

The geology, geochronology, structure and geochemistry of the
Wild Rogue Wilderness remnant of the Coast Range ophiolite, southwest Oregon:
implications for the magmatic and tectonic evolution of the Coast Range ophiolite

by

Stefan B. Kosanke

A Dissertation

Submitted to the University at Albany, State University of New York
in Partial Fulfillment of
the Requirements for the Degree of
Doctor of Philosophy

College of Arts & Sciences

Department of Earth and Atmospheric Sciences

2000

ABSTRACT

The Wild Rogue Wilderness ophiolite (WRWO) has been correlated with the Coast Range ophiolite (CRO) and overlying Great Valley Sequence in California. The WRWO occurs on the east limb of a large Cretaceous syncline within a folded thrust sheet. The basement units strike NE, are subvertical and fault bounded and include from east to west: (1) a sheeted dike complex having gabbro screens; (2) a ductily, but heterogeneously deformed metatonalite containing abundant mylonites; (3) a heterogeneously deformed metagabbro having a relic magmatic foliation overprinted by solid-state deformation at amphibolite facies and lower grade conditions; (4) a 0.5 - 0.9 km wide, high-strain zone consisting of mafic and silicic ultramylonites and mylonites; (5) undeformed pillow basalts cut by mafic and silicic dikes; (6) quartz gabbro to tonalite (Half Moon Bar diorite), (7) poorly exposed metavolcanic rocks, including at least some volcanoclastics in the uppermost section of this unit.

The following events have been identified in the Wild Rogue Wilderness: (1) pre-ophiolite deformation and (regional?) amphibolite facies metamorphism (unit 3; ~171 Ma); (2) formation of the ophiolite, related normal faulting and subseafloor hydrothermal alteration (units 1, 2, and 5; ~164 Ma); (3) Post-ophiolite arc-related magmatism (units 6 and 7; 153-160 Ma); and (4) Nevadan-age ductile deformation (unit 4 and mylonites in units 2 and 3; ~149 Ma).

The trace-element analysis indicates that the WRWO consists of rocks having magmatic affinities to normal mid-ocean ridge basalt, island-arc tholeiite, calc-alkaline basalt and boninite. Compositional variations within units and between units cannot be explained with differences in the degree of partial melting and/or fractionation. A highly heterogeneous source is inferred, which was probably variably depleted by previous melting and variably re-enriched with a subduction component.

The evolution of the WRWO is similar to that of the CRO and the Josephine ophiolite, which is consistent with previously proposed models that invoke rifting of the volcanic arc built on western N. America. The geochemical diversity of the WRWO is indicative of formation in a fore-arc or intra-arc setting similar to that of the Miocene Tonga arc, SW Pacific. Rift-propagation and melting of heterogeneous, inherited mantle may have played an important role in the magmatic evolution of the WRWO.

ACKNOWLEDGMENTS

A great deal of thanks and gratitude go to my advisor, Dr. Gregory D. Harper for his guidance, support, and encouragement. Dr. Harper provided me with a very exciting project in which we both shared great interest. Additional thanks go to my thesis committee members. Their insightful comments and helpful suggestions greatly improved the quality of this work. Also, this work benefited greatly from many productive discussions with Charles Knaack and Richard Conrey at Washington State University regarding the precision and accuracy of trace element analysis by ICP-MS. The trace element analysis was conducted at the Union College Geology Department under the direction of Kurt Hollocher. I thank Kurt Hollocher for sharing his expertise. Thanks go to Matt Heizler and Jason Saleeby, who provided the isotopic ages for this study. Also, I like to thank my fellow students Steffi Dannenmann, Angela Coulton, Mike Edwards, Bruno Ciscato, Nick Hayman and Young Do Park for helpful discussions. I am particularly indebted to my wife, Tobi, for her frequent assistance and unceasing support.

Financial support for this project, including field work, ICP-MS analysis and electron microprobe analysis was provided through Student Research Grants from the Geological Society of America, Sigma Xi Grant in-Aid of Research, SUNY Albany Benevolent Foundation, and the Gregg Ranch Foundation. I thank these organizations for their support.

I would like to thank the caretakers of the Rogue River Ranch, Laura and Loren Rush. Without their generosity and help, I would not have had such pleasant and memorable field seasons in the Wild Rogue Wilderness. Additional thanks go to Michael Haschke for assistance in the first field season and to Sean Oakley, the forest warden, for keeping an eye on my safe return from bushwhacks and backpack excursions. Finally, I wish to thank my parents. Without their continuous support and encouragement, I would not have come this far.

TABLE OF CONTENT

CHAPTER ONE

| | |
|--------------------|---|
| INTRODUCTION | 1 |
|--------------------|---|

CHAPTER TWO

| | |
|---------------------------------------------------------------------------------------------------------------------------------|-----------|
| GEOLOGY, PETROGRAPHY AND GEOCHRONOLOGY OF THE ROGUE WILDERNESS REMNANT OF THE COAST RANGE OPHIOLITE, SW OREGON | 19 |
| 2.1 INTRODUCTION | 19 |
| 2.2 GEOGRAPHIC SETTING AND PREVIOUS WORK | 20 |
| 2.3 THE ROGUE WILDERNESS REMNANT OF THE COAST RANGE OPHIOLITE | 24 |
| 2.4 SERPENTINITES | 33 |
| 2.5 METAGABBRO UNIT | 33 |
| 2.5.1 Lithology | 33 |
| 2.5.2 Structure and metamorphism | 34 |
| 2.5.3 Evidence for ductile deformation in the metagabbro unit | 40 |
| 2.5.4 Interpretation of metamorphic hornblende and age constraints | 49 |
| 2.5.5 Hornblende quartz diorite in metagabbro unit | 51 |
| 2.5.6 Contact between metagabbro unit and metatonalite unit | 52 |
| 2.6 METATONALITE UNIT | 55 |
| 2.6.1 Lithology | 55 |
| 2.6.2 Evidence for magma mingling | 60 |
| 2.6.3 Mylonites | 61 |
| 2.6.4 Metatonalite unit compared to oceanic plagiogranites | 69 |
| 2.6.5 Contact with the sheeted dike complex | 70 |
| 2.6.6 Age constraints | 72 |
| 2.7 SHEETED DIKE COMPLEX | 72 |
| 2.7.1 Gabbroic screens | 76 |

| | |
|-----------------------------------------------------------------|-----|
| 2.7.2 Sheeted Dikes | 82 |
| 2.7.3 Cross cutting relationships | 89 |
| 2.7.4 Hydrothermal metamorphism of sheeted dikes | 90 |
| 2.7.5 Age constraints | 93 |
| 2.8 PILLOW UNIT | 93 |
| 2.8.1 Pillowed submarine flows | 94 |
| 2.8.2 Dikes | 99 |
| 2.8.3 Structure | 102 |
| 2.8.4 Age constraints | 103 |
| 2.9. MULE MOUNTAIN VOLCANICS | 104 |
| 2.9.1 Volcanic breccia | 106 |
| 2.9.2 Basalt and basaltic andesite flows | 108 |
| 2.9.3 Andesites and dacites | 110 |
| 2.9.4 Mudstones and sandstones | 113 |
| 2.9.5 Hydrothermal metamorphism | 115 |
| 2.9.6 Age constraints | 116 |
| 2.10 POST-OPHIOLITE INTRUSIONS | 117 |
| 2.10.1 Muscovite garnet tonalite dikes in metagabbro unit | 117 |
| 2.10.2 Half Moon Bar Diorite | 121 |
| 2.11. BLOSSOM BAR SHEAR ZONE | 127 |
| 2.11.1 Lithology and fabric | 127 |
| 2.11.2 Age constraints | 137 |
| 2.12 MYRTLE GROUP | 137 |

CHAPTER THREE

| | |
|-----------------------------------------------------------------------------------------------------------------------------------------------------------------------------------------------------------------------------------------------------------------------------------|------------|
| APPLICATION OF HOLLAND AND BLUNDY'S (1994) AMPHIBOLE-PLAGIOCLASE GEOTHERMOMETER: CONSTRAINTS AND IMPLICATIONS FOR THE INTERPRETATION OF THE THERMAL HISTORY OF THE HALF MOON BAR DIORITE AND THE METAGABBRO UNIT IN THE WILD ROGUE WILDERNESS, SW OREGON | 140 |
|-----------------------------------------------------------------------------------------------------------------------------------------------------------------------------------------------------------------------------------------------------------------------------------|------------|

| | |
|------------------------|-----|
| 3.1 INTRODUCTION | 140 |
|------------------------|-----|

| | |
|----------------------------------------------------------------------------------|-----|
| 3.2 METHOD | 143 |
| 3.2.1 Selection and analysis of coexisting plagioclase-hornblende pairs | 143 |
| 3.2.2 The amphibole-plagioclase geothermometer | 146 |
| 3.2.3 Restrictions for the use of the amphibole-plagioclase thermometers | 147 |
| 3.2.4 Recalculation of amphibole analyses | 148 |
| 3.2.5 Classification of amphiboles | 149 |
| 3.2.6 Calculation of temperatures | 152 |
| 3.2.7 Uncertainties | 160 |
| 3.3 PRESSURE ESTIMATES | 160 |
| 3.3.1 Estimate of pressure of crystallization using geological constraints | 160 |
| 3.3.2 Aluminum-in-hornblende barometers | 162 |
| 3.4 DISCUSSION | 165 |
| 3.4.1 Half Moon Bar diorite | 165 |
| 3.4.2 Hornblende quartz diorite in metagabbro unit | 170 |
| 3.4.3 Metagabbro unit | 173 |
| 3.5 SUMMARY | 178 |

CHAPTER FOUR

| | |
|-----------------------------------------------------------------------------------------------------------------------|------------|
| STRUCTURAL AND METAMORPHIC HISTORY OF THE WILD ROGUE WILDERNESS REMNANT OF THE COAST RANGE OPHIOLITE | 181 |
| 4.1 INTRODUCTION | 181 |
| 4.2 PALEOSTRESS ANALYSIS | 188 |
| 4.3 POST-OPHIOLITE SEDIMENTARY ROCKS AND STRUCTURES | 190 |
| 4.3.1 Eocene cover | 190 |
| 4.3.2 Post-Mid-Eocene faults | 193 |
| 4.3.3 Franciscan Complex | 200 |
| 4.3.3.1 Yolla Bolly terrane | 200 |
| 4.3.3.2 Sixes River Terrane | 204 |
| 4.3.4 Myrtle Group | 205 |
| 4.3.4.1 Riddle Formation | 205 |

| | |
|--------------------------------------------------------------------------------------------------------------|-----|
| 4.3.4.2 Days Creek Formation | 206 |
| 4.4 ORIENTATION OF PLANAR FEATURES IN THE PILLOW UNIT AND MULE MOUNTAIN VOLCANICS | 207 |
| 4.5 POSSIBLE RE-ORIENTATION OF THE OPHIOLITE TO PALEOHORIZONTAL | 211 |
| 4.6 STRUCTURE OF THE SHEETED DIKE COMPLEX | 212 |
| 4.6.1 Diabasic and microdioritic dikes | 212 |
| 4.6.2 Igneous layering | 220 |
| 4.6.3 Amphibole shear bands and amphibole veins | 221 |
| 4.6.4 Cemented faults | 225 |
| 4.6.4.1 Domains A and B | 227 |
| 4.6.4.2 Domain D | 231 |
| 4.6.4.3 Discussion of the fault geometry | 235 |
| 4.7 DUCTILE TO BRITTLE DEFORMATION IN THE BLOSSOM BAR SHEAR ZONE, METATONALITE AND METAGABBRO UNITS | 236 |
| 4.7.1 Sense of shear criteria | 236 |
| 4.7.2 Deformation in the metagabbro unit | 246 |
| 4.7.2.1 Magmatic foliation | 246 |
| 4.7.2.2 Shear foliation and sense of shear | 248 |
| 4.7.2.3 Brittle deformation and crosscutting relationships | 250 |
| 4.7.2.4 Estimate of temperature of solid-state deformation | 251 |
| 4.7.2.5 Transition from magmatic flow to solid-state deformation? | 254 |
| 4.7.3 Deformation in the metatonalite unit | 256 |
| 4.7.3.1 Shear foliation and sense of shear | 257 |
| 4.7.3.2 Brittle deformation and crosscutting relationships | 260 |
| 4.7.4 Blossom Bar shear zone | 265 |
| 4.7.4.1 Shear foliation and sense of shear | 265 |
| 4.7.4.2 Brittle deformation and crosscutting relationships | 266 |
| 4.7.5 Estimates of the temperatures of deformation in the metatonalite unit and Blossom Bar shear zone | 266 |
| 4.7.6 Deformation of late intrusions in the metagabbro unit | 269 |
| 4.7.6.1 Shear foliation and sense of shear | 269 |
| 4.7.6.2 Brittle deformation and crosscutting relationships | 270 |
| 4.7.7 Summary | 270 |
| 4.7.8 Using the results of the structural study | 271 |

| | |
|-------------------------------------------------------------------------------------------|-----|
| 4.7.8.1 Occurred ductile deformation and brittle faulting in the same stress field? | 271 |
| 4.7.8.2 Determination of the stress tensor for ductile deformation | 275 |
| 4.8 DISCUSSION | 279 |
| 4.8.1 Possible pre-ophiolite deformation and metamorphism | 279 |
| 4.8.2 Formation of the ophiolite, related deformation and hydrothermal alteration | 282 |
| 4.8.2.1 Direction of seafloor spreading and early normal faulting | 284 |
| 4.8.2.2 The fault geometry in the sheeted dike complex | 289 |
| 4.8.2.3 Possible near ridge-axis rotation of sheeted dikes | 294 |
| 4.8.2.4 Summary of oceanic deformation of ophiolite | 298 |
| 4.8.3 Post-ophiolite structural history | 299 |
| 4.8.3.1 Late magmatism and hydrothermal alteration | 299 |
| 4.8.3.2 Post-ophiolite ductile deformation | 300 |
| 4.9 SUMMARY AND CONCLUSION | 306 |

CHAPTER FIVE

| | |
|------------------------------------------------------------------------------------------------------------|------------|
| THE GEOCHEMISTRY OF THE WILD ROGUE WILDERNESS REMNANT OF THE COAST RANGE OPHIOLITE, SW OREGON | 308 |
| 5.1 INTRODUCTION | 308 |
| 5.2 ANALYTICAL METHODS | 311 |
| 5.3 ELEMENT MOBILITY | 313 |
| 5.4 INTERPRETATION OF CHONDRITE- AND N-MORB NORMALIZED TRACE ELEMENT PATTERNS | 315 |
| 5.5 GEOCHEMISTRY OF IGNEOUS ROCKS FROM THE OPHIOLITE UNITS | 322 |
| 5.5.1 Metagabbro unit | 322 |
| 5.5.1.1 Rock classification | 322 |
| 5.5.1.2 Magmatic affinities | 325 |
| 5.5.1.3 Petrogenesis | 332 |
| 5.5.1.3a Crystal Fractionation | 332 |
| 5.5.1.3b Partial melting | 338 |
| 5.5.2 Hornblende quartz diorite in the metagabbro unit | 339 |
| 5.5.2.1 Rock classification | 339 |
| 5.5.2.2 Magmatic affinities | 343 |
| 5.5.3 Metatonalite unit | 343 |

| | |
|-----------------------------------------------------------------------------------------|-----|
| 5.5.3.1 Rock classification | 343 |
| 5.5.3.2 Magmatic affinities | 344 |
| 5.5.3.3 Petrogenesis | 351 |
| 5.5.3.3a Possible origin of the metatonalite unit | 351 |
| 5.5.3.3b Crystal fractionation models | 353 |
| 5.5.3.3c Magma mixing | 361 |
| 5.5.4 Sheeted dike complex | 364 |
| 5.5.4.1 Rock classification | 364 |
| 5.5.4.1a Gabbroic screens | 364 |
| 5.5.4.1b Sheeted dikes | 370 |
| 5.5.4.2 Magmatic affinities | 377 |
| 5.5.4.2a Gabbroic screens | 377 |
| 5.5.4.2b Dikes of geochemical group 1 | 381 |
| 5.5.4.2c Dikes of geochemical group 2 | 387 |
| 5.5.4.3 Chromian Spinel in dikes of geochemical group 2 | 390 |
| 5.5.4.4 Element mobility | 392 |
| 5.5.4.5 Petrogenesis | 394 |
| 5.5.4.5a Crystal Fractionation | 394 |
| 5.5.4.5b Source heterogeneity and magma mixing | 397 |
| 5.5.5 Pillow unit | 400 |
| 5.5.5.1 Rock classification | 400 |
| 5.5.5.2 Magmatic affinities | 403 |
| 5.5.5.3 Chromian Spinel in a pillow sample | 410 |
| 5.5.5.4 Element mobility | 412 |
| 5.5.5.5 Petrogenesis | 413 |
| 5.5.5.5a Crystal Fractionation | 413 |
| 5.5.5.5b Mantle heterogeneity and magma mixing | 413 |
| 5.5.6 Comparison of ophiolite units | 416 |
| 5.5.6.1 Metagabbro unit | 418 |
| 5.5.6.2 Calc-alkaline samples from the metatonalite unit and sheeted dike complex | 419 |
| 5.5.6.3 Tholeiitic samples from the sheeted dike complex and pillow unit | 423 |
| 5.5.6.4 High Ca-boninitic component in sheeted dike complex and pillow unit | 424 |
| 5.5.7 Geochemical diversity in modern tectonic settings | 424 |
| 5.6 GEOCHEMISTRY OF THE MULE MOUNTAIN VOLCANICS | 427 |
| 5.6.1 Rock classification | 427 |
| 5.6.2 Magmatic affinities | 431 |
| 5.6.3 Chromian spinel in a sample from the Mule Mountain volcanics | 440 |
| 5.6.4 Element mobility | 442 |

| | |
|--------------------------------------------------------------------|-----|
| 5.6.5 Petrogenesis | 443 |
| 5.6.5.1 Crystal fractionation | 443 |
| 5.6.5.2 Mantle heterogeneity and magma mixing | 448 |
| 5.7 POST OPHIOLITE INTRUSIVE ROCKS | 448 |
| 5.7.1 Half Moon Bar Diorite | 449 |
| 5.7.1.1 Rock classification | 449 |
| 5.7.1.2 Magmatic affinities | 452 |
| 5.7.1.3 Fractionation | 457 |
| 5.7.2 Muscovite garnet tonalite dikes in the metagabbro unit | 458 |
| 5.7.2.1 Rock classification | 458 |
| 5.7.2.2 Magmatic affinities | 460 |
| 5.7.2.3 Fractionation | 463 |
| 5.8 THE ZR/Y VS. ZR DISCRIMINATION DIAGRAM | 464 |
| 5.8.1 Ophiolite units | 465 |
| 5.8.2 Mule Mountain volcanics | 465 |
| 5.9 SUMMARY | 468 |
| 5.9.1 Metagabbro unit | 468 |
| 5.9.2 Metatonalite unit | 469 |
| 5.9.3 Sheeted dike complex | 469 |
| 5.9.4 Pillow unit | 470 |
| 5.9.5 Mule Mountain volcanics | 472 |
| 5.9.6 Post-ophiolite intrusions | 473 |

CHAPTER SIX

| | |
|--------------------------------------------------------------------------------------------------------------------------------------------------------------------------------------------------------------------------------------------|------------|
| RELATIONS OF THE WILD ROGUE WILDERNESS OPHIOLITE WITH THE COAST RANGE OPHIOLITE AND JOSEPHINE OPHIOLITE: IMPLICATIONS FOR THE TECTONIC AND MAGMATIC EVOLUTION OF MID- TO LATE-JURASSIC OPHIOLITES IN CALIFORNIA AND SW OREGON | 474 |
| 6.1 INTRODUCTION | 474 |
| 6.2 POSSIBLE CORRELATION OF THE WILD ROGUE WILDERNESS OPHIOLITE WITH TWO BELTS OF LATE-JURASSIC OPHIOLITES | 476 |
| 6.2.1 Eastern belt of ophiolites | 481 |
| 6.2.2 Western belt of ophiolites | 483 |

| | |
|----------------------------------------------------------------------------------------------|------------|
| 6.2.3 The Wild Rogue Wilderness ophiolite: a bridging link | 485 |
| 6.3 GEOCHEMISTRY OF THE COAST RANGE OPHIOLITE AND JOSEPHINE OPHIOLITE . | 489 |
| 6.3.1 The Coast Range ophiolite remnant at Llanada, California | 489 |
| 6.3.2 The Coast Range ophiolite remnant at Black Mountain, California | 491 |
| 6.3.3 The Coast Range ophiolite remnant at Point Sal, California | 492 |
| 6.3.4 The Stonyford volcanic complex | 494 |
| 6.3.5 The Coast Range ophiolite remnant at Snow Camp Mountain, SW Oregon | 499 |
| 6.3.6 The Josephine ophiolite, northern California SW Oregon | 501 |
| 6.3.7 Summary | 505 |
| 6.4 MODELS FOR THE TECTONIC AND MAGMATIC EVOLUTION OF THE COAST RANGE OPHIOLITE | 506 |
| 6.4.1 Subduction initiation and the multi-stage evolution of the Coast Range ophiolite | 507 |
| 6.4.1.1 The geochemical evolution of the Coast Range ophiolite, California | 507 |
| 6.4.1.2 The geochemical evolution of the Wild Rogue Wilderness ophiolite, SW Oregon ... | 510 |
| 6.4.1.2a Island-arc tholeiites | 510 |
| 6.4.1.2b Boninites | 511 |
| 6.4.1.2c Calc alkaline rocks | 512 |
| 6.4.1.2d Mid ocean ridge basalts | 515 |
| 6.4.1.3 Discussion of the magmatic evolution of the Wild Rogue Wilderness ophiolite | 515 |
| 6.4.2 The Lau basin as a modern analogue for the Coast Range ophiolite | 517 |
| 6.4.2.1 The tectonic evolution of the Tonga-Lau arc/back-arc basin system | 518 |
| 6.4.2.2 The geochemical evolution of the Tonga-Lau arc/back-arc basin system | 519 |
| 6.4.2.3 Formation of the Wild Rogue Wilderness ophiolite by fore-arc rifting | 529 |
| 6.4.3 Discussion | 531 |
| CHAPTER SEVEN | |
| SUMMARY | 534 |
| APPENDIX A | |
| PETROGRAPHIC SUMMARY OF SAMPLES FROM THE WILD ROGUE WILDERNESS, SW OREGON | 543 |

APPENDIX B

AGE SPECTRA, K/CA AND RADIOGENIC YIELD DIAGRAMS FOR THE DATED HORNBLENDES AND MUSCOVITES561

APPENDIX C

COMPOSITION OF CLINOPYROXENE, PLAGIOCLASE AND CR-SPINEL IN SAMPLES FROM THE WILD ROGUE WILDERNESS, SW OREGON (ELECTRON MICROPROBE ANALYSIS)566

APPENDIX D

FAULT SLIP DATA AND SENSE OF SHEAR DETERMINED IN FOLIATED AND MYLONITIC ROCKS FROM THE WILD ROGUE WILDERNESS, SW OREGON581

APPENDIX E

QUALITY CHECK OF THE TRACE ELEMENT ANALYSIS BY INDUCTIVELY COUPLED PLASMA MASS SPECTROMETRY (ICP-MS) AT THE UNION COLLEGE GEOLOGY DEPARTMENT, SCHENECTADY, NY598

E.1 INTRODUCTION598

E.2 SAMPLE PREPARATION599

 E.2.1 Internal standards599

 E.2.2 Acid digestion procedure599

 E.2. 1.1 Weighing and dissolution procedure600

 E.2.1.2 Dilution procedure604

E.3 ICP-MS INSTRUMENT OPERATION604

 E.3.1 Instrumentation604

 E.3.2 Drift606

 E.3.3 Interference606

E.4 CALIBRATION607

 E.4.1 Sequence of analysis607

 E.4.2 Standards607

 E.4.3 Blanks611

E.5 CALCULATION OF CONCENTRATIONS612

| | |
|--------------------------------------------------------------------------------|-----|
| E.6 EVALUATION OF DATA | 613 |
| E.6.1 Determination of detection limits | 613 |
| E.6.2 Determination of precision | 614 |
| E.6.3 Determination of accuracy | 615 |
| E.6.3.1 Comparison with standards | 615 |
| E.6.3.2 Inter-laboratory comparison | 617 |
| E.7 TEST RUNS | 617 |
| E.7.1 First test run, 06/12/1995, synthetic standard used | 617 |
| E.7.1.1 Strategy and methods | 617 |
| E.7.1.2 Limits of detection | 619 |
| E.7.1.3 Precision | 619 |
| E.7.1.4 Accuracy | 623 |
| E.7.1.5 Inter-laboratory comparison | 623 |
| E.7.1.6 Problems with Ta and Nb | 628 |
| E. 7.1.7 Evaluation of dissolution | 630 |
| E.7.2 Second test run, 11/17/95, NIST-278 and NTST-688 used as standards | 631 |
| E.7.2.1 Strategy and methods | 631 |
| E.7.2.2 Limits of detection | 632 |
| E.7.2.3 Precision | 632 |
| E.7.2.4 Accuracy | 635 |
| E.7.2.5 Inter-laboratory comparison | 635 |
| E.7.2.6 Problems with Ta and Nb | 639 |
| E.8 ANALYTICAL RUNS | 640 |
| E.8.1 Introduction | 640 |
| E.8.2 First analytical run, 02/23/96 | 642 |
| E.8.2.1 Limits of detection | 642 |
| E.8.2.2 Precision | 642 |
| E.8.2.3 Accuracy | 642 |
| E.8.2.4 Resolution of problem with Ta and Nb | 647 |
| E.8.3 Second analytical run, 08/19/96 | 648 |
| E.8.3.1 Limits of detection | 648 |
| E.8.3.2 Precision..... | 648 |
| E.8.3.3 Accuracy | 648 |
| E.8.3.4 Evaluation of dissolution | 653 |

| | |
|------------------------------------------------------------------------------------------------------------------------------------------------------------------------------------------|------------|
| E.8.4 Third analytical run, 09/10/97 | 654 |
| E.8.4.2 Limits of detection | 654 |
| E.8.4.3 Precision | 655 |
| E.8.4.4 Accuracy | 655 |
| E.8.5 Fourth analytical run, 09/19/97 | 660 |
| E.8.5.1 Limits of detection | 660 |
| E.8.5.2 Precision | 660 |
| E.8.5.3 Accuracy | 665 |
| E.8.5.4 Selection of data | 665 |
| E.9 COMMENTS ON USE OF ICP-MS AT UNION COLLEGE AND CONCLUSIONS | 665 |
| E.10 SUPPLEMENT: EVALUATION OF THE FIFTH ANALYTICAL RUN; ANALYSIS OF SAMPLES FROM THE COAST RANGE OPHIOLITE REMNANTS AT LLANADA AND BLACK MOUNTAIN | 668 |
| E.10.1 Introduction | 668 |
| E.10.2 Fifth analytical run, 11/11/97 | 677 |
| E.10.2.1 Limits of detection | 677 |
| E.10.2.2 Precision | 677 |
| E.10.2.3 Accuracy | 677 |
| E.10.2.4 Varying performance of the ICP-MS instrument or incomplete dissolution? | 682 |
| E.10.3 Comparison with XRF and INAA data | 683 |
| E.10.3.1 Comparison with XRF data | 683 |
| E.10.3.2 Comparison with INAA data | 683 |
| E.10.4. Summary | 684 |
| APPENDIX F | |
| ANALYTICAL DATA OBTAINED BY ICP-MS AT THE UNION COLLEGE GEOLOGY DEPARTMENT, SCHENECTADY, NY (WILD ROGUE WILDERNESS, SNOW CAMP MOUNTAIN, BLACK MOUNTAIN AND LLANADA) | 689 |
| REFERENCES | 713 |

LIST OF FIGURES

Chapter 1

| | |
|---------------------------------------------------------------------------------------------------------|----|
| 1.1 Generalized geologic map of central and northern California and SW Oregon | 3 |
| 1.2 Simplified geological map of SW Oregon | 5 |
| 1.3 Tectonostratigraphic diagram comparing CRO and Josephine ophiolite | 7 |
| 1.4 Model postulating a mid ocean ridge origin for the Coast Range ophiolite | 9 |
| 1.5 Model postulating the CRO formed in an exotic island arc terrane | 11 |
| 1.6 CRO and Josephine ophiolite formed by rifting of the volcanic arc built on western N. America | 13 |
| 1.7 Model postulating the CRO formed during the initiation of subduction (infant arc crust) | 15 |
| 1.8 Model of Cretaceous continental margin of western North America | 17 |

Chapter 2

| | |
|--------------------------------------------------------------------------------------------------|----|
| 2.1a Simplified geologic map of SW Oregon | 22 |
| 2.1b Interpretative cross section through Snow Camp Mountain terrane | 23 |
| 2.2a Simplified geologic map of the Wild Rogue Wilderness | 27 |
| 2.2b Geological cross sections through Wild Rogue Wilderness along lines BB' and CC' | 28 |
| 2.3 Schematic reconstruction of the ophiolite | 31 |
| 2.4 Photograph of typical medium grained gabbro of the metagabbro unit | 36 |
| 2.5 Close up photograph of outcrop in metagabbro unit | 37 |
| 2.6 Photograph of compositionally layered metagabbro | 38 |
| 2.7 Photograph showing the relationship between three different phases of gabbro | 39 |
| 2.8 Photomicrograph of fine grained mafic dike in metagabbro | 42 |
| 2.9 Photomicrograph of plagioclase in weakly foliated mafic dike in metagabbro | 43 |
| 2.10 Photograph of slabbed and polished sample from a mylonite zone in the metagabbro unit | 44 |
| 2.11 Photomicrograph of typical mylonitic metagabbro | 45 |
| 2.12a Photomicrograph showing typical plagioclase porphyroclasts in the metagabbro unit | 46 |

| | |
|----------------------------------------------------------------------------------------------------------|----|
| 2.12b Photomicrograph showing typical augen-shaped hornblende porphyroclast in the metagabbro unit | 46 |
| 2.13 Photomicrograph showing a shear band cut by an epidote vein (metagabbro unit) | 47 |
| 2.14 Photograph of slabbed and polished metagabbro protomylonite | 53 |
| 2.15 Photograph of prominent brittle fault with shear zone exposed at mile 46 at the Rogue River | 54 |
| 2.16 Photograph of metatonalite and dioritic enclaves in the metatonalite unit | 57 |
| 2.17 Photograph of metatonalite containing two globular fine-grained dioritic enclaves | 58 |
| 2.18 Photomicrograph of granophyric texture in metatonalite | 59 |
| 2.19 Photograph of a zone of strongly foliated rock within the metatonalite unit | 63 |
| 2.20 Photomicrograph showing fabric of typical mylonite (type 1) in the metatonalite unit | 64 |
| 2.21 Photomicrograph showing fabric of typical mylonite (type 2) in the metatonalite unit | 65 |
| 2.22 Photomicrograph of porphyroclast of albite in matrix of recrystallized quartz (metatonalite) | 66 |
| 2.23 Photomicrograph of large, relic quartz grain in a monomineralic layer of quartz (metatonalite) | 67 |
| 2.24 Photograph of fault contact between the metatonalite unit and the sheeted dike complex | 71 |
| 2.25 Outcrop map of sheeted dikes in the Rogue River canyon near Stair Creek Falls | 74 |
| 2.26 Photograph of layered cumulate gabbro screen in the sheeted dike complex | 77 |
| 2.27 Photograph of layered cumulate gabbro in sheeted dike complex near the Coffee Pot | 78 |
| 2.28 Traced thin section showing relict igneous texture of cumulate gabbro | 79 |
| 2.29 Photograph of polished hand sample showing a narrow shear band in cumulate gabbro | 80 |
| 2.30 Photograph of a quartz-bearing dike of group two intruding a gabbroic host rock | 84 |
| 2.31 Photomicrograph showing texture typical of aphyric diabasic dikes (sheeted dike complex) | 86 |
| 2.32 Slabbed and polished sample of a microdioritic dike containing olivine xenocrysts | 87 |
| 2.33 Photomicrograph showing translucent brown Cr-spinel in partially resorbed olivine xenocryst | 88 |
| 2.34 Photograph of an exposed fault surface with patches of pistachio green ep+qtz mineralization | 91 |
| 2.35 Photograph of one of several faults across which an abrupt change in dike orientations was observed | 92 |
| 2.36 Photograph of water polished outcrop of pillows | 96 |
| 2.37 Photograph of pillow exposed in Huggins Canyon | 97 |
| 2.38 Photomicrograph of center of pillow showing typical intergranular texture | 98 |

| | |
|------------------------------------------------------------------------------------------------------|-----|
| 2.39 Photomicrograph of granophyric texture in dikes intruding pillows | 100 |
| 2.40 Photograph of leucocratic dike in the pillow unit near Brushy Bar | 101 |
| 2.41 Photograph of hand sample of typical breccia in the Mule Mountain volcanics | 107 |
| 2.42 Photomicrograph of the intergranular texture of the basalt sample O/C-81a (Mule Mountain) | 109 |
| 2.43 Photomicrograph of the trachytic texture of an aphyric andesite (Mule Mountain volcanics) | 111 |
| 2.44 Photomicrograph of plagioclase phenocryst in dacite (Mule Mountain volcanics) | 112 |
| 2.45 Photograph of sedimentary rocks in the uppermost Mule Mountain volcanics | 114 |
| 2.46 Photograph showing outcrop of late tonalitic dikes in the metagabbro unit | 118 |
| 2.47 Photomicrograph showing the texture of a foliated tonalite dike (metagabbro unit) | 119 |
| 2.48 Polished sample of muscovite-garnet tonalite dike having S/C-type fabric | 120 |
| 2.49 Photograph of a net-vein breccia about 200 m west of the fault exposed at Brushy Bar | 123 |
| 2.50 Photograph of medium-grained Half Moon Bar diorite intruded by a porphyritic dike | 124 |
| 2.51 Photomicrograph of amphibole in sample O/C-377 from the HMB diorite | 125 |
| 2.52 Photograph of S/C-type mylonite from the Blossom Bar shear zone | 129 |
| 2.53 Photograph of mylonite and ultramylonite (Blossom Bar shear zone) | 130 |
| 2.54 Photograph of a strongly foliated, mafic rock (Blossom Bar shear zone) | 132 |
| 2.55 Photograph of a strongly foliated chlorite schist (Blossom Bar shear zone) | 133 |
| 2.56 Photograph of an undeformed and a foliated volcanic breccia (Blossom Bar shear zone) | 135 |
| 2.57 Photograph of hand sample of 1.5 m wide epidote+actinolite zone (Blossom Bar shear zone) | 136 |

Chapter 3

| | |
|-----------------------------------------------------------------------------------------------------------|-----|
| 3.1 Columnar section, showing reconstruction of ophiolite | 142 |
| 3.2 Photomicrograph of HMB diorite showing typical, strongly zoned plagioclase | 145 |
| 3.3 Classification of amphiboles using electron microprobe data | 151 |
| 3.4 Diagram illustrating P-T conditions of equilibration of hornblende-plagioclase pairs (HMB diorite) .. | 167 |
| 3.5 Temperature variations versus Mg-# in samples O/C-118a and O/C-376 (HMB diorite) | 168 |
| 3.6 Diagram illustrating P-T conditions of equilibration of hornblende-plagioclase pairs (O/C-229) | 171 |

| | |
|----------------------------------------------------------------------------------------------------|-----|
| 3.7 Temperature variations versus Mg-# in sample O/C-229 (hbl qtz gabbro in metagabbro unit) | 172 |
| 3.8 Diagram illustrating P-T conditions of equilibration of hbl-plag pairs (metagabbro unit) | 176 |
| 3.9 Temperature variations versus Mg-# in samples from the metagabbro unit | 177 |

Chapter 4

| | |
|---------------------------------------------------------------------------------------------------------------------------|-----|
| 4.1a Simplified geologic map of SW Oregon | 184 |
| 4.1b Interpretative cross section along line AA' in figure 4.1a | 185 |
| 4.2 Stratigraphic nomenclature in the Tyee Basin after Baldwin (1974) | 192 |
| 4.3 Stereographic projections of faults after the method of Hoepfner (1955) | 196 |
| 4.4 Stereographic projections of post-Eocene faults and results of paleostress analysis | 198 |
| 4.5 Stereographic projections of structural data from the Dothan Formation | 203 |
| 4.6 Stereographic projections of poles to planar features (pillow unit and Mule Mountain volcanics) | 209 |
| 4.7 Geologic map showing structural domains A through F in the sheeted dike complex | 215 |
| 4.8 Stereographic projection of pole to mean dike orientations for domains A through F | 217 |
| 4.9 Stereographic projections of poles to dikes after correcting for Tertiary and Cretaceous folding | 218 |
| 4.10 Results of the paleostress analysis of structural data from domains A and B | 224 |
| 4.11 Results of the paleostress analysis of structural data from domains A and B (continued) | 229 |
| 4.12 Results of the paleostress analysis of structural data from domain D | 233 |
| 4.13 Summary of the criteria used to infer the sense-of-shear in mylonitic rocks | 239 |
| 4.14a Photomicrograph of fabric in a mafic mylonite from the metagabbro unit (O/C-374b.4) | 243 |
| 4.14b Photomicrograph of a C/C'-type fabric in a chlorite-rich mylonite from the metatonalite unit | 243 |
| 4.14c Photomicrograph of plagioclase porphyroclast having a low-angle, synthetic microfault | 244 |
| 4.14d Photomicrograph of plagioclase porphyroclast having two high-angle, antithetic microfaults | 244 |
| 4.14e Photomicrograph of mylonite consisting of alternate layers of quartz and epidote \pm chlorite | 245 |
| 4.15 Stereographic projections of foliations and lineations in samples from the Wild Rogue Wilderness. 259 | |
| 4.16 Results of paleostress analysis of cemented faults in the metatonalite unit | 263 |
| 4.17 Determination of the shear stress τ on C_1 and C_{sz} for different stress fields (after Means, 1989) | 274 |

| | |
|--------------------------------------------------------------------------------------------------------|-----|
| 4.18 Determination of stress tensor (shearing in Blossom Bar shear zone and metatonalite unit) | 278 |
| 4.19 Summary and interpretation of isotopic ages in the Rogue Wilderness remnant of the CRO | 280 |
| 4.20 Stereographic projections of structural data (domains A and B) after correcting for folding | 287 |
| 4.21 Model for fault block rotation in the sheeted dike complex | 288 |
| 4.22 Analysis of unfolded structural data of domains A, B and D | 292 |
| 4.23 Model of the spreading and fault geometry of the Troodos ophiolite | 297 |
| 4.24 Stereographic projections of foliations and lineations after correcting for folding | 304 |
| 4.25 Cartoons depicting the directions of spreading (~164 Ma) and thrusting (~150 Ma) | 305 |

Chapter 5

| | |
|---------------------------------------------------------------------------------------------------------------------|-----|
| 5.1 Simplified geologic map of the Wild Rogue Wilderness and sample localities | 310 |
| 5.2 Chondrite and N-MORB normalized REE and trace element patterns (reference samples) | 318 |
| 5.3 Chondrite and N-MORB normalized REE and trace element patterns (metagabbro unit) | 327 |
| 5.4 Cr vs. Y tectonic discrimination diagram (metagabbro unit) | 330 |
| 5.5 Hf/3-Th-Ta tectonic discrimination diagram (metagabbro unit) | 331 |
| 5.6 MgO variation diagrams of samples from the metagabbro unit | 336 |
| 5.7 Chondrite and N-MORB normalized REE and trace element patterns (hbl Qtz diorite in metagabbro) ... | 342 |
| 5.8 Chondrite and N-MORB normalized REE and trace element patterns (metatonalite unit) | 348 |
| 5.9 MgO variation diagrams of samples from the metatonalite unit | 355 |
| 5.10 Incompatible trace element ratios in tonalite-trondhjemite samples plotted against SiO ₂ | 358 |
| 5.11 N-MORB normalized trace element patterns showing the effects of allanite fractionation (metatonalite) | 360 |
| 5.12 N-MORB normalized trace element diagram showing the effects of mixing (metatonalite unit) | 363 |
| 5.13 MgO variation diagrams of samples from the sheeted dike complex | 372 |
| 5.14 Rock classification of diabasic and microdioritic dikes in the Zr/TiO ₂ vs. Nb/Y diagram | 376 |
| 5.15 Chondrite and N-MORB normalized REE and trace element patterns (gabbro screens) | 379 |
| 5.16 Hf/3-Th-Ta tectonic discrimination diagram (sheeted dike complex) | 382 |

| | |
|----------------------------------------------------------------------------------------------------------------------|-----|
| 5.17 Chondrite and N-MORB normalized REE and trace element patterns (sheeted dikes) | 385 |
| 5.18 Cr vs. Y tectonic discrimination diagram (sheeted dike complex) | 388 |
| 5.19 Composition of Cr-spinels in dikes of geochemical group 2 | 391 |
| 5.20 Diagrams showing effects of mixing of MORB with IAT and IAT with CAB (sheeted dike complex) .. | 399 |
| 5.21 Rock classification of samples from the pillow unit in the Zr/TiO ₂ vs. Nb/Y diagram | 404 |
| 5.22 Chondrite and N-MORB normalized REE and trace element patterns (pillow unit) | 407 |
| 5.23 Hf/3-Th-Ta tectonic discrimination diagram (pillow unit) | 408 |
| 5.24 Cr vs. Y tectonic discrimination diagram (pillow unit) | 409 |
| 5.25 Composition of Cr-spinel in a sample from the pillow unit | 411 |
| 5.26 Diagrams illustrating the effects of mixing vs. variable degrees of partial melting (pillow unit) | 415 |
| 5.27 Th/Yb vs. Ta/Yb tectonic discrimination diagram (Wild Rogue Wilderness ophiolite) | 421 |
| 5.28 Rock classification of samples from the Mule Mountain volcanics in the Zr/TiO ₂ vs. Nb/Y diagram ... | 432 |
| 5.29 Chondrite and N-MORB normalized REE and trace element patterns (Mule Mountain volcanics) . | 435 |
| 5.30 Hf/3-Th-Ta tectonic discrimination diagram (Mule Mountain volcanics) | 438 |
| 5.31 Cr vs. Y tectonic discrimination (Mule Mountain volcanics) | 439 |
| 5.32 Composition of Cr-spinel in a sample from the Mule Mountain volcanics | 441 |
| 5.33 MgO variation diagrams of samples from the Mule Mountain volcanics | 446 |
| 5.34 Rock classification of diabasic dikes intruding HMB diorite using the Zr/TiO ₂ vs. Nb/Y diagram.... | 453 |
| 5.35 Chondrite and N-MORB normalized REE and trace element patterns (Half Moon Bar diorite) | 455 |
| 5.36 Hf/3-Th-Ta tectonic discrimination diagram (Half Moon Bar diorite) | 456 |
| 5.37 Chondrite and N-MORB normalized REE and trace element patterns (Musc-gar-tonalite) | 462 |
| 5.38 Zr/Y vs. Zr tectonic discrimination diagram of Pearce and Norry (1979) and Pearce (1983) | 467 |
| 5.39 Cross section showing the units of the Wild Rogue Wilderness, sample ages, and magmatic affinities | 471 |

Chapter 6

| | |
|----------------------------------------------------------------------------------------------------|-----|
| 6.1 Generalized geologic map of California and SW Oregon showing major accretionary terranes | 478 |
| 6.2 Tectonostratigraphic diagram comparing two belts of Jurassic ophiolites | 480 |

| | |
|---------------------------------------------------------------------------------------------------------|-----|
| 6.3 Cr-Y discrimination diagram showing data from the Coast Range ophiolite | 496 |
| 6.4 Hf/3-Th-Ta discrimination diagram showing data from the Coast Range ophiolite | 497 |
| 6.5 Tb/Yb and Ta/Yb discrimination diagram showing data from the Coast Range ophiolite | 498 |
| 6.6 Cr vs. Y tectonic discrimination diagram showing the fields for Josephine lavas and dikes | 503 |
| 6.7 Hf/3-Th-Ta discrimination diagram showing the fields for Josephine lavas and dikes | 504 |
| 6.8 Hf/3-Th-Ta tectonic discrimination diagram showing samples from the Rogue Wilderness ophiolites ... | 514 |
| 6.9 Location map of the Lau Basin after Hergt and Farley (1994) | 521 |
| 6.10 Diagrams showing the tectonic evolution of the Lau Basin | 522 |
| 6.11 Th/Yb vs. Ta/Yb discrimination diagram showing data from the Lau Basin, SW Pacific | 526 |
| 6.12 Hf/3-Th-Ta discrimination diagram showing data from the Lau Basin, SW Pacific | 527 |

Chapter 7

| | |
|---------------------------------------------------------------------------------------------------------|-----|
| 7.1 Simplified geologic map of the Wild Rogue Wilderness | 540 |
| 7.2 Cross section showing units of the Wild Rogue Wilderness, sample ages and magmatic affinities | 541 |

List of Plates

Plate 1: Geological map of the Wild Rogue Wilderness, southwest Oregon (scale 1:24,000)

(in back pocket)

List of Tables

Chapter 2

| | |
|----------------------------------------------------------------------------|----|
| Table 2.1a: Summary of $^{40}\text{Ar}/^{39}\text{Ar}$ apparent ages | 32 |
| Table 2.1b: Summary of U/Pb zircon ages | 32 |
| Table 2.2: List of mineral abbreviations | 32 |

Chapter 3

| | |
|---------------------------------------------------------------------------------------------------------------------------------------------------------------------------------------------|-----|
| Table 3.1: Microprobe analyses of hornblende in samples from the Half Moon Bar diorite | 154 |
| Table 3.2: Microprobe analyses of hornblende in O/C-229 (hornblende quartz diorite in metagabbro unit) . | 156 |
| Table 3.3: Microprobe analyses of hornblende in samples from the metagabbro unit | 157 |
| Table 3.4: Chemical analyses and proportional formula for run products (Poli, 1993) and results of temperature calculations using the geothermometers of Blundy and Holland (1994) | 180 |

Chapter 5

| | |
|---------------------------------------------------------------------------------------------------------------------------------------|-----|
| Table 5.1a: Major and trace element compositions of samples from the metagabbro unit | 323 |
| Table 5.1b: Major and trace element composition of hornblende quartz diorite in the metagabbro unit..... | 340 |
| Table 5.2: Major and trace element compositions of samples from the metatonalite unit | 345 |
| Table 5.3a: Major and trace element compositions of samples from the sheeted dike complex (gabbro screens) | 365 |
| Table 5.3b: Major and trace element compositions of samples from the sheeted dike complex (diabasic and microdioritic dikes) | 367 |
| Table 5.4: Major and trace element composition of samples from the pillow unit | 401 |
| Table 5.5 Major and trace element composition of samples from the Mule Mountain volcanics | 428 |
| Table 5.6: Major and trace element composition of samples from the Half Moon Bar diorite | 450 |
| Table 5.7: Major and trace element composition of dikes in the metagabbro unit | 459 |

CHAPTER ONE

INTRODUCTION

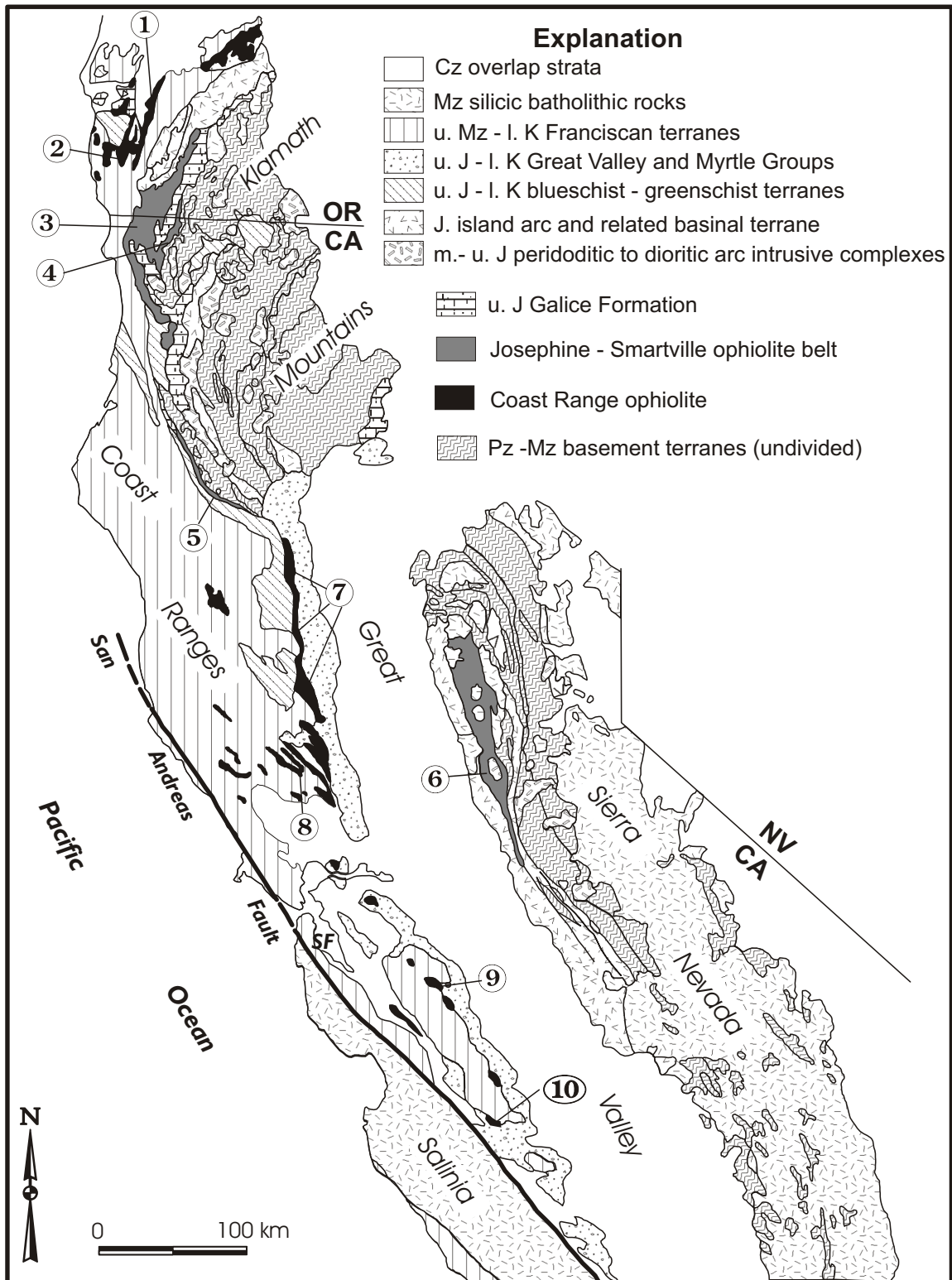
Jurassic ophiolites are an important element of the North American Cordillera, and understanding their origin is essential for correctly interpreting the tectonic evolution of the North American continental margin. Exposures of the Jurassic Coast Range ophiolite representing deformed and structurally dismembered segments of oceanic crust and uppermost mantle are widely distributed and extend along the western North American margin from southern California to Oregon (Hopson et al., 1981, Blake et al., 1985a) and even further north to Washington (Garver, 1988). In northern California and southwestern Oregon the Jurassic ophiolites occur in two belts (figure 1.1): an eastern belt defined by the 165-160 Ma Josephine and Smartville ophiolites and a western belt consisting of 170-155 Ma ophiolite remnants collectively called the Coast Range ophiolite (CRO) lying positionally beneath the fore-arc sediments of the Great Valley Group (GVG). Note that the Myrtle Group in Oregon is correlative with the GVG in California (Imlay et al, 1959, Blake et al., 1985a).

The Josephine ophiolite (JO) is conformably overlain by a sequence of radiolarian chert and tuffaceous cherts (volcanopelagic sequence), which is conformably overlain by shale, sandstone, graywacke, and conglomerate of the Galice Formation. The coeval Late Middle Jurassic to Late Jurassic JO and Rogue-Chetco island arc complex (Illinois River batholith and Rogue Formation) are overlapped by the Galice Formation (Pessagno and Blome, 1990) (figure 1.2 and 1.3). Typically, basal Rogue Formation strata are intercalated with the hemipelagic strata of the Galice Formation, and are overlain by middle Oxfordian to Kimmeridgian flysch deposits of the Galice Formation. The provenance of the Galice Formation is tied to both, the Rogue-Chetco island arc complex and older terranes of the Klamath Mountains (Miller and Saleeby, 1987). The rock assemblage in and around the margins of the Josephine ophiolite include fragments correlative with the upper Triassic to lower Jurassic Rattlesnake Creek terrane (Wyld and Wright, 1988; Yule, 1996). The Rattlesnake Creek terrane is constrained to have accreted to

Figure 1.1

Generalized map showing major accretionary terranes but also mid- to late Jurassic ophiolitic and related rocks of California and SW Oregon. Map modified from Harper et al. (1985). Two belts of mid- to late Jurassic ophiolites include the Coast Range ophiolite (western belt), and the Josephine - Smartville ophiolites (eastern belt). Numbers refer to the localities listed below.

1. Wild Rogue Wilderness: 164 Ma (Saleeby, 1984)
2. Snow Camp Mountain: 169 Ma (Saleeby et al., 1984).
3. Josephine ophiolite: 162 Ma (Harper et al., 1994)
4. Preston Peak 'ophiolite' (Saleeby and Harper, 1993)
5. Devils Elbow remnant of the JO: 164 Ma (Wyld and Wright, 1988)
6. Smartville ophiolite: 160-164 Ma (Edelman et al, 1989; Saleeby et al, 1989).
7. Northern Coast Range ophiolite remnants (e.g., Elder Creek, Paskenta, Stonyford)
8. Black Mountain
9. Del Puerto: 155-157 Ma (Hopson et al., 1981; Evarts et al., 1992)
10. Llanada: 164 Ma (Hopson et al., 1981)



N. America by mid-Jurassic time (Wright and Wyld, 1994). Around 155-150 Ma, the JO was emplaced by underthrusting under western North America during the Nevadan Orogeny and is unconformably overlain by strata as old as Valanginian (figure 1.2 and 1.3) that are correlative with the GVG and Myrtle Group (Saleeby et al., 1982; Harper and Wright, 1984; Wright and Fahan, 1988; Harper et al., 1994, Blake et al, 1985a). The beginning of flysch sedimentation (Galice Formation) during middle Oxfordian time may mark the onset of the Nevadan Orogeny (Harper et al., 1994; figure 1.3). The Josephine-Smartville ophiolite belt and overlying sediments (Galice formation) were regionally metamorphosed to at least prehnite-pumpellyite facies (Harper et al., 1988; Harper et al., 1994), and intruded by calc-alkaline dikes and sills (figure 1.3) (Harper et al., 1994). The belt of rocks correlative with the Rattlesnake Creek terrane within and along the margins of the Josephine ophiolite (Wyld and Wright, 1988; Yule 1996; figure 1.3) are interpreted to represent rifted fragments of the N. American continental margin that were carried outboard as the Josephine marginal basin widened due to seafloor spreading. The marginal basin between N. America and the Rogue-Chetco island arc complex was the site of deposition of the volcanopelagic sequence and the Galice Formation. To summarize, the JO is well studied and it is generally accepted that the JO formed by back-arc spreading after rifting of a Mid-Jurassic arc built on western North America (Harper, 1984; Harper and Wright, 1984; Harper et al., 1994; Miller and Saleeby, 1987; Wyld and Wright, 1988; Yule, 1996).

The CRO differs greatly in its sedimentary and structural history from the JO. In California (e.g. Llanada), sedimentation of the volcanopelagic sequence lasted much longer on the CRO than on the JO (figure 1.3). While the Josephine ophiolite was underthrust beneath western N. America, deposition of various volcanoclastic sediments on the CRO continued (tuffaceous cherts, lahars, volcanic breccia, volcanoclastic sandstones were deposited on CRO remnants in central and southern California; additionally ophiolite derived breccias were deposited on CRO remnants in northern California). Also, the deposition of the fore-arc sediments of the basal Great Valley Group on the CRO appears to overlap in time with the Nevadan orogeny. Evidence of regional metamorphism has not been reported from any of the Coast Range ophiolite remnants (e.g., Hopson et. al., 1981 and 1997; Lagabrielle et al, 1986; Robertson, 1989, 1990). Thus, the CRO and overlying sediments are apparently not affected by the Nevadan orogeny (Hopson

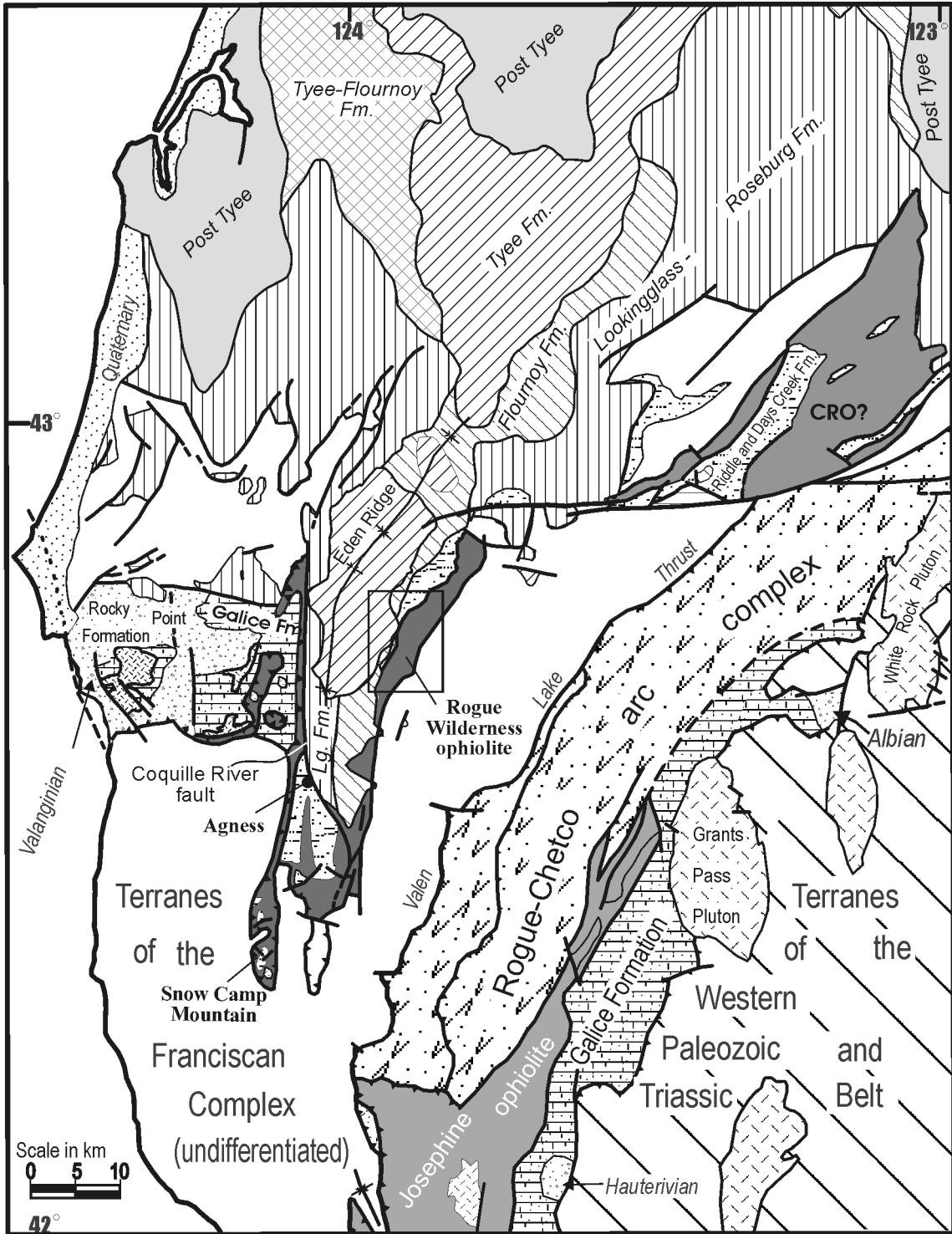


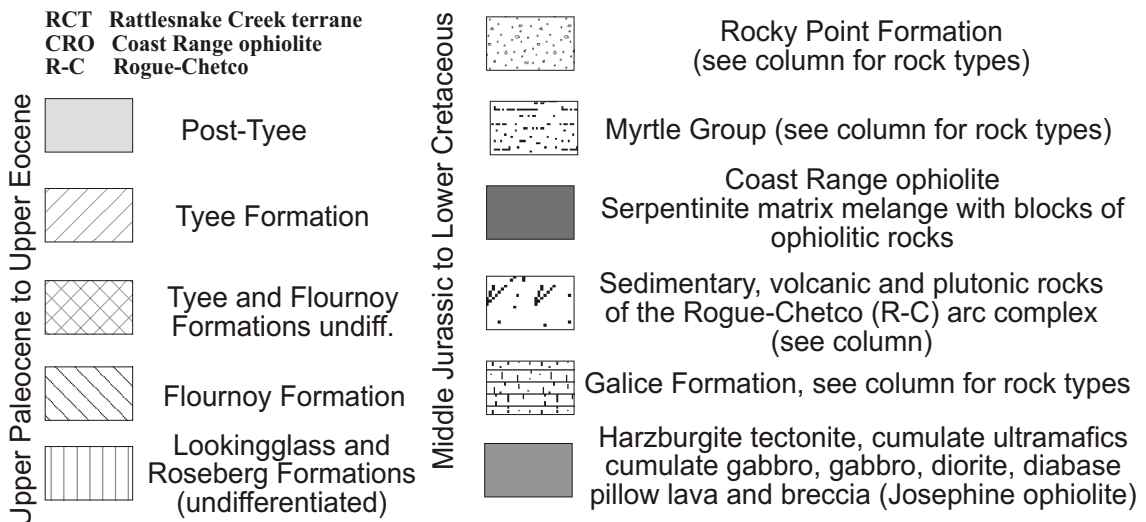
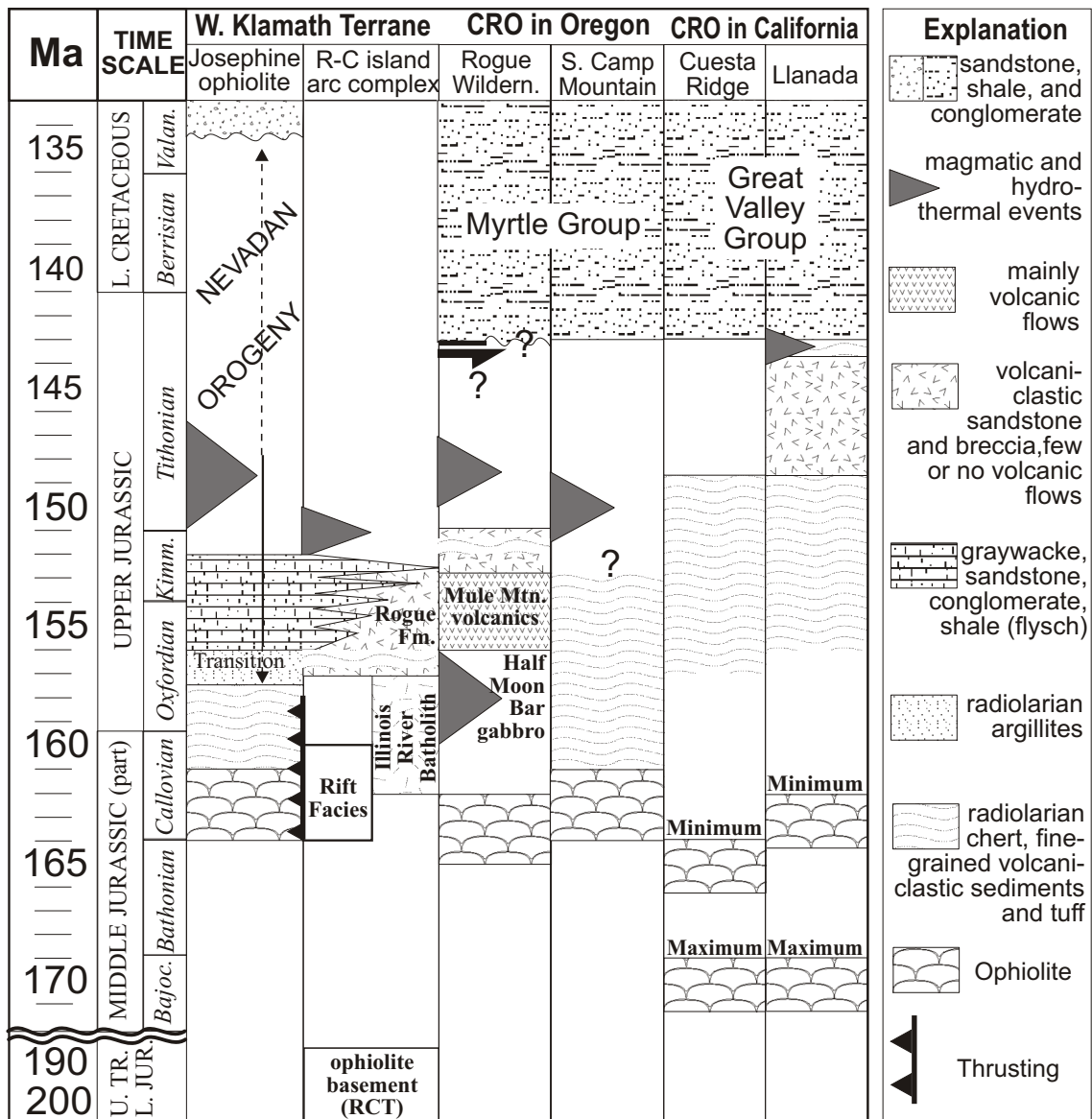
Figure 1.2

Simplified geological map of SW Oregon. The area of the field map is outlined (box).

See figure 1.3 for explanation.

Figure 1.3

Tectonostratigraphic diagram comparing Coast Range ophiolite (CRO) - basal Great Valley Group (volcanopelagic sequence) succession with the Josephine ophiolite - Galice succession. Minimum and estimated maximum possible ages of the Coast Range ophiolite remnant at Cuesta Ridge and Llanada are based on U/Pb and Pb/Pb isotopic ages, respectively (Hopson et al., in Dickinson et al., 1996). Terrigenous sedimentation on Coast Range ophiolite - volcanopelagic sequence began with basal strata of the Great Valley Group in the latest Jurassic. Ages for the Josephine ophiolite are from Harper et al. (1994), for the Rogue Chetco island arc complex from Yule (1996), for the Coast Range ophiolite remnant at Cuesta Ridge and Llanada from Hopson et al. (in Dickinson et al., 1996). The data for the Snow Camp mountain area and the Wild Rogue Wilderness are from Saleeby et al. (1984) and Saleeby (1984), respectively. Additionally, the $^{40}\text{Ar}/^{39}\text{Ar}$ and U/Pb data obtained for this study for the Half Moon Bar gabbro and the Mule Mountain volcanics are used. The cherts within and above pillows near Snow Camp Mountain contain radiolarians of Callovian to mid Oxfordian age (Pessagno written communication, 1996).



et al., 1981; Hopson et al. in Dickinson et al., 1996). Note that the CRO and volcanopelagic sediments in California are conformably overlain by the Great Valley Group, which is equivalent to the Myrtle Group in Oregon (figure 1.3).

The origin of the CRO is controversial and a number of different hypotheses for the genesis of the CRO have been suggested. Three tectonic models are summarized and discussed in a recent article (Dickinson et al., 1996): (1) The CRO formed by sea-floor spreading at a mid-ocean ridge near the paleoequator and was transported north toward a subduction zone in front of the North American continental-margin arc (figure 1.4); (2) The CRO formed by back-arc spreading behind an intra-oceanic island arc that subsequently collided with the North American continental-margin arc during the Nevadan Orogeny (figure 1.5); (3) The CRO formed by fore-arc spreading within the fore-arc region of the North American continental-margin arc during oblique subduction and trench roll back (figure 1.6). A fourth model, not discussed in Dickinson et al. (1996), has been suggested by Stern and Bloomer (1992): the CRO formed by generation by seafloor spreading above a nascent subduction zone similar to the Eocene Izu-Bonin-Mariana arc (figure 1.7). Model (1) and model (2) imply an exotic origin for the CRO with respect to North America, model (3) and model (4) imply, similar to the JO, a parautochthonous origin for the CRO with respect to North America.

The first model, proposed by Hopson and others (in Dickinson et al., 1996), suggests formation of the CRO by sea-floor spreading at a mid-oceanic ridge near the paleoequator (figure 1.4). Most CRO remnants are depositionally overlain by a volcanopelagic sequence consisting of radiolarian chert, fine-grained volcanoclastic sediments and tuff. Some CRO remnants contain also a sandy-fragmental volcanoclastic facies (figure 1.3). Hopson and others (in Dickinson et al., 1996) interpret these observations as follows: the oceanic plate was drawn progressively closer to the coeval Sierran-Klamath volcanic arc that fringed western North America. Sedimentation of tuffaceous radiolarites began as the oceanic plate was transported northeast through the distal tefra fringe and then transported further into the proximal volcanoclastic apron (figure 1.4). Finally, the basal GVG strata represent a terrigenous clastic apron that prograded over the deep oceanic floor following onset of the Nevadan Orogeny. The ophiolite must have been accreted to N. America during deposition of the upper Jurassic to Cretaceous GVG (figures 1.3 and

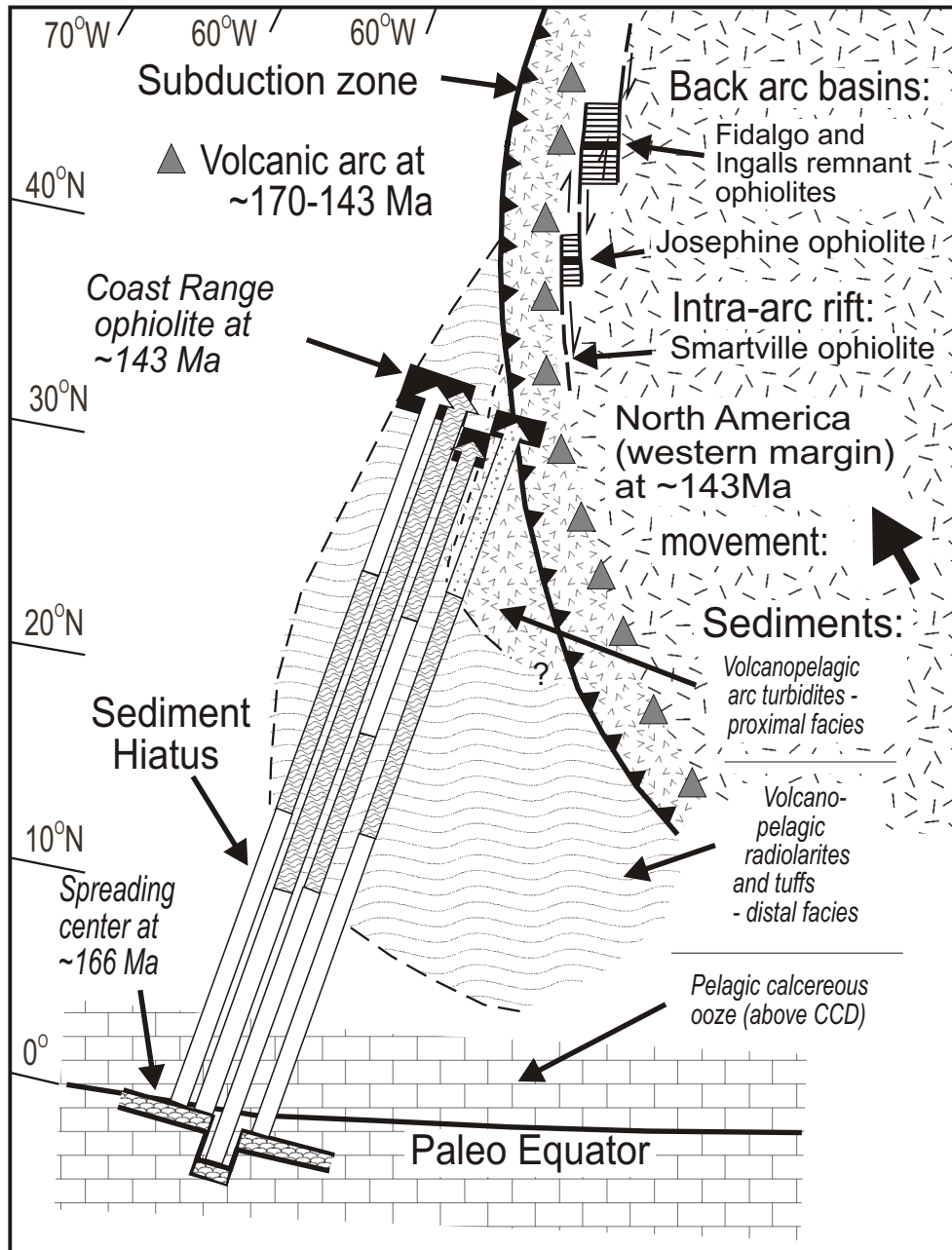


Figure 1.4

Tectonic model for the Coast Range ophiolite after Hopson et al. (in Dickinson et al.; 1996).

This model involves seafloor spreading at a mid-ocean ridge followed by accretion to

N. America by latest Jurassic time.

1.4). Also, this model invokes an exotic origin for the CRO with long northward transport. However, large northward motions of the CRO inferred from paleomagnetism may not be valid, because new paleomagnetic data from some CRO remnants suggest there were no substantial northward motions (Hagstrum and Murchey, 1996; Hull et al., 1997). This model also predicts mid-ocean ridge basalt (MORB) chemistry of igneous rocks of the CRO, but island arc and boninitic affinities are found throughout the CRO (e.g., Shervais 1990; Shervais et al., in review; this study). However, arc-like lavas have been recovered from the Chile-rise near the Chile trench, an active oceanic spreading ridge located west of South America (Klein and Karston, 1995). Also, arc-like lavas occur at the oceanic spreading center in the Woodlark basin (Perfit et al., 1987). The Woodlark basin and Woodlark spreading center are currently being subducted beneath the New Georgia Group, part of the Solomons island arc (Perfit et al., 1987). These examples indicate that arc-like lavas occur at oceanic spreading centers and may not be uncommon.

The second model was proposed by Ingersoll and Schweickert (1986) who suggested that the CRO formed by back-arc spreading behind an east-facing intra-oceanic island arc (figure 1.5a) that collided at ~159 Ma and became amalgamated with the North American continental margin (figure 1.5b and 1.5c). As the island arc collided, volcanic activity of both volcanic arcs ceased (~157 Ma, figure 1.5b) and continued later after a new subduction zone initiated in the former back-arc basin of the oceanic-arc complex (figure 1.5c). The CRO was trapped in the fore-arc region of the new volcanic arc and formed the basement on which sediments of the GVG were deposited. The Smartville ophiolite (intra-arc rift) and the CRO (back-arc basin) are both considered to be part of an exotic island arc - backarc basin complex, and the JO is considered to be parautochthonous with respect to North America. However, recent studies suggest the Smartville ophiolite formed in the same marginal basin as the JO, and the deformation previously attributed to the Nevadan Orogeny predates ophiolite generation (Wright and Fahan, 1988; Saleeby et al., 1992). The model of Ingersoll and Schweickert (1986) is also based on a 157 ± 2 Ma radiometric age for the JO (Saleeby et al., 1982) which has been shown to be too young (Harper et al., 1994). Further potential problems with this model, which envisions supra-subduction zone affinity, are discussed by Saleeby in Dickinson et al. (1996). This model also evokes an exotic origin of the CRO.

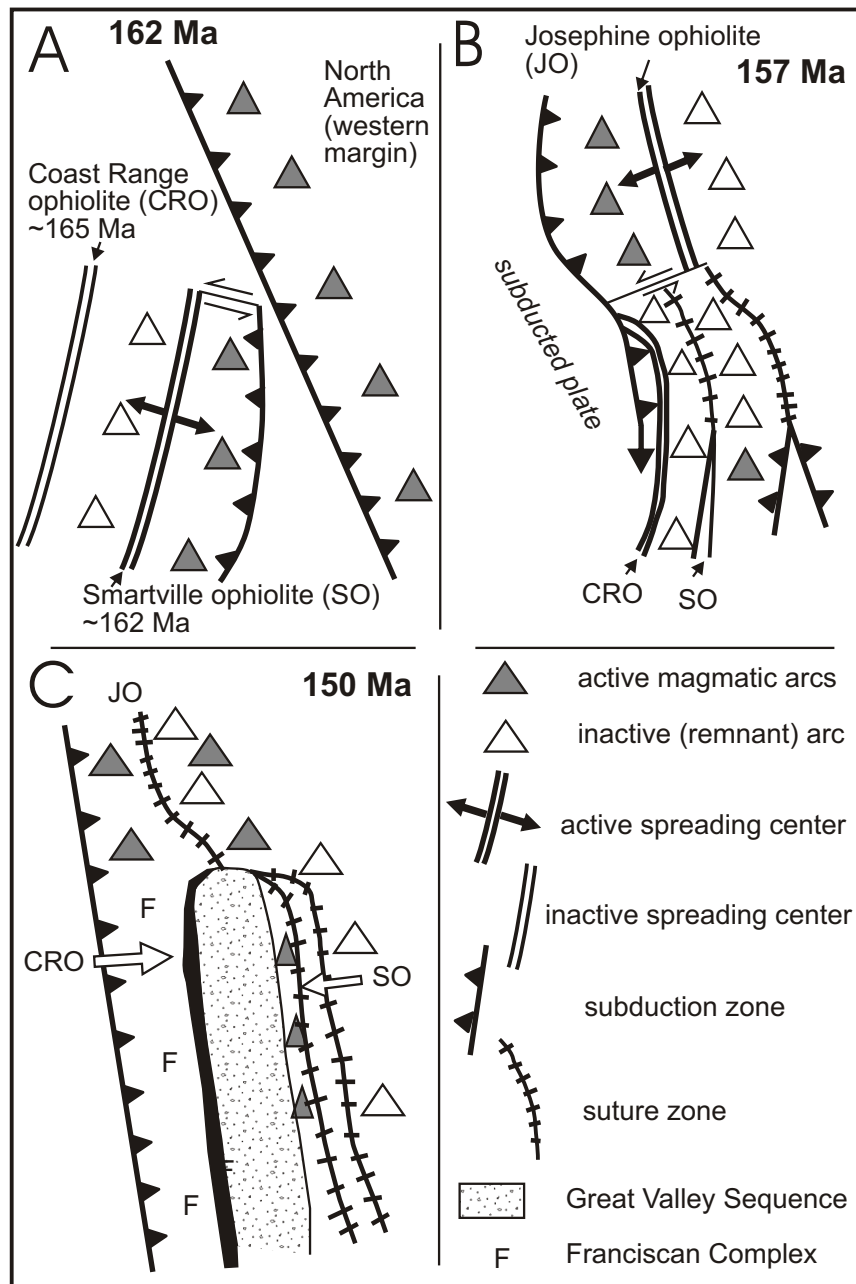


Figure 1.5

Tectonic model for the Coast Range ophiolite after Ingersoll and Schweikert (1986)

This model involves back-arc spreading in an intra-oceanic arc that collided with N. America during the late Jurassic Nevadan orogeny.

The third hypothesis discussed by Saleeby in Dickinson et al (1996) is based on the model proposed by Harper and Wright (1984), Wyld and Wright (1988), Harper et al. (1985) and Saleeby et al (1992). These authors propose that the CRO and JO were generated in a single fore-arc (or intra-arc) basin in front of (or within) the North American Sierran-Klamath arc (figure 1.6). Harper and Wright (1984) proposed that the mid-Jurassic magmatic arc built on older accreted terranes of the Klamath Mountains began to migrate westward relative to North America. This resulted in the formation of a back-arc basin and remnant arc. In late Jurassic time, the back-arc basin widened and arc-magmatism migrated eastward resulting in the intrusion of numerous calc-alkaline dikes and sills in the back-arc basin. During the Nevadan orogeny, the arc and back-arc basin was thrust underneath the remnant arc built on western N. America. Saleeby and Harper (1993) and Saleeby et al. (1992) proposed a more complex model involving the formation of transtensional rifts within and in front of the magmatic arc built on western N. America. These transtensional rifts were connected by right-lateral transform faults and formed after the postulated oblique collision of the Insular Superterrane at ~170-165 Ma (Siskiyou Orogeny). Further extension of the N. American continental margin arc has been postulated to be the result of trench-roll back during oblique subduction (Saleeby et al., 1992). Similarly, Harper et al. (1985, 1994) proposed that the JO formed by rifting of the Sierran-Klamath arc built on western North America. A major deformation and regional metamorphic event, similar in style to the Nevadan orogeny (i.e. collision unrelated) affected the magmatic arc at 165-170 Ma largely prior to rifting of the arc (Harper and Wright, 1984; Harper et al, 1994; Wright and Fahan, 1988). Harper et al. (1985) and Harper et al. (1994) suggest that the intra-arc rifts are connected by left-lateral transform faults (figure 1.6). The models involving rifting of the magmatic arc built on western N. America evoke a parautochthonous origin of the JO and CRO and predict that rifted older basement should be associated with the CRO, JO and Smartville ophiolite. Such fragments have been found associated with the Josephine ophiolite (Wyld and Wright, 1988; Harper et al 1994; Yule et al., 1992; Yule 1996), but have not been found in the CRO. This third model implies a supra-subduction zone origin of the CRO and is consistent with the occurrence of unusual high MgO and Cr 'boninitic' lavas in the CRO (e.g., Shervais 1990). Boninites are found in many fore-arcs of Pacific volcanic arcs (e.g.,

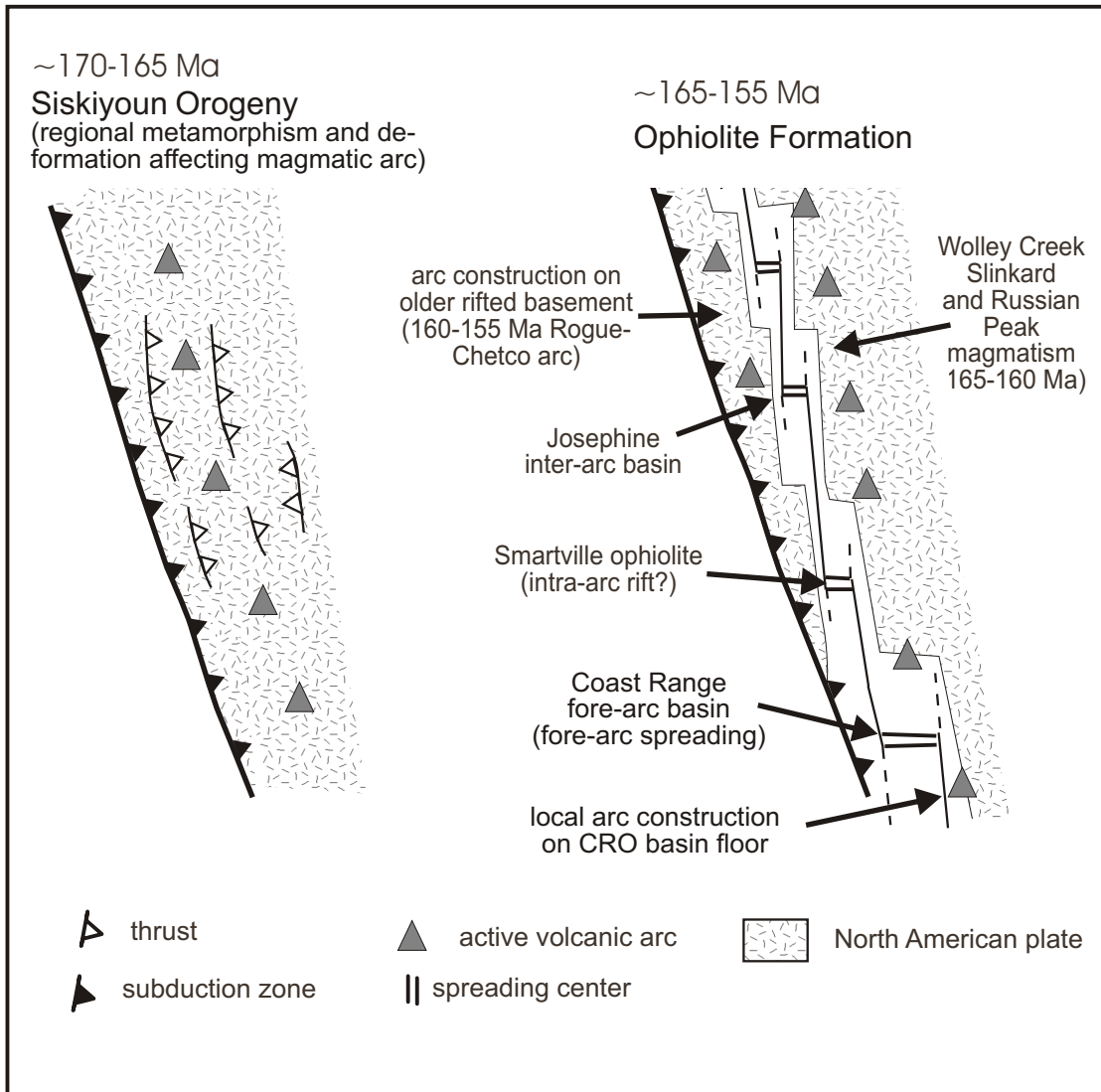


Figure 1.6

Tectonic model for the generation of the Josephine ophiolite and Coast Range ophiolite (CRO) after Harper and Wright (1984), Wyld and Wright (1988), Saleeby and Harper (1993), Saleeby et al. (1992), and Harper et al. (1985, 1994). This model involves spreading within the fore-arc of the Mid-Jurassic Sierran-Klamath arc during oblique subduction and trench rollback (see also figure 1.7).

Crawford, 1989; Stern and Bloomer, 1992). Note that high-Ca boninites are known from back-arcs such as the Valu-Fa ridge in the Lau basin (e.g., Kamenetsky et al. 1997).

The fourth model, proposed by Stern and Bloomer (1992), evokes formation of the CRO related to subduction nucleation along an active Mid-Jurassic transform boundary similar to the Eocene Izu-Bonin-Mariana arc (figure 1.7). For comparison, a cross section of model 3 is shown in figure 1.7. According to the model of Stern and Bloomer (1992), sinking and subduction of the oceanic lithosphere resulted in the trench moving away with respect to North America, and the JO and CRO formed by subsequent extension of the upper plate into the “gap” (figure 1.7). However, the analogy with the Eocene Izu-Bonin-Mariana arc is weak, because subduction was occurring before the “arc infancy phase” of the CRO. For example, radiometric ages for plutons indicate that arc-magmatism in the Sierran-Klamath arc occurred almost continuously in the interval 215-85 Ma (e.g., Stern et al, 1981; Chen and Moore, 1982, Wright and Fahan, 1988; Hacker et al., 1993; Wright and Wyld, 1994). Unlike model 4, which invokes initiation of subduction and subsequent arc-magmatism in mid-Jurassic time (figure 1.7), model 3 is consistent with arc-magmatism in the Sierran-Klamath arc prior to and contemporaneous with the formation of the JO and CRO.

Although the different models of the formation of the CRO are mutually exclusive, they have fundamental areas of agreement such as the interpretation of the rock assemblage of the CRO and JO. It is generally accepted that the CRO and JO represent an assemblage of mafic crust and portions of lithosphere of oceanic character that was formed by seafloor spreading. However, an important aspect of this controversy is whether the CRO is exotic with respect to North America (Ingersoll and Schweikert, 1986, Lagabrielle et al., 1986, Hopson et al, 1981, 1991, 1997, Dickinson et al., 1996) or not (Stern and Bloomer, 1992, Harper et al., 1985; Saleeby and Harper, 1993). These tectonic models have to be reevaluated as new data becomes available. For example, a Jurassic ophiolite remnant that possesses characteristics of both belts of ophiolites, would help to constrain one of the mutually exclusive models of the origin of the Coast Range ophiolite that proposed an exotic origin. Assuming that such a “bridging link” exists, the Coast Range ophiolite should be interpreted to have formed within the same volcanic arc -

Model 3 (see figure 1.6)

Model 4 (Stern and Bloomer, 1992)

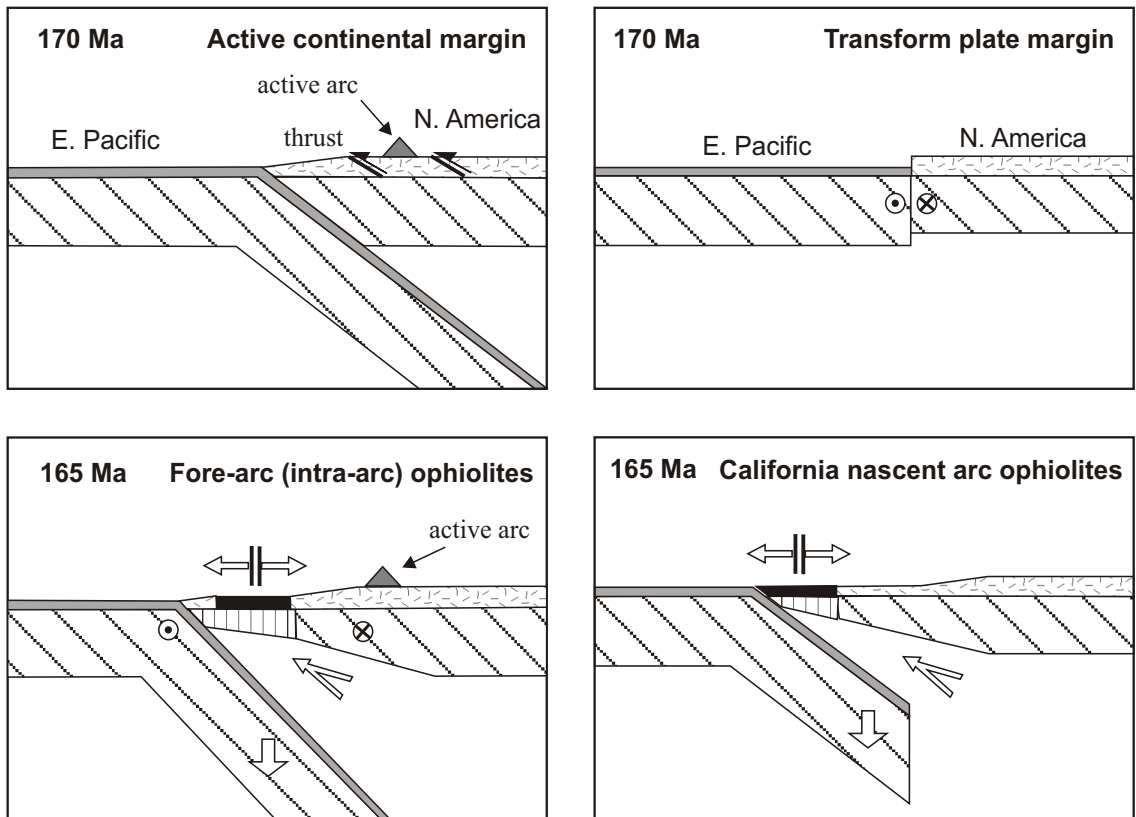


Figure 1.7

Tectonic model for the Coast Range ophiolite after Stern and Bloomer (1992) compared to the model shown in figure 6 (after Harper and Wright, 1984; Wyld and Wright, 1988; Saleeby and Harper 1993; and Harper et al., 1985, 1994). The model invokes extension of the North American plate into the 'gap' that resulted from the sinking and subduction of the Pacific plate.

Thus, the CRO represents 'infant arc crust' formed by seafloor spreading.

marginal basin system as the Josephine-Smartville ophiolite belt and, therefore, is native with respect to North America.

In California, the west flank of the CRO is bounded by the Coast Range ‘thrust’, and the east flank is overlain by the upper Jurassic basal Great Valley sequence (figure 1.3). The east flank of the Franciscan complex was thrust beneath or is otherwise faulted against the CRO (e.g., Ingersoll, 1979; Dickinson and Seely, 1979). The “stacking” from west to east is: Franciscan complex, Coast Range “thrust”, CRO, Great Valley sequence (figure 1.8). It is generally agreed that (1) the Sierra Nevada composite batholith (Sierran-Klamath arc) to the east of the CRO and Great Valley sequence represent the deeply eroded roots of the Jurassic-Cretaceous magmatic arc that formed as a result of east-directed subduction of oceanic lithosphere beneath western N. America (e.g., Page, 1972); (2) the Franciscan complex of the California Coast Ranges farther west of the Sierran-Klamath arc is interpreted to be the accretionary complex that was paired with the Sierran-Klamath arc (e.g., Hamilton, 1969, Hamilton, 1978); and (3) the deposition of the Great Valley Group on the CRO occurred within the fore-arc of the Cretaceous Sierran-Klamath arc (e.g., Seiders and Blome, 1988). Obviously, models of the emplacement of the CRO must be consistent with the CRO being part of the fore-arc crust in front of the Sierran-Klamath arc since Cretaceous time (figure 1.8).

This thesis is a study of the ophiolite remnant exposed in the Wild Rogue Wilderness which provides much new data to better constrain the origin of the CRO. The Wild Rogue Wilderness remnant of the CRO was largely unstudied prior to this investigation. This thesis reports the findings of a comprehensive geologic field investigation of a late-Middle Jurassic ophiolite remnant exposed in the Wild Rogue Wilderness, SW Oregon (plate 1). The objectives of this study were threefold: (1) determine the internal structure and pseudostratigraphy of the ophiolite, and document constraints on the fault- and spreading- geometry of the ophiolite and its subsequent evolution; (2) constrain the post-ophiolite structural and metamorphic history; and (3) constrain the likely tectonic setting using major and trace element data from the Coast Range ophiolite in SW Oregon. Data obtained from investigations (2) and (3) are used to determine whether the ophiolite remnant in the Wild Rogue Wilderness is correlative with the eastern (Josephine-Smartville) or western (CRO) belt of late-Mid Jurassic ophiolites.

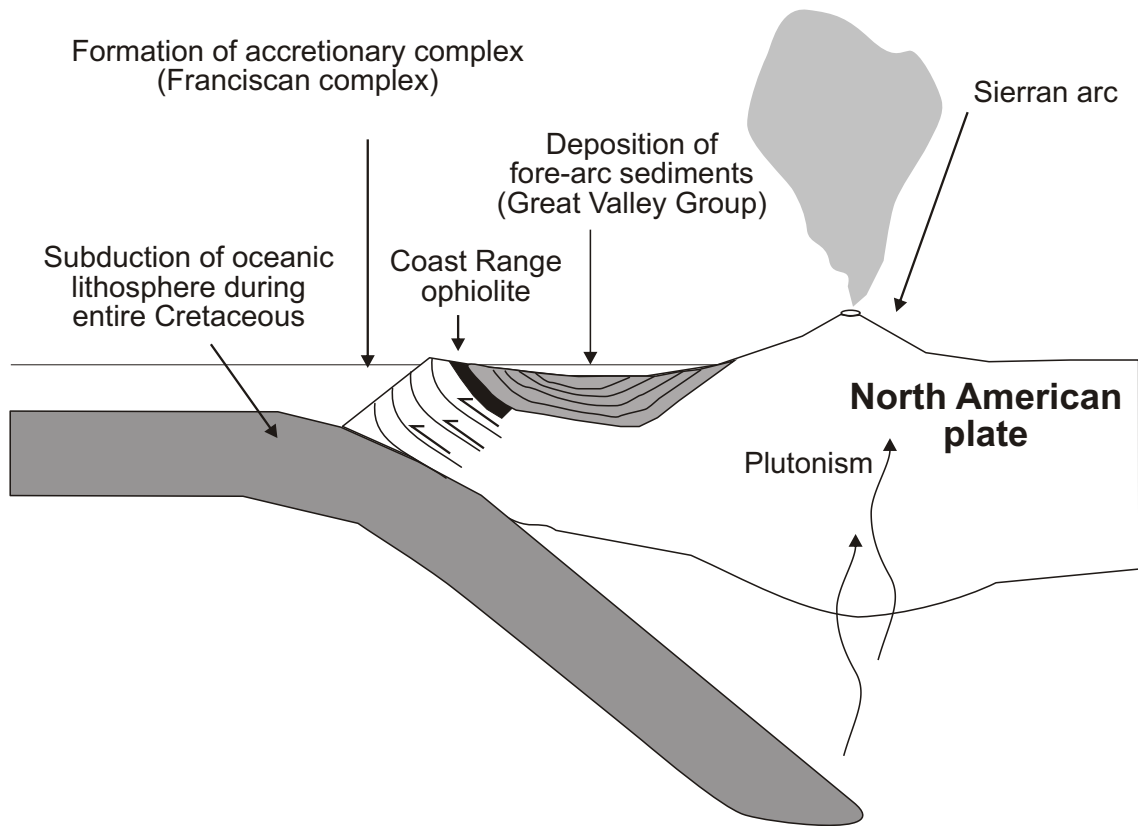


Figure 1.8

Model modified after Page (1972) showing subduction of oceanic lithosphere beneath western North America during the Cretaceous.

Previously, the Rogue Wilderness ophiolite was interpreted to represent a klippe thrust westward from the Klamath Mountain province and, thus, be a tectonic outlier of the Josephine ophiolite (Coleman and Lanphere, 1991; Blake et al, 1982; Roure and Blanchart, 1983). In contrast, Blake et al. (1985a) correlated the Rogue Wilderness ophiolite (Snow Camp terrane) with the Coast Range ophiolite in California which is largely based on lack of Nevadan-age deformation and conformably overlying Myrtle Group (Great Valley Group-equivalent strata) (Imlay et al., 1959, Blake et al., 1985a). The findings of this study, concerning the second objective, were rather surprising in that the Rogue Wilderness ophiolite seems in part correlative with the Josephine ophiolite, and to some extent to the Coast Range ophiolite and, thus, may represent the “missing link”, which, in California is likely covered by thick sediments of the Great Valley Group. Thus, the results of this study have important implications for the interpretation of the tectonic evolution of the North American Cordillera.

CHAPTER TWO

GEOLOGY, PETROGRAPHY AND GEOCHRONOLOGY OF THE ROGUE WILDERNESS REMNANT OF THE COAST RANGE OPHIOLITE, SW OREGON

2.1 Introduction

The area of study is located in the Wild Rogue Wilderness, SW Oregon about 20 km northeast of Agness, and about 30 km north-northwest of the Josephine ophiolite (figure 2.1a). The ophiolitic basement is overlain by the sedimentary rocks of the Myrtle Group. Imlay et al. (1959) and Blake et al. (1985a) correlated the Myrtle Group with the Great Valley sequence in California. The ophiolitic basement and overlying strata of the Myrtle Group in SW Oregon form the “Snow Camp terrane” (Blake et al, 1985a). This terrane is a folded thrust sheet overlying terranes of the Franciscan complex (figure 2.1a and 2.1b), with thrusting and folding constrained to have occurred by early Tertiary. Similar to most Coast Range ophiolite remnants in California, the ophiolite remnant in the Rogue Wilderness is structurally disrupted, with ophiolitic units bounded by faults. The best exposures of the ophiolite remnant occur in the deep canyon along the Rogue River within the Wild Rogue Wilderness (figure 2.2). All ophiolitic units are present, except for ultramafic rocks, although these occur further south along strike. Abundant ultramafic rocks occur even further south in the Snow Camp Mountain area (figure 2.1a).

Blake et al. (1985a) correlated the ophiolite remnant and overlying Myrtle Group in the Rogue Wilderness area and the Snow Camp Mountain area with the Coast Range ophiolite (CRO) and Great Valley sequence in California. In contrast, Coleman and Lanphere (1991), Blake et al. (1982), and Blanchet and Roue (1986), suggested the ophiolite remnants in the Rogue Wilderness area and the Snow Camp Mountain area is a klippe of the Josephine ophiolite. The ophiolite remnant in the study area is interpreted to be part of the CRO for the following reasons: (1) the ophiolitic rocks are depositionally overlain by Great Valley Group - equivalent strata (i.e. Myrtle Group) in the Snow Camp Mountain area

(Harper, unpublished field mapping 1997-98); (2) there is no evidence of Nevadan regional metamorphism nor related penetrative deformation (Blake et al., 1985a; this study); (3) the ophiolitic rocks are disrupted in a style similar to most Coast Range ophiolite remnants in California (e.g., Hopson et al., 1981); and (4) an outlier of the Galice Formation occurs 10-15 km west of the ophiolite in the study area (figure 2.1a), and shows the regional metamorphism and slaty cleavage typical of the Galice Formation, whereas the ophiolite remnant in the Wild Rogue Wilderness and overlying sediments are not penetratively deformed nor underwent regional metamorphism.

2.2 Geographic setting and previous work

The Wild Rogue Wilderness is located within the Klamath Mountains Province of Oregon about 60 km northwest of Grants Pass (figure 2.1a). It is a very rugged and heavily vegetated terrain with steep topography. Relatively good access is provided by a road that leads to Marial just outside the eastern boundary of the central part of the Wilderness area (plate 1). Excellent water polished outcrops are found along the Rogue River and numerous creeks. Natural exposures occur along ridge crests and on mountain tops as well as in gullies and steep cliffs on the flanks of mountains. Of course, man-made exposures are rare in the roadless Wilderness, but can be found along a washed out 4WD-road within the Wilderness boundary and in abandoned prospects and gold mines.

Geologic studies with accompanying geologic maps covering parts or the entire area of the Wild Rogue Wilderness include those of Wells (1955), Wells and Peck (1961), Baldwin (1969), Rud (1971), Baldwin and Rud (1972), Kent (1972), Ramp et al. (1977), Ramp and Floyd (1980), Gray et al. (1982) and Ramp and Moring (1986). The most detailed study was conducted in 1978-1980 as part of an evaluation of the mineral resource potential of the Wild Rogue Wilderness by the U.S Geological Survey, the Oregon Department of Geology and Mineral Industries, and the U.S Bureau of Mines. The results were summarized in a 1:48,000 scale geologic map (Gray et al., 1982). In conjunction with this investigation, Ramp and Gray (1980) identified a spectacular sheeted dike complex in fault contact with the Late Jurassic to Early Cretaceous Dothan Formation (part of the Franciscan complex). Furthermore, Gray et al. (1982) mapped several fault-bounded units, including pillow lava and gabbro, which, together

Figure 2.1

- A. Simplified geologic map of SW Oregon. The geologic map of Tertiary strata in Oregon is modified from Chan and Dott (1983) and Niem and Niem (1990), and the geologic map of pre-Tertiary rocks is modified from Walker and MacLeod (1991) and Blake et al. (1985a). The structural data suggest that the Rogue Wilderness ophiolite occurs on the east-limb of a large Cretaceous syncline (folded thrust sheet).
- B. Interpretative cross section along line AA' (figure 2.1a). The Snow Camp terrane, consisting of an ophiolitic basement and late Jurassic to early Cretaceous fore-arc sediments (Myrtle Group), is interpreted as the remnant of a folded thrust sheet that is thrust over the terranes of the Franciscan complex (Yolla Bolly terrane and Sixes River terrane) (Blake et al., 1985a). This remnant appears to be preserved in a graben and is largely covered by Tertiary strata with great unconformity.

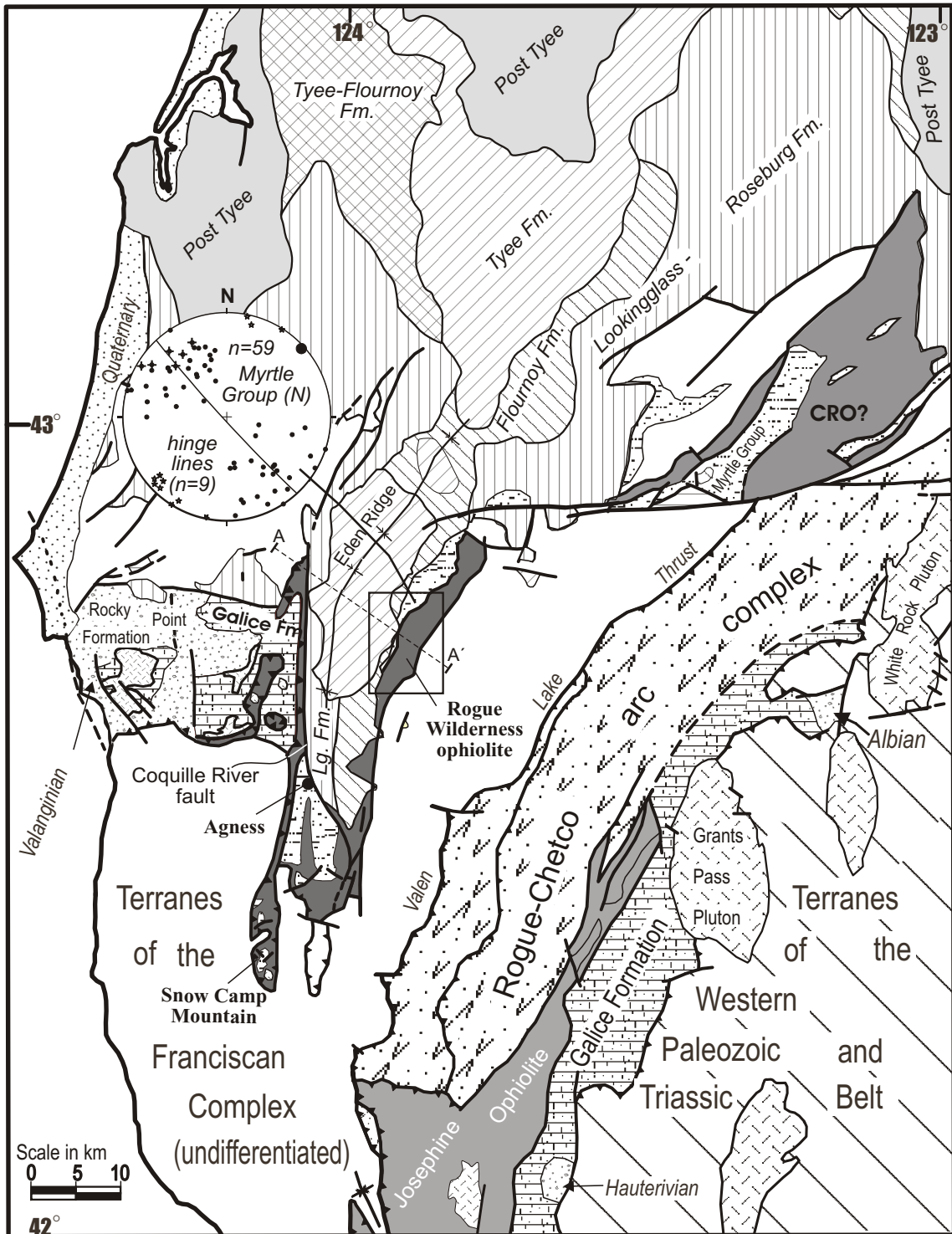
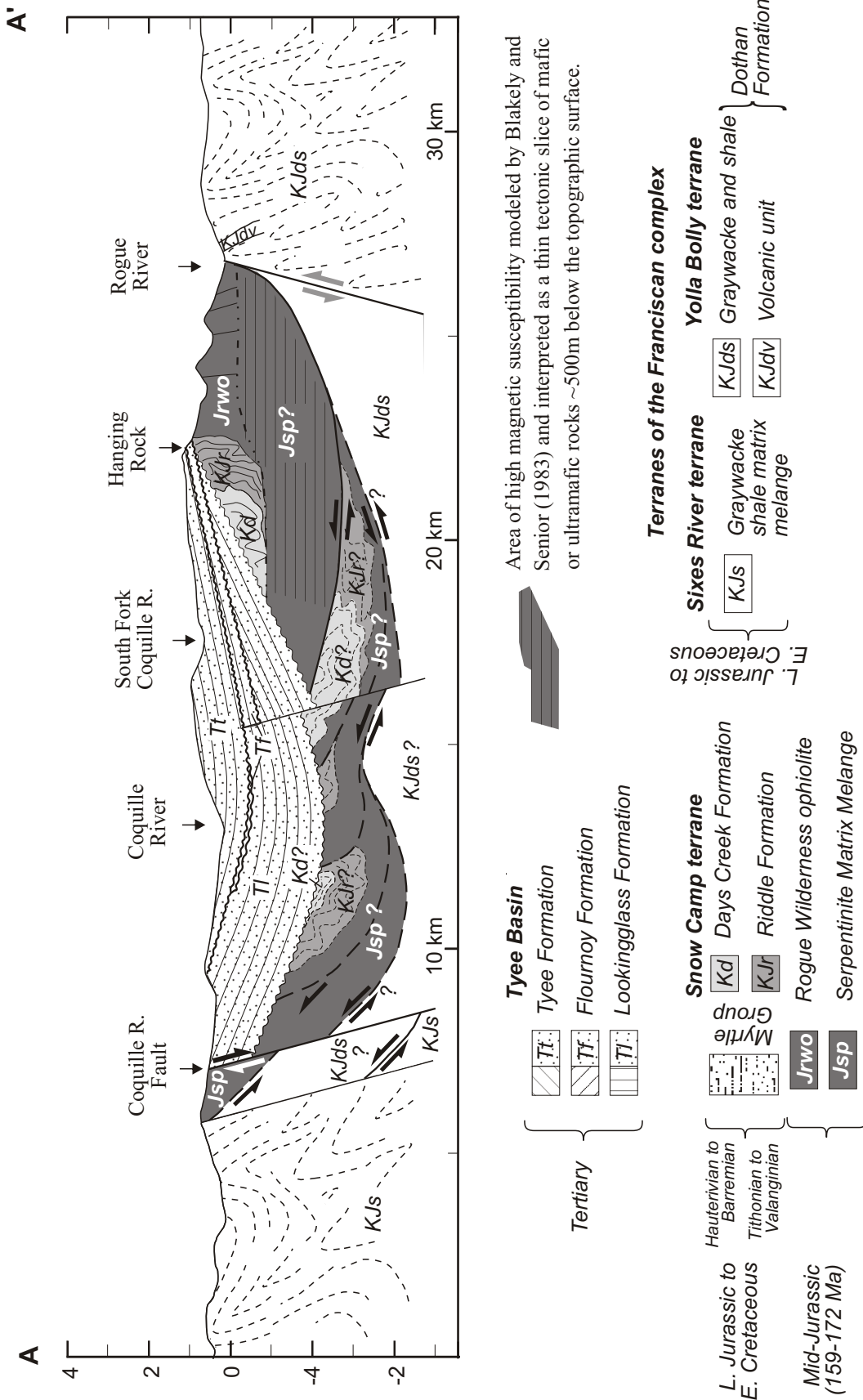


Figure 2.1a

Simplified geologic map of SW Oregon showing the area of the field map (box).

See figure 4.1b for legend.



with the sheeted dike complex, seem to form an incomplete and dismembered ophiolite sequence. However, detailed descriptions of rock units and their structures are not provided by these authors, and some deformed rocks were misidentified. Gray et al. (1982) also mapped a thick sequence of andesitic and dacitic flows intercalated with tuffs and volcanic breccia and interpreted these rocks as being related to a volcanic arc environment.

Gray and Peterson (1982) obtained geochemical data by semi-quantitative emission spectrographic analysis of rock and stream sediment samples. Unfortunately, the data, which consist only of the results of the semi-quantitative analysis of nine trace metals and three major elements, provide no constraints on the magmatic affinities of the igneous rocks in the Wild Rogue Wilderness.

Scarce radiometric age data are available and include hornblende- and mica- K/Ar ages reported by Gray and McKee (1981) and zircon U/Pb ages reported by Saleeby (1984). In addition, the K-Ar dates of Gray and McKee (1981) appear to be of little value: three of four K-Ar dates from the Wild Rogue Wilderness are most likely too young which could be related to Ar-loss in the samples.

Blakely and Senior (1983) present the data of an aeromagnetic survey of the Earth's total field in the Wild Rogue Wilderness superimposed on the geologic map of Gray et. al. (1982). Blakely and Senior (1983) inferred that a thin tectonic slice of rocks with high magnetic susceptibility lays may be less than 500 m below the topographic surface west of the fault contact with the Dothan formation (figure 2.1b).

2.3 The Rogue Wilderness remnant of the Coast Range ophiolite

The middle to late Jurassic volcanic and plutonic rocks in the Wild Rogue Wilderness occur as steeply dipping fault-bounded units on the eastern limb of a large Cretaceous syncline (folded thrust sheet?) that has a gently northeast dipping fold axis (figure 2.1a and 2.1b). The Dothan Formation (part of the Franciscan complex) is known to underlie (structurally) the Snow Camp Mountain terrane in Snow Camp Mountain area (Blake et al., 1985a) (see also chapter 4). Other constraints on the construction of the cross section in figure 2.1b are discussed in chapter 4 in more detail.

The fault-bounded volcanic and plutonic units trend northeast-southwest (figure 2.2a) and form the igneous basement of the late Jurassic to early Cretaceous fore-arc sediments of the Myrtle Group. Both

the Myrtle Group and its igneous basement are nearly vertical and are unconformably overlain by gently dipping Eocene sedimentary rocks in the western part of the Wilderness (figures 2.1 and 2.2). A prominent fault, inferred to be a terrane boundary (Blake et al, 1985a, this study) forms the eastern confines of the igneous basement. Shale, graywacke and a block of greenstone, all part of the late Jurassic to early Cretaceous Dothan Formation (Yolla Bolly terrane of the Franciscan complex) are exposed east of this fault. Note that the block of metavolcanic rocks east of the sheeted dike complex could be part of the ophiolite. Perhaps, a thin fault slice correlative with the Rogue Wilderness remnant of the CRO was incorporated into the sedimentary rocks of the Dothan Formation during Cretaceous thrusting and folding.

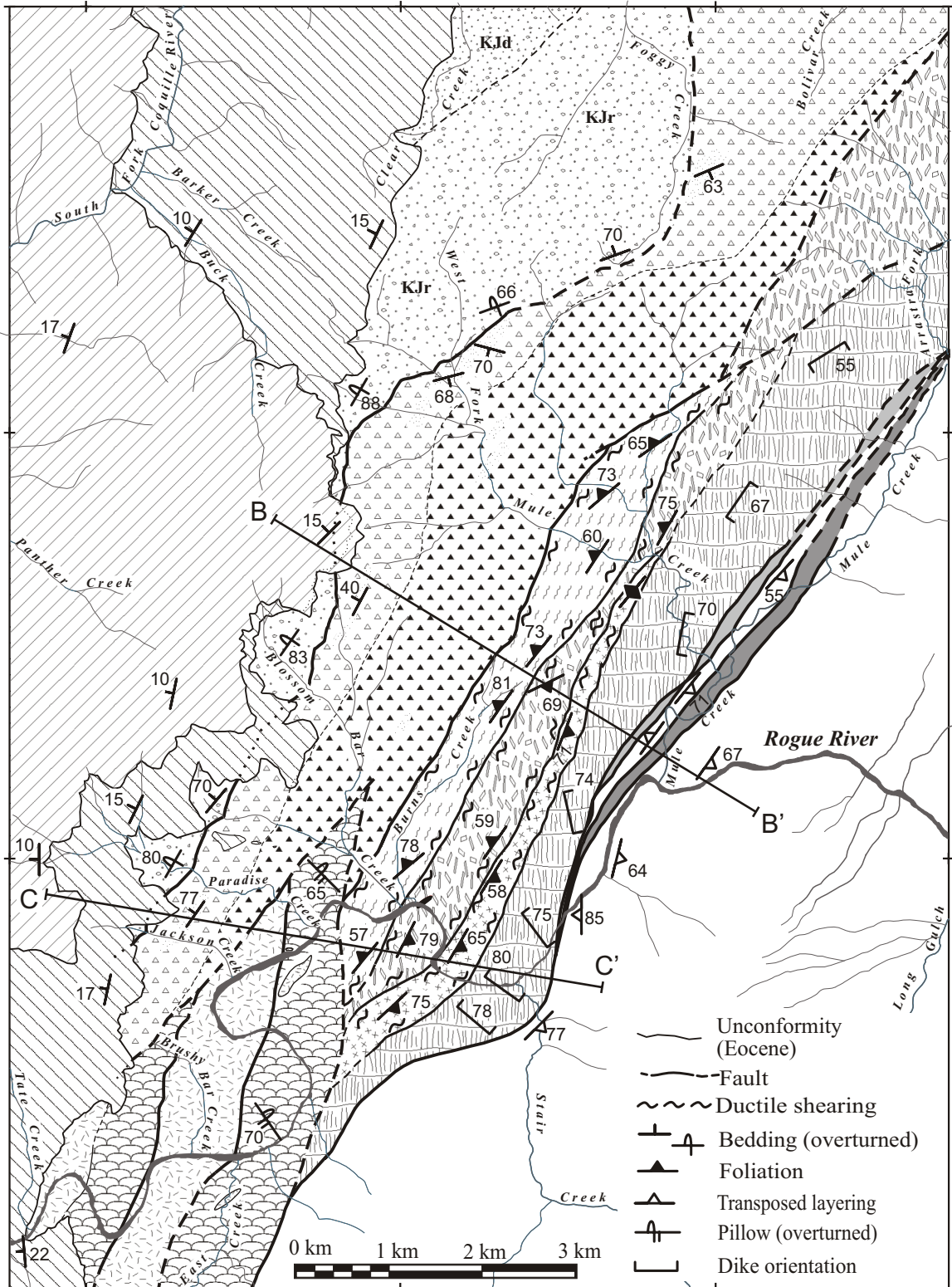
The only contact not exposed on the Rogue River is between the sedimentary rocks of the Myrtle Group and its igneous basement, because it is buried beneath Eocene sedimentary rocks. However, this contact is exposed further north on the west fork of Blossom Bar Creek (plate 1), and outcrops of heavily fractured and sheared rocks occur between metavolcanic rocks and sedimentary rocks of the Myrtle Group, implying a fault contact. All other contacts between the units are exposed along the Rogue River. The structural thickness of the igneous basement in the Wild Rogue Wilderness ranges between 4 and 5 km, and the fault-bounded igneous units and overlying Myrtle Group dip steeply northeast or southwest (figure 2.2b).

The Blossom Bar shear zone, possibly representing a shear contact between the metagabbro unit and the Mule Mountain volcanics (figure 2.2a and 2.2b), is defined as a separate unit because of its considerable size (0.8 km wide) and distinctive assemblage of variably strained rocks. The Blossom Bar shear zone as well as the metagabbro, metatonalite and sheeted dike units are cut by a late fault juxtaposing pillow lavas at their southern terminations (figure 2.2a).

Several of the fault-bounded units identified in the Wild Rogue Wilderness are characteristic of the distinctive rock assemblage of ophiolites (e.g., Penrose conference report, 1972, Coleman, 1977), especially the thick sheeted dike complex. The typical units of ophiolites, however, ranging upward from peridotite tectonite, ultramafic cumulates, gabbro cumulates and gabbro to sheeted dikes and, finally, pillow lavas is only partially preserved (figure 2.3). The likely ophiolitic units are fault bounded and out of sequence. East of the Blossom Bar shear zone, the units include from west to east (1) metagabbro unit,

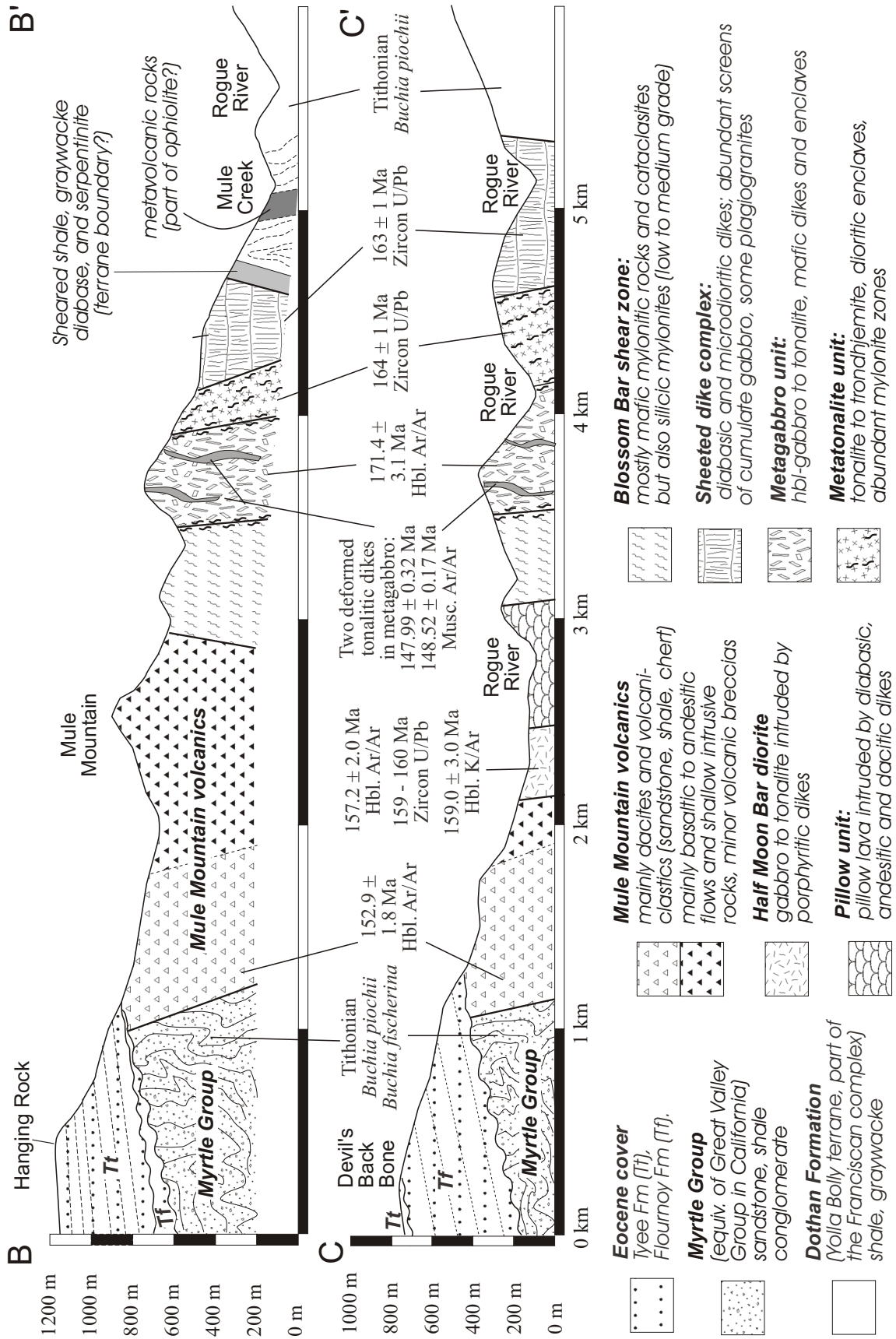
Figure 2.2

- A. Simplified geologic map of the Wild Rogue Wilderness (see plate 1) showing mapped units and structural data. The Myrtle Group and its igneous basement are part of the Snow Camp terrane in SW Oregon. The Dothan Formation (Yolla Bolly terrane) is part of the Franciscan complex.
- B. Cross sections along lines BB' and CC' (figure 2.2a). Isotopic and fossil ages are given. Line BB' is subparallel to line AA' in figure 2.1a.



| | | | | |
|-----------------------------------------|---|--|--------------------------|----------------|
| Tertiary | { | | Tye and Flournoy Fms. | (Myrtle Group) |
| Late Jurassic - early Cretaceous | { | | Days Creek & Riddle Fms. | |
| | { | | Dothan Formation | |
| Late Jurassic | { | | Blossom Bar shear zone | |
| | { | | Half Moon Bar diorite | |

| | | | |
|----------------------------------------|---|--|-------------------------|
| Middle Jurassic - Late Jurassic | { | | Mule Mountain volcanics |
| | { | | Pillows |
| | { | | Sheeted dikes |
| | { | | Metatonalite |
| | { | | Metagabbro |



(2) metatonalite unit and (3) sheeted dike complex. Note that, if the Myrtle Group and its ophiolitic basement were restored to paleohorizontal using a 90° clockwise rotation around the fold axis shown in figure 2.1 (see chapter 4), the sequence consisting of metagabbro, metatonalite, and sheeted dikes would be inverted compared to the typical ophiolite pseudostratigraphy. This indicates the ophiolite remnant is dismembered, which is typical of the CRO remnants in California (e.g. Hopson et al., 1981). However, the presence of a large, ductile (high-T) shear zone is unusual and has been reported only from this remnant of the CRO (Kosanke and Harper, 1996). Pillowed submarine flows (pillow unit) and other extrusive and shallow intrusive volcanic rocks (Mule Mountain volcanics) are exposed west of the Blossom Bar shear zone (figure 2.2a and 2.2b). The pseudostratigraphic level of the ophiolite changes abruptly across the Blossom Bar shear zone.

The relatively wide range of isotopic ages determined in samples from mapped units indicate that older plutonic rocks (metagabbro; hornblende $^{40}\text{Ar}/^{39}\text{Ar}$ cooling age of 171.4 ± 3.1 Ma) as well as younger intrusive (Half Moon Bar diorite; hornblende $^{40}\text{Ar}/^{39}\text{Ar}$ cooling age of 157.2 ± 2.0 Ma and zircon U/Pb ages of 159-160 Ma) and extrusive rocks (Mule Mountain volcanics; hornblende $^{40}\text{Ar}/^{39}\text{Ar}$ cooling age of 152.9 ± 1.8 Ma) occur in the Wild Rogue Wilderness (Kosanke et al., 1999). Also, the cooling age of the mylonitic tonalite-dikes (muscovite $^{40}\text{Ar}/^{39}\text{Ar}$ of ~ 148 Ma) indicate that a late Jurassic deformational event affected the Rogue Wilderness ophiolite. The presence of younger and older rocks indicate that not all mapped units are part of the ophiolite remnant. Thus, the igneous basement of the Snow Camp terrane exposed in the Wild Rogue Wilderness is a composite unit.

The reconstructed ophiolite sequence (figure 2.3) would have presumably consisted of, from base to top, serpentinites, metatonalite (164 ± 1 Ma), sheeted dikes (163 ± 1 Ma), and an exceptionally thick extrusive sequence. The metagabbro unit has a cooling age of 171.4 ± 3.1 Ma (hornblende $^{40}\text{Ar}/^{39}\text{Ar}$ analysis), which is significantly older than the age of the sheeted dike complex. The metagabbro unit could have a much older igneous age. In subsequent chapters, it is discussed whether or not the metagabbro is part of the ophiolite. The age of the pillowed extrusive sequence is constrained by the intrusion of the Half Moon Bar diorite (159-160 Ma). Also, cherts within pillowed volcanic flows in the Snow Camp Mountain area yielded well-preserved radiolaria which are of Callovian to middle Oxfordian age (chert samples taken

by G.D. Harper, 1996; biostratigraphic/chronostratigraphic determination by E.A. Pessagno, 1996). It is likely that the pillow unit in the Wild Rogue Wilderness are also of Callovian to middle Oxfordian age. Probably the pillow unit is as old as the other ophiolitic units (163-164 Ma). The uppermost portion of the Mule Mountain volcanics may represent a younger upper volcanic member, and thus, may not be part of the ophiolite. However, the uppermost crustal sequence of the Rogue Wilderness ophiolite consisting of pillow unit and Mule Mountain volcanics is very similar to the Del Puerto ophiolite, California, which has also an exceptionally thick extrusive sequence containing 157 Ma volcanic rocks (Evarts, 1977; Hopson et al., 1981; Evarts et al., 1992), suggesting an extended magmatic history (Kosanke et al., 1999).

The inferred ophiolite pseudostratigraphy is shown in figure 2.3, depicting also the types of contacts from one pseudostratigraphic level to another. In general, the units are separated by faults. The metagabbro unit may or may not be part of the ophiolite. Assuming the metatonalite unit represents plutonic rocks comagmatic with the sheeted dikes and pillows, it forms the “high-level gabbro” (diorites and plagiogranites can be present) of the ophiolite. Xenoliths and stopped blocks are common in high-level gabbro such as the Josephine ophiolite (Harper, 1984). The screens of gabbro in the sheeted dike complex represent the top-most fragments of high-level gabbro, and the dikes in the pillow unit represent the highest appearance of the dike swarm. The cherts found interlayered with volcanoclastic sediments near the top of the Mule Mountain volcanic unit are interpreted to mark the top of the ophiolite. The dated dacitic sample (153 Ma) near the contact with the Myrtle Group occurs above the cherts and is not part of the ophiolite.

The middle and upper crustal sections of an ophiolite sequence are preserved in the Wild Rogue Wilderness ranging upward from high-level gabbro to the extrusive sequence (Rogue Wilderness ophiolite). The lower members of an ophiolite assemblage, such as the cumulate sequence (although present as screens in the sheeted dike complex) and mantle sequence, are not present.

In subsequent sections, the units are described from base to top following the ophiolite pseudostratigraphy in figure 2.3 (serpentinites, metagabbro unit, metatonalite, sheeted dikes, pillows). The youngest units, which are not part of the ophiolite are described last (Mule Mountain volcanics?, post-ophiolite intrusions, Myrtle Group).

Figure 2.3

**Reconstruction of the
Rogue Wilderness ophiolite**

Columnar section showing likely reconstruction of ophiolitic units identified in the Wild Rogue Wilderness compared to a typical pseudostratigraphy (e.g., Penrose conference, 1972) of ophiolites shows only the middle and upper crustal section is preserved. The metagabbro unit may not be part of the ophiolite

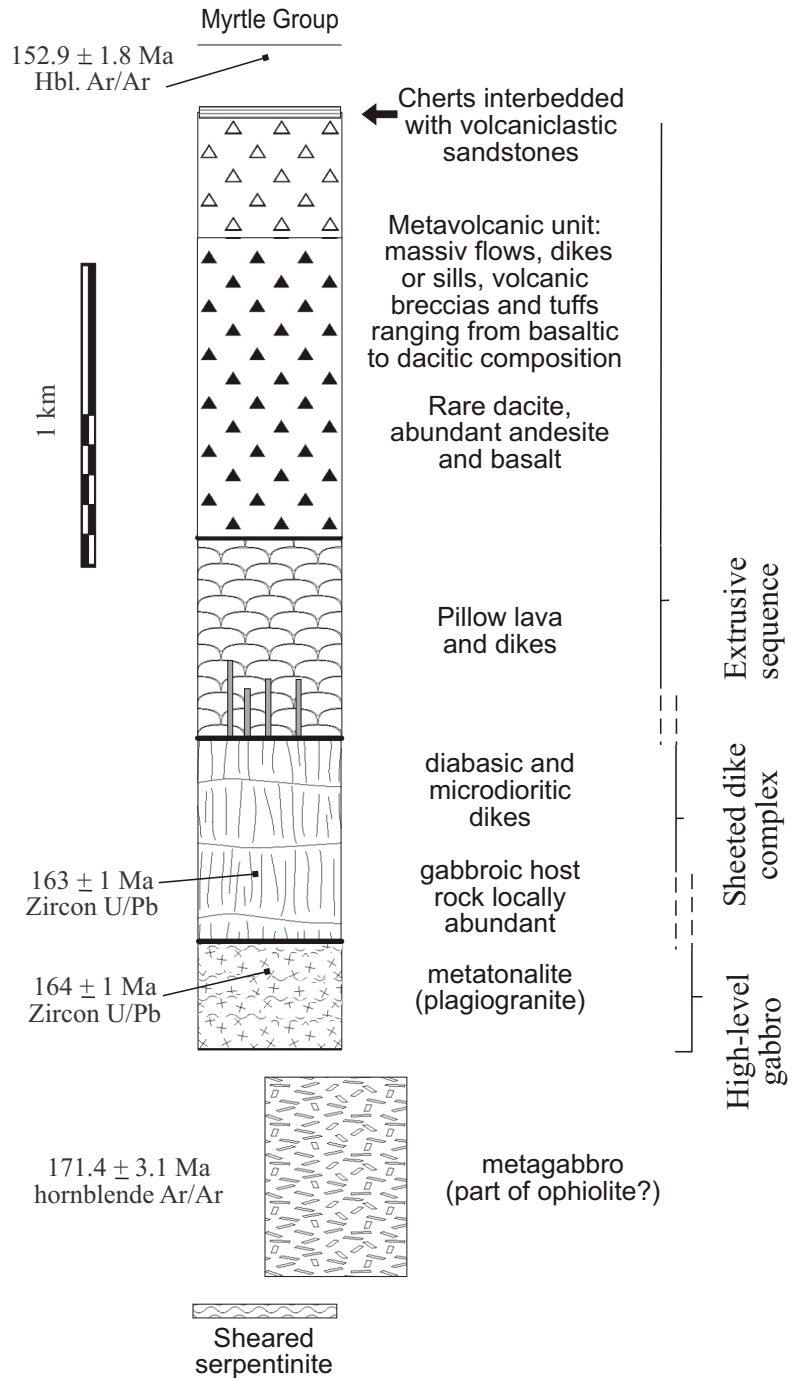


Table 2.1a: Summary of $^{40}\text{Ar}/^{39}\text{Ar}$ apparent ages

| Sample | Unit | Longitude Latitude | Description | Min- eral | Plateau or preferred age (Ma \pm 2s) | MS WD | % ^{39}Ar in plateau |
|--------------------------------------------------------|--------------|-------------------------|-------------------|--------------|--------------------------------------------------------------------|--------------|-------------------------------------|
| O/C-376 | HMB diorite | 123°56'28" 42°41'31" | hbl qtz diorite | hbl | 157.2 \pm 2.0 | 1.96 | 91.1 |
| O/C-373b 1 st run 2 nd run | metagabbro | 123°54'39" 42°42'05" | hbl gabbro | hbl | 171.4 \pm 3.1 [†] 166.5 \pm 5.3 174.0 \pm 3.9 | 0.64 3.33 | 100.0 100.0 |
| GDH-5a | MM volcanics | 123°54'18" 42°45'36" | hbl plag dacite | hbl | 152.9 \pm 1.8 | 2.09 | 84.1 |
| GH-97-20 | metagabbro | 123°54'42" 42°42'11" | musc gar tonalite | mus c | 147.99 \pm 0.32 | 4.03 | 97.4 |
| O/C-372b | metagabbro | 123°54'38" 42°42'01" | musc gar tonalite | mus c | 148.52 \pm 0.17 | 1.57 | 98.2 |

The $^{40}\text{Ar}/^{39}\text{Ar}$ ages were determined at the New Mexico Geochronology Research Laboratory by Matthew Heizler (see appendix B for analytical and age calculation methods and age spectrum diagrams).

HMB Half Moon Bar

MSWD mean sum weighted deviates

MM Mule Mountain

[†] weighted mean of O/C-373b runs

Table 2.1b: Summary of U/Pb zircon ages

| Sample | Unit | Longitude / Latitude | Description | Age |
|--------|---------------------|------------------------|-----------------|----------------|
| SC-1 | Sheeted dike compl. | 123°53'57" / 42°41'53" | anorthosite | 163 \pm 1 Ma |
| SC-2 | metatonalite unit | 123°54'37" / 42°41'49" | trondhjemite | 164 \pm 1 Ma |
| SC-11 | HMB diorite | 123°56'32" / 42°41'38" | hbl leucogabbro | 160 \pm 1 Ma |
| SC-12 | HMB diorite | 123°56'22" / 42°40'48" | trondhjemite | 159 \pm 1 Ma |
| SC-13 | HMB diorite | 123°57'30" / 42°40'39" | trondhjemite | 159 \pm 1 Ma |

The U/Pb ages were determined on abraded zircon separates at the California Institute of Technology, Pasadena by Jason B Saleeby (written communication, 1999).

Table 2.2: Mineral abbreviations

| | | | | | |
|-----|---------------|------|---------------|------|-------------------|
| ab | albite | ep | epidote | ox | oxide (opaque) |
| ac | actinolite | gar | garnet | plag | plagioclase |
| an | anorthite | hbl | hornblende | pr | prehnite |
| ap | apatite | lau | laumontite | pu | pumpellyite |
| cc | calcite | mt | magnetite | qtz | quartz |
| chl | chlorite | musc | muscovite | su | sulfide |
| cpx | clinopyroxene | ol | olivine | ti | titanite (sphene) |
| cz | clinozoisite | opx | orthopyroxene | | |

2.4 Serpentinites

Several, 1 to 20 meter-wide and tens-of-meter long slivers of sheared serpentinite are exposed along the fault between the sheeted dike complex and the Dothan formation and along the east margin of the Dothan volcanic unit (plate 1). These slivers may represent serpentinitized remnants of upper mantle section of ophiolite, which is the thickest member of most ophiolite sequences. A thick unit of serpentinites occur 10 km along strike to south of mapped area (Gray et al., 1982; Ramp and Moring, 1986). Also, serpentinites crop out west, east and south of Agness (figure 2.1a).

2.5 Metagabbro unit

2.5.1 Lithology

The metagabbro unit is composed of a suite of foliated, medium grained plutonic rocks ranging in composition from hornblende gabbro to tonalite-trondhjemite. All of these contain abundant mafic enclaves and are intruded by mafic, fine grained deformed dikes. Compositional layering as observed in most ophiolites could not be identified in the field, and the more fractionated, felsic phases seem to be randomly distributed throughout the unit. Possibly, magmatic- and solid-state deformation, which evidently affected this unit, obliterated any zoning or stratification.

Table A1a (appendix A) gives a petrographic summary of discussed samples from the metagabbro unit. The main phase in the metagabbro unit is a medium grained, mesocratic hornblende gabbro that hosts fine grained mafic dikes and enclaves (figure 2.4, figure 2.5). The mafic gabbro as well as the mafic dikes and enclaves are relatively uniform in composition and differ mainly in grain size and texture. They consist of 45-55% dark green, uniformly colored hornblende and 40-50% zoned plagioclase with calcic cores (An_{68-85}), and a few percent magnetite and accessory apatite. In most outcrops, the gabbro is foliated (figure 2.5) but is locally isotropic having a hypidiomorphic granular texture.

The minor, but more fractionated phases in the metagabbro unit include medium- to fine-grained leucocratic gabbro, quartz-bearing gabbro, quartz-gabbro and tonalite-trondhjemite (figure 2.6). The abundance of the minor phases in the metagabbro unit decreases from mesocratic gabbro (most abundant)

to leucocratic gabbro to quartz gabbro to tonalite-trondhjemite (least abundant). Similar to the main-phase gabbro, they consist of hornblende, calcic plagioclase (An 48-68), magnetite and apatite, in addition to a variable amount of quartz. The minor, fractionated rocks are also foliated, intruded by mafic dikes and contain mafic enclaves (figure 2.6). Leucocratic gabbro and other felsic rock types form schlieren in the medium grained main-phase metagabbro (figure 2.7).

Peraluminous tonalitic dikes that contain no mafic enclaves also occur in the metagabbro unit. These tonalites are compositionally distinct from all other quartzo-feldspathic rocks in the metagabbro unit. Also they appear to be younger (muscovite $^{40}\text{Ar}/^{39}\text{Ar}$ cooling age of 148 Ma). Therefore, they are described in a later section (2.10.1).

2.5.2 Structure and metamorphism

The metagabbro unit is in fault contact with the metatonalite unit to the east and the Blossom Bar shear zone to the west (figure 2.2a and 2.2b). The basic structure of the metagabbro unit is defined by a NE-SW trending and steeply dipping foliation (figures 2.5, 2.6 and 2.7) and gently NE plunging mineral lineation. Typically, the fine grained gabbroic enclaves are elongate, flattened, and aligned subparallel with foliation in the host gabbro (figure 2.4).

The enclaves are often irregular, globular or lenticular in shape and have pointed or wispy terminations (figure 2.5). These are characteristics of enclaves that indicate magma mingling and flow (Vernon et al., 1988). Mafic dikes intruding the gabbro have no chilled margins and are subparallel with the magmatic foliation. Also, the dikes are attenuated, and locally folded. Isolated, deformed dikes grade along strike of the foliation into zones that contain abundant enclaves suggesting disruption of the dikes due to deformation. The enclaves as well as the dikes display a foliation and lineation subparallel to that in the host gabbro (figure 2.5).

Similarly, the minor phases in the metagabbro unit, such as leuco-gabbro, quartz-bearing gabbro, quartz gabbro and tonalite-trondhjemite, are also intruded by mafic dikes and/or contain mafic enclaves. Typically, the fine grained dikes and enclaves are highly attenuated and usually occur as laminae and schlieren of less than 3 cm width and up to several meters length, are tabular or lenticular in shape, and

display a foliation and lineation subparallel to that of the medium grained felsic host rock (figure 2.6). The boundaries between mafic and more felsic laminae are relatively sharp, some 'mixing', however, was observed: tiny fractions of the fine grained mafic enclaves consisting of only few crystals occur within the more felsic laminae. Also, thin laminae, wispy lenses, and even single grains of the felsic rock types are found within the fine grained mafic intrusions producing a schlieren-type layering (figure 2.7). Furthermore, late, fine grained mafic dikes having a foliation subparallel to that in the host rock cut medium- to fine-grained gabbro having schlieren-type layering (figure 2.7). These field observations indicate that the foliation and mineral lineation (defined by the alignment of igneous minerals, figure 2.8) occurred due to magmatic flow and, thus, the layering is interpreted as magmatic flow foliation. Alignment of minerals and enclaves, as well as attenuation, folding and disruption of dikes to smaller fragments (elongate enclaves, thin tabular selvages, clusters of grains) are interpreted to have occurred in a magmatic environment. The stretched enclaves, thin tabular selvages, and irregular schlieren probably represent magma globules that were deformed in a magmatic environment (Vernon, 1984, Vernon et al, 1988) (see also chapter 4).

Other structures and metamorphic features in the metagabbro unit include retrograde alteration of mafic and quartzo-feldspathic rocks, epidiosites, mylonitic zones, cataclasites, mineralized faults and veins and micro-shear bands. Typically, plagioclase is replaced by $cz+ab\pm ep\pm chl\pm musc$ and appears cloudy in thin section. Hornblende is uniform, dark-green in color implying a metamorphic origin. However, relic cpx in amphibole was not observed. Mineral assemblages identified in crosscutting veins include $ep\pm qtz$, $pr\pm qtz$, $pu\pm qtz$, $qtz+su$. The mineral assemblages in the metagabbro, mineralized faults, and veins appear to be very similar to other ophiolites for which subseafloor hydrothermal alteration is inferred (e.g., Josephine ophiolite: Harper et al, 1988; Alexander et al., 1993; Troodos ophiolite: Schiffmann and Smith, 1988; Semail ophiolite, Gregory and Taylor, 1984). Also, the complete replacement of the metagabbro by epidiosite ($ep+qtz\pm chl$) involves metamorphism and a very high water/rock ratio which can be provided during subseafloor hydrothermal alteration (e.g. Schiffmann and Smith, 1988; Harper et al., 1988). Crosscutting relationships of magmatic flow foliation and mylonites as well as mineralized cataclasites, faults and veins indicate that deformation was contemporaneous with cooling and hydrothermal alteration;



Figure 2.4

Photograph of typical medium grained gabbro of the metagabbro unit (O/C-385.1) containing abundant fine grained mafic enclaves. The enclaves and the host gabbro are very similar in composition and contain hornblende, calcic plagioclase, and accessory magnetite and apatite. The enclaves are elongate and aligned parallel to the magmatic flow foliation of the host gabbro. Two mineralized faults (cataclastic) cut the gabbro at moderate angles to the flow foliation (lower half of the photograph). The upper of the two faults developed within a 2 cm wide ductile shear band indicating a change from ductile to brittle deformation with decreasing temperature. The lens cap is 5.5 cm in diameter.

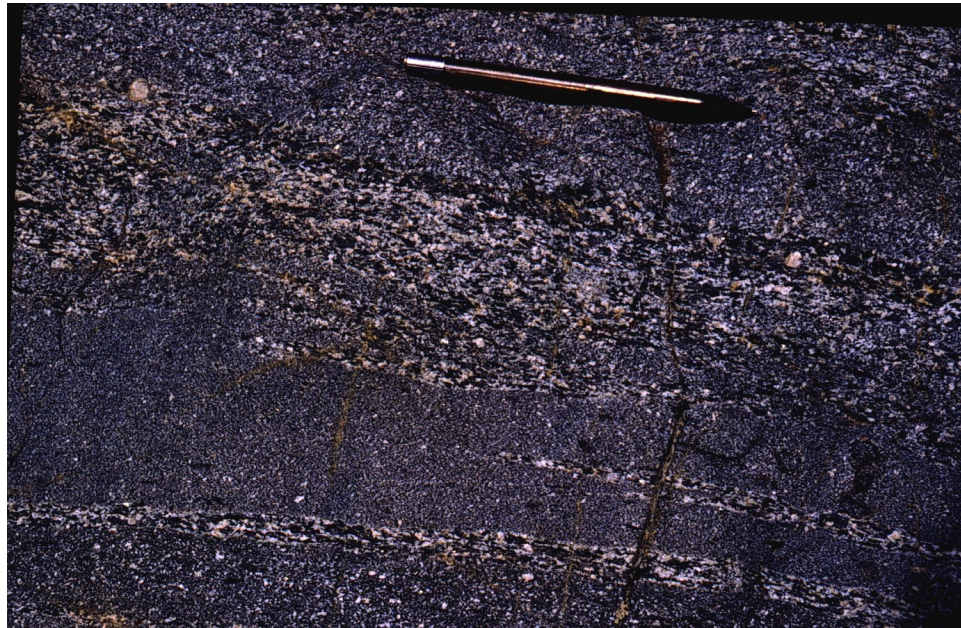


Figure 2.5

Close-up photograph of outcrop in metagabbro unit consisting mainly of mafic enclaves (O/C-385.2). The flow foliation in the fine grained enclaves is subparallel to that in the medium grained host gabbro. The terminations of the enclaves are pointed or wispy, and small selvages (~ 1 cm) occur within the medium grained gabbro. Overall, a continuum in shape of gabbroic enclaves exists ranging from deformed, dike-like intrusions to round and ellipsoidal enclaves (figure 2.4) and ultimately to thin, tabular or ellipsoidal selvages and schlieren (this photograph and figure 2.6). Note pen for scale.

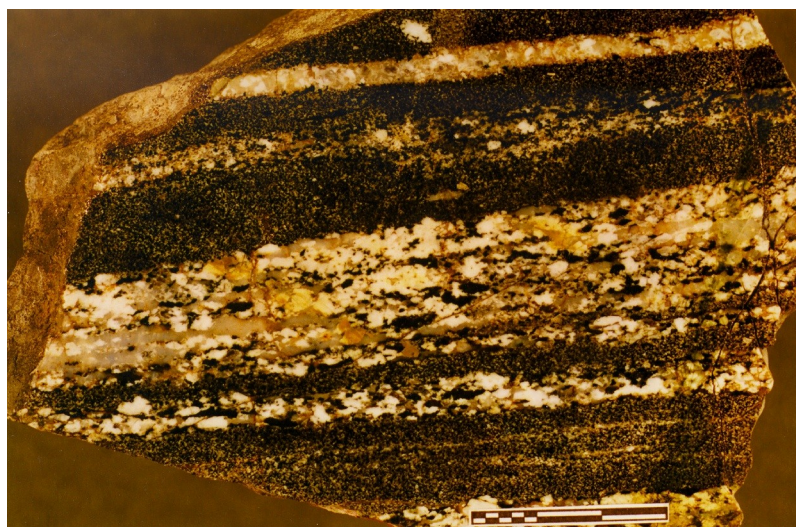


Figure 2.6

Photograph of compositionally layered metagabbro (GH-97-16b) characterized by laminae and lenses of fine-grained gabbro in medium-grained leucocratic quartz-gabbro and tonalite. The fine grained mafic metagabbro probably intruded the felsic fractionates of a plutonic suite ranging in composition from hornblende gabbro to tonalite-trondhjemite. Schlieren, thin tabular selvages and single crystals (arrow) of the felsic rock occur in the fine grained mafic layers. Tiny selvages (red outline) of mafic rock, occasionally consisting of only a few crystals, occur within the felsic laminae as well. Thus, mechanical mixing of felsic and mafic magma is inferred. Note also that the quartz grains are stretched, and dynamic recrystallization of quartz is evident in thin section. The magmatic flow foliation is clearly overprinted by solid-state deformation. The structures are interpreted as follows: the mafic magma intruded a crystal rich felsic magma as dikes, which was followed by attenuation and mixing due to magmatic flow resulting in a thinly banded rock. Later ductile shearing overprinted the magmatic foliation. The scale bar is 3 cm long.

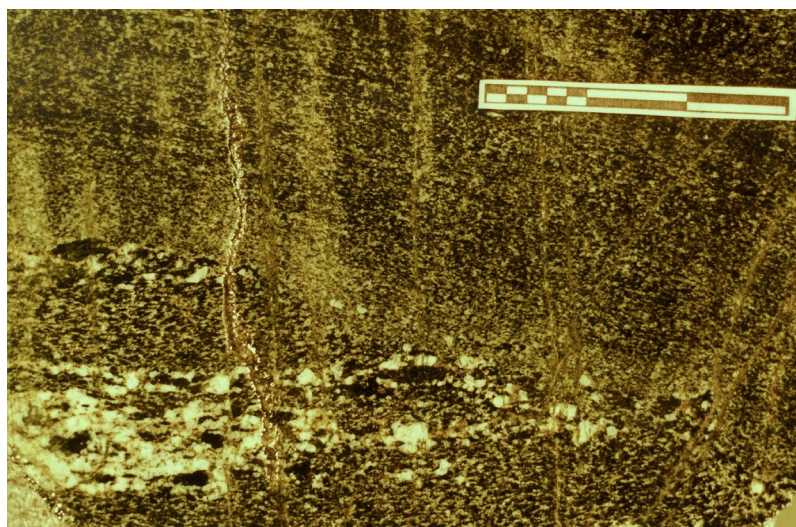


Figure 2.7

Photograph showing the relationship between three different phases of gabbro (O/C-374b) easily distinguishable by their grain size. The two oldest phases are the medium grained leuco-gabbro (largest grain size) and the mafic metagabbro (second largest grain size). Mixing of these two magmatic phases and magmatic flow produced the schlieren-type layering. Note that clusters of grains (red outline) or single grains of one phase can be found within the other. The gabbro with the schlieren-type layering was subsequently cut by a late mafic dike (smallest grain size) which has no chilled margins and a magmatic flow foliation subparallel to the host rock and. The alignment of the minerals in the late dike is likely due to continued magmatic deformation after dike intrusion. Single, coarse-grained crystals from the leuco-gabbro occur as xenocrysts in the mafic dike (arrow). The scale bar is 3 cm long.

that is deformation ranges from hypersolidus through retrogressive hydrothermal metamorphism.

Therefore, it is necessary to discuss evidence for ductile deformation in context with metamorphism.

2.5.3 Evidence for ductile deformation in the metagabbro unit

Common features indicating solid-state ductile deformation in metagabbro samples with magmatic flow foliation (figure 2.8) include bent plagioclase grains and tapered deformation twins (figure 2.9). These features occur in most samples and can be attributed to crystal plastic behavior (e.g., Passchier and Trouw, 1996). Evidence for intense grain size reduction due to dynamic recrystallization, neocrystallization or grain abrasion was only found in samples that show a fabric similar to proto-mylonites and mylonites. Several mylonitic samples are distinguished based on composition and fabrics.

Quartz-free mylonitic samples were taken from rare, narrow bands (1-15 cm) cutting magmatic foliation at low to medium angles (e.g., figure 2.4, ductile shear band paralleled by brittle fault). Most of these shear bands occur close to the contacts of the metagabbro unit with the Blossom Bar shear zone and with the metatonalite unit, whereas only a few mafic mylonitic rocks are found within the central portion of the metagabbro unit. The matrix of these mylonitic rocks is extremely fine grained (figure 2.10) and, in places, wraps around plagioclase and hornblende porphyroclasts (figure 2.11). Generally, replacement of plagioclase by metamorphic minerals in the mylonite zones is much more complete than anywhere else in the metagabbro unit. In all except one of the mylonitic samples, plagioclase is replaced by $cz+ab+ep\pm chl\pm musc$ and forms cloudy aggregates which are stretched into long ribbons and, occasionally, occur as thin, cloudy laminae between fine grained laminae of hornblende. Similarly, most plagioclase porphyroclasts are replaced by $cz+ab+ep\pm chl\pm musc$ and appear cloudy in thin section. Commonly, they are ovoid or augen-shaped and fractured. The least altered plagioclase porphyroclasts display wedge-shaped twinning and undulatory extinction. In the only mylonitic sample that shows no evidence of retrograde alteration of plagioclase whatsoever (sample O/C-384), plagioclase porphyroclasts with recrystallized edges occur within an extremely fine grained matrix of hornblende and recrystallized plagioclase. Grain size reduction of plagioclase by dynamic recrystallization is inferred for sample O/C-384.

Other common features in all mylonitic samples include ubiquitous fractures and microfaults in plagioclase porphyroclasts (figure 2.11). Occasionally, plagioclase grains are elongated from breaking along microfractures, forming bookshelf structures. Hornblende porphyroclasts are augen-shaped (figure 2.11), and they usually retain a dark-green, uniform color. An investigation in one of the mylonitic samples (O/C-13-S22) determining the asymmetry of the pleochroism using the method of Hall (1984) revealed that about 65% of the hornblende-augen have a lattice preferred orientation. This method revealed that the a-axes are inclined in an uniform direction in 65% of the hornblende-augen that have c-axes subparallel with foliation. This may be attributed to glide on (100) [001] (Dollinger and Blacic, 1975; Biermann, 1981). Fractures and microfaults in hornblende porphyroclasts are ubiquitous and, in places, hornblende crystals are bent. Distinct domains having slightly different extinction angles within the bends suggests that the strain is accommodated by microfracturing. Interestingly, the fine-grained hornblende in the matrix of the mylonitic zones is often uniform and dark-green in color. Probably, they are minute cleavage fragments that were not altered during retrograde conditions. The abundant brittle features in hornblende suggest that grain size reduction of hornblende occurred mainly by fracturing and grain abrasion accompanied by little or no alteration of hornblende. Brodie and Rutter (1985) point out that the distinction between grain size reduction produced by cataclasis and recrystallization is difficult to make for amphibole aggregates, and criteria applied to quartz aggregates cannot be extended to metabasic rocks. Thus, an interpretation of the microstructures in the fine grained amphibole matrix is difficult to make, i.e. whether grain size reduction occurred by cataclasis/grain abrasion in a deforming matrix or recrystallization/neocrystallization. Consequently, the classification of such rocks is problematic, i.e. whether they represent foliated cataclasites or mylonites.

The mylonite zones occurring in quartz-free gabbroic rocks are usually parallel to or cut by mineralized cataclasites, faults or veins. In thin section, randomly oriented rock fragments with mylonitic fabric are found in an extremely fine grained, coherent matrix. Clearly, a cataclastic flow fabric overprints the mylonitic fabric. Cement of the cataclasis and veins contain ep, chl, pr, ab, qtz, su, cc. The crosscutting relationships of mineralized faults and veins indicate retrograde conditions during deformation.

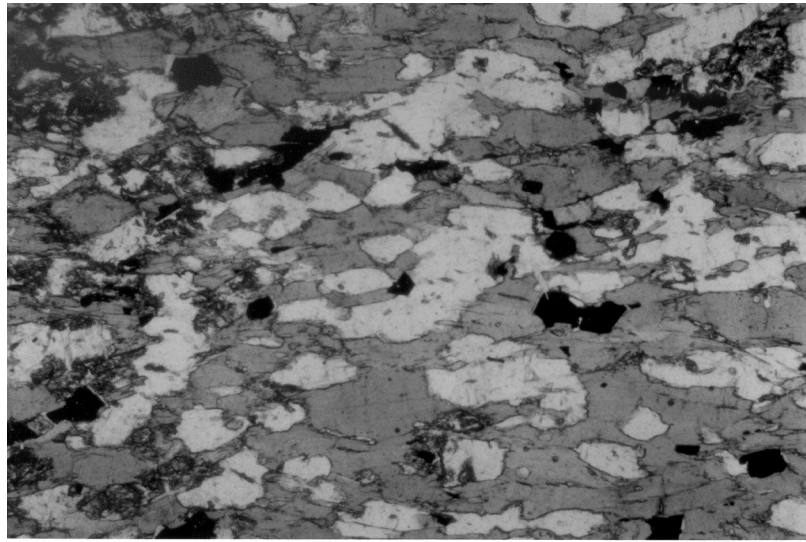


Figure 2.8

Photomicrograph of fine grained mafic dike in metagabbro (O/C-374b) showing typical texture and composition of gabbroic rocks in the metagabbro unit. Plagioclase is white, hornblende gray and magnetite black. Plagioclase and hornblende are aligned (crystal shape fabric) defining the foliation and range from anhedral to subhedral in shape. The width of the photograph is 2.14 mm.

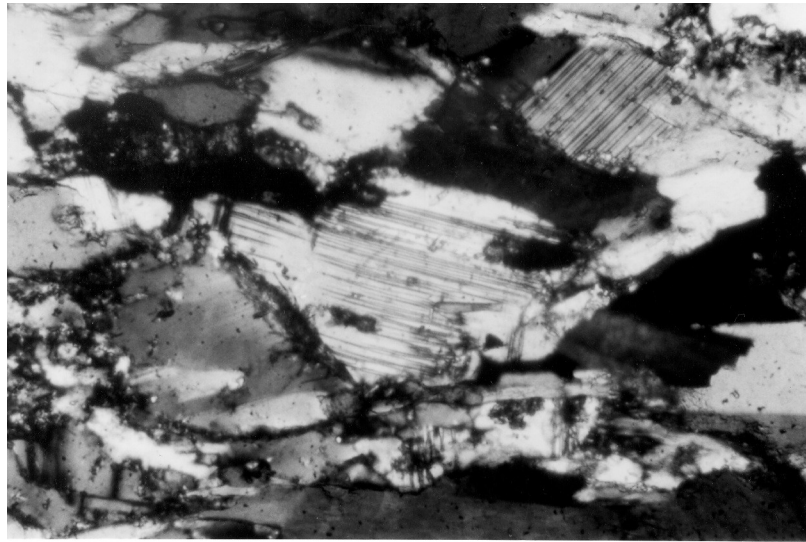


Figure 2.9

Photomicrograph of plagioclase in weakly foliated mafic dike in metagabbro (O/C-374b). Typically, plagioclase grains in most samples have tapering deformation twins. The wedge-shaped twins are thought to indicate temperatures of deformation between 300°C and 400°C (Passchier and Trouw, 1996, p.49). The width of the photograph is 0.54 mm.

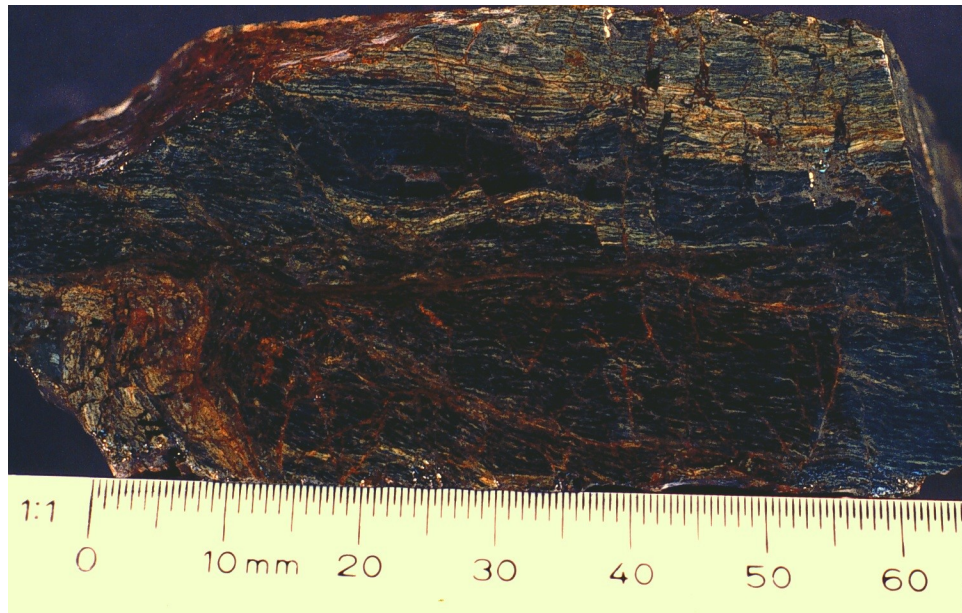


Figure 2.10

Photograph of slabbed and polished sample from a narrow (13cm) mylonite zone (O/C-13-S22.1) which is paralleled by a prominent mineralized fault in the metagabbro unit. Fracturing and cataclastic overprint of mylonites in the metagabbro unit is common. The sample is strongly foliated, and the extremely fine grain size compared to other gabbroic rocks indicates intense grain size reduction during solid-state deformation.



Figure 2.11

Photomicrograph of typical mylonitic metagabbro (from figure 2.10, O/C-13-S22.2) showing plagioclase and hornblende porphyroclasts in a fine grained matrix. Porphyroclasts are ovoid or augen-shaped and occasionally have tails. The matrix consists of fine hornblende and a range of greenschist facies minerals such as actinolite, chlorite, epidote, clinozoisite, and albite. The width of the photomicrograph is 2.14 mm.

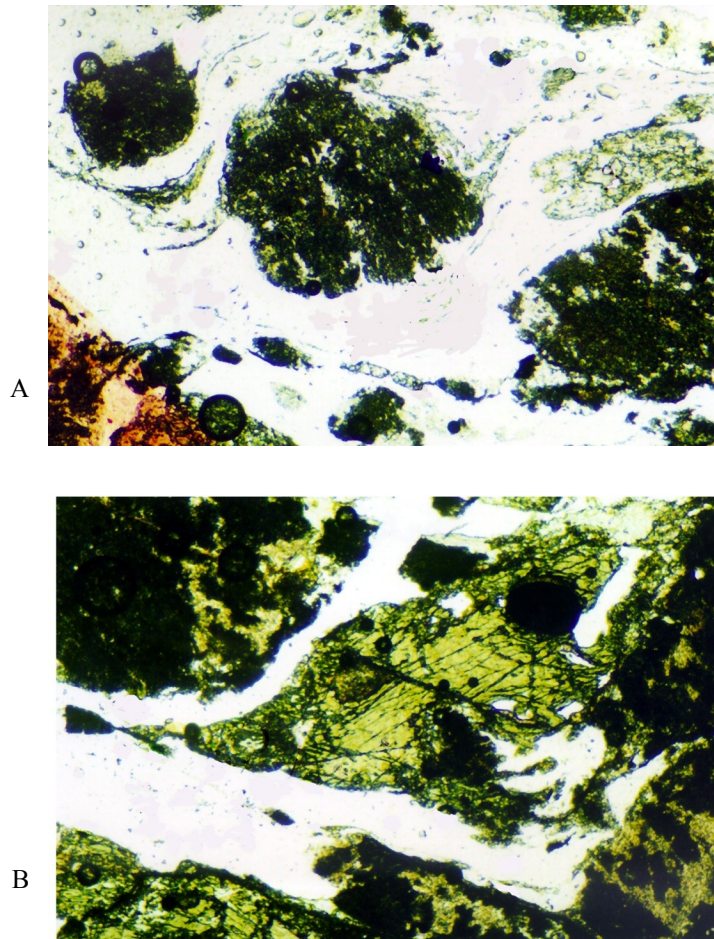


Figure 2.12

- A. Photomicrograph showing typical plagioclase porphyroclasts in quartz bearing rocks (O/C-13-S28) in the metagabbro unit. Plagioclase is completely replaced by a dark cloudy mass consisting of epidote or clinozoisite, chlorite and possibly albite. The matrix consists of very fine-grained, strongly recrystallized quartz. Grain size reduction of what used to be plagioclase probably occurred by abrasion during deformation. The height of the photograph is 2.14 mm. The sense of shear is dextral.
- B. Photomicrograph showing typical augen-shaped hornblende porphyroclast in quartz bearing rocks (O/C-13-S28) in the metagabbro unit. Hornblende is uniformly colored and the wings of these porphyroclasts consist of same-color hornblende as well as of epidote and chlorite. Epidote and chlorite occur also as alteration in fractures and cracks in hornblende. The height of the photograph is 2.14 mm. The sense of shear is dextral.

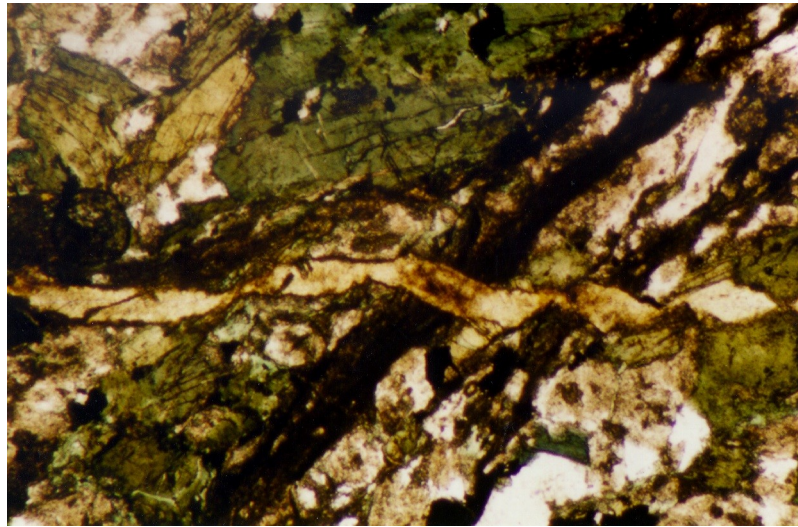


Figure 2.13

Photomicrograph showing a shear band cut by an epidote vein (ep). The dark cloudy mass in the shear band consists of very fine-grained chlorite and epidote. This sample (O/C-229) is from a section of hornblende-quartz diorite within the metatonalite unit and consists of variably colored hornblende (hbl), plagioclase (pl) and quartz (qz). The width of the photomicrograph is 2.14 mm.

The minor, fractionated phases in the metagabbro unit contain variable amounts of quartz. Such quartz-bearing rocks are ductily deformed (e.g. figure 2.6). Actually, the greatest number of shear bands that indicate strain due to ductile deformation coincide with the quartz-bearing and quartz-rich phases in the metagabbro unit. These zones are characterized by a moderate to strong foliation with augen-shaped or ovoid plagioclase and hornblende (figure 2.12), whereas the interlayered mafic rocks show little strain and retain largely a magmatic flow fabric. In moderately deformed quartz-rich rocks (i.e. protomylonites), hornblende and plagioclase retain their subhedral shape whereas quartz is moderately recrystallized. Relic, elongate grains show sweeping undulatory extinction and consist of subgrains. Hornblende is, as elsewhere in the metagabbro unit, dark-green, uniformly colored. The wings protruding from augen-shaped porphyroclasts consist of dark-green hornblende fragments, epidote and chlorite (figure 2.12b). Grain size reduction of hornblende apparently occurred by fracturing and abrasion accompanied by some alteration to chlorite and epidote. In contrast, plagioclase is completely replaced forming dark-cloudy ovoid masses with s- or d-type wings (figure 2.12a). The cloudy masses inferred to represent replaced plagioclase seem to become 'eroded' during deformation. Grain size reduction of quartz occurred mainly by dynamic recrystallization (subgrain rotation probably dominant). Interestingly, S/C-type structures are often observed in mylonites that formed in quartz-bearing rocks of the metagabbro unit. Strongly recrystallized quartz seems to form C-type shear bands, and the S-plane is defined by the obliquity of hornblende augen or prisms.

Quartz-rich rocks in the metagabbro unit are strongly foliated and commonly, much finer grained than the quartz-bearing and quartz-free mylonitic rocks. Quartz-rich, strongly deformed rocks in the metagabbro unit can be classified as mylonites and ultramylonites which predominantly consist of epidote, quartz, chlorite and albite. These mylonites are very similar to the mylonites in the metatonalite unit (section 2.6.3).

In thin section, mafic as well as quartz-bearing rocks having predominantly magmatic fabric have <<1 mm wide, relatively continuous shears which are cut by epidote veins. Microprobe analysis revealed fine grained chlorite and epidote in the microshears (figure 2.13).

2.5.4 Interpretation of metamorphic hornblende and age constraints

Petrographic descriptions of regionally metamorphosed (Laird, 1982) and hydrothermally altered metabasic rocks (Alexander et al., 1993; Harper et al., 1988; Cann, 1977) may be summarized as follows: pale green actinolite and actinolitic hornblende are part of the metamorphic assemblage in metabasic rocks that were altered during greenschist to lower amphibolite facies metamorphic conditions, whereas dark-green to greenish brown hornblende are characteristic of amphibolite facies conditions. Furthermore, regionally metamorphosed rocks equilibrate over a long period of time at relatively constant P-T conditions typically resulting in an uniform color of amphiboles. In contrast, relatively fast cooled oceanic rocks contain variably colored amphiboles that partially equilibrated over a large range of temperatures ranging from igneous (brown hornblende) to amphibolite (green brown and dark green) to greenschist facies (pale green).

The dark-green hornblende in the metagabbro unit is in contact with plagioclase having oligoclase composition (and occasionally less calcic). The core to rim zoning in the igneous plagioclase is bytonite (An₇₅₋₈₁) to Andesine/Labradorite (~An₅₀). Oligoclase in contact with hornblende could be part of igneous zoning of plagioclase, however, the results of the determination of the temperatures of equilibration using the hornblende-plagioclase geothermometer of Holland and Blundy (1994) indicate metamorphic temperatures of equilibration (~600°C at 2kbar) based on mineral compositions (chapter 3). It appears that there is an amphibolite facies metamorphic assemblage present consisting of calcic hornblende and oligoclase.

The greenschist facies minerals (ab+ep+cz+chl±musc±qtz±ac) in samples from the metagabbro unit, especially in ductile to brittle deformed rocks, indicate that deformation and hydrothermal alteration are closely interlinked, and that much of the solid-state deformation occurred at greenschist facies conditions. However, the dark-green, uniformly colored hornblende in the metagabbro appears to be relatively unaltered (rare ac and ac-hbl, some ep+chl seem to replace dark-green hbl), suggesting that the hornblende did not re-equilibrate at lower amphibolite facies or greenschist facies conditions. It appears that the dark-green hornblende and oligoclase equilibrated at amphibolite facies metamorphic conditions prior to solid state deformation.

It is suggested that the metagabbro unit was metamorphosed during earlier regional metamorphism or plutonism for the following reasons: (1) hornblende is uniform, dark green in color similar to amphibole in regionally metamorphosed rocks (e.g., Laird, 1982), and dissimilar to amphibole formed during subseafloor hydrothermal metamorphism (e.g., Alexander et al., 1993; Harper et al; 1988; Cann, 1977), (2) hornblende and plagioclase (oligoclase) equilibrated at temperatures of ~600°C (assuming 2 kbar), based on mineral compositions of hornblende-plagioclase pairs (chapter 3). The greenschist facies mineral assemblage found in cement of crosscutting faults, cataclasites, and veins indicate retrograde conditions. The type of alteration (i.e. epidiosites) and the mineral assemblage indicating retrograde conditions are typical of subseafloor hydrothermal alteration. Later greenschist facies hydrothermal metamorphism clearly overprinted the amphibolite facies mineral assemblage. (3) The hornblende $^{40}\text{Ar}/^{39}\text{Ar}$ cooling age of 171.4 ± 3.1 Ma determined for sample O/C-373b from the metagabbro unit (table 2.1a; Heizler, written communication, 1998) evidently marks the end of regional amphibolite facies metamorphism. Hornblende generally closes to Ar-diffusion at temperatures ~500°C (e.g. Harrison, 1981). The age spectrum diagram of the $^{40}\text{Ar}/^{39}\text{Ar}$ dating analysis is shown in appendix B. This age is much older than the zircon U/Pb age of the sheeted dike complex and the metatonalite unit (figure 2.3, table 2.1), indicating the metagabbro unit is not part of the ophiolite and could have had a different magmatic and metamorphic history than the other ophiolitic units. If the metagabbro unit is a fragment of an older basement terrane, the metagabbro unit is not comagmatic with the sheeted dike complex and pillows. The metagabbro unit differs from the ophiolitic units in terms of major- and trace element compositions as discussed in subsequent chapter.

To summarize, rare, pale-green and patchy colored amphiboles such as actinolitic-hornblende and actinolite occur together with older, dark green uniformly colored hornblende in samples from the metagabbro unit. The pale green amphiboles as well as other greenschist to prehnite-pumpellyite facies minerals are interpreted to have formed during relatively short-lived retrograde hydrothermal alteration, whereas the dark green, uniformly colored hornblende is thought to have formed during regional metamorphism/plutonism at temperatures of about 600°C based on the results from amphibole-hornblende thermometry (chapter 3).

2.5.5 Hornblende quartz diorite in metagabbro unit

A small section within the metagabbro unit (~30 m wide, min. 70 m long) consisting of hornblende quartz diorite (HQ diorite) is exposed near the contact with the Blossom Bar shear zone (plate 1). A petrographic summary of samples from this diorite is listed in appendix A (table A1b). In contrast to the hornblende gabbro in the metagabbro unit showing magmatic flow foliation, the HQ diorite is isotropic to weakly foliated. The HQ diorite is medium-grained (2-3 mm) and has a hypidiomorphic granular texture. Quartz (5-15%) forms anhedral, interstitial grains and shows almost always undulatory extinction. Plagioclase (45-55%) forms zoned, subhedral to euhedral crystals that display simple and polysynthetic twinning. Plagioclase compositions range from An₆₈ in cores to albite occurring as patchy replacement. The rims have compositions ranging from about An₅₆ to An₃₈. Replaced plagioclase (ab +ep ±chl ±musc), especially the calcic cores, appear cloudy in thin section. Hornblende (35-50%) commonly occurs as subhedral, prismatic crystals, and dark green to brownish green prismatic varieties occur together with patchy, pale green hornblende and/or actinolite. The amphiboles in the HQ diorite are somewhat more variable within a thin section, than the dark-green uniformly colored hornblende in the metagabbro unit. Also, hornblende in HQ diorite is less variable in terms of color and texture than the amphibole in the Half Moon Bar diorite. The variably colored hornblende are a disequilibrium assemblage. The hornblende is interpreted as igneous in origin on the basis of its strong color and pleochroism and subhedral to euhedral, prismatic shape, and relic zoning. The pale-green amphiboles are metamorphic minerals possibly replacing cpx and/or magmatic hornblende and usually occur together with chlorite, epidote ± magnetite. The samples from the HQ diorite contain up to 6% anhedral oxide, and other accessory phases include rod-like apatite euhedra, biotite intergrown with hornblende and trace amounts of zircon.

Enclaves are locally abundant, 0.5 cm to several dm in diameter, and identical in composition to the HQ diorite. The enclaves are fine grained (0.3-0.6 mm) and have hypidiomorphic granular texture. Plagioclase is the predominant mineral (~50%). Zoning in the subhedral to euhedral plagioclase (An₆₈) is not observed. Quartz forms anhedral interstitial crystals (~6%) indicating its crystallized. Mafic minerals include subhedral, prismatic hornblende (~40%), anhedral oxide (~4%), and accessory apatite. The

enclaves may represent fragments of the more rapidly cooled walls of the small intrusion or could have formed by magma mingling, similar to the enclaves found in the metatonalite and metagabbro units.

Quartz is weakly recrystallized and commonly shows undulose extinction and less commonly subgrains. Intense grain size reduction of quartz by dynamic recrystallization was observed only near the micro-shear bands (e.g. figure 2.13). Clearly, this localized ductile deformation post-dates the intrusion of the HQ diorite. Crosscutting relationships of veins and mineralized faults in the HQ diorite are also very similar to that of the metagabbro unit (see section 2.5.2).

The boundaries of the HQ diorite section in the metagabbro unit are not well-defined, and it is not clear whether the HQ diorite is a younger intrusion in the metagabbro unit or represents a more fractionated phase of the host metagabbro. The Zircon U/Pb age of a dioritic sample (SC-3) collected about 50 m east of the contact between metagabbro unit and Blossom Bar shear zone was determined, and a discordant age of 157 was obtained (Saleeby, written communication 1997). The reanalysis of the zircon separates using an abrasion technique yielded complex discordant ages which cannot be resolved (Saleeby, written communication 1999). These data indicate that the HQ diorite is at least 157 Ma, but it could be as old as the hornblende $^{40}\text{Ar}/^{39}\text{Ar}$ cooling age of the sample from the metagabbro unit (171.4±3.1 Ma) or even older.

2.5.6 Contact between metagabbro unit and metatonalite unit

The western boundary of the metatonalite unit consists of a strongly foliated epidote+quartz mylonite and is in contact with a compositionally layered and well-foliated zone that forms the eastern boundary of the metagabbro unit (figure 2.2a and 2.2b). The contact appears to be transitional and there is evidence for crystal plastic deformation and ductile-brittle shearing in both units forming a ~50 m wide shear zone between the metagabbro and metatonalite units. This zone is characterized by southwest-northeast trending and steeply dipping, discontinuous laminae and layers (figure 2.14) that consist of rocks identified elsewhere in the metagabbro unit as well as the metatonalite unit; but they are generally more deformed. For example, augen-shaped hornblende in metagabbro and recrystallized quartz in more felsic rocks are common. The variably thick laminae and layers in the contact zone include medium-grained,

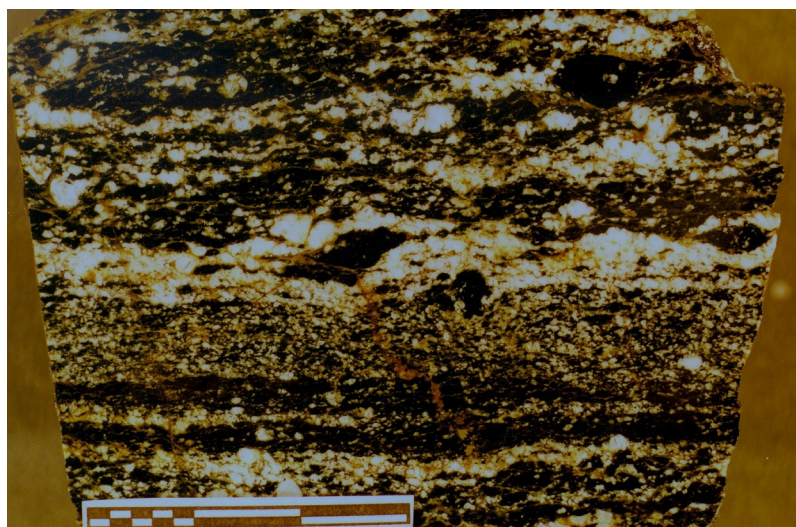


Figure 2.14

Slabbed and polished metagabbro protomylonite (O/C-371) from the shear zone between the metatonalite and metagabbro units (figures 2.2a and 2.2b). This photograph shows a typical, strongly foliated metagabbro having compositional banding. The lamination is similar to that of less deformed metagabbro and reflects the compositional variations in the metagabbro unit and is probably a primary igneous feature (i.e. magmatic flow) that was later overprinted by a tectonic foliation. Augen-shaped hornblende are common in rocks from this contact zone as well as stretched and fractured plagioclase crystals. The sense of shear is dextral. The scale bar is 3 cm long.



Figure 2.15

Photograph of prominent brittle fault with shear zone exposed at mile 46 at the Rogue River. The photograph is taken looking due north. The sharp contact is the brittle fault (the cliff is about 8 m high). Foliated metagabbro occurs to the left of the fault (northwest), and a 50 m wide ductile-brittle shear zone between the metagabbro unit and the metatonalite unit occurs to the right of the fault (southeast). The fault is subparallel to the shear foliation in the metagabbro to the left and the shear zone to the right of the fault. The 50 m wide shear zone to the right of the fault consists of strongly foliated and banded mylonitic rocks similar to the metagabbro unit (figure 2.14) and metatonalite unit (section 2.6.3). Epidosite mylonites become more abundant towards the metatonalite unit, and about 50 m southeast of this fault, only epidosite-mylonites typical of the metatonalite unit occur.

strongly foliated hornblende quartz gabbro (or quartz diorite?), fine- and medium-grained foliated hornblende gabbro, medium to fine-grained strongly foliated laminae of tonalite with mylonitic fabric, and $ep+qtz\pm chl$ mylonites (epidosite mylonites) that become more and more abundant towards the metatonalite unit. The compositional layering and highly variable texture of deformed rocks in the fault zone most likely reflect the compositional and textural variations of the metagabbro unit (figure 2.14). The 50 m wide contact zone is cut on its northwestern margin by a prominent brittle fault subparallel to the foliation (figure 2.15).

2.6 Metatonalite unit

2.6.1 Lithology

The metatonalite unit consists of variably strained rocks including isotropic and foliated tonalites, and mylonites and ultramylonites derived from metatonalite. Most of the rocks in the metatonalite unit show evidence of crystal plastic deformation, and meter-wide zones characterized by intense dynamic recrystallization and grain size reduction are abundant. The widest mylonitic zone is about ~20-30 m wide, consists of epidosite mylonites, and occurs at the western margin of the metatonalite unit (figure 2.2a and 2.2b). The foliation and mylonitic zones trend southwest-northeast and dip steeply northwest. Only about one third of this unit consists of fairly isotropic rocks in which primary igneous textures are well-preserved. The isotropic rocks include fine-grained metatonalite-trondhjemite (leucotonalite) and minor dioritic enclaves (figure 2.16 and 2.17).

A petrographic summary of representative samples is given in appendix A (table A2). Tonalite, the dominant phase of the isotropic portion of the metatonalite unit, is medium-grained (1.5 -2 mm), hypidiomorphic granular and often has a granophyric texture (figure 2.18). Quartz (30-40%) forms anhedral grains and almost always has undulatory extinction. Plagioclase (50-60%) forms subhedral to euhedral lath-shaped crystals that display scarce (relict) simple and polysynthetic twinning. The plagioclase is albite in all samples as determined from carlsbad-albite twinning. Replaced plagioclase ($cz +ab +ep \pm chl \pm musc$) appears cloudy in thin section (figure 2.18), and hornblende (10-15%) occurs as both subhedral

prismatic crystals and as interstitial grains between plagioclase laths. In contrast to the hornblende in the metagabbro unit, the amphiboles are variable in color within a thin section; light-brown (sometimes dark blue-green) prismatic varieties occur together with patchy, pale green hornblende and nearby actinolite. The brown hornblende is interpreted as igneous in origin on the basis of its strong color and pleochroism. In contrast, the pale-green amphiboles (ac) are metamorphic minerals and usually occur together with chl + ep ± mt. For example, samples OC-368G and SC-2 contain ragged cores of relic cpx within ac + chl + ep ± mt. Dark colored (magmatic?) hornblende is often rimmed by pale amphibole as well. These textures indicate that cpx and hbl are replaced by a greenschist facies mineral assemblage consisting of ac + chl + ep ± mt. Tonalite contains 1-4% anhedral oxide and other accessory phases including subhedral titanite, rod-like apatite euhedra and trace amounts of zircon.

Trondhjemites, minor constituent of the isotropic rocks, are also medium grained (1 - 2 mm), hypidiomorphic granular and often have granophyric texture (figure 2.18). In one sample, a myrmekitic texture was observed. Trondhjemite contains slightly more quartz (40-45%) and plagioclase (50-55%) than the tonalite and is lighter in color. As described above, plagioclase is completely replaced (e.g. figure 2.18). Mafic and accessory minerals include subhedral clinopyroxene (5-9 %), oxide <1%, titanite and trace amounts of zircon. Clinopyroxene is commonly partially replaced by fibers of ac and specks of magnetite and is rimmed by chlorite and pale-green amphibole.

Dark-gray dioritic enclaves, 0.5 cm to 1.5 m in diameter, are locally abundant within the light colored tonalite and trondhjemite (figure 2.16). The dioritic enclaves are fine grained (0.3-0.6 mm) and hypidiomorphic granular. Subhedral to euhedral plagioclase is the predominant mineral (50-55%). Determination of the primary An content is not possible due to complete replacement of plagioclase by cz + ab + ep ± chl ± musc. Quartz forms anhedral interstitial crystals (10-20%) and thus, crystallized late. Mafic minerals include subhedral prismatic hornblende (25-35%), anhedral as well as rare skeletal oxide (3-6%), and accessory apatite. Skeletal oxide possibly represents a quench texture in the microdioritic enclaves. Amphiboles are interpreted to be both magmatic and metamorphic in origin based on their form (i.e., blocky/prismatic or fibrous amphiboles) and color (i.e., deeply and uniformly colored or pale and patchy) in thin section.

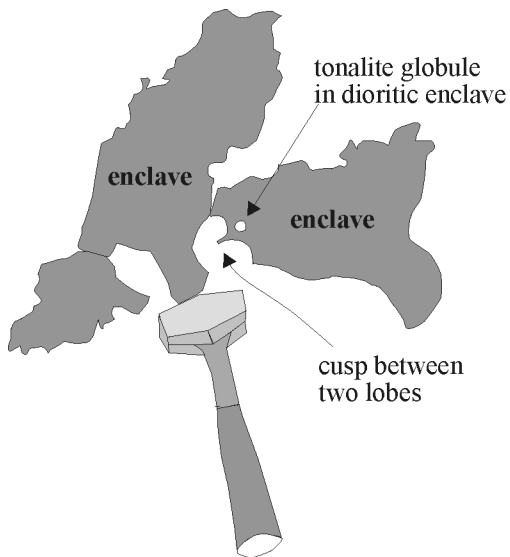
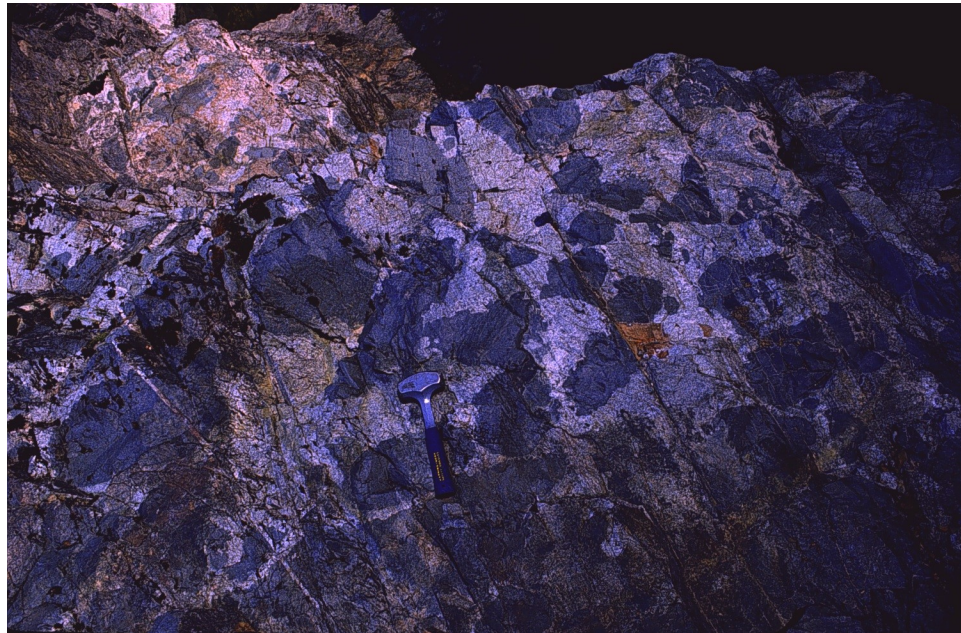


Figure 2.16

Photograph of metatonalite (light colored) and dioritic enclaves (dark) in O/C-10 at the Rogue River. Diorite enclaves in this outcrop become less abundant from bottom to top. Most of the enclaves in this outcrop appear to be angular. However, the enclaves are angular because of the cusped shapes of the enclave margins. Note the cusp between two concave lobes of the enclave margin. A small inclusion of tonalite occurs in the dioritic enclave. Other enclaves are globular and have lobate margins (figure 2.17). These features are interpreted as due to magma mingling.

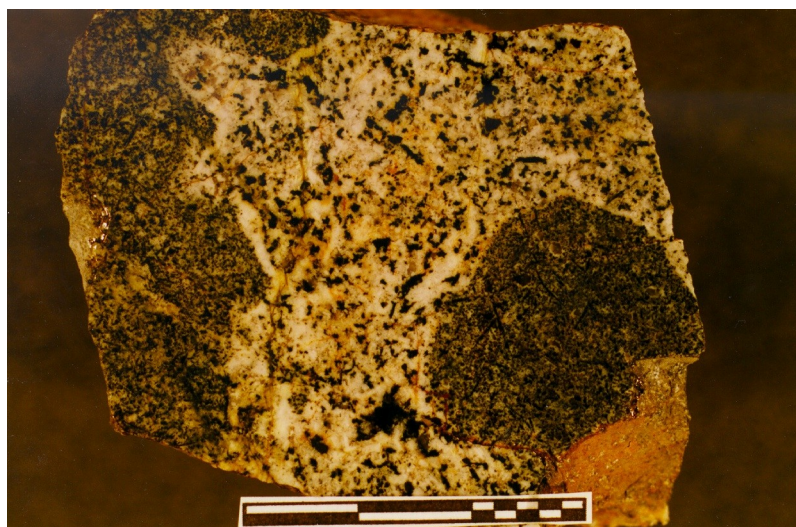


Figure 2.17

Slabbed and polished hand sample from the metatonalite unit (O/C-11) showing two globular fine-grained dioritic enclaves in medium-grained hornblende tonalite. Acicular hornblende similar to that of the hornblende tonalite occurs in the fine-grained diorite. Note that the enclave to the left has a lobate margin. Scale bar is 3 cm.

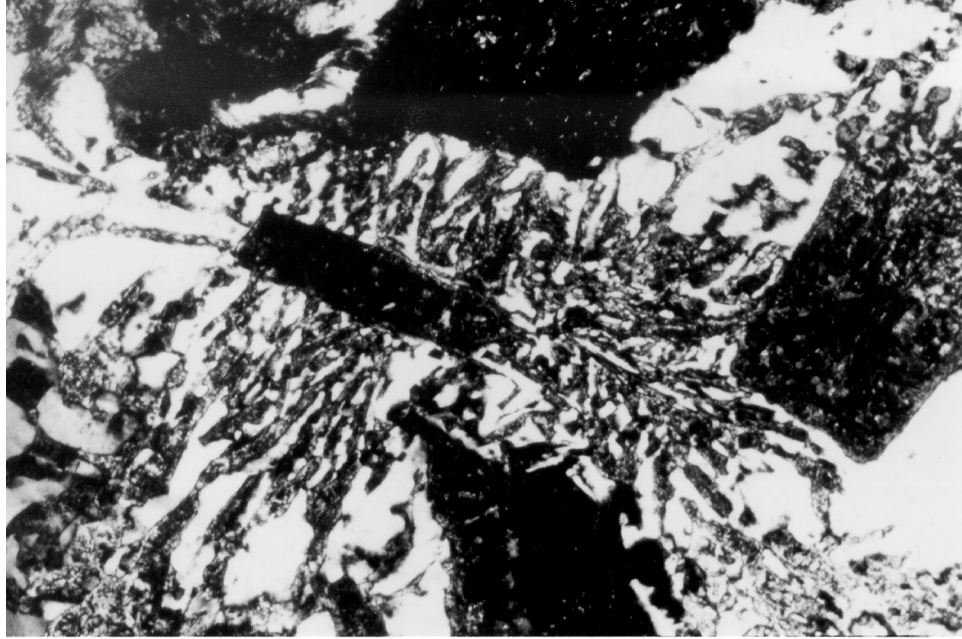


Figure 2.18

Plane light microphotograph of granophyric texture in metatonalite (O/C-368G). Plagioclase in this microphotograph is dark gray to black (cloudy masses of cz or ep + ab \pm chl \pm musc) and quartz is white. Radiate intergrowths of quartz and feldspar arranged about euhedral plagioclase crystals is common. The width of the microphotograph is 2.14 mm.

The diorite, tonalite and trondhjemite are petrographically distinct from the quartz-bearing rocks in the metagabbro unit. The rocks in the metatonalite unit do not contain uniformly colored hornblende, but have variably colored amphiboles similar to amphiboles in ophiolitic rocks which are constrained to have undergone seafloor hydrothermal metamorphism (Alexander et al., 1993; Harper et al. 1988). Another difference is that metatonalite is isotropic (except for the mylonitic rocks) and generally does not have a magmatic flow foliation. These differences suggest that the metagabbro unit and metatonalite unit are not related. Yet, the metagabbro unit and metatonalite unit are structurally conformable (compare figures 2.2b and 2.3) unlike the extrusive sequence west of the Blossom Bar shear zone.

2.6.2 Evidence for magma mingling

Several structures observed in the field, hand samples and thin section resemble those of microgranitoid enclaves (Vernon, 1984) that have been inferred or constrained to have formed by magma mingling (e.g. Eberz and Nicholls, 1988; Vernon et al., 1988; Vernon, 1991):

- (1) Inclusions of tonalite occur in the enclaves (figure 2.16) strongly suggesting that both types of rocks were in a magmatic stage as the diorite intruded the tonalite.
- (2) Although the contacts between the tonalite and diorite are almost always sharp, they are often lobate or cusped (figure 2.16 and figure 2.17) suggesting the tonalite was in a magmatic state when the diorite was intruded.
- (3) In some outcrops, small subangular and globular enclaves occur as appendages that are apparently attached to dike-like intrusions of diorite suggesting the enclaves could have formed as 'pillow' dikes.
- (4) The globular and rounded shape of many enclaves (figure 2.17) is inconsistent with fracturing and brecciation of completely solidified diorite during intrusion of the tonalite. Globules and lobate 'pillows' are likely to form when two liquids with limited miscibility are brought in contact.
- (5) The dioritic enclaves lack any older or inherited internal structures or textures. For example, if the enclaves represented xenoliths from the sheeted dike complex, at least some of the larger enclaves should exhibit the typical structures of the sheeted dikes (e.g. chilled margins) or gabbroic screens (e.g. planar lamination).

(6) The aspect ratios of elongated enclaves is up to 7:1, measured in a portion of the metatonalite unit where subsequent solid state deformation is essentially absent (only undulose extinction of quartz observed, no quartz ribbons or grain size reduction by dynamic recrystallization). This suggests that the relatively large finite strain indicated by the enclave elongation is likely the result of deformation of the tonalite and diorite when both were in a magmatic state (i.e. magmatic flow).

(7) The relatively uniform and very fine grain size of the enclaves indicate rapid crystallization; that is, 'quenching' of the dioritic magma as it came in contact with cooler tonalitic magma. This is consistent with a quench texture such as skeletal oxide observed in one sample. Quenching occurs because a more mafic magma (diorite) becomes dispersed through a felsic magma (tonalite) and crystallizes more rapidly because it is more undercooled than the felsic magma.

(8) The mineral assemblage in the enclaves is the same as those in the tonalite. Only the proportions of the minerals are different.

The microdioritic enclaves in the metatonalite unit are, based on these observations, interpreted to have formed by the injection of a more mafic magma (diorite) into a felsic magma (tonalite-trondhjemite) and, therefore, represent globules of magma ("pillows") that were 'quenched' in a plutonic environment. Also, the elongation of enclaves in outcrops where solid state deformation is insignificant is interpreted as due to deformation by magmatic flow. Microgranitoid enclaves deformed by magmatic flow are common in high-level granitoid plutons (Vernon, 1984).

2.6.3 Mylonites

The metatonalite unit contains several zones of strongly foliated rocks (figure 2.19) previously mapped as silicic tuffs (Gray et al., 1982). Samples from such zones show evidence of intense ductile deformation, have a stretching lineation, and contain fabric elements with a monoclinic shape symmetry indicative of non-coaxial deformation. Field and petrographic evidence suggests that the protoliths of these mylonites include tonalite-trondhjemite, dioritic enclaves, quartz-epidote veins and epidiosites (granoblastic epidote+quartz±chlorite). Epidiosites in ophiolites are inferred to have formed by subseafloor hydrothermal

metamorphism. The formation of epidiosites involves extreme Ca-metasomatism which is only likely by hydrothermal metamorphism where water/rock ratios can be very high (e.g., Harper et al., 1988).

The mylonites are variably colored, and include dark gray-green, pistachio green, light brown, and white (figure 2.19). The color variations occur in mm to dm wide, often discontinuous and tapering bands, parallel to the foliation and give the rock a banded appearance. In hand sample, the mylonitic foliation is planar or wavy and is defined by <1 mm wide laminae or microlithons rich in quartz separated by laminae of fine grained, greenish minerals. Reliable determination of the sense of shear, the orientation of the stretching lineation, and the percentage of porphyroclasts as compared to matrix was not possible in the field, mainly because of the extremely small grain size of the mylonites in the metatonalite unit. Sense of shear was determined from characteristic fabric elements of mylonites evident in thin sections cut perpendicular to foliation and parallel to stretching lineation as discussed in chapter 4.

An attempt was made to classify the mylonites according to the percentage of matrix as compared to porphyroclasts (Sibson, 1977). The classification of Sibson (1977) requires an artificial distinction between porphyroclast and matrix, which is often very ambiguous. Therefore, the classification was somewhat simplified and only protomylonites (0-10% matrix), mylonites (10-90% matrix) and ultramylonites (90-100% matrix) were distinguished (see chapter 4).

Porphyroclasts in the mylonites include any of the following minerals: epidote (figure 2.20 and 2.21), albitized plagioclase (figure 2.22), hornblende (see figure 2.12b), and quartz (figure 2.23). They occur in a fine grained matrix of recrystallized quartz (figure 2.22 and 2.23) and disseminated greenschist-facies minerals. Generally, the mylonites in the metatonalite unit can be classified into two types based on the characteristics of the foliation: Type 1 mylonites have a foliation that is defined by clearly separable, alternating layers rich in quartz \pm albite, and cloudy mineral aggregates of mainly Ca-Al-silicates (i.e., ep, cz, pr?) as well as some chl, musc, and ac (figure 2.20). The spacing of the layering decreases with strain, but the bands remain clearly discernible. Type 1 mylonites are usually light colored including pistachio green, light blue-green, beige and whitish colors. Type 2 mylonites have a foliation that is comparable to a domain spaced cleavage (figure 2.21). It appears that rough cleavage domains rich in chlorite separate quartz-rich microlithons. The microlithons consist mainly of aggregates of recrystallized quartz and



Figure 2.19

Photograph of a zone of strongly foliated rock within the metatonalite unit. These rocks are characterized by extremely fine grain sizes, tightly spaced foliation and compositional (color) banding. The color of the mylonites is highly variable; they are bright white, beige, pistachios green, bluish-green, dark-green, gray-green, and rust-brown, depending on strain, composition of protolith, and weathering. The lens cap is 5.5 cm in diameter.



Figure 2.20

Photomicrograph showing fabric of typical mylonite (type 1) in the metatonalite unit. Porphyroclasts are epidote and saussuritized plagioclase. Only few large quartz grains are preserved in quartz-rich layers. Typically, quartz porphyroclasts are stretched, contain subgrains and/or show undulatory extinction and laterally grade into strongly recrystallized quartz. The foliation is characterized by quartz \pm albite ribbons (clear) that alternate with laminae consisting of fine grained mineral aggregates (dark-green layers) which include mainly ep or cz, but may also include ac, chl, pr, musc, pu(?). The foliation wraps around porphyroclasts. The width of the photograph is 6 mm.

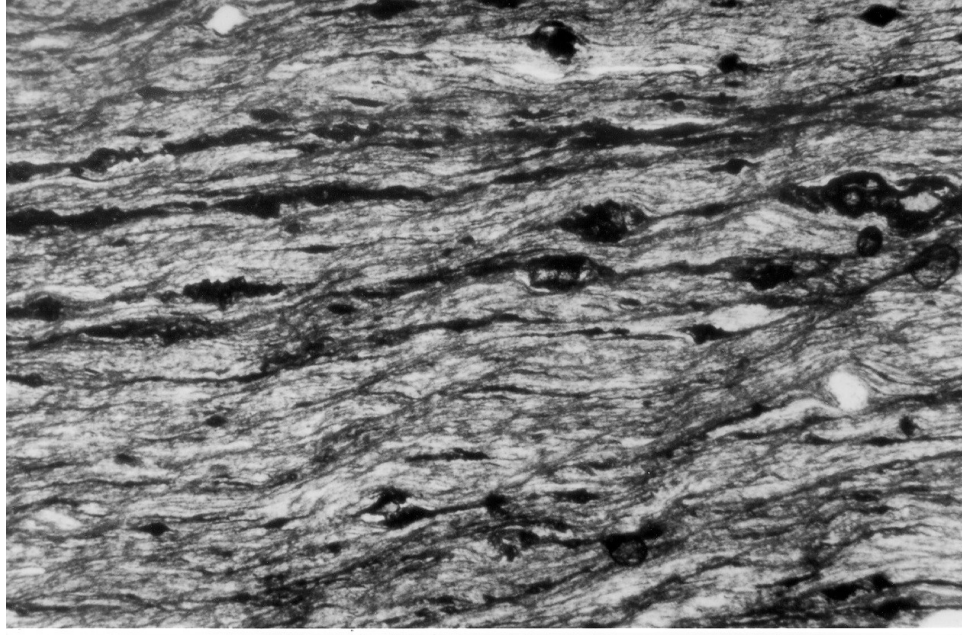


Figure 2.21

Photomicrograph showing fabric of typical mylonite (type 2) in the metatonalite unit. Porphyroclasts consists of saussuritized plagioclase, epidote and quartz. The foliation is characterized by cleavage domains rich in chlorite (dark gray) separating microlithons rich in recrystallized quartz (light gray/cloudy).

Elongate microlithons define the foliation (C). Asymmetrical extensional shear bands (C') consisting mainly of chlorite typically form in type-2 mylonites. Grain size reduction of epidote porphyroclasts results in planar, discontinuous layers consisting of epidote fragments (black, discontinuous layers). The cloudy appearance of microlithons in thin section is due to abundant disseminated alteration phases. The width of the photograph is 2.14 mm.



Figure 2.22

Photomicrograph of porphyroblast of albite (center) occurring in a matrix of recrystallized quartz (metatonalite unit, O/C-9-S12). The largest albite fragment shows a Carlsbad twin as well as undulatory and patchy extinction. It seems as if albite consists of several subgrains. The large, twinned fragment is surrounded by numerous smaller albite fragments in a matrix of recrystallized quartz. Possibly, a fine grained albite-quartz mixture forms with progressive deformation. Although the undulatory extinction and formation of subgrains could be due to dislocation glide, abundant microscopic cracks and fractures in albite are consistent with predominantly cataclastic deformation of albite in a matrix of quartz, indicating relatively low temperatures of deformation (<450C). The width of the photograph is 0.6 mm.

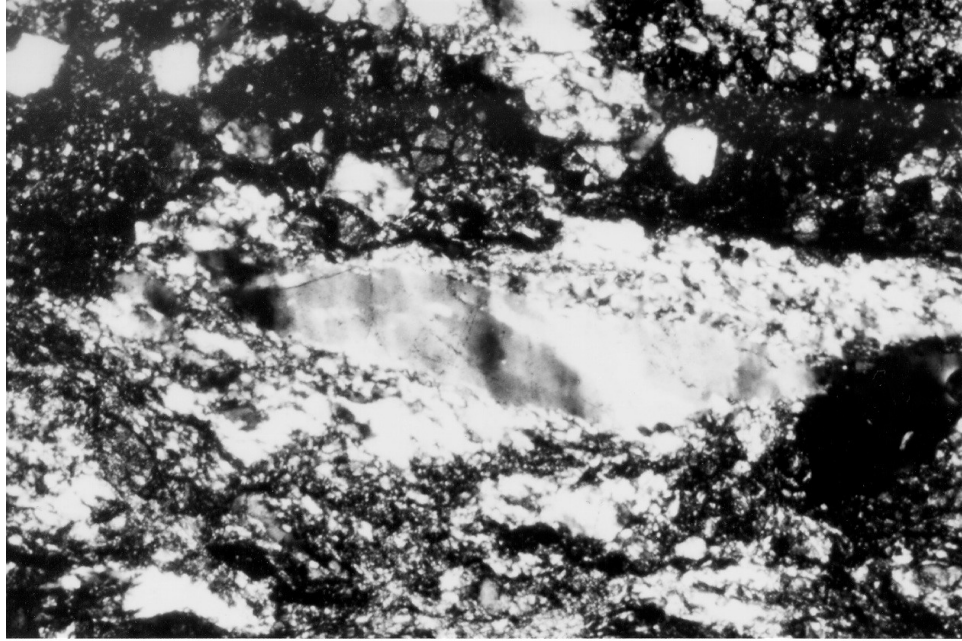


Figure 2.23

Photomicrograph of large, relic quartz grain in a monomineralic layer of quartz showing several subgrains and undulose extinction. Note that the relic quartz grain passes laterally into domains of small, dynamically recrystallized grains. This indicates that the temperature of deformation was high enough for climb assisted dislocation glide allowing subgrain rotation recrystallization. The width of the photograph is 2.14 mm.

disseminated minerals too small to reliably identify using transmitted light microscopy. However, the disseminated minerals are probably similar to type 1 mylonites,; i.e. chl, ep, cz, musc and ab. Type 2 mylonites are usually dark in color (dark-green and gray-green), due to the relatively high chlorite content. Asymmetric extensional shear bands (C'-surfaces) consist mainly of chlorite and are typically developed in type-2 mylonites (figure 2.21).

Evidently, there is a transition between both types of mylonites, probably depending on the chlorite- and epidote-content. For example, increasing strain in type 2 mylonites containing abundant epidote porphyroclasts has produced relatively planar, almost continuous layers of epidote grains occurring within the type 2 matrix. Figure 2.21 shows an example of how grain size reduction caused epidote porphyroclasts to become more fragmented and stretched resulting in thin, discontinuous layers. Also, asymmetric extensional shear bands in some type 1 mylonites rich in chlorite were observed.

The shape of plagioclase porphyroclasts is highly variable ranging from almost euhedral plagioclase having slightly rounded edges to augen-shaped and ovoid forms (figure 2.22). Subangular plagioclase occurs typically in type 2 mylonites, whereas augen-shaped and ovoid forms predominate in type-1 mylonites. Regardless of their occurrence, plagioclase is albitized and/or replaced by cloudy, fine grained mineral aggregates. Also, bookshelf structures and microfaults with high angle antithetic or low-angle synthetic offsets are common in plagioclase porphyroclasts. Stress induced twinning and undulatory extinction in plagioclase was not found (possibly due to high degree of alteration?). Often, plagioclase resembles winged porphyroclasts (figure 2.20). Usually, the wings or tails consist of dark, cloudy mineral aggregates contrasting with the lighter colored, albitized plagioclase porphyroclasts. This suggests that the mineralogy of the porphyroclastic wings is different from the porphyroclast implying metamorphism during deformation.

Grain size reduction of epidote/clinozoisite with progressive deformation is evident from the observation that the size of epidote/clinozoisite porphyroclasts decreases proportionally with the size of recrystallized quartz grains. The least deformed epidote-quartz rock contains a boudinaged epidote vein in a moderately recrystallized quartz matrix. With decreasing grain size of recrystallized quartz, the

abundance and angularity of large epidote porphyroclasts become less. At the highest inferred strain, epidote is fragmented into tiny grains that form cloudy-looking laminae defining (together with other greenschist facies minerals) the compositional banding foliation of the mylonites. Epidote rarely forms structures that resemble winged s-type or d-type porphyroclasts. Subtle stair-stepping of porphyroclasts is found, however, and the monoclinic shape fabric may be used as a sense of shear indicator. For example, when a cloudy epidote-rich band on one side of an epidote porphyroclast is slightly elevated as compared to the cloudy layer on the other side, the sense of shear may be inferred. Grain size reduction of epidote with progressive deformation thus appears to have been a likely process. Rare, undeformed epidote + quartz veins cut the mylonitic foliation, but undeformed epidote zones do not.

The occurrence of boudinaged epidote veins, grain size reduction of epidote with progressive deformation, occurrence of mylonites with compositions identical to epidotes (ep + qtz ± chl), and presence of undeformed epidote veins crosscutting foliation can be interpreted as follows: the formation of epidotes and most ep + qtz veins preceded ductile deformation and grain size reduction. That is, ductile deformation took place in a previously hydrothermally metamorphosed tonalite. However, retrograde hydrothermal metamorphism probably took place during ductile deformation, because deformed and undeformed epidote veins crosscut the foliation. If ductile deformation and hydrothermal alteration occurred simultaneously, recrystallization processes or microfracturing in partially altered plagioclase facilitated access for metamorphic (hydrothermal) fluids causing the breakdown and complete replacement of plagioclase. Continued deformation resulted in the abrasion of replaced plagioclase. Thus, neocrystallization or nucleation could have been important during grain size reduction (Fitz Gerald and Stünitz, 1993a). Also, grain boundary sliding accommodated by diffusive mass transfer (Brodie and Rutter, 1985) as well as granular flow (Fitz Gerald and Stünitz, 1993b) are likely processes resulting in ductile flow in the fine grained aggregates that formed by the breakdown of plagioclase.

2.6.4 Metatonalite unit compared to oceanic plagiogranites

Tonalites and trondhjemites occurring in ophiolites or 'oceanic' settings are collectively called 'plagiogranites' (Coleman and Peterman, 1975). In many ophiolites, plagiogranites typically occur as small

screens or intrusions at the base of the sheeted dike complex and are in close association with a large underlying cumulate sequence that represent the high-level gabbro (e.g. Oman ophiolite, Josephine ophiolite). The plagiogranites are thought to represent differentiates of basaltic liquids (Coleman and Peterman, 1975, Coleman and Donato, 1989, Dixon-Spülber and Rutherford, 1979, 1983), which is consistent with the observation that they are volumetrically insignificant in ophiolites as well as among dredged or drilled rocks from the ocean floor. Only a tiny fraction of the original volume of a fractionating tholeiitic basalt magma consists of differentiates with such felsic composition (> 90% fractionation, Dixon-Spülber and Rutherford, 1983). The locale of the metatonalite unit between the sheeted dike complex and the metagabbro unit compares favorably with the typical pseudostratigraphic position of plagiogranites in ophiolites (e.g. Oman ophiolite, Bay of Island ophiolite). However, the large volume of tonalitic rocks in the Wild Rogue Wilderness is problematic in that, if they were derived from the fractionation of basalt, a large cumulate sequence should be present and should be in close association with the metatonalite unit (the metagabbro unit is not part of a cumulate sequence and is not related to the metatonalite). Furthermore, the metagabbro unit is most likely not part of the ophiolite stratigraphy, and may be a fragment of regionally metamorphosed basement terrane. Thus, the absence of a related cumulate sequence suggests that the metatonalite unit may not represent ‘oceanic’ plagiogranites, and may be a silicic intrusion related to a volcanic arc or the product of melting of sialic crust. On the other hand, the missing cumulate sequence may not be preserved in the study area due to the structural disruption of the ophiolite. To avoid genetic implications using the term ‘plagiogranite’, the conventional, non-generic terms tonalite and trondhjemite (Le Maitre et al., 1989) are used in the description and the naming of this unit (see also chapter 5).

2.6.5 Contact with the sheeted dike complex

A prominent brittle fault is exposed on the Rogue River (figure 2.24) about 500 m downstream of Stair Creek Falls. The metatonalite, exposed to the west of the fault is strongly foliated, and type 1 (figure 2.20) and type 2 (figure 2.21) mylonites were identified within a distance of at least 25 m from the fault. The mylonitic foliation is subparallel to the SW-NE-trending and steeply SE-dipping fault. The diabasic



Figure 2.24

Photograph of outcrop (facing north) showing the brittle fault contact (in steep shadow) between the metatonalite unit (west) and the sheeted dike complex (east). The metatonalite has a mylonitic foliation subparallel to the fault, whereas the sheeted dike complex within 15 m of the fault is heavily fractured and brecciated. The fault breccia is cemented by epidote and quartz. Also, this fault breccia is cut by prehnite veins. Other secondary minerals include chlorite and sulfide.

rocks exposed to the east of the fault are heavily fractured within a distance of about 15 m of the fault. The difference in brecciation and ductile flow in the sheeted dike complex and the metatonalite unit may be due to the higher temperature of deformation needed for crystal plastic formation in diabase. The fault gouge and fragments in this 15 m wide breccia zone are cemented by epidote and quartz, and this fault breccia is also cut by prehnite veins. Samples taken from the fault surface that is very conspicuously exposed at the Rogue River (figure 2.24), indicate also some quartz and sulfide in crosscutting veins. Outcrops of heavily fractured and subsequently cemented rocks are also found in the lower drainage of Mule Creek between outcrops of diabasic rocks and metatonalite. The metatonalite unit pinches out further north (figure 2.2a), and the sheeted dike complex is in shear contact with the metagabbro unit.

2.6.6 Age constraints

The zircon U/Pb age of a sample from the metatonalite unit (SC-2) has been determined, and a concordant age of 164 ± 1 Ma was obtained (table 2.1b; Saleeby, written communication 1999). The 164 Ma metatonalite unit is structurally overlain by the older metagabbro unit and structurally underlain by the sheeted dike complex (figure 2.2b) which gives the same age as the metatonalite.

2.7 Sheeted dike complex

A spectacular sheeted dike complex is exposed in the Wild Rogue Wilderness (figure 2.2a). The sheeted dike complex was first described by Ramp and Gray (1980). Excellent, almost continuous water polished exposures of subparallel diabasic and microdioritic dikes occur along the Rogue River and the lower part of Mule Creek. Weathered outcrops of subparallel dikes occasionally stand out along ridge crests and near mountain tops. Other exposures where chilled margins and diabasic texture of dikes can be observed includes gullies. Chilled margins are not generally evident in natural weathered outcrops.

The structure of the sheeted dike complex is reflected in the attitude of the dikes which changes more than 90° in strike from the southern domain along the Rogue River (WNW striking and steeply dipping) to the northern domain (NNE striking dikes and moderately steep dips) about 10 km further

northeast (figure 2.2a). In outcrop, the dikes are subparallel, and the variation of their attitudes generally ranges between 0° to 25° , resulting in dikes that pinch out at low angles (figure 2.25). Dikes that cut sheeting at high angles are rare. Most dikes that occur at intermediate angles with other dikes were intruded along faults, and therefore, appear to cut older dikes at intermediate angles (usually less than 45°).

The chilled margins of dikes are well preserved and can easily be identified in water polished outcrops and hand sample. However, the sheeting, a characteristic feature of dike complexes of ophiolites, is somewhat obscured by numerous faults in outcrop, veins, and fractures cutting dikes at various angles. Nevertheless, the excellent outcrops along the Rogue River allow the study of the complex intrusive relationships (figure 2.25). As a result of dikes intruding others, many dikes were split and have no or only one chilled margin. Locally, dike splitting caused displacement of segments of a single dike over several to tens of meters. In some cases, dikes were also intruded along the margins of older dikes resulting in chilled margins facing each other. Ramp and Gray (1980) reported that the number of chilled margins is greater on the north side of the west-northwest striking and steeply dipping dikes by a ratio of 3:2. A similar degree of one-way chilling is indicated in the randomly selected section of dikes shown in figure 2.25. Kidd and Cann (1974) argued that one-way chilling in dike swarms is consistent with an ocean-floor spreading model, and that a greater number of chilled margins must face away from the axis of a the spreading center than towards it. Accordingly, the sheeted dike complex in the Wild Rogue Wilderness could have formed at a spreading center lying to the south of the complex in its present orientation.

Typically, the diabasic and microdioritic dikes are 0.5 to 1.5 m wide (figure 2.4), but vary from as little as 1 cm to 8 m wide. Overall, the sheeted dike complex consists of 60% -100% dikes having well defined chilled margins and up to 40% screens of plag-cpx cumulate gabbro. Locally, screens of plagiogranite (qtz+plag rich intrusive rocks in ophiolites; Coleman and Peterman, 1975) were found as well. Along the well-exposed Rogue River section, estimates of the percentage of gabbro as compared to the sheeted diabasic dikes reveals that the abundance of gabbroic screens increases slightly from west (>30% gabbro) to east (40% gabbro). This increase, also reported by Ramp and Gray (1980), however, is abrupt across a probable oceanic fault zone occurring about 150 m downstream from the contact with the

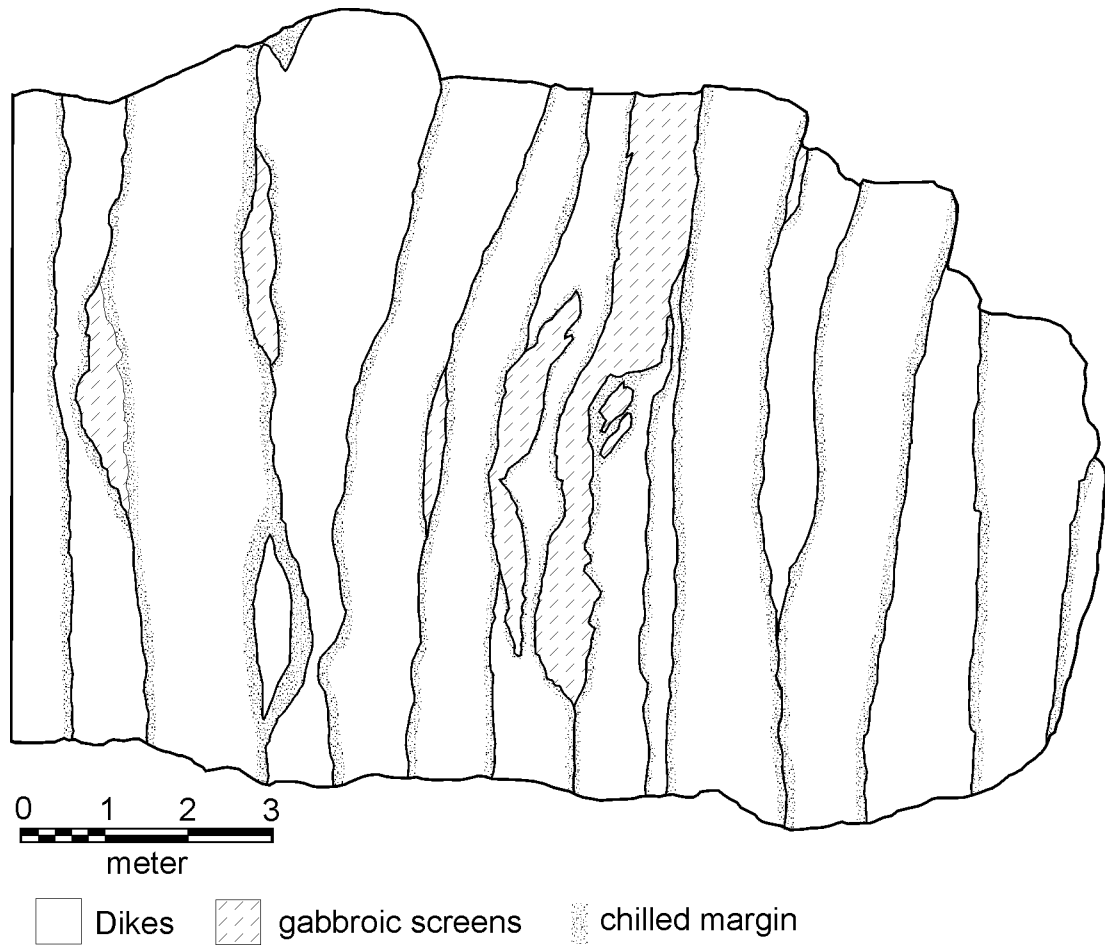


Figure 2.25

Outcrop map of sheeted dikes in the Rogue River canyon near Stair Creek falls shows the typical relationships between dikes and gabbroic screens. This map is traced from a photograph taken from opposite canyon wall. The vertical cliff faces NW perpendicular to the strike of the dikes. In this randomly selected section of sheeted dikes, nine chilled margins face NE whereas only six face SW. Ramp and Gray (1981) also reported that the number of chilled margins is greater on the northeast side.

Dothan Formation. Across the oceanic fault zone, the strike of the steeply dipping dikes is 10°-30° different than elsewhere along the Rogue River, and a sudden decrease in the abundance of gabbroic screens is evident. This suggests fault block rotation during deformation.

Screens of gabbro and rare plagiogranite were also found in the northern domains which have distinctly different dike orientations than on the Rogue River. Unfortunately, a general increase or decrease of the abundance of gabbro screens in this domain could not be mapped due to the small size of scattered outcrops. The upstream increase of gabbroic screens along the Rogue River section may be used to reconstruct the ophiolite to its original orientation at the ridge axis, as the increase of the proportion of gabbro screens could indicate the direction of down-section in an ophiolite stratigraphy. Assuming the sheeted dike complex is subvertical at the Rogue River section, the direction of down-section is from northwest to southeast, which is also consistent with the overlying sedimentary rocks of the Myrtle Group (figure 2.2b). However, the evidence for original up and down should be carefully evaluated when used for reconstruction or structural model of the ophiolite. The above mentioned structural complications, such as faulting and rotation of dikes across cemented fault zones, could be the result of deformation processes near the ridge axis. Fault orientations and related rotation perhaps provide additional clues about the orientation of the Rogue River ophiolite.

All samples collected from the sheeted dike complex are highly altered (appendix A, tables A3a and A3b). The igneous phases are replaced between 80% and 100% by a mineral assemblage indicating greenschist to lower amphibolite facies hydrothermal metamorphism (detailed descriptions in sections 2.7.1 and 2.7.2). Despite this high degree of alteration, igneous textures are often well preserved and primary minerals, if completely replaced, can often be inferred. Therefore, the classification of rocks is given in terms of protoliths (i.e. diabase instead of meta-diabase or microdiorite instead of meta-microdiorite). In addition to the conventional rock classification (Streckeisen 1973, 1976), the terminology for layered intrusions as suggested by Irvine (1982) is adopted for the classification of the gabbroic screens. Accordingly, the term 'cumulate' is used in a descriptive sense and does not necessarily imply formation by crystal settling as originally defined by Wager et al. (1960).

2.7.1 Gabbroic screens

Most slivers and lenses in the sheeted dikes consist of fine- to medium-grained plag-cpx cumulate gabbro having a weak planar lamination defined by the alignment of tabular plagioclase. Many screens of cumulate gabbro contain irregular layers and laminae of leucogabbro (figure 2.26 and 2.27) which are mostly parallel to the planar lamination. Other common features include elongate bodies of anorthosite in cumulate gabbro which are sometimes rimmed by discontinuous ultramafic layers. Usually, the planar bodies of anorthosite or leucogabbro are irregular in thickness, ranging from 0.5 cm to 0.3 m, are tapered and lensoid in shape and can have a lateral extent of up to 3 m. The contacts of the anorthosite layers are often very sharp and appear to be concordant with the planar lamination. Some of the anorthosite layers may be misidentified in the field as plagiogranite sills (or vice versa) because of the intense alteration making textures difficult to identify in the field. In places, schlieren, lenses, and bands of cumulate leucogabbro and anorthosite give the layering a wispy appearance (figure 2.27). At one locality (OC-357), a small, concordant lens of gabbro pegmatite was found.

The anorthosites and leucogabbros are adcumulates whereas the more mafic gabbros appear to be mesocumulates based on an estimate of the abundance of the cumulus relative to post cumulus phases (Irvine, 1982). Plagioclase is relatively uniform in size (0.5-1.5 mm), generally subhedral and completely replaced by a dark cloudy mass consisting of $cz/ep + ab \pm chl \pm mica$. Nearly all cpx has been replaced by metamorphic (hydrothermal amphiboles). Relict cpx was found in only two samples, occurring as ragged cores within hornblende. Optical properties determined in thin section indicate cpx is diopside. The amphiboles are highly variable in color and texture within a thin section; they are patchy, pale to deep green and sometimes brown-green in color. The amphiboles probably range from actinolite (pale green) to actinolitic hornblende (dark colors) based on analysis of similar colored hydrothermal amphiboles in ophiolites and ocean gabbros (e.g., Harper et al., 1988). Fibrous and acicular varieties occur as well as up to 4 mm large patchy colored oikocrysts (figure 2.28). The poikilitic texture in two mesocumulate samples, one of which is shown in figure 2.28, is interpreted to reflect a primary igneous texture (cpx is replaced by amphibole). Interstitial Fe-Ti oxides constitute usually less than 2% of the cumulate gabbros and occasionally show a trellis pattern indicative of oxidation-exsolution ilmenite that occurs at high

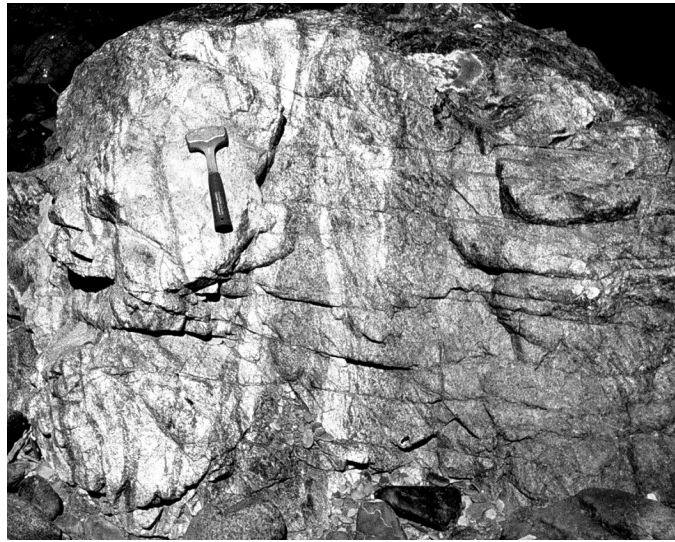


Figure 2.26

Photograph of layered cumulate gabbro seen in the sheeted dike complex on the Rogue River near Stair Creek Falls. This photograph shows irregular leucocratic (anorthosite) layers and laminae in a fine grained plag-cpx cumulate gabbro. Many screens contain irregular layers and lenses of anorthosite with occasional ultramafic rims. Note hammer for scale.

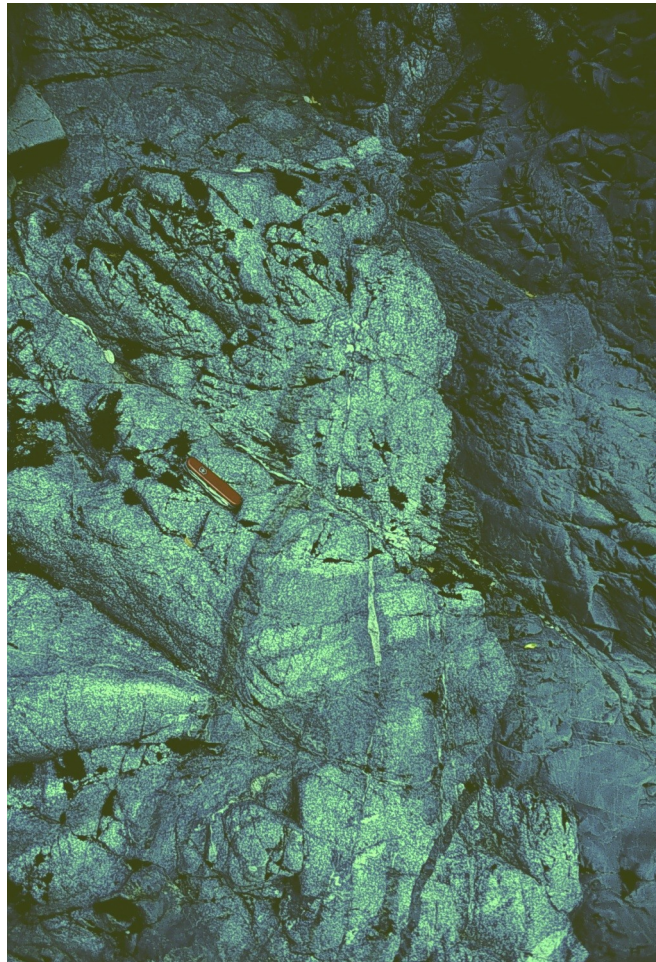


Figure 2.27

Layered cumulate gabbro in sheeted dike complex near the Coffee Pot (whirlpool on the Rogue River above Stair Creek falls). This photograph was taken looking northwest and shows wispy leucocratic layers and laminae in a fine grained plag-cpx cumulate gabbro cut by a chilled dike. The mafic dike to the right cuts the layering at a high angle. Note that the epidote vein having an amphibole alteration halo (2cm right of the knife) is truncated by the dike. All structures are cut and offset by a epidote + quartz vein (fault) located 4 cm above the knife. The length of the knife is 10 cm.

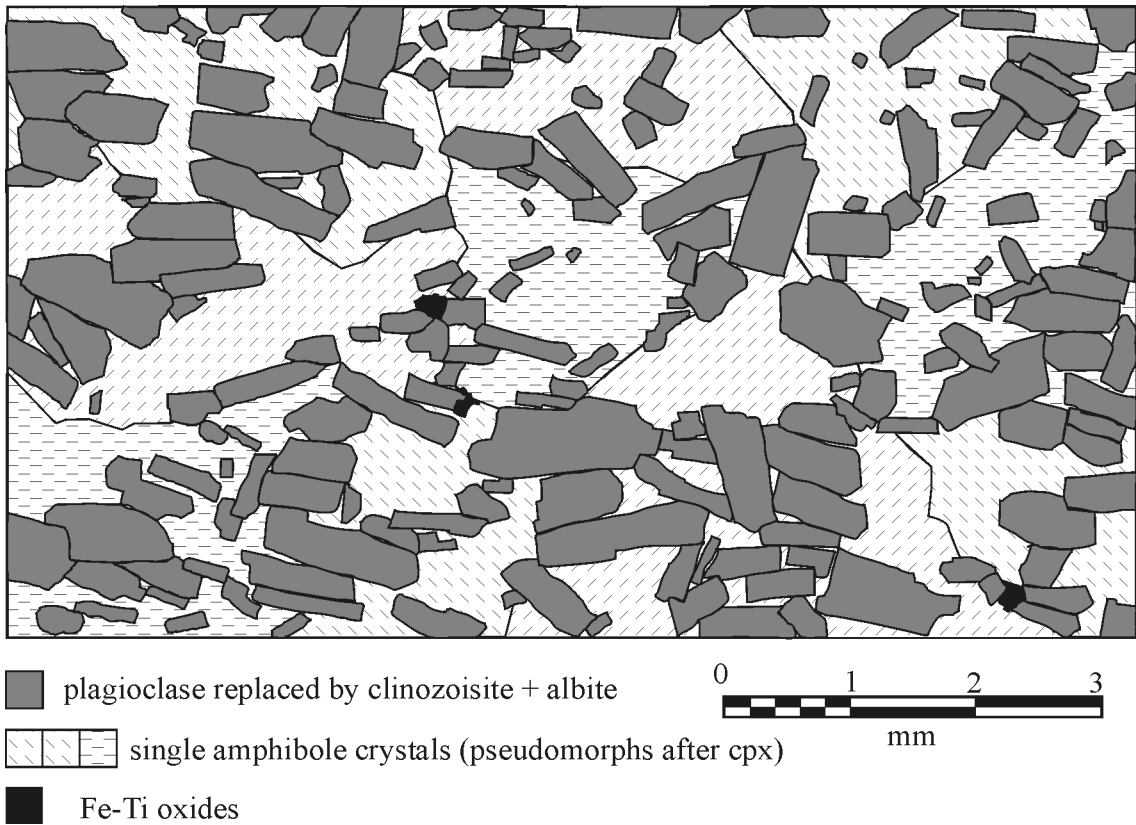


Figure 2.28

Part of thin section was traced to show relict igneous texture of cumulate gabbro (O/C-360). Subhedral plagioclase is poikilitically enclosed in much larger pyroxene oikocrysts, the latter are replaced by patchy and pale green amphibole often containing small specks of opaque minerals. The plagioclase displays a weak preferred orientation defining the planar lamination of the cumulate gabbro.

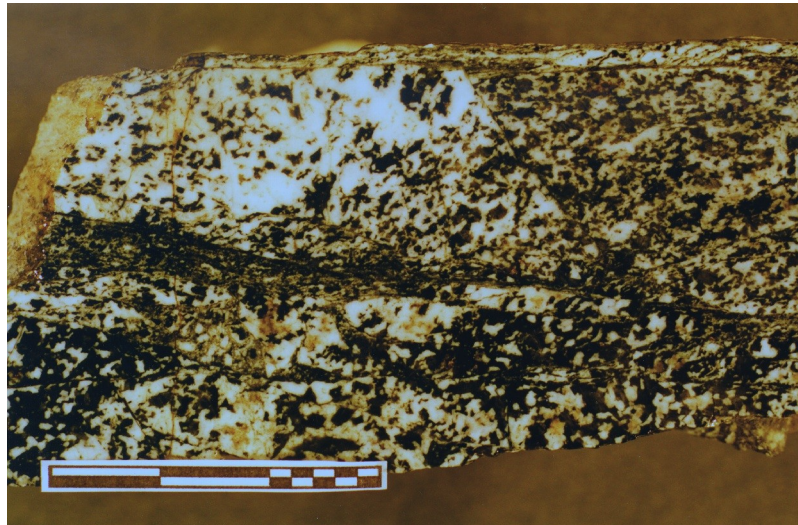


Figure 2.29

Photograph of polished hand sample showing a narrow shear band in cumulate gabbro. The shear bands probably formed at high temperature as indicated by deformed amphibole forming in the shear bands. They occur at high angles with respect to the layering in cumulate gabbro. Also, the shear bands are only found in gabbroic screens and are cut by dikes. Scale bar is 3 cm.

temperatures ($> 600^{\circ}\text{C}$, Wooldridge et al, 1990, Lattard, 1995). Fe-Ti oxides are almost completely absent in the anorthosite layers.

Petrographically, the cumulate gabbro occurring as screens in the sheeted dike complex is distinct from the gabbro typically found in the metagabbro unit. The metagabbro unit contains deformed mafic dikes and enclaves subparallel to magmatic foliation, and the metagabbro does not have a cumulate texture. The main phase metagabbro is coarser grained than the cumulate gabbro in the sheeted dike complex, and mafic to silicic rocks in the metagabbro unit contain uniformly, dark-green colored hornblende. Thus, the variable color of the amphibole in the gabbroic screens, which replaced cpx and almost certainly formed during ocean ridge hydrothermal metamorphism, contrasts strongly with the uniformly colored, dark-green hornblende in the metagabbro suggesting a different igneous and metamorphic history (discussed earlier in section 2.5.4).

Other structures, which occur in the gabbroic screens and are cut by dike intrusions, include amphibole veins, amphibole rimmed epidote veins (figure 2.27), ductile shear bands (figure 2.29) and epidosite zones. The amphibole veins and the amphibole rich (ductile?) shear bands formed probably at temperatures of amphibolite facies conditions ($>400^{\circ}\text{C}$, table 2 of Alexander et al., 1993). However, only remnants of an amphibolite facies assemblage are preserved, such as some patchy, pale-brown and dark-green hornblende replacing clinopyroxene. An amphibolite- transitional to greenschist facies assemblage consisting of ab, ac, ac-hbl, ep, cz, chl, and ti almost completely overprints earlier amphibolite facies assemblages. In addition to variable amphibole compositions, these low-T assemblages are indicative of retrograde metamorphism which is very common in some ophiolite and oceanic gabbros (Harper et al., 1988 and references therein). Interestingly, the ductile shear bands (figure 2.29) occur at relatively low angles with respect to the dike intrusions ($<30^{\circ}$), and the amphibole veins are mostly subparallel to sheeted dikes (figures 2.27). Perhaps, the ductile shear bands and amphibole veins formed in the same extensional regime that gave rise to repeated injection of magma into cracks and fractures in the cumulate gabbro, ultimately resulting in the formation of the sheeted dike complex (see chapter 4). Epidosites and hornblende rimmed epidote veins in the cumulate gabbro are cut by sheeted dikes suggesting hydrothermal circulation and alteration accompanied the intrusion of dikes.

2.7.2 Sheeted Dikes

The color of the dikes depends mainly on grain size and weathering, and subordinately on modal composition and intensity of hydrothermal alteration (e.g., epidiosites are pistachio green). Chilled margins as well as aphanitic, cm-wide dikes are dark-gray or black and appear in water polished outcrops as almost glassy (figure 2.30). Otherwise, the fine grained dikes are gray-green, rarely porphyritic, and have a diabasic texture. Dikes having abundant disseminated pyrite have brown bands on weathered surfaces (limonite), or occur as brown dikes subparallel to the dark-gray and gray-green dikes.

Petrographically, two types of dikes were distinguished in thin section in the sheeted dike complex, and shown in a subsequent chapter to be chemically distinct. The first group includes diabasic dikes consisting of plag + cpx \pm ox. Most of these diabasic dikes are aphyric and only those that are porphyritic typically have less than 5% phenocrysts of cpx, plag, or cpx + plag (pseudomorphs). The igneous texture is well preserved in the strongly recrystallized diabasic dikes, and a subophitic texture is evident (figure 2.31). Occasionally, a distinct grading can be observed in rare phenocryst-rich dikes: the amount and size of phenocrysts in the chilled margins is markedly less than in the center of the dike, and phenocrysts may occur in layers parallel to the dike margin. The graded distribution of phenocrysts in dike intrusions is not unusual and may reflect flow differentiation of magma in the dikes. The ordered distribution and alignment of phenocrysts is thought to result from laminar flow (Ross, 1986). Generally, the diabasic dikes do not exceed widths larger than 3 m.

The second group of dikes includes aphyric, quartz-bearing microdiorites with plag + cpx + qtz \pm ox \pm ti and hypidiomorphic granular texture, which is very similar to the texture of dikes of petrographic group 1, except for the presence of quartz. Interstitial quartz in dikes of group 2 ranges from 3%-12%. Dikes of the second group can be up to 8 m wide and medium grained in the center. Apart from these rare, extremely wide dike intrusions, they are not significantly different in their width compared to the dikes of the first group.

A subgroup of these dioritic dikes (2a) contain olivine xenocrysts (figure 2.30, 2.32) that show signs of resorption. The xenocrysts usually contain octahedra of brown translucent Cr-spinel (figure 2.33). A graded and layered distribution of the olivine xenocrysts in dikes is rare or absent; instead, the

distribution is very heterogeneous. Irregular zones and patches with abundant olivine xenocrysts (up to 30%) may occur in dioritic dikes that are otherwise almost or completely devoid of xenocrysts (figure 2.30). In such heterogeneous dikes, the texture can range from hypidiomorphic granular in patches having no or only few olivine xenocrysts (interstitial qtz present) to subophitic in patches of the same dike having abundant olivine xenocrysts (no qtz present). Figure 2.32 shows a polished sample from a domain within a dike containing abundant, partially resorbed olivine xenocrysts in a ground mass having a subophitic texture. The heterogeneous distribution of olivine xenocrysts probably reflects turbulent flow and/or mixing of magmas during dike injection. Possibly, a relatively silicic magma, which gave rise to the microdioritic dikes, mixed with a mafic magma containing abundant olivine phenocrysts to produce the hybrid-dikes characterized by highly variable texture and heterogeneous composition (e.g. figure 2.30), and resorption of olivine (figure 2.33). The lobate margins of olivine pseudomorphs indicated that resorption occurred. Olivine and quartz are not stable together, and the reaction is $ol + qtz \rightarrow opx$. If orthopyroxene was present, it is now replaced. However, reaction rims were not found probably due to intense hydrothermal alteration.

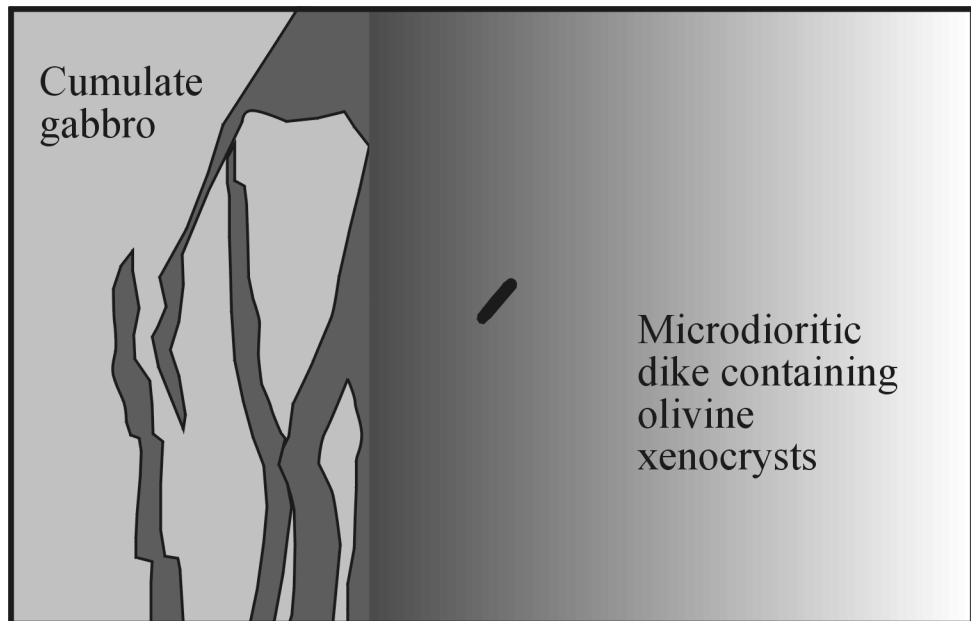
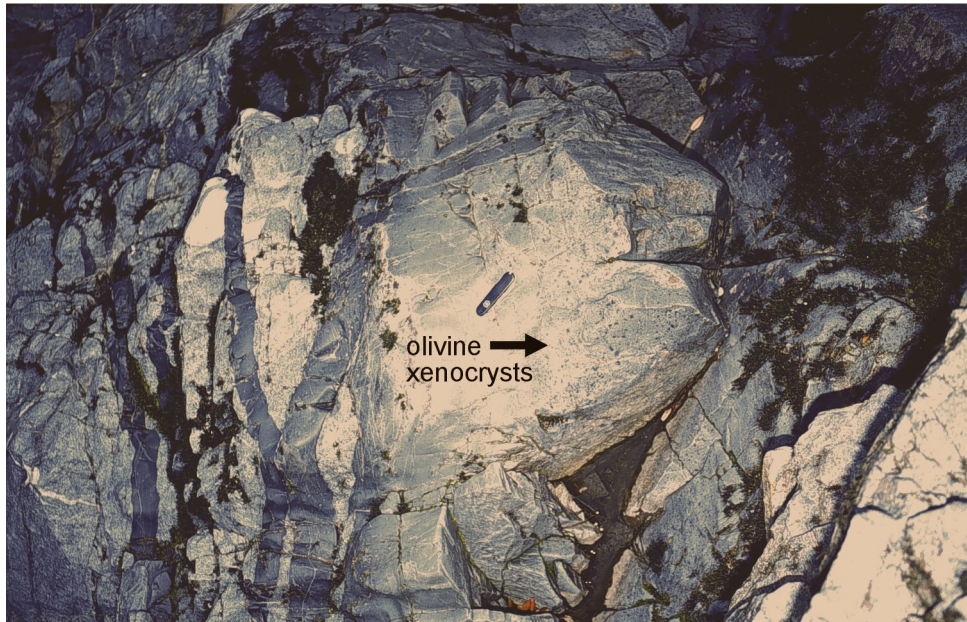
A rare, greenish gray, fine grained porphyritic dike, affected by ductile deformation, is exposed in the lower drainage of the Mule Creek near the contact with the metatonalite unit (O/C-325). The dike intrudes cumulate gabbro and contains few, partially replaced cpx phenocrysts as well as abundant, completely replaced and deformed olivine(?) phenocrysts or xenocrysts (these are ellipsoidal, cloudy mineral aggregates containing some fibrous actinolite). The ellipsoidal, fine grained mineral aggregates contain euhedral Cr-spinel, and are, therefore, interpreted as deformed pseudomorphs of olivine phenocrysts. The ground mass is foliated and appears to consist entirely of greenschist facies minerals (ac + ab + chl + ep) and Fe-Ti oxides. Possibly, these ol + cpx phenocryst bearing dikes represent the mafic end member of the two magmas that mixed resulting in the possibly hybrid dikes (group 2a) described above.

The composition of relic cpx found in O/C-325 was determined by electron microprobe analysis, and the data are listed in appendix C (table C1) The end member composition of cpx phenocrysts in O/C-325 is $Wo_{39,3-42,5}En_{49,3-52,6}Fs_{6,2-8,6}$.

Figure 2.30

Photograph of a quartz-bearing dike of group two intruding a gabbroic host rock (O/C-4-S3). The main dike contains a small domain rich in olivine xenocrysts (right and above knife) whereas the remainder of the dike is almost devoid of olivine xenocrysts. The small dikes fed by the main intrusion are actually completely free of olivine xenocrysts. Unfortunately, such narrow, xenocryst-free dikes of group 2 can rarely be traced to a large dike intrusion with clearly identifiable interstitial quartz and/or olivine xenocrysts. Most of the time, they are indistinguishable in the field from phenocryst-free dikes of group 1. The chaotic distribution of olivine xenocrysts in quartz-bearing microdioritic dikes may indicate turbulent flow and/or magma mixing. The microdioritic dike shown in this photograph intrudes dikes of group 1 about 6 m above this outcrop.

The knife is 10 cm long.



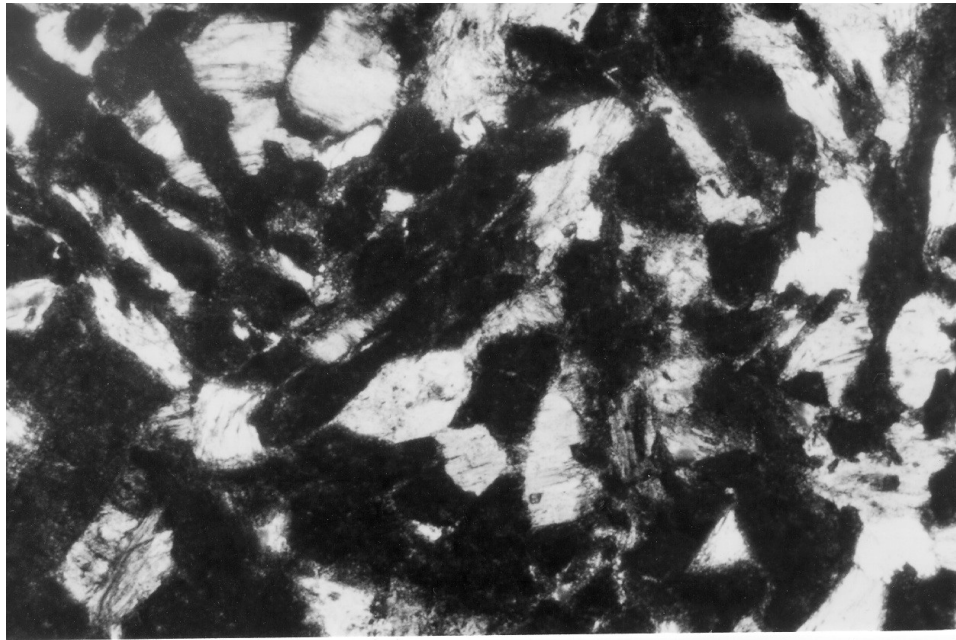


Figure 2.31

Photomicrograph showing texture typical of aphyric diabasic dikes (O/C-58) in the sheeted dike complex of the Rogue Wilderness remnant of the CRO. Clinopyroxene replaced by pale to light green amphibole (white in b/w photograph) is subophitically intergrown with laths of plagioclase pseudomorphed by a cloudy, dark mass consisting of clinozoisite + albite \pm chlorite \pm mica (almost black in b/w photograph). The width of the photograph is 2.16 mm.

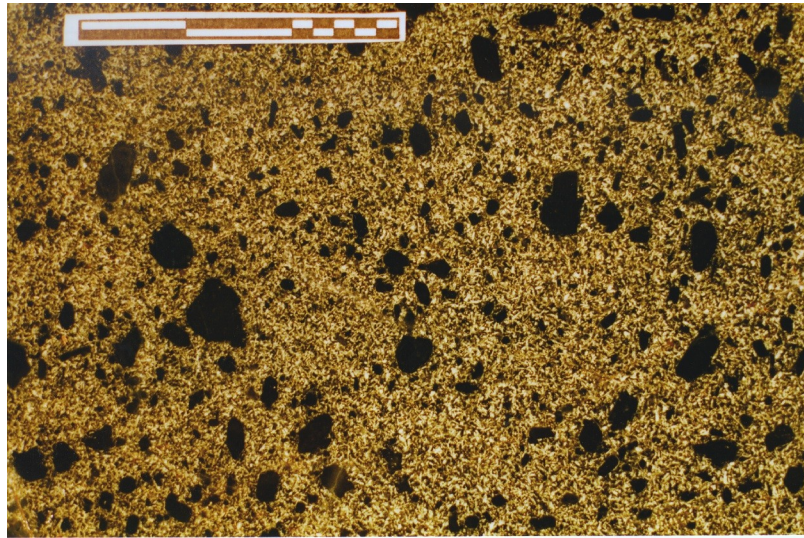


Figure 2.32

Slabbed and polished sample (O/C-4-S3) of a microdioritic dike having abundant olivine xenocrysts (pseudomorphed). The sampled dike consists of several irregular domains (figure 2.30): xenocryst rich parts within the dike contain no or little quartz and have subophitic texture whereas areas without xenocrysts have up to 12% interstitial quartz and hypidiomorphic granular texture. The irregular and heterogeneous distribution of the xenocrysts in a compositionally and texturally variable dike suggests mixing of magmas. The scale bar is 3 cm long.

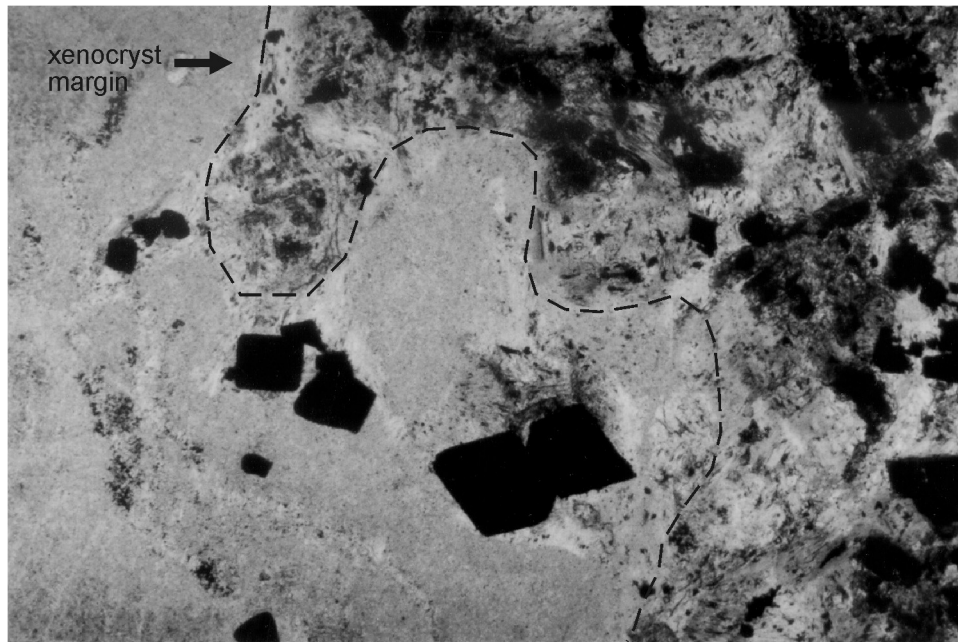


Figure 2.33

Photomicrograph showing translucent brown Cr-spinel (large black diamonds in b/w photograph) in partially resorbed olivine xenocryst (O/C-4-S3b). The resorption of the olivine xenocrysts may result in Cr-spinel crystals occurring in the ground mass (Cr-Spinel in matrix not shown). The ground mass consists of pyroxene and plagioclase; pyroxene is replaced by pale, fibrous amphibole (light gray, cloudy) whereas the dark-gray to black, cloudy masses represent plagioclase replaced by clinozoisite + albite ± chlorite ± mica. In this thin section, interstitial quartz is not present. Few percent of Fe-Ti oxides are present as well (small black minerals in the matrix). The width of the photograph is 2.16 mm.

2.7.3 Cross cutting relationships

Establishing the cross-cutting relationships of dike groups is important to constrain a model of the magmatic evolution of the ophiolite. The relationships observed in the field are summarized below: both groups of dikes are found cutting cumulate gabbro (e.g. figure 2.30). Furthermore, five diabasic dikes (group 1) are intruded by microdioritic dikes (group 2 and 2a) suggesting group 1 dikes are older than group 2 dikes. A certain sequence of intrusion of dikes of group 2 and subgroup 2a could not be identified (i.e., whether microdioritic dikes containing olivine xenocrysts are older or younger than microdioritic dikes having no olivine xenocrysts). Perhaps a continuous(?) episode of formation of group 2 dikes (microdiorites) was interspersed with an event of magma mixing characterized by the simultaneous intrusion of group 2 and subgroup 2a dikes (microdiorites with or without olivine xenocrysts). After the possible episode of magma mixing ended, only group 2 dikes continued to form. Also, magma mixing may explain the scarcity of cpx- and olivine phyric dikes that could represent the mafic end member of hypothesized magma mixing. On the other hand, the timing of intrusions of group 2 and subgroup 2a dikes is extremely difficult to establish because of the compositional and textural heterogeneity of dikes of subgroup 2a. Similarly, possible misidentification of fine-grained, phenocryst- or xenocryst-free dikes in the field poses a problem to establish and document the crosscutting relationships in greater detail, requiring chemical analyses to distinguish the two types of dikes based on composition (discussed in chapter 5).

There are at least two different types of dikes (group 1 and group 2) which can be distinguished petrographically and geochemically (chapter 5). However, differences in the attitude and alteration of group 1 and group 2 dikes are not observed. The typical secondary mineral assemblage (ac, ab, ep, cz, chl, ti, qtz) in all dikes indicates lower amphibolite to greenschist facies conditions. This is very similar to the above described assemblage in the gabbroic host rock. Furthermore, the same crosscutting relationships of hydrothermal veins and mineralized faults are observed in both groups of dikes suggesting that groups 1 and 2 were essentially contemporaneous.

2.7.4 Hydrothermal metamorphism of sheeted dikes

Figures 2.27 and 2.34 show examples of the cross cutting relationships observed in the sheeted dike complex. The amphibole rimmed epidote vein cuts plagioclase-cumulate gabbro, and both are cut by a diabasic dike (figure 2.27). Figure 2.34 shows the surface of a fault with preserved patches of epidote + quartz mineralization which is cut by white prehnite + quartz veins. In general, the following mineral assemblages in crosscutting structures, such as mineralized faults and veins, are identified in the field, hand samples and thin sections and are listed from oldest to youngest: (1) amphibole veins and shears are cut by (2) amphibole-rimmed epidote veins (3) followed by epidosite zones and epidote ± quartz veins, followed by (4) prehnite ± quartz and amphibole ± quartz veins followed by (5) quartz + sulfide followed by (6) pumpellyite ± quartz followed by (7) calcite-veins. Large, prominent faults in the sheeted dike complex are usually mineralized by quartz + sulfide and are easily recognized by their rust-brown color and occasional yellow stains as a result of weathering and oxidation (figure 2.35).

It appears that the dikes intruded into a gabbroic host that maintained over the period of time of dike formation a relatively constant temperature. This is inferred from the following observations which include my own as well as unpublished field mapping of Haschke (written communication, 1994): (1) diabasic and microdioritic dikes cut amphibole-rich shear bands, amphibole rimmed epidote veins, and epidosites which formed primarily in the gabbroic host rock; (2) dikes that cut mineralized faults, epidote ± quartz-, prehnite- or pumpellyite veins were not found. Only few dikes intruded low-angle faults; (3) amphibole rimmed epidote veins are rarely observed in dike; (4) epidosite zones, epidote-, prehnite- and pumpellyite veins cut gabbroic host rock and dikes alike. These crosscutting relationships together with the secondary mineral assemblages in gabbro and dikes may be used to constrain the thermal history of the host rock as the dikes intruded.

The cumulate gabbro cooled (high-T oxidation of Fe-Ti oxides) to temperatures of lower amphibolite- to greenschist facies metamorphic conditions in a subseafloor environment. Amphibole veins, amphibole-rich shear bands, amphibole rimmed epidote veins, and epidosites formed in gabbroic rocks. Similar amphibole veins in ophiolites are constrained to have formed at temperatures $\geq 400^{\circ}\text{C}$ (e.g., Alexander et al, 1993). The formation of epidosites in ophiolites is constrained to have occurred at

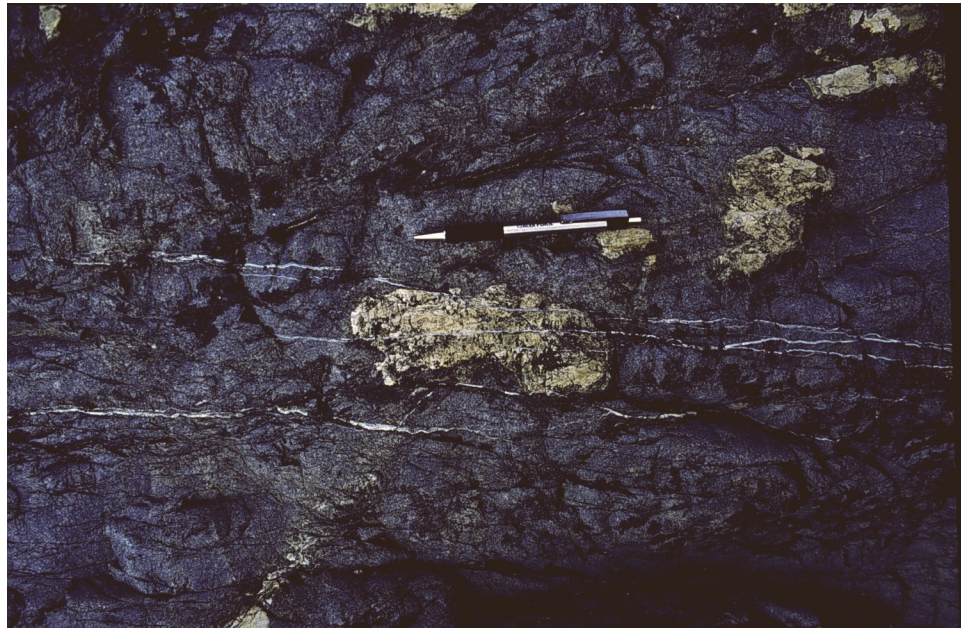


Figure 2.34

Photograph of an exposed fault surface with patches of pistachio green ep+qtz mineralization. Recent abrasion by cobbles along the bank of the Rogue River left these small patches of epidote on the fault surface. White prehnite + quartz veins cut the fault at high angles suggesting retrograde conditions during deformation. The pen is 14 cm long.



Figure 2.35

Photograph of one of several faults across which an abrupt change in dike orientations was observed at the Rogue River section of the sheeted dike complex. The distinctly different orientation of dikes across a large fault zone suggests rotation of fault blocks during deformation. This fault is cemented by quartz and sulfide. The weathering color of the fault is rust brown.

temperatures between 250°C and 400°C involving extreme Ca-metasomatism and high water/rock ratios (e.g. Harper et al, 1988). The dikes essentially formed after the ubiquitous formation of amphibole veins and amphibole-rimmed epidote veins and before the wide-spread appearance of epidote + quartz veins (350°C - 250°C). Gabbroic screens as well as dikes continued to cool and are cut by epidote zones, and epidote-, prehnite and pumpellyite veins ($\leq 300^\circ\text{C}$).

2.7.5 Age constraints

The maximum age of the sheeted dike complex is constrained by the Zircon U/Pb age of a plagiogranite dike intruding a gabbroic screen (SC-1) both of which are cut by a dike (Coleman written communication, 1996). A concordant age of 163 ± 1 Ma was obtained (table 2.1b; Saleeby, written communication, 1999). This suggests the metatonalite unit (164 ± 1 Ma) and sheeted dike complex are very similar in age and, perhaps, are comagmatic (further discussed in chapter 5).

2.8 Pillow unit

The pillow unit (and Half Moon Bar diorite) is a wedge shaped unit that truncates the Blossom Bar shear zone, metagabbro unit, metatonalite unit and sheeted dike complex (figure 2.2a), and the pillow unit may have been faulted against the other units by tectonic wedging. The best exposures of the fault-bounded pillow unit occur along the Rogue River in Huggins Canyon and the confluence of Paradise Creek (plate 1). This extrusive sequence consists primarily of pillow lava but, locally, dikes or sills are abundant. The pillows range in composition from basaltic andesite (most abundant) to andesite (least abundant), and the dikes range in composition from basaltic andesite (most abundant) to dacite/rhyolite (rare). The relative proportions of dikes/sills as compared to pillows are difficult to estimate as well as the relative abundance of mafic versus silicic dikes (bimodal in composition?). The shapes of pillows at several localities indicate overturned submarine volcanic flows which strike northwest-southeast and dip moderately southwest.

2.8.1 Pillowed submarine flows

Typically, the pillows are closely packed containing very little inter-pillow matrix. The dark gray-green pillows range from 0.5 m to 1 m in diameter and often appear subspherical in outcrop (figure 2.36). The spaces in between individual pillows are commonly 1 cm to 10 cm, occasionally up to 30 cm in size and contain chert, pillow clasts, and metatuff. This material is often replaced by epidosite (figure 2.37) or other assemblages characteristic of seafloor hydrothermal alteration. Hyaloclastic fragments in the inter-pillow matrix as well as the glassy rims of pillows are not preserved. Probably, the tuffaceous component consisted originally of hyaloclastic material which formed by granulation of glassy pillow rims upon quenching. Larger fragments could have been derived by spalling of the glassy crust of pillows and/or fracturing of pillows due to rapid cooling. The secondary mineral assemblage replacing glass includes primarily chlorite but also (clino)zoisite, epidote, quartz, prehnite, sulfide and jasper. Epidosites in spaces between pillows are ubiquitous (figure 2.37), suggesting large amounts of hydrothermal fluid passed through between pillows and fractures, ultimately resulting in the complete replacement of glass as well as destruction of primary minerals and textures (epidosites have a granoblastic texture).

Gray et al. (1982) reported that thin beds of shale intercalated with basaltic flow rocks occur in this pillow unit. Unfortunately, the localities of the outcrops are not provided by them, and in the course of two field seasons, the reported (terrigenous?) interflow sediments were not found in the pillow unit. Note that tuffaceous sediments intercalated with andesitic and dacitic flows occur in the Wild Rogue Wilderness. However, these rocks are assigned to the Mule Mountain volcanics (see next section) and not the pillow unit. Overall, it appears that predominantly chemical sediments, such as red radiolarian chert trapped in between pillows, occur in the pillow unit. Unfortunately, the cherts contain only poorly preserved radiolarians because of the pervasive hydrothermal alteration evident in the pillow unit. Sampled radiolarians lacked diagnostic features and could not be identified (E. Pessagno, personal communication, 1995).

In water-polished outcrops, pillows with dark, chilled margins of up to 3 cm width can be identified (e.g. figure 2.37). Amygdules are abundant and occur in more than 50% of the pillows. Typically, only few amygdules are distributed in the center of pillows (figure 2.38), whereas most are

concentrated in the up to 3 cm wide chilled rims (figure 2.37). Neither concentric zones of amygdules nor more than an estimated 10% -15% amygdules in the rims were observed. Pillows are intensely fractured and occasionally display semi-radial and/or concentric cooling fractures. Vesicles and fractures are filled with a wide variety of metamorphic minerals. Even within a single thin section, infillings are highly variable and can be any two to four of the following minerals: ab, ep, qtz, cz, chl, pr, pu, cc, ti (e.g. figure 2.38).

The petrographic summary of representative samples from the pillow unit is given in appendix A (table A4). Typically, pillows are slightly porphyritic (< 5% phenocrysts), and range overall from aphyric to glomerophyric with up to 25% of phenocrysts. Often, the phenocrysts of cpx+plag, plag, or cpx are completely replaced, but can be identified in thin section by the well-preserved crystal form. Many phenocrysts are only twice (or more) as large as grains in the matrix (microphenocrysts). Well preserved quench textures, such as variolites and skeletal crystals of swallow tail and hollow plagioclase, are rarely preserved. Away from the chilled margins, pillows show intergranular (or intersertal?) textures (figure 2.38).

The secondary mineral assemblage in the pillows is $ab + chl + ep + ti + qtz \pm ac \pm pu \pm pr \pm musc \pm cc$. Locally, disseminated sulfide in pillows is evident as rust brown stains in weathered pillow basalts. Cpx is partially to completely replaced both as phenocryst and in the matrix, usually by actinolite \pm magnetite. Based on optical characteristics, the composition of cpx is augite. Plagioclase is albitized and/or replaced by a fine grained cloudy mineral aggregate. Compared to other CRO remnants, the alteration of the pillows is extreme (e.g., Schiffmann et al., 1991).

The vesicles (amygdules) indicate that the magma degassed upon eruption releasing volatiles that could not be kept dissolved due to the lower confining pressure of the environment of eruption. Obviously, the amount of vesicles that form in the pillows depends not only on the primary volatile content of the magma, but also on the depth of water at which the lavas erupted (Harper, 1982). Radiolarian cherts occur as interpillow matrix implying eruption of lavas in deep ocean. Thus, the formation of vesicles in pillow rims occurred probably at considerable depth of water suggesting a relatively high primary volatile content of the magma. High vesicularity related to a high volatile-content of the erupting lava is characteristic for a volcanic arc environment and many back-arc basins (e.g., Matveyenko and Khain, 1988), in contrast to



Figure 2.36

Photograph of water polished outcrop near Paradise Bar on the Rogue River just above the summer water-level. Interpillow material is eroded out, and the round and subspherical shapes of the pillows are exceptionally well-exposed. Just few meters above this outcrop (above winter water-level), the pillow-shapes are not identifiable because of poor exposure and strong weathering.



Figure 2.37

Photograph of pillow exposed in Huggins Canyon (O/C-228). The interpillow material in this outcrop is completely recrystallized and consists of epidote+quartz±chlorite (epidosite). The veins, possibly representing cooling fractures, contain epidote and quartz. Vesicles in this pillow occur in the dark rim (originally glassy) and are filled with prehnite+quartz or quartz±chlorite (white amygdules). Only a few meters downstream of this outcrop, chert occurs in the interpillow matrix suggesting abyssal conditions of eruption. Vesicles occurring in glassy rims of pillows that erupted at considerable water depth indicate high volatile content of the magma (e.g. Harper, 1982).

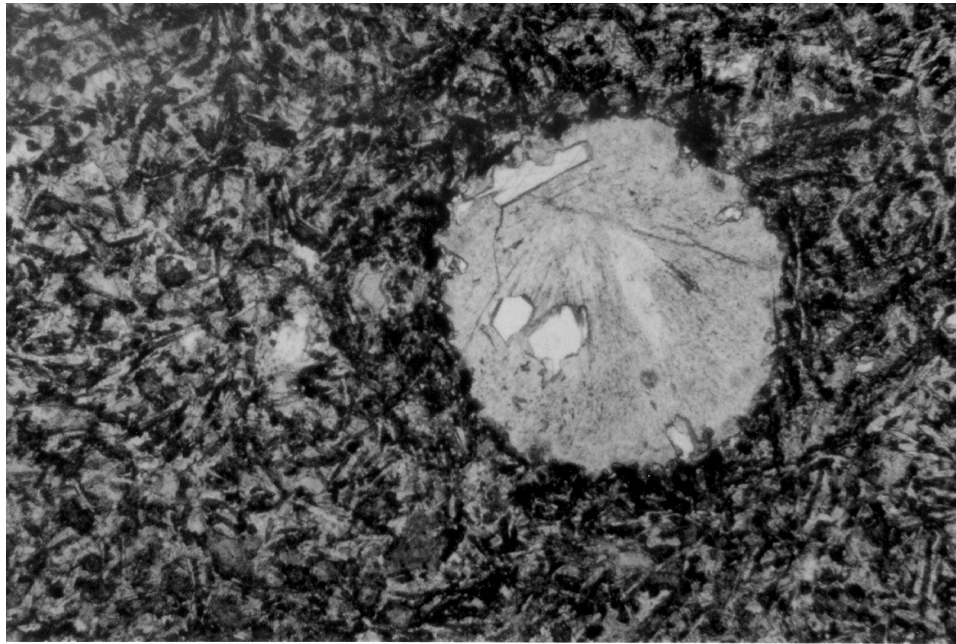


Figure 2.38

Photomicrograph of center of pillow (O/C-227A) showing typical intergranular (intersertal?) texture of pillows away from chilled margins. Laths of plagioclase and clinopyroxene as well as the interstitial matrix are partially to completely replaced obscuring much of the original texture. The metamorphic assemblage in the pillows includes albite + chlorite + epidote + titanite + quartz \pm actinolite \pm pumpellyite \pm prehnite \pm muscovite \pm calcite. Few vesicles occur in the centers of most pillows. The vesicle is filled with radiating epidote, quartz and disseminated flakes of chlorite. The width of the photomicrograph is 2.14 mm.

non-vesicular mid ocean ridge basalts. However, some basalt glasses from the Mid-Atlantic ridge contain microvesicles which formed by outgassing of CO₂ of lavas erupted at the Azores platform (Kingsley and Schilling, 1995).

2.8.2 Dikes

Two types of dikes are identified in the pillow unit based on their color and composition. The first group of dikes includes fine grained diabasic to andesitic dikes which are indistinguishable in color from the pillows (dark gray-green). These dikes are typically 30 cm to 50 cm in width, rarely contain any phenocrysts and have chilled margins on both sides. Close examination of the dikes in the pillow unit, however, reveal similar intrusive relationships as in the sheeted dike complex. Some dikes were split and intruded by younger dikes resulting in “half-” and “marginless” dikes. Although the dikes are indistinguishable in color from the pillows, they contain some modal quartz unlike the pillows (quartz in ground mass). They consist of cpx (30-40%), plag (50-55%), qtz (1-10%) and <5% Fe-Ti oxides and have a subophitic texture in diabasic dikes and intergranular to granophyric (figure 2.39) textures in quartz-bearing dikes. The degree of alteration and the secondary mineral assemblage is similar to that of the pillows. Although some of the quartz formed probably due to alteration (i.e. when occurs as replacement of primary minerals), most of it represents an igneous phase, inferred from the textural relationships. Granophyric textures are common (figure 2.39) and probably formed in an igneous regime. Similar to the granophyric texture identified in samples from the metatonalite unit (e.g. figure 2.18), radiating intergrowth of quartz and plagioclase are arranged about euhedral, equant plagioclase crystals (figure 2.39). Also, quartz occurs as an interstitial phase and probably crystallized late. Overall, the dikes in the pillow unit differ texturally and compositionally from the porphyritic dikes in the Half Moon Bar diorite (described in later section). Apart from the granophyric texture, the dikes in the pillow unit resemble most closely the aphyric diabasic dikes in the sheeted dike complex and thus, may be related.

The second group of dikes intruding the pillow unit include white to beige dacitic dikes (figure 2.40) which are scattered throughout the eastern fault slice of the pillow unit (figure 2.2a). The light color of the dikes contrasts strongly with the dark host rock. The dacitic dikes are porphyritic and contain



Figure 2.39

Photomicrograph of granophyric texture in dikes intruding pillows (O/C-226a). These dikes are indistinguishable in color from the pillows and appear to be mafic at first glance. However, they contain up to 10% primary quartz which is either intergrown with plagioclase and/or occurs as late, interstitial phase between laths of plagioclase and clinopyroxene. Similar to the granophyric texture in samples from the metatonalite unit (figure 2.18), radiate intergrowth of quartz and plagioclase are arranged about euhedral, equant plagioclase crystals. The width of the photomicrograph is 2.14 mm.



Figure 2.40

Photograph of leucocratic dike in the pillow unit near Brushy Bar (O/C-231). These light colored dikes consist essentially of plagioclase and quartz, are porphyritic (15-20% plag, 5-10% qtz and $\ll 1\%$ cpx phenocrysts) and contain a similar metamorphic assemblage as the pillows (ab, ep, chl, pr, pu). The width of the dikes is highly variable ranging from few centimeters to 2 meters. Note hammer for scale.

abundant, ~1 mm phenocrysts of plag (15-20%), qtz (5-10%) and scarce cpx (<<1%). The matrix is xenomorphic granular and consists mainly of plagioclase and quartz. Fe-Ti oxides (opaque specks in thin section) occur in trace amounts. Plagioclase is saussuritized and cpx altered mainly to chlorite. Other secondary phases include ab, ep, cz, pr, and pu. These dikes differ compositionally and texturally from the tonalitic dikes in the metagabbro unit. However, they are very similar to the tonalitic rocks intruding the western fault-slice of the pillow unit. The felsic dikes could represent highly fractionated dikes related to the Half Moon Bar diorite, which locally intrudes the pillow unit (Gray et al., 1984), or they could represent highly fractionated dikes that have the same source as the pillowed submarine flows (further discussed in chapter 5).

2.8.3 Structure

The sheeted dike complex, metatonalite unit, metagabbro unit and the Blossom Bar shear zone (figure 2.2a) are truncated along a fault by the easternmost part of the pillow unit. The fault is partially exposed at the Rogue River near Blossom Bar, where the pillow unit is clearly faulted against mylonites of the Blossom Bar shear zone. The pillow unit and Half Moon Bar diorite may represent a tectonic wedge (figure 2.2a) emplaced before the deposition of Lower Eocene strata. The nature of the contact of the pillow unit with the (overlying?) Mule Mountain volcanics is not clear. Several outcrops of heavily brecciated and sheared rocks in the bed of Blossom Bar Creek indicate the existence of a fault zone. However, one should keep in mind that similar fault rocks occur within the pillow- as well as within the Mule Mountain volcanics, and the outcrops of fault rocks in the Blossom Bar Creek may not qualify as the unit boundary. Perhaps, both extrusive units are in depositional contact. Although an exact boundary between the extrusive units may not be drawn in the geologic map, the lithological and petrographic (and age?) differences between the pillow unit and the Mule Mountain volcanics justify the subdivision of the extrusive sequence into two distinct units.

The fault that represents the terrane boundary between the Yolla Bolly terrane (part of the Franciscan complex) and Snow Camp Mountain terrane forms also a large portion of the eastern boundary of the pillow unit. The western fault-slice of the pillow unit is unconformably overlain by gently west-

dipping Tertiary sedimentary rocks. In the center of the pillow unit occurs a tapering fault slice exposing the Half Moon Bar diorite. At several localities, abundant tonalitic dikes, possibly related to the Half Moon Bar diorite, intrude the pillows (figure 2.2a).

The pillowed submarine volcanic flows appear to be overturned (they strike NW-SE and dip moderately SW) as inferred from the shapes of pillows at several localities (figure 2.2a). The orientation of these flows is approximately perpendicular to the dikes in the northernmost section of the sheeted dike complex. This relationship could be coincidence, because the pillow unit and the sheeted dike complex are different fault slices, and the sheeted dike complex is internally complexly deformed (i.e., rotation of fault blocks).

2.8.4 Age constraints

The minimum age of the pillow unit is constrained by the intrusion of the Half Moon Bar diorite. The hornblende $^{40}\text{Ar}/^{39}\text{Ar}$ age (157.2 ± 2.0 Ma, Heizler, written communication, 1998) and the K-Ar age (159 ± 3 Ma, Gray and McKee, 1981) determined in samples from the Half Moon Bar diorite are consistent with the new zircon U/Pb ages of 159 - 160 Ma (Saleeby, written communication, 1999) determined in three samples from the Half Moon Bar diorite. These ages indicate the pillows formed in late Jurassic time or earlier.

Pillowed volcanic flows also occur in the Snow Camp Mountain area about 50 km south of the Wild Rogue Wilderness along strike (figure 2.1a). Interpillow chert yielded well-preserved radialaria which are of Callovian to middle Oxfordian age (chert samples taken by G.D. Harper, 1996; biostratigraphic / chronostratigraphic determination by E.A. Pessagno, 1996). Assuming the ophiolite remnants near Snow Camp Mountain and in the Wild Rogue Wilderness are part of the same terrane, it is very likely that the pillowed submarine flows exposed in the Wild Rogue Wilderness are also of Callovian to Middle Oxfordian age (~164-158 Ma).

2.9. Mule Mountain volcanics

The Mule Mountain volcanic unit is exposed in the northwestern part of the Wild Rogue Wilderness and forms a thick, fault-bounded unit consisting of volcanic flows, shallow intrusives and volcanoclastic rocks. The maximum structural thickness is 2.5 km (figure 2.2a). Exposures which clearly show the contact relationships between Mule Mountain volcanic unit and the sedimentary rocks of the Myrtle Group were not found. On one hand, heavily fractured and sheared rocks occur between scattered outcrops of conglomerates and volcanic flow rocks in the west fork of Blossom Bar Creek suggesting a fault separates the Mule Mountain volcanics and the Myrtle Group (Riddle and Days Creek Formations). The outcrop distribution of the upper volcanic unit indicates a northeast-southwest striking and steeply dipping contact. A low angle thrust fault between the Myrtle Group and Mule Mountain volcanics as suggested by Baldwin and Rud (1972) and later adopted by Gray et al. (1982), could not be confirmed. On the other hand, the attitude of volcanoclastic sediments and locally interbedded chert is subparallel to this contact as well as subparallel to the sedimentary layers of the Myrtle Group suggesting that depositional (conformable or non-conformable) contact relationships are possible.

To the east, the Mule Mountain volcanic unit is in contact with the Blossom Bar shear zone. Strongly foliated volcanic breccias characteristic of the Mule Mountain volcanics occur within and along the western margin of the Blossom Bar shear zone indicating that ductile deformation post-dates the Mule Mountain volcanics.

The Mule Mountain volcanic unit can be subdivided into two sections: The lower section consists of basaltic to andesitic flows and shallow intrusives intercalated with volcanic breccia, all of which crop out to within 400-500 m east of the Myrtle Group (figure 2.2a and 2.2b). Attempts to differentiate between the basaltic and andesitic rocks in the field based on the phenocryst assemblage and the color were unsuccessful. A petrographic summary of representative samples from the lower section of the Mule Mountain volcanics is presented in appendix A (table A5). It seems that the metabasalts and metaandesites, as defined by geochemistry, have similar phenocryst assemblages, and the color is primarily controlled by the metamorphic mineral assemblage as well as the degree of weathering. In general, the volcanic rocks range from aphyric to highly porphyritic (up to ~30-35%) and have usually one to three of the following

phenocrysts: olivine (inferred from pseudomorphs), clinopyroxene (relict), plagioclase and magnetite. The volcanic rocks range from greenish black to various shades of gray and green to purplish red and brown. Pillow-like features are not observed in the Mule Mountain volcanic unit. However, the flows are often amygdaloidal or vesicular, and in places contain extremely elongate vesicles or amygdules indicating flow of a relatively viscous lava. Also, diabasic to andesitic dikes or sills intrude flow rocks.

Gray et al (1982) reported that the portion that is defined as the lower section of the Mule Mountain volcanic unit consists mainly of plagioclase-bearing and clinopyroxene-bearing andesite flows. However, in contrast to the study of Gray et al (1982), it is suggested that most rocks in the lower part of the Mule Mountain volcanics are more similar to basalt and basaltic andesites than andesite. This is primarily based on the classification of representative samples using 'immobile' trace elements (see chapter 5). Overall, caution should be applied using the classifications based on modal composition (QAPF) or major elements (TAS) as outlined by Le Maitre et al. (1989), because of potential element mobility related to the alteration of the volcanic rocks. For example, secondary quartz is common in the Mule Mountain volcanics, and basalts could be erroneously classified as andesites using the TAS classification if silica was added from hydrothermal fluids. Also, modes of igneous minerals as well as primary An-content of plagioclase (rarely preserved) are difficult (in many cases impossible) to determine in these fine-grained, metamorphosed rocks.

The upper section of the Mule Mountain volcanic unit, near the contact with the sedimentary rocks of the Myrtle Group, varies in thickness ranging between 100-1000 m (figure 2.2a), and consists mainly of volcanogenic sandstones and volcanic flows and shallow intrusives of dacitic composition. Intercalated are basaltic and andesitic rocks, volcanoclastic sandstones as well as thinly laminated mudstones and minor amounts of radiolarian chert. Thick volcanoclastic sandstones found on north side of upper West Fork of Mule Creek and in Bolivar Creek (Harper, unpublished petrographic data) are an important part of the upper section of the Mule Mountain volcanic unit (figure 2.2a). The bedding and the fold axis of the uppermost section of the Mule Mountain volcanics are subparallel to the bedding and fold axis of the structurally(?) overlying Myrtle Group (chapter 4). The upper section of the Mule Mountain volcanic unit coincides with the dacite to dacitic andesite flows of Gray et al (1982). In general, the dacitic

rocks are characterized by a light-brown to beige color and commonly have one of two phenocryst assemblages: (1) plagioclase + quartz + clinopyroxene, and (2) plagioclase + hornblende ± quartz. The various rock types in the Mule Mountain volcanic unit are described in the following sections in more detail.

2.9.1 Volcanic breccia

Figure 2.41 shows a sample of a typical volcanic breccia from the Mule Mountain volcanic unit consisting of unsorted, angular rock fragments in a extremely fine grained matrix (mostly chlorite). Individual clasts identified in the breccia range from broken phenocrysts (<1 m m) to volcanic rock fragments of up to 30 cm in size. The clasts are angular to subangular in shape and consist of a large range of different volcanic rocks which can be distinguished based on their texture, phenocryst assemblage and color. The clasts are aphyritic or porphyritic volcanic rocks and, if porphyritic, they have one to three of the following phenocrysts: olivine, clinopyroxene, plagioclase and magnetite. Many clasts have abundant amygdules. In general, the reddish brown and purplish red clasts contain abundant disseminated hematite and secondary quartz whereas the green clasts contain dominantly chlorite and epidote as secondary phases. The various colors of the clasts correlate well with certain secondary mineral assemblages. Overall, the clasts are characterized by a wide variety of primary and secondary mineral assemblages as well as textures and colors suggesting that alteration of clasts occurred prior to brecciation and that the clasts were eroded from a variety of volcanic rocks. The secondary mineral assemblages in the clasts, in the fillings of vesicles and in the matrix of the breccia, and the type of alteration are suggestive of subseafloor hydrothermal metamorphism. The differently altered volcanogenic clasts indicate that subseafloor hydrothermal alteration occurred prior to brecciation, transport and deposition. However, the recrystallization and mineralization of the matrix as well as veins cutting breccias indicate that hydrothermal metamorphism also postdates deposition; i.e. volcanism and hydrothermal alteration were essentially synchronous.

In the west fork of Mule Creek the breccias are in sharp contact with volcanic flow rocks and do not grade from intact flows to brecciated rocks. A breccia in gradational contact with a flow would

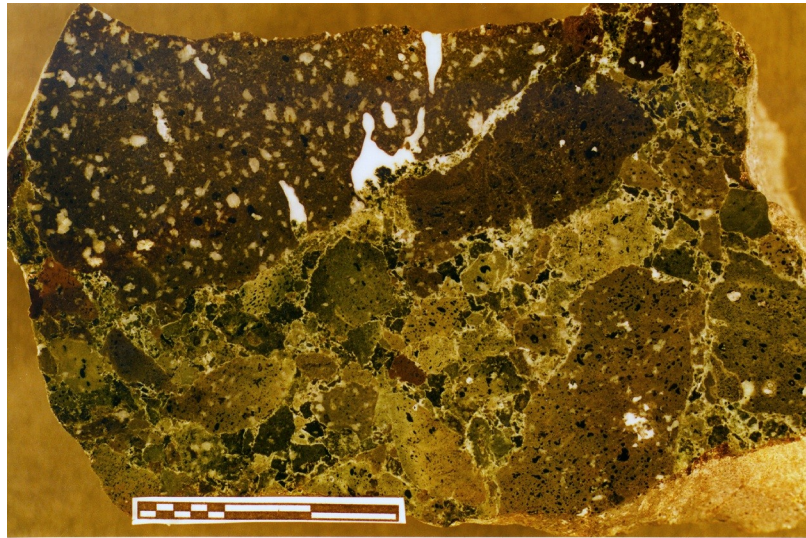


Figure 2.41

Photograph of slabbed and polished hand sample of typical breccia in the Mule Mountain volcanic unit. Volcanic flow rocks of basaltic to andesitic composition are intercalated with these volcanic breccias. The fragments are angular to subangular in shape and consist of volcanic rocks of various composition as well as broken phenocrysts. The color of the volcanic rocks is primarily determined by the secondary mineral assemblage. Reddish or purplish brown colors indicate abundant disseminated hematite whereas green colors correlate with abundant chlorite and epidote. The fragments with different colors in this breccia suggest that they were derived from a volcanic source characterized by heterogeneous alteration. Transport and redeposition of fragments must have occurred after the heterogeneous alteration of the volcanic rocks. The scale bar is 3 cm long.

suggest that the breccia formed by autobrecciation during flow which would result in breccias containing fragments with similar textures and colors. However, the breccias contain fragments of volcanic rocks having different textures and compositions, clasts are variably colored, and the breccia is in sharp contact with extrusive rocks. Thus, the variably colored breccias are interpreted as a talus breccia, or they could have formed due to submarine pyroclastic flows.

2.9.2 Basalt and basaltic andesite flows

The volcanic rocks, classified as basalt and basaltic andesites using ‘immobile’ trace elements, are porphyritic and contain up to 25% phenocrysts of ol +plag +cpx or of cpx + plag ± mt (appendix A, table A5). Olivine pseudomorphs were found only in sample O/C-81a, and olivine is completely replaced. Plagioclase is usually <1 mm and appears to be unzoned. Determination of the An content in relatively unaltered plagioclase phenocrysts (GDH-7 and GDH-8) indicate calcic plagioclase compositions (An₇₅₋₈₀) consistent with a basaltic composition of the volcanic rocks. Ewart (1976) showed that calcic labradorite-bytownite (~An₇₅) is the predominant compositional range for plagioclase phenocrysts in most modern orogenic basalts and basaltic andesites, and labradorite (~An₆₅) for plagioclase phenocryst in andesites. However, andesites can have highly An-rich pheno- or xenocrysts, such as some andesites from Japan. In basaltic sample O/C-81a, the cpx phenocrysts reach sizes of up to 8 mm and contain, as well as olivine pseudomorphs (figure 2.42), euhedral, translucent Cr-spinel. Results of the microprobe analysis of compositions of cpx phenocrysts in O/C-81a are listed in appendix C (table C2). Cpx phenocrysts are Ti-poor augite, and the end member composition is Wo_{40.9-45.6}En_{47.7-49.6}Fs_{5.5-10.1}. Phenocrysts of Ca-poor pyroxene are not found in any of the samples, but this could be due to alteration (opx alters readily like olivine whereas cpx is usually little altered). The matrix is composed of euhedral laths of plagioclase, subhedral to anhedral brownish augite, Fe-Ti oxides and interstitial chlorite (figure 2.42) (interstitial glass or hypocrySTALLINE material is altered to chlorite). The ground mass textures range from intersertal or intergranular (e.g. figure 2.42) to pilotaxitic. Additionally, hyalophitic textures are also recognized in some breccia clasts: fine grained laths of plagioclase and augite are enclosed in a matrix of chlorite probably replacing glass.

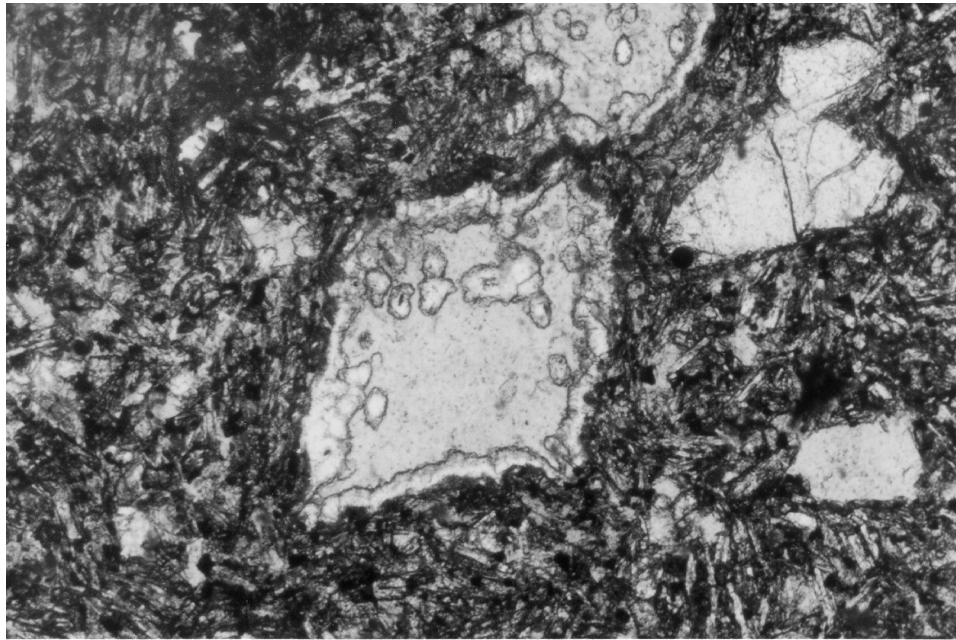


Figure 2.42

Photomicrograph of the intergranular texture of the basalt sample O/C-81a. The matrix is composed of lath-shaped, euhedral plagioclase, subhedral to anhedral augite and Fe-Ti oxides. Two phenocrysts of unaltered clinopyroxene (augite) are shown to the right and two larger olivine pseudomorphs consisting of quartz and chlorite in the center. Alteration and replacement of igneous phases by a wide range of secondary minerals is common. Clinopyroxene is relatively well-preserved. The width of the photomicrograph is 2.14 mm.

2.9.3 Andesites and dacites

Two samples of andesitic composition are identified using the trace element classification. One sample is aphyric (O/C-147) and the other is porphyritic (O/C-217) and contains predominantly plagioclase phenocrysts (13%) and only few percent phenocrysts of cpx (2%) and magnetite (2%). The magnetite phenocrysts are only identified in thin section because of their small grain size. Both samples are amygdaloidal and have a trachytic texture. Acicular and lath-shaped plagioclase are predominant in the matrix, are aligned due to flow, and have the tendency to be arranged in bands (figure 2.43). However, this poorly defined banding is not visible in hand samples. The color of the samples is relatively uniform which is related to the secondary minerals: one sample (O/C-217) contains disseminated hematite and secondary quartz and has a purplish red color, whereas the other sample (O/C-147) has a secondary mineral assemblage consisting mainly of quartz, epidote and chlorite resulting in a dark green color. Igneous matrix components besides plagioclase include some Fe-Ti oxides, granular pyroxene and chlorite. Overall, characteristics that could be used in the field to distinguish basalts from the andesites are not found.

The light brown to beige dacitic flows and/or shallow intrusives have either phenocrysts of plag + qtz + cpx, or of plag + hbl ± quartz (appendix A, table A5). Plagioclase porphyroclasts are predominant in all dacitic rocks and constitute up to 30%. They are 0.5 - 2 mm in size, euhedral in shape and often contain glass (now chlorite) inclusions (figure 2.44). However, plagioclase is usually completely replaced and albitized (cloudy in thin section). Quartz phenocrysts in the cpx phyric dacites are 1 - 3 mm and form up to 10% of the dacitic rocks. Usually, they have round outlines as well as embayment structures indicating partial resorption. Well-preserved quartz phenocrysts have the characteristic crystal form of b-quartz. Also, fractured or brecciated phenocrysts of plagioclase and quartz occur which are similar to broken phenocrysts abundant in Great Basin ash-flow tuffs (Best and Christiansen, 1997). However, broken phenocrysts in the dacitic flows in the Wild Rogue Wilderness appear to be rare. Best and Christiansen (1997) suggested that breakage of phenocrysts may occur by vesiculation of the melt that was entrapped as inclusions in the crystals. During explosive eruptions the magma is rapidly decompressed, and the vesiculating melt in the inclusions may exert enough pressure to blow phenocrysts apart. Best and Christiansen (1997) propose the name phenoclasts for these broken phenocrysts. Apparently, ash-flow

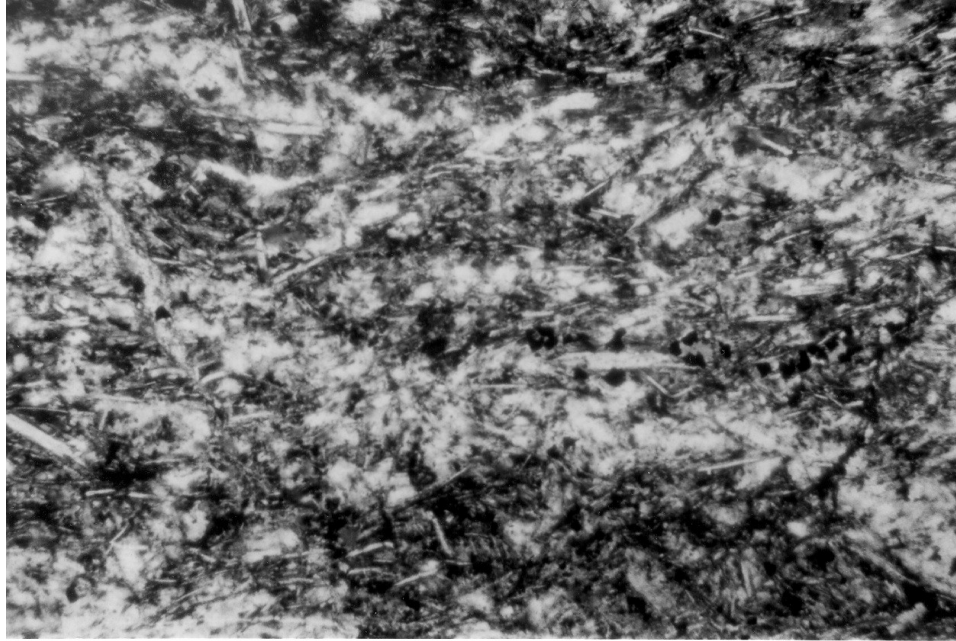


Figure 2.43

Photomicrograph of the trachytic texture of an aphyric andesitic sample in the Mule Mountain volcanics (O/C-186). Acicular and lath-shaped plagioclase are aligned and have the tendency to be arranged in bands. Note the two lighter colored bands stretching from left to right. Other matrix components include granular pyroxene, Fe-Ti oxides and a wide range of secondary minerals such as chlorite (replacing glass), albite, epidote, quartz, prehnite, and hematite. The width of the photomicrograph is 0.6 mm.

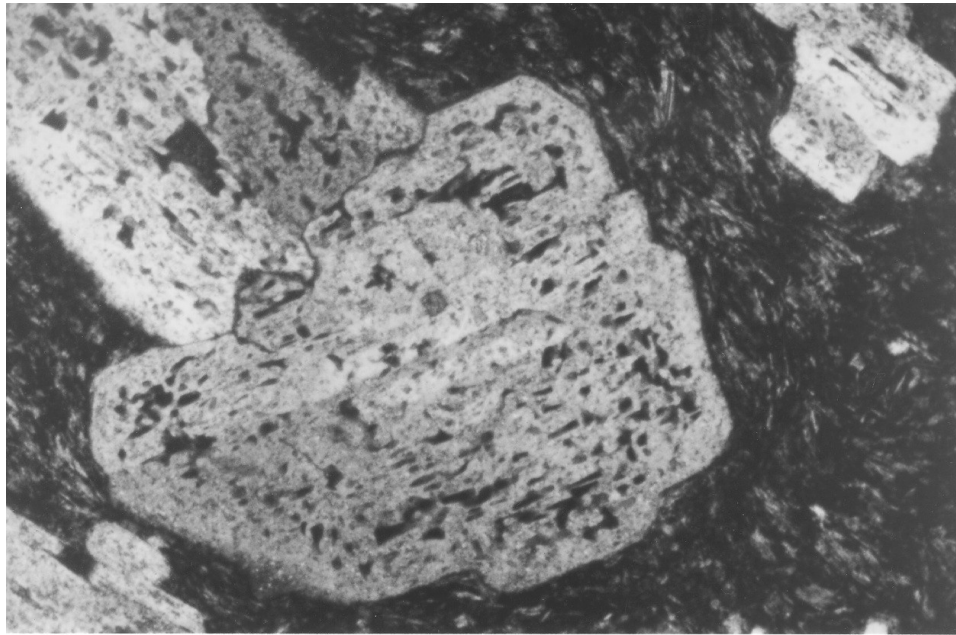


Figure 2.44

Photomicrograph of plagioclase phenocryst in dacitic sample from the Mule Mountain volcanics (GDH-2b). The twinned plagioclase phenocrysts contain abundant inclusions of chlorite probably replacing glass (crossed Nicols). The width of the photograph is 2.14 mm.

tuffs from explosive eruptions contain abundant phenocrasts which are diagnostic of such deposits, whereas phenocrasts are rare in lava flows associated with the explosive deposits (Best and Christiansen, 1997). Perhaps this mechanism explains some of the highly fractured quartz in the dacite flows. Euhedral clinopyroxene is clear to light brown in thin section, ≤ 1 mm in size, and constitute up to 15% of the rock. Minerals partially replacing pyroxene include chlorite and prehnite. Hornblende phenocrysts are brown-green to dark brown in thin section, are euhedral in shape, and occasionally contain inclusions of euhedral apatite. Hornblende phenocrysts form usually less than 10% of the hornblende-phyric dacites and range from unaltered to partially- to completely-replaced crystals. Unaltered hornblende is light brown to greenish brown in color. Typical secondary minerals replacing hornblende include chlorite, pumpellyite, and prehnite. The matrix of the dacitic rocks consists predominantly of feldspar (albite) and quartz. Only a few percent of Fe-Ti oxides ($<2\%$) and chlorite ($<5\%$) is found in the matrix. Sericite appears to be common throughout these rocks.

2.9.4 Mudstones and sandstones

Strongly weathered outcrops of sedimentary rocks (figure 4.45) are scattered in the upper (westernmost) section of the Mule Mountain volcanic unit. These sediments appear to be in depositional contact with the dacitic flows as observed in an outcrop along the 4WD road leading to the Golden Bullet Mine (Old Red Mine). Individual beds range from 1cm to about 20 cm in thickness (figure 4.45) and are well-laminated. Sandstones, mudstones and cherts are interbedded at this locality. The thinly laminated beds occasionally contain radiolarians (up to $\sim 20\%$), and the clastic constituents are too fine grained (10 mm) to be identified in the altered sedimentary rocks. Chlorite and sericite appear to be ubiquitous and perhaps replace glass or other fine-grained volcanoclastic material. The thinly laminated rocks appear to be radiolarian-bearing metatuffs. Other layers contain coarser clasts which can be up to 0.8 mm in size. These clasts consist mainly of saussuritized plagioclase, altered pyroxene, epidote, some magnetite and minor quartz. The shapes of the crystals range from anhedral to almost euhedral. Also, a layer graded from sand to mud was observed in a polished hand sample. Overall, the fine grained, radiolarian-bearing, well-laminated sediments seem to be interlayered with graded beds that carry a sandy, volcanogenic component.



Figure 2.45

Photograph of sedimentary rocks exposed on the 4WD road leading to the Golden Bullet (Old Red) Mine in the Wild Rogue Wilderness. Layers range from about 1 cm to 20 cm in thickness and are thinly laminated. The clastic component is extremely fine grained (mud), and can be up to 0.8 mm in size (sand) and is probably of volcanogenic origin. Occasionally, the thin laminae contain radiolarians in an extremely fine grained matrix suggesting deep ocean deposition. A polished hand sample from this outcrop shows graded bedding.

This indicates that deposition occurred in relatively deep water within reach of the fringes of turbidity currents. Apparently, the 'background' sedimentation of radiolarians and fine grained detritus was periodically interspersed with coarser grained volcanogenic deposits that were carried by turbidity currents. Note that the fine-grained secondary minerals identified in the sedimentary rocks (e.g. chlorite, epidote) as well as the altered clasts (e.g. saussuritized plagioclase, partially replaced cpx) could have been derived from volcanic rocks that were weathered and/or metamorphosed prior to transport and deposition (similar to the alteration of clasts in the volcanic breccias). However, abundant veins (e.g., prehnite, calcite) indicate that alteration must have also occurred after deposition. Furthermore, no terrigenous component in these sediments has been found (Harper, 1999; unpublished petrographic data). Future, more detailed studies applying sandstone petrology and Nd-isotope analysis of fine grained-rocks may constrain the source region(s) of these sediments, which can be important for regional interpretations.

2.9.5 Hydrothermal metamorphism

Typically, clinopyroxene is well-preserved and in places partially replaced by chlorite and quartz. Well-preserved cpx is common in volcanic rocks from CRO remnants in California (e.g. Giaramita et al, 1998). Actinolite replacing cpx is rarely observed in the Mule Mountain volcanics. Plagioclase is saussuritized and typical secondary minerals include ab, ep, cz, chl, and musc. Secondary minerals in amygdules, veins and faults include ep, chl, qtz, pr, pu, cc, and lau. One amygdule in sample O/C-147 contains quartz, chlorite and garnet (hydrogrossular?). A large cavity in sample O/C-81a contains spherical 'ghost' structures in an assemblage consisting of epidote, chlorite and quartz which could have been chalcedony or zeolite. This would suggest that low-T weathering or alteration (palagonite, zeolite or chalcedony) was replaced by a later mineral assemblage indicating higher temperatures of formation (greenschist). Overall, variable alteration in basalt, andesite, dacite, and sedimentary rocks (e.g., figure 2.41) as well as the mineral assemblages in veins indicate subseafloor hydrothermal metamorphism. (e.g., Evarts and Schiffmann, 1983; Harper et al, 1988; Schiffmann et al., 1991)

The bulk (lower section) of the Mule Mountain volcanics consists of hydrothermally metamorphosed plag + cpx phyric rocks ranging in composition from basalt to basaltic andesite. This

conclusion is based on the chemical classification and petrography of representative samples as well as the observations in the field. Hydrothermally metamorphosed basalts containing ol + plag + cpx phenocryst with inclusions of Cr-spinel, plag + cpx phyric andesites, volcanic breccias and other volcanoclastic sediments represent volumetrically minor constituents. The uppermost section of the Mule Mountain volcanics consists of hydrothermally metamorphosed plag + cpx +qtz or plag+hbl phyric dacites, volcanogenic sandstones and minor tuffaceous(?) mudstones.

2.9.6 Age constraints

Gray and McKee (1981) reported hornblende K-Ar and pyroxene K-Ar dates for a dacite (133.4 ± 4 Ma) and an andesite (122.6 ± 8 Ma), respectively. Gray and McKee (1981) noted, referring to above ages: “regional geologic considerations suggest that K-Ar age is young; however, age has not been verified by other isotopic dates”. Obviously, the ages are much younger than overlying basal Myrtle (Tithonian, ~151-144 Ma). Probably, the anomalously young ages are related to Ar-loss in the samples and, therefore, should not be used.

A new $^{40}\text{Ar}/^{39}\text{Ar}$ date from hornblende separates in a plag+hbl-phyric dacite (GDH-5a) was obtained (table 2.1a; Heizler, written communication, 1998). The age spectrum diagram of the $^{40}\text{Ar}/^{39}\text{Ar}$ dating analysis of hornblende are shown in appendix B. Hornblende is igneous in origin and the calculated plateau age of $152.9 \text{ Ma} \pm 1.8 \text{ Ma}$ almost certainly indicates the date of crystallization, because the fine grained volcanic rock cooled rapidly through the “Ar-closure temperature” for hornblende. It is unlikely that the plateau age represents a metamorphic age because secondary minerals (e.g., pumpellyite), which partially replace igneous hornblende, formed at temperatures of metamorphism ($<350^\circ\text{C}$) significantly below the temperature at which hornblende closes to argon-diffusion ($\sim 500^\circ\text{C}$, Harrison, 1981).

Radiolarian-bearing metatuffs were sampled in the uppermost section of the Mule Mountain volcanics below (southeast) of the dated dacite, but have not yet yielded well-preserved species providing further age-constraints (E. Pessagno, personal communication, 1996-1997). Harper (unpublished data) reported that a section of interbedded chert and volcanoclastic sandstone occurs above the dated chert (Callovian to middle Oxfordian age) on and within the Snow Camp Mountain pillows. The interbedded

cherts in the Snow Camp Mountain area are not dated, but they are very similar to the interbedded interval in the uppermost section of the Mule Mountain volcanics exposed on the 4WD-road leading to the Old Red Mine (Harper, 1999; unpublished data). This correlation implies that the Mule Mountain volcanics below the interbedded chert could be part of the ophiolite (figure 2.3).

2.10 Post-ophiolite intrusions

2.10.1 Muscovite garnet tonalite dikes in metagabbro unit

Younger dikes of tonalitic composition occur in the metagabbro unit (figure 2.46). They are medium to coarse grained, consist of quartz, plagioclase, few percent garnet and muscovite, and do not contain hornblende (figure 2.47). Typically, they are foliated and occasionally display a mylonitic fabric (figures 2.47 and 2.48). The tonalites occur parallel magmatic foliation or form low to medium angles with magmatic foliation (figure 2.46). The petrographic summary of tonalitic dikes in the metagabbro unit is given in appendix A (table A6).

These dikes are variably deformed and range from moderately foliated samples (figure 2.47) that have stretched and somewhat dynamically recrystallized quartz grains to samples with clearly mylonitic fabric (figure 2.48). Typically, plagioclase is saussuritized, and in samples with mylonitic fabric, it is broken into subangular fragments (figure 2.48). In places, the abundant subangular fragments give this rock an appearance similar to cataclasites. S/C-type foliation is developed with C-shears consisting of muscovite and chlorite (figure 2.48). Variably wide (50-300 mm) quartz ribbons are parallel C-surfaces and wrap around plagioclase porphyroclasts. Larger, relict quartz grains show undulose extinction and/or contain subgrains which pass laterally into small recrystallized grains. Disseminated flakes of muscovite and chlorite occur in recrystallized quartz as well.

Two muscovite garnet tonalite dikes were analyzed for muscovite $^{40}\text{Ar}/^{39}\text{Ar}$, and cooling ages of 148.52 ± 0.17 Ma (O/C-372b) and 147.99 ± 0.45 Ma (GH-97-20) were obtained at the New Mexico Geochronology Research Laboratory by M. Heizler (table 2.1a; written communication, 1998). The age spectrum diagram of the $^{40}\text{Ar}/^{39}\text{Ar}$ dating analysis of muscovite are shown in appendix B. These ages



Figure 2.46

Photograph showing outcrop of late tonalitic dikes in the metagabbro unit (O/C-372b). The tonalite occurs parallel magmatic layering as well as dike like intrusions cutting layering at low to medium angles. The tonalite contains plagioclase, quartz, muscovite and garnet and is typically very coarse grained. The composition and texture is unlike all other quartzo-feldspathic rocks in the metagabbro unit. See hammer for scale.

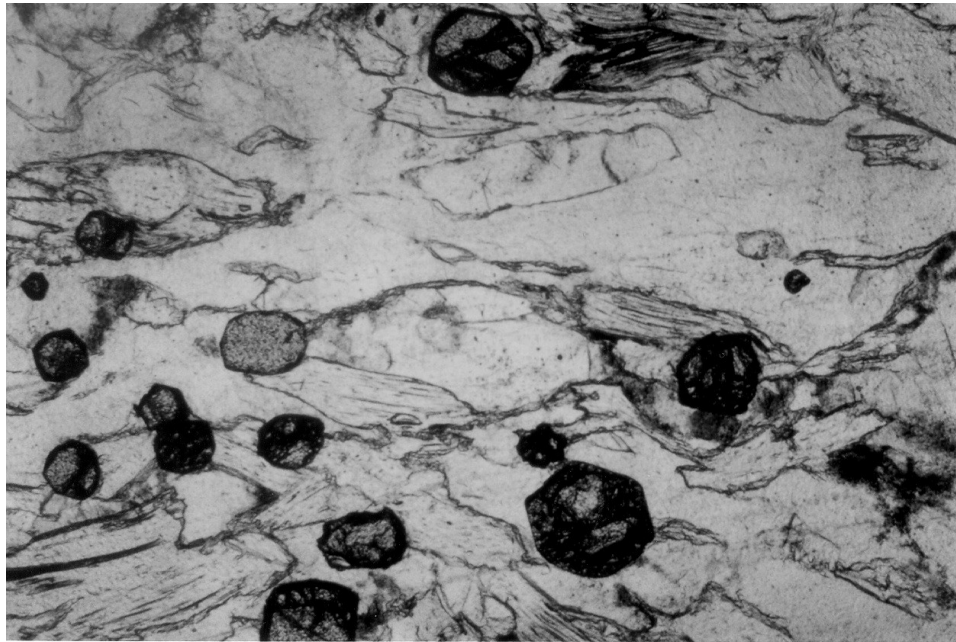


Figure 2.47

Photomicrograph showing the texture of a foliated tonalite dike (GH-97-20). The tonalite consists of weakly recrystallized quartz (clear, low relief), plagioclase (grayish, medium relief), muscovite (cleavage, high relief) and euhedral garnet (dark, high relief). The garnet-muscovite tonalites are compositionally distinct from all other quartzo-feldspathic rocks in the metagabbro unit. Muscovite separates of this samples yielded a $^{40}\text{Ar}/^{39}\text{Ar}$ cooling (below 350°C) age of 147.99 ± 0.45 Ma. The width of the photomicrograph is 2.14 mm.

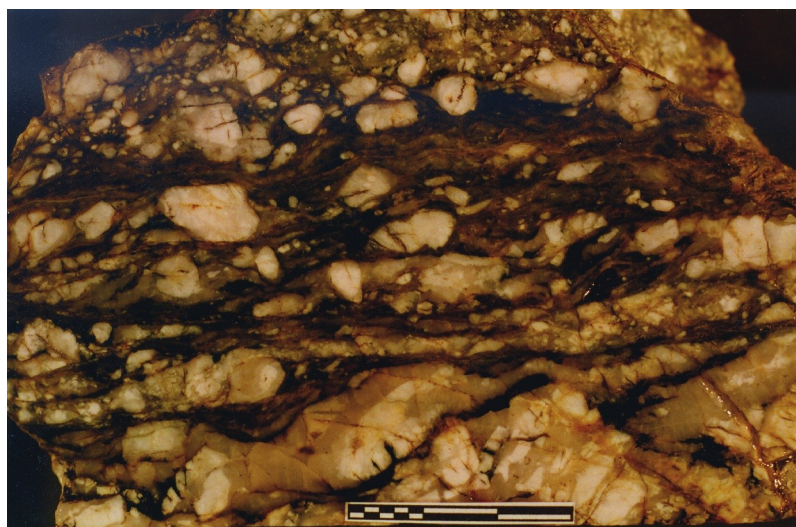


Figure 2.48

Slabbed and polished sample of muscovite-garnet tonalite intrusion having S/C-type fabric (GH-97-6). The rock consists of plagioclase (white), quartz (clear), muscovite (often altered to chlorite and appears dark green to black) and garnet (similar to figure 2.47). Plagioclase is heavily fractured, and muscovite-poor portions of the tonalite (arrow) look similar to cataclasites. Muscovite and chlorite occur in C-type shears (subhorizontal). S-planes trend from upper right to lower left. Sense of shear is dextral. Muscovite separates of a sample from the same dike (O/C-372b) yielded a $^{40}\text{Ar}/^{39}\text{Ar}$ cooling age of 148.52 ± 0.17 Ma. The scale bar is 3 cm long.

probably mark the end of widespread ductile deformation in the Rogue Wilderness area (see chapter 4). Muscovite closes to Ar-diffusion at around 350°C, depending on grain size and cooling rate (McDougall and Harrison, 1988; Hames and Bowring, 1994).

2.10.2 Half Moon Bar Diorite

The bulk of the Half Moon Bar diorite (HMB diorite) occurs as a fault-bounded unit between the western and eastern fault-slices of the pillow unit (figure 2.2a). The intrusive relationships between HMB diorite and pillow basalt are exposed within the western fault-slice of the pillow unit (figure 2.49).

Amygdaloidal basaltic rocks with minor red chert or jasper as well as diabasic rocks occur west of a ~30 m wide fault zone that is well-exposed at the western end of Brushy Bar. A few tonalitic dikes intrude the pillow basalt and diabasic dikes near the fault zone, but they become more abundant further west forming intrusive breccias similar to a net-vein breccia (figure 2.49). Finally, the intrusive breccias grade into 100% plutonic rocks of gabbroic to dioritic composition which are unconformably overlain by Tertiary sediments near Tate Creek. As the plutonic rocks become more abundant in western direction, they become also coarser grained and appear to grade from tonalite to more mafic compositions and are similar to the diorite exposed around Half Moon Bar. The dacitic dikes intruding the eastern fault-slice of the pillow unit (e.g. figure 2.40) are very similar to the tonalite in the net-vein breccia (figure 2.49). The tonalite-dikes scattered throughout the pillow unit are most likely related to the intrusion of the HMB diorite.

Locally, the diorite shows a compositional layering and is intruded by 2 cm - 30 cm wide porphyritic dikes (figure 2.50). The layering is characterized by changes in the modal composition, and layers of tonalite or leuco-diorite alternating with diorite are easily identified by the color banding. The petrographic classification of the HMB diorite is somewhat difficult due to the necessary distinction between diorite and gabbro based on the An-content of plagioclase (e.g., Le Maitre et al., 1989). Gray et al (1982) reported that the main phase in this unit is a hornblende quartz diorite. In this study, it is confirmed that the main phase is a hornblende quartz diorite based on the following determinations in representative samples: (1) although plagioclase have very calcic cores (An₈₂₋₇₅), the average compositions of the strongly zoned plagioclase in mafic samples are usually dominated by the rims (An₆₈₋₁₇) and not the calcic cores

(An₈₂₋₇₅). Thus, the average compositions estimated for representative plagioclase grains are usually just below An₅₀. However, within the same thin section, some plagioclase grains have also average compositions above An₅₀. Most importantly, the geochemical analyses of representative samples from this unit are consistent with a dioritic composition as discussed in subsequent chapter.

The petrographic summary of representative samples from the HMB diorite is given in appendix A (table A7). Hornblende quartz diorite, the dominant phase of the HMB diorite, is medium grained (2-3 mm) and idiomorphic to hypidiomorphic granular (figure 2.50). Quartz (5% - 15%) forms anhedral grains and shows sometimes undulatory extinction. Plagioclase (45-65%) forms subhedral to euhedral and strongly zoned crystals that display simple and polysynthetic twinning. Albite is ubiquitous in all samples and occurs as patchy replacement of plagioclase. Replaced plagioclase (ab ±ep ±chl ±musc) appears cloudy in thin section, and predominantly calcic cores are affected by this alteration (figure 2.51). Hornblende quartz diorite contains 1-3% anhedral oxide, and other accessory phases include trace amounts of biotite, apatite and titanite.

In contrast to the uniformly green colored hornblende in samples from the metagabbro unit, amphibole (30 - 45%) in HMB diorite is highly variable in color within thin section and occurs in three different forms: (1) as brown to greenish-brown, subhedral to euhedral prismatic crystals suggesting an igneous origin, (2) as brownish green mantles around relict cpx (corona texture, figure 2.51), which may have formed as the result of incomplete reaction of cpx with melt or late-stage magmatic fluids, and (3) as pale- to dark-green, occasionally fibrous amphibole replacing cpx as well as hornblende of type (1) and (2). Microprobe analysis of amphiboles in sample O/C-376 indicate that the brown and greenish brown varieties are Mg-hornblende whereas the dark green to pale green, occasionally fibrous varieties are actinolitic hornblende and actinolite (chapter 3). Petrographically, the corona texture is most difficult to constrain, because cpx is usually completely replaced by actinolite ± magnetite ± epidote ± chlorite. In places, tiny, ragged cores of cpx occur in fibrous amphibole, all of which are rimmed by brownish-green hornblende giving the amphibole a zoned appearance (figure 2.51). Possibly, the (hypothesized) reaction of cpx with melt or late stage fluids resulted in brownish-green hornblende coronas and was followed by hydrothermal or deuteric alteration resulting in the partial replacement of the remaining cpx cores by pale-



Figure 2.49

Photograph of a net-vein breccia about 200 m west of the fault exposed at Brushy Bar. The zone containing the net-vein breccias and intrusive breccias probably represents the wall or roof zone of the HMB diorite. The tonalite in the net-vein breccia is very similar to the tonalite dikes scattered throughout the pillow unit (figure 2.40) suggesting that the silicic dikes in the pillow unit could be related to the HMB diorite. Zircon separates of a sample (SC-13) from about this locality yielded a concordant U/Pb age of 159 Ma.

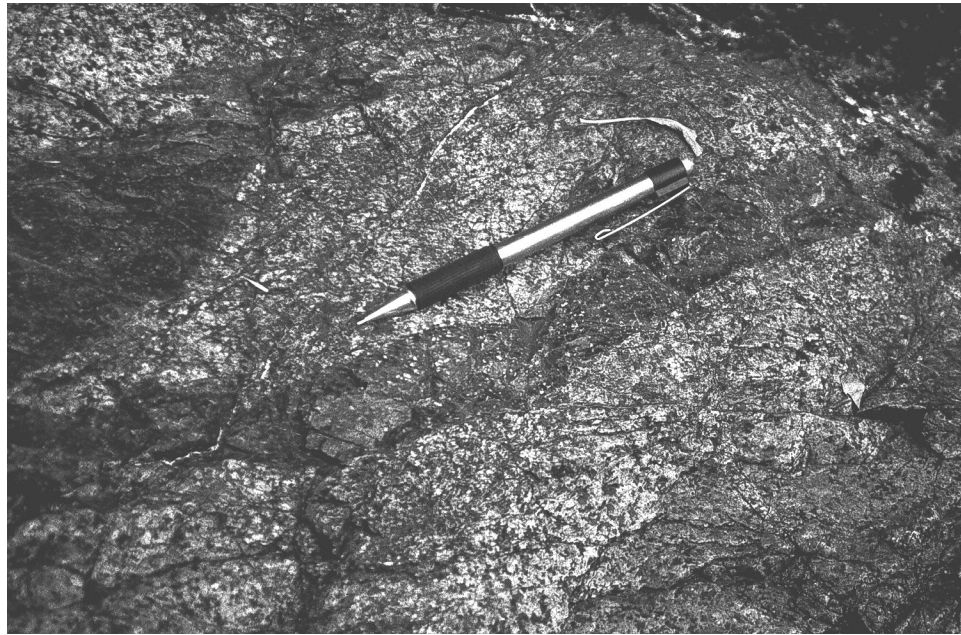


Figure 2.50

Photograph of medium-grained Half Moon Bar diorite intruded by a porphyritic dike (O/C-177). This dike is about 3 cm wide. Dikes in the HMB diorite are as wide as 30 cm and contain phenocrysts of plagioclase, clinopyroxene (pseudomorphs) and magnetite. Clinopyroxene phenocrysts in the porphyritic dikes are typically replaced by uniformly colored brownish-green amphibole.

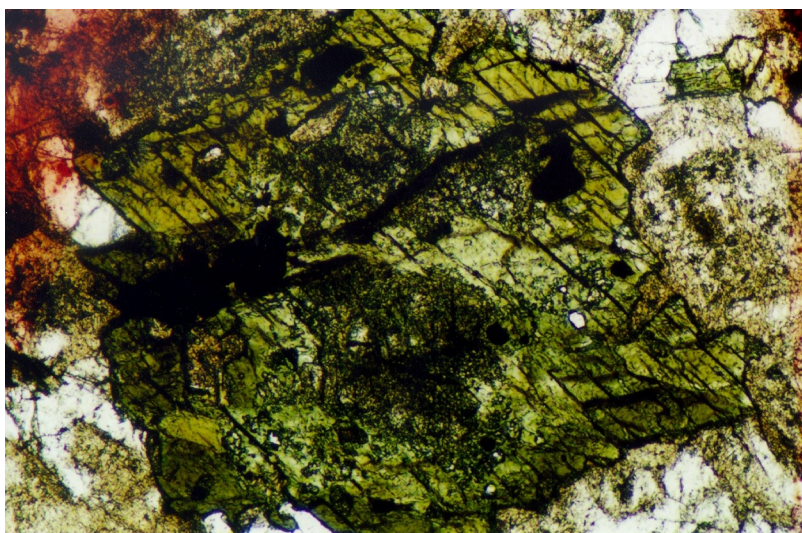


Figure 2.51

Photomicrograph of amphibole in sample O/C-377 from the HMB diorite. Dark brown-green hornblende occurs as a poorly defined rim around lighter colored, pale-green amphibole and dark, cloudy mineral aggregates. The assemblage in the cloudy aggregates includes actinolite, magnetite, chlorite, epidote. Occasionally, relic igneous cpx is preserved. The dark colored rim consists of calcic Mg-hornblende and is interpreted as a corona that formed by the incomplete reaction between cpx and melt or late stage magmatic fluids. Metamorphism (deuteric or hydrothermal alteration) followed upon crystallization of the diorite and the remaining cpx may have been replaced by cloudy mineral aggregates and pale colored amphibole. Plagioclase, especially the calcic cores are replaced as well. The width of the photomicrograph is 2.14 mm.

to dark-green, fibrous amphibole. Regardless of the specific textures and their interpretations, the gradational relationship from clearly primary hornblende to varieties that are probably late magmatic followed by metamorphic amphibole indicates that the crystallization of the diorite from the melt was followed by retrograde hydrothermal or deuteritic alteration.

Quartz-bearing diorites or gabbros (~ 3 % qtz), a minor constituent of the HMB diorite, are also medium grained (3 mm), hypidiomorphic granular and contain strongly zoned, subhedral to euhedral plagioclase (45-55%). Green, fibrous amphibole partially replacing cpx (40-45%) is predominant, whereas the brown, prismatic hornblende as well as the hornblende coronas are rare or absent. Quartz (2-5%) occurs as an interstitial phase and thus, crystallized late. Quartz-bearing diorite contains about 3-4% anhedral oxide.

The leucocratic and more fractionated, felsic phases contain basically the same mineral assemblage as the main-phase diorite but in different proportions and have hypidiomorphic to xenomorphic textures. For example, typical leucotonalite (or trondhjemite) intruding pillow basalt, exposed 200 m downstream of Solitude Bar (SC-13) contains 51% plagioclase, 47% quartz, 2% hornblende, accessory biotite and oxide, and trace amounts of apatite and titanite (figure 2.49).

The dark colored dikes intruding HMB diorite (figure 2.50) are highly porphyritic and contain variable amounts of phenocrysts (<1 mm). They range from almost black to dark gray-green in color. The phenocryst assemblage includes plagioclase (10-30%), clinopyroxene (pseudomorphs) and/or hornblende (3-20%), and magnetite (1-3%). Clinopyroxene phenocrysts are usually replaced by blocky, brownish green hornblende, and plagioclase is strongly saussuritized. The fine grained matrix has a subophitic texture and consists of lath-shaped plagioclase, pyroxene(?) replaced by amphibole, and Fe-Ti oxides. Petrographically, the porphyritic dikes appear to be similar to the plag+cpx phyric shallow intrusives or flows within the Mule Mountain volcanics. One mafic dike (O/C-174C) in the HMB diorite contains dacitic xenoliths that strongly resemble dacitic dikes found in the pillow unit (e.g., figure 2.40), suggesting that fractionation of HMB diorite related magmas was followed by mafic dike intrusions. The beige, felsic xenolith contains phenocrysts of plagioclase (35%), quartz (20%), hornblende (3%) and magnetite (1%) in a fine-grained, felsic matrix.

Other structures in the HMB diorite include <1 mm wide micro-shear bands identified in thin section (similar to figure 2.13) as well as mineralized faults and hydrothermal veins. Ductile deformation in the HMB diorite is subordinate and includes weak undulous extinction of quartz and the micro-shear bands. The mineral assemblages identified in the crosscutting structures (i.e. veins and faults) indicate decreasing temperatures of formation: The ductile shear bands have compositions similar to epidiosites (ep+cz+qtz+chl) and are usually cut by ep+qtz-veins followed by pr+qtz followed by qtz±su followed by laumontite- and calcite veins. The partial replacement of primary phases and the formation of hydrothermal veins and mineralized faults presumably followed closely upon the crystallization of the diorite from the melt.

Gray and McKee (1981) reported a hornblende K-Ar age of 159.5 ± 3 Ma for a sample (79WG221) collected near Half Moon Bar. This age is in good agreement with the new $^{40}\text{Ar}/^{39}\text{Ar}$ age of 157.2 ± 2.0 Ma determined from hornblende separates of sample O/C-376 (table 2.1a; Heizler, written communication, 1998). The age spectrum diagram of the $^{40}\text{Ar}/^{39}\text{Ar}$ dating analysis are shown in appendix B. Sample SC-13 is from the western fault slice of the Half Moon Bar diorite, and has a concordant zircon U/Pb age of 159 Ma, Two samples from the eastern fault slice of the Half Moon Bar diorite were dated using the zircon U/Pb method and have concordant ages of 160 Ma (SC-11) and 159 Ma (SC-12) . The zircon ages and sample localities were provided by J. Saleeby (table 2.1b; written communication 1999).

2.11. Blossom Bar Shear zone

2.11.1 Lithology and fabric

The best exposures of the 0.8-0.9 km wide shear zone, exposed between the metagabbro unit and the Mule Mountain volcanic unit, are found along the Rogue River at Blossom Bar. The structure of this unit is defined by a northeast-southwest trending and steeply dipping foliation and a steeply northeast plunging stretching lineation (chapter 4). In most outcrops, a gently folded layering which is parallel to foliation can be identified, and the 1 cm to 2 m thick layers usually consist of distinctly different rocks. Individual layers may be felsic or mafic in composition and appear to be derived from plutonic, volcanic or

possibly sedimentary protoliths. Relatively undeformed blocks in the Blossom Bar shear zone include aphyric and porphyritic volcanic flow rocks (with or without amygdules), gabbroic and diabasic rocks, quartz-bearing and quartz-rich volcanic and plutonic rocks, and volcanic breccia. Basically, all of these rocks are described in previous sections and most likely derived from the metatonalite unit, metagabbro unit, and Mule Mountain volcanics. Various representative samples indicating intense ductile deformation are discussed below:

The deformed plutonic rocks in the Blossom Bar shear zone (e.g. figure 2.52 and 2.53) are similar in composition and fabric to the mafic and felsic plutonic rocks in the metagabbro and metatonalite unit. For example, some samples from the Blossom Bar shear zone are much like the felsic phases (e.g. figure 2.6) and muscovite±garnet-bearing tonalite dikes (e.g. figure 2.48) which are part of the metagabbro unit. Other samples from the Blossom Bar shear zone are similar to the protomylonites and mylonites identified in the metatonalite unit (e.g. figure 2.19). Near the contact with the metagabbro unit, deformed plutonic rocks of gabbroic composition having augen-shaped hornblende are common, and their fabrics resemble that of samples from the contact zone between metagabbro and metatonalite units (figure 2.14). Additionally, a medium- to fine-grained S/C-type mylonite (figure 2.52), which is somewhat different in its mineral composition than any of the previously described samples, occurs in the shear zone. This S/C-type mylonite is exposed in the Mule Creek and consists mainly of strongly recrystallized quartz (~35%), saussuritized plagioclase (~50%), and contains the mafic phases biotite, muscovite, hornblende and oxide (~Σ 15%) (see also chapter 4).

Many of the quartz-rich mylonites in the Blossom Bar shear zone are comparable in composition and fabric to type 1 (figure 2.20) and type 2 (figure 2.21) mylonites identified in the metatonalite unit, and they seem to be derived from plagioclase + quartz rich protoliths (e.g. figure 2.53). Similar to the mylonites in the metatonalite unit (section 2.6.3), the mylonites and ultramylonites in the Blossom Bar shear zone consist mainly of quartz, epidote and chlorite and little or non of the original texture and composition is preserved. Interestingly, epidote-mylonites or ultramylonites occur not only in the quartzo-felspathic layers, but are also very common in the mafic layers (e.g. figure 2.54) that probably

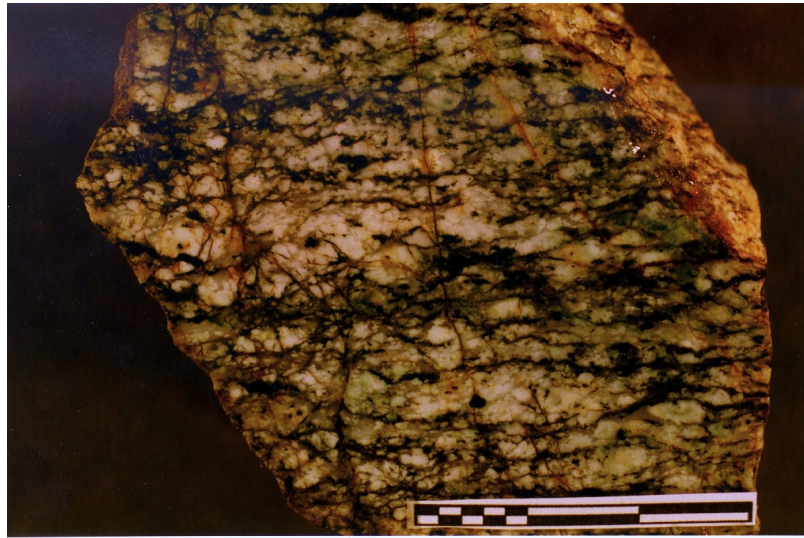


Figure 2.52

Photograph of polished hand sample (O/C-417) of S/C-type mylonite from the Blossom Bar shear zone. The rock consists of strongly recrystallized quartz, saussuritized plagioclase, biotite, muscovite and hornblende. The porphyroclasts of plagioclase and hornblende are heavily fractured. C-planes are horizontal and S-planes trend upper right to lower left. The shear sense is dextral. The scale bar is 3 cm.

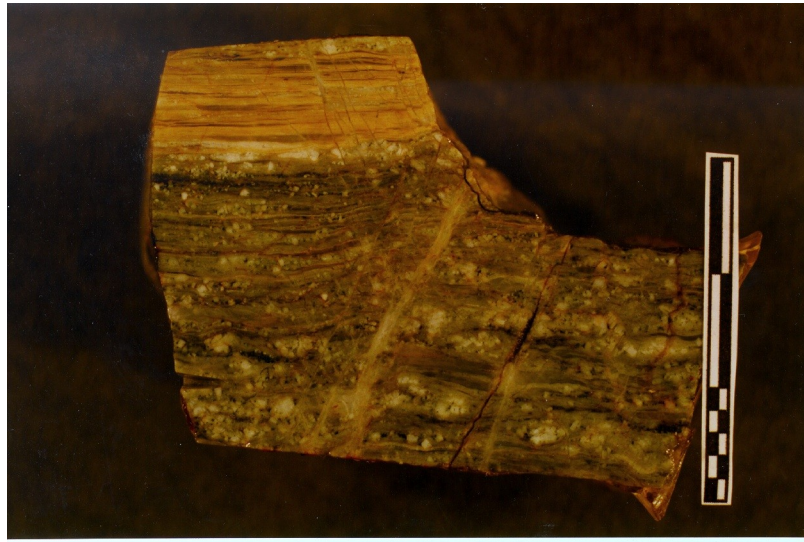


Figure 2.53

Photograph of a polished hand sample (O/C-230-S61) of mylonite (gray-green) and ultramylonite (pistachio green) sampled in a quartzo-feldspathic block at Blossom Bar on the Rogue River. The contact between mylonite and ultramylonite is sharp. The foliation of the mylonite is defined by discontinuous layers or lozenge-shaped domains of recrystallized quartz containing various porphyroclasts. The discontinuous layers or domains are separated by < 1mm bands (C-type shears?) consisting of a fine grained mineral aggregate of mostly epidote or clinozoisite. Plagioclase porphyroclasts are heavily fractured and fragments are completely replaced. The ultramylonite consists of quartz ribbons occurring in a fine grained, pistachio green matrix. In thin section, the matrix appears dark cloudy to almost opaque, and consists probably mostly of epidote. Other minerals in the cloudy matrix may include clinozoisite, albite, chlorite, and mica. The scale bar is 3 cm.

consist of sheared volcanic or dike rocks. The strong alteration and replacement of the felsic and mafic rocks by epidosite may have occurred prior to and/or during deformation.

The bulk of the Blossom Bar shear zone appears to consist of strongly foliated mafic rocks (figures 2.54 and 2.55) which seem to contain abundant secondary (metamorphic) quartz¹. Zones of 'epidosite-mylonites' are common and are always parallel foliation. In places, relatively large (2-7 mm) porphyroclasts of epidote occur in an extremely fine grained (aphanitic) matrix perhaps representing amygdules in deformed volcanic flow rocks. This suggests that some alteration (e.g., deposit of epidote in vesicles) occurred prior to deformation. Other, relatively large porphyroclasts (0.5-2 mm) include amphibole possibly replacing cpx and saussuritized plagioclase which may be relict phenocrysts in mafic volcanic rocks. The porphyroclasts are usually heavily fractured and, in places, have wings of the same mineral or mineral aggregates. Occasionally, the amphibole porphyroclasts are augen-shaped. Chlorite, amphibole (pale green actinolite), epidote and recrystallized quartz are identified in the fine grained matrix. Also, other minerals such as clinozoisite, albite, and mica are likely to occur in the matrix but are difficult to identify with the optical microscope due to the small grain size. The fabric of the foliated, mafic rocks (figure 2.54) is characterized by abundant asymmetrical extensional shear bands similar to type 2 mylonites (figure 2.21). However, the mafic foliated rocks contain much less quartz than the mylonites in the metatonalite unit. This fabric is discernible with the naked eye in relatively coarse grained polished hand samples (figure 2.54) which could have been derived from diabasic protoliths. A similar fabric can be found in much finer grained deformed mafic rocks using the petrographic microscope. Possibly, the coarser grained rocks represent shallow mafic intrusives whereas the foliated, aphanitic rocks are deformed volcanic flows or dikes. Alternatively, the difference in grain size could be related to different amounts of strain.

¹ It is not possible to distinguish between primary and secondary quartz in the sheared rocks. Thus, the seemingly mafic rocks containing secondary quartz could represent rocks of intermediate or silicic composition.

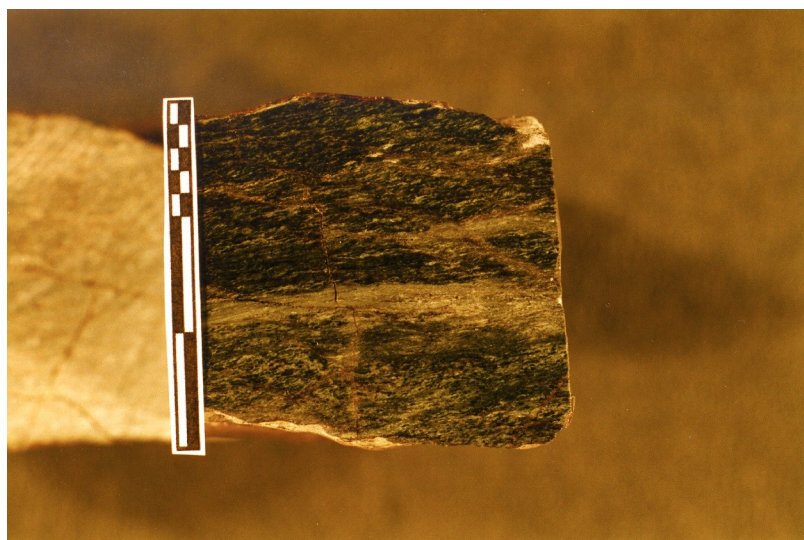


Figure 2.54

Photograph of a polished hand sample of a strongly foliated, mafic rock (O/C-45-S41) showing the characteristic fabric of foliated mafic rocks in the Blossom Bar shear zone. This sample is relatively coarse-grained possibly representing a deformed, phenocryst-free, shallow intrusive rock. Pistachio green 'epidosite-mylonite' zones (2-3 mm wide) occur parallel foliation. Igneous minerals are completely replaced and are arranged at low angles to foliation (long axis trend upper right to lower left). Amphibole (pale green in thin section) is augen-shaped and possibly replaces cpx. Plagioclase is replaced by a fine grained, cloudy mineral aggregate (cz+ep+ab±chl±mica), and secondary(?) quartz is strongly recrystallized. The extensional shear bands trend upper left to lower right. In places, chlorite is altered and the extensional shear bands may show up as rust brown, oblique bands. The scale bar is 3 cm.

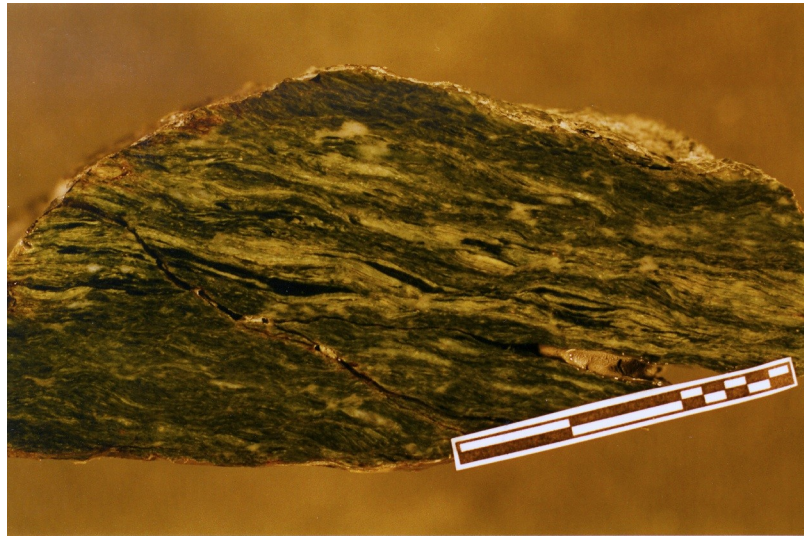


Figure 2.55

Photograph of a polished hand sample (O/C-238) of a strongly foliated rock consisting primarily of chlorite, actinolite and calcite. The foliation ranges from spaced to continuous. The microlithons or discontinuous layers (white to pale green) consist primarily of calcite, minor quartz and some disseminated chlorite, actinolite and epidote. The cleavage domains (dark green) consist primarily of chlorite and minor actinolite. The black lenses in this hand sample consist of actinolite. The scale bar is 3 cm.

Other foliated mafic rocks, frequently found in the Blossom Bar shear zone, may be classified as chlorite+actinolite schists (figure 2.55). These strongly foliated rocks are dark green in color, break easily along foliation, and consist primarily of chlorite, actinolite, and calcite. The foliation is spaced, zonal or continuous depending on the amount of calcite \pm quartz which form microlithons between cleavage domains of chlorite \pm actinolite. The microlithons are few tens of mm to 1 mm thick, and consist primarily of recrystallized calcite and minor quartz (also recrystallized). Calcite contains abundant deformation twins. Fine-grained, disseminated minerals in the microlithons include flakes of chlorite, acicular actinolite and granular epidote. Also, actinolite forms up to 2 mm thick and several cm long lenses that occur parallel foliation. Relict textures are not found, and the protoliths of these strongly foliated rocks cannot be constrained with available data. Perhaps, the chlorite schist formed from mafic volcanic rocks or tuffaceous sediments.

Volcanic breccias are locally abundant and range from undeformed to strongly foliated (figure 2.56). The undeformed breccias are very similar to the volcanic breccia described in section 9.1 (figure 2.41) and consist of fragments with distinct compositions and textures in a fine grained, cemented matrix. The textures of the fragments suggest that they are derived primarily from mafic volcanic rocks (i.e.

amygdaloidal, hyalophitic², and pilotaxitic textures) and secondarily from shallow intrusives (i.e. diabasic texture). The aspect ratios of clasts in undeformed breccias are between 1 and 2, and in foliated breccias in which individual fragments could still be identified between 2 and 15. Progressive deformation could ultimately result in strongly foliated rocks similar to the samples shown in figures 2.54 and 2.55.

A peculiar rock, resembling in outcrop a foliated breccia, is exposed in the lower part of Blossom Bar Creek (figure 2.57) in a \sim 1.5 m wide outcrop. The foliation is defined by alternating greenish black and pistachio green, discontinuous bands of variable thickness and length. The foliation is subparallel to the main structural trend. A sample taken from this zone lacks any relict (primary) textures and consists of only two minerals: granoblastic epidote (grain size of 0.5-1 mm) and acicular actinolite. Perhaps, the sample is from an extremely large vein or mineralized gash that formed during deformation in the Blossom Bar shear

² Chlorite probably replaces quartz

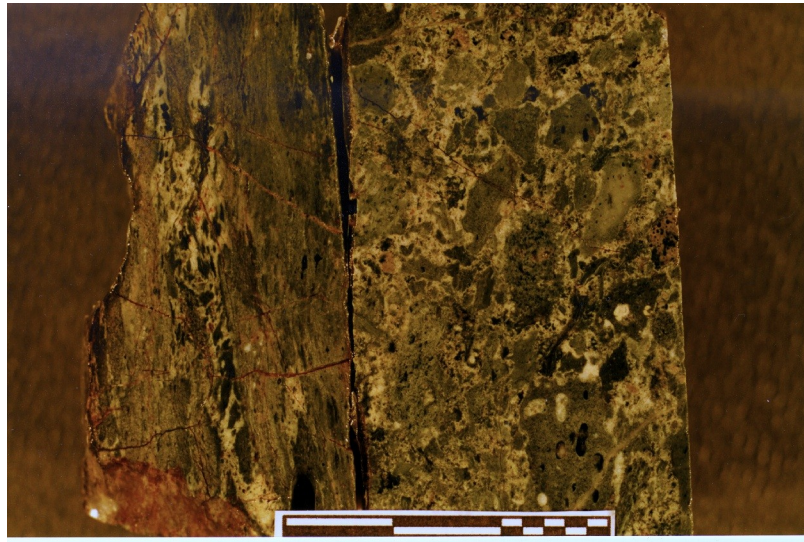


Figure 2.56

Photograph of two polished thin section chips showing an undeformed (O/C-201c) and a foliated volcanic breccia (O/C-419) from the Blossom Bar shear zone. The fragments in the deformed breccia (left) are elongate and aligned subparallel foliation. The undeformed breccia (right) is very similar to the volcanic breccias in the Mule Mountain volcanic unit. The clasts are of variable composition, texture and color indicating sedimentary transport and deposition (see figure 2.41). The scale bar is 3 cm.

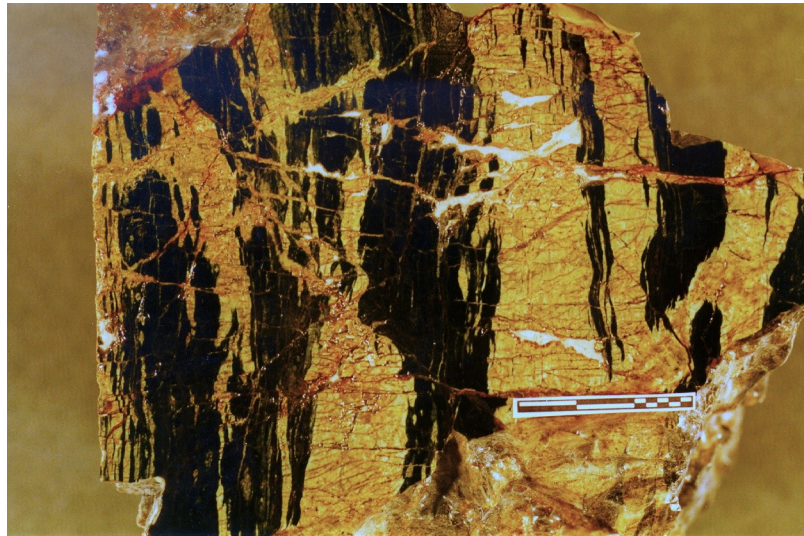


Figure 2.57

Photograph of polished hand sample of 1.5 m wide epidote+actinolite zone (O/C-382) occurring in the Blossom Bar shear zone. The sample consists of granoblastic epidote (pistachios green to yellow) and acicular actinolite (greenish black). Fibrous veins cut foliation (defined by the color banding) at high angles. The scale bar is 3 cm.

zone and was subsequently deformed. Abundant veins cut foliation at high angles (figure 2.57) and contain curved fibers of actinolite and granular epidote. The curvature of the fibers suggests that the fibers in the small veins grew parallel to the instantaneous stretching axes that changed orientation (rotated) with time.

2.11.2 Age constraints

A deformed tonalite (SC-10) from the Blossom Bar shear zone was dated (J. Saleeby, personal communication). Zircon separates from this sample yielded concordant ages of 164 Ma which are the same as that of the metatonalite unit. The zircon U/Pb age of SC-10 clearly indicates that the Blossom Bar shear zone is younger than 164 Ma.

The Blossom Bar shear zone appears to be younger than the Mule Mountain volcanic unit as indicated, for example, by the undeformed and foliated breccias (figure 2.56) which are similar to the volcanic breccias frequently found in the Mule Mountain volcanic unit (figure 2.41). The age of the Mule Mountain volcanic unit is constrained by the $^{40}\text{Ar}/^{39}\text{Ar}$ date determined from hornblende separates of a dacite (152.9 ± 1.8 Ma) and overlying, unmetamorphosed sedimentary rocks of the Myrtle Group (basal Myrtle group is Tithonian, 151-144 Ma). Furthermore, the muscovite $^{40}\text{Ar}/^{39}\text{Ar}$ ages of two deformed tonalitic dikes (148.52 ± 0.17 Ma and 147.99 ± 0.45 Ma) sampled in the metagabbro unite are interpreted to essentially mark the end of ductile deformation because muscovite closes to Ar-diffusion at about 350°C , which is just above the lower limit of crystal plastic flow of quartz ($\sim 300^\circ\text{C}$) (discussed in more detail in chapter 4). The ductile deformation can, thus, be bracketed between ~ 153 Ma and 148 Ma.

2.12 Myrtle Group

Imlay et al. (1959) raised part of the Myrtle Formation of Diller (1898) to the rank of a group and divided it into two new formations, the Riddle Formation and Days Creek Formation. The Myrtle Group has been correlated with the Great Valley sequence in California (Imlay et al., 1959, Blake et al, 1985a).

The sedimentary rocks of the Riddle Formation are exposed west of the Rogue Wilderness remnant of the CRO, and the best exposures occur along the 4WD road from Camp Hope leading to the

Golden Bullet Mine (Old Red Mine), and in Blossom Bar Creek. The sedimentary rocks exposed directly at the western boundary of the Rogue Wilderness remnant consist of conglomerates (0.5 to 10 m thick beds), conglomeratic sandstone (0.1 to 0.5 m thick beds) and minor amounts of siltstone (<0.1 m thick beds). The conglomerates contain predominantly chert pebbles and a minor amount of well rounded clasts of aphanitic and porphyritic greenstone in a sandy matrix. The pebbles range from 1 cm to 8 cm in size. In three outcrops in Blossom Bar Creek and along the 4WD-road just outside of the western boundary of the Wild Rogue Wilderness near the head of Mule Creek (West Fork), the conglomerate is overturned, as indicated by graded bedding. The underside of graded beds dips 060°-080° southeast.

Rud (1971) recognized four distinct sections above the 'basal' chert-pebble conglomerate. Rud (1971) reports that the thickness or stratigraphic order could not be constrained due to the intensely folded and faulted nature of the Riddle formation and lack of continuous exposures, but that the dip of beds decreases from east to west. The stratigraphic sections above the chert-pebble conglomerate at the contact with the Rogue Wilderness remnant of the CRO include (Rud, 1971): (1) A section of siltstone and sandstone (7.5 - 75 cm thick beds) containing lenses of conglomerate. The conglomerate consists mainly of chert pebbles and minor amounts of graywacke pebbles. *Buchia piochii* is very abundant. (2) A section of conglomerates and conglomeratic sandstones containing pebbles of chert, graywacke and minor amounts of greenstone. (3) A section of siltstone containing abundant wood fragments and the fossil *Buchia piochii* followed by interbedded sandstone and siltstone. (4) A 10 m thick section of coarse conglomerate containing rounded, up to 30 cm large fragments of chert, graywacke and greenstone in a silt matrix.

Gray et al. (1982) report that, in addition to *Buchia piochii*, the fossil *Buchia fischerina* is present in the Wild Rogue Wilderness. These fossils indicate that the Riddle formation was deposited during the latest Jurassic (Tithonian). The Riddle Formation is thought to have been deposited in deep water by a combination of turbidity currents, submarine debris flow and accumulation of submarine ooze (Gray et al., 1982, Blake et al., 1985a).

About 2 km northwest from the western boundary of the Rogue Wilderness remnant of the CRO, the Riddle Formation appears to be conformably overlain by the lower Cretaceous Days Creek Formation (Rud, 1971). The beds of the Days Creek formation also strike north 030°-040° east, but they dip

moderately steep (40°-60°) northwest (Rud, 1971). Increasingly shallower dips from east to west are consistent with the interpretation that the sedimentary rocks of the Myrtle Group occur on the east-limb of a syncline. Rud (1971) reports that the sedimentary rocks of the Days Creek formation in the area northwest of the Rogue Wilderness remnant of the CRO consist of fine to medium grained fossiliferous sandstone with abundant plant debris near the base, a massive sandy siltstone with abundant *Buchia crassicolis* (Keyserling), sandy siltstone that weathers to spheroidal forms, a sandstone section containing abundant wood fragments as well as siltstone pods and lenses of chert-pebble conglomerate, and a 15m thick section of conglomerate containing subrounded fragments of red, black, and gray colored chert, as well as metavolcanic fragments. The conglomerate is overlain by sandy siltstone.

CHAPTER THREE

APPLICATION OF HOLLAND AND BLUNDY'S (1994) AMPHIBOLE- PLAGIOCLASE GEOTHERMOMETER: CONSTRAINTS AND IMPLICATIONS FOR THE INTERPRETATION OF THE THERMAL HISTORY OF THE HALF MOON BAR DIORITE AND THE METAGABBRO UNIT IN THE WILD ROGUE WILDERNESS, SW OREGON.

3.1 Introduction

A reconstruction of the ophiolite in the Wild Rogue Wilderness is shown in figure 3.1. Based on radiometric ages and the types of rocks, the ophiolite consists from base to top of metatonalite (164 Ma), sheeted dike complex (163 Ma), pillow lavas and possibly a 2 km thick sequence of other metavolcanic rocks (Mule Mountain volcanics). The pillow unit is intruded by the Half Moon Bar diorite (HMB diorite), which was dated using the zircon U/Pb (158-160 Ma) and hornblende $^{40}\text{Ar}/^{39}\text{Ar}$ (157.2 ± 2.0 Ma) methods (chapter 2). The metagabbro unit contains a small intrusion of hornblende quartz diorite (HQ diorite), and is in structural contact with the ophiolite remnant exposed in the Wild Rogue Wilderness. As indicated by the hornblende $^{40}\text{Ar}/^{39}\text{Ar}$ cooling age, the metagabbro unit is at least 171.4 ± 3.1 Ma. (Heizler, personal comm. 1998), because hornblende $^{40}\text{Ar}/^{39}\text{Ar}$ ages mark the time when hornblende in the plutonic rocks closed to Ar-diffusion which is at $\sim 500^\circ\text{C}$ (Harrison, 1981). Cooling below $\sim 500^\circ\text{C}$ may occur very shortly after crystallization (i.e., fast cooling). This is the case for the HMB diorite: the igneous age (zircon U/Pb) of 159-160 Ma and the cooling age of 157.2 ± 2.0 Ma overlap within error of the analyses. The other possibility is that a significant period of time can pass between crystallization and cooling below 500°C , or the rocks could have been reheated and then cooled below $\sim 500^\circ$ (i.e., regional metamorphism). Thus, the metagabbro could be significantly older than the cooling age of 171.4 ± 3.1 Ma, and a reliable zircon U/Pb age would help to resolve this problem.

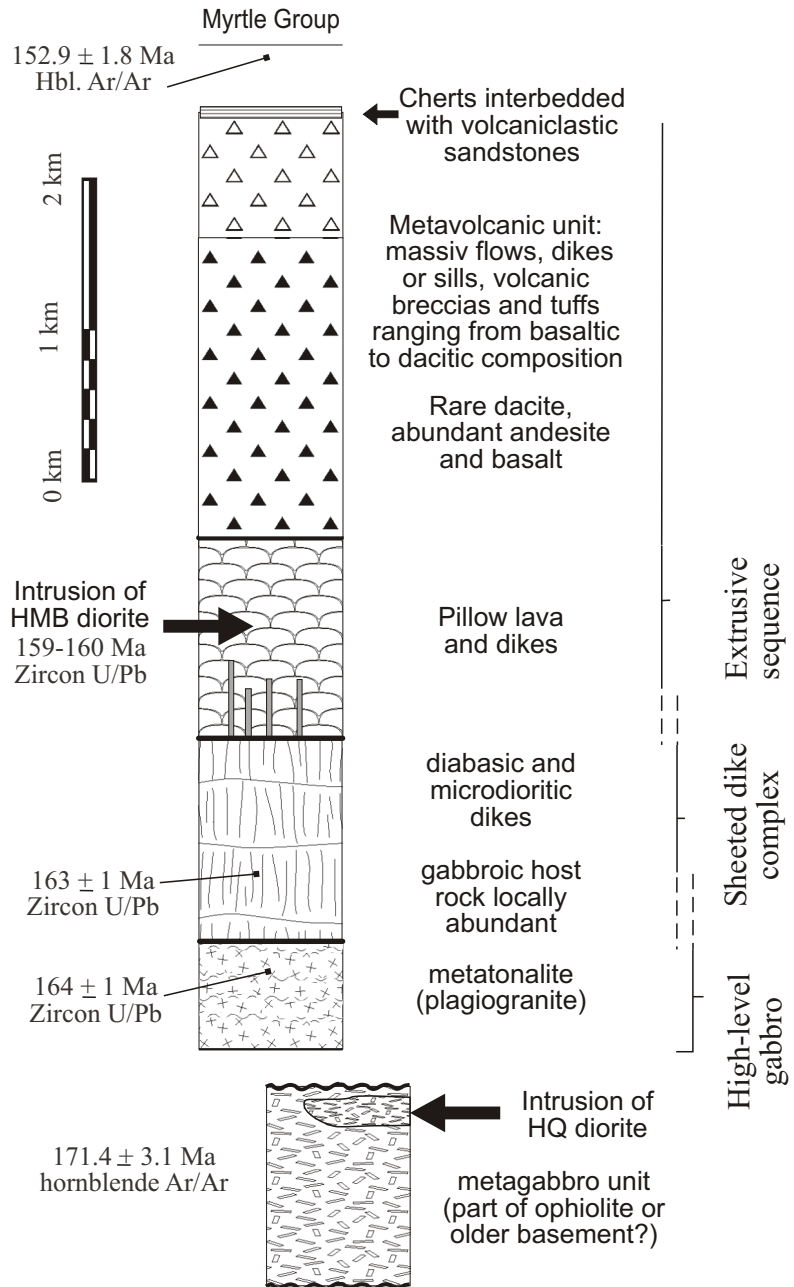
Hornblende from the HMB diorite are highly variable in color suggesting that the hornblende partially equilibrated under retrograde conditions. In contrast, the hornblende in the metagabbro unit is uniformly dark-green in color suggesting it could have equilibrated under regional metamorphic conditions. It is important to determine the nature of the metamorphism of the metagabbro, because it can have important implications for regional correlation. The significance of determining the temperature of equilibration of the hornblende for further interpretation of the metagabbro unit is briefly outlined below, and two opposing possibilities are considered:

- (1) On condition that the hornblende is igneous in origin (i.e. if it has near-solidus compositions) and only partially re-equilibrated during retrograde, hydrothermal metamorphism, the metagabbro unit may be interpreted as an ophiolitic unit forming part of the high-level gabbro of the Rogue Wilderness ophiolite (figure 3.1). In other words, if the metagabbro unit is indeed an ophiolitic unit, some of the hornblende should indicate magmatic temperatures and have frozen-in solidus compositions, because fast cooling of high-level gabbro in an oceanic setting would prevent widespread and complete re-equilibration at temperatures significantly below the solidus: Blundy and Holland (1992) stated that, for example, Al-diffusion in amphibole will be negligible if pluton cooling times are on the order of 10^6 years and if the diffusion coefficient for Al in amphibole is significantly less than 10^{-16} $\text{cm}^2 \text{s}^{-1}$. Depending to some extent on crustal thickness and spreading rate, the oceanic crust at 3 km below sea floor cools below temperatures of 500°C in less than $1.2 \cdot 10^6$ years (Sleep, 1975, Morton and Sleep; 1985, McCarthy et al., 1988). Petrographic evidence from hornblende-gabbro occurring in an oceanic setting is consistent with the prediction that a range of equilibration temperatures (near-solidus to greenschist facies) should be observed in such rocks. Cann (1977) summarized the petrographic relations as follows: "Every gradation is seen within such rocks from hornblendes that are clearly primary, through varieties that are pale brown, to green hornblendes with textural relationships that show them clearly to be secondary. Such a gradational relationship demonstrates clearly that metamorphism has followed very closely upon the crystallization of the gabbros from the melt, and hence that it takes place very early in the history of the ocean crust."
- (2) In case that all the amphiboles in selected samples from the metagabbro unit (MRH-78/1, MRH-78/2, O/C-373) are metamorphic in origin, i.e. equilibration occurred significantly below the solidus, an

Figure 3.1

**Reconstruction of the
Rogue Wilderness ophiolite**

Columnar section showing likely reconstruction of ophiolitic units identified in the Wild Rogue Wilderness compared to a typical pseudostratigraphy (e.g., Penrose conference, 1972) of ophiolites shows only the middle and upper crustal section is preserved. The metagabbro unit may not be part of the ophiolite. A small intrusion of hornblende quartz diorite (HQ diorite) occurs in the meta-gabbro unit. The Half Moon Bar diorite (HMB diorite) intruded the pillows.



interpretation has to be sought which is consistent with metamorphic temperatures that persisted over a long period of time to allow for re-equilibration at temperatures significantly below the solidus. Metamorphic amphiboles that re-equilibrated over a lengthy period of time are commonly uniformly colored, and, depending on metamorphic grade and rock composition, colors of amphiboles in metamorphosed mafic rocks range from light-green in greenschist facies, to darker blue-green in epidote-amphibolite facies, or dark green in amphibolite facies (Laird, 1982 p. 115). Petrographically, this contrasts with the variably colored hornblende in oceanic settings. These amphiboles formed in a relatively short(?) period of time over a large range of temperatures and variable interaction with fluids (i.e. deuteritic and seawater). Metamorphic temperatures persisting over a long period of time may occur during (a) regional metamorphism, and (b) regional plutonism. The heat released from several plutons intruding over a protracted period of time could keep earlier intruded plutons at elevated temperatures for a very long period of time. The late-stage magmatic, hydrothermal fluids released during cooling aid in diffusion processes furthering re-equilibration.

Currently, reliable thermobarometers applicable for many hornblende- and plagioclase-bearing assemblages are scarce. However, the improved geothermometer of Holland and Blundy (1994) for amphibole-plagioclase assemblages appears to be promising. It seems to produce reliable results and was, therefore, selected for this study. The application of the geothermometer of Holland and Blundy (1994) is outlined below and the temperatures of equilibration of three different intrusions are calculated. The thermometry results are discussed, and conclusions, supported by geologic and petrographic evidence, are made. These conclusions should allow to better constrain the interpretation of (1) new hornblende $^{40}\text{Ar}/^{39}\text{Ar}$ ages, (2) regional correlation, and (3) reconstruction of the Rogue Wilderness remnant of the CRO.

3.2 Method

3.2.1 Selection and analysis of coexisting plagioclase-hornblende pairs

The analyses of hornblende in selected samples were carried out at Rensselaer Polytechnique Institute on the JEOL 733X electron microprobe operating at 15 keV accelerating voltage and 15.5 nA

sample current. Analyses were obtained using a beam size of 1 to 2 μ and integrated count times of 30 s. A natural hornblende standard was run at the beginning and end of each microprobe session to ensure accurate analyses. Coexisting plagioclase was analyzed using a defocused beam and integrated count times of 5 s. Tobi Kosanke and David Wark are gratefully acknowledged assisting in the analysis.

Plagioclase that is in direct contact with hornblende are thought to represent coexisting phases, and the contact of phases was confirmed in thin section prior to analysis (figure 3.2). All of the compositions of coexisting plagioclase were determined by microprobe analysis, and the albite proportion (X_{Ab}) is listed in tables 3.1, 3.2 and 3.3. The data of the microprobe analysis of coexisting plagioclase is given in appendix C (tables C3, C4 and C5). The An-content of plagioclase was also determined using carlsbad-albite twinning and the corresponding determinative table in Tröger (1974). The results agree well with the microprobe analysis.

It is important to point out that plagioclase in all samples is partially or completely replaced and albitized, probably due to retrograde hydrothermal alteration. In thin section, replacement of plagioclase appears patchy, and igneous (or metamorphic?) zoning is often extremely obscured. Albite is ubiquitous, and it was analyzed in saussuritized plagioclase and occurs in veins as well as in association with clinzoisite (\pm ep \pm chl \pm musc) replacing plagioclase. Albite that occurs in saussuritized plagioclase, in veins or as patchy rims is interpreted as a secondary (retrograde) alteration phase and is probably not in equilibrium with the adjoining amphibole (complete re-equilibration at the low temperatures indicated by the alteration assemblage is unlikely). Therefore, albite compositions (Ab_{100-95}) were rejected, and the next lower Ab-content determined in the same grain was selected for pairing of the plagioclase-hornblende compositions (tables 3.1, 3.2 and 3.3). This is similar to the method of Ague (1997) who excluded albite-enriched regions along grain margins and cracks that were inferred to have formed during low-T chemical exchange with hydrothermal fluids.

Combining the plagioclase compositions determined optically and by microprobe analysis, compositional zoning of analyzed plagioclase grains could be reconstructed and the most likely plagioclase composition coexisting with hornblende selected. In general, the calcic cores and somewhat less calcic rims



Figure 3.2

Photomicrograph of HMB diorite sample O/C-376 showing typical, strongly zoned plagioclase coexisting with quartz (yellow, upper right) and hornblende (dark blue, lower left). Plagioclase is saussuritized, has calcic cores (dark center, An₇₃₋₈₂) and normal igneous zoning ranging from labradorite to oligoclase. Patchy albitization is inferred from variable replacement of grains combined with analysis by electron microprobe. Relict carlsbad-albite twinning is visible. Overall, hornblende in the HMB diorite is in contact with plagioclase ranging in composition from andesine to oligoclase, whereas actinolite is predominantly in contact with albite. The width of the photograph is 2.14 mm, and polarizers are crossed. The selected thin section is somewhat thick (50 μ m), but shows twinning and zoning better in the altered samples.

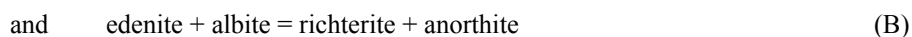
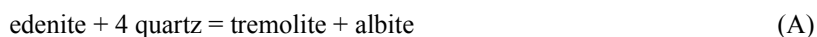
(An₈₂₋₆₃ in samples from the metagabbro unit, An₈₀₋₆₅ in HQ-diorite intruding metagabbro, and An₇₆₋₆₀ in HMB diorite intruding pillows) are not in contact with hornblende (figure 3.2), whereas the sodic rims ranging from oligoclase appear to be coexisting with hornblende and quartz (if present). It is believed that good control is achieved on the composition of plagioclase that most likely coexists with hornblende. Back-scattered electron (BSE) imaging is a powerful tool for determining alteration in hornblende and plagioclase, especially if used in high-contrast mode. Thus, BSE images should be obtained to better constrain whether or not altered plagioclase and hornblende were analyzed.

Although a relatively large data set is presented, it is not well-constrained whether or not the data sets of plagioclase-hornblende pairs (tables 3.1, 3.2 and 3.3) are representative and reflect the overall compositional variability of the samples. Given these limitations, the application of the thermometers of Holland and Blundy (1994) should be evaluated in the light of geologic and petrographic evidence. Overall, the calculated temperatures can be considered as meaningful results based on the assumptions that (1) the hornblende-plagioclase pairs represent indeed coexisting pairs, and (2) the model of Holland and Blundy (1994) for non-ideal interactions in calcic amphiboles approximates the temperature dependence of the compositions of involved phases.

Better constraints for the coexistence of plagioclase and hornblende may be obtained by selecting the least altered samples and acquiring X-ray maps of parts of the thin sections of selected samples. With a X-ray map, the compositional variations of plagioclase and hornblende are revealed, which are not always visible using the petrographic microscope, or deducible from spot-analyses of single grains. With help of the X-ray maps, the most likely coexisting plagioclase-hornblende pairs can be selected and analyzed. Ideally, this approach enables to obtain a data set which is representative of the compositional variability of hornblende-plagioclase pairs in a sample.

3.2.2 The amphibole-plagioclase geothermometer

Holland and Blundy (1994) developed an improved geothermometer for amphibole plagioclase assemblages using a semi-empirical evaluation of amphibole thermodynamics. They examined the composition-dependence of the ideal (mixing-on-sites) equilibrium constants for the equilibria:



However, non-ideal interactions in calcic amphiboles are taken into account, in contrast to their earlier amphibole-plagioclase geothermometer (Blundy and Holland, 1990), which is based on the Al^{VI} content of amphibole coexisting with plagioclase. Basically, Holland and Blundy (1994) evaluated for the reactions (A) and (B) all possible within-site and cross-site interactions between the components [] (vacancy), K, Na, Ca, Mg, Fe^{2+} , Fe^{3+} , Al, Si on the A, M4, M1, M3, M2 and T1 crystallographic sites of amphibole. They argue that, adopting the model of the simplest (symmetrical) form of non-ideal interactions, the effects of only eight linearly independent combinations of the 36 possible interaction energy terms need to be considered. Similar to their earlier amphibole-plagioclase geothermometer, plagioclase non-ideality was modeled using Darken's quadratic formalism. The values for the eight interaction parameters (also the values for apparent enthalpy, entropy and volume changes for each reaction) were obtained applying a regression of experimental and natural data of amphibole-plagioclase pairs for which the temperature and pressure of equilibrium are well constrained. Based on this semi-empirical thermodynamic evaluation of natural and experimental data used for the calibration, Holland and Blundy (1994) formulated two new geothermometers: edenite-tremolite thermometer (A) and edenite-richterite thermometer (B).

3.2.3 Restrictions for the use of the amphibole-plagioclase thermometers

In their paper, Holland and Blundy (1994) pointed out several restrictions in terms of amphibole- and plagioclase-compositions, and they estimated the range of pressure and temperature for which this thermometer is applicable. For example, the data used for the calibration of the geothermometers ranges from 400-1000°C and 1-15 kbar for plagioclase-amphibole pairs with a broad range of bulk compositions. Thus, they argue that the thermometers should perform well within this range of pressures and temperatures.

Holland and Blundy (1994) caution against the use of their thermometers to kaersutites or Ti-rich richterites due to the fact that Ti was ignored determining the equations for the thermometers. Ti (and Mn) was found to be insignificant concerning the effects on the thermometers, and ignoring Ti poses no

problem using amphibole-plagioclase pairs of a wide range of compositions. However, it may be significant for high-Ti amphiboles, because Ti may occupy T1-sites in such amphiboles.

For the calibration of the geothermometers, Holland and Blundy (1994) also ignored the substitution of Mg and Fe into the M4-site partly because of the limitations on estimations of Fe³⁺ from microprobe data (determination of Fe and Mg in M4-sites is extremely imprecise). Apparently, ignoring the substitution of Mg and Fe into the M4 site is only a potential problem at high temperatures and/or in calcium poor environments.

Thermometers A and B may be applied for silica-saturated rocks whereas for silica-undersaturated rocks only thermometer B can be applied. Further restrictions for the use of thermometer A are: T in the range 400-900°C, amphiboles must have Na^A > 0.02 pfu, Al^{vi} < 1.8 pfu, and Si in the range 6.0-7.7 pfu and plagioclase with X_{an} < 0.90. Restrictions for the use of thermometer B are: T in the range 500-900°C, plagioclase must lie in the range 0.1 < X_{an} < 0.9, and amphiboles must have X_{Na}^{M4} > 0.03, Al^{vi} < 1.8 pfu, and Si in the range 6.0-7.7 pfu. The data used in this study are screened to conform with all above restrictions.

3.2.4 Recalculation of amphibole analyses

A detailed outline of the amphibole recalculation is given in Holland and Blundy (1994), and it is, therefore, not necessary to restate the details of this method inhere. Basically, the amphibole recalculation follows a method similar to that of Spear and Kimball (1984), and Robinson et al. (1982), however, the method is somewhat extended. First, the microprobe data of hornblende are recalculated on the basis of 23 oxygens (if not already done during the analysis) assuming all Fe as FeO with a cation sum (Σ). Then, Fe^{total} is recast as Fe²⁺ and Fe³⁺ so that the given crystal-chemical constraints on the upper and lower limits of ferric iron in amphiboles are satisfied. Too little ferric iron has been allocated if: (1) $\Sigma > 16$, (2) Si > 8, (3) $\Sigma - \text{Na} + \text{K} > 15$, (4) Ca > 2, and (5) all iron as ferrous (minimum possible). Too much ferric iron has been allocated if: (6) Si + Al_{total} < 8, (7) $\Sigma - \text{K} < 15$, (8) $\Sigma - \text{Na} - \text{K} - \text{Ca} < 12.9$, (9) Fe³⁺ > 2 - Al^{vi} - Ti, and (10) all iron as ferric (maximum possible). This method also enables to determine whether or not the analysis can be made stoichiometric (Holland and Blundy, 1994).

Amphibole analyses used in this study were recalculated according to the method outlined above, and the data which did not conform with the stated crystal-chemical constraints, or could not be made stoichiometric, were discarded. (N.B. for Minpet-users: The program Minpet version 2.02 offers five options to recalculate amphibole analyses: (1) Iron as Fe²⁺, (2) Cations 15-NK, (3) Cations 15-K, (4) Cations 13-CNK, and (5) average of the 15-NK and 13-CNK methods. When option (5) was selected, more of the recalculated amphibole data agreed with the 10 crystal-chemical constraints listed above than selecting any other option).

From the recalculated amphibole analyses (given in cations), eight site terms must be determined for the thermometers. The required site terms are found as follows:

$$\begin{aligned}
 X_{\text{Si}}^{\text{T1}} &= (\text{Si} - 4) / 4 \\
 X_{\text{Al}}^{\text{T1}} &= (8 - \text{Si}) / 4 \\
 X_{\text{Al}}^{\text{M2}} &= (\text{Al} + \text{Si} - 8) / 2 \\
 X_{\text{K}}^{\text{A}} &= \text{K} \\
 X_{\text{I}}^{\text{A}} &= 3 - \text{Ca} - \text{Na} - \text{K} - \text{cm} \\
 X_{\text{Na}}^{\text{A}} &= \text{Ca} + \text{Na} + \text{cm} - 2 \\
 X_{\text{Na}}^{\text{M4}} &= (2 - \text{Ca} - \text{cm}) / 2 \quad (\text{note: } X_{\text{Na}}^{\text{M4}} > 0.03) \\
 X_{\text{Ca}}^{\text{M4}} &= \text{Ca} / 2
 \end{aligned}$$

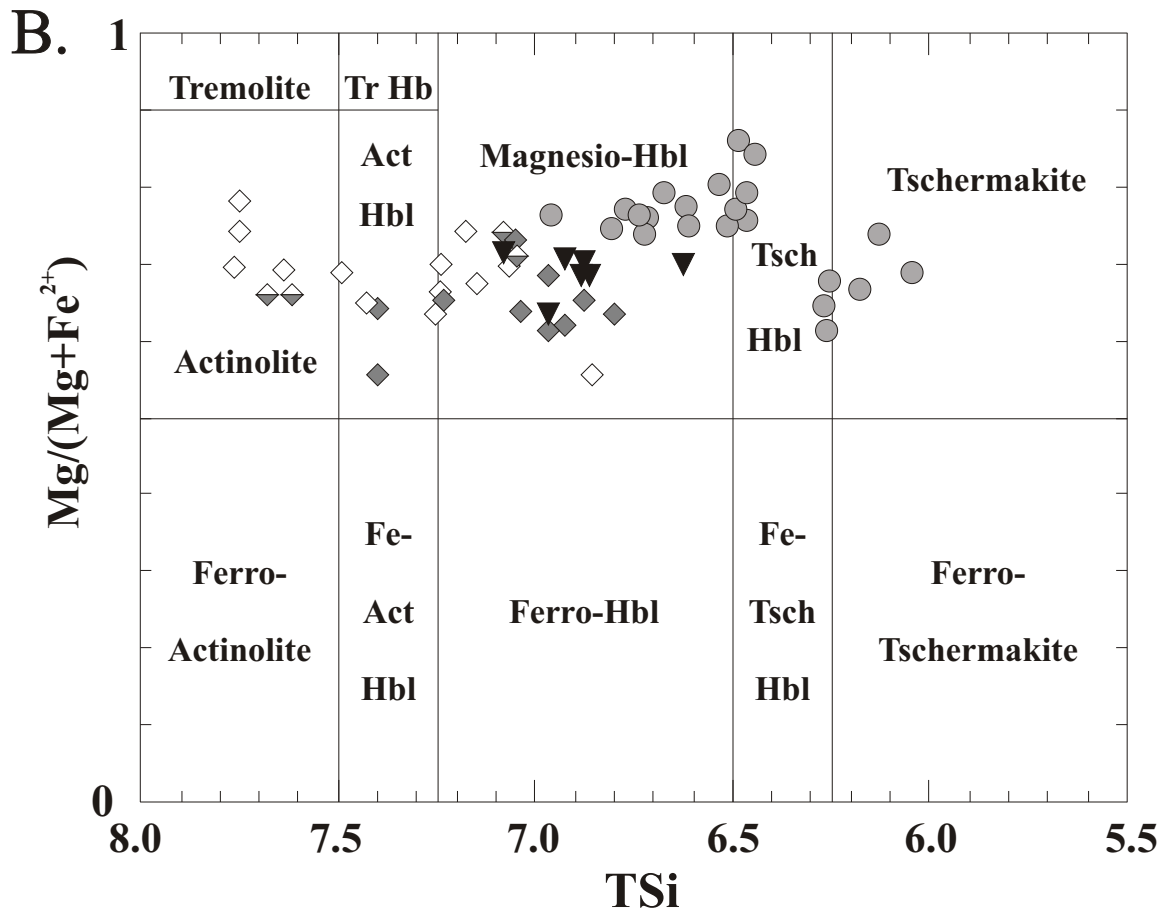
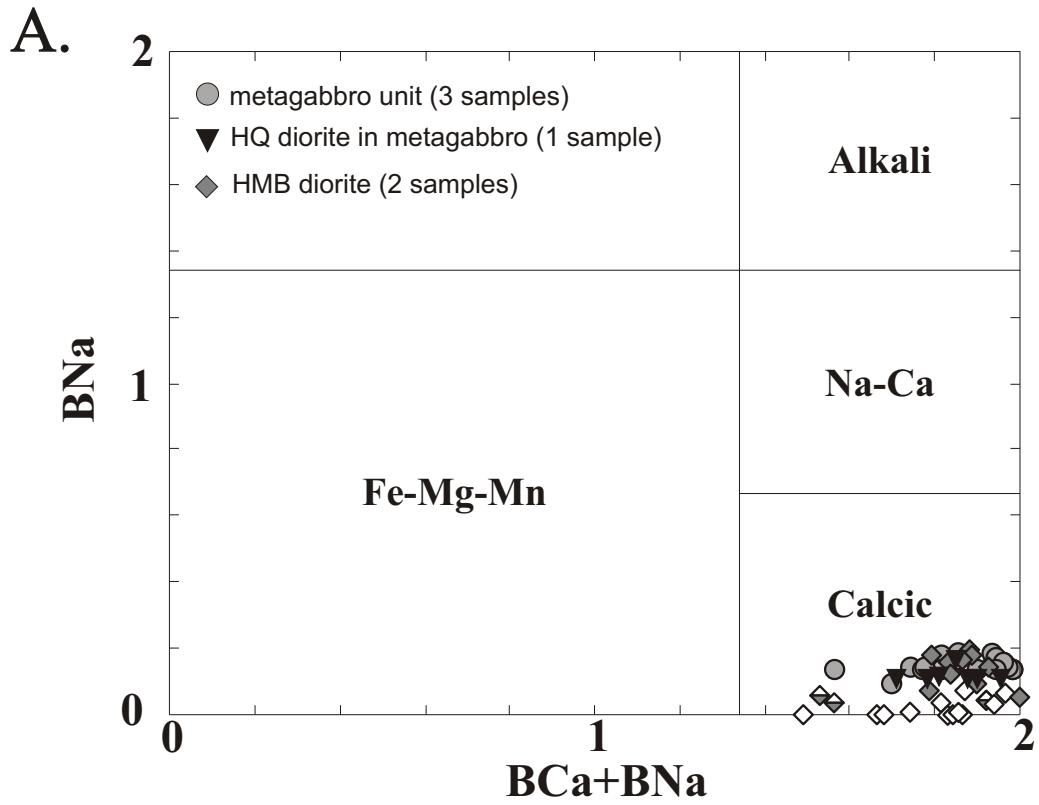
X_i^Φ terms denote the molar fraction of the species i in crystallographic site Φ , and cm denotes the “cummingtonite” substitution and is determined as follows: $\text{cm} = \text{Si} + \text{Al} + \text{Ti} + \text{Fe}^{3+} + \text{Fe}^{2+} + \text{Mg} + \text{Mn} - 13$

3.2.5 Classification of amphiboles

The classification of the amphiboles is shown in figure 3.3 in which the recalculated amphibole analysis (tables 3.1, 3.2 and 3.3) are plotted. All data points fall within the field of calcic amphiboles (figure 3.3a), and the compositional requirements for the application of the thermometers are met for most amphiboles. The empty symbols denote the analyses (data not listed in tables 3.1, 3.2 and 3.3) that could not be used for the thermometry calculations, mainly because the requirements for enough Na in the M4 (or B)-site ($X_{\text{Na}}^{\text{M4}} > 0.03$) and/or the A-site ($\text{Na}^{\text{A}} > 0.02$ pfu) were not met. The half-filled symbols represent

Figure 3.3

- A. Classification of amphiboles determining the principle group. The samples from the metagabbro unit (n = 3), the intrusion of HQ diorite (n = 1) in the metagabbro unit, and the HMB diorite (n = 2) contain exclusively calcic amphiboles. Many amphibole compositions are not suitable for the application of the thermometers A and B (empty symbols), mainly because they contain not enough Na in the B- (or M4-) site. Few amphibole were suitable for the application of thermometer A, but not thermometer B (half filled symbols).
- B. Further subdivision of calcic amphiboles based on tetrahedral Si and Mg-# (also: $ANa + AK < 0.5$ and $Ti < 0.5$). The amphiboles are relatively magnesian and range in composition from tschermakite to actinolite.



analyses of amphiboles in assemblages with quartz meeting the requirements for thermometer A, but not for thermometer B. Overall, the amphiboles that could not be used for the thermometry calculations are predominantly actinolite and actinolitic hornblende (figure 3.3b).

The three different plutonic units sampled in the Wild Rogue Wilderness are also characterized by distinctly different compositions of hornblende. The amphiboles analyzed in three quartz-free samples from the metagabbro unit range in composition from Mg-hornblende to tschermakite, whereas the HMB diorite intruding the pillows indicates compositions ranging from Mg-hornblende to actinolite. A compositional gap, or bimodal composition is indicated by the data from the metagabbro unit. The reason for this gap is not known (i.e. exsolution lamellae or zoning were not observed in thin section). Finally, the amphibole-data of the sample from the HQ diorite in the metagabbro plot entirely in the Mg-hornblende field between the data points of the other two units.

3.2.6 Calculation of temperatures

The microprobe data were transferred to a spreadsheet format, and all calculations were performed using a macro written for Microsoft Excel and the equations given in Holland and Blundy (1994). The temperatures for assemblages with quartz were calculated using the edenite-tremolite thermometer (A) as well as the edenite-richterite thermometer (B). The temperatures for assemblages without quartz were calculated using only the edenite-richterite thermometer (B). Holland and Blundy (1994) presented the following two equations:

$$(A) \quad T = \frac{-76.95 + 0.79 \cdot P + Y_{ab} + 39.4 \cdot X_{Na}^A + 22.4 \cdot X_K^A + (41.5 - 2.89 \cdot P) \cdot X_{Al}^{M2}}{-0.0650 - R \cdot \ln \left(\frac{27 \cdot X_{\square}^A \cdot X_{Si}^{T1} \cdot X_{ab}^{plag}}{256 \cdot X_{Na}^A \cdot X_{Al}^{T1}} \right)}$$

where the Y_{ab} term is given by: if $1.0 > X_{ab} > 0.5 \rightarrow Y_{ab} = 0$
 if $0.1 < X_{ab} < 0.5 \rightarrow 12.0 \cdot (1 - X_{ab})^2 - 3$

$$(B) \quad T = \frac{78.44 + Y_{ab-an} - 33.6 \cdot X_{Na}^{M4} - (66.8 - 2.92 \cdot P) \cdot X_{Al}^{M2} + 78.5 \cdot X_{Al}^{T1} + 9.4 \cdot X_{Na}^A}{0.0721 - R \cdot \ln \left(\frac{27 \cdot X_{Na}^{M4} \cdot X_{Si}^{T1} \cdot X_{an}^{plag}}{64 \cdot X_{Ca}^{M4} \cdot X_{Al}^{T1} \cdot X_{ab}^{plag}} \right)}$$

where the Y_{ab-an} term is given by: if $0.9 > X_{ab} > 0.5 \rightarrow Y_{ab-an} = 3.0$

if $0.1 < X_{ab} < 0.5 \rightarrow 12.0 \cdot (2 \cdot X_{ab} - 1) + 3$

the X_i^{ϕ} terms for amphibole are determined as discussed in section 3.2.4, T is the temperature in Kelvins, P is the pressure in kbar, $R = 0.0083144 \text{ kJ K}^{-1} \text{ mol}^{-1}$, and X_a^{plag} terms denote the molar fraction of component **a** (albite or anorthite) in coexisting plagioclase.

Before applying the geothermometers to hornblende-plagioclase compositions of plutonic rocks from the Wild Rogue Wilderness, the correctness of the calculation procedure must be tested. This was done applying the programmed Microsoft Excel macro to a test data set for which Holland and Blundy (1994) already calculated the temperatures. The test data are from an experimental study of Poli (1993). He experimentally investigated in a basaltic system the phase relationships and phase compositions through the transformation from feldspar-amphibolite to eclogite. The average microprobe analyses of plagioclase-amphibole pairs of three experimental runs (Poli, 1993) are listed at the end of this chapter in table 3.4 as well as the P-T conditions of these experiments. The temperatures that were calculated with the Microsoft Excel macro agree with the temperatures provided by Holland and Blundy (1994) indicating the macro was programmed correctly. Note also that these temperatures agree well with the temperatures of the experimental runs suggesting the geothermometers produce meaningful results.

The calculated temperatures (in °C) at various pressures (in kbar) are presented for the HMB diorite, HQ diorite, and metagabbro in tables 3.1, 3.2, and 3.3, respectively. The temperatures are calculated using the microprobe analyses of the hornblende-plagioclase pairs listed in these tables. The average temperatures for each sample as well as the standard deviation (1σ) are given. The electron microprobe analysis of coexisting plagioclase is given in Appendix C (tables C3, C4, and C5).

Table 3.1a: Results of microprobe analysis and temperature calculations, HMB diorite

Microprobe analysis of coexisting hornblende-plagioclase pairs in O/C-118a

| Analysis | 68 | 70 | 80 | 76 | 78 | 79 | 81 |
|--------------------------------|-------|-------|-------|-------|-------|-------|-------|
| Location | 1 | 2 | 5 | 3 | 4 | 5 | 5 |
| SiO ₂ | 47.43 | 47.74 | 48.62 | 42.94 | 50.47 | 52.93 | 48.20 |
| TiO ₂ | 0.85 | 0.31 | 1.33 | 0.23 | 0.17 | 0.06 | 0.14 |
| Al ₂ O ₃ | 6.54 | 6.12 | 6.36 | 8.64 | 4.91 | 2.31 | 6.47 |
| FeO | 16.56 | 15.11 | 17.43 | 17.86 | 18.19 | 16.07 | 16.61 |
| MnO | 0.20 | 0.27 | 0.19 | 0.27 | 0.20 | 0.40 | 0.31 |
| MgO | 13.34 | 13.81 | 13.07 | 14.14 | 11.14 | 15.53 | 14.74 |
| CaO | 10.62 | 11.37 | 10.35 | 7.76 | 12.65 | 9.80 | 9.36 |
| Na ₂ O | 1.11 | 0.64 | 1.27 | 0.21 | 0.52 | 0.25 | 0.40 |
| K ₂ O | 0.25 | 0.11 | 0.21 | 0.07 | 0.11 | 0.09 | 0.08 |
| Total | 96.90 | 95.49 | 98.81 | 92.12 | 98.36 | 97.45 | 96.32 |

Recalculation of amphibole analysis following Holland and Blundy (1994)

| | | | | | | | |
|------------------|-------|-------|-------|-------|-------|-------|-------|
| Si | 6.967 | 7.060 | 7.035 | 6.568 | 7.398 | 7.680 | 7.057 |
| Al | 1.033 | 0.940 | 0.965 | 1.432 | 0.602 | 0.320 | 0.943 |
| | 8 | 8 | 8 | 8 | 8 | 8 | 8 |
| Al | 0.099 | 0.126 | 0.118 | 0.125 | 0.246 | 0.075 | 0.172 |
| Ti | 0.094 | 0.034 | 0.145 | 0.026 | 0.019 | 0.006 | 0.016 |
| Fe ³⁺ | 0.693 | 0.721 | 0.522 | 1.240 | 0.272 | 0.216 | 0.721 |
| Mg | 2.921 | 3.045 | 2.819 | 3.226 | 2.435 | 3.360 | 3.217 |
| Fe ²⁺ | 1.193 | 1.074 | 1.397 | 0.383 | 1.957 | 1.343 | 0.875 |
| Mn | 0 | 0 | 0 | 0 | 0.024 | 0 | 0 |
| Ca | 0 | 0 | 0 | 0 | 0.047 | 0 | 0 |
| | 5 | 5 | 5 | 5 | 5 | 5 | 5 |
| Fe ²⁺ | 0.148 | 0.074 | 0.192 | 0.662 | 0.000 | 0.391 | 0.438 |
| Mn | 0.025 | 0.033 | 0.023 | 0.034 | 0.000 | 0.050 | 0.038 |
| Ca | 1.670 | 1.801 | 1.605 | 1.273 | 1.939 | 1.524 | 1.468 |
| Na | 0.157 | 0.091 | 0.181 | 0.032 | 0.061 | 0.036 | 0.056 |
| | 2 | 2 | 2 | 2 | 2 | 2 | 2 |
| Na | 0.160 | 0.093 | 0.174 | 0.032 | 0.086 | 0.036 | 0.056 |
| K | 0.046 | 0.020 | 0.039 | 0.013 | 0.020 | 0.017 | 0.015 |
| | 0.207 | 0.112 | 0.213 | 0.044 | 0.106 | 0.053 | 0.071 |

Mg-# of amphibole and composition of coexisting plagioclase (see also appendix C)

| | | | | | | | |
|-----------------|-------|-------|-------|-------|-------|-------|-------|
| Mg-# | 0.685 | 0.726 | 0.640 | 0.755 | 0.554 | 0.660 | 0.710 |
| X _{Ab} | 0.643 | 0.646 | 0.639 | 0.823 | 0.905 | 0.924 | 0.639 |

Calculation of temperatures using thermometers A and B at pressure P

| P (kbar) | A: T (°C) | | | | | | | average 1σ | |
|----------|-----------|-----|-----|-----|-----|-----|-----|------------|----|
| 1 | 761 | 704 | 750 | 654 | 579 | 510 | 656 | 659 | 84 |
| 2 | 751 | 696 | 741 | 647 | 573 | 502 | 649 | 651 | 83 |
| 3 | 741 | 687 | 731 | 639 | 568 | 495 | 642 | 643 | 82 |
| 4 | 731 | 678 | 721 | 631 | 562 | 488 | 634 | 635 | 81 |
| P (kbar) | B: T (°C) | | | | | | | | |
| 1 | 752 | 686 | 755 | - | - | - | - | 731 | 32 |
| 2 | 753 | 688 | 756 | - | - | - | - | 732 | 31 |
| 3 | 755 | 690 | 758 | - | - | - | - | 734 | 31 |
| 4 | 756 | 692 | 760 | - | - | - | - | 736 | 31 |

Table 3.1b: Results of microprobe analysis and temperature calculations, HMB diorite

Microprobe analysis of coexisting hornblende-plagioclase pairs in O/C-376

| Analysis | 40 | 41 | 48 | 49 | 53 | 55 | 64 |
|--------------------------------|-------|-------|-------|-------|-------|-------|--------|
| Location | 2 | 2 | 1 | 1 | 3 | 3 | 5 |
| SiO ₂ | 47.45 | 46.09 | 50.05 | 47.88 | 47.19 | 50.93 | 53.87 |
| TiO ₂ | 1.10 | 1.23 | 0.48 | 1.19 | 1.00 | 0.10 | 0.24 |
| Al ₂ O ₃ | 6.83 | 7.46 | 5.11 | 6.55 | 7.01 | 4.01 | 2.62 |
| FeO | 18.40 | 18.08 | 17.05 | 18.45 | 17.58 | 17.31 | 15.73 |
| MnO | 0.35 | 0.34 | 0.41 | 0.40 | 0.43 | 0.49 | 0.26 |
| MgO | 11.99 | 11.85 | 13.45 | 12.10 | 12.42 | 13.64 | 14.75 |
| CaO | 10.82 | 10.80 | 11.06 | 10.87 | 11.38 | 11.01 | 12.34 |
| Na ₂ O | 1.40 | 1.34 | 0.87 | 1.32 | 1.20 | 0.51 | 0.34 |
| K ₂ O | 0.28 | 0.36 | 0.25 | 0.26 | 0.32 | 0.18 | 0.09 |
| Total | 98.62 | 97.55 | 98.73 | 99.02 | 98.53 | 98.17 | 100.24 |

Recalculation of amphibole analysis following Holland and Blundy (1994)

| | | | | | | | |
|------------------|-------|-------|-------|-------|-------|-------|-------|
| Si | 6.928 | 6.801 | 7.235 | 6.968 | 6.875 | 7.399 | 7.620 |
| Al | 1.072 | 1.199 | 0.765 | 1.032 | 1.125 | 0.601 | 0.380 |
| | 8 | 8 | 8 | 8 | 8 | 8 | 8 |
| Al | 0.102 | 0.097 | 0.105 | 0.090 | 0.079 | 0.086 | 0.056 |
| Ti | 0.120 | 0.137 | 0.051 | 0.130 | 0.109 | 0.011 | 0.025 |
| Fe ³⁺ | 0.650 | 0.730 | 0.505 | 0.589 | 0.715 | 0.459 | 0.254 |
| Mg | 2.610 | 2.606 | 2.899 | 2.624 | 2.697 | 2.954 | 3.111 |
| Fe ²⁺ | 1.518 | 1.429 | 1.440 | 1.567 | 1.400 | 1.490 | 1.554 |
| Mn | 0 | 0 | 0 | 0 | 0 | 0 | 0 |
| Ca | 0 | 0 | 0 | 0 | 0 | 0 | 0 |
| | 5 | 5 | 5 | 5 | 5 | 5 | 5 |
| Fe ²⁺ | 0.079 | 0.072 | 0.116 | 0.090 | 0.026 | 0.154 | 0.052 |
| Mn | 0.043 | 0.042 | 0.050 | 0.049 | 0.053 | 0.060 | 0.032 |
| Ca | 1.692 | 1.707 | 1.713 | 1.695 | 1.776 | 1.714 | 1.870 |
| Na | 0.186 | 0.178 | 0.120 | 0.165 | 0.144 | 0.071 | 0.046 |
| | 2 | 2 | 2 | 2 | 2 | 2 | 2 |
| Na | 0.210 | 0.206 | 0.122 | 0.206 | 0.195 | 0.072 | 0.046 |
| K | 0.052 | 0.068 | 0.045 | 0.048 | 0.060 | 0.033 | 0.016 |
| | 0.262 | 0.274 | 0.168 | 0.254 | 0.255 | 0.105 | 0.062 |

Mg-# of amphibole and composition of coexisting plagioclase (see also appendix C)

| | | | | | | | |
|-----------------|-------|-------|-------|-------|-------|-------|-------|
| Mg-# | 0.620 | 0.634 | 0.651 | 0.613 | 0.654 | 0.642 | 0.659 |
| X _{Ab} | 0.672 | 0.557 | 0.445 | 0.716 | 0.475 | 0.880 | 0.836 |

Calculation of temperatures using thermometers A and B at pressure P

| P (kbar) | A: T (°C) | | | | | | | average 1σ | |
|----------|-----------|-----|-----|-----|-----|-----|-----|------------|-----|
| 1 | 775 | 823 | 728 | 762 | 833 | 607 | 550 | 725 | 100 |
| 2 | 764 | 812 | 719 | 752 | 821 | 599 | 542 | 716 | 98 |
| 3 | 754 | 801 | 709 | 741 | 810 | 591 | 534 | 706 | 97 |
| 4 | 744 | 790 | 700 | 731 | 799 | 582 | 526 | 696 | 96 |
| P (kbar) | B: T (°C) | | | | | | | | |
| 1 | 757 | 812 | 791 | 721 | 818 | 561 | - | 743 | 88 |
| 2 | 758 | 813 | 793 | 733 | 819 | 562 | - | 746 | 88 |
| 3 | 760 | 815 | 795 | 734 | 820 | 563 | - | 748 | 88 |
| 4 | 761 | 816 | 796 | 735 | 821 | 565 | - | 749 | 88 |

Table 3.2: Results of microprobe analysis and temperature calculations, HQ diorite

Microprobe analysis of coexisting hornblende-plagioclase pairs in O/C-229

| Analysis | 125 | 134 | 135 | 136 | 137 | 138 | 139 |
|--------------------------------|-------|-------|-------|-------|-------|-------|-------|
| Location | 2 | 4 | 5 | 5 | 5 | 5 | 5 |
| SiO ₂ | 47.72 | 46.37 | 48.08 | 47.46 | 48.45 | 48.24 | 49.10 |
| TiO ₂ | 1.06 | 0.90 | 1.36 | 0.82 | 0.27 | 1.25 | 1.01 |
| Al ₂ O ₃ | 7.56 | 9.08 | 7.78 | 7.25 | 7.75 | 6.77 | 6.46 |
| FeO | 16.05 | 18.20 | 16.44 | 17.12 | 17.68 | 15.93 | 14.60 |
| MnO | 0.39 | 0.51 | 0.55 | 0.38 | 0.37 | 0.51 | 0.54 |
| MgO | 13.48 | 13.16 | 13.41 | 12.91 | 11.98 | 13.65 | 14.55 |
| CaO | 10.92 | 10.46 | 11.06 | 11.37 | 11.97 | 11.63 | 10.82 |
| Na ₂ O | 1.18 | 0.78 | 0.86 | 0.80 | 0.79 | 0.78 | 0.81 |
| K ₂ O | 0.16 | 0.23 | 0.19 | 0.18 | 0.24 | 0.21 | 0.19 |
| Total | 98.53 | 99.68 | 99.72 | 98.30 | 99.50 | 98.97 | 98.08 |

Recalculation of amphibole analysis following Holland and Blundy (1994)

| | | | | | | | |
|------------------|-------|-------|-------|-------|-------|-------|-------|
| Si | 6.874 | 6.627 | 6.859 | 6.881 | 6.966 | 6.926 | 7.069 |
| Al | 1.126 | 1.373 | 1.141 | 1.119 | 1.034 | 1.074 | 0.931 |
| | 8 | 8 | 8 | 8 | 8 | 8 | 8 |
| Al | 0.157 | 0.155 | 0.166 | 0.120 | 0.278 | 0.072 | 0.164 |
| Ti | 0.115 | 0.097 | 0.146 | 0.089 | 0.030 | 0.135 | 0.110 |
| Fe ₃₊ | 0.703 | 0.976 | 0.647 | 0.781 | 0.646 | 0.686 | 0.508 |
| Mg | 2.895 | 2.803 | 2.851 | 2.791 | 2.567 | 2.922 | 3.121 |
| Fe ₂₊ | 1.130 | 0.969 | 1.189 | 1.219 | 1.479 | 1.185 | 1.097 |
| Mn | 0 | 0 | 0 | 0 | 0 | 0 | 0 |
| Ca | 0 | 0 | 0 | 0 | 0 | 0 | 0 |
| | 5 | 5 | 5 | 5 | 5 | 5 | 5 |
| Fe ₂₊ | 0.102 | 0.230 | 0.126 | 0.076 | 0.001 | 0.040 | 0.152 |
| Mn | 0.048 | 0.062 | 0.066 | 0.047 | 0.045 | 0.062 | 0.066 |
| Ca | 1.687 | 1.601 | 1.690 | 1.765 | 1.844 | 1.789 | 1.669 |
| Na | 0.163 | 0.107 | 0.118 | 0.111 | 0.110 | 0.109 | 0.112 |
| | 2 | 2 | 2 | 2 | 2 | 2 | 2 |
| Na | 0.167 | 0.108 | 0.120 | 0.113 | 0.112 | 0.110 | 0.114 |
| K | 0.029 | 0.041 | 0.035 | 0.033 | 0.043 | 0.039 | 0.035 |
| | 0.195 | 0.150 | 0.155 | 0.146 | 0.155 | 0.150 | 0.149 |

Mg-# of amphibole and composition of coexisting plagioclase (see also appendix C)

| | | | | | | | |
|-----------------|-------|-------|-------|-------|-------|-------|-------|
| Mg-# | 0.702 | 0.700 | 0.684 | 0.683 | 0.634 | 0.704 | 0.714 |
| X _{Ab} | 0.56 | 0.56 | 0.53 | 0.51 | 0.46 | 0.59 | 0.75 |

Calculation of temperatures using thermometers A and B at pressure P

| P (kbar) | A: T (°C) | | | | | | | average 1σ | |
|----------|-----------|-----|-----|-----|-----|-----|-----|------------|----|
| 1 | 784 | 788 | 765 | 776 | 719 | 761 | 687 | 754 | 35 |
| 2 | 775 | 779 | 757 | 767 | 713 | 751 | 679 | 746 | 34 |
| 3 | 766 | 770 | 748 | 757 | 707 | 741 | 671 | 737 | 33 |
| 4 | 757 | 761 | 740 | 748 | 702 | 731 | 663 | 729 | 32 |
| P (kbar) | B: T (°C) | | | | | | | | |
| 1 | 775 | 769 | 756 | 768 | 711 | 750 | 654 | 740 | 40 |
| 2 | 777 | 771 | 759 | 770 | 715 | 751 | 657 | 743 | 40 |
| 3 | 780 | 773 | 761 | 772 | 719 | 752 | 659 | 745 | 40 |
| 4 | 782 | 776 | 764 | 774 | 724 | 753 | 662 | 748 | 40 |

Table 3.3a: Results of microprobe analysis and temperature calculations, metagabbro

Microprobe analysis of coexisting hornblende-plagioclase pairs in MRH-78/1

| Analysis | 141 | 143 | 145 | 150 | 151 | 156 | 165 |
|--------------------------------|-------|-------|-------|-------|-------|-------|-------|
| Location | 1 | 1 | 1 | 2 | 3 | 4 | 4 |
| SiO ₂ | 41.45 | 46.04 | 42.68 | 43.68 | 45.26 | 46.06 | 42.70 |
| TiO ₂ | 0.58 | 0.43 | 0.46 | 0.52 | 0.50 | 0.90 | 0.59 |
| Al ₂ O ₃ | 13.74 | 10.84 | 15.32 | 14.64 | 12.05 | 11.38 | 14.45 |
| FeO | 20.49 | 14.07 | 15.56 | 15.71 | 13.80 | 15.14 | 15.75 |
| MnO | 0.28 | 0.50 | 0.37 | 0.32 | 0.43 | 0.59 | 0.44 |
| MgO | 11.21 | 13.07 | 10.46 | 10.89 | 13.24 | 13.20 | 11.46 |
| CaO | 9.15 | 11.74 | 11.92 | 12.04 | 11.53 | 11.00 | 11.82 |
| Na ₂ O | 0.97 | 1.39 | 1.47 | 1.37 | 1.29 | 1.41 | 1.52 |
| K ₂ O | 0.12 | 0.13 | 0.21 | 0.13 | 0.08 | 0.17 | 0.14 |
| Total | 97.99 | 98.21 | 98.43 | 99.30 | 98.18 | 99.86 | 98.85 |

Recalculation of amphibole analysis following Holland and Blundy (1994)

| | | | | | | | |
|------------------|-------|-------|-------|-------|-------|-------|-------|
| Si | 6.044 | 6.612 | 6.176 | 6.253 | 6.462 | 6.510 | 6.131 |
| Al | 1.956 | 1.388 | 1.824 | 1.747 | 1.538 | 1.490 | 1.869 |
| | 8 | 8 | 8 | 8 | 8 | 8 | 8 |
| Al | 0.403 | 0.444 | 0.785 | 0.720 | 0.489 | 0.405 | 0.572 |
| Ti | 0.063 | 0.046 | 0.050 | 0.056 | 0.053 | 0.095 | 0.064 |
| Fe ³⁺ | 1.395 | 0.748 | 0.751 | 0.770 | 0.915 | 0.852 | 1.015 |
| Mg | 2.437 | 2.797 | 2.256 | 2.323 | 2.818 | 2.782 | 2.453 |
| Fe ²⁺ | 0.702 | 0.941 | 1.131 | 1.110 | 0.726 | 0.866 | 0.875 |
| Mn | 0 | 0.024 | 0.027 | 0.021 | 0 | 0 | 0.021 |
| Ca | 0 | 0 | 0 | 0 | 0 | 0 | 0 |
| | 5 | 5 | 5 | 5 | 5 | 5 | 5 |
| Fe ²⁺ | 0.401 | 0.000 | 0.000 | 0.000 | 0.008 | 0.072 | 0.000 |
| Mn | 0.034 | 0.037 | 0.018 | 0.018 | 0.051 | 0.071 | 0.032 |
| Ca | 1.429 | 1.806 | 1.847 | 1.847 | 1.764 | 1.667 | 1.818 |
| Na | 0.136 | 0.156 | 0.135 | 0.135 | 0.177 | 0.190 | 0.150 |
| | 2 | 2 | 2 | 2 | 2 | 2 | 2 |
| Na | 0.138 | 0.231 | 0.276 | 0.245 | 0.181 | 0.195 | 0.271 |
| K | 0.021 | 0.024 | 0.037 | 0.025 | 0.016 | 0.030 | 0.025 |
| | 0.160 | 0.255 | 0.314 | 0.270 | 0.197 | 0.226 | 0.297 |

Mg-# of amphibole and composition of coexisting plagioclase (see also appendix C)

| | | | | | | | |
|-----------------|-------|-------|-------|-------|-------|-------|-------|
| Mg-# | 0.688 | 0.748 | 0.666 | 0.677 | 0.793 | 0.748 | 0.737 |
| X _{Ab} | 0.883 | 0.766 | 0.766 | 0.853 | 0.794 | 0.719 | 0.719 |

Calculation of temperatures using thermometer B. Pressure P is assumed.

| P (kbar) | T (°C) | | | | | | | average | 1σ |
|----------|--------|-----|-----|-----|-----|-----|-----|---------|----|
| 2 | 651 | 635 | 583 | 553 | 630 | 689 | 670 | 630 | 44 |
| 4 | 661 | 648 | 603 | 572 | 643 | 701 | 686 | 645 | 42 |
| 6 | 672 | 660 | 624 | 590 | 657 | 712 | 702 | 660 | 39 |
| 8 | 682 | 673 | 645 | 609 | 670 | 724 | 717 | 674 | 37 |
| 10 | 692 | 685 | 666 | 627 | 684 | 736 | 733 | 689 | 35 |

Table 3.3b: Results of microprobe analysis and temperature calculations, metagabbro

Microprobe analysis of coexisting hornblende-plagioclase pairs in MRH-78/2

| Analysis | 41 | 43 | 49 | 51 | 52 | 54 |
|--------------------------------|-------|-------|-------|-------|-------|-------|
| Location | 2 | 2 | 1 | 4 | 4 | 4 |
| SiO ₂ | 44.82 | 45.09 | 44.48 | 45.90 | 46.28 | 44.93 |
| TiO ₂ | 0.76 | 0.82 | 0.88 | 0.89 | 0.77 | 0.76 |
| Al ₂ O ₃ | 11.24 | 10.11 | 10.81 | 10.14 | 8.91 | 8.85 |
| FeO | 15.62 | 13.50 | 13.21 | 13.99 | 14.54 | 15.29 |
| MnO | 0.31 | 0.37 | 0.48 | 0.59 | 0.52 | 0.54 |
| MgO | 13.41 | 14.46 | 13.95 | 13.78 | 14.37 | 14.95 |
| CaO | 10.36 | 11.75 | 11.44 | 10.87 | 10.58 | 10.31 |
| Na ₂ O | 1.04 | 1.04 | 1.17 | 1.22 | 1.33 | 1.25 |
| K ₂ O | 0.21 | 0.10 | 0.13 | 0.08 | 0.10 | 0.09 |
| Total | 97.77 | 97.24 | 96.55 | 97.46 | 97.39 | 96.96 |

Recalculation of amphibole analysis following Holland and Blundy (1994)

| | | | | | | |
|------------------|-------|-------|-------|-------|-------|-------|
| Si | 6.462 | 6.482 | 6.446 | 6.615 | 6.676 | 6.536 |
| Al | 1.538 | 1.518 | 1.554 | 1.385 | 1.324 | 1.464 |
| | 8 | 8 | 8 | 8 | 8 | 8 |
| Al | 0.371 | 0.193 | 0.290 | 0.336 | 0.190 | 0.050 |
| Ti | 0.082 | 0.089 | 0.096 | 0.096 | 0.083 | 0.083 |
| Fe ³⁺ | 0.952 | 1.124 | 1.042 | 0.831 | 0.939 | 1.060 |
| Mg | 2.883 | 3.097 | 3.014 | 2.962 | 3.091 | 3.241 |
| Fe ²⁺ | 0.711 | 0.497 | 0.558 | 0.775 | 0.697 | 0.566 |
| Mn | 0 | 0 | 0 | 0 | 0 | 0 |
| Ca | 0 | 0 | 0 | 0 | 0 | 0 |
| | 5 | 5 | 5 | 5 | 5 | 5 |
| Fe ²⁺ | 0.220 | 0.002 | 0.001 | 0.080 | 0.118 | 0.235 |
| Mn | 0.037 | 0.045 | 0.060 | 0.073 | 0.064 | 0.066 |
| Ca | 1.599 | 1.810 | 1.777 | 1.679 | 1.635 | 1.606 |
| Na | 0.144 | 0.143 | 0.163 | 0.168 | 0.184 | 0.093 |
| | 2 | 2 | 2 | 2 | 2 | 2 |
| Na | 0.147 | 0.146 | 0.166 | 0.172 | 0.188 | 0.259 |
| K | 0.038 | 0.019 | 0.023 | 0.015 | 0.019 | 0.017 |
| | 0.185 | 0.164 | 0.190 | 0.187 | 0.207 | 0.276 |

Mg-# of amphibole and composition of coexisting plagioclase (see also appendix C)

| | | | | | | |
|-----------------|-------|-------|-------|-------|-------|-------|
| Mg-# | 0.756 | 0.861 | 0.844 | 0.776 | 0.791 | 0.802 |
| X _{Ab} | 0.876 | 0.876 | 0.825 | 0.773 | 0.823 | 0.823 |

Calculation of temperatures using thermometer B. Pressure P is assumed.

| P (kbar) | T (°C) | | | | | | average | 1σ |
|----------|--------|-----|-----|-----|-----|-----|---------|----|
| 2 | 616 | 654 | 668 | 667 | 688 | 712 | 668 | 29 |
| 4 | 626 | 659 | 676 | 677 | 693 | 713 | 674 | 27 |
| 6 | 636 | 664 | 684 | 686 | 699 | 714 | 680 | 25 |
| 8 | 646 | 669 | 692 | 696 | 704 | 716 | 687 | 23 |
| 10 | 655 | 674 | 700 | 705 | 709 | 717 | 693 | 22 |

Table 3.3c: Results of microprobe analysis and temperature calculations, metagabbro

Microprobe analysis of coexisting hornblende-plagioclase pairs in O/C-373

| Analysis | 6 | 13 | 14 | 15 | 23 | 25 | 26 | 27 | 29 |
|--------------------------------|-------|-------|-------|-------|-------|-------|-------|-------|-------|
| Location | 1 | 4 | 4 | 4 | 3 | 3 | 3 | 3 | 3 |
| SiO ₂ | 47.95 | 42.90 | 47.39 | 47.03 | 43.28 | 44.20 | 47.29 | 47.43 | 48.92 |
| TiO ₂ | 0.70 | 0.31 | 0.65 | 0.90 | 0.39 | 0.55 | 0.74 | 0.45 | 0.69 |
| Al ₂ O ₃ | 9.05 | 14.88 | 10.23 | 9.84 | 14.85 | 11.14 | 9.32 | 9.81 | 7.80 |
| FeO | 14.66 | 16.02 | 13.85 | 14.40 | 16.46 | 14.14 | 13.36 | 14.26 | 13.17 |
| MnO | 0.52 | 0.28 | 0.56 | 0.48 | 0.28 | 0.41 | 0.45 | 0.37 | 0.42 |
| MgO | 14.30 | 10.10 | 14.23 | 13.93 | 10.04 | 12.67 | 14.16 | 14.27 | 14.60 |
| CaO | 10.74 | 11.32 | 10.77 | 10.68 | 11.80 | 11.47 | 11.46 | 11.05 | 11.86 |
| Na ₂ O | 1.07 | 1.39 | 1.09 | 0.98 | 1.73 | 1.21 | 1.01 | 0.98 | 0.98 |
| K ₂ O | 0.11 | 0.15 | 0.10 | 0.10 | 0.15 | 0.17 | 0.09 | 0.11 | 0.08 |
| Total | 99.09 | 97.34 | 98.86 | 98.34 | 98.97 | 95.96 | 97.89 | 98.74 | 98.53 |

Recalculation of amphibole analysis following Holland and Blundy (1994)

| | | | | | | | | | |
|------------------|-------|-------|-------|-------|-------|-------|-------|-------|-------|
| Si | 6.806 | 6.268 | 6.719 | 6.726 | 6.263 | 6.490 | 6.773 | 6.736 | 6.961 |
| Al | 1.194 | 1.732 | 1.281 | 1.274 | 1.737 | 1.510 | 1.227 | 1.264 | 1.039 |
| | 8 | 8 | 8 | 8 | 8 | 8 | 8 | 8 | 8 |
| Al | 0.319 | 0.828 | 0.428 | 0.382 | 0.793 | 0.416 | 0.345 | 0.377 | 0.267 |
| Ti | 0.075 | 0.033 | 0.070 | 0.097 | 0.042 | 0.060 | 0.080 | 0.048 | 0.074 |
| Fe ³⁺ | 0.699 | 0.756 | 0.689 | 0.676 | 0.631 | 0.904 | 0.697 | 0.764 | 0.603 |
| Mg | 3.025 | 2.200 | 3.008 | 2.970 | 2.166 | 2.774 | 3.024 | 3.021 | 3.097 |
| Fe ²⁺ | 0.882 | 1.182 | 0.805 | 0.876 | 1.360 | 0.832 | 0.855 | 0.790 | 0.959 |
| Mn | 0 | 0 | 0 | 0 | 0.008 | 0.013 | 0 | 0 | 0 |
| Ca | 0 | 0 | 0 | 0 | 0 | 0 | 0 | 0 | 0 |
| | 5 | 5 | 5 | 5 | 5 | 5 | 5 | 5 | 5 |
| Fe ²⁺ | 0.159 | 0.019 | 0.148 | 0.172 | 0.000 | 0.000 | 0.048 | 0.139 | 0.005 |
| Mn | 0.063 | 0.034 | 0.068 | 0.058 | 0.027 | 0.038 | 0.054 | 0.045 | 0.051 |
| Ca | 1.633 | 1.771 | 1.636 | 1.636 | 1.829 | 1.806 | 1.758 | 1.682 | 1.809 |
| Na | 0.145 | 0.175 | 0.148 | 0.135 | 0.145 | 0.157 | 0.140 | 0.134 | 0.134 |
| | 2 | 2 | 2 | 2 | 2 | 2 | 2 | 2 | 2 |
| Na | 0.148 | 0.219 | 0.151 | 0.137 | 0.342 | 0.186 | 0.142 | 0.136 | 0.137 |
| K | 0.020 | 0.028 | 0.018 | 0.019 | 0.027 | 0.031 | 0.017 | 0.020 | 0.015 |
| | 0.168 | 0.246 | 0.168 | 0.156 | 0.368 | 0.218 | 0.159 | 0.156 | 0.152 |

Mg-# of amphibole and composition of coexisting plagioclase (see also appendix C)

| | | | | | | | | | |
|-----------------|-------|-------|-------|-------|-------|-------|-------|-------|-------|
| Mg-# | 0.744 | 0.647 | 0.759 | 0.739 | 0.614 | 0.769 | 0.770 | 0.765 | 0.763 |
| X _{Ab} | 0.807 | 0.735 | 0.735 | 0.791 | 0.745 | 0.823 | 0.823 | 0.773 | 0.773 |

Calculation of temperatures using thermometer B. Pressure P is assumed.

| P (kbar) | T (°C) | | | | | | | | | average | 1σ |
|----------|--------|-----|-----|-----|-----|-----|-----|-----|-----|---------|----|
| 2 | 630 | 579 | 638 | 622 | 587 | 628 | 611 | 628 | 633 | 617 | 20 |
| 4 | 639 | 602 | 650 | 633 | 609 | 639 | 620 | 639 | 640 | 630 | 15 |
| 6 | 648 | 625 | 663 | 644 | 631 | 650 | 630 | 649 | 648 | 643 | 11 |
| 8 | 657 | 648 | 675 | 654 | 652 | 662 | 639 | 660 | 655 | 656 | 9 |
| 10 | 666 | 671 | 687 | 665 | 674 | 673 | 649 | 670 | 663 | 669 | 10 |

3.2.7 Uncertainties

Basically, the magnitude of the uncertainties of the calculated temperatures is equal to the size of the temperature residuals of the regression of experimental and natural data to calibrate the thermometers (Holland and Blundy, 1994). For thermometer A, the maximum of the temperature residuals ($T_{\text{experimental}}$ or T_{natural} minus $T_{\text{calculated}}$) is 87°C, the standard deviation (1σ) of the residuals is 35°C. For thermometer B, the maximum of the residuals is 98°C, the standard deviation of the residuals is 38°C. Holland and Blundy (1994) also pointed out that the stated temperature uncertainties ($\pm 35^\circ\text{C}$ and $\pm 38^\circ\text{C}$) may enlarge for iron-rich amphiboles with very different oxidation states from those of the calibrant data set where the scheme of recasting of Fe_{total} into Fe^{2+} and Fe^{3+} can become uncertain. Due to the fact that a very large experimental and natural data set has been used for the calibration of the thermometers, the indicated uncertainties also include the typical errors of the analytical techniques employed (microprobe or wet chemical analysis) as well as the typical errors recasting Fe_{total} as Fe^{2+} and Fe^{3+} (if no wet-chemical analysis available). Provided the analyzed plagioclase-hornblende pairs are coexisting, and the pressure is assumed correctly, the obtained temperatures of equilibration are accurate within $\pm 70\text{-}80^\circ\text{C}$ on a 95% confidence level. Note also that the temperature variations calculated for each sample in tables 3.1, 3.2 and 3.3 (expressed as 1σ) are well within the temperature uncertainties indicated above.

3.3 Pressure estimates

It is readily determined from equations (A) and (B) (section 3.2.6) that an accurate temperature estimate depends also on a well-constrained determination of the pressure of equilibration. The pressure of crystallization of the gabbroic rocks can be estimated based on (1) geological evidence, and (2) composition of hornblende.

3.3.1 Estimate of pressure of crystallization using geological constraints

Although most of the HMB diorite occurs as a structurally bound unit, small gabbroic intrusions in the pillow unit, and a fault slice of diorite containing roof pendants of pillow basalt were mapped,

indicating the HMB diorite intruded near the base of the volcanic section of the Rogue Wilderness ophiolite (figure 3.1). The pillowed volcanic section represents the transition zone between a sheeted dike complex and an extrusive sequence as indicated by the occurrence of abundant diabasic dikes intruding the pillow basalt. Because only a fault slice of the extrusive sequence is preserved (max. structural thickness ~1 km), the original thickness as well as the water depth must be estimated to infer the pressure at the base of the extrusive sequence. The water depth of 5-10 Ma old oceanic or marginal basin crust is about 3 - 4 km (Sclater et al., 1971; Sclater, 1972), and the average thickness of the extrusive sequence of the oceanic floor is about 1.6 km as inferred from seismic velocities and ocean drilling (e.g., Vogt et al., 1969; Christensen and Salisbury, 1975) as well as from seismic studies in ophiolites (e.g., Christenson and Smewing, 1981; Casey et al., 1981). Taking into account that the Mule Mountain volcanics in the Wild Rogue Wilderness could represent an overlying volcanic pile at the time the HMB diorite intruded (max. structural thickness is almost 3 km), the pressure at the base of the extrusive sequence ranges between 0.85-1.5 kbar.

Unfortunately, the pressure of crystallization for the metagabbro unit and the HQ diorite occurring in the metagabbro unit near the contact with the Blossom Bar shear zone is difficult if not impossible to estimate using geological constraints. Assuming the metagabbro unit is part of the ophiolite and the HQ-diorite intruded the metagabbro (high-level gabbro) in an oceanic setting (figure 1), the pressure of equilibration may be inferred. The average water depth of 5-10 Ma year old crust is 3 - 4 km, and the average depth of high-level gabbro is 3 to 3.5 km (Christensen and Salisbury, 1975). The pressure inferred from the maximum structural thickness of units possibly overlying the metagabbro and HQ-diorite (figure 1) include from base to top high-level gabbro (~1 km), sheeted dike complex (~1 km), and pillow unit (~1 km) and is consistent with the pressure estimates using the average oceanic crust (1.3 kbar). However, it is also possible that the Mule Mountain volcanics and the HMB diorite were overlying units at the time the quartz-diorite intruded. Thus, the estimated pressure based on geological evidence is about 1.3 kbar and may be as high as 2.5 kbar for the HQ diorite. On the other hand, it is also possible that the structurally bound metagabbro unit and the HQ diorite within it are not part of the ophiolite but represent older(?), regionally metamorphosed basement and are structurally juxtaposed to the ophiolitic units. If this

is the case, the pressure of equilibration for the HQ-diorite and metagabbro remains unknown unless a meaningful, empirical pressure estimate can be obtained.

3.3.2 Aluminum-in-hornblende barometers

Field and experimental studies have shown that in the presence of the appropriate buffer assemblage, the total Al-content in hornblende is proportional to the crystallization pressure; Aluminum-in-hornblende (AH) barometers include the field-based calibrations of Hammarstrom and Zen, (1986) and Hollister et al. (1987) as well as the experimental calibrations by Johnson and Rutherford (1989) and Schmidt, (1992). These AH barometers have widely been used to estimate the pressure of emplacement of batholiths (e.g., Ague, 1997; Ague and Brandon, 1996; Anderson and Smith, 1995), and problems with the practical application have been discussed (Anderson, 1997; Patterson and Miller, 1998). The practical application of the AH barometers can produce meaningful results, however, it requires attention to several issues (Ague and Brandon, 1996):

(1) Pressure determination based on hornblende composition should be done on samples that contain hornblende in textural equilibrium with biotite, K-feldspar, quartz, plagioclase, titanite, and Fe-Ti oxides (Hammarstrom and Zen, 1986; Hollister et al., 1987; Johnson and Rutherford, 1989, Schmidt, 1992). The critical mineral assemblage required for AH barometers is not present in any of the investigated gabbros from the Wild Rogue Wilderness. Samples from the HMB diorite and HQ diorite contain quartz, plagioclase, hornblende, Fe-Ti-oxides, and trace amounts of titanite and biotite. They do not contain K-feldspar. Ague and Brimhall (1988) report that pressure estimates for rocks that lack K-feldspar are somewhat too high compared to those where the critical mineral assemblage is present. A pressure estimate based on hornblende composition may be made for the HMB diorite and the HQ diorite, but the obtained pressures have to be considered as the uppermost pressure limit. A pressure estimate cannot be made for the metagabbro as these samples lack quartz, K-feldspar, titanite and biotite.

(2) Pressure estimates based on the composition of Fe-rich amphiboles, which crystallized under very low oxygen fugacities, are systematically too high (Ague and Brimhall, 1988; Anderson and Smith, 1993). This

is not a problem in this study, because the amphiboles in the gabbro and diorite samples from the Wild Rogue Wilderness are Mg-rich (figure 3.3).

(3) Amphiboles which formed during low-temperature, subsolidus alteration (e.g., hornblende rims altered to actinolite) cannot be used, because the AH barometers are calibrated for hornblende that have “frozen-in” solidus compositions (see section 3.4).

(4) The composition of hornblende is a function of temperature as well as pressure (Spear, 1981; Hammarstrom and Zen, 1986; Blundy and Holland, 1994; Holland and Blundy, 1994). Edenite-type substitutions are thought to be related to increases in temperature (Holland and Blundy, 1994, Anderson and Smith, 1995). This type of substitution enriches hornblende in Al^{IV} but not Al^{VI} and therefore, if the AH barometer assemblage equilibrates at temperatures different from the temperatures of barometer calibration, then pressure estimates will be incorrect (Ague and Brandon, 1996). Thus, only hornblendes that are inferred to have equilibrated at solidus conditions can be used for the pressure estimates using the AH barometers.

There seems to be conclusive evidence that the total Al-content of hornblende (Al^{Tot}) coexisting with quartz, plagioclase, K-feldspar, biotite, titanite, Fe-Ti-oxides, supercritical fluids and melt linearly increases with increasing P (Hammarstrom and Zen, 1986; Hollister et al., 1987; Johnson and Rutherford, 1988). Such aluminum-in-hornblende barometers have widely been used, and they are calibrated for plutons of granitic, dioritic and tonalitic composition. The equations are as follows:

$$P = 5.03 Al^{Tot} - 3.92 \quad \text{Hammarstrom and Zen (1986)}$$

$$P = 5.64 Al^{Tot} - 4.76 \quad \text{Hollister et al. (1987)}$$

$$P = 4.28 Al^{Tot} - 3.54 \quad \text{Johnson and Rutherford (1988)}$$

Also, Ague (1997) successfully estimated the P-T conditions of equilibration for 19 rocks from Mesozoic batholiths in California evaluating a P-sensitive reaction (tremolite + phlogopite + 2 anorthite + 2 albite = 2 pargasite + 6 quartz + K-feldspar) and using simultaneously the thermometers A and B of Holland and Blundy (1994). A comparison with the AH barometers indicates that these barometers principally produce valid results, although absolute values differed up to ± 1.5 kbar from Ague's (1997) approach.

Using the average of $Al^{Tot} = 1.16 \pm 0.17$ pfu of Mg-hornblende in two samples from the HMB diorite (table 3.1), the calculated pressures of equilibration are 1.9 ± 0.8 kbar, 1.8 ± 0.9 kbar, and 1.4 ± 0.7 , respectively (note that only hornblendes are used which are thought to have equilibrated at near-solidus temperatures, see section 3.4.1). Similar to the results of Ague and Brimhall (1988) reported from batholiths in California, pressure estimates using the AH barometers on samples without K-feldspar are too high (1.4-1.9 kbar) compared to the pressure estimates using geological constraints (0.85-1.5 kbar). However, the pressure estimates using the AH barometers agree within error with the geological constraints for the HMB diorite.

The average of $Al^{Tot} = 1.37 \pm 0.13$ pfu of Mg-hornblende in sample O/C-229 (table 3.2) yields pressures of 2.5 ± 0.7 kbar, 2.4 ± 0.7 kbar, and 1.9 ± 0.6 kbar, respectively (note that only hornblendes are used which are thought to have equilibrated at near-solidus temperatures, see section 3.4.2). However, these results cannot be evaluated using pressure estimates based on geological constraints (see section 3.3.1).

Another estimate of the pressure of crystallization may be obtained from the intercept of the thermometers A and B in a P-T diagram (e.g. figure 3.4). For example, Ague (1997) noted that the curve representing the P-sensitive reaction (tremolite + phlogopite + 2 anorthite + 2 albite = 2 pargasite + 6 quartz + K-feldspar) intercepts in a P-T diagram in or near the point of intersection of thermometers A and B. This suggests that the thermometers and barometer equilibrated (simultaneously) under similar P-T conditions, and it is hypothesized that the point of intercept of thermometers A and B may be used in some instances as barometric indicator. However, Holland and Blundy (1994) caution against the use of the intersection of the thermometers as a barometric indicator because the coefficients were not optimized on the basis of minimizing pressure residuals.

3.4 Discussion

3.4.1 Half Moon Bar diorite

Assuming pressures between 1 to 4 kbar, the temperature of equilibration of coexisting plagioclase - hornblende pairs was determined using thermometers A and B (table 3.1). The resulting curves are plotted in a P-T diagram (figure 3.4). The shaded bars around curves A and B represent $\pm 1\sigma$ standard deviation. Note that the data points in figure 3.4 represent average temperatures of equilibration of hornblende-plagioclase pairs for which both thermometers are applicable (i.e. analyses 68, 70, 78, 80, 40, 41, 48, 49, 53 and 55 in table 3.1 were used to calculate the average temperature and 1σ). Curves A and B are almost pressure insensitive, because the calculated temperature changes only slightly as the assumed pressure increases. Figure 3.4 shows that the temperature estimates using thermometers A and B are indistinguishable in the range 0 to 4.5 kbar. Interestingly, curves A and B intersect in the P-T diagram at about 1.8 kbar, and the pressure indicated by the point of intersection is in relative good agreement with the pressure inferred from geological constraints (0.85-1.5 kbar) and the AH barometers (1.4-1.9 kbar).

The solidus of the HMB diorite is probably very close to the experimentally determined quartz diorite solidus of other Coast Range diorites in California (Piwinski, 1973). The wet quartz diorite solidus (samples CP2-1, DR510, and DR126) determined by Piwinski (1973) is shown in figure 3.4. The shaded bars representing the range of pressure and temperature estimates have a point of interception in the P-T diagram at $745 \pm 25^\circ\text{C}$ and 1.2 ± 0.3 kbar which lies on the wet solidus of quartz diorite. It is therefore likely that the amphiboles equilibrated at near-solidus conditions (figures 3.4).

The results of the temperature calculations (table 3.1) are presented in figure 3.5 on a plot of temperature versus Mg-# of hornblende (molar $\text{Mg}/(\text{Mg}+\text{Fe}^{2+})$). The pressure used was 2 kbar. The wet solidus of quartz diorite at 2 kbar is $\sim 725^\circ\text{C}$ and at 1 kbar $\sim 780^\circ\text{C}$ (samples CP2-1, DR510, and DR126 in Piwinski, 1973). The bulk of the calculated temperatures lies between 830°C and 640°C indicating that most amphiboles have frozen-in solidus compositions and only few amphiboles re-equilibrated at lower amphibolite facies conditions.

A cooling trend is clearly indicated in figure 3.5 which is characterized by the negative correlation of temperatures with Mg-#. The amphibole becomes more magnesian with cooling which is a significant feature of near- and sub-solidus cooling trends and is observed in many plutons (e.g. Czamanske and Wones, 1973). This has been demonstrated experimentally; the amphibole Mg-# is strongly dependent on fO_2 for specific bulk compositions and is highest under oxidizing conditions (Spear, 1981). Evidently, the HMB diorite underwent oxidation during cooling which may be attributed to the activity of supercritical(?) fluids that were released during cooling and the latest stages of crystallization. This interpretation is consistent with the formation of secondary, patchy pale-brown to brownish-green hornblende in the HMB diorite. Furthermore, the cooling trend is discontinued below 640°C, and partial(?) re-equilibration of amphibole characterized by lower Mg-# as well as lower Al^{IV} appears to have occurred significantly below the solidus. The four data points indicating the lowest temperatures of equilibration correspond to the actinolitic hornblende and actinolitic compositions shown in figure 3.3 (analyses 78, 79, 55 and 64; table 3.1). These amphiboles coexist with plagioclase having the highest Ab-content. The partial(?) re-equilibration at temperatures significantly below the solidus may require the presence of fluids to facilitate, for example, mass transport and the diffusion of Al in amphibole. A likely process is the hydrothermal circulation of seawater which is driven by the heat of the cooling pluton at the base of the submarine extrusive sequence. Actually, there is abundant petrographic evidence for retrograde hydrothermal alteration in the igneous basement studied in the Wild Rogue Wilderness, including the HMB diorite and pillow unit (chapter 2).

It has been demonstrated that the amount of Al in hornblende strongly depends on pressure (Hammarstrom and Zen, 1986; Hollister et al., 1987; Johnson and Rutherford, 1988) and temperature (Blundy and Holland, 1990; Holland and Blundy, 1994; Anderson and Smith, 1995). However, there is much debate what parameters most strongly affect amphibole compositions (e.g., Hammarstrom and Zen, 1992; Rutherford and Johnson, 1992; Blundy and Holland, 1992a, 1992b; Poli and Schmidt, 1992; Anderson, 1997). The enormous variability of compositions of amphibole is mainly attributed to pressure, temperature, rock composition, activity of silica, composition of fluids and fO_2 . Although the appropriateness of the compositional variability of amphiboles as thermometers or barometers is still

Half Moon Bar diorite

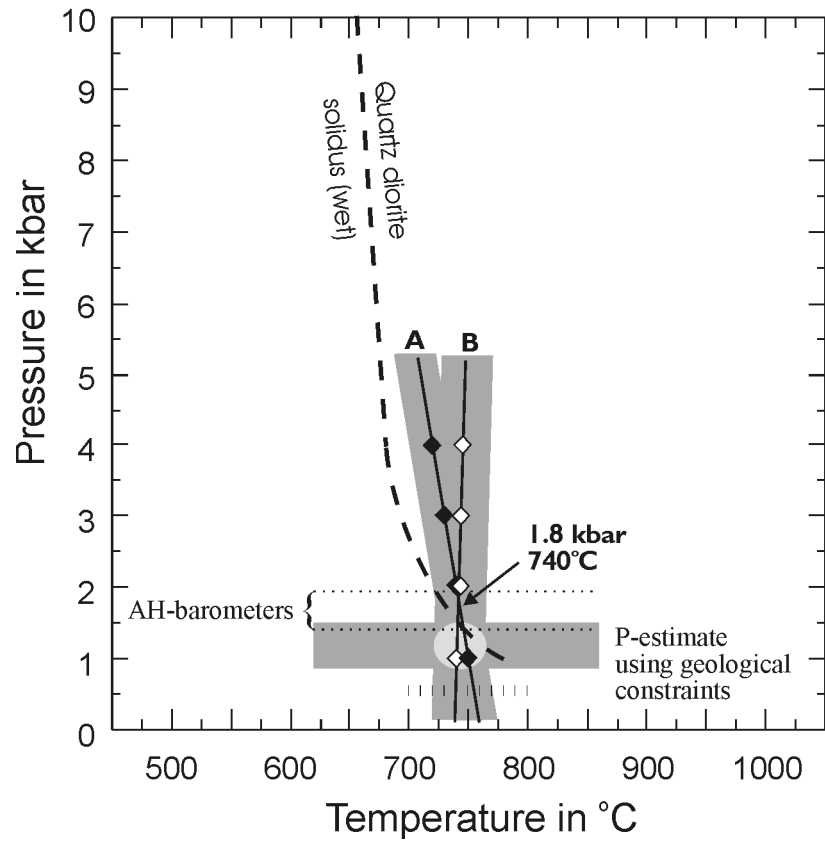


Figure 3.4

P-T diagram showing the range of inferred pressures and temperatures of equilibration of hornblende-plagioclase pairs in two samples from the Half Moon Bar (HMB) diorite. Pressure estimates using geological constraints range between 0.85 and 1.5 kbar. Al^{Tot} -in-hornblende geobarometers indicate maximum pressures of 1.4 - 1.9 kbar. These independent pressure estimates coincide with the point of interception of thermometers A and B. At pressures between 0.85 and 1.5 kbar, the average temperature of equilibration calculated using thermometers A and B is $745 \pm 25^\circ\text{C}$. For reference, the wet quartz-diorite solidus (Piwinski, 1973) is shown. Evidently, the HMB diorite equilibrated at solidus conditions.

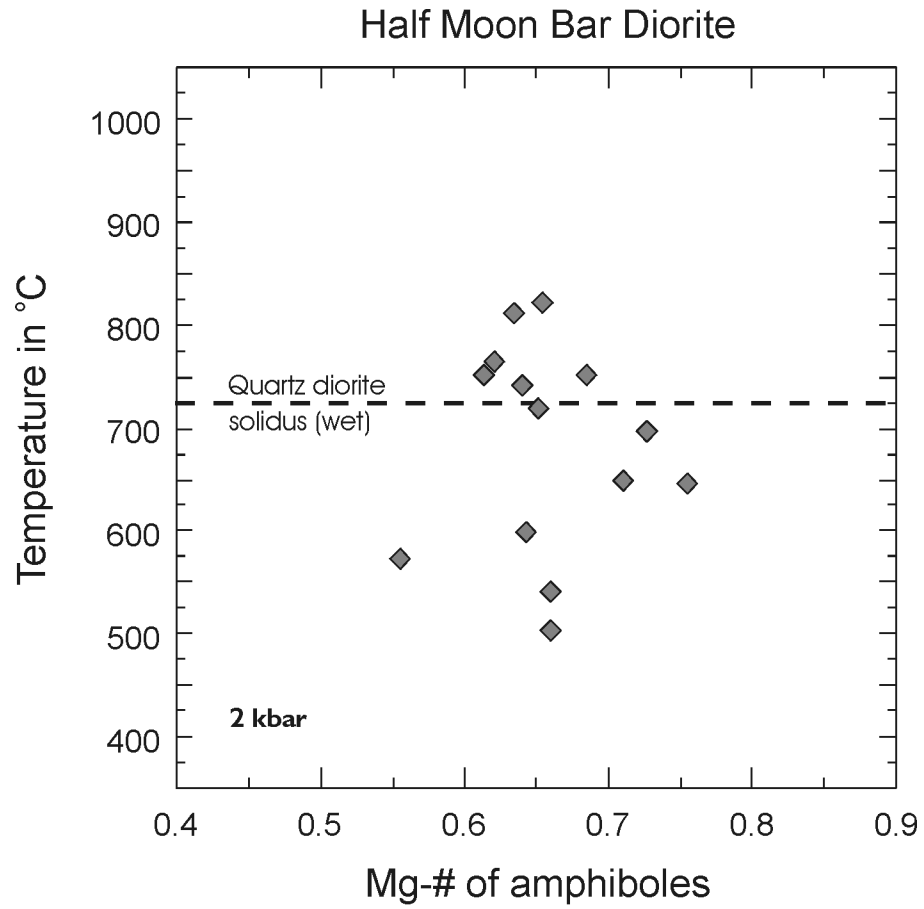


Figure 3.5

Temperature variations versus Mg-# in samples O/C-118a and O/C-376. Temperatures are calculated using thermometer A at 2 kbar (table 3.1). For reference, the wet quartz-diorite solidus at 2 kbar is shown (Piwinski, 1973). Oxidation at near solidus conditions is indicated by the increase in Mg-# with cooling.

poorly understood, it appears that the equations for Al-in hornblende barometers produce meaningful results when the assumptions are satisfied on which the calibration of the barometers are based. The assumptions are: (1) the limited variance of assemblages of minerals, melt and fluid in granitoids near solidus conditions preclude compositional variability other than that attributable to pressure, (2) amphibole freezes in its composition at the solidus, and (3) the solidus is at a relatively uniform temperature. These assumptions are probably met for many granitoids with a simple thermal history which have a frozen-in solidus composition and negligible re-equilibration at low temperatures. They are most likely true for the HMB diorite as indicated by the near-solidus compositions of most of the amphibole (figure 3.4 and 3.5). It appears that the thermometers and barometers equilibrated at similar P-T conditions. As a result, the calculated pressures using the Al^{Tot}-in-hornblende barometers agree reasonably well with the pressure inferred from the geological constraints as well as with the thermometer A and B intercept. Possibly, in cases when the hornblende compositions reflect frozen-in solidus compositions and quartz is present, the intercept of thermometer A and B can be used as a barometric indicator (figure 3.4) as well as the Al^{Tot}-in hornblende.

Field evidence suggests the HMB diorite intruded near the base of a pillowed submarine extrusive sequence which may have been overlain by a thick volcanic pile (Mule Mountain volcanics). Field and petrographic evidence indicate that the HMB diorite was subsequently metamorphosed during retrograde hydrothermal alteration. The hornblende in the HMB diorite ranges from magmatic hornblende to patchy, pale-brown and green amphiboles that are clearly secondary. This assemblage is cut by various veins including ep, ep+qtz, pr, cc, and qtz+su, and cross-cutting relationships suggest retrograde conditions. The results of the geothermometers and geobarometers are entirely consistent with the geological constraints indicating near-solidus equilibration at about 830°C - 650°C and 1-2 kbar. Cooling occurred under oxidizing conditions (figure 3.5) probably related to the release of late-stage, supercritical fluids as the temperature decreased. Subsequently, the near-solidus assemblage re-equilibrated only partially at much lower temperatures during retrograde hydrothermal alteration resulting in assemblages containing among others albite and actinolite (table 3.1). Probably, the heat released during cooling of the pluton was the driving energy of the hydrothermal circulation of sea water, resulting in fast(?) cooling of the intrusion (i.e.

wide-spread re-equilibration of hornblende at lower temperatures did not occur). Consequently, the hornblende $^{40}\text{Ar}/^{39}\text{Ar}$ cooling age of 157.2 ± 2.0 Ma (sample O/C-376) is very close to the crystallization age of the HMB gabbro. Indeed, the hornblende $^{40}\text{Ar}/^{39}\text{Ar}$ cooling age overlaps within error with the U/Pb zircon ages of this unit (159-160 Ma).

Finally, it appears that the thermometers A and B of Holland and Blundy (1994) perform well using the hornblende-plagioclase pairs in samples from the HMB diorite. For example, the calculated temperatures coincide with the solidus of a quartz-diorite of similar composition as the HMB-diorite (figure 3.4), and petrographic evidence supports the presence of magmatic hornblende. It is also hypothesized that the intercept of thermometer A and B can be used as barometric indicator for the HMB diorite, and that, similar to Al^{Tot} -in-hornblende barometers, the thermometer A-B intercept method requires frozen-in solidus compositions.

3.4.2 Hornblende quartz diorite in metagabbro unit

The application of the Al^{Tot} -in-hornblende barometers of Hammarstrom and Zen (1986), Hollister et al. (1987), and Johnson and Rutherford (1988) yield pressures ranging between 1.9 and 2.5 kbar, which are thought to give an upper limit on the pressure of crystallization (section 3.3.2). The Al^{Tot} -in hornblende pressures agree within error with the pressure estimate based on the assumption that the HQ diorite intruded high-level gabbro (3 - 3.5 km below sea floor; Christensen and Salisbury, 1975).

Figure 3.6 shows that the temperature of equilibration of plagioclase-hornblende pairs is $745 \pm 25^\circ\text{C}$ assuming pressures of crystallization range between 1.3 and 2.5 kbar. These P-T conditions indicate that the hornblendes in the HQ diorite have frozen-in solidus compositions. Similar to the HMB diorite, the interception of the bars representing pressure estimates with the bars representing calculated temperatures (thermometers A and B) coincides in the P-T diagram with the point of interception of thermometers A and B (figure 3.6). This second example of coinciding pressures strengthens the hypothesis that the point of interception of thermometers A and B may be used, under certain circumstances, as a barometric indicator; probably when equilibration occurred near-solidus conditions.

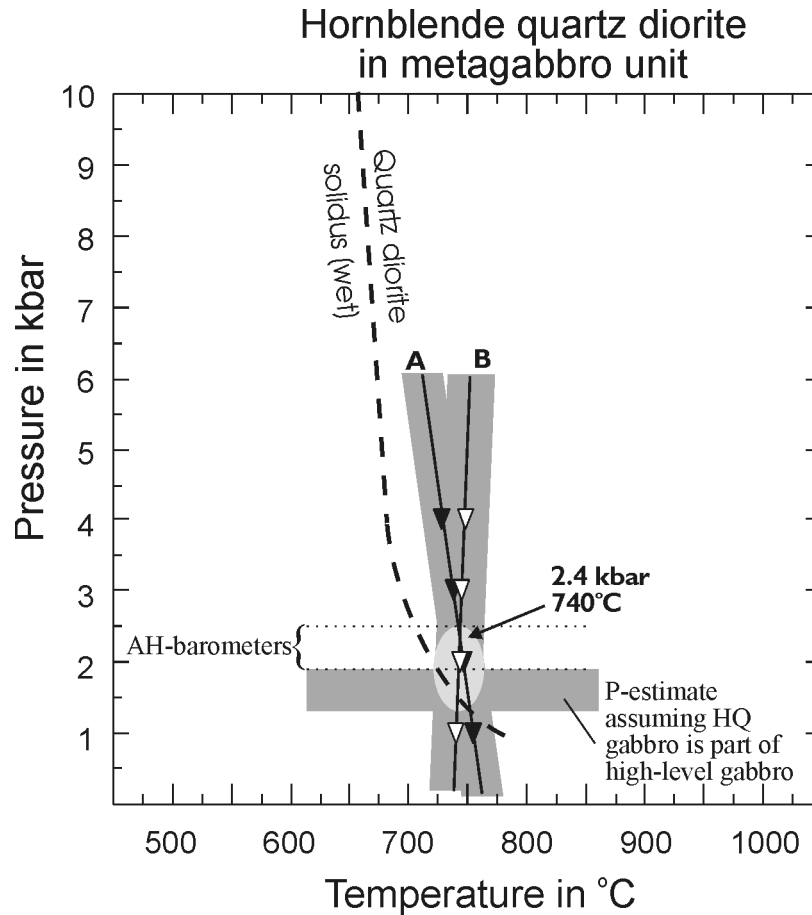


Figure 3.6

P-T diagram showing the range of inferred pressures and temperatures of equilibration of hornblende-plagioclase pairs in a samples from the hornblende quartz (HQ) diorite in the metagabbro unit. Pressure estimates assuming the HQ diorite intruded high-level gabbro range between 1.3 and 1.9 kbar. However, this is highly speculative, because the metagabbro unit is a fault-bounded unit. Al^{Tot} -in-hornblende geobarometers indicate maximum pressures of 1.9 - 2.5 kbar. These independent pressure estimates coincide with the point of interception of thermometers A and B. At pressures between 1.3 and 1.9 kbar, the average temperature of equilibration calculated using thermometers A and B is $745 \pm 25^\circ C$. For reference, the wet quartz-diorite solidus (Piwinskii, 1973) is shown. Evidently, the HMB diorite equilibrated at solidus conditions.

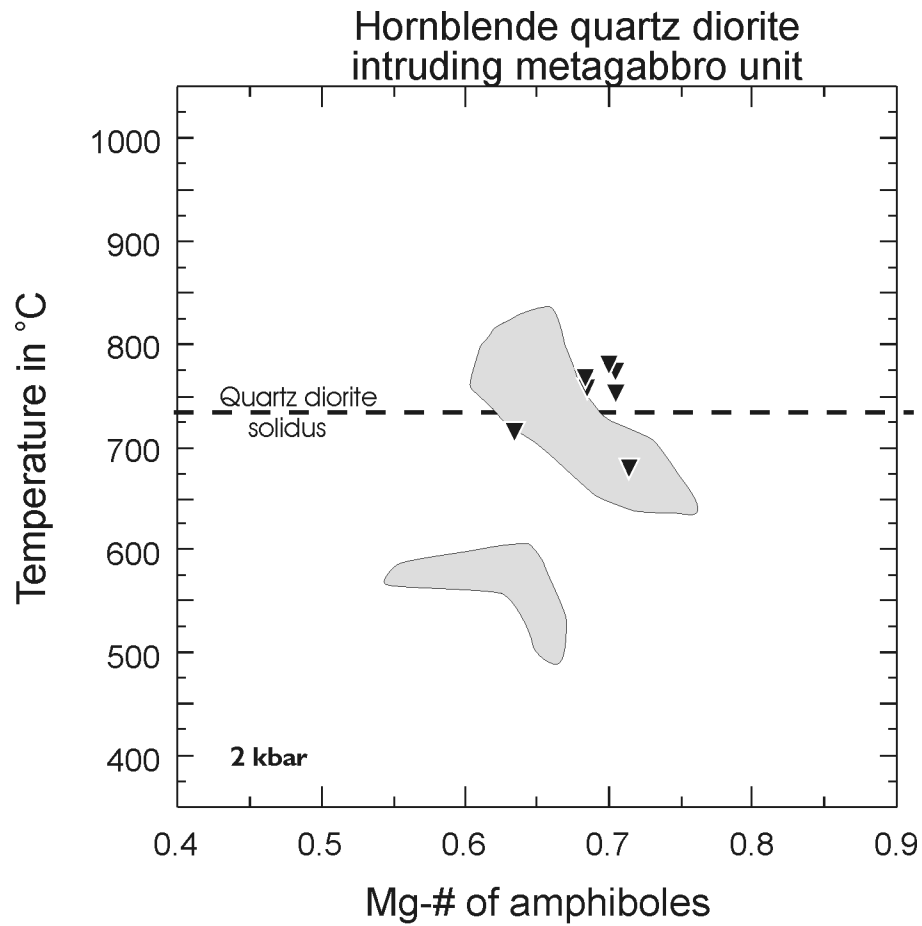


Figure 3.7

Temperature variations versus Mg-# in sample O/C-229. Temperatures are calculated using Thermometer A at 2 kbar (table 3.2). For comparison, the results from figure 3.5 (HMB diorite) are shown as well (shaded fields). The horizontal line indicates the water saturated solidus of quartz diorite at 2 kbar (Piwinski, 1973). Similar to the HMB diorite, the HQ diorite equilibrated at near solidus conditions. The Mg-# of hornblendes in the HQ gabbro increases only slightly over a temperature range of $\sim 100^{\circ}\text{C}$ ($800^{\circ}\text{C} \rightarrow 700^{\circ}\text{C}$) suggesting that oxidation during cooling was not an important process in the HQ diorite.

The results of the temperature calculation (table 3.2) are plotted in a diagram of temperatures versus Mg-# (figure 3.7). The pressure used is 2 kbar based on above constraints. For comparison, fields comprising the results from the HMB diorite are shown. The data points plot around the water saturated solidus of quartz diorite. The solidus of the HQ diorite intruding the metagabbro unit is probably very close to shown experimentally determined solidus (Piwinskii, 1973). Evidently, equilibration occurred at near- to sub-solidus conditions similar to the HMB diorite. However, the data points cluster strongly (with one exception) and do not indicate a pronounced cooling trend. The Mg-# appears to increase only slightly with decreasing temperatures suggesting that oxidization during cooling was not an important process. In thin section, actinolite coexisting with albite is observed in most samples from the HQ-diorite intruding the metagabbro unit but was not analyzed. Therefore, partial re-equilibration at much lower temperatures is likely, but cannot be illustrated in figure 3.7 because of the lack of data.

The temperature and pressure conditions at which the HQ diorite crystallized cannot be uniquely inferred using available geological evidence (section 3.3.1). Therefore, above results of geothermometry and geobarometry may provide important data to better constrain the interpretation of the HQ diorite in the metagabbro unit. In view of the fact that (1) the results of geothermometry and geobarometry agree well with the field and petrographic evidence for the HMB diorite (see section 3.4.1), (2) HMB diorite and HQ diorite are very similar in composition (both are hbl Qtz diorites), and (3) the results for HMB diorite and HQ diorite are very similar (figures 3.4 to 3.7), the calculated pressures and temperatures of equilibration for the HQ diorite represent meaningful results and may be used interpreting both, the HQ diorite and the metagabbro unit. Hornblende and plagioclase in the HQ diorite in the metagabbro unit appear to have equilibrated at around 2 kbar and 750°C.

3.4.3 Metagabbro unit

The pressure estimate for the metagabbro unit using geological constraints follows the same line of evidence as for the HQ diorite intrusion as discussed in section 3.3.1. Therefore, if the metagabbro unit is not an ophiolitic unit, pressure estimates based on geological evidence are not available. Unfortunately, neither the Al^{Tot} -in hornblende barometers can be applied as barometric indicator nor the intersection of

thermometers A and B, because the investigated assemblage is quartz undersaturated (plagioclase + hornblende + magnetite + apatite; whole rock analysis indicates ~48% SiO₂). Consequently, only the temperatures calculated for various pressures using thermometer B (table 3.3) can be illustrated in a P-T diagram (figure 3.8). As the assumed pressure increases from 2 kbar to 8 kbar, the calculated temperature increases only slightly ($635 \pm 38^\circ\text{C} \rightarrow 670 \pm 28^\circ\text{C}$) as indicated by the curve B. For reference, the principal metamorphic facies (Spear, 1990, p.17) as well as the water saturated solidus of gabbro (Holloway and Burnham, 1972) and of quartz diorite (Piwinski, 1977) are shown. Evidently, the average of analyzed hornblende-plagioclase pairs in three quartz-free samples from the metagabbro unit indicate temperatures of equilibration at amphibolite facies conditions. This result is entirely consistent with the uniform dark-green color of the hornblende observed in all samples from the metagabbro unit. Note also that the curve intersects the water saturated solidus of quartz-diorite at about 8 kbar and 670°C. This point of intersection may place an upper limit on the pressures, because the more fractionated phases in the metagabbro unit ranging in composition from quartz gabbro to tonalite do not have a gneissic or re-melted texture. The textural evidence suggests metamorphic conditions remained below the quartz diorite solidus.

The results from petrography and geothermometry strongly point to a metamorphic origin of the hornblende, and the hypothesis that the metagabbro unit represents part of the high-level gabbro of the Rogue Wilderness remnant of the CRO (figure 3.1) is not consistent with such data (see introduction, section 3.1). Because the metagabbro unit is perhaps not part of ophiolite (i.e. high-level gabbro), the only constraints on the pressure of (re)equilibration of hornblende in the metagabbro unit is given by the results from the HQ diorite. The HQ diorite in the metagabbro equilibrated at around 2 kbar based on the Al^{tot}-in-hornblende barometers (1.9 - 2.5 kbar) and the intercept of thermometers A and B (2.4 kbar). Interestingly, the hornblende-plagioclase pairs in the HQ diorite seem to have equilibrated at a higher temperature (near-solidus conditions) than those in the samples from the metagabbro unit. It is possible that the HQ diorite intruded the metagabbro unit toward the end of amphibolite metamorphism, or later. Therefore, the hornblende-plagioclase pairs in the HQ diorite did not re-equilibrate at amphibolite facies conditions.

The results of the temperature calculations (table 3.3) are presented in figure 3.9 on a plot of temperature versus Mg-# of hornblende (molar $\text{Mg}/(\text{Mg}+\text{Fe}^{2+})$), and are compared to the results of previously discussed diorites (shaded fields). The pressure used was 2 kbar, and the bulk of the calculated temperatures lies between 600°C and 675°C. The solidus of the metagabbro lays probably somewhere around the wet solidus of basalt which occurs at around 850°C at 2 kbar pressure (Yoder and Tilley, 1962, Holloway and Burnham, 1972). Thus, the amphiboles appear to have re-equilibrated at temperatures significantly below solidus conditions (figures 3.8 and 3.9) implying that the metagabbro was metamorphosed for a protracted period of time at an average temperature between 600°C and 675°C.

A broken, poorly defined cooling (or heating?) trend is indicated in figure 3.9 by the data from the metagabbro unit. This trend is characterized by a positive correlation of temperatures with Mg-#. The amphibole becomes less magnesian with decreasing temperature, which is opposite to the cooling trend of the HMB diorite (upper light-shaded field). The reason for this trend is not known. The amphiboles in the metagabbro samples indicating the lowest temperatures of equilibration (< 600°C) are tschermakite and tschermakitic hornblende (figure 3.3).

Overall, petrographic evidence suggests the dark-green, uniformly colored hornblende in the metagabbro unit could be metamorphic in origin, and the dark-green color may indicate amphibolite facies conditions (Laird, 1982 p. 115). The results from the application of geothermometer B to the quartz under-saturated metagabbro samples is entirely consistent with the petrographic evidence, and metamorphism at average temperatures between 600°C - 675°C depending on pressure (figure 3.8) are calculated. Inferred upper and lower limits on the pressure are 8 kbar and 2 kbar, respectively. The re-equilibration of hornblende and plagioclase occurred at temperatures significantly below the wet solidus of gabbro suggesting the metamorphic conditions were maintained over a protracted period of time (> 10⁶ Ma). Consequently, the hornblende ⁴⁰Ar/³⁹Ar age of 171.4 ± 3.1 Ma (sample O/C-373b) appears to represent the time of cooling from amphibolite facies metamorphism. The crystallization age of the metagabbro and HQ diorite may be substantially older.

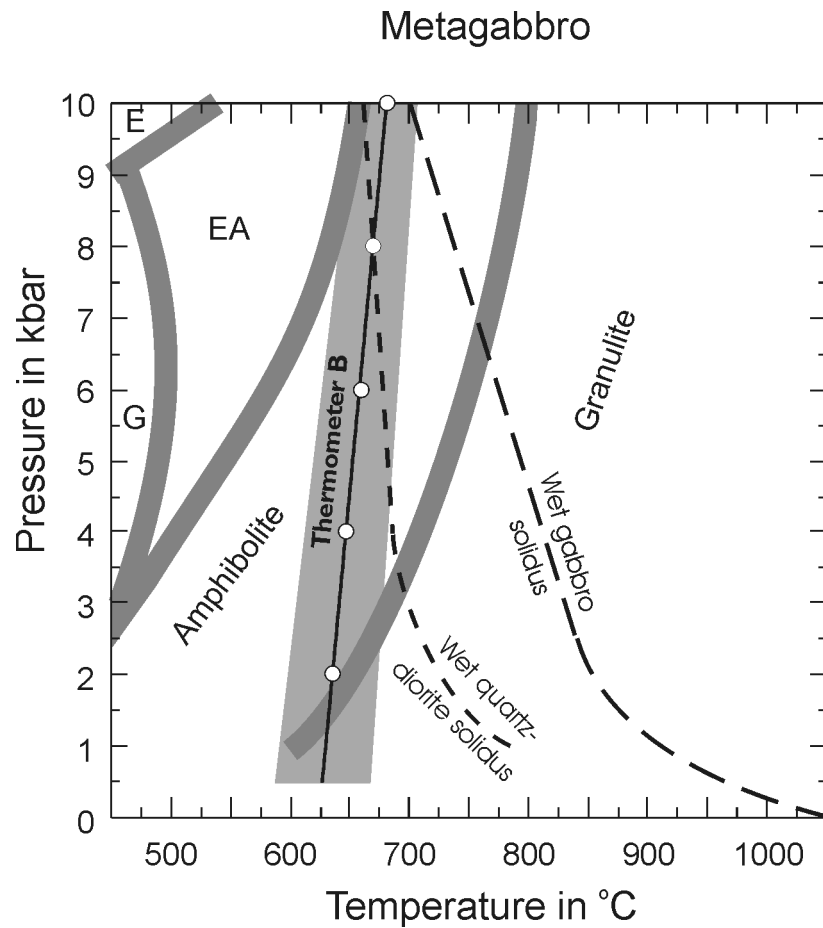


Figure 3.8

P-T diagram showing the principle metamorphic facies (after Spear, 1993; p.17). **E** denotes eclogite facies, **EA** epidote-amphibolite facies, and **G** greenschist facies. For reference, the water saturated solidi of gabbro and quartz diorite are plotted as well. Thermometer B of Holland and Blundy (1994) was used to calculate the temperatures at 2, 4, 6, 8 and 10 kbar (table 3.3). Evidently, the metagabbro (samples MRH-78/1, MRH-78/2 and O/C-373) equilibrated at conditions significantly below the water saturated solidus of gabbro (after Holloway and Burnham, 1972). Metamorphism occurred at amphibolite facies conditions. The intersection of curve B with the solidus of quartz diorite (Piwinskii, 1973) at 8 kbar may be considered as an upper limit on the pressure of metamorphism. Evidence of re-melting of quartz-bearing/ quartz-rich phases in the metagabbro unit was not observed.

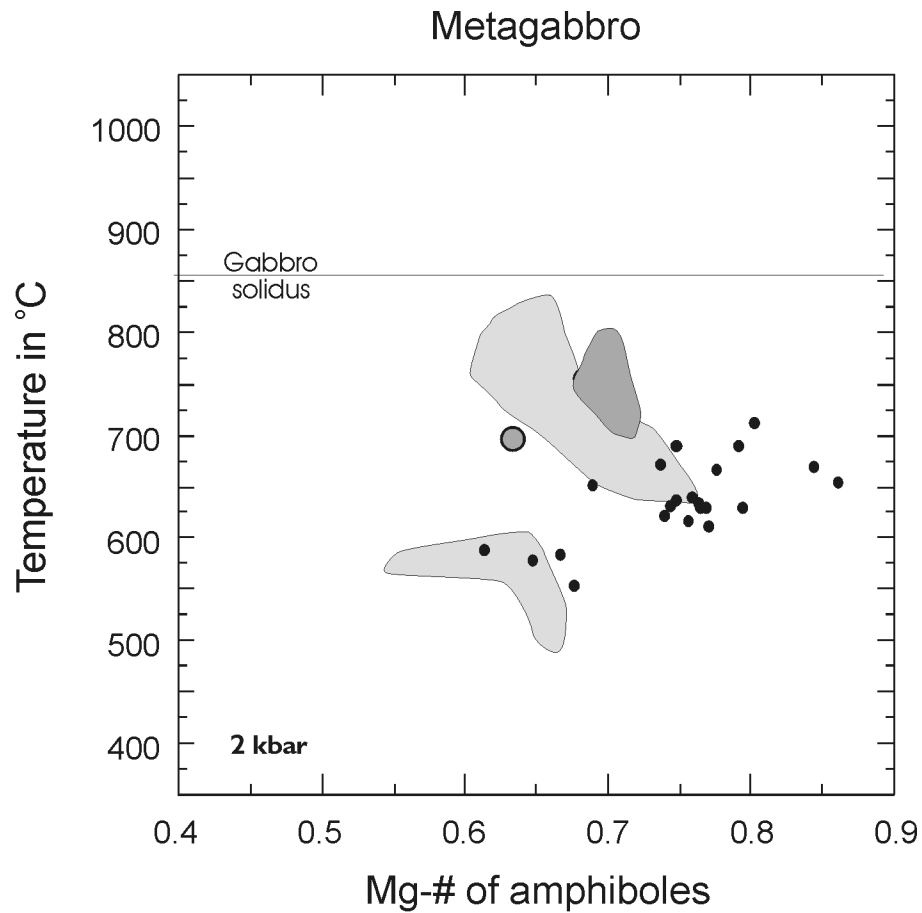


Figure 3.9

Temperature variations versus Mg-# in samples MRH-78/1, MRH-78/2 and O/C-373 from the metagabbro unit. Temperatures are calculated using thermometer B at 2 kbar (table 3.3). For comparison, the results from figures 3.5 and 3.7 are shown as well (HMB diorite: light-shaded fields; HQ diorite: dark-shaded fields). The horizontal line indicates the water saturated solidus of gabbro at 2 kbar (Holloway and Burnham, 1972). Unlike the HMB and HQ diorites, the metagabbro equilibrated significantly below solidus conditions. It is not clear whether or not the positive correlation of Mg-# with temperature represents a cooling or heating trend. Nevertheless, the conditions of equilibration of the metagabbro were much different than for the HMB and HQ gabbro.

3.5 Summary

I have attempted to obtain better constraints on the P-T conditions of equilibration for three different plutonic rocks mapped in the Wild Rogue Wilderness, SW Oregon. The studied samples include O/C-118a and O/C-376 from the HMB diorite (table 3.1), O/C-229 from the HQ diorite in the metagabbro unit (table 3.2), and MRH-78/1, MRH-78/2 and O/C-373 from the metagabbro unit (table 3.3). The results from the temperature estimates using thermometers A and B of Holland and Blundy (1994), accompanied by various pressure estimates, are evaluated and interpreted in the light of available geologic and petrographic evidence. Overall, the empirical results agree well with the geologic and petrographic constraints. Consequently, the results presented below should be taken in consideration interpreting the units from which the samples are taken for this study.

- (1) The HMB diorite equilibrated near the solidus of quartz diorite at about 1 - 2 kbar and 750°C. Probably, cooling occurred relatively fast under oxidizing conditions, and some of the hornblende-plagioclase pairs re-equilibrated at temperatures significantly below the solidus (< 600°C) suggesting that metamorphism followed closely upon crystallization. Thus, the hornblende $^{40}\text{Ar}/^{39}\text{Ar}$ age of 157.2 ± 2 Ma closely represents the crystallization age.
- (2) The HQ diorite intruding the metagabbro unit equilibrated also near the solidus of quartz diorite at about 1.5 - 2.5 kbar and 750°C. Possibly, the conditions and history of intrusion and cooling of the HQ gabbro are very similar to the HMB gabbro. However, more microprobe data is needed to empirically constrain this hypothesis.
- (3) Equilibration of the metagabbro unit occurred at amphibolite facies conditions. Inferred upper and lower limits for the pressure are 8 kbar and 1.5 kbar, respectively, and the calculated average temperatures using thermometer B range between $635 \pm 38^\circ\text{C}$ (determined at 2 kbar) and $670 \pm 28^\circ\text{C}$ (determined at 8 kbar). These results appear to be inconsistent with the interpretation of the metagabbro unit is part of the high-level gabbro of the Rogue Wilderness ophiolite (figure 3.1), and the hornblende $^{40}\text{Ar}/^{39}\text{Ar}$ age of 171.4 ± 3.1 Ma could represent the time of the end of regional metamorphism or plutonism.

(4) Also, it was noted that the intercept of thermometers A and B coincided with the pressures estimated from geological evidence as well as Al-in-hornblende barometers. It is hypothesized that the intercept of thermometers A and B may be used as a barometric indicator when hornblende-plagioclase pairs equilibrated near solidus conditions and largely retained near-solidus compositions throughout subsequent thermal history (e.g., retrograde seafloor hydrothermal alteration).

Table 3.4: Chemical analyses and proportional formula for run products (Poli, 1993) and results of temperature calculations using the geothermometers of Blundy and Holland (1994)

Microprobe analyses of run products (Poli, 1993)

| Run-# | R8a | R5a | R11c |
|----------------------------------|--------|-------|--------|
| SiO ₂ | 44.63 | 46.44 | 47.17 |
| TiO ₂ | 0.07 | 0.04 | 0.04 |
| Al ₂ O ₃ | 13.57 | 10.68 | 12.96 |
| FeO | 13.36 | 12.21 | 11.1 |
| Fe ₂ O ₃ * | 3.71 | 3.39 | 3.08 |
| MnO | 0.07 | 0.64 | 0.02 |
| MgO | 9.54 | 10.76 | 11.33 |
| CaO | 11.1 | 10.64 | 10.43 |
| Na ₂ O | 2.24 | 1.86 | 2.56 |
| K ₂ O | 0.07 | 0.15 | 0.04 |
| H ₂ O* | 2.05 | 2.03 | 2.1 |
| Total | 100.41 | 98.84 | 100.83 |

Recalculation of microprobe analysis of amphiboles following method of Holland and Blundy (1994) with site-allocation following Robinson et al. (1982)

| | | | |
|------------------|-------|-------|-------|
| Si | 6.534 | 6.846 | 6.746 |
| Al | 1.466 | 1.154 | 1.254 |
| | 8 | 8 | 8 |
| Al | 0.873 | 0.701 | 0.928 |
| Ti | 0.008 | 0.004 | 0.004 |
| Fe ³⁺ | 0.408 | 0.458 | 0.380 |
| Mg | 2.082 | 2.364 | 2.416 |
| Fe ²⁺ | 1.629 | 1.424 | 1.272 |
| Mn | 0 | 0.049 | 0 |
| Ca | 0 | 0 | 0 |
| | 5 | 5 | 5 |
| Fe ²⁺ | 0.008 | 0 | 0.007 |
| Mn | 0.009 | 0.031 | 0.002 |
| Ca | 1.741 | 1.680 | 1.598 |
| Na | 0.242 | 0.289 | 0.394 |
| | 2 | 2 | 2 |
| Na | 0.394 | 0.243 | 0.315 |
| K | 0.013 | 0.028 | 0.007 |
| | 0.407 | 0.270 | 0.322 |

Compositions of coexisting plagioclase

| | | | |
|-----------------|------|-----|-----|
| X_{ab}^{plag} | 0.75 | 0.8 | 0.8 |
| X_{an}^{plag} | 0.25 | 0.2 | 0.2 |

* Poli (1993) recalculated H₂O and Fe₂O₃ wt. percent on the basis of 2OH and Fe³⁺/Fe(total) = 0.2 in the formula, respectively

P-T conditions of experimental runs (Poli, 1993)

| Run-# | R8a | R5a | R11c |
|----------|-----|-----|------|
| P (kbar) | 8 | 10 | 12 |
| T (°C) | 650 | 640 | 650 |

Results applying geothermometers (A) and (B)

1. Temperatures calculated by Holland and Blundy (1994; p.442)

| | | | |
|------------|-----|-----|-----|
| (A) T (°C) | 629 | 618 | 626 |
| (B) T (°C) | 633 | 629 | 631 |

2. Temperatures calculated using the Microsoft Excel macro programmed for this study with the equations given in the text

| | | | |
|------------|-----|-----|-----|
| (A) T (°C) | 629 | 618 | 629 |
| (B) T (°C) | 633 | 629 | 641 |

CHAPTER FOUR

STRUCTURAL AND METAMORPHIC HISTORY OF THE WILD ROGUE WILDERNESS REMNANT OF THE COAST RANGE OPHIOLITE

4.1 Introduction

The principal map units and main structures are depicted in figures 4.1a and 4.1b showing a simplified geologic map of SW Oregon, inserted stereographic projections, and an interpretative cross section, respectively. The cross section line AA' intersects approximately the apex of the bend in the Tertiary Eden Ridge syncline. The structural data obtained during mapping of units east and west of the Rogue Wilderness ophiolite as well as the structural data compiled from published maps are divided into two sets, north (N) and south (S) of the cross section line AA'. Sources of the compiled data include Niem and Niem (1990), Gray et al. (1982), Ramp and Moring (1986), Ramp et al. (1977), Coleman (1972), Rud (1971). The structural framework of the study area and relevant terranes are discussed in section 4.2.

The Snow Camp terrane, SW Oregon, consists basically of ophiolitic basement rocks overlain by sediments of the Myrtle Group (figure 4.1a and 4.1b). The ophiolitic basement of the Snow Camp Mountain terrane is disrupted in a style similar to most Coast Range ophiolite (CRO) remnants in California, where the ophiolitic units are separated by faults, ophiolitic units occur out of sequence, and sections of the ophiolite stratigraphy are not exposed or preserved. In the Wild Rogue Wilderness, the basement units strike north 30°-40° east, are subvertical and fault bounded. The units from east to west are (1) sheeted dike complex, (2) metatonalite, (3) metagabbro, (4) Blossom Bar shear zone, (5) pillowed submarine flows, (6) Mule Mountain volcanics. Ultramafic rocks are not exposed, except for small slivers of serpentinite. However, the magnetic modeling experiments of Blakely and Senior (1983), which are based on an aeromagnetic survey of the Earth's total field in the vicinity of the Wild Rogue Wilderness (flown in 1978 at an elevation of 4000 ft), indicate that the weakly magnetic rocks exposed on the surface are not the source for the major anomalies and steep gradients observed in the Wild Rogue Wilderness.

Blakely and Senior (1983) suggested that a thin, but widespread tectonic slice of mafic or ultramafic rocks, which may be less than 500 m below the topographic surface, is the source. The result of the magnetic modeling experiments of Blakely and Senior (1983) may be used to constrain the cross section (figure 4.1b).

The overlying sedimentary rocks of the Myrtle Group in the study area consist mainly of gray siltstones, sandstones and conglomerates, strike north 030° - 040° east and dip steeply southeast or northwest. They were previously correlated with the Great Valley sequence in California and are interpreted to have been deposited in a fore-arc basin (Imlay et al., 1959; Blake et al, 1985a). The upper Jurassic to lower Cretaceous Myrtle Group comprises the Riddle and Days Creek Formation (figure 4.1b) both of which are exposed west of the Rogue Wilderness remnant of the CRO. The following suggest that Rogue Wilderness remnant of the CRO may occur on the east-limb of a large Cretaceous syncline: (1) The sedimentary rocks of the upper Jurassic to lower Cretaceous Riddle Formation have attitudes similar to the strike and dip of the basement units and are subvertical near the contact with the Rogue Wilderness ophiolite (Myrtle Group (N) in figure 4.1). (2) About 2 km west from the basal conglomerate, the Riddle Formation is conformably overlain by the lower Cretaceous Days Creek Formation (Rud, 1972). Here, the beds dip moderately northwest. At outcrop-scale, the beds are openly to tightly folded, and the hinges of outcrop-scale folds plunge gently northeast or southwest (Myrtle Group (N) in figure 4.1). The poles to bedding define a crude girdle whose pole ($047^{\circ}/03^{\circ}$) indicates the approximate orientation of the syncline. The pole to the girdle and the subparallel hinge lines measured in outcrop-scale folds define an axis (R_c) which provides a rotation axis to unfold Cretaceous strata and possibly restore the ophiolitic basement to paleohorizontal.

However, the hypothesis that the Rogue Wilderness ophiolite occurs on the east-limb of a large Cretaceous syncline is not uniquely constrained, and the construction of a cross section, such as that in figure 4.1b, is speculative. The interpretation of the geology and structure of the Snow Camp terrane south of the southernmost exposures of Tertiary strata may be used to place constraints on the construction of a cross section along line AA'. Unfortunately, the minimum distance to project the structure of the

Figure 4.1

A. Simplified geologic map of SW Oregon. The geologic map of Tertiary strata in Oregon is modified from Chan and Dott (1983) and Niem and Niem (1990), and the geologic map of pre-Tertiary rocks is modified from Walker and MacLeod (1991). The structural data are from the following sources:

Myrtle Group (S); Coleman (1972), Ramp et al. (1977)

Myrtle Group (N); Rud (1971), Ramp et al. (1977), Gray et al. (1982), this study

Eocene strata (S); Ramp et al. (1977), Gray et al. (1982), Ramp and Moring (1986),

Niem and Niem (1990), this study

Eocene strata (N); Rud (1971), Ramp et al. (1977), Gray et al. (1982), Niem and Niem (1990),
this study

B. Interpretative cross section along line AA' (figure 4.1a). The Snow Camp terrane, consisting of an ophiolitic basement and late Jurassic to early Cretaceous fore-arc sediments (Myrtle Group), is interpreted as the remnant of a folded thrust sheet that is thrust over the terranes of the Franciscan complex (Yolla Bolly terrane and Sixes River terrane) (Blake et al., 1985a). This remnant appears to be preserved in a graben and is largely covered by Tertiary strata with great unconformity. The angular unconformities between the Tertiary formations and increase of intensity of folding with age indicate that Tertiary strata was deposited in a growing syncline. The cross section of the southern Tyee basin (i.e., tertiary strata) from Hanging Rock to the Coquille River Fault is based on the report of Niem and Niem (1990). The following data are incorporated in the construction of the cross section: (1) the steeply dipping normal fault at the eastern boundary of the Rogue Wilderness ophiolite displaced Tertiary strata (Ramp and Moring, 1986; this study); (2) an area of high magnetic susceptibility (ultramafic rocks or serpentinite) occurs ~ 500 m below the topographic surface (Blakely and Senior, 1983); (3) the ophiolitic units are subvertical and fault bounded (Gray et al., 1982; this study); (4) the beds of the Myrtle Group are subvertical near the contact with the Rogue Wilderness ophiolite, and are intensely folded (this study), and the dip of the beds decreases westwards towards younger strata (Rud, 1971); (5) the structure of the ophiolitic basement may be characterized by a succession of imbricate thrust sheets (Roure and Blanchet, 1983; Harper, unpublished field mapping, 1999).

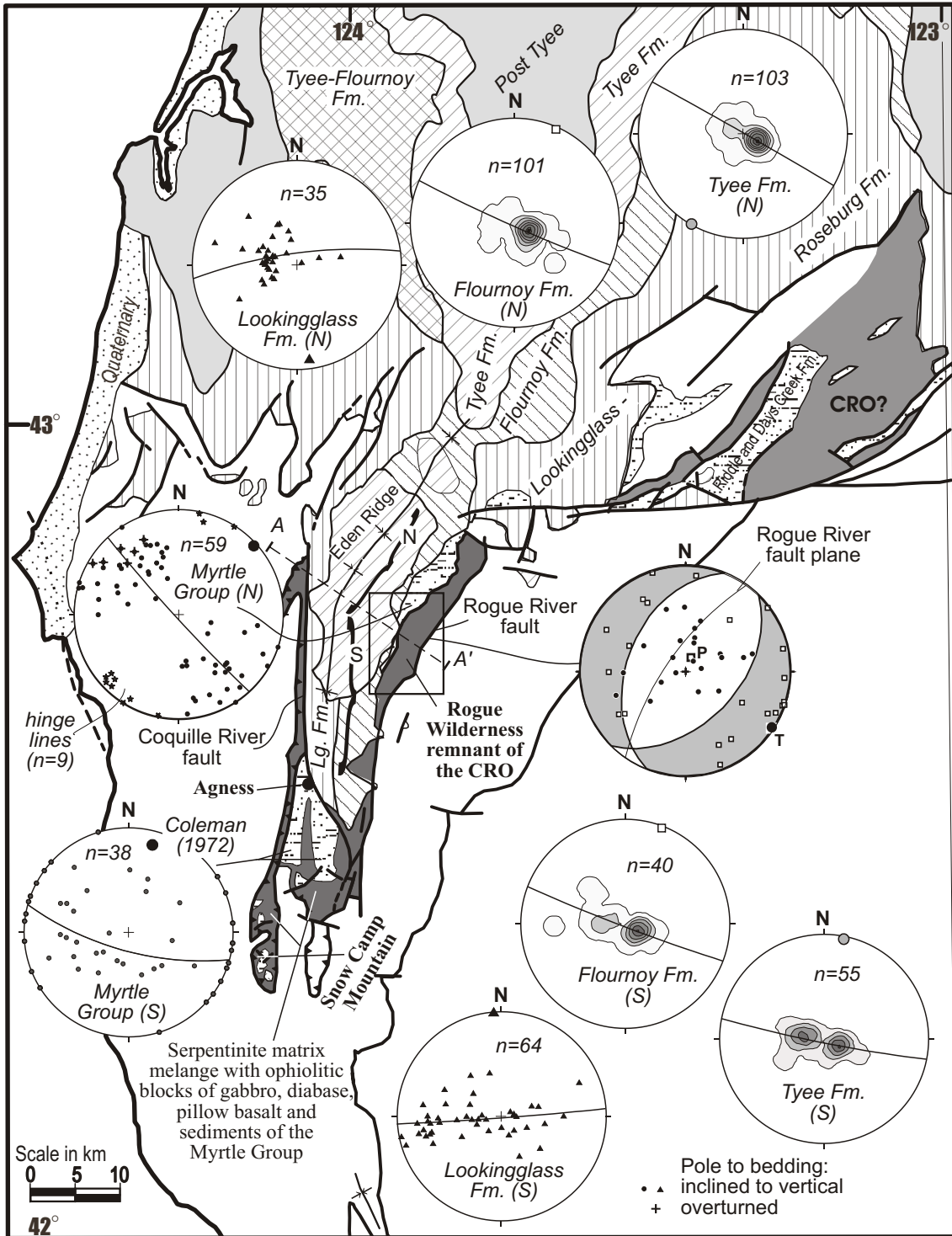


Figure 4.1a

Simplified geologic map of SW Oregon showing the area of the field map (box) and lower hemisphere stereographic projections of structural data from sedimentary units up to 50 km north (N) and south (S) of the cross section line AA'. See figure 4.1b for legend.

southernmost Snow Camp terrane into the plane of the cross section AA' is 30 km, and the projection must be made across the southern part of the Coquille River fault.

Coleman (1972) mapped the area adjacent to the Colebrook schist and provided data of the attitude of sedimentary rocks of the Myrtle Group south of the southernmost extent of the Tyee basin near Agness, Oregon. The poles to bedding are plotted in a stereographic projection in figure 4.1a (Myrtle group (S)). Coleman (1972) suggested that the sedimentary rocks of the Myrtle group occur in two synclines. However, the poles to bedding scatter and poorly define a girdle whose pole indicates a gently NNE plunging fold axis ($015^{\circ}/14^{\circ}$). The trend of the fold axis is distinct in orientation compared to that of the northern outcrops of the Myrtle Group ($047^{\circ}/03^{\circ}$). This might be the result of a clockwise rotation of about 30° around a subvertical axis. The bending of the fold axis probably postdates Cretaceous-folding (Frei et al., 1982).

Roure and Blanchet (1983) interpreted the Snow Camp terrane near Snow Camp Mountain (about 50 km south from the Rogue Wilderness remnant of the CRO and 20 km south from the southernmost extent of the Tyee basin) as a folded thrust sheet that has been thrust over the terranes of the Franciscan complex (Colebrook schist and Yolla Bolly terrane). They suggest, similar to Blake et al. (1982), that the ophiolitic rocks and overlying Myrtle Group represent klippen thrust westward from the Klamath Mountains. According to the interpretation of Roure and Blanchet (1983), the ophiolitic basement of the Snow Camp terrane occurs in a succession of imbricated thrust slices, while the (depositionally?) overlying sedimentary rocks of the Myrtle Group occur in synclines bounded by normal faults (Roure and Blanchet, 1983).

Harper (unpublished field mapping, 1999) reported that the area near Agness is an imbricated zone of serpentinite and sedimentary rocks of the Myrtle group. In this area, steeply dipping slices of serpentinite alternate with sedimentary rocks of the Myrtle group, the strike and dip of beds change rapidly, and medium scale folds (~ 100 m) occur. These preliminary data indicate that the internal structure of the Snow Camp terrane is more complex than suggested by Coleman (1972) and Roure and Blanchet (1983). The area needs to be remapped in order to present a meaningful interpretation of the structure of the Snow Camp terrane and its contact relationship with the terranes of the Franciscan complex. Such an

investigation should prove very fruitful as there are many more logging roads now than when Coleman (1972) and Roure and Blanchet (1983) mapped.

Since the interpretation of the structure of the Snow Camp terrane 30-50 km south of the Rogue Wilderness remnant of the CRO was incorporated in the construction of the cross section in figure 4.1b, the question has to be addressed whether or not the ophiolite remnant is similar to the ophiolitic basement exposed along strike 30-50 km further south. The ophiolitic basement 30-50 km south of the Rogue Wilderness ophiolite consists of a serpentinite matrix melange containing blocks of hypabyssal intrusive and extrusive rocks. Harper (unpublished field mapping, 1997, 1998) reported that an essentially intact, ~ 6 km² block of peridotite, gabbro, sheeted dikes, and locally pillow lavas occurs at Snow Camp mountain. In contrast, only tiny slivers of sheared serpentinite occur in the Wild Rogue Wilderness area (chapter 2), and the Rogue Wilderness remnant of the CRO consists mainly of hypabyssal intrusive and extrusive rocks. However, the geomagnetic modeling experiments of Blakely and Senior (1983) indicate that a thin, but widespread slice of mafic or ultramafic rocks (serpentinite) occur as close as 500 m below the topographic surface of the Wild Rogue Wilderness, suggesting a similar rock assemblage as in the Snow Camp area 50 km further south.

The Rogue Wilderness remnant of the CRO and overlying sedimentary rocks of the Myrtle Group are interpreted to represent the remnants of a folded thrust sheet (e.g., Blake et al., 1982; Blake, 1985a, Roure and Blanchet, 1983; Coleman and Lanphere, 1991) that was transported over the late Jurassic to early Cretaceous rocks of the Yolla Bolly, Picket Peak and Sixes River terranes (of the Franciscan complex). In principle, this interpretation is consistent with the traditional model of Ingersoll (1979) and Dickinson and Seely (1979) that is based on studies in northern and central California. They suggest that the east flank of the Franciscan complex was thrust beneath the Coast Range ophiolite and regard the Franciscan rocks as part of the subduction complex accreted near the trench that was paired with the Sierran-Klamath arc. According to this model, the west flank of the Coast Range ophiolite is bound by the Coast Range 'thrust', and the east flank is overlain by the Great Valley sequence. This interpretation is depicted in figure 4.1b, where a thrust fault (the Coast Range 'thrust') is shown at depth. However, a more complex structural evolution of the Snow Camp terrane is possible, and, in analogy to studies in the

California Coast Ranges, may involve any one of the following processes resulting in the disruption of the ophiolite: tectonic wedging (Phipps and Unruh, 1992; Unruh et al., 1991; Wentworth et al., 1984), thin-skinned imbrication (Suppe, 1979; Ring and Brandon, 1994), translation and dispersal along strike-slip faults (McLaughlin et al., 1988), or attenuation by extensional faulting (Jayko et al., 1987; Harms et al., 1992).

4.2 Paleostress analysis

Paleostress techniques have been used and developed over the last two decades to define regional stress tensors using fault slip data. Particularly, the programs developed by Reches (1987), Angelier (1979), Lisle (1988), and Marrett and Allmendinger (1990) have been used in many field studies and, thus, are often cited in the literature. Four paleostress programs are used in this field study to analyze fault slip data and determine the directions of the principal stress axes. In this section, the programs are briefly described and basic assumptions discussed.

The paleostress programs require the input of the attitude of the fault as well as the direction and sense of slip for a minimum number of faults. Then, the orientation of a single stress field is returned which provides the best fit to the fault slip data. Although the different paleostress programs are based on different methods to solve the inverse problem, they rely on the same basic assumptions (Schimmrich, 1991). These assumptions are: (1) Slip occurs in the direction of maximum resolved shear stress; (2) all faults formed in one “generation”, which means, slip on all faults in the data set occurs under a single, static stress field; (3) faults move independently and there is no interaction between faults; alternatively, faults must have “infinitesimal” offsets; and (4) faults are planar. Specific assumptions for certain methods, if there are any, are pointed out in the description of the paleostress programs below.

The program ROMSA (Lisle, 1988) is based on the graphical method of Angelier and Mechler (1977), and thus, does not rely on additional assumptions. The program ROMSA returns the compound likelihood P_{total} of a user-provided direction X being the direction of the maximum principal stress. In addition to P_{total} , ROMSA gives the best estimate for the direction of the minimum principal stress. To present the results, the compound likelihood P_{total} for a sufficient number of X are plotted in a

stereographic projection and contoured (e.g. figure 4.4c). The direction X which has the highest compound likelihood (P_{\max}) is interpreted as the most likely orientation of the maximum principal stress. The best estimate for the direction of the minimum principal stress returned by ROMSA usually is within the area of the lowest compound likelihood (e.g. figure 4.4c). This method not only gives a best-fit result but also visually indicates how good the stress tensor satisfies the fault data. Large areas of low values of P_{\max} (e.g., 50 - 60%) implies that the solution is not compatible with a significant portion of the fault data suggesting that any one (or all) of the basic assumptions are not satisfied (e.g. figure 4.12c). Small areas of high values of P_{\max} (e.g. 80-100%) implies that the fault data can be adequately represented by a single static stress fields (e.g. figure 4.10c).

FAULTKIN (Marrett and Allmendinger, 1990) is a program that returns, similar to ROMSA, results based on a graphical solution. FAULTKIN determines the compressional (P) and extensional (T) axes for each fault, which can be displayed in a convenient way similar to the “fault plane solutions” presented by earthquake seismologists (e.g. figure 4.1a). The P and T axes are parallel to the m-plane and form 45° angles with the fault plane (figure 4.3). Then, the P-axis (or alternatively the T-axis) can be contoured. The maximum contour per 1% area is interpreted to represent the common P-axis (or T-axis) of all faults. Alternatively, FAULTKIN can also return the linked Bingham Distribution for the P and T axes, which is exactly equivalent to an unweighted moment tensor summation (a moment tensor sum in which all faults are assumed to be weighted equally) in order to obtain the common P and T axes of all faults. Essentially the same assumption is made graphically, when contouring P and T axes. In this study, the common P and T axis returned by FAULTKIN are calculated using the linked Bingham Distribution. Note that the common P and T axes for the fault slip data are not the maximum and minimum principal stresses. As mentioned above, the P and T axes form 45° angles with the fault plane and could occur at low angles ($\sim 15^\circ$) with the maximum and minimum principal stresses.

TENSOR (based on the method developed by Angelier, 1979 and Angelier et al., 1981) and STRESS (based on the method developed by Reches, 1987) determine the orientations of the principal stress axes by minimizing the angular deviations between the observed slip direction along a fault and the direction of the maximum resolved shear stress determined from the stress tensor. However, STRESS,

also relies on the assumption that the magnitudes of the shear (τ) and normal stresses (σ_n) on the fault satisfy the Colomby yield criterion [$\tau = C + \mu \cdot (\sigma_n - P_{H_2O})$]. Thus, assumptions about the coefficient of friction (Byerlee suggests $\mu = 0.85$), the cohesion (Byerlee suggests $C = 0$ for upper crustal rocks) and the fluid pressure P_{H_2O} have to be made. In this study, the following values were assumed: $\mu = 0.85$, $C = 0$, and $P_{H_2O} = 0.1$. The fluid pressure P_{H_2O} affects only the normal stress and not the tensor configuration. Tests showed that the orientations of the principal stress axes returned by STRESS did not change significantly on varying cohesion (C), but the orientations of the principal stress axes returned by STRESS varied substantially using different coefficients of friction (μ).

Schimmrich (1991) tested the stress inversion programs TENSOR, STRESS, and ROMSA and found that they return consistent results if the basic assumptions listed above are satisfied and the fault data set contain faults of variable orientation. Thus, if the programs return contradicting results, or ROMSA returns low values for the maximum compound likelihood, one can infer that the basic assumptions listed above are probably not satisfied, and the determined orientations of the principal stress axis must be discarded or interpreted accordingly.

4.3 Post-ophiolite sedimentary rocks and structures

4.3.1 Eocene cover

The Rogue Wilderness ophiolite and the sedimentary rocks of the Myrtle Group are overlain with great angular unconformity by early Eocene strata for which the stratigraphic nomenclature in the Tyee Basin (after Baldwin, 1974) is adopted (figure 4.2). Baldwin (1974) divided the Eocene strata in the Tyee basin, Oregon, into three formations separated by regional unconformities (figure 4.2). The Eocene sedimentary rocks within the Eden Ridge syncline include, from oldest to youngest, Lookingglass, Flournoy and Tyee formations (figures 4.1a and 4.1b). These data are consistent with the interpretation of Baldwin (1974) that unconformities separate the Lookingglass, Flournoy and Tyee formations (figure 4.1a and 4.1b). Clearly, folding and faulting in the Eden Ridge syncline occurred during sedimentation in Early to Middle Eocene time for which evidence is summarized below (figures 4.1a and 4.1b): West of the

Rogue Wilderness ophiolite, the sedimentary rocks of the Lookingglass formation occur in a shallow syncline (e.g. Niem and Niem, 1990) with gently east- and west-dipping limbs ($\sim 20^\circ$ - 25°). Unlike the Tyee and Flourney formations, the Lookingglass formation is affected by intense faulting and smaller scale folding ($\lambda \leq 150$ m) resulting in moderately dipping beds (figure 4.1a, Lookingglass formation (N)+(S)). An exception is near the Coquille River fault where beds dip steeply to the east probably due to drag folding. In the southernmost extension of the Tyee basin, the Flourney formation and Lookingglass formation are separated by a fault or fault zone (figure 4.1a and 4.1b) (Chan and Dott, 1983; Niem and Niem, 1990). As a result, the sedimentary rocks of the Lookingglass formation are exposed only on the west-limb of the Eden-Ridge syncline, whereas the younger rocks of the Flourney formation are found on the east-limb (Chan and Dott, 1983, Niem and Niem. 1990). Exceptions are small structural windows exposing the angular unconformity between the Flourney and Lookingglass formations on the east-limb (e.g. Gray et al, 1982).

The Tyee formation underlying Eden ridge overlaps the fault or fault zone which separates the Lookingglass formation from the Flourney formation in the southernmost extension of the Tyee basin (Chan and Dott, 1983), suggesting an unconformity could separate the Tyee and Flourney formations. The maxima of the contoured poles to bedding of Tyee and Flourney Formations can be separated (figure 4.1a), which is consistent with the occurrence of an angular unconformity between the Tyee and Flourney formations. Most beds (located on the east limb of the syncline) in the Tyee Formation strike north 024° - 030° east and dip 13° - 15° northwest as indicated by the contoured maximum of 38% (figure 4.1a, Tyee (S)) while most beds (also located on the east limb of the syncline) in the Flourney formation strike north 027° - 033° east and dip 10° - 12° northwest as indicated by the contoured maximum of 48% (figure 4.1a, Flourney (S)). Furthermore, the outcrop patterns in the southernmost extension of the Tyee Basin show clearly that the contact is an angular unconformity (e.g., Gray et al, 1982).

North of the line AA', however, the maxima of the contoured poles to bedding of the Tyee and Flourney formations are indistinguishable: the contoured maximum of 66% indicates that most beds in the Tyee Formation north of line AA' strike north 026° - 029° east (Tyee (N)) and dip 12° - 14° northwest, and

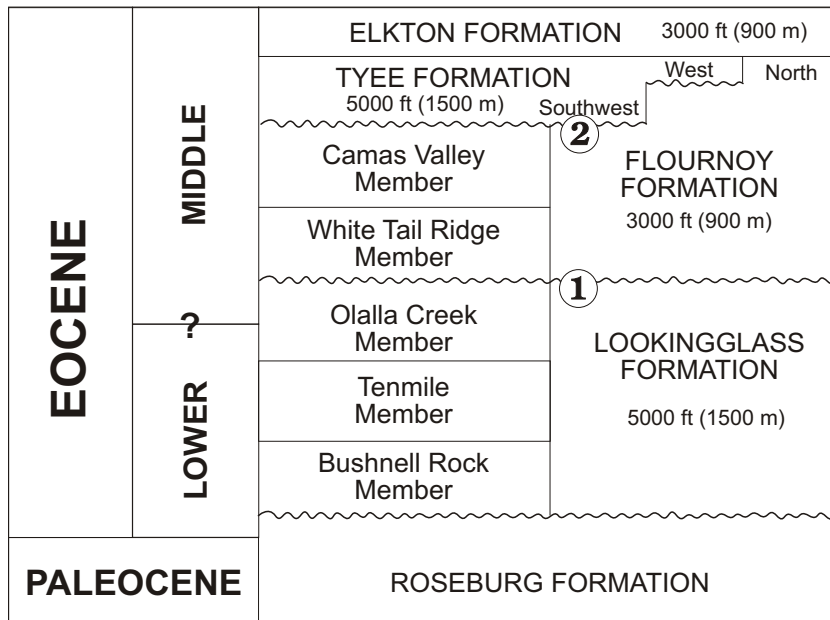


Figure 4.2

Stratigraphic nomenclature in the Tyee Basin after Baldwin (1974). An angular unconformity separates the Lookingglass and Flournoy formations in the Eden Ridge syncline (1). In the southernmost extension of the Tyee basin, the Flournoy and Tyee formations are separated by an angular unconformity (2), which appears to change to a disconformity north of line AA' (figure 4.1a).

the Flournoy (N) maximum of 63% indicates that most beds in the Flournoy Formation north of line AA' strike north 024°-034° and dip 11.5°-13.5° northwest, suggesting that the Flournoy and Tyee formations are separated by a disconformity north of line AA'. Obviously, the angular unconformity with 1°-2° difference in attitude above and below disappears further north and is only clearly mappable south of line AA'. For example, Molenaar (1985) questions the regional unconformity between the Tyee and Flournoy formations. Overall, the poles to the girdles plotted for the Tyee Formation indicate a subhorizontal axis of the Eden-Ridge syncline. However, the trend of the axis changes about 20° clockwise from south to north (Tyee (S), 011° / 03° → Tyee (N), 210° / 01°), which may reflect original bending of the hinge line.

The axis of the Eden Ridge syncline may be used as the rotation axis R_T to unfold Tertiary sedimentary rocks as well as restore the sedimentary rocks of the Myrtle Group and the ophiolitic basement to their orientation prior to Tertiary folding. The Eden ridge syncline west of the study area is subhorizontal and has an azimuth of 30°.

4.3.2 Post-Mid-Eocene faults

The rocks of the Snow Camp terrane appear to occur in a Tertiary graben which is bounded by the Coquille River fault to the west and a previously unnamed, eastern fault, which will be referred to as the "Rogue River fault" in this chapter (figures 4.1a and 4.1b). The drag-folded layers of the Lookingglass formation, and the occurrence of older rocks in the foot wall, indicate normal displacement on the Coquille River fault which dips steeply to the east. The Rogue River fault cuts the sediments of the Flournoy formation indicating a component of normal displacement of at least 400 ft (~125 m) about 11 km south of line AA', and of at least 800 ft (250 m) about 19 km south of line AA' (Ramp and Moring, 1986).

The Rogue River fault is along a terrane boundary between two terranes of completely different metamorphic history (figure 4.1b). The Yolla Bolly terrane, east of the Rogue River fault, underwent high-P metamorphism and the Snow Camp terrane, west of the Rogue River fault, was not regionally metamorphosed (Blake et al, 1985a; this study), implying large offset between these terranes. Considering this, the Rogue River fault is either (1) a relatively minor, post-Mid-Eocene fault with at least 800 ft offset, or (2) it is the original fault (terrane boundary) that has had minor reactivation in post-Mid-Eocene.

Interpretation (2) is preferred for the following reasons: an up to 150 m wide zone of thinly laminated (< 1 mm to 1 cm) and sheared metasedimentary and metavolcanic rocks occurs east of the Rogue Wilderness ophiolite, directly in contact with the sheeted dike complex. The foliation in this zone strikes northeast and dips steeply northwest or southeast. It is unlikely that minor displacement in post-Mid-Eocene time (interpretation (1)) would result in a 150 m wide zone containing intensely sheared and thinly laminated metasedimentary and metavolcanic rocks. Also, the metavolcanic unit occurring east of the terrane boundary could be a fault-slice correlative with the Snow Camp terrane (figure 4.1b). This unit could have been incorporated into the sedimentary rocks of the Yolla Bolly terrane during Cretaceous thrusting and folding.

Small faults containing uncemented fault gouge (<1 cm wide) and polished, lustrous fault surfaces occur within the zone of intensely sheared and thinly laminated metasedimentary and metavolcanic rocks. The polished, lustrous faults are likely to provide kinematic constraints for the latest movement along the Rogue River fault. Two populations of fault-slickenside measurements were taken at two localities along the Rogue River fault zone. The attitude of polished, striated fault surfaces as well as the trend and plunge of the striations were measured at the banks of the Rogue River (n=8) and Mule Creek (n=14). The sense of slip was determined using either offset markers or the sense-of-slip criteria of Petit (1987) for brittle faults if no offset markers were present.

Throughout this chapter, the fault slip data are presented in 'Hoeppner plots', and the convention of plotting and classifying faults is shown in figure 4.3. The faults, striation and sense-of-slip from two localities in the Rogue River fault zone are illustrated in a 'Hoeppner plot' in figure 4.4a, and the corresponding data are listed in appendix D (table D1). Using the plotting convention outlined in figure 4.3, the faults are subdivided according to their main component of slip (figure 4.4a): the combined data set consists of 16 normal faults, 4 right-lateral and 2 left-lateral strike-slip faults.

The fault slip data from each locality probably consist of a subset of minor faults or secondary fractures which formed in the fault zone between the Rogue Wilderness ophiolite and the Dothan formation. When both data sets are analyzed separately using four different stress inversion methods, both

Figure 4.3

Plots of a normal fault, reverse fault, right-lateral strike slip fault, and a left-lateral strike slip fault after the method of Hoepfner (1955). The lower hemisphere stereographic projections show the fault plane, the striation on the fault plane, and the sense and direction of movement (assumed to be parallel striation). The M-plane is defined as a plane perpendicular to the fault plane and parallel to the striation. The slip linear is defined as an arrow affixed to the pole to the fault plane and parallel to the trace of the M-plane. Normal faults have slip linears pointing towards the center, reverse faults have slip linears pointing away from the center, right-lateral and left-lateral strike slip faults have slip linears approximately parallel to the circumference of the stereographic projection. Additionally, the compressional (P) and tensional (T) axis are plotted.

To facilitate the identification of the type of fault in the Hoepfner plots, the following convention is applied throughout this chapter: if the striation on a fault has a pitch between 0° - 45° and 135° - 180° , the fault is labeled as a strike slip fault (left or right lateral), if the striation on a fault has a pitch between 45° - 135° , the fault is labeled as a dip-slip fault (normal or reverse).

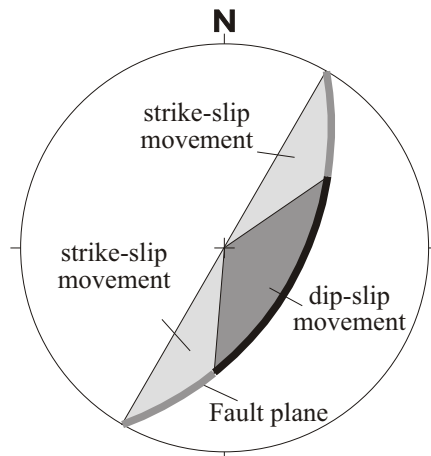
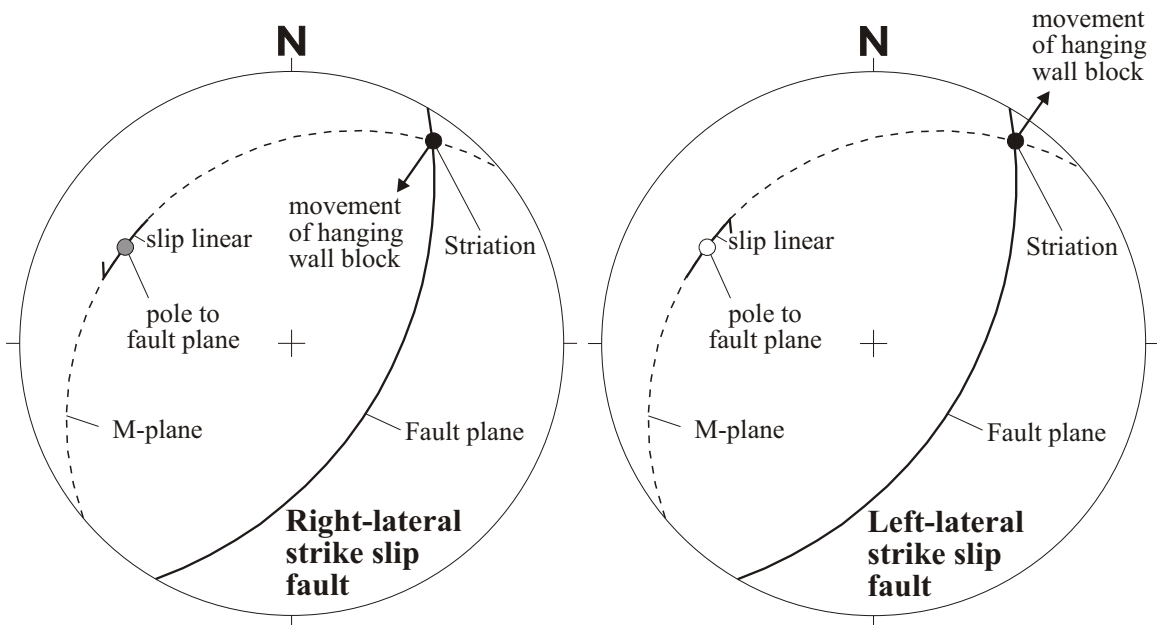
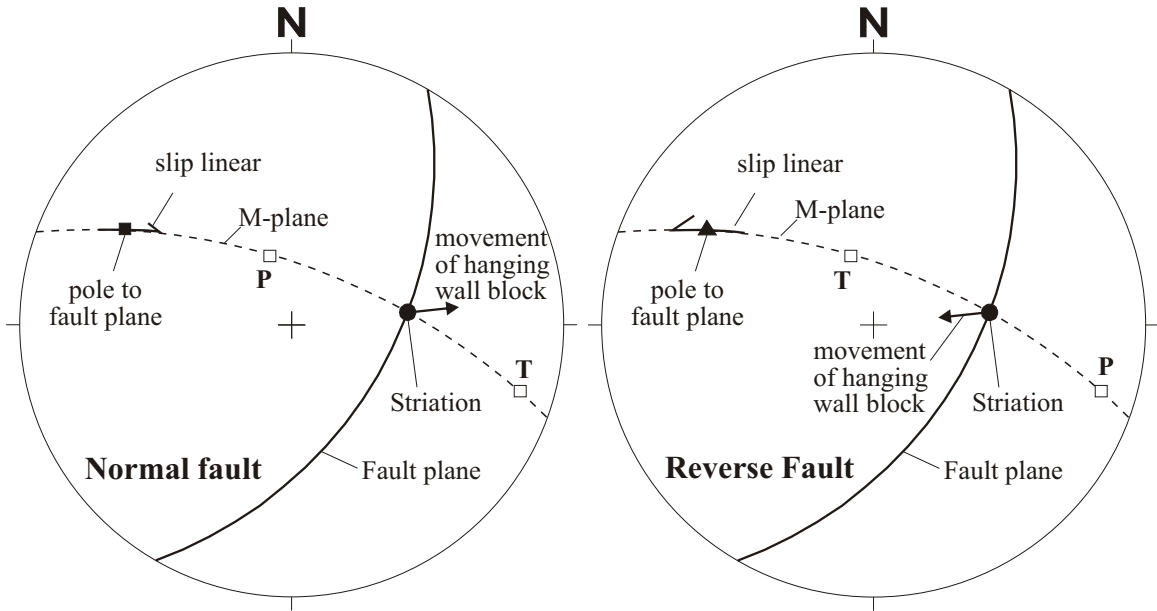
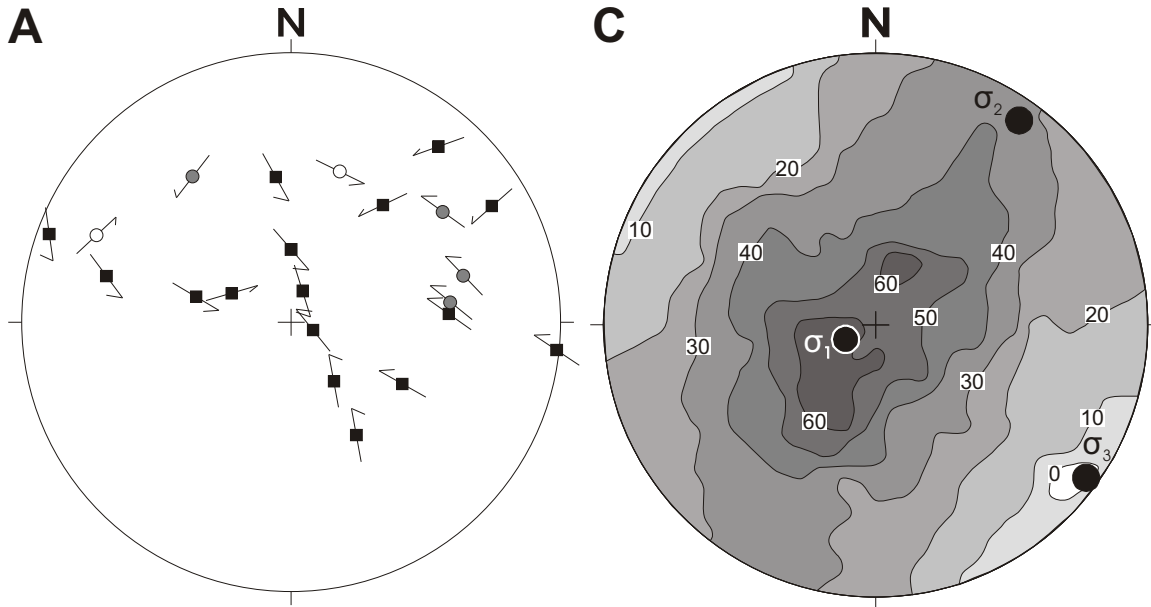


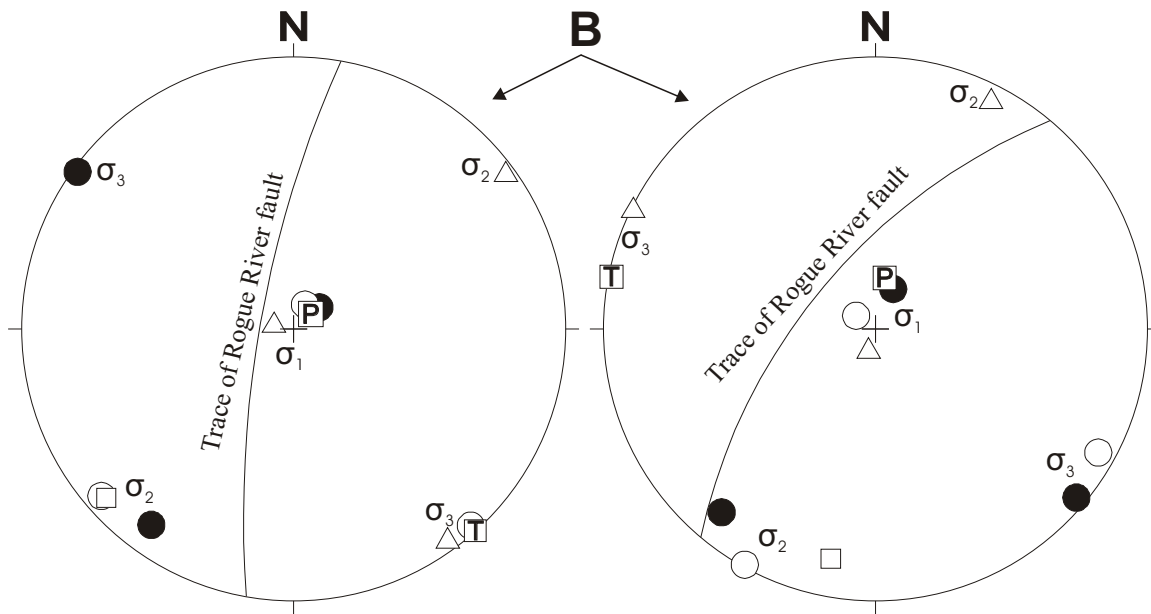
Figure 4.4

Lower hemisphere, equal area stereographic projections of poles to post-Eocene faults (4.4a) and the results of the paleostress analysis (4.4b and 4.4c) using the data shown in figure 4.4a.

- a. Poles to post-Eocene faults and their slip vectors (Hoepfner, 1955). The arrows affixed to the poles to faults indicate the direction of slip of the hanging wall block (see figure 4.3).
- b. Results of the paleostress analysis using four different programs: solid circle - ROMSA (Lisle, 1988); circle - TENSOR (Angelier, 1979); square - FAULTKIN (Allmendinger et al., 1994); triangle - STRESS (Reches, 1987). The principal stress axis σ_1 , σ_2 , and σ_3 are calculated separately for two data sets: (1) Rogue River locality (n = 8); and (2) Mule Creek locality (n = 14). The orientation of the foliation in the Rogue River fault is indicated for both localities.
- c. Solution of the analysis of the combined data sets (n = 22) using ROMSA (Lisle, 1988). The contours express the most probable orientation of σ_1 ($245^\circ / 80^\circ$). The maximum compound likelihood is $P_{\text{Total}} = 67.4\%$ (contour interval = 10%). The corresponding σ_2 and σ_3 orientations are $035^\circ / 09^\circ$ and $126^\circ / 05^\circ$, respectively.



- right-lateral strike slip fault (n = 4)
- left-lateral strike slip fault (n = 2)
- normal fault (n = 16)



Rogue River locality (8 faults)

Mule Creek locality (14 faults)

- ROMSA
- TENSOR
- △ STRESS
- FAULTKIN

fault population yield similar results as shown in figure 4.4b. The maximum principal stress σ_1 is subvertical, the intermediate principal stress σ_2 and the minimum principal stress σ_3 are subhorizontal. In the Rogue River locality, σ_2 is not parallel and σ_3 is not perpendicular to the foliation in the Rogue River fault zone, suggesting that reactivation of the fault zone was not parallel to the older foliation.

The results of the paleostress analysis of the combined data sets using ROMSA (Lisle, 1988) are shown in figure 4.4c. The maximum principal stress σ_1 has an azimuth of 245° and a plunge of 80° . The best σ_3 -direction returned by ROMSA is $126^\circ / 05^\circ$. The σ_2 -direction ($035^\circ / 09^\circ$) is determined stereographically as the normal to plane containing the calculated directions of σ_1 and σ_3 . In figure 4.4c, the likelihood (P_{Total}) for X being the direction of σ_1 is contoured. The maximum compound likelihood for $X = 245^\circ / 80^\circ$ being the direction of σ_1 is $P_{\text{Total}} = 67.4\%$ indicates that about two thirds of the fault slip data are compatible with the obtained solution. The fact that P_{Total} is less than 100% may indicate that the basic assumptions on which the paleostress analyses rely are not satisfied. Reactivation of the Rogue River fault is thought to have occurred, perhaps the criteria to distinguish Tertiary faults from earlier deformation are not sufficient, and a mixed data set in table 4.1 is analyzed. Nevertheless, the results of the paleostress analysis in figure 4.4c are consistent with the normal displacement of Tertiary strata 11 km and 18 km south of line AA' (figure 4.1a). Also, the "fault plane solution" using the program FAULTKIN (Allmendinger et al., 1994, see for description of methods Marrett and Almendinger, 1990) of the combined data sets as well as the fault plane determined from outcrop patterns is shown in figure 4.1a. The "fault plane solution" diagram clearly indicates normal displacement along the Rogue River fault. The compressional axis ($P = 023^\circ/79^\circ$) is subvertical whereas the extensional axis ($T = 123^\circ/02^\circ$) is horizontal and normal to the strike of the Rogue River fault. The axis σ_2 ($214^\circ/11^\circ$) is subhorizontal, paralleling the Rogue River fault. Neither of the planes ($202^\circ/44^\circ$ and $044^\circ/48^\circ$), which separate the quadrants of compression (shaded) and extension (white), appear to be parallel to the Rogue River fault (figure 4.1a). However, the strike of these planes is subparallel to the Rogue River fault. Outcrop patterns suggest a steeply, northwest dipping fault (60° - 90°) which strikes north 030° - 040° east. The results of the stress inversion are in good agreement with the geological constraints such as the normal displacement of Tertiary strata evident south of the area of study (Ramp and Moring, 1986). The orientation of the Rogue

River fault, as inferred from the map pattern, is consistent with the stress field determined from the analysis of small faults implying NW-SE extension in post-Mid-Eocene time.

4.3.3 Franciscan Complex

4.3.3.1 Yolla Bolly terrane

“Dothan Formation” is a name used in Oregon for a succession of sedimentary rocks that are part of the Yolla Bolly terrane of the Franciscan complex (Blake et al., 1985a). The sedimentary rocks of the Dothan Formation are exposed east of the Rogue Wilderness ophiolite and consist mainly of variably thick layers of fractured metagraywacke and sheared argillite. Sedimentary structures, such as graded bedding, indicate that the sediments were deposited by turbidity currents. The presence of the index fossil *Buchia piochii* (Ramp, 1969) and radiolarians found in chert horizons (Gray et al., 1982) indicate that the Dothan Formation was deposited during the latest Jurassic (Tithonian) and early Cretaceous. The beds strike north 10° - 50° east and have moderate to steep southeast dips (figure 4.5a). Overall, the poles to the layers scatter considerably, but they form a broad girdle whose pole ($208^{\circ} / 01^{\circ}$) indicates an average subhorizontal northeast-southwest trending fold axis.

The beds of metagraywacke alternate with layers of argillite which usually contain a weak slaty cleavage or appear sheared. The metagraywacke beds range from few cm to up to 5 m in thickness and are laterally discontinuous, especially in sections consisting predominantly of argillite. Many of the thin graywacke beds occurring in a fine grained matrix are folded (figure 4.5b) and boudinaged (figure 4.5d) or phacoidal in shape. In contrast, thick layers of graywacke are fractured and only vaguely lenticular in shape. Sections (~ 20-50 m thick) that consist predominantly of thick bedded graywacke seem to be stratigraphically intact and form coherent strata. Locally, the cleavage in the fine grained rocks is well-developed. The cleavage in several outcrops strikes north 020° - 040° east and dips 80° to 90° southeast (figure 4.5c), forming the axial plane of northwest verging folds (inclination in modern orientation). Other structural elements in the fine-grained, shaly layers include locally a weakly developed pencil-cleavage, isoclinal folds, coupled folds and kink-bands, open to tight sinusoidal and chevron folds, and drag-folded layers adjacent to micro-faults or shear-bands. Slump folds may occur as well. However, they were not

positively identified. In addition to lateral discontinuity of the bedding and the presence of isoclinal and rootless folds, the bedding is in places parallel to the axial-plane cleavage or to sheared argillite layers suggesting local transposition of the layering.

The measured fold hinges are variable in their orientation (figure 4.5b) suggesting multiple generations of folds or folding and rotation of hinges during simple shear. However, a detailed study was not undertaken to constrain different fold generations ($F_1, F_2 \dots$) and foliations ($S_0, S_1, S_2 \dots$) to relate these structures to various deformation phases ($D_1, D_2 \dots$). The outcrop map of an exposure having steeply dipping layers shows a typical example of a fold that probably formed due to drag in sheared argillite suggesting right-lateral offset along a fault (figure 4.5d). A cleavage parallel to the axial plane was not observed in this outcrop of sheared argillite. The distinctly different orientations of the two hinge lines in this two-dimensional outcrop map are also consistent with the geometry of a sheath fold. The field investigation of the Dothan Formation adjacent to the Rogue Wilderness ophiolite, revealed that most of the steeply dipping folds (i.e. coupled folds and drag-folds) occur in argillite rich sections and are consistent with drag due to right lateral shearing.

A laterally tapering, up to 200 m thick unit of greenschist facies volcanic rocks occurs about 150-250 m east of the fault contact with the Rogue Wilderness ophiolite (figure 4.1b, plate 1). This unit is subparallel to the general structural trend. Additionally, 5 m to 30 m blocks of metavolcanic rocks have been observed in a matrix of argillite and metagraywacke suggesting some disruption of this volcanic unit has occurred.

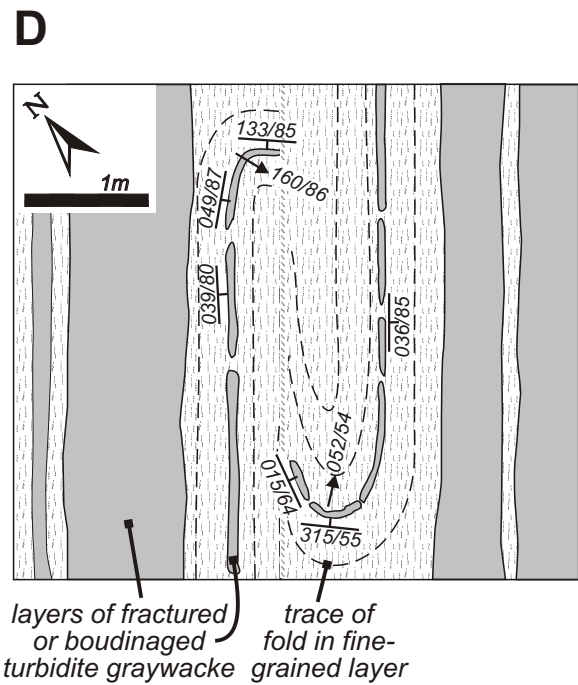
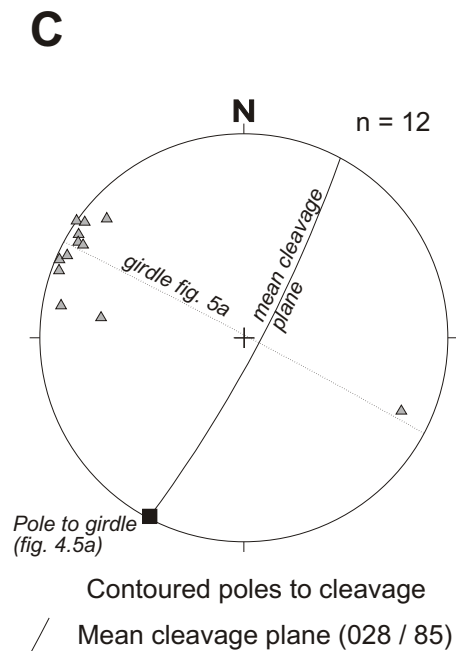
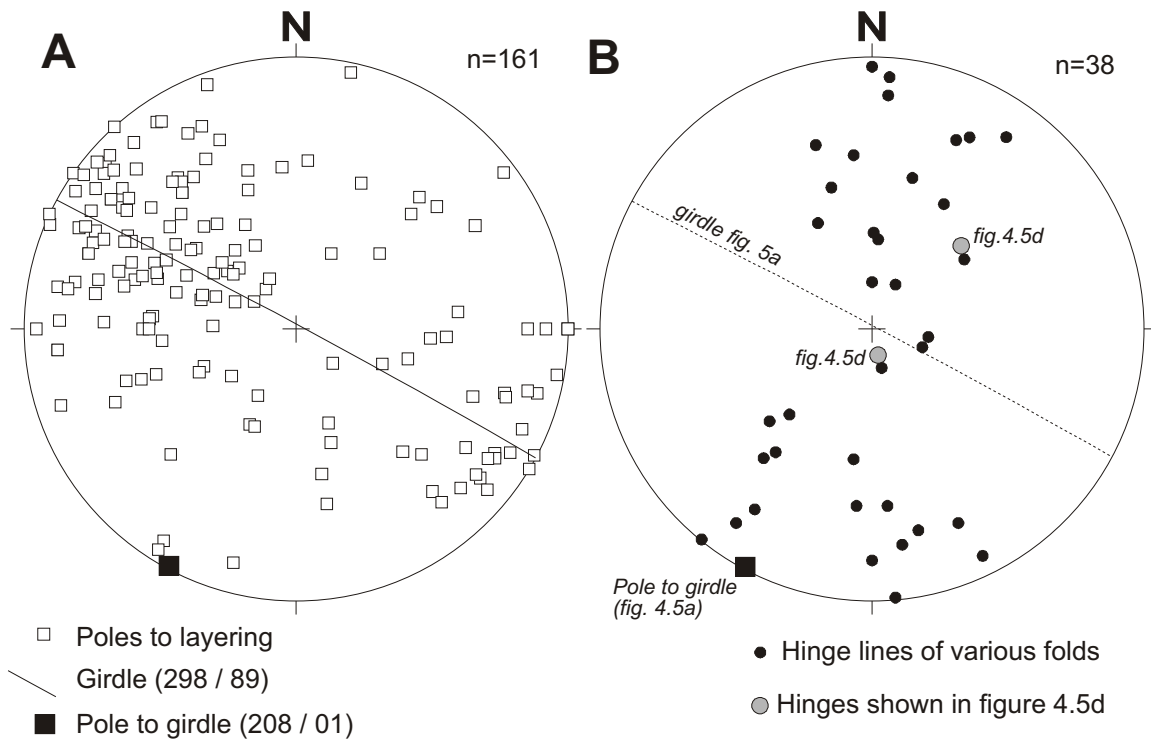
The sedimentary rocks directly in contact with the sheeted dike complex of the Rogue Wilderness ophiolite are thinly laminated (< 1 mm to 1 cm thick laminae) and intensely sheared. The foliation strikes northeast and dips steeply northwest or southeast. The blocks of metavolcanic rock caught up in this zone are also intensely sheared. This zone of intensely sheared rocks is up to 150 m wide, and could represent the terrane boundary between the Dothan Formation and the Rogue Wilderness ophiolite. However, outcrop pattern indicate that the Dothan volcanic unit and the zone of intensely sheared sedimentary and metavolcanic rocks are truncated at a low angle (plate 1). This can be explained with later faulting along a fault subparallel to the terrane boundary.

Figure 4.5

Lower hemisphere, equal area stereographic projections of structural data of the Dothan Formation (a, b, and c) and simplified outcrop map (d).

- a. Poles to layering in the Dothan formation. The best-fit girdle and the pole to this girdle ($208^{\circ} / 01^{\circ}$) are shown.
- b. Hinge lines of outcrop-scale folds. Steeply plunging fold hinges are often associated with drag-folds in sheared argillite (figure 4.5d).
- c. Contoured poles to cleavage. Based on observations in outcrops, the cleavage plane probably represents the axial plane of subvertical, slightly west verging folds.
- d. Outcrop map of sheared argillite and boudinaged graywacke at China Bar. The apparent offset of bedding in this outcrop is dextral. The hinge lines plunge at almost 90° to each other.

Structural data for the Dothan Formation east of the Rogue Wilderness ophiolite



Because of the tectonic mixing of the sedimentary and igneous rocks typically found in the Dothan Formation (e.g. Wiggins, 1980), the distinctive deformational style characterized by the stratal discontinuity, and the lack of exotic blocks, the Dothan Formation in this area can be classified as a “dismembered formation” (rather than melange or broken formation) using the nomenclature proposed by Raymond (1984).

The Yolla Bolly terrane is part of the Franciscan complex, which is considered to be a type example of an accretionary complex that formed during subduction of Pacific lithosphere beneath western N. America (e.g., Hamilton, 1978). Typical characteristics include high degrees of structural disorder (largely broken formation and melange) and presence of high P/T metamorphic assemblages. The Franciscan complex has been subdivided into terranes (Blake et al, 1985a, 1985b), and these terranes become older and show higher grades of metamorphism from west to east (Coastal Belt, Central Belt and Eastern Belt). Fossils from the Yolla Bolly terrane (part of the Eastern belt) indicate the oldest rocks in the accretionary complex are of latest Jurassic age (Tithonian) (Blake and Jones, 1974; Blake et al., 1988). The Coastal Belt of the Franciscan complex contain fossils that indicate that the youngest rocks are of Tertiary (Miocene) age (McLaughlin et al., 1982).

4.3.3.2 Sixes River Terrane

Rocks of the Sixes River terrane do not crop out in the Wild Rogue Wilderness area. However, the Sixes River terrane is shown in the cross section in figure 4.1b and is, therefore, briefly discussed. The Sixes River terrane is part of the Franciscan complex and is correlated with the Central Belt of the Franciscan complex in the California Coast Ranges (Blake et al., 1985b). Highly sheared mudstones, sandstone and conglomerate occur together with abundant tectonic blocks of high-grade blueschist and eclogite (Blake et al., 1985a, 1985b) forming a tectonic melange (Raymond, 1984). Fossils indicate that the sediments accumulated in latest Jurassic and early Cretaceous time (Blake and Jones, 1974). The Yolla Bolly terrane is thought to be thrust over the Sixes River terrane (Blake et al, 1985b).

4.3.4 Myrtle Group

In this study, the stratigraphic nomenclature of Imlay et al. (1959) is adopted. Imlay et al. (1959) raised part of the Myrtle Formation of Diller (1898) to the rank of a group and divided it into two new formations, the Riddle Formation and Days Creek Formation. The type section for the Myrtle Group is located 10 miles east of Riddle along the South Umpqua River (Imlay et al., 1959). The Myrtle Group has previously been correlated with the Great Valley sequence in California (Imlay et al., 1959, Blake et al. 1985a).

In the study area, the beds strike north 030° - 040° east and dip steeply southeast or northwest (figure 4.1a, Myrtle (N)). The strike and dips of the beds change rapidly (Rud, 1971; this study), and at outcrop-scale, the beds are openly to tightly folded. The hinges of outcrop-scale folds dip gently northeast or southwest (figure 4.1a, Myrtle Group (N)). The beds of the Riddle formation appear to dip steeper than the beds of the Days Creek formation, suggesting that the sedimentary rocks of the Myrtle Group occur in a large syncline (Rud, 1971). The rotation axes R_c is defined as the axis of the syncline, which is thought to be parallel to the pole to the girdle in figure 4.1a (Myrtle group (N); pole to girdle = 047° / 03°). The axis R_c may be used to restore the sedimentary rocks of the Myrtle Group and ophiolitic basement to the orientation prior to Cretaceous folding.

4.3.4.1 Riddle Formation

The sedimentary rocks of the Riddle Formation are exposed west of the Rogue Wilderness remnant of the CRO, and the best exposures occur along the 4WD road from Camp Hope leading to the Old Red Mine, and in Blossom Bar Creek. The sedimentary rocks exposed directly at the western boundary of the Rogue Wilderness ophiolite consist of conglomerates (0.5 to 10 m thick beds), conglomeratic sandstone (0.1 to 0.5 m thick beds) and minor amounts of siltstone (<0.1 m thick beds). The conglomerates contain predominantly chert pebbles and a minor amount of well rounded clasts of aphanitic and porphyritic greenstone in a sandy matrix. The pebbles range from 1 cm to 8 cm in size. In three outcrops in Blossom Bar Creek and along the 4WD-road just outside of the western boundary of the

Wild Rogue Wilderness near the head of Mule Creek (West Fork), the conglomerate is overturned, as indicated by graded bedding. The underside of graded beds dips 060°-080° southeast.

Rud (1971) recognized four distinct sections above the 'basal' chert-pebble conglomerate. Rud (1971) reports that the thickness or stratigraphic order could not be constrained due to the intensely folded and faulted nature of the Riddle formation and lack of continuous exposures, but that the dip of beds decreases from east to west. The stratigraphic sections above the chert-pebble conglomerate at the contact with the Rogue Wilderness remnant of the CRO include (Rud, 1971): (1) A section of siltstone and sandstone (7.5 - 75 cm thick beds) containing lenses of conglomerate. The conglomerate consists mainly of chert pebbles and minor amounts of graywacke pebbles. *Buchia piochii* is very abundant. (2) A section of conglomerates and conglomeratic sandstones containing pebbles of chert, graywacke and minor amounts of greenstone. (3) A section of siltstone containing abundant wood fragments and the fossil *Buchia piochii* followed by interbedded sandstone and siltstone. (4) A 10 m thick section of coarse conglomerate containing rounded, up to 30 cm large fragments of chert, graywacke and greenstone in a silt matrix.

Gray et al. (1982) report that in addition to *Buchia piochii*, the fossil *Buchia fischerina* is present in the Wild Rogue Wilderness. These fossils indicate that the Riddle formation was deposited during the latest Jurassic (Tithonian). The Riddle Formation is thought to have been deposited in deep water by a combination of turbidity currents, submarine debris flow and accumulation of submarine ooze (Gray et al., 1982).

4.3.4.2 Days Creek Formation

About 2 km northwest from the western boundary of the Rogue Wilderness ophiolite, the Riddle Formation appears to be conformably overlain by the lower Cretaceous Days Creek Formation (Rud, 1971). The beds of the Days Creek formation also strike north 030°-040° east, but they dip moderately steep (40°-60°) northwest (Rud, 1971). Increasingly shallower dips from east to west are consistent with the interpretation that the sedimentary rocks of the Myrtle Group occur on the east-limb of a syncline. Rud (1971) reports that the sedimentary rocks of the Days Creek formation in the area northwest of the Rogue Wilderness remnant of the CRO consist of fine to medium grained fossiliferous sandstone with abundant

plant debris near the base, a massive sandy siltstone with abundant *Buchia crassicolis* (Keyserling), sandy siltstone that weathers to spheroidal forms, a sandstone section containing abundant wood fragments as well as siltstone pods and lenses of chert-pebble conglomerate, and a 15m thick section of conglomerate containing subrounded fragments of red, black, and gray colored chert, as well as metavolcanic fragments. The conglomerate is overlain by sandy siltstone.

Conglomerate and sandstone with lenses of pebble conglomerate reported by Rud (1971) does not occur in the type section of the Days Creek formation about 10 miles east of Riddle along the South Umpqua River (Imlay et al., 1959). Perhaps, the structure of the Myrtle Group west of the Rogue Wilderness ophiolite is more complex than recognized by Rud (1971). Conglomerates typical of the Riddle formation crop out among sandstones and siltstones of the Days Creek formation perhaps due to thrust faulting. Clearly, this area needs to be remapped and ages of continuous stratigraphic sections determined (if fossils present and outcrop conditions permit) in order to determine whether the sedimentary rocks of the Myrtle Group occur in a large syncline, or form an imbricated zone.

4.4 Orientation of planar features in the pillow unit and Mule Mountain volcanics

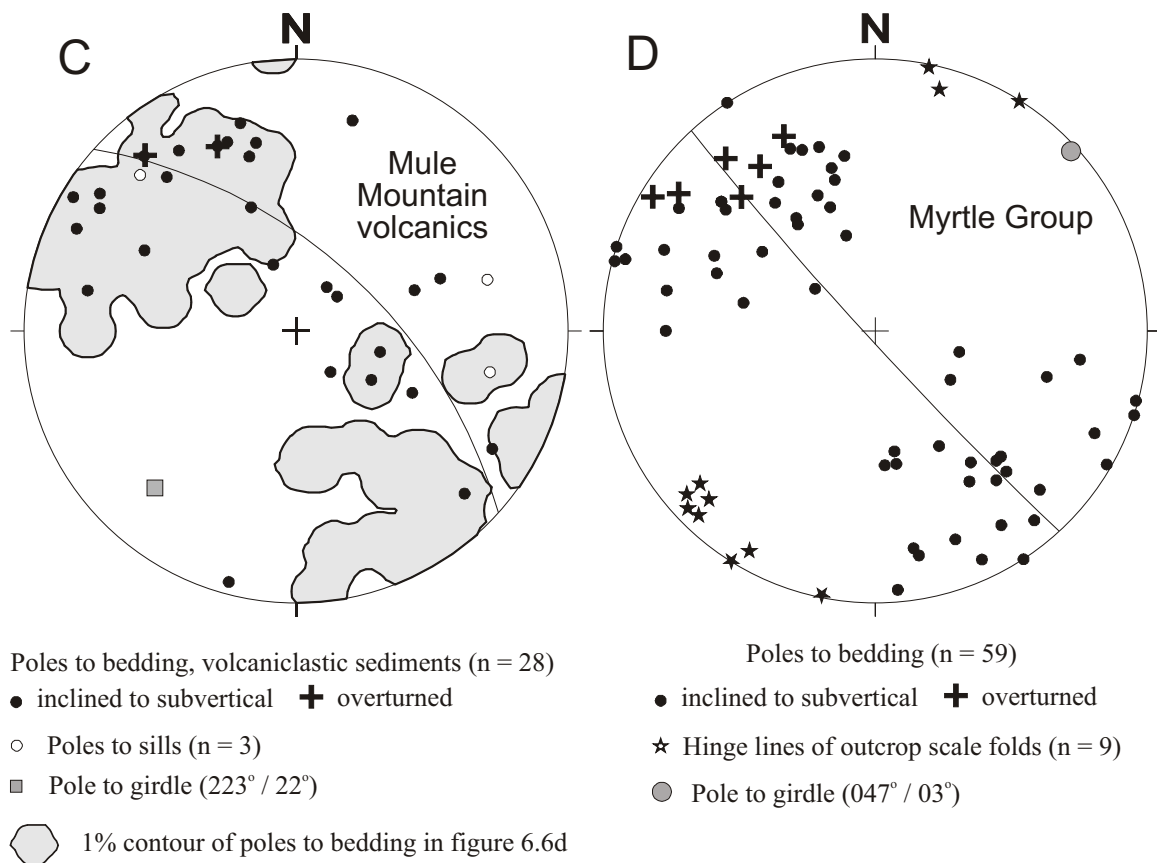
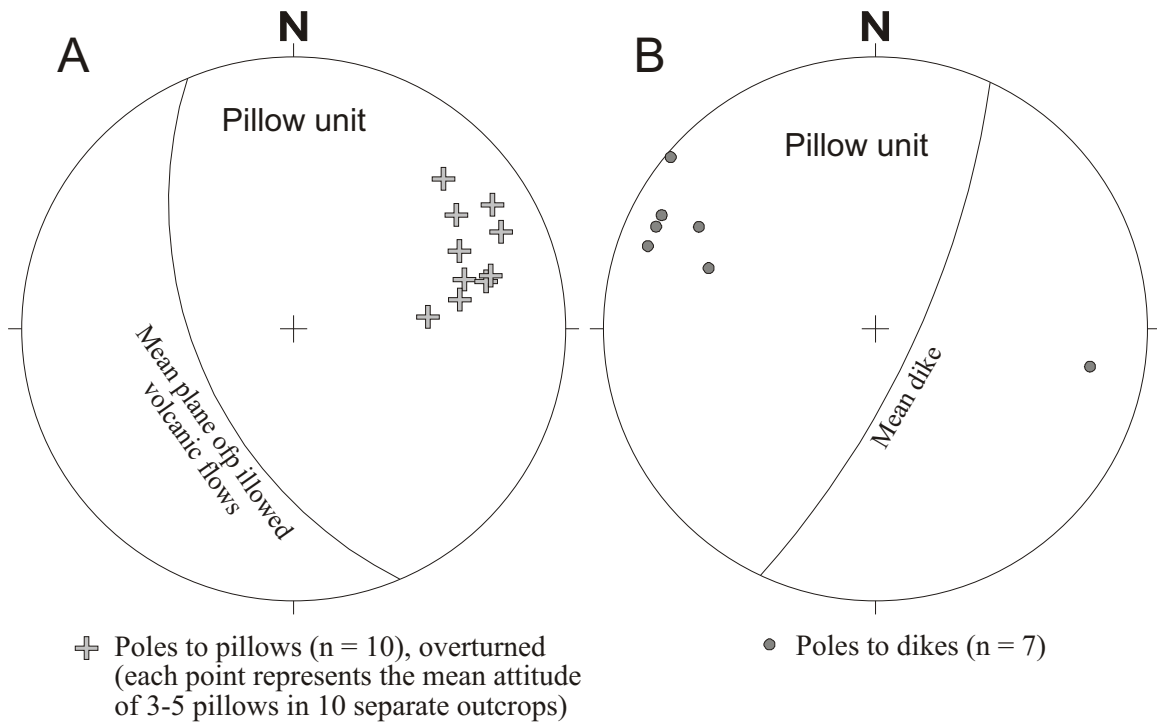
Pillow structures in the pillow unit are relatively spherical and it is often not possible to determine the orientation of the flows. However, the top and bottom of relatively flat pillows could be identified in few outcrops, and the attitude of these are somewhat constrained. Generally, these flows strike northwest-north and dip steeply to the southwest (figure 4.6a). In the present coordinates, the submarine volcanic flows are overturned (i.e. flat undersides and “tails” are up).

The diabasic and dacitic dikes and intrusions cut the volcanic flows at high angles. Overall, the dikes strike northeast-north and dip steeply southeast (figure 4.6b). The acute angle between the submarine volcanic flows and the dikes is about 60°. Interestingly, the dikes in the pillow unit are subparallel to the dikes in domain E in the sheeted dike complex (figure 4.7). This could be coincidence because these dikes occur in different fault slices across the Blossom Bar shear zone. However, the parallelism of the dikes in the pillow unit and the dikes in domain E in the sheeted dike complex could also indicate the units are related and underwent similar rotations during deformation.

Figure 4.6

Lower hemisphere, equal area stereographic projections of poles to pillows (a), of poles to dike margins for dikes cutting pillows (b), and poles to bedding of volcanoclastic sediments (c). For comparison, the structural data for the Myrtle Group west of the Rogue Wilderness ophiolite are plotted (d).

- a. The attitude of 3-5 relatively flat pillows was measured in 10 outcrops. The submarine volcanic flows are overturned based on shape of pillows. The mean plane of the pillowed volcanic flows is shown.
- b. Dacitic and diabasic dikes intruding the pillow unit cut the pillowed flows at high angles. The acute angle between the mean plane of the pillowed volcanic flows and the mean dike is about 60° .
- c. The poles to bedding of volcanoclastic sandstones and radiolarian-bearing, tuffaceous mud- and siltstones are shown as well as the poles to sills (Mule Mountain volcanics). These poles define a broad girdle.
- d. The poles to bedding in the Myrtle Group define a broad girdle. The pole to the girdle is subparallel to most of the subhorizontal hinge lines measured in outcrop scale folds.



Planar features in the Mule Mountain volcanics include bedded volcanoclastic sandstones (they could be part of the Myrtle Group?), thinly laminated radiolarian-bearing, tuffaceous mud- and siltstones (argillites) as well as sills and dikes. Although the poles to bedding and sills scatter considerably, they form a broad girdle with the pole ($223^\circ / 22^\circ$) defining a southwest-plunging fold axis (figure 4.6c). Most poles to bedding and sills overlap with the structural data from the Myrtle group, and the fold axis of the Mule Mountain volcanics has almost the same trend as the fold axis of the Myrtle Group (figure 4.6d). However, the fold axis in the Mule Mountain volcanics plunges 22° towards 223° in contrast to the subhorizontal fold axis of the Myrtle Group ($047 / 03^\circ$). The difference in the plunge of the fold axis can be explained in two ways: (1) The uppermost section of the Mule Mountain volcanics is positionally overlain by the Myrtle Group, and the beds were originally parallel. During subsequent deformation the sedimentary rocks of the Myrtle Group were rotated differently than the Mule Mountain volcanics. Alternatively, the sedimentary beds in both units could have remained essentially parallel after deformation. However, the attitudes of the bedding planes vary greatly, which means, the strike and dips change rapidly from outcrop to outcrop resulting in large scatter of poles to bedding in the stereographic plots. Consequently, a large number of measurements from both units is necessary to test whether or not the attitudes of the fold axes are statistically similar, and that the beds could have been parallel. (2) The Mule Mountain volcanics are unconformably overlain by the Myrtle Group. In this case, the angular relationship between the fold axes may suggest an angular unconformity between the Mule Mountain volcanics and the sedimentary rocks of the Myrtle Group. If a statistical treatment of the data shows that the fold axes are indeed statistically different, possibility (1) could still not be ruled out.

The contact relationship between the uppermost section of the Mule Mountain volcanics and the Myrtle Group cannot be determined with existing data, and more work is needed. Unfortunately, the outcrop conditions near the contact between the Mule Mountain volcanics and Myrtle Group are very poor, and this critical contact may not be exposed in the Wild Rogue Wilderness. Considering the scatter of the data in the Mule Mountain volcanics and the Myrtle group (figures 4.6c and 4.6d), the difference in the plunge of the fold axes is probably not significant, and it is possible that the Myrtle group lays

depositionally on the Rogue Wilderness remnant of the CRO. This would be similar to the CRO remnants in California which are depositionally overlain by the Great Valley sequence (e.g. Hopson et al., 1981).

4.5 Possible re-orientation of the ophiolite to paleohorizontal

The volcanic flows and sediments overlying the ophiolitic basement provide control on the orientation of the Snow Camp terrane prior to Cretaceous and Tertiary folding. The fold axes which were determined in figures 4.1a, 4.6c and 4.6d, may be used as the rotation axes for the reorientation. The Cretaceous fold axis in the Myrtle Group trends 047° and plunges 03° northeast (figure 4.6d), and the strata at the contact with the Mule Mountain volcanics is subvertical. The trend of the fold axis of the sedimentary rocks in the Mule Mountain volcanics is subparallel (223°) to the Myrtle Group, but it plunges 22° southwest (figure 4.6c). Compared to Cretaceous folding, the rotation of the Snow Camp terrane due to Tertiary folding was small (maximum dip of oldest Eocene strata in the east-limb of Eden Ridge syncline is 25°). The fold axis of the Eden ridge syncline trends 030° and is subhorizontal.

The ophiolite can be restored using the Tertiary and Cretaceous fold axes as rotation axes which are defined as R_T and R_C , respectively. However, instead of unfolding around two rotation axes (Tertiary rotation axis $R_T = 030^\circ/00^\circ$ and Cretaceous rotation axis $R_C = 047^\circ/03^\circ$) an equivalent clockwise rotation of 90° can be performed around a single, horizontal rotation axis R which has an azimuth of 045° . For example, a clockwise rotation of 90° around $R = 045^\circ/00^\circ$ restores the subvertical sedimentary strata of the Myrtle Group near the contact with the Mule Mountain volcanics to subhorizontal so that the beds are normally graded.

If there is indeed an angular unconformity between the sedimentary strata in the uppermost section of the Mule Mountain volcanics and the Myrtle Group (section 4.4), a rotation around $R = 045^\circ/00^\circ$ could not suffice to restore the ophiolite to paleohorizontal. However, the trend and plunge of the fold axis of the upper metavolcanic unit would be 247° and 01° , respectively after a 90° clockwise rotation around R .

The traditional model of Ingersoll (1979) and Dickinson and Seely (1979) for the Coast Range ophiolite suggests that the east flank of the Franciscan complex was thrust beneath the Coast Range

ophiolite, and the Franciscan rocks are part of the subduction complex accreted near the trench that was paired with the Sierran-Klamath arc. This model is based on studies in northern and central California, where the tectonostratigraphy, from west to east, consists of (1) Franciscan complex; (2) Coast Range ophiolite, which is bound by the Coast Range 'thrust' to the west; and (3) Great Valley sequence which conformably overlies the Coast Range ophiolite on its east flank. The 'stacking' in SW Oregon is opposite and, from west to east, consists of: (1) Sedimentary rocks of the Myrtle Group (correlated with Great Valley sequence in California), (2) Rogue Wilderness ophiolite, and (3) Franciscan rocks (figure 4.1b). Perhaps, the 'stacking' in SW Oregon is 'reversed' (with reference to 'normal' stacking in California), because the Rogue Wilderness remnant of the CRO and overlying Myrtle Group are located on the east-limb of a large Cretaceous syncline which is part of a folded thrust sheet. This is consistent with the interpretation that the Rogue River fault (figure 4.1a) is a terrane boundary (section 4.3.3.1) and had had only minor reactivation in post-Mid-Eocene time (section 4.3.2). The regional comparison, and the fact that the general structural trend in the study area is southwest-northeast (figure 6.1a) provide good constraints for rotating the entire sequence (Myrtle Group, Rogue Wilderness ophiolite, Franciscan) around the rotation axis $R = 045^{\circ}/00^{\circ}$ in a clockwise direction.

4.6 Structure of the sheeted dike complex

4.6.1 Diabasic and microdioritic dikes

The principal structures of the sheeted dike complex are (1) sheeting defined by subparallel dikes and (2) igneous layering in the gabbroic screens. The orientations of the dikes were determined throughout the sheeted dike complex by measuring the attitude of the chilled margins in outcrops. Dikes that cut sheeting at high angles are rare, and mostly include dikes intruded along faults and, therefore, appear to cut older dikes at intermediate angles (usually less than 45°). Commonly, the dikes are subparallel and may cut each other at low angles. Overall, the attitudes of the chilled margins of the dikes measured in individual outcrops vary between 0° - 30° . This variation is reflected in the scatter of the poles to dike margins plotted in the stereographic projections for the various domains in figure 4.7. A systematic

difference in attitude between diabasic and microdioritic dikes was not observed, suggesting the intrusion of both types of dikes could have occurred during one episode of deformation under one static stress field. On the other hand, the intrusion of late dikes could have occurred under the influence of a different stress field, and the late dikes could have intruded parallel to older dikes following the anisotropy of the sheeting rather than intruding perpendicular to the direction of maximum extension.

Six domains having similar dike orientations are outlined in figure 4.7 (domains A to F). The individual measurements of the attitude of the chilled margins are plotted as poles to dikes. Additionally, the mean orientations of dikes are represented by great circles, so that the average strike and dip of the mean dike in each domain can be easily read from the stereonet plots in figure 4.7. Statistically, domains A and B cannot be distinguished. However, it was useful to split the large data set obtained along the Rogue River into domain A and B.

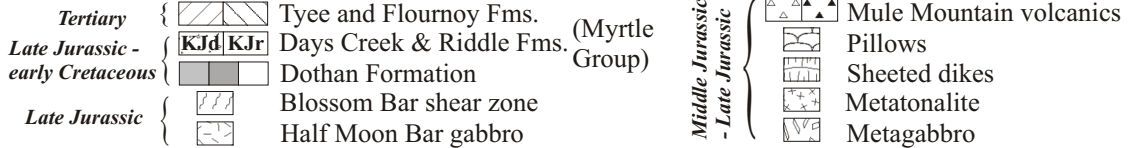
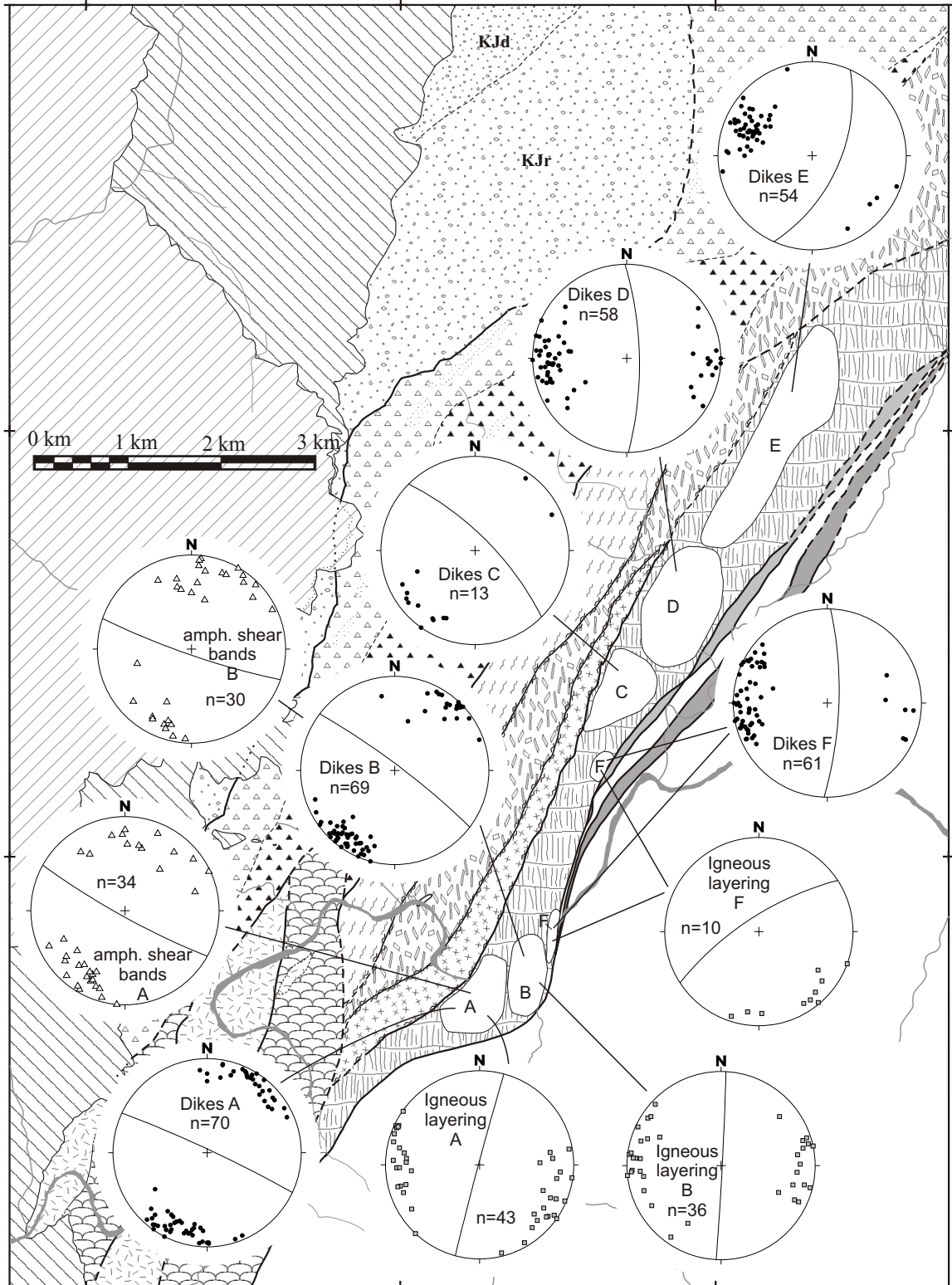
Overall, the strike of the steeply dipping dikes changes about 90° from an average of 295° in domain A to an average of 024° in domain E. The dikes near the fault contact with the Dothan Formation (domain F) strike north-south and dip steeply east, similar to the dikes in domain D. The change of attitude of the dikes from domain B to domain F is not gradual, but occurs abruptly across several, steeply dipping, mineralized faults described in chapter 2. Ramp and Gray (1981) interpreted the change of the attitude of the dikes near the fault contact with the Dothan Formation as due to drag-folding along the Rogue River fault. However, drag-folding would result in a gradual rather than an abrupt change of dike attitudes as the dikes are bent into parallelism with the Rogue River fault. Thus, it appears that the markedly different attitudes of the dikes identified in the various domains are more likely due to variable rotation of relatively rigid fault blocks.

The progressive change of the attitude of the dikes from domain A through F is constrained to have occurred prior to Cretaceous folding for the following reasons: the faults across which an abrupt change of the dike orientation is observed are cemented with hydrothermal minerals such as sulfide and quartz, and epidote and quartz (see chapter 2). Clasts of epidotes occur within the fault zones. Epidotes form in excess of 200°C (probably $>250^\circ\text{C}$) depending on pressure and fluid composition (Harper et al.,

Figure 4.7

Geologic map of the Rogue Wilderness ophiolite showing the structural domains A to F in the sheeted dike complex. The structural data of each domain are presented in lower hemisphere, equal area stereographic projections. Three types of planar structures are illustrated:

1. Diabasic and microdioritic dikes; the individual measurements of the attitude of the chilled margins are plotted as poles to dike margins (solid circles; dikes A to F). The great circles indicate the mean strike and dip of the dikes in each domain (discussed in section 4.6.1).
2. Igneous layering in screens of cumulate gabbro; the data include poles to planar lamination and poles to compositional layering (squares; igneous layering A, B, and F). The mean orientations are plotted as great circles for each domain (discussed in section 4.6.2).
3. Amphibole veins and shear bands; the poles to amphibole veins and shear bands in screens of cumulate gabbro are plotted (triangles; amph. shear bands A and B). The great circles indicate the average strike and dip of these planar structures which are subparallel to the sheeted dikes in domains A and B (discussed in section 4.6.3).



1988 and references therein). Also, this type of mineralization is not found in the upper Jurassic to lower Cretaceous sedimentary rocks of the Myrtle Group. Niem and Niem (1990) reported published (Law et al., 1984) and unpublished (Mobile, 1980) vitrinite reflectance numbers (R_o) measured in 47 samples from the Myrtle Group ranging between 0.56 % to 1.05 %. These values indicate a maximum paleotemperature of 70°C to 120°C, suggesting the sedimentary rocks of the Myrtle Group are unmetamorphosed. This leads to the conclusion that the faults across which an abrupt change of the dike orientation is observed predate the deposition of the Myrtle Group and, thus, post-Myrtle/pre-Eocene Cretaceous thrusting and folding.

The great amount of fluid required for epidotization (water/rock >10000; Harper, 1995 and references therein) implies faulting during hydrothermal metamorphism, presumably at the ridge axis. The faults which separate the rotated blocks could thus be 'oceanic'; that is, they were active when the ophiolite formed at a spreading center (163-164 Ma). Probably, most of the progressive change of the attitude of the dikes from domain A through F is related to 'oceanic' tilting. Some of the rotation could have occurred later, because younger(?) epidote and prehnite veins cut the foliation of ductile to brittle deformation. Ductile deformation is constrained to have ended at ~149 Ma, because the muscovite $^{39}\text{Ar}/^{40}\text{Ar}$ ages of ~149 Ma, determined in two samples of ductily deformed muscovite-garnet tonalite, mark the time of cooling below 350°C. At this temperature, muscovite closes to Ar-diffusion (Hames and Bowring, 1994), and strain is thought to be accommodated predominantly by brittle fracturing and cataclastic flow (depending on rock composition, strain rate, and water content which is discussed in section 4.7).

Regardless of the orientation of the sheeted dike complex prior to Cretaceous folding and the timing of the rotation of the fault blocks, a common tilt axis T for all dikes (or mean dikes) in the present coordinates can be found so that the attitudes of the dikes in any one of the domains can be reproduced by rotating the dikes around the axis T (figure 4.8). This is based on the assumption that dike injection was subvertical and, therefore, all dikes possessed similar attitudes.

In order to simplify the illustration, only the pole to mean dike orientations for each domain is plotted in figure 4.8. For example, as the pole to mean dike of domain A rotates about the axis T with constant angle φ_A (= angle between pole A and axis T) it will describe a small circle on the stereonet

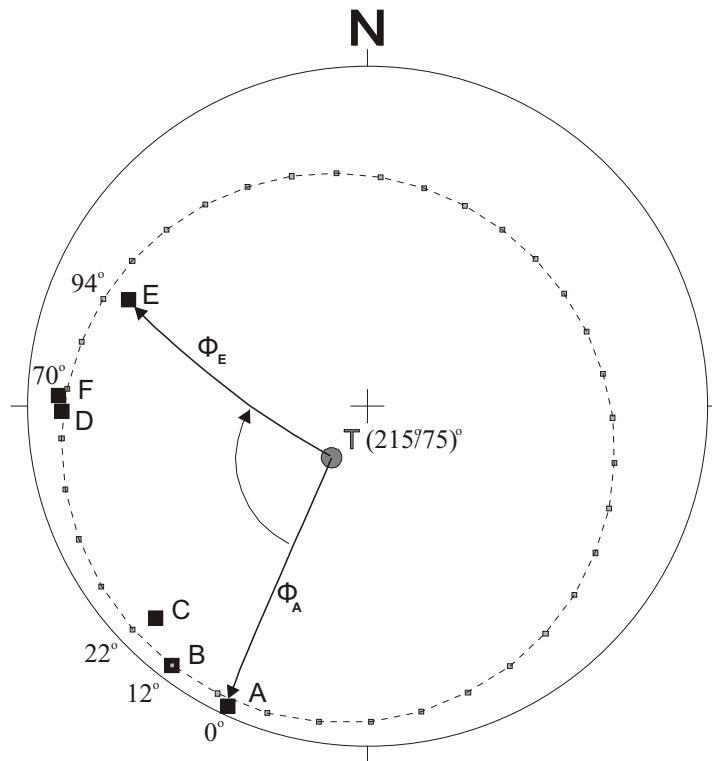


Figure 4.8

Lower hemisphere, equal area stereographic projection of pole to mean dike orientations for domains A through F (figure 4.7). The stippled, ellipse depicts the common small circle to poles A to F. The inferred rotation axis T is located in the center of the small circle. Assuming all dikes originally possessed similar attitudes prior to rotation by tilting of rigid fault blocks, it is possible to reproduce the orientation of the dikes in any one of the domains by simply rotating the dikes of anyone of the domains around T. For example, if it is assumed that the dikes in domain A remained in their original orientation since they formed, a clockwise rotation of a rigid fault block of about 94° around T would suffice to explain the orientation of the dikes in domain E. Φ_i is the angle between the tilt axis T and the poles to the mean dikes in domain i.

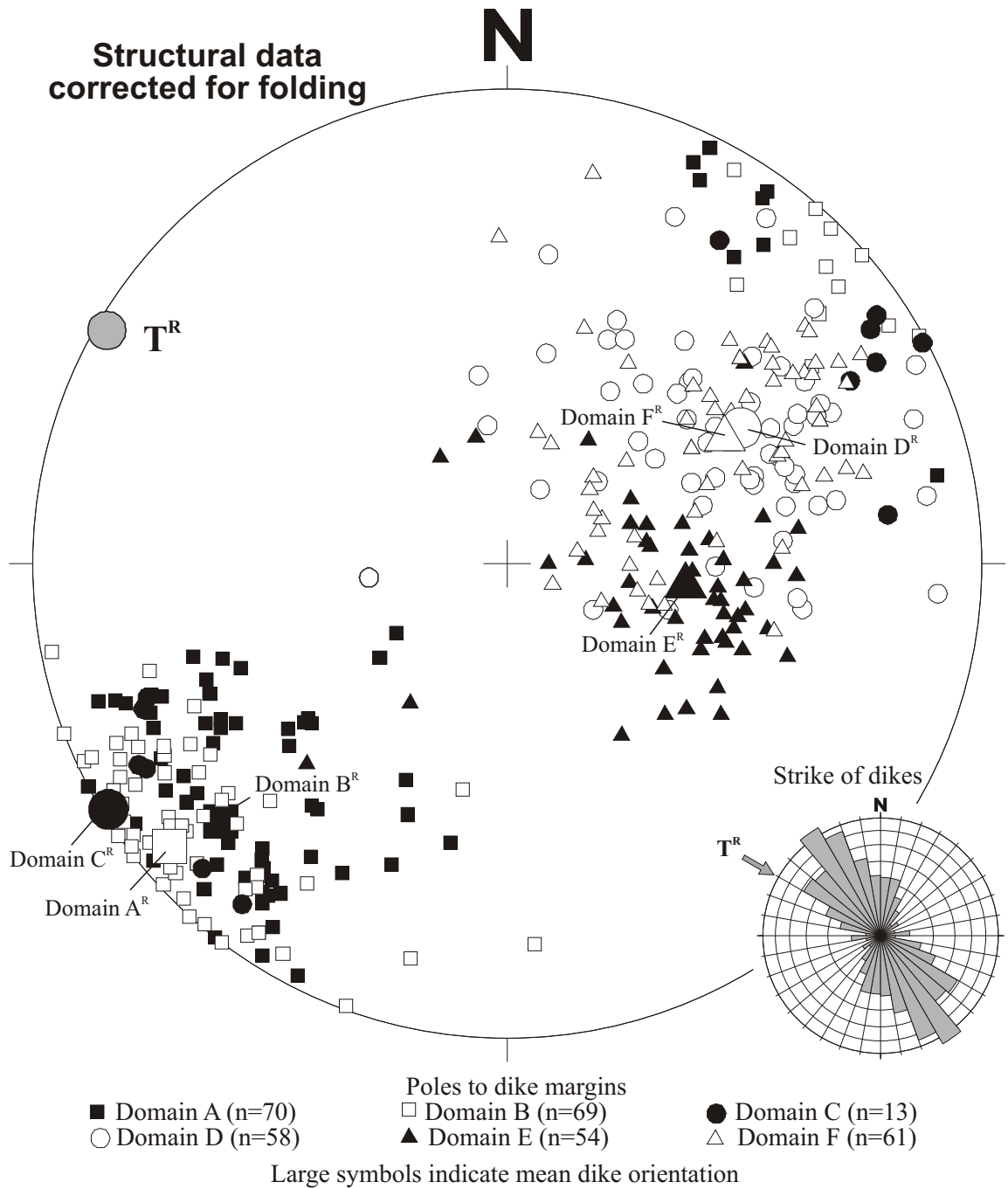


Figure 4.9

Lower hemisphere, equal area stereographic projections of poles to dikes after correcting for Tertiary and Cretaceous folding. Also, the mean dike orientations and the inferred tilt axis from figure 4.8 are shown after correcting for Tertiary and Cretaceous folding. The inset shows that 85% of the dikes strike north 010°-060° west. The restored tilt axis T^R is at an angle to the maximum of the strike of the dikes.

(figure 4.8). Since the attitudes of the dikes of the domains B, C, D, E and F should be reproduced by rotating A around T, all poles to the mean dikes must be located on or close to a common small circle (stippled circle in figure 4.8). This means, the tilt axis T must be selected so that the angles φ_A , φ_B , φ_C , φ_D , φ_E , and φ_F are approximately equal. In this case, φ_i averages about 70° . Using these relationships, T was determined having an azimuth of 215° and plunge of 75° . If the mean dike of domain A is selected as reference, and the dikes of domain A are tilted around the subvertical axis T, attitudes similar to the dikes of domain B are obtained after a clockwise rotation of 12° , dikes of domain C after 22° , domain D&F after 70° , and domain E after 94° (figure 4.8).

As discussed in section 4.5, the entire terrane was probably rotated in Cretaceous time during thrusting and folding, and the structural data from the sheeted dike complex must be restored to the orientation prior to Cretaceous deformation using the rotation axis R (defined in section 4.5). Unfolding around R results in dike orientations ranging from subvertical to subhorizontal (figure 4.9). The strike of the dikes is variable, but dikes which strike northwest-southeast are most abundant. About 85% of the sheeted dikes strike north 010° - 060° west (inset in figure 4.9). The unfolded data in figure 4.9 could give the orientation of the dikes at the spreading center and, thus, the inferred orientation of the ridge axis.

The subvertical tilt axis T in figure 4.8 becomes horizontal (T^R) with unfolding (figure 4.9). However, the restored tilt axis T^R is not parallel to the maximum of the strike of the dikes (inset in figure 4.9). Two interpretations of these data are presented: (1) tilting of the dikes occurred near the ridge axis (evidence for 'oceanic' faulting discussed above), but the rotation axis T^R was not parallel to the ridge axis; (2) 'oceanic' tilting of the dikes occurred around a rotation axis parallel to the spreading ridge. However, later deformation (e.g., ~ 149 Ma ductile-brittle deformation, Cretaceous folding) resulted in variable, but minor rotations of the domains outlined in figure 4.7. Therefore, the inferred axis T (figure 4.8) or T^R (figure 4.9) does not represent the rotation axis for 'oceanic' tilting of the dikes, but is a combination of mostly 'oceanic' tilting and minor tilting during later deformation.

To summarize, the sheeted dike complex is subdivided in several domains each characterized by dikes having similar attitude (figure 4.7). Domains B and F are separated by faults containing cement alteration typical of seafloor hydrothermal metamorphism. The deformation of the sheeted dike

complex in the Rogue Wilderness ophiolite, such as the progressive 110° to 200° clockwise change in strike, may have occurred due to variable rotation of rigid fault blocks at the spreading center. Restored structural data from the sheeted dike complex (figure 4.9) suggest that the trend of the ridge-axis is north 010°-060° west, and that 'oceanic' tilting could have occurred oblique to the ridge axis.

4.6.2 Igneous layering

The igneous layering in the Rogue Wilderness ophiolite, clearly visible in most screens of cumulate gabbro in the sheeted dike complex, is defined by the alignment of tabular plagioclase (planar lamination) and numerous concordant lenses¹ or layers of anorthosite and mesocratic cumulate gabbro (chapter 2). The alignment of euhedral to subhedral plagioclase (chapter 2, figure 2.28) may have occurred during flow and/or compaction of a partially crystallized cumulate gabbro (Nicolas, 1992).

Although only a rough estimate of the angle between dikes and igneous layering can be made because of the large variation of the attitude of the igneous layering, it becomes clear that the cumulate layering occurs at a high-angle with respect to the sheeted dikes (figure 4.7). For example, the subvertical igneous layers in domains A and B strike approximately north (figure 4.7), and the acute angle between the northwest-striking dikes and the igneous layering ranges between 50° and 80°. Similarly, the cumulate layering in domain F is at a high angle to the north-south striking dikes, and the acute angle between the dikes and the northeast-striking igneous layering in domain F is about 60°. Obviously, the cumulate gabbro and the sheeted dikes were rotated as coherent blocks (around the subvertical axis T). The angle between the dikes and cumulate layering is about 60° in the Josephine ophiolite ~40-50 km southwest of the thesis area (Harper, 1982).

After unfolding using the rotation axis R, the dikes in domains A and B are subvertical and strike, on average, north 040° west (figure 4.9), and the mean igneous layering strikes north 045° west and dips 35° southwest. The ridge-axis was probably oriented about north 045° west parallel to the strike of the

¹ Lenses of anorthosite having sharp boundaries are often not quite concordant.

subvertical dikes and the strike of the southwest-dipping igneous layering (discussed in section 4.8.2 in more detail).

Sinton and Detrick (1992) show, based on seismic refraction and tomography from mid-ocean ridges, that a large, mainly molten magma chamber beneath the ridge axis does not exist. Therefore, it is more likely that the layers and shape fabric in ophiolitic gabbros were generated during magmatic/ductile flow of a crystal mush with as little as 10% melt present (Nicolas et al., 1993). The geometry of the flow of the crystal mush, which is recorded in the layered and foliated gabbros (Nicolas et al., 1988, Nicolas, 1992), may be controlled by the shape of the magma chamber and driven by the flow of the underlying mantle. Thus, the layering and foliation of ophiolitic gabbros may provide important clues to infer the spreading structure of the ophiolite (e.g., Dewey and Kidd, 1977)

4.6.3 Amphibole shear bands and amphibole veins

Numerous, up to 1 cm wide amphibole veins and shear bands crosscut the cumulate gabbro screens in the sheeted dike complex (chapter 2, figure 2.29). The shear bands and amphibole veins cut the igneous layering at high angles and are subparallel to the sheeted dikes (figure 4.7, domains A and B). The igneous layering is offset along the amphibole shear bands, so shear clearly occurred. The amphibole veins and shear bands are not found in the dikes. They are cut by dikes, and thus formed before the intrusion of the dikes.

In thin section, the shear bands and amphibole veins consist of variably colored, brown to pale green amphibole. Unfortunately, microstructures that would conclusively indicate the main mechanism of deformation were not found. High-T ductile deformation may have been important, however, any trace of crystal plastic deformation is obliterated by later, pervasive hydrothermal alteration that has replaced amphibole. The planar lamination near the shear band shown in figure 2.29 (chapter 2) is rotated into a parallel orientation with the shear band, and several laths of amphibole are bent suggesting dextral offset. Bending of amphibole and rotation of the planar lamination into parallelism with the shear band suggest ductile deformation. Other shear bands do not show any rotation of the planar lamination and have broken laths of amphibole suggesting brittle failure and cataclastic flow occurred in some of the shear bands.

Amphibole veins that show no offsets across them are likely to represent pure extensional structures (mode I cracks). Thus, the structures that formed most likely by tensile parting include the dikes and the amphibole veins. Both structures are roughly parallel (figure 4.7) and probably formed under the same regional stress field. Since tensile fractures tend to form perpendicular to the direction of the minimum stress, the σ_3 -direction can be inferred from the orientation of the dikes and the amphibole veins. The poles to all extensional structures in domains A and B are contoured in figure 4.10a to illustrate the approximate direction of the minimum principal paleostress axis σ_3 . The σ_3 -direction in domains A and B is approximately given by the maximum contoured area of 15.3 % per 1% area. This maximum indicates a σ_3 direction plunging 10° towards 220° .

In several outcrops, the igneous layering is offset up to 10 cm along thin amphibole shear bands (chapter 2, figure 2.29). Unfortunately, a striation or stretching lineation in the shear bands could not be measured directly in the field. However, when at least two marker layers with different attitudes are offset by the same shear band, the plunge and trend of the slip line can be determined. The data collected in the field include the attitudes of several shear bands and marker layers as well as the magnitude and direction of the apparent offsets indicated in the plane of the outcrop. Using these data, the trend and plunge of the slip line and the sense of slip along eleven shear bands was determined. Four shear bands were determined in domain A, seven in domain B. The data of the attitude of shear bands and their associated slip directions are listed in appendix D (table D2) and are shown in a 'Hoepfner-plot' in figure 4.10b. In the present coordinates, nine shear bands are right-lateral strike-slip faults, and most of them have a small thrust-component. The remaining two shear bands are normal faults with a small left-lateral component.

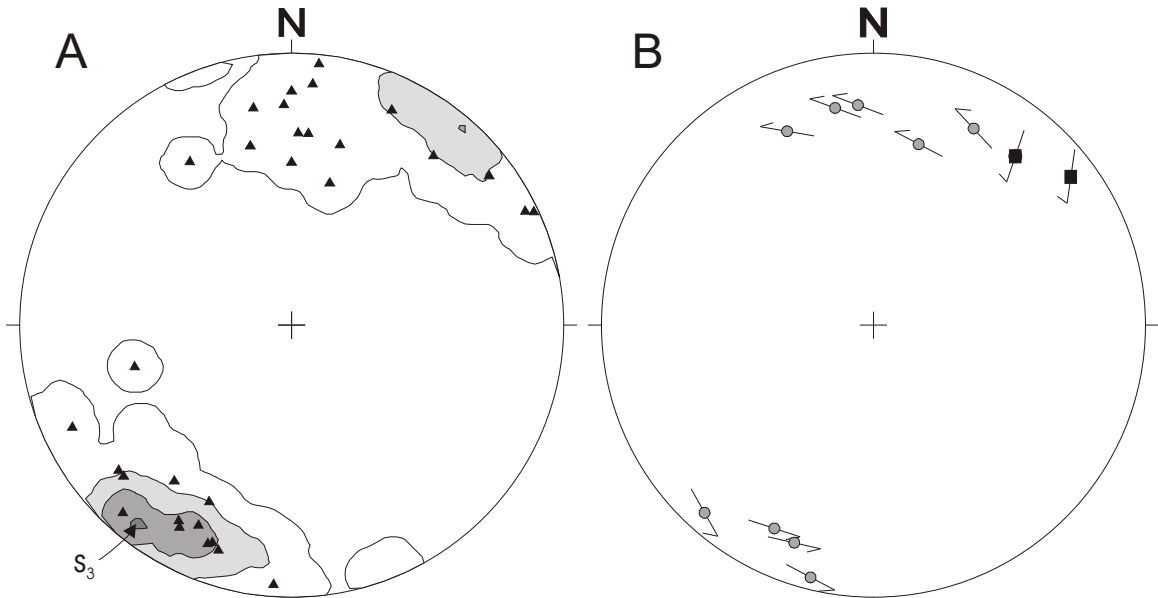
The results of the stress inversion using the data set plotted in figure 4.10b are shown in figure 4.10c and 4.10d. Using ROMSA (Lisle, 1988), the maximum principal stress σ_1 is determined with an azimuth of 131° and a plunge of 29° . The results returned by ROMSA (figure 4.10c) are compared with the results produced by three other stress inversion programs. Overall, the solutions of these four stress inversion techniques agree well (figure 4.10d). The solution obtained by ROMSA has a compound likelihood (P_{Total}) of 100%. This high value of P_{Total} implies that the solution is compatible with all of the shear band data. Furthermore, the best σ_3 -direction returned by ROMSA ($228^\circ / 15^\circ$) and the other stress

Figure 4.10

Analysis of structural data of domains A and B: Lower hemisphere, equal area stereographic projections of contoured poles to dikes and amphibole veins (a), of poles to shear bands (b), and the results of the paleostress analysis (c, d) using data shown in (b).

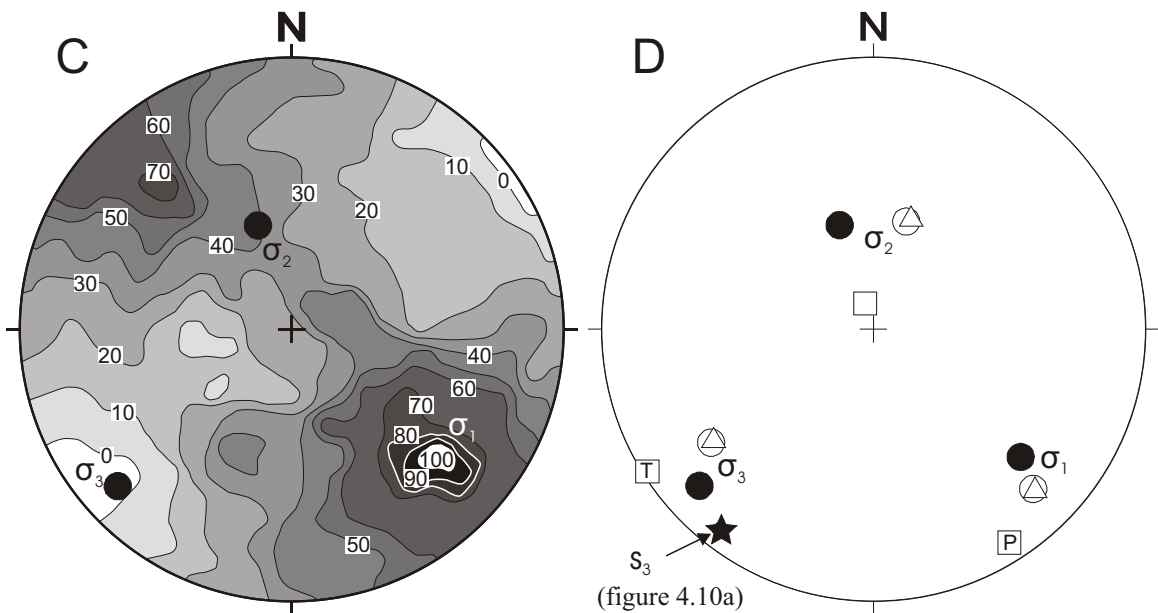
- a. The poles to dike margins ($n = 139$) and amphibole veins ($n = 31$) in domains A and B are contoured. The contour intervals are given in percent. Additionally, the poles to amphibole veins are shown. The amphibole veins shown in this diagram indicate no offsets, and the dikes and amphibole veins are interpreted to have formed by tensile fracturing (mode 1 cracks). The direction of maximum extension (minimum principal stress σ_3) is given by the maximum of the contoured poles to dike margins and amphibole veins.
- b. Poles to amphibole shear bands and their slip vectors (Hoepfener, 1955). The arrows affixed to the poles to shear bands indicate the direction of slip of the hanging wall block (see figure 4.3).
- c. Paleostress solution for the shear bands illustrated in figure 4.10b ($n = 11$) using ROMSA (Lisle, 1988). The contours express the most probable orientation of σ_1 ($131^\circ / 29^\circ$). The maximum compound likelihood is $P_{\text{Total}} = 100\%$. The corresponding σ_2 and σ_3 orientations are $341^\circ / 57^\circ$ and $228^\circ / 15^\circ$, respectively. Note that calculated σ_3 corresponds to estimate of σ_3 in figure 4.10a.
- d. Comparison of the results of the paleostress analysis for the amphibole shear bands illustrated in figure 10b using four different programs: filled circle - ROMSA (Lisle, 1988); open circle - TENSOR (Angelier, 1979); square - FAULTKIN (Allmendinger et al., 1994); triangle - STRESS (Reches, 1987). Note that the FAULTKIN returns the orientations of the compressional (P) and extensional axis (T). Small differences exist between the principal stress axis computed by the various programs. Note that the estimate for σ_3 (tensile fractures, figure 4.10a) is very close to the minimum principal stress axis computed for the shear band data.

Amphibole veins and shear bands, domain A and B



Contours include dikes ($n = 139$) and amphibole veins ($n = 31$) of domains A and B
 contour lines: 0.6, 5.3, 10.0, 15.3% / 1% area
 ▲ poles to amphibole veins

● Right-lateral strike-slip/oblique-slip faults ($n = 9$)
 ■ Normal faults ($n = 2$)



ROMSA

(figure 4.10a)

● ROMSA △ STRESS
 ○ TENSOR □ FAULTKIN

inversion programs (figure 4.10d) agree well with the estimate of the minimum principal stress axis inferred from the structures that are interpreted to have formed by tensile fracturing (figure 4.10a).

To correct for Tertiary and Cretaceous folding, the structural data from domains A and B, must be rotated around axis R.(045° / 00°) in a clockwise direction. After unfolding, the amphibole veins and shear bands in domains A and B are subvertical to moderately steep and strike, on average, north 045° west (see section 4.8.2). The amphibole shear bands with right-lateral offset (figure 4.10b) become steeply dipping shear bands with normal displacement, and those with normal displacement (figure 4.10b) become steeply dipping shear bands with right-lateral offset after correcting for Tertiary and Cretaceous folding.

Furthermore, the direction of the reoriented maximum principal stress σ_1^R is subvertical and the direction of the re-oriented minimum principal stress σ_3^R is perpendicular to the strike of the dikes, which is consistent with tectonic extension at the spreading center in a direction perpendicular to the dikes.

4.6.4 Cemented faults

Cemented faults are an important feature of the sheeted dike complex. The cemented faults may have formed at or near the ridge axis (~ 164 Ma) under the same stress field as the sheeted dikes, amphibole veins and shear bands. If the faults can be constrained to have formed at or near the ridge axis, a model of the fault- and spreading- geometry of the ophiolite at mid-crustal level can be developed.

Almost all faults in the sheeted dike complex are cemented and crosscut by veins. The cemented fault gouge and the veins contain mineral assemblages characteristic of subseafloor hydrothermal alteration (chapter 2, figures 2.24 and 2.35). Those faults which are not cemented usually exhibit extremely lustrous, striated surfaces; these faults may have formed or reactivated relatively late (Tertiary?), and are, therefore, not included in this analysis. In this study, only faults that are cemented with epidote \pm quartz or prehnite \pm quartz are analyzed. These faults are easily recognized in water-polished outcrops: the fault gouge that is cemented by epidote \pm quartz is pistachio-green, and the gouge cemented by prehnite \pm quartz is white and appears chalky where weathered. Most of the faults have a thickness less than 5 cm, and are probably minor faults and subsidiary shear fractures. Only 10% of the measured faults have a thickness greater than

5 cm and appear to be major faults with substantial offset (offset larger than outcrop). Typically, the faults can be traced only for a few decimeters to meters, because they get covered or they cannot be traced across crosscutting faults (perhaps they end in crosscutting fault). Most fault surfaces are approximately planar at this scale, and only some are curved or irregular. In these cases, several measurements were necessary to obtain an average orientation in order to reduce the ambiguity of the attitude. Overall, there was little or no ambiguity concerning the attitude of the faults.

The exposed fault surfaces are partially or completely covered with lineated, cemented gouge. Often, only remnants of the cemented gouge are present, and the striated wall rock underneath is exposed (chapter 2, figure 2.34). The ridges and grooves in the fault surfaces and the lineated gouge can be used to ascertain the direction of slip along the fault. Probably, the grooves in the wall rock formed by 'asperity ploughing' (Means, 1987). When the cemented gouge is chipped away from the wall rock, one can see that the cemented gouge often forms a cast of the ridges and grooves created by asperity ploughing.

In a water-polished outcrop (O/C-7), a dike is parallel to other dikes in the lower half of the outcrop but bends sharply 30° to 40° following the orientation of a cemented fault. Thus, at least one of the faults is intruded by a diabasic dike. This is interpreted as an 'oceanic' fault because the fault formed before the intrusion of the dike. If all faults in the data set are oceanic in origin, insights into the fault- and spreading-geometry at mid-crustal levels of the ophiolite may be gained. This requires also that the sheeted dike complex can be uniquely restored to paleohorizontal.

The veins and faults in the data set are interpreted to have formed near the ridge axis for the following reasons: (1) at least one fault was intruded by a dike; (2) the mineral assemblages in faults and adjacent wall rocks are typical of hydrothermal metamorphism; and (3) the geometry of the faults after restoring to paleohorizontal is consistent with this interpretation (discussion in section 4.8.2). However, many of the faults and veins analyzed in this study may also have formed during later episodes of deformation which were also characterized by retrograde hydrothermal alteration (chapter 2). For example, the ductily deformed muscovite-garnet tonalite having a muscovite $^{40}\text{Ar}/^{39}\text{Ar}$ cooling age of 149 Ma in the metagabbro unit is cut by prehnite veins and contains mineral assemblages typical of greenschist facies hydrothermal metamorphism.

4.6.4.1 Domains A and B

Within domains A and B (see figure 4.7 for location), the attitude of 145 epidote- and prehnite-cemented faults and the orientation of the corresponding striations were measured. The sense of slip of 54 of the 145 faults was determined using offset markers and the criteria for the sense of movement on slickenside fault surfaces of Petit (1987). For clarity, the fault data for which the sense of slip is not known are shown in figure 4.11a (n=91), while the data of faults with known sense of slip are shown in figure 11b (n=54). The fault slip data are listed in appendix D (table D3). Comparing figures 4.11a and 4.11b, it becomes clear that the data in figure 4.11b represent an almost equivalent subset of the total data in terms of attitudes of the faults and orientation of the slickenside lineation. The frame of reference is given by the contoured poles to the dikes as illustrated in figure 4.11a.

A strong clustering of the poles to faults, corresponding to conjugate fault sets, is not observed. The distribution appears almost random. Note that the data set includes abundant secondary fractures which formed near major faults or fault zones. The geometry of several small faults with respect to a large fault was determined suggesting that some of the small faults could be R, T, and R'-type fractures. Only 10% of all faults occur parallel to the dikes or cut dikes at very low angles, and they plot within the 5% per 1% area contour line (figure 4.11a).

The faults are subdivided according to their main component of displacement in the present-day coordinates: the bulk of the faults are thrusts (n = 21), followed by left-lateral (n = 16) and right-lateral (n = 15) strike-slip faults of which most also have a significant thrust component. Only two faults indicate predominantly normal displacement. Many of the right-lateral strike slip faults (with a small thrust component), cutting dikes at low angles (figure 4.11b), are very similar in orientation and displacement to the amphibole shear bands (figure 4.10b). Probably, these cemented faults formed during the same episode of deformation, but at lower temperature under the same stress field as that which produced the amphibole veins and shear bands, explaining the same attitude and displacement.

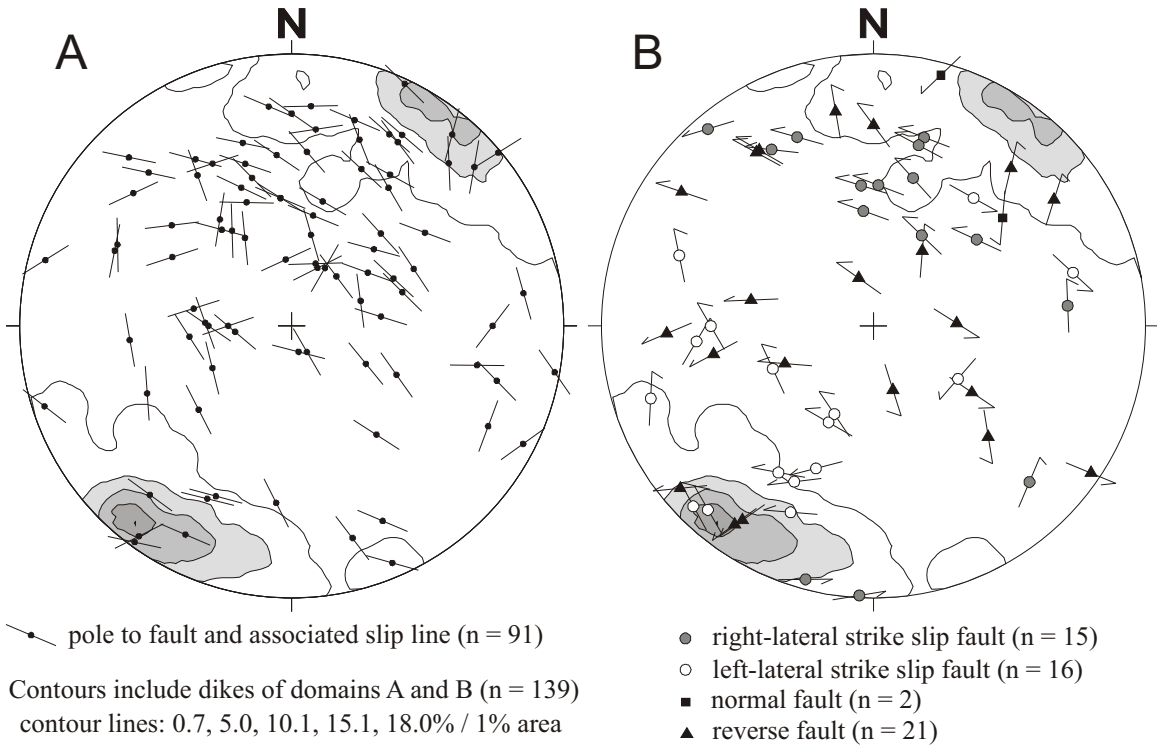
As discussed in section 4.2, the orientation of the fault planes and the sense and direction of slip (figure 4.11b) can be used to compute the stress tensor which best satisfies all fault data. To solve this inverse problem, four different stress inversion programs are applied. The results of the stress inversion

Figure 4.11

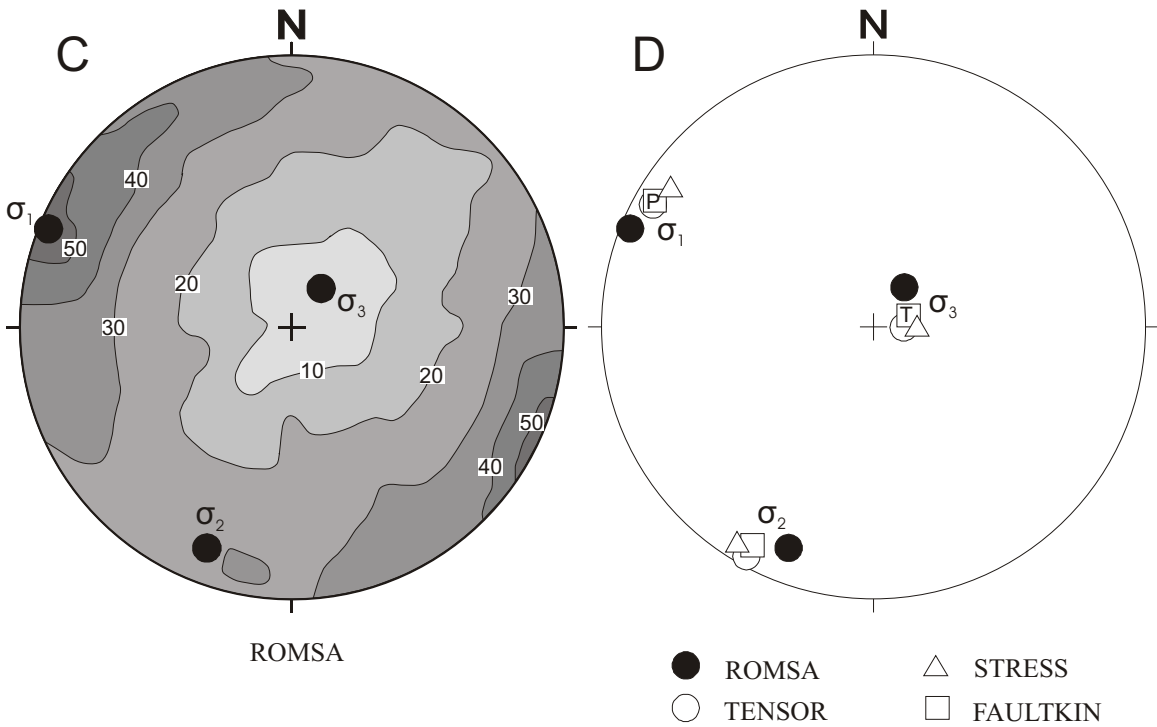
Analysis of structural data of domains A and B: Lower hemisphere, equal area stereographic projections of poles to cemented faults superimposed on contoured poles to dikes (a, b), and the results of the paleostress analysis (c, d) using data shown in (b).

- a. Poles to 91 cemented faults (filled circles) superimposed on the contoured plot of poles to dikes. The direction of slip along the fault is indicated by the line affixed to the poles similar to the Hoepfner plot in figure 4.3. The sense of slip was not determined in outcrop, therefore, only the directions, but not the sense of slip are shown.
- b. Poles to 54 cemented faults where sense of shear could be determined and their slip vectors (Hoepfner, 1955). The arrows affixed to the poles to cemented faults indicate the direction of slip of the hanging wall block (see figure 4.3).
- c. Stress inversion solution for cemented faults of figure 4.11b ($n = 54$) using ROMSA (Lisle, 1988). The contours (in %) express the most probable orientation of σ_1 ($292^\circ / 04^\circ$). The maximum compound likelihood is $P_{\text{Total}} = 56.4\%$. The calculated σ_2 and σ_3 orientations are $201^\circ / 14^\circ$ and $038^\circ / 75^\circ$, respectively.
- d. Comparison of the results of the paleostress analysis using four different programs: solid symbol - ROMSA (Lisle, 1988); circle - TENSOR (Angelier, 1979); square - FAULTKIN (Allmendinger et al., 1994); triangle - STRESS (Reches, 1987). The principal stress axes computed by the four different programs for the fault slip data shown in figure 4.11b agree well. Note that the principal stress axes σ_2 and σ_3 are switched compared to the axes shown in figure 4.10d. The σ_1 -directions in figures 4.10d and 4.11d are subparallel.

Brittle faults, domain A and B



Contours include dikes of domains A and B (n = 139)
contour lines: 0.7, 5.0, 10.1, 15.1, 18.0% / 1% area



using ROMSA are shown in figure 4.11c and are compared to the solutions obtained applying three other techniques (figure 4.11d). Using ROMSA (Lisle, 1988), the maximum principal stress σ_1 is determined with an azimuth of 292° and a plunge of 04° . The best σ_3 -direction returned by ROMSA is $038^\circ / 75^\circ$. Knowing the σ_1 - and σ_3 -directions, σ_2 ($201^\circ / 14^\circ$) is determined stereographically. As illustrated in figure 4.11c, the maximum compound likelihood for $X = 292^\circ / 04^\circ$ being the direction of σ_1 is very low ($P_{\text{Total}} = 56.4\%$). This low value implies that just more than half of the fault data are compatible with the obtained solution. Possible explanations for this low value are: (1) the fault slip data include faults that were active during more than one deformational event in which each event had a different regional stress field, or (2) it includes faults that did not move in the direction of the shear stress, such as transfer faults. In transfer faults, slip is controlled by the interaction between differentially moving faults, so it violates a basic assumption in the paleostress analysis (section 4.2). However, the results produced by ROMSA are almost identical with the solutions of the other stress inversion programs (figure 4.11d).

Interestingly, the principal stress axis σ_2 in figure 4.11d is approximately parallel to the σ_3 -direction in figure 4.10d, which is subhorizontal and roughly perpendicular to the strike of the dikes, while the maximum principal stress directions in figures 4.10d and 4.11d are subparallel. In both figures, the σ_1 -directions are subparallel to the strike of the dikes. If the stress field would have remained exactly the same after the formation of the amphibole veins and shear bands (and if the veins formed near or at the ridge axis), all three principal stress axes in figures 4.11d should be subparallel to the principal stress axes in figure 4.10d. This suggests that either the regional stress field changed after the formation of the amphibole veins and shear bands and the intrusion of the dikes, or many (or all of the) cemented faults formed off-axis under a different stress field, or a combination of both, or other assumptions made in the paleostress analysis are not satisfied (section 4.2).

The structural data from domains A and B must be corrected for Cretaceous and Tertiary folding (rotation around axis R). After unfolding, most of the strike slip faults in figure 4.11a and 4.11b become normal faults (detailed discussion in section 4.8.2), and the strike directions of the normal faults are subparallel to the strike of the restored dikes or occur at low angles to the dikes. Abundant normal faults are consistent with an extensional environment at the ridge axis. However, a large number of strike-slip

faults are still present after correction for Cretaceous and Tertiary folding. Most strike slip faults occur at high angles with respect to the strike of the dikes, suggesting they could be transfer faults. This could explain the low maximum compound likelihood for obtained solution (figure 4.11c).

The direction of the reoriented maximum principal stress σ_1^R is subvertical and the direction of the reoriented minimum principal stress σ_3^R is parallel to the strike of the restored dikes. This is not consistent with tectonic extension at the spreading center in a direction perpendicular to the dikes. Possible explanations will be discussed in section 4.8.2 in more detail.

4.6.4.2 Domain D

Within domain D (see figure 4.7 for location), the attitude of 24 cemented faults and the orientation of the corresponding striations and sense of slip were determined (appendix D, table D4). For reference, the contoured stereographic projection of the poles to dikes in domain D is shown in figure 4.12a. The steeply dipping dikes strike north-south, and, as previously discussed, they are tilted about 60° to 70° clockwise around the axis T with respect to the dikes of domains A and B (figure 4.8). With an anti-clockwise rotation of 70° (or 290° clockwise) about axis T, the dikes of domain D can be reoriented so that they have attitudes similar to the dikes in domains A and B (figure 4.12a).

The fault slip data are plotted in a stereographic projection and are subdivided according to their main component of slip (figure 4.12b). Half of the faults analyzed in domain D ($n = 12$) are right-lateral, 5 are left-lateral strike slip faults and 7 are thrust faults in present-day coordinates. Similar to the cemented faults in domains A and B (figure 4.11b), some of the faults that are subparallel to the sheeted dikes are right-lateral transform faults (figure 4.12b). It is not clear whether all of the faults contained in this domain underwent a clockwise rotation of 60° to 70° around T (figure 4.8), or whether the faults formed during and/or after the rotation of the dikes with respect to domains A and B.

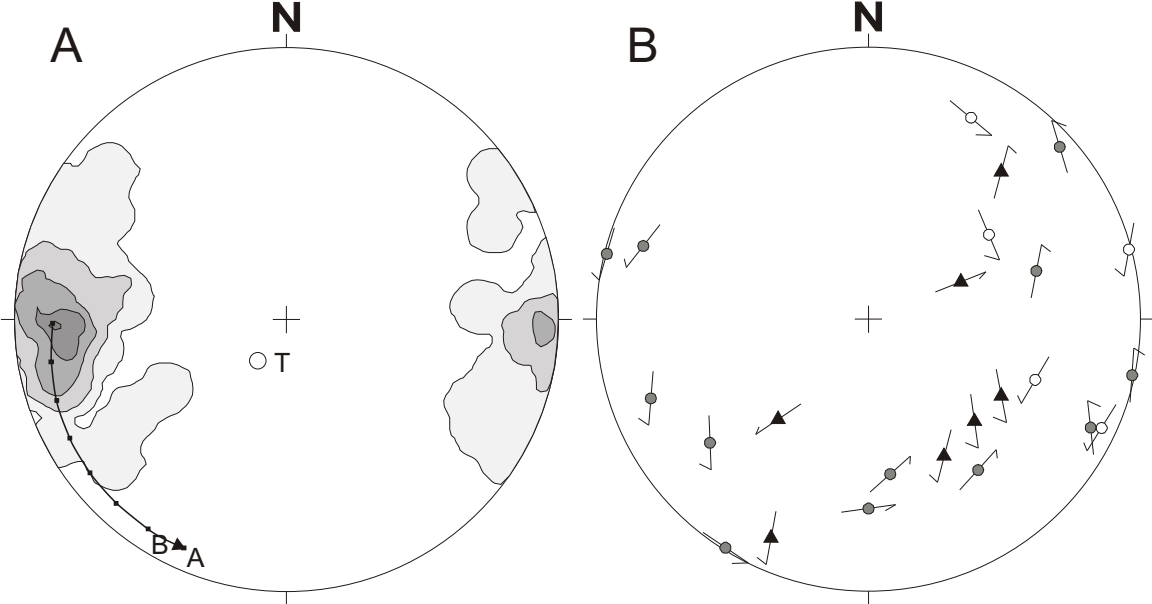
The orientation of the principal stress axis were determined using the fault slip data plotted in figure 4.12b and four different stress inversion programs. The results of the stress inversion using ROMSA are shown in figure 4.12c and are compared to the solutions obtained from three other techniques (figure 4.12d). Using ROMSA (Lisle, 1988), the maximum principal stress σ_1 is determined with an azimuth of

Figure 4.12

Analysis of structural data of domain D: Lower hemisphere, equal area stereographic projections of poles to dike margins (a), of poles to cemented faults (b), and the results of the paleostress analysis (c, d) using data shown in (b).

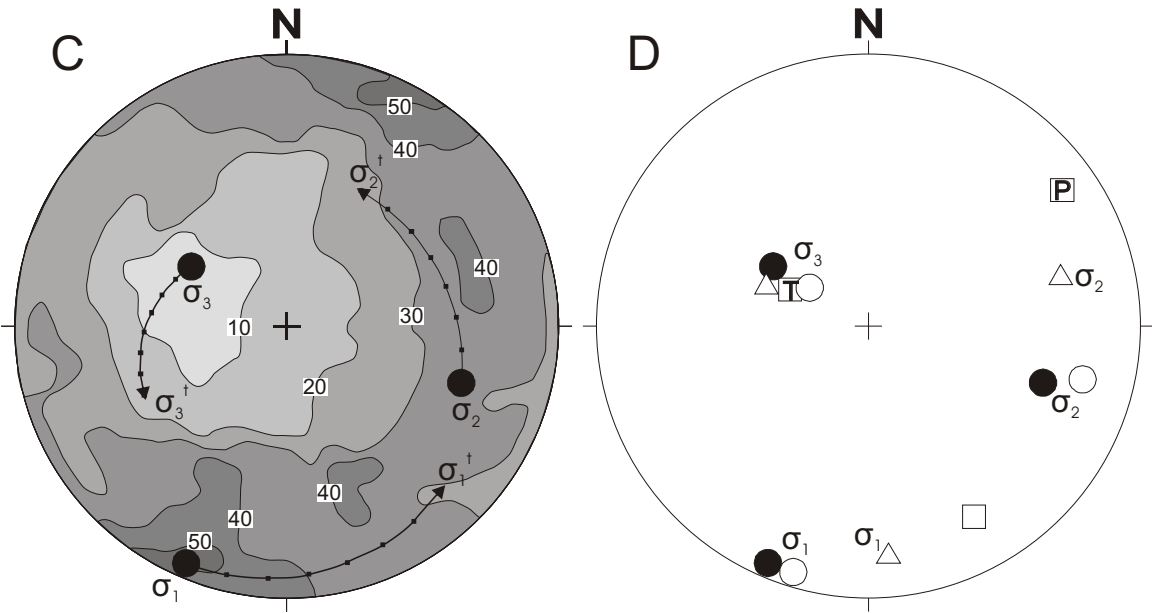
- a. Contoured plot of poles to dikes in domain D. The contour intervals are given in percent. The dikes in domain D are rotated $60^\circ - 70^\circ$ clockwise around a subvertical axis ($T = 215^\circ / 75^\circ$) with respect to the mean poles of dikes of domains A and B shown as “A” and “B” (figure 4.8, also compare figures 4.11a and 4.12a). The arrow indicates the position of the maximum contour assuming an anti-clockwise rotation of the mean dike pole to that of A by 70° around T.
- b. Poles to cemented faults and their slip vectors (Hoeppener, 1955). The arrows affixed to the poles to cemented faults indicate the direction of slip of the hanging wall block (see figure 3). Most faults suparallel to the sheeted dikes are right-lateral transfer faults.
- c. Paleostress analysis solution for cemented faults illustrated in figure 12b ($n = 24$) using ROMSA (Lisle, 1988). The contours express the most probable orientation of σ_1 ($203^\circ / 06^\circ$). The maximum compound likelihood is $P_{\text{Total}} = 56.4\%$. The corresponding σ_2 and σ_3 orientations are $108^\circ / 33^\circ$ and $302^\circ / 56^\circ$, respectively. The arrows show the position of the principal stress axes after the cemented faults are rotated 70° in an anticlockwise direction around tilt-axis T.
- d. Comparison of the results of the paleostress analysis using four different programs: filled circle - ROMSA (Lisle, 1988); open circle - TENSOR (Angelier, 1979); square - FAULTKIN (Allmendinger et al., 1994); triangle - STRESS (Reches, 1987). Significant differences exist between the principal stress axes computed by the four different programs for the data shown in figure 4.12b. Note that the principal stress axes σ_1 and σ_2 are variable whereas all programs computed similar σ_3 -directions.

Brittle faults, domain D



Contours include dikes of domain D (n = 58)
 contour lines: 1.7, 5.2, 10.3, 15.5, 19.0% / 1% area

- right-lateral strike-slip faults (n = 12)
- left-lateral strike-slip faults (n = 5)
- ▲ reverse faults (n = 7)



- ROMSA
- TENSOR
- △ STRESS
- FAULTKIN

203° and a plunge of 06°. The best σ_3 -direction returned by ROMSA is 302° / 56°, and the stereographically determined σ_2 -direction is 108° / 33°. Similar to the paleostress analysis for faults in domains A and B (figure 4.11c), the maximum compound likelihood P_{Total} for $X = 203^\circ / 06^\circ$ being the direction of σ_1 is low ($P_{\text{Total}} = 54.2\%$), implying almost half of the fault data are incompatible with the obtained solution. Note that all programs computed very similar directions for the minimum principal stress σ_3 (figure 4.12d). However, the σ_1 - and σ_2 -directions vary, and significant differences exist between the solutions of the various programs. Only the results obtained from ROMSA (Lisle, 1988) and TENSOR (Angelier, 1979) overlap.

The positions of the principal stress axes of ROMSA are illustrated after an anti-clockwise rotation of 70° around the axis T and labeled σ_1^T , σ_2^T and σ_3^T (figure 4.12c). If all of the cemented faults formed prior to the rotation of the dikes relative to domains A and B and were not reactivated during this deformation, the restored stress axis σ_1^T , σ_2^T and σ_3^T should overlap with the principal stress axis σ_1 , σ_2 and σ_3 computed for the cemented faults in domains A and B (figure 4.11c). This is not the case, although this rotation returns the direction of the maximum principal stress to an orientation subparallel to σ_1 in figure 4.11c. The analyzed fault populations in domains A, B and D probably contain faults that might have experienced slip prior to, during and/or after the rotation of the dikes.

The structural data from domain D must be corrected for Cretaceous and Tertiary folding (using axis R) similar to that of domains A and B. After unfolding, dikes in domain D dip moderately steep southwest (figure 4.). After unfolding, most faults in domain D are strike-slip faults, and there are only two normal faults that are consistent with extension perpendicular to the sheeted dikes. The number of strike-slip faults and reverse faults in present-day coordinates (figure 4.12d) are only slightly reduced after unfolding (detailed discussion in section 4.8.2). After correcting for Cretaceous and Tertiary folding, the minimum principal stress axis σ_3 , which is best constrained by the paleostress analyses in figure 4.12d, plunges gently southeast.

To restore the dikes, faults and principal stresses in domain D to paleohorizontal, two rotations have to be performed. The deformation path is thought to be as follows: (1) dikes of domain D were rotated around axis T with respect to dikes in domains A and B in late Jurassic time, probably near the

ridge axis (figure 4.9); (2) then, the entire ophiolite was rotated around R during Cretaceous and Tertiary folding. The low maximum compound likelihood for the best-fit σ_1 -direction (figure 4.12c) and the differences between the solutions of the various stress inversion programs (figure 4.12d) probably reflect this complexity. Thus, a well-constrained interpretation of the stress axes corrected for folding and near-ridge axis(?) deformation cannot be presented (discussed in detail in section 4.8.2). It is possible that the epidote and prehnite mineralized faults in domain D formed near the ridge axis and experienced slip prior to, during and/or after the rotation of the dikes around the subhorizontal axis T^R (figure 4.9).

4.6.4.3 Discussion of the fault geometry

When viewed in the present-day coordinates, normal faults are very rare in the sheeted dike complex, and strike-slip, oblique-slip, and reverse faults dominate in the investigated domains (figures 4.10b, 4.11b, and 4.12b). This is not consistent with the findings of many studies of modern oceanic crust (e.g. Escartin and Lin, 1998, Dilek et al, 1998) and ophiolites (e.g. Alexander et al., 1993, Dilek and Thy, 1998) describing the fault- and spreading- geometry of spreading centers. Geophysical evidence from mid-ocean and marginal-basin spreading ridges and field evidence from ophiolite studies support the idea that normal faulting along high- and low-angle faults (Mutter and Karson, 1992) at the ridge axis is an important process of crustal extension (e.g., Dilek and Thy, 1998; Mutter and Karson, 1990; Escartin and Lin, 1998). This implies that the sheeted dike complex has been rotated with respect to paleohorizontal.

A rotation axis R has been found to unfold structural data. The geological constraints for rotation around R are discussed in section 4.5. The structures in the sheeted dike complex, including the epidote and prehnite mineralized faults, were restored using these geological constraints. Many of the strike-slip, oblique-slip, and reverse faults in present-day coordinates become normal faults rotating the fault slip data around R (section 4.8.2). The occurrence of normal faults subparallel to the strike of the sheeted dikes imply structural extension perpendicular to the ridge axis, which is consistent with the findings of the studies of modern oceanic crust and ophiolites. Thus, the geometry of the normal faults can be seen as additional constraint for restoring the ophiolite to paleohorizontal using the rotation axis R. However,

differential rotation of rigid fault blocks seems to have occurred (rotation around T^R , figure 4.9) probably near the spreading axis and, thus, is older than Cretaceous and Tertiary folding (rotation around R).

4.7. Ductile to brittle deformation in the Blossom Bar shear zone, metatonalite and metagabbro units

4.7.1 Sense of shear criteria

There are a large number of studies and reviews describing criteria for deducing shear sense in quartzo-feldspathic rocks (e.g. Simpson and Schmid, 1983; Simpson, 1986, Hanmer and Passchier, 1991; Passchier and Trouw, 1996). Evaluations of shear sense indicators are also published (e.g., Simpson and Schmid; 1983), and Passchier and Williams (1996) discussed conflicting shear sense indicators in non-ideal sections (i.e. orientation of the plane of the outcrop, hand sample or thin section with respect to foliation and stretching lineation). There are also published reviews, discussions and evaluations of the sense-of-shear criteria with special reference to sheared mafic and ultramafic rocks indicating that most of the criteria, which are successfully applied to deduce the sense of shear in quartzo-feldspathic rocks, are also applicable to similar fabrics in mafic and ultramafic rocks (e.g., Norell et al., 1989, Cannat et al., 1991).

The criteria for deducing shear sense in quartzo-feldspathic rocks were used in this study, because most mylonitic rocks sampled in the Wild Rogue Wilderness are 'typical' quartzo-feldspathic mylonites consisting mainly of quartz, feldspar (plagioclase) and phyllosilicates (e.g., chlorite, mica). The sampled rocks consist of up to 60% plagioclase, although it is saussuritized (typically 80-100%) and appears cloudy in thin section. Most of the samples contain primary and/or secondary quartz (up to ~40 - 50 %), and chlorite (a phyllosilicate) is ubiquitous (appendix D, table D5). The sense of shear of a small number of ductily deformed mafic rocks was determined using the same criteria because similar fabrics were observed in quartz-rich and mafic samples. Not only these criteria, which were established in quartzo-feldspathic rocks, could be successfully applied for quartz-rich as well as mafic rocks from the Rogue Wilderness ophiolite, but also the nomenclature which is commonly used for deformed rocks of quartzo-feldspathic composition was largely retained (figure 4.13, table D5).

Figure 4.13

Summary of the criteria used to infer the sense-of-shear (after Passchier and Trouw, 1996, p. 105) in mylonitic rocks from the metatonalite unit, metagabbro unit and the Blossom Bar shear zone. First, the thin sections are cut parallel to lineation and perpendicular to foliation, then the sense of shear was determined and the thin sections were reoriented to determine the shear sense in present-day coordinates. Consistent results between samples were obtained (see text).

Figure 4.13a

- Grain shape fabric

An oblique foliation, also termed oblique grain shape fabric (GSF), occurs in samples containing monomineralic layers of recrystallized quartz. During non-coaxial progressive deformation, the fabric forming elements developing in the monomineralic layers do not track the rotating principal directions of finite strain (Means, 1981). Thus, the angular relationship between the mylonitic foliation and the elongate shape of most of the grains allow to deduce the shear sense if the oblique GSF developed during the formation of the mylonite. The geometric relationship between C and the elongate shape of the grains developing in sinistral shear is shown.

- S/C and C/C'

Hanmer and Passchier (1991) interpret S-planes ('schistosity') and C-planes ('cisaillement') as follows: S-planes represent a strain-sensitive flattening (*sensu lato*) fabric which attempts to track the XY plane of the finite strain ellipsoid during progressive deformation, while C-planes are discrete narrow shear zones which are taken to lie parallel to the flow plane of the progressive deformation. In a S/C fabric, C is a pervasive foliation and S is (ideally) deflected or cut by C-foliation. C'-planes are called asymmetric extensional shear bands because they lie at an angle with respect to the flow plane of the progressive deformation.

Figure 4.13a continued

- Microfaults in porphyroclasts

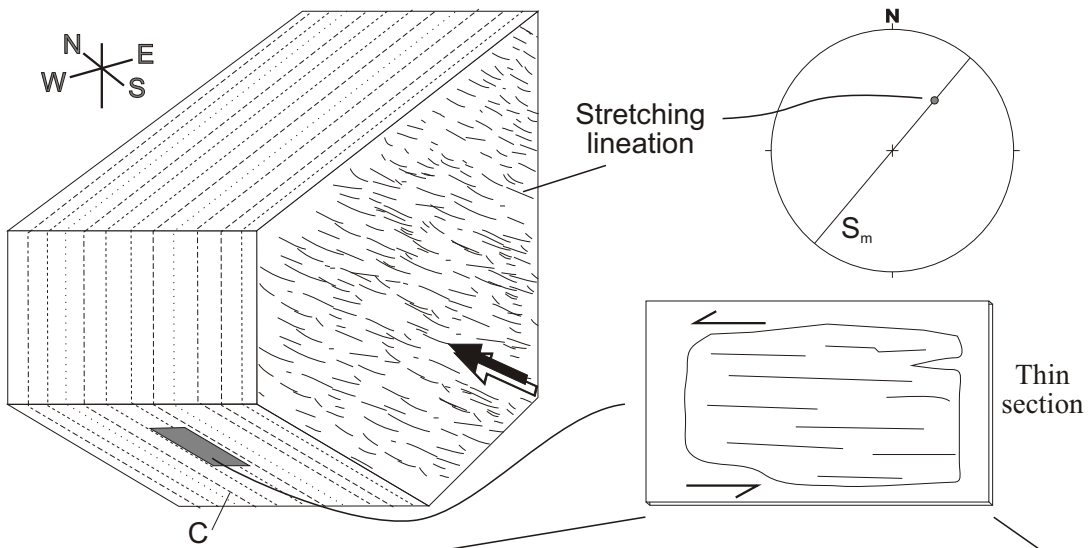
Rigid minerals occurring in a soft, plastically deforming matrix, often show cracks along weak planes, such as cleavage planes, apparently because they cannot accommodate large strains by crystal plastic mechanisms. With continued shearing the rigid grains rotate and the fragments of each grain slide past each other along the fractures, allowing grains to extend in the direction of flow (Hanmer and Passchier, 1991). Two types of microfaults are distinguished: high angle fractures (50° - 130°) with antithetic offsets and low-angle fractures (0° - 20° and 160° - 180°) with synthetic offsets. The angles in between (20° - 50° and 130° - 160°) are ambiguous because rotation of the fractured grain may cause initial high angle fractures to change orientation (Simpson and Schmid, 1983).

- Other sense of shear indicators

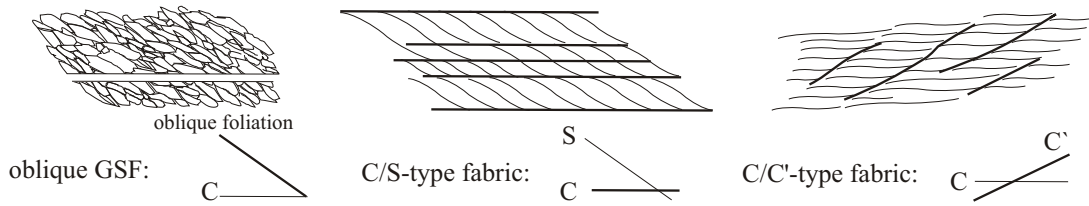
Other sense-of-shear indicators found in thin section include tiling of rigid minerals or mineral fragments and deformed quartz veins which could be used as displacement markers.

Hanmer and Passchier (1991) pointed out that tiling structures are not a reliable shear-sense indicator because the interpretation of the formation of the tiling structures is not unique. Therefore, the tiling structures are only reported as an additional shear sense indicator which may or may not agree with the other sense-of-shear criteria used in this study. Tiling structures are interpreted to form when rigid inclusions in a soft matrix are subjected to non-coaxial flow and interfere with each other and block each other's rotational behavior. In sinistral shear, the inclusions block at left-stepping overlaps forming structures resembling imbricated dominos or tipped books on a bookshelf.

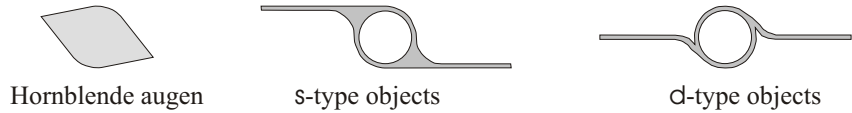
Several mylonites (appendix D) contain quartz veins which are less recrystallized than the quartz in the matrix. Quartz in the veins shows subgrains and undulatory extinction. Typically, the veins are less than 0.3 mm wide, they do not contain disseminated flakes of other minerals commonly found in the matrix, and the boundaries of the quartz veins are relatively sharp. These characteristics were used to trace the quartz veins under the microscope, and it was noted that some quartz veins are offset as they cut cloudy layers of fine-grained, fractured epidote and other Ca-Al-silicates. This was used to determine the sense of shear.



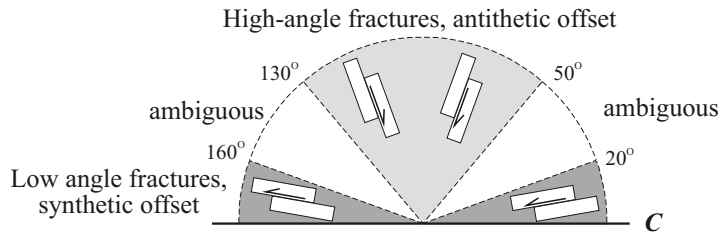
Foliation and shear bands:



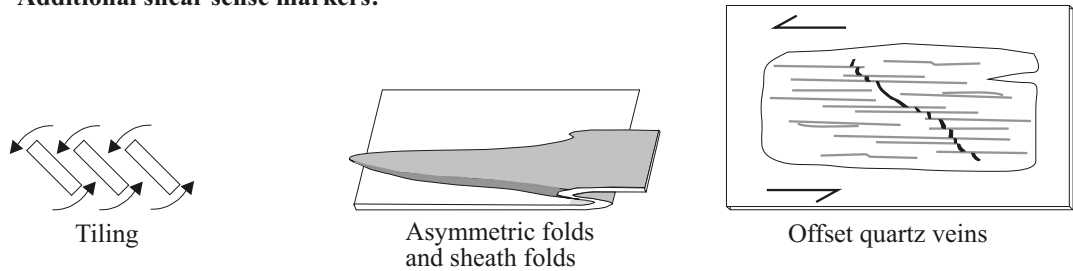
Porphyroclasts:



Microfaults in rigid inclusions:



Additional shear sense markers:



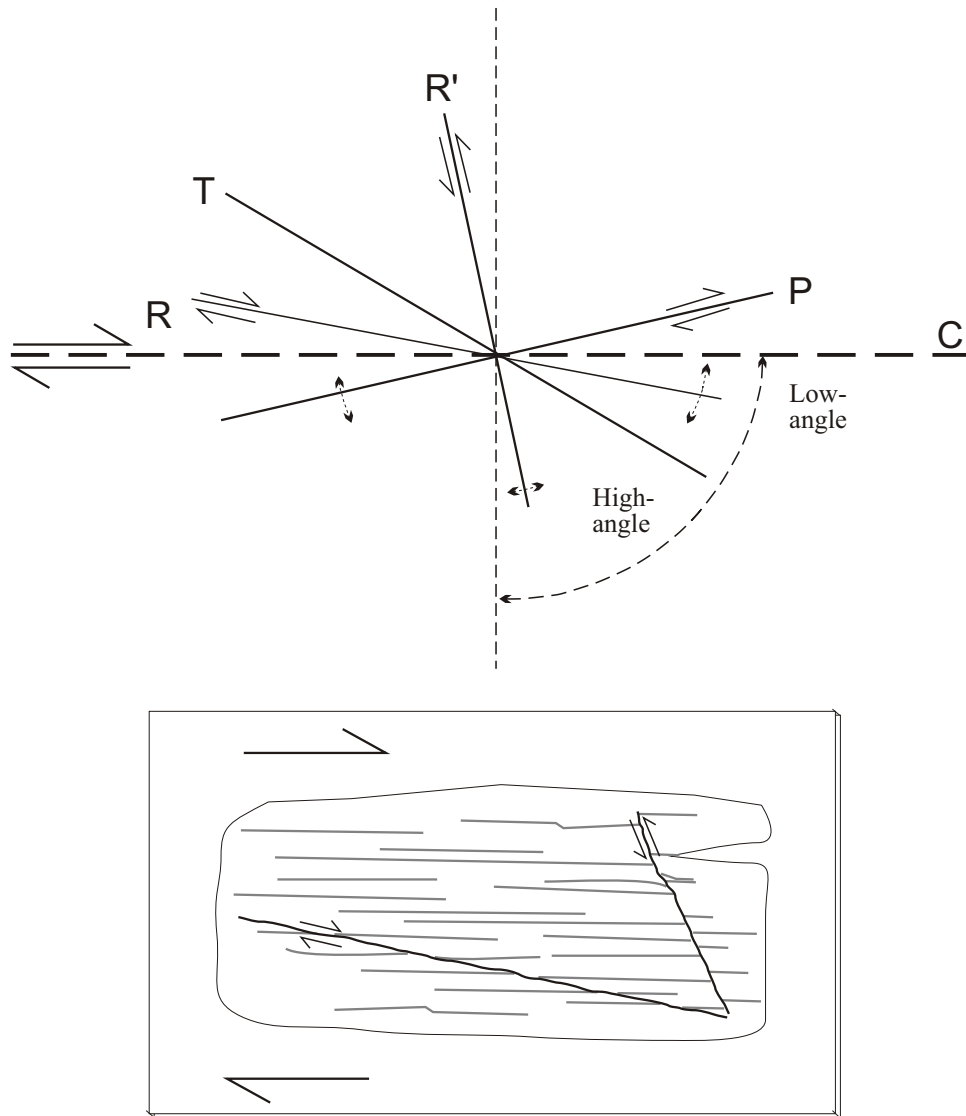


Figure 4.13b

Riedel-type shears

In thin sections, cut parallel to stretching lineation and normal to foliation, microfaults occur at high and low angles with respect to the mylonitic foliation (next page), and the mylonitic foliation is occasionally offset along such microfaults (typically < 0.2 mm offset). The sense of shear on these microfaults is interpreted as that of secondary shear fractures similar to Riedel shears in brittle fault zones.

The mylonitic foliation C, which is taken to lie parallel to the flow plane of the progressive deformation (Lister and Snoke, 1984), is defined by alternating lenses and layers with different mineral composition such as quartz rich and Ca-Al-silicate rich layers (e.g., figure 4.14e). Hand samples of fine-grained mylonitic rocks were cut and polished parallel to the foliation, and the orientation of the stretching lineation was determined on these polished surfaces (figure 4.13) often with the help of a magnifying stereoscope. The shear sense indicators and the fabric elements observed in thin section cut parallel to the mylonitic lineation and perpendicular to the foliation are schematically summarized in figure 4.13, and photomicrographs of representative fabrics are shown in figures 4.14a through 4.14e.

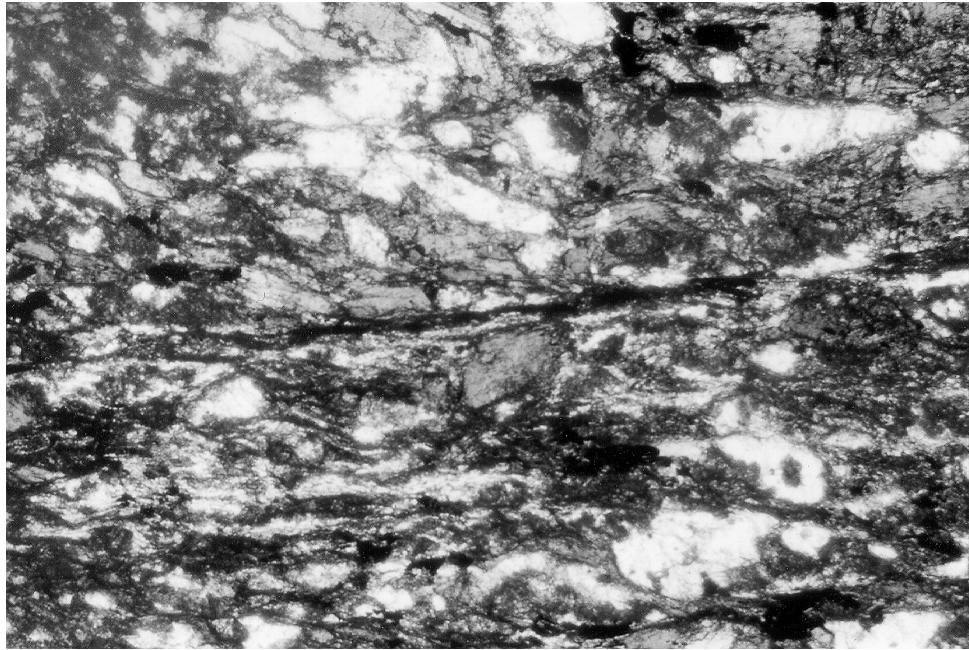
In thin sections, cut parallel to stretching lineation and normal to foliation, microfaults occur at high and low angles with respect to the mylonitic foliation (figure 4.13), and the mylonitic foliation is occasionally offset along such microfaults (typically < 0.2 mm offset). The geometry of some of the microfaults resemble that of anti-Riedel and Riedel-type secondary fractures (figure 4.13b). These microfaults, cemented with hydrothermal minerals (prehnite \pm quartz, quartz \pm sulfide, or pumpellyite), may be used, as additional shear sense indicators. The geometry of the secondary shear fractures and their displacement with respect to the main shear plane for sinistral shear is shown in figure 4.13b. The sense of shear inferred from these microfaults interpreted as Riedel-type shears is consistent with the other sense-of-shear indicators for samples from the metatonalite unit (O/C-9-S12), metagabbro unit (O/C-13-S22, O/C-371A, O/C-373b.4, O/C-371b.2 O/C-373C, and the Blossom Bar shear zone (O/C-17-S31) (appendix D, table D5).

After the shear sense in all of the thin sections was determined, the thin sections were reoriented to their position in the field as depicted in figure 4.13. The results, such as the attitude of the shear foliation, the orientation of the stretching lineation and the sense of shear, are summarized in appendix D (table D6). Note that the block diagram in figure 4.13 actually can be viewed as a model of the kinematic framework orienting the flow in the field. In highly strained rocks that underwent non-coaxial progressive deformation, as for example in studied mylonites, the finite strain ellipsoid (i.e. maximum finite strain X_p) as well as planar and linear features rotated towards the flow plane during deformation (e.g., Hanmer and

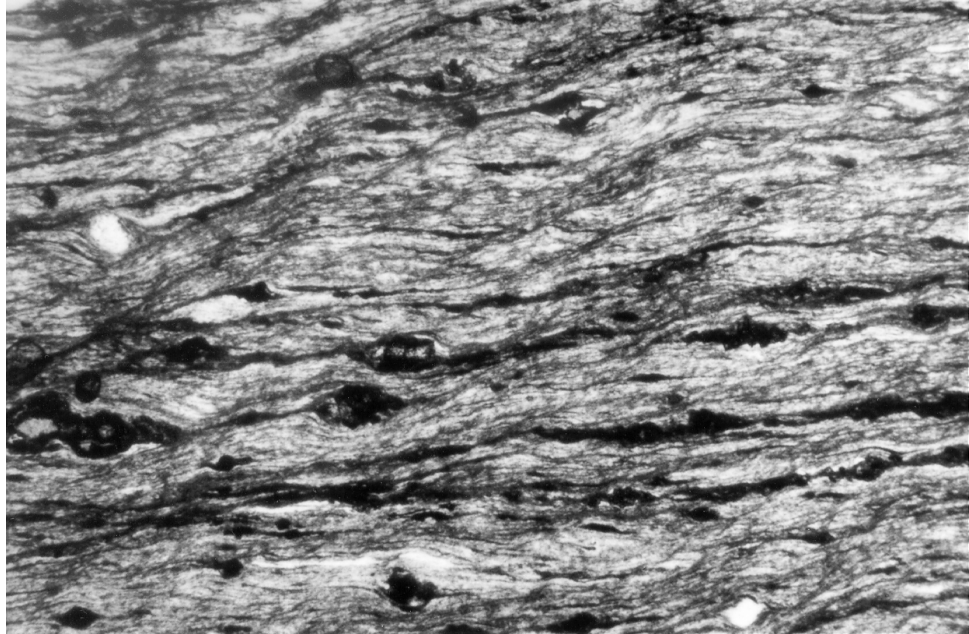
Figure 4.14

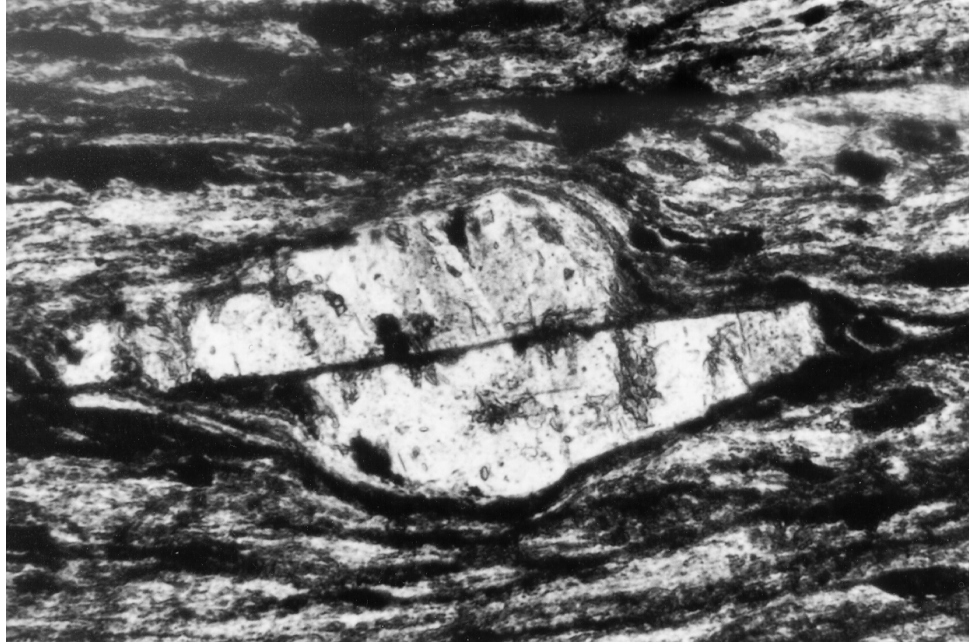
- A. Fabric in a mafic mylonite from the metagabbro unit (O/C-374b.4). This fabric has a similar geometry as S/C-type fabrics in quartzo-feldspathic rocks. The S-foliation (upper left to lower right) is defined by the alignment of elongate plagioclase and hornblende, whereas the transecting C-planes (horizontal) consist of extremely fine grained minerals (probably Ca-Al-silicates, chlorite, magnetite). The sense of shear is sinistral. The width of the photomicrograph is 2.12 mm (plane light).
- B. Example of a C/C'-type fabric in a chlorite-rich sample from the metatonalite unit (sample O/C-368e). The C'-planes trending from upper right to lower left are also termed "asymmetric extensional shear bands". The sense of shear is sinistral. Note the inclusions with tails indicating the same sense of shear. The width of the photomicrograph is 2.12mm (plane light).
- C. Fractured plagioclase porphyroclast with a low-angle, synthetic microfault (sample O/C-368e). The sense of shear is sinistral. The width of the photomicrograph is 0.54 mm (plane light).
- D. Fractured plagioclase porphyroclast with two high-angle, antithetic microfaults (sample O/C-368e). The sense of shear is sinistral. The width of the photomicrograph is 2.12 mm (crossed Nichols).
- E. Mylonite consisting of alternate layers of quartz and epidote \pm chlorite. Winged porphyroclasts of plagioclase and epidote can be used as sense of shear indicators, if porphyroclasts developed a monoclinic shape symmetry similar to σ - and δ -type objects (see figure 13). In this photomicrograph most porphyroclasts with monoclinic shape symmetry indicate sinistral shear (some σ -type inclusions seem to indicate dextral shear).

A

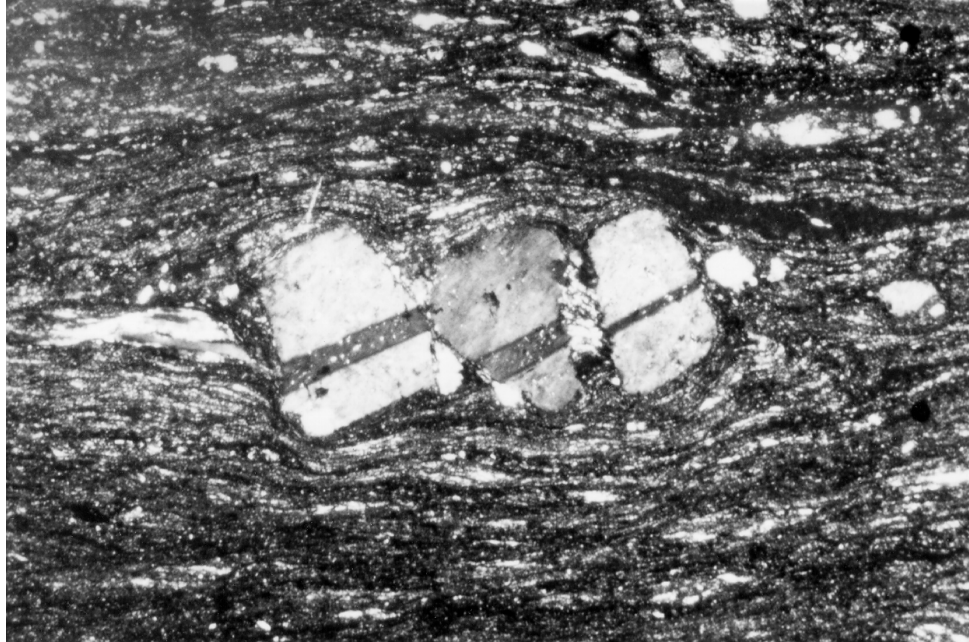


B





C



D

E



Passchier, 1991). This is used to infer that the shear or flow plane lies subparallel to the mylonitic foliation, and that the stretching lineation closely tracks the shear direction.

4.7.2 Deformation in the metagabbro unit

A definition of magmatic flow following Nicolas (1992) is presented first, before microstructural evidence is discussed in section 7.2.1. The term ‘magmatic flow’ applies to deformation of a crystallizing melt and includes both, ‘suspension flow’ and ‘submagmatic flow’. According to Nicholas (1992), suspension flow applies to the deformation of a crystallizing magma in which minerals are in suspension. The number of grains increases with crystallization and, as a result, the interaction of the grains during deformation increases (Nicholas 1992). Below a ‘critical melt fraction’, which is 30-35% for granitic melts (Van der Molen and Paterson, 1979), crystals form a rigid framework, and the deformation under such conditions is then called ‘submagmatic flow’ (Paterson et al., 1989). In section 4.7.2.1, no distinction is made between ‘submagmatic flow’ and ‘suspension flow’. In section 4.7.2.5, evidence for ‘submagmatic flow’ is discussed and whether or not magmatic flow passed continuously into solid state deformation as the rock crystallized completely.

4.7.2.1 Magmatic foliation

Except for few blocks of isotropic metagabbro and rare pegmatitic gabbro, the mafic dikes and enclaves as well as the medium-grained host metagabbro range from weakly to strongly foliated. The foliation is defined by the alignment of anhedral to subhedral hornblende laths and anhedral to subhedral tabular plagioclase. Locally, deformed dikes and enclaves are parallel to the foliation defined by the alignment of igneous minerals. The preferred orientation of hornblende laths also defines the mineral lineation. In thin section, the texture can be described as allotriomorphic to hypidomorphic granular (e.g., chapter 2, figure 2.9).

The orientations of the foliation and mineral lineation in the metagabbro unit are shown in figure 4.15a. The mean foliation strikes northeast and dips steeply southeast and the mineral lineation plunges northeast. The foliation and lineation (figure 15a) is interpreted to have formed due to magmatic flow for

the following reasons: (1) In outcrop, there is a continuum in shape of gabbroic enclaves ranging from deformed dike-like intrusions to round and ellipsoidal enclaves (chapter 2, figure 2.4) and ultimately to thin, tabular selvages, irregular schlieren (chapter 2, figure 2.5) and clusters of grains (chapter 2, figure 2.7). Assuming the enclaves are passive strain markers, an increase of the finite strain may be inferred from the shape of the enclaves which seem to become more elongate and thinner with increasing deformation. The host metagabbro and the enclaves have igneous textures suggesting that magmatic flow is the most likely interpretation to explain this apparent increase in strain (Paterson et al., 1989, Vernon et al 1988). (2) In samples with mostly subhedral grains, the strain due to crystal plastic deformation appears to be independent of the degree of alignment of the minerals and elongation of the enclaves. The crystal plastic deformation evident in these samples include wedge shaped twins in plagioclase (chapter 2, figure 2.8) and occasionally bends in plagioclase and hornblende grains. The small, but nearly constant amount of strain accommodated by the plastically distorted crystal lattices cannot satisfactorily explain the increasing rotation and alignment of plagioclase and hornblende with increasing elongation of enclaves. (3) A cursory investigation of the lattice preferred orientation using the method of Hall (1984) indicates that, in samples with predominantly subhedral minerals, hornblende shows no evidence of a lattice preferred orientation. Only a shape preferred orientation was found; i.e. the c-axis (the long axis of hornblende) is subparallel foliation suggesting alignment due to magmatic flow (Nicolas, 1992). Brodie and Rutter (1985) and Paterson et al. (1989) pointed out that even euhedral hornblende may be aligned in both magmatic and solid state foliation and can display similar microstructures in magmatic and metamorphic rocks. Hornblende is, therefore, not reliable discriminating magmatic or solid-state flow (Paterson et al., 1989). However, the alignment of subhedral hornblende parallel with relict igneous plagioclase suggests that both, plagioclase and hornblende were aligned due to magmatic flow. (4) In places, the aligned plagioclase retained igneous microtextures such as zoning and carlsbad and albite twinning. Unfortunately, the twinning is usually obscured or destroyed due to retrograde hydrothermal replacement and albitization of plagioclase as well as by stress-induced twinning. Nevertheless, when relict albite- and carlsbad- twinning is present, they are almost invariably parallel to the direction of elongation of plagioclase (which is subparallel with foliation) providing strong evidence that the alignment of igneous plagioclase occurred

during magmatic flow (Paterson et al., 1989). Consequently, the foliation in the gabbro is interpreted to be primarily a magmatic flow foliation overprinted by later solid-state deformation.

4.7.2.2 Shear foliation and sense of shear

Various mylonitic rocks were sampled from 2 cm to several meter wide zones in the metagabbro unit. The mylonitic zones occur subparallel to the magmatic foliation or cut it at low to intermediate angles. The mylonitic rocks are described below and the sense of shear criteria found in thin section discussed (see also table D5 in appendix D).

The matrix of quartz-free mylonitic rocks is extremely fine grained (chapter 2, figure 2.10) and, in places, wraps around plagioclase and hornblende porphyroclasts (chapter 2, figure 2.11). In all, except one of the mafic mylonitic samples, plagioclase is replaced by $cz + ab + ep \pm ch \pm mu$ and forms cloudy aggregates which are stretched into long ribbons and, occasionally, occur as thin, cloudy laminae between fine grained laminae of hornblende defining the mylonitic foliation (O/C-13-S22, O/C-13-S23, O/C-324, O/C-216 and O/C-427b, appendix D). Plagioclase porphyroclasts are similarly altered. The most common sense of shear indicators in the quartz-free mylonitic rocks includes augen-shaped hornblende porphyroclasts, low-angle synthetic and high-angle antithetic microfaults in plagioclase and hornblende porphyroclasts as well as tiling of plagioclase fragments (see figure 4.13 and 4.14). The asymmetry of the pleochroism of hornblende in O/C-13-S22 was determined using the method of Hall (1984), and about 65% of the hornblende-augen have a lattice preferred orientation consistent with sinistral shear. A C/S-type fabric is also observed in narrow shear bands (1-4 mm wide) occurring in the samples O/C-373C and O/C-374b.4. A photomicrograph of this C/S(?) type fabric is shown in figure 4.14a. The S(?) plane is defined by the alignment of elongate plagioclase and hornblende, whereas the transecting C(?) planes consist of extremely fine grained minerals (probably Ca-Al silicates, chlorite and magnetite). This fabric could be a C/C' (?) type fabric, if the orientation of S and C with respect to the shear zone boundary was misinterpreted. However, this would not change the interpretation of the sense of shear. Samples O/C-216 and O/C-384 are compositionally layered, and the extremely thin layers are thought to be parallel to the shear zone boundary. Individual layers are transected by asymmetric extensional shear bands. This type of

fabric is very similar to a C/C'-type fabric. The fabrics similar to C/S and C/C'-type shear bands in O/C-216, O/C-373C, O/C-374b.4, and O/C-384 indicate the same sense of shear as that inferred from other sense of shear indicators (appendix D, table D5). In sample O/C-384, fresh plagioclase porphyroclasts with recrystallized edges occur within an extremely fine grained matrix of hornblende and recrystallized plagioclase suggesting grain size reduction by dynamic recrystallization.

Those mylonitic rocks in the metagabbro unit that contain less than ~20% quartz are relatively coarse grained and are moderately to strongly foliated (O/C-13-S28, O/C-371B.1, O/C-371B.2, GH-97-15a, O/C-228, O/C-229). They contain subhedral to augen-shaped hornblende and subhedral to ovoid, altered plagioclase with wings (chapter 2, figure 2.12) in a strongly recrystallized matrix of quartz. Subgrains, lattice preferred orientation, and undulatory extinction is commonly observed in quartz. An oblique grain shape fabric, which served as sense of shear criteria (figure 4.13), seems to occur only in mono-mineralic layers of quartz. Also, hornblende-augen could be used as sense of shear criteria in some samples (appendix D, table D5). However, plagioclase is completely replaced forming dark-cloudy ovoid masses with wings that cannot be reliably distinguished as to be part of a σ - or δ -type inclusion. A fabric that closely resembles a C/S-type fabric is observed in O/C-13-S28. Strongly recrystallized quartz with tiny, disseminated flakes of chlorite(?) appear to form relatively continuous (C-type?) shear bands which clearly transect the S(?)-planes. The S-planes are defined by the shape preferred orientation of subhedral hornblende and plagioclase. The sense of shear inferred from the geometric relationship of these C(?) - and S(?) -planes is consistent with three other sense-of-shear indicators observed in the same thin section (appendix D, table D5).

Quartz-rich rocks (>20%) in the metagabbro near the contact with the metatonalite unit have a strong mylonitic foliation which is defined by alternate, very thin layers of strongly recrystallized quartz and epidote + chlorite (O/C-371A and O/C-13S26, appendix D). These mylonites are very similar to most mylonites in the metatonalite unit. Sense of shear criteria found in thin section include oblique grain shape fabric in mono-mineralic layers of quartz, microfaults in porphyroclasts (epidote, plagioclase) and porphyroclasts with σ -type wings (epidote, plagioclase).

The orientations of the shear foliation and stretching lineation are shown in figure 4.15b. The mean shear plane strikes north 039° east and dips 83° southeast, and the mean stretching lineation trends 040° and dips 30°. The mean shear plane is assumed to represent the flow plane and the mean stretching lineation the flow direction. The sense of shear (appendix D, tables D5 and D6) as determined in thin section is indicated by the arrow in figure 4.15b. The inferred sense of shear is dextral with a thrust component.

4.7.2.3 Brittle deformation and crosscutting relationships

The mylonitic zones are paralleled or crosscut by >2 cm to 1.5 m wide faults and are cut by extensional veins. Faults and veins in the metagabbro unit are mineralized, and the mineral assemblages identified in faults and veins include ep + ch + qz, ep + ch, ep(±qz), ch, qz, pr ± qz, ab, qz + sulf, pu ± qz, cc. Microshears (~ 0.1 mm wide), containing extremely fine grained minerals, are parallel to as well as cut the shear foliation of a ductily deformed sample at a low angle (thin section O/C-229). As observed in another thin section (O/C-14-S22), the mylonitic foliation is overprinted by a cataclastic fabric: strongly foliated fragments showing variable orientations occur in a fine-grained matrix consisting of chlorite and quartz. The cataclastic zone in hand sample O/C-14-S22 is 1.5 cm wide and parallel foliation.

The metagabbro is strongly altered, and contains 1 cm to 50 cm wide zones of epidotes as well as epidote, prehnite and quartz + sulfide mineralized faults and veins. The mineral assemblages in veins, faults and adjacent wall rocks are identical to these in the sheeted dike complex, and indicate retrograde hydrothermal metamorphism. Interestingly, many mylonites in the metatonalite and metagabbro unit and Blossom Bar shear zone are essentially strongly sheared epidotes (quartz + epidote + chlorite), which are cut by ep+qz and pr- veins. This implies that mylonites could have developed in pre-existing epidosite zones and/or that epidotization took place as the mylonites formed. The crosscutting relationships in outcrop, hand sample and thin section indicate that mylonites and epidotes formed first in the metagabbro. Then, microshears developed parallel to the shear foliation (or at low angles). Subsequently, ep±qz mineralized faults and veins formed as well as cataclastic overprint of some of the mylonites. These structures are cut by prehnite pr±qz mineralized faults and veins and albite veins. The latest veins

identified in thin section are qz- and $pu \pm qz$ -veins followed by calcite-veins. The mineral assemblages found in metagabbro, faults, and veins indicate retrograde hydrothermal metamorphism typical of subseafloor hydrothermal alteration (e.g., Harper et al., 1988; Alexander et al., 1993).

4.7.2.4 Estimate of temperature of solid-state deformation

The mafic rocks in the metagabbro unit consist mainly of plagioclase and hornblende and are considered in the following discussion as a two-phase aggregate. Little is known about the plastic properties of amphiboles (Brodie and Rutter, 1985; Passchier and Trouw, 1996). Nevertheless, Brodie and Rutter (1985) propose that metabasic rocks deformed at temperatures in excess of 600°C show evidence of plastic deformation of amphibole, provided it is a load supporting phase. Otherwise, it deforms in a brittle manner, even at very high temperatures, or is deformed due to creep by grain boundary diffusion.

Deformation in the metagabbro unit occurred at temperatures mostly below 600°C, based on Brodie and Rutter's (1985) generalization and the observation that amphiboles are typically fractured and show neither mechanical twinning nor kink bands. However, the sample that has a weak crystallographic preferred orientation of hornblende (O/C-13-S22) may have deformed at temperatures above 600°C based on an experimental study of Dollinger and Blacic (1975) suggesting glide on (100)[001] in hornblende occurs between 600°C-750°C.

Clear evidence for grain size reduction by dynamic recrystallization of plagioclase is found in only one sample (O/C-384). Otherwise, plagioclase shows undulatory extinction, stress-induced twinning or is fractured. The lowest limit of dynamic recrystallization of plagioclase is thought to occur at a temperature of about 450°C (Passchier and Trouw, 1996), and is an important process at temperatures around and in excess of 550°C (Brodie and Rutter, 1985; Fitz Gerald and Stuenitz, 1993a, 1993b). In contrast, undulatory extinction, tapered deformation twins, and bookshelf structures seem to prevail at low grade conditions (300-400°C) (Passchier and Trouw, 1996). Using plagioclase as a the temperature gauge, deformation of the metagabbro probably occurred at temperatures below 500°C. However, the sample that contains unaltered, recrystallized plagioclase (O/C-384), may have deformed at a higher temperature; that is, when grain size reduction by subgrain rotation recrystallization is predominant (>500°C).

Some ductile deformation in mylonitic mafic rocks is estimated to have occurred at temperatures above 500°C, based on the study of the microstructures in quartz-free mylonitic rocks summarized above. However, evidence of brittle failure of plagioclase and hornblende, the ubiquitous occurrence of deformation twins in plagioclase, and the greenschist facies mineral assemblage in deformed rocks indicate that deformation continued below temperatures of 500°C and was perhaps dominated by cataclastic deformation processes in mafic rocks. Additionally, the likely presence of fluids aiding diffusive mass transfer could have enhanced crystal plasticity (Fitz Gerald and Stuenitz, 1993a). For example, in the presence of fluids, plagioclase can be replaced by a fine-grained mineral assemblage during deformation. The metamorphic and contemporaneous deformation by grain boundary sliding accommodated by diffusive mass transfer could have been an important mechanism of ductile deformation below 500°C (Brodie and Rutter, 1985). This process may explain the formation of cloudy, fine grained layers that formed from plagioclase (ab, cz, ep, chl, musc) between layers of hornblende in mafic mylonitic rocks.

Temperature estimates of ductile deformation are also made interpreting the microstructures in quartz bearing rocks. The characteristics of the quartz fabrics may be summarized as follows: relics of old, elongate quartz grains containing subgrains have fine-grained recrystallized edges and pass laterally into bands or layers of small dynamically recrystallized grains. Evidence for grain boundary migration, such as bulging grain boundaries, were rarely observed. Occasionally, a crystallographic preferred orientation is found and oblique grain shape fabric of recrystallized quartz. These fabrics indicate that recrystallization of quartz is dominated by subgrain rotation recrystallization (climb-accommodated dislocation creep), and minor grain boundary migration recrystallization. This is thought to occur at temperatures between 400°C and 700°C (Passchier and Trouw, 1996). However, the lower part of this temperature range (400°C -500°C) is inferred to be more likely in consideration of the observation that (1) plagioclase deformed mainly by brittle fracturing in a recrystallized matrix of quartz, and not by dynamic recrystallization. Grain size reduction accompanied by nucleation and neocrystallization is possible since plagioclase is often completely replaced in shear bands (Fitz Gerald and Stuenitz, 1993a); (2) grain-boundary migration recrystallization of quartz appears to be less dominant than subgrain rotation recrystallization (see above summary of quartz fabric), (3) textures that indicate rapid recovery due to higher temperatures are not

observed (such as a honeycomb texture), and (4) the alteration of plagioclase, which appears to be closely interlinked with deformation (e.g. chapter 2, figure 2.12), suggest green schist facies rather than amphibolite facies conditions.

Other common features of solid-state deformation include ubiquitous undulatory extinction in quartz (300-400°C), fracturing and bending of plagioclase and hornblende, the development of c-type shears consisting of chlorite and muscovite (often paralleled by quartz ribbons) and the formation of cataclastic shear zones.

Retrograde conditions during deformation are inferred from the following observations: (1) mylonitic fabric is overprinted by cataclastic flow, (2) faults and veins cut mylonites, and (3) cataclasites, faults and veins are mineralized with mineral assemblages indicating retrograde hydrothermal alteration. The cross-cutting relationships are summarized below which include the observations made in the field, hand samples and thin sections. The crosscutting structures and their typical secondary mineral assemblages are presented from oldest to youngest: (1) mylonites and epidiosites (ep + chl + qz) are followed by (2) microshears (ep + chl) followed by (3) ep ± qz mineralized veins and faults followed by and cataclasites (ep + chl + qz) followed by (4) pr ± qz- mineralized veins and faults and ab-veins followed by (5) qz ± su- and pu ± qz-veins, and (6) cc-veins.

The timing of the formation of epidiosites and mylonites is not entirely clear. Some mylonites in the metagabbro unit have a composition similar to epidiosites and consist entirely of quartz, epidote and chlorite. Either, epidotization occurred prior to deformation or the rocks underwent alteration as they were deformed resulting in mylonites with a composition similar to epidiosites. Interestingly, ep ± qz veins are sometimes deformed in quartz-bearing mylonites suggesting that ductile processes accompanied brittle deformation in the stability field of epidote + quartz veins. Estimates of temperatures of formation of hydrothermal veins and alteration of mafic rocks in high-level gabbro/sheeted dike transition zone are compiled in table 2 of Alexander et al. (1993). Assuming a similar stratigraphic level for the metagabbro (~1.5 kbar) and similar composition of hydrothermal fluids, the temperatures of brittle deformation can be inferred using Alexander et al.'s (1993) compilation. It is suggested that temperatures of deformation decreased with time beginning with the formation of ductile shear zones in mafic rocks (~600°C). With

decreasing temperature, ductile deformation concentrated in quartz rich rocks (<500°C) and stress induced twins in plagioclase in mafic rocks formed. Grain boundary sliding assisted by diffusive mass transfer, or similar fluid-enhanced crystal plastic deformation processes, at greenschist facies conditions may have been important processes during deformation of both mafic and silicic rocks. Epidote + quartz veins formed ($\leq 400^{\circ}\text{C}$) followed by $\text{pr} \pm \text{qz}$ veins ($\leq 300^{\circ}\text{C}$) followed by $\text{qz} + \text{su}$ and $\text{pu} \pm \text{qz}$ ($150\text{-}250^{\circ}\text{C}$) suggesting brittle deformation followed ductile deformation. Described microstructures are interpreted as indicative of temperatures of 600°C - 400°C for ductile deformation. Brittle failure appeared to become an important process at temperatures $\leq 400^{\circ}\text{C}$ (epidote veins appear).

It is suggested that the end of ductile deformation occurred at around 149 Ma. This is inferred from the muscovite $^{40}\text{Ar}/^{39}\text{Ar}$ cooling ages determined in two deformed tonalitic dikes (Heizler, written communication, 1998). Muscovite closes to argon-diffusion in the temperature range of $350\text{-}400^{\circ}\text{C}$, depending on grain size and cooling rate (McDougall and Harrison, 1988; Hames and Bowring, 1994).

4.7.2.5 Transition from magmatic flow to solid-state deformation?

Evidence for magmatic flow at temperatures in excess of about 850°C (gabbro solidus at 2 kbar, Holloway and Burnham, 1972) and later superimposed moderate- to low-temperature solid-state deformation ($150\text{-}600^{\circ}\text{C}$) is presented in sections 4.7.2.2 through 4.7.2.4. In addition, the possibility is explored that magmatic flow could have passed continuously into solid state flow as the cooling and crystallizing gabbroic magma was deformed. This is a distinct possibility because the mean magmatic foliation and lineation are subparallel to the mean shear foliation and stretching lineation (figure 4.15a and 4.15b).

Paterson et al. (1989) referred to the transitional stages as 'submagmatic flow' which operates at and below a 'critical melt fraction' of about 30-35% liquid (Van der Molen and Paterson, 1979) when crystals begin to form a solid framework in a crystallizing magma, and the framework deforms by brittle fracturing under high strain rates (under low strain rates by grain-boundary and phase-boundary migration), and high-temperature solid-state deformation operating below solidus-temperatures. The deformation of a framework of interlocking grains with an interstitial liquid fraction present may occur in

numerous ways. For example: (1) plasticity of crystals is facilitated at wet grain boundaries by rapid diffusion within the liquid, but it is also accompanied by rapid recovery because of the high temperature. Thus, evidence for plastic deformation of grains may not be preserved. (2) Weakening and deformation of the solid framework of interlocking grains, which supports the tectonic stress, may be accomplished by re-melting of particles at grain-grain contacts, or by grain-boundary and phase-boundary migration in the presence of melt (Means and Park, 1993; Means and Park, 1994). Alignment of particles may be accomplished without leaving any trace of crystal plastic deformation. (3) Fracturing of crystals in the presence of melt is also possible during submagmatic deformation. Such fractures, described in granitoids, are characterized by infillings with minerals that crystallized from late-stage melts. These features are termed submagmatic microfractures (Bouchez et al., 1992).

Textures resulting from submagmatic flow could be indistinguishable from the textures produced by suspension flow, and caution interpreting flow processes is necessary (Means and Park, 1993). Furthermore, submagmatic microfractures were not observed in the samples from the metagabbro unit suggesting either they did not form in the crystallizing gabbroic magma, or submagmatic flow did not occur.

Is there any evidence for submagmatic flow? The felsic schlieren in the medium grained gabbro (e.g., chapter 2, figure 2.7) could be an indication of submagmatic deformation. Some of the felsic schlieren may represent late-stage melts that segregated by solid compaction during submagmatic flow (e.g. Higgins, 1991). Segregated melts having a composition similar to quartz-diorite may solidify at temperatures as low as 750°C (solidus of quartz diorite at 2 kbar, Piwinski, 1973). Nicholas (1992) pointed out that a strong preferred orientation is not accomplished by the mechanical rotation of particles during solid compaction alone. Consequently, flow alignment must have occurred prior to, or simultaneously with, solid compaction if this type of melt segregation played any role in the development of textures and microstructures observed in the metagabbro unit.

The magmatic flow foliation (e.g. chapter 2, figure 2.7) in deformed and disrupted dikes may have formed by submagmatic flow. Perhaps, the host gabbro reached the critical melt fraction and deformed by fracturing at high strain rates associated with the injection of the dikes. The lack of chilled

margins indicates that dikes and host gabbro had very similar temperatures when the dikes were intruded. Subsequent deformation occurred by flow during which dikes and host gabbro were still in a magmatic state resulting in the disruption of the dikes and the flow texture in the dikes subparallel to that in the host gabbro.

The textures and microstructures described in mylonitic rocks from the metagabbro unit indicate that solid-state deformation occurred at temperatures significantly below solidus conditions ($\leq 600^{\circ}\text{C}$, section 7.2.4). The study of more samples from the metagabbro unit may reveal relict textures which are characteristic of high-T, near-solidus deformation. However, they have not been found, and the preservation of igneous microstructures and textures (i.e. carlsbad albite twinning in zoned, subhedral plagioclase) indicates that intense deformation at high-T conditions did not play an important role.

Overall, evidence for ‘submagmatic flow’ is inconclusive. Submagmatic flow may have played an important role in the alignment of igneous minerals and the formation of magmatic layering in the metagabbro unit, but it is poorly constrained with available data. Microstructural evidence indicating near-solidus solid-state deformation was not found, and currently available data indicate that magmatic flow ($>850^{\circ}\text{C}$) did not pass continuously into the observed medium- to low-grade solid state deformation ($\leq 600^{\circ}\text{C}$, section 4.7.2.4).

4.7.3 Deformation in the metatonalite unit

The metatonalite unit consists predominantly of tonalitic to trondhjemitic intrusive rocks. Subordinately, microdioritic enclaves and dikes occur in the metatonalite unit. Based on observations in the field, hand sample and thin section, the enclaves are interpreted to have formed by the injection of a more mafic magma (diorite) into a felsic magma (tonalite-trondhjemite) and, therefore, represent globules of magma (“pillows”) that were ‘quenched’ in a plutonic environment (see chapter 2, figure 2.16 and 2.17).

The metatonalite unit contains several zones of strongly foliated rocks previously mapped as silicic tuffs (Gray et al., 1982). Samples from such zones are compositionally layered, show evidence of intense ductile deformation, have a stretching lineation and contain fabric elements with a monoclinic shape

symmetry indicative of non-coaxial deformation. Field and petrographic evidence suggests that the protoliths of these mylonites include tonalite-trondhjemite, dioritic enclaves, quartz-epidote veins and epidotes (see chapter 2).

4.7.3.1 Shear foliation and sense of shear

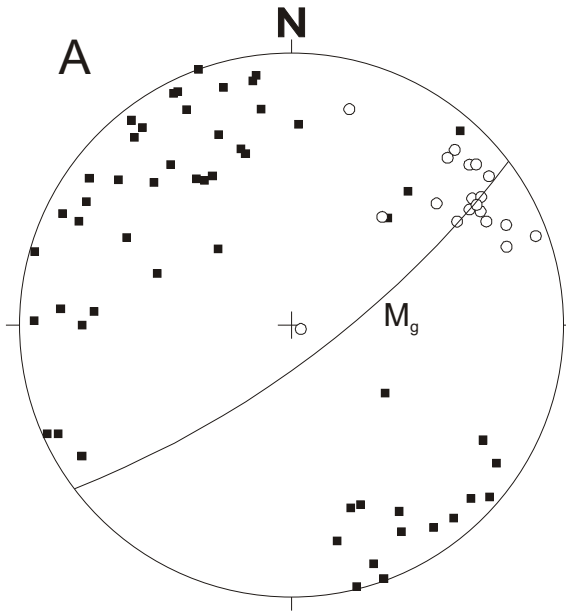
The mylonites in the metatonalite unit are classified as type 1 and type 2 mylonites (see chapter 2). Type-1 mylonites are very quartz-rich and have a foliation that is defined by clearly separable, alternating layers of quartz \pm albite and cloudy mineral aggregates of mainly Ca-Al-silicates (i.e. ep, cz, pr?) as well as some chl, musc, and ac (type-1 mylonites occur also in the Blossom Bar shear zone, see example in figure 4.14e). The sense of shear indicators typically developed in type-1 mylonites include: (1) oblique grain shape fabric developed in monomineralic layers of quartz; (2) asymmetric extensional shear bands (C'-planes) transect compositional layering (C-planes) at low angles; (3) porphyroclasts of epidote with wings consisting of cloudy epidote (see figure 4.14e), (4) plagioclase porphyroclasts with wings consisting of a cloudy mineral aggregate; (5) mantled quartz porphyroclasts; (6) albite porphyroclasts with high-angle antithetic and low-angle synthetic microfaults; (7) quartz veins showing undulatory extinction are offset along cloudy layers (figure 4.13). Quartz in veins is weakly recrystallized (undulatory extinction), while quartz in the layers is usually strongly recrystallized and has a strong lattice preferred orientation.

Type-2 mylonites have a foliation that is comparable to a domainal spaced cleavage (figure 4.14b). The cleavage domains are rich in chlorite separating quartz-rich microlithons. The microlithons consist mainly of aggregates of recrystallized quartz and small amounts of disseminated minerals. Type 2 mylonites are richer in chlorite and poorer in quartz than type 1 mylonites. The sense of shear indicators identified in type 2 mylonites include: (1) well-developed C' shear planes consisting mainly of chlorite (figure 4.14b); (2) albite porphyroclasts with low-angle synthetic and high-angle antithetic microfaults (figures 4.14c and 4.14d, respectively), (3) winged porphyroclasts of epidote, cloudy plagioclase and hornblende. Similar to type 1 mylonites, quartz is also strongly recrystallized and has a lattice preferred orientation. However, an oblique grain shape fabric was not found.

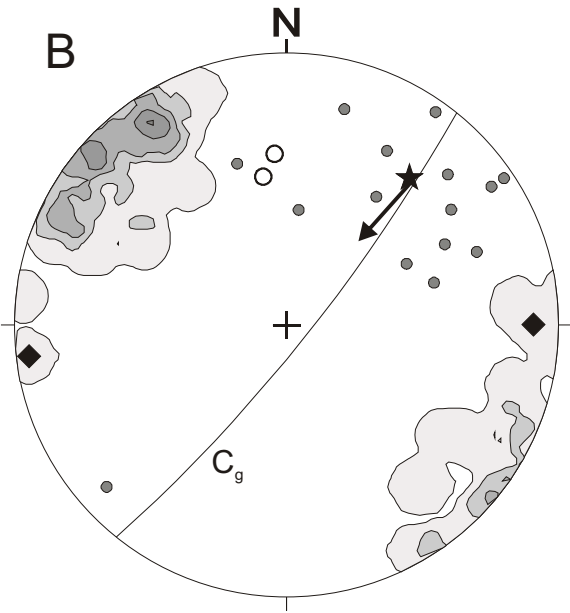
Figure 4.15

Lower hemisphere, equal area stereographic projections of foliations and lineations in the metagabbro unit, metatonalite unit and Blossom Bar shear zone.

- A. Poles to magmatic foliation in the metagabbro unit. The mean magmatic foliation M_g is shown as a great circle. The lineation is defined by the preferred orientation of subhedral hornblende and is interpreted as magmatic in origin (see text).
- B. Contoured poles to shear foliation in the metagabbro unit. The mean shear foliation C_g is shown as a great circle, which is subparallel to the magmatic foliation M_g . The stretching lineations scatter considerably, but the group mean of the stretching lineation plots close the great circle C_g . Sense of shear is dextral with a thrust-component.
- C. Contoured poles to shear foliation in the metatonalite unit. The mean shear foliation is plotted as a great circle (C_t). The mean shear foliation C_t is very similar in attitude to the mean shear foliation in the metagabbro unit. The stretching lineations are more clustered in the metatonalite unit than in the metagabbro unit. Shear sense is dextral with a thrust component.
- D. Contoured poles to shear foliation in the Blossom Bar shear zone. The strike of the mean shear foliation (C_{sz}) is subparallel to the shear foliation in the metagabbro unit and the metatonalite unit. However, the mean shear foliation dips steeply northwest. Also, most stretching lineations plunge steeply northwest. The sense of shear is normal.

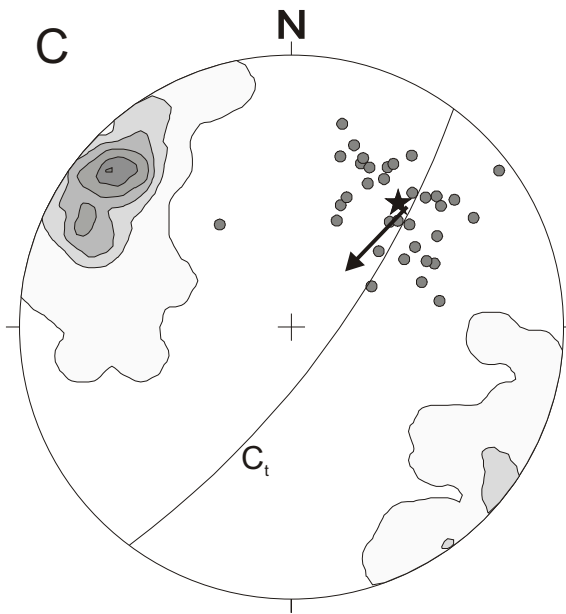


- pole to magmatic foliation (n=54)
- magmatic mineral lineation (n=19)

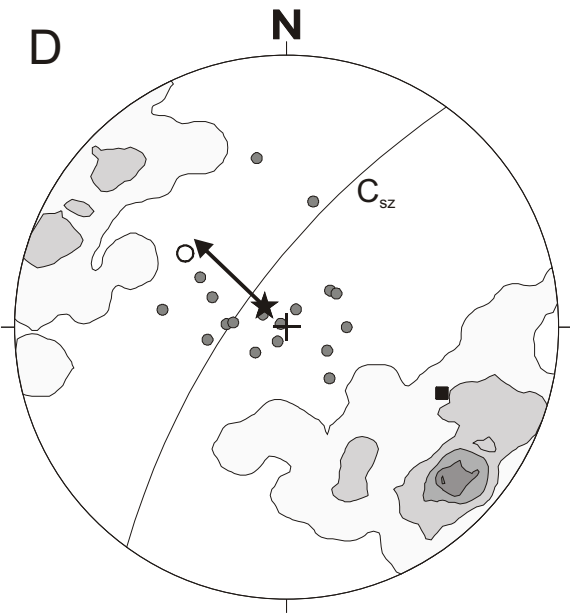


- Contours include shear foliation in metagabbro unit (n = 47)
 contour lines: 2.1, 6.4, 10.6, 14.9, 19.2% / 1% area
- stretching lineation (n = 17)
 - ★ mean stretching lineation

- pole to foliation
 - ◆ stretching lineation
- } O/C-372b, GH-97-6



- Contours include shear foliation in metatonalite unit (n = 115)
 contour lines: 0.9, 5.2, 10.4, 14.8, 20.0, 22.6% / 1% area
- stretching lineation (n = 34)
 - ★ mean stretching lineation



- Contours include foliation in Blossom Bar shear zone (n = 104)
 contour lines: 1.0, 4.8, 9.6, 14.4, 17.3% / 1% area

- stretching lineation (n = 19)
 - ★ mean stretching lineation
 - pole to foliation
 - stretching lineation
- } (O/C-17-S32)

The mean shear foliation in the metatonalite unit strikes north 037° east and dips 78° southeast, and the mean stretching lineation trends 040° and dips 39° (figure 4.15c). The sense of shear (appendix D, tables D5 and D6) as determined in thin section is also shown in figure 4.15c. The arrow indicates the inferred sense of shear is dextral with a thrust component.

4.7.3.2 Brittle deformation and crosscutting relationships

In outcrop, striated faults cut the mylonitic foliation at various angles. The faults are few mm to cm thick, and the offsets are in the range of several cm to ~2 m. In this study, small mineralized faults with striated surfaces were analyzed. These faults are cemented predominantly with white minerals which may include, as observed in microfaults and veins in thin section, quartz and prehnite (most common, see appendix D, table D5), but also calcite, pumpellyite, and laumontite (less common, see appendix D, table D5). Pistachio-green mineralization indicative of epidote is common in faults and veins cutting relatively undeformed metatonalite (which could represent oceanic brittle deformation), but is rare in veins cutting mylonites. Very small epidote veins and quartz+epidote veins are observed cutting mylonitic foliation (MRH-73, O/C-366b, O/C-372b.2), however, quartz in these veins is recrystallized as indicated by undulatory extinction. Ductily deformed epidotes (most type 1 mylonites are similar to epidotes in composition) and boudinaged epidote veins occur in the metatonalite unit (O/C-368d) suggesting that epidotization and formation of epidote veins is older than, or contemporaneous (or both) with ductile deformation.

The attitude of 19 cemented faults, the orientation of the associated striae and the sense of slip were determined. If no clear offset markers could be identified, the criteria of Petit (1987) for the sense of movement on fault surfaces were used. Stepped surfaces are the most common types of shear sense markers. The fault data (n = 19) are listed in appendix D (table D7) and presented in a Hoeppner-plot in figure 4.16b. In the present coordinates, the subdivision of the faults according to their main component of slip is as follows: three right-lateral strike-slip faults, eight left-lateral strike-slip faults, five reverse faults and three normal faults. Also, the faults appear to be clustered (clusters 1 through 5).

Faults that occur at low angles with respect to the foliation (#1 and #5) indicate right-lateral offsets with a thrust component (#5) or reverse displacement with a significant right-lateral component (cluster #1). The movement along faults in clusters #1 and #5 is sympathetic with the direction of transport along the mean shear plane C_1 (compare slip linears in figures 4.16a and 4.16b). In contrast, most of the faults that occur at relatively high angles with respect to the foliation are left-lateral strike-slip faults (clusters #2 and #3) or thrust faults with a significant left-lateral component. The largest component of the movement of the faults in clusters #2 and #3 is antithetic with respect to the sense of shear along C_1 (compare slip linears in figures 4.16a and 4.16b). The three dimensional geometry of the faults in figure 4.16b was compared to Riedel shears in brittle fault zones, and the orientations of the planes and striations do not match the attitude and displacement of P, R and R' subsidiary shear fractures in brittle fault zones (compare with figure 4.13b). Thus, the faults in figure 4.16b are not similar to Riedel-type shears except, perhaps, faults in cluster #5. The projection of the faults into the plane of thin sections cut perpendicular to shear foliation and parallel stretching lineation results in a two dimensional fault geometry that is similar to that of Riedel shears. Also the projected offsets would match the displacement on R, R' and P fractures (compare with figure 4.13b). Thus, the microfaults observed in thin section may not be Riedel-type shears.

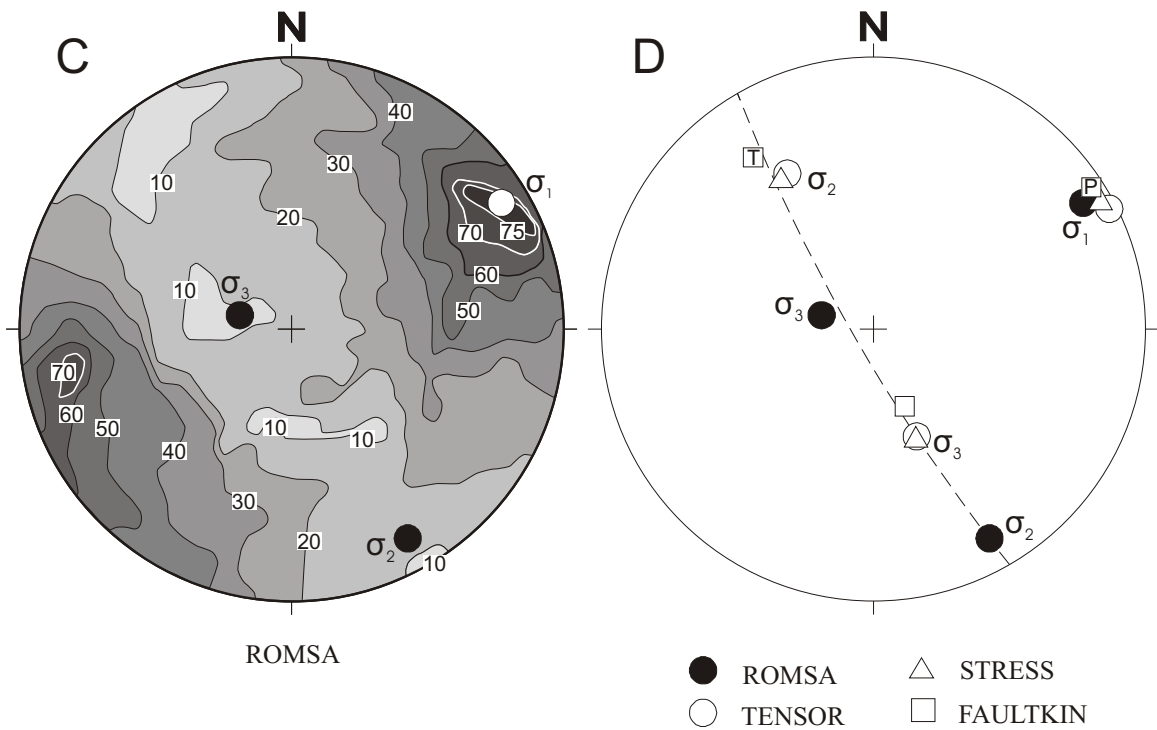
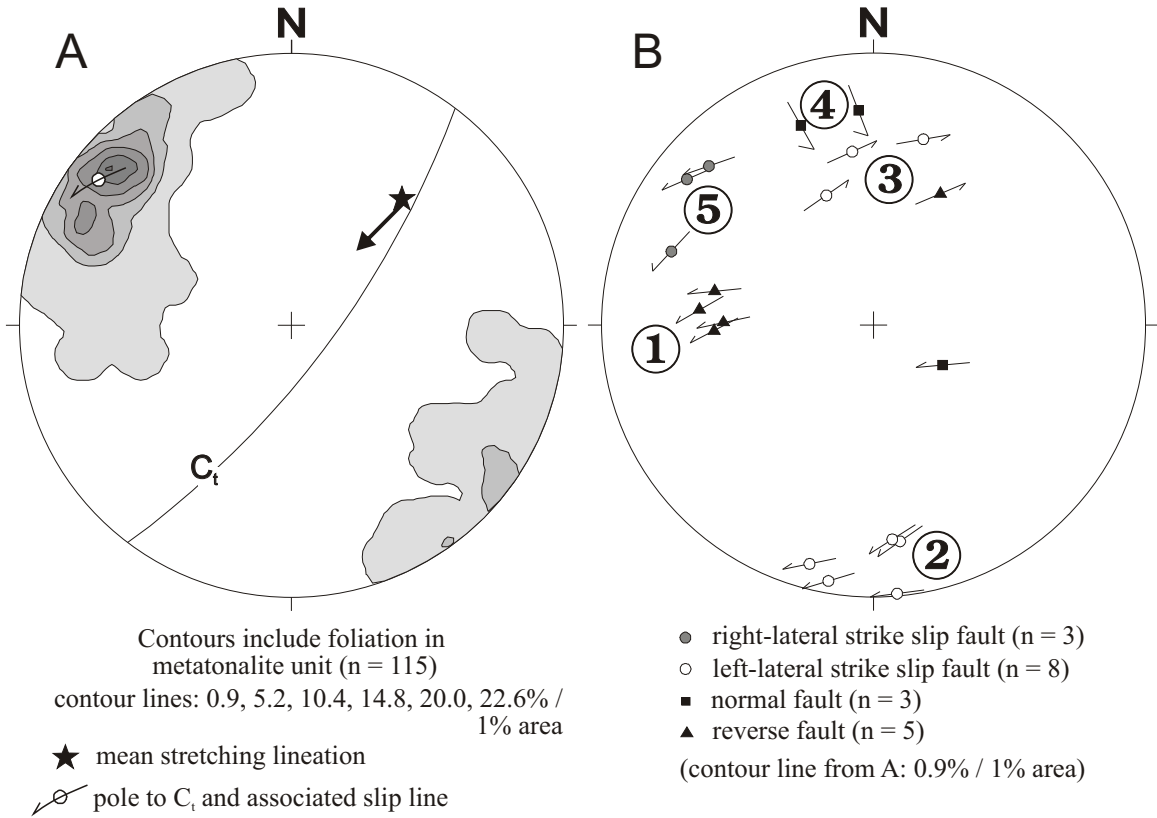
The orientation of the principal stress axis which best fit the fault data in figure 4.16b are determined, and the solution obtained from the stress inversion program of Lisle (1988) are shown in figure 4.16c and are compared to the results from three other techniques (figure 4.16d). Using ROMSA (Lisle, 1988), the maximum principal stress σ_1 is determined with an azimuth of 062° and a plunge of 18° . The best σ_3 -direction computed by ROMSA is $273^\circ / 69^\circ$. Knowing the σ_1 - and σ_3 -directions, the orientation of the intermediate principal stress axis σ_2 is found stereographically, which is $154^\circ / 11^\circ$. Unlike the results of previous paleostress analyses of cemented faults (figures 4.11c and 4.12c), the maximum compound likelihood P_{Total} for $X = 059^\circ / 11^\circ$ being the direction of σ_1 is high ($P_{\text{Total}} = 75.1\%$). This value of P_{Total} indicates that three quarters of the fault data are compatible with the obtained solution. The four paleostress programs computed almost identical directions for the maximum principal stress σ_1 (figure 4.12d). The directions of the other stress axis differ between methods, and the σ_2 - and σ_3 -axis plot in a plane normal to σ_1 . Only the results for σ_2 - and σ_3 returned by TENSOR (Angelier, 1979) and STRESS

Figure 4.16

Lower hemisphere, equal area stereographic projections of mean shear plane C_1 and stretching lineation in the metatonalite unit (a), of poles to cemented faults (b), and the results of the paleostress analysis (c, d) using data shown in (b).

- a. The contours of poles to shear foliation from figure 4.16a are shown as well as the mean shear plane C_1 and the mean stretching lineation. The arrow indicate the direction of transport (dextral-thrust). Additionally, the pole to C_1 with associated slip vector is shown (see figure 4.3).
- b. Poles to cemented faults and their associated slip vectors (Hoeppener, 1955). The arrows affixed to the poles to cemented faults indicate the direction of slip of the hanging wall block (see figure 4.3). Faults occurring at low angles with respect to the foliation (#1 and #5) have synthetic offsets (dextral-thrust), and faults occurring at high angles with respect to the foliation (# 2, #3 and #4) have antithetic offsets (sinistral-thrust) with respect to shear parallel C_1 in the direction of the mean stretching lineation.
- c. Solution of the analysis of cemented faults illustrated in figure 16b ($n = 19$) using ROMSA (Lisle, 1988). The contours (in %) express the most probable orientation of σ_1 ($062^\circ / 18^\circ$). The maximum compound likelihood is $P_{\text{Total}} = 77.1\%$ (contour interval = 10%). The corresponding σ_2 and σ_3 orientations are $154^\circ / 11^\circ$ and $273^\circ / 69^\circ$, respectively.
- d. Comparison of the results of the paleostress analysis using four different programs: solid symbol - ROMSA (Lisle, 1988); circle - TENSOR (Angelier, 1979); square - FAULTKIN (Allmendinger et al., 1994); triangle - STRESS (Reches, 1987). Significant differences exist between the principal stress axes computed by the four different programs for the data shown in figure 16b. Note that all programs computed almost identical σ_1 (T) directions whereas the programs returned various σ_2 - and σ_3 - directions which plot within the $\sigma_2\sigma_3$ plane normal to σ_1 .

Shear foliation and brittle faults, metatonalite unit



(Reches, 1987) are equivalent. Note that the direction of the minimum principal stress σ_3 and the tensional axis T is calculated by the different paleostress programs so that σ_3 and the tensional axis T plot within one of three contoured areas where the compound likelihood P_{Total} for X being the direction of σ_1 is lowest (< 10%). This means, the likelihood for Z being the direction of σ_3 is highest in the areas with $P_{\text{total}} < 10\%$. Clearly, there is not a unique solution for the σ_3 -direction(s). The direction of the intermediate and minimum principal stress may not be determined correctly when σ_2 and σ_3 are similar in magnitude; that is, when the stress ratio $\varphi = (\sigma_2 - \sigma_3)/(\sigma_1 - \sigma_3)$, which is a measure of the shape of the stress ellipsoid, is close to zero. In the extreme case of axial compression ($\sigma_1 > \sigma_2 = \sigma_3$) the value of φ is zero. If this is the case, a cone-shaped fault array would form in isotropic rocks. Alternatively, different solutions from the different programs may be returned when the population of fault slip data consists entirely of faults of very similar attitude and displacement. In contrast, the stress inversion programs usually return reliable results when faults of highly variable orientation are analyzed which experienced slip under a single static stress field (Schimmrich, 1991).

The mineralized faults cutting mylonitic foliation may have formed during the transition from predominantly ductile to predominantly brittle deformation under the same stress field as that of ductile shear in the metatonalite unit. It is possible that some or all of the faults formed later under a different stress field. Thus, the stress axis found from the paleostress analysis of faults in the metatonalite unit may or may not represent the stress field during ductile-brittle deformation.

The results of the paleostress analysis of epidote- and prehnite-mineralized faults in domains A and B (figure 4.11) and domain D (figure 4.12) are not similar to the results of the paleostress analysis of prehnite and quartz-mineralized faults in the metatonalite unit (figure 4.16). This suggests that not all faults formed in one “generation”; that is, slip on the faults in the data sets occurred not under a single, static stress field.

4.7.4 Blossom Bar shear zone

4.7.4.1 Shear foliation and sense of shear

The most unusual structural feature of the field area is the 0.5-0.9 km wide Blossom Bar shear zone exposed west of the metagabbro unit. This shear zone contains mylonites, ultramylonites, cataclasites and relatively undeformed, weakly foliated rocks. The different protoliths of foliated and mylonitic rocks in the Blossom Bar shear zone include metavolcanic rocks (flows and volcanic breccia), quartz-hornblende metagabbro, metatonalite, and metadiabase. Metavolcanic rocks appear to be most abundant in this shear zone. Also, a large portion of the Blossom Bar shear zone consists of a very thinly foliated rock consisting mostly of chlorite \pm quartz \pm calcite. Individual layers in the Blossom Bar shear zone range from few cm to several m in thickness, and are gently folded. Locally, dragfolding due to faulting is observed.

Deformed plutonic rocks in the Blossom Bar shear zone are similar in composition and fabric to the mafic and felsic plutonic rocks in the metagabbro and metatonalite unit. Type 1 and type 2 mylonites (see figures 14b and 14e) in the Blossom Bar shear zone are very similar to these in the metatonalite unit (O/C-230-S61, O/C-230-S62, O/C-233, O/C-17-S31, O/C-17-S34, O/C-17-S35, appendix D, table D5). Also, the Blossom Bar shear zone contains felsic mylonitic rocks (O/C-234 and O/C-237) similar to quartz-rich mylonites in the metagabbro unit. Samples that are similar to the muscovite \pm garnet-bearing tonalite dikes (GH-97-6, O/C-372b) in the metagabbro unit or also present in the Blossom Bar shear zone (O/C-17-S32, O/C-19-S34). Additionally, a fine-grained S/C-type mylonite (O/C-417a), which is somewhat different in the mineral composition than any of the previously described samples, occurs at the contact with the metagabbro unit (could be an intrusion in the metagabbro unit). This S/C-type mylonite is exposed in the Mule Creek and consists mainly of strongly recrystallized quartz (~35%), saussuritized plagioclase (~50%), and contains the mafic phases biotite, muscovite, hornblende and oxide ($\sim \Sigma$ 15%). Overall, the same sense of shear indicators are found in the mylonites from the Blossom Bar shear zone as in equivalent rocks in the metatonalite unit and metagabbro unit (appendix D, table D5).

Dark green, strongly foliated rocks consisting of (secondary?) quartz and abundant chlorite are most common in the Blossom Bar shear zone. Many of the dark green, very fine grained mylonitic rocks could be derived from porphyritic volcanic rocks. A C/C'-type fabric is most commonly observed

(O/C-45-S42, O/C-236, O/C-238, O/C-418A), as well as winged porphyroclasts and porphyroclasts containing microfaults. Quartz is strongly recrystallized and has a lattice preferred orientation.

On average, the layers and shear foliation strike northeast and dip steeply northwest (figure 4.15d). The stretching lineation dips steeply southeast to northwest, and the inferred sense of shear is normal (figure 4.15d). The orientation of the shear foliation and stretching lineation as well as the inferred sense of shear in the Blossom Bar shear zone differ significantly from the metagabbro unit and metatonalite unit.

4.7.4.2 Brittle deformation and crosscutting relationships

The mylonitic foliation in the Blossom Bar shear zone is cut by mineralized faults and veins as well as non-mineralized faults. Faults exposed in outcrop are few mm to cm thick, and the offsets are in the range of several cm to ~5 m. Minerals in veins crosscutting mylonitic foliation include epidote, prehnite \pm quartz, quartz, and calcite. Similar to the metagabbro unit, epidote veins cutting foliation are rare, and prehnite \pm quartz-, quartz-, and calcite-veins are predominant (appendix D, table D5). In the lower part of Blossom Bar Creek is a ~1.5 m wide layer which consists of granoblastic epidote and acicular actinolite (O/C-382). This layer could be a large vein or mineralized gash that formed during deformation in the Blossom Bar shear zone and was subsequently deformed. The crosscutting relationships found in outcrop, hand sample and thin section indicate the following relative ages from oldest to youngest: (1) mylonites, epidotes and epidote+actinolite veins formed; followed by (2) epidote veins; followed by (3) prehnite \pm quartz veins, followed by (4) quartz and calcite veins. Similar veins and crosscutting relationships are observed in the metatonalite unit and metagabbro unit.

4.7.5 Estimates of the temperatures of deformation in the metatonalite unit and Blossom Bar shear zone

Estimates of the temperatures of ductile deformation are based on the interpretation of the microstructures of quartz and plagioclase and the secondary mineral assemblages in deformed rocks.

Quartz forms small, dynamically recrystallized grains which have a strong lattice preferred orientation and occasionally an oblique grain shape fabric (appendix D, table D5). Large, relic quartz grains show subgrain structures and/or sweeping undulatory extinction. An oblique foliation in quartz is thought to develop in the combined regime of grain boundary migration- and subgrain rotation recrystallization, which is inferred to occur at medium- to high-grade conditions (Passchier and Trouw, 1996). The presence of a fluid phase aiding diffusion, however, may enhance grain boundary migration processes, and the oblique grain shape fabric formed probably at lower temperatures (low- to medium-grade). This is consistent with the observation that grain size reduction of plagioclase occurred predominantly by fracturing and/or grain abrasion suggesting the temperature at which dynamic recrystallization of plagioclase becomes important was not reached (450-550°C, Passchier and Trouw, 1996). Also, wedge-shaped deformation twins in plagioclase which form at temperatures above 500°C are not observed. Although plagioclase forms winged porphyroclasts in a fine grained matrix, typical core and mantle structures are not developed that would indicate grain size reduction by dynamic recrystallization. The cores and wings consist of a cloudy mineral aggregate indicative of replacement of plagioclase at green-schist facies conditions (ab + ep or ab + cz). Neocrystallization during deformation may have been an important process (Fitz Gerald and Stuenitz, 1993a, 1993b). Overall, it is estimated that the deformation occurred at low- to medium-grade conditions ($\leq 500^\circ\text{C}$).

At very low temperatures ($\sim 300^\circ\text{C}$), quartz deforms predominantly by brittle fracturing, pressure solution and solution transfer of material (Passchier and Trouw, 1996). The textures characteristic of this type of deformation include fractures in grains, undulose extinction, evidence for pressure solution and redeposition of the material such as in veins. The mylonitic samples from the Blossom Bar shear zone and the metatonalite unit contain abundant quartz veins which are also deformed and show undulose extinction. This may indicate redeposition of quartz during deformation. Thus, it is estimated that the minimum temperature for crystal plasticity is about 300°C.

Mylonites consisting of epidote quartz and chlorite could have formed in previously epidotized rocks or epidotization could have taken place during deformation. Epidosites in ophiolites occurring at mid-crustal levels (sheeted dike complex) are inferred to have formed between approximately 350° and

450° degree (Josephine ophiolite: Harper et al., 1988) which is well within the temperature range estimates for ductile deformation. Furthermore, crosscutting relationships of mylonites, mineralized faults and hydrothermal veins suggest retrograde conditions during deformation. The deformational structures together with characteristic mineral assemblages are, from oldest to youngest: (1) mylonites cut by $ep \pm qz$ veins and qz -veins (quartz in these veins is recrystallized) followed by (2) $pr \pm qz$ veins and $pu \pm qz$ veins (quartz in veins is usually not recrystallized), followed by (3) lau veins.

A boudinaged epidote vein in a quartz-rich, strongly recrystallized matrix was found (metatonalite unit, O/C-368d). Also, quartz veins are very rare in quartz-rich mylonitic rocks while they are much more abundant in mafic mylonitic rocks. As discussed in section 4.7.2.4, ductile deformation in mafic rocks probably ceased at a higher temperature than in quartz-rich rocks. It appears that ductile deformation continued in the quartz-rich rocks after (and during) the formation of epidote + quartz veins (epidote veins become deformation and, perhaps, destroyed), while mafic rocks deformed predominantly by brittle fracturing (and epidote and quartz veins are preserved). An increase in the fluid pressure P_f or the strain rate can cause fracturing in an otherwise ductily deforming rock (fracturing as a result of an increase in P_f is called hydrofracturing). Thus, variations in P_f and/or the strain rate may have played an important role in the formation of observed crosscutting relationships.

The crosscutting relationships suggests that ductile deformation took place within the temperature range of formation of epidotes (350°C and 450°C, Harper et al, 1988) to epidote + quartz veins (220°C to 405°C, Alexander et al., 1993 and references therein). Furthermore, undeformed prehnite and pumpellyite veins cutting across quartz-rich mylonites are much more abundant than epidote + quartz veins, suggesting that brittle deformation is predominant as prehnite + quartz veins (200-300°C) and pumpellyite \pm quartz veins (150-330°C) formed (table 2 of Alexander et al., 1993). Finally, prehnite veins are cut by laumontite veins. The upper limit of the stability of laumontite at 1 kbar is 250°C (Liou, 1971). Clearly, the crosscutting relationships indicate retrograde conditions.

4.7.6 Deformation of late intrusions in the metagabbro unit

Muscovite separates of two muscovite-garnet tonalite dikes in the metagabbro unit yielded $^{40}\text{Ar}/^{39}\text{Ar}$ cooling ages of 149 Ma (GDH-97-6 and GH-97-20; note that O/C-372b is from same dike as GH-97-20). Rocks of similar composition and fabric occur in the Blossom Bar shear zone. They consist of plagioclase, quartz, and muscovite (O/C-17-S32, O/C-19-S34). A 2 m wide layer of deformed tonalite containing biotite (O/C-417a) occurs between the metagabbro unit and Blossom Bar shear zone in Mule Creek. However, the sampled tonalitic rocks in the Blossom Bar shear zone do not contain garnet. Probably, they are not related to the garnet bearing tonalites. However, it is very likely that the muscovite $^{40}\text{Ar}/^{39}\text{Ar}$ cooling age of the tonalitic rocks in the Blossom Bar shear zone would yield the same cooling ages, because these rocks are similarly foliated and show evidence of ductile deformation such as recrystallization of quartz. Thus, the tonalitic rocks from the Blossom Bar shear zone are described in this section together with the garnet muscovite tonalites from the metagabbro unit.

4.7.6.1 Shear foliation and sense of shear

Commonly, a C/S-type fabric is observed in the samples consisting mainly of quartz and saussuritized plagioclase and having a small percentage of muscovite. The latter is usually intergrown with, or replaced by chlorite (O/C-372b, O/C-417A, GDH-97-6; appendix D, table D5). The C-type shears are continuous and consist of phyllosilicates separating microlithons of quartz and plagioclase (chapter 2, figures 2.46 and 2.52). Also, the C-type shear bands anastomose around plagioclase porphyroclasts, some of which have σ -type wings. Variably wide (50-300 μm) quartz ribbons are parallel C-surfaces and also wrap around plagioclase porphyroclasts. Often, the S-planes are not clearly defined in thin section and are more easily recognized in hand samples. Large, relic quartz grains show undulose extinction and/or contain subgrains which pass laterally into small recrystallized grains. In two samples, an oblique grain shape fabric of recrystallized quartz was identified (O/C-372b and O/C-417a). Commonly, very small flakes of muscovite and chlorite occur in the matrix of strongly recrystallized quartz. The tonalitic rocks in the Blossom Bar shear zone contain abundant broken porphyroclasts (appendix D, table D5) in a matrix of

recrystallized quartz. These samples appear similar to cataclasites because of the abundant broken fragments, and sense of shear indicators could not be identified.

The shear foliation of the tonalitic samples in the metagabbro unit (O/C-372b, GH-97-6) is not parallel to the mean shear foliation in the metagabbro unit, but the shear foliation of the tonalitic rocks (O/C-17-S32) in the Blossom Bar shear zone is subparallel to that of the host unit. However, the orientation of the stretching lineations and the sense of shear determined in these samples is consistent with the overall sense of shear in the metagabbro and metatonalite units (figure 4.15b and 4.15d).

The microstructures in the garnet muscovite tonalites are very similar to those of silicic rocks in the metatonalite unit and Blossom Bar shear zone. Thus, the estimate of temperature of ductile deformation for the gar musc tonalites is the same as for the silicic rocks in the other units (300-500°C, section 4.7.5).

4.7.6.2 Brittle deformation and crosscutting relationships

The tonalitic samples containing muscovite from the metagabbro unit and Blossom Bar shear zone are crosscut by prehnite \pm quartz veins. Epidote veins crosscutting foliation are not found. However, epidote occurs in a vein in a large, broken plagioclase porphyroclast in GH-97-6. Also, small epidote grains occur in other plagioclase porphyroclasts and within the recrystallized matrix of quartz.

4.7.7 Summary

The shear foliation in the metatonalite unit, metagabbro unit and Blossom Bar shear zone strike northeast and have subvertical dips (figure 4.15). The stretching lineation in the metatonalite unit (figure 4.15c) and metagabbro unit (figure 4.15b) plunge moderately steep NE, whereas in the Blossom Bar shear zone the stretching lineations are subvertical (figure 4.15c) strongly suggesting distinct directions of transport. In the present-day coordinates, the sense of shear in the metagabbro and metatonalite units is dextral with a reverse component (appendix D, table D6) whereas in the Blossom Bar shear zone the sense-of-shear criteria indicate normal displacement (the average shear plane is used as reference plane to determine the mode of shearing in each unit).

The microstructures in samples from the metagabbro unit are interpreted as indicative of temperatures of 600°C - 400°C for ductile deformation in mafic to quartz-bearing rocks. Brittle failure in the metagabbro unit appeared to become an important process at temperatures $\leq 400^\circ\text{C}$. Deformed, quartz-rich rocks in the metagabbro unit (GH-97-6, GH-97-20, O/C-372b), metatonalite unit and Blossom Bar shear zone have microtextures that are interpreted to have formed during ductile deformation at low- to medium-grade conditions (300 to 500°C). It cannot be determined whether epidotes formed before or only during ductile deformation. However, the mineral assemblages in veins and faults crosscutting ductily deformed rocks in these units indicate retrograde conditions.

The paleostress analysis of quartz and prehnite mineralized faults in the metatonalite unit shows that the direction of the maximum principal stress is well-characterized, but different programs determined different directions for the intermediate and minimum principal stress axes (figure 4.16). The faults could have formed in axial compression ($\sigma_1 > \sigma_2 = \sigma_3$), or any of the basic assumptions on which the paleostress analyses rely are not satisfied. The determined principal stress axes shown in figure 4.16 differ significantly from the paleostress analysis of epidote and prehnite mineralized faults in the sheeted dike complex (figures 4.10, 4.11 and 4.12), strongly suggesting slip on the faults in the data sets occurred in more than one stress field.

4.7.8 Using the results of the structural study

4.7.8.1 Occurred ductile deformation and brittle faulting in the same stress field?

In this section, the question is addressed whether or not the analyzed faults in the metatonalite unit formed during the same deformational event as the ductily sheared rocks. If the brittle faults formed during the same deformational event under the same stress field, the principal stress axes determined from the stress inversion in figure 4.16 should produce “slip” on the average shear planes of the metatonalite unit (C_t), metagabbro unit (C_m) and the Blossom Bar shear zone (C_{sz}) in the direction of the stretching lineations L_t , L_m and L_{sz} , respectively (figure 4.15). Basically, it is tested if the stress field that is consistent with slip on the brittle faults is also consistent with ductile shearing in the Blossom Bar shear zone, metagabbro unit and metatonalite unit as a whole. Because the shear plane and sense and direction of shear

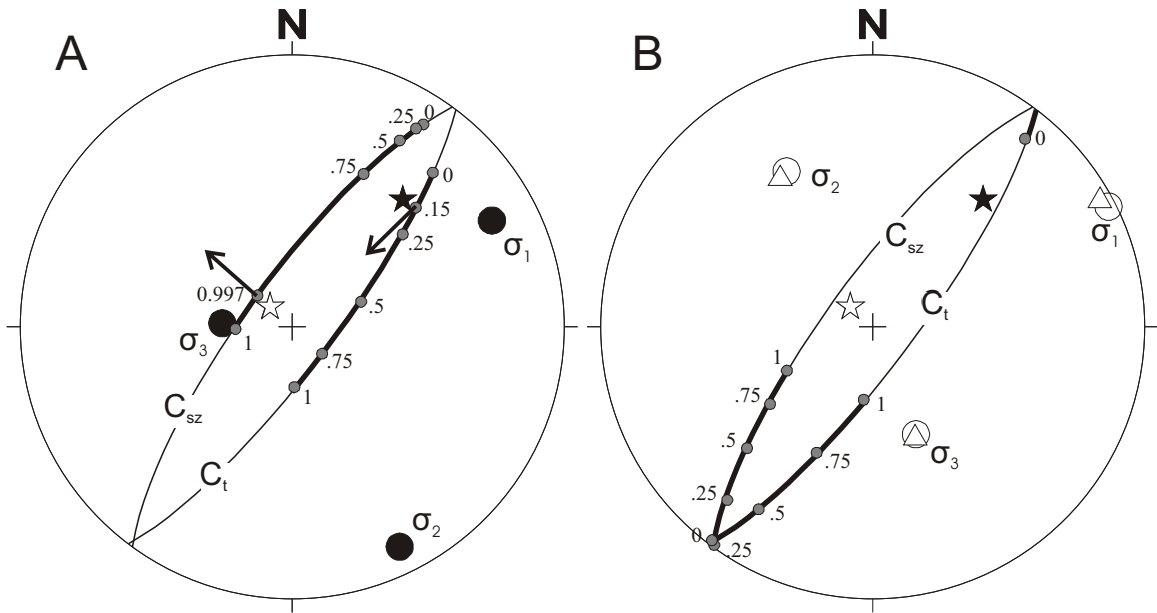
is very similar in the metagabbro unit and the metatonalite unit, only the average shear planes and stretching lineations from the metatonalite unit and the Blossom Bar shear zone are considered. The basic assumptions of this evaluation are: (1) the brittle-ductile shear foliation in the metatonalite unit and Blossom Bar shear zone are planes of discontinuity similar to brittle faults and can be represented by the mean shear planes C_t and C_{sz} ; (2) slip occurs in the direction of the shear stress τ on the planes C_t and C_{sz} ; and, (3) the stretching lineations L_i are parallel to τ on the shear planes.

Are any of the three solutions of the paleostress analysis in figures 4.16d consistent with slip on C_t and C_{sz} subparallel to the direction of the stretching lineation L_t and L_{sz} ? Knowing the principal stresses (i.e. orientation and magnitude), the directions of the shear stress τ on C_t and C_{sz} can be found with a simple stereographic construction (Means, 1989). The stereographic construction of Means (1989) yields the relative magnitudes, expressed as the stress ratio $\varphi = (\sigma_2 - \sigma_3) / (\sigma_1 - \sigma_3)$, if the direction of slip is known (assumption 2: slip occurs in the direction of τ). Using the method of Means (1989) and the principal stress directions of figure 4.16d, the shear stresses on C_t and C_{sz} are determined for the stress ratios $\varphi = 0, 0.25, 0.5, 0.75$ and 1 (figure 4.17). The results for the foliation plane C_g are not shown because they are very similar to C_t . Three different constructions are made to evaluate the solutions returned by ROMSA, TENSOR/STRESS and FAULTKIN. (A.) ROMSA, figure 4.17a: τ is either parallel to the mean stretching lineation in the metatonalite unit (L_t) or to the mean stretching lineation in the Blossom Bar shear zone (L_{sz}). The shear stress τ cannot be parallel to L_t and L_{sz} at the same time, because slip occurs along C_t in the direction of L_t if $\varphi = 0.15$, and slip along C_{sz} occurs in the direction of L_{sz} if $\varphi = 0.997$. The values of φ describe two fundamentally different stress fields, the first is close to uniaxial compression ($\varphi=0$), the second is similar to uniaxial tension ($\varphi=1$). This indicates that the stress axis returned by ROMSA cannot produce shear on the shear planes in the direction of observed stretching lineations. (B.) TENSOR/STRESS, figure 4.17b: τ occurs always at an angle to the stretching lineation L_t and L_{sz} , regardless of the value of φ . This indicates that slip on C_t and C_{sz} would occur in directions much different from observed L_t and L_{sz} if the shown stress axes would represent the regional stress field of ductile deformation. (C.) FAULTKIN, figure 4.17c: τ on C_t is parallel to L_t if $\varphi = 0.96$. However, τ on C_{sz} occurs always at an angle with L_{sz} regardless of the value of φ . This indicates that slip on C_{sz} would occur in a

Figure 4.17

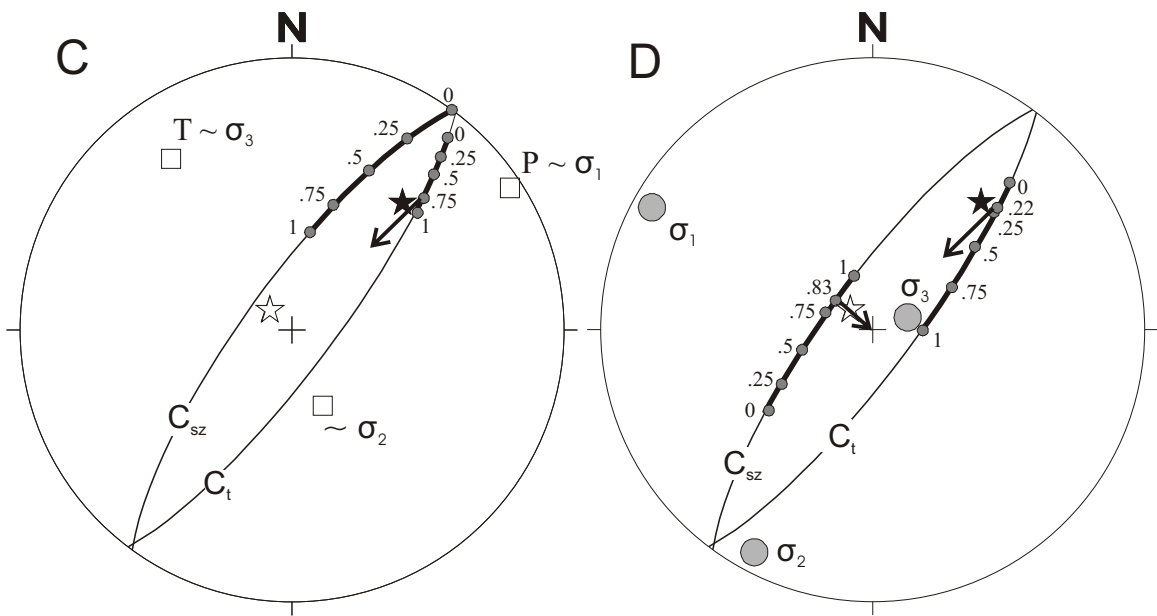
Lower hemisphere, equal area stereographic projections of the mean shear plane C_t and C_{sz} as well as corresponding mean stretching lineations L_t and L_{sz} in the metatonalite unit and Blossom Bar shear zone, respectively. The directions of the shear stress τ on C_t and C_{sz} for different stress fields are determined using the graphical method of Means (1989).

- a. The shear stress on C_t is parallel to the mean stretching lineation L_t if $\varphi = 0.15$, while the shear stress on C_{sz} is parallel to the mean stretching lineation L_{sz} if $\varphi = 0.997$.
- b. The shear stress on C_t and C_{sz} is not parallel to L_t and L_{sz} , respectively, for any value of φ .
- c. The shear stress on C_t is parallel to the mean stretching lineation L_t if $\varphi = 0.96$, whereas the shear stress on C_{sz} is not parallel to L_{sz} for any value of φ .
- d. The shear stress on C_t is parallel to the mean stretching lineation L_t if $\varphi = 0.22$, whereas the shear stress on C_{sz} is parallel to the mean stretching lineation L_{sz} if $\varphi = 0.83$. The direction of the shear stress is opposite to the sense of shear determined in mylonitic samples from the Blossom Bar shear zone.



● Stress axes determined by analysis of brittle faults in metatonalite unit using ROMSA

○ △ Stress axes determined by analysis of brittle faults in metatonalite unit using TENSOR and STRESS



□ P and T axes determined by analysis of brittle faults in metatonalite unit using FAULTKIN

● Mean of results from the paleostress analysis of brittle faults in the sheeted dike complex (domains A and B, figure 4.11d)

Explanation

☆ Mean stretching lineation (L_{sz}) in Blossom Bar shear zone
 ★ Mean stretching lineation (L_i) in metatonalite unit

C_t Mean foliation plane metatonalite unit
 C_{sz} Mean foliation plane Blossom Bar shear zone

● Shear stress τ on C_i for various values of ϕ
 $\phi = (\sigma_2 - \sigma_3) / (\sigma_1 - \sigma_3)$

／ All possible directions of τ in the foliation plane C_i ($0 < \phi < 1$)

direction much different from observed L_{sz} if the shown stress axes would represent the regional stress field of ductile deformation. The results of this evaluation clearly show that the stress field that produced slip on the brittle faults in the metatonalite unit could not have produced “slip” along the mean shear planes C_t and C_{sz} in the direction of the mean stretching lineations L_t and L_{sz} , respectively.

The same procedure is used to test whether or not the orientations of the principal stress axes determined from the paleostress analysis of epidote and prehnite mineralized faults in the sheeted dike complex (figure 4.11d) are consistent with slip on C_t and C_{sz} in the directions of the stretching lineations L_t and L_{sz} . Figure 4.17d shows that τ is parallel to L_t when $\varphi = 0.22$ and parallel to L_{sz} when $\varphi = 0.83$. Not only are the stress ratios different, but also the direction of slip on L_{sz} is opposite to that determined in thin section. Clearly, the stress field that best fits the fault slip data from the sheeted dikes (domains A and B, figure 4.11d) cannot produce slip on C_t and C_{sz} in a direction parallel to L_t and L_{sz} . Further evaluation of the results show that the stress field that best fits the fault slip data from domain D (figure 4.12d) cannot produce slip on C_t and C_{sz} in a direction parallel to L_t and L_{sz} (evaluation not shown in figure 17).

The results illustrated in figure 4.17 clearly show that neither the solutions of the paleostress analysis of prehnite and quartz mineralized faults in the metatonalite unit nor the solution of the paleostress analysis of epidote and prehnite mineralized faults in the sheeted dike complex are consistent with slip on C_t and C_{sz} in the direction of L_t and L_{sz} (assuming slip occurs in the direction of the shear stress τ). This strongly suggests that some or all analyzed faults in the metatonalite unit and sheeted dike complex formed in different stress fields than the stress field which produced shearing along C_t and C_{sz} in the metatonalite unit and Blossom Bar shear zone, respectively. This result is consistent with the interpretation that the mineralized faults in the sheeted dike complex are “oceanic” in origin.

4.7.8.2 Determination of the stress tensor for ductile deformation

Is there a stress tensor that is compatible with simultaneous “slip” along the mean shear planes C_t , C_g and C_{sz} in the directions of the stretching lineations L_t , L_g and L_{sz} in the metatonalite unit, metagabbro unit and Blossom Bar shear zone? This problem was solved performing a stress inversion using TENSOR (Angelier, 1979) which relies on the assumption that slip occurs parallel to the maximum resolved shear

stress. The “fault slip data” put into the program included the orientation of the mean shear foliations C_t , C_g and C_{sz} (assumed to represent fault planes), the mean stretching lineations L_t , L_g and L_{sz} (assumed to represent slip linears) and the sense of shear (section 4.7). The stress tensor that satisfies these data was computed by the paleostress program ($\sigma_1 = 145^\circ/66^\circ$, $\sigma_2 = 298^\circ/21^\circ$, $\sigma_3 = 032^\circ/10^\circ$, $\varphi = 0.72$). However, TENSOR may return erroneous results if the faults are very similar in terms of orientation and displacement, and/or only a very small number of faults is analyzed (Schimmrich, 1991). Therefore, the results returned by TENSOR were evaluated.

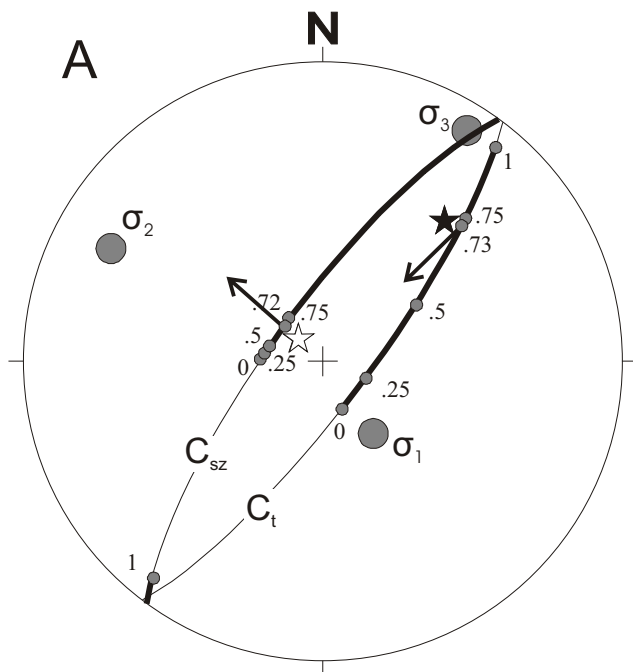
The evaluation of the orientation of the stress axes returned by TENSOR is illustrated in figure 4.18a. The shear stress τ on C_t and C_{sz} was constructed using the directions of the principal stress axes determined by TENSOR (see method of Means, 1989). As shown in figure 4.18a, τ on C_t is parallel to L_t , and τ on C_{sz} is parallel to L_{sz} for equal values of $\varphi = 0.72$. The graphically determined values of φ are equal to the value of φ returned by TENSOR. Clearly, the stress tensor found using the paleostress analysis satisfies the “fault slip” data.

In what direction would the prehnite and quartz mineralized faults in the metatonalite unit slip, if the stress tensor that is compatible with slip on C_t and C_{sz} parallel to L_t and L_{sz} is applied to the prehnite and quartz mineralized faults? The stress axes of figure 4.18a ($\sigma_1 = 145^\circ/66^\circ$, $\sigma_2 = 298^\circ/21^\circ$, $\sigma_3 = 032^\circ/10^\circ$ and $\varphi \sim 0.72$) were used to predict the direction of slip on the fault planes shown in figure 4.16b, assuming slip occurs in the direction of τ (method of Means, 1989). The results of this analysis are presented in a ‘Hoeppner plot’ in figure 4.18b.

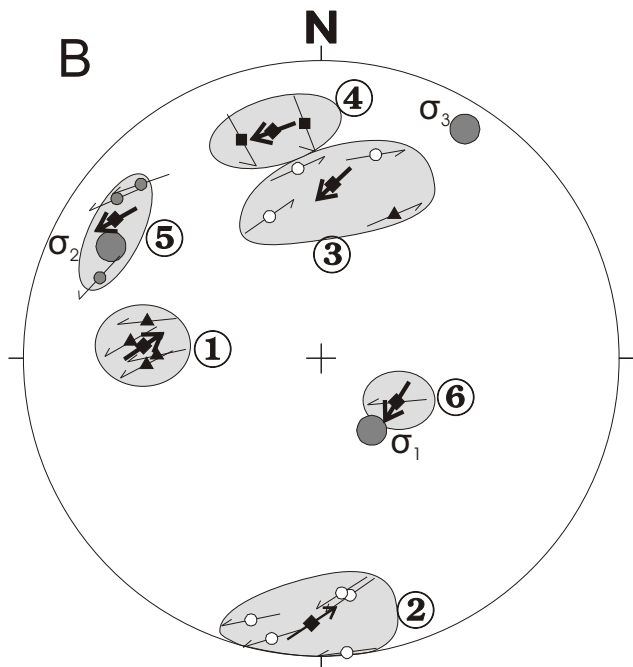
The vector, representing the shear stress τ on the faults #1 through #6, is shown in an orientation so that, if slip occurs in the direction of τ , the movement of the hangingwall block is indicated. Thus, the vectors representing τ can be directly compared to the slip linears of the faults determined in outcrop (figure 4.18b). The stress field shown in figure 4.18b produces slip on faults in clusters #1, #2 and #3 in a direction opposite to that observed in outcrop (offset markers or sense-of-shear criteria of Petit, 1987). Slip on the faults in cluster #5 is consistent with the stress tensor. The remaining faults (#4 and #6) would slip at high angles with respect to the observed striation.

Figure 4.18

- a. Lower hemisphere, equal area stereographic projections of the mean shear plane C_t and C_{sz} and corresponding mean stretching lineations L_t and L_{sz} in the metatonalite unit and Blossom Bar shear zone, respectively. The directions of the principal stresses were obtained from the stress inversion using the mean shear planes C_t , C_g , and C_{sz} , the stretching lineations L_t , L_g , and L_{sz} and the sense of shear determined in thin section as “fault-slip data”. The results of the stress inversion and the predicted sense of shear on the shear planes C_t and C_{sz} are shown. It is demonstrated that the determined stress tensor is compatible with the sense and direction of ductile shearing in the Blossom Bar shear zone and metatonalite unit.
- b. The stress tensor of figure 18a is used to predict the sense of slip on faults cutting mylonitic foliation in the metatonalite unit. It is assumed that slip occurs in the direction of the maximum resolved shear stress on planes 1 through 6. The predicted sense of shear is opposite to observed sense of shear for faults #1, #2, and #3. The predicted sense of shear is consistent with fault #5, and the predicted sense of shear occurs at a high to intermediate angle with respect to observed sense of shear in faults #4 and #6.



- ☆ Mean stretching lineation Blossom Bar shear zone
- ★ Mean stretching lineation metatonalite unit
- Shear stress τ on C_i for various values of ϕ
 $\phi = (\sigma_2 - \sigma_3) / (\sigma_1 - \sigma_3)$
- M_t Mean foliation plane metatonalite unit
- M_{sz} Mean foliation plane Blossom Bar shear zone
- Section of foliation plane in which τ lies assuming $0 < f < 1$



- right-lateral strike slip fault (n = 3)
- left-lateral strike slip fault (n = 8)
- normal fault (n = 3)
- ▲ reverse fault (n = 5)
- ↘ Mean pole to fault clusters. The vector indicates the direction of shear stress τ (hangingwall block is assumed to slip in direction of τ)

The result that the predicted slip direction of faults #1, #2 and #3 is opposite to the slip direction observed in the field can be explained in several ways: (1) the sense of shear was not correctly determined in outcrop. This is not very likely because offset markers were used for 50% of the faults. (2) The shear fractures formed or were reactivated during later deformation; or (3) the brittle shear fractures and ductile shear planes could have interacted with each other (wall-rock flow and fault-slip could be coupled) so that slip did not occur in the direction of the shear stress, but is a function of strain. Further study of the relationship between finite strain and stress is necessary in the ductily sheared rocks from the Wild Rogue Wilderness.

4.8 Discussion

The main textural and structural features of the rocks of the study area are reviewed as well as the temperature constraints from metamorphic mineral assemblages, microstructure and hornblende-plagioclase geothermometry (chapter 3) and discussed in the light of the new isotopic ages determined in samples from the mapped units. A summary of the sample ages using the $^{40}\text{Ar}/^{39}\text{Ar}$ and U/Pb analytical methods is shown in figure 4.19. A multistage evolution of the ophiolite exposed in the Wild Rogue Wilderness is recognized and at least three distinct episodes of deformation and metamorphism are recorded in the basement rocks of the study area (figure 4.19).

4.8.1 Possible pre-ophiolite deformation and metamorphism

The oldest deformational phase is recognized in the metagabbro unit (figure 4.19). Subhedral plagioclase and hornblende in the metagabbro are aligned and define a relict foliation and lineation (figure 4.15a) which is interpreted to have formed by magmatic flow (section 4.7.2.1). Pillowed and attenuated mafic dikes intruding the gabbro occur subparallel to the mineral foliation. These structures are interpreted to have formed by intrusion of mafic magma in a deforming, partially crystallized gabbro.

The magmatic texture and flow foliation (figure 4.15a) are overprinted, but not completely erased by inferred amphibolite facies metamorphism. Amphibolite grade conditions could have been maintained over a long period of time in an area of extended plutonism, such as a volcanic arc, or during regional

| Ma | Sample ages and units | Interpretation |
|---------------------------|------------------------------------------------------------------------------------------------------------------|---------------------------------------------------------------------------------------------------------------------------------------------------------------------------------|
| —145— — — — — | Metagabbro unit garnet muscovite tonalite dikes (muscovite $^{40}\text{Ar}/^{39}\text{Ar}$) | Intrusion and ductile deformation of muscovite garnet tonalite dikes marking episode of wide-spread ductile deformation in the Wild Rogue Wilderness. |
| —150— — — — — | Uppermost section of Mule Mountain volcanics (hornblende $^{40}\text{Ar}/^{39}\text{Ar}$) | Deposition of arc-related volcanogenic sedimentary rocks; episode of arc-related extrusive and intrusive magmatism and subsequent (subseafloor) hydrothermal metamorphism. |
| —155— — — — — | Half Moon Bar gabbro (hornblende $^{40}\text{Ar}/^{39}\text{Ar}$: 157 ± 2 Ma zircon U/Pb: 159-160 Ma) | |
| —160— — — — — | Pillow unit* | Formation and subsequent extensional deformation of the Rogue Wilderness ophiolite during seafloor spreading, including normal faulting and subseafloor hydrothermal alteration |
| —165— — — — — | Sheeted dike complex Metatonalite unit (zircon U/Pb 164 ± 1 Ma) | |
| —170— — — — — | Metagabbro unit (muscovite $^{40}\text{Ar}/^{39}\text{Ar}$ 171.4 ± 3.1 Ma) | Amphibolite facies (regional?) metamorphism of gabbroic rock with relic magmatic foliation |
| —175— | | |

* The minimum age of the pillow unit is constrained by the intrusion of the Half Moon Bar gabbro

Figure 4.19: Summary and interpretation of isotopic ages in the Rogue Wilderness remnant of the CRO.

metamorphism. Probably the most distinguishable feature of this (regional?) metamorphic event is the uniform, dark-green color of the hornblende, uncharacteristic for oceanic gabbros (Cann, 1977). Equilibrium temperatures of hornblende-plagioclase pairs in three metagabbro samples range between $635 \pm 38^\circ\text{C}$ (assuming 2 kbar) and $670 \pm 28^\circ\text{C}$ (assuming 8 kbar) using the improved hornblende-plagioclase geothermometer of Holland and Blundy (1994). Locally, mylonites may have formed during the amphibolite facies metamorphic (and deformational) event such as sample O/C-384 in which plagioclase porphyroclasts show recrystallized edges and occur in a fine-grained matrix of recrystallized plagioclase and disseminated flakes of hornblende. Intense grain size reduction of plagioclase by recrystallization occurs apparently at temperatures in excess of 550°C (Fitz Gerald and Stuenitz, 1993a and references therein). Later, solid-state deformation evident in the metagabbro unit is characterized by a upper greenschist facies mineral assemblage (and lower grade) as well as by fragmentation of plagioclase in sheared rocks, suggesting later deformation occurred at lower temperatures ($\leq 500^\circ$; see section 4.7.2.4 and 4.7.5).

The weighted mean of two separate hornblende $^{40}\text{Ar}/^{39}\text{Ar}$ analyses of sample O/C-373b from the metagabbro unit indicates a cooling age of 171.4 ± 3.1 Ma. This is interpreted to mark the end of amphibolite-facies metamorphism. Similar, Mid-Jurassic cooling-ages (169-173 Ma) are reported by Hacker et al. (1995), and Wright and Fahan (1988) in the Klamath Mountains province, and constrain the age of Middle Jurassic regional deformation and metamorphism in this area (Wright and Fahan, 1988; Siskiyou event of Coleman et al., 1988). This regional event apparently coincides with the reestablishment of oceanic arc magmatism after a ~ 20 Ma hiatus of the volcanoplutonic arc built on western North America (Yule, 1996). Saleeby and Harper (1993) proposed that a collision with an insular superterrane in mid Jurassic time could have occurred explaining the Mid Jurassic cooling ages of rocks in the Klamath Mountains province. In contrast, Harper et al. (1994) called this event a magmatic arc orogeny (model 3 in chapter 1, figure 1.6).

Note that the cooling ages of the metagabbro unit do not overlap within error of the analyses with the crystallization age of the sheeted dike complex and the metatonalite unit (164 ± 1 Ma). It is very likely that the metagabbro unit is not comagmatic with the sheeted dike complex and does not represent

the upper plutonic sequence of the Rogue Wilderness remnant of the CRO. Also, the differences in the geochemistry and magmatic affinity of the metagabbro unit and screens of cumulate gabbro in the sheeted dike complex indicate that the metagabbro unit is not part of the ophiolite (chapter 5). The distinct age and metamorphic mineral assemblage of the metagabbro (uniformly colored hornblende in contact with oligoclase: hornblende-plagioclase pairs equilibrated at ~635-670°C) are consistent with the hypothesis that the metagabbro unit represents a fragment of rifted Mid-Jurassic (North American) basement rocks (e.g., Rattle Snake Creek terrane; Wright and Wyld, 1994), and the metagabbro unit could be older rift-facies in the Rogue Wilderness remnant of the CRO. Within the framework of this interpretation, the hornblende $^{40}\text{Ar}/^{39}\text{Ar}$ cooling age of 171.4 ± 3.1 could mark the time of break-up and rifting of the Mid-Jurassic arc built on western North America (the metagabbro cooled below 500°C, and hornblende closed to Ar-diffusion).

The retrograde mineral assemblage evident in crosscutting veins and faults may have formed during cooling from amphibolite facies conditions in mid-Jurassic time, which could have taken place during the initial stages of the opening of the marginal basin by rifting of the Mid-Jurassic arc. Or, the retrograde assemblages may have formed much later during one or more of the following deformational and metamorphic phases outlined in the following subsections.

4.8.2 Formation of the ophiolite, related deformation and hydrothermal alteration

The second phase of deformation is characterized by the formation of the metatonalite unit, sheeted dike complex, and the pillow unit marking an episode of construction of new oceanic crust by magmatic processes. This phase was also characterized by tectonic extension and seafloor hydrothermal alteration.

After the metagabbro cooled below amphibolite facies temperatures, opening of a marginal basin occurred by seafloor spreading (~163-164 Ma). This is indicated by the occurrence of a large swarm of parallel dikes intruding cumulate gabbro (figure 4.7, domains A through F). In the sheeted dike complex, and probably in the metatonalite unit and metagabbro unit, this phase is also characterized by brittle fragmentation, faulting, and pervasive lower amphibolite to greenschist grade and lower hydrothermal

alteration near the spreading axis. Similarly, extensive fragmentation, cataclasis and ubiquitous hydrothermal alteration is evident in the pillow unit, however, the grade is somewhat lower and more localized (greenschist facies and lower grade hydrothermal alteration). Perhaps, the epidosite zones in the metagabbro unit, metatonalite unit, sheeted dike complex and the pillow unit are the most characteristic features of this episode. The rocks in the epidosite zones underwent extreme calcium metasomatism typified by large losses of Na₂O and MgO and gain of CaO (i.e. basalt or gabbro is metasomatized to granoblastic ep - Qtz - chl zones typically near fractures and faults). This metasomatism requires extremely high water-rock ratios (Harper et al., 1988). The epidiosites occurring in narrow, often dike-parallel zones, in the Rogue Wilderness ophiolite is similar to these of many other ophiolites (e.g. Harper et al. 1988; Alexander and Harper, 1992; Bettison-Varga et al., 1995; Evarts and Schiffmann, 1983; Schiffmann, et al., 1991). This type of alteration is inferred to have occurred in a subseafloor setting near the ridge axis where large quantities of seawater-derived fluids are circulated through fractures and faults in the crust within a short period of time. The epidosite zones are interpreted to mark the pathways of discharge of highly reacted seawater-derived fluids (discharge zones Harper et al. 1988, Bettison-Varga et al., 1995). Note that a dike crosscuts an epidosite zone in the sheeted dike complex, indicating that the alteration occurred near the ridge axis.

The age of the sheeted dike complex is constrained by the zircon-U/Pb age of 163 ± 1 Ma determined in an anorthosite layer occurring in a screen of cumulate gabbro (SC-1) cut by diabasic dikes. A sample from the metatonalite unit (SC-2) yields a zircon-U/Pb age of 164 ± 1 Ma. The minimum age of the pillow unit is constrained by the intrusion of the Half Moon Bar diorite (157.2 ± 2.0 Ma using hornblende ⁴⁰Ar/³⁹Ar; and 159 -160 Ma using zircon U/Pb methods). The pillow unit is probably comagmatic with the sheeted dike complex. Overall, these isotopic ages, marking the formation of the ophiolite, agree well with the ages of other, late-Jurassic ophiolite remnants exposed along the western margin of North America (e.g., Harper et al. 1994, Hopson et al, 1981).

4.8.2.1 Direction of seafloor spreading and early normal faulting

Aspects of this constructional (magmatic construction) as well as deformational episode are discussed below in more detail, and a possible model of the fault- and spreading-geometry of the Rogue Wilderness ophiolite is proposed, which is based on detailed mapping of the sheeted dike complex and the analysis of brittle faults presented in section 4.6.s

The history of events, recorded in the rocks of the sheeted dike complex, can be determined using crosscutting relationships, petrography and structural analysis. The following sequence of events is inferred: (1) intrusion and crystallization of layered cumulate gabbro followed by formation of amphibole veins and shear bands; (2) injection of diabasic and microdioritic dikes into gabbro (assuming dikes are originally subvertical); (3) pervasive alteration of the gabbro and dikes as indicated by a lower amphibolite to greenschist facies mineral assemblages, formation of epidiosites and extensive faulting (possible tilting of fault blocks around rotation axis T, figure 4.9); (4) diabasic and microdioritic dikes are injected into faults or cut epidiosites, indicating overlap of dike injection and faulting associated with formation of epidote + quartz and prehnite + quartz veins as cement (possible tilting of fault blocks, figure 4.9); (5) formation of veins indicating retrograde hydrothermal metamorphism, i.e. prehnite + quartz and pumpellyite + quartz veins (possible continued tilting of fault blocks).

The model of the fault- and spreading-geometry at the mid-crustal level of the Rogue Wilderness ophiolite relies on the following assumptions: (1) the sheeted dike complex can be restored to paleohorizontal by unfolding the Tertiary and Cretaceous synclines, and the correction for Tertiary and Cretaceous folding can be approximated with a clockwise rotation of about 90° around a horizontal axis (R trending 045° (figures 4.1a and 4.1b, section 4.5); (2) the restored structures formed at or near the ridge axis and not during earlier or later episodes of deformation, and (3) dikes were injected subvertically perpendicular to the direction of the minimum principal stress.

Figure 4.20 shows the stereographic projections of planar structures in the sheeted dike complex in domains A and B after correcting for Tertiary and Cretaceous folding. These structures are inferred to have formed during events (1) and (2) and include the cumulate layering in the gabbroic screens (figure 4.20a), the amphibole veins and shear-bands (figure 4.20b and 4.20c), and the diabasic and microdioritic

dikes (figure 4.20d). Note that the strike of the mean dike (north 049° west) is parallel to the strike of the mean cumulate layering (north 045° west) as well as to the strike of the amphibole veins and shear bands (north 045° west) in the gabbroic screens (figure 4.20).

The mean igneous layering strikes north 045° west and dips 36° southwest and forms an angle of about 60° with the steeply dipping dikes (figure 4.20a). Although the amphibole veins and shear bands in domains A and B were rotated around R (figure 4.20b) they seem to be unchanged in attitude compared to figure 4.10a, because the rotation axis R is approximately normal to these planar structures. As a result, the restored amphibole veins and shear bands strike northwest and dip steeply northeast (figure 4.20b). However, the amphibole shear bands with right-lateral offset in the present-day coordinates (figure 4.10b) become normal faults, and two shear bands with normal displacement become right-lateral strike-slip faults after correcting for Cretaceous and Tertiary folding (figure 4.20c). Additionally, the rotated principal stress axes are shown (mean of the analysis in figure 4.10d using four different techniques). The stress axes determined from the fault-slip data of amphibole shear bands is consistent with normal faulting and extension perpendicular to the dikes (σ_1 is vertical, σ_2 is horizontal and parallel to the dikes, and σ_3 is horizontal and perpendicular to the dikes). Also, the direction of σ_3 in figure 4.20c is subparallel to the direction of extension related to injection of subvertical dikes (figure 4.20d). These data indicate that normal faulting must have followed closely upon the crystallization of the cumulate gabbro (event 1) and preceded and overlapped with the intrusion of subvertical dikes (event 2). Early normal faulting and intrusion of dikes probably occurred under the same stress field. Overall, the geometric relationships of the igneous layering, amphibole veins and shear bands, sheeted dikes and calculated stress axes suggest that an adequate rotation axis and rotation angle were used to restore the ophiolite (sheeted dike complex) to paleohorizontal (section 4.5).

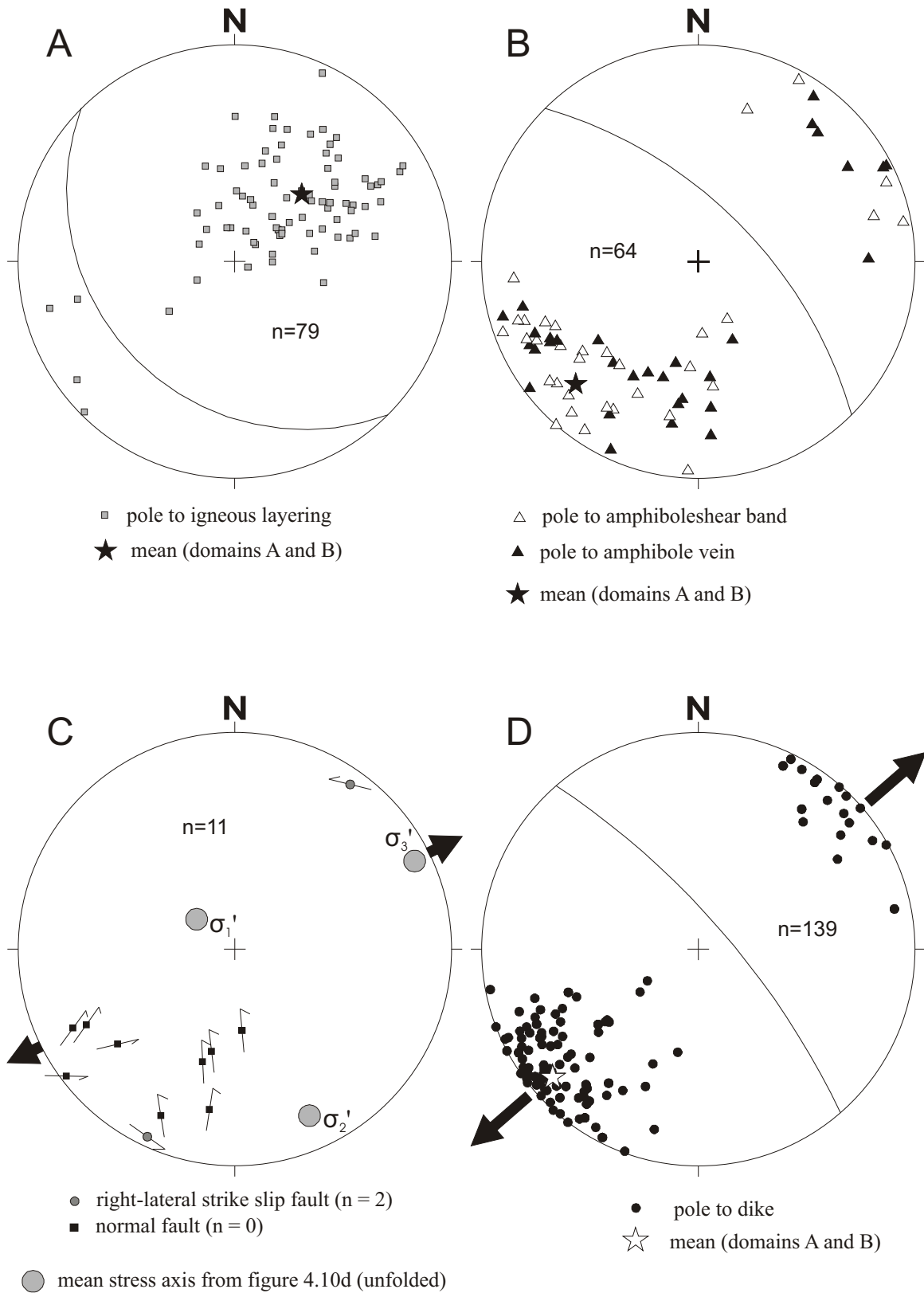
Figure 4.21 shows a schematic diagram of the structure of the sheeted dike complex in domains A and B. Consistent results between methods for the direction of the minimum principal stress were obtained (figure 4.10), suggesting the stress field remained static during events (1) and (2). The σ_3^R -direction is horizontal and roughly perpendicular to the strike of the dikes (figure 4.20c and 4.20d), σ_2^R is also

Figure 4.20

Lower hemisphere, equal area stereographic projections of structural data of domains A and B after correcting for Tertiary and Cretaceous folding.

- a. The mean igneous layering in the screens of cumulate gabbro dips 35° southwest and strikes north 045° west.
- b. The amphibole veins and shear bands remain subvertical after correcting for Tertiary and Cretaceous folding, are subparallel to the sheeted dikes (d) and occur at a high angle with respect to the igneous layering (a).
- c. The arrows affixed to the poles to cemented faults indicate the direction of slip of the hanging wall block (see figure 4.3). The solution of the paleostress analysis of the cemented faults (after correcting for Tertiary and Cretaceous folding) is consistent with extension by normal faulting.
- d. Most of the dikes are subvertical and subparallel to the amphibole veins and shear bands. Only few have relatively shallow dips. The average direction of extension for subvertical dike-injection is shown assuming dikes were injected perpendicular to the direction of the minimum principal stress.

Structural data from the sheeted dike complex corrected for Cretaceous and Tertiary folding



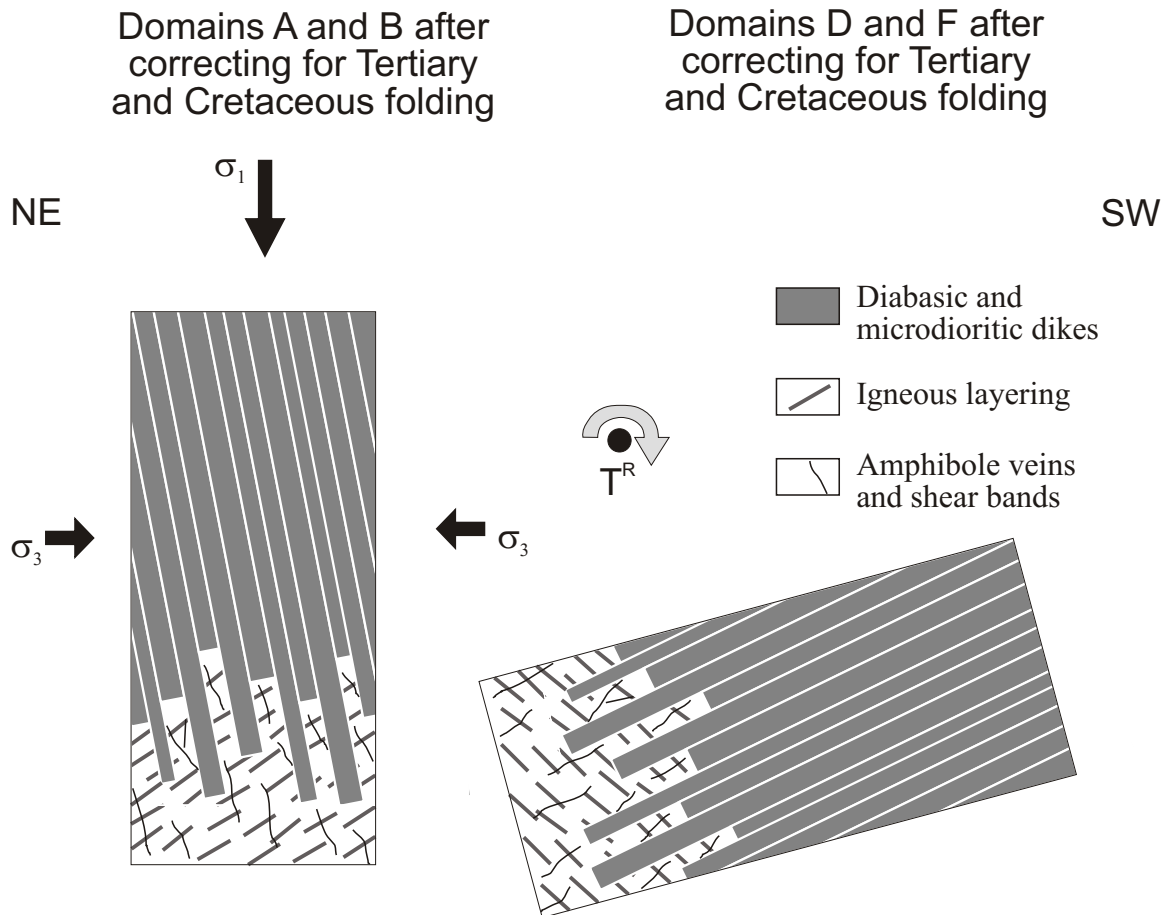


Figure 4.21

Geometric relationships of structures in domains A and B after correcting for Tertiary and Cretaceous folding. The intrusion and crystallization of the cumulate gabbro, containing moderately steep, southwest-dipping layers (figure 4.20a), is followed by the formation of steeply northeast-dipping amphibole veins and shear bands (figures 4.20b and 4.20c). Most of the shear bands indicate normal displacement, whereas amphibole veins are interpreted as mode 1 cracks. The formation of the amphibole veins and the shear bands is consistent with SW-NE directed extension by tensile parting and normal faulting, respectively. Then, SW-NE directed extension occurs by subvertical injection of diabasic and microdioritic dikes (figure 4.20d) into cumulate gabbro truncating older structures. Tilting of dikes determined in other domains is inferred around a horizontal axis (T^R) subparallel to the strike of the dikes (see figure 4.9).

horizontal and approximately parallel to the strike of the dikes, and σ_1^R is subvertical. The mode of faulting is normal and is consistent with an extensional tectonic regime near a spreading center. The geometric relationship between the dikes and the igneous layering is consistent with NE-SW spreading (figure 4.21).

4.8.2.2 The fault geometry in the sheeted dike complex

Figures 4.22a and 4.22b show the same fault-slip data as figures 4.11a and 4.11b, respectively, only they are corrected for Cretaceous and Tertiary folding. The poles to faults and associated slip lines in figure 4.22a are remarkably consistent with the poles to faults and associated slip vectors in figure 4.22b, suggesting that a representative set of faults is obtained to determine the principal stress axes.

Most of the faults in figures 4.22b, and probably these faults in figure 4.22a that have subparallel striations to these in figure 4.22b, are normal faults. More than half of all faults (52%) plot in the stippled fields representing 42% of the area. Obviously, most of the normal faults are not parallel to the sheeted dikes but occur at an angle with respect to the average strike of the dikes. For better comparison, the contoured poles to sheeted dikes (figure 4.22a) as well as a rose diagram of the strikes of dikes are plotted (figure 4.22c). The average angle between the mean of the dike and the mean of the high-angle normal faults in the stippled fields is about 55° (figure 4.22a and 4.22b). Note also, that most of the faults parallel to the sheeted dikes are strike-slip or oblique-slip faults, and not normal faults. Most strike-slip and oblique-slip faults are perpendicular to the normal faults in the stippled fields, and most of these strike-slip faults indicate right-lateral displacement (figure 4.22b). It is possible that the high-angle strike slip faults are transfer faults which, via oblique-slip or strike-slip, allow the juxtaposition of normal faults with different displacement characteristics. The analyzed faults have the same cement (epidote + quartz or prehnite + quartz) suggesting the normal faults and strike-slip faults (possible transfer faults) were active synchronously. The presence of transfer faults among analyzed fault-slip data would explain the low maximum compound likelihood for X being the direction of σ_1 in figure 4.10c; the displacement along transfer faults is not parallel to the maximum resolved shear stress, but is controlled by the differential displacement along the faults which are connected by the transfer fault. Thus, basic assumptions of the paleostress analysis are not satisfied if transfer faults are included in the fault-slip data (section 4.2).

However, normal faults and strike-slip faults (possible transfer faults) are consistent with the fault regime near a spreading center.

The mean of the results of the paleostress analysis using four different methods (figure 4.11d) is corrected for Tertiary and Cretaceous folding and plotted in figure 4.22b. The rotated minimum principal stress axis (σ_3^R) forms a low-angle ($\sim 20^\circ$) with the mean strike of dikes, and the rotated intermediate principal stress axis (σ_2^R) forms a low angle with the mean pole to dikes (figure 4.22b). Only the maximum principal stress axis (σ_1^R) is subvertical and subparallel to the σ_1^R - direction determined from the paleostress analysis of amphibole shear bands (figure 4.20c). The direction of the minimum principal stress in figure 4.22b is not consistent with tectonic extension perpendicular to the strike of the dikes, but with extension parallel to the strike of the dikes. The change of the stress axes between event 1 (crystallization of cumulate gabbro and formation of amphibole veins) and event 3 (extensive faulting and hydrothermal alteration) could be related to the violation of assumptions of the paleostress analysis (i.e. transfer faults). Other possible explanations are discussed below.

Some of the normal faults in figure 4.22b are very similar in terms of attitude and displacement to the amphibole shear bands in figure 4.20c, suggesting that the cemented faults formed in a similar stress field that produced slip in the amphibole shear bands (i.e. near the ridge axis). Also, the observation that most normal faults are oblique to the strike of the dikes is not necessarily contradictory to the interpretation that the epidote and prehnite mineralized faults formed near a ridge axis. This leads to intriguing possible explanations why the shear fractures with normal displacement show this obliquity with respect to the strike of the sheeted dikes and why a change of the stress axis could have occurred. The stress field could have changed over time or switched suddenly (σ_2^R and σ_3^R are flipped in figures 4.20c and figure 4.22b), but the change of the direction of extensional faulting must have occurred sometime after the intrusion of most of the dikes assuming dikes were injected perpendicular to the direction of the minimum principal stress.

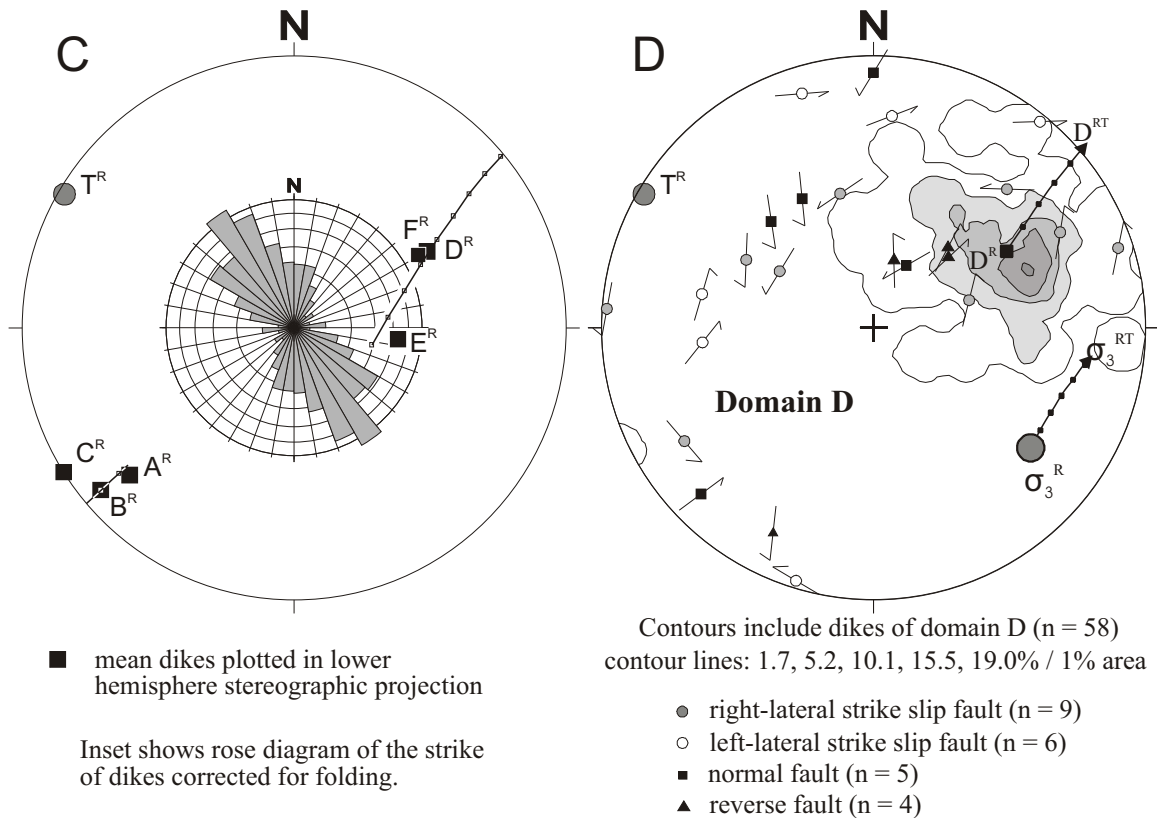
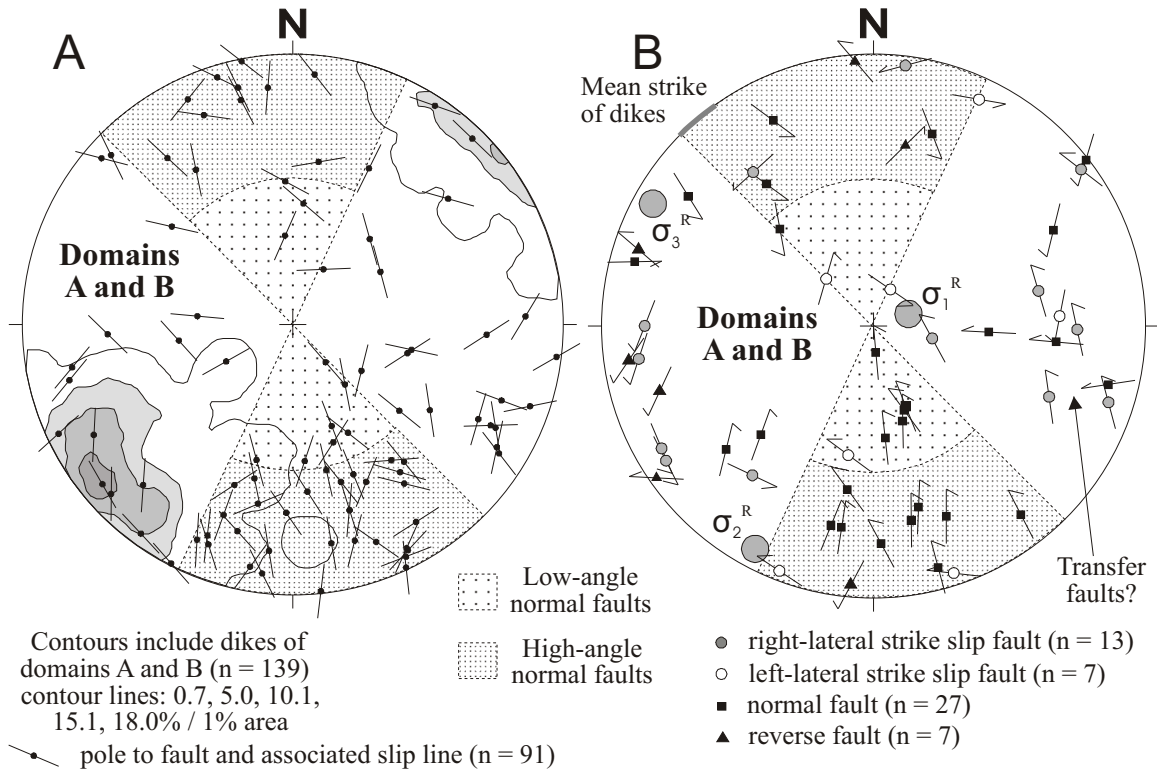
The findings of studies of modern oceanic spreading centers indicate that the oceanic spreading centers are not continuous, planar features, transected only every 600 ± 300 km by transform faults, but

Figure 4.22

Analysis of unfolded structural data of domains A, B and D: Lower hemisphere, equal area stereographic projections of contoured poles to dikes of domains A and B (a), of poles to cemented faults in domains A and B (a, b), poles to mean dike of domains A through F (c), and of contoured poles to dikes and poles to cemented faults in domain D (d).

- a. Poles to cemented faults (solid symbols) and associated slip line superimposed on the contours of poles to dikes of domains A and B after correcting for Tertiary and Cretaceous folding. The sense of slip on these faults was not determined. However, the direction of slip along the fault is indicated by the line affixed to the poles (figure 4.3). The sense of slip is probably the same as of similar faults in figure 4.22b (note the parallelism of faults and striae in figures 4.22a and 4.22b).
- b. Poles to cemented faults and their slip vectors (Hoepfner, 1955). The arrows affixed to the poles to cemented faults indicate the direction of slip of the hanging wall block (see figure 4.3). Most high- and low-angle normal faults (stippled field) occur at an angle with the sheeted dikes. Many faults parallel to the sheeted dikes are strike-slip faults. Other strike-slip faults occurring at a high angle to the strike of the dikes could be transfer faults. Note the similarity between normal faults in figure 4.22b and amphibole shear bands in figure 4.20c.
- c. Pole to mean dike of domains A through F and the best-fit Rotation axis T^R after correcting for Tertiary and Cretaceous folding (compare with figure 4.9). The unfolded rotation axis T^R is subhorizontal and occurs at a low angle to the strike of the subvertical dikes (A^R , B^R and C^R). For reference, the rose diagram indicating the strike of the dikes is shown.
- d. Pole to fault and associated slip vectors of domain D superimposed on the contoured poles to dike of domain D after correcting for Tertiary and Cretaceous folding. Faults of domain D are dissimilar to faults in domains A and B. Perhaps, many of the faults are tilted strike-slip or tilted normal faults that formed before or during the tilting of the dikes around T^R . Rotation of dikes and faults around T^R may restore the dikes in domain D to paleohorizontal. D^{RT} and σ_3^{RT} indicate rotation of D and σ_3 around R (unfolding), and rotation of D^R and σ_3^R around the rotation axis T^R (figure 4.21).

Structural data from the sheeted dike complex corrected for Cretaceous and Tertiary folding



show discontinuities at different scales (MacDonald et al., 1988). These discontinuities include, from largest to smallest scale: (1) transforms and propagating rifts, (2) overlapping spreading centers, (3) transfer zones and accommodation zones (e.g. due to opposing half-grabens), and (4) offsets of the ridge-axial summit (devals). In any of these settings, normal faults could form at various angles with respect to the strike of the dikes. Also, dikes may not necessarily intrude parallel to the ridge axis near discontinuities, such as transform-ridge intersections (e.g., Fjader et al., 1994). Therefore, the assumption that the dikes are parallel to the ridge-axial plane is not always true. The obliquity of the normal faults (and possible transfer faults) with respect to the dikes could be the result of formation of the sheeted dike complex and subsequent deformation in any one of these ridge discontinuities.

The main conclusion of the paleostress analysis is that the different directions of the stress axes in figures 4.20c and 4.22b reflect a complex evolution of the sheeted dike complex which could involve a change of the stress field after event 2 (injection of subvertical dikes). This interpretation is consistent with the observed obliquity of normal faults with respect to the sheeted dikes. However, the directions of the stress axes in figure 4.22b cannot be interpreted as the directions of the principal stresses of the new stress field, because the analyzed faults could be of multiple generation and/or the data set may include transfer faults. If the strike-slip faults in figure 4.22b are transfer faults, then faults were analyzed which do not slip in the direction of the shear stress. Thus, the basic assumption made for the stress inversion, that slip occurs in the direction of the shear stress, is not satisfied (section 4.2).

Unless the faults in the sheeted dike complex can be chronologically separated and stages of the change of the stress-field defined based on geologic evidence, the hypothesis of a non-static stress field near the ridge axis is difficult to constrain. Currently, the obliquity of epidote and prehnite mineralized faults with respect to the strike of the dikes is the only hint for such a scenario. The identification of multiply striated surfaces in the field and determination of the conditions during faulting using for example fluid inclusions and isotopic evidence may be a first step towards constraining this hypothesis.

4.8.2.3 Possible near ridge-axis rotation of sheeted dikes

The mean dikes of domains A through F and the best-fit tilt axis T (figure 4.8) are shown in figure 4.9 and 4.22c after correction for Tertiary and Cretaceous folding. The poles labeled A^R , B^R , and C^R closely reflect the inferred original position of dikes at the spreading center. The restored subvertical dikes (A^R , B^R , and C^R) strike, on average, north, 032° - 042° west (figure 4.22c). The poles labeled D^R , E^R and F^R are the restored poles to mean dikes of the remaining domains. Assuming that dike intrusion was predominantly subvertical, the dikes D^R , E^R and F^R reflect the position of dikes that are rotated $\sim 45^\circ$ and $\sim 75^\circ$ to the northeast about T^R from a vertical position. Note that T^R , the best-fit rotation axis, is in a subhorizontal position ($300^\circ / 03^\circ$) and occurs at an low angle with the mean strike of the subvertical dikes ($\sim 30^\circ$). The rotation of subvertical dikes around a horizontal axis is schematically depicted in figure 4.21.

Figure 4.22d shows the pole to fault and associated slip vectors of domain D after they were rotated around R to correct for Tertiary and Cretaceous folding. For reference, the contoured poles of dikes of domain D are plotted. Also, the mean of the minimum principal stress axis of figure 4.12d is shown after correcting for folding. After unfolding, most faults in domain D do not resemble faults in domains A and B in terms of attitude and displacement. However, some of the faults plotted in figure 4.22d are strike-slip or normal faults that could have formed before or during rotation of the dikes around T. Interestingly, the trend of the σ_3^R -directions in figures 4.22b and 4.22d and the best fit rotation axis T^R are subparallel.

The possibility of the rotation of faults should be taken in consideration interpreting the results of the paleostress analysis in domain D. A hypothetical scenario may involve faults which slipped initially in response to the stress field of figure 4.20c. Then the faults could have been cemented and tilted around T^R without any further slip occurring on them (the faults could have been cemented prior to rotation around T^R). Some of the cemented faults could have been reactivated reaching a favorable orientation during rotation, or new faults formed during rotation. Alternatively, faults are rotated while slip occurs on the fault plane until the fault is no longer in a position in which slip can occur. Basically, as the faults are cemented and rotated, the stress tensor that describes slip in the direction of the shear stress on these faults is rotated an equal amount. Differential rotation of faults would result in obtaining a stress tensor

that describes essentially a multitude of stress tensors using variably tilted faults in the paleostress analysis. The geologist interpreting the results of the paleostress analysis, not recognizing that faults could have been rotated, may conclude that the stress field changed with time, but in this case, the regional stress field may have been static (only the fault blocks were rotated).

The successive steepening of initially horizontal features such as sedimentary beds or volcanic flows as well as the successive shallowing of initially vertical features such as dikes is often observed in terranes that have undergone large tectonic extension. Slow- to intermediate-spreading ridges are sites not only of magmatic extension but also of substantial tectonic extension and crustal stretching (Dilek et al., 1998). The tectonic extension at slow- to intermediate-spreading ridges with low magma supply is accommodated by ductile shear zones (e.g., southwest Indian Ridge, Site 735b: Cannat et al., 1991), and/or low- and high-angle brittle faults and detachment surfaces (e.g., eastern Atlantic: Collier et al. 1997, Reston et. al, 1996; Juan de Fuca ridge: Minshull and Hall, 1997; MAR: Karson, 1990). Exposures of gabbroic rocks and serpentinized ultramafic rocks are common at slow-spreading ridges suggesting that upper crustal sequences are missing due to normal faulting and large-magnitude amagmatic extension (Dilek et al, 1998). Substantial rotation of fault blocks (up to 100°) associated with tectonic extension has been inferred in the MARK area using paleomagnetic evidence (Reston et. al., 1996). Also, successive steepening of sedimentary layers due to displacement along a listric normal fault is inferred at the Juan De Fuca Ridge (Minshull and Hall, 1997). Similarly, many well-preserved ophiolites, which have been inferred to be of slow-spreading origin, contain a broad spectrum of structures suggestive of amagmatic (structural) extension. One of these characteristic features is extensional faulting associated with rotation of fault blocks (e.g., Harper, G.D., 1982b, Alexander and Harper, 1992). Typical structures include planar and listric normal faults, structural grabens, and detachment surfaces documented within the lower crustal and/or mantle sequences. (e.g., Josephine ophiolite: Norell and Harper, 1988; Alexander and Harper, 1992; Troodos ophiolite: Allerton and Vine, 1987; Kizildag ophiolite: Dilek and Delaloye, 1992, Dilek et al, 1998). Generally, the models of the spreading structure derived from the study of modern oceanic crust and ophiolites of slow- to intermediate-spreading environments show the following features: a large, low-angle normal fault is inferred at depth (main detachment fault) bounding a fault mosaic comprised of listric

and/or planar rotational faults (figure 4.23). Tilting of blocks bound by rotational faults, occurs in response to large-magnitude extension along a major detachment during amagmatic cycles.

Substantial tilting (up to 75°) of subvertical dikes around a horizontal axis is inferred from the structure of the sheeted dike complex of the Rogue Wilderness ophiolite (figures 4.9, 4.21 and 4.22c). Tilting probably occurred near the ridge axis, because faults across which a significant change of the attitude of the dikes is observed (figure 4.7, domains B and F) contain cemented gouge typical of subseafloor hydrothermal alteration. Furthermore, the sheeted dike complex of the Rogue Wilderness ophiolite underwent pervasive hydrothermal alteration similar to ophiolites for which a slow-spreading environment is inferred. Based on these observations and comparison with modern oceanic crust and ophiolites, it is suggested that the Rogue Wilderness remnant of the CRO formed at a slow- to intermediate-spreading ridge, and that dike rotation (figure 4.21) could have occurred in response to structural extension as depicted in the model in figure 4.23. This model of the spreading structure of the Troodos ophiolite (after Allerton and Vine, 1987) is selected as an example, because it is constrained by detailed mapping and additional paleomagnetic data. The model shows, as constrained by the paleomagnetic data and orientation of dikes (Allerton and Vine, 1987), up to $78^\circ \pm 22^\circ$ tilting of dikes within a distance of only 5 to 10 km. Similar geometric relationships are observed in the sheeted dike complex of the Rogue Wilderness remnant of the CRO. However, there are two observations that indicate a somewhat more complex evolution. First, the strike of most of the normal shear fractures is not parallel to the dikes, and the geometry and kinematics of the normal faults and possible transfer faults (figures 4.22a and 4.22b) is not entirely consistent with structural extension perpendicular to the ridge axial plane. Second, the subhorizontal rotation axis T^R (figure 4.22c) is not exactly perpendicular to the ridge axial plane as inferred from the orientation of the sheeted dikes. The obliquity of these faults may be related to structural extension in the vicinity of a ridge discontinuity.

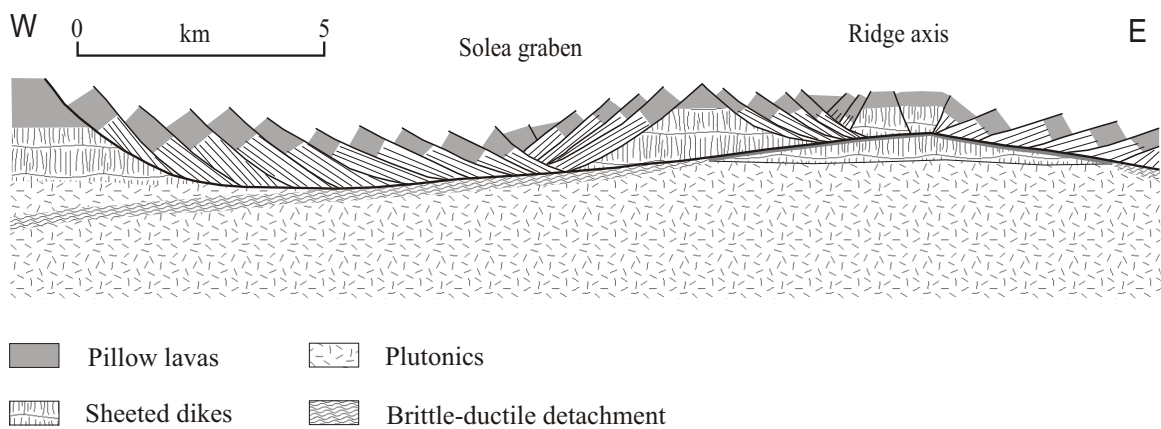


Figure 4.23

Model of the spreading and fault geometry of the Troodos ophiolite depicting the formation of the Solea graben (after Allerton and Vine; 1987). A detachment fault is inferred at depth bounding a fault mosaic comprised of listric and/or planar rotational faults. Tilting of blocks bound by rotational faults occurs in response to large-magnitude extension along the detachment during amagmatic cycles.

4.8.2.4 Summary

The evidence for normal faulting, hydrothermal alteration, and fault block rotation near the ridge axis, as well as for a likely change of the stress field after the intrusion of most of the dikes (event 2), is summarized below:

- The direction of extension during events 1 (crystallization of the cumulate gabbro and formation of amphibole veins and shear bands) and event 2 (intrusion of most of the dikes) occurred very likely perpendicular to the strike of subvertical dikes (figure 4.20c, 4.20d and figure 4.21) suggesting NW-SE (present orientation) directed extension.
- A dike was found truncating an epidosite zone, and another was found intruding (paralleling) a fault, indicating faulting occurred near the ridge axis.
- Cemented faults separate domains B and F at the Rogue River, and a sudden change of the orientation of the dikes is observed across these faults (figures 4.7).
- After correcting for Tertiary and Cretaceous folding, most cemented faults in domains A and B are high- or low-angle normal faults (figures 4.22a and 4.22b), and possible transfer faults occur at high-angles with respect to the normal faults. Several cemented faults are parallel to the amphibole shear bands.
- Both the strike of the cemented normal faults (figures 4.22a and 4.22b) and the subhorizontal axis T^R , which may represent the rotation axis of the dikes during structural extension (figure 4.21), are not parallel to the strike of the dikes (figure 4.22c). The obliquity of T^R and the normal faults with respect to the sheeted dikes suggest that extension may not have occurred perpendicular to the ridge axial plane after event (2).

Considering these constraints, it is possible that a change or disturbance of the regional stress field after event (2) may have played a role in the evolution of sheeted dike complex exposed in the Wild Rogue Wilderness. Possible sites at (or near) a spreading center where a change of the regional stress field during spreading and/or tectonic extension is likely to occur include: (1) ridge-transform intersections, (2) ridge discontinuities such as propagating rifts and overlapping spreading centers, and (3) accommodation/transfer zones or ridge offsets. Furthermore, the pervasive hydrothermal alteration evident

in the sheeted dike complex as well as inferred rotation of sheeted dikes (figure 4.21), possibly due to large-magnitude extension by normal faulting (figure 4.23), are characteristics for slow- to intermediate-spreading ridges.

4.8.3 Post-ophiolite structural history

4.8.3.1 Late magmatism and hydrothermal alteration

It is inferred that arc-related magmatism and associated hydrothermal alteration followed the formation of the Rogue Wilderness remnant of the CRO (figure 4.19). The intrusion of the 159-160 Ma Half Moon Bar diorite into the pillow unit and the formation of the upper most section of the Mule Mountain volcanics mark the arc-related intrusive, extrusive and hydrothermal phase.

Hornblende separates of sample GDH-5a (plagioclase and hornblende phyric dacite) from the metavolcanic unit yielded a $^{40}\text{Ar}/^{39}\text{Ar}$ age of 152.9 ± 1.8 Ma. Sample GDH-5a was taken from the uppermost section of the Mule Mountain volcanics which consists mainly of volcanicalstic sandstone, dacitic extrusive and shallow intrusive rocks and minor thinly laminated, tuffaceous mudstone and chert. No isotopic ages are obtained from the 2.0-2.5 km thick lower section of the Mule Mountain volcanics which consists of a succession of basaltic to andesitic flows and shallow intrusives intercalated with volcanic breccia. The sample age of 152.9 ± 1.8 Ma (GDH-5a) is interpreted as the minimum age of the lower section of the Mule Mountain volcanics. The predominance of extrusive rocks and coarse, volcanogenic sediments in the Mule Mountain volcanics suggest that it formed in proximity to a volcanic center. However, intercalated, thinly laminated mudstones and chert suggest also that a small “volcanopelagic” succession is present and deposition occurred in relatively deep water.

The phase of intrusion of arc-related magmas into the pillow unit and extrusion of arc-related magmas in the Mule Mountain volcanics is characterized by subsequent brittle fragmentation, cataclasis, and greenschist grade and lower hydrothermal alteration. However, the intensity of faulting and alteration is much less compared to that of the sheeted dike complex. Samples from the Half Moon Bar diorite and Mule Mountain volcanics are moderately altered (cpx is preserved) and show a mineral assemblage typical of greenschist facies (and lower grade) hydrothermal alteration. Numerous, crosscutting veins and faults

(epidote, prehnite, pumpellyite, quartz) in both, the Mule Mountain volcanics and the Half Moon Bar diorite, indicate retrograde conditions. Epidote is not as common in the Mule Mountain volcanics as in the Half Moon Bar diorite and seems to occur more localized. In addition to subseafloor hydrothermal metamorphism, magmatic fluids released during cooling of the intrusion may have played a role in the alteration of the Half Moon Bar diorite and surrounding rocks (deuteric alteration). Petrographic evidence together with calculated near-igneous temperatures of equilibration (820°C to 650°C at 2 kbar) of hornblende-plagioclase pairs suggest cooling of the pluton under increasingly oxidizing conditions (see chapter 3). The overlap of the hornblende $^{40}\text{Ar}/^{39}\text{Ar}$ cooling age (157.2 ± 2.0 Ma) and the zircon U/Pb age (159-160 Ma) are consistent with rapid cooling of the pluton in a subseafloor environment.

The ages of the Half Moon Bar diorite and the upper section of the Mule Mountain volcanics coincide with the ages of volcanoplutonic arc rocks associated with two distinct belts of late Jurassic ophiolites in California and Oregon; these are the Josephine ophiolite and the Coast Range ophiolite.

4.8.3.2 Post-ophiolite ductile deformation

This episode is characterized by (1) the formation of the Blossom Bar shear zone, (2) mylonite zones and penetrative foliation in the metatonalite unit, and (3) localized shear foliation in the metagabbro unit, especially in quartz-rich rocks in the metagabbro unit. The Blossom Bar shear zone represents a major ductile-brittle, greenschist facies shear zone with a width of ~900 m. The subparallel mylonitic zones in the metagabbro unit and metatonalite unit total about 150 m. With an estimated average shear strain ratio of 1:10, a transport distance of about 10 km is obtained (note that most of the stretched quartz grains in compositionally layered mylonites have a much larger aspect ratio). Microstructural data and metamorphic mineral assemblages indicate that temperatures of ductile deformation ranged between 300°C to 500°C in these three units (sections 8.7.2 and 8.7.5).

The strike of the shear foliation in the Blossom Bar shear zone, the metagabbro unit and metatonalite unit are parallel (figure 4.15), the temperatures of deformation are similar, and similar metamorphic mineral assemblages occur in mylonitic samples from the various units. In view of these similarities, the Blossom Bar shear zone, the mylonitic zones in the metatonalite unit, and the shear

foliation in the metagabbro unit are interpreted to have formed during the same deformational/metamorphic event. However, the orientation of the stretching lineation in the metatonalite and metagabbro units plunge much shallower (figures 4.15b and 4.15c) than the stretching lineation in the Blossom Bar shear zone (figure 4.15d).

The age of the Blossom Bar shear zone is bracketed by the age of the metavolcanic unit (~153 Ma) and the deposition of the sediments of the Myrtle group (Late Tithonian, ~143 Ma). Foliated volcanic breccias occur within the Blossom bar shear zone (chapter 2, figure 2. 56) suggesting that rocks of the metavolcanic unit are incorporated in the shear zone during ductile deformation. The vitrinite reflectance R_o determined in samples from the Myrtle group (Niem and Niem, 1990) indicate maximum temperatures ranging between 70°C ($R_o = 0.56\%$) and 120°C ($R_o = 1.01\%$), indicating the overlying sedimentary rocks are unmetamorphosed. The muscovite $^{40}\text{Ar}/^{39}\text{Ar}$ ages of two ductily deformed muscovite garnet tonalite dikes are in agreement with these age constraints (figure 4.19). Muscovite separates of two mylonitic muscovite-garnet tonalites, intruding the metagabbro unit, yielded cooling ages of 148.52 ± 0.17 Ma (O/C-372b) and 147.99 ± 0.45 Ma (GH-97-20). Note that the sense of shear determined in sample O/C-372b is consistent with that of the shear zone, although some differences in the orientation of the foliation and stretching lineation exists (figure 4.15b). The ages, indicating cooling to $<350^\circ\text{C}$ (muscovite closes to Ar-diffusion), coincide with the Nevadan orogeny (e.g. Harper et al., 1994) and are interpreted to mark the end of wide-spread ductile deformation evident in the Rogue Wilderness ophiolite (ductile deformation was constrained to have occurred between 300 and 500°C). The Josephine ophiolite and overlying sediments of the Galice formation were regionally metamorphosed during the Nevadan orogeny (Harper et al., 1994). However, there is no evidence for regional metamorphism in the Rogue Wilderness ophiolite (e.g., laumontite veins occur in samples from the metatonalite unit, metagabbro unit, Mule Mountain volcanics). The muscovite $^{40}\text{Ar}/^{39}\text{Ar}$ cooling ages of ductily deformed tonalites clearly indicate Nevadan age deformation.

Figures 4.24a, 4.24c, and 4.24d show the contoured poles to shear foliation in the metatonalite unit, metagabbro unit and the Blossom Bar shear zone, respectively, after correcting for Tertiary and Cretaceous folding. In the new coordinates, the shear foliation in all three units is subhorizontal or dip

gently, and the stretching lineation trend S to SE. The trend of the stretching lineation in the Blossom Bar shear zone is about 45° - 50° different from that in the metatonalite and metagabbro units. Also, the stress axes evaluated in figure 4.18 are shown after correction for folding (σ_i^R in figures 4.24a, 4.24c, and 4.24d). As discussed in section 4.7.8.2, these stress axes are compatible with the sense and direction of transport during ductile deformation, assuming that slip (shear) occurred in the direction of the shear stress on the mean shear planes C_t , C_g and C_{sz} .

Figure 4.24b shows the poles to cemented faults and associated slip vectors of figure 4.18b after correcting for Tertiary and Cretaceous folding. As discussed in section 7.8, the observed sense and direction of transport parallel C_t , and C_{sz} could not have occurred in the stress field that produced slip on the brittle faults (figure 4.24b). It is possible that the principal stress axes in figure 4.24b describe a later episode of deformation than the stress axes in figures 4.24a, 4.24c and 4.24d.

The tectonostratigraphic column in figure 4.25 depicts the structurally bounded units in the Wild Rogue Wilderness after correcting for Tertiary and Cretaceous folding. This interpretation is consistent with the traditional model of Ingersoll (1979) and Dickinson and Seely (1979), showing the sediments of the Myrtle Group (equivalent to Great Valley sequence) on top, and the Franciscan rocks (Dothan Formation) at the bottom. In these new coordinates, the Blossom Bar shear zone is thrust northwest over the metatonalite and metagabbro units as well as the sheeted dike complex (figure 4.24d, figure 4.25). The Blossom Bar shear zone could represent the thrust zone between the Mule Mountain volcanics and the structural block consisting of metagabbro unit, metatonalite unit and sheeted dike complex. However, the contact relations between the Blossom Bar shear zone and the Mule Mountain volcanics are not clear, whether this contact is a thrust or (later) normal fault.

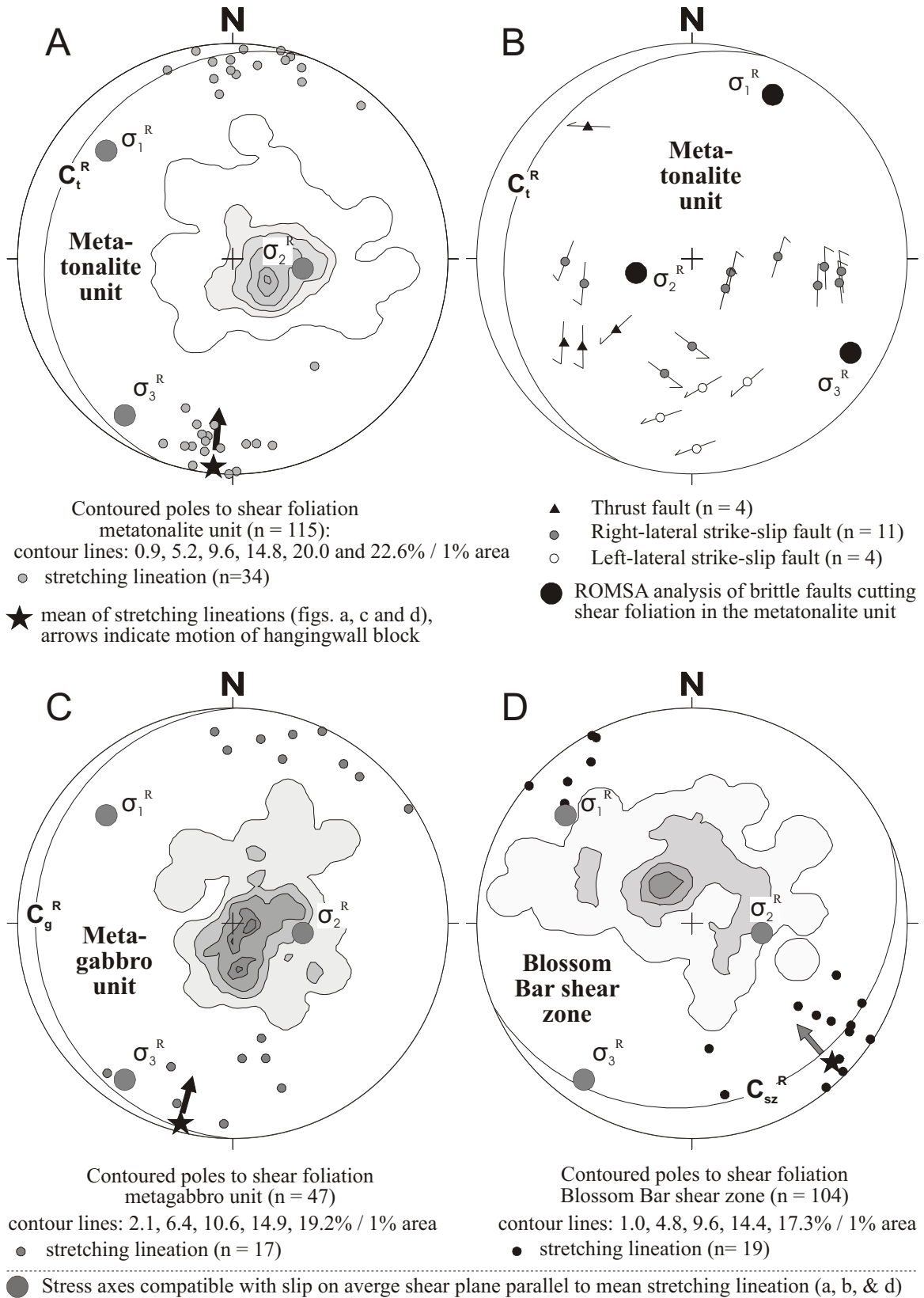
The stretching lineation and sense-of-shear indicators suggest that the plutonic units (metagabbro unit and metatonalite unit) were transported north with respect to the sheeted dike complex (figures 4.24a, 4.24c, figure 4.25). Also, the stratigraphically lower units (plutonic units) occur on top of a stratigraphically higher unit (sheeted dike complex) suggesting thrusting. However, the attitude of the average shear planes and trend of the stretching lineation in the metatonalite unit and metagabbro unit are indicative of strike slip transport on shallowly east-dipping shear planes (figures 4.24a, and 4.24c).

Figure 4.24

Structural data of the metatonalite unit (a, b), metagabbro unit (c), and Blossom Bar shear zone (d) after correcting for Tertiary and Cretaceous folding (lower hemisphere, equal area stereographic projections).

- a. The mean shear plane (C_t^R) dips shallowly west, and the mean stretching lineation trends south. The sense of shear indicators are consistent with top to the north transport (metagabbro unit is hangingwall block). The reoriented stress axes of figure 18a are shown.
- b. The poles to faults cutting mylonitic foliation in the metatonalite unit and associated slip vectors are shown. Cemented faults which occur at low angles with the subhorizontal foliation are sympathetic with the sense of shear in the mylonites. The reoriented stress axes of figure 4.16c are shown. The stress field that produced slip on the brittle faults in the metatonalite unit could not have produced slip on mean foliations (C_t^R , C_g^R , C_{sz}^R) in the directions of the mean stretching lineations.
- c. The mean shear plane (C_g^R) gently dips west, and the mean stretching lineation trends south. The sense of shear indicators are consistent with top to the north transport (Blossom Bar shear zone is hangingwall block). The reoriented stress axes of figure 4.18a are shown.
- d. The mean shear plane (C_{sz}^R) gently dips southeast, and the mean stretching lineation trends also southeast. The sense of shear indicators are consistent with top to the north thrusting (Mule Mountain volcanics is hangingwall block). The reoriented stress axes of figure 18a are shown.

Structural data corrected for folding



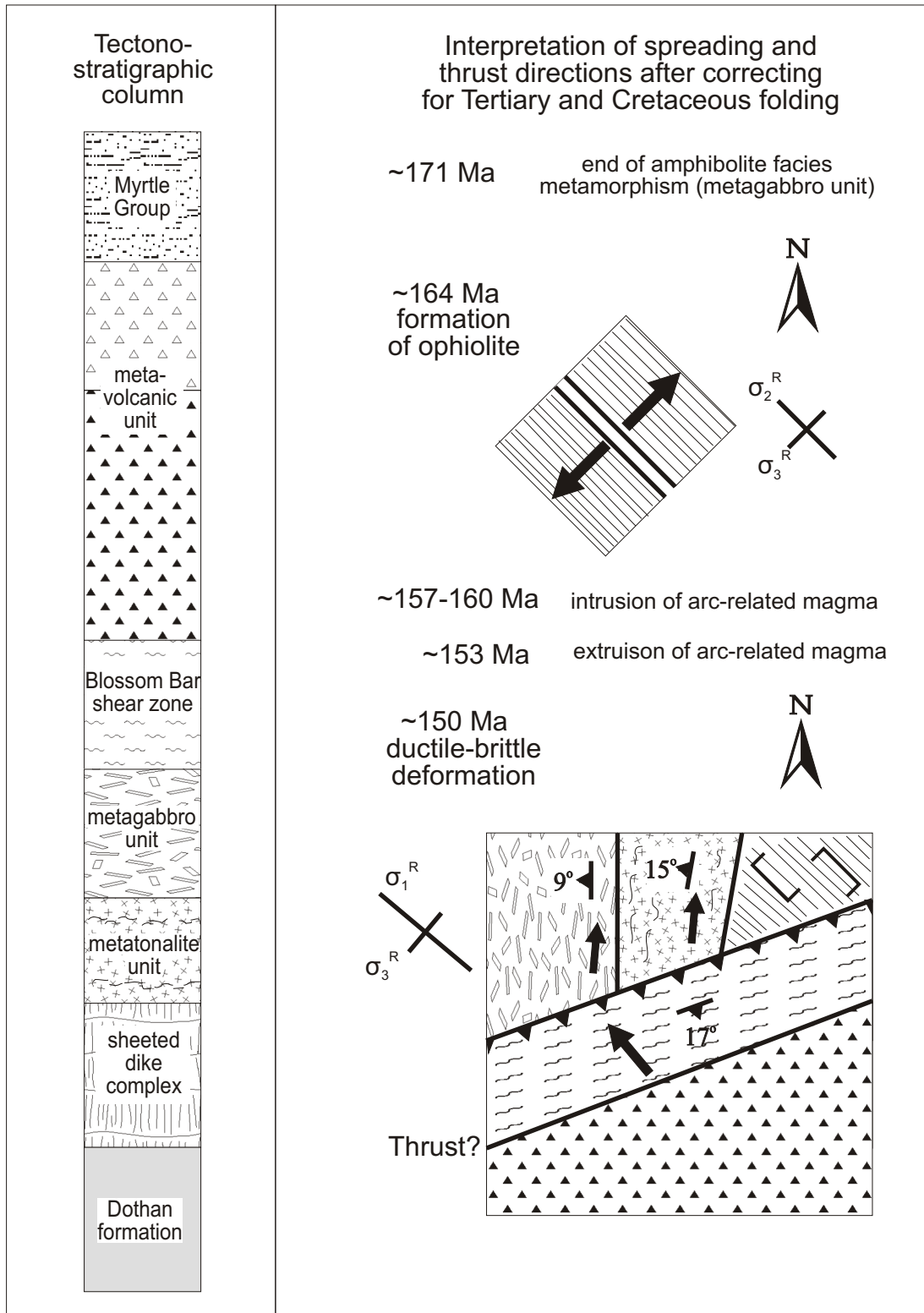


Figure 4.25: Cartoons depicting the directions of spreading at ~164 Ma, and directions of thrusting at ~150 Ma (not corrected for possible rotation around subvertical axis)

It has been demonstrated that the stress axes depicted in figure 4.25 (see also figure 4.24a, 4.24c and 4.24d) are consistent with strike slip movement in the metatonalite and metagabbro units as well as with thrusting in the Blossom Bar shear zone (section 8.7.8.2). After correcting for Cretaceous and Tertiary folding, the maximum and minimum principal stresses are subhorizontal and the intermediate stress axis is subvertical.

8.9 Summary and Conclusion

The structural data presented and discussed in this chapter are a self important contribution towards a better understanding of the formation and deformation of a fragment belonging to same-age (late Jurassic) ophiolites which are widely dispersed in western North America. Combined with the new age data, constraints for the interpretation of the origin and tectonic evolution of the Coast Range ophiolite are found. The main findings of this study include:

- The tectonostratigraphy from east to west includes: (1) a sheeted dike complex having cumulate gabbro screens, (2) a ductily but heterogeneously deformed metatonalite unit, (3) a similarly deformed metagabbro unit showing evidence of early amphibolite facies (regional?) metamorphism, (4) a 500 to 900 m wide ductile-brittle shear zone (Blossom Bar shear zone) consisting of silicic to mafic mylonites and ultramylonites, (5) undeformed pillow basalts intruded by tonalitic and mafic dikes, (6) Half Moon Bar diorite (hbl-qtz gabbro to diorite to tonalite) intruding the pillow unit, and (7) 2.5 km thick Mule Mountain volcanics.
- The ophiolite seems to occur on the east limb of a folded thrust sheet. All of the units strike NE and are subvertical and fault bounded. It is suggested that the units can be restored to paleohorizontal by correcting for Cretaceous and Tertiary folding (rotation axis $R = 045^{\circ}/00^{\circ}$, $\sim 90^{\circ}$ clockwise rotation).
- The metagabbro unit with a hornblende- $^{40}\text{Ar}/^{39}\text{Ar}$ cooling age represent a (regionally?) metamorphosed plutonic unit that may be correlative with older basement terrane occurring in the rift facies of the Josephine ophiolite. To constrain this hypothesis, a fractionated phase of the metagabbro, which is more likely to contain zircon than the main phase, should be dated using improved U/Pb dating technique. If this unit represents older Klamath ophiolitic basement, ages of ~ 200 Ma are expected (Rattle Snake Creek terrane).

- The formation of the ophiolite is typified by the crystallization of a plutonic sequence, repeated injection of subvertical dikes and extrusion of pillowed submarine volcanic flows. Normal faulting followed closely upon the crystallization of the cumulate gabbro which is inferred analyzing amphibole shear bands in screens of cumulate gabbro. Spreading and early normal faulting occurred in SW-NE (present orientation) direction. Deformation after the intrusion of most of the dikes probably involved large-magnitude tectonic extension associated with differential rotation of rigid fault blocks around a subvertical axis. A change of the stress field near the ridge axis is possible (consistent with paleostress analysis of cemented shear fractures) suggesting a complex evolution of the ophiolite, perhaps related to formation in or near a ridge discontinuity such as a propagating spreading center or ridge-transform intersection.
- An episode of plutonism (~157-160 Ma) and volcanism (~153 Ma) associated with brittle fracturing and retrograde greenschist facies hydrothermal alteration is recognized. This late magmatic episode could be related to a nearby arc.
- Extensive ductile-brittle deformation was identified in three different units which include (1) Blossom Bar shear zone, (2) metagabbro unit, and (3) metatonalite unit. Within the framework of proposed reorientation to paleohorizontal, the sense-of-shear indicators are consistent with top-to-the-northwest thrusting on a shallowly inclined shear plane (the Blossom Bar shear zone may represent the thrust fault). Thrusting may have been accompanied by strike-slip faulting juxtaposing plutonic rocks next to the sheeted dike complex (and probably on top of the sheeted dike complex).

CHAPTER FIVE

THE GEOCHEMISTRY OF THE WILD ROGUE WILDERNESS REMNANT OF THE COAST RANGE OPHIOLITE, SW OREGON

5.1 Introduction

A large variety of igneous rocks with widely differing trace element composition can be found in oceanic arc / back-arc systems, including normal and enriched mid-ocean ridge basalts (N-MORB, E-MORB), back-arc basin basalts (BABB), island arc tholeiites (IAT), calc-alkaline basalts (CAB; many calc-alkaline lavas are of andesitic composition), and boninites (BON; high-Mg andesites).

BABB typically erupt in suprasubduction zone ridge settings, such as the Mariana back arc basin, and are intermediate in trace element and isotopic composition between N-MORB and IAT (e.g., Hochstaedter et al., 1990a, 1990b, Hawkins and Melchior, 1985, Volpe et al., 1990, Hawkins et al., 1990).

IAT and CAB and their differentiates erupt in volcanic arcs and have high H₂O and Al₂O₃ and low FeO* and TiO₂ contents, and are selectively enriched in large ion lithophile elements and depleted in high field strength elements compared to N-MORB (Pearce, 1982, 1983; Pearce et al. 1995a; Hochstaedter et al., 1996; Borg et al., 1997; Ewart et al., 1994). The isotopic signature is different from N-MORB and generally high ⁸⁷Sr/⁸⁶Sr and low ¹⁴³Nd/¹⁴⁴Nd and ¹⁷⁶Hf/¹⁷⁷Hf reflect the addition of a subduction component to the sub-arc mantle (e.g., White and Patchett, 1984).

Primitive arc magmas are believed to have been generated by partial melting of the metasomatized mantle wedge overlaying the down-going slab. Two components are inferred to produce the characteristic trace element signature of arc magmas (e.g., Ellam and Hawkesworth, 1988; Hochstaedter et al., 1990b; Pearce, 1983; Pearce et al., 1984a; Pearce and Parkinson, 1993; Stern et al., 1993): (1) the slab component which is believed to represent the material transferred from the down-going slab to the overlying mantle wedge, and (2) the mantle before the addition of the subduction component. Based on trace element and isotopic data as well as experimental evidence, the slab component can be one or more of the following: a

hydrous fluid released by dehydration of the down-going oceanic crust (e.g., Tatsumi et al, 1986; Saunders et al., 1991; Philippot and Selverstone, 1991; Ayers and Watson, 1991; Ellam and Hawkesworth, 1988; Pearce, 1983; Pearce et al., 1995a, 1995b; Stolper and Newman, 1994; Peate et al., 1997; Borg et al., 1997; Stolz et al., 1996); melts derived from a subducted slab (Ringwood, 1974; Edwards et al., 1993; Sajona et al., 1993; Rapp et al., 1994; Yogodzinski et al., 1994; Stolz et al., 1996); a sedimentary component (Hole et al., 1984; Ellam and Hawkesworth, 1988; Peate et al., 1997; Pearce et al., 1995a); and continental crust (Honthaas et al., 1998; Hildreth and Moorbath, 1988; Pearce, 1983). Most authors favor the hypothesis of the addition of a hydrous fluid released by dehydration of the down-going oceanic crust that occurs at about 100 km depth.

The mantle (before subduction contribution) beneath oceanic arcs is believed to be similar to the mantle from which N-MORB is derived or somewhat more refractory than N-MORB-like mantle (Hawkins et al., 1990; Hawkins and Melchior, 1985; Pearce et al., 1995a, 1995b; Peate et al., 1997; Taylor et al., 1992). In contrast, the metasomatized mantle source of boninites is considerably more refractory than the sources for MORB or IAB which is thought to be the result of previous melting and melt extraction (Crawford et al., 1989; Sobolev and Danyushevsky, 1994; Fallon and Crawford, 1991; Monzier et al. 1993; Beccaluva and Serri, 1988). Furthermore, enriched mantle sources, similar to that of E-MORB and ocean island basalt (OIB) are inferred to have contributed to some arc magmas (e.g., Pearce, 1983; Stern et al., 1990, 1993; Lagabrielle et al., 1994; Ikeda and Yuasa, 1989). In addition to the N-MORB, E-MORB, and OIB mantle sources, continental lithosphere is believed to undergo melting beneath continental arcs (e.g. Pearce, 1983; Conrey et al., 1997).

Finally, the lower arc crust as well as the down-going slab are potential sources of partial melts. Silicic magmas in convergent margin settings may have formed by anatexis of sub-arc crust or partial melting of subducted, altered oceanic crust (e.g., Ringwood, 1974; Helz, 1976; Cole, 1979 and 1981; Beard and Lofgren, 1991; Rapp et al., 1991).

In this chapter, the major- and trace element composition of samples from the Wild Rogue Wilderness remnant of the Coast Range ophiolite are presented and the magmatic affinities of the altered rocks determined using ‘immobile’ trace elements. The simplified geologic map of the Wild Rogue

Wilderness and sample localities are shown in figure 5.1. The analytical data are interpreted using most recent models for arc-magmatism, and a comparison of the various units is made. The analyzed samples from the Wild Rogue Wilderness show a very large compositional diversity. Not only are certain units geochemically distinct from each other, but also different magma types are identified within a single unit, including MORB, IAT, CAB and their differentiates. In order to assess this unusual compositional diversity, the analytical results are discussed in the light of recent models for arc-magmatism (e.g., Pearce and Parkinson, 1993) which ascribe magma generation to decompression melting in the mantle wedge triggered by fluid released from dehydration of the subducted slab. Using this model, the variations of incompatible trace element abundance ratios in primitive magmas can be explained with three principal factors which include: (1) variable input of a 'slab component'; (2) differing degrees of partial melting; and (3) the composition of the mantle wedge prior to input of the 'slab-component' (Pearce and Parkinson, 1993). Note that the samples from the Rogue Wilderness ophiolite are fractionated and hydrothermally altered, and the trace element variations must be interpreted taking these additional variables into account.

5.2 Analytical methods

A complete description and discussion of the analytical methods is given in appendix E. Major elements and five trace elements (Ba, Cr, Ni, Sc and V) were analyzed by standard XRF technique on pressed powder pellets at the McGill University, Montreal, Canada. The basalt V-25-1T2 was analyzed with each batch of samples ($n = 3$) to monitor the accuracy and precision of the analyses. The XRF data of V-25-1T2 compare well with the wet chemical analysis of this sample. SiO_2 , Al_2O_3 , Fe_2O_3^* , and CaO agree within 1%, MnO, MgO and Na_2O agree within 2%, and TiO_2 , K_2O and P_2O_5 within 4-7% of the wet chemical analysis of V-25-1T2.

Ba, Cr, Sc, Ni, and V have been analyzed by XRF and, in most samples, Ba, Cr, and V also by ICP-MS. In general, good agreement between the analytical techniques exists, and most XRF data agree within 10% of the analysis by ICP-MS. Large differences are found between XRF and ICP-MS data (10 - 40 %) when the concentration of a trace element is below three to five times the detection limit of the XRF analysis. The detection limit of the ICP-MS technique is at least an order of magnitude lower than the

detection limit of XRF analysis for Ba, Cr and V. Consequently, the ICP-MS data are preferred because the trace elements are analyzed with higher accuracy and precision.

Mafic samples were analyzed by inductively coupled plasma mass spectrometry (ICP-MS) at Union College (UC), Schenectady, NY. The samples were powdered in an Al₂O₃ ball mill and dissolved in pressurized Teflon vials using a mixed acid attack (hydrofluoric acid and nitric acid). This procedure is outlined in appendix E in more detail. A small amount of hydrofluoric acid was added to the dissolved sample in the Teflon vial prior to preparing the dilute analytical solution. Adding HF is necessary to stabilize Ta and Nb in the dilute acid solution throughout the analytical run (appendix E).

The analytical data obtained at UC represent the average of the analysis of at least two separately prepared sample solutions. Higher accuracy is obtained with the analysis of duplicates. Also, this method allows to test whether or not the samples were dissolved completely. The analysis of duplicates yielded virtually identical data for each sample indicating all samples dissolved completely. The precision and accuracy were monitored by analyzing 8 to 12 solutions of the basalt standard BCR-1 as unknowns throughout each analytical run. The average relative standard deviation of 32 analyses (1σ) for Dy, Ho, Er and Tm is smaller than 3%; for Y, Zr, Nb, Ba, La, Ce, Pr, Nd, Sm, Eu, Gd, Tb, Yb, Lu, Hf, Ta and Th, smaller than 4%; for V, Cr, Rb and U, smaller than 8%; and for Pb smaller than 10%. The analysis of BCR-1 as an unknown sample is very accurate as indicated by comparing the analytical results for BCR-1 with the recommended standard values (Govindaraju, 1994): V, Rb, Sr, Cs, Ba, Ce, Pr, Sm, Eu, Gd, Tb, Dy, Ho, Hf, Th and U were analyzed within better than 2%; Zr, La, Nd, and Yb within better than 3%; Er, Ta, and Pb within better than 5%; and Y, Nb, Tm, and Lu within better than 8% of the recommended standard values of BCR-1.

Evolved igneous rocks, which often contain chemically resistant minerals, such as zircon, cannot be dissolved completely using the acid digestion method. These samples were analyzed at the Washington State University Geoanalytical Laboratory (WSU). Complete dissolution of zircon-bearing samples is achieved by fusing the samples with a flux (Lithiumborate) prior to acid digestion, which is routinely done at WSU.

The precision on a single sample (BCR-P) analyzed over a four month period at WSU is as follows: the relative standard deviation (1σ) of 24 analyses of BCR-P is smaller than 2% for Ba, La, Ce, Pr, Nd, Gd, Tb, Dy, Ho, Er, Tm, Yb, Lu, Rb, Y, and Hf ; smaller than 4% for Sm, Eu, Nb, Cs, Ta and Pb; and smaller than 10% for Th and U.

The accuracy of the analysis at WSU was monitored by analyzing the Cornell basalt standard PAL-889 (recollection of USGS standard W-1) as an unknown. Generally, the discrepancies between analytical results and standard values for PAL-889 are small indicating good accuracy of the analysis: Y, Ba, La, Sm, Eu, Tb, Dy, Er, Tm, Lu, and Hf were analyzed within 5%, Sr, Ce, Pr, Nd, Gd, Ho, Yb, and Ta within 8% of the recommended standard values. Only Zr, Nb, Cs, Pr, and U indicate larger than 10% difference between the analytical results and the selected standard values, but this difference is because well-characterized standard values for these elements are not available (appendix E).

Furthermore, the accuracy of the analysis was estimated using an inter-laboratory comparison. Several samples previously analyzed at UC were re-analyzed at WSU, and the results of both laboratories agree well. In general, the results obtained at WSU agree within 10% of the analytical results obtained at UC. This indicates that both laboratories produced results with high accuracy and precision.

5.3 Element mobility

Most primary minerals in rock samples from the different units in the Wild Rogue Wilderness are partially to completely replaced (chapter 2, appendix A). The metamorphic assemblages are interpreted to have formed during subseafloor hydrothermal alteration and in the metagabbro unit, metatonalite unit and Blossom Bar shear zone by subsequent deformation accompanied by hydrothermal alteration. This interpretation is based on field and petrographic evidence as outlined in chapters 2 and 4. Extensive element mobility can occur during subseafloor hydrothermal alteration (e.g., Mottl, 1983; Alt et al., 1986; Harper et al., 1988; Harper, 1995) and, therefore, an understanding of this process is necessary for correctly interpreting geochemical variations in analyzed samples.

The pattern of hydrothermal metamorphism in many ophiolites is characterized by a downward increase in metamorphic grade (e.g. Evarts and Schiffmann, 1983; Harper et al., 1988; Schiffmann et al.,

1991) that generally dies out in the gabbroic unit. This 'background' alteration is interpreted to be the result of down-welling sea water that reacts with basalt at increasingly higher temperature and pressure and decreasing water / rock ratios with depth. This 'recharge' alteration is characterized by prograde metamorphism under a steep thermal gradient. Then, the highly reacted sea-water derived fluids rise along grain boundaries (diffuse discharge) or through fractures and fault zones (fault-controlled discharge, e.g., Alexander et al., 1993) to the seafloor where the fluids are expelled forming axial hot-springs. Epidosites (epidote- and quartz-rich rock with granoblastic texture) are believed to have formed in such zones of upflowing hydrothermal fluids under high water/rock ratios (Harper et al, 1988; Bettison-Varga et al, 1995).

In zones of down-welling, the reaction of seawater with basalt results in removal of Mg^{2+} from seawater and leaching of Ca^{2+} from the rock (Mottl, 1983; Seyfried et al., 1988). This takes place over a wide range of temperatures. Basalt and diabase affected by this type of alteration are enriched in Mg and depleted in Ca relative to primary igneous values. The mass exchange generally becomes less downward due to decreasing seawater/rock ratios.

Epidosites occur throughout all units in the Wild Rogue Wilderness. They are areas of extreme calcium metasomatism and are believed to represent zones of discharge alteration superimposed on the background alteration. The epidosites appear to be similar to those in the Josephine ophiolite (Harper et al, 1988) and Troodos ophiolite (Bettison-Varga et al., 1995) which are generally depleted in Cu, Zn, Na_2O , K_2O , and MgO and are enriched in CaO, Sr, and often Eu, compared to fresh diabase or basalt.

Most major elements and many trace elements experience redistribution during subseafloor hydrothermal alteration based on observational data from ophiolites (e.g., Harper et al, 1988; Bettison-Varga et al., 1995) and basalts recovered from the ocean floor (e.g., Mottl, 1983; Alt et al., 1986; Staudigel et al., 1996) as well as experimental data (e.g., Mottl, 1983; Seyfried, 1987; Seewald and Seyfried, 1990). Redistribution of virtually all major elements has been reported except for Ti, which is generally immobile. Gains or losses of SiO_2 , Al_2O_3 , FeO^* , MnO, MgO, CaO, Na_2O compared to primary igneous values can occur depending on temperature, pressure, and fluid composition.

Also, the mobility of elements can be assessed by comparing their ionic potential (ionic charge / ionic radius). Elements with low ionic potential, also called low field strength elements (LFS), are generally mobile in aqueous solutions (Pearce, 1983, 1996; Rollinson, 1993). LFS elements include Cs, Rb, K, Ba, Sr, divalent Eu and divalent Pb. Also, many transition elements such as Cu, Fe, Zn, Ni and Mn are mobile (Seewald and Seyfried, 1990). In contrast, elements with high ionic potential, also called high field strength elements, are generally immobile in aqueous solutions under a wide range of metamorphic conditions (Pearce, 1983, 1996; Rollinson, 1993). HFS elements include Ta, Nb, Zr, Hf, Th, Ti, Y, Sc and the MREE and HREE.

In areas of extreme metasomatism, redistribution of generally immobile elements may occur such as during the formation of epidiosites or silicification. Valsami and Cann (1992) reported that REE, especially LREE, were mobile under these extreme alteration conditions, while other HFS elements (Ti, Zr, Y, Nb and HREE) appear immobile. Because of the potential problem of the redistribution of generally 'immobile' elements under the conditions of extreme metasomatism, epidiosites and mineralized rocks were not analyzed in this study.

Often element mobility can be deduced from bivariate diagrams in which 'mobile' elements are plotted against an 'immobile' element (such as Zr). A strong correlation between incompatible elements suggests that the variation is due to igneous processes such as crystal fractionation. However, this method cannot be applied if different magmatic suites are sampled because they are characterized by different primary compositions and incompatible trace element ratios, which is the case for the Wild Rogue Wilderness remnant of the CRO. Evidence for little or no major element mobility are discussed in the sections on metatonalite and sheeted dikes.

5.4 Interpretation of Chondrite- and N-MORB normalized trace element patterns

The diagrams in figure 5.2a show the Chondrite- normalized REE abundance patterns for average N-MORB, island arc tholeiite (IAT), calc alkaline basalt (CAB) and Boninite (BON). Average N-MORB is depleted in light rare earth elements (LREE) with respect to heavy rare earth elements (HREE). This depletion reflects the character of the upper mantle from which N-MORB is derived by partial melting

(Sun and McDonough, 1989). Continued melting and melt extraction results in depletion of incompatible elements in the convecting upper mantle. LREE behave more incompatibly than HREE during most partial melting processes and, therefore, are more depleted in the convecting upper mantle. The REE fractionation is expressed using the chondrite normalized $(La/Yb)_n$ ratio, which is about 0.55 for average N-MORB.

The N-MORB normalized diagrams in figures 5.2b through 5.2d are a convenient means of graphically presenting the trace element data of a sample. Characteristic patterns for various magma types can be recognized, and interpretations of the character of the mantle source can be made based on these patterns (e.g., Pearce and Parkinson, 1993). The N-MORB normalized trace element abundance patterns of the selected island arc reference samples are shown in figure 5.2b through 5.2d. The patterns of IAT, CAB and BON have a characteristic 'arc-signature' which is typified in the relative enrichment of LILE (Sr, K, Rb and Ba) and relative depletion of the high-field strength (HFS) elements Ta and Nb.

The elements in the N-MORB normalized diagram behave incompatibly during most partial melting and fractional crystallization processes (Pearce, 1983; Sun and McDonough, 1989), except perhaps Sr and Eu which may be compatible in plagioclase, Y and HREE, which are compatible in garnet, and Ti which is compatible in magnetite, titanite and ilmenite (Pearce, 1983). During partial melting of the upper mantle, the incompatible elements are concentrated into the magma, and the abundance ratio of two incompatible elements having identical mineral/melt partition coefficients remains constant during partial melting, regardless of the degree of melting. As a result, the ratio of elements having identical mineral/melt partition coefficients reflects that of the source. In contrast, the ratio of two incompatible elements with different mineral/melt partition coefficients will vary with the degree of partial melting. However, the differences between mineral/melt partition coefficients of elements in the N-MORB normalized diagrams in figure 5.2 are small so that as long as there is $\geq 15\%$ melting (equilibrium or fractional melting) the abundance ratio of any of these elements does not differ significantly from that of the source. Similar relationships are found with fractional crystallization. Lower than 60-80% fractional crystallization does not result in significant changes of the ratios either, except at very high degrees of fractionation where the crystallization of accessory phases in which certain trace elements are highly compatible, such as zircon (Zr, Hf), results in notable changes of certain trace element abundance ratios. In general, fractional crystallization and partial melting change the level, but not the shape of the patterns in the N-MORB normalized diagrams (Pearce, 1983, Pearce and Parkinson, 1993).

The elements on the N-MORB normalized diagrams are arranged (after Pearce 1983) according to their relative incompatibility during partial melting of the mantle, because the mineral/melt partition coefficients play such an important role. The elements are also split into two groups: elements that are generally mobile in aqueous solutions (Sr, K, Rb, Ba), and elements that are thought to be immobile during most metamorphic processes (Th through Yb). The systematic relationships amongst incompatible trace elements are discussed in more detail in Pearce (1983), Sun and McDonough (1989), and Pearce and Parkinson (1993). The authors suggest that the order of incompatibility in oceanic magmas is $Rb \approx Ba > Th > Nb = Ta \approx K > La > Ce > Pr \approx Sr > Zr = Hf \approx Sm > Gd \approx Ti > Dy > Ho = Y > Yb$. The incompatibility of 'mobile' elements increases from right (Sr) to left (Ba) while the incompatibility of 'immobile' elements increases from left (Yb) to right (Th).

Differences between the various patterns of IAT, CAB and BON are interpreted in the light of the most recent models for arc magmatism which ascribe magma generation to decompression melting in the mantle wedge triggered by the introduction of hydrous fluids released by dehydration of the subducted slab (e.g., Plank and Langmuir, 1988; Hawkesworth et al., 1991; Pearce and Peate, 1995). Pearce (1983) proposed a simple method for estimating the relative contributions of the 'slab-component' and 'mantle-component' in volcanic arc basalts. This method is based on the assumption that the HFS elements, including Ta, Nb, Zr, Hf, Ti, Y and HREE (Dy to Lu) are dominantly mantle-derived (Pearce, 1983; Pearce et al. 1984a; Pearce and Parkinson, 1993; Pearce et al., 1995a, b; Hochstaedter et al., 1990a,b). The mantle-derived elements are marked with solid symbols in figure 5.2b through 5.2d. If this assumption is true, the HFS elements can be used to quantify the composition of the mantle source before the addition of the 'slab-component', and also allows to determine which elements make up the slab-component (i.e. the elements that are enriched relative to the HFS). The slab-derived elements are marked with open symbols in figure 5.2b through 5.2d. The stippled line at a lower composition shows the interpolated and extrapolated composition for a hypothetical basalt generated by melting of the mantle wedge before subduction contribution. The composition of the hypothetical basalt can be interpolated and extrapolated

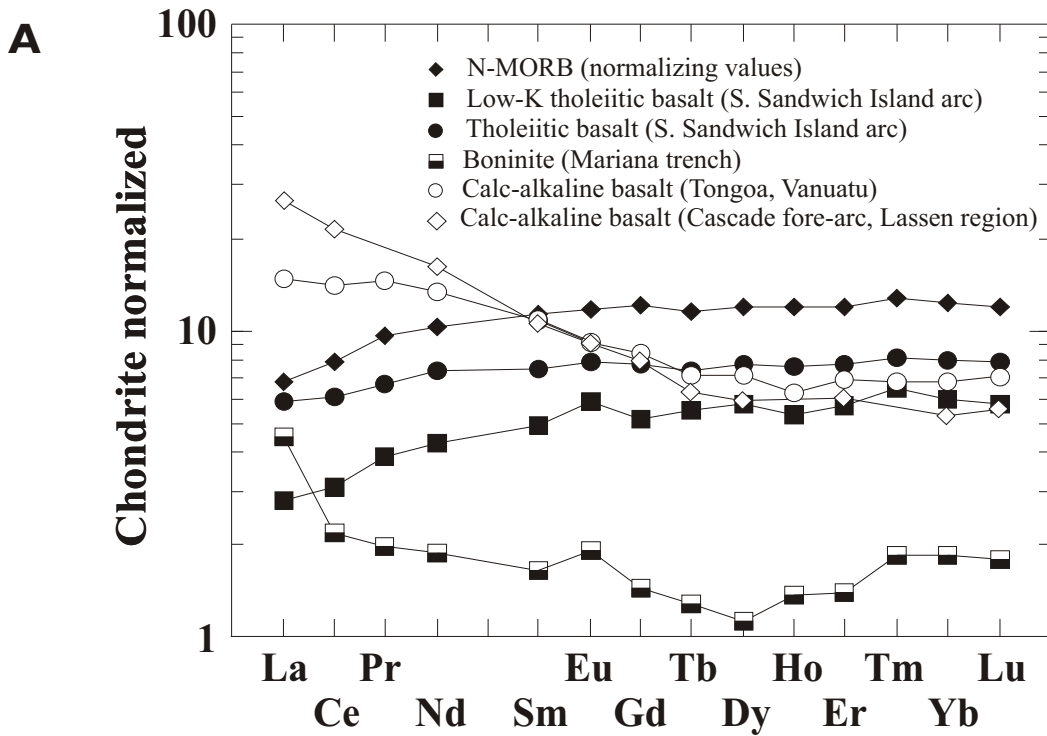
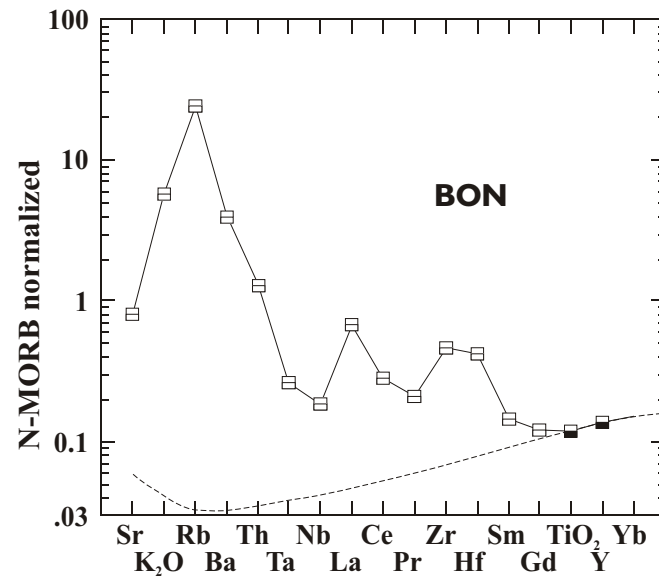
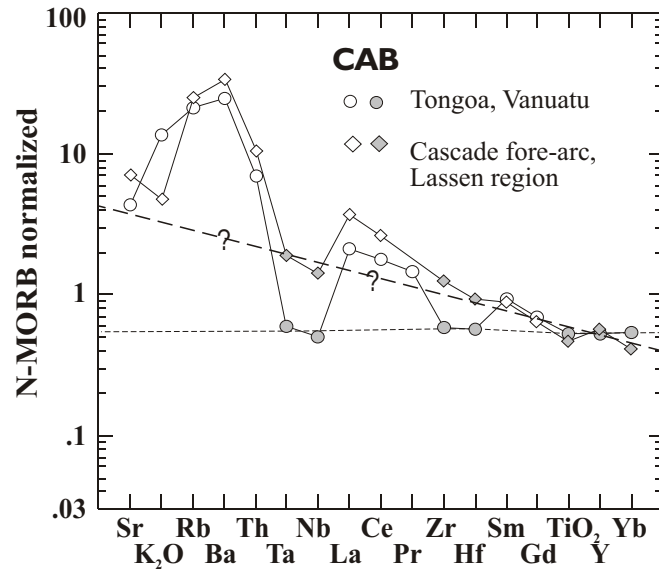
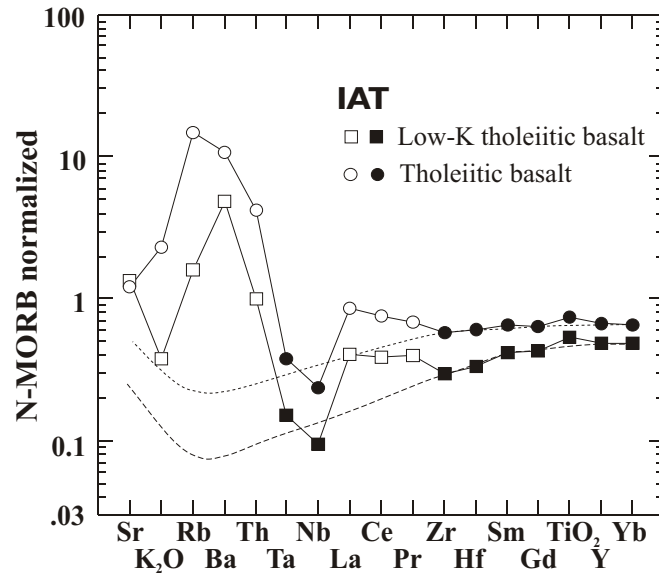


Figure 5.2

A. Chondrite normalized rare earth element distribution patterns of normal mid ocean ridge basalt

(MORB), island arc tholeiite (IAT), calc-alkaline basalt (CAB). Average N-MORB values are from Sun and McDonough (1989), the data for the IAT reference samples are from Pearce et al. (1995a), the BON reference sample is from Pearce and Parkinson (1993), and the CAB reference sample is from Pearce et al. (1995b) (Tonga) and Borg et al. (1997) (Cascade fore-arc). The chondrite normalizing values of Taylor and McLennan (1985) are used throughout this chapter.

B-D. (next page) Diagrams showing N-MORB normalized major and trace element distribution patterns of IAT, CAB and BON. Fractional crystallization and variations in the degree of partial melting (see text) change the level of the pattern, but have little effect on the shape (e.g., Pearce, 1983). Elements shown with open symbols are thought to be derived by significant subduction contribution whereas elements shown with solid symbols are thought to be derived almost entirely from the mantle wedge. The stippled lines in the diagrams for IAT, CAB and BON indicate the extrapolated compositions for elements in a hypothetical basalt derived by partial melting of the mantle prior to subduction contribution (after Pearce, 1983; Pearce and Parkinson, 1993).



using the order of incompatibility listed above. For example, K, Ta, and Nb are almost identical in their incompatibility. Thus, K in the hypothetical basalt should be as depleted as Ta and Nb. Rb, Ba and Th are slightly more incompatible than Ta and Nb and should be more depleted than Ta and Nb.

Both reference samples for island arc tholeiites (IAT) have significantly lower REE abundances than N-MORB. The low-K tholeiite reference sample is relatively more depleted in LREE than average N-MORB, whereas the tholeiitic reference sample is more enriched in LREE than N-MORB (figure 5.2a). The $(La/Yb)_n$ of the low-K tholeiite and arc tholeiite reference samples are 0.47 and 0.73, respectively. Lower-than-N-MORB REE concentrations and lower $(La/Yb)_n$ ratios can be explained with a more refractory mantle source than the N-MORB mantle and/or high degrees of melting (Pearce, 1983; Pearce and Parkinson, 1993; Pearce et al., 1995a). IAT have often higher $(La/Yb)_n$ ratios than N-MORB, which is thought to be the result of a subduction contribution rich in LREE relative to HREE (Pearce, 1983; Pearce and Parkinson, 1993; Saunders et al., 1991). Crustal contamination apparently does not play an important role in tholeiites erupting in oceanic island arcs and, therefore, is not responsible for the $(La/Yb)_n$ ratios higher than N-MORB. The IAT reference samples are characterized by low abundances of the elements Ta through Yb, while the LILE and Th are selectively enriched. LREE (La, Ce, Pr, and Nd) are also enriched with respect to the inferred mantle composition before subduction contribution (figure 5.2b). Overall, the abundances of all incompatible trace elements in the low-K tholeiite is much lower than in the arc tholeiite despite there is no apparent difference in the degree of fractionation (both IAT are primitive). Ta and Nb are more depleted in the low-K tholeiite than in the tholeiite, and as a result their Ta/Yb and Nb/Yb ratios differ significantly indicating that the mantle source of the low-K tholeiite is more depleted (or the low-K tholeiite may be derived by higher degrees of dynamic melting; Pearce et al., 1995a).

CAB are notably enriched in LREE (figure 5.2a). The $(La/Yb)_n$ ratio of the reference sample from Tongoa is 2.2, and of primitive low-K calc-alkaline basalts from the Cascade fore-arc in the Lassen region is 5.00. Similar to the IAT reference samples, the abundance of HREE in CAB is lower than that of N-MORB ($7 \times$ chondritic). This pattern can be explained with high degrees of melting of a mantle that has been enriched with a subduction contribution high in LREE (Pearce, 1983, Pearce and Parkinson, 1993, Pearce 1995b). Crustal contamination in primitive CAB from an island arc is unlikely. CAB are similarly

depleted in HREE and Yb, but much more enriched in LILE, Th and LREE, and less depleted in Ta and Nb than IAT (figure 5.2c). Unlike IAT, MREE are enriched in CAB, and the line representing the composition of the hypothetical basalt produced by melting of the mantle wedge before subduction contribution is parallel to N-MORB (Tonga) or slopes downward from right to left (Cascade fore-arc). The high Ta and Nb values of the lavas from the Cascade fore-arc are higher than typical N-MORB reflecting “within-plate” enrichment of the subarc-mantle in continental arc settings (Pearce, 1983). Note that the boundary between CAB and IAT is transitional as variations in relative depletion in HFS elements and relative enrichment in LILE, Th and LREE exist.

BON have extremely low REE abundances and are characterized by an U-shaped REE distribution pattern with $(La/Yb)_n > 1$ (figure 5.2a). REE and most other HFS elements in BON (figure 5.2d) are much more depleted than in IAT and CAB. The extremely low concentrations of incompatible elements in BON, such as HREE (e.g. Yb), indicate high degrees of melting of a refractory mantle source (significantly more depleted than the global N-MORB reservoir). $(La/Yb)_n$ ratios > 1 and high LILE and Th concentrations reflect the enrichment with a subduction contribution rich in LREE, LILE and Th (Pearce and Parkinson, 1993). As shown in figure 5.2d, Nb and Ta and sometimes Zr and Hf appear to be enriched relative to the inferred composition of the mantle wedge before subduction contribution. Pearce and Parkinson (1993) suggested that the enrichment in Ta, Nb, Zr and Hf could be due to the addition of a slab melt.

The ratios of incompatible elements expressing the relative depletion of HFSE and relative enrichment of LILE, Th and LREE, can be used to distinguish and compare different magmatic suites and identify different mantle sources. Incompatible element ratios (of immobile trace elements) are used in tectonic discrimination diagrams to identify the magmatic affinities of altered rocks. Ratios used include Hf/Th, Th/Ta, Th/Yb, and La/Yb which give a measure of the relative subduction enrichment. Ta/Yb, Zr/Y, and Nb/Yb ratios give a measure of the mantle depletion using average N-MORB as a reference. Incompatible trace element ratios involving ‘immobile’ trace elements such as Ba/Zr should be interpreted with caution, because rock samples are altered and primary minerals in the Wild Rogue Wilderness remnant of the CRO are replaced.

In summary, the normalized diagrams are convenient to present graphically the complete trace element data of a sample for the purpose of pattern recognition. Different magma types can be determined, and patterns of samples can be compared in order to determine whether or not they are related by fractionation. The advantage of REE- and N-MORB- normalized diagrams is that the patterns change little with crystal fractionation or variations in the degree of partial melting. Only the absolute concentrations of the incompatible elements change with fractionation or partial melting. Thus, samples that derived from a similar source and are related by crystal fractionation have parallel patterns on chondrite- and N-MORB-normalized diagrams. In contrast, crossing REE and trace element distribution patterns indicate that the samples are most likely not related by crystal fractionation, and other possibilities such as magma mixing, contamination, variable degrees of melting, dynamic melting, and different mantle sources, or a combination of these factors have to be considered.

5.5 Geochemistry of igneous rocks from the ophiolite units

5.5.1 Metagabbro unit

5.5.1.1 Rock classification

Nine samples from the metagabbro unit were analyzed; three samples are from the medium grained main phase gabbro (O/C-373b, MRH-23, MRH-78.2), two sample are from deformed, fine-grained mafic dikes (O/C-373a, O/C-374b), and one is from a deformed, fine-grained mafic enclave (MRH-78.1). The sample locations are shown in figure 5.1, the analytical data are listed in table 5.1a, and the petrographic data are listed in appendix A (table A1). The metagabbro samples contain 40-55% plagioclase, 40-55% hornblende, 1-3% oxide and accessory apatite as inclusions in hornblende. Plagioclase is cloudy in thin section but often retains a relict igneous texture and composition; plagioclase is strongly zoned, shows relict carlsbad-albite twinning and has calcic cores (An_{78-82}) and calcic to sodic rims (An_{63-16}). Hornblende is dark-green and uniformly colored. Relict magmatic textures, such as zoning and albite-carlsbad twinning in plagioclase, and relict magmatic foliation and lineation, are preserved. However, it is not clear whether or not hornblende is igneous in origin. If hornblende is igneous in origin, then it

Table 5.1a: Major and trace element composition of samples from the metagabbro unit

| Sample | O/C-373a | O/C-373b | O/C-374b | MRH-23 | MRH-78/1 | MRH-78/2 |
|--------------------------------|-----------|----------|-----------|---------|--------------|----------|
| Rock type | def. dike | gabbro | def. dike | gabbro | def. enclave | gabbro |
| SiO ₂ | 42.79 | 44.01 | 43.14 | 44.00 | 43.31 | 44.14 |
| TiO ₂ | 0.86 | 0.82 | 0.64 | 0.75 | 0.87 | 0.77 |
| Al ₂ O ₃ | 19.00 | 18.87 | 21.58 | 18.74 | 19.47 | 20.30 |
| Fe ₂ O ₃ | 14.08 | 12.50 | 12.78 | 12.39 | 13.42 | 11.28 |
| MnO | 0.25 | 0.25 | 0.22 | 0.30 | 0.24 | 0.22 |
| MgO | 6.61 | 6.65 | 5.58 | 7.39 | 6.35 | 5.98 |
| CaO | 12.21 | 11.95 | 11.73 | 12.43 | 11.85 | 12.47 |
| Na ₂ O | 1.50 | 1.73 | 1.62 | 1.34 | 1.72 | 1.71 |
| K ₂ O | 0.16 | 0.15 | 0.23 | 0.15 | 0.27 | 0.23 |
| P ₂ O ₅ | 0.13 | 0.16 | 0.08 | 0.09 | 0.14 | 0.23 |
| BaO | 20 | 22 | 82 | 46 | 41 | 36 |
| Cr ₂ O ₃ | 48 | 67 | 0 | 138 | 40 | 61 |
| LOI | 2.51 | 3.03 | 2.69 | 3.08 | 2.26 | 2.91 |
| Total | 100.15 | 100.16 | 100.32 | 100.73 | 99.95 | 100.29 |
| Ni | 20 | 30 | 4 | 46 | 21 | 22 |
| Sc xrf/icp | 48/n.d. | 42/n.d. | 29/25 | 51/n.d. | 49/n.d. | 1 |
| V xrf/icp | 349/373 | 326/333 | 221/247 | 328/343 | 331/372 | 270/285 |

Major elements (in wt%) and Ba, Cr, Ni, Sc, and V (in ppm) were analyzed by standard XRF technique on pressed powder pellets at McGill University, Montreal. Additionally, Sc was analyzed by ICP-MS at Washington State University and V at Union College

Table 5.1a cont.

| Sample | O/C-373a | | O/C-373b | | O/C-374b | | MRH-23 | MRH-78/1 | | MRH-78/2 | |
|--------|----------|-------|----------|-------|----------|-------|--------|----------|------|----------|--|
| | UC | UC | WSU | UC | WSU | UC | UC | UC | WSU | | |
| Cr | 29 | 46 | n.d. | 9 | n.d. | 75 | 27 | 37 | n.d. | | |
| Rb | 1.8 | 1.6 | 1.9 | 2.5 | 2.8 | 1.5 | 3.6 | 3.1 | 2.8 | | |
| Sr | 448 | 454 | 449 | 436 | 422 | 386 | 476 | 510 | 500 | | |
| Y | 24 | 22 | 24 | 11 | 12 | 19 | 20 | 20 | 21 | | |
| Zr | 23 | 22 | 21 | 14 | n.d. | 18 | 24 | 19 | n.d. | | |
| Nb | 0.37 | 0.40 | 0.40 | 0.22 | 0.25 | 0.28 | 0.45 | 0.42 | 0.42 | | |
| Cs | 0.33 | 0.32 | 0.33 | 0.41 | 0.39 | 0.20 | 0.76 | 0.41 | 0.39 | | |
| Ba | 31 | 29 | 34 | 43 | 41 | 29 | 47 | 55 | 58 | | |
| La | 2.55 | 3.00 | 3.26 | 1.61 | 1.81 | 1.92 | 3.57 | 3.80 | 3.99 | | |
| Ce | 9.98 | 11.1 | 10.8 | 5.38 | 5.57 | 7.63 | 11.9 | 12.3 | 11.6 | | |
| Pr | 2.15 | 2.27 | 2.16 | 1.04 | 1.03 | 1.63 | 2.24 | 2.30 | 2.13 | | |
| Nd | 13.4 | 13.5 | 12.8 | 6.00 | 5.70 | 9.75 | 12.4 | 12.9 | 11.5 | | |
| Sm | 4.10 | 4.08 | 4.27 | 1.77 | 1.89 | 2.96 | 3.50 | 3.67 | 3.74 | | |
| Eu | 1.31 | 1.29 | 1.40 | 0.66 | 0.72 | 1.11 | 1.20 | 1.18 | 1.23 | | |
| Gd | 4.69 | 4.50 | 4.52 | 1.88 | 2.03 | 3.11 | 3.74 | 4.07 | 3.95 | | |
| Tb | 0.74 | 0.68 | 0.74 | 0.30 | 0.32 | 0.49 | 0.58 | 0.62 | 0.62 | | |
| Dy | 4.54 | 4.15 | 4.60 | 1.89 | 2.12 | 3.14 | 3.53 | 3.80 | 3.91 | | |
| Ho | 0.88 | 0.81 | 0.94 | 0.39 | 0.43 | 0.66 | 0.70 | 0.73 | 0.78 | | |
| Er | 2.64 | 2.43 | 2.57 | 1.14 | 1.22 | 1.95 | 2.05 | 2.20 | 2.21 | | |
| Tm | 0.42 | 0.38 | 0.37 | 0.18 | 0.18 | 0.30 | 0.32 | 0.34 | 0.33 | | |
| Yb | 2.44 | 2.30 | 2.35 | 1.14 | 1.16 | 1.90 | 1.96 | 2.05 | 1.98 | | |
| Lu | 0.35 | 0.34 | 0.37 | 0.18 | 0.19 | 0.29 | 0.28 | 0.30 | 0.32 | | |
| Hf | 0.89 | 0.84 | 1.00 | 0.55 | 0.76 | 0.77 | 0.90 | 0.73 | 0.90 | | |
| Ta | 0.013 | 0.014 | 0.02 | 0.017 | 0.02 | 0.02 | 0.01 | 0.02 | 0.03 | | |
| Pb | 0.50 | 0.46 | 0.64 | 0.51 | 0.76 | 0.184 | 0.514 | 0.567 | 0.69 | | |
| Th | 0.02 | 0.04 | 0.14 | 0.02 | 0.06 | 0.02 | 0.04 | 0.06 | 0.10 | | |
| U | 0.02 | 0.02 | 0.04 | 0.02 | 0.1 | 0.01 | 0.02 | 0.03 | 0.1 | | |

UC... Trace element analysis by ICP-MS at Union College

WSU... Trace element analysis by ICP-MS at Washington State University

All trace elements are given in ppm.

n.d. ... not determined

<d.l. ... below detection

re-equilibrated at amphibolite facies conditions. This was determined from the composition of coexisting plagioclase-hornblende pairs using Holland and Blundy's (1994) geothermometer (chapter 3). Assuming hornblende is igneous in origin, the samples can be classified as hornblende gabbro based on the modes (Streckeisen, 1976, LeMaitre et al., 1989). The metagabbro unit is heterogeneously deformed, and observed textures are interpreted to have formed by magmatic and subsequent solid state deformation (chapter 4).

The total alkalis vs. silica (TAS) diagram of Cox et al. (1979) for volcanic rocks was adapted by Wilson (1989) for the chemical classification of plutonic rocks. The samples from the metagabbro unit have low SiO_2 (44-46 %; on volatile-free basis and total iron as FeO^*) and low $\text{K}_2\text{O} + \text{Na}_2\text{O}$ (table 5.1a). They plot in the field for subalkalic gabbro using the TAS diagram of Wilson (1989) (not shown). Unfortunately, this classification is based on 'mobile' elements and should be used with caution. However, very low Nb/Y ratios (0.015-0.23) and low Zr/ TiO_2 ratios (22-28) in samples from the metagabbro unit are consistent with a mafic, subalkalic composition of the magma.

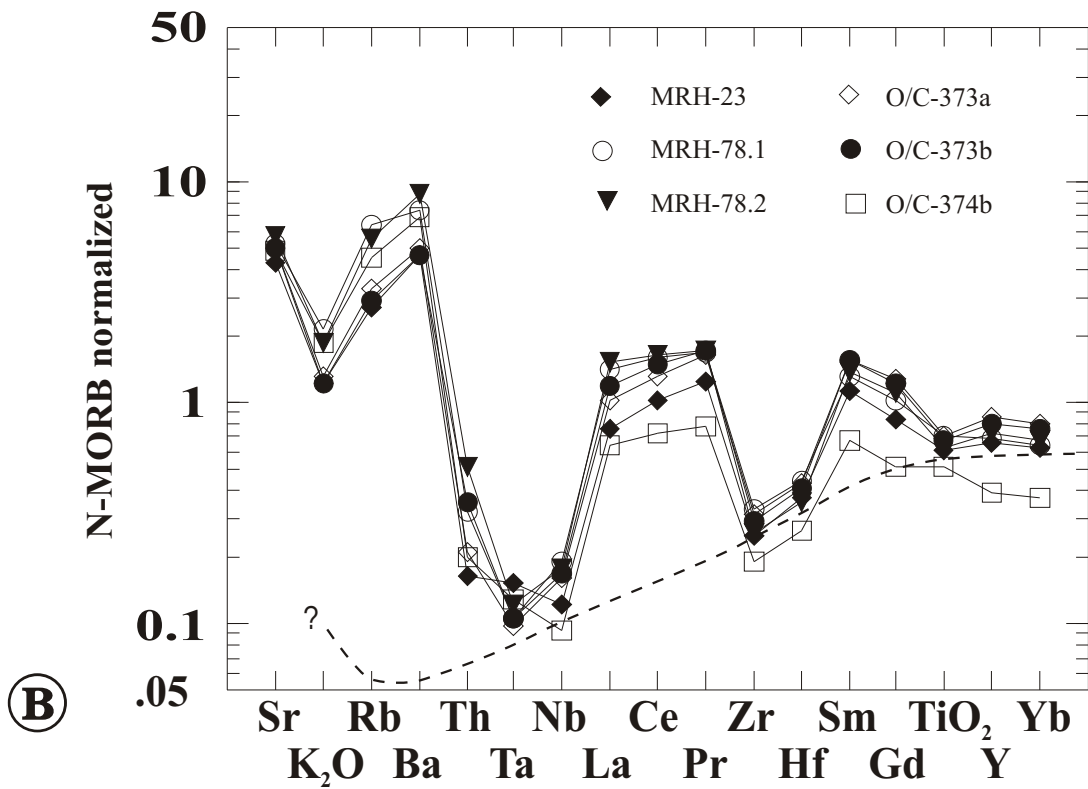
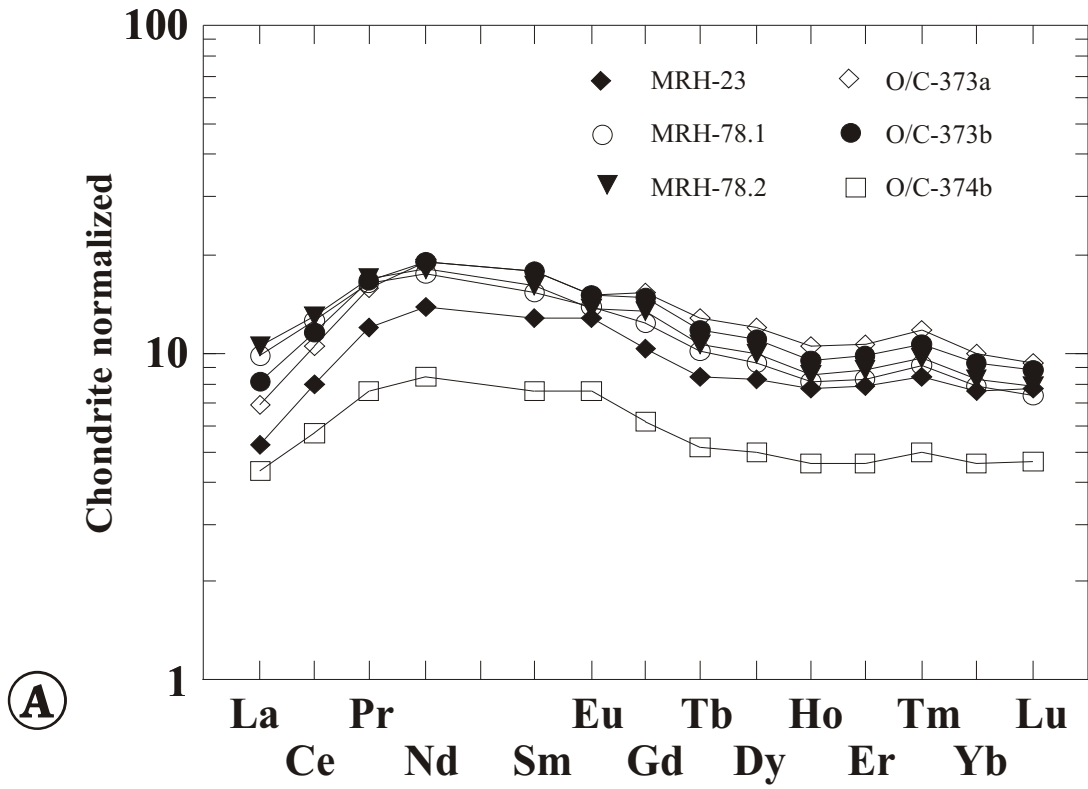
5.5.1.2 Magmatic affinities

The chondrite normalized REE distribution patterns of the metagabbro samples have an unusual shape (figure 5.3a). They are flat in the HREE (5-10 \times chondritic) and strongly convex-up in the LREE. Two samples have a positive and four samples have a negative Eu anomaly. Such convex-up characteristics of REE patterns centered on Nd are not found in the continental crust and are not very common in rocks that crystallized from mantle-derived liquids (e.g., Barrat and Nesbitt, 1996).

The N-MORB normalized pattern has an arc-signature that is typified in the depletion of high field-strength elements (HFSE) and enrichment of large ion lithophile elements (LILE). The comparison with N-MORB shows that the metagabbro samples are strongly depleted in Hf, Zr, Nb, Ta and Th relative to MORB, whereas the REE have concentrations similar to N-MORB (figure 5.3b). Most LILE (Ba, Rb and Sr) are notably enriched relative to N-MORB. The consistent patterns for K, Rb, B, and Sr suggest that alteration did not change the abundances of LILE significantly. Thus, the selective enrichment of LILE is probably a primary signature. Th is depleted compared to N-MORB. However, it is still enriched relative

Figure 5.3

- A. Chondrite normalized REE distribution patterns of samples from the metagabbro unit. The patterns are parallel suggesting that the samples could be related by fractionation. The shape of the REE distribution pattern is very unusual: the LREE show a convex-up pattern centered on Nd. Such patterns are not observed in the continental crust and are very rare in mantle-derived liquids.
- B. N-MORB normalized major and trace element distribution patterns of samples from the metagabbro unit. The patterns show characteristics of arc-related rocks. Compared to N-MORB, the elements Ta, Nb, Hf, and Zr are strongly depleted, LILE are enriched, and REE are similar to N-MORB. This is enriched with respect to Ta and Nb, but depleted compared to N-MORB.



to Ta and Nb which is characteristic of arc magmas. This pattern is similar to the low-K tholeiite reference sample in figure 5.2b. However, certain differences exist, such as the extreme depletion of Hf and Zr, and very small Th-enrichment relative to Ta and Nb. A dashed line is drawn in figure 5.3b similar to the stippled lines in figure 5.1b that represents the inferred mantle composition before subduction contribution. It becomes clear that both LILE and LREE, MREE and Th are significantly enriched relative to the dashed line in figure 5.3b. I infer that LILE, Th, LREE and MREE constitute a subduction contribution to a very depleted mantle (very low Ta/Yb and Nb/Y ratios). Note that MREE in IAT are not significantly enriched by subduction contribution (figure 5.2b), but they are notably enriched in CAB (figure 5.1c). Another difference between the metagabbro samples and the IAT reference samples in figure 5.2b (and most other arc lavas) is the relative depletion of Ta and Nb. Most samples from the metagabbro unit, have Nb/Ta ratios (up to 29) significantly higher than the average value of 17.5 (e.g., Stolz et al., 1996). Most mantle-derived rocks have a Nb/Ta ratio similar to (or somewhat lower than) the chondritic value of 17.5 (e.g., Stolz et al., 1996), indicating that during most mantle melting and crystal fractionation processes Ta and Nb are not fractionated. The Nb/Ta ratios in the metagabbro samples are most likely very accurate considering the high quality of the trace element analysis by ICP-MS (appendix E). High Nb/Ta ratios have been reported from potassic HFSE-enriched calc-alkaline and K-rich alkaline rocks from the Sunda arc (Stolz et al., 1996). However, the samples from the metagabbro unit are subalkalic gabbros with much lower K.

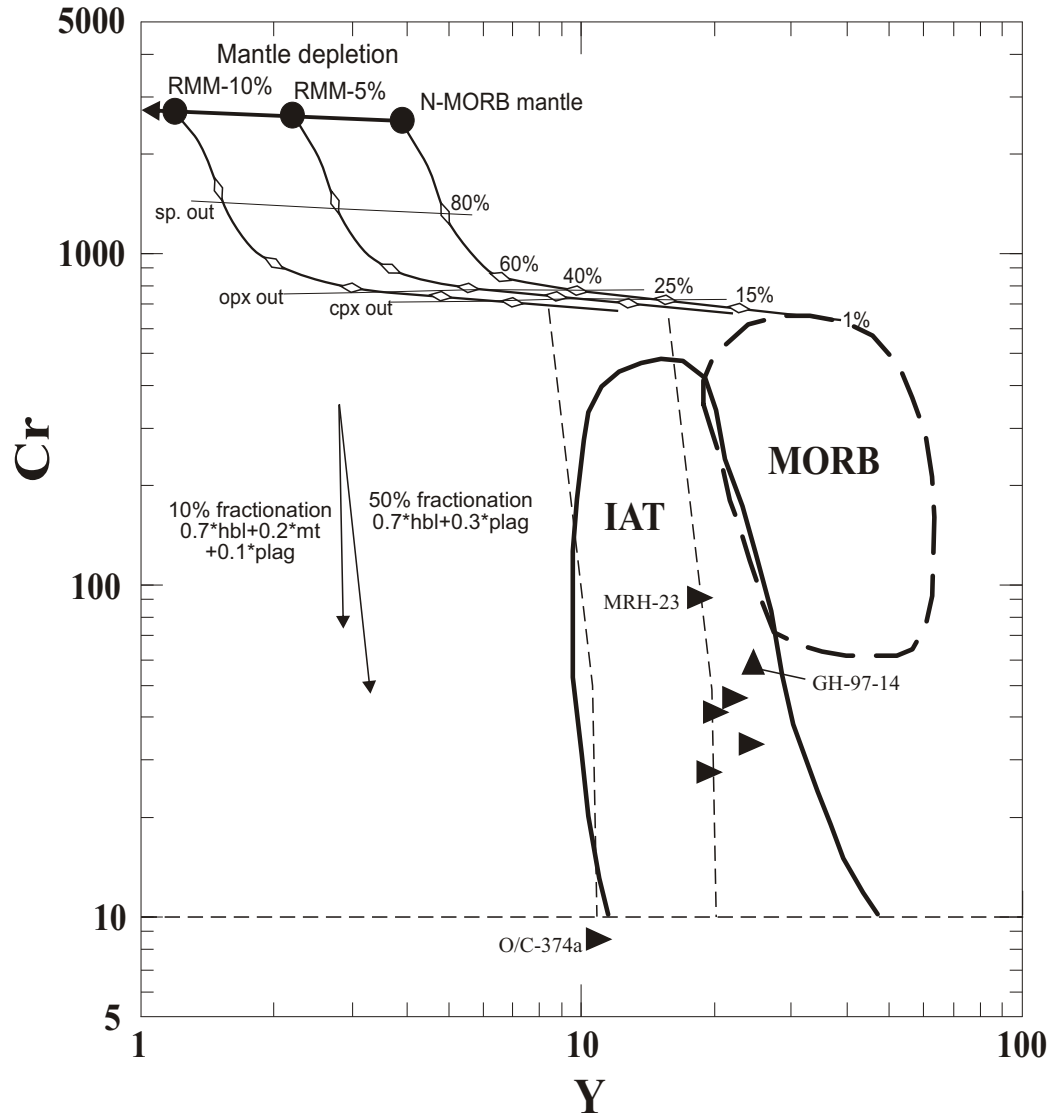
The metagabbro samples plot in the Cr vs. Y discrimination diagram of Pearce (1982) within the field for island arc basalts (figure 5.4). Cr is lower than in typical MORB, which is consistent with an origin in an island arc setting. The low Cr levels indicate that the samples are fairly evolved.

Almost all geochemical information can be conveniently summarized in the ternary Hf/3-Th-Ta diagram of Wood et al. (1979) (figure 5.5a). The Hf/3-Th-Ta diagram records mantle ratios of these, and thus source heterogeneities, independent of variations resulting from fractional crystallization and variations in the degree of partial melting (Wood, 1980; Dudas, 1992). The effects of mantle enrichment and depletion are shown with the petrogenetic pathways in figure 5.5b (after Pearce et al., 1984). “Within-plate” mantle enrichment events cause increase of Th and Ta relative to Hf, and the mantle composition

Figure 5.4

Cr vs. Y tectonic discrimination diagram of Pearce (1982) showing fields for mid-ocean ridge basalts (MORB) and island arc tholeiite (IAT) (the latter field also includes calc-alkaline and alkalic basalts from oceanic arcs). The samples from the metagabbro unit (sideways triangle) plot within the VAB field. Upright triangle is the hornblende quartz diorite in the metagabbro unit which may be much younger.

The curves indicate the degree of melting of variously depleted mantle sources are calculated using the equation for fractional melting modified and extended after Hertogen and Gubels (1976) to take into account non-modal melting as well as depletion of phases with progressive melting. RMM-5% and RMM-10% are the residual MORB mantle compositions after 5% and 10% melt extraction, respectively. The N-MORB mantle composition and the rate of phase disappearance are taken from Pearce and Parkinson (1993). The N-MORB mantle consists of 57.5% olivine, 2.0% spinel, 27.0% opx and 12.5% cpx and contains 2500 ppm Cr and 3.9 ppm Y. Cpx is depleted after 15%, opx after 40%, and spinel after 80% melting of the N-MORB mantle. The initial mantle composition and the initial rate of phase disappearance, given in Pearce and Parkinson (1993), were used to determine the mineral proportion for each melting step as well as the composition of RMM-5% and RMM-10%, and the rate of phase disappearance during melting of RMM-5% and RMM-10% (subvertical lines labeled cpx out, opx out, and sp out). The mineral/melt partition coefficients at 1300°C compiled in Pearce and Parkinson (1993) are used to calculate the melting curves. Following Pearce and Parkinson (1993), incomplete melt extraction is incorporated into the melting model by treating trapped melt as a phase with a partition coefficient of 1. The mass fraction of trapped melt is assumed to be 0.01 (see Pearce and Parkinson, 1993). The arrows indicating fractionation of hbl + plag and hbl + plag + mt are calculated using the equation for Rayleigh fractionation and mineral/melt partition coefficients for basaltic liquids compiled in Rollinson (1993). The dashed lines show possible petrogenetic pathways based on calculated fractionation vectors (fractionation of hbl + plag followed by hbl + plag + mt from two different parental magmas). O/C-374b has very low abundances of incompatible trace elements, including Y, suggesting that the parental magma of O/C-374b was generated by higher degrees of melting than the parental magma of the other samples. Alternatively, the mantle source of O/C-374b could have been more refractory than that of the other samples.



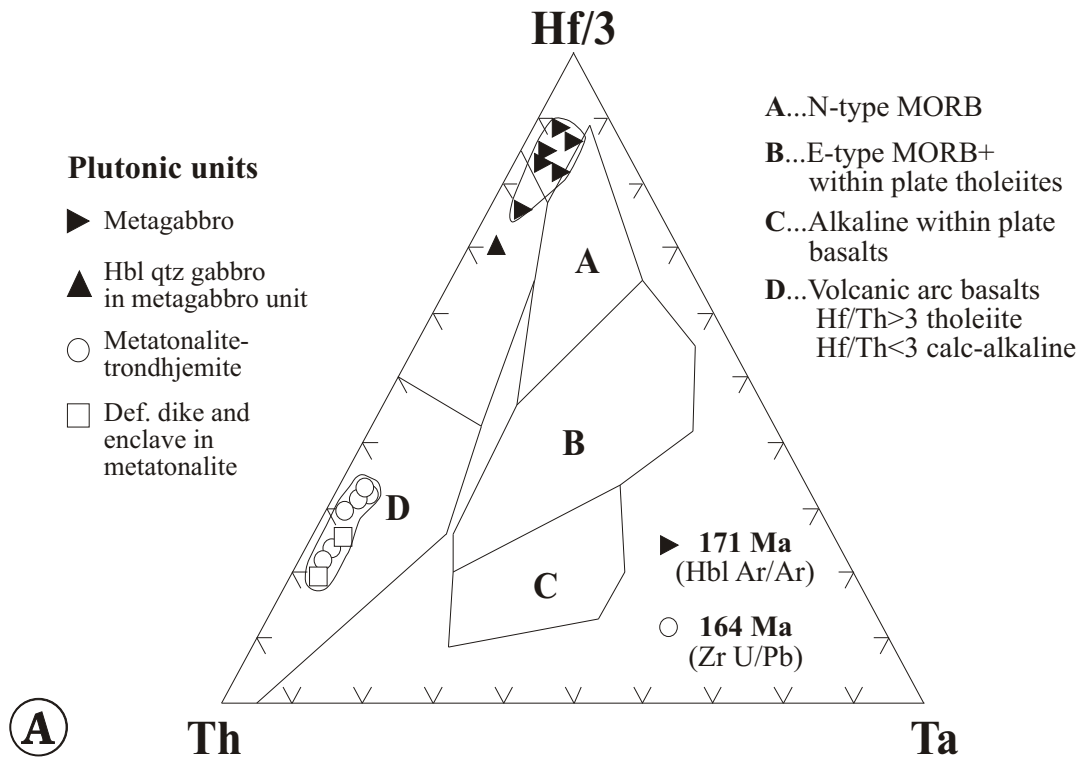
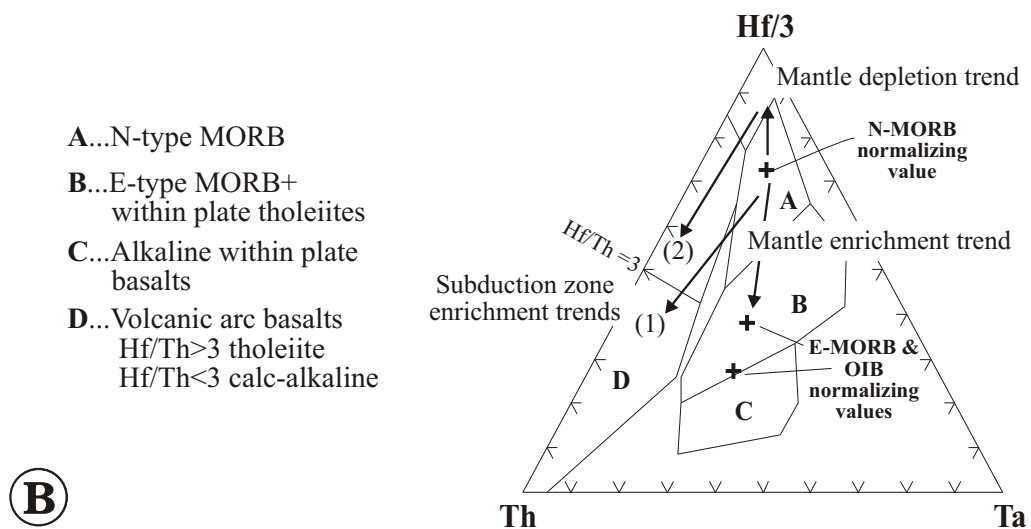


Figure 5.5A.

Hf/3-Th-Ta tectonic discrimination diagram of Wood et al. (1979). The samples from the metagabbro unit plot at depleted N-MORB compositions and overlap with the field of island arc tholeiite. The hbl-Qtz diorite (GH-97-14) which intrudes (?) the metagabbro and may be much younger (chapter 2) plots well within the IAT field. All samples from the metatonalite unit plot in the calc-alkaline field.



B. Petrogenetic pathways in the Hf/3-Th-Ta diagram of Wood et al. (1979). See text for explanation

moves towards field C, while mantle depletion events move the mantle composition towards the Hf-apex. In contrast, a “subduction zone contribution” moves the mantle composition towards the Th-apex into the volcanic arc field. Two arrows are shown marking the subduction zone enrichment: (1) the subduction component is added to a depleted mantle ; and (2) to a N-MORB-like mantle. Magmas derived from a mantle having composition (1) have lower Ta/Yb and Ta/Hf ratios than magmas derived from a mantle with composition (2). Clearly, the metagabbro unit is derived from a highly depleted mantle source. The metagabbro is so depleted that the samples fall outside of the N-MORB field. Only one samples from the metagabbro unit is displaced towards the Th-apex and plots in the IAT field.

5.5.1.3 Petrogenesis

5.5.1.3a Crystal Fractionation

The MgO variation diagrams for the samples from the metagabbro unit are shown in figure 5.6. The MgO content of metagabbro samples ranges from 7.7 - 5.7% with SiO₂ content from 44 - 46%. Although some scatter occurs, trends are clearly evident. SiO₂, CaO and MnO decrease, and TiO₂, Al₂O₃, and FeO*, increase with decreasing MgO content (greater fractionation). The fractionation trend show a cusp at about 6.7% MgO in the TiO₂ vs. MgO (figure 5.6b), FeO* vs. MgO (figure 5.6d) and V vs. MgO (figure 5.6j) diagrams. The cusp at about 6.7% MgO is interpreted to mark the onset of Fe-Ti oxide fractionation. The Al₂O₃ content of the metagabbro samples is very high for igneous rocks, ranging between 19.7 and 22.2%, which is higher than most magmas, but similar to the Al₂O₃ content of plagioclumulate gabbros (e.g., Pearce, 1996). Commonly, accumulation of plagioclase is indicated by a positive Eu anomaly. Most samples from the metagabbro unit have a negative Eu-anomaly (figure 5.3a) suggesting fractionation of plagioclase. However, the development of an Eu anomaly depends also on the oxygen fugacity of the magma which determines whether Eu occurs predominantly as Eu²⁺ (compatible in plag) or Eu³⁺ (incompatible in plag similar to other REE).

The scatter in the data in the MgO variation diagrams, especially in plots of SiO₂, FeO* and K₂O vs. MgO, could be explained with removal or addition of mobile elements during, for example, hydrothermal (epidote veining) or amphibolite facies metamorphism (veined material was avoided for

analysis). However, the consistent patterns in the N-MORB normalized diagram (figure 5.3) and the strong correlation of Na₂O with MgO (figure 5.6g) indicate that alteration probably did not result in significant redistribution of these elements. This implies that much of the variation in figure 5.6 is primary.

Sample O/C-374b, which has the lowest MgO content, has also the lowest REE and trace element abundances (figure 5.3). If the low MgO content were a result of fractionation, sample O/C-374b would have the highest rather than the lowest concentrations of incompatible elements. Thus, sample O/C-374b is probably not related to the other samples by crystal fractionation. O/C-374b was probably derived from the same source as the other samples because of the relatively parallel REE and N-MORB normalized patterns, but may have formed from a melt produced by higher degrees of melting.

Various magmatic differentiation models were tested using least-square regressions on mass-balance equations in order to determine the best-fit model of fractionating phases and their proportions to the observed fractionation trends in figure 5.6. The calculations were performed using a spreadsheet program, with calculations made using the equations given in Stomer and Nicholls (1978). Various models of fractionation involving hornblende (average composition), pyroxene (Wo-En-Fs), plagioclase (An-Ab), olivine (Fo-Fa), apatite and Fe-Ti oxides (il + mt) were applied in order to find the best fit model to observed trends. The composition of hornblende must be known for the mass balance calculation because of the complex compositions of amphiboles in igneous rocks. The composition of hornblende used for the testing of fractionation models were determined by electron microprobe (see chapter 3, table 3.1), and an average hornblende composition has been entered in the spreadsheet table containing the composition of the phases that were added or subtracted from the “initial magma” (MRH-23) to arrive at the “derivative magmas” (MRH-78.1 and MRH-78.2). The lowest residuals, or the best fit solution, are obtained when 36% hornblende and 16% calcic plagioclase are subtracted from MRH-23 (sample with highest MgO content). This subtraction produces the trend from 7.7% (MRH-23) to about 6.5% MgO (figure 5.6). The “derivative magma” is similar in composition to MRH-78.1. The proportions of the end member compositions of plagioclase are also constrained by the least-square mass balance calculation. The composition of plagioclase given by the best-fit solution (An₈₅) is remarkably similar to the An-contents determined in cores of relict igneous plagioclase (An₈₆₋₈₂; microprobe analyses and optical determination).

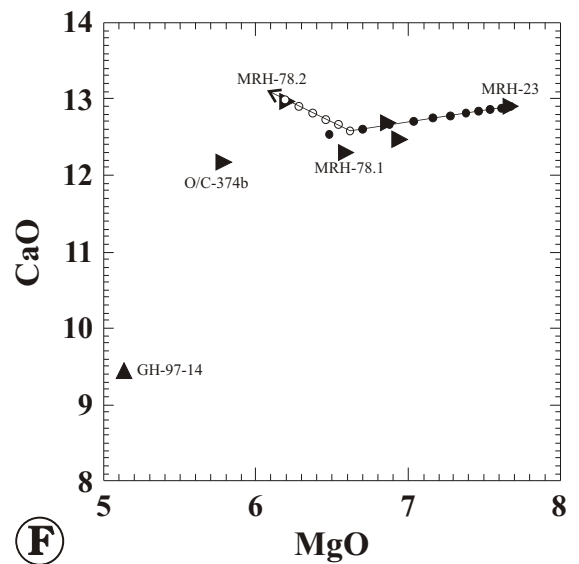
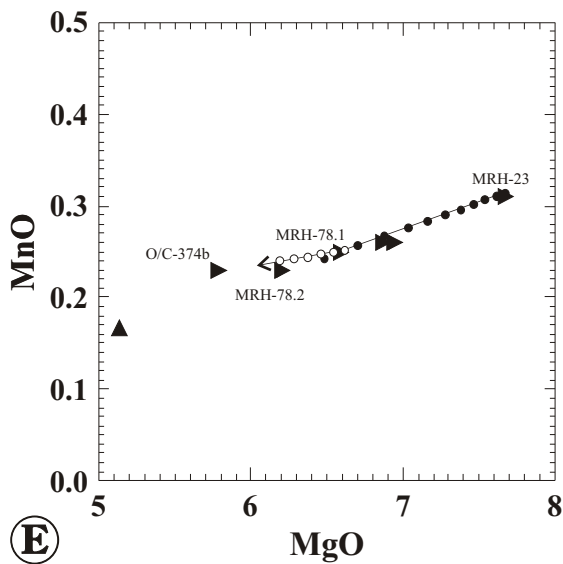
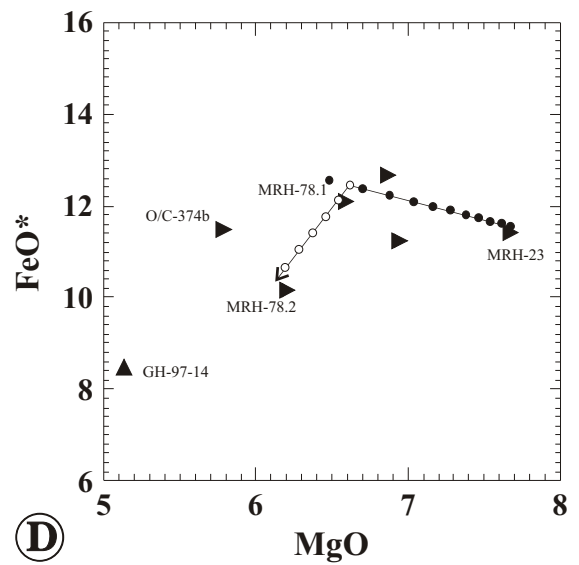
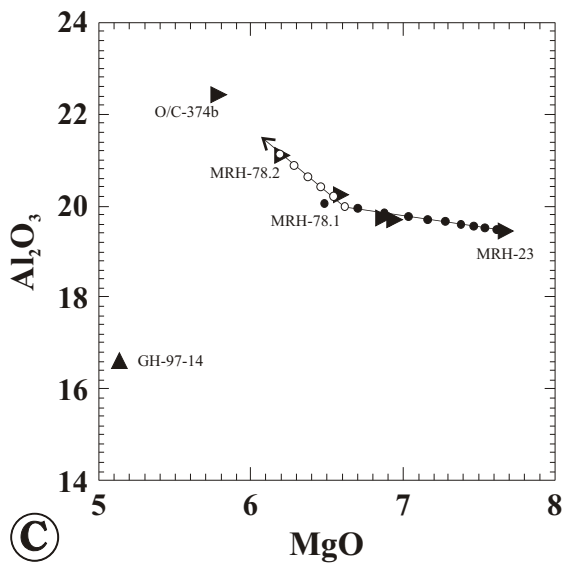
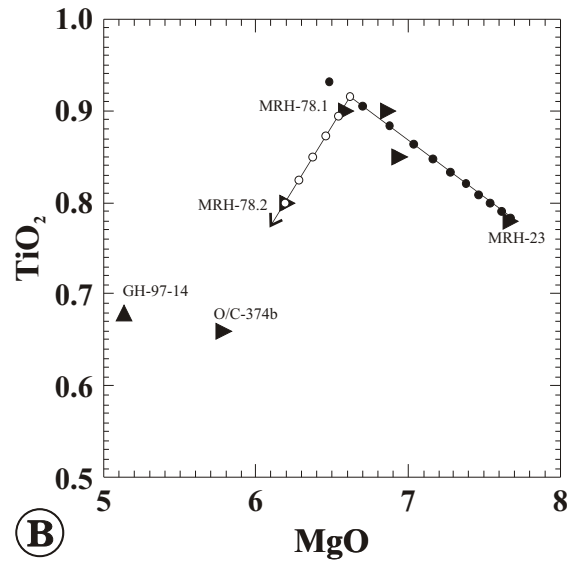
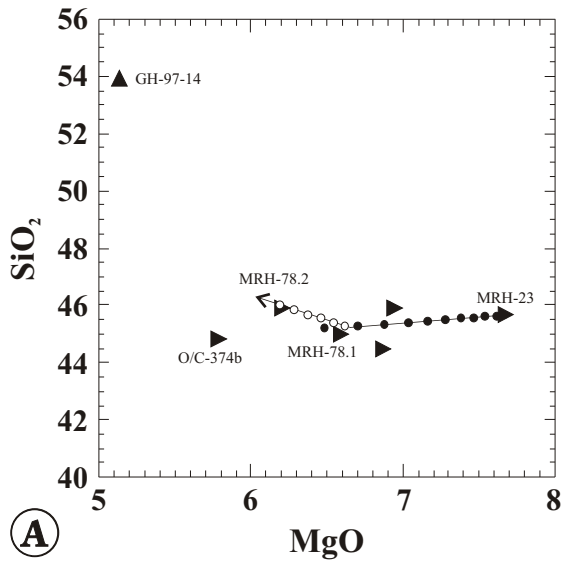
Continued crystal fractionation from about 6.7% to 6.2 % MgO is best explained with fractionation (subtraction) of 7.3% hornblende, 1.9% magnetite and 0.9% plagioclase (An_{50}). The subtraction of hornblende, magnetite and plagioclase yields a composition similar to MRH-78.2. The presence of magnetite containing small amounts of TiO_2 is corroborated by microprobe analysis (assuming it is igneous). Thus, the observed trends in the MgO variation diagrams (figure 5.6) can be reproduced using a two stage model of fractionation: (1) hornblende + plagioclase fractionation is followed by (2) hornblende + magnetite + plagioclase fractionation.

The trends of V plotted against MgO (figure 5.6j) is subparallel to that of TiO_2 and FeO^* (figure 5.6b and 5.6d). It appears that V behaves incompatibly during fractionation of hornblende + plagioclase and highly compatibly during fractionation of hornblende + magnetite + plagioclase. Estimates of the hornblende/melt (k_V^{hbl}) and magnetite/melt (k_V^{mt}) partition coefficients have been made using the results of the mass balance calculations and the equation for fractional crystallization. The partition coefficients are estimated assuming that $k_V^{plag} = 0$. The estimated partition coefficients $k_V^{hbl} = 1.25$ and $k_V^{mt} = 16$ are lower than published mineral/melt partition coefficients in melts of basaltic to basaltic andesite composition ($k_V^{hbl} = 3.4$ and $k_V^{mt} = 26$, compilation in Rollinson, 1993; p.108). Initially, Ti and V increase with decreasing MgO and the Ti/V-ratio remains almost constant with increasing fractionation as shown in a plot of V vs. Ti in figure 5.6k (part of discrimination diagram of Shervais, 1982). The increase of Ti and V with decreasing MgO corresponds to the subtraction of plagioclase + hornblende from MRH-23. This suggests that the hornblende/melt bulk partition coefficients for Ti and V were similar ($D_{Ti}^{hbl} \cong D_V^{hbl}$). Below 6.5% MgO, V and Ti decrease with decreasing MgO which corresponds to the subtraction of hornblende + magnetite + plagioclase. V decreases faster than Ti, and, as a result, the Ti/V ratio increases rapidly with fractionation (figure 5.6k). V appears to be more compatible in magnetite than Ti, which is in agreement with published partition coefficients (compilation of partition coefficients in Rollinson, 1993). The behavior of V, whether it is incompatible, compatible or highly compatible depends largely on its ionic radius (Shervais, 1982) which in turn depends on the oxidation state. V can occur naturally as V^{3+} , V^{4+} and V^{5+} whereas Ti occurs naturally only as Ti^{4+} . The oxidation state depends on fO_2 (oxygen fugacity) of the magma.

Figure 5.6

A - J: MgO variation diagrams of samples from the metagabbro unit (sideways triangle) and the hornblende quartz diorite intrusion in the metagabbro unit (upright triangle, GH-97-14) which may or may not be related. MgO decreases with increasing fractionation. The trends are produced by subtraction of plagioclase (An_{85}) + hornblende (closed dots) followed by subtraction of plagioclase (An_{50}) + hornblende + magnetite (open dots) from the most primitive sample (MRH-23). SiO_2 decreases with increasing fractionation until the onset of fractionation of hornblende + magnetite + plagioclase.

K: The V vs. Ti diagram shows the fields for island arc tholeiite (IAT) and normal ocean floor basalt (OFB) after Shervais (1982). The samples from the metagabbro unit plot within the IAT field. The Ti/V ratio remains constant as Ti and V increase with fractionation of hornblende + plagioclase (closed dots). Then, the Ti/V ratio increases as Ti and V decrease with fractionation of hornblende + titanomagnetite + plagioclase (open dots).



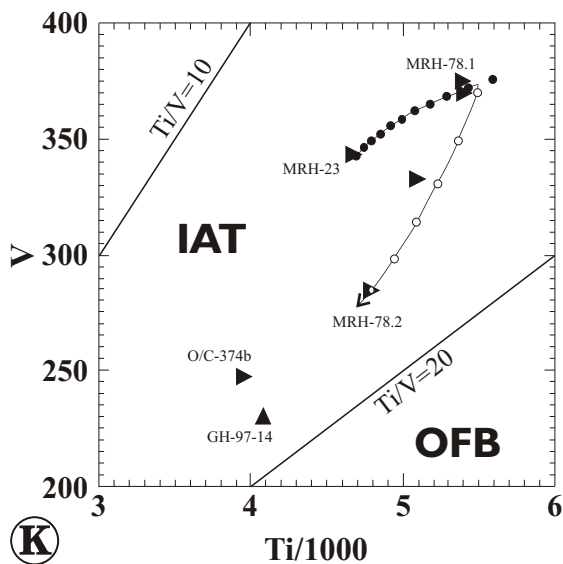
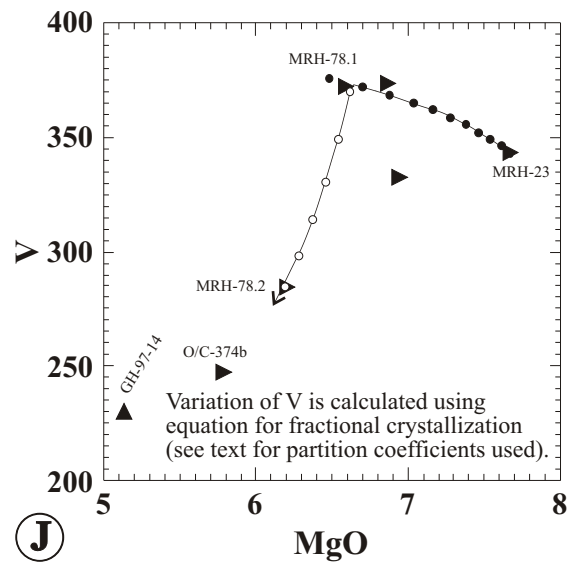
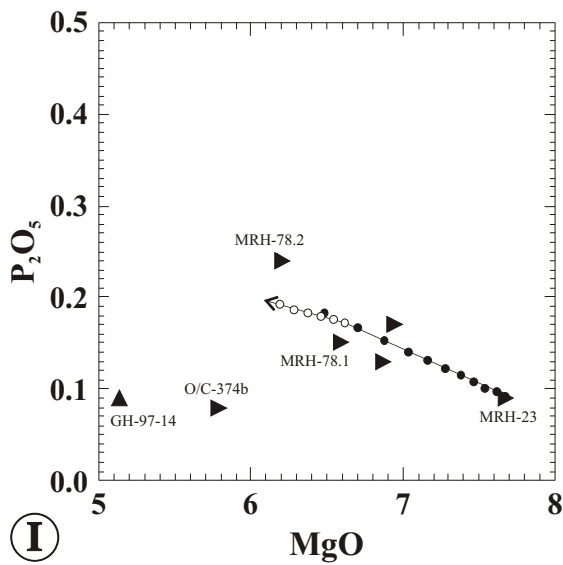
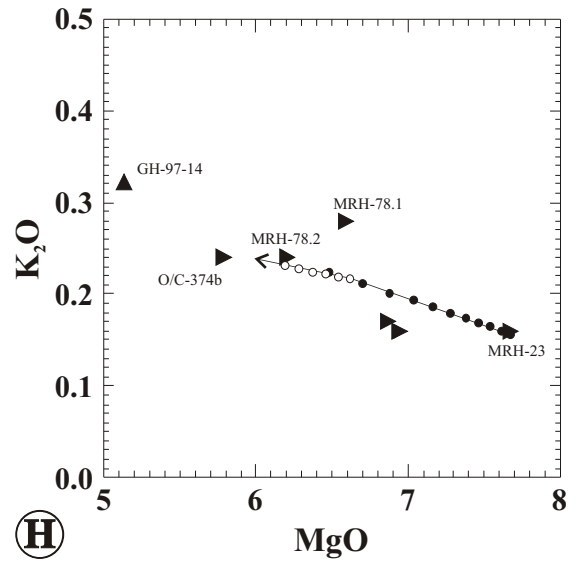
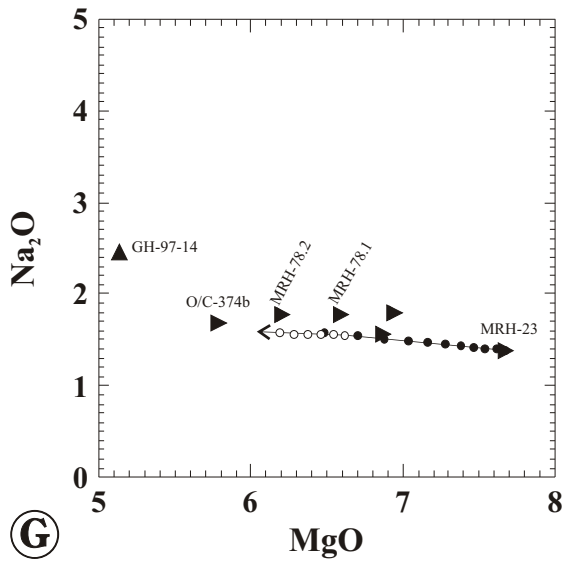


Figure 5.6 cont.

Subtraction of
 $0.692 \cdot \text{hornblende} + 0.308 \cdot \text{plagioclase (An}_{85})$
 (5% increments)

Subtraction of
 $0.723 \cdot \text{hornblende} + 0.089 \cdot \text{plagioclase (An}_{50})$
 $+ 0.189 \cdot \text{magnetite}$
 (2% increments)

Fractionation of hornblende + plagioclase (An_{85}) followed by hornblende + magnetite + plagioclase (An_{50}) can explain the major and trace element (V) variations of five samples. Other fractionation models involving different combinations of minerals (e.g., cpx + plag, cpx + plag + mt) do not fit observed trends in the MgO variation diagrams. Thus, the results of the modeling as well as relict igneous textures suggest that hornblende could be igneous in origin. However, the temperatures of equilibration of hornblende-plagioclase pairs and evidence of high-T ductile deformation are consistent with subsolidus equilibration of the dark-green, uniformly colored hornblende. Hornblende and plagioclase apparently (partially?) re-equilibrated during amphibolite facies metamorphism (chapter 3), but the samples retained largely the compositional variations that reflect igneous processes.

5.5.1.3b Partial melting

The fractionation vector for 50% fractionation of plagioclase + hornblende and 10% fractionation of hornblende + magnetite + plagioclase is shown in the Y-Cr diagram (figure 5.4). The low Cr-levels (<100 ppm) indicate that the samples are evolved. Even the most primitive sample (MRH-23) appears to be fairly fractionated based on the low Cr-level. O/C-374b is the most evolved sample based on the MgO (figure 5.6) and Cr (figure 5.4) concentrations. The fractionation vectors in figure 5.4 may be used to infer the petrogenetic pathway. The REE distribution patterns and N-MORB normalized patterns of O/C-374b are parallel to those of the other samples (figures 5.3a and 5.3b), but are at significantly lower levels (5-8 \times chondritic instead of 10-12 \times chondritic). The parental magma of O/C-374b perhaps was generated by significantly higher degrees of melting than the other samples. This would explain the low levels of incompatible elements such as REE and Y in O/C-374b (figures 5.3 and 5.4). Alternatively, O/C-374b could have formed by partial melting of a refractory mantle source depleted in incompatible elements and the other samples by partial melting of a more fertile mantle source. The hypothesis that the parental magma of O/C-374b was derived by high degrees of melting of the same mantle source as the other samples is preferred because of the parallel chondrite and N-MORB normalized patterns (figure 5.3).

5.5.2 Hornblende quartz diorite in the metagabbro unit

5.5.2.1 Rock classification

GH-97-14 is a sample from a 50 m-wide section of a quartz-bearing, medium grained plutonic rock in the metagabbro unit 100m east of the Blossom Bar shear zone. The contact relationships between this quartz-bearing rock and the metagabbro are not clear because of the complex deformation in the metagabbro unit. It is probably an intrusion in the metagabbro unit. The sample location is shown in figure 5.1, the analytical data are listed in table 5.1b, and the petrographic data are listed in appendix A (table A1). GH-97-14 is hypidiomorphic granular and consists of ~45% euhedral to subhedral plagioclase, ~10% interstitial quartz, ~40% subhedral hornblende, 5% oxide and trace amounts of biotite and apatite. Plagioclase is altered and cloudy in thin section, quartz is weakly recrystallized and shows undulatory extinction, and hornblende is variably colored (pale/light green to dark green). Igneous clinopyroxene is not found in any samples from this intrusion (appendix A, table A1). The secondary mineral assemblage partially replacing igneous minerals include actinolite, epidote, albite, chlorite, prehnite and pumpellyite. This is similar to the alteration observed in many of the metagabbros. Relict plagioclase ranges in composition from bytownite (An_{80}) and labradorite (An_{68-58}) in the cores to oligoclase (An_{21}) in the rims. Hornblende is constrained to be igneous in origin, because it re-equilibrated at near-solidus conditions based on the composition of coexisting plagioclase-hornblende pairs using Holland and Blundy's (1994) geothermometer (see chapter 3). Thus, samples from the 50 m wide section in the metagabbro unit ~100 m east of the Blossom Bar shear zone can be classified as hornblende quartz diorite based on the modes (Streckeisen, 1976, LeMaitre et al., 1989). GH-97-14 has significantly higher SiO_2 , lower Al_2O_3 and lower CaO than the samples from the metagabbro unit (figure 5.6). GH-97-14 plots in the field for subalkalic diorite using the TAS diagram of Wilson (1989) (not shown). Very low Nb/Y ratios (0.024) and low Zr/TiO₂ ratios (70.8) determined for sample GH-97-14 are consistent with a mafic to intermediate, subalkalic composition.

Table 5.1b: Major and trace element composition of hornblende quartz diorite in the metagabbro unit

| Sample | GH-97-14 | Sample | GH-97-14 |
|--------------------------------|----------|--------|----------|
| Rock type | diorite | | WSU |
| SiO ₂ | 53.95 | Cr | n.d. |
| TiO ₂ | 0.68 | Rb | 1.8 |
| Al ₂ O ₃ | 16.63 | Sr | 260 |
| Fe ₂ O ₃ | 9.42 | Y | 25 |
| MnO | 0.17 | Zr | 48 |
| MgO | 5.13 | Nb | 0.58 |
| CaO | 9.43 | Cs | 0.13 |
| Na ₂ O | 2.46 | Ba | 76 |
| K ₂ O | 0.32 | La | 3.71 |
| P ₂ O ₅ | 0.09 | Ce | 10.0 |
| BaO | 92 | Pr | 1.67 |
| Cr ₂ O ₃ | 87 | Nd | 8.78 |
| LOI | 1.74 | Sm | 3.06 |
| Total | 100.08 | Eu | 0.91 |
| | | Gd | 3.72 |
| Ni | 24 | Tb | 0.65 |
| Sc xrf/icp | 39/39.5 | Dy | 4.11 |
| V | 230 | Ho | 0.91 |
| | | Er | 2.56 |
| | | Tm | 0.39 |
| | | Yb | 2.50 |
| | | Lu | 0.39 |
| | | Hf | 1.62 |
| | | Ta | 0.03 |
| | | Pb | 0.89 |
| | | Th | 0.19 |
| | | U | 0.07 |

Major elements (in wt%) and Ba, Cr, Ni, Sc, and V (in ppm) were analyzed by standard XRF technique on pressed powder pellets at McGill University, Montreal. Additionally, Sc was analyzed by ICP-MS at Washington State University WSU... Trace element analysis by ICP-MS at Washington State University All trace elements are given in ppm.

n.d. ... not determined

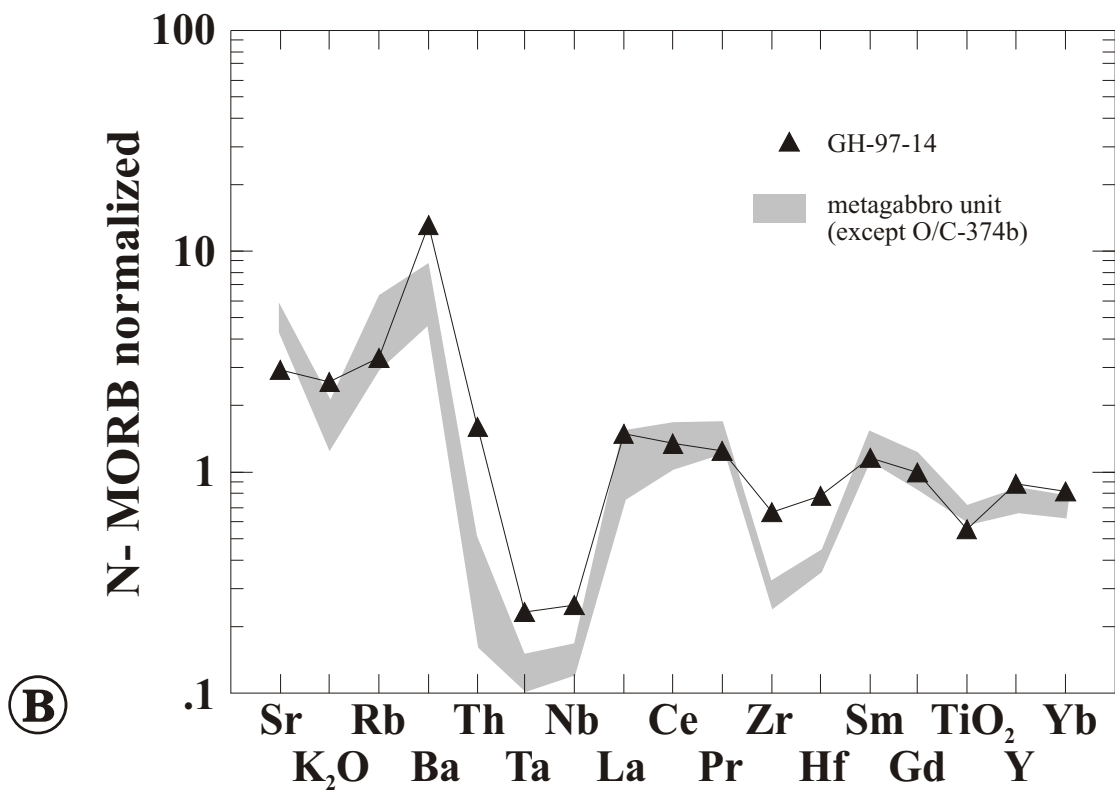
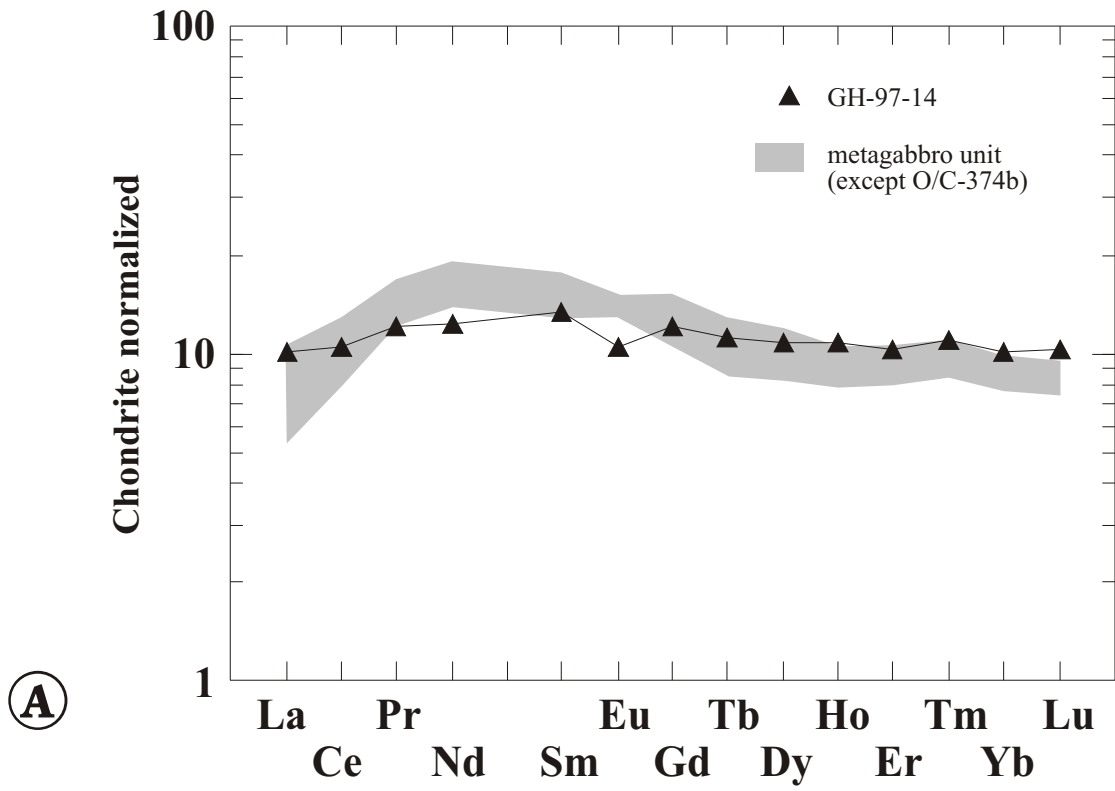
<d.l. ... below detection

Figure 5.7

- A. Chondrite normalized REE distribution pattern of the hornblende quartz diorite in the metagabbro unit.

The pattern of GH-97-4 differs from that of the samples from the metatonalite unit indicating it cannot be related by fractionation to the metatonalite unit. However, the shape of the REE distribution pattern is similar to that of the metagabbro unit in that it has a slightly convex-up shape centered on Nd.

- B. N-MORB normalized major and trace element distribution patterns of GH-97-14. The patterns show characteristics of arc-related rocks. Compared to N-MORB, the elements Ta, Nb, Hf, and Zr are strongly depleted, LILE are enriched, and REE are similar to N-MORB. It is enriched with respect to Ta and Nb, and similar compared to N-MORB.



5.5.2.2 Magmatic affinities

The chondrite normalized REE distribution pattern of GH-97-14 is shown in figure 5.7a. GH-97-14 has a slightly convex-up REE distribution pattern, a negative Eu-anomaly, and a $(La/Yb)_n$ ratio of 1.07. The REE pattern differs from the strongly convex-up REE patterns of samples from the metagabbro unit suggesting that GH-97-14 is not related by fractionation to the metagabbro unit.

The N-MORB normalized trace element distribution pattern in figure 5.7b shows that GH-97-14 is depleted in HFSE and selectively enriched in LILE and Th, while REE concentrations are similar to N-MORB. These are characteristics typical of IAT (figure 5.2a and 5.2b) The hornblende quartz diorite in the metagabbro unit is more enriched in Th and less depleted in Ta, Nb, Zr and Hf than the samples from the metagabbro unit. The differences in the N-MORB normalized patterns indicate that GH-97-14 and the metagabbro unit are most likely not related by fraction implying different sources or contamination of the GH-97-14 magma.

GH-97-14 has a lower Cr-content than N-MORB and plots on the boundary of the field for island arc basalt in the Cr vs. Y tectonic discrimination diagram of Pearce (1982) (figure 5.4). Furthermore, GH-97-14 is classified as island-arc tholeiite using the Th-Hf/3-Ta discrimination diagram in figure 5.5 and the Ti vs. V plot in figure 5.6.

5.5.3 Metatonalite unit

5.5.3.1 Rock classification

Eight samples from the metatonalite unit were analyzed. Six samples are from the main phase and range in composition (mode) from tonalite to trondhjemite. Based on estimated modes (Streckeisen, 1976; LeMaitre et al., 1989), GH-97-2b, GH-97-3 and O/C-368g are classified as trondhjemite and O/C-367, O/C-368b and O/C-11-S16a as tonalite (appendix A, table A2). Additionally, a deformed, fine-grained dike (O/C-11-S16b) and an undeformed, fine-grained enclave (O/C-368f) have been analyzed. The dike and the enclave are intermediate in composition (quartz diorite). The sample localities are shown in figure 5.1, the analytical data are listed in table 5.2, and petrographic data are listed in appendix A (table A2).

The tonalite-trondhjemite samples contain 45-60% plagioclase, 20-45% quartz, 5-25% mafic minerals (hornblende or clinopyroxene), accessory oxide, titanite and apatite. Titanite appears to be metamorphic in origin because it commonly replaces Fe-Ti oxides. The samples are foliated (tectonic foliation, see chapter 4) to undeformed with igneous textures preserved (granophyric, hypidiomorphic granular). Plagioclase is replaced by albite and clinozoisite and is cloudy in thin section. Hornblende is greenish brown (pleochroic) and interpreted to be igneous in origin. Dark-green to light-green amphibole occurs also as fibrous (uralitic) replacement of pyroxene.

The dioritic dikes and enclaves contain ~55% plagioclase, 10-15% quartz and 30-35% hornblende, 2-3% opaque minerals and accessory apatite. Plagioclase is replaced by clinozoisite/epidote and albite and appears cloudy in thin section. Hornblende is variable in color ranging from light green to dark green-brown (strongly pleochroic). Occasionally, dark-brown hornblende occurs as well. Relict cpx has not been found in the dioritic samples. The texture in the undeformed enclave is hypidiomorphic granular. Assuming amphibole is magmatic in origin such as the dark-brown hornblende, the dike and the enclave can be classified as hornblende quartz diorite based on the modes (Streckeisen, 1976, LeMaitre et al., 1989).

5.5.3.2 Magmatic affinities

The chondrite normalized REE distribution pattern of samples from the metatonalite unit range from flat (figure 5.8a) to moderately fractionated (figure 5.8c and 5.8d). The level of the HREE is relatively constant in all samples (8-12*chondritic) whereas the concentration of the LREE is variable (10-50*chondritic). $(La/Yb)_n$ ratios range from 1.33 to 5.04. Sample O/C-11-S16b, a deformed dike in metatonalite, is the least evolved rock (lowest SiO₂- and highest MgO- and Cr- contents, table 5.2), but is significantly more enriched in LREE than any of the other samples and has a $(La/Yb)_n$ ratio of 5.04 (figure 5.8d). Sample O/C-368f (figure 5.8d), an enclave of intermediate composition, has a $(La/Yb)_n$ ratio similar to GH-97-3, O/C-367 and O/C-368g (figure 5.8b), but O/C-368f has much higher Cr and MgO and less SiO₂ than GH-97-3, O/C-367 and O/C-368g. As shown in figure 5.8a through 5.8d, SiO₂ is inversely correlated with $(La/Yb)_n$. The deformed dike (O/C-11-S16b) and the enclave (O/C-368f) have a strong

Table 5.2: Major and trace element composition of samples from the metatonalite unit

| Sample | GH-97-2b | GH-97-3 | O/C-11 S16a | O/C-367 | O/C-368B | O/C-368G | O/C-11 S-16b | O/C-368f |
|--------------------------------|----------|----------|----------------|----------|----------|----------|-----------------|----------|
| | trondhj. | trondhj. | tonalite | tonalite | tonalite | trondhj. | def. dike | enclave |
| SiO ₂ | 73.64 | 71.58 | 65.78 | 67.39 | 65.54 | 70.80 | 55.79 | 59.78 |
| TiO ₂ | 0.38 | 0.64 | 0.76 | 0.65 | 0.57 | 0.59 | 0.76 | 0.59 |
| Al ₂ O ₃ | 12.93 | 13.99 | 13.10 | 13.66 | 14.33 | 13.82 | 15.50 | 14.42 |
| Fe ₂ O ₃ | 2.15 | 1.49 | 4.95 | 5.70 | 6.04 | 2.10 | 8.34 | 9.97 |
| MnO | 0.02 | 0.03 | 0.08 | 0.08 | 0.03 | 0.03 | 0.17 | 0.04 |
| MgO | 0.77 | 1.07 | 1.83 | 1.01 | 1.86 | 1.17 | 4.88 | 3.20 |
| CaO | 4.79 | 4.29 | 7.59 | 4.97 | 5.60 | 5.26 | 7.97 | 6.64 |
| Na ₂ O | 3.87 | 5.79 | 3.00 | 4.22 | 4.28 | 4.90 | 3.74 | 4.05 |
| K ₂ O | 0.18 | 0.16 | 0.24 | 0.18 | 0.31 | 0.17 | 0.08 | 0.20 |
| P ₂ O ₅ | 0.10 | 0.27 | 0.29 | 0.19 | 0.15 | 0.17 | 0.25 | 0.09 |
| BaO | 59 | 117 | 84 | 89 | 67 | 67 | 118 | 160 |
| Cr ₂ O ₃ | 25 | 35 | 33 | 26 | 122 | 33 | 18 | 60 |
| LOI | 1.26 | 0.85 | 1.92 | 1.57 | 1.40 | 0.95 | 2.86 | 1.57 |
| Total | 100.10 | 100.18 | 99.57 | 99.64 | 100.15 | 99.99 | 100.37 | 100.59 |
| Ni | <d/l | <d/l | 9 | <d/l | 193 | 12 | 15 | <d/l |
| Sc xrf/icp | 16/13 | 15/17 | 17/22 | 23/18 | 16/19 | 17/14 | 11/n.d. | 31/33 |
| V xrf/icp | 33/n.d. | 44/n.d. | 107/n.d. | 33/n.d. | 113/n.d. | 52/n.d. | 181/178 | 191/210 |

Major elements (in wt%) and Ba, Cr, Ni, Sc, and V (in ppm) were analyzed by standard XRF technique on pressed powder pellets at McGill University, Montreal. Additionally, Sc was analyzed by ICP-MS at Washington State University and V at Union College

Table 5.2 cont.

| Sample | GH-97-2b | GH-97-3 | O/C-11 | O/C-367 | O/C-368B | O/C-368G | O/C-11 | O/C-368f | |
|--------|----------|---------|-------------|---------|----------|----------|-------------|----------|------|
| | WSU | WSU | S16a WSU | WSU | WSU | WSU | S-16b UC | UC | WSU |
| Cr | n.d. | n.d. | n.d. | n.d. | n.d. | n.d. | 9 | 32 | n.d. |
| Rb | 2.1 | 1.7 | 2.0 | 1.4 | 2.7 | 1.1 | 0.4 | 1.1 | 1.3 |
| Sr | 266 | 222 | 316 | 303 | 322 | 259 | 380 | 286 | 276 |
| Y | 27 | 22 | 26 | 30 | 18 | 22 | 24 | 26 | 27 |
| Zr | 109 | 70 | 85 | 97 | 74 | 78 | 62 | 39 | n.d. |
| Nb | 2.38 | 2.22 | 2.04 | 2.01 | 1.33 | 1.60 | 2.34 | 1.69 | 1.42 |
| Cs | 0.17 | 0.08 | 0.06 | 0.05 | 0.17 | 0.06 | 0.04 | 0.05 | 0.05 |
| Ba | n.d. | n.d. | n.d. | n.d. | n.d. | n.d. | 46 | 86 | 85 |
| La | 4.89 | 6.87 | 13.25 | 11.83 | 9.05 | 7.16 | 17.1 | 8.99 | 9.18 |
| Ce | 9.57 | 17.1 | 27.4 | 23.8 | 17.8 | 16.3 | 37.2 | 24.0 | 22.9 |
| Pr | 1.35 | 2.40 | 3.55 | 3.15 | 2.16 | 2.21 | 4.76 | 3.43 | 3.18 |
| Nd | 6.99 | 11.4 | 16.3 | 14.6 | 9.59 | 10.7 | 19.9 | 15.5 | 14.3 |
| Sm | 2.67 | 3.36 | 4.41 | 4.31 | 2.59 | 3.17 | 4.46 | 3.90 | 4.16 |
| Eu | 1.07 | 1.17 | 1.23 | 1.37 | 0.98 | 1.09 | 1.07 | 0.94 | 1.02 |
| Gd | 3.44 | 3.64 | 4.55 | 4.83 | 2.90 | 3.60 | 4.48 | 4.22 | 4.39 |
| Tb | 0.63 | 0.58 | 0.74 | 0.83 | 0.48 | 0.59 | 0.68 | 0.68 | 0.77 |
| Dy | 4.20 | 3.65 | 4.69 | 5.50 | 3.12 | 3.87 | 4.10 | 4.48 | 4.88 |
| Ho | 0.93 | 0.78 | 0.98 | 1.17 | 0.66 | 0.83 | 0.82 | 0.94 | 1.02 |
| Er | 2.58 | 2.21 | 2.60 | 3.30 | 1.86 | 2.30 | 2.35 | 2.78 | 2.91 |
| Tm | 0.40 | 0.32 | 0.38 | 0.49 | 0.27 | 0.35 | 0.35 | 0.43 | 0.44 |
| Yb | 2.49 | 2.06 | 2.38 | 3.10 | 1.79 | 2.15 | 2.29 | 2.75 | 2.84 |
| Lu | 0.40 | 0.32 | 0.39 | 0.49 | 0.30 | 0.34 | 0.35 | 0.42 | 0.46 |
| Hf | 3.22 | 2.13 | 2.57 | 3.05 | 2.40 | 2.60 | 1.88 | 1.37 | 1.90 |
| Ta | 0.16 | 0.12 | 0.13 | 0.13 | 0.1 | 0.1 | 0.13 | 0.082 | 0.09 |
| Pb | 0.68 | 0.68 | 0.78 | 0.69 | 0.48 | 0.42 | 0.64 | 0.40 | 0.67 |
| Th | 2.10 | 2.17 | 2.91 | 2.11 | 1.84 | 1.66 | 2.48 | 1.25 | 1.31 |
| U | 0.22 | 0.33 | 0.81 | 0.66 | 0.29 | 0.28 | 0.55 | 0.30 | 0.43 |

UC... Trace element analysis by ICP-MS at Union College

WSU... Trace element analysis by ICP-MS at Washington State University

All trace elements are given in ppm.

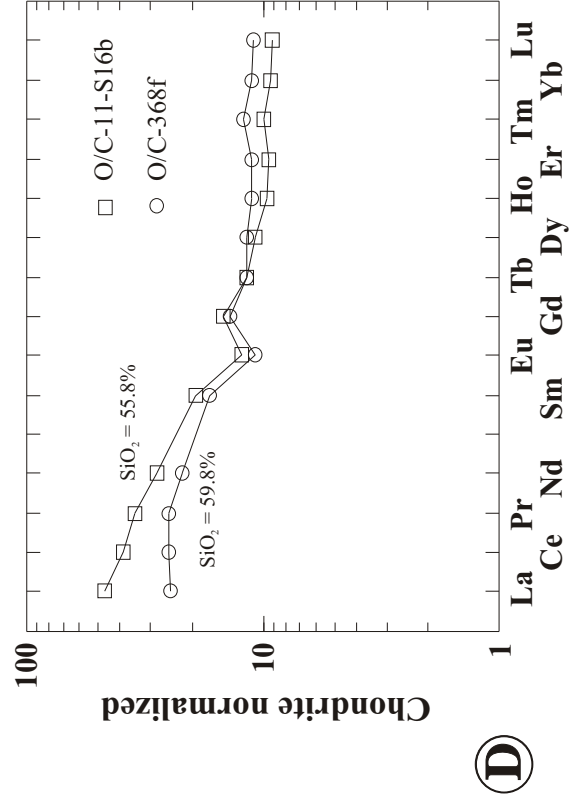
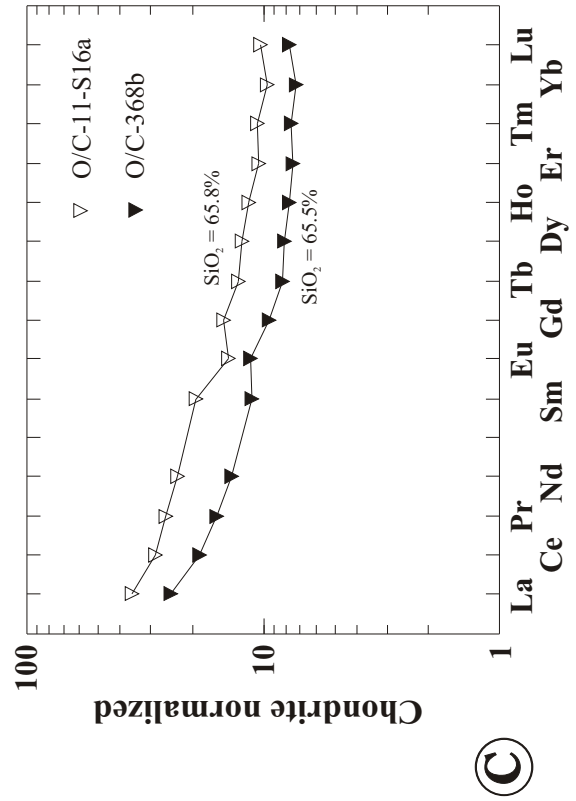
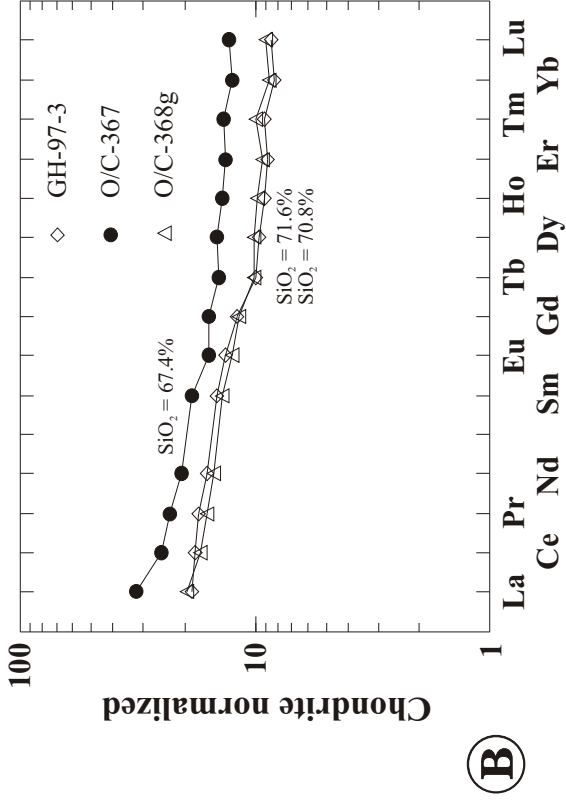
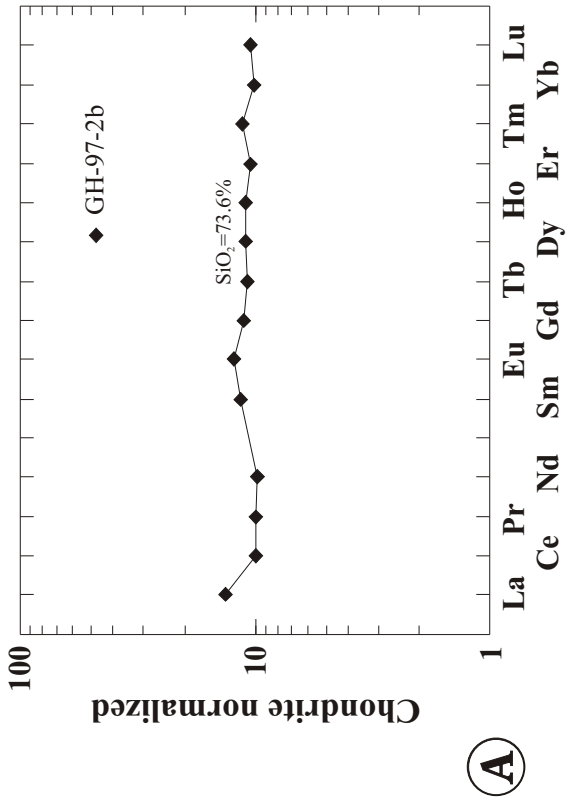
n.d. ... not determined

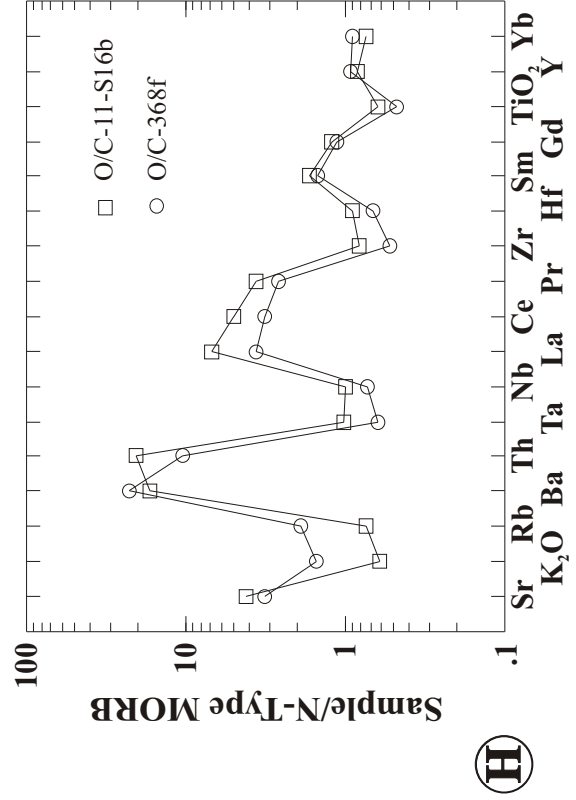
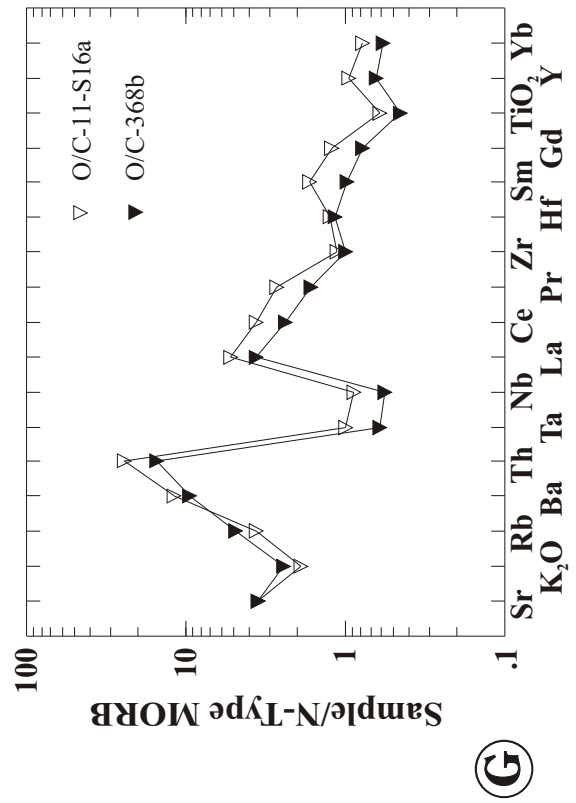
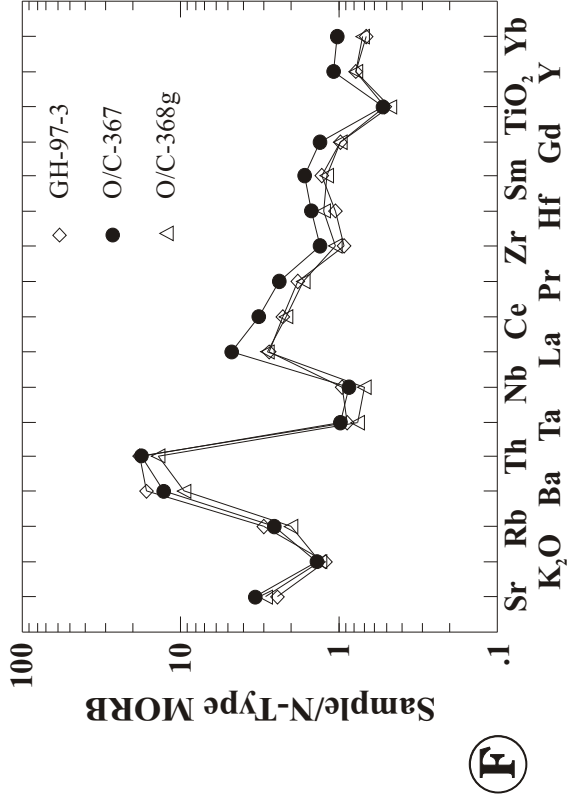
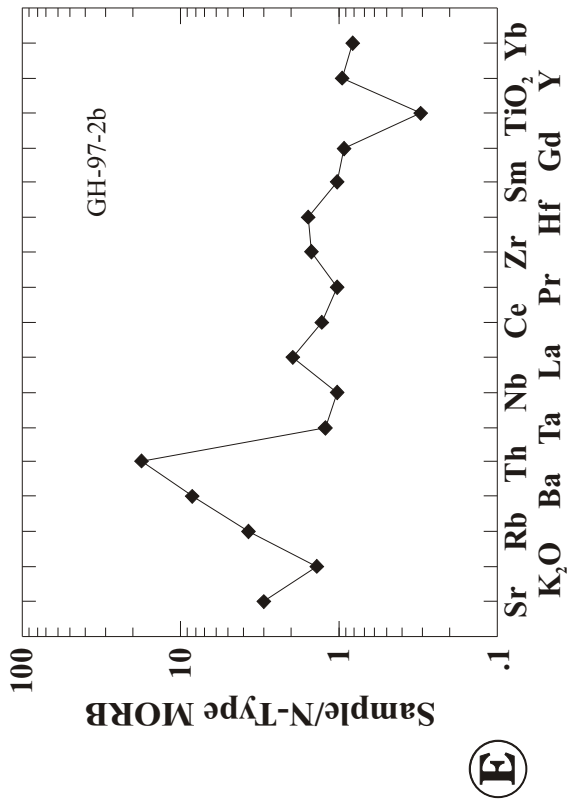
<d.l. ... below detection

Figure 5.8

A - D: Chondrite normalized REE distribution diagrams of samples from the metatonalite unit. The patterns vary from flat to moderately LREE enriched. Sample GH-97-2b (figure 5.8a) has a $(La/Yb)_n$ ratio of 1.33. The ratios of samples GH-97-3, O/C-367 and O/C-368f ranges from 2.21 to 2.58 (figure 5.8b), and of samples O/C-11-S16a and O/C-368b from 3.42 to 3.77 (figure 5.8c). The deformed dike (O/C-11-S16b) in the metatonalite has the highest $(La/Yb)_n$ ratio of 5.04 (figure 5.8d), while the $(La/Yb)_n$ ratio of the enclave (O/C-368f) is similar to that of GH-97-3, O/C-367 and O/C-368f (figure 5.8b). In general, SiO_2 contents increase with decreasing $(La/Yb)_n$.

E - H: N-MORB normalized trace element distribution diagram of samples from the metatonalite unit. Ta, Nb, Zr and Hf are depleted while LILE, Th, and LREE are selectively enriched. These patterns are typical of calc-alkaline rocks, except LREE in the most silicic samples (GH-97-2b, GH-97-3, O/C-368g) are not very enriched (figure 5.8e and 5.8f).





negative Eu-anomaly suggesting fractionation of plagioclase (figure 5.8d). In contrast, the trondhjemite-tonalite samples have either a positive Eu-anomaly, no Eu-anomaly, or a very small negative Eu-anomaly (figure 5.8a, b and c).

The N-MORB normalized trace element variation patterns in figures 5.8e through 5.8h show that Th and Ba are strongly enriched compared to N-MORB. In most samples, LREE are also enriched compared to N-MORB. The strong enrichment of Th (15-30*N-MORB), LILE, and LREE and negative Ta and Nb anomaly is a characteristic signature of calc-alkaline rocks commonly occurring at volcanic arcs (compare with figure 5.2c). The consistent patterns of the LILE indicate that these elements were not mobile, and the low K₂O- and Rb-contents could be a primary signature. K₂O- and Rb are not, or only slightly, enriched compared to N-MORB while Sr and Ba are significantly more enriched than N-MORB. A strong negative K₂O anomaly is often observed in magmas generated at island arcs built on oceanic crust (see figure 5.2b).

Potassium feldspar is not found in samples from the metatonalite unit. The lack of relict potassium feldspar, of potassium-rich secondary phases, or any evidence of replacement of potassium feldspar, suggests that only trace amounts, if any, of potassium feldspar crystallized. This is reflected in the low concentrations of K₂O in the samples (< 0.5% K₂O) (figure 5.9h). Low K₂O concentrations (< 1%) are typical for “oceanic plagiogranites” (Maniar and Piccoli, 1989; Coleman and Peterman, 1975) as well as island arc plutons.

Crystallization and fractionation of Fe-Ti oxides (and perhaps titanite) is reflected in the large negative Ti-anomaly (figure 5.8e through 5.8h). The chondrite and N-MORB normalized REE and trace element patterns are variable and suggest that the samples are not related by crystal fractionation implying different sources.

A diagram of Al₂O₃ vs. SiO₂ is shown in figure 5.9j including a regression line through the data. Barker (1979) and Arth (1979) proposed a simple classification of trondhjemites. They suggested that tonalite-trondhjemite suites can be classified in low- and high-Al₂O₃ types. The separation is made at 15% Al₂O₃ and 70% SiO₂ (Barker, 1979), and at 14.5% Al₂O₃ and 1.5 ppm Yb (Arth, 1979). The trondhjemite samples from the metatonalite unit are, according to this classification scheme, low-Al₂O₃, high-Yb type

trondhjemites (14% Al_2O_3 at 70% SiO_2 ; $\text{Al}_2\text{O}_3 < 14.5\%$ with $\text{Yb} > 1.5$ ppm). Arth (1979) recognized that low- Al_2O_3 type trondhjemites (high-Yb types) have, in general, flat or mildly fractionated REE patterns and originate in oceanic environments whereas the high- Al_2O_3 types (low-Yb types) have strongly fractionated REE patterns with very low HREE contents and generally are associated with continental collision zones and continental margin arcs.

The tectonic discrimination of granitoids using major elements such as that of Maniar and Piccoli (1989) and Barker (1979) is ambiguous because the samples are metamorphosed, and mobile elements, such as LILE, are easily added or removed. Therefore, a classification using ‘immobile’ trace elements is more accurate. Dudas (1992) evaluated petrogenetic trace element discrimination diagrams and found that a number of discrimination diagrams commonly used for basaltic rocks, such as the Th-Hf/3-Ta diagram of Wood et al. (1979), are also applicable for granitic rocks, because certain elemental abundance ratios are relatively insensitive to fractionation. In addition to Hf, Ta, and Th, the best ‘immobile’ discriminant elements for granitic rocks include Y, Nb, and Yb (Pearce et al., 1984b; Dudas, 1992; Foerster et al., 1997). As shown in figure 5.5a, the samples from the metatonalite unit plot well within the calc-alkaline field in the Th-Hf/3-Ta diagram of Wood et al. (1979).

5.5.3.3 Petrogenesis

5.5.3.3a Possible origin of the metatonalite unit

Figures 5.8a through 5.8d illustrate the change of the REE patterns with SiO_2 . The $(\text{La}/\text{Yb})_n$ ratios are plotted against SiO_2 and MgO in figures 5.10a and 5.10b, respectively, and an inverse correlation of $(\text{La}/\text{Yb})_n$ ratios with fractionation is observed. The enclave (O/C-368f) and the deformed dike (O/C-11-S16b) do not plot along the trend defined by the tonalite-trondhjemite samples (circles). Fractionation of pyroxene or hornblende could shift the composition of the dike and the enclave towards the trend defined by the tonalite-trondhjemite samples, because fractionation of pyroxene and hornblende typically decreases MgO and increases SiO_2 while the La/Yb ratios (and other trace element ratios) do not change significantly. It is possible that the tonalite-trondhjemite evolved from a compositionally diverse, mafic parent (i.e. O/C-368f and O/C-11-S16b). Other incompatible trace element abundance ratios are

plotted against SiO_2 in figure 5.10. Silica is selected as a measure of crystal fractionation. The incompatible trace element ratios Ce/Lu (figure 5.10c), Th/Ta (figure 5.10d), and La/Ta (figure 5.10e) decrease with increasing SiO_2 (bulk REE increases with decreasing SiO_2). What are possible reasons for this correlation?

The origin of felsic rocks in ophiolites and modern arc settings is controversial and several possible explanations are summarized below: In addition to the possibility that metasomatic alteration could have modified the primary composition (gain of Na_2O and SiO_2 , loss of K_2O), a mafic magma potentially can assimilate large amounts of crustal material resulting in formation of silicic rocks. Typically, crustal rocks are characterized by high La/Yb ratios and high SiO_2 . The more crustal material is assimilated by a mafic liquid, the higher the SiO_2 contents and La/Yb ratios. Samples from such a suite would indicate a positive correlation between La/Yb ratios and SiO_2 . The trends shown in figures 5.10a and 5.10b are opposite to the trend that would be produced by crustal assimilation. Thus, crustal assimilation is unlikely.

Also, tonalites-trondhjemites (plagiogranites) or the volcanic equivalent, low-K rhyolites, could have formed by fractional crystallization from a mafic parent, such as a low-K basaltic magma, under hydrous conditions (Dixon-Spilber and Rutherford, 1983; Coleman and Peterman, 1975, Coleman and Donato, 1979), or as a late stage immiscible liquid during fractional crystallization (Dixon and Rutherford, 1979) (very unlikely unless mafic magma is very high in Fe), or they could have formed by hydrous partial melting of greenstones, amphibolites, or eclogites (Barker, 1979; Helz, 1976; Cole, 1979, 1981; Beard and Lofgren, 1991; Rapp and Watson, 1995). In any case, the composition of the melt depends on the composition of the source material, the pressure and temperature of melting, residual phases, mixing, assimilation and fractionation.

Enrichment of LREE relative to HREE caused by partial melting of a mantle source is generally very small unless residual garnet is present in the source. Garnet involvement is highly unlikely, because the samples are high-Y, low- Al_2O_3 tonalites-trondhjemites (figure 5.9j). Typically, garnet is present in high-Al type trondhjemites which are strongly depleted in HREE and Y. For example, melts generated by partial melting of the subducted slab are dacitic in composition (Ringwood, 1974) and would show pronounced HREE depletion and LREE enrichment because of equilibration with garnet eclogite. Partial melting with garnet as residual phase in the source would result in much stronger LREE enrichment

relative to HREE and much lower HREE and Y abundances than observed in the metatonalite samples. Thus, partial melting with garnet as residual phase in the source is unlikely. Also, garnet is not found in any of the samples from the metatonalite unit suggesting that garnet fractionation is unlikely. Consequently, other hypotheses such as crystal fractionation involving certain accessory phases or magma mixing have to be considered.

5.5.3.3b Crystal fractionation models

LREE are highly compatible in allanite and monazite whereas HREE and Ta are significantly less compatible. Similarly, Th is strongly compatible in allanite whereas Ta is significantly less compatible than Th, La and Ce (compilation of distribution coefficients in Rollinson, 1993). Therefore, the LREE concentrations would decrease much faster than HREE resulting in a flattening of the REE pattern with increasing fractionation (e.g., figure 5.8). Also, Th, La and Ce would decrease much faster than Ta with fractionation of allanite. Thus, it is possible that the inverse correlation of the incompatible trace element ratios with SiO₂ in figure 5.10 could be related to fractionation of allanite. To test this hypothesis, the changes of the trace element concentrations with crystal fractionation are modeled.

First, the minerals that could have fractionated in addition to allanite must be determined using the major element composition of the samples. The MgO content of samples from the metatonalite unit ranges from 5.0% to 0.8% with SiO₂ content from 58%-75% (figure 5.9a). The SiO₂ content increases with decreasing MgO and ranges from 58-61% in the enclaves (squares) and from 68-75% in the tonalite-trondhjemite samples (circles). Although the data scatter, several trends can be identified: TiO₂, Al₂O₃, FeO*, MnO, CaO, and P₂O₅ decrease with decreasing MgO content. This is consistent with fractionation of Mg-rich mafic mineral(s), such as pyroxene or hornblende in addition to plagioclase, Fe-Ti oxides, and apatite. The calculation of various crystal fractionation models relies on the following assumption: the tonalite-trondhjemite samples were derived from similar parental magmas which evolved along similar liquid lines of descent. Using a least square regression on mass balance equations, a best fit result was found so that the trends defined by the tonalite-trondhjemite samples (circles) could be reproduced in most MgO variation diagrams (figure 5.9a, b, c, d, e, and i). Subtraction of 14.4% plagioclase (An₆₇), 10.5%

orthopyroxene, 1.0 % ilmenite, and 0.4% apatite from a composition similar to O/C-11-S16a results in a daughter composition similar to that of the most silicic sample (GH-97-2b). The subtraction is equivalent to 26.3% fractionation of an assemblage with the proportions $X^{plag} = 0.547$, $X^{opx} = 0.401$, $X^{il} = 0.037$, and $X^{ap} = 0.015$. However, the data scatter around the best-fit crystal fractionation trends suggesting differences in the primary composition, variations due to element mobility (e.g., scatter of Na₂O and CaO as a result of albitization of plagioclase), or both. Thus, this model should be interpreted with caution.

Fractionation of plag + opx + il + ap results in an increase of SiO₂ and REE while the incompatible trace element ratios remain almost unchanged (not shown). This was determined using the equation for Rayleigh fractionation, the partition coefficients compiled in Rollinson (1993), and the mineral proportions $X^{plag} = 0.547$, $X^{opx} = 0.401$, $X^{il} = 0.037$, and $X^{ap} = 0.015$. However, the most silicic sample (GH-97-2b, figure 5.8a) has lower LREE than O/C-11-S16a (figure 5.8c). The decrease of LREE with increasing fractionation can be modeled assuming that onset of allanite fractionation occurred at a composition similar to that of O/C-11-S16a. The amount of allanite fractionation was determined using a least-square regression. The following parameters are given for the least square regression: (1) initial REE and trace element composition (O/C-11-S16a, figure 5.11a); (2) final REE and trace element composition (GH-97-2b, figure 5.11a), (3) variation of the REE and trace element concentrations as a function of fractionation of plag + opx + il + ap (Rayleigh fractionation); and (4) trace element partition coefficients for allanite in dacitic to rhyolitic melts (Rollinson, 1993). The following parameters were determined by the least square regression: (1) the weight proportion of allanite in the fractionating mineral assemblage (plag + opx + il + ap + al), which is $X^{al} = 0.0017$; (2) the total amount of fractionation based on variations of the trace element composition (which is similar to the amount of fractionation constrained by the major element composition); a total of 26.9% crystal fractionation from the starting composition (O/C-11-S16a) produces a trace element composition similar to that of the most silicic sample (figure 5.11a).

Figure 5.11a shows the predicted N-MORB normalized pattern after 26.9% crystal fractionation of O/C-11-S16a in comparison with GH-97-2b. Figure 5.11b shows the predicted N-MORB normalized trace element pattern after 14.6% crystal fractionation of O/C-11-S16a in comparison with O/C-368g. The REE and trace element composition of O/C-368g and GH-97-2b can be reproduced very accurately

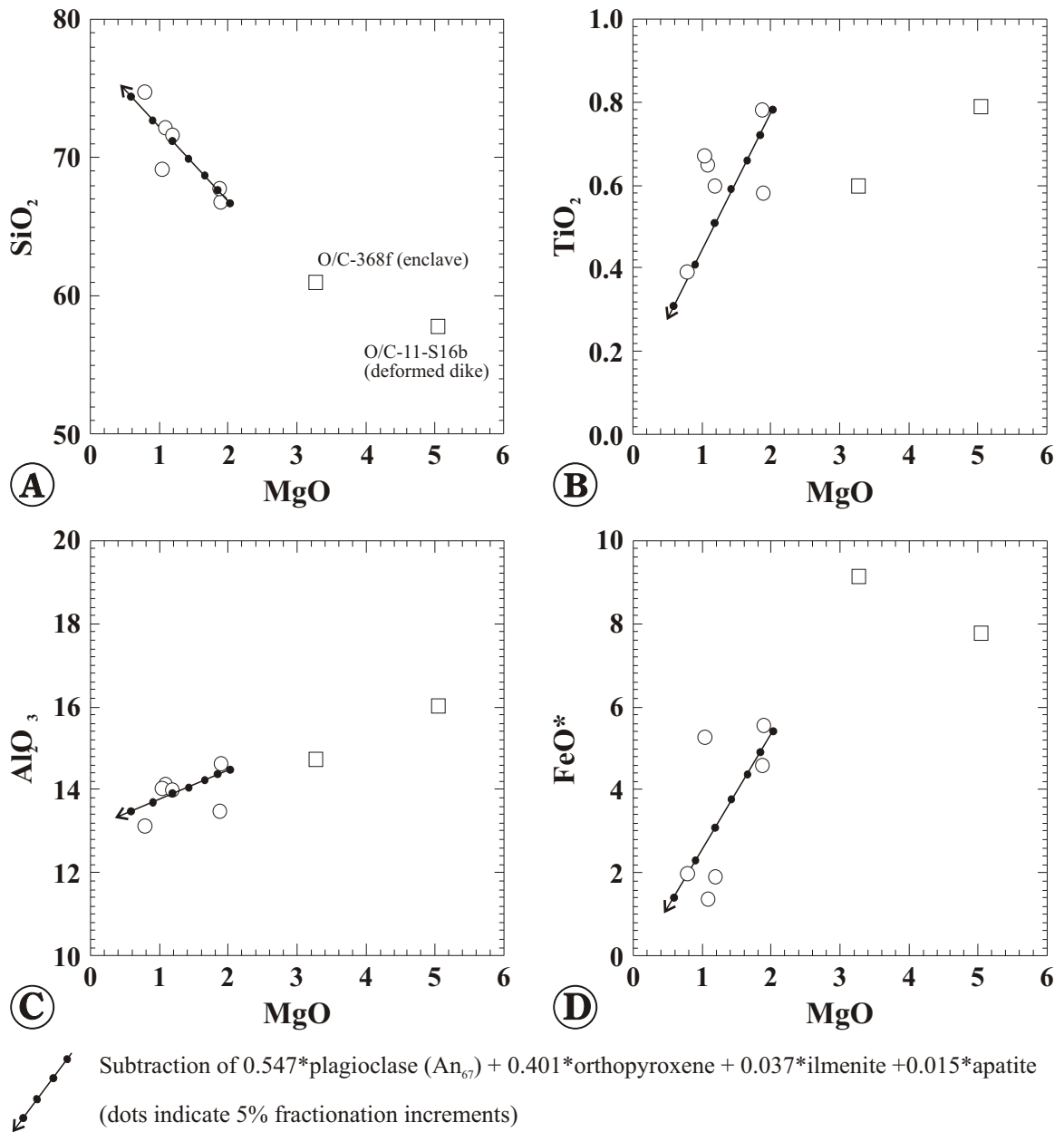


Figure 5.9

A-I: MgO variation diagrams of samples from the metatonalite unit. The trends are modeled by subtraction of plagioclase + orthopyroxene + ilmenite + apatite from a composition similar to O/C-11-S16a and O/C-368b. SiO_2 increases with increasing fractionation while MgO, TiO_2 , Al_2O_3 , FeO^* , MnO, CaO, and P_2O_5 decrease.

J: Al_2O_3 vs. SiO_2 bivariate plot showing the classification of trondhjemites after Barker (1979).

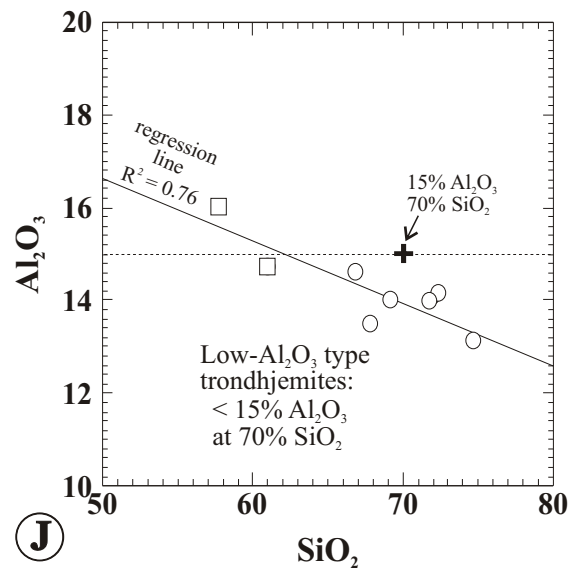
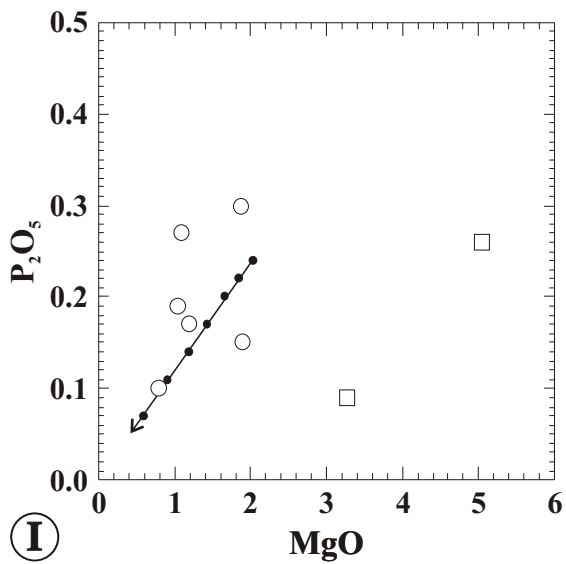
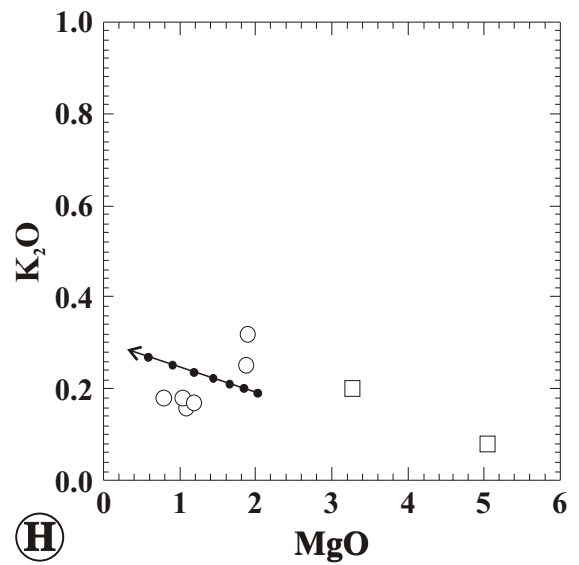
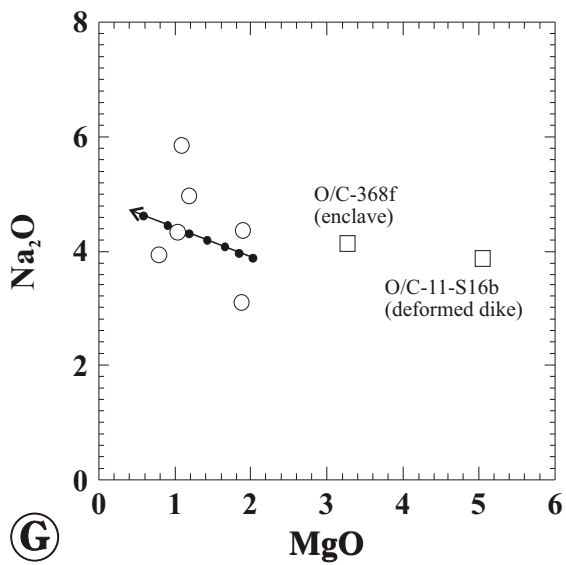
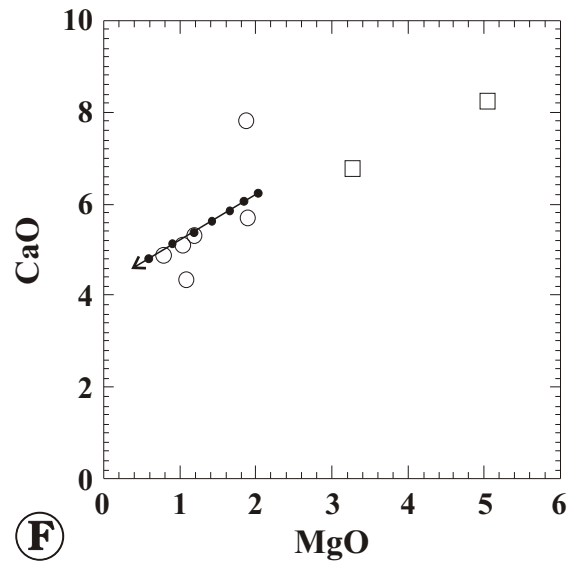
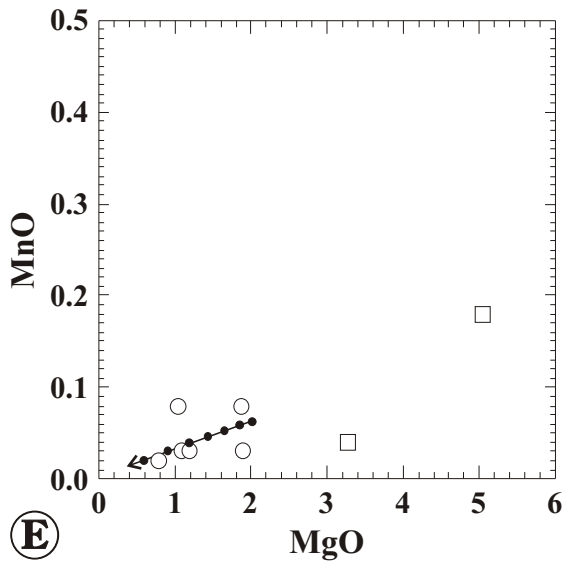
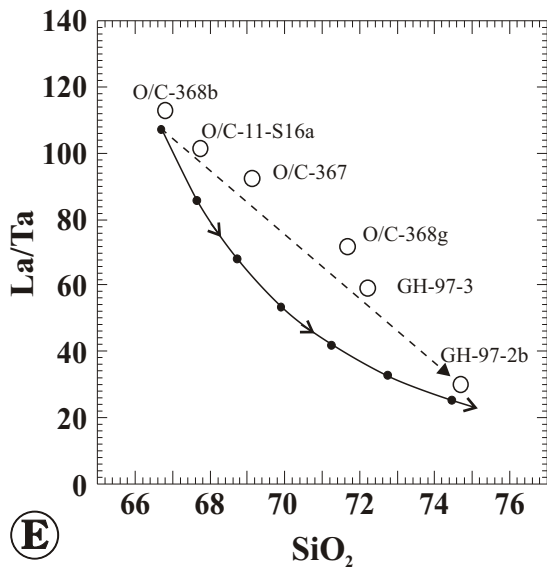
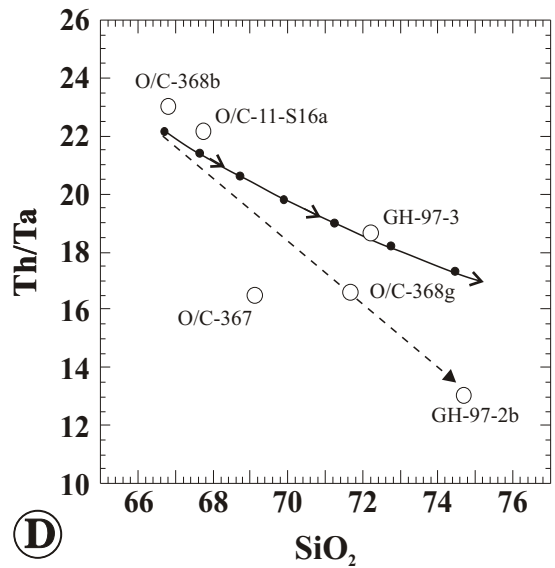
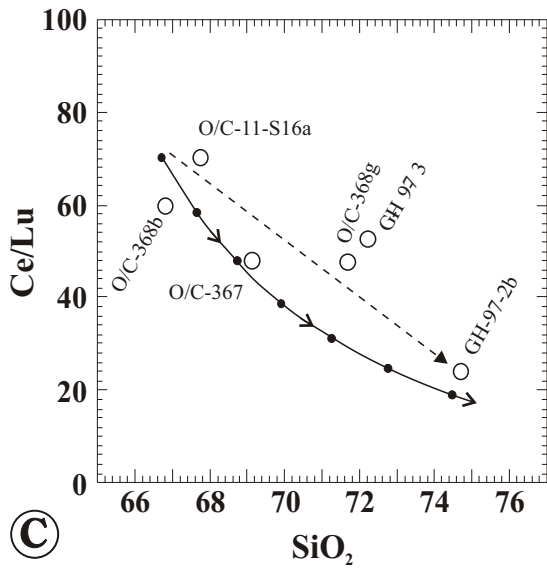
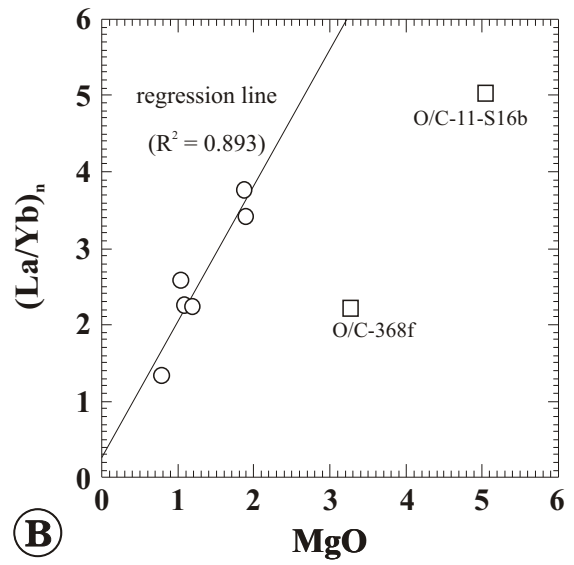
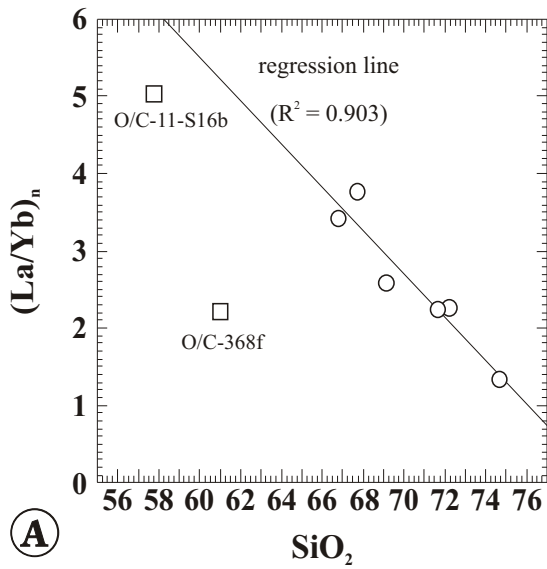


Figure 5.10

A - B: Chondrite normalized La/Yb ratios of samples from the metatonalite unit plotted against SiO₂ and MgO. The ratios decrease with increasing SiO₂ and decreasing MgO. The arrows indicate that fractionation of Mg-rich mafic phases (e.g., hornblende, pyroxene) + plagioclase + Fe-Ti oxides results in increase of SiO₂ and decrease of MgO but does not change the (La/Yb)_n ratios significantly. Fractionation involving allanite or magma mixing may explain the strong correlation between (La/Yb)_n and fractionation index (SiO₂ and MgO).

C - E: Trace element ratios in tonalite-trondhjemite samples plotted against SiO₂. Ce/Lu, Th/Ta and Ta/La decrease with increasing SiO₂ content. Fractionation of plagioclase + orthopyroxene + ilmenite + apatite + allanite (solid curve) can explain the decrease of these trace element ratios with increasing SiO₂. Alternatively, different magmas and magma mixing (dashed line) is also likely.

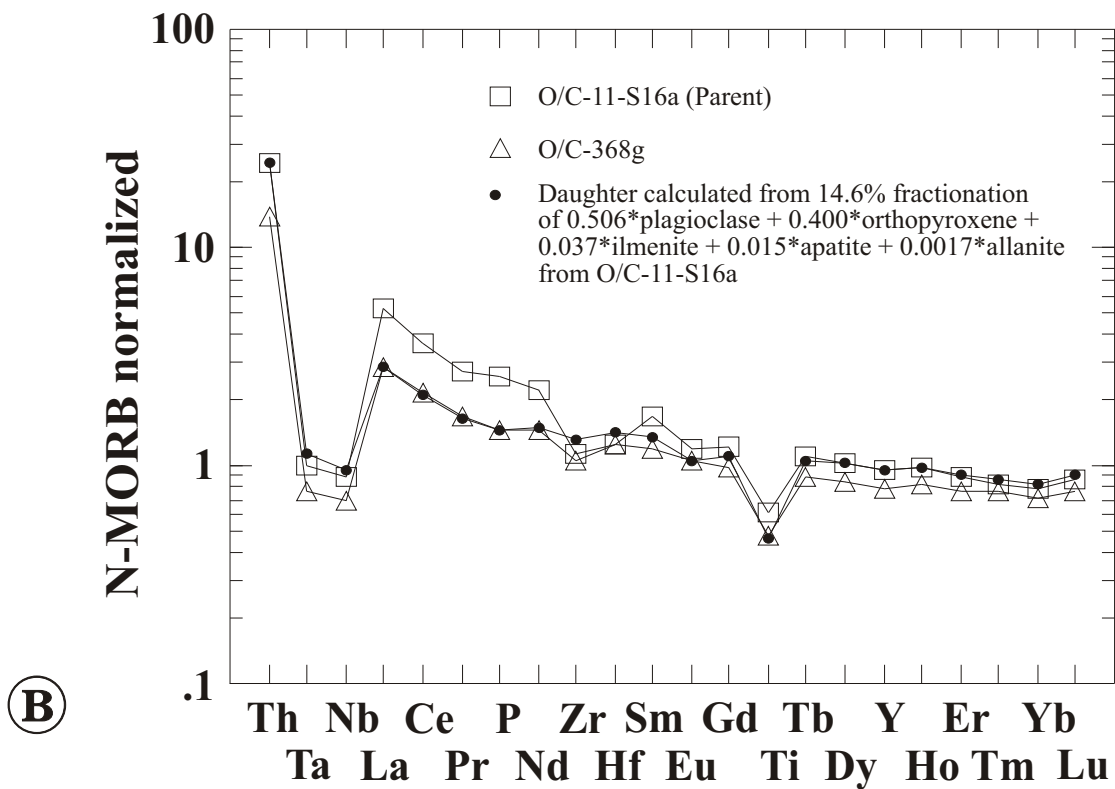
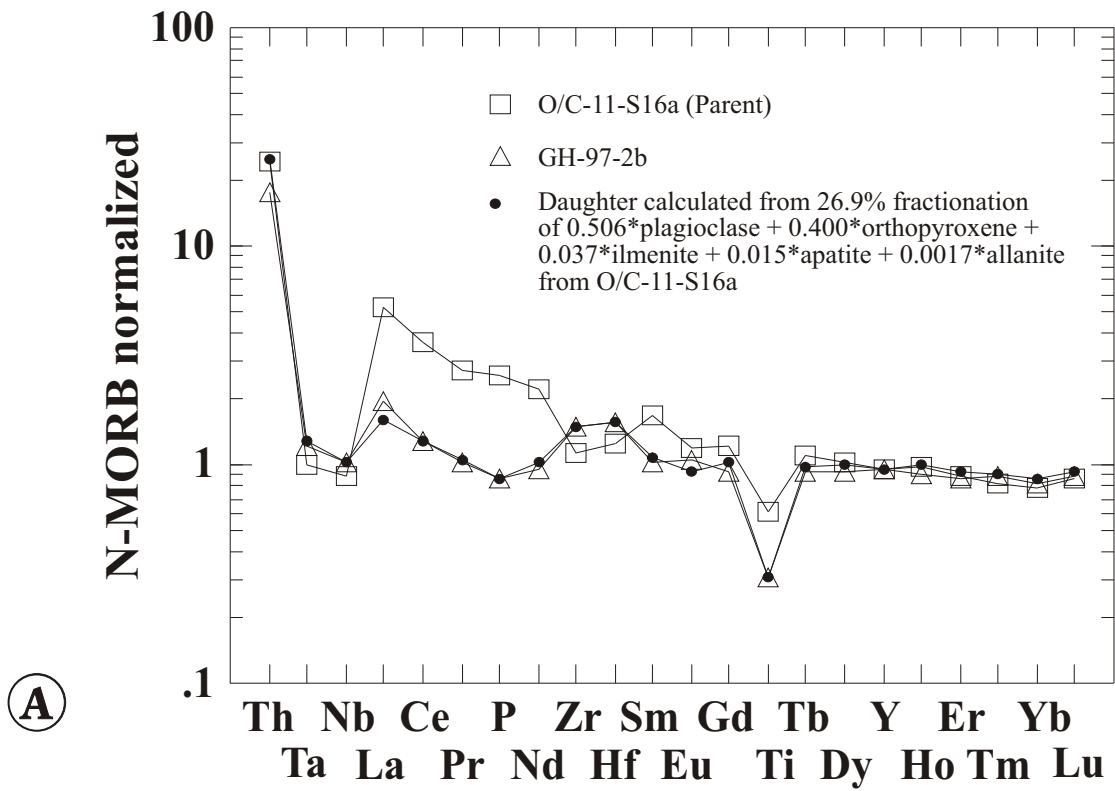


Fractionation trends (5% increments):
 $0.506 * \text{plagioclase} + 0.400 * \text{orthopyroxene} +$
 $0.037 * \text{ilmenite} + 0.015 * \text{apatite} +$
 $0.0017 * \text{allanite}$

Magma mixing

Figure 5.11

N-MORB normalized REE and trace element variation patterns showing the effects of crystal fractionation in the metatonalite unit. (A) The REE and trace element composition of GH-97-2b is reproduced by 26.9% fractionation from O/C-11-S-16a. (B) The REE and trace element composition of O/C-368g is reproduced by 14.6% fractionation from O/C-11-S-16a. Fractionation involving allanite can explain the variations of REE, in the samples, however, it cannot explain the variations of Th, Ta, and Nb (figure 5.11a and 5.11b), and Th/Ta ratios with SiO₂ (figure 5.10).



assuming 14.6% and 26.9% crystal fractionation of an assemblage consisting of 54.6 % plagioclase, 40.0 % orthopyroxene, 3.7 % ilmenite, 1.5% apatite and 0.17% allanite. Clearly, these calculations demonstrate that much of the trace element variations in the tonalite-trondhjemite samples can be explained with fractionation of allanite.

Figures 5.10c through 5.10e show the calculated variations of selected trace element ratios with fractionation of plag +opx + il +ap +al. The calculated crystal fractionation trends largely reproduce the trends defined by the tonalite-trondhjemite samples, suggesting that fractionation of allanite could have played an important role. However, the analytical data scatter around the calculated trends indicating variations due to element mobility (i.e., SiO₂), or differences in the composition of the parental magmas (or both). Also, the scatter of the data around calculated crystal fractionation trends may reflect crystallization and fractionation of other accessory phases (e.g., titanite, zircon) that were not taken into account in this simple model.

5.5.3.3c Magma mixing

The mixing lines are shown in figure 5.10. Most tonalite-trondhjemite samples plot close to or on the mixing lines. Furthermore, the complete REE and trace element composition of O/C-368g can be calculated using a simple mixing model. A least square regression on the mixing equations using immobile trace elements yields the best fit result. GH-97-2b and O/C-11-S16a are mixed in proportions such that a composition most similar to O/C-368g is obtained. The resulting N-MORB normalized trace element pattern obtained by this mixing is very similar to that of O/C-368g (figure 5.12). Clearly, magma mixing is a plausible model that can explain the trace element variations of samples from the metatonalite unit.

Although most of the trace element variations in tonalite-trondhjemite samples could be successfully reproduced with crystal fractionation, allanite fractionation is not sufficient to explain the full range of trace element variations in the samples. Thus, magma mixing is considered to have played an important role for the following reasons: (1) The enclave (O/C-368f) has lower SiO₂ and higher MgO and Cr than the deformed dike (O/C-11-S16b) but has a lower La/Yb ratio (figure 5.10a and 5.10b). O/C-368f and O/C-11-S16b form a 'trend' of decreasing (La/Yb)_n ratios with increasing fractionation (figure 5.10a

and 5.10b). This 'trend' is subparallel to that of the tonalite-trondhjemite samples indicating that the intermediate samples have a similar range of $(La/Yb)_n$ ratios as the silicic samples. The compositional diversity in the intermediate samples cannot be related to allanite fractionation because crystallization and fractionation of allanite is unlikely in a relatively mafic magma (allanite saturation is not reached). Perhaps the tonalite-trondhjemite suite evolved from a compositionally diverse, andesitic parent as depicted in figures 5.10a and 5.10b. (2) The differences in the chondrite and N-MORB normalized REE and trace element patterns of O/C-368f and O/C-11-S16b (see figures 5.8d and 5.8h) cannot be explained with crystal fractionation implying compositionally diverse magmas were present. (3) The Th/Ta ratios decrease much slower with modeled fractionation of allanite than observed for the samples, and more samples fit the mixing line than the fractionation trend (figure 5.10d). (4) Most samples plot closer to the mixing line than to the fractionation curve in figure 5.10e, and a linear decrease (or increase) of incompatible trace element ratios with increasing SiO_2 (or decreasing MgO) is characteristic of mixing or contamination and is not consistent with fractionation of allanite (figure 5.10e).

Based on these observations, it is suggested that the strong correlation of LREE/HREE, La/Ta and Th/Ta ratios with SiO_2 and MgO (figure 5.10) is caused by some type of contamination or mixing process. Contamination can involve the interaction of two miscible magmas, or assimilation of country rock by partial to complete melting of the wall rock or of xenoliths (assimilation of arc lithosphere by an upwelling magma), or variable partial melting and mixing of an upwelling two-component (or multi-component) source region. These processes are overprinted by subsequent fractionation and possible element mobility due to hydrothermal alteration. The identification of end members and uniquely constraining any of the possible mixing processes is not possible using major and trace elements alone. The hypothesis of mixing or contamination can be tested, and perhaps constrained, using Sr and Nd isotopes. Also, the Sr and Nd isotopic signature of samples from the metatonalite unit may reveal more information about the source of the metatonalite unit.

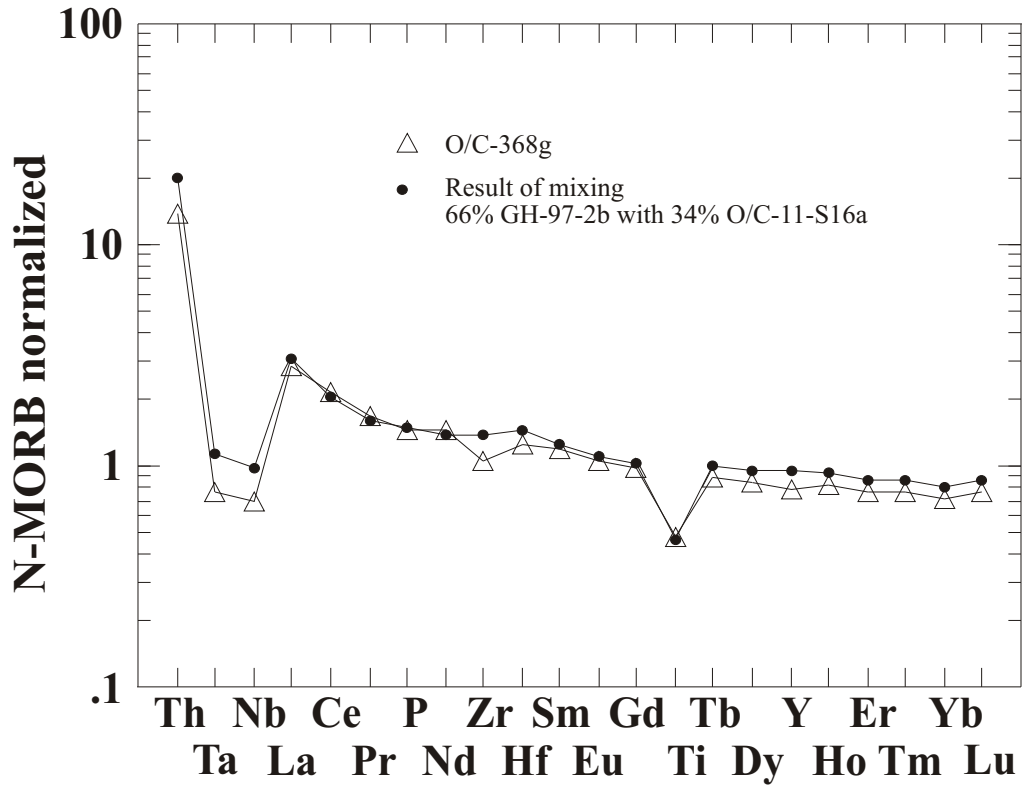


Figure 5.12

N-MORB normalized REE and trace element variation diagram showing the effects of mixing. GH-97-2b and O/C-11-S16a are mixed in proportions such that a composition most similar to O/C-368g is obtained. The composition of O/C-368g and the composition obtained by mixing GH-97-2b and O/C-11-S16a agree well suggesting that magma mixing is a likely process.

5.5.4 Sheeted dike complex

Nineteen samples from the sheeted dike complex were analyzed; fourteen samples are from various dikes and five samples are from gabbro screens. The sample localities are shown in figure 5.1. The analytical data for the gabbro screens are listed in table 5.3a and for the sheeted dikes in table 5.3b. The petrographic data are listed in appendix A (table A3).

5.5.4.1 Rock classification

5.5.4.1a Gabbroic screens

The cumulate gabbro samples (O/C-358, O/C-360 and GH-97-23) contain 45-80% plagioclase, 20-65% pyroxene and <1% oxide. Clinopyroxene and plagioclase are pseudomorphed, and can be identified in thin section based on the secondary mineral assemblages and shape. Clinopyroxene is replaced by variably colored amphibole and magnetite, while plagioclase is commonly replaced by clinozoisite and albite. The primary plagioclase composition could not be determined in thin section because of 100% alteration. Other fine grained mineral aggregates observed in thin section could be altered olivine and/or orthopyroxene. Cumulate textures are well preserved in all samples, except for GH-97-27 which may have been a very fine grained cumulate. Two samples taken from layers consisting almost entirely of plagioclase (GH-97-25 and GH-97-27) were analyzed as well. GH-97-25 shows an adcumulate texture.

The analytical data of cumulate gabbro samples are presented in the MgO variation diagrams in figure 5.13 together with the analytical data of 14 sheeted dikes and 7 samples from the metatonalite unit. Samples O/C-358, O/C-360 and GH-97-23 lie on a straight line in all MgO variation diagrams. The position of O/C-358, O/C-360 and GH-97-23 on that line can be explained with accumulation of varying amounts of calcic plagioclase (plag) and a mafic mineral assemblage (mafic). The composition of plagioclase can be determined using the y-axis intercepts of the regression lines in the MgO variation diagrams in figures 5.13a ($\text{SiO}_2 = 46.7\%$), 5.13c ($\text{Al}_2\text{O}_3 = 33.4\%$), 5.13f ($\text{CaO} = 15.9\%$), and 5.13g ($\text{Na}_2\text{O} = 2.8\%$). These data suggest plagioclase has a composition of about An_{85} , which is typical for plagioclase in mafic cumulates in ophiolites. Assuming the mafic mineral assemblage contains 0% Al_2O_3 , the weight proportions of plagioclase and the mafic mineral assemblage can be estimated using the lever rule in a plot

Table 5.3a: Major and trace element composition of samples from the sheeted dike complex (cumulate gabbro and anorthosite)

| Sample | GH-97-23 | GH-97-25 | GH-97-27 | O/C-358 | OC-360 |
|--------------------------------|----------|-------------|-------------|----------|----------|
| | cum gab. | anorthosite | anorthosite | cum gab. | cum gab. |
| SiO ₂ | 45.77 | 53.58 | 54.30 | 47.87 | 47.43 |
| TiO ₂ | 0.15 | 0.35 | 1.51 | 0.26 | 0.16 |
| Al ₂ O ₃ | 24.65 | 26.00 | 24.16 | 14.39 | 19.53 |
| Fe ₂ O ₃ | 4.06 | 1.40 | 0.82 | 8.11 | 6.32 |
| MnO | 0.06 | 0.02 | 0.02 | 0.13 | 0.09 |
| MgO | 4.27 | 0.61 | 0.34 | 10.32 | 6.92 |
| CaO | 14.89 | 8.45 | 9.78 | 14.23 | 14.13 |
| Na ₂ O | 2.07 | 5.49 | 6.42 | 1.27 | 2.04 |
| K ₂ O | 0.12 | 1.75 | 0.48 | 0.20 | 0.15 |
| P ₂ O ₅ | 0.02 | 0.02 | 0.49 | 0.02 | 0.01 |
| BaO | 23 | 409 | 141 | 0 | 32 |
| Cr ₂ O ₃ | 100 | 355 | 93 | 407 | 231 |
| LOI | 4.26 | 2.28 | 1.73 | 2.81 | 3.17 |
| Total | 100.34 | 100.03 | 100.09 | 99.66 | 100.01 |
| Ni | 28 | 9 | 3 | 90 | 70 |
| Sc xrf/icp | 19/19.2 | 0/7.5 | 10/6.7 | 55/n.d. | 42/n.d. |
| V xrf/icp | 60/n.d. | 42/n.d. | 98/n.d. | 167/191 | 138/156 |

Major elements (in wt%) and Ba, Cr, Ni, Sc, and V (in ppm) were analyzed by standard XRF technique on pressed powder pellets at McGill University, Montreal. Additionally, Sc was analyzed by ICP-MS at Washington State University and V at Union College

Table 5.3a cont.

| Sample | GH-97-23 | GH-97-25 | GH-97-27 | O/C-358 | OC-360 |
|--------|----------|----------|----------|---------|--------|
| | WSU | WSU | WSU | UC | UC |
| Cr | n.d. | n.d. | n.d. | 291 | 157 |
| Rb | 2.0 | 33 | 6.9 | 3.7 | 1.4 |
| Sr | 234 | 298 | 297 | 188 | 274 |
| Y | 4 | 8 | 33 | 6 | 5 |
| Zr | 8 | 9 | 127 | 9 | 7 |
| Nb | 0.22 | 0.31 | 2.59 | 0.15 | 0.12 |
| Cs | 0.11 | 0.98 | 0.37 | 0.08 | 0.06 |
| Ba | n.d. | n.d. | n.d. | 29 | 46 |
| La | 0.87 | 0.77 | 3.30 | 0.72 | 0.67 |
| Ce | 1.63 | 1.95 | 9.49 | 1.68 | 1.48 |
| Pr | 0.25 | 0.33 | 1.53 | 0.28 | 0.24 |
| Nd | 1.23 | 1.96 | 8.48 | 1.56 | 1.28 |
| Sm | 0.43 | 0.88 | 3.47 | 0.61 | 0.45 |
| Eu | 0.29 | 0.39 | 1.29 | 0.29 | 0.25 |
| Gd | 0.59 | 1.24 | 4.90 | 0.87 | 0.62 |
| Tb | 0.09 | 0.22 | 0.88 | 0.15 | 0.11 |
| Dy | 0.65 | 1.44 | 5.85 | 1.05 | 0.75 |
| Ho | 0.14 | 0.30 | 1.25 | 0.22 | 0.16 |
| Er | 0.39 | 0.78 | 3.42 | 0.66 | 0.48 |
| Tm | 0.05 | 0.11 | 0.52 | 0.10 | 0.08 |
| Yb | 0.35 | 0.64 | 2.97 | 0.63 | 0.47 |
| Lu | 0.05 | 0.09 | 0.40 | 0.09 | 0.07 |
| Hf | 0.25 | 0.35 | 3.97 | 0.27 | 0.18 |
| Ta | 0.016 | 0.014 | 0.20 | 0.01 | 0.01 |
| Pb | 0.45 | 0.58 | 0.90 | 0.45 | 0.54 |
| Th | 0.10 | 0.16 | 0.8 | 0.1 | 0.1 |
| U | 0.051 | 0.060 | 0.4 | 0.04 | 0.03 |

UC... Trace element analysis by ICP-MS at Union College

WSU... Trace element analysis by ICP-MS at Washington State University

All trace elements are given in ppm.

n.d. ... not determined

<d.l. ... below detection

Table 5.3b: Major and trace element composition of samples from the sheeted dike complex
(Diabasic and microdioritic dikes)

| Sample | O/C-1S1 | O/C-1S2 | O/C-4S3 | O/C-5S4 | O/C-6S5 | O/C-58 | O/C-325* |
|--------------------------------|---------|---------|----------|---------|----------|---------|-----------|
| Rock type | Diab | Diab | Microdio | Diab | Microdio | Diab | Def. dike |
| SiO ₂ | 51.51 | 53.53 | 54.55 | 53.36 | 55.74 | 49.36 | 48.44 |
| TiO ₂ | 1.13 | 1.11 | 0.80 | 0.74 | 0.62 | 0.89 | 0.56 |
| Al ₂ O ₃ | 16.28 | 15.22 | 14.14 | 14.96 | 14.83 | 15.87 | 11.83 |
| Fe ₂ O ₃ | 9.90 | 11.69 | 8.61 | 8.48 | 8.66 | 10.13 | 9.46 |
| MnO | 0.10 | 0.10 | 0.09 | 0.08 | 0.09 | 0.18 | 0.20 |
| MgO | 5.47 | 4.17 | 7.13 | 6.07 | 5.79 | 7.09 | 14.40 |
| CaO | 8.88 | 8.13 | 8.98 | 9.37 | 8.65 | 11.66 | 7.07 |
| Na ₂ O | 4.36 | 3.67 | 2.29 | 3.69 | 3.66 | 2.30 | 1.72 |
| K ₂ O | 0.11 | 0.27 | 0.46 | 0.05 | 0.15 | 0.29 | 0.03 |
| P ₂ O ₅ | 0.10 | 0.10 | 0.13 | 0.07 | 0.13 | 0.08 | 0.10 |
| BaO | 129 | 202 | 221 | 85 | 134 | 124 | 0 |
| Cr ₂ O ₃ | 189 | 52 | 546 | 103 | 319 | 124 | 1584 |
| LOI | 2.59 | 2.00 | 2.63 | 2.95 | 2.10 | 2.76 | 5.79 |
| Total | 100.50 | 100.06 | 99.93 | 99.87 | 100.50 | 100.67 | 99.83 |
| Ni | 49 | 38 | 150 | 40 | 62 | 46 | 415 |
| Sc | 34 | 29 | 23 | 37 | 23 | 32 | 29 |
| V xrf/icp | 276/270 | 348/376 | 255/258 | 204/200 | 252/260 | 241/233 | 202/200 |

* contains ~25% olivine xeno- or phenocrysts and ~5% cpx phenocrysts

| Sample | O/C-333 | O/C-356 | O/C-357b | O/C-362 | MRH-45b | MRH-45a | MRH-111 |
|--------------------------------|---------|---------|----------|----------|----------|----------|---------|
| | Diab | Diab | Diab | Microdio | Microdio | Microdio | Diab |
| SiO ₂ | 49.33 | 49.32 | 51.76 | 57.81 | 56.99 | 56.64 | 50.71 |
| TiO ₂ | 0.87 | 1.1 | 0.58 | 0.7 | 0.7 | 0.63 | 0.93 |
| Al ₂ O ₃ | 14.68 | 15.05 | 15.94 | 15.26 | 15.94 | 14.83 | 15.82 |
| Fe ₂ O ₃ | 9.41 | 10.3 | 7.93 | 7.46 | 7.1 | 7.5 | 11.94 |
| MnO | 0.16 | 0.15 | 0.1 | 0.06 | 0.08 | 0.12 | 0.17 |
| MgO | 8.83 | 7.58 | 7.3 | 4.68 | 4.56 | 5.79 | 7.79 |
| CaO | 11.81 | 11.34 | 11.83 | 9.31 | 9.15 | 9.33 | 5.27 |
| Na ₂ O | 2.05 | 2.93 | 2.33 | 3.21 | 3.16 | 2.78 | 2.13 |
| K ₂ O | 0.15 | 0.29 | 0.16 | 0.19 | 0.32 | 0.37 | 0.05 |
| P ₂ O ₅ | 0.09 | 0.11 | 0.06 | 0.12 | 0.17 | 0.1 | 0.36 |
| BaO | 86 | 159 | 140 | 119 | 162 | 151 | 100 |
| Cr ₂ O ₃ | 433 | 306 | 133 | 140 | 150 | 387 | 75 |
| LOI | 2.7 | 2.04 | 2.14 | 1.89 | 2.25 | 2.35 | 5.13 |
| Total | 100.17 | 100.29 | 100.18 | 100.75 | 100.48 | 100.53 | 100.34 |
| Ni | 82 | 64 | 43 | 41 | 33 | 77 | 23 |
| Sc | 44 | 47 | 41 | 35 | 24 | 17 | 40 |
| V xrf/icp | 225/200 | 253/251 | 175/186 | 247/231 | 258/241 | 223/269 | 197/194 |

Major elements (in wt%) and Ba, Cr, Ni, Sc, and V (in ppm) were analyzed by standard XRF technique on pressed powder pellets at McGill University, Montreal. Additionally, V was analyzed by ICP-MS at Union College

Table 5.3b cont.

| Sample | O/C-1S1 | O/C-1S2 | O/C-4S3 | O/C-5S4 | O/C-6S5 | O/C-58 | O/C-325* |
|--------|---------|---------|---------|---------|---------|--------|----------|
| | UC | UC | UC | UC | UC | UC | UC |
| Cr | 204 | 14 | 326 | 54 | 190 | 73 | 1125 |
| Rb | 0.37 | 3.08 | 9.1 | 0.13 | 0.92 | 3.9 | 0.20 |
| Sr | 181 | 253 | 282 | 73 | 279 | 197 | 113 |
| Y | 21 | 23 | 19 | 20 | 13 | 17 | 15 |
| Zr | 73 | 51 | 61 | 44 | 47 | 44 | 49 |
| Nb | 2.77 | 1.72 | 1.66 | 1.25 | 1.22 | 1.84 | 1.02 |
| Cs | 0.12 | 0.27 | 0.36 | 0.03 | 0.05 | 0.24 | 0.08 |
| Ba | 37 | 86 | 155 | 21 | 85 | 52 | 11 |
| La | 3.45 | 5.51 | 5.90 | 1.82 | 7.80 | 4.05 | 5.63 |
| Ce | 8.61 | 14.8 | 12.5 | 4.80 | 14.7 | 9.73 | 11.8 |
| Pr | 1.33 | 2.30 | 1.78 | 0.79 | 1.86 | 1.49 | 1.72 |
| Nd | 6.91 | 11.20 | 8.32 | 4.27 | 7.94 | 7.43 | 7.54 |
| Sm | 2.19 | 2.93 | 2.31 | 1.52 | 1.90 | 2.17 | 2.07 |
| Eu | 0.73 | 1.28 | 0.68 | 0.58 | 0.79 | 0.87 | 0.63 |
| Gd | 2.89 | 3.50 | 2.73 | 2.31 | 2.12 | 2.71 | 2.33 |
| Tb | 0.52 | 0.60 | 0.46 | 0.47 | 0.35 | 0.47 | 0.38 |
| Dy | 3.42 | 3.82 | 3.01 | 3.34 | 2.17 | 3.06 | 2.43 |
| Ho | 0.73 | 0.82 | 0.63 | 0.75 | 0.46 | 0.64 | 0.52 |
| Er | 2.08 | 2.36 | 1.85 | 2.24 | 1.32 | 1.82 | 1.56 |
| Tm | 0.32 | 0.36 | 0.29 | 0.35 | 0.21 | 0.28 | 0.24 |
| Yb | 2.11 | 2.35 | 1.91 | 2.23 | 1.38 | 1.80 | 1.52 |
| Lu | 0.32 | 0.36 | 0.29 | 0.34 | 0.22 | 0.28 | 0.23 |
| Hf | 1.86 | 1.57 | 1.81 | 1.42 | 1.51 | 1.26 | 1.37 |
| Ta | 0.18 | 0.095 | 0.099 | 0.079 | 0.088 | 0.13 | 0.063 |
| Pb | 0.42 | 0.58 | 0.54 | 0.33 | 0.71 | 0.12 | 0.85 |
| Th | 0.29 | 0.61 | 1.06 | 0.32 | 1.39 | 0.32 | 0.83 |
| U | 0.12 | 0.37 | 0.40 | 0.12 | 0.39 | 0.12 | 0.31 |

UC... Trace element analysis by ICP-MS at Union College

WSU... Trace element analysis by ICP-MS at Washington State University

All trace elements are given in ppm.

n.d. ... not determined

<d.l. ... below detection

* contains ~25% olivine xeno- or phenocrysts and ~5% cpx phenocrysts

Table 5.3b cont.

| Sample | O/C-333 | O/C-356 | O/C-357b | O/C-362 | MRH-45b | MRH-45a | MRH-111 |
|--------|---------|---------|----------|---------|---------|---------|---------|
| | UC | UC | UC | UC | UC | UC | UC |
| Cr | 260 | 185 | 79 | 69 | 278 | 84 | 35 |
| Rb | 1.3 | 3.0 | 1.9 | 1.98 | 6.5 | 5.0 | 0.34 |
| Sr | 146 | 179 | 202 | 310 | 256 | 347 | 252 |
| Y | 17 | 22 | 14 | 18 | 13 | 21 | 19 |
| Zr | 35 | 65 | 32 | 56 | 48 | 69 | 35 |
| Nb | 1.73 | 3.07 | 0.93 | 1.43 | 1.32 | 1.99 | 0.73 |
| Cs | 0.10 | 0.25 | 0.29 | 0.11 | 0.21 | 0.14 | 0.06 |
| Ba | 38 | 92 | 85 | 78 | 96 | 93 | 20 |
| La | 2.39 | 3.32 | 2.39 | 8.05 | 6.26 | 19.10 | 3.90 |
| Ce | 6.36 | 9.30 | 4.99 | 17.8 | 12.2 | 37.3 | 9.42 |
| Pr | 1.02 | 1.44 | 0.73 | 2.56 | 1.62 | 4.98 | 1.56 |
| Nd | 5.22 | 7.48 | 3.65 | 11.85 | 7.45 | 22.37 | 8.39 |
| Sm | 1.68 | 2.37 | 1.27 | 2.98 | 1.86 | 5.21 | 2.58 |
| Eu | 0.65 | 0.91 | 0.45 | 1.00 | 0.57 | 1.80 | 0.87 |
| Gd | 2.32 | 3.11 | 1.78 | 3.14 | 2.10 | 4.87 | 3.17 |
| Tb | 0.42 | 0.57 | 0.32 | 0.49 | 0.35 | 0.69 | 0.52 |
| Dy | 2.74 | 3.68 | 2.18 | 2.99 | 2.22 | 3.92 | 3.32 |
| Ho | 0.57 | 0.78 | 0.46 | 0.61 | 0.47 | 0.77 | 0.71 |
| Er | 1.68 | 2.22 | 1.35 | 1.74 | 1.36 | 2.11 | 2.02 |
| Tm | 0.26 | 0.34 | 0.21 | 0.27 | 0.21 | 0.31 | 0.31 |
| Yb | 1.64 | 2.18 | 1.40 | 1.71 | 1.45 | 1.99 | 1.99 |
| Lu | 0.25 | 0.32 | 0.21 | 0.26 | 0.24 | 0.30 | 0.32 |
| Hf | 1.03 | 1.71 | 0.92 | 1.70 | 1.50 | 2.04 | 1.09 |
| Ta | 0.11 | 0.19 | 0.067 | 0.083 | 0.081 | 0.095 | 0.044 |
| Pb | 0.29 | 0.44 | 0.24 | 0.44 | 0.46 | 0.60 | 0.69 |
| Th | 0.18 | 0.22 | 0.25 | 1.53 | 0.99 | 2.19 | 0.53 |
| U | 0.092 | 0.076 | 0.14 | 0.60 | 0.27 | 0.68 | 0.18 |

UC... Trace element analysis by ICP-MS at Union College

WSU... Trace element analysis by ICP-MS at Washington State University

All trace elements are given in ppm.

of Al_2O_3 vs. MgO: O/C-358 contains 43% plag and 57% mafic minerals; O/C-360 contains 60% plag and 40% mafic minerals; and GH-97-23 contains 75% plag and 25% mafic minerals.

The regression line in a plot of Al_2O_3 vs. MgO intercepts the x-axis at MgO = 19.5%. Assuming the mafic minerals contain no significant amounts of Al_2O_3 (i.e., olivine, clinopyroxene, and orthopyroxene) the weight-% of oxides making up the mafic mineral assemblage can be determined: for MgO = 19.5%, then $\text{Al}_2\text{O}_3 = 0\%$, $\text{SiO}_2 = 52.8\%$, $\text{FeO}^* = 12.6\%$, $\text{CaO} = 13.7\%$, $\text{Na}_2\text{O} = 0.20\%$, $\text{TiO}_2 = 0.40\%$. This composition can be recalculated as normative mineral composition (CIPW norm) which is 56.2% diopside, 40.6% hyperstene, 0.1% olivine, and 3.2% Fe-Ti oxides. According to these estimates, the samples range in composition from gabbronorite (O/C-358 and O/C-360) to leuco-gabbronorite (GH-97-23). This calculation (and classification) is only valid if the bulk rock composition did not change significantly due to alteration. The linear relationships of elements suggest little element mobility.

Samples GH-97-25 and GH-97-27 consist almost entirely of plagioclase (replaced entirely by secondary minerals which appear cloudy in thin section. The composition of GH-97-25 and GH-97-27 is similar to labradorite ($\text{SiO}_2 \sim 55\%$, $\text{Al}_2\text{O}_3 \sim 26\%$, $\text{CaO} \sim 9\%$, and $\text{Na}_2\text{O} \sim 6\%$). The major element composition and textures clearly indicate that these layers are cumulates. Obviously, GH-97-25 and GH-97-27 do not plot along the “accumulation trend” of O/C-358, O/C-360 and GH-97-23, because GH-97-25 and GH-97-27 have a different (calculated) plagioclase composition (oligoclase) than O/C-358, O/C-360 and GH-97-23 (bytownite).

The concentration of TiO_2 and P_2O_5 in GH-97-27 is much higher than in GH-97-25 whereas K_2O is much higher in GH-97-25 than in GH-97-27. Redistribution of K_2O is likely in highly altered rocks, while P_2O_5 and TiO_2 were probably ‘immobile’. Perhaps a small amount of highly fractionated melt rich in incompatible elements has been trapped between the cumulus phases in GH-97-27 causing large differences in incompatible element concentrations between the samples GH-97-25 and GH-97-27.

5.5.4.1b Sheeted dikes

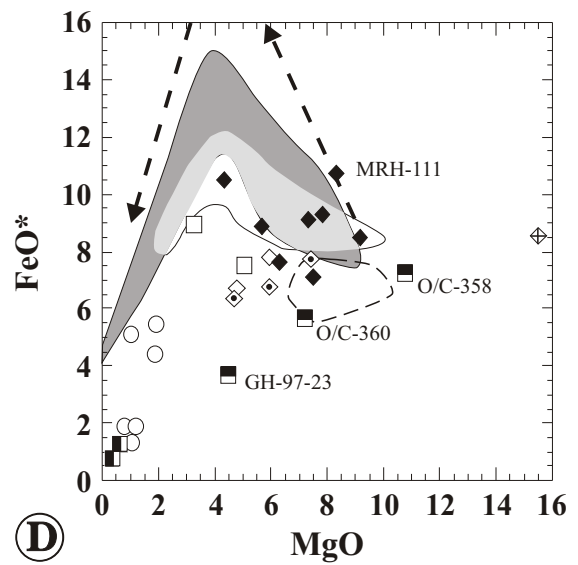
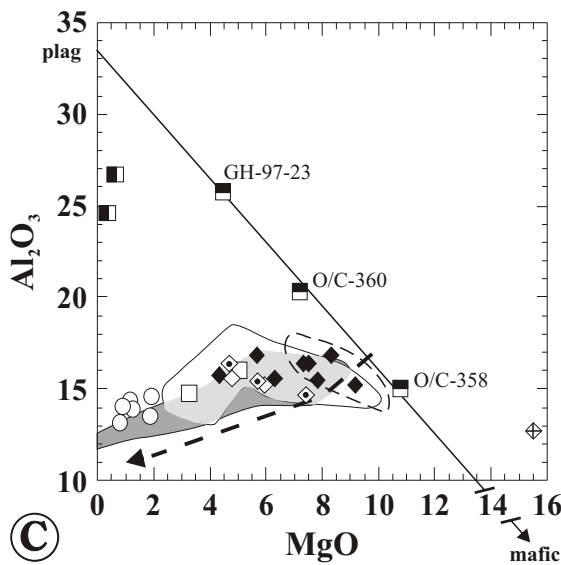
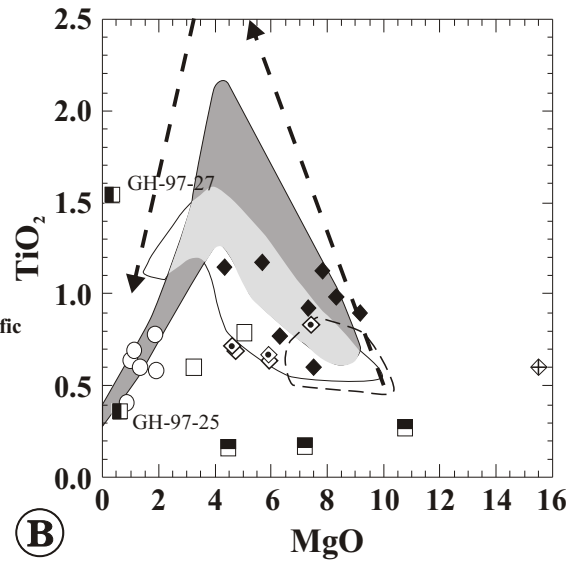
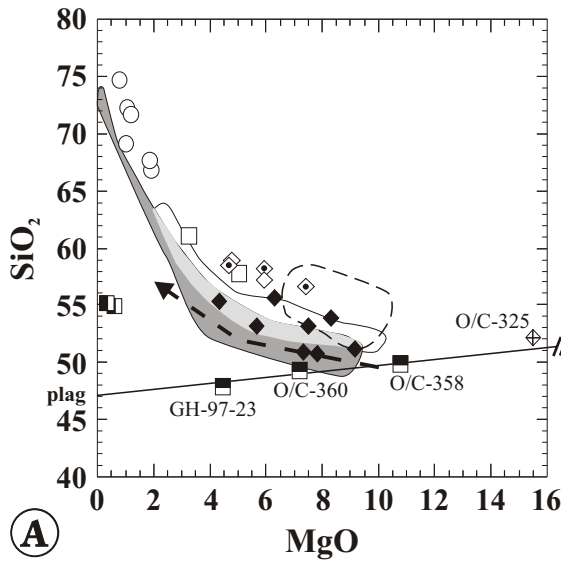
The dikes are subdivided into two geochemical groups based on ‘immobile’ trace elements (section 5.5.4.2). The petrographic descriptions are given for each group and characteristics that may be

Figure 5.13

A - I: MgO variation diagrams of samples from the sheeted dike complex. Three samples from the cumulate gabbro screens lay on a straight line between plagioclase (plag) and a mafic mineral assemblage (mafic) suggesting different amounts of accumulation of plagioclase and mafic minerals. Figures 5.13 a, c, f, and g give the composition of plagioclase which is bytownite ($\sim\text{An}_{85}$). Based on CIPW norm calculations, the mafic mineral assemblage consists of 56.2% cpx, 40.5% opx, 0.1% olivine and 3.2% Fe-Ti oxides. The Fe/Mg ratio in cpx, opx and olivine is 0.28 (see text). In most MgO variation diagrams, the dikes of geochemical group 1 are distinct from dikes of geochemical group 2 (figures 5.13a, b, c, d, and f). The dikes of group 1 follow a tholeiitic fractionation trend similar to rift-related lavas recovered at ODP Leg 135 Site 839 in the Lau Basin, SW Pacific. Three dikes of group 1 have higher TiO_2 for a given MgO than Site 839 lavas (figure 5.13b) and appear to be similar to lavas dredged at the Eastern Lau Spreading center. In contrast the dikes of group 2 (and the samples from the metatonalite unit) follow a calc-alkaline fractionation trend. The analytical data of samples from the metatonalite unit are plotted for comparison. These data seem to form an extension of the trends defined by the microdioritic dikes.

J: FeO/MgO vs. SiO_2 discrimination diagram of Miyashiro (1974).

The field for ODP Leg 135 Site 839 (IAT) is defined by analyses published in Ewart et al. (1994a, 1994b), Hawkins and Allan (1994), Hawkins (1995), Hergt and Hawksworth (1994), and Pearce et al. (1995b). The field for the Eastern Lau Spreading Center (MORB-IAT) is defined by analyses published in Hawkins and Melchior (1985), Hawkins (1995), Frenzel et al. (1990), Davis et al. (1990), Boespflug et al. (1990), and Pearce et al. (1995b). The field for CAB from the Lassen region, California is defined by analyses published in Borg et al. (1997) and Conrey et al. (1997). The fractionation trend for N-MORB (dashed arrow) is from Hochstaedter et al. (1990a).



Metatonalite unit

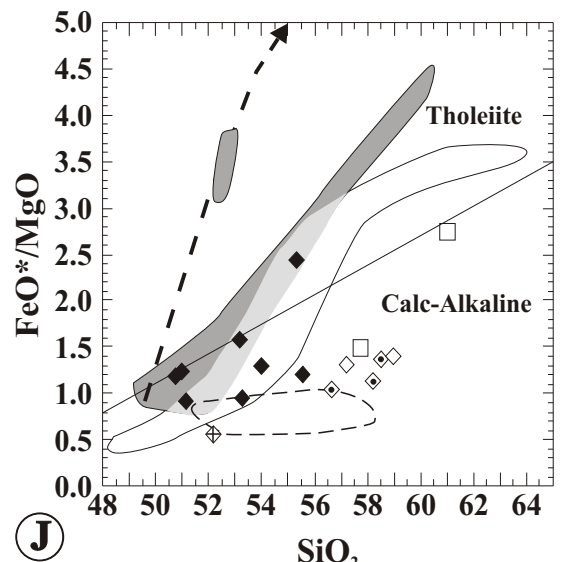
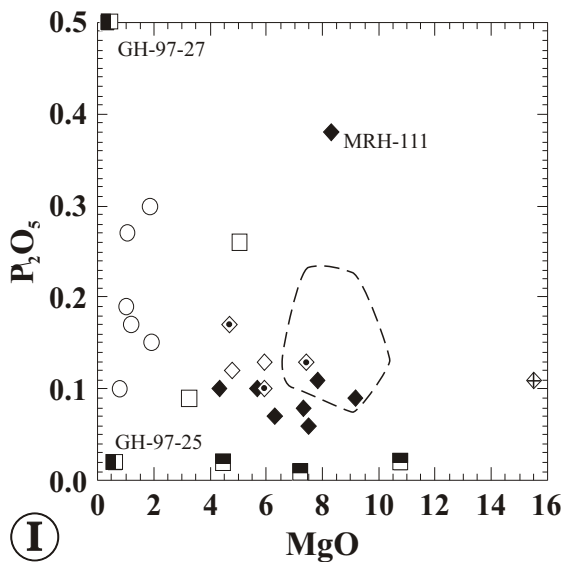
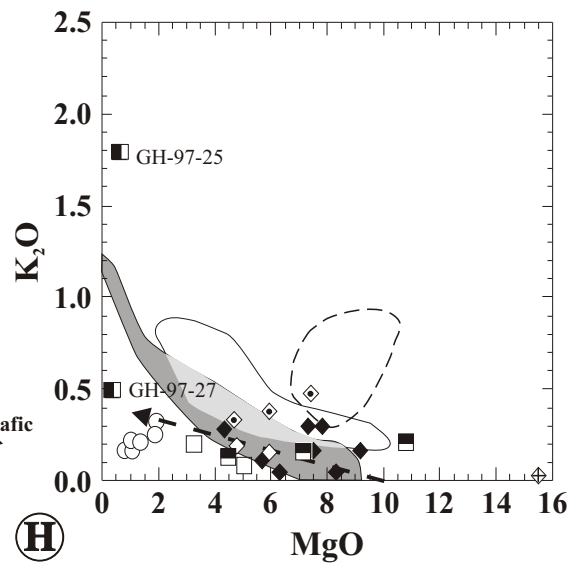
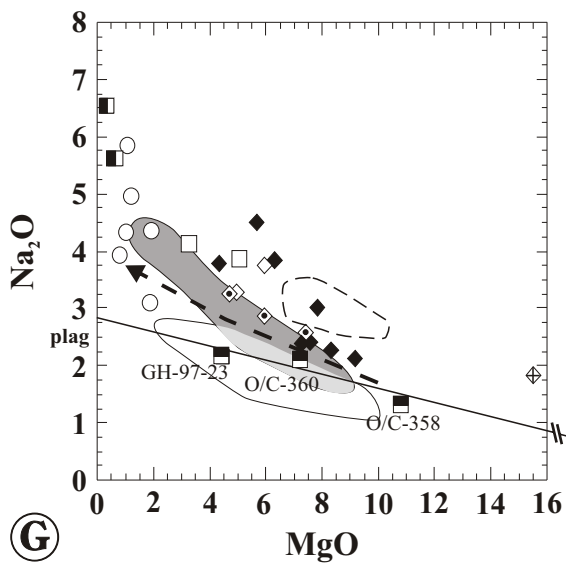
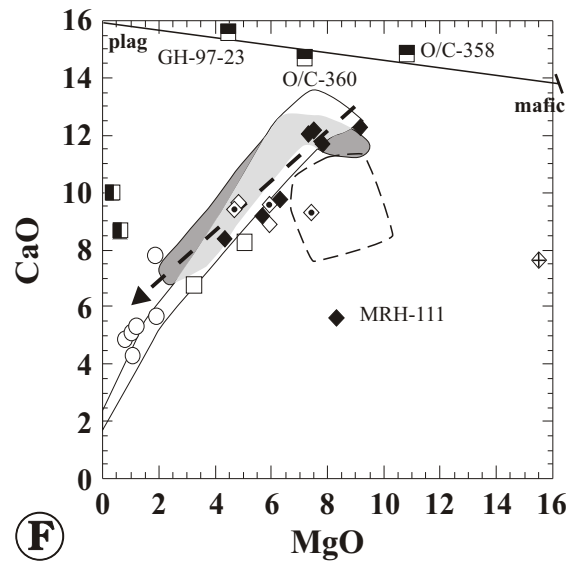
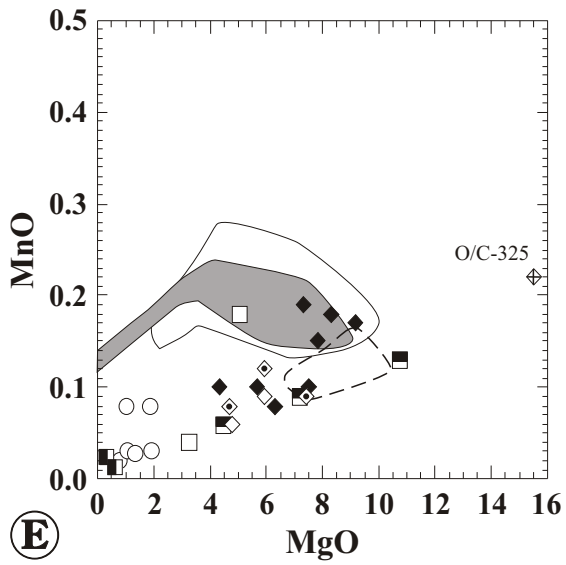
- Tonalite-trondhjemite
- Dioritic dike and enclave

Sheeted dike complex

- ◆ diabasic dikes (geochemical group 1)
- ◆ diabasic and microdioritic dikes, (geochemical group 2)
- ◇ w/o ol-xenocrysts
- ◇ with 1-6% ol-xenocrysts
- ◇ with ~25% olivine

- Gabbro screens
- cumulate gabbro
- plagioclasite

- Primitive calc-alkaline basalts with highest Sr/P ratios from the Lassen region, Cascade arc, California
- IAT: ODP Leg 135 Site 839, Lau Basin, SW Pacific
- Trans. IAT-MORB: Dredge samples, Eastern Lau Spreading Center
- ▲ Fractionation trend of N-MORB



used to distinguish these groups in thin section are pointed out. The mineral compositions in both groups of dikes are inferred since plagioclase and pyroxene are almost 100% replaced by albite + clinozoisite/epidote and amphibole \pm magnetite, respectively (appendix A, table A3). Both groups of dikes have similar degrees of alteration and contain the same metamorphic mineral assemblages replacing igneous minerals as well as the same crosscutting veins (see chapter 2).

The first geochemical group (MRH-111, O/C-1-S1, O/C-1-S2, O/C-5-S4, O/C-58, O/C-333, O/C-356b, and O/C-357) includes diabasic dikes originally consisting of 50-56% clinopyroxene and 42-49% plagioclase and <4% oxide. In general, the diabasic dikes are aphyric. Of eight analyzed diabasic samples, only two contain small amounts of phenocrysts; O/C-356 contains ~2% plagioclase- and ~2% clinopyroxene phenocrysts, and MRH-111 contains ~2% clinopyroxene phenocrysts (phenocrysts are pseudomorphed). The igneous textures are well preserved and range from ophitic to subophitic. Quartz has not been found in dikes of group 1, except in and adjacent to quartz veins. Quartz, most likely secondary in origin (occurs as replacement of igneous minerals), is rare or absent in the ground mass of dikes of geochemical group 1.

The second geochemical group (MRH-45a, MRH-45b, O/C-4-S3, O/C-6-S5, O/C-325 and O/C-362) includes diabasic and microdioritic dikes consisting of 41-47% plagioclase, 40-50% pyroxene, 1-14% quartz, <2% oxide and accessory titanite. Most oxide is probably secondary in origin (magnetite) as it is very fine-grained and occurs together with amphibole replacing pyroxene. Interstitial titanite is translucent light-brown and it does not occur as replacement of ilmenite. Thus, titanite is probably igneous in origin. Three of these dikes contain variable amounts of olivine xenocrysts that contain translucent dark-brown Cr-spinel (chapter, 2 figures 2.31 and 2.32). Olivine is completely replaced by a fine grained/fibrous mineral aggregate, but textures, such as lobate xenocryst rims, indicating resorption are still preserved. The distribution of olivine xenocrysts in many dikes is highly heterogeneous. Samples that contain large amounts of olivine contain no quartz, whereas samples from the same dike with only few olivine xenocrysts contain quartz. Also, the amount of olivine in different parts of the same dike is negatively correlated with modal quartz. The textures in a single dike of group 2a can vary from ophitic (no modal quartz present) to hypidiomorphic granular (quartz present interstitially). Quartz is probably igneous in

origin because it occurs interstitially, and because an inverse correlation between the amount of olivine xenocrysts and modal quartz is observed. This correlation suggests that resorption of olivine occurred in a silica over-saturated melt (i.e., olivine + quartz = orthopyroxene). Some SiO_2 , however might have formed by alteration.

Two samples were analyzed that contain no xenocrysts (O/C-6-S5 and O/C-362), and three samples were analyzed containing between 1% and ~6% olivine xenocrysts (MRH-45a, MRH-45b, O/C-4-S3). Additionally, a deformed dike (O/C-325) located ~ 20 m east of the contact with the metatonalite unit was analyzed. The deformed dike contains ~5% fractured clinopyroxene phenocrysts (cpx composition listed in appendix C) and elongate masses (up to 1 cm long and 4 mm in diameter) of fine grained mineral aggregates. The elongate masses of fine grained mineral aggregates constitute ~25% of the sample and are interpreted as deformed olivine phenocrysts (xenocrysts?), because the fine grained masses contain Cr-spinel similar to the olivine xenocrysts (pseudomorphed) in samples MRH-45a, MRH-45b, and O/C-4-S3. The high percentage of phenocrysts (xenocrysts?) in O/C-325 are probably due to accumulation.

In thin section, samples of geochemical group 2 can be distinguished from samples of geochemical group 1 provided the samples are relatively-coarse grained so that interstitial quartz and titanite in samples of geochemical group 2 can be identified (a distinction in the field could not be made). Other differences, such as differing metamorphic mineral assemblages were not observed. Also, samples of geochemical group 2 that contain neither interstitial quartz nor titanite cannot be distinguished from samples of geochemical group 1.

Figure 5.14 shows the Zr/TiO_2 vs. Nb/Y classification diagram of Winchester and Floyd (1977) with fields revised by Pearce (1996). The dikes of the first geochemical group plot at and below the lower field boundary of the 10% probability contour for subalkaline basalts defined by the total alkali vs. silica (TAS) rock classification. The dikes of the second geochemical group plot also in the field for subalkaline basalts, but they have higher Zr/TiO_2 ratios than the dikes of the first group suggesting the dikes of group 2 are more evolved or have a different primary composition. The compositional differences between the geochemical groups are most pronounced in a plot of SiO_2 vs. MgO (figure 5.13a). The MgO content of group 1 samples ranges from 9.6 - 4.3% with SiO_2 content from 50.8 - 55.3%, whereas the MgO content

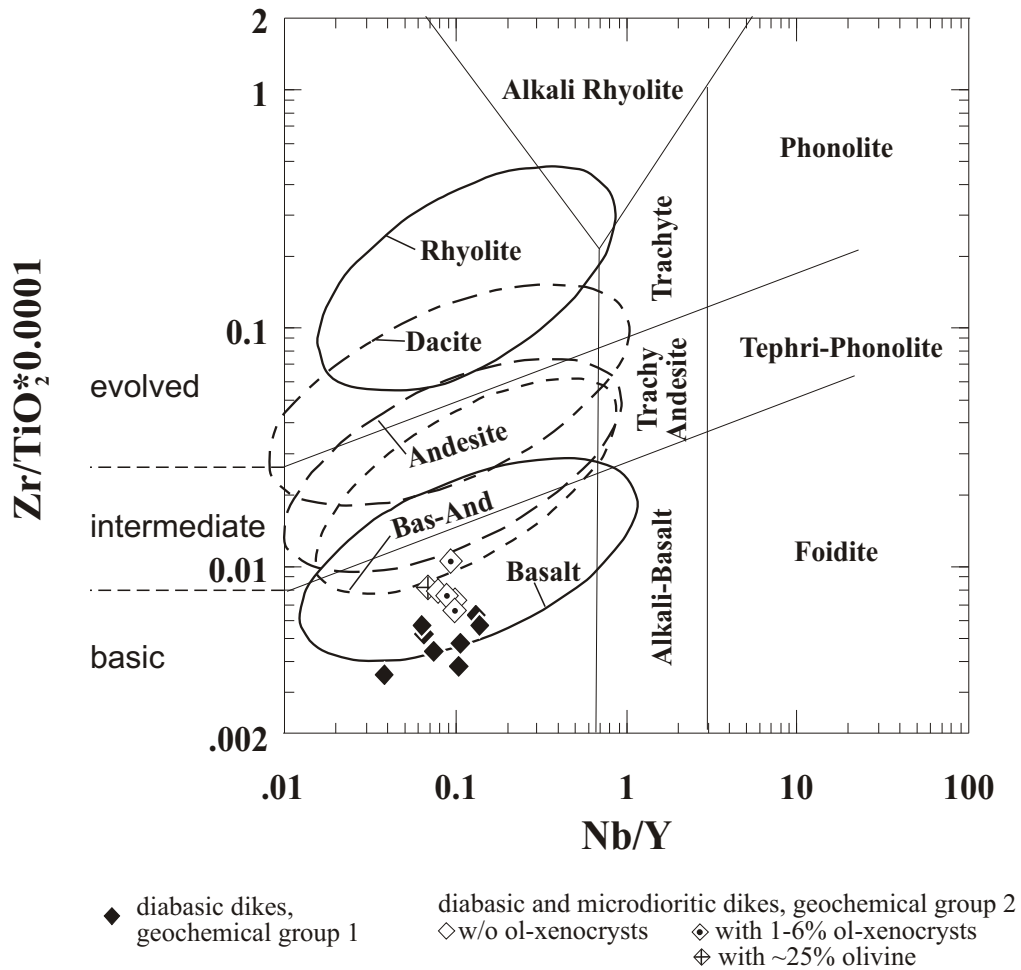


Figure 5.14

Zr/TiO_2 vs. Nb/Y diagram of Winchester and Floyd (1977) with fields revised by Pierce (1996).

Additionally, the 10% probability ellipses for TAS-defined rock types from subalkaline series are shown (after Pierce, 1996). The 10% probability ellipses overlap substantially. Dikes of geochemical group 2 have higher Zr/TiO_2 ratios than dikes of geochemical group 1.

of samples of group 2 (except O/C-325 which has ~25% olivine accumulation) ranges from 7.4 - 4.8% with SiO₂ content from 56.6 - 59.0%. Assuming no significant addition of SiO₂ due to hydrothermal alteration, the composition of samples of group 1 ranges from basalt to basaltic andesite while group 2 samples are andesitic in composition. Differences between the petrographic groups are not as pronounced in the other plots (figures 5.13b through 5.13i), and substantial overlap exists. At a given MgO, group 1 samples are, on average, higher in TiO₂, slightly higher in Al₂O₃, higher in FeO*, CaO, NaO, MnO, and lower in SiO₂, Ni, and Cr than group 2 samples.

O/C-325 is a foliated dike and its igneous minerals are deformed and 100% replaced, only some relict clinopyroxene is present. Elongated masses of fine grained metamorphic mineral aggregates define the lineation and contain abundant Cr-spinel, suggesting that these aggregates represent deformed and replaced olivine phenocrysts or xenocrysts. Mass balance calculations show that the major element variations between samples containing 1-6% olivine xenocrysts and O/C-325 are best explained by 30% accumulation of olivine, a few percent of clinopyroxene and minor amounts of calcic plagioclase. The results of the mass balance calculation constrain the mineral composition of this sample which supports the petrographic data. Also, high Ni and Cr contents are consistent with accumulation of olivine containing abundant Cr-spinel.

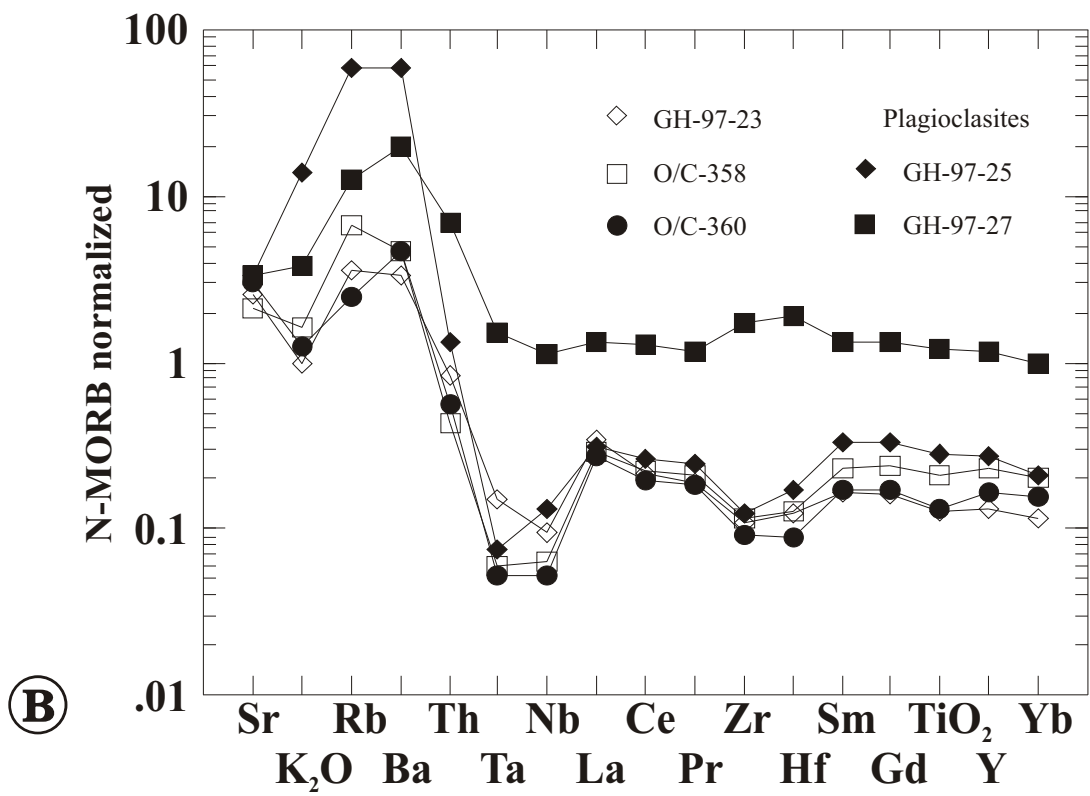
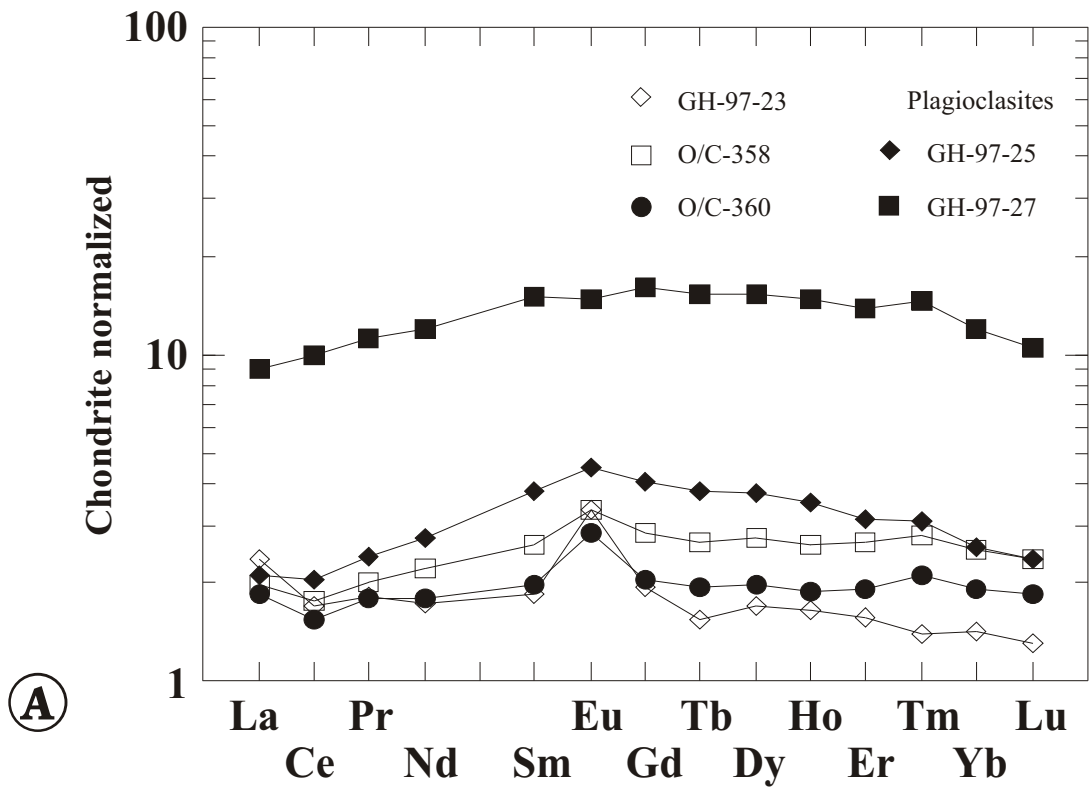
5.5.4.3 Magmatic affinities

5.5.4.3a Gabbroic screens

The chondrite- and N-MORB normalized REE and trace element distribution patterns are shown in figure 15a and 15b, respectively. The REE concentration of GH-97-23, Gh-97-25, O/C-358 and O/C-360 is very low ranging between 1.5 and 4 × chondritic, consistent with these samples being cumulates. However, GH-97-27 has significantly higher REE and trace element concentrations than the other samples. On one hand, the high concentrations of incompatible elements seems inconsistent with the interpretation that GH-97-27 is a cumulate. On the other hand, the major element composition, especially high Al₂O₃- and low SiO₂- contents (figure 5.13a and 5.13c), indicate that GH-97-27 is not an highly evolved, silicic

Figure 5.15

- A. Chondrite normalized REE distribution diagrams of samples from gabbroic screens in the sheeted dike complex. The patterns vary from flat to LREE depleted. The LREE depletion could reflect the composition of the parental magma. The positive Eu-anomaly increases with decreasing REE abundance suggesting accumulation of plagioclase.
- B. N-MORB normalized trace element distribution diagram of samples from the gabbroic screens in the sheeted dike complex. The patterns have a strong arc signature indicating selective enrichment of LILE and Th and relative depletion of Ta, Nb as well as Zr and Hf. Compared to island arc tholeiites (figure 5.2), the patterns of the cumulates are shifted down indicating very low abundance of incompatible elements. GH-97-27 is a sample consisting almost entirely of plagioclase similar to GH-97-25. However, the high concentrations of incompatible trace elements in GH-97-27 compared to the other cumulate samples suggest the presence of highly fractionated melt in between cumulate phases.



rock, such as a plagiogranite. Perhaps the enrichment in incompatible elements is caused by a highly fractionated melt entrapped in between cumulus plagioclase.

Zircon-separates have been obtained from sample SC-1, which occurs in similar outcrop relationship as GH-97-25 and GH-97-27 (Coleman, personal communication 1996), and is petrographically indistinguishable from GH-97-25. The presence of zircon in a cumulate gabbro screen is unusual, because Zr is strongly partitioned in the melt. The hypothesis of a highly fractionated melt occurring in between cumulus phases may explain the presence of zircon in these samples. Zr-saturation in a melt of tholeiitic composition is reached only at high degrees of fractionation (DeLong and Chatelain, 1990; Watson, and Harrison, 1983), and zircon may have crystallized in the residual melt entrapped between cumulus plagioclase.

The cumulate gabbro samples have a positive Eu-anomaly that increases with decreasing total REE abundance. This is indicative of plagioclase accumulation. Europium forms predominantly Eu^{2+} under the relatively reducing conditions of a mafic magma of MORB or IAT composition. Eu^{2+} is less incompatible in plagioclase than Eu^{3+} and other REE (which occur in trivalent state). Thus, Eu becomes relatively enriched during accumulation of plagioclase.

The relative depletion in LREE compared to HREE is likely related to cumulate processes. The partition coefficients between basaltic melt and clinopyroxene, orthopyroxene and olivine is lower for LREE than for HREE (e.g., compilation of partition coefficients in Rollinson, 1993). During fractionation of these minerals, the residual melt becomes more enriched in LREE than in HREE, and the cumulates become more depleted in LREE than in HREE. Thus, the parental magma could have been less LREE depleted than the cumulates.

A strong arc-signature is evident in the N-MORB normalized trace element patterns. The patterns are characterized by relative depletion of HFSE (Ta, Nb, Hf, Zr) and selective enrichment of LILE and Th. Fractionation and accumulation processes do not result in significant changes of the trace element patterns, nor occur large changes of abundance ratios of incompatible trace elements (e.g., Dudas, 1992). Thus, the cumulate rocks can be classified using the Hf/3-Th-Ta discrimination diagram (figure 5.16). The samples

plot in the volcanic arc basalt field in the Hf/3-Th-Ta discrimination diagram indicating magmatic affinities to island arc tholeiite transitional to calc-alkaline basalt.

5.5.4.2b Dikes of geochemical group 1

The chondrite- and N-MORB normalized trace element variation diagrams of dikes of geochemical group 1 are shown in figures 5.17a through 5.17f. The dikes of group 1 have been subdivided into four different subgroups based on their Th/Ta ratios and chondrite normalized La/Yb ratios.

The chondrite normalized REE distribution pattern for O/C-5-S4 (“subgroup” 1a) indicates relative depletion of LREE ($(La/Yb)_n = 0.55$) (figure 5.17a). The pattern in the N-MORB normalized trace element variation diagram (figure 5.16b) shows a slight depletion of Ta and Nb and significant enrichment of Th and Ba (figure 5.17b). O/C-5-S4 has a Th/Ta ratio of 4.03. The often highly mobile elements Rb and K are also depleted. From La to Yb, the pattern is parallel to N-MORB, but O/C-4-S5 has significantly lower HFSE concentrations than N-MORB ($\sim 0.7 \times$ N-MORB) suggesting either higher degrees of melting or a mantle source that is more depleted than the typical N-MORB mantle. O/C-5-S4 has chondrite- and N-MORB normalized trace element patterns typical of IAT (see figure 5.2).

The second and third geochemical subgroups (subgroups 1b and 1c) consist of two samples each (figures 5.17c and 5.17d). These samples have flat chondrite normalized REE patterns with $(La/Yb)_n$ ratios ~ 1 (0.98 to 1.16) (figure 5.17c). The N-MORB normalized diagram shows that HREE in the second subgroup (O/C-1-S1 and O/C-356) are slightly depleted, LREE and Th are similar to N-MORB, while Ba is significantly enriched. Although Ba can be highly mobile and may have been redistributed during hydrothermal alteration, the Ba concentration could be primary because of the consistent enrichment in Ba in all samples from the sheeted dike complex. O/C-1-S1 and O/C-356 are neither depleted in Ta, Nb, Zr and Hf nor are they enriched in Th. The Th/Ta are similar to that of N-MORB and range from 1.1 -1.5. Obviously, the trace element characteristics of O/C-1-S1 and O/C-356 are more similar to N-MORB than to IAT (compare with figure 5.2), although high Ba suggests some arc signature. Also, O/C-1-S1 and O/C-356 plot in the tectonic discrimination diagrams within the N-MORB field (figures 5.16, 5.18).

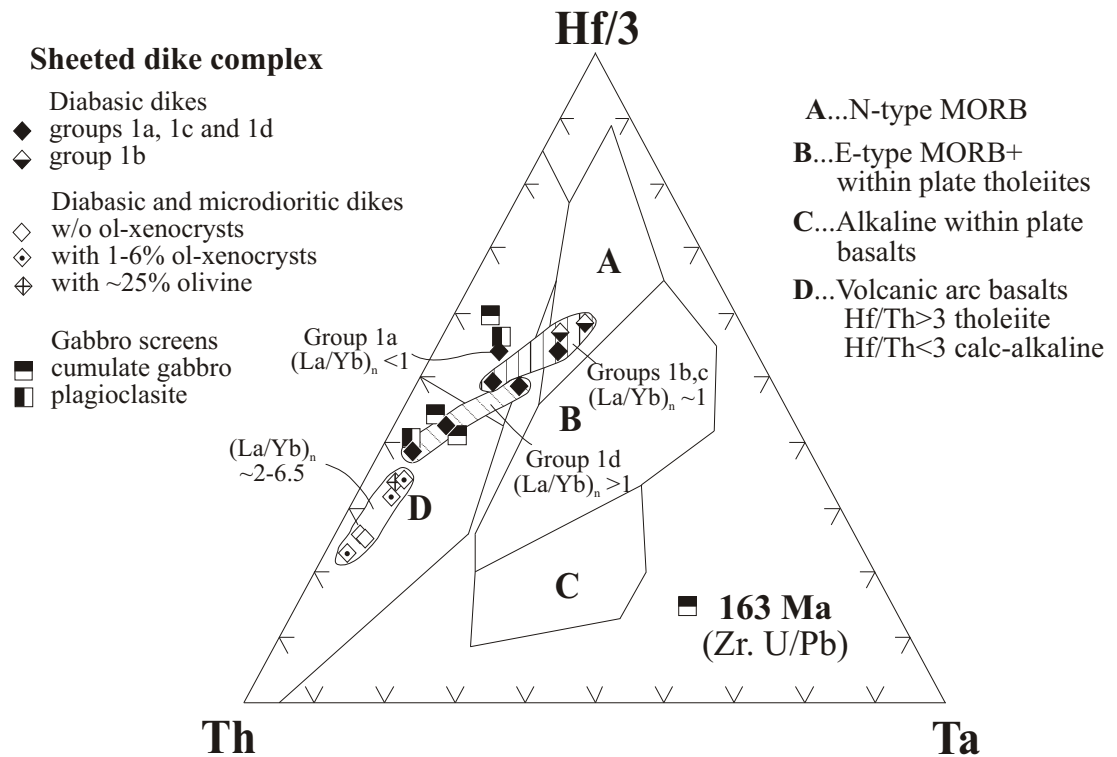


Figure 5.16

Hf/3-Th-Ta tectonic discrimination diagram with fields after Wood et al. (1979). The samples from the gabbro screens (cumulate gabbro and plagioclase) plot in the volcanic arc field. The dikes of geochemical group 1 plot in the field for N-MORB and IAT. The dikes of geochemical group 2 plot in the field for calc-alkaline rocks.

The N-MORB normalized patterns of O/C-1S1 and O/C-356 slope downwards from Th to Y. Note that the mantle-melt bulk distribution coefficients increase from Th to Y (section 5.4). The decreasing abundance from Th to Y can be explained with low degrees of melting of a N-MORB-like mantle because low degrees of melting results in relative enrichment of highly incompatible elements compared to less incompatible elements. Alternatively, the slope can be explained with high degrees of melting of a mantle source that is more enriched than the average N-MORB mantle.

O/C-333 and O/C-357b, defining subgroup 1c, also have flat REE patterns similar to O/C-1S1 and O/C-356 (figure 5.17c). However, the N-MORB normalized diagram (figure 5.17d) reveals relative depletion of Ta and Nb, and selective enrichment of Th and LILE. The Th/Ta ratios are higher than for subgroup 1b and range between 1.6 and 3.7. The N-MORB patterns of O/C-333 and O/C-357b are characteristic of IAT (compare with figure 5.2).

The fourth geochemical subgroup comprises three samples (O/C-1-S2, O/C-58, MRH-111; group 1d) which are slightly enriched in LREE. The $(La/Yb)_n$ ratios range from 1.32 to 1.58 (figure 5.17e). The N-MORB normalized trace element patterns of O/C-1-S2, O/C-58 and MRH-111 are somewhat similar to O/C-333 and O/C-357b (group 1c) and are characterized by relative depletion of Ta, Nb, Zr, and Hf and selective enrichment of Th and LILE (figure 5.13f). These patterns are typical of many volcanic arc basalts (see figure 5.2). However, O/C-1-S2, O/C-58 and MRH-111 are more enriched in LREE and have a higher range of $(La/Yb)_n$ and Th/Ta (2.4 - 12.1) ratios than O/C-333 and O/C-357b (figure 5.17d).

Further subdivision of the geochemical subgroups could be made based on other incompatible trace element ratios using immobile elements (e.g. Ta/Yb, Zr/Yb, Th/Yb). For example, samples O/C-357b and O/C-333 of group 1c differ significantly in their Th/Ta, Ta/Yb, Th/Yb, and Zr/Y ratios (variations are much larger than analytical uncertainty). Also, O/C-1-S2, O/C-58 and MRH-111 (group 1d) differ significantly in these ratios suggesting different parental magmas. Probably, none of the samples of geochemical group 1 are related by fractionation, and the variations in incompatible trace element ratios are due to source heterogeneity, variable amounts of (crustal?) contamination or magma mixing.

Almost all REE patterns (figures 5.17a, c and e) have a slight negative Ce-anomaly (greater than analytical uncertainty). The Ce-anomaly is characteristic of many arc related rocks and is thought to

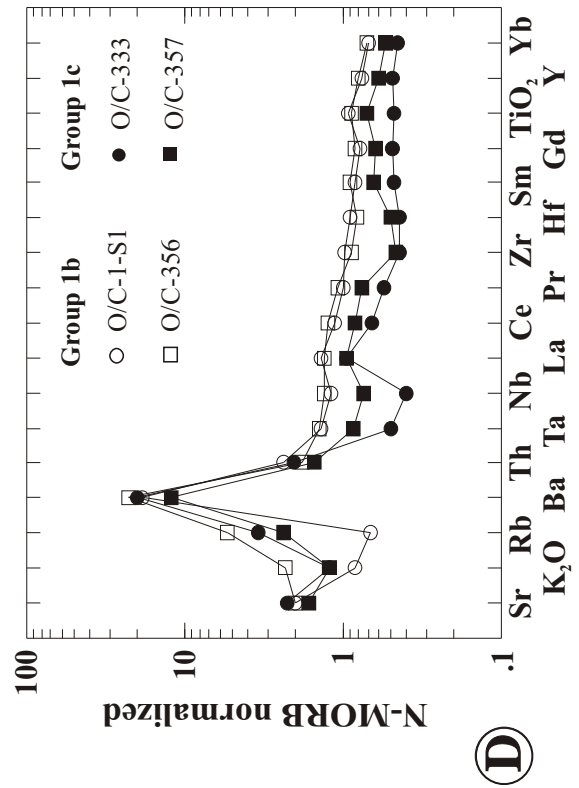
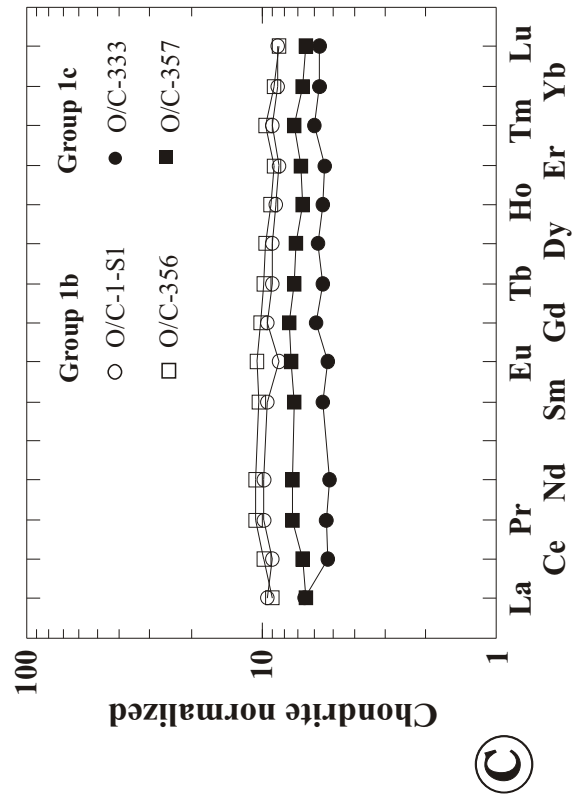
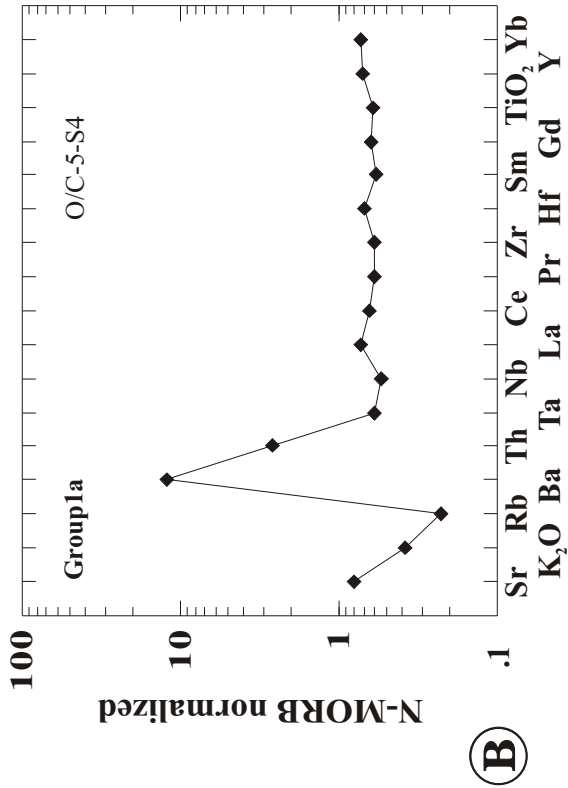
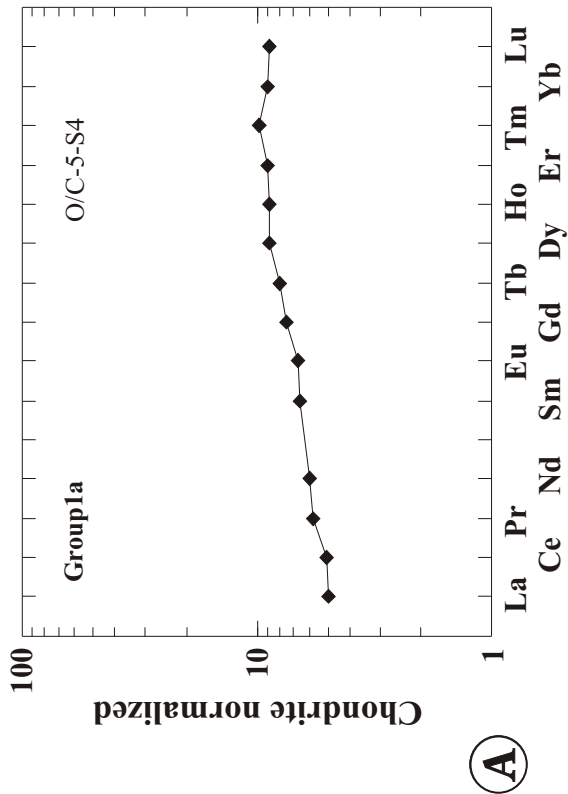
Figure 5.17

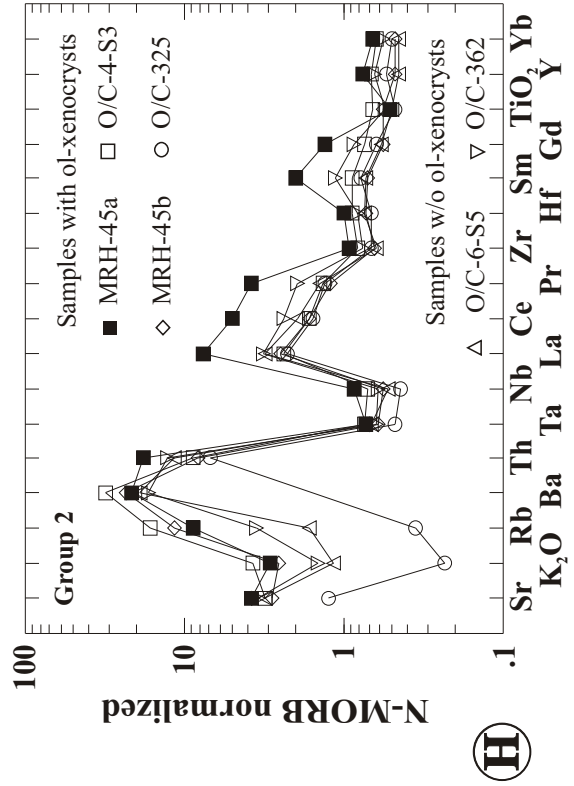
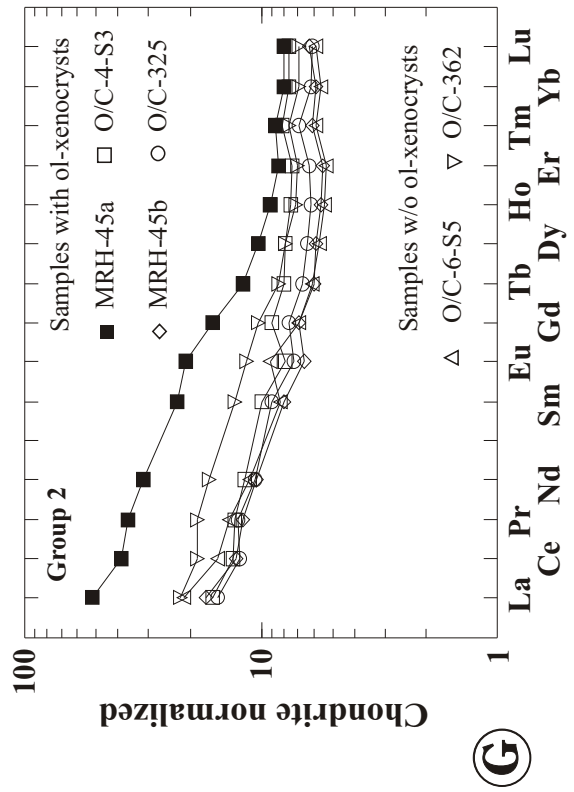
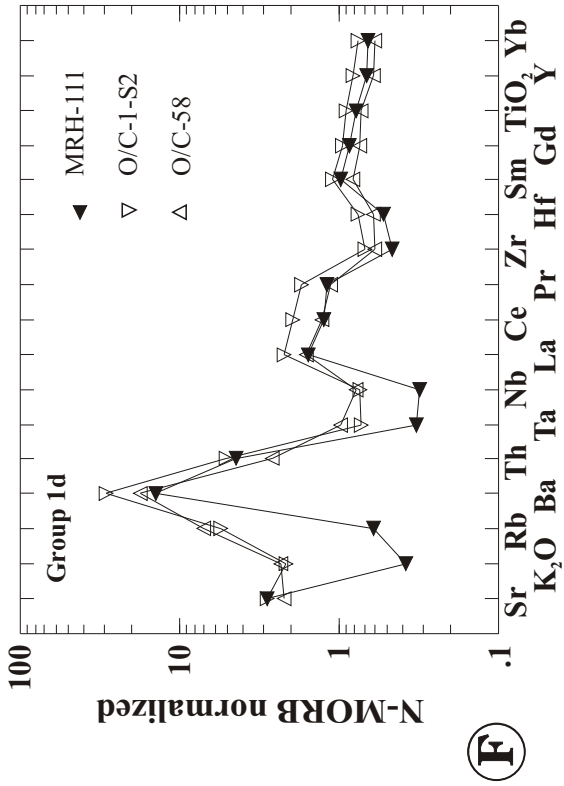
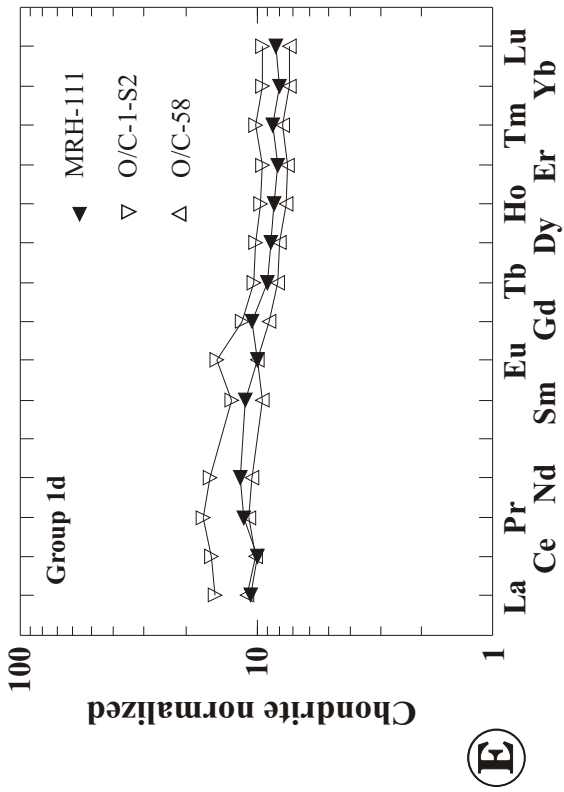
A - F: Chondrite and N-MORB normalized REE and trace element distribution diagrams of dikes of geochemical group 1. The REE patterns vary from LREE depleted (figure 5.17a) to flat (figure 5.17c) to slightly LREE enriched (figure 5.17e). Sample O/C-5-S4 has a $(La/Yb)_n$ ratio of 0.55. The ratios of samples O/C-1-S1, O/C-356, O/C-333 and O/C-357b range from 0.98 to 1.16, and of samples MRH-111, O/C-1-S2 and O/C-58 from 1.32 to 1.58.

Two distinct N-MORB normalized trace element variation diagrams are recognized. O/C-1-S1 and O/C-356 (subgroup 1b) are similar to N-MORB showing a pattern that gently slopes from Th to Yb. The patterns of the other dikes (subgroups 1a, 1c and 1d) are characterized by relative depletion of HFSE (e.g., negative Ta- and Nb- anomaly) and selective enrichment of LILE and Th, which is typical of IAT (see figure 5.2).

G - H: Chondrite and N-MORB normalized REE and trace element distribution diagrams of dikes of geochemical group 2. The dikes of group 2 are much more enriched in LREE ($(La/Yb)_n > 2$) than the dikes of group 1. However, similar to the dikes of group 1, $(La/Yb)_n$ ratios vary greatly ranging between 2.1 and 6.5.

The patterns in the N-MORB normalized diagram are characterized by very strong enrichment of LILE, Th and LREE, while Ta and Nb as well as Zr and Hf are depleted. The Ta/Yb ratios are similar to that of N-MORB whereas the levels of Ta and Nb are only 0.4 to 0.7 \times N-MORB. These are characteristics of CAB (see figure 5.2).





indicate a subduction contribution derived from pelagic sediments (e.g., Hole et al., 1984), but can also result from hydrothermal alteration (e.g., Ludden and Thompson, 1979).

The Hf/3-Th-Ta tectonic discrimination diagrams in figure 5.16 are largely independent of fractionation (e.g., Dudas, 1992), and these elements are generally 'immobile'. Samples of subgroup 1b (O/C-1-S1 and O/C-356) plot in the N-MORB field. The remaining dikes (subgroups 1a, 1c and 1d) plot in the arc field in the Th-Hf/3-Ta diagram, except O/C-333 which plots in the N-MORB field near the dikes of subgroup 1b. Apparently, the dikes of subgroup 1c are transitional between N-MORB and IAT. The dikes of subgroup 1d are transitional between IAT and calc-alkaline basalt.

The samples with N-MORB-like trace element patterns, O/C-1-S1 and O/C-356 (subgroup 1b), plot in the Cr vs. Y tectonic discrimination diagram of Pearce (1982) in the MORB field (half-filled diamonds, figure 5.18). The remaining samples of geochemical group 1 (subgroups 1a, 1c and 1d) plot well within the field for island arc basalts. The difference in Y concentrations between MORB-like and IAT-like dikes can be explained with higher degrees of melting or a more depleted mantle source.

5.5.4.2c Dikes of geochemical group 2

The chondrite- and N-MORB normalized trace element variation diagrams of dikes of geochemical group 2 are shown in figures 5.17g and 5.17h, respectively. These dikes have LREE enriched patterns and much higher $(La/Yb)_n$ ratios than dikes of geochemical group 1 (figures 5.17a, c, and e). The $(La/Yb)_n$ ratios of five dikes range between 2.09 and 3.82. Only MRH-45a has a significantly higher $(La/Yb)_n$ ratio of 6.49. The $(La/Yb)_n$ ratios and the amount of olivine xenocrysts (or SiO_2 and MgO) in the sample are not correlated.

The N-MORB normalized trace element patterns show that Th and LREE are highly enriched compared to the HFSE, and MREE are also notably enriched with respect to Zr, Hf, Y and HREE (figure 5.17h). The patterns in the N-MORB normalized trace element variation diagram in figure 5.17h are typical of rocks of the calc-alkaline series (compare with figure 5.2c). The negative TiO_2 -anomaly is probably due to fractionation of Fe-Ti oxides. This is consistent with the decrease of FeO^* and TiO_2 with MgO as shown in figures 5.13b and 5.13d.

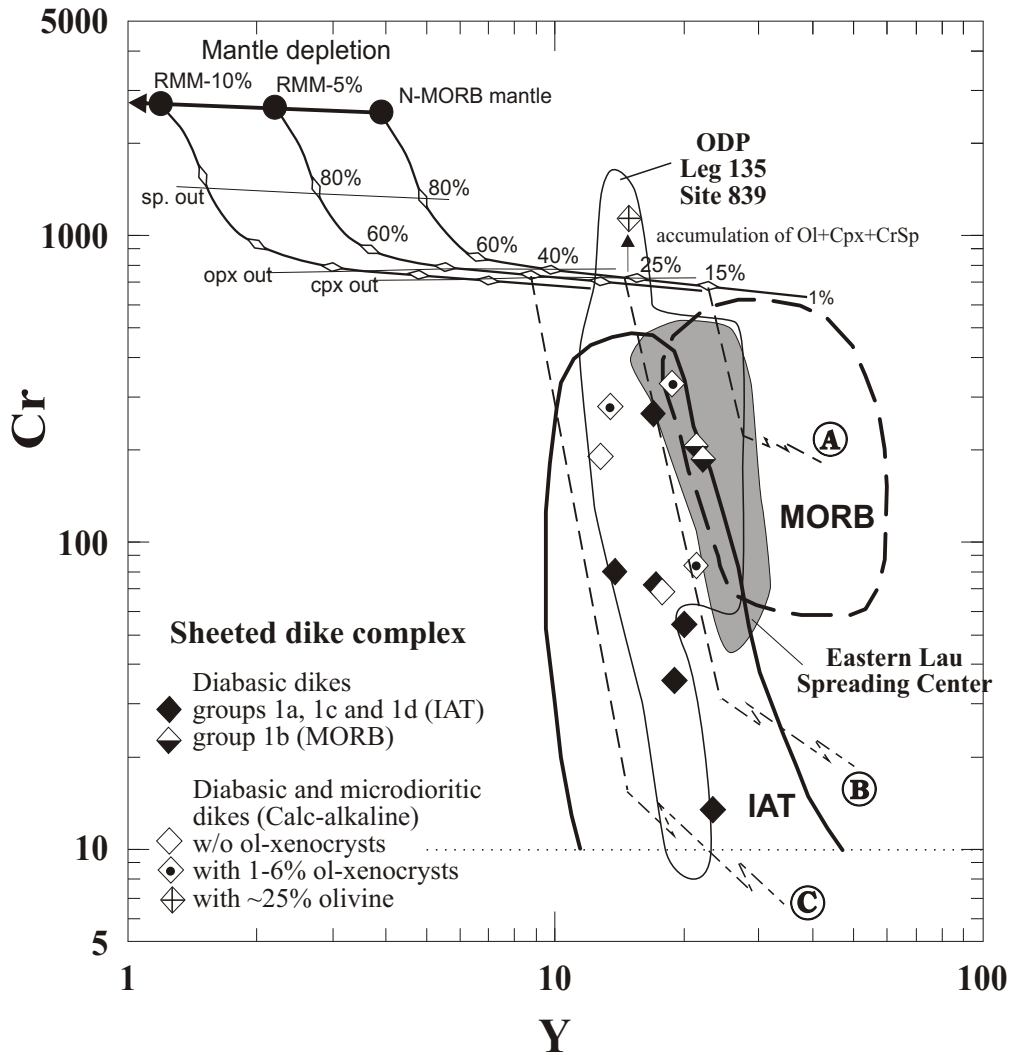


Figure 5.18

Cr vs. Y tectonic discrimination diagram of Pearce (1982) showing the fields for mid ocean ridge basalts (MORB) and island arc tholeiites (IAT) (the latter field also includes calc-alkaline and alkalic basalts from oceanic arcs). The modeled melting curves of the N-MORB mantle and the residual MORB mantle after 5% (RMM-5%) and 10% (RMM-10%) melt extraction are calculated as outlined in figure 5.4. The fractional crystallization trends for MORB (A), IAT (B) and boninite (C) are taken from Pearce et al. (1984a). The steep vector represents crystallization of olivine + Cr-spinel ± clinopyroxene, and the shallower vector represents crystallization of olivine + Cr-spinel + clinopyroxene + plagioclase. The dikes having trace element patterns similar to IAT and CAB have lower Y-contents than the dikes with N-MORB like patterns suggesting either higher degrees of partial melting or a more depleted mantle source.

Similar to the dikes of geochemical group 1, the REE patterns of dikes of group 2 show a Ce-anomaly suggesting a subduction contribution derived from pelagic sediments (Hole et al., 1984), or depletion of Ce could have occurred as a result of seafloor hydrothermal alteration. Also, the chondrite and N-MORB-normalized REE and trace element distribution patterns cross each other, and the $(La/Yb)_n$ and Th/Ta ratios differ between samples suggesting that the dikes of group 2 are not related by crystal fractionation. The heterogeneous distribution of olivine xenocrysts indicates that magma mixing could have occurred.

The dikes of geochemical group 2 plot in the Hf/3-Th-Ta tectonic discrimination diagram within the calc-alkaline field (figure 5.16). This is consistent with the interpretation of the N-MORB normalized trace element patterns (figure 5.17h). Note that the dikes of geochemical group 2 plot in the same field in the Hf/3-Th-Ta tectonic discrimination diagram as the samples from the metatonalite unit (figure 5.5). Also, the REE pattern of sample MRH-45a (figure 5.17h) is very similar to that of the deformed dike (O/C-11-S16b) and the enclave (O/C-368f) in the metatonalite unit (figure 5.8d), except that samples O/C-11-S16b and O/C-368f have a strong negative Eu-anomaly, and MRH-45a has a slightly positive Eu-anomaly. A number of incompatible trace element ratios, such as La/Yb, Th/Yb, Ta/Yb, and Zr/Y, of dikes of petrographic group 2 differ from O/C-11-S16b and O/C-368f suggesting that the deformed dike and enclave in the metatonalite unit and the dikes of petrographic group 2 are not related by fractionation.

Although the calc-alkaline dikes (group 2) are andesitic in composition based on their SiO₂ content, the Zr/TiO₂ ratios are very low (figure 5.14) and the Cr concentrations are very high (figure 5.18) for andesites. The olivine pseudomorphs in the dikes of group 2 have inclusions of euhedral Cr-spinel. The Cr content is positively correlated with the amount of olivine xenocrysts in the sample. For example, O/C-325 contains ~25% olivine xenocrysts and has a Cr content of >1000 ppm (figure 5.18). Probably, the Cr-concentration in most samples of petrographic group 2 does not reflect the amount of fractionation, but indicates the amount of mixing or accumulation of olivine xenocrysts. The samples of group 2 plot similar to samples of group 1 in the island arc field with Y < 25 ppm, but have, in general, higher Cr-contents.

5.5.4.3 Chromian Spinel in dikes of geochemical group 2

Cr-spinel is widely used as a petrogenetic indicator of the environment of crystallization (e.g., Dick and Bullen, 1984; Allan, 1994, Clynne and Borg, 1997). The composition of Cr-spinel in igneous rocks is variable and correlates with the major element composition of co-existing primitive liquids (Dick and Bullen, 1984). A strong correlation exists between the Cr# of spinel and modal mineralogy of the host peridotite (for residual peridotites) suggesting that the composition of Cr-spinel may be used as an indicator of partial melting (Dick and Bullen, 1984) and source fertility (Fujii, 1989; Clynne and Borg, 1997). Also, Cr-spinel is a liquidus phase in many primitive basaltic melts, and its composition can be used to determine the Mg# of the primitive melt (Allan, 1994; Forsythe and Fisk, 1994).

Three samples from the sheeted dike complex containing Cr-spinel were analyzed (O/C-4-S3, MRH-45a, O/C-325). The majority of Cr-spinels occur as inclusions within olivine xenocrysts in these dikes. Only very few Cr-spinels were found in the matrix. O/C-325 has in addition to ~25% deformed and replaced olivine phenocrysts (or xenocrysts?) about 1% relict clinopyroxene phenocrysts containing Cr-spinels. Relict cpx does not occur in any other dikes from the sheeted dike complex. The analytical data of Cr-spinel from the sheeted dike complex are listed in appendix C (table C6). Fe^{2+} and Fe^{3+} were calculated by cation normalization to 3 cations per 4 oxygens. The Mg# [$100 \cdot \text{Mg}/(\text{Mg} + \text{Fe}^{2+})$] of Cr-spinel in group 2 dikes is highly variable (1.7-75.0), while the Cr# [$100 \cdot \text{Cr}/(\text{Cr} + \text{Al})$] is fairly constant (71.4 - 80.7) (figure 5.19). In general, translucent, dark brown Cr-spinel have Mg# ranging between ~ 45 - 75.

Chromites which have opaque rims, are completely opaque in thin section, and/or appear mottled in backscattered images have Mg# lower than ~ 45 (appendix C). This indicates that Cr-spinel gained FeO in exchange for MgO during hydrothermal alteration. The Cr# of altered vs. unaltered Cr-spinel is unchanged, indicating that the Cr# is not affected by alteration. The analyses in figure 5.19 were screened so that only unaltered Cr-spinels are plotted. However, the extent of the variations of the Mg# due to fractionation/re-equilibration and alteration is not known.

Differences in the Cr# between Cr-spinel trapped in olivine xenocrysts and Cr-spinel in the matrix are not observed, but the Mg# of Cr-spinel within olivine xenocrysts is higher than of Cr-spinel in the matrix for samples O/C-4-S3 (Mg# = 67.2 and 43.9) and MRH-45a (Mg# = 63.9 and 59.2). Furthermore,

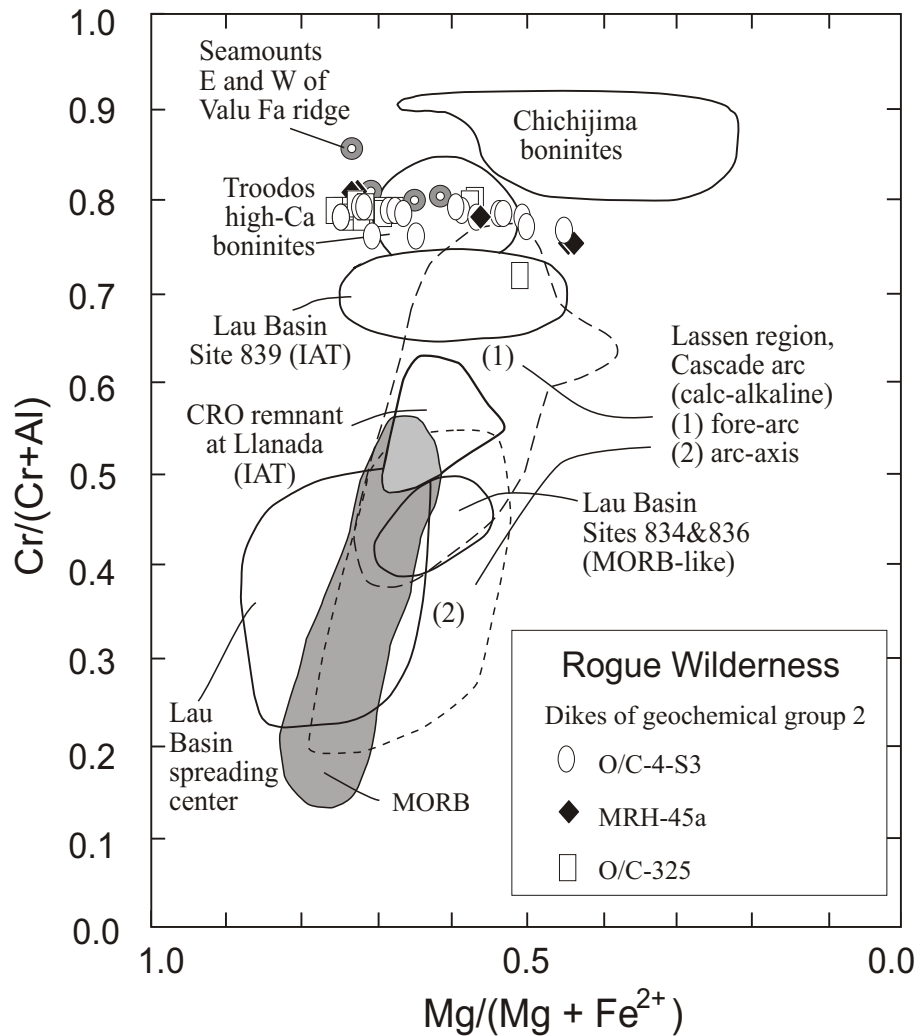


Figure 5.19

Comparison of the composition of Cr-spinel in dikes of geochemical group 2 (sheeted dike complex) with chromites from modern island arcs, the Troodos ophiolite, and the Coast Range ophiolite (CRO remnant at Llanada). The fields for Chichijima, Troodos, and the Lau Basin are from Meffre et al. (1996), for MORB from Dick and Bullen (1984), for the Coast Range ophiolite remnant at Llanada from Giaramita et al. (1998), and for the Cascade arc from Clynne and Borg (1997).

Cr-spinels in relict clinopyroxene in O/C-325 have slightly lower Cr/(Cr+Al) ratios (Cr# = 74.5) and lower Mg# (Mg# = 50.9) than Cr-spinel in olivine phenocrysts (Cr# = 78.5, Mg# = 69.3).

The Cr/(Cr+Al) ratios of Cr-spinel in samples from the sheeted dike complex are significantly higher than those of chromites from MORB and basalts from the Lau Spreading Centers (figure 5.19). The Cr/(Cr+Al) ratios are similar to Cr-spinels occurring in high-Ca boninites in the Troodos ophiolite (Cameron, 1985) and slightly higher than in island arc tholeiites in the Lau Basin (Site 839) as well as slightly higher than in calc-alkaline volcanic rocks from the Mt. Lassen region in California (Clynne and Borg, 1997). The Cr-spinel bearing dikes from the sheeted dike complex have magmatic affinities to CAB (figure 5.16) but contain Cr-spinel with Cr/(Cr+Al) ratios typical of high-Ca boninites suggesting magma mixing.

5.5.4.4 Element mobility

Based on the Zr/TiO₂ vs. Nb/Y rock classification, the sheeted dike samples are subalkaline basalts (figure 5.14). However, based on the SiO₂-content, group 1 consists of basalts and basaltic andesites, and group 2 of basaltic andesites and andesites. There appears to be a discrepancy between the rock classification based on the silica content (TAS) and the rock classification using immobile trace elements (figure 5.14). Perhaps, SiO₂ has been added as a result of hydrothermal metamorphism. Also, MgO is often very mobile in subseafloor hydrothermal alteration (e.g., Mottl, 1983). Thus, the problem of element mobility needs to be addressed. Both groups of dikes contain the same metamorphic assemblages: pyroxene is replaced by amph ± mt and plagioclase by ab + cz. Also, the samples are carefully selected for the geochemical analysis; they are essentially free of veins (i.e., no retrograde alteration).

Based on the following lines of evidence, I suggest that redistribution of major elements may have been insignificant in samples from the sheeted dike complex: (1) The relative good correlation between Al₂O₃ and MgO for both groups of dikes (figure 5.13c) implies that MgO is conserved. (2) CaO and Na₂O are correlated with MgO (figures 5.13f and 5.13g) suggesting these elements are immobile. For example, albitization of calcic plagioclase (Ca-plagioclase → albite + quartz + Ca²⁺) would result in substantial scatter of the data and destroy the correlation in diagrams of CaO vs. MgO and Na₂O vs. MgO. (3) The

linear trends for the cumulate gabbro samples in figure 5.13 suggest that element mobility in the gabbro screens was insignificant. (4) LILE (Sr, K₂O, Rb, and Ba) have consistent patterns in the N-MORB normalized diagrams (figure 5.15 and 5.17) suggesting these elements were immobile. (5) A comparison with the lower sheeted dikes of the Josephine ophiolite is helpful evaluating possible element mobility. The amphibolite facies assemblages (amph + plag + mt) in the lower sheeted dikes of the Josephine ophiolite are constrained to have formed by hydrothermal metamorphism at low water/rock ratios (Harper et al., 1988; Alexander et al., 1993). The linear trends in MgO variation diagrams formed by the samples from the lower sheeted dikes of the Josephine ophiolite indicate that redistribution of “mobile” elements was insignificant. These linear trends are constrained to reflect primary variations (Harper, in review). It is likely that the conditions of hydrothermal metamorphism in the sheeted dike complex of the Rogue Wilderness ophiolite were very similar to the lower sheeted dikes of the Josephine ophiolite, because of similar levels of the ophiolite pseudostratigraphy and similar metamorphic assemblages and replacement textures. Thus, extensive redistribution of “mobile” elements (away from epidosite zones) is not likely in the sheeted dike complex of the Rogue Wilderness ophiolite.

Unfortunately, the element mobility cannot be independently evaluated by plotting “mobile” elements against an “immobile” element, such as Zr, because the samples from the sheeted dike complex are from different magmatic suites and differ greatly in their incompatible trace element compositions (section 5.5.4.2). Thus, the poor correlation of MgO or SiO₂ with Zr (not shown) is most likely related to differences in the primary composition of the samples rather than mobility of MgO or SiO₂. Also, one cannot determine with existing data whether or not SiO₂ has been added as a result of hydrothermal metamorphism. However, the differences in the SiO₂-contents (figure 5.13a) probably reflect primary differences between the dikes of group 1 and group 2, because dikes of group 2 have igneous quartz and dikes of group 1 contain no quartz.

5.5.4.5 Petrogenesis

5.5.4.5a Crystal Fractionation

Two geochemical groups have been identified based on immobile trace elements: (1) dikes with geochemical characteristics ranging between IAT and N-MORB; and (2) dikes with geochemical characteristics similar to CAB. Obviously the dikes are not related by crystal fractionation. However it is possible that the samples of geochemical group 1 were derived from “similar” parental magmas (i.e., the parental magmas are slightly different in trace element composition but similar in major element composition) and evolved along similar (parallel) liquid lines of descent. The same could be true for dikes of geochemical group 2.

Although the major element data scatter, both geochemical groups of dikes as well as the gabbro screens define distinct trends in the MgO variation diagrams. The scatter in the data could be related to differences in the primary composition rather than element mobility (section 5.5.4.3). The dikes of geochemical group 1 indicate trends of increasing SiO₂, TiO₂, FeO*, Na₂O, and Al₂O₃ (Al₂O₃ stays almost constant with fractionation) with decreasing MgO (figures 5.13a, b, c, d, and g), while CaO and MnO decrease with decreasing MgO (figure 5.13e and f). These trends fall within the fields of lavas and volcanic glass grains from the ELSC and ODP site 839. The dikes of geochemical group 1 have significantly higher SiO₂ and Al₂O₃, and lower FeO* and TiO₂ (TiO₂ < 1.2%), than N-MORB. Also, SiO₂ in the dikes of geochemical group 1 increases much faster with increasing FeO*/MgO (a fractionation index) than N-MORB (figure 5.13j). On one hand, the SiO₂, MgO and FeO* concentrations could have been modified as a result of hydrothermal alteration, and the major element composition may not reflect the magmatic affinity. For example, MRH-111 plots well outside of the trend defined by the samples of geochemical group 1, indicating that MRH-111 may have gained FeO*, MgO, and P₂O₅ (usually immobile) partly in exchange for CaO. On the other hand, low TiO₂- and high Al₂O₃-contents compared to N-MORB are probably primary because TiO₂ and Al₂O₃ are ‘immobile’.

Although the dikes of geochemical group 1 are altered, the major element composition is very similar to lavas recovered in the Lau Basin, SW Pacific (figure 5.13). The lavas and volcanic glass grains recovered at Site 839 have magmatic affinities to island arc tholeiite (Ewart et al., 1994; Hawkins and

Allan, 1994), while lavas from the ELSC have magmatic affinities more similar to N-MORB (Hawkins, 1995). Many lavas from the ELSC have compositions transitional between N-MORB and IAT (Pearce et al., 1995b). Compared to N-MORB, site 839 lavas have significantly higher SiO_2 - and Al_2O_3 -, and lower TiO_2 - and FeO^* - contents. Al_2O_3 increases to a point of inflection at $\text{MgO} = 4.5\%$ which marks the point of plagioclase fractionation. In contrast, Al_2O_3 in N-MORB decreases continually because plagioclase starts to crystallize much earlier. Also, TiO_2 and FeO^* in lavas from site 839 are displaced to lower concentrations than N-MORB, indicating early crystallization of Fe-Ti-oxides. Similarly, lavas from the ELSC have higher Al_2O_3 and lower TiO_2 and FeO^* compared to N-MORB (figure 5.13). The trends of TiO_2 and FeO^* are similar in shape to those of N-MORB but displaced towards lower concentrations at a given MgO content. High Al_2O_3 and/or a trend of increasing Al_2O_3 with decreasing MgO is characteristic of volcanic arc basalts and can be related to elevated H_2O contents which delays crystallization of plagioclase (Sisson and Grove, 1993a, 1993b; Stolper and Newman, 1994). Similar to the lavas from the ELSC and ODP site 839, the trend on Al_2O_3 vs. MgO (figure 5.13c) defined by the dikes of geochemical group 1 can be explained by delayed fractionation of plagioclase suggesting high primary H_2O content of the magmas.

The dikes of geochemical group 2 in the sheeted dike complex define trends in the MgO variation diagrams that are clearly distinct from the dikes of geochemical group 1 (figure 5.13a, b, c, d, and f). As shown in figure 5.13, the deformed dike in the metatonalite unit (O/C-11-S16b) generally falls on the trends defined by group 2. Also, the enclave in metatonalite (O/C-368f) and the other samples from the metatonalite unit plot in most MgO variation diagrams on an extension of the trend defined by the dikes of geochemical group 2. It appears that the samples from the metatonalite unit lie on the continuation of the liquid line of descent of dikes of geochemical group 2 (figures 5.13a, b, c, d, e, f, and g). The most primitive sample of the dikes of group 2 (O/C-4-S3) plots in the field of primitive calc-alkaline basalts (0.07-1.27 Ma) from the Lassen region, California. These fresh, primitive calc-alkaline basalts contain olivine and Cr-spinel phenocrysts, have relatively high MgO contents (7-10%) as well as high SiO_2 (54-58%) and high Sr/P ratios (Borg et al., 1997). The microdioritic dikes could have evolved from a magma similar to the calc-alkaline basalts from the Lassen region.

Compared to group 1, SiO₂-contents of dikes of group 2 are higher and Al₂O₃-contents are lower (figures 5.13a and 5.13c). However, Al₂O₃ in dikes of group 2 increases more steeply with decreasing MgO than in dikes of group 1. An important characteristic of dikes of geochemical group 2 is that the trends of FeO* and TiO₂ are not parallel to the tholeiitic trends in figures 5.13b and 5.13d. FeO* and TiO₂ do not increase to a point of inflection but decrease continually with increasing MgO, which is typical of calc-alkaline trends, suggesting even earlier crystallization and fractionation of Fe-Ti oxides.

Overall, the dikes from the sheeted dike complex of the Rogue Wilderness ophiolite appear to evolve along two different fractionation trends. The first trend is defined by the dikes of geochemical group 1 and is characterized by increasing or constant TiO₂ and FeO* with fractionation (figure 5.13b and 5.13d). SiO₂ increases little with decreasing MgO, and on a plot of FeO*/MgO vs. SiO₂ (figure 5.13j), the dikes of petrographic group 1 form a trend that crosses the tholeiite / calc-alkaline discriminant line of Miyashiro (1974). Thus, the first trend can be referred to as tholeiitic because FeO*/MgO and TiO₂ rise with decreasing MgO with relatively slight increase in SiO₂.

The second trend is defined by the dikes of geochemical group 2 and appears to be aligned with the trend of samples from the metatonalite unit. Al₂O₃ in group 2 dikes appears to increase with fractionation to an inferred point of inflection at about 4% MgO, and then decreases in the samples from the metatonalite unit (figure 5.13c). In contrast to group 1, TiO₂ and FeO* in dikes of group 2 decrease with fractionation (figures 5.13b and 5.13d), and the FeO/MgO* values increase much less with increasing SiO₂ (figure 5.13j). Also, the deformed dike (O/C-11-S16b) and the enclave (O/C-368f) in the metatonalite unit plot within the calc-alkaline field of Miyashiro (1974). Clearly, the samples of petrographic group 2 and the samples from the metatonalite unit define a calc-alkaline differentiation trend.

The trends defined by the samples of geochemical group 2 do not intercept the line along which the cumulate gabbro samples O/C-358, O/C-360 and GH-97-23 plot (line between plagioclase and mafic mineral assemblage; figure 5.13). In contrast, the trends defined by the samples of geochemical group 1 intercept this line in all MgO variation diagrams. This indicates that the cumulate gabbro could not have formed by fractionation of a magma similar in composition to dikes of geochemical group 1. The

composition of the cumulate gabbro is consistent with accumulation of crystals from fractionation of a tholeiitic parent magma similar to that for group 1 dikes.

5.5.4.5b Source heterogeneity and magma mixing

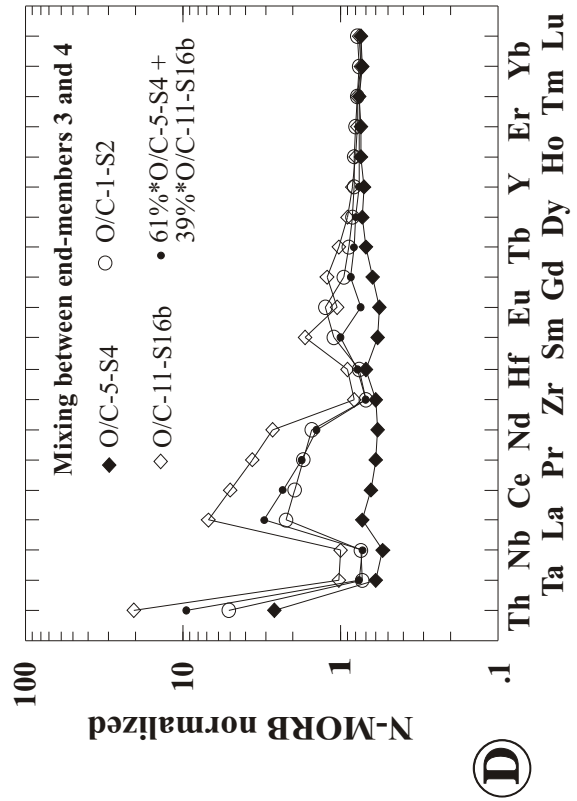
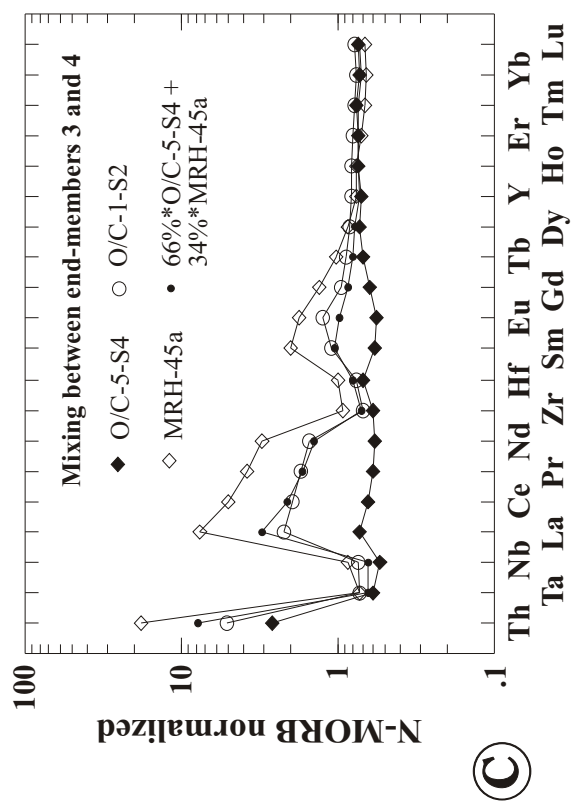
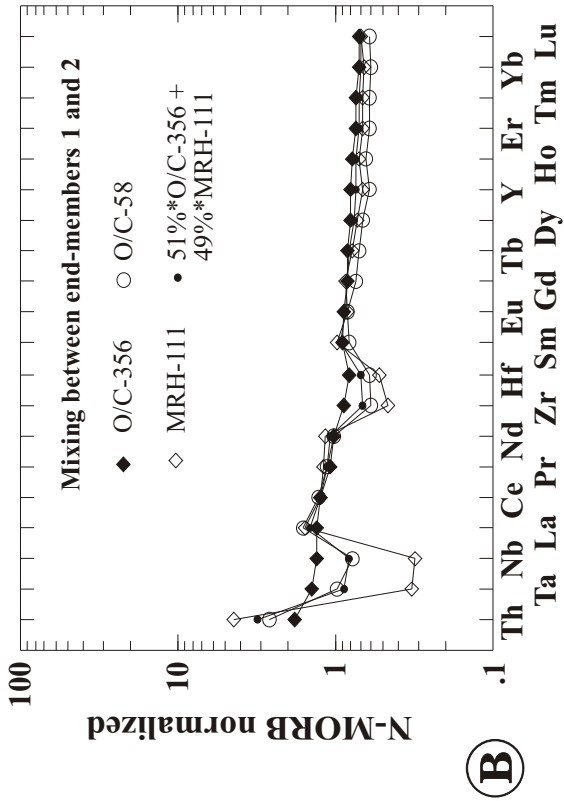
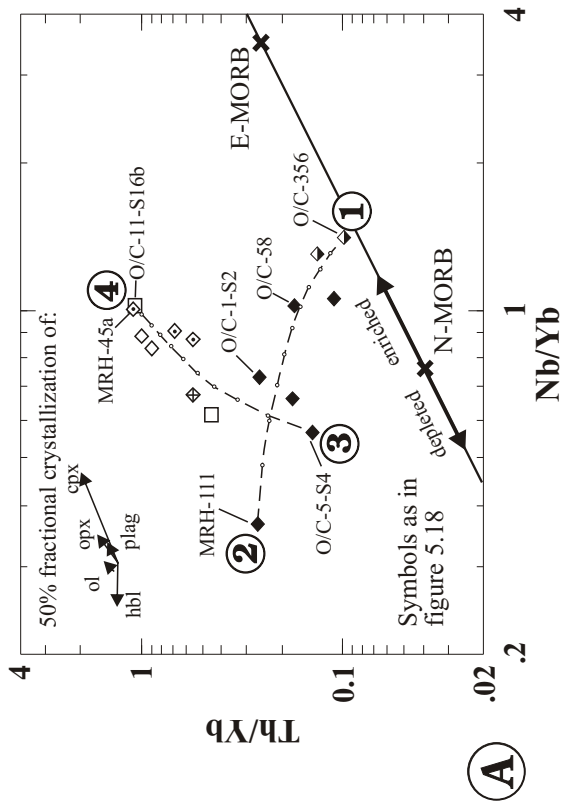
The N-MORB normalized trace element patterns show that the dikes of geochemical groups 1 and 2 have distinct negative Ta- and Nb - anomalies and variable enrichment of Th, LILE and LREE (figure 5.17). The variations of the incompatible trace element ratios is discussed using the Th/Nb ratio as an example to show that the differences in these patterns cannot be explained with crystal fractionation implying different sources. In order to evaluate the Th/Nb ratios in dikes of geochemical groups 1 and 2, it is useful to normalize Th and Nb to Yb, because Yb varies the least (figure 5.17).

The Nb/Yb ratios in dikes of geochemical group 1 decrease with little increase of the Th/Yb ratios (figure 5.20a). In contrast, the Nb/Yb ratios in dikes of geochemical group 2 increase with increasing Th/Yb ratios. Note that the deformed dike (O/C-11-S16b) and the enclave (O/C-368f) in the metatonalite unit lie on the trend defined by the dikes of geochemical group 2. For reference, the variations of the Th/Yb and Nb/Yb ratios in MORB are shown in figure 5.20a. The variations of the Th/Yb and Nb/Yb ratios observed for both groups of dikes and the samples from the metatonalite unit are much larger than the length of any of the vectors for 50% fractional crystallization of cpx, opx, ol, hbl, and plag. Clearly, these variations cannot be explained with crystal fractionation. Also, most of the compositional differences cannot be explained by variable degrees of melting of a homogenous mantle source.

The model shown in figure 5.20a postulates four different mantle sources in order to explain the range of trace element compositions observed in the sheeted dikes. According to this model, partial melting of mantle source 1 produces magmas with flat REE patterns (figure 5.17c) and MORB-like Th/Yb ratios (group 1b; figure 5.17d). In the Th/Yb vs. Nb/Yb diagram (figure 5.20a), source 1 magmas are intermediate in composition between N-MORB and E-MORB. Partial melting of source 2 produces magmas which are slightly LREE enriched (figure 5.17e), strongly depleted in Ta and Nb (MRH-111; figure 5.17f), and have three times higher Th/Yb ratios than magmas from source 1 (figure 5.20a). The mixing of magma 1 (O/C-356) with magma 2 (MRH-111) in proportions of 51:49 results in a new

Figure 5.20

- A. Plot of Th/Yb vs. Nb/Yb for samples from the sheeted dike complex and metatonalite unit. The solid line indicates the variations of the Th/Yb and Nb/Yb ratios in MORB (from Pearce, 1982; Pearce and Peate, 1995; Pearce et al., 1995a, Pearce and Parkinson, 1993). The crosses on that line give the normalizing values for N-MORB and E-MORB. Also, the mantle depletion and enrichment trends relative to N-MORB are shown. Mixing of magmas derived by partial melting of four different mantle sources can explain the range of trace element compositions observed in dikes of geochemical group 1 (half-filled and solid diamonds) and dikes of geochemical group 2 (empty diamonds) from the sheeted dike complex as well as the deformed dike (O/C-11-S16b) and the enclave (O/C-368f) from the metatonalite unit (empty squares). The broken lines indicate the mixing curves between the different magmas.
- B. Mixing of O/C-356 (end member 1) and MRH-111 (end member 2) results in a composition similar to O/C-58.
- C. Mixing of O/C-5-S4 (end member 3) and MRH-45a (end member 4) results in a composition similar to O/C-1-S2.
- D. Mixing of O/C-5-S4 (end member 3) and O/C-11-S16b (end member 4) results in a composition similar to O/C-1-S2.



composition which is remarkably similar to O/C-58 (figure 5.20b). However, any mixture of magma 1 (flat REE pattern) and magma 2 (slightly LREE enriched) will differ in composition from O/C-5-S4, because the mixture will be LREE enriched and O/C-5-S4 is LREE depleted (figure 5.17a). Therefore, O/C-5-S4 is thought to represent the composition of the magma produced by partial melting of source 3. The fourth end member composition could be the deformed dike (O/C-11-S16b) in the metatonalite unit or MRH-45a from the sheeted dike complex (figure 5.19), because these samples have very similar Th/Yb and La/Yb ratios (see figures 5.8 and 5.17). Mixing of magma 3 (O/C-5-S4) and magma 4 (MRH-45a) in proportions of 66:34 results in a composition similar to O/C-1-S2 (figure 5.20c). Also, mixing of O/C-5-S4 and O/C-11-S16b in proportions of 61:39 produces a similar result (figure 5.20d). Mixing of end members 3 and 4 seems to be a good model, because it can explain the complete range of chondrite normalized REE patterns of samples from the sheeted dike complex (and perhaps the metatonalite unit) ranging from LREE-depleted (figure 5.17a) to slightly LREE enriched (figure 5.17e) to strongly LREE enriched patterns (figure 5.17g).

The presented mixing model is not unique because of the large range of trace element compositions of samples from the sheeted dike complex. However, this model explains the trace element compositions of most samples using the fewest possible end members. Also these models clearly show that magma mixing could have occurred in crustal magma chambers before intrusion of the dikes.

Further evidence for magma mixing comes from the analyses of Cr-spinels found in olivine-xenocryst bearing dikes (figure 5.19). Note that olivine xenocrysts are often very heterogeneously distributed in the dikes of geochemical group 2 (chapter 2). The high Cr/(Cr+Al) ratios of Cr-spinels indicate that high-Ca boninitic magmas were present at or near the ridge axis and mixed with calc-alkaline magmas.

5.5.5 Pillow unit

5.5.5.1 Rock classification

The localities of samples from the pillow unit are shown in figure 5.1, the analytical data are listed in table 5.4, and the petrographic data are listed in appendix A (table A4). The analyzed samples of pillows

Table 5.4: Major and trace element composition of samples from the pillow unit

| Sample | O/C-113 diab. dike | O/C-186 diab. dike | O/C-224 pillow | O/C-227a pillow | O/C-227b diab. dike |
|--------------------------------|-----------------------|-----------------------|-------------------|--------------------|------------------------|
| SiO ₂ | 53.81 | 55.54 | 53.82 | 53.69 | 54.04 |
| TiO ₂ | 0.51 | 1.06 | 0.74 | 0.79 | 0.96 |
| Al ₂ O ₃ | 14.78 | 13.94 | 15.64 | 14.49 | 13.61 |
| Fe ₂ O ₃ | 9.99 | 12.28 | 10.97 | 9.98 | 13.29 |
| MnO | 0.17 | 0.18 | 0.17 | 0.19 | 0.18 |
| MgO | 4.03 | 4.06 | 4.83 | 4.57 | 4.33 |
| CaO | 12.40 | 5.12 | 6.58 | 8.40 | 6.95 |
| Na ₂ O | 2.21 | 5.60 | 5.35 | 3.30 | 3.58 |
| K ₂ O | 0.26 | 0.15 | 0.11 | 0.41 | 0.29 |
| P ₂ O ₅ | 0.07 | 0.12 | 0.07 | 0.09 | 0.08 |
| BaO | 81 | 36 | 120 | 125 | 130 |
| Cr ₂ O ₃ | 89 | 29 | 62 | 36 | 57 |
| LOI | 2.01 | 2.14 | 2.06 | 4.52 | 3.24 |
| Total | 100.28 | 100.23 | 100.41 | 100.47 | 100.61 |
| Ni | 27 | 11 | 25 | 14 | 15 |
| Sc xrf/icp | 37/n.d. | 38/n.d. | 35/n.d. | 37/n.d. | 42/n.d. |
| V xrf/icp | 261/277 | 307/375 | 366/387 | 223/263 | 353/428 |

| Sample | O/C-379 pillow | O/C-380 pillow | Pb-1 pillow | O/C-231a rhyol. dike |
|--------------------------------|-------------------|-------------------|----------------|-------------------------|
| SiO ₂ | 57.65 | 56.15 | 54.50 | 78.08 |
| TiO ₂ | 1.06 | 0.90 | 0.85 | 0.26 |
| Al ₂ O ₃ | 13.49 | 14.46 | 14.05 | 12.09 |
| Fe ₂ O ₃ | 11.50 | 12.09 | 13.52 | 0.89 |
| MnO | 0.18 | 0.16 | 0.19 | 0.01 |
| MgO | 3.02 | 2.66 | 4.73 | 0.32 |
| CaO | 5.54 | 3.10 | 5.52 | 0.78 |
| Na ₂ O | 5.34 | 5.90 | 5.05 | 6.48 |
| K ₂ O | 0.04 | 0.04 | 0.05 | 0.14 |
| P ₂ O ₅ | 0.11 | 0.08 | 0.08 | 0.05 |
| BaO | 98 | 122 | 106 | 29 |
| Cr ₂ O ₃ | 24 | 17 | 39 | 47 |
| LOI | 2.17 | 4.22 | 1.98 | 0.72 |
| Total | 100.15 | 99.80 | 100.58 | 99.85 |
| Ni | 4 | <d/l | 12 | 6 |
| Sc xrf/icp | 22/n.d. | 37/n.d. | 19/n.d. | 16/11.6 |
| V xrf/icp | 306/312 | 166/167 | 284/312 | 11/n.d. |

Major elements (in wt%) and Ba, Cr, Ni, Sc, and V (in ppm) were analyzed by standard XRF technique on pressed powder pellets at McGill University, Montreal. Additionally, Sc was analyzed by ICP-MS at Washington State University and V at Union College

Table 5.4 cont.

| Sample | O/C-113 | O/C-186 | O/C-224 | O/C-227a | O/C-227b | O/C-379 | O/C-380 | Pb-1 | O/C-231a |
|--------|---------|---------|---------|----------|----------|---------|---------|-------|----------|
| | UC | UC | UC | UC | UC | UC | UC | UC | WSU |
| Cr | 53.5 | 18.0 | 42.5 | 27.0 | 32.5 | 9.7 | 8.0 | 19.9 | n.d. |
| Rb | 3.87 | 0.74 | 0.84 | 5.38 | 3.98 | 0.20 | 0.19 | 0.42 | 1.58 |
| Sr | 163 | 87 | 161 | 179 | 169 | 58 | 61 | 61 | 58.65 |
| Y | 13.4 | 28.8 | 17.5 | 19.2 | 22.9 | 25.5 | 32.1 | 21.0 | 30.33 |
| Zr | 30.8 | 68.4 | 30.0 | 49.4 | 45.4 | 57.6 | 35.5 | 40.4 | 86.25 |
| Nb | 0.61 | 1.62 | 0.83 | 1.39 | 0.68 | 1.29 | 0.64 | 0.69 | 1.16 |
| Cs | 0.07 | 0.02 | 0.10 | 0.76 | 0.32 | 0.05 | 0.05 | 0.02 | 0.06 |
| Ba | 62.5 | 38.7 | 46.7 | 99.2 | 74.7 | 24.0 | 28.7 | 22.6 | 45.41 |
| La | 2.14 | 3.35 | 2.13 | 2.90 | 2.15 | 3.16 | 1.84 | 1.93 | 3.51 |
| Ce | 5.17 | 8.99 | 5.29 | 7.19 | 5.59 | 8.36 | 4.78 | 5.30 | 8.62 |
| Pr | 0.85 | 1.56 | 0.89 | 1.16 | 1.03 | 1.46 | 0.90 | 0.96 | 1.39 |
| Nd | 4.64 | 8.86 | 4.98 | 6.37 | 5.88 | 7.90 | 5.22 | 5.47 | 7.43 |
| Sm | 1.57 | 2.97 | 1.71 | 2.05 | 2.00 | 2.65 | 2.03 | 1.92 | 2.85 |
| Eu | 0.59 | 1.02 | 0.64 | 0.78 | 0.75 | 0.94 | 0.85 | 0.63 | 0.65 |
| Gd | 2.04 | 3.98 | 2.41 | 2.67 | 2.70 | 3.56 | 3.03 | 2.73 | 3.73 |
| Tb | 0.36 | 0.70 | 0.44 | 0.47 | 0.50 | 0.63 | 0.56 | 0.49 | 0.71 |
| Dy | 2.36 | 4.76 | 2.92 | 3.11 | 3.41 | 4.20 | 3.85 | 3.33 | 4.86 |
| Ho | 0.51 | 1.03 | 0.64 | 0.66 | 0.74 | 0.92 | 0.85 | 0.74 | 1.07 |
| Er | 1.51 | 3.03 | 1.87 | 1.97 | 2.16 | 2.63 | 2.45 | 2.14 | 3.04 |
| Tm | 0.23 | 0.46 | 0.30 | 0.30 | 0.33 | 0.41 | 0.39 | 0.34 | 0.51 |
| Yb | 1.58 | 3.00 | 1.98 | 2.06 | 2.21 | 2.63 | 2.55 | 2.26 | 3.20 |
| Lu | 0.25 | 0.48 | 0.31 | 0.32 | 0.37 | 0.42 | 0.42 | 0.36 | 0.54 |
| Hf | 0.99 | 2.09 | 1.02 | 1.39 | 1.40 | 1.79 | 1.25 | 1.34 | 2.95 |
| Ta | 0.037 | 0.092 | 0.063 | 0.096 | 0.037 | 0.087 | 0.038 | 0.060 | 0.10 |
| Pb | 2.29 | 1.06 | 0.52 | 0.90 | 1.13 | 1.46 | 0.91 | 0.47 | 0.53 |
| Th | 0.33 | 0.38 | 0.32 | 0.32 | 0.30 | 0.34 | 0.21 | 0.25 | 0.69 |
| U | 0.14 | 0.16 | 0.14 | 0.14 | 0.12 | 0.16 | 0.11 | 0.15 | 0.26 |

UC... Trace element analysis by ICP-MS at Union College

WSU... Trace element analysis by ICP-MS at Washington State University

All trace elements are given in ppm.

n.d. ... not determined

<d.l. ... below detection

are aphyric (O/C-379 and O/C-380) to slightly porphyritic (<5% phenocrysts) and contain phenocrysts of plag + cpx (O/C-224a), plag (Pb-1) or cpx (O/C-227a). Occasionally, small (~0.2 mm) magnetite phenocrysts are found. Plagioclase is albitized and often cloudy in thin section and cpx is mostly replaced by amphibole + chlorite ± magnetite. The groundmass consists of laths of plagioclase, clinopyroxene and granular oxide as well as 'intersertal' chlorite inferred to replace glass. The pillows have an intergranular texture. An intersertal texture is likely where chlorite appears to replace glass. Many pillows are highly vesicular and/or amygdaloidal.

The diabasic dikes (O/C-113, O/C-186, and O/C-227b) consist of ~45-50% plagioclase, 43-45% clinopyroxene and 1-5% oxide. Small amounts of quartz (<5%) occur interstitially indicating that quartz could be igneous in origin. One dike (not analyzed) contains ~20% quartz and has a granophyric texture. The analyzed dikes are aphyric and have a subophitic texture. The secondary mineral assemblage in the dikes is identical to that of the pillows.

A sample from a silicic dike (O/C-231a) in the pillow unit is analyzed. The dike contains phenocrysts of plagioclase (14%), quartz (5.5%) and some clinopyroxene (<1%). Minerals identified in the groundmass include plagioclase, quartz, and trace amounts of oxide. The secondary mineral assemblage includes epidote, chlorite, prehnite and pumpellyite. This dike may be related to the Mule Mountain volcanics and could be much younger than the pillow unit.

In the Winchester-Floyd classification using Zr/TiO₂ vs. Nb/Y, the samples from the pillow unit plot in the field for subalkalic basalts, except the silicic dike (O/C-231a) which plots in the center of the probability ellipse for dacites (figure 5.21). However, five samples from the pillow unit (O/C-186, O/C-224, O/C-379, O/C-380 and Pb-1) plot in the trachyandesite field using the total alkali vs. silica classification (the Na₂O+K₂O vs. SiO₂ diagram is not shown) suggesting significant enrichment in Na₂O and/or SiO₂ mobility.

5.5.5.2 Magmatic affinities

The chondrite- and N-MORB normalized trace element variation diagrams are shown in figures 5.22a and 5.22c. The samples from the pillow unit can be subdivided into two geochemical groups based

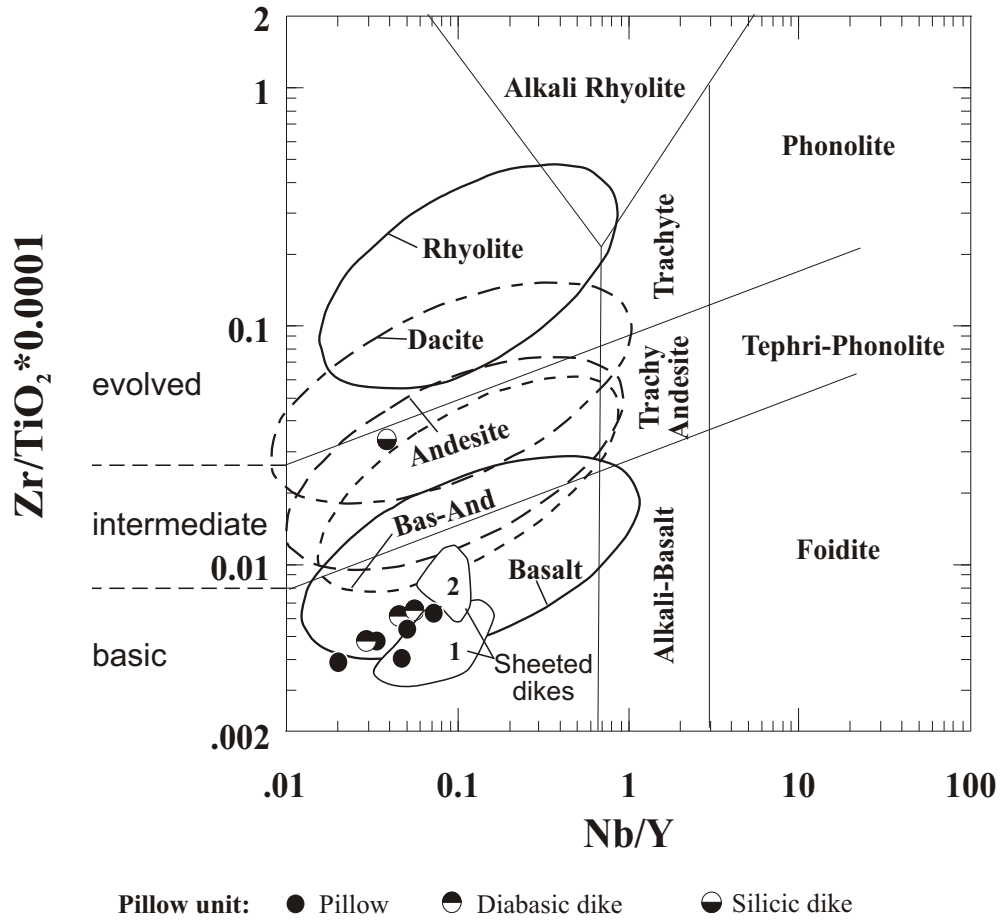


Figure 5.21

Zr/TiO₂ vs. Nb/Y diagram of Winchester and Floyd (1977) with fields revised by Pierce (1996).

Additionally, the 10% probability ellipses for TAS-defined rock types from subalkaline series are shown (after Pierce, 1996). The 10% probability ellipses overlap substantially. The samples from the pillow unit plot in the field for subalkaline basalts. For comparison, the fields for the dikes of geochemical groups 1 and 2 are shown. The basic samples from the pillow unit have higher Zr/TiO₂ ratios than dikes of geochemical group 1 from the sheeted dike complex.

on their chondrite normalized trace element ratios. The first group of samples has depleted LREE patterns, and the second group has slightly LREE depleted to flat chondrite normalized REE patterns.

The $(La/Yb)_n$ ratios of samples having depleted LREE patterns range from 0.51 to 0.79 (figure 5.22a). The pattern of the silicic dike (OC-231a) is also LREE depleted, but plots at significantly higher levels which can be interpreted as due to high degrees of fractionation. Furthermore, the parallel REE patterns indicate that O/C-231a could have evolved from the same magma as the other samples of this group. The negative Eu-anomaly suggests extensive fractionation of plagioclase.

The second group includes samples with almost flat REE distribution patterns. Note that the chondrite normalized values of Pr and Nd are equal to the chondrite normalized values of Yb and Lu. Only La and Ce are slightly depleted (figure 5.22c). Therefore, the $(La/Yb)_n$ ratios range from 0.80 to 1.00. Similar to group 1, the REE patterns show a prominent negative Ce-anomaly, which could be related to a subduction component derived from pelagic sediments (Hole et al., 1984). Alternatively, the negative Ce-anomaly could have developed as a result of interaction with seawater during hydrothermal alteration (Ludden and Thompson, 1979).

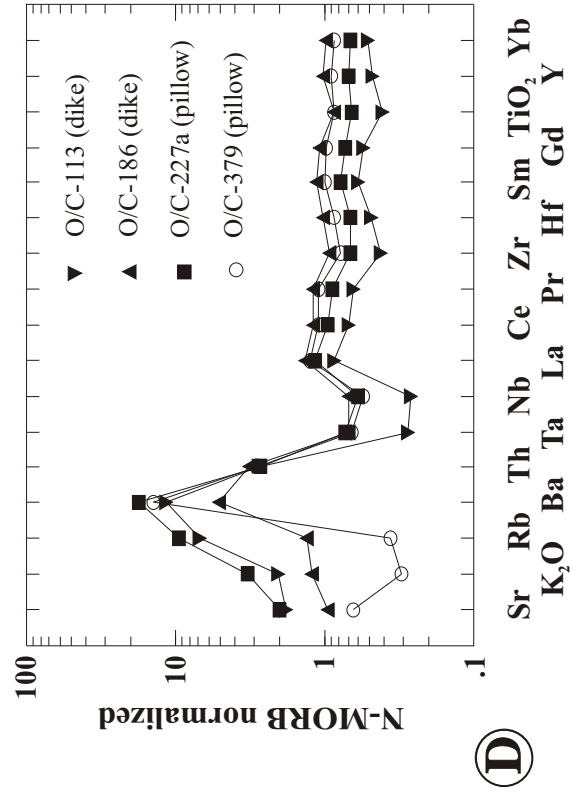
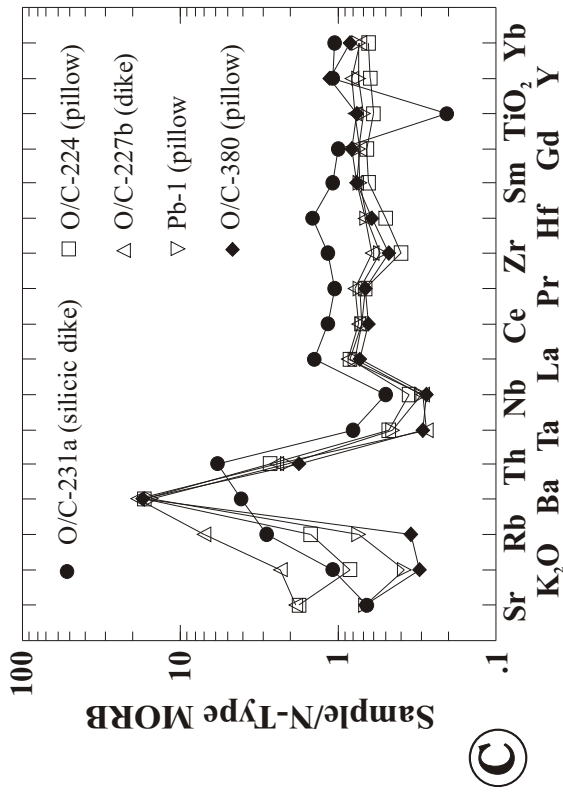
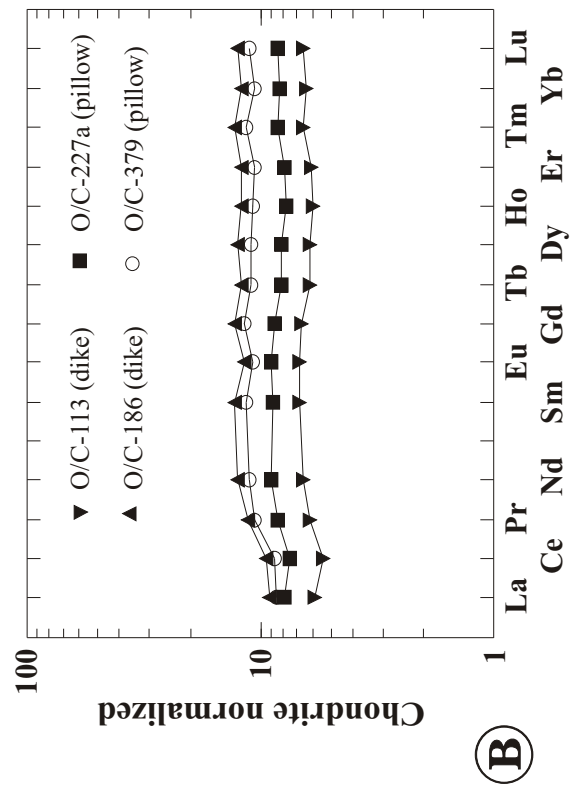
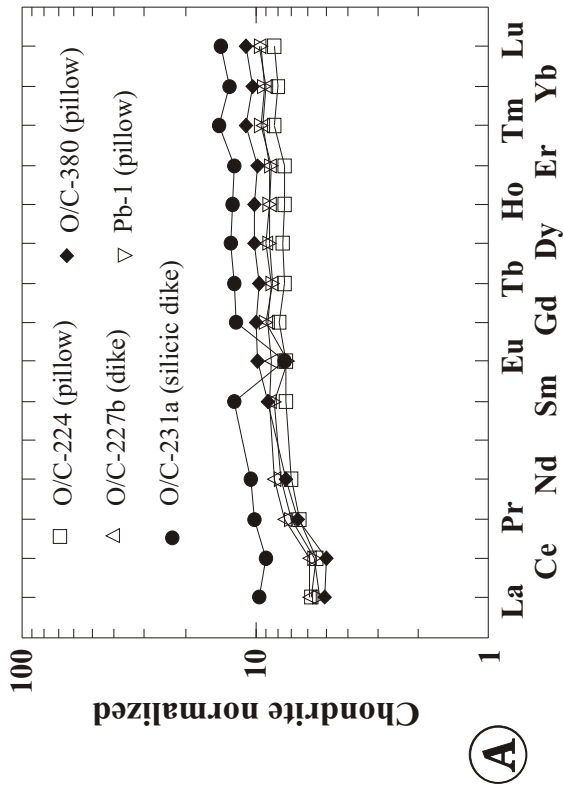
The N-MORB normalized trace element variation diagrams of samples from the pillow unit are shown in figures 5.22b and 5.22d. LILE and Th are selectively enriched and HFSE are variably depleted. These are characteristics of island-arc tholeiites (compare with figure 5.2). The strong scattering of LILE can be related to a variable slab component and/or element mobility due to hydrothermal alteration.

Note that samples of the same geochemical group have different incompatible trace element ratios, even of 'immobile' trace elements. For example, O/C-113 is more depleted in Ta and Nb than the other samples of the same group. Thus, not only are $(La/Yb)_n$ ratios variable, which was used to subdivide samples from the pillow unit into two groups, but other incompatible trace element ratios, such as Th/Ta, Ta/Yb, Th/Hf, and Zr/Y, differ. The variation in incompatible trace element ratios is probably not due to alteration, because these elements are 'immobile' in low grade metamorphic conditions. Also, crystal fractionation does not result in large variations of these ratios suggesting the differences are related to source heterogeneity and/or variable degrees of melting.

Figure 5.22

A - B: Chondrite normalized REE distribution diagrams of samples from the pillow unit. The patterns range from LREE depleted to almost flat. All samples have a pattern with a strong negative Ce-anomaly. The $(La/Yb)_n$ ratios of the first group of samples (O/C-224, O/C-227b, O/C-231a, O/C-379 and PB-1) range from 0.51 to 0.79. The chondrite normalized values for Pr and Nd are smaller than the normalized values for Yb and Lu. Samples of the second group (O/C-113, O/C-186, O/C-227a and O/C-379) have almost flat REE patterns with $(La/Yb)_n$ ratios from 0.8 to 1.00. The chondrite normalized values for Pr and Nd are equal to the normalized values for Yb and Lu; only La and Ce are slightly depleted.

C - D: N-MORB normalized trace element distribution diagram of samples from the pillow unit. The HFSE Ta, Nb, Zr, and Hf are variably depleted and LILE, Th and LREE are selectively enriched. Highly mobile elements, such as Rb and K, may have been redistributed during hydrothermal alteration. The patterns of all samples are similar to IAT (figure 5.2).



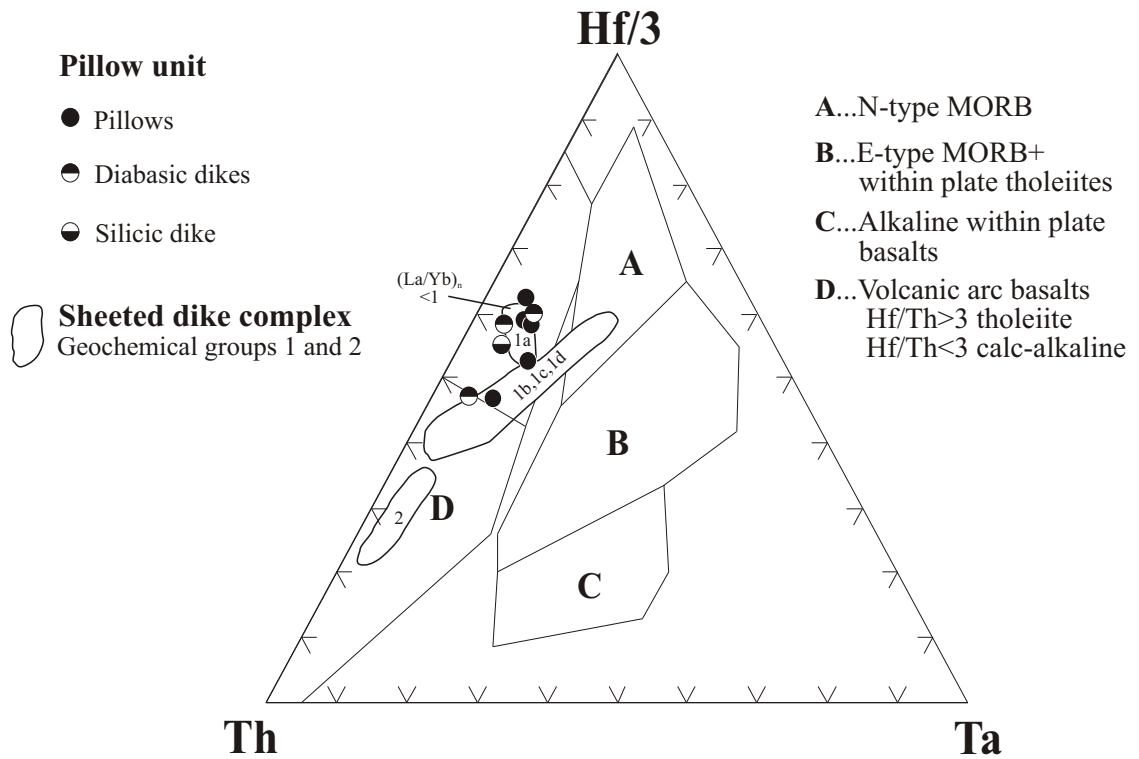


Figure 5.23

Hf/3-Th-Ta tectonic discrimination diagram with fields after Wood et al. (1979). The samples from the pillow unit plot in the field for island-arc tholeiite. For comparison the fields for dikes of geochemical group 1 (N-MORB and IAT) and dikes of geochemical group 2 (calc-alkaline) from the sheeted dike complex are shown.

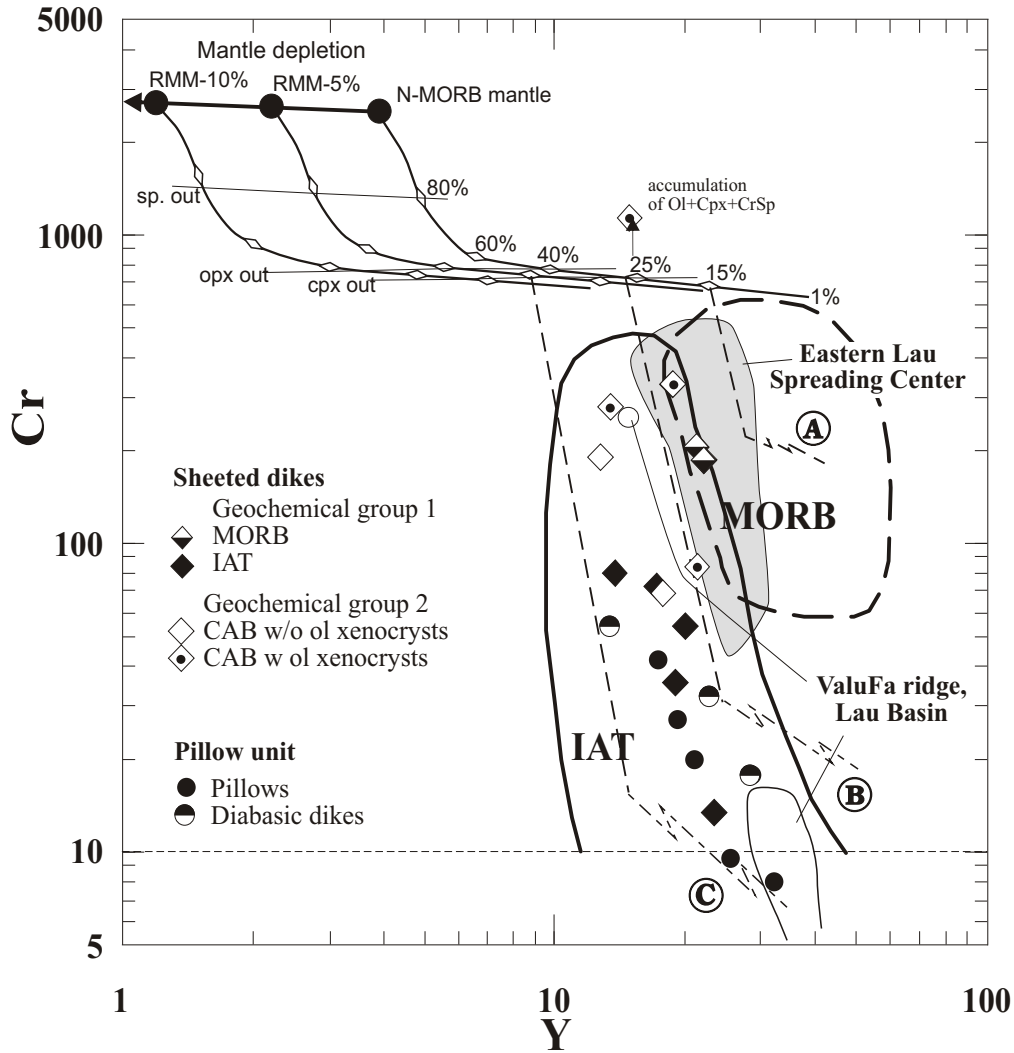


Figure 5.24

Cr vs. Y tectonic discrimination diagram of Pearce (1982) showing the fields for mid ocean ridge basalts (MORB) and island arc tholeiite (IAT) (the latter field also includes calc-alkaline and alkalic basalts from oceanic arcs). The modeled melting curves of the N-MORB mantle and the residual MORB mantle after 5% (RMM-5%) and 10% (RMM-10%) melt extraction are calculated as outlined in figure 5.4. The fractional crystallization trends for MORB (A), IAT (B) and boninite (C) are taken from Pearce et al. (1984a). The steep vector represents crystallization of olivine + Cr-spinel ± clinopyroxene, and the shallower vector represents crystallization of olivine + Cr-spinel + clinopyroxene + plagioclase. The samples from the pillow unit plot in the field for volcanic arc basalts.

The samples from the pillow unit plot in the IAT field in the Hf/3-Th-Ta diagram of Wood et al. (1979) (figure 5.23). In this diagram, the samples from the pillow unit define a much smaller field than the samples from the sheeted dike complex. The samples from the pillow unit have LREE depleted patterns ($(La/Yb)_n < 1$), whereas most samples from the sheeted dike complex have flat REE patterns (i.e., groups 1b and 1c) or LREE enriched patterns (i.e., group 1d). Only one dike (O/C-5-S4) and the gabbroic screens from the sheeted dike complex have LREE depleted patterns. Most samples from the pillow unit plot in or near the sheeted dike samples that have LREE depleted patterns (figure 5.23).

On the Cr-Y tectonic discrimination diagram of Pearce (1982), the samples plot in the field for island arc basalts (figure 5.24). The fractionation vectors in the Cr-Y diagram show that Cr decreases rapidly as mafic phases, such as olivine, clinopyroxene, and Cr-spinel, fractionate (figure 5.24) while Y increases only slightly. However, fractionation of plagioclase + mafic minerals results in a much larger increase of Y while Cr decreases not as fast. The slope of the trend defined by the samples from the pillow unit is subparallel to the vector indicating fractionation of mafic minerals suggesting delayed fractionation of plagioclase. Also, low Cr-contents are consistent with the interpretation that the samples from the pillow unit are more evolved than the sheeted dikes of geochemical group 1 (see also figure 5.21).

5.5.5.3 Chromian Spinel in a pillow sample

Sample O/C-224b, a pillow basalt from the pillow unit contains euhedral Cr-spinel in the matrix and Cr-spinel within clinopyroxene (cpx is completely replaced). The analyses of unaltered chromites are shown in figure 5.25, and the analytical data are listed in appendix C (table C7). Cr-spinel in the matrix has about the same Mg# as Cr-spinels within clinopyroxene phenocrysts (Cr-spinel in matrix: Mg# = 62.0; Cr-spinel in cpx: Mg# = 61.8). However, the Cr/(Cr+Al) ratios of Cr-spinel in the matrix (Cr# = 81.5) are higher than of Cr-spinels within clinopyroxene phenocrysts (Cr# = 76.7). The Cr-spinel within clinopyroxene phenocrysts plot in the field for the sheeted dike complex while the Cr-spinel in the matrix plots above this field. The difference in the Cr# indicates that the analyzed Cr-spinel in the matrix is probably a xenocryst.

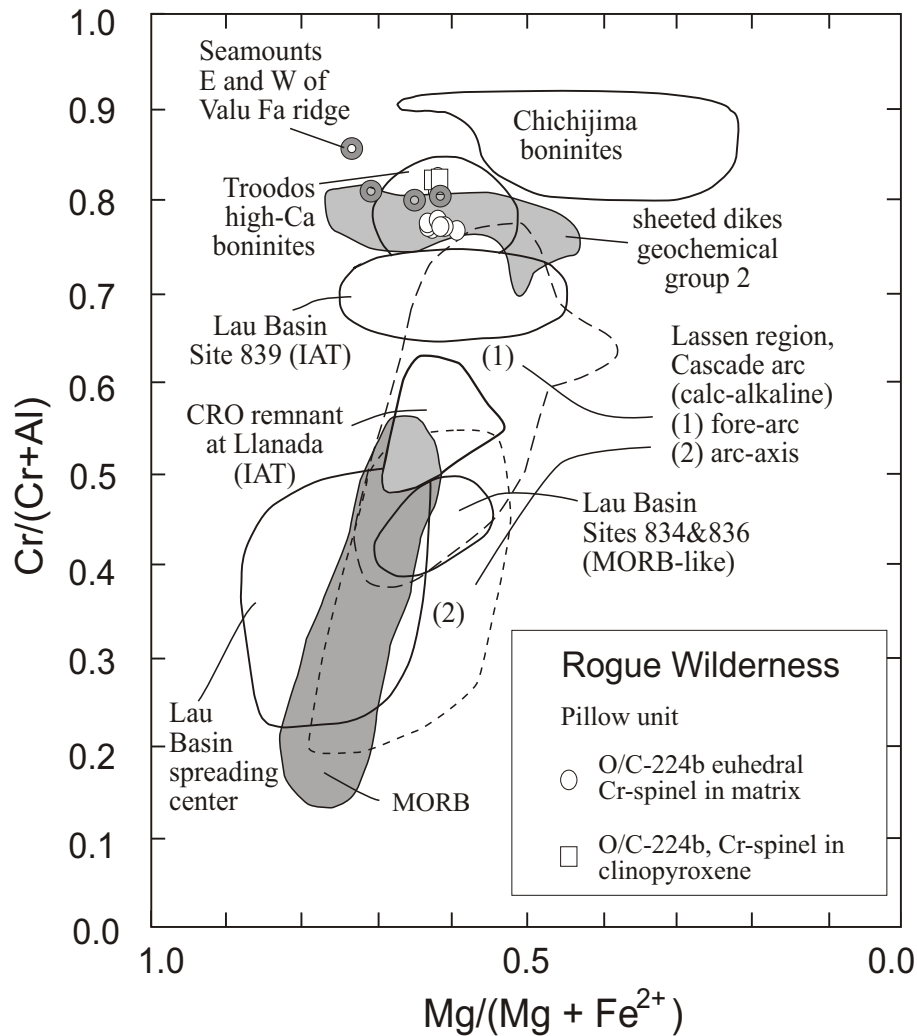


Figure 5.25

Comparison of the composition of Cr-spinel in a sample from the pillow unit (O/C-224b) with chromites from modern island arcs, the Troodos ophiolite, and the Coast Range ophiolite (CRO remnant at Llanada). The fields for Chichijima, Troodos, and the Lau Basin are from Meffre et al. (1996), for MORB from Dick and Bullen (1984), for the Coast Range ophiolite remnant at Llanada from Giaramita et al. (1998), and for the Cascade arc from Clynne and Borg (1997). The field for the dikes of geochemical group 2 from the sheeted dike complex is shown as well.

The Cr/(Cr+Al) values of Cr-spinel in O/C-224b are similar to Cr-spinel occurring in high-Ca boninites in the Troodos ophiolite (figure 5.25) implying a high-Ca boninitic magma was present as the pillows formed. However, the pillows, including O/C-224b have magmatic affinities to IAT (figure 5.22b, 5.23, 5.24). The high Cr/(Cr+Al) values of Cr-spinel and the whole-rock trace element composition of O/C-224b can be explained with mixing of an IAT magma with a high-Ca boninitic component.

5.5.5.4 Element mobility

According to the TAS rock classification (not shown), the pillows and diabasic dikes in the pillow unit range in composition from basaltic andesite to andesite/trachyandesite. The silicic dike (O/C-231a) has a very low MgO content (0.3%), high SiO₂ (78.9%), high Na₂O (6.5%) and low K₂O (table 5.4), and the silicic dike can be classified as a high-Na rhyolite. However, using the Zr/TiO₂ vs. Nb/Y classification, the pillows and diabasic dikes plot in the field for subalkalic basalts, and the silicic dike O/C-231a plots in the field for subalkalic dacite (figure 5.20). This suggests extensive Na metasomatism and / or SiO₂ mobility. Other evidence for element mobility includes: (1) the correlation of Al₂O₃ with MgO in samples from the pillow unit is very poor (not shown) suggesting MgO is not conserved in contrast to the samples from the sheeted dikes; (2) the discrepancy between the rock classification using TAS and the Zr/TiO₂ vs. Nb/Y diagram (figure 5.20) indicates that Na-metasomatism occurred; (3) the lack of a correlation in a diagram of Na₂O + CaO vs. MgO suggests mobility of these elements related to albitization of plagioclase; (4) the concentrations of LILE vary in samples from the pillow unit (figure 5.22b and 5.22d) much more than in samples from the sheeted dike complex (figure 5.17) suggesting redistribution of Ba, Rb, K and Sr in the pillow unit.

Similar to samples from the pillow unit, an independent evaluation of the mobility of elements by plotting “mobile” elements against an “immobile” element, such as Zr, is not possible, because the samples from the pillow unit are not from a single magmatic suite (section 5.5.5.5b). For example, the samples vary strongly in incompatible trace element ratios such as Ta/Yb (0.014 - 0.047), Th/Hf (0.16 - 0.34), and Zr/Y (~1.1 - 2.6). The correlation between Zr vs. MgO is very poor (not shown) because of mobility of MgO in addition to differences in the primary compositions.

5.5.5.5 Petrogenesis

5.5.5.5a Crystal Fractionation

The MgO variation diagrams of samples from the pillow unit are not shown because of inferred mobility of most major elements. However, a comparison of the major- and trace-element composition of samples from the pillow unit with the dikes of geochemical group 1 (sheeted dike complex) reveals that the samples from the pillow unit could be more fractionated than group 1 sheeted dikes. The samples from the pillow unit and group 1 sheeted dikes have very similar magmatic affinities (IAT), but at a given Nb/Y ratio, the samples from the pillow unit have higher Zr/TiO₂ ratios than group 1 sheeted dikes (figure 5.21). It is likely that the Zr/TiO₂ ratios are higher, because of higher degrees of fractionation. This interpretation is consistent with the samples from the pillow unit having, on average, higher SiO₂, lower MgO and lower Cr-contents than the group 1 sheeted dikes (e.g., figure 5.24).

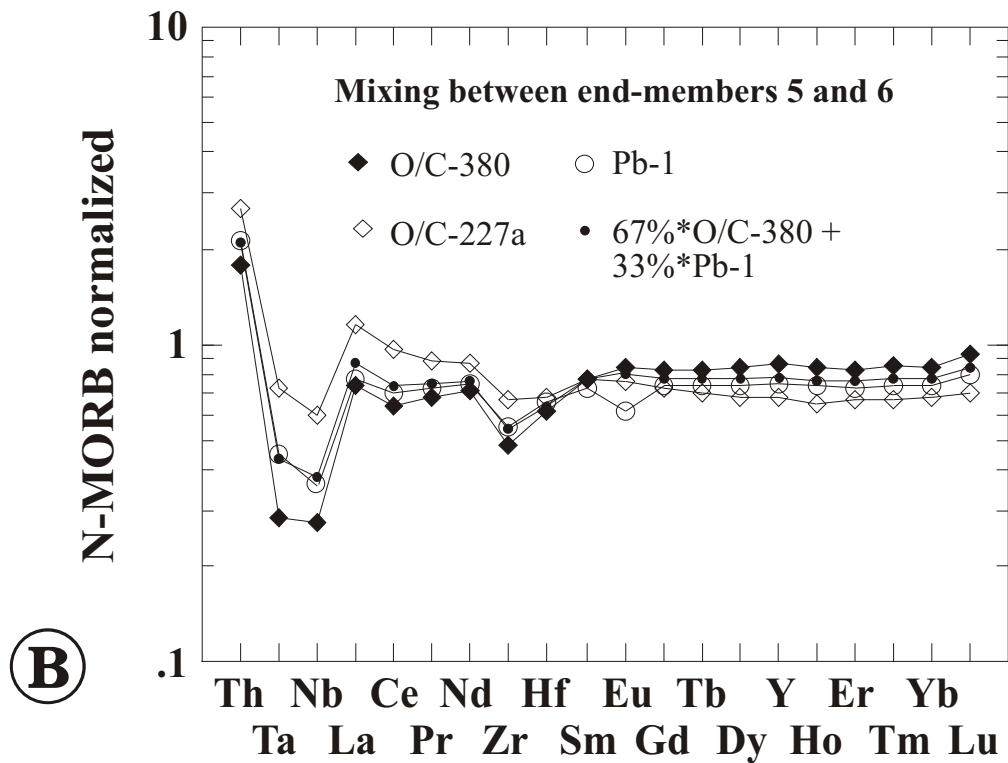
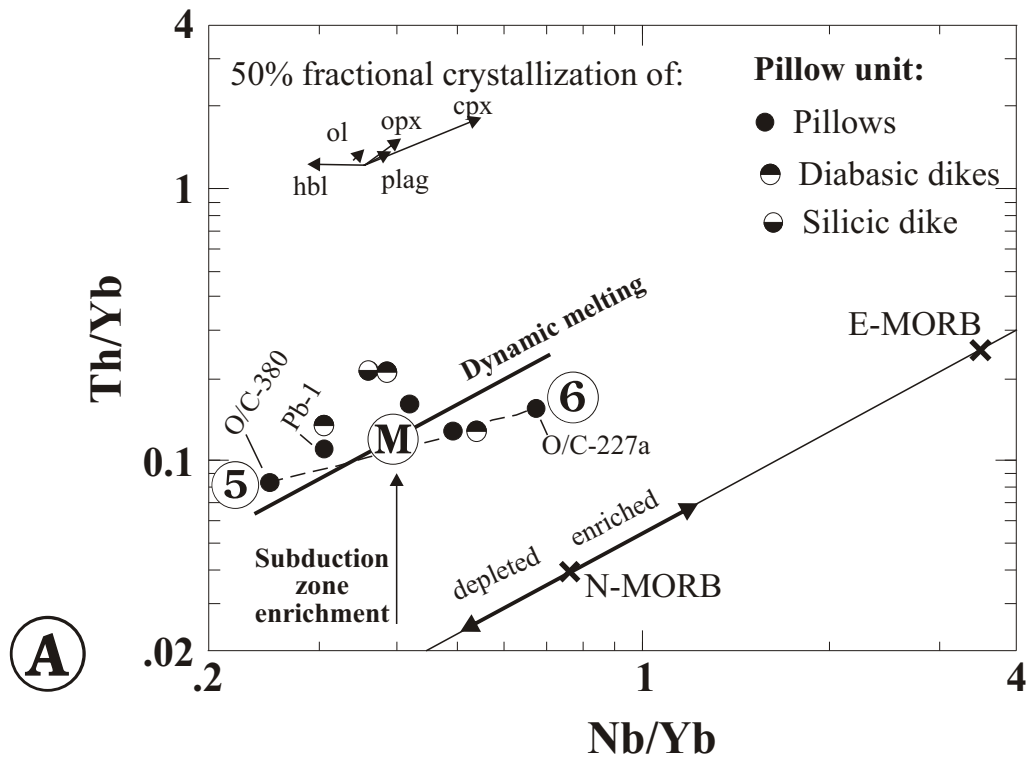
Furthermore, the chondrite and N-MORB normalized REE and trace element patterns of the silicic dike O/C-231a are remarkably parallel to the patterns of O/C-224, O/C-227b, and Pb-1 in figures 5.22a and 5.22b (O/C-380 has a lower La/Yb ratio). Perhaps, the silicic dike is related to one of these samples by crystal fractionation explaining the parallel patterns. The strong negative Ti-anomaly of O/C-231a is probably related to crystallization and fractionation of Fe-Ti oxides. If the silicic dike is related to other samples from the pillow unit, then the pillow unit could be bimodal in composition as indicated in figure 5.21. This hypothesis can be tested by analyzing more samples from the pillow unit and dating these silicic dikes.

5.5.5.4b Mantle heterogeneity and magma mixing

The variations of the incompatible trace element ratios Th/Yb and Nb/Yb in samples from the pillow unit are shown in figure 5.26a. For reference, the variations of these ratios in basalts from non-subduction settings (N-MORB and E-MORB) are shown. Obviously, the difference of the Th/Yb and Nb/Yb ratios in O/C-380 and O/C-227a cannot be explained with crystal fractionation, because large amounts of fractional crystallization results only in relatively small changes of these ratios (figure 5.26a).

Figure 5.26

- A. Plot of Th/Yb vs. Nb/Yb for samples from the pillow unit. The solid line indicates the variations of the Th/Yb and Nb/Yb ratios in MORB (from Pearce, 1982; Pearce and Peate, 1995; Pearce et al., 1995a; Pearce and Parkinson, 1993). The crosses on that line give the normalizing values for N-MORB and E-MORB. Also, the mantle depletion and enrichment trends relative to N-MORB are shown. Dynamic melting of a mantle source M with selective tapping of the melting column produces a trend that runs parallel to the MORB array (Pearce et al., 1995a). Alternatively, mixing of magmas derived by partial melting of two different mantle sources can explain the range of trace element compositions observed in samples from the pillow unit. The broken lines indicate the mixing curves between the different magmas.
- B. Mixing of O/C-380 (end member 5) and O/C-227a (end member 6) results in a composition similar to Pb-1.



Although the samples from the pillow unit scatter in figure 5.26a, they define a trend that is subparallel to the MORB array. Pearce et al. (1995a) argued that the addition of a constant subduction component to a constant mantle composition followed by dynamic melting can produce a trend that runs parallel to the MORB array. The petrogenetic pathway according to the model of Pearce et al. (1995a) is as follows: the addition of a constant subduction component results in a constant mantle composition (M in figure 5.26a). Dynamic melting of the mantle M with selective tapping of the melting column produces a trend that is parallel to the MORB trend. Other trace element ratios, such as Ta/Yb, La/Yb, Ce/Yb, Zr/Yb, Hf/Yb, and Gd/Yb, plotted against Nb/Yb (not shown) also produce trends that run subparallel to the MORB array suggesting the variations of the incompatible trace element ratios in samples from the pillow unit are related to dynamic melting of a relatively homogeneous mantle. Alternatively, fractional melting of a compositionally heterogeneous mantle could produce different magmas with distinct trace element compositions, such as those of O/C-380 and O/C-227a. Magma mixing could explain compositions between end member compositions 5 and 6 (figure 5.26a). For example, O/C-380 has a LREE depleted pattern, O/C-227a has a LREE enriched pattern, and Pb-1 has a flat REE pattern in the N-MORB normalized diagram (figure 5.26b). Mixing sample O/C-380 with sample O/C-227a in proportions of 67:33 results in a composition similar to that of Pb-1. Not only is the REE pattern of Pb-1 accurately reproduced using this mixing model, but also the depletion of Ta, Nb, Zr and Hf as well as the enrichment of Th relative to N-MORB are accurately modeled.

5.5.6 Comparison of ophiolite units

The comparison of the geochemical data of the ophiolite units is presented in the Th/Yb vs. Ta/Yb diagram in figure 5.27a. The Th/Yb vs. Ta/Yb diagram is a very useful diagram to summarize the geochemical data from the Rogue Wilderness ophiolite. The Th/Ta ratio normalized to Yb in figure 5.27a effectively discriminates basalts from non-subduction settings (divergent and intraplate settings) from subduction settings (Pearce, 1982).

In contrast to the Hf/3-Th-Ta diagram, the Th/Yb vs. Ta/Yb diagram is, to some extent, sensitive to partial melting and fractionation, because of small, but noticeable differences in the bulk partition

coefficients of the discriminant elements Th, Ta, and Yb ($D_{Th} \cong D_{Ta} < D_{Hf} < D_{Yb}$). To illustrate the effects of partial melting, the melting curves for a mantle similar in composition to the N-MORB mantle and a residual MORB mantle (depleted by 5% melt extraction) are calculated and plotted in figure 5.27a. Overall, the variations due to mantle source depletion or “within-plate” enrichment are larger than of partial melting, and the Th/Yb ratio is an excellent indicator of mantle source depletion.

In general, high degrees of fractionation causes Th and Ta to become more enriched in the residual liquid than Yb, resulting in an increase of Th/Yb and Ta/Yb ratios. However, low to medium degrees of fractionation have a negligible effect on Th/Yb and Ta/Yb ratios as illustrated with the fractionation vectors for hornblende, olivine, orthopyroxene, clinopyroxene, plagioclase and magnetite (figure 5.27a).

Th is thought to be a subduction-derived element while Ta and Yb are mantle-wedge derived (Pearce et al., 1984; Pearce and Parkinson, 1993; Pearce et al., 1995a, see also figure 5.2). Consequently, the Th/Yb ratio is a measure of the subduction component added to the mantle-wedge as illustrated in figure 5.27a with a vertical vector.

In order to recognize or preclude possible genetic relationships between the various units, three different petrogenetic pathways in the Th/Yb vs. Ta/Yb diagram are shown in figure 5.27b (after Pearce et al., 1995a). The first pathway (pathway A) shows the effects of the addition of a variable subduction component to a constant mantle composition. The resulting trend is a vertical line (figure 5.27b). The second pathway (pathway B) shows the effects of the addition of a constant subduction component to a variably depleted mantle. The addition of a constant subduction component to a mantle enriched with a within-plate component will not change the Th/Yb ratio very much. In contrast, the addition of the same subduction component to a refractory mantle results in significant increase of the Th/Yb ratio. Thus, a constant subduction component added to a variably depleted mantle results in a subhorizontal trend as indicated by vector B (figure 5.27b). The third petrogenetic pathway (C) shows the effects of the addition of a constant subduction component to a constant mantle composition followed by dynamic melting. A single point is displaced from the MORB array by an amount determined by the magnitude of the subduction contribution. Dynamic melting of this mantle with selective tapping of the melting column

produces a trend that runs parallel to the MORB trend (Pearce et al., 1995a). The difference between fractional melting and dynamic melting is that during fractional melting, the incompatible trace element ratios Th/Yb and Ta/Yb cannot decrease below that of the original mantle composition. Nevertheless, trends produced by fractional melting and dynamic melting are both parallel to the mantle array. Obviously, partial melting or dynamic melting of variable sources A and B is also possible and will generate a complex scatter across the diagram (Pearce et al., 1995a).

5.5.6.1 Metagabbro unit

The samples from the metagabbro unit have very low Ta/Yb ratios suggesting the metagabbro unit is derived from a highly depleted mantle source (figure 5.27a). Most samples have higher Th/Yb ratios than basalts from non-subduction settings suggesting a small subduction contribution. The samples plotting above the MORB array may be classified as “depleted” IAT. The metagabbro samples have an unusual REE pattern that can be described as a convex-up LREE pattern centered on Nd (figure 5.3). Thus, the metagabbro unit could not have formed by partial melting (i.e., dynamic melting with selective tapping of the melting column) of the mantle sources from which the metatonalite unit, sheeted dike complex, or pillow unit formed. It appears that the metagabbro unit is unrelated to the other units, and thus, the metagabbro unit may not be part of the ophiolite.

The intrusion of the hornblende quartz diorite in the metagabbro unit (GH-97-14) plots at the lower end of the field for IAT having depleted LREE patterns. However, GH-97-14 differs significantly from these samples because it has a $(La/Yb)_n$ ratio of 1.03, and the REE pattern of GH-97-14 has a slightly convex-up shape (figure 5.7a). The composition of GH-97-14 can be explained with assimilation of gabbroic wall rock if the initial composition of the magma, which intruded and assimilated the metagabbro, was similar to samples with flat chondrite normalized REE patterns. Preliminary calculations indicate that assimilation of ~33% metagabbro by a magma having a composition similar to O/C-113 (figure 5.22c and 5.22d) results in a contaminated magma composition similar to GH-97-14 (assuming simple mixing). Additionally, the samples from the metagabbro unit, GH-97-14 and O/C-113 appear to define a mixing trend in figure 5.27a. Thus, the hornblende quartz diorite appears to be the only plutonic rock in the

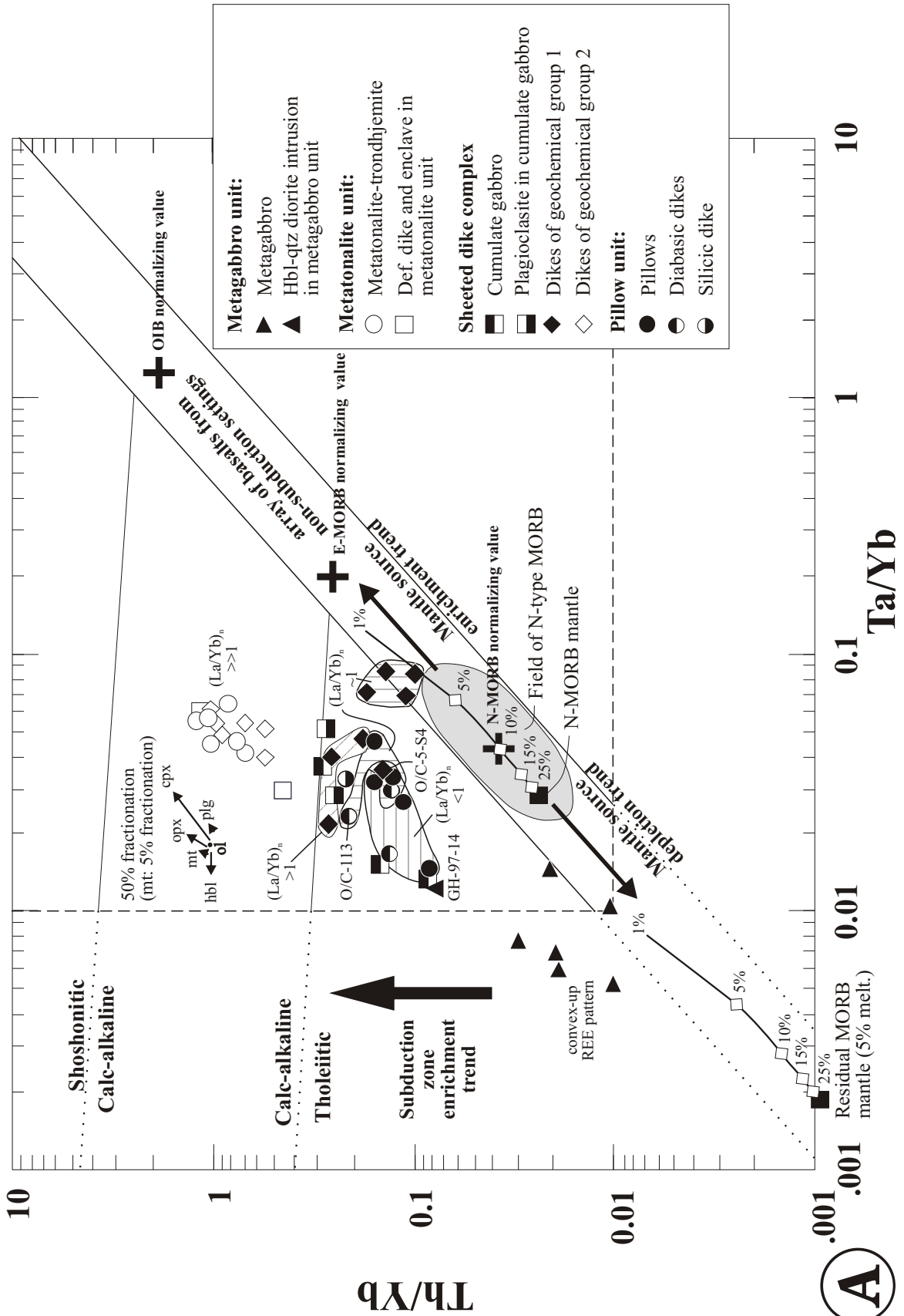
metagabbro unit that can be petrogenetically related to another ophiolitic unit. However, it is likely that the latent heat of crystallization during fractional crystallization drove assimilation of the wall rock. This process is known as AFC (e.g., Powell, 1984). Thus, additional samples from the hornblende quartz diorite intrusion need to be analyzed in order to recognize possible AFC processes. Then, AFC should be incorporated into a more realistic model of wall rock assimilation. Also, the analysis of Sr- and Nd-isotopes in samples from the metagabbro unit, pillow unit, sheeted dike complex and the hornblende quartz gabbro intrusion in the metagabbro unit is essential constraining the hypothesis of wall rock assimilation. Constraining the hypothesis of assimilation of metagabbro is important to correctly interpret the zircon U/Pb ages of SC-3, a sample from the hornblende quartz diorite intrusion.

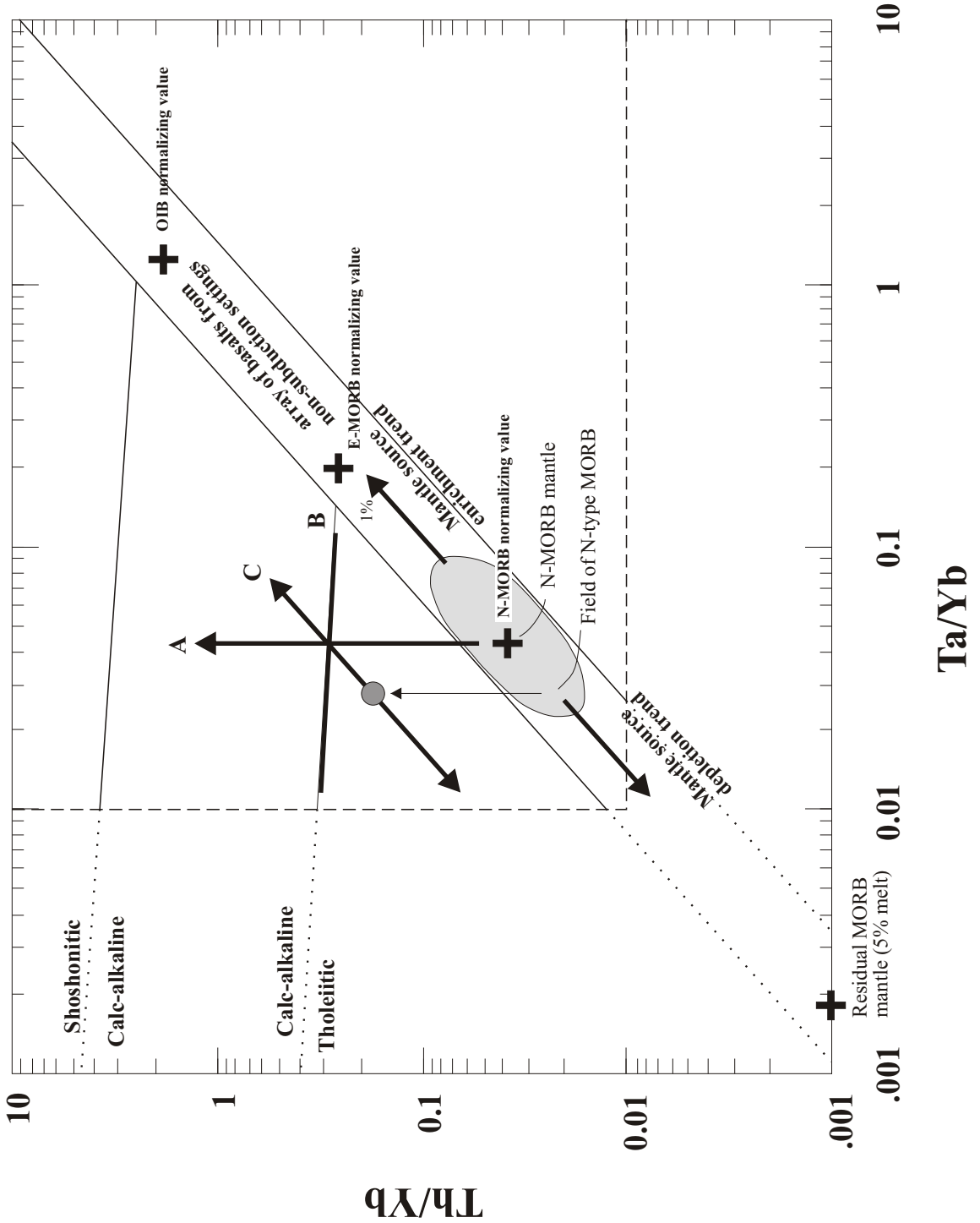
5.5.6.2 Calc-alkaline samples from the metatonalite unit and sheeted dike complex

The samples from the metatonalite unit overlap in the Th/Yb vs. Ta/Yb (figure 5.27a) and the Hf/3-Th-Ta (figures 5.5 and 5.16) discrimination diagrams with the dikes of geochemical group 2 from the sheeted dike complex implying similar mantle sources. These samples plot along a line subparallel to the MORB array, but displaced towards significantly higher Th/Yb ratios (figure 5.27a). Furthermore, the La/Yb ratios in the calc-alkaline samples from both units are strongly correlated with the Th/Yb and Ta/Yb ratios. The variations of the La/Yb, Th/Yb, and Ta/Yb ratios could reflect variable degrees of partial melting of a relatively homogeneous mantle source; i.e., dynamic melting with selective tapping of the melting column (figure 5.27b). Overall, the similarities in the trace element composition as well as variations in incompatible trace element ratios between samples from the metatonalite unit and group 2 sheeted dikes suggest that the metatonalite unit and part of the sheeted dike complex (i.e., calc-alkaline dikes) are related. In addition to variations related to variable degrees of partial melting, both magma mixing (figure 5.10, 5.12, and 5.20) and allanite fractionation (figure 5.11) could have played an important role in the evolution of some of the calc-alkaline samples.

Figure 5.27

- A. Th/Yb vs. Ta/Yb tectonic discrimination diagram of Pearce (1982) showing samples from the Rogue Wilderness ophiolites. The melting curves for N-MORB mantle and residual MORB mantle (after 5% melt extraction) are calculated using the distribution coefficients in Pearce and Parkinson (1993), and the equations for fractional melting modified to take into account non-modal melting (see also figure 5.4). Variations due to partial melting are parallel to the MORB mantle array. N-MORB, E-MORB and OIB normalizing values are given as well as vectors showing mantle source depletion- and enrichment- trends. Elevated Th/Yb ratios compared to the mantle array indicate enrichment with a subduction component. Variations due to fractional crystallization are relatively small as shown by vectors indicating crystal fractionation.
- B. Possible petrogenetic pathways in the Th/Yb vs. Ta/Yb tectonic discrimination diagram. Pathway **A** indicates the trend produced by variable addition of a subduction component to a constant mantle composition. Pathway **B** shows the trend resulting from the addition of a constant subduction component to a variably depleted mantle (addition of Th to a mantle with high Th/Yb ratios does not affect the Th/Yb ratios significantly, but the addition of the same amount of Th to a mantle with very low Th/Yb ratios results in a large increase of the Th/Yb ratios; thus pathway B is not parallel to the array of basalts from non-subduction settings). Pathway **C** shows the trend produced by the addition of a constant subduction component to a constant mantle composition followed by dynamic melting. Dynamic or fractional melting of variable sources A and B results in a complex scatter across the diagram (after Pearce et al, 1995a).





5.5.6.3 Tholeiitic samples from the sheeted dike complex and pillow unit

The samples from the gabbro screens, the dikes of geochemical group 1 from the sheeted dike complex and the samples from the pillow define two distinct fields in the Th/Yb vs. Ta/Yb discrimination diagram (figure 5.27a). Four sheeted dike samples plot on and around the upper boundary of the array of basalts from non-subduction settings. These samples have flat chondrite normalized REE patterns and have magmatic affinities to MORB transitional to IAT. The remaining samples from the sheeted dike complex and the pillow unit define a broad, slightly elongate field subparallel to the array of basalts from non-subduction settings, but at significantly elevated Th/Yb ratios typical of IAT (figure 5.27a). As a group, the IAT samples from the sheeted dike complex and the pillow unit become more depleted in LREE with decreasing Ta/Yb and Th/Yb ratios (figure 5.27). However, there are many samples that deviate substantially from this general trend (e.g., MRH-111). The large scatter of these data could have been produced following any one of the pathways or a combination of the pathways shown in figure 5.27b. Basically, the variability of the trace element composition of the IAT samples can be explained with a variably depleted mantle source re-enriched with a variable subduction component resulting in a heterogeneous mantle. Possible models of mixing of magmas produced by partial melting of various mantle sources are shown in figures 5.20 and 5.26. For example, the trace element composition of O/C-58 can be explained with mixing of a MORB-like (O/C-356) and an IAT-like magma (MRH-111).

Only one sample from the sheeted dike complex (O/C-5-S4) plots in the area where the fields comprising samples from the pillow unit having flat REE patterns and samples having LREE depleted patterns overlap each other (figure 5.27a). Also, two gabbro screens from the sheeted dike complex have similar Th/Yb and Ta/Yb ratios as the samples from the pillow unit. The similarity of the trace element composition of samples from the pillow unit and the sheeted dike complex suggests that these samples could have been derived from a similar mantle source. Thus, the pillow unit and part of the sheeted dike complex (i.e., cumulate gabbro, diabasic dike O/C-5-S4) could be related.

5.5.6.4 High Ca-boninitic component in sheeted dike complex and pillow unit

Cr-spinels occur in dikes of geochemical group 2 containing olivine xenocrysts and in a pillow sample from the pillow unit. The Cr/(Cr+Al) ratios of Cr-spinels in samples from both units are very similar and are as high as the Cr/(Cr+Al) ratios of Cr-spinels in high-Ca boninites from the Troodos ophiolite (figure 5.19 and 5.25). This implies that high-Ca boninitic magmas were present as the pillow unit and the calc-alkaline dikes formed. It is possible that the pillow sample and the calc-alkaline dikes from the sheeted dike complex contain the same high-Ca boninitic component implying both units are comagmatic.

5.5.7 Geochemical diversity in modern tectonic settings

The samples from the Rogue Wilderness ophiolite are geochemically diverse having magmatic affinities to MORB, IAT and CAB (figures 5.5, 5.16, 5.23 and 5.27a). High Cr/(Cr+Al) ratios of Cr-spinels in a pillow sample and in calc-alkaline dikes containing olivine xenocrysts are interpreted as evidence for the presence of high-Ca boninitic component in the sheeted dike complex and the pillow unit (figure 5.19 and 5.25). Are there any modern analogues where such a large geochemical and compositional diversity can be found?

For example, the back-arc basin crust of the Lau Basin, SW Pacific is composed of geochemically diverse rocks indicating a large range of different magma types (e.g., Ewart et al., 1994; Hawkins, 1995). However, the rocks recovered at a single site in the Lau Basin are not as geochemically diverse as the sheeted dike complex. The Lau Basin, which is inferred to have formed by fore-arc rifting (e.g., Parson and Wright, 1996), is a back-arc basin situated between the Lau ridge remnant arc and the Tonga ridge. The latter has an active volcanic arc (Tofua arc). The Tonga Trench lies to the east of the Tonga Ridge marking the boundary between the Pacific plate and the Indo-Australian plate. Sea-floor spreading in the Lau Basin occurs on the Eastern Lau and Central Lau Spreading Centers. The southernmost extension of the Eastern Lau Spreading Center, the Valu Fa Ridge, is a rift that propagates into the Lau-Havre arc-crust as close as 40 km west of the active Tofua arc (Parson and Wright, 1996). The rocks recovered from the Lau Basin have magmatic affinities ranging from N-MORB (e.g., Site 834: Hergt and Farley, 1994;

Eastern Lau Spreading Center: Hawkins and Melchior, 1985) to transitional (e.g., Sites 835 and 836; Hawkins and Allan, 1994; Ewart et al., 1994b) to IAT (e.g., Site 839: Ewart et al., 1994a; Valu Fa ridge: Jenner et al., 1994; Frenzel et al., 1990; modern arc volcanics: Ewart et al., 1994b; Pearce et al., 1995b). Furthermore, Site 839 basalts contain Cr-spinel having Cr/(Cr+Al) values varying from 0.52 and 0.80 and Mg# varying from 0.27 to 0.75 (Allen, 1994). The compositions of Cr-spinels having high Cr# (0.75-0.80) are similar to Cr-spinels from primitive, boninitic or low-Al₂O₃ arc basalts (Allan, 1994). Cr-spinel megacrysts in Site 839 basalts are strongly zoned in Mg# (the Mg# decreases from core to rim), but display little zoning in Cr# reflecting disequilibrium reactions in the rocks (Foresythe and Fisk, 1994). Allan (1994) concludes that the Cr-spinel megacrysts within Site 839 lavas grew from primitive melts that have characteristics of primitive low-Al₂O₃ arc basalts derived from highly depleted harzburgite or lherzolite. Allen (1994) explains zoning in these Cr-Spinel megacrysts with magma mixing between primitive, spinel-bearing magmas and evolved, spinel-barren magmas shortly before eruption. The high Cr/(Cr+Al) values of these Cr-spinel megacrysts (0.75-0.8) are consistent with the interpretation that primitive, high-Ca boninitic magmas were present at site 839 and mixed with IAT-like magmas. Furthermore, Kamenetsky et al. (1997) identified two fundamentally different primitive primary melt compositions based on melt-inclusion compositions of magmas erupted at near-axis seamounts on either side of the Valu Fa Ridge. One magma type is a H₂O-rich, high-Ca, low Al₂O₃ magnesian basalt (similar to ankamarites), and the other is a low-Ca boninite-like magma. Magmas erupted at the nearby Valu Fa ridge have magmatic affinities to IAT (e.g., Boespflug et al., 1990; Pearce et al., 1995b).

Sigurðsson et al. (1993) reported a large range of magma types at the Hunter Ridge - Hunter Fracture Zone in the southernmost North Fiji Basin. The latter is located between the Pacific plate and Indo-Australian plate. The North Fiji Basin is an active back-arc basin bounded to the north by the inactive Vityaz trench, the Vanuatu arc in the west, the Hunter Ridge - Hunter Fracture zone in the south, and Fiji in the east. The India-Australian plate is subducted underneath the North Fiji Basin (marked by the New Hebrides trench) in a N70°E direction. Subduction becomes more oblique south of the Hunter Ridge, eventually shifting to inferred transform motion along the Hunter Fracture zone. The southernmost tip of the main spreading center of the North Fiji Basin is believed to propagate southward into the Hunter ridge

(Maillet et al., 1989). South of the Hunter-Ridge, a small pull-apart basin may be linked via a transform fault zone with the spreading center transecting the Hunter ridge (Maillet et al., 1989). Sigurdsson et al. (1993) defined nine magmatic groups based on major element glass chemistry and olivine and spinel compositions in samples dredged from 26 sites in the Hunter Ridge - Hunter Fracture Zone area. These include two groups of boninites, two groups of IAT, two groups of N-MORB, E-MORB, olivine porphyritic andesites and basaltic andesites and Na-rhyolites (Sigurdsson et al. 1993).

The third example where geochemically diverse rocks occur is the Izu- Mariana fore-arc region. Subduction of the Pacific plate beneath the Philippine Sea plate began by the middle Eocene resulting in the formation of the proto Mariana arc system (Hussong and Uyeda, 1981). The Parece Vela and Shikoku Basins formed by spreading between 30-17 Ma removing the Palau-Kyushu Ridge (now a remnant arc) from the locus of arc-magmatism. Another remnant arc to the east, the West Mariana Ridge formed from 29-5 Ma and was isolated when spreading began in the Mariana back-arc basin (or Mariana trough) (e.g., Taylor, 1992). The Mariana island arc as well as the back arc spreading center have been active since 5-6 Ma (Hussong and Uyeda, 1981). Johnson and Fryer (1990) reported new chemical data from samples dredged in the Marianas fore-arc. In addition to IAT and boninite (e.g., Taylor et al., 1992), MORB-like and OIB lavas were recovered from the Marianas fore-arc (Johnson and Fryer, 1990).

The volcanic and plutonic rocks from the Rogue Wilderness ophiolite are compositionally diverse because the rocks are not only basaltic in composition (see figures 5.14 and 5.21): mylonitic to undeformed felsic plutonic rocks of the metatonalite unit form part of the ophiolite. However, the silicic dike having magmatic affinities to IAT in the pillow unit (O/C-231a) may be younger than the ophiolite remnant (discussed in subsequent sections). The major- and trace element characteristics of the metatonalite are similar to low-K (high-Na) arc-rhyolites and dacites that have been described from various oceanic arc systems including the fore-arc region (e.g., Tonga: Bloomer et al., 1994; Marianas: Bloomer, 1987), the volcanic front (e.g., Tonga: Cunningham and Anscombe, 1985) and the back-arc region (ValuFa ridge: Frenzel et al., 1990; Sumisu rift: Hochstaedter et al., 1990a,b; Ikeda and Yuasa, 1989). Also, Sigurdsson et al. (1993) report that various high-Na rhyolites were dredged from the Hunter Ridge -

Hunter fracture zone near the southernmost (propagating) end of the main spreading center of the North Fiji Basin.

5.6 Geochemistry of the Mule Mountain volcanics

5.6.1 Rock classification

The analytical data of 14 samples from the Mule Mountain volcanics are listed in table 5.5 and the petrographic data are summarized in appendix A (table A5). Most volcanic flows and dikes in the Mule Mountain volcanics are porphyritic. Two of the analyzed samples (O/C-81a and O/C-81b) contain phenocrysts of olivine (pseudomorphed), clinopyroxene, and plagioclase. O/C-81a and O/C-81b are samples from the same flow but they differ markedly in their phenocryst content. There are as much as 25% and up to 1 cm large clinopyroxene phenocrysts in this flow. O/C-81a contains 6.3% plag, 10.5% cpx and 6.9% ol phenocrysts while O/C-81b contains 2% plag, 3% cpx, and 2% ol. Translucent, euhedral Cr-spinel occurs in olivine (pseudomorphed) and pyroxene phenocrysts. Consequently, the sample having a higher phenocryst content (O/C-81a) has also significantly higher Cr-concentration, indicating it is an accumulate. Four samples (GDH-7, GDH-8, O/C-82 and O/C-217) contain clinopyroxene and plagioclase phenocrysts. Three samples that were analyzed are aphyric (O/C-80, O/C-88 and O/C-147). The groundmass in the porphyritic sample is intergranular, and the texture in O/C-80 and O/C-147 (aphyric samples) is trachytic. O/C-88 is a sample taken from within the Blossom Bar shear zone and has a tectonic foliation. Samples O/C-217 and O/C-147 contain abundant quartz in the ground mass. However, it is not clear whether quartz is primary or formed from the alteration and/or redistribution of SiO₂ during hydrothermal alteration.

Additionally, four samples taken from dacitic flows (or sills) in the uppermost section of the Mule Mountain volcanics were analyzed. Overall, two different phenocryst assemblages are identified in the dacitic samples: GDH-1 and GDH-2b have phenocrysts of clinopyroxene, plagioclase and quartz, and the ground mass has a trachytic flow texture similar to O/C-217 and O/C-147. GDH-2a and GDH-5a have phenocrysts of plagioclase and hornblende, and the texture of the ground mass is xenomorphic granular.

Table 5.5: Major and trace element composition of samples from the Mule Mountain volcanics

| Sample | O/C-80 | O/C-81a | O/C-81b* | O/C-82 | O/C-88 | O/C-147 | O/C-217 |
|--------------------------------|------------|---------|----------|---------|---------|---------|---------|
| SiO ₂ | 61.14 | 48.99 | 50.02 | 54.58 | 52.29 | 67.74 | 68.25 |
| TiO ₂ | 0.71 | 0.51 | 0.51 | 0.72 | 0.93 | 0.79 | 0.88 |
| Al ₂ O ₃ | 14.36 | 14.49 | 13.80 | 16.05 | 15.05 | 14.13 | 14.13 |
| Fe ₂ O ₃ | 8.93 | 9.61 | 9.67 | 10.06 | 11.35 | 5.70 | 6.06 |
| MnO | 0.13 | 0.15 | 0.15 | 0.17 | 0.17 | 0.10 | 0.11 |
| MgO | 2.41 | 9.99 | 10.29 | 3.84 | 5.10 | 1.36 | 1.28 |
| CaO | 2.64 | 10.36 | 11.04 | 7.86 | 10.18 | 1.71 | 1.22 |
| Na ₂ O | 5.94 | 1.49 | 1.34 | 3.47 | 1.15 | 6.29 | 5.64 |
| K ₂ O | 0.83 | 0.48 | 0.49 | 0.39 | 0.05 | 0.08 | 0.08 |
| P ₂ O ₅ | 0.11 | 0.05 | 0.05 | 0.10 | 0.09 | 0.19 | 0.22 |
| BaO | 499 | 132 | 198 | 156 | 0 | 118 | 272 |
| Cr ₂ O ₃ | 27 | 564 | 741 | 52 | 154 | 24 | 18 |
| LOI | 2.78 | 4.05 | 3.17 | 2.93 | 3.82 | 2.21 | 2.07 |
| Total | 99.98 | 100.26 | 100.67 | 100.22 | 100.23 | 100.31 | 99.93 |
| Ni xrf | <d.l. | 121 | 126 | 20 | 43 | <d.l. | <d.l. |
| Sc xrf/icp | <d.l./n.d. | 45/n.d. | 45/n.d. | 17/n.d. | 39/n.d. | 14/n.d. | 15/17 |
| V xrf/icp | 156/130 | 219/239 | 225/238 | 300/328 | 336/363 | 50/26 | 40/31 |

* contains ~11% cpx, 7% olivine and ~6% plagioclase phenocrysts

| Sample | GDH-1 | GDH-2A | GDH-2B | GDH-5A | GDH-7 | GDH-8 | SC-15JS |
|--------------------------------|----------|---------|----------|---------|---------|---------|----------|
| SiO ₂ | 67.89 | 67.89 | 68.83 | 66.64 | 53.05 | 52.91 | 53.12 |
| TiO ₂ | 0.40 | 0.39 | 0.39 | 0.40 | 0.58 | 0.61 | 0.72 |
| Al ₂ O ₃ | 13.72 | 14.38 | 13.64 | 14.51 | 15.77 | 16.31 | 14.75 |
| Fe ₂ O ₃ | 5.26 | 4.32 | 5.86 | 4.90 | 9.37 | 9.62 | 11.30 |
| MnO | 0.06 | 0.10 | 0.13 | 0.10 | 0.13 | 0.16 | 0.15 |
| MgO | 1.67 | 1.32 | 2.10 | 1.85 | 5.47 | 5.45 | 5.16 |
| CaO | 1.95 | 1.54 | 0.76 | 1.99 | 7.41 | 9.52 | 4.05 |
| Na ₂ O | 5.39 | 6.73 | 5.90 | 6.67 | 3.87 | 2.26 | 4.08 |
| K ₂ O | 0.57 | 1.31 | 0.25 | 1.04 | 0.24 | 0.42 | 0.16 |
| P ₂ O ₅ | 0.06 | 0.09 | 0.06 | 0.09 | 0.06 | 0.09 | 0.05 |
| BaO | 194 | 448 | 64 | 239 | 54 | 79 | 56 |
| Cr ₂ O ₃ | 29 | 0 | 20 | 31 | 74 | 101 | 80 |
| LOI | 2.53 | 1.76 | 2.48 | 1.75 | 4.37 | 2.75 | 7.00 |
| Total | 99.54 | 99.83 | 100.43 | 99.98 | 100.37 | 100.15 | 100.58 |
| Ni xrf | 10.05 | 8.04 | 6.03 | 3.01 | 42 | 33 | 23 |
| Sc xrf/icp | 13/24 | 20/18 | 25/24 | 24/19 | 27 | 44 | 33/44 |
| V xrf/icp | 104/n.d. | 72/n.d. | 114/n.d. | 92/n.d. | 232/232 | 258/281 | 194/n.d. |

Major elements (in wt%) and Ba, Cr, Ni, Sc, and V (in ppm) were analyzed by standard XRF technique on pressed powder pellets at McGill University, Montreal. Additionally, Sc was analyzed by ICP-MS at Washington State University and V at Union College

Table 5.5 cont.

| Sample | O/C-80 | O/C-81a | O/C-81b* | O/C-82 | O/C-88 | O/C-147 | O/C-217 | |
|--------|--------|---------|----------|--------|--------|---------|---------|-------|
| | UC | UC | UC | UC | UC | UC | UC | WSU |
| Cr | 7 | 381 | 515 | 33 | 94 | 14 | 11 | n.d. |
| Rb | 9.59 | 6.72 | 7.13 | 6.17 | 0.18 | 0.25 | 0.79 | 0.98 |
| Sr | 134 | 150 | 148 | 228 | 233 | 75 | 59 | 60.0 |
| Y | 17.9 | 12.9 | 12.5 | 19.8 | 23.1 | 44.6 | 41.0 | 46.5 |
| Zr | 74 | 25 | 23 | 41 | 48 | 112 | 113 | n.d. |
| Nb | 1.57 | 0.39 | 0.37 | 0.76 | 0.72 | 2.18 | 2.14 | 1.83 |
| Cs | 0.12 | 0.34 | 0.36 | 0.34 | 0.04 | 0.02 | 0.04 | 0.03 |
| Ba | 608 | 140 | 137 | 103 | 17 | 96 | 321 | 194 |
| La | 3.67 | 1.29 | 1.28 | 2.63 | 2.33 | 5.59 | 4.99 | 5.41 |
| Ce | 8.51 | 3.37 | 3.27 | 6.58 | 6.48 | 14.9 | 13.57 | 13.60 |
| Pr | 1.30 | 0.59 | 0.57 | 1.07 | 1.15 | 2.53 | 2.33 | 2.28 |
| Nd | 6.37 | 3.21 | 3.17 | 5.86 | 6.48 | 13.6 | 12.7 | 12.4 |
| Sm | 2.01 | 1.18 | 1.11 | 2.01 | 2.29 | 4.57 | 4.18 | 4.63 |
| Eu | 0.56 | 0.48 | 0.45 | 0.68 | 0.85 | 1.39 | 1.21 | 1.40 |
| Gd | 2.56 | 1.64 | 1.59 | 2.65 | 3.11 | 6.04 | 5.38 | 6.10 |
| Tb | 0.44 | 0.30 | 0.29 | 0.46 | 0.56 | 1.06 | 0.94 | 1.17 |
| Dy | 2.95 | 2.09 | 1.99 | 3.18 | 3.77 | 7.01 | 6.49 | 7.79 |
| Ho | 0.62 | 0.45 | 0.43 | 0.70 | 0.81 | 1.49 | 1.43 | 1.68 |
| Er | 1.87 | 1.33 | 1.27 | 2.09 | 2.36 | 4.42 | 4.31 | 4.92 |
| Tm | 0.30 | 0.21 | 0.20 | 0.33 | 0.37 | 0.70 | 0.67 | 0.72 |
| Yb | 1.97 | 1.40 | 1.34 | 2.15 | 2.41 | 4.46 | 4.29 | 4.72 |
| Lu | 0.32 | 0.22 | 0.21 | 0.33 | 0.37 | 0.67 | 0.66 | 0.76 |
| Hf | 2.25 | 0.76 | 0.71 | 1.34 | 1.51 | 3.59 | 3.58 | 3.50 |
| Ta | 0.097 | 0.033 | 0.035 | 0.051 | 0.053 | 0.14 | 0.14 | 0.15 |
| Pb | 1.19 | 0.99 | 1.05 | 1.78 | 1.06 | 1.18 | 2.87 | 3.36 |
| Th | 0.69 | 0.20 | 0.19 | 0.39 | 0.30 | 0.75 | 0.72 | 0.76 |
| U | 0.32 | 0.10 | 0.08 | 0.19 | 0.12 | 0.31 | 0.39 | 0.40 |

UC... Trace element analysis by ICP-MS at Union College

WSU... Trace element analysis by ICP-MS at Washington State University

All trace elements are given in ppm.

n.d. ... not determined

<d.l. ... below detection

* contains ~11% cpx, 7% olivine and ~6% plagioclase phenocrysts

Table 5.5 cont.

| Sample | GDH-1 | GDH-2A | GDH-2B | GDH-5A | GDH-7 | GDH-8 | SC-15JS |
|-----------|-------|--------|--------|--------|-------|-------|---------|
| Mag. type | WSU | WSU | WSU | WSU | UC | UC | WSU |
| Cr | n.d. | n.d. | n.d. | n.d. | 49 | 75 | n.d. |
| Rb | 5.91 | 18.14 | 3.51 | 12.87 | 2.66 | 4.44 | 2.14 |
| Sr | 133 | 137 | 140 | 101 | 220 | 194 | 104 |
| Y | 34.4 | 28.7 | 42.5 | 22.5 | 19.9 | 17.8 | 5.9 |
| Zr | 69 | 92 | 67 | 82 | 38 | 36 | n.d. |
| Nb | 1.14 | 2.51 | 1.02 | 2.19 | 0.69 | 0.72 | 1.03 |
| Cs | 0.07 | 0.07 | 0.09 | 0.05 | 0.25 | 0.32 | 0.04 |
| Ba | 163 | 385 | 76 | 223 | 52 | 90 | 44.3 |
| La | 3.93 | 10.96 | 4.05 | 8.97 | 2.97 | 3.02 | 2.96 |
| Ce | 8.85 | 20.46 | 8.79 | 17.8 | 6.69 | 7.09 | 5.93 |
| Pr | 1.47 | 2.85 | 1.63 | 2.34 | 1.16 | 1.17 | 0.80 |
| Nd | 7.86 | 13.0 | 9.03 | 10.7 | 5.62 | 5.76 | 3.49 |
| Sm | 2.96 | 3.47 | 3.36 | 2.89 | 1.88 | 1.86 | 0.84 |
| Eu | 0.76 | 0.95 | 0.85 | 0.78 | 0.64 | 0.67 | 0.41 |
| Gd | 4.18 | 3.92 | 5.11 | 3.16 | 2.65 | 2.44 | 0.89 |
| Tb | 0.76 | 0.68 | 0.96 | 0.54 | 0.47 | 0.43 | 0.15 |
| Dy | 5.12 | 4.35 | 6.63 | 3.68 | 3.16 | 2.90 | 1.06 |
| Ho | 1.14 | 0.93 | 1.46 | 0.79 | 0.68 | 0.65 | 0.21 |
| Er | 3.36 | 2.69 | 4.09 | 2.24 | 2.04 | 1.98 | 0.69 |
| Tm | 0.49 | 0.42 | 0.62 | 0.35 | 0.32 | 0.32 | 0.11 |
| Yb | 3.12 | 2.63 | 3.90 | 2.26 | 2.02 | 1.99 | 0.79 |
| Lu | 0.49 | 0.44 | 0.61 | 0.37 | 0.30 | 0.31 | 0.16 |
| Hf | 2.31 | 2.70 | 2.31 | 2.41 | 1.19 | 1.15 | 1.46 |
| Ta | 0.091 | 0.17 | 0.085 | 0.16 | 0.041 | 0.041 | 0.08 |
| Pb | 1.93 | 2.74 | 2.67 | 3.16 | 2.93 | 2.87 | 3.41 |
| Th | 0.58 | 2.32 | 0.58 | 2.01 | 0.38 | 0.42 | 0.59 |
| U | 0.24 | 0.69 | 0.23 | 0.59 | 0.17 | 0.35 | 0.68 |

Hornblende separates of GDH-5a yielded an $^{40}\text{Ar}/^{39}\text{Ar}$ age of 152.9 ± 1.8 Ma, which is ~10 Ma younger than the Rogue Wilderness ophiolite.

SC-15 was sampled by J. Saleeby in a quarry just outside of the northwestern boundary of the Wild Rogue Wilderness. Primary minerals as well as igneous textures are not preserved in this highly altered rock. SC-15 contains abundant sulfide minerals. SC-15 appears to be basic in composition based on immobile trace element ratios (figure 5.28).

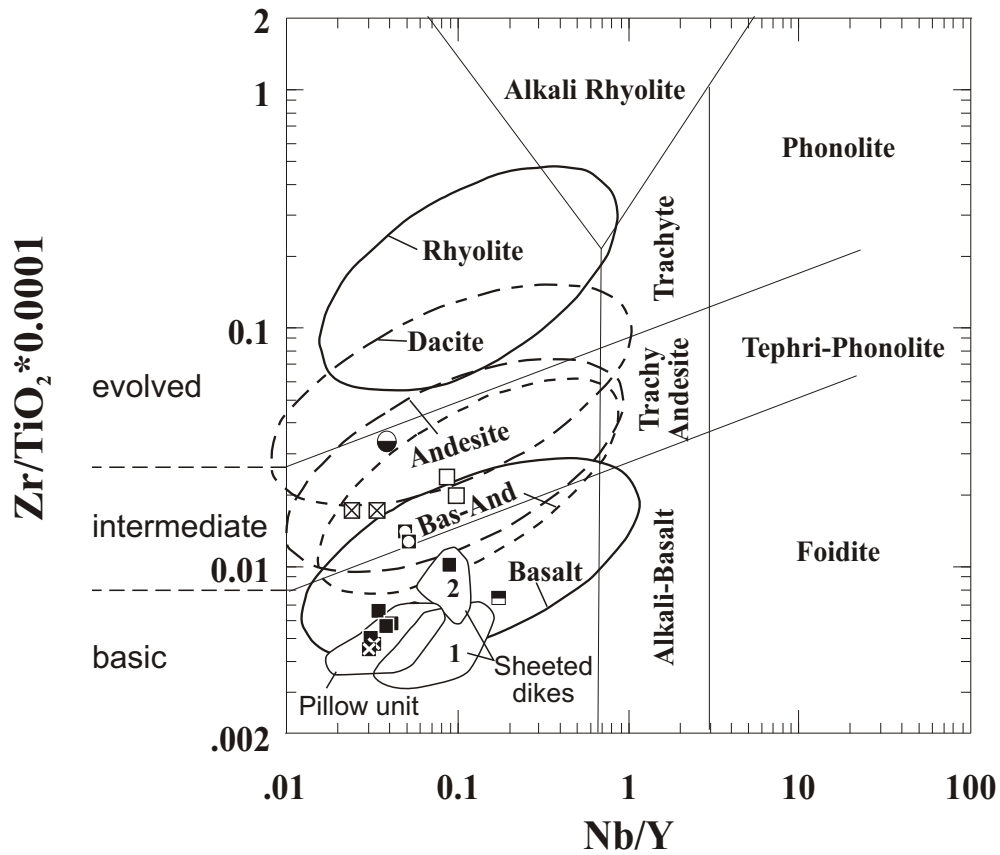
Figure 5.28 shows the Winchester-Floyd classification using Zr/TiO_2 vs. Nb/Y . Eight samples from the Mule Mountain volcanics plot in the field for subalkalic basalts (basic compositions) and six samples in the field for subalkalic andesites (intermediate compositions).

Most basic samples (O/C-81a, O/C-81b, O/C-81, O/C-88, GDH-7 and GDH-8) from the Mule Mountain volcanics overlap with the field for the pillow unit, and one basic sample (O/C-80) plots in the field for dikes of geochemical group 2 from the sheeted dike complex. Interestingly, GDH-1 and GDH-2b contain quartz phenocrysts and thus, are petrographically classified as dacites. However, these samples plot just below the lower boundary of the 10% probability ellipse for dacites in figure 5.28 implying that GDH-1 and GDH-2b have very low Zr/TiO_2 ratios for dacites.

5.6.2 Magmatic affinities

Similar to the pillow unit and the sheeted dike complex, the samples from the Mule Mountain volcanics can be subdivided into different geochemical groups based on their chondrite normalized REE distribution patterns. O/C-81a, O/C-81b, O/C-88, GDH-1 and GDH-2b have LREE depleted patterns and the chondrite-normalized La/Yb ratios range between 0.66 and 0.74 (figure 5.29a). These LREE depleted patterns are very similar to the patterns of samples from the pillow unit with $(\text{La}/\text{Yb})_n$ ratios ranging from 0.51 to 0.79 (figure 5.22a). Also, the patterns of GDH-1 and GDH-2b are remarkably similar to O/C-231a (silicic dike in the pillow unit). The dacitic samples GDH-1 and GDH-2b have a large negative Eu-anomaly suggesting fractionation of plagioclase.

O/C-82, O/C-147, and O/C-217 (figure 5.29c) have almost flat chondrite normalized REE distribution patterns, and the chondrite normalized values of Pr and Nd are equal to the normalized values



- Mule Mountain volcanics:**
- Silicic dike in pillow unit (O/C-231a, plag+cpx+qtz phyric)
 - Basic volcanic rocks (plag+cpx phyric or aphyric)
 - ⊠ Accumulate volcanic rocks (ol+cpx+plag phyric)
 - GDH-2a and GDH-5a (hbl + plag phyric)
 - ⊠ GDH-1 and GDH-2b (plag+cpx+qtz phyric)
 - O/C-147 (aphyric) and O/C-217 (plag+cpx phyric)
 - SC-15

Figure 5.28

Zr/TiO₂ vs. Nb/Y diagram of Winchester and Floyd (1977) with fields revised by Pierce (1996).

Additionally, the 10% probability ellipses for TAS-defined rock types from subalkaline series are shown (after Pierce, 1996). The 10% probability ellipses overlap substantially. The samples from the Mule Mountain volcanics plot in the field for subalkaline basalts and andesites. For comparison, the fields for the dikes of geochemical groups 1 and 2 from the sheeted dike complex and the field for samples from the pillow unit are shown.

of Y and Lu. Only La and Ce are slightly depleted, and the $(La/Yb)_n$ ratios are smaller than 1 (0.82-0.90). These REE distribution patterns of O/C-82, O/C-147, and O/C-217 are similar to samples from the pillow unit with $(La/Yb)_n$ ratios of 0.80 to 1.00 (figure 5.22c).

Samples O/C-80, GDH-7 and GDH-8 have flat chondrite-normalized REE distribution patterns (figure 5.29e). La and Ce are not depleted and the $(La/Yb)_n$ ratios are larger than 1 (1.05-1.33). The REE distribution patterns of O/C-80, GDH-7 and GDH-8 are similar to those of samples from the sheeted dike complex with flat to slightly enriched REE patterns and $(La/Yb)_n$ ratios of 0.98 to 1.12 (figure 5.17e).

The N-MORB normalized trace element distribution patterns of samples with LREE depleted and flat REE patterns are presented in figures 5.29b, 5.29d, and 5.29f. The N-MORB normalized patterns indicate that HFSE, such as Ta, Nb, Zr, and Hf, are variably depleted and Th and LILE are selectively enriched in these samples. The N-MORB normalized patterns are typical of IAT (see also figure 5.2). Interestingly, O/C-80 differs from the other IAT samples. O/C-80 has a positive Zr and Hf anomaly, whereas the other samples are depleted in Zr and Hf. The reason for the positive Hf and Zr anomaly in O/C-80 is not known. However, a positive Zr and Hf anomaly is observed in many boninite suites (e.g., Izu-Bonin fore-arc, Site 786; Murton et al., 1992). Overall, the samples from the Mule Mountain volcanics with $(La/Yb)_n$ ratios ≤ 1 have chondrite- and N-MORB- normalized REE and trace element distribution patterns similar to those of samples from the pillow unit (figure 5.22).

The plot in figure 5.29g shows the LREE enriched patterns of GDH-2a and GDH-5a which have $(La/Yb)_n$ ratios of 2.84 and 2.99, respectively. The N-MORB-normalized trace element distribution patterns (figure 5.29h) show that LILE, Th, and LREE are significantly enriched compared to N-MORB, while Ta, Nb, Zr, Hf, Y and HREE are similar to N-MORB. The N-MORB patterns of GDH-2a and GDH-5a are typical of volcanic rocks of calc-alkaline affinity (figure 5.2). Thus, the chondrite- and N-MORB-normalized REE and trace element distribution patterns of samples containing hornblende and plagioclase phenocrysts (GDH-2a and GDH-5a) differ significantly from all other samples from the Mule Mountain volcanics. Note that Th and LILE are more enriched in the calc-alkaline dacites (GDH-2a, GDH-5a; figure 5.29h) than in the tholeiitic dacites (GDH-1, GDH-2b, O/C-231a; figure 5.29b). The chondrite and N-MORB normalized REE and trace element distribution patterns of GDH-2a and GDH-5a

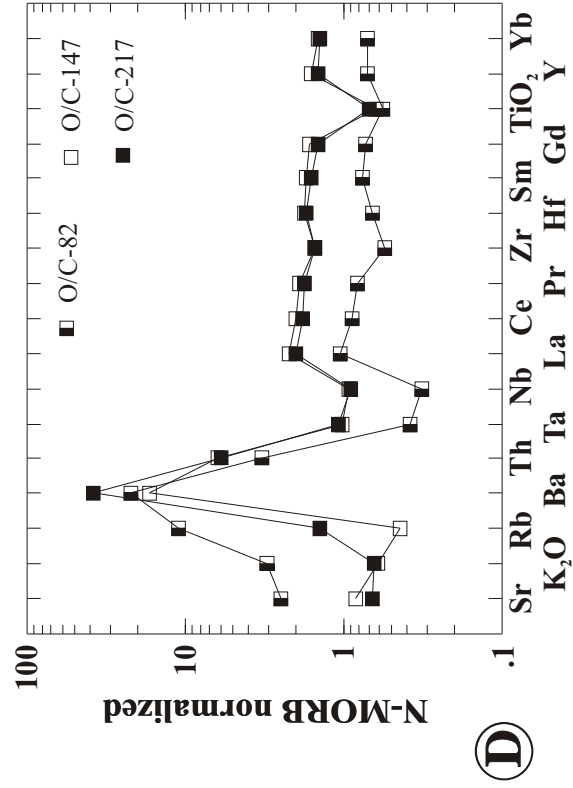
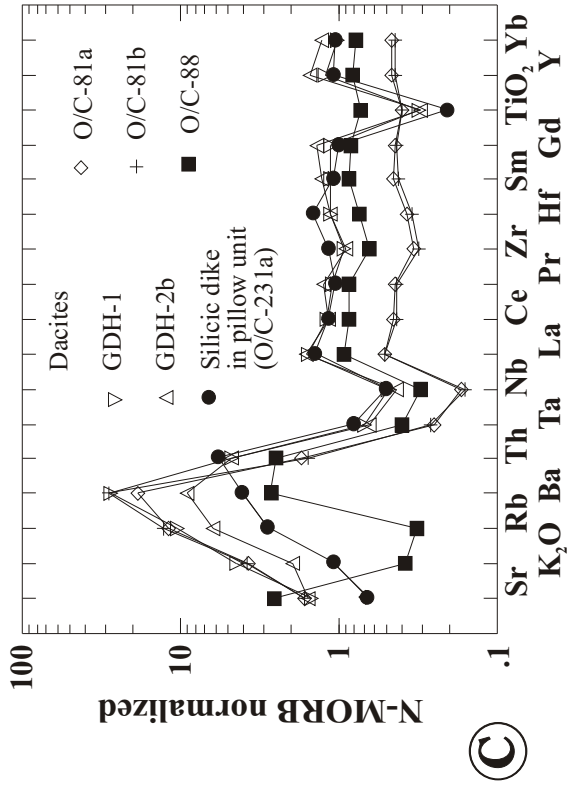
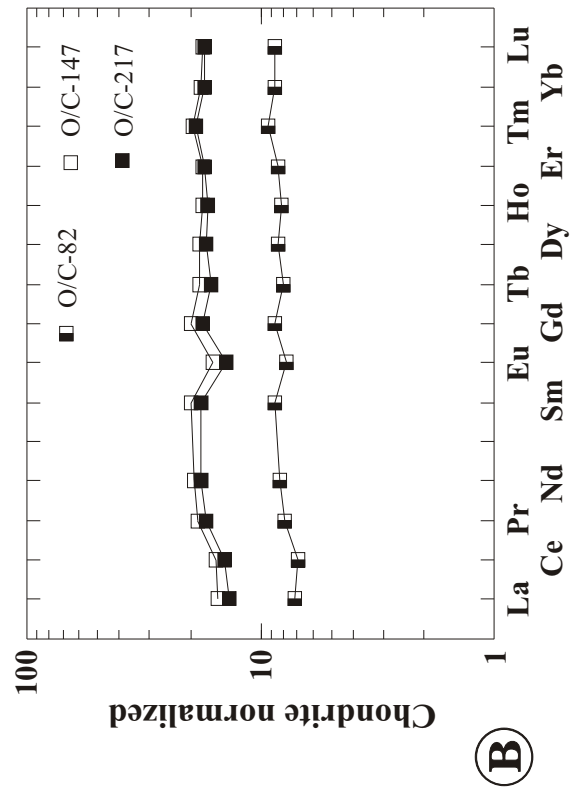
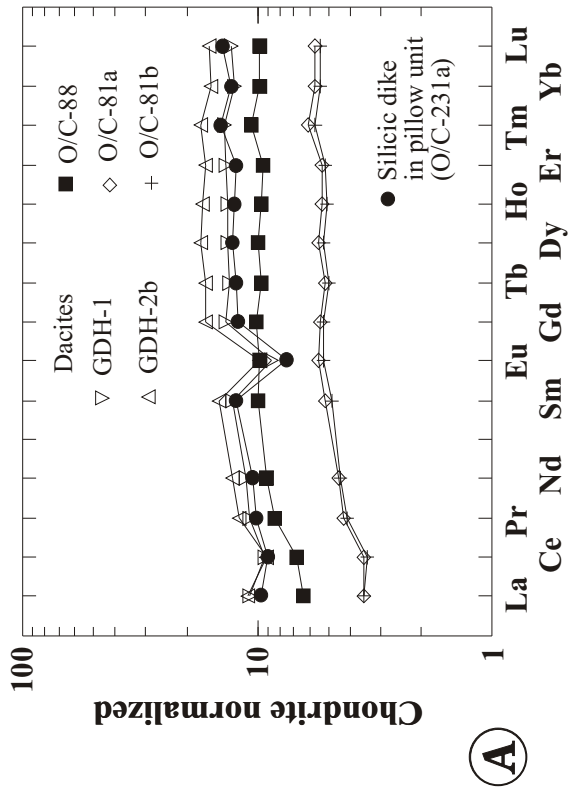
Figure 5.29

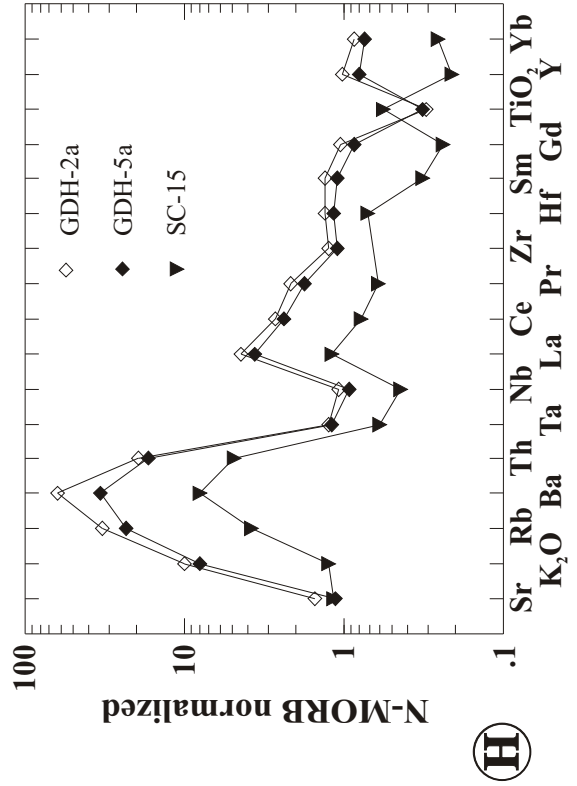
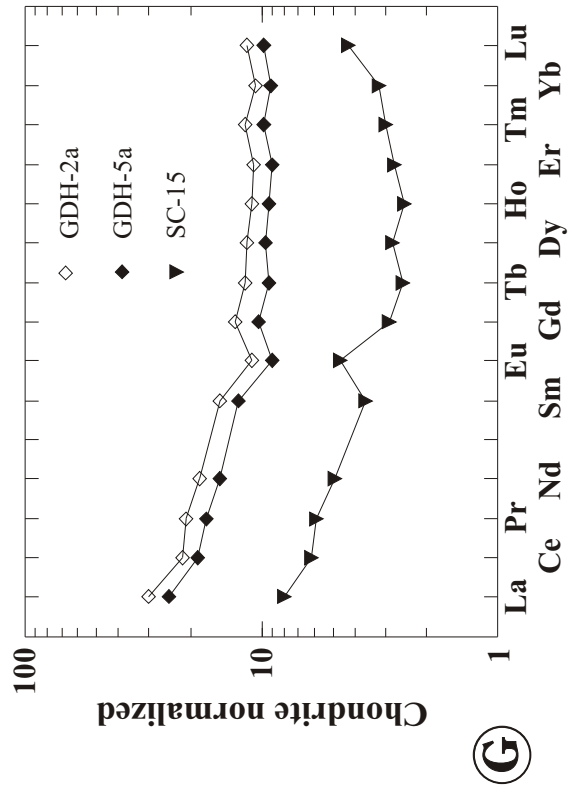
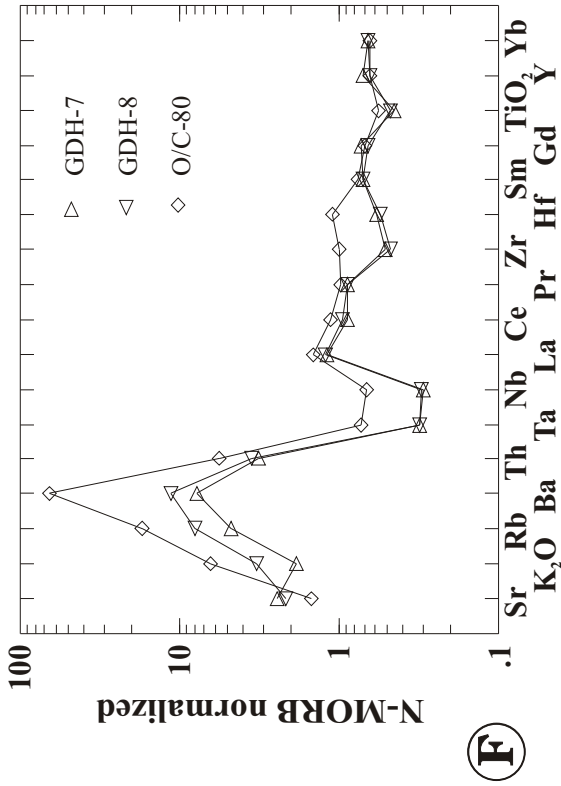
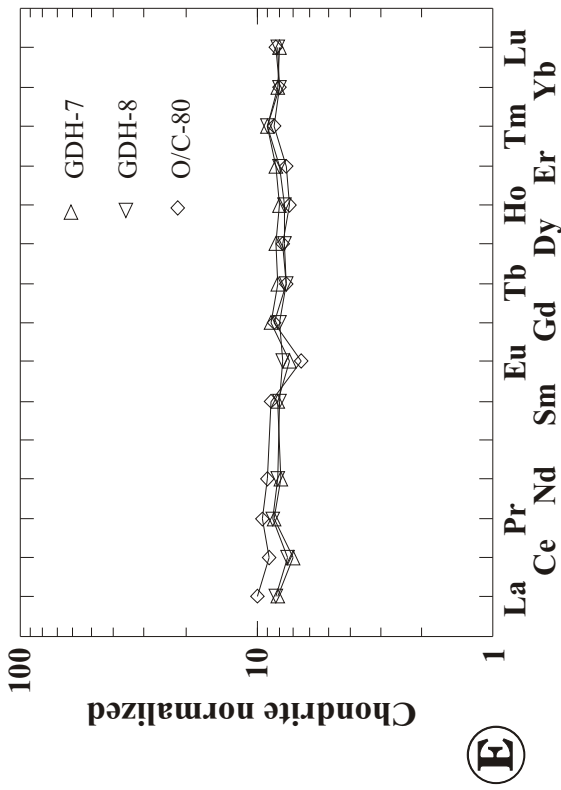
A - F: Chondrite and N-MORB normalized REE and trace element distribution diagrams of samples from the Mule Mountain volcanics having LREE depleted to flat REE patterns. Samples GDH-1, GDH-2b, O/C-81a, O/C-81b and O/C-88 have LREE depleted patterns and $(La/Yb)_n$ ratios between 0.66 and 0.74 (figure 5.29a). The $(La/Yb)_n$ ratios of samples O/C-82, O/C-147, and O/C-217 range from 0.82 to 0.9 (figure 5.29c), and of samples GDH-7, GDH-8, and O/C-80 from 1.05 to 1.33 (figure 5.29e).

The N-MORB normalized patterns of these samples are characterized by relative depletion of HFSE (e.g., negative Ta- and Nb- anomaly) and selective enrichment of LILE and Th, which is typical of IAT (see figure 5.2). In contrast to the other samples in figures 5.29a through 5.29f, O/C-80 has a slightly positive Hf- and Zr-anomaly which is often observed in boninites (see figure 5.2).

G - H: Chondrite and N-MORB normalized REE and trace element distribution diagrams of samples having LREE enriched patterns. Two distinct REE patterns are recognized (figure 5.29g). The REE patterns of GDH-2a and GDH-5a indicate a $(La/Yb)_n$ ratio of ~ 3 and are flat from Gd to Lu. In contrast, the REE pattern of SC-15 is U-shaped similar to boninites (see figure 5.2).

The N-MORB normalized patterns of GDH-2a and 5a are typical of calc-alkaline rocks. LILE, Th and LREE are highly enriched and Ta and Nb as well as Zr and Hf are depleted. Depletion of TiO_2 is most likely related to fractionation of Fe-Ti oxides. The N-MORB normalized pattern of SC-15 is very similar to that of boninites. LILE Th, LREE and Hf (Zr not analyzed) are enriched compared to HREE, MREE and Ta and Nb (see figure 5.2).





are similar to dikes of geochemical group 2 in the sheeted dike complex (figure 5.17g and 5.17h). However, the sheeted dike complex is dated at 163 ± 1 Ma, whereas hornblende separates of GDH-5a yielded an $^{40}\text{Ar}/^{39}\text{Ar}$ cooling age of 153 ± 1.8 Ma, showing that the hornblende + plagioclase phyric dacites are not comagmatic with the sheeted dike complex.

SC-15 has a $(\text{La}/\text{Yb})_n$ ratio similar to GDH-2a and GDH-5a ($(\text{La}/\text{Yb})_n = 2.52$). However, the shape of the REE distribution pattern differs significantly (figure 5.29g); SC-15 has an U-shaped REE pattern and very low concentrations of REE ($0.25\text{-}8.0 \times$ chondritic). The REE distribution pattern is similar to that of boninites (compare with figure 5.2). The N-MORB normalized trace element distribution pattern of SC-15 has a characteristic arc signature, such as enrichment of LILE, Th and LREE relative to Ta, Nb and HREE. The concentrations of HREE and Y are extremely low ($0.1\text{-}0.2 \times$ N-MORB) which is characteristic of boninites. This suggests that SC-15 formed by high degrees of partial melting of a depleted mantle source. Also, a characteristic feature of the N-MORB normalized patterns of boninites is shown in figure 5.29h (compare with BON in figure 5.2); the pattern of SC-15 has a positive Hf-anomaly (Zr not analyzed). The nature of the positive Ti-anomaly is not known.

Most samples from the Mule Mountain volcanics plot in the field for IAT in the Hf/3-Th-Ta discrimination diagram of Wood et al. (1979) (figure 5.30). Also, these samples overlap with the field comprising the samples from the pillow unit suggesting much of the pillow unit and the Mule Mountain volcanics crystallized from similar magmas. Only the dacites having LREE enriched patterns (GDH-2a and GDH-5a), the boninitic sample (SC-15), and O/C-80 plot in the tectonic discrimination diagrams within the calc-alkaline field (figure 5.30). GDH-2a and GDH-5a overlap with the field for dikes of geochemical group 2 from the sheeted dike complex. Note that the Hf/3-Th-Ta discrimination diagram of Wood et al. (1979) has no field for boninites. However, rocks of boninitic affinity can be distinguished in the Cr vs. Y diagram, because boninites have very low Y concentrations and plot in general left of the field for island arc basalts (figure 5.31).

Most basic samples (see figure 5.28 for subdivision in basic and intermediate compositions) from the upper volcanic unit plot on the Cr vs. Y tectonic discrimination diagram within the field for island arc basalts (figure 5.31) overlapping with the fields of the pillow unit and the sheeted dike complex. Only O/C-

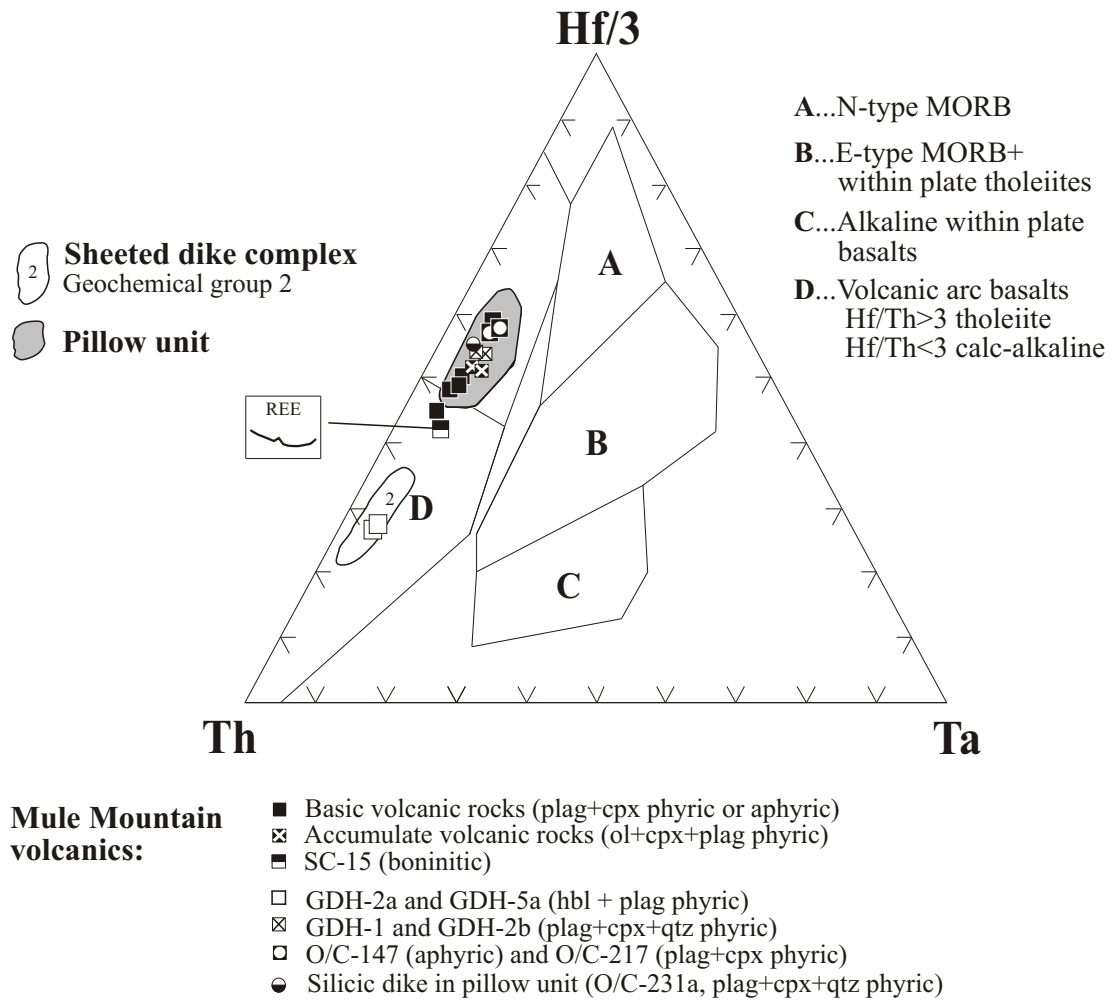


Figure 5.30

Hf/3-Th-Ta tectonic discrimination diagram with fields after Wood et al. (1979). The samples from the Mule Mountain volcanics plot in the field for island-arc tholeiite and calc-alkaline rocks. For comparison the fields for the pillow unit and the dikes of geochemical group 2 (calc-alkaline) from the sheeted dike complex are shown.

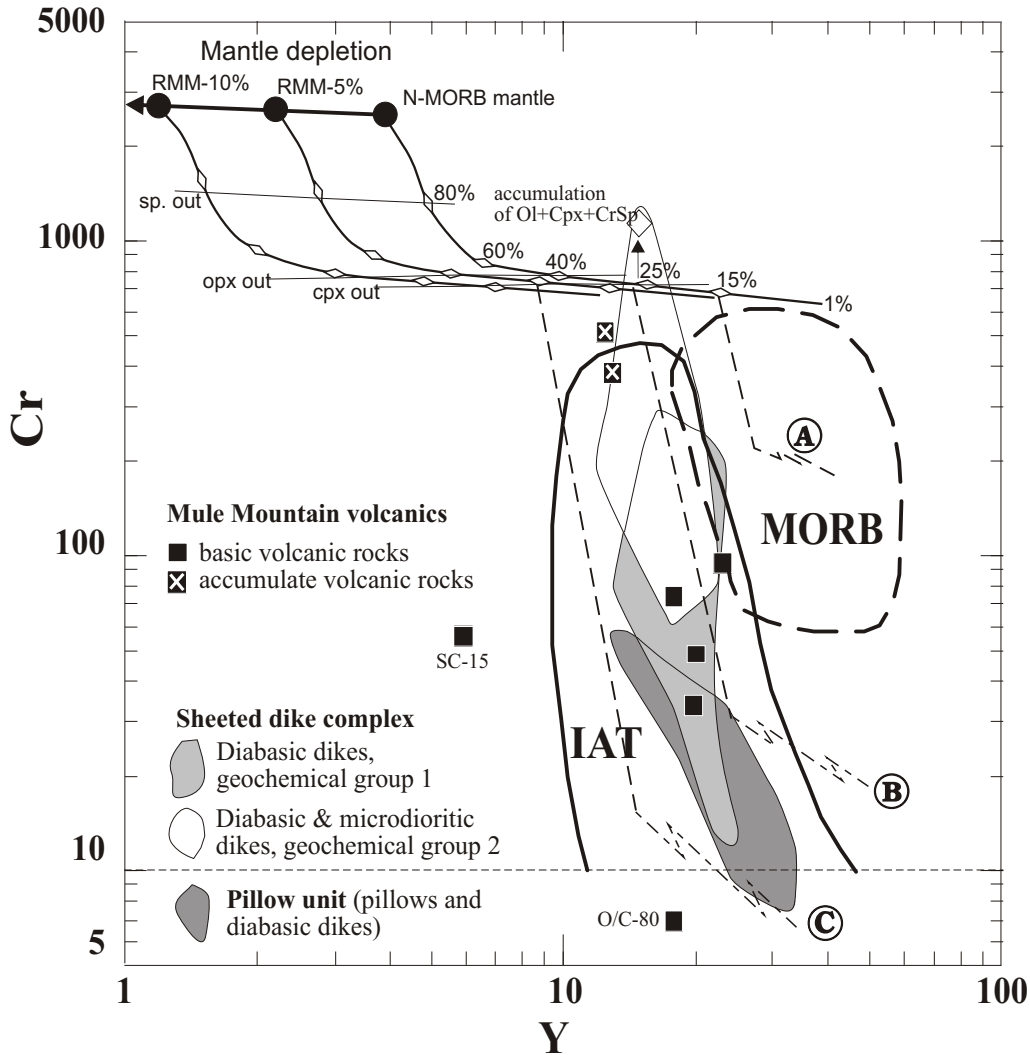


Figure 5.31

Cr vs. Y tectonic discrimination diagram of Pearce (1982) showing the fields for mid ocean ridge basalts (MORB) and island arc tholeiite (IAT) (the latter field also includes calc-alkaline and alkalic basalts from oceanic arcs). The modeled melting curves of the N-MORB mantle and the residual MORB mantle after 5% (RMM-5%) and 10% (RMM-10%) melt extraction are calculated as outlined in figure 5.4. The fractional crystallization trends for MORB (A), IAT (B) and boninite (C) are taken from Pearce et al. (1984a). The steep vector represents crystallization of olivine + Cr-spinel ± clinopyroxene, and the shallower vector represents crystallization of olivine + Cr-spinel + clinopyroxene + plagioclase. The samples from the Mule Mountain volcanics plot in the field for island arc basalts, except SC-15 and O/C-80. For comparison, the fields for the sheeted dike complex and the pillow unit are plotted.

80 and SC-15 have lower Y concentrations. The low Y concentrations of SC-15 and O/C-80 suggest that these samples evolved from magmas derived by high degrees of melting of a depleted mantle source. Note, however, that the petrogenetic pathways in figure 5.31 indicates general fractionation trends. Thus, O/C-80 could have been derived by melting of a highly depleted mantle source followed by crystal fractionation (pathway 3) or by melting of a depleted mantle source followed by similar crystal fractionation resulting in strong depletion of Cr (pathway 2). O/C-81a and O/C-81b have very high Cr contents, mainly because of Cr-spinel occurring in abundant clinopyroxene phenocrysts. O/C-81a and b appear to be very similar to clinopyroxene-rich tholeiitic lavas (IAT) in some western Pacific island arcs including Vanuatu (Barsdell, 1988) and Kamtchatka (Kamenetsky et al., 1995).

5.6.3 Chromian spinel in a sample from the Mule Mountain volcanics

Sample O/C-81b from the Mule Mountain volcanics contains euhedral Cr-spinels in the matrix and Cr-spinels within clinopyroxene and olivine phenocrysts (olivine is completely replaced by secondary minerals). The analyses of unaltered chromites are shown in figure 5.32, and the analytical data are listed in appendix C (table C8). Clinopyroxene phenocrysts have a composition of $Wo_{40.9-45.6} En_{47.7-49.6} Fs_{5.5-10.1}$ and $Mg \cdot 100 / (Mg + Fe^{2+})$ ratios of 82.7 to 91.5 (appendix C). Cr-spinels in olivine pseudomorphs have about the same Mg# as Cr-spinels within clinopyroxene phenocrysts (Cr-spinel in olivine: Mg# = 51.4; Cr-spinel in cpx: Mg# = 51.8), but the Mg# is lower in Cr-spinels in the matrix (Mg# = 42.0). Furthermore, the Cr/(Cr+Al) ratios of Cr-spinel in the matrix (Cr# = 77.6) and clinopyroxene phenocrysts (Cr# = 78.0) are significantly higher than of Cr-spinels within olivine pseudomorphs (Cr# = 61.9). Overall, the sample from the Mule Mountain volcanics (O/C-81b) contains Cr-spinels having a wide range of Cr#. One analysis of Cr-spinel within olivine pseudomorphs has a Cr/(Cr+Al) ratio similar to Cr-spinel in lavas from the Coast Range ophiolite remnant at Llanada (Giaramita et al., 1998), the other analysis is similar to Cr-spinel in lavas of Site 839 (Allan, 1994). Cr-spinels in clinopyroxene phenocrysts are similar to Cr-spinel in the boninite series of Chichijima, Bonin islands (Umino, 1986) as well as high-Ca boninites from the Troodos ophiolite (Cameron, 1985). Such a wide range of Cr# indicates disequilibrium and Cr-spinel may have crystallized from different melts generated by different extents of melting or from a variably depleted

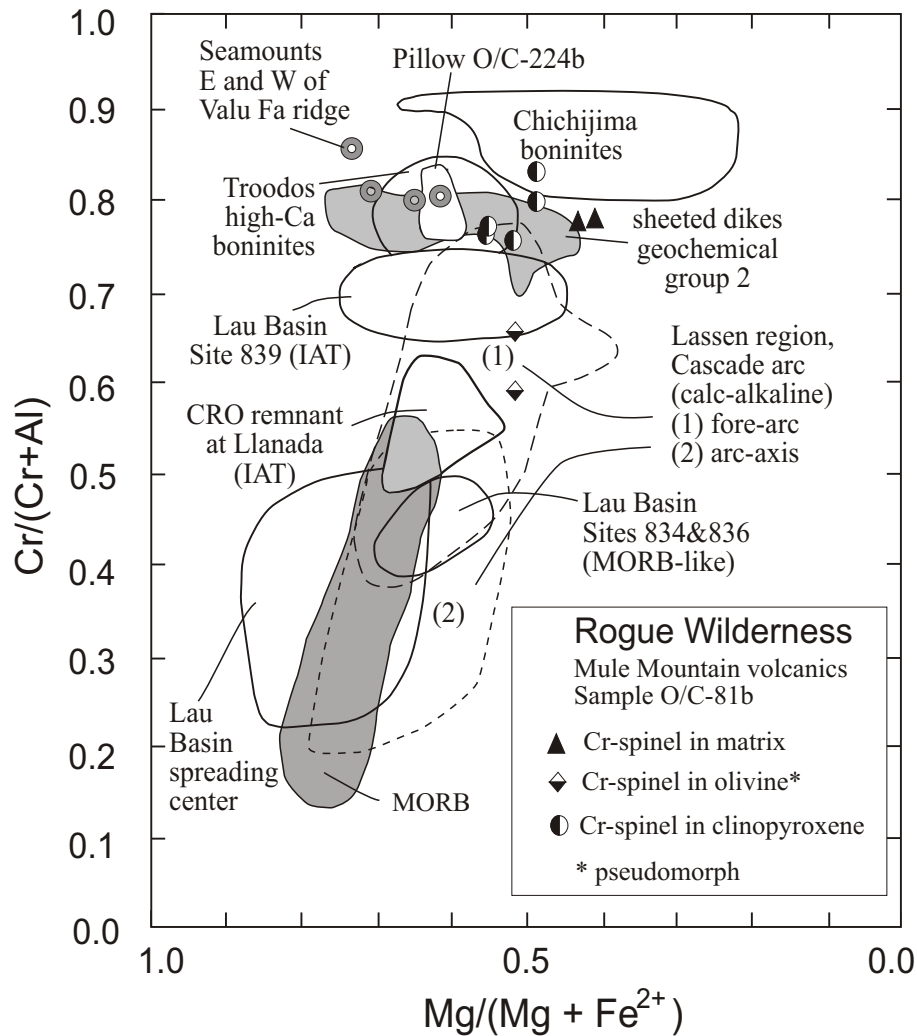


Figure 5.32

Comparison of the composition of Cr-spinel in a sample from the Mule Mountain volcanics (O/C-81b) with chromites from modern island arcs, the Troodos ophiolite, and the Coast Range ophiolite (CRO remnant at Llanada). The fields for Chichijima, Troodos, and the Lau Basin are from Meffre et al. (1996), for MORB from Dick and Bullen (1984), for the Coast Range ophiolite remnant at Llanada from Giaramita et al. (1998), and for the Cascade arc from Clynne and Borg (1997). The field for the dikes of geochemical group 2 (sheeted dike complex) is shown as well as the field for the pillow unit (O/C-224b).

mantle source, because an increase of the Cr# with little change in the Mg# of spinel is related to an increase of the degree of partial melting (Dick and Bullen, 1984) and the degree of mantle depletion (Fujii, 1989; Clyne and Borg, 1997).

5.6.4 Element mobility

The Zr vs. MgO bivariate plot of samples from the Mule Mountain volcanics are shown in figure 5.33a. The samples having parallel chondrite and N-MORB-normalized REE and trace element patterns in figure 5.29a and 5.29b form a linear trend in figure 5.33a (samples are connected by a dashed line), suggesting MgO was conserved. Samples O/C-82, GDH-7, and GDH-8 have trace element compositions similar to the samples connected by the dashed line in figure 5.34a. Furthermore, samples O/C-82, GDH-7, and GDH-8 plot close to this trend, suggesting that O/C-82, GDH-7, and GDH-8 evolved along a similar liquid line of descent. Further evidence for no or insignificant element mobility includes: (1) The positive correlation between Zr/TiO_2 and SiO_2 in figure 5.33b suggests that SiO_2 was conserved. Zr/TiO_2 is selected as a fractionation index which is also used in figure 5.28. The calc-alkaline samples GDH-2a and GDH-5a do not plot along this trend, because they have different primary compositions. (2) The relative good correlation between Al_2O_3 and MgO (figure 5.34d) for samples having relatively similar trace element compositions (i.e., GDH-1, GDH-2b, O/C-231a, O/C-81a and b, O/C-88, O/C-82, GDH-7, and GDH-8) implies that MgO is conserved. (3) CaO is correlated with MgO, except for O/C-88 (figures 5.34g) suggesting CaO was immobile in most samples. (4) LILE (Sr, K_2O , Rb, and Ba) have smooth and parallel patterns in the N-MORB normalized diagrams (figure 5.29), except for O/C-88, O/C-147 and O/C-217, suggesting these elements were immobile in most samples. (5) In contrast to the samples from the pillow unit (for which element mobility has been inferred), the samples from the Mule Mountain volcanics form linear trends in most MgO variation diagrams (figures 5.33c, d, e, f, g, h, and k).

5.6.5 Petrogenesis

5.6.5.1 Crystal fractionation

The analytical data of 14 samples from the Mule Mountain volcanics are presented in the oxide-MgO covariation diagrams in figure 5.33c through 5.33k. Additionally, the compositional fields for the pillow unit, the dikes of geochemical groups 1 and 2 from the sheeted dike complex and the samples from the metatonalite unit are shown. MgO in samples from the Mule Mountain volcanics are strongly correlated with Zr, and SiO₂ is strongly correlated with Zr/TiO₂ (figures 5.33a and 5.33b) for samples having similar trace element compositions (i.e., GDH-1, GDH-2b, O/C-231a, O/C-81a and b, O/C-88, O/C-82, GDH-7, and GDH-8). This suggests that the increase of SiO₂ and decrease of MgO in samples having similar trace element compositions is related to crystal fractionation (or increase of MgO and decrease of SiO₂ is related to accumulation), and that the major element composition is not strongly affected by alteration (section 5.6.4).

The MgO content of the samples from the Mule Mountain volcanics ranges from 10.7 to 1.3% and SiO₂ content ranges from 51.5 to 70.7% (figure 5.34c). There is a compositional gap which occurs between 10.5% and 6% MgO. SiO₂ increases only slightly within the range of the compositional gap. Samples O/C-81a and b, O/C-82, O/C-88, GDH-7, and GDH-8 contain between 51% and 57% SiO₂. The remaining, dacitic samples have SiO₂ contents between 68% and 72% (GDH-1, GDH-2a, GDH-2b, GDH-5a, O/C-147 and O/C-217). O/C-80 has significantly lower SiO₂ and higher FeO, but not much lower MgO than the dacitic samples. O/C-80 appears to be transitional between the mafic and silicic samples from the upper volcanic unit. SC-15 has significantly higher SiO₂ at a given MgO than the other mafic samples (figure 5.34c). This could be related to alteration or could reflect a high primary SiO₂-content such as that of boninitic fractionates.

The trends of the data plotted in the MgO variation diagrams show points of inflection where the rate of increase or decrease of the element abundance changes with increasing fractionation (figure 5.33). A point of inflection is located at about 3.5% MgO in a plot of SiO₂ vs. MgO (figure 5.33c). Also, TiO₂, FeO* and MnO (figures 5.33d, 5.33f and 5.33g) increase slightly from 10.5% MgO to about 3.5% MgO. These trends are characteristic of tholeiitic fractionation trends. Then, the concentrations of TiO₂, FeO*

and MnO decrease rapidly with increasing fractionation. Rapid decrease of FeO, MnO, and TiO₂ is consistent with fractionation of Fe-Ti oxides. Therefore, the inflection at 3.5% MgO probably marks the onset of crystallization of Fe-Ti oxides.

GDH-7 and GDH-8 have the highest Al₂O₃ content and seem to mark the point of inflection in the Al₂O₃ vs. MgO plot (figure 5.34e). Al₂O₃ increases from 14.5% to 16.5% and then decreases to 14% with decreasing MgO suggesting that fractionation of plagioclase was predominant when MgO in the magma was less than 5-6%. The Increase of Al₂O₃ with increasing MgO can be explained with delayed crystallization of plagioclase. High volatile (H₂O) content of the parental magma causes suppression of plagioclase crystallization and enrichment of Al₂O₃ (Sisson and Grove, 1993a,b).

CaO decreases sharply with fractionation in samples with >8% MgO. The decrease of CaO and Al₂O₃ with decreasing MgO is consistent with fractionation of plagioclase and clinopyroxene. The point of inflection in the CaO vs. MgO plot cannot be inferred due to the compositional gap.

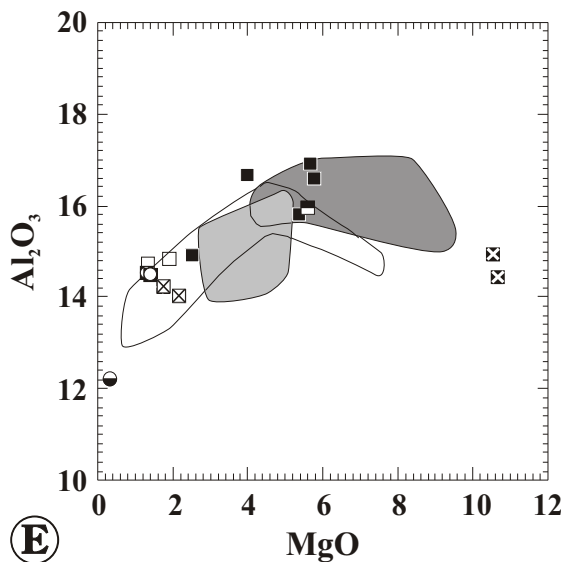
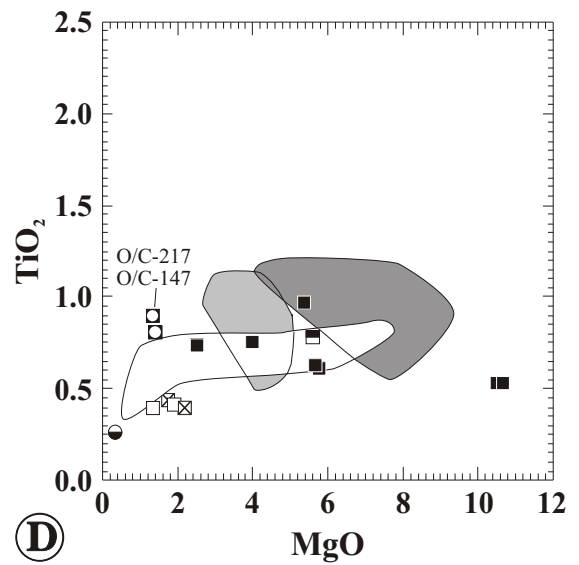
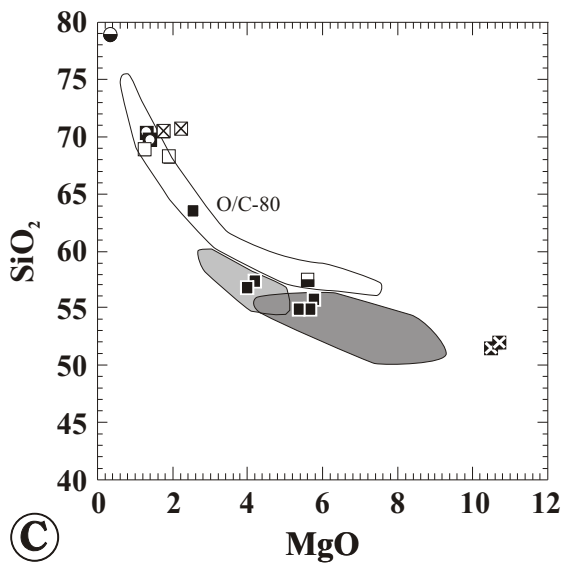
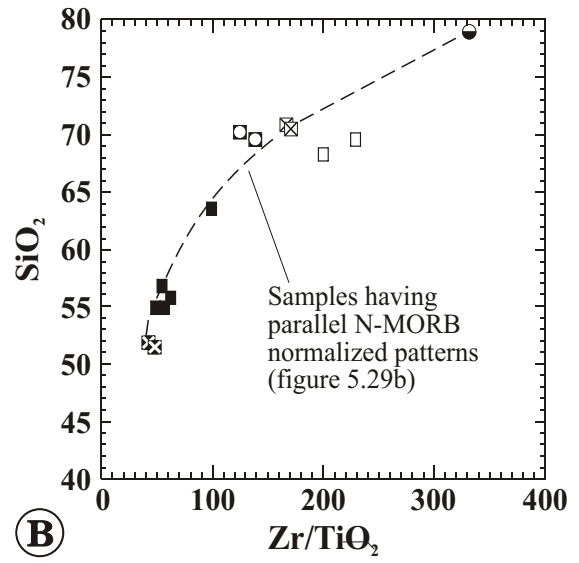
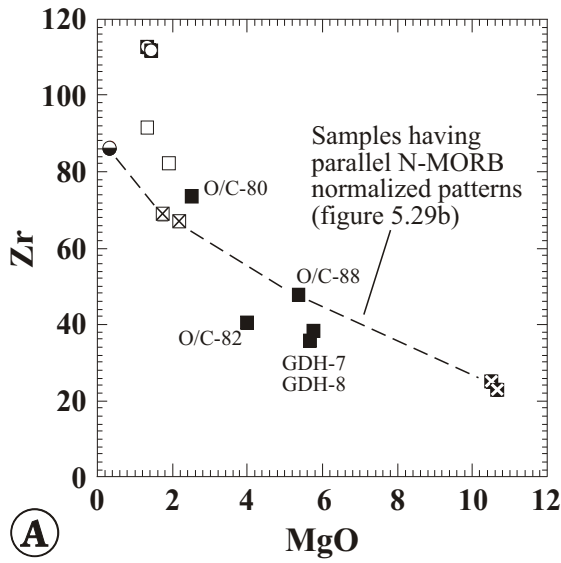
The Na₂O- and K₂O- concentrations scatter in the MgO variation diagram, suggesting hydrothermal fluids reacted with the rock resulting in enrichment or depletion of mobile elements such as Na and K. Samples may have gained Na₂O due to albitization of plagioclase.

The major element composition of O/C-147 (aphyric dacite) and O/C-217 (slightly porphyritic dacite, <<1% phenocrysts) is very similar to the strongly porphyritic dacites GDH-1, GDH-2a, GDH-2b and GDH-5a. However, O/C-147 and O/C-217 have significantly higher TiO₂ and P₂O₅ concentrations than the other dacitic samples (figure 5.33d and 5.33k) suggesting they derived from different magmas than GDH-1, GDH-2a, GDH-2b and GDH-5a.

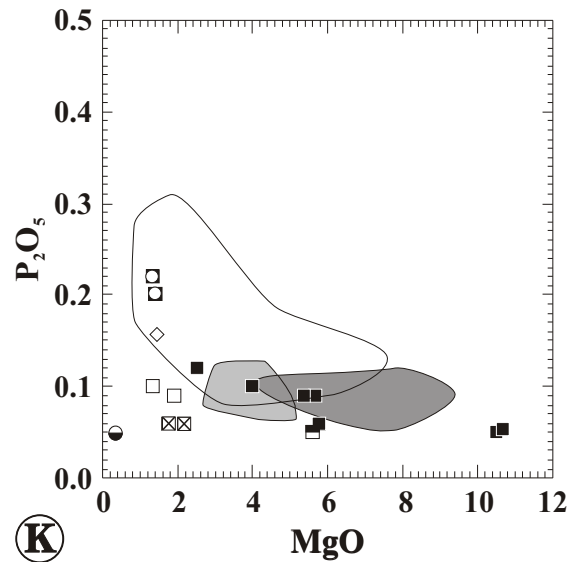
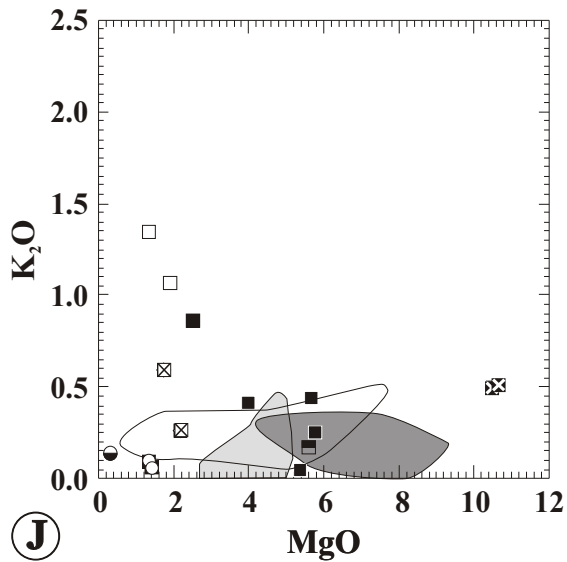
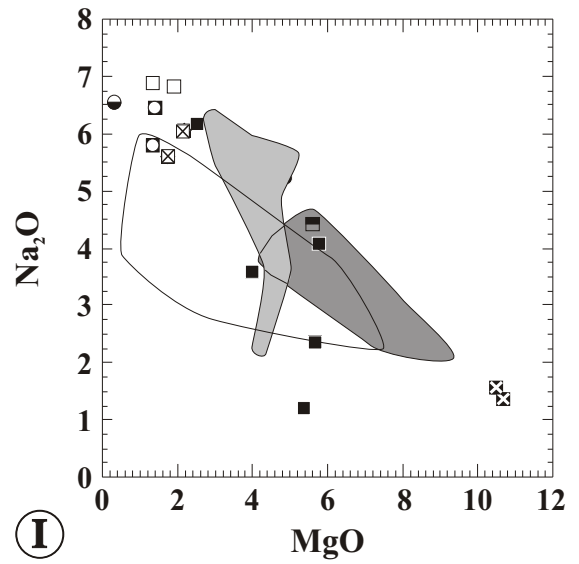
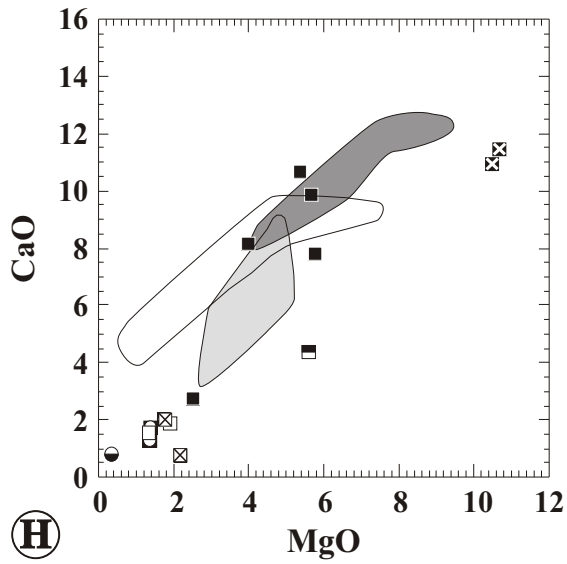
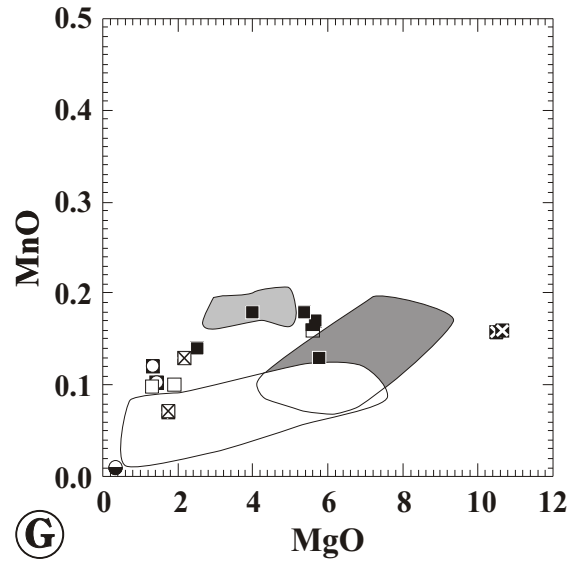
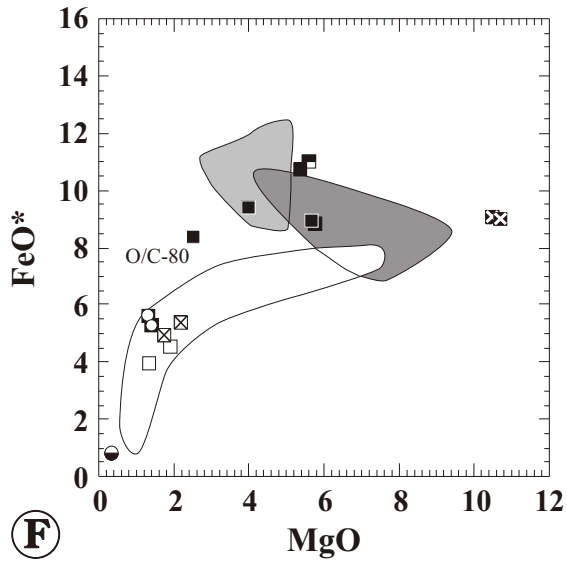
The dacitic samples GDH-1, GDH-2a, GDH-2b and GDH-5a cannot be distinguished based on the major element composition, because the differences are very small as illustrated in the MgO variation diagrams (figure 5.33). Only the hornblende + plagioclase phyric samples (open squares) are more enriched in K₂O than the cpx + plag + Qtz phyric samples (open square containing X). Clearly, the analyses of major elements is not sufficient to determine whether these dacites derived from tholeiitic or calc-alkaline parental magmas.

Figure 5.33

- A:** Zr vs. MgO variation diagram of samples from the Mule Mountain volcanics. The samples having parallel MORB normalized patterns lay on a straight suggesting MgO was immobile.
- B:** SiO₂ vs. Zr/TiO₂ diagram of samples from the Mule Mountain volcanics. The strong correlation between Zr/TiO₂, a fractionation index (figure 5.28), and SiO₂ suggests SiO₂ was not mobile.
- C - K:** MgO variation diagrams of samples from the Mule Mountain volcanics. For comparison, the fields for the metatonalite unit + dikes of geochemical group 2, the dikes of geochemical group 1 and the pillow unit are shown. In most MgO variation diagrams, the samples having similar trace element compositions form curvilinear trends (figures 5.33c, d, e, f, g, h, and k). These samples follow a tholeiitic fractionation trend (see text). Silicic samples derived from tholeiitic parental magmas (GDH-1, GDH-2b) cannot be distinguished from silicic samples derived from calc-alkaline parental magmas (GDH-2a, GDH-5a) based on the major elements.



- Basic samples (plag+cpx phyric or aphyric)
- ⊠ Accumulate samples (ol+cpx+plag phyric)
- SC-15 (highly altered boninitic sample)
- GDH-2a and GDH-5a (hbl + plag phyric)
- ⊠ GDH-1 and GDH-2b (plag+cpx+qtz phyric)
- O/C-147 (aphyric) and O/C-217 (plag+cpx phyric)
- Silicic dike in pillow unit, O/C-231a (plag+cpx+qtz phyric)
- Dikes of geochemical group 1, sheeted dike complex
- Dikes of geochemical group 2, sheeted dike complex; samples from the metatonalite unit
- Pillows and diabasic dikes, pillow unit



The major element composition of samples O/C-81a and 81b is very similar to high-Ca boninites as defined by Crawford et al. (1989), such as $\text{SiO}_2 < 56\%$, $\text{CaO} > 9\%$, $\text{FeO}^* > 7.5\%$ and $\text{CaO}/\text{Al}_2\text{O}_3 = 0.7 - 1.0$. Although O/C-81a and 81b have $\text{SiO}_2 = 49-50\%$, $\text{FeO}^* = 9.6\%$ and $\text{CaO}/\text{Al}_2\text{O}_3 = 0.7-0.8$, they have significantly higher TiO_2 , higher Al_2O_3 and lower Mg# (lower MgO and similar FeO^* content) compared to the reference suite, the Troodos Upper Pillow lavas ($\text{TiO}_2 < 0.36$, $\text{Al}_2\text{O}_3 = 11-15\%$, and Mg# of 65 - 75). The high MgO content of O/C-81a and 81b could be related to accumulation of clinopyroxene and olivine.

5.6.5.2 Mantle heterogeneity and magma mixing

The samples from the Mule Mountain volcanics in figure 5.29b and 5.29d have N-MORB normalized trace element distribution patterns similar to the samples from the pillow unit in figures 5.22b and 5.22d, respectively. Thus, a mixing model similar to that shown in figure 5.26 can be calculated for the samples from the Mule Mountain volcanics (not shown). In addition to the IAT, the Mule Mountain volcanics comprises rocks having boninitic and calc-alkaline affinities. Partial melting of at least three different mantle sources can explain the occurrence of three different magma types in the Mule Mountain volcanics. Mixing between the different magma types (IAT, BON and CAB) cannot be constrained using the trace element data. However, the analysis of Cr-spinels in O/C-81b provides evidence for magma mixing between different magma types. Sample O/C-81b has magmatic affinities to IAT, but it contains Cr-spinels having $\text{Cr}/(\text{Cr}+\text{Al})$ ratios typical of boninites. This implies that boninitic magmas were present and mixed with IAT magma. This interpretation is consistent the large range of compositions of Cr-spinels in O/C-81b implying disequilibrium (figure 5.32).

5.7 Post ophiolite intrusive rocks

The Half Moon Bar diorite (HMB) is the largest, post-ophiolite intrusion in the Wild Rogue Wilderness and occurs as a fault slice in contact with the pillow unit. Locally, small dioritic intrusions, probably related to the HMB diorite, crop out within the pillow unit. Also, the HMB diorite contains basaltic, andesitic, and rhyolitic xenoliths. Hornblende separates of sample O/C-376 from the HMB diorite

yielded a $^{40}\text{Ar}/^{39}\text{Ar}$ cooling age of 157.2 ± 2.0 Ma. Gray and McKee (1981) reported a K/Ar age of 159 ± 3.0 Ma determined in a sample from the same locality as O/C-376 (figure 5.1). Saleeby, (personal communication, 1999) reported concordant zircon U/Pb ages for samples from the HMB diorite (figure 5.2). Sample SC-11 has a concordant age of 160 ± 2 Ma, and SC-12 and SC-13 of 158 ± 1.5 Ma. The $^{40}\text{Ar}/^{39}\text{Ar}$ and the K/Ar cooling ages are in excellent agreement with the U/Pb zircon ages.

Two muscovite garnet tonalite dikes (GH-97-6 and GH-97-20) intruding the metagabbro unit were sampled for major- and trace elements analysis. For $^{40}\text{Ar}/^{39}\text{Ar}$ dating, O/C-372b was collected from the same dike as GH-97-6 near the contact with the metatonalite unit (figure 5.1). Muscovite separates of two dikes (O/C-372b and GH-97-20) yielded $^{40}\text{Ar}/^{39}\text{Ar}$ ages of 148.52 ± 0.17 Ma and 147.99 ± 0.45 Ma, respectively. There are no U/Pb zircon ages from the muscovite garnet tonalite dikes. Potentially, the tonalitic dikes could have formed much earlier than 149 Ma, because the $^{40}\text{Ar}/^{39}\text{Ar}$ ages mark the age of cooling below 350°C .

5.7.1 Half Moon Bar Diorite

5.7.1.1 Rock classification

Seven samples from the HMB diorite are analyzed for major and trace elements, including O/C-376, and the analytical data are listed in table 5.6. The sample localities are shown in figure 5.1, and the petrographic data are summarized in appendix A (table A7). Four medium grained dioritic samples from the HMB diorite were analyzed. They consist of 45-64% plagioclase, 28-45% hornblende, 5-12% quartz, and <4% oxide. Plagioclase is altered and cloudy in thin section, but zoning is easily identified, and calcic cores are partially preserved (An_{76-82}). The rims are zoned ranging in composition from andesine to oligoclase ($\geq \text{An}_{17}$). Amphibole ranges in composition from magnesio-hornblende to actinolite. Rare, dark-brown to greenish brown (pleochroic) hornblende is interpreted to be igneous in origin (see also chapters 2 and 3). Igneous clinopyroxene is not very common in three samples and appears to be replaced by amphibole (actinolite) + magnetite (magmatic and/or metamorphic reactions). O/C-174a differs from the other samples in that it contains mostly clinopyroxene instead of hornblende. All samples contain

Table 5.6: Major and trace element composition of samples from the Half Moon Bar diorite

| Sample | OC-174b dike | OC-375c dike | OC-375d dike | O/C-118A gabbro | O/C-174A gabbro | O/C-376 gabbro | O/C-377 gabbro |
|--------------------------------|-----------------|-----------------|-----------------|--------------------|--------------------|-------------------|-------------------|
| SiO ₂ | 56.87 | 58.62 | 56.03 | 52.15 | 56.53 | 56.88 | 59.59 |
| TiO ₂ | 0.56 | 0.58 | 0.61 | 0.74 | 0.60 | 0.55 | 0.49 |
| Al ₂ O ₃ | 15.57 | 16.22 | 16.60 | 16.23 | 14.74 | 15.98 | 15.59 |
| Fe ₂ O ₃ | 9.46 | 8.67 | 9.20 | 10.65 | 8.51 | 9.18 | 8.82 |
| MnO | 0.17 | 0.11 | 0.14 | 0.14 | 0.14 | 0.13 | 0.13 |
| MgO | 4.54 | 3.41 | 3.94 | 5.24 | 6.06 | 3.80 | 3.49 |
| CaO | 7.72 | 8.36 | 8.71 | 9.35 | 6.96 | 8.19 | 7.04 |
| Na ₂ O | 2.90 | 2.89 | 3.32 | 2.98 | 3.71 | 2.95 | 2.44 |
| K ₂ O | 0.41 | 0.23 | 0.28 | 0.60 | 0.74 | 0.43 | 0.47 |
| P ₂ O ₅ | 0.11 | 0.12 | 0.11 | 0.06 | 0.12 | 0.15 | 0.09 |
| BaO | 281 | 199 | 254 | 227 | 267 | 248 | 245 |
| Cr ₂ O ₃ | 80 | 38 | 27 | 75 | 205 | 39 | 23 |
| LOI | 1.99 | 1.49 | 1.32 | 1.81 | 2.00 | 1.42 | 1.68 |
| Total | 100.38 | 100.75 | 100.32 | 100.03 | 100.19 | 99.71 | 99.88 |
| Ni xrf | 10.05 | <d.l. | 6.03 | 18.09 | 121.57 | 18.08 | 6.03 |
| Sc xrf/icp | 24/n.d. | 33/n.d. | 46/n.d. | 43/45 | 40/41 | 32/35 | 30/33 |
| V xrf/icp | 221/243 | 220/235 | 246/256 | 344/n.d. | 235/n.d. | 224/n.d. | 188/n.d. |

Major elements (in wt%) and Ba, Cr, Ni, Sc, and V (in ppm) were analyzed by standard XRF technique on pressed powder pellets at McGill University, Montreal. Additionally, Sc was analyzed by ICP-MS at Washington State University and V at Union College

Table 5.6 cont.

| Sample | OC-174b | OC-375c | OC-375d | O/C-118A | O/C-174A | O/C-376 | O/C-377 |
|--------|---------|---------|---------|----------|----------|---------|---------|
| | UC | UC | UC | WSU | WSU | WSU | WSU |
| Cr | 44.0 | 18.5 | 18.1 | n.d. | n.d. | n.d. | n.d. |
| Rb | 5.19 | 2.94 | 2.88 | 7.98 | 10.1 | 4.93 | 5.81 |
| Sr | 358 | 370 | 410 | 337 | 407 | 357 | 374 |
| Y | 16.9 | 18.6 | 17.4 | 15.4 | 20.3 | 19.3 | 25.4 |
| Zr | 51 | 56.8 | 50.3 | 33 | 53 | 49 | 48 |
| Nb | 1.45 | 1.67 | 1.45 | 0.99 | 1.48 | 1.32 | 1.87 |
| Cs | 0.528 | 0.665 | 0.66 | 1.018 | 1.148 | 0.709 | 0.635 |
| Ba | 216 | 157.7 | 188 | 211 | 262 | 223 | 223 |
| La | 5.47 | 6.10 | 5.21 | 4.23 | 4.59 | 5.38 | 7.13 |
| Ce | 11.9 | 13.30 | 11.8 | 9.9 | 10.4 | 11.9 | 16.3 |
| Pr | 1.75 | 1.95 | 1.76 | 1.45 | 1.54 | 1.73 | 2.41 |
| Nd | 8.2 | 8.97 | 8.20 | 6.7 | 7.6 | 8.4 | 11.4 |
| Sm | 2.20 | 2.35 | 2.16 | 1.93 | 2.36 | 2.50 | 3.25 |
| Eu | 0.70 | 0.68 | 0.65 | 0.63 | 0.75 | 0.71 | 0.72 |
| Gd | 2.36 | 2.58 | 2.42 | 2.29 | 2.92 | 2.80 | 3.51 |
| Tb | 0.40 | 0.43 | 0.42 | 0.40 | 0.51 | 0.48 | 0.62 |
| Dy | 2.70 | 2.95 | 2.79 | 2.67 | 3.57 | 3.31 | 4.15 |
| Ho | 0.59 | 0.64 | 0.60 | 0.57 | 0.74 | 0.69 | 0.94 |
| Er | 1.75 | 1.89 | 1.81 | 1.59 | 2.03 | 1.91 | 2.66 |
| Tm | 0.27 | 0.30 | 0.28 | 0.25 | 0.31 | 0.30 | 0.41 |
| Yb | 1.81 | 1.97 | 1.86 | 1.53 | 1.98 | 1.89 | 2.54 |
| Lu | 0.28 | 0.31 | 0.30 | 0.25 | 0.32 | 0.31 | 0.41 |
| Hf | 1.55 | 1.74 | 1.55 | 1.05 | 1.64 | 1.46 | 1.68 |
| Ta | 0.079 | 0.094 | 0.083 | 0.067 | 0.093 | 0.081 | 0.11 |
| Pb | 0.53 | 0.68 | 0.75 | 1.06 | 0.87 | 0.86 | 0.75 |
| Th | 1.06 | 1.22 | 1.01 | 0.62 | 1.04 | 1.05 | 1.14 |
| U | 0.39 | 0.44 | 0.29 | 0.2 | 0.28 | 0.29 | 0.40 |

UC... Trace element analysis by ICP-MS at Union College

WSU... Trace element analysis by ICP-MS at Washington State University

All trace elements are given in ppm.

n.d. ... not determined

<d.l. ... below detection

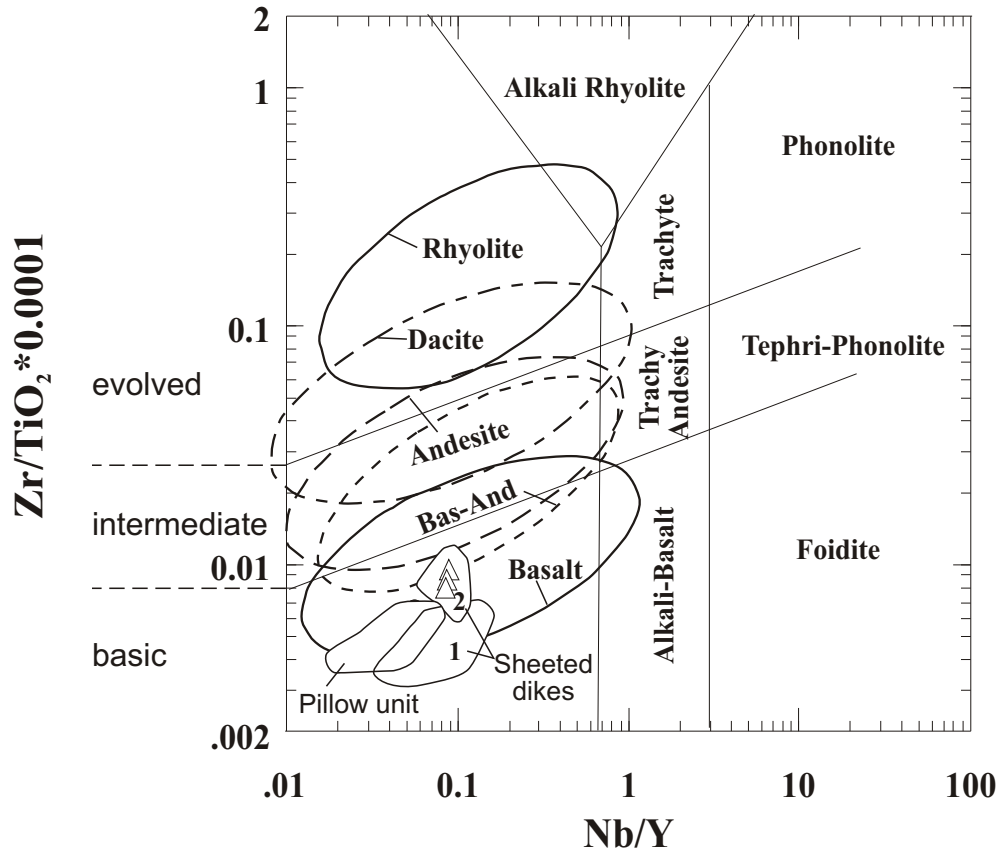
interstitial quartz which crystallized late and texturally appears clearly to be igneous. Typically, quartz is not recrystallized, unless it occurs in the vicinity of narrow (< 1 mm wide), ductile-brittle shear bands identified in thin section. The metamorphic mineral assemblage in the diorite includes epidote, clinozoisite, albite, actinolite, magnetite, quartz, chlorite, prehnite, laumontite and calcite.

The samples from the HMB diorite range in composition from quartz gabbro (O/C-174a) to hornblende quartz gabbro (O/C-118a) to hornblende quartz diorite (O/C-376 and O/C-377) based on the modes and estimated average compositions of plagioclase (Streckeisen, 1976, LeMaitre et al., 1989). However, all plutonic samples plot in the field for subalkalic diorite using the TAS diagram of Wilson (1989) (not shown). Low Nb/Y ratios (0.064 - 0.073) and low Zr/TiO₂ ratios (44-96) determined for the plutonic samples are consistent with a mafic to intermediate, subalkalic composition.

Also, three porphyritic dikes cutting the HMB-diorite were analyzed. The dikes contain phenocrysts of plagioclase (12-22%), clinopyroxene (7-19%, pseudomorphed by pale green hornblende) and magnetite (1-3%). The secondary mineral assemblage is similar to the HMB diorite and includes epidote, clinozoisite, albite, actinolite, magnetite, quartz, chlorite, prehnite, laumontite and calcite. Figure 5.34 shows the Zr/TiO₂ vs. Nb/Y classification diagram of Winchester and Floyd (1977) with fields revised by Pearce (1996). The dikes plot at and below the lower field boundary of the 10% probability contour for subalkaline basaltic andesites defined by the total alkali vs. silica (TAS) rock classification. The Nb/Y ratios (0.083 - 0.096) and Zr/TiO₂ ratios (80-96) of these dikes is very similar to the dikes of geochemical group 2 from the sheeted dike complex (figure 5.34).

5.7.1.2 Magmatic affinities

The chondrite normalized trace element patterns of samples from the HMB gabbro are shown in figures 5.35a and 5.35b. The samples from the HMB diorite and the dikes have almost parallel REE distribution patterns with (La/Yb)_n ratios ranging between 1.66 and 2.22. All REE patterns have a negative Ce-anomaly. O/C-176a is slightly less enriched in LREE than the other samples. The (La/Yb)_n ratio of O/C-176a is 1.66 and of the other samples 1.99 - 2.22. Thus, the REE patterns of O/C-174b and O/C-376



△ Dikes in the Half Moon Bar diorite

Figure 5.34

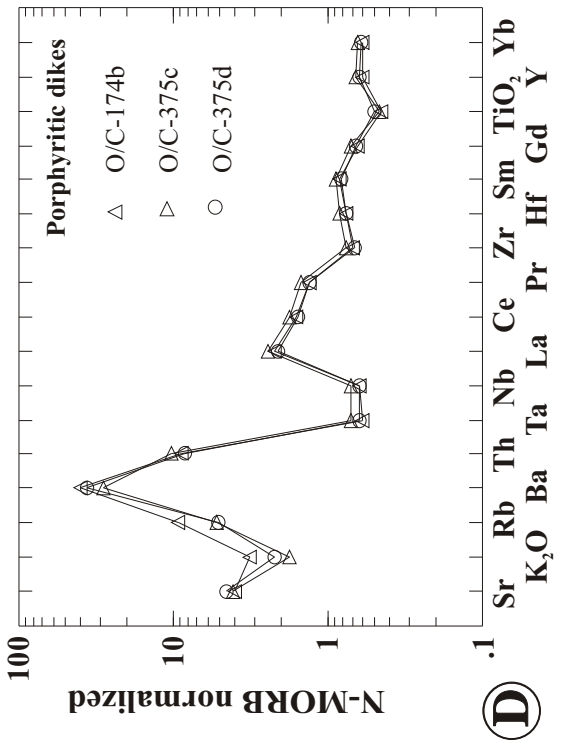
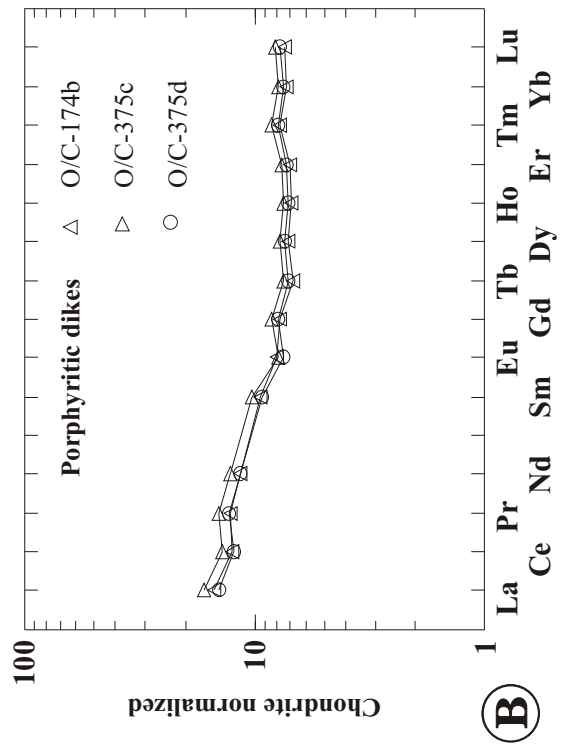
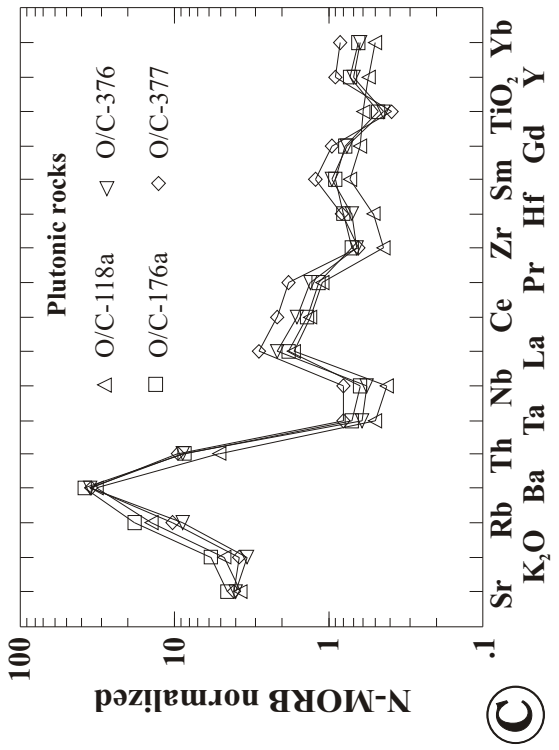
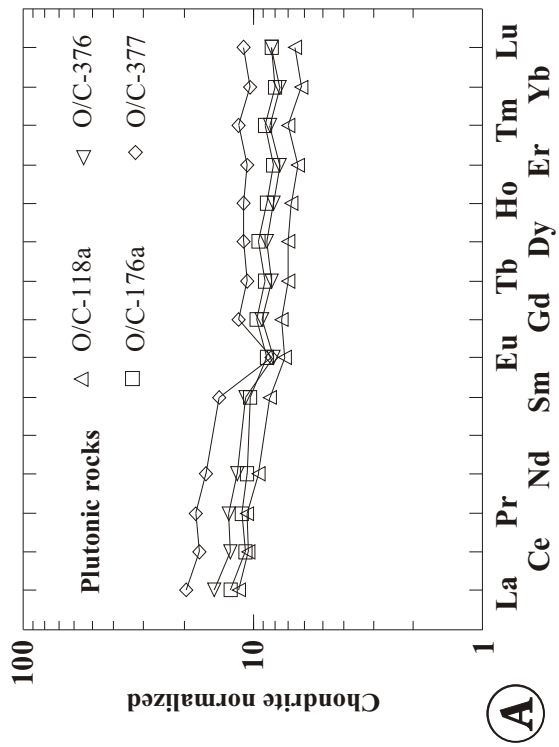
Zr/TiO₂ vs. Nb/Y diagram of Winchester and Floyd (1977) with fields revised by Pierce (1996).

Additionally, the 10% probability ellipses for TAS-defined rock types from subalkaline series are shown (after Pierce, 1996). The 10% probability ellipses overlap substantially. The dikes in the Half Moon Bar diorite have similar Zr/TiO₂ and Nb/Y ratios as dikes of geochemical group 2 from the sheeted dike complex.

Figure 5.35

A - B.: Chondrite normalized REE distribution patterns of samples from the Half Moon Bar diorite and porphyritic dikes intruding diorite. The patterns are LREE enriched, and the range of the chondrite normalized La/Yb ratios is very limited (1.66-2.22). All samples have a negative Ce-anomaly.

C - D: N-MORB normalized trace element distribution diagram of samples from the Half Moon Bar diorite and porphyritic dikes intruding diorite. The HFSE are depleted and LILE, Th and LREE are strongly enriched. The negative TiO₂ anomaly increases with increasing incompatible trace element abundance suggesting fractionation of Fe-Ti oxides. The patterns are parallel suggesting the samples are related by fractionation. The patterns are typical of rocks of calc-alkaline affinity (compare with figure 5.2).



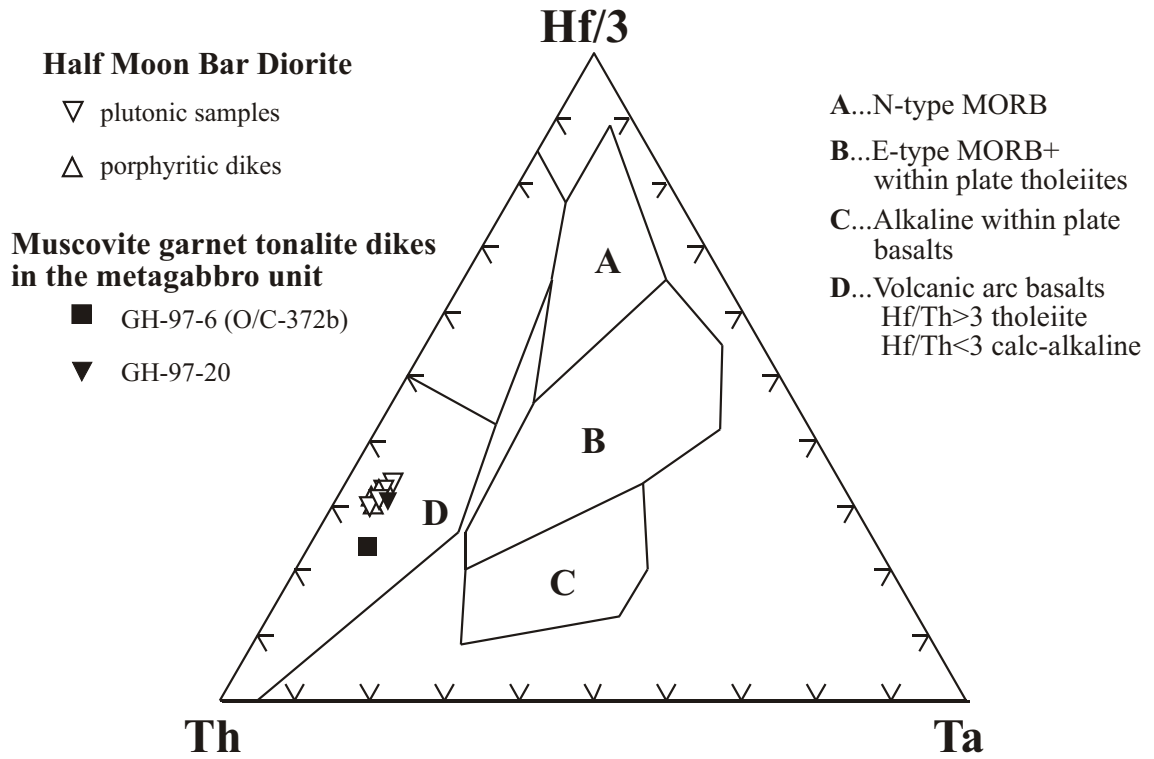


Figure 5.36

Hf/3-Th-Ta tectonic discrimination diagram with fields after Wood et al. (1979). The samples from the Half Moon Bar diorite plot in the field for calc-alkaline rocks.

cross each other. O/C-176a not only has a different mineral (appendix A) and major element composition (table 5.6), it also differs slightly in the REE composition.

The N-MORB normalized trace element distribution patterns of the samples from the HMB diorite and the dikes are also parallel (they vary only in their level), indicating that incompatible trace element ratios remained constant during fractionation (figure 5.35c and 5.35d). Ta, Nb, Zr and Hf are strongly depleted ($0.4-0.8 \times$ N-MORB), whereas LREE, Th and LILE are selectively enriched. The relative enrichment of Th and LREE is significantly higher than the Th and LILE enrichment in island-arc tholeiites. All samples from the HMB-diorite show patterns characteristic of rocks of calc-alkaline affinity (compare with figure 5.2). Also, these samples plot in the calc-alkaline field in the Hf/3-Th-Ta tectonic discrimination diagram (figure 5.36).

5.7.1.3 Fractionation

The parallel chondrite- and N-MORB- normalized REE and trace element patterns of samples from the HMB diorite (figure 5.35) indicate that the plutonic samples as well as the porphyritic dikes are from the same source and might be related by crystal fractionation. SiO_2 and Zr/TiO_2 as well as SiO_2 and Zr are strongly correlated in all samples (SiO_2 increases with increasing Zr/TiO_2 ratios as well as increasing Zr) suggesting that SiO_2 increases with increasing fractionation and that SiO_2 was immobile in the HMB diorite. However, Zr and MgO are poorly correlated suggesting MgO was not conserved in the samples from the Half Moon Bar diorite (subseafloor hydrothermal and or deuteric alteration, chapters 2 and 3). Thus, the MgO variation diagrams are not shown.

O/C-118a has the lowest SiO_2 content, the lowest Zr/TiO_2 ratios and, thus, appears to be the most primitive sample. The N-MORB normalized pattern of O/C-118a has no negative TiO_2 -anomaly. However, the negative TiO_2 -anomaly of the other samples increases with increasing SiO_2 content, which is consistent with crystallization and fractionation of Fe-Ti oxides. In addition to TiO_2 , V decreases with increasing fractionation, which is characteristic of the calc-alkaline series (Shervais, 1982).

The REE pattern of the most primitive sample (O/C-118a) has no negative Eu-anomaly (figure 5.35a). In the other samples, the Eu-anomaly increases with increasing REE-enrichment suggesting fractionation of plagioclase.

The samples from the HMB diorite and the porphyritic dikes have parallel chondrite- and N-MORB normalized trace element distribution patterns (figure 5.35). Only the REE pattern of O/C-176a varies slightly, which could be explained with higher degrees of partial melting. Also, the samples from the HMB gabbro cluster in the Hf/3-Th-Ta discrimination diagram (figure 5.26) indicating little compositional diversity. This implies the HMB diorite was derived by partial melting of a homogeneous mantle source.

5.7.2 Muscovite garnet tonalite dikes in the metagabbro unit

5.7.2.1 Rock classification

Two silicic dikes in the metagabbro unit were analyzed for major and trace elements, and the analytical data are listed in table 5.7. The sample localities are shown in figure 5.1. GDH-97-20 occurs approximately in the center of the metagabbro unit, the other dike about 400m further southeast, near the contact with the metatonalite unit. The petrographic data are summarized in appendix A (table A6). The dikes GH-97-6 (re-sampled dike O/C-372b) and GH-97-20 consist of 40-50% plagioclase, 40-45% quartz, 8-15% muscovite and up to 7% garnet. GH-97-20 contains significantly more garnet than GH-97-6 (trace amounts). Additionally, trace amounts of biotite occur in sample GH-97-6. Both dikes are foliated, and GH-97-20 has a S/C-type fabric. The secondary mineral assemblage includes epidote, chlorite, albite and prehnite. These silicic dikes in the metagabbro unit can be classified as muscovite garnet tonalites based on the modes (Streckeisen, 1976, LeMaitre et al., 1989). The samples have low Nb/Y ratios (0.10 - 0.32) but moderate to high Zr/TiO₂ ratios (377-1270) which are consistent with an intermediate to evolved, subalkalic composition.

Table 5.7: Major and trace element composition of dikes in the metagabbro unit

| Sample | GH-97-6 tonalite | GH-97-20 tonalite | Sample | GH-97-6 WSU | GH-97-20 WSU |
|--------------------------------|---------------------|----------------------|--------|----------------|-----------------|
| SiO ₂ | 74.76 | 74.34 | Cr | n.d. | n.d. |
| TiO ₂ | 0.17 | 0.03 | Rb | 6.4 | 48.8 |
| Al ₂ O ₃ | 12.69 | 15.05 | Sr | 236 | 97 |
| Fe ₂ O ₃ | 2.04 | 1.31 | Y | 4.9 | 45 |
| MnO | 0.05 | 0.80 | Zr | 64 | 41 |
| MgO | 0.92 | 0.25 | Nb | 1.57 | 4.64 |
| CaO | 3.17 | 0.83 | Cs | 0.32 | 0.63 |
| Na ₂ O | 4.03 | 3.09 | Ba | 165 | 1716 |
| K ₂ O | 0.54 | 2.43 | La | 6.34 | 16.4 |
| P ₂ O ₅ | 0.04 | 0.06 | Ce | 10.8 | 31.5 |
| BaO | 187 | 1958 | Pr | 1.04 | 3.71 |
| Cr ₂ O ₃ | 27 | 27 | Nd | 3.38 | 14.43 |
| LOI | 1.64 | 1.80 | Sm | 0.65 | 3.61 |
| Total | 100.08 | 100.20 | Eu | 0.28 | 0.43 |
| Ni | <d.l. | <d.l. | Gd | 0.65 | 3.94 |
| Sc xrf/icp | 17/4.8 | 11/3.8 | Tb | 0.10 | 0.81 |
| V | 23 | <d.l. | Dy | 0.70 | 6.03 |
| | | | Ho | 0.15 | 1.34 |
| | | | Er | 0.47 | 3.92 |
| | | | Tm | 0.08 | 0.61 |
| | | | Yb | 0.51 | 4.08 |
| | | | Lu | 0.10 | 0.61 |
| | | | Hf | 2.27 | 1.86 |
| | | | Ta | 0.13 | 0.20 |
| | | | Pb | 1.48 | 8.71 |
| | | | Th | 1.52 | 1.78 |
| | | | U | 1.20 | 0.55 |

Major elements (in wt%) and Ba, Cr, Ni, Sc, and V (in ppm) were analyzed by standard XRF technique on pressed powder pellets at McGill University, Montreal. Additionally, Sc was analyzed by ICP-MS at Washington State University WSU... Trace element analysis by ICP-MS at Washington State University All trace elements are given in ppm.

n.d. ... not determined

<d.l. ... below detection

5.7.2.2 Magmatic affinities

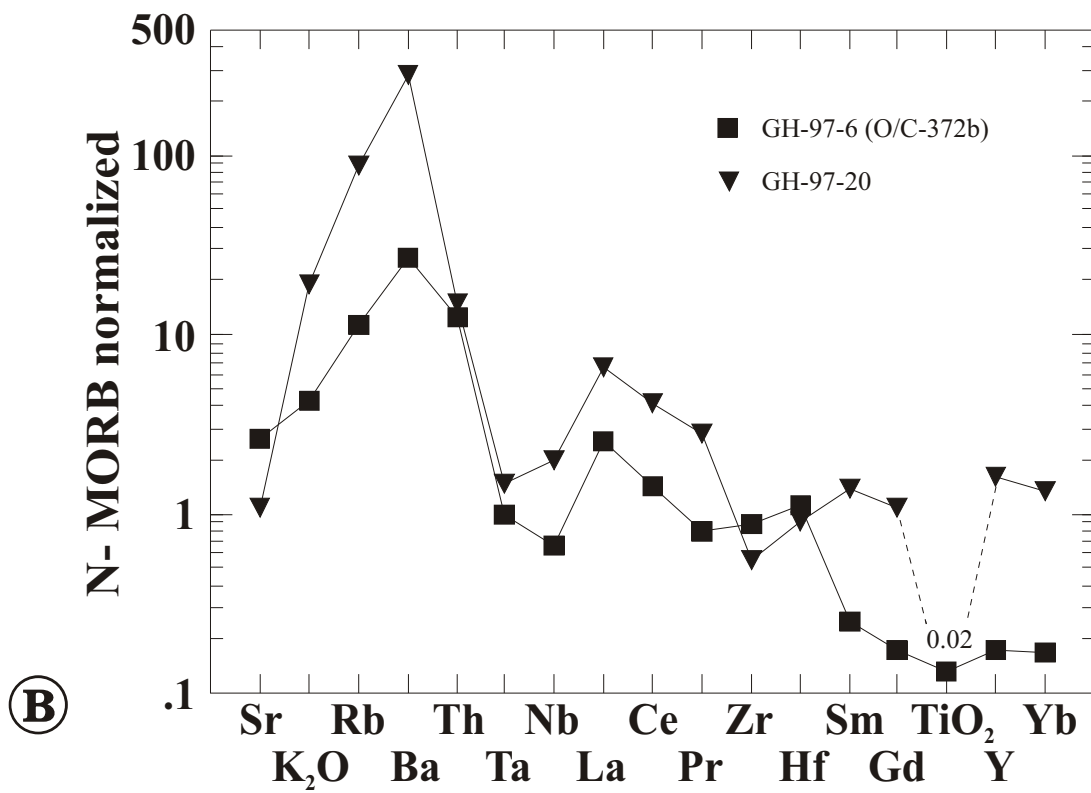
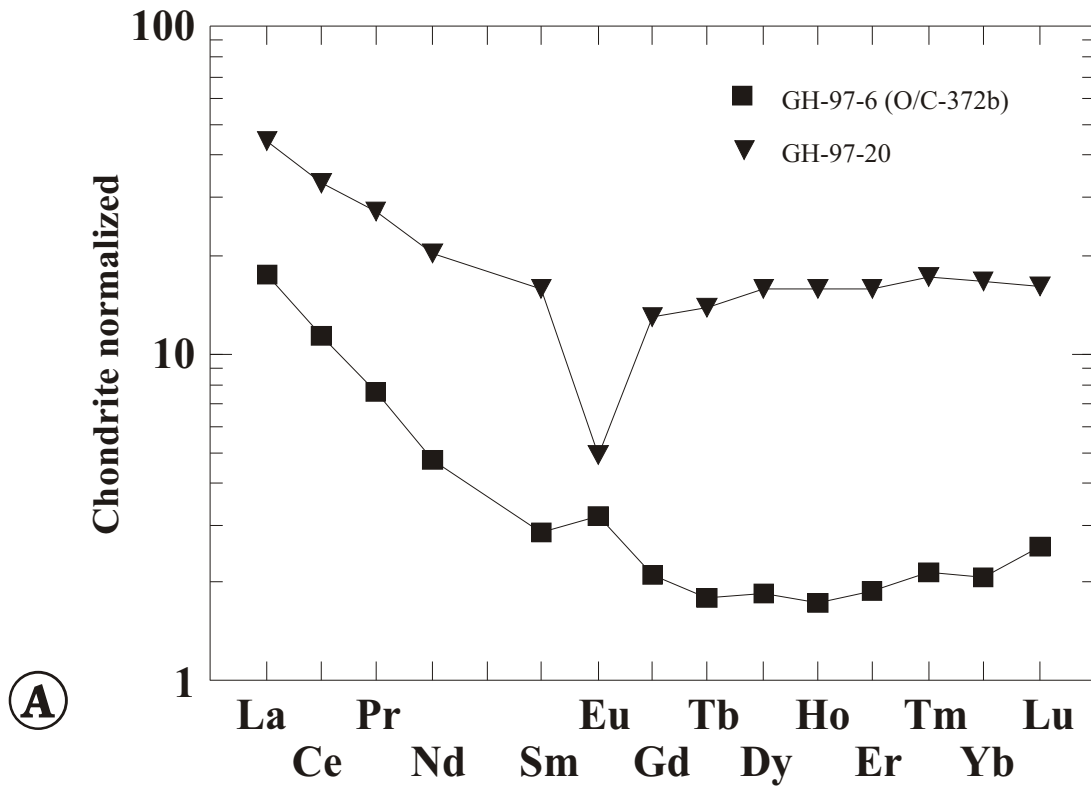
GH-97-6 and GH-97-20 are tonalitic dikes containing significantly higher Al_2O_3 at a given SiO_2 -content than all other silicic rocks in the Rogue Wilderness. Although, GH-97-6 has much lower Al_2O_3 and contains much less garnet and muscovite than GH-97-20, it still contains more Al_2O_3 than O/C-231a, the silicic dike sampled in the pillow unit. Also, GH-97-20 has the highest K_2O concentration of all samples from the Rogue Wilderness. However, one has to keep in mind that K_2O has probably been removed from many volcanic and plutonic rocks during hydrothermal alteration. If the tonalite dikes were not altered, they could be classified using the major element discrimination diagrams of Maniar and Piccoli (1989). However, in addition to presenting a classification based on major elements, Maniar and Piccoli (1989) summarized the petrographic data of the reference suites. They report that muscovite is found in continental arc-, continental collision-, and post-orogenic- granitoids, but other peraluminous minerals, such as garnet, seem to occur only in continental collision granitoids. Thus, a mineralogical classification may be used. Clearly, the high Al_2O_3 content (table 5.7) and the presence of muscovite and garnet in the tonalitic dikes indicate that these dikes are peraluminous.

The chondrite- and N-MORB-normalized REE and trace element distribution patterns of the muscovite garnet tonalite dikes are shown in figures 5.37a and 5.37b, respectively. The patterns differ significantly in level and shape from each other as well as from all other rocks sampled in the Wild Rogue Wilderness. Both samples are strongly enriched in LREE compared to HREE. GH-97-6 has a $(\text{La}/\text{Yb})_n$ ratio of 8.56, and GH-97-20 has a $(\text{La}/\text{Yb})_n$ ratio of 2.72. Furthermore, GH-97-20 has a large, negative Eu-anomaly, while GH-97-6 has a slight positive Eu-anomaly.

The N-MORB normalized trace element distribution pattern of GH-97-20 indicates depletion of HFSE (Ta, Nb, Zr and Hf) and selective enrichment of LILE, Th and LREE. An important feature is that the HREE are not depleted in GH-97-20. This is a characteristic pattern of volcanic arc granitoids (e.g., Pearce et al., 1984b). Only TiO_2 is extremely depleted perhaps due to fractionation and/or low TiO_2 content of the source. Clearly, the trace element pattern of GH-97-20 is very similar to rocks of calc-alkaline affinity (compare with CAB in figure 5.2) suggesting generation in a volcanic arc. However, GH-97-20 has a very high Al_2O_3 content and is peraluminous according to Shand's index. Also, GH-97-20

Figure 5.37

- A. Chondrite normalized REE distribution patterns of two muscovite garnet tonalite dikes in the metagabbro unit. The REE patterns are flat in the HREE and increase steeply from Sm to La which is characteristic of garnet fractionation or garnet as residual phase in the source. The patterns differ in level and shape which can be explained with fractionation (GH-97-6) or accumulation (GH-97-20) of garnet.
- B. N-MORB normalized trace element distribution diagram of two muscovite garnet tonalite dikes in the metagabbro unit. The patterns resemble that of rocks of calc-alkaline affinity. However, there are important differences such as strong depletion of Ti, Y, and Yb.



contains peraluminous minerals such as muscovite and garnet. Therefore, GH-97-20 would be classified as continent collision granitoid using the tectonic discrimination scheme of Maniar and Piccoli (1989). Pearce et al. (1984b) and Förster et al. (1997) reported that many peraluminous continental collision granitoids have trace element characteristics similar to volcanic arc granitoids, such as depletion of HFSE and enrichment of LILE (especially Rb), Th and LREE. Also, many of the collision granitoids plot in the tectonic discrimination diagram of Pearce et al. (1984b) within the volcanic arc granite field (Förster et al., 1997). Furthermore, peraluminous silicic igneous rocks have been reported from continental arcs such as the Macusani rhyolite in the Andean arc (Pichavant et al., 1987; Pichavant and Montel, 1988).

The N-MORB normalized trace element pattern of GH-97-6 is different from GH-97-20. GH-97-6 is also depleted in Ta and Nb, but it has extremely low HREE concentrations, and is enriched in LILE, Th, LREE, Zr and Hf relative to Ta, Nb and HREE. The pattern of GH-97-6 is typical for collision related granitoids for which a sedimentary source is inferred (Pearce et al., 1984b). Interestingly, GH-97-6 has a relatively low Al_2O_3 -content and is metaluminous, which would lead to the classification as volcanic arc granitoid using the discrimination scheme of Maniar and Piccoli (1989).

Also, the muscovite garnet tonalite dikes are plotted in the Hf/3-Th-Ta discrimination diagram of Wood et al. (1979). Both dikes plot in the calc-alkaline field in figure 5.36, which is consistent with the N-MORB patterns showing certain arc-characteristics.

5.7.2.3 Fractionation

The low abundances of HREE and the strong enrichment of LREE in GH-97-6 ($(La/Yb)_n = 8.56$) may be explained with garnet fractionation or with equilibration with residual garnet in the source. The compatibility of REE in garnet increases with increasing atomic weight. In a liquid of rhyolitic composition, all REE except La, Ce, and Eu are compatible in garnet (compilation of k_d 's in Rollinson, 1993). Thus, fractionation of garnet causes the melt to become depleted in all REE, except La, Ce, and Eu. Also, garnet could have accumulated in GH-97-20. For example, GH-97-6 contains only trace amounts of garnet whereas GH-97-20 contains ~7% garnet. Accumulation of garnet may explain the high

HREE and Y abundances compared to GH-97-6. Furthermore, the large negative Eu-anomaly could be the combined effect of fractionation of plagioclase and accumulation of garnet.

5.8 The Zr/Y vs. Zr discrimination diagram

Pearce (1983) proposed a discrimination diagram to distinguish between continental- and island-arc settings using the Zr/Y ratios of volcanic arc basalts. The original Zr/Y vs. Zr diagram of Pearce and Norry (1979) is shown in figure 5.38a. This diagram illustrates that, based on the Zr/Y ratio, basalts from ocean island arcs and mid ocean ridges overlap, but within plate basalt settings can be distinguished. Once the arc-characteristics are established from other trace element ratios (e.g., N-MORB normalized diagram), further distinction has been found between continental and oceanic arc settings (figure 5.38b). Pearce (1983) showed that basalts erupted at oceanic arcs plot in the original island-arc tholeiite field of Pearce and Norry (1979), whereas basalts from continental arcs plot towards higher Zr/Yb ratios, that is, in the original within plate field. Pearce and Norry (1979) evaluated the variations of the Zr/Y ratios in various volcanic suites, and they found that the Zr/Y ratio changes little with increasing Zr in each volcanic suite used to compile the Zr/Y vs. Zr diagram. Pearce and Norry (1979) argued that varying degrees of open- and closed-system fractional crystallization or of partial melting does not result in large variations of the Zr/Y ratio, and that the Zr/Y ratio is a good measure of the degree of source depletion or enrichment. Thus, the higher Zr/Yb ratios in lavas from continental arcs reflect that sub-continental lithosphere rather than the convecting upper mantle undergoes melting (Pearce, 1983).

The arc-characteristics of the samples from the Rogue Wilderness ophiolite and the Mule Mountain volcanics have clearly been established in previous sections. The subdivision into “basic”, “intermediate”, and “evolved” compositions after Pearce (1996) was used for the volcanic rocks (figures 5.14, 5.21, and 5.28). Then, the volcanic rock samples having “basic” compositions are plotted in the Zr/Y vs. Y diagrams in figure 38a and 38b. Additionally, the samples from the metagabbro unit, the hbl-qtz diorite intrusion in the metagabbro unit, and the dike and enclave in the metatonalite unit are plotted (these samples are also “basic” in composition based on Zr/TiO₂ ratios).

5.8.1 Ophiolite units

The samples from the metagabbro unit have extremely low Zr/Y ratios. Two metagabbro samples plot just above the lower field boundary for island-arc tholeiites, and four samples plot below this boundary (figure 5.38a). Low Zr/Y ratios are consistent with the interpretation that the metagabbro unit formed by partial melting of a highly depleted mantle source (see also figure 5.5). However, the hornblende quartz gabbro intrusion has a higher Zr/Y ratio, similar to the other samples from the Wild Rogue Wilderness ophiolite (figure 5.38a and 5.28b).

The IAT dikes from the sheeted dike complex and the samples from the pillow unit as well as the deformed dike and the enclave in the metatonalite unit plot in the island-arc tholeiite field of Pearce and Norry (1979). The MORB-like dikes plot near the normalizing value for N-MORB (figure 5.38a). The dikes of geochemical group 2 from the sheeted dike complex plot above the upper boundary of the island-arc tholeiite field (figure 5.38a).

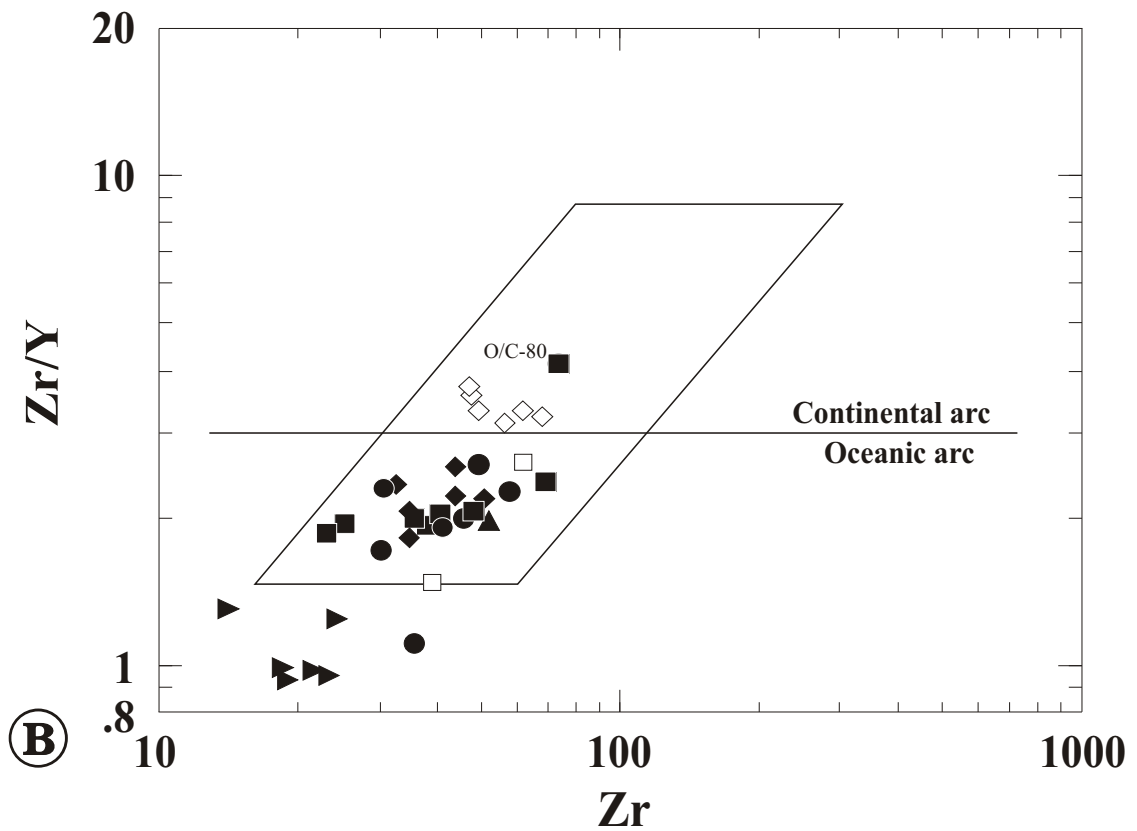
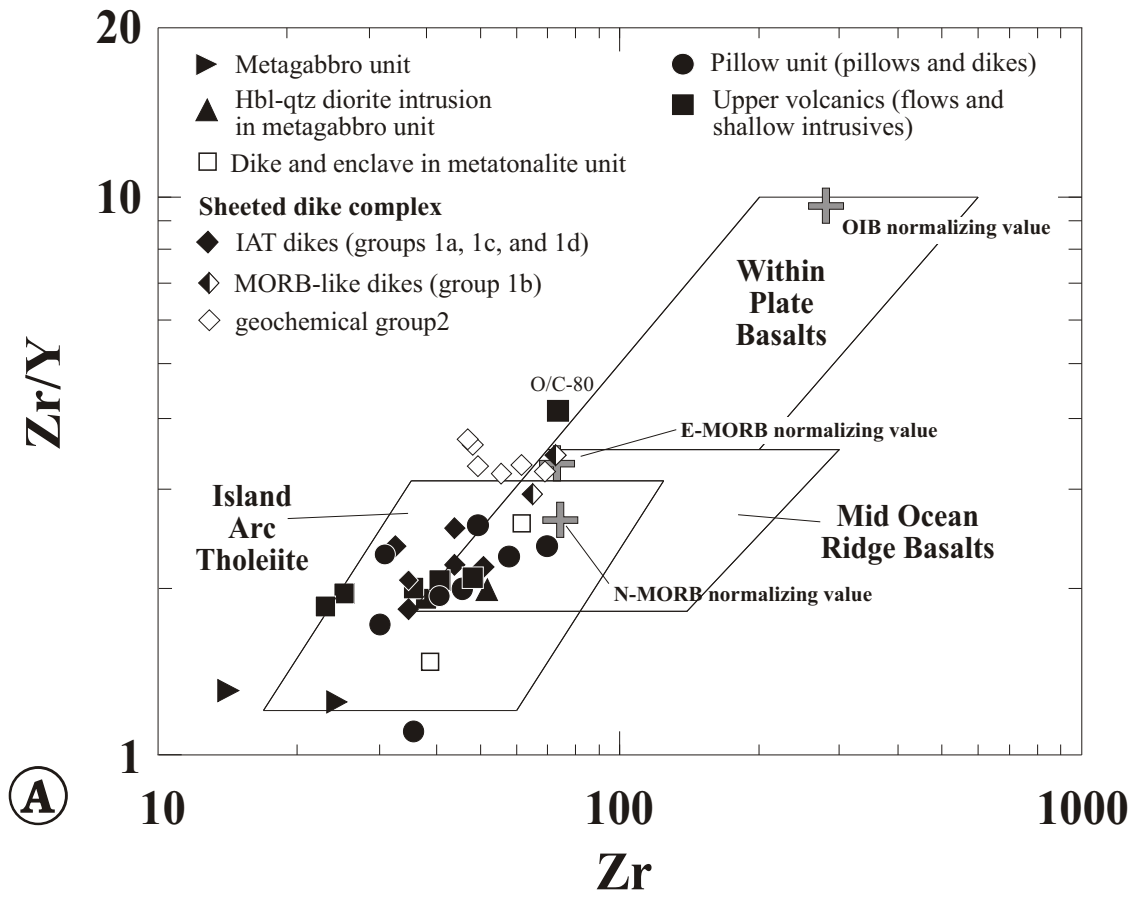
The samples from the metatonalite unit, the sheeted dike complex, and the pillow unit having arc-characteristics are plotted in figure 5.38b. Only the dikes of geochemical group 2 from the sheeted dike complex plot in the field for continental arcs. The elevated Zr/Y ratios of the dikes of geochemical group 2 suggest an enriched mantle source having geochemical characteristics of subcontinental lithosphere (Pearce, 1983).

5.8.2 Mule Mountain volcanics

Most samples from the Mule Mountain volcanics are very similar in their trace element composition to the pillow unit. These samples plot in the island-arc tholeiite field in figures 5.38a and in the field for oceanic arcs in figure 5.38b. Only O/C-80 plots in the field for continental arcs (figure 5.38b) suggesting that magmas derived from an enriched mantle source, having geochemical characteristics of subcontinental lithosphere, were present as the Mule Mountain volcanics formed.

Figure 5.38

- A. Zr/Y vs. Zr tectonic discrimination diagram of Pearce and Norry (1979) to distinguish island arc basalts, MORB and within plate basalts. Note large overlap field between MORB and IAT.
- B. Zr/Y vs. Zr tectonic discrimination diagram of Pearce (1983). Once it is established that the basalts erupted in an arc setting, the Zr/Y ratio can be used to distinguish oceanic and continental arc settings. The dikes of geochemical group 2 from the sheeted dike complex plot in the continental arc field while the IAT dikes, all samples from the pillow unit and most samples from the upper volcanic unit plot in the island arc field.



5.9 Summary

The rocks from the Wild Rogue Wilderness remnant of the Coast Range ophiolite and the Mule Mountain volcanics are petrogenetically diverse. A diagram summarizing the age and magmatic affinities of the various units is shown in figure 5.39.

5.9.1 Metagabbro unit

- The metagabbro unit can be classified as having magmatic affinities to island arc tholeiite using tectonic discrimination diagrams (figures 5.4, 5.6, 5.7k, 5.27a, 5.38a). However, the metagabbro has a very unusual trace element composition which is characterized by convex-up REE distribution patterns centered on Nd (figure 5.3a), high Nb/Ta ratios (up to 29), very strong depletion of HFSE compared to LILE and REE (figure 5.3b), and very low Ta/Yb (figure 5.27a) and Zr/Y ratios (figure 5.38b). These ratios indicate that the metagabbro unit was probably derived from a depleted mantle source (figures 5.5, 5.27a). The metagabbro unit is geochemically distinct from the metatonalite unit, sheeted dike complex and the pillow unit (figure 5.27a). Additionally, the $^{40}\text{Ar}/^{39}\text{Ar}$ cooling age of 171.4 ± 3.1 Ma is significantly older than the other ophiolitic units (163 ± 1 Ma and 163 ± 1 Ma) suggesting that the metagabbro unit may not be an integral part of the ophiolite stratigraphy.
- The hornblende quartz diorite (GH-97-14) in the metagabbro unit has a trace element composition which is distinct from the metagabbro unit (figure 5.7). GH-97-14 has magmatic affinities to IAT (figure 5.4, 5.5 and 5.27a), but it has a less pronounced convex-up REE pattern than the metagabbro (figure 5.7a), and the HFSE are significantly less depleted than in the metagabbro unit (figure 5.7b). Overall, the trace element composition of GH-97-14 is transitional between samples from the pillow unit (or IAT dikes from the sheeted dike complex) and the metagabbro unit (figure 5.27a). The “transitional” trace element composition of GH-97-14 may be explained with assimilation of metagabbro by a magma similar in composition to the pillows or the IAT dikes in the sheeted dike complex.

5.9.2 Metatonalite unit

- The metatonalite unit is a fault-bounded unit consisting of tonalites and trondhjemites as well as dioritic enclaves and dikes. All samples from this unit have calc-alkaline magmatic affinities (figure 5.5, 5.27a). However, this unit is compositionally heterogeneous which is likely due to magma mixing (figure 5.12). Perhaps, fractionation involving allanite played an important role as well (figure 5.11). The 164 ± 1 Ma metatonalite unit is interpreted to be an integral part of the ophiolite stratigraphy because its U/Pb zircon age is indistinguishable from the sheeted dike complex (163 ± 1 Ma) and dikes of calc-alkaline affinity occur in the sheeted dike complex. It cannot be determined whether the metatonalite unit formed in a suprasubduction zone spreading center setting (i.e. plagiogranite) or represents an off-axis intrusion of silicic arc-magmas.

5.9.3 Sheeted dike complex

- The screens in the sheeted dike complex consist of cumulate gabbro containing layers of plagioclase. Most cumulate gabbro and plagioclase samples have very depleted REE patterns with a pronounced Eu-anomaly and depleted N-MORB normalized trace element patterns typical of gabbroic cumulates (figure 5.15). A plagioclase sample (GH-97-27) contains high concentrations of incompatible trace elements (including Zr) suggesting a highly fractionated melt was trapped in between cumulus phases. Zircon separates from a similar sample (SC-1) yielded a concordant U/Pb age of 163 ± 1 Ma. The cumulate gabbro samples have magmatic affinities to island arc tholeiite (figures 5.15 and 5.16).
- Two groups of dikes can be distinguished in the sheeted dike complex based on their trace element composition, mineral composition and texture. The first geochemical group includes diabasic dikes having magmatic affinities to N-MORB and IAT (figures 5.15, 5.18, 5.27a, and 5.17a through 5.17f). The second group includes microdioritic and diabasic dikes having magmatic affinities to CAB (figures 5.15, 5.18, 5.27a, and 5.17h). A subgroup of dikes of geochemical group 2 contain olivine xenocrysts. Cr-spinels within olivine xenocrysts have Cr/(Cr+Al) ratios similar to high-Ca boninites. This implies that boninitic magmas were present as the sheeted dikes formed and mixed with calc-alkaline magmas.

- The incompatible trace element ratios of dikes of geochemical group 1 are highly variable indicating that almost none of these dikes are related by crystal fractionation. The variations of the trace element ratios of dikes of group 1 can be explained with magma mixing (figure 5.20a). For example, mixing between MORB (O/C-356) and IAT (MRH-111) produces a trace element composition similar to that of O/C-58 (figure 5.20b).
- Similar to the samples from the metatonalite unit, the dikes of petrographic group 2 have a large range of $(La/Yb)_n$ ratios (2.1 to 6.5; figure 5.17h). Thus, the dikes of group 2 cannot be related by crystal fractionation. However, magma mixing can explain the variations of the trace element compositions. For example, mixing between an IAT-dike having LREE depleted patterns (O/C-5-S4) and a calc-alkaline dike from the sheeted dike complex or the metatonalite unit (MRH-45a or O/C-11-S16b) produces a trace element composition similar to that of O/C-1-S2 (figure 5.20c and 5.20d). Also, mixing of samples O/C-5-S4 and MRH-45a in various proportions can explain the large range of $(La/Yb)_n$ ratios of dikes of geochemical group 2.
- The dikes of geochemical group 2 have high Zr/Y ratios typical of basalts from continental volcanic arcs (figure 5.38). The higher Zr/Yb ratios in group 2 dikes suggest that a source similar to sub-continental lithosphere rather than the convecting upper mantle underwent melting (Pearce, 1983).
- It is likely that various degrees of melting of a heterogeneous mantle source as well as magma mixing or contamination resulted in the large magmatic diversity of samples from the sheeted dike complex.

5.9.4 Pillow unit

- The samples from the pillow unit have magmatic affinities similar to IAT (figure 5.23, 5.24). They have lower Cr, Ni and MgO, and higher Zr/TiO₂ and SiO₂ than group 1 sheeted dikes (tables 5.4 and 5.5, figures 5.21 and 5.24). These data suggest that the pillows and diabasic dikes in the pillow unit are more evolved than the dikes of geochemical group 1 from the sheeted dike complex.

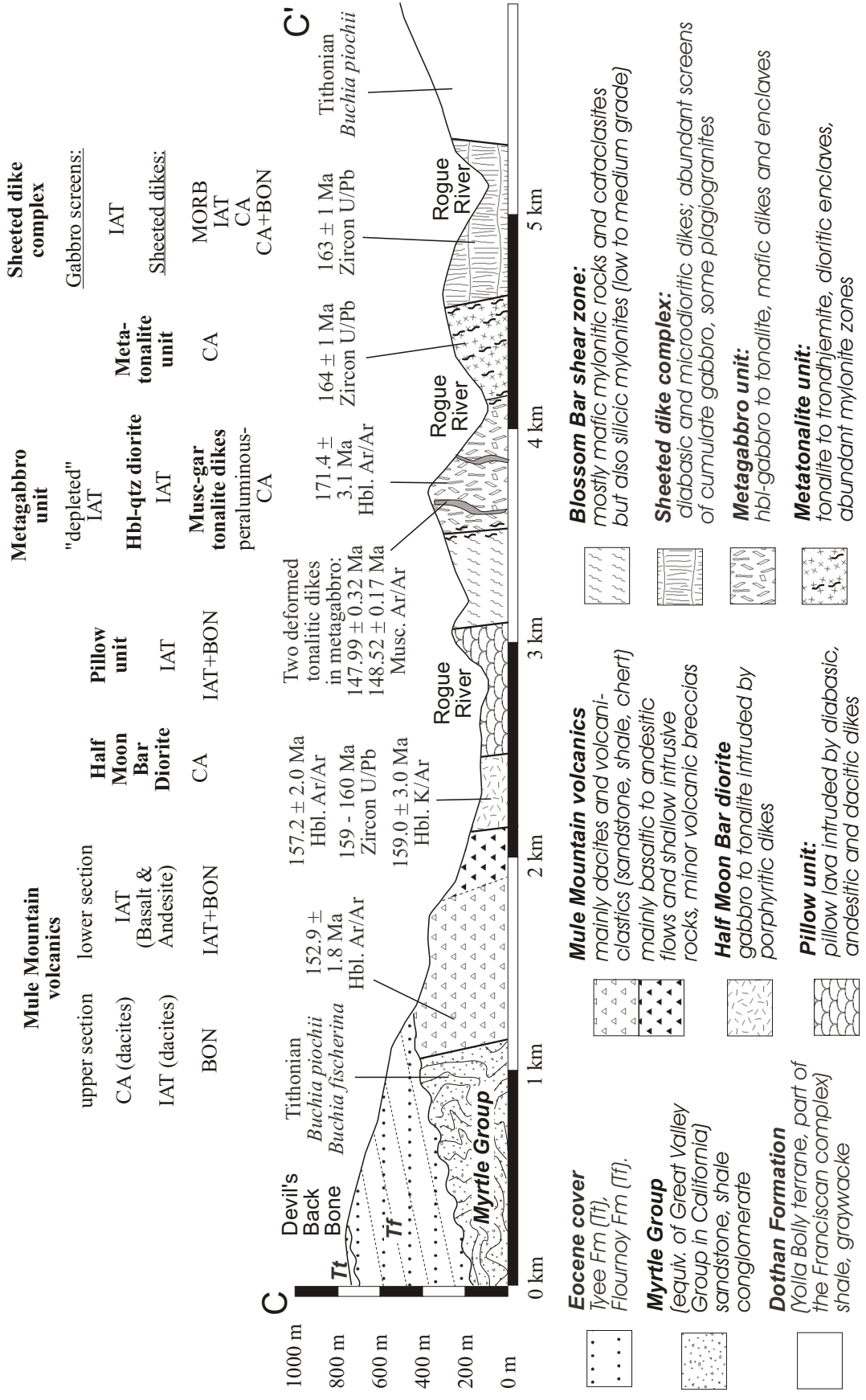


Figure 5.39: Cross section showing the units of the Wild Rogue Wilderness, sample ages and magmatic affinities.

- One diabasic dike (O/C-5-S4) and two cumulate gabbro screens (GH-97-27 and O/C-358) in the sheeted dike complex have incompatible trace element ratios similar to samples from the pillow unit (figures 5.23 and 5.27a), indicating the sheeted dike complex and the pillow unit could be related. However, most samples from the sheeted dike complex have different incompatible trace element ratios such as higher $(La/Yb)_n$ than the pillow unit. At least four geochemical groups identified in the sheeted dike complex were not sampled in the pillow unit: (1) MORB-like samples, (2) IAT having flat REE patterns, (3) IAT having LREE enriched patterns, and (4) calc-alkaline dikes.
- Variations of the trace element ratios in samples from the pillow unit can be explained with magma mixing or dynamic melting with selective tapping of the melting column (figure 5.26). Also, O/C-224b is a pillow having magmatic affinities to IAT, but it contains Cr-spinel having Cr/(Cr+Al) ratios similar to high-Ca boninites (figure 5.24). This implies boninitic magmas were present and mixed with IAT.

5.9.5 Mule Mountain volcanics

- The Mule Mountain volcanics have been divided into a lower and upper section (chapter 2). Samples from the lower section have magmatic affinities to IAT (figures 5.30 and 5.31) and range in composition from basalt to andesite (figure 5.28). Most samples from the lower section of the Mule Mountain volcanics are very similar in their trace element composition to the pillow unit (i.e., IAT having LREE-depleted to flat REE distribution patterns, figure 5.29a through 5.29f).
- Samples from the upper section have magmatic affinities to IAT, CAB and BON (figures 5.30 and 5.31) and are predominantly dacitic in composition (figure 5.28). Thus, at least two different magmatic types identified in the upper section of the Mule Mountain volcanics are not found in the lower section of the Mule Mountain volcanics and the pillow unit: (1) IAT with slightly LREE enriched patterns, and (2) volcanic rocks having boninitic affinities.
- O/C-81a and b have magmatic affinities to IAT and contain Cr-spinels within clinopyroxene- and olivine-phenocrysts as well as in the matrix. The Cr-spinels have a large range of Cr/(Cr+Al) ratios. They are similar to Cr-spinels in IAT, high-Ca boninite and low-Ca boninite (figure 5.32). This implies that boninitic magmas were present and mixed with IAT.

- Two dacitic samples from the Mule Mountain volcanics (upper section) and one silicic dike from the pillow unit have very similar N-MORB normalized trace element patterns (GDH-1, GDH-2b and O/C-231a) as the basic samples (O/C-81a and b; figure 5.29b), suggesting they evolved from similar, tholeiitic parents.
- O/C-80, a sample having trace element characteristics between CAB and IAT (figures 5.29f and 5.30) has high Zr/Y ratios typical of basalts from continental volcanic arcs (figure 5.38). The high Zr/Yb ratio suggests that a source similar to sub-continental lithosphere may have been present (Pearce, 1983).

5.9.6 Post-ophiolite intrusions

- The 158-160 Ma Half Moon Bar diorite is faulted against the pillow unit, but intrusions of HMB diorite occur also in the pillow unit (see chapter 2). The HMB diorite and crosscutting porphyritic dikes have magmatic affinities to CAB (figure 5.36). The N-MORB normalized trace element patterns of the samples from the HMB diorite are parallel (figure 5.35) suggesting they derived by partial melting of a homogeneous source.
- Peraluminous tonalitic dikes (high Al₂O₃ content and muscovite + garnet bearing) intruding the metagabbro unit have geochemical characteristics ranging between volcanic arc and collision related granitoids (figures 5.36 and 5.37) and may be derived by melting of a sedimentary source. The muscovite ⁴⁰Ar/³⁹Ar cooling age of 149 Ma only provides a minimum age.

CHAPTER 6

RELATIONS OF THE WILD ROGUE WILDERNESS OPHIOLITE WITH THE COAST RANGE OPHIOLITE AND JOSEPHINE OPHIOLITE: IMPLICATIONS FOR THE TECTONIC AND MAGMATIC EVOLUTION OF MID- TO LATE-JURASSIC OPHIOLITES IN CALIFORNIA AND SW OREGON

6.1 Introduction

The comparison of the analytical data of samples from the Wild Rogue Wilderness with samples recovered from modern arc systems is an important step for interpreting the magmatic and tectonic evolution of the Coast Range ophiolite. Recent studies of the magmatism in modern arc/backarc- basin systems suggest that factors such as the degree of mantle depletion (or enrichment) prior to melting, degree of partial melting, and the degree of fractionation are influenced or governed by tectonic processes such as maturation of the volcanic arc, rifting of the volcanic arc, transition from rifting to spreading in the incipient back-arc basin, ridge propagation within the back-arc basin (or into the volcanic front), 'ridge-jump' away or towards the volcanic arc, widening of the back-arc basin, and the formation of seamounts on rifted arc crust. These processes ultimately have an influence on the composition of the magmas. Additionally, magmatic heterogeneities are introduced when an oceanic ridge intersects a trench (i.e., subduction of an spreading ridge), or when a seamount chain is subducted. Notably, the influence of fluids released from the subducting slab into the mantle appears to decrease with increasing distance from the volcanic front (Pearce et al., 1995). Also, hot spots, such as in the northern Tonga arc and Lau back arc basin, can have an influence on the composition of the magmas (e.g., Hawkins, 1995).

In view of the complex evolution of modern arc - backarc systems, the documentation of the different magma types in the CRO and their absolute and relative ages are very important in order to infer

possible tectonic processes that may have governed or influenced the magmatic evolution of the CRO.

Perhaps, if more CRO remnants are studied in detail, a general pattern of the interplay between tectonic and igneous processes may emerge. This could lead to a well constrained model of a multistage evolution of the CRO such as that advanced by Shervais et al. (in review).

In addition to the strong influence that tectonic processes have on magma composition, magmatic heterogeneity could also be a result of an inherited, highly heterogeneous mantle source. Perhaps the mantle source prior to rifting and spreading of the CRO was highly heterogeneous at variable scales due to previous episodes of subduction or from a “within-plate” component. During fore-arc or intra-arc rifting, as new undepleted asthenosphere rises from depth, heterogeneous mantle could become entrained into the melting column and may result in the generation of compositionally diverse magmas. Thus, the composition of magmas in the CRO could be controlled by two factors: (1) tectonic processes such as those inferred to have been important in the evolution of marginal basins; (2) by the mantle composition prior to partial melting and formation of the Coast Range ophiolite.

Also, the comparison of the age data for the Rogue Wilderness ophiolite with that of the Coast Range ophiolite in California and the coeval Josephine ophiolite have to be made, and implications resulting from that comparison must be considered proposing a tectonic model for the magmatic evolution of the Coast Range ophiolite.

Previously, the Rogue Wilderness ophiolite was interpreted to represent a klippe thrust westward from the Klamath Mountain province and, thus, be a tectonic outlier of the Josephine ophiolite (Coleman and Lanphere, 1991; Roure and Blanchart, 1983). In contrast, Blake et al. (1985a) correlated the Rogue Wilderness ophiolite (Snow Camp terrane) with the Coast Range ophiolite in California which is largely based on the correlation of the Myrtle Group in Oregon with the Great Valley sequence in California (Imlay et al., 1959; Blake et al., 1985b). The findings of the comparison of the tectonic evolution of the Coast Range ophiolite in California, with that of the Rogue Wilderness ophiolite in SW Oregon, and the Josephine ophiolite in northern California /SW Oregon are rather surprising in that the Rogue Wilderness ophiolite seems in part correlative with the Josephine ophiolite, and to some extent with the Coast Range ophiolite. Thus, the Rogue Wilderness ophiolite may represent the “missing link” that ties the Coast Range

ophiolite to the parautochthonous Josephine ophiolite. Consequently, a model of the magmatic evolution of the Coast Range ophiolite should also incorporate the data available for the Josephine ophiolite and the Rogue Wilderness/Snow Camp Mountain ophiolites.

6.2 Possible correlation of the Wild Rogue Wilderness ophiolite with two belts of Late-Jurassic ophiolites

Two belts of late Jurassic ophiolites with distinct sedimentary and structural history are exposed in California and Oregon (figure 6.1). The eastern belt of ophiolites comprises the Josephine ophiolite (Harper et al., 1994), Smartville ophiolite (Edelman et al., 1989), and the Devils Elbow remnant (Wyld and Wright, 1988) all of which are constrained to have formed by rifting of a Mid-Jurassic arc built on western North America. During the Nevadan orogeny (figure 6.2), the Josephine ophiolite was emplaced by underthrusting (~155-150 Ma) and subject to variable degrees of deformation and low grade regional metamorphism. The northern portion of the Josephine ophiolite, closest to the Rogue Wilderness ophiolite, underwent prehnite-pumpellyite facies regional metamorphism, and is characterized by the development of folds and slaty cleavage in the conformably overlying sediments of the Galice Formation (Harper, 1994). Also, numerous calc-alkaline dikes and sills (~150-145 Ma) were intruded during the Nevadan orogeny (Harper et al., 1994). Finally, the Josephine ophiolite and overlying Galice Formation are unconformably overlain by Great-Valley-sequence-equivalent strata as old as Valanginian (figure 6.2).

In contrast, the western belt of late Jurassic ophiolite remnants, collectively called the Coast Range ophiolite, is conformably overlain by the Great Valley sequence with the basal member as old as late Tithonian (e.g. Hopson et al., 1981). Also, the CRO remnants at California are depositionally overlain by volcanopelagic sediments as old as late Tithonian (figure 6.2). Thus, the Coast Range ophiolite was not affected by the Nevadan orogeny, and the CRO and depositionally overlying volcanoclastic (volcanopelagic) sediments were not regionally metamorphosed nor were they penetratively deformed. Evidence of deformation that can be clearly linked to the Nevadan orogeny is not documented in the Coast Range ophiolite. Despite these fundamental differences in the structural and metamorphic evolution, there

Figure 6.1

Generalized map showing major accretionary terranes but also mid- to late Jurassic ophiolitic and related rocks of California and SW Oregon. Map modified from Harper et al. (1985). Two belts of mid- to late Jurassic ophiolites include the Coast Range ophiolite (western belt), and the Josephine - Smartville ophiolites (eastern belt). Numbers refer to the localities listed below.

1. Wild Rogue Wilderness: 164 Ma (Saleeby, 1984)
2. Snow Camp Mountain: 169 Ma (Saleeby et al., 1984).
3. Josephine ophiolite: 162 Ma (Harper et al., 1994)
4. Preston Peak 'ophiolite' (Saleeby and Harper, 1993)
5. Devils Elbow remnant of the JO: 164 Ma (Wyld and Wright, 1988)
6. Smartville ophiolite: 160-164 Ma (Edelman et al, 1989; Saleeby et al, 1989).
7. Northern Coast Range ophiolite remnants (e.g., Elder Creek, Paskenta, Stonyford)
8. Black Mountain
9. Del Puerto: 155-157 Ma (Hopson et al., 1981; Evarts et al., 1992)
10. Llanada: 164 Ma (Hopson et al., 1981)

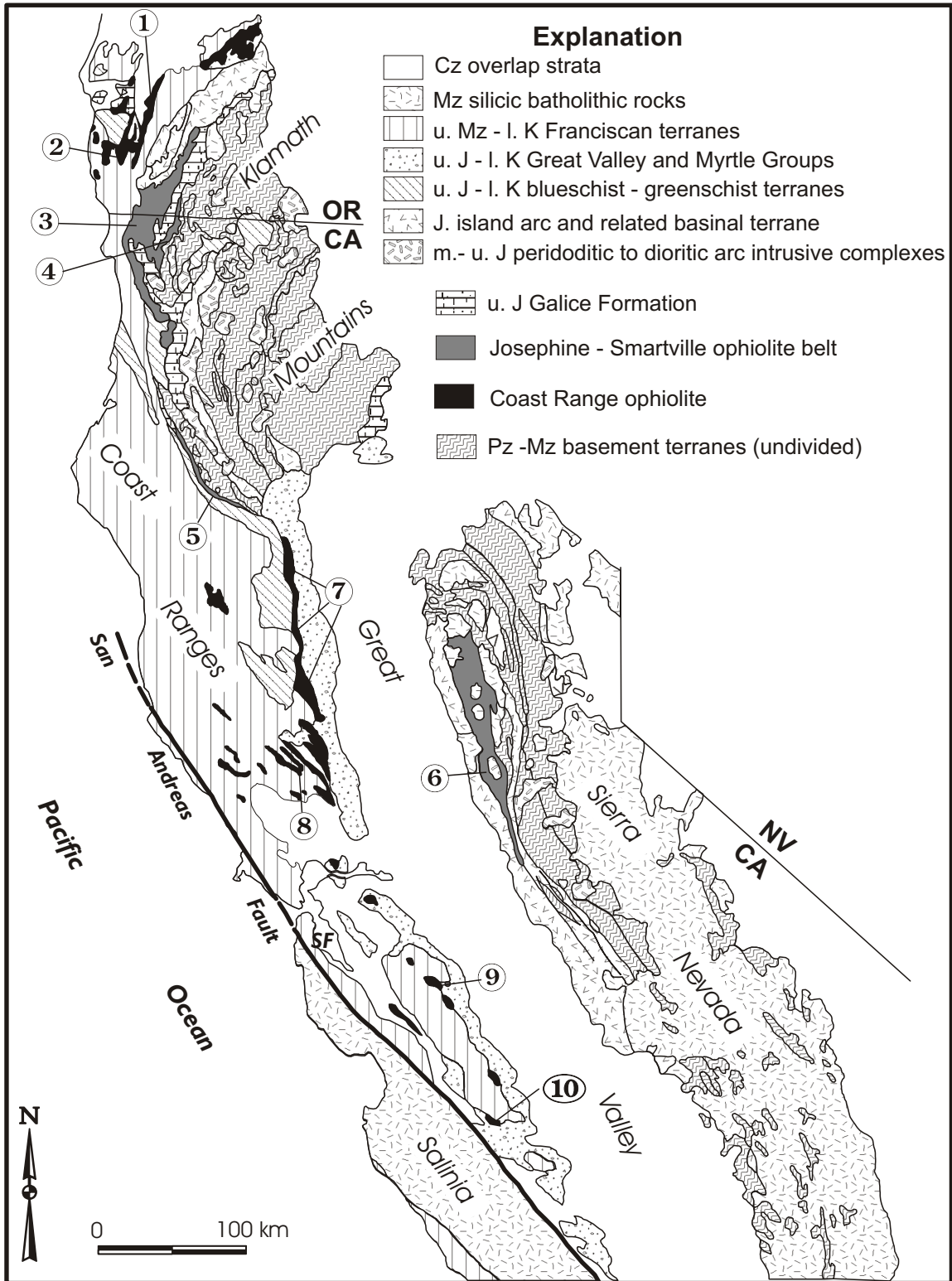


Figure 6.2

Tectonostratigraphic diagram comparing Coast Range ophiolite (CRO) - basal Great Valley Group (volcanopelagic sequence) succession with the Josephine ophiolite -Galice succession. The age range for the northern Coast Range ophiolite remnants is based on the compilation of isotopic ages in Robertson (1990) as well as on ages of interlava radiolarian cherts (Oxfordian-Kimmeridgian). Dated northern CRO remnants include Harbin Springs (164 ± 2 Ma zircon U/Pb, and 169 ± 2 Ma titanite U/Pb), Elder Creek (155 ± 5 Ma and 163 ± 5 Ma hornblende K/Ar), Paskenta (166 ± 3 Ma and 162 ± 3 Ma hornblende K/Ar). Minimum and maximum possible ages of the Coast Range ophiolite remnant at Cuesta Ridge, Point Sal and Llanada are based on U/Pb and Pb/Pb isotopic ages, respectively (Hopson et al. in Dickinson et al., 1996). The age for the CRO remnant at Del Puerto are from Evarts et al. (1992). Terrigenous sedimentation on Coast Range ophiolite - volcanopelagic sequence began with basal strata of the Great Valley Group in the latest Jurassic. Ages for the Josephine ophiolite are from Harper et al. (1994) and Harper et al. 1996), for the Rogue Chetco island arc complex from Yule (1996). The zircon U/Pb age for a gabbro in the Snow Camp Mountain area is from Saleeby et al. (1984) and radiolarian ages from E. Pessagno (samples collected by G.D. Harper, unpublished field mapping, 1997). The age data for the Rogue Wilderness are summarized in chapter 2 (Saleeby; 1984; Saleeby personal communication, 1999; Heizler, personal communication 1998).

are also characteristics both belts of ophiolites share: (1) both belts of ophiolites range in magmatic affinity from mid-ocean-ridge basalts to island-arc tholeiites (discussed in subsequent sections), and (2) young, arc-related extrusive, intrusive and sedimentary rocks of similar age (post-ophiolite ages) are closely associated with both belts of ophiolites.

The Rogue Wilderness ophiolite and related units are discussed in the regional frame work outlined above. In the following sections, the tectonostratigraphy of the Wild Rogue Wilderness ophiolite is compared with the Josephine ophiolite as well as the Coast range ophiolite in order to assess whether the Wild Rogue Wilderness ophiolite, is correlative with the Josephine-Smartville belt or the Coast Range ophiolite (figure 6.2).

6.2.1 Eastern belt of ophiolites

The Josephine ophiolite is bounded (underthrust) on the northwest by arc-related terranes composed of late Jurassic, extrusive, intrusive and volcanoclastic sedimentary rocks. Garcia (1979, 1982) defined this rock assemblage as the Rogue-Chetco island arc complex which includes the Illinois River batholith (Chetco complex) and the Rogue Formation. The gabbroic to tonalitic rocks of the Illinois River batholith are mainly of calc-alkaline magmatic affinity (Garcia, 1982), and U/Pb zircon data from the main phase gabbro and the late stage tonalite indicate ages of crystallization at 157-161 Ma and 155-157 Ma, respectively (Yule, 1996).

The Rogue Formation consists of basaltic to dacitic rocks of calc-alkaline to island arc tholeiite magmatic affinity and include volcanic flows, volcanic breccia, and predominantly volcanoclastic turbidites forming a stratified sequence (Garcia, 1979). An U/Pb zircon age of 157 ± 1.5 Ma (Saleeby, 1984) is reported for a zircon-bearing dacitic tuff breccia in the type Rogue Formation along the Rogue River, and a hornblende- $^{40}\text{Ar}/^{39}\text{Ar}$ age of 153.4 ± 0.6 Ma for a crystal-lithic tuff breccia (Yule, 1996). Also, Middle Oxfordian Tuffaceous cherts occur overlying the Rogue Formation (Pessagno and Blome, 1992).

The volcanopelagic succession, which conformably overlays the 162 ± 2 Ma Josephine ophiolite (Harper, 1983; Pinto-Auso and Harper, 1985; Harper, 1996), consists of interbedded siliceous argillite, and radiolarian chert. The volcanoclastic component of these sediments was most likely derived from the

Rogue-Chetco island arc complex or remnant arc which is interpreted to represent a Late Jurassic magmatic arc bordering the coeval Josephine marginal basin.

Both the Rogue Formation and the Josephine ophiolite are overlain by metasedimentary sequences (Galice Flysch) derived from an active arc and older Klamath basement (Harper, 1994, Miller and Saleeby, 1995) perhaps marking the onset of the Nevadan orogeny (Harper et al., 1994) (figure 6.2). During the Nevadan orogeny, the arc terranes and the Josephine ophiolite were stacked into a series of east-dipping thrust sheets, and numerous 146 to 151 Ma calc-alkaline dikes and sills were intruded into the Josephine ophiolite, Rogue-Chetco island arc complex and overlying sedimentary rocks (Harper et al., 1994).

Note also that older, basement terrane is found locally within the margins of the Josephine ophiolite and interpreted as rift facies (Wyld and Wright, 1988). The basement terrane in the rift facies is typified by ophiolitic rocks of MORB and within-plate basalt magmatic affinity and have been correlated with the late Triassic Rattlesnake Creek terrane (Wyld and Wright, 1988; Yule, 1996). Thus, the Josephine ophiolite is constrained to be native with respect to North America and probably formed by rifting of a Mid-Jurassic arc built on western North America.

Furthermore, Wright and Fahan (1988) described a Middle Jurassic event (“Siskiyou” event of Coleman et al., 1988) of regional deformation, metamorphism and thrust faulting (~ 175-170 Ma), which was also accompanied by arc magmatism. Saleeby and Harper (1993) invoke the collision of the Insular Superterrane with the continental margin (model 3, chapter 1) at this time to explain this regional event. According to Saleeby and Harper’s (1993) model, the oblique collision of the Insular Superterrane resulted in localized transtensional rifts preceding the opening of the Josephine basin. Hacker et al. (1995) and Yule (1996) suggest that profound changes in plate motion of the subducting oceanic crust resulted in the 175-170 Ma regional deformation and metamorphism of the western North American as well as subsequent formation of transtensional rifts.

6.2.2 Western belt of ophiolites

Several of the southern remnants of the ~165 Ma Coast Range ophiolite in California are depositionally overlain by young, extrusive rocks and volcanogenic sedimentary rocks (e.g. Hopson et al., 1981, Robertson, 1989, 1990). Also, young, arc-related intrusive, rocks locally occur as well. A volcanopelagic succession representing the distal to proximal volcanoclastic apron of an active volcanic arc overlies the Coast Range ophiolite in most of the studied localities in southern and Central California (e.g., Point Sal, Stanley Mountain, Cuesta Ridge and Llanada; figure 6.2) (Hopson et al., 1981, 1997, Robertson, 1989). The volcanopelagic succession consists mainly of tuff, tuffaceous chert, and minor volcanoclastic sandstone including tuffaceous sandstone and crystal tuff. At Llanada, a more proximal facies is present consisting of volcanoclastic sandstone and breccia intercalated with lahars and flows of meta-andesitic, -dacitic and -rhyolitic composition (figure 6.2). Biostratigraphic data from the various ophiolite remnants indicate that the volcanoclastic/pelagic succession is Oxfordian to Tithonian age (Hopson et al., 1981, 1997). Also, mafic to silicic dikes and/or sills occur at several localities intruding the Coast Range ophiolite and its volcanoclastic cover (e.g., Llanada and Cuesta Ridge). Hydrothermal alteration related to these magmatic events affected the sedimentary cover and preceded deposition of the sediments of the Great Valley sequence. Hopson et al. (in Dickinson et al., 1996) propose an hiatus after the formation of the oceanic (or marginal-basin) crust (~ 170 -160 Ma) prior to the deposition of the volcanopelagic succession overlying the ophiolite remnants. This hiatus is based on paleontologic ages in the sediments and radiometric ages on the ophiolite. Thus, the length and even the presence of such a hiatus depends on the accuracy of the geologic time scale.

Hopson et al. (1981) report an U/Pb zircon age of 155 ± 2 Ma for an undeformed plagiogranite porphyry that cuts sheared, foliated hornblende diorite in the upper part of the plutonic member of the Del Puerto Canyon remnant of the Coast Range ophiolite, and Evarts et al. (1992) report that a tonalite related to the cumulates of the Del Puerto ophiolite remnant is 157 ± 5 Ma (hornblende- $^{40}\text{Ar}/^{39}\text{Ar}$). Thus, the minimum age of the plutonic member of the ophiolite is constrained to be 155 - 157 Ma. Furthermore, Evarts et al. (1992) report that mafic to felsic dikes cutting the cumulates of the ophiolite are 149 ± 5 Ma and 150 ± 6 Ma (fission track zircon), a rhyolite near the top of the 2.5 km thick volcanic member is $150 \pm$

2 Ma (hornblende- $^{40}\text{Ar}/^{39}\text{Ar}$), and an andesite clast in the Lotta Creek Formation (thin bedded tuffaceous cherts interlayered with non-ophiolitic volcanoclastic turbidites), which positionally overlays the volcanic member of the ophiolite, is also 150 ± 2 Ma (hornblende- $^{40}\text{Ar}/^{39}\text{Ar}$). Evarts (1977). The young flows and fine-grained dike rocks associated with the Del Puerto ophiolite have primarily calc-alkaline magmatic affinity, and few are even boninite-like (Evarts et al., 1992). These geochemical and age constraints reveal an extended magmatic history related to a nearby active volcanic arc (formation in a fore-arc).

The Coast Range ophiolite remnants in northern California are overlain by 0 to 500 m thick Kimmeridgian to early Tithonian ophiolite-derived breccia (figure 6.2). Clasts in the breccia-unit also include calc-alkaline extrusive and intrusive rocks derived from an (unexposed) volcanic arc (Robertson, 1990). The breccia unit is locally conformably overlain by a 0-10m thick transitional unit (Tithonian) containing ophiolite-derived sediments and minor arc-derived silicic volcanic and tuffaceous sediments (Robertson, 1990). This assemblage is positionally overlain by the Tithonian basal Great Valley sequence. At one locality (Mt. St. Helena) the breccia unit is intruded by a dike/sill.

To summarize, the sediments overlying the Coast range ophiolite include not only a distal facies (tuffaceous volcanopelagic sequence) but also locally an accumulation of plutonic and volcanic debris of more-or-less proximal source such as volcanoclastic breccias and sandstones (Digger Creek, Black Mountain, Del Puerto and Llanada) or ophiolite breccia (northern Coast Range ophiolites). At some localities, the deposition of volcanoclastic sediments overlaps with arc-related magmatism as inferred from the presence of interbedded (arc-related) basaltic to rhyolitic flow rocks and dikes (Llanada, Del Puerto, Mt. St. Helena). Also, the ophiolitic breccias contain rare clasts derived from the erosion of a volcanic arc (Robertson, 1990). The age of volcanic activity is constrained mainly by radiolarian ages (also few radiometric ages) to a period ranging between Oxfordian and Tithonian time (figure 6.2). These data suggest that the breccia clasts are derived from the erosion of rocks typically found in island-arc environments (diorite, quartz-diorite, rhyolite, dacite, andesite), and/or from the erosion of ophiolitic basement highs (northern Coast Range ophiolite remnants).

6.2.3 The Wild Rogue Wilderness ophiolite: a bridging link

The cooling age of the metagabbro unit in the Wild Rogue Wilderness (171.4 ± 3.1 Ma) overlaps with the U/Pb zircon age of a gabbro (169 ± 1 Ma) in the Snow Camp Mountain area 30 km south of the area of study (Saleeby et al., 1984), suggesting that the metagabbro in the Wild Rogue Wilderness could be part of the ophiolite in SW Oregon. It is possible the metagabbro unit has an older igneous age and was (regionally?) metamorphosed; cooling below 500°C occurred at around 171.4 ± 3.1 Ma. The only event of regional extent at this time is the “Siskiyou” event of Coleman et al. (1988) affecting the North American continental margin between 175-170 Ma (figure 6.2). If the metagabbro unit represents a plutonic fragment that was affected by the “Siskiyou” event, the metagabbro unit represents a “rift facies” in the Rogue Wilderness ophiolite, and its cooling age probably marks the opening of the marginal basin in which the Rogue Wilderness ophiolite formed (and the metagabbro unit should contain ophiolitic dikes). If this is the case, not only does the Josephine ophiolite contain a rift facies (late Triassic Rattlesnake Creek terrane) which is on line of evidence that ties the Josephine ophiolite to the western North American margin (Wright and Wyld, 1994; Yule, 1996), but also the Rogue Wilderness ophiolite is associated with a fragment that may be native to North America. Whether the metagabbro is Rattlesnake Creek terrane affinity will need to be tested by obtaining an igneous age on the metagabbro.

No ophiolitic dikes (i.e., sheeted dikes) and dikes related to the metatonalite unit cutting metagabbro were found. However, the geochemical data of samples from the metagabbro unit and a hbl-qtz diorite in the metagabbro unit suggest an IAT magma similar in composition to group 1 sheeted dikes or the pillow unit may have assimilated metagabbro wall rock (chapter 5). The zircon U/Pb age data for the hbl-qtz diorite (SC-3) in the metagabbro unit cannot be interpreted uniquely; either zircon lost most of its Pb or older (xenocrystic) zircon was present (Saleeby personal communication, 1999). Overall, the minimum age for the hbl-qtz diorite is ~153 Ma and the maximum age is ~170 Ma. Clearly, the geochemical data and the age data for the hbl-qtz diorite are not enough evidence to interpret the hbl-qtz diorite as an ophiolite-related intrusion. Thus, without clear evidence for ophiolite related dikes and intrusions, the metagabbro unit cannot be interpreted as “basement” for the ophiolite. The metagabbro unit appears to be some exotic fault slice with unknown origin.

Calc-alkaline plutonic intrusions of the size and age of the Half Moon Bar Diorite (zircon U/Pb age of 158.5 ± 1.5 and 160 ± 1 Ma; hbl $^{40}\text{Ar}/^{39}\text{Ar}$ age of 157.2 ± 2.0 Ma) are not reported from any of the Coast Range ophiolite remnants. However, plutonic rocks of similar magmatic affinity and age occur in the intrusive portion of the Rogue-Chetco island arc complex (161 ± 1 Ma to 157 ± 1 Ma Illinois River batholith, Yule 1996) structurally underlying the Josephine ophiolite (figure 6.2).

Two muscovite-garnet tonalites, intruding the metagabbro unit, yield muscovite- $^{40}\text{Ar}/^{39}\text{Ar}$ cooling ages of 147.99 ± 0.32 and 148.52 ± 0.17 Ma (figure 6.2). These dikes are deformed and hydrothermally altered (chapter 2). The muscovite-garnet tonalites are peraluminous in composition (chapter 5) suggesting the dikes may be a product of partial melting of metasedimentary rocks (e.g., White and Chappell, 1979). In order to constrain the hypothesis of a metasedimentary origin, the garnet muscovite tonalite dikes should be analyzed for Sr, Nd, and O isotopes. Also, the igneous age for these tonalites should be determined in order to correlate these rocks with similar rocks in the Klamath Mountains. For example, rocks similar in composition to the peraluminous tonalite dikes in the metagabbro unit occur in late Middle-Jurassic plutons intruding older basement terranes in the Klamath Mountain province (i.e., 155-161 Ma Greyback Belt). A late-stage, two-mica granite occurs in the Slinkard pluton (161 Ma, zircon U/Pb) and late-stage peraluminous hornblende-biotite granites in the Ashland (161 Ma, zircon U/Pb) and Grayback (157 Ma, hbl K/Ar) plutons (Barnes, et al., 1990; 1992). Initial $^{87}\text{Sr}/^{86}\text{Sr}$ and $\delta^{18}\text{O}$ values for these plutons indicate that the magmas assimilated crustal rocks or mixed with crustal melts prior to final emplacement (Barnes et al., 1992). The late-stage two-mica granite and peraluminous hornblende-biotite granite could be representative of crustal melts, and their compositions suggest a graywacke-like source (Barnes et al., 1990, Gribbles et al, 1990). In late Middle-Jurassic time the Klamath province was, at least in part, underlain by metasedimentary rocks, and late Middle-Jurassic arc magmatism resulted in heating and partial melting of metasedimentary rocks at relatively deep crustal levels (Barnes et al., 1992). Clearly, determining the igneous age of the muscovite garnet tonalite dikes and analyzing them for Sr, Nd and O isotopes is critical for constraining the origin of these dikes.

The ophiolite in the Wild Rogue Wilderness, SW Oregon, includes an upper plutonic sequence (metatonalite unit and screens of cumulate gabbro), sheeted dikes, and pillow lavas. Structurally (?)

overlying with the pillow lava is a 2.5 km thick metavolcanic unit (Mule Mountain volcanics) having a lower section consisting of meta-basaltic and -andesitic flows, and an upper section of volcanoclastic rocks intercalated with meta-andesitic to -dacitic flows and/or sills (figure 6.2). Presently, it cannot be excluded that the lower section of the Mule Mountain volcanics represents an ophiolitic unit related to the pillows. Nevertheless, the upper section, containing a 152.9 ± 1.8 Ma dacitic flow overlaps in age with the volcanoclastic succession locally overlying the Coast Range ophiolite in California and consists of rocks typically encountered in an arc setting. The lower section of the Mule Mountain volcanics in the Wild Rogue Wilderness is dominated by volcanic extrusive and shallow intrusive rocks suggesting close proximity to a volcanic center. The upper section contains volcanic flows as well. In contrast, most Coast Range ophiolite remnants are overlain by fine-grained volcanoclastic rocks. However, the lithology of the strata overlying the various Coast Range ophiolite remnants (figure 6.2) appears to be a function of the proximity to an volcanic center, and abundant volcanic breccias, volcanogenic sandstones and flow rocks are present in some CRO remnants. Overall, the age, magmatic affinity, and, to some degree, the lithology of the Mule Mountain volcanics are similar to the volcanoclastic strata overlying many Coast Range ophiolite remnants (figure 6.2).

The Nevadan orogeny is not only typified by 155-150 Ma thrusting, regional metamorphism and development of folds and slaty cleavage, but also characterized by a period (~ 150 - 145 Ma) of intrusion of numerous calc-alkaline dikes and sills (figure 6.2) which are widely distributed in the Josephine ophiolite and overlying Galice Flysch (e.g., Harper et al., 1994). Interestingly, late magmatic and hydrothermal events are also reported from several Coast Range ophiolite remnants (e.g. Cuesta Ridge, Llanada). Perhaps, the magmatic and hydrothermal events represent distal echoes of the Nevadan orogeny in the Coast Range ophiolite.

Nevadan thrusting in the Klamath Mountains province is constrained to 155-150 with cooling below ~300C by ~135 Ma, except for the amphibolite sole of the Josephine ophiolite which has muscovite $^{40}\text{Ar}/^{39}\text{Ar}$ ages (slow cooling) of 150-146 Ma (Harper et al., 1994, 1996). Commonly, the Nevadan structures in the Klamath Mountain province at the latitude of the CRO include a northeast striking, southeast dipping regional foliation and syn-metamorphic, shallowly NE-SW plunging tight folds (Yule,

1996). The orientation of these structures, however, are variable (e.g., some folds are vertically plunging). Also, post-Nevadan deformation has to be taken into account; for example the regional foliation is approximately horizontal after restoration for post-Nevadan deformation.

The muscovite- $^{40}\text{Ar}/^{39}\text{Ar}$ ages of 147.99 ± 0.32 and 148.52 ± 0.17 Ma (figure 6.2) determined in two mylonitic muscovite-garnet tonalites mark cooling to $< 350\text{-}400\text{C}$. The closure temperature for argon diffusion in muscovite depends on the cooling rate (McDougall and Harrison, 1988). These cooling ages are interpreted to represent the end of wide-spread ductile deformation in the Wild Rogue Wilderness (chapter 4). The Blossom Bar shear zone and related mylonitic zones in the Rogue Wilderness ophiolite formed during the time of the Nevadan dike- and sill-event identified in the Klamath Mountains province. The subhorizontal foliation and NE-SW trending stretching lineation (after correcting for Cretaceous and Tertiary folding, chapter 4) in the Blossom Bar shear zone are consistent with NW-SE thrusting. As discussed in chapter 4, the Mule Mountain volcanics (top) are interpreted to have been thrust NW over the metagabbro unit, metatonalite unit and sheeted dike complex (bottom) along a subhorizontal shear zone (see chapter 4 for reorientation of foliation in the Blossom Bar shear zone). Thus, the Blossom Bar shear zone and related mylonites are likely to represent Nevadan structures in the Rogue Wilderness ophiolite.

The Josephine ophiolite and overlying Galice Formation are unconformably overlain by strata that is correlative with the Great Valley sequence; however, the oldest sediments are of Valanginian age (~ 135 Ma) (Sliter et al., 1984; Harper et al., 1994). In contrast, the Rogue Wilderness ophiolite is overlain (depositionally?) by sediments as old as Tithonian as indicated by the presence of *Buchia piochii* and *Buchia fischerina* in the basal layers of the Myrtle group (figure 6.2). The Myrtle group is also correlative with the Great Valley sequence in California (Imlay et al, 1959, Blake et al., 1985b) which conformably overlays the volcanoclastic cover of the Coast Range ophiolite.

The Rogue Wilderness ophiolite has a structural and stratigraphical evolution which is similar in part to that of the Josephine ophiolite and in part to that of the Coast Range ophiolite in California (figure 6.2). Thus, I suggest that the Rogue Wilderness ophiolite may be the 'missing link' between these two belts of ophiolites, which, if present in California, is now buried beneath the sedimentary rocks of the Great

Valley sequence. Based on this correlation, I conclude that the Coast Range ophiolite formed in the same arc-system as the Josephine ophiolite.

6.3 Geochemistry of the Coast Range ophiolite and Josephine ophiolite

The localities of several CRO remnants in California and Oregon are shown in figure 6.1 as well as the same age Josephine and Smartville ophiolites further east. The samples from the Rogue Wilderness ophiolite and related units are plotted in tectonic discrimination diagrams and compare to the geochemical data compiled from the CRO in California (Llanada, Black Mountain, Point Sal, Stonyford) and SW Oregon (Snow Camp Mountain) as well as to the geochemical data from the Josephine ophiolite (figure 6.3 through 6.7).

6.3.1 Comparison with the Coast Range ophiolite remnant at Llanada, California

The plutonic section of the CRO remnant at Llanada includes small fault slices of tectonite harzburgite, cumulate ultramafics and cumulate plutonic rocks such as gabbro, feldspathic wehrlite, and olivine gabbro and melagabbro. A sheeted dike complex is not present. The volcanic rocks at Llanada can be divided in two sections: (1) a lower volcanic member consisting mostly of mafic pillows or massive lava flows, and (2) an upper volcanic member consisting of siliceous volcanic rocks ('keratophyre'), siliceous tuffs and tuffaceous breccias, volcanic sandstone, mudstone, basaltic to andesitic breccias, and andesitic conglomerates (Hopson et al., 1981; Lagabrielle et al., 1986; Giaramita, 1998). The age data shown on figure 6.2 are from Hopson et al. (1981) and Hopson et al. in Dickinson et al. (1996).

Analytical data of samples from the lower volcanic section (i.e. ophiolitic unit) include those of Lagabrielle et al. (1986), Shervais (1990) and Giaramita et al. (1998). The samples of Giaramita et al. (1998) have been re-analyzed by ICP-MS at Union College, and the ICP-MS data listed in appendix F are preferred for the comparison in figures 6.3 through 6.5, because of higher accuracy for Ta using ICP-MS. Otherwise, the analytical data of Giaramita et al. (1989) are very similar to the ICP-MS data indicating that

both sets of data are accurate (appendix E). Additionally, data from Lagabrielle et al. (1986) and Shervais (1990) are shown in figure 6.3. Most samples plot within the arc field in the Cr-Y diagram.

The samples from Llanada plot in distinct fields in figures 6.3, 6.4 and 6.5. One group of samples are slightly LREE enriched (LL91 -8, -10, -13, -14) and plot on the boundary between island-arc tholeiites and calc-alkaline lavas (figures 6.4 and 6.5). The Cr-content in these samples is low (figure 6.3) and SiO₂ is high (~56-60%) which could be due to fractionation of olivine + Cr-spinel + pyroxene. The low-Cr samples from Llanada overlap somewhat with the fields of samples from the Rogue Wilderness ophiolite (group 1 sheeted dikes, pillow unit) and the Mule Mountain volcanics (figure 6.4 and 6.5).

The sample with the highest Y-content (LL91-9) has a LREE depleted chondrite normalized pattern and plots well within the N-MORB field in figure 6.3. This sample is depleted in Th and Ta and plots close to the Hf-apex in figure 6.4. Furthermore, this sample plots almost within the array of basalts from non-subduction settings in figure 6.5, but it has significantly lower Ta/Yb ratios than typical N-MORB. The low Ta/Yb ratio combined with the high Y concentration can be explained with low degrees of partial melting of a depleted mantle source (figures 6.3 and 6.5).

The remaining samples have high Cr-concentrations and plot in the IAT field in figure 6.3 (i.e., LL91 -1, -2, -3a, 5, -6, -7, -11, -16, -18 from Giaramita et al. (1998); and C₂₋₂, C_{3.1a}, C_{3.1b}, C_{5.1b} from Lagabrielle et al. (1986)). However, these samples overlap from the N-MORB to the IAT field in the Hf/3-Th-Ta diagram (figure 6.4). Also, they plot very close to the array of basalts from non-subduction settings in the Th/Yb vs. Ta/Yb diagram (figure 6.5). This indicates that the high-Cr samples from Llanada are transitional between N-MORB and IAT.

These groups of samples from Llanada can be distinguished in a plot of Ti vs. V (figure 7 of Giaramita et al., 1998): the SiO₂ rich (Cr-depleted) samples have arc-like Ti/V ratios (~10), the sample depleted in Th and Ta (LL91-9) has a MORB-like Ti/V ratio (~23), and the remaining high-Cr samples have Ti/V ratios transitional between IAT and MORB (~15-21).

To summarize, the lavas from the lower volcanic member of the CRO remnant at Llanda are compositionally diverse, and at least three different groups of samples have been identified. The variations in trace element abundance ratios can be explained with various degrees of melting and/or mantle depletion

as well as variable input of a subduction component. The most silicic samples (low Cr) have the highest subduction contribution, are derived by high degrees of melting of a mantle source that is similar to N-MORB mantle (same Ta/Yb ratios as N-MORB mantle) and have trace element characteristics which are transitional between IAT and CAB (figures 6.4 and 6.5). The bulk of the samples ($\text{SiO}_2 < 50\%$, high Cr) are derived by high degrees of melting of a similar mantle source (Ta/Yb ratios similar to N-MORB-mantle). However, they have a much smaller subduction contribution than the high- SiO_2 samples and are transitional to N-MORB. Finally, LL91-9 has very low Ta/Yb and Th/Yb ratios (much lower Ta/Yb ratios than typical N-MORB), suggesting a depleted mantle source. The geochemical variations suggest that a heterogeneous mantle source underwent variable degrees of partial melting ultimately resulting in the production of petrologically diverse lavas in the CRO remnant at Llanada. Most importantly, the range of the geochemical variations in the CRO remnant at Llanada are similar to that in the Wild Rogue Wilderness ophiolite. This indicates that large geochemical variations may not be uncommon in the CRO.

6.3.2 The Coast Range ophiolite remnant at Black Mountain, California

The Black Mountain ophiolite remnant (figure 6.1, locality 8) consists of a thin strip of serpentinized peridotite, an adjacent strip of uralitic gabbro and a diabase sill complex underlying much of Geysers Peak (Hopson et al., 1981; Lagabrielle, 1986). The sill complex and the pillow lavas are separated by a steep, NNE-trending fault. The pillow lavas at Black Mountain are overlain by a sedimentary breccia containing largely ophiolitic clasts such as microgabbro, diabase, diorite, and basalt. The sedimentary sequence also contains mudstones and sandstones as well as tuff and tuffaceous radiolarian chert which may mark the top of the ophiolite at Black Mountain (Hopson et al., 1981; Lagabrielle et al., 1986, Giaramita et al., 1998). Isotopic ages for the CRO remnant at Black Mountain have not been reported.

The ICP-MS data for the CRO remnant at Black Mountain are listed in appendix F. Additionally, analytical data from Black Mountain pillow lavas reported by Blake and Jones (1981) are shown in figure 6.3, and by Lagabrielle et al. (1986) in figure 6.4.

Most samples plot within the MORB-field in the Cr-Y tectonic discrimination diagram (figure 6.3). Several samples have lower Cr-, but similar Y-concentrations, than N-MORB suggesting

differentiation of island-arc tholeiite magma. Interestingly, the samples analyzed by Blake and Jones (1981) plot well within the IAT field in the Cr vs. Y diagram (figure 6.3).

The lavas from the CRO remnant at Black Mountain have MORB-like Ti/V ratios (~23-35). However, the samples define a linear trend in the Hf/3-Th-Ta diagram extending from the N-MORB field to the IAT field (figure 6.4). Also, the samples define a linear trend in the Th/Yb vs. Ta/Yb diagram (figure 6.5). The Ta/Yb ratios are similar to N-MORB, but the Th/Yb ratios vary significantly ranging from N-MORB like values to IAT-like values. The variable Th/Yb, but constant Ta/Yb ratios in the pillow lavas can be explained with variable input of a subduction component to a constant MORB-mantle source (e.g., Pearce et al., 1995a).

The lower-than-N-MORB Cr-concentrations (figure 6.3) suggest that plagioclase fractionation was suppressed, probably due to elevated H₂O contents. Fractionation of clinopyroxene before the onset of fractionation of plagioclase results in a rapid decrease of Cr in a basaltic magma. This interpretation is consistent with the petrographic data: the samples contain rare phenocrysts of augite and olivine (pseudomorphed), as well as up to 15% vesicles, but no plagioclase. The elevated H₂O content is probably related to the input of a subduction component which also caused variable enrichment in Th.

The Black Mountain lavas have many MORB-like characteristics, but elevated Th/Ta ratios and IAT-like fractionation trends in the Cr vs. Y diagram suggest a suprasubduction zone origin. Compared to the Wild Rogue Wilderness ophiolite, the pillow lavas from Black Mountain are compositionally relatively homogeneous. This may be related to the smaller data set. Nevertheless, the sheeted dike complex of the Wild Rogue Wilderness ophiolite contains dikes ranging in composition from N-MORB to IAT (figures 6.3, 6.4 and 6.5). Especially the samples O/C-1-S1 and O/C-356b from the sheeted dike complex (chapter 5) have very similar N-MORB normalized trace element patterns as the pillow lavas from Black Mountain.

6.3.3 Comparison with the Coast Range ophiolite remnant at Point Sal, California

The locality of the CRO remnant at Point Sal is not on the map in figure 6.1 (Point Sal is further south of map). The remnant at Point Sal is a nearly complete ophiolite consisting of serpentinite, harzburgite, dunite, layered cumulate gabbros, intrusive wehrlites-clinopyroxenites, isotropic gabbro,

diorite, quartz diorite and some plagiogranite, a sheeted sill complex, and lower and upper volcanic sections overlain by tuffaceous radiolarian cherts (Hopson and Frano, 1977; Hopson et al., 1981). The lower volcanic section of the Point Sal ophiolite consists chiefly of pillowed and massive submarine flows of plag-cpx-phyric and aphyric basalts. Dikes related to the underlying sheeted sill complex occur within the lower volcanic section and decrease up-section. Also, interpillow radiolarian chert and silicic dikes (“keratophyre”) are found. The upper volcanic section also consists of pillowed and massive submarine flows, but they are ol-cpx-phyric and aphyric basalts. Some interpillow limestone occurs (Hopson and Frano, 1977; Hopson et al., 1981). The age data for the CRO remnant at Point Sal are summarized in figure 6.2.

The only studies reporting trace elements for volcanic rocks and diabasic dikes are those of Menzies et al. (1977a, 1977b) and Shervais (1990). Menzies et al. 1977a, 1977b analyzed 19 volcanic samples for REE, Na, Sc, Cr, Fe, Co, Ni, Hf, Ta, and Th by instrumental neutron activation analysis (INAA) at the Planetary and Earth Science Division of Johnson space center.

The samples from the pillow section of the Point Sal ophiolite are shown in figure 6.4. A sample from the upper volcanic section plots within the N-MORB field (A) while five samples from the lower volcanic section plot in the MORB, IAT and CAB fields. This range of compositions is similar to that of the sheeted dike complex in the Rogue Wilderness ophiolite (dikes of geochemical groups 1 and 2). The data must be interpreted with caution because of potentially large analytical uncertainties. For example, several samples plot in the field for E-type MORB and within plate basalts (field B) and outside the field boundaries of Wood et al. (1979) (figure 6.4). Depending on counting time, the very low levels of Ta (typical of depleted island arc rocks) could have been below detection for INAA. However, it is suggested that the upper and lower volcanic sections of the Point Sal ophiolite are compositionally heterogeneous, and that lavas with affinities similar to N-MORB, IAT and CAB are present (figure 6.4).

The trace element data of Menzies et al. (1977a,b) and Shervais et al. (1990) are also plotted in the Cr vs. Y diagram of Pearce (1982) (figure 6.3). Menzies et al. (1977a,b) did not analyze for Y, but it is possible to substitute Yb for Y, because Y behaves similar to Ho and the HREE (Sun and McDonough, 1989). The chondritic Y/Yb ratio is 9.1, which is almost identical to the Y/Yb ratios in the primitive mantle

($Y/Yb = 9.2$), average E-MORB ($Y/Yb = 9.3$) and average N-MORB ($Y/Yb = 9.2$) suggesting that this ratio stays constant during most mantle melting processes (Sun and McDonough, 1989). Most lavas from the upper and lower volcanic section have low Cr (<100 ppm) and plot in the arc field of the Cr-Y ($Yb*9.2$) discrimination diagram. These lavas plot within or close to the field of the pillow unit of the Rogue Wilderness ophiolite. One sample from the lower lavas of the Point Sal ophiolite has high Y ($Yb*9.2$) concentrations, similar to N-MORB. However, the Cr-content of this sample is lower than typical N-MORB and the lavas from Black Mountain, suggesting fractionation of a IAT magma. Also, there are three samples from the upper and lower lavas of the Point Sal ophiolite which have very high Cr-concentrations and low Y ($Yb*9.2$) concentrations. The low Y ($Yb*9.2$)-concentrations are typical of boninites indicating extremely high degrees of melting of a N-MORB-like mantle or high degrees of melting of a depleted (residual) mantle (figure 6.3).

The available trace element data from the Point Sal ophiolite indicate that both, the lower and upper volcanic sections are compositionally heterogeneous. Most samples have magmatic affinities similar to island arc tholeiite. However, the lower volcanic section appears to contain lavas with magmatic affinities to CAB, IAT, N-MORB (figure 6.4) and boninites (figure 6.3) while the upper volcanic section appears to contain lavas similar to N-MORB (figure 6.4), IAT and boninites (figure 6.3). Only more analyses will establish the magmatic affinities of the lavas in the upper and lower volcanic sections. The pillow lavas of the Point Sal ophiolite provide an opportunity to study and document the compositional diversity in the CRO at this locality.

6.3.4 The Stonyford volcanic complex

The Stonyford volcanic complex lies in the northern Coast Ranges (locality 5, figure 6.1) and consists chiefly of pillowed volcanic flows, and minor diabase, pillow breccia and intercalated radiolarian chert (Hopson et al, 1981; MacPherson, 1983; Shervais and Kimbrough 1987; Shervais et al. in review). Radiolaria in the intercalated chert sections are early Tithonian (Hopson et al, 1981; Shervais et al., in review). Thus, volcanism overlapped with the sedimentation of the volcanopelagic sequence elsewhere in the Coast Range ophiolite(see figure 6.2). The volcanic rocks of the Stonyford volcanic complex have a

Figure 6.3

Comparison of geochemical data from the Wild Rogue Wilderness ophiolite with that from the Coast Range ophiolite remnants at Llanada, Black Mountain, Point Sal and Snow Camp Mountain in the Cr-Y discrimination diagram of Pearce (1982).

Figure 6.4

Comparison of geochemical data from the Wild Rogue Wilderness ophiolite with that from the Coast Range ophiolite remnants at Llanada, Black Mountain, Point Sal, Stonyford and Snow Camp Mountain in the Hf/3-Th-Ta discrimination diagram of Wood (1979).

Figure 6.5

Comparison of geochemical data from the Wild Rogue Wilderness ophiolite with that from the Coast Range ophiolite remnants at Llanada, Black Mountain, Point Sal and Snow Camp Mountain in the Th/Yb and Ta/Yb discrimination diagram of Pearce (1982).

Figures 6.3 through 6.5 (references for compilation of analytical data)

- Llanada: Lagabriele et al. (1986), Shervais (1990), Giaramita et al. (1998), and ICP-MS data obtained at Union College (appendix F).
- Black Mountain: Blake and Jones (1981), Lagabriele et al. (1986), Giaramita et al. (1998), and ICP-MS data obtained at Union College (appendix F).
- Point Sal: Menzies et al. (1977a, 1977b) and Shervais (1990).
- Stonyford: the analytical data are from Shervais (unpublished data)
- Snow Camp Mountain: ICP-MS data obtained at Union College (appendix F)

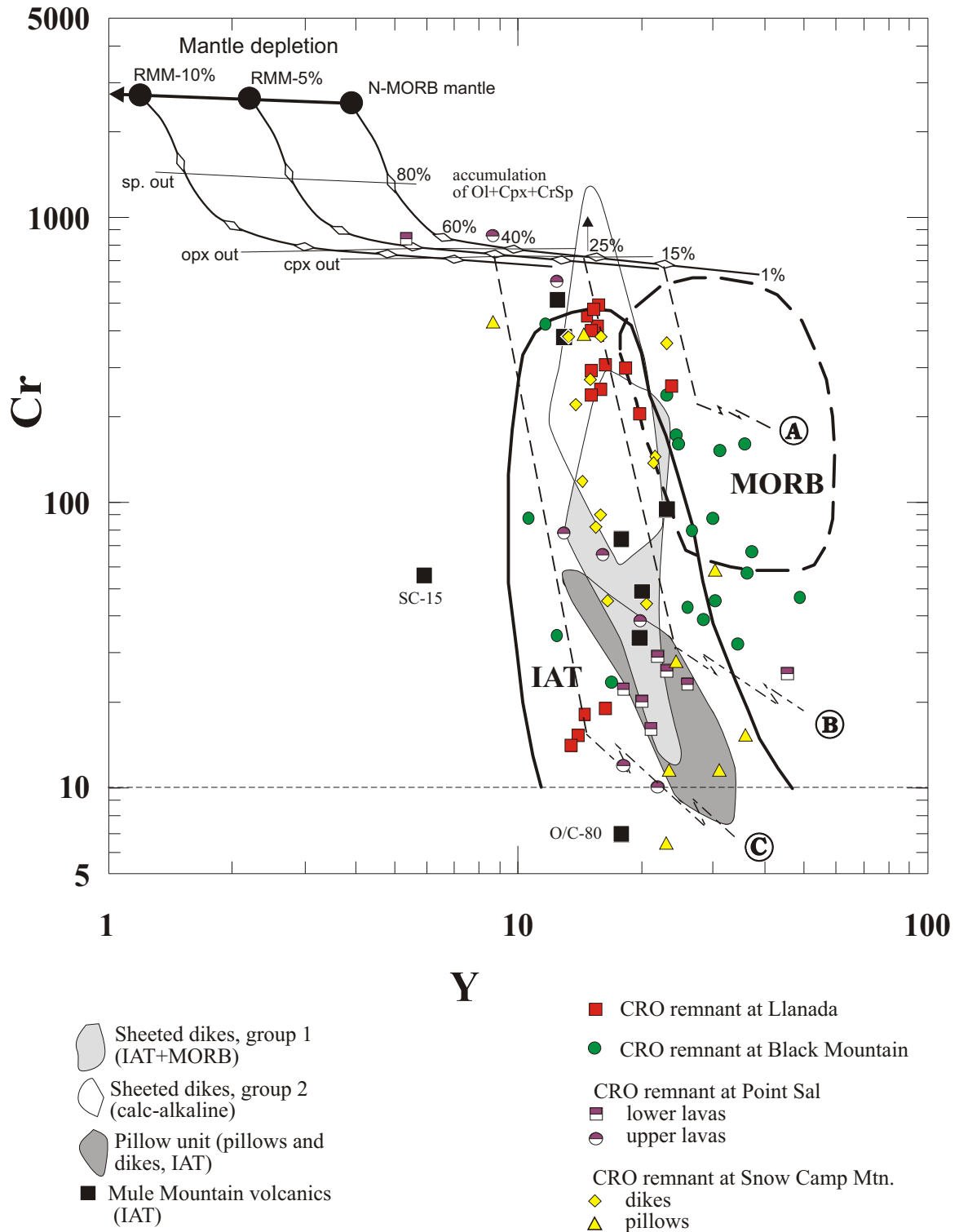


Figure 6.3: Comparison in the Cr vs. Y diagram of Pearce (1982). The fractionation paths for N-MORB (A), IAT (B) and Boninites (C) are shown (after Pearce et al.; 1984a). See figure 5.4 (chapter 5) for calculation of melting curves for N-MORB mantle and Residual MORB mantle (RMM).

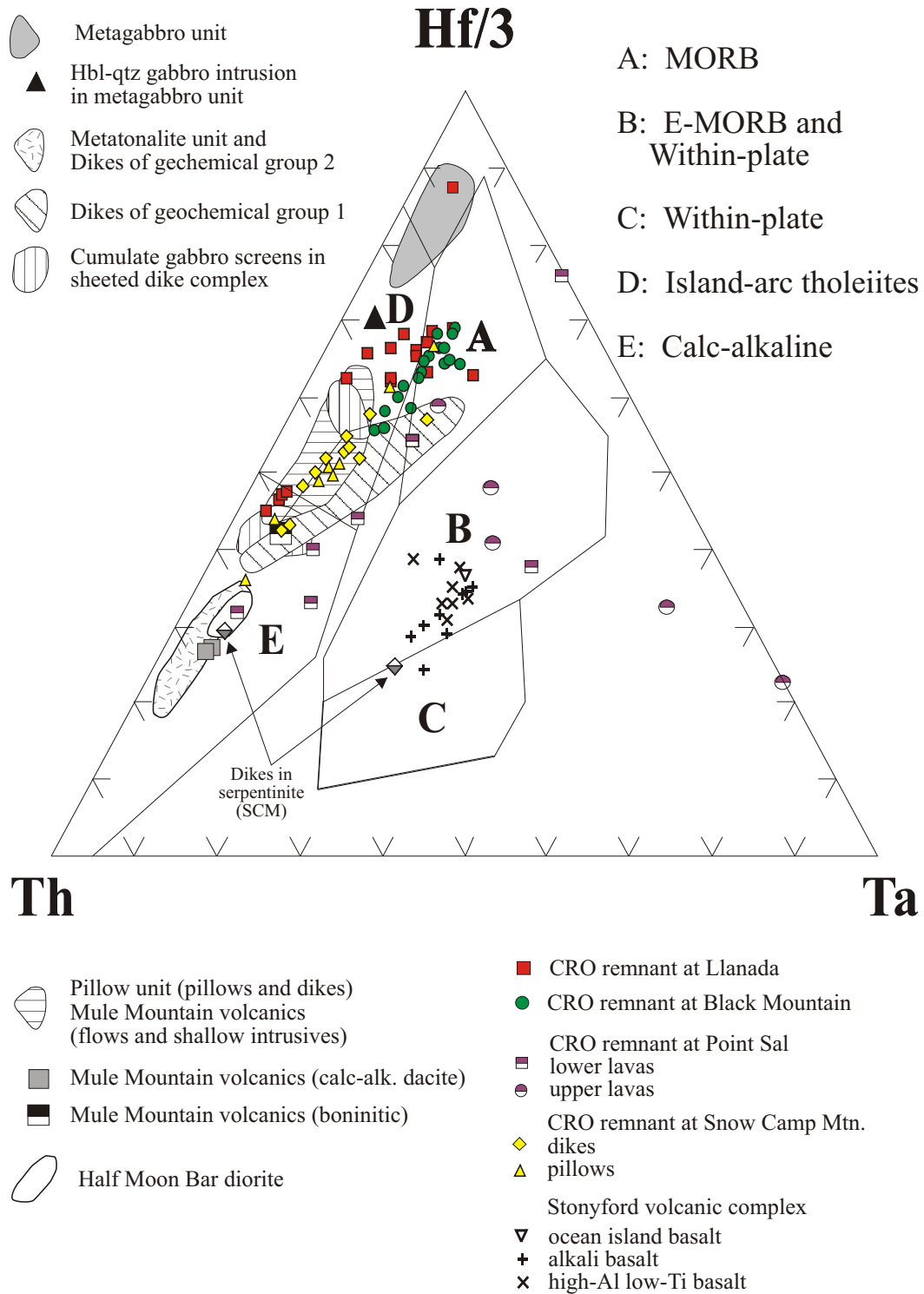


Figure 6.4: Comparison in the Hf/3-Th-Ta diagram of Wood (1979).

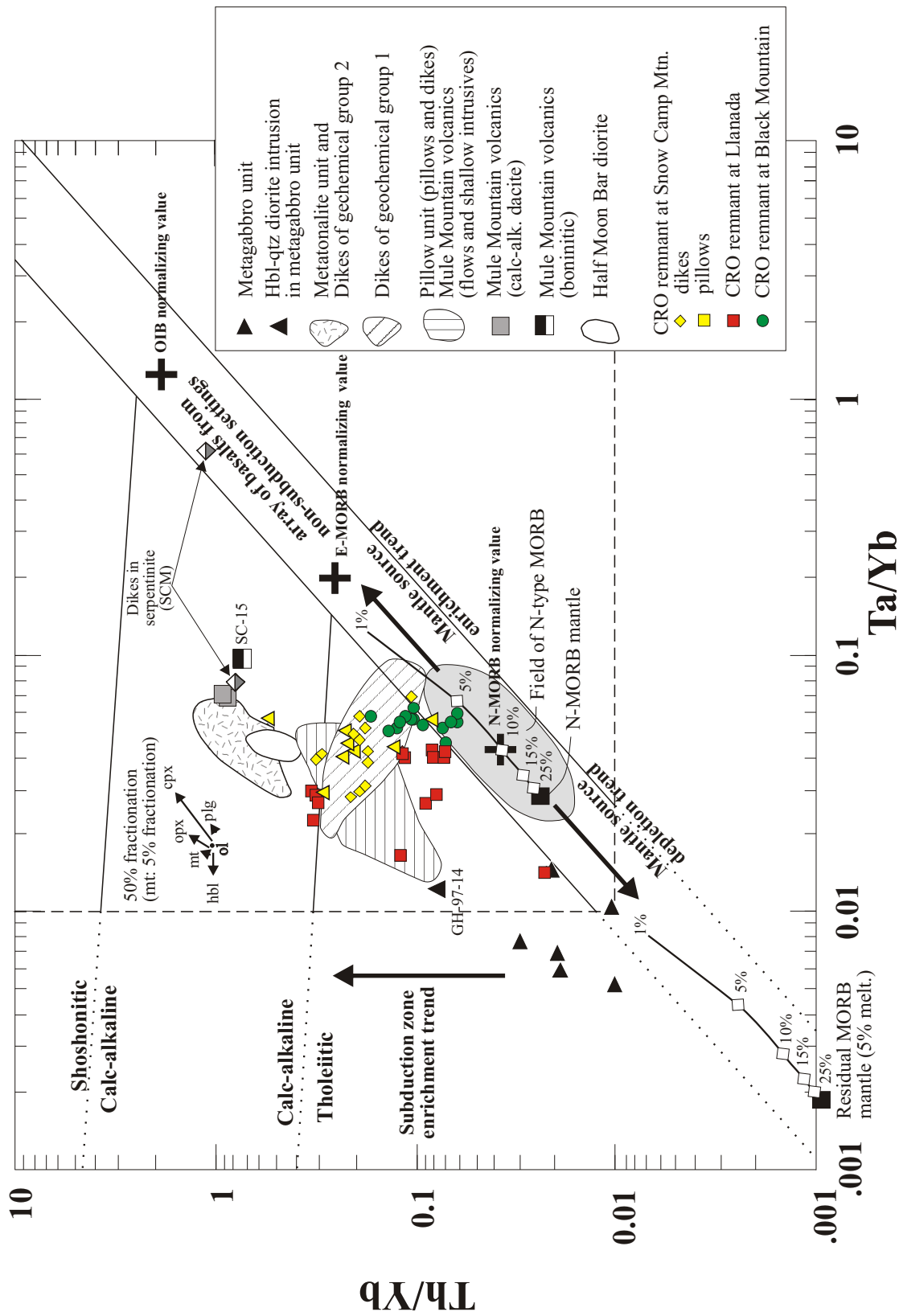


Figure 6.5: Comparison in the Th/Yb vs. Ta/Yb diagram of Pearce (1982). See chapter 5 for calculation of melting curves.

stratigraphic thickness of up to ~2.5 km and occur in four large tectonic blocks within or overlying a sheared serpentinite matrix melange (Shervais et al., in review). Dismembered remnants of the CRO are structurally below the largest blocks of the Stonyford volcanic complex.

Shervais et al. (in review) distinguishes three petrologic groups which are intercalated at all stratigraphic levels of the Stonyford volcanic complex. These groups are (1) ocean island basalts (OIB); (2) transitional alkali basalts and basaltic glasses; and (3) high-Al, low-Ti tholeiites. Basalts and glasses from the Stonyford complex (Shervais, unpublished data) plot in the Hf/3-Th-Ta diagram in the E-MORB and within-plate fields (figure 6.4). Based on their thickness and composition the Stonyford volcanics have been interpreted as a seamount (Hopson et al., 1981; MacPherson, 1983; Shervais and Kimbrough 1987; Shervais et al., in review). Clearly, the Stonyford volcanic complex is unique within the Coast Range ophiolite.

6.3.5 The Coast Range ophiolite remnant at Snow Camp Mountain, SW Oregon

Much of Snow Camp Mountain, SW Oregon, is underlain by a serpentinite matrix melange. Blocks within the serpentinite matrix melange consist of ophiolitic blocks containing uralitic gabbro intruded by mafic dikes (dike-gabbro transition), pillow lavas and chert (Harper, unpublished field mapping) and form a rock assemblage that is similar to that in the Wild Rogue Wilderness. However, in the Wild Rogue Wilderness, only few slivers of serpentinite are exposed.

Several of the analyzed dike samples are either chilled against uralitic gabbro (SM-96-2a, SM-96-2b.1, SM-96-2d.1, SM-96-3d) or other diabasic dikes (SM-96-2c.1, SM-96-2c.2, SC-27, SC-28, and SC-45). Also, two diabasic dikes (SM-96-8b, SM-96-11) intruding serpentinite and two diabasic dikes (SM-96-3b, SM-96-5a.1) intruding ultramafic rocks have been sampled and analyzed. Additionally, seven pillow samples (SM-96-10b, SM-96-10c, SM-96-10d, SM-96-12e, SM-96-13a, SM-96-13b, SM-96-13c) and one clast from a pillow breccia (SM-96-12a) have been analyzed. The trace element data, listed in appendix F, were obtained by ICP-MS analysis at Union College, Schenectady, NY. The SiO₂-content, ranging between 52% and 62%, is relatively high and may not be primary due to addition of hydrothermal

SiO₂. However, this range of SiO₂-contents is similar to the sheeted dike complex and the pillow unit in the Rogue Wilderness ophiolite (SiO₂ = 50%-60%).

The pillows and dikes intruding gabbro plot in the IAT field in the Cr vs. Y diagram (figure 6.3). A sample from a diabasic dike has a high Y concentration and plots well within the N-MORB field. Also, a pillow sample has a low Y concentration and plots outside the IAT field, typical of boninites. The pillow samples from the Snow Camp Mountain area have lower MgO and Cr-contents (figure 6.3) than the diabasic dikes, suggesting the pillows are more fractionated than the dikes. The same observation is made in the Rogue Wilderness ophiolite; the pillow unit appears to be more fractionated than the diabasic sheeted dikes.

The diabasic dikes from the Snow Camp Mountain area (which intrude gabbro and other diabasic dikes) plot in the N-MORB and IAT fields in the tectonic discrimination diagrams and also cross the boundary to the CAB field (figures 6.4 and 6.5). Essentially, the dikes from the Snow Camp Mountain area plot in the same field as group 1 sheeted dikes from the Rogue Wilderness area (figures 6.5 and 6.6). Thus, the compositional range in the Snow Camp Mountain ophiolite is similar to that of the dikes of geochemical group 1 in the sheeted dikes of the Rogue Wilderness ophiolite.

All pillow samples, except SM-96-12a, plot in the IAT and MORB fields in the tectonic discrimination diagrams in figure 6.4. The sample SM-96-12a is relatively more enriched in Th and plots in the CAB field. SM-96-12a has high Cr (~400 ppm, figure 6.3), high SiO₂, low Y, low HREE, and low TiO₂. Also, the LREE are enriched relative to the HREE. The extremely low Yb-content of SM-97-12a is typical of boninites and can be interpreted as due to high degrees of melting of a depleted mantle source (in figure 6.3, SM-97-12a plots left of arc-field). Pearce and Parkinson (1993) note that boninites often appear to be re-enriched in Nb and Ta, and thus the Ta/Yb or Nb/Yb ratios do not reflect the depleted nature of boninites (SM-96-12a plots well within the CAB field in figures 6.4 and 6.5). The Cr vs. Y diagram is effective to identify boninites using immobile trace elements; boninites plot in general left of the island-arc tholeiite field in figure 6.3.

To summarize, the diabasic dikes intruding gabbro in the Snow Camp Mountain area range in composition from N-MORB to IAT and are transitional to CAB. These dikes are similar in composition to

the dikes of geochemical group 1 of the sheeted dike complex in the Wild Rogue Wilderness. The pillows range in composition from N-MORB to IAT to boninite. Thus, the samples from the CRO remnant at Snow Camp Mountain, SW Oregon, are compositionally diverse, and have a similar range of compositional diversity as that for the Rogue Wilderness ophiolite and the Point Sal ophiolite (figures 6.34 and 6.4). The variations in trace element abundance ratios and large differences in magmatic affinities can be explained by various degrees of partial melting or variable mantle depletion as well as variable input of a subduction component.

The dikes intruding the serpentinite matrix melange are distinct from all other samples in the Snow Camp Mountain area. In figure 6.4 and 6.5, one dike (SM-96-11) plots in the calc-alkaline and the other dike (SM-96-8b) in the within-plate field. These samples have the highest Ta/Yb ratios of all samples from the Snow Camp Mountain area suggesting an enriched mantle source or crustal contamination (Pearce, 1983). Probably, these dikes are not related to the ophiolite and may have intruded during the emplacement of the ophiolite. SM-96-11 (calc-alkaline) could be related to the Nevadan-age calc-alkaline dikes and sills intruding the Josephine ophiolite and overlying Galice formation in the Klamath Mountains province (145-150 Ma dike and sill event). SM-96-8b could be related to Oligocene alkaline intrusive complex to the SW (Emily Peak). Isotopic ages are necessary to constrain possible correlations.

6.3.6 The Josephine ophiolite, northern California SW Oregon

The 162 ± 1 Ma Josephine ophiolite is a complete ophiolite (Harper, 1984). It consists of harzburgite tectonite, cumulate ultramafic, cumulate gabbro, high-level gabbro and diorite, a sheeted dike complex and a 0.4 km thick sequence of pillow lava and breccia. The Josephine ophiolite is conformably overlain by the Galice Formation (Harper 1983), which consists at the base of a thin, siliceous pelagic sequence and grades upwards into a thick sequence of turbidites (Harper, 1996) (see also figure 6.2).

A large geochemical data base for the Josephine lavas and sheeted dikes is available which includes the data from Harper (1984, 1988, 1995, in review); Harper et al. (1988), Alexander and Harper (1993), and Coulton et al. (1995). Fields for the data from the Josephine ophiolite are outlined in the Cr vs. Y (figure 6.6) and Hf/3-Th-Ta (figure 6.7) diagrams. These fields comprise previously unpublished

analyses of dikes and lavas from the Josephine ophiolite and are taken from Harper (in review). The field for Josephine dikes and lower extrusives overlaps with the N-MORB and IAT field in the Cr vs. Y diagram indicating that the Josephine lavas and sheeted dikes have transitional IAT-MORB magmatic affinities (figure 6.6). This is also shown in the Hf/3-Th-Ta diagram (figure 6.7): the field comprising plagiogranites, sheeted dikes and lavas from the Josephine ophiolite extends from the field for N-MORB to IAT. However, the upper lavas of the Josephine ophiolite plot entirely in the MORB field in the Hf/3-Th-Ta diagram (figure 6.7). Most of the upper lavas are Fe-Ti basalts or Fe-Ti rich. The high Fe- and Ti-content in these lavas is the result of high degrees of fractionation of N-MORB-like magma (Harper, in review). Harper (in review) suggested that the formation of the Fe-Ti lavas was related to the propagation of a back-arc spreading center into island-arc lithosphere.

Additionally, lavas and dikes having high Cr- and low Y- concentrations occur in the Josephine ophiolite (figure 6.6). These rocks have magmatic affinities to boninites (Harper, in review). The field for the boninitic lavas and dikes from the Josephine ophiolite is shown in the Hf/3-Th-Ta diagram extending from IAT to CAB (figure 6.7). Harper (in review) reports that IAT, MORB and boninite are all interlayered in the lower extrusive sequence of the Josephine ophiolite, while MORB-like lavas and Fe-Ti basalts occur in the upper extrusive sequence.

Most dikes of geochemical group 1 from the Wild Rogue Wilderness ophiolite plot in the field for Josephine lavas and dikes (figure 6.6 and 6.7) indicating transitional IAT-MORB magmatic affinities. However, two dikes of geochemical group 1 are more enriched in Th than the Josephine lavas and dikes. Clearly, lavas and dikes that are transitional between IAT and CAB do not occur in the Josephine ophiolite. Also, calc-alkaline rocks similar to the dikes of geochemical group 2 and the metatonalite unit are absent in the Josephine ophiolite (figure 6.7).

In the Cr vs. Y diagram, the samples from the pillow unit of the Wild Rogue Wilderness ophiolite plot in the same field as the sheeted dikes and lower extrusives of the Josephine ophiolite (figure 6.6). However, the pillow samples from the Rogue Wilderness ophiolite are more depleted in Ta relative to Hf than the Josephine lavas and dikes (figure 6.7).

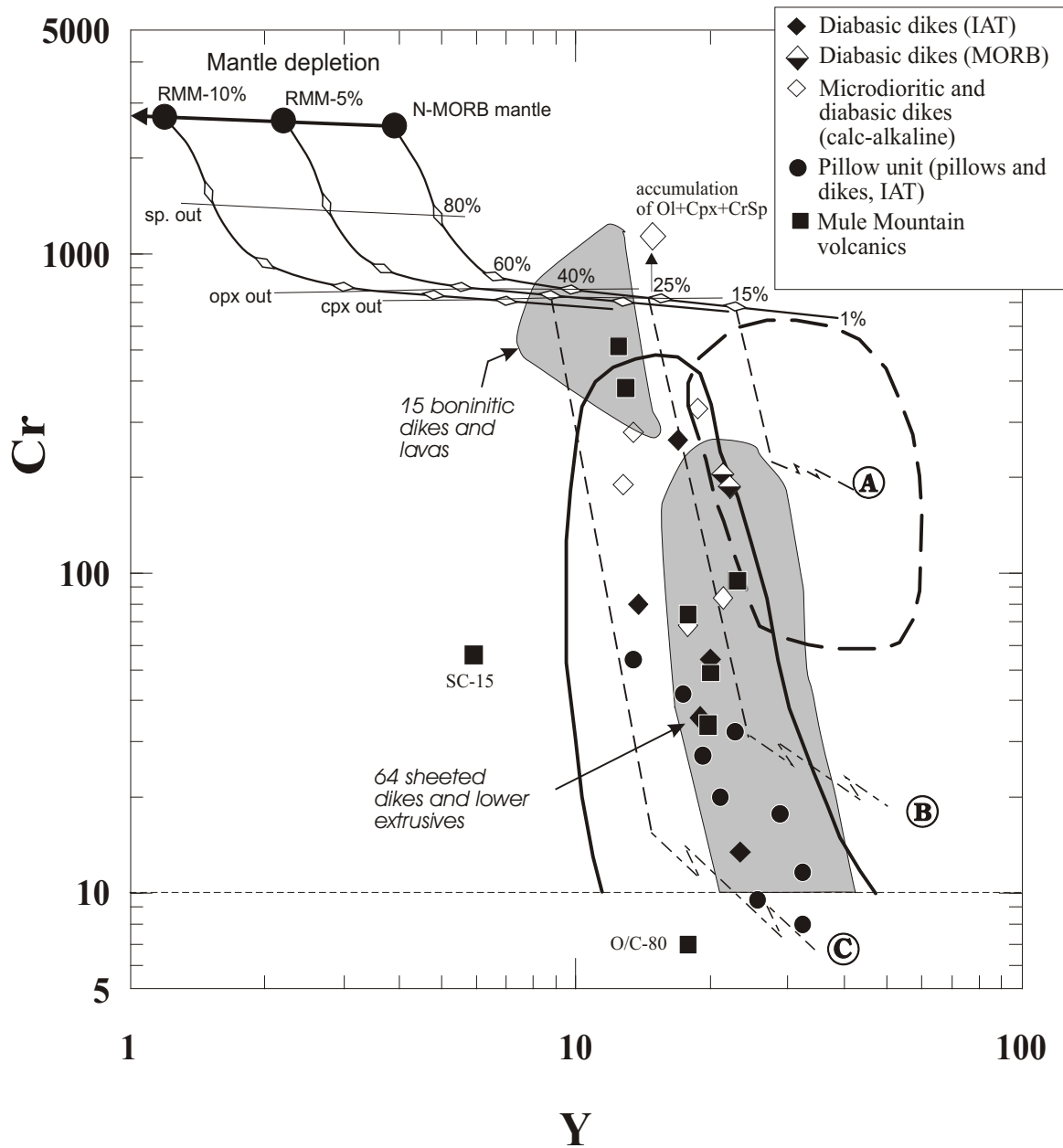
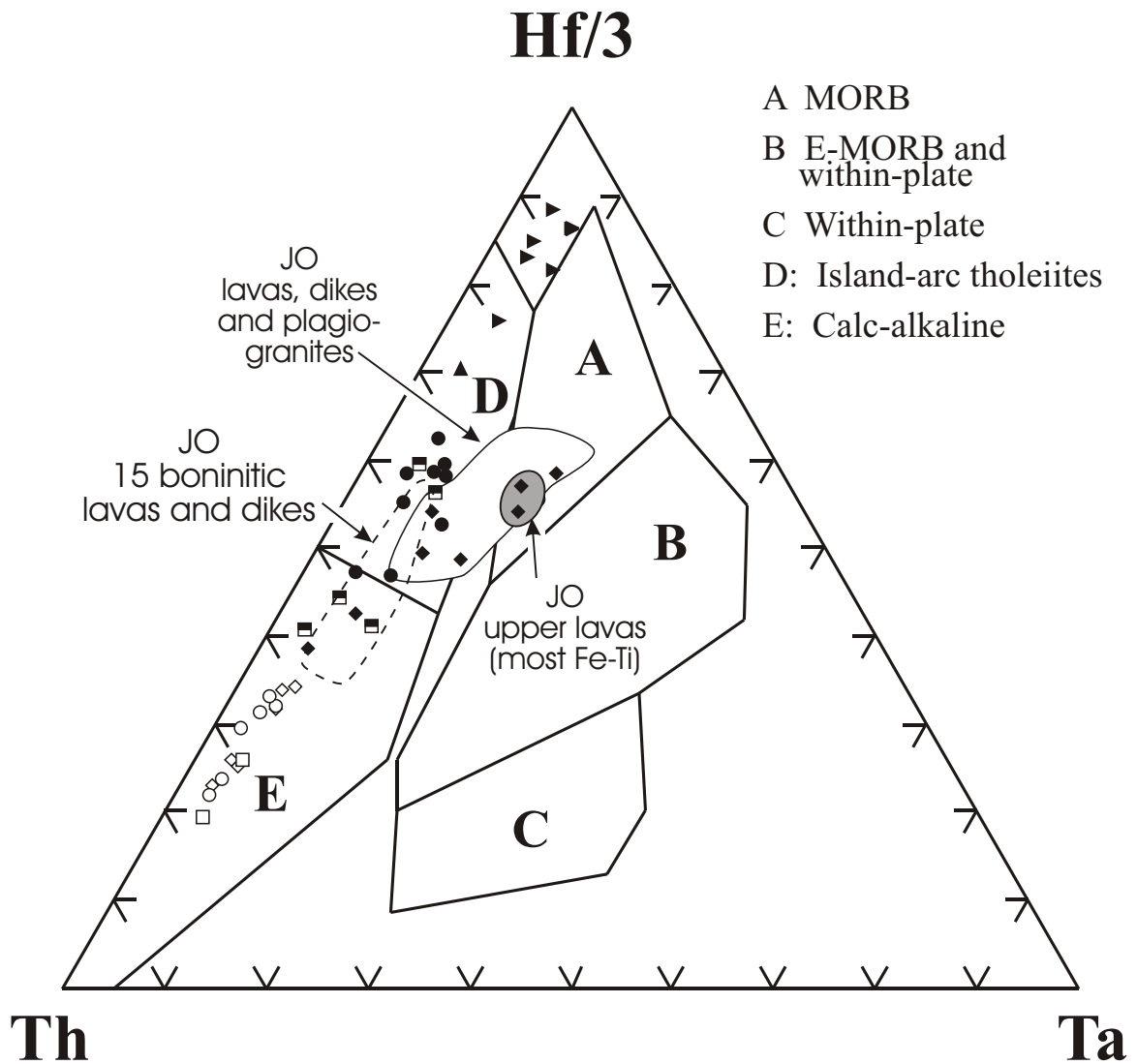


Figure 6.6

Comparison between the Josephine ophiolite and Wild Rogue Wilderness ophiolite in the Cr vs. Y tectonic discrimination diagram of Pearce (1982) showing fields for mid-ocean ridge basalts (MORB) and island arc tholeiite (IAT) (the latter field also includes calc-alkaline and alkalic basalts from oceanic arcs). The fields for the Josephine ophiolite are taken from Harper (in review). The fractionation paths for MORB (A), IAT (B) and boninite (C) are shown (after Pearce et al., 1984). See figure 5.4 (chapter 5) for calculation of the melting curves for MORB-mantle and residual MORB-mantle.



Wild Rogue Wilderness ophiolite

Plutonic units

- ▶ Metagabbro
- ▲ Hbl-qtz diorite in metagabbro
- Metatonalite-trondhjemite
- Def. dike and enclave in metatonalite

Sheeted dike complex

- ◆ Dikes of group 1
- ◇ Dikes of group 2
- Cumulate gabbro screens

Pillow unit

- Pillows and dikes

Figure 6.7

Comparison between the Josephine ophiolite and Wild Rogue Wilderness ophiolite in the Hf/3-Th-Ta tectonic discrimination diagram of Wood (1979). The fields for the Josephine ophiolite are taken from Harper (in review).

Samples having boninitic affinities were not found in the sheeted dike complex and the pillow unit of the Rogue Wilderness ophiolite. However, the composition of Cr-spinels in dikes of geochemical group 2 and in a pillow samples indicate that boninitic magmas were present as sheeted dikes and the pillows of the Rogue Wilderness ophiolite formed. Also, samples having boninitic affinities occur in the Mule Mountain volcanics (figure 6.6).

The lavas and dikes from the Josephine ophiolite are geochemically diverse ranging in composition from MORB to IAT to boninite. However, the geochemical diversity for the Josephine ophiolite is not as large as that for the Rogue Wilderness ophiolite. Calc-alkaline ophiolitic rocks are absent in the Josephine ophiolite. The occurrence of calc-alkaline rocks indicates a large subduction component in the Wild Rogue Wilderness ophiolite.

6.3.7 Summary

The geochemical data in this (see geochemistry chapter) and earlier studies (this section) clearly show that most extrusive and hypabyssal intrusive rocks from almost all studied Coast Range ophiolite remnants have suprasubduction zone affinities. Typical arc-characteristics include depletion of HFSE and selective enrichment in LILE and Th, lower Fe, Ti, Yb and Y concentrations than N-MORB, as well as low Ti/V, low Zr/Y, and low Ti and Zr (Menzies et al., 1977a, 1977b; Blake and Jones, 1981; Shervais and Kimbrough, 1985; Lagabrielle et al., 1986; Shervais, 1990; Giaramita et al., 1998, Shervais et al. in review). Most extrusive and intrusive rocks from the CRO are similar to IAT, or are transitional between N-MORB and IAT. Boninitic lavas (Shervais, 1990) as well as silicic samples with calc-alkaline affinities have been reported from the CRO (Menzies et al., 1977a, 1977b, Shervais, 1990, Shervais et al., in review, this study). Only the Stonyford volcanic complex consists largely of within-plate basalts, and the remnant at Black Mountain consist largely of MORB-like rocks, but the suite still shows suprasubduction zone affinities (Giamitra et al, 1998; Shervais et al., in review).

The Josephine ophiolite has a similar range of magmatic affinities (i.e., MORB, IAT and boninitic lavas; Harper in review) as the CRO in California and Oregon. Only calc-alkaline rocks do not occur in the

Josephine ophiolite (calc-alkaline dikes intrude the Josephine ophiolite and overlying Galice Formation during Nevadan orogeny).

6.4 Models for the tectonic and magmatic evolution of the Coast Range ophiolite

Two models for the tectonic evolution of the Coast Range ophiolite are discussed below (models 3 and 4; chapter 1). These models are consistent with the correlation made between the Coast Range ophiolite and the Josephine ophiolite (section 6.2), because these models predict that the CRO is native with respect to North America (i.e., the Coast Range ophiolite formed in the same arc - marginal basin system as the Josephine ophiolite).

Arc-like lavas have been recovered from segments of oceanic spreading ridges, such as the Chile rise near the Chile trench (Klein and Karston, 1995) and at the Woodlark spreading center in the Woodlark basin (Perfit et al., 1987). However, boninitic and calc-alkaline lavas, which occur at several CRO localities (section 6.3), have not been recovered from oceanic spreading centers. The model of Hopson et al. (in Dickinson et al, 1996) (see model 1, chapter 1) is considered unlikely, because it predicts MORB and locally transitional MORB-IAT magmatic affinities of igneous rocks of the CRO. Also, the model of Hopson et al (in Dickinson et al. 1996) postulates that the CRO is exotic with respect to North America.

The model proposed by Ingersoll and Schweickert (1986) and Dickinson et al. (1996) postulates that the CRO formed by back-arc spreading behind an east-facing intra-oceanic island arc that collided at ~159 Ma and became amalgamated with the North American continental margin (model 2, chapter 1). Although this model envisions suprasubduction zone affinity, there are several difficulties with it (Saleeby et al., 1992, Saleeby in Dickinson et al, 1996). For example, the implied late Jurassic collisional suture within the western Sierra and Klamath Mountain province cannot be defined (likely structures for a suture are older than late Jurassic; i.e. >169 Ma), and the entire subduction complex and fore-arc region of both the exotic arc system and the arc built on western N. America are missing (Saleeby et al., 1992).

6.4.1 Subduction initiation and the multi-stage evolution of the Coast Range ophiolite

6.4.1.1 The geochemical evolution of the Coast Range ophiolite, California

The most comprehensive study of the CRO is that of Shervais et al. (in review), providing an excellent review and synthesis of the field setting, relative ages of magmatic episodes, and geochemical data of several CRO remnants. Shervais et al. (in review) proposed, based on field and geochemical evidence, that the CRO of California had a multistage magmatic history. They identify at least four plutonic and volcanic suites having different petrochemical affinities and suggest that these suites correspond to progressive stages in the evolution of the CRO in a fore-arc setting above an east-dipping subduction zone. This subduction zone is postulated to have formed in the Mid-Jurassic as a transform zone was converted to a subduction zone (Stern and Bloomer, 1992) (see chapter 1 figure 1.7). Shervais et al. (in review) reported that three distinct magmatic types occur in most remnants of the CRO.

The first magmatic suite is characterized by low Ti (0.7-1.2%) and Cr (<50 ppm) over a range of SiO₂ from 53-66% as well as low Zr/Ti and Ti/V ratios. These rocks have magmatic affinities to island arc tholeiite and less commonly low-K calc-alkaline. Shervais et al. (in review) ascribe this first magmatic series, consisting of dunites, layered and foliated cumulate gabbros, some isotropic gabbros, portions of the sheeted dike complex, and the “lower” volcanic series (dominantly basaltic andesites), to the formation of incipient island arc crust above a nascent subduction zone. Basically, Shervais et al. (in review), envision a setting similar to the Eocene Izu-Bonin-Mariana arc (transition from transform to subduction zone; see model 4, chapter 1) as suggested by Stern and Bloomer (1992).

The second magmatic series of Shervais et al. (in review) consisting of wehrlites, clinopyroxenites, associated gabbros and gabbro-norites, portions of the sheeted complex and the “upper” volcanic series, is characterized by high Cr over a range of SiO₂, low TiO₂, low Zr/Ti and Ti/V. Shervais et al. (in review) report that the “upper” volcanic series in the CRO includes “tholeiitic ankaramites” and boninites. According to this model, melting of the mantle wedge and subsequent melt extraction of stage 1 magmas depleted the mantle wedge of the nascent subduction zone. Then, stage 2 (boninitic) magmas were produced by re-melting of previously depleted mantle requiring that the melting zone of stage 2 magmas was partially or completely isolated from undepleted asthenosphere (i.e., no or only local

“mixing” between depleted and undepleted mantle). Continued rifting of the young island arc crust, which formed during stage 1, allowed the intrusion of primitive, unfractionated ankaramite and boninite magmas (Shervais et al., in review).

The third magmatic series of Shervais et al. (in review) includes hornblende diorites, quartz diorites, plagiogranites, portions of the sheeted complex, and the volcanoclastic cover. The volcanoclastic rocks are predominantly of andesite to rhyolite composition, have calc-alkaline magmatic affinities, and rest on massive lavas and pillow lavas, but lie beneath the radiolarian cherts and clastic sediments that define the upper surface of the ophiolite. Shervais et al. (in review) ascribe the calc-alkaline magmatism to the influx of new, undepleted mantle into the melting zone as response to convection in the mantle wedge as the subduction zone matures. Melting of the undepleted mantle is augmented by the addition of enriched fluids from the subducted slab.

The fourth magmatic series of Shervais et al. (in review), include oceanic basalts and late dikes of MORB- composition. Only few remnants (Elder Creek, Mount Diabolo, Del Puerto Canyon, Cuesta Ridge, Geyser Peak/Black Mountain) contain MORB-like rocks which crosscut or overlie all of the older igneous rock series. Shervais et al. (in review) present two interpretations of the late MORB-like rocks in the CRO: (1) the composition changes from calc-alkaline to MORB-like lavas due to continued rifting of the arc to form a back-arc basin, or (2) MORB-like magmas, that generated at a spreading center, leak through the overlying plate as the spreading center is subducted. Shervais et al. (in review) favor the second interpretation.

The studies of Shervais et al. (in review), Shervais and Kimbrough (1985) and Shervais (1990) as well as the compilation of the data from the CRO in section 6.3 clearly show that the CRO contains petrographically and geochemically distinct suites including MORB- and OIB-like lavas, island-arc tholeiites, boninites, and calc-alkaline lavas. The same range of magmatic affinities has been identified in the Rogue Wilderness ophiolite (except OIB) and rocks recovered from the fore-arc region of the Izu-Bonin-Mariana arc (e.g., Johnson and Fryer, 1990). The presence of petrologically diverse rocks in the CRO supports the idea that the CRO formed in a fore-arc region (Kosanke and Harper, 1997, Giaramita et

al., 1998) and perhaps had a similar evolution as the infant (Eocene) Izu-Bonin-Mariana arc (Stern and Bloomer, 1992; Shervais et al., in review).

The model of Shervais et al. (in review) may explain much of the geochemical variability in the CRO. However, the compilation of the geochemical data from the CRO (figure 6.3, 6.4 and 6.5) indicates that there is geochemical variability which may not be explained using this model. For example, both volcanic series in the Point Sal ophiolite contain volcanic flows having very high Cr- and extremely low Yb- contents (Menzies et al. 1977a) suggesting that lavas having boninitic magmatic affinities occur in both volcanic sections of the Point Sal ophiolite (figure 6.3). In fact, the sample with the lowest Yb- concentration, indicating the highest degree of partial melting or highest degree of mantle source depletion, is from the lower and not the upper pillow lavas. Most samples from the upper and lower pillow lavas at Point Sal have arc-like Yb-concentrations and low Cr-concentrations which is common in island arc tholeiites (figure 6.3).

The pillow lavas sampled from the lower volcanic member at Llanada are also geochemically heterogeneous. As shown in figure 6.3, most samples seem to be derived by high degrees of melting of a N-MORB-like mantle or lower degrees of melting of a depleted mantle source. Only two samples, one in the middle (LL91-9) and one at the top (LL91-18) of the volcanic member, have low Ta/Yb ratios consistent with formation by re-melting of a depleted mantle source. However, one of the “depleted” samples (LL91-9) plots in the N-MORB field in figure 6.3 indicating it formed by low degrees of melting. Also, the Cr# of Cr-spinels in samples from the lower volcanic member at Llanada ranges between 48 and 62, and thus it is slightly higher than the Cr# of Cr-spinels in N-MORB ($100 * Cr / (Cr + Al) = 12-58$) and much lower than of high-Ca and low Ca-boninites (72 - 85 and 80 - 92, respectively). There is no indication that the lavas from Llanada are “depleted” similar to boninites are “tholeiitic ankamarite”. Therefore, the pillow lavas should correspond to the first magmatic series according to the model of the multi-stage evolution of the CRO, and not to the second magmatic series as suggested by Shervais et al. (in review). Furthermore, the Zr/Y ratios in samples from Llanada increase from base to top. This is not consistent with the model of Shervais et al. (in review) proposing that the melting zone of stage 2 magmas may have been isolated from convective exchange with undepleted asthenosphere, resulting in melting of a

previously depleted mantle source. This would result in increasingly depleted magmas in the second stage. However, an increase of Zr/Y ratios at Llanada is consistent with the interpretation that the lavas became more enriched. If the increase of Zr/Y ratios can be linked to an increase of the mantle fertility, these data would imply exactly an opposite mantle source evolution through time than that suggested by Shervais et al. (in review).

6.4.1.2 The geochemical evolution of the Wild Rogue Wilderness ophiolite, SW Oregon

Can the geochemical heterogeneity in the Rogue Wilderness ophiolite be explained with the model of the multi-stage evolution of the CRO as suggested by Shervais (in review)? The Wild Rogue Wilderness remnant of the CRO has almost the same range of magmatic affinities as the entire Coast Range ophiolite in California (figure 6.4). The magma types include MORB, IAT and “depleted” IAT, CAB, and boninites. Only OIB is not present in the Wild Rogue Wilderness (figure 6.4). In addition to isotopic ages for several units (figure 6.3), several crosscutting relationships were mapped in the Wild Rogue Wilderness. The field, geochemical and geochronological data can be used to test the model of the multi-stage evolution of the Coast Range ophiolite.

6.4.1.2a Island-arc tholeiites

Extrusive and intrusive rocks from the Wild Rogue Wilderness ophiolite having compositions similar to the first magmatic series (island-arc tholeiites) of Shervais et al. (in review) may include the hornblende-quartz diorite intrusion in the metagabbro unit (figure 6.8a), most diabasic dikes from the sheeted dike complex (figure 6.8b), and all samples from the pillow unit (except the silicic dike O/C-231a which is probably younger) (figure 6.8c). These samples have magmatic affinities to island-arc tholeiite and were sampled from the ophiolitic units. Also, the Mule Mountain volcanics chiefly consist of volcanic flows having IAT affinities (figure 6.8d). However, the age of most of this unit is uncertain, because only a calc-alkaline dacite from the uppermost section was dated (152.9 ± 1.8 Ma).

A silicic dike in the pillow unit (O/C-231a) and four dacitic samples from the Mule Mountain volcanics (O/C-147, O/C-217, GDH-1, GDH-2b) have IAT affinities. Altered silicic rocks such as O/C-

231a, O/C-147, O/C-217, GDH-1, and GDH-2b are often referred to as “keratophyres” in the literature, and have been reported from numerous CRO remnants. The N-MORB- and chondrite- normalized patterns for several mafic samples from the pillow unit and the Mule Mountain volcanics are parallel to the silicic samples from the Rogue Wilderness ophiolite (chapter 5) and other CRO remnants suggesting that the mafic and silicic rocks evolved from similar parental magmas. Shervais et al. (in review) suggested that the “keratophyre” dikes and sills intruded during the third stage of the evolution of the CRO, and that stage 3 is characterized by calc-alkaline magmatism. Based on the trace element data from the Rogue Wilderness ophiolite, however, I suggest that caution must be applied interpreting “keratophyres” and other silicic rocks in the CRO as having formed during the third magmatic series, because many of the altered silicic samples from the Rogue Wilderness ophiolite and Mule Mountain volcanics have magmatic affinities similar to island-arc tholeiites and likely formed by fractional crystallization of mafic, tholeiitic magmas. It becomes clear that more age data should be obtained, especially of the highly evolved silicic rocks having IAT affinities. These rocks may contain enough zircon for dating.

6.4.1.2b Boninites

Volcanic rocks from the Wild Rogue Wilderness having compositions similar to the second magmatic series (tholeiitic ankamarites and boninites) of Shervais et al. (in review) may include samples O/C-81a, O/C-81b and SC-15 in the Mule Mountain volcanics (figure 6.8d, see also chapter 5). O/C-81a and b have low Ti/V ratios (< 20), high Cr-, and low Y- concentrations and plot in the field for Josephine boninitic dikes and lavas (figure 6.6). O/C-81a and b contain large and abundant phenocrysts of clinopyroxene that also contain Cr-spinel (O/C-81b contains much less phenocrysts but is from the same flow). Cr-spinels within O/C-81b have high Cr/(Cr+Al) ratios similar to high-Ca boninites. SC-15 has even lower HFSE and HREE concentrations than O/C-81a and O/C-81b, an U-shaped REE pattern (figure 6.8, see also chapter 5), and plots outside of the arc field in the Cr-Y discrimination diagram (figure 6.6). Very low Y-concentrations are characteristics of boninites and consistent with the interpretation of formation by very high degrees of melting of a depleted mantle source. Unlike most boninites, SC-15 has very low Cr-concentrations suggesting that SC-15 fractionated from a boninitic magma. According to the model of

Shervais et al. (in review), much of the Mule Mountain volcanics may have formed during stages 1 (IAT) and 2 (boninitic).

Additionally, Cr-spinels in a pillow sample (O/C-224b) and in calc-alkaline dikes containing olivine xenocrysts have high Cr/(Cr+Al) ratios similar to high-Ca boninites. This implies that boninitic magmas were present and mixed with IAT in the pillow unit and with CAB in the sheeted dike complex. It appears that magmas of stages 1, 2, and 3 (after Shervais in review) were simultaneously present in the Wild Rogue Wilderness ophiolite. Another possibility is that the lavas in the pillow unit are transitional between stages 1 and 2 while the calc-alkaline dikes having a boninitic component (i.e., Cr-spinels) are transitional between stages 2 and 3. Note that dikes of geochemical group 2 cut dikes of geochemical group 1.

6.4.1.2c Calc alkaline rocks

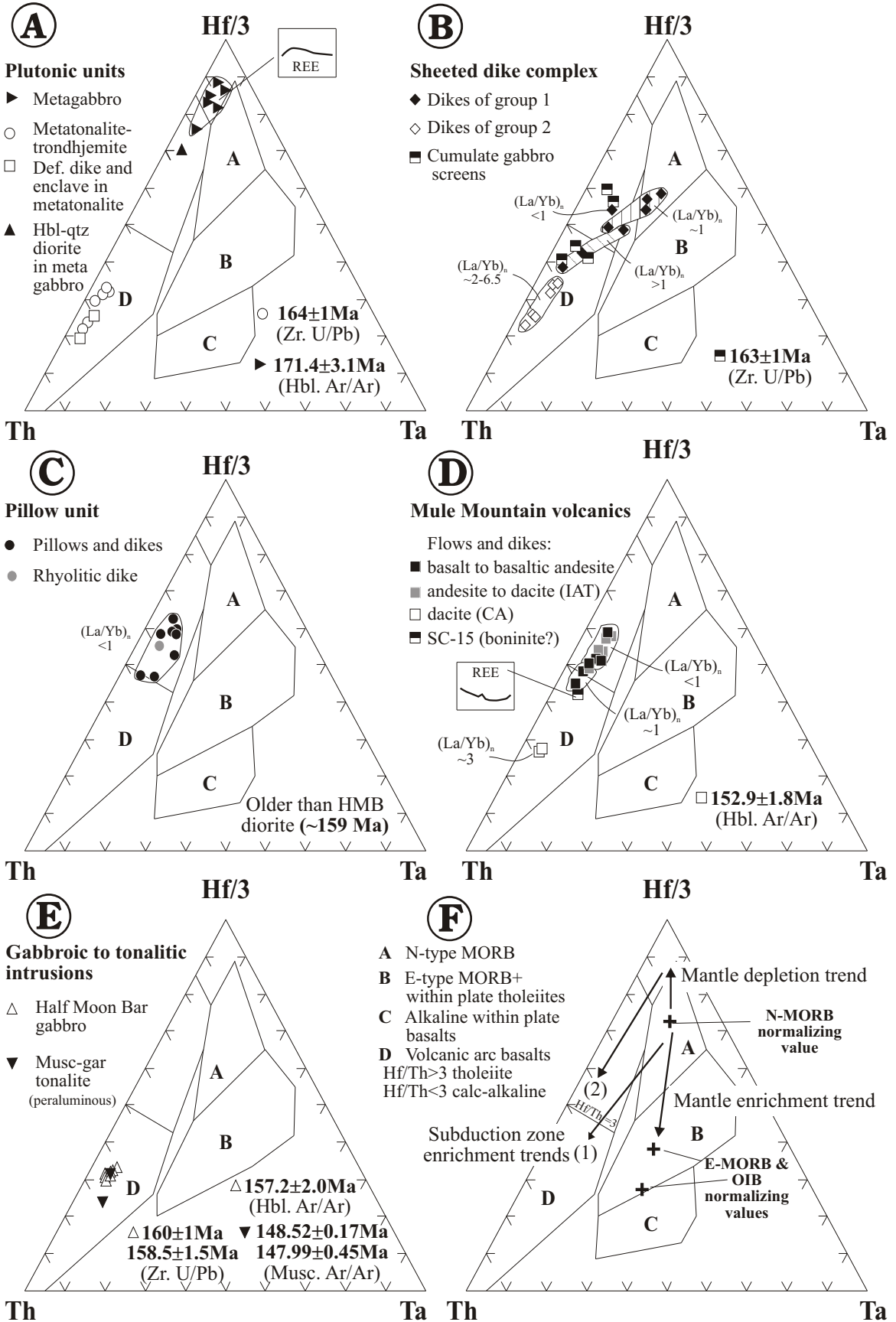
Extrusive and intrusive rocks having compositions similar to the third magmatic series (calc-alkaline rocks) of Shervais et al. (in review) would include the metatonalite unit (figure 6.8.a), the dikes of geochemical group 2 in the sheeted dikes complex (figure 6.8b), the Half Moon Bar diorite (figure 6.8e), and the hornblende + plagioclase phyric dacites (GDH-2a and GDH-2b) from the upper most section of the Mule Mountain volcanics (figure 6.8.d). Although, the silicic samples in the pillow (O/C-231a) unit and upper volcanic unit (O/C-147, O/C-217, GDH-1, GDH-2b) as well as the hornblende-quartz diorite (GH-97-14) are indistinguishable in terms of major element composition from calc-alkaline samples, the trace element data clearly indicate that O/C-231a, O/C-147, O/C-217, GDH-1, GDH-2b and GH-97-14 evolved from arc-tholeiitic parents.

A sample (SC-2) from the metatonalite unit yielded an U/Pb zircon age of 164 ± 1 Ma. This is, within analytical error, the same age as the U/Pb zircon age of SC-1, a plagioclase layer from a cumulate gabbro screen in the sheeted dike complex (163 ± 1 Ma). The lack of sheeted dike diabases in the metatonalite unit implies it may be younger. The cumulate gabbro screens and the plagioclase layers have magmatic affinities similar to island arc tholeiites (figure 6.8b, see also chapter 5). Outcrop relationships indicate that both groups of dikes intruded cumulate gabbro. The age data and crosscutting relationships

Figure 6.8

Hf/3-Th-Ta tectonic discrimination diagram showing samples from the Rogue Wilderness ophiolites.

- A. The samples from the metagabbro unit plot at depleted N-MORB compositions and overlap with the field for island-arc tholeiites. All samples from the metatonalite unit plot in the calc-alkaline field.
- B. The samples from the sheeted dike complex plot in the N-MORB field, island-arc tholeiite field and calc-alkaline field. Dikes of petrographic group 1 (diabasic dikes) range from N-MORB to island-arc tholeiite in composition whereas dikes of petrographic group 2 (diabasic and microdioritic dikes) are calc-alkaline. The screens of cumulate gabbro have IAT and transitional IAT-CA magmatic affinities. This diagram also shows that the $(La/Yb)_n$ ratios increase with increasing Th/Hf ratios.
- C. All samples from the pillow unit plot within the island-arc tholeiite field. One dike from the sheeted dike complex and two cumulate gabbro samples overlap with the field of the pillow unit and also have $(La/Yb)_n < 1$.
- D. Most samples from the Mule Mountain volcanics plot in the island-arc tholeiite field, and two dacitic samples plot well within the calc-alkaline field. The field containing samples with $(La/Yb)_n < 1$ overlaps completely with the field of the pillow unit suggesting that the pillow unit and part of the Mule Mountain volcanics are related. SC-15 appears to be a boninite having an U-shaped REE pattern and low concentrations of HFS elements. Similar to the samples from the sheeted dike complex, the $(La/Yb)_n$ ratios increase slightly with increasing Th/Hf ratios.
- E. The samples from the Half Moon Bar diorite plot in a very small cluster in the calc-alkaline field. Small variations in incompatible trace element ratios indicate the samples are related by fractionation of a common parental liquid. Also, the muscovite garnet tonalite dikes in the metagabbro unit plot in the calc-alkaline field.
- F. Petrogenetic pathways in the Hf/3-Th-Ta diagram of Wood et al. (1979) after Pearce et al. (1984). The vectors show mantle depletion due to previous partial melting and mantle enrichment from a “within-plate” component. Vectors (1) and (2) indicate enrichment of normal and depleted mantle with Th derived from a subducted slab.



indicate that magmas of calc-alkaline (metatonalite unit and dikes of group 2) and tholeiitic (cumulate gabbro dikes of group 1) affinities formed at about the same time

Hornblende separates of a sample from the HMB diorite yielded an $^{40}\text{Ar}/^{39}\text{Ar}$ cooling age of 157.2 ± 2.0 Ma, and of GDH-5a an $^{40}\text{Ar}/^{39}\text{Ar}$ cooling age of 152.9 ± 1.8 Ma. Zircon separates of samples from the Half Moon Bar diorite intrusion (calc-alkaline) unit yielded concordant U/Pb ages between 158.5 ± 1.5 Ma and 160 ± 1 Ma. It appears that tholeiitic and calc-alkaline magmas were intruded at 164 Ma (sheeted dikes and metatonalite unit, figure 6.8d), and calc-alkaline magmas were produced during at least two subsequent episodes (HMB diorite at 157-160 Ma, and metavolcanic unit at 152.9 ± 1.8 Ma). Thus, at least three episodes of calc-alkaline magmatism have been identified, which is inconsistent with the model of Shervais et al. (in review) who propose that calc-alkaline magmas correspond to the third of four progressive stages of the magmatic evolution of the CRO.

6.4.1.2d Mid ocean ridge basalts

Dikes having compositions similar to the fourth magmatic series of Shervais et al. (in review) includes two MORB-like dikes (O/C-1-S1 and O/C-356) in the sheeted dike complex (figure 6.8b, see also chapter 5). The MORB-like dikes are very thin and cut other diabasic dikes, one of which has magmatic affinities to island-arc tholeiite (O/C-1-S2). The N-MORB dikes as well as the calc-alkaline dikes could be the youngest dikes in the sheeted dike complex. However, mixing of MORB- and IAT-end members in crustal magma chambers can explain the composition of samples of transitional MORB-IAT composition. This is demonstrated in chapter 5 (figure 5.20) using a simple mixing model. Thus, MORB and IAT magmas could have been produced at the same time during seafloor spreading and the formation of the sheeted dikes.

6.4.1.3 Discussion of the magmatic evolution of the Wild Rogue Wilderness ophiolite

The sheeted dike complex in the Rogue Wilderness is perhaps an ideal locality to test the model of the multi-stage evolution of the CRO, because all magmatic series identified in the CRO are also present in the sheeted dike complex of the Wild Rogue Wilderness ophiolite, except OIB. The geochemical data

from the sheeted dike complex indicate that different dikes have different magmatic affinities including IAT, CAB, and N-MORB (figure 6.8b, see also chapter 5) as well as a boninitic component in some calc-alkaline dikes. Also, a dike (MRH-111) having low Ta/Yb ratios has been identified, suggesting that magmas could have formed by melting of a previously depleted mantle source. The crosscutting relationships and magmatic affinities of cumulate gabbro, diabasic dikes (N-MORB and IAT) and microdioritic dikes (calc-alkaline) should be determined along the Rogue River in a continuous, section of the sheeted dike complex. Such a detailed study of the sheeted dike complex would allow to determine whether the different magmas formed in a specific order which Shervais et al. (in review) would predict to be IAT - BON - CAB - MORB, or different magmas formed simultaneously suggesting a highly heterogeneous (inherited) mantle source. Additionally, igneous titanite and possibly zircon commonly found in the microdioritic dikes could be dated to provide control on the age of the calc-alkaline magmatism in the sheeted dike complex, unless they are <2 Ma apart (resolution of age).

Based on the compiled geochemical data for several CRO remnants and the data obtained from the Wild Rogue Wilderness remnant of the CRO, I suggest that suites having different petrochemical affinities do not necessarily correspond to progressive (successive) stages in the evolution of the Coast Range ophiolite, but reflect the geochemical heterogeneity that is characteristic of lavas erupted in a fore-arc setting. For example, the model of Shervais et al. (in review) does not explain the occurrence of more than one episode of calc-alkaline magmas in the Wild Rogue Wilderness ophiolite. Also, the model of Shervais et al. (in review) is not entirely consistent with the observation that lavas having magmatic affinities to IAT and boninites are intercalated in the extrusive sequence. Although the Wild Rogue Wilderness ophiolite contains the same types of rocks having the same range of magmatic affinities as the Coast Range ophiolite in California, the complete set of geochemical and age data from the units of the Rogue Wilderness ophiolite are not consistent with the model of the multistage evolution of the CRO as suggested by Shervais et al. (in review).

In order to better understand why magmas of such widely differing petrochemical affinities are generated during the formation of the CRO, which is thought to represent ancient marginal basin crust, a modern example of the tectonic evolution of a marginal basin is reviewed below. This will provide a

modern analogue and help to identify processes that could have played an important role in the tectonic evolution of the CRO and develop a model for the Coast Range ophiolite that fits all field, geochemical, and age data.

6.4.2 The Lau basin as a modern analogue for the Coast Range ophiolite

Stern and Bloomer (1992) and Shervais et al. (in review) envision the origin of the CRO as due to the generation of incipient island arc crust above a nascent subduction zone similar to the Eocene Izu-Bonin-Mariana arc. This oceanic arc was initiated as a large transform zone was converted into a subduction zone by major plate reorganization (Stern and Bloomer, 1992 and references therein). However, Stern and Bloomer (1992) noted that this view is problematic, because there is evidence subduction was underway before the “arc infancy phase” of the CRO (stage 1 of Shervais et al., in review): arc-magmatism in the Sierran arc occurred almost continuously in the interval 215-85 Ma (e.g. Chen, 1982) and in the Klamath arc since ~174 Ma (Wright and Fahan, 1988). An alternative model for the CRO should incorporate these constraints. In this context, the evolution of the Lau Basin offers an attractive modern analogue for the CRO. A map of the Lau basin, SW Pacific is shown in figure 6.9 and a model of its evolution in figure 6.10.

Before the drilling transect in the Lau Basin (ODP leg 135), it was assumed that the magmatism in back-arc spreading centers evolves from arc-like basalts during the initial arc-rifting stage to N-MORB with time as the basin widens and the locus of arc magmatism moves away from the volcanic front (Hawkins and Melchior, 1985). Similarly, Shervais et al. (in review) hypothesized that the change calc-alkaline to MORB-like magmatism (third to fourth magmatic series) could be related to continued spreading. This would result in a compositionally zoned back-arc basin crust with the margins having arc-like characteristics (IAT, CAB), and lavas erupted at the spreading center having compositions similar to N-MORB (Hawkins and Melchior, 1985). However, the results from ODP leg 135 (Lau Basin - Tonga Ridge drilling transect) indicate spatial and temporal heterogeneity. The trace element data of the Lau Basin - Tonga Ridge drilling transect and other cruises are compiled, grouped according to the stages of

back-arc evolution and plotted in the Hf/3-Th-Ta and Th/Yb vs. Ta/Yb tectonic discrimination diagrams (figures 6.11 and 6.12).

6.4.2.1 The tectonic evolution of the Tonga-Lau arc/back-arc basin system

The detailed study of the Lau-Tonga arc system, SW Pacific, an active, 1000-km long, back-arc basin associated with Pacific-Australian plate convergence (figure 6.9), provided new insights of the magmatic and tectonic evolution of this system. A summary of the evolution of the Lau Basin after Parson et al., (1994), Parson and Hawkins, (1994), and Parson and Wright (1996) is given below: (1) In response to changes in relative plate motion between Pacific and Australian plate, incipient, symmetrical rifting occurred in the fore-arc region (Tonga Platform) at ~5.6 Ma (figure 6.10b). N-MORB-like lavas erupted during the earliest episode of fore-arc rifting (ODP-site 834). The Lau Ridge (now a remnant arc, figure 6.9) continued as an active volcanic arc for at least 4 Ma after rifting began (Parson et al., 1994). (2) Distributed and heterogeneous half-graben rifting occurred (figure 6.10c) which was associated with rapid half-graben sediment infilling and pooling of MORB-like and arc-like rift magmatism (ODP-sites 835, 837, 838 and 839). As the crust was structurally stretched and thinned, the arc-front began to migrate trenchward. The second stage lasted about ~3 Ma after the initial rifting resulting in the basin and range topography of the western Lau Basin, analogous to half-graben formation currently occurring in the offshore Taupo volcanic zone off New Zealand, but behind the volcanic front (Parson and Wright, 1996). (3) A propagating rift was initiated at ~ 4.5 Ma (Parson and Hawkins, 1994). The propagator started from the trace of the Peggy Ridge (figure 6.9) and propagated south through the basin complex. The earliest magmatism related to spreading at Site 836 is ~0.8 Ma (figure 6.10d), and dominantly N-MORB-like magmas occur. Currently, the southern rift tip of the ELSC propagates into the active Tofua arc. The southernmost spreading segment of the ELSC (Valu Fa ridge) is only 40 km west of the arc volcano Ata (figure 6.9). (4) A second propagating rift was initiated on the Peggy Ridge at about 1.5-1.2 Ma and has overtaken and “replaced” the ELSC (Parson and Hawkins, 1994). As shown in figure 9, the Central Lau spreading center (CLSC) has propagated southward into the older oceanic crust generated at the ELSC. A small ridge segment is located between the failing (ELSC) and propagating (CLSC) tips of the spreading

ridges. This ridge segment is termed the intermediate Lau spreading center (ILSC). The modern lavas at the spreading centers are mostly similar to N-MORB, except for the ELSC south of 21S and the ValuFa ridge (e.g., Pearce et al., 1995b).

6.4.2.2 The geochemical evolution of the Tonga-Lau arc/back-arc basin system

Initial rifting was characterized by the eruption of MORB-like lavas that ponded in the rift basins (e.g., Hergt and Farley, 1994; Hawkins and Allan, 1994) recorded by volcanic rocks drilled at Site 834, located in a 2700 m-deep half-graben at the western most margin of the extensional basin (figures 6.9 and 6.10). These volcanic rocks range in composition from low- K tholeiite basalt to basaltic andesite. The lavas are highly vesicular (40-50%) despite the considerable water depth (Hawkins and Allan, 1994), implying high volatile contents in the magmas compared to MORB from mid ocean ridges. Most samples are very similar to N-MORB, but important differences exist such as the addition of a variable slab-component evident in the elevated H₂O content, selective enrichment of LILE and high (but variable) Th/Yb ratios (figure 6.12). The site-834 lavas have, on average, lower Ta/Yb ratios than N-MORB (figure 6.12) and plot much closer to the Hf-apex in the Hf/3-Th-Ta ternary diagram than N-MORB (figure 6.11). Variations in the Ta/Yb ratios indicate that the lavas were derived by partial melting of variably depleted or enriched mantle or variable degrees of partial melting (figure 6.12). Hergt and Farley (1994) interpret the trace element and isotope (Pb, Sr, Nd) signature of Site 834 lavas as the result of the influx of “fresh” Pacific MORB-mantle during fore-arc extension. The influx of Pacific MORB-mantle implies that rifting in the fore-arc region was associated with decompressional melting of asthenospheric mantle rising from depth, and previously melted lithosphere, such as the mantle directly beneath the volcanic front, became entrained in the rising column of Pacific MORB-mantle. As a result, “undepleted” and “depleted” lavas, having some or no arc signature, respectively are closely associated.

Sites 835, 837, 838 and 839 are located in the western Lau Basin (figure 6.9), and the minimum ages of recovered igneous rocks are constrained by foraminifera in overlying sediments to have formed during the rifting phase (Site 835: ~3.5 Ma; Sites 837 and 838: ~2 Ma; Site 839: ~1.25- >2.2 Ma). Tuffaceous sediments interbedded with these lavas indicate numerous, short-lived arc-composition

Figure 6.9

Location map of the Lau Basin after Hergt and Farley (1994) showing bathymetry, location of Lau and Tonga ridges, and drill-hole sites (Leg 135 and DSDP Site 203). CLSC, ILSC and ELSC are the Central Intermediate and Eastern Lau Spreading centers, respectively. The three spreading segments between the islands of Niuafu'ou and Tafahi form the King's triple junction. Also shown (dashed lines extending from the Peggy Ridge to the Valu Fa ridge) is the approximate boundary between the older western and eastern Lau Basin crustal Provinces. The western Lau Basin has horst-and-graben topography as a result of tectonic extension of arc crust while the eastern Lau basin crust formed by true seafloor spreading (Parson and Hawkins, 1994).

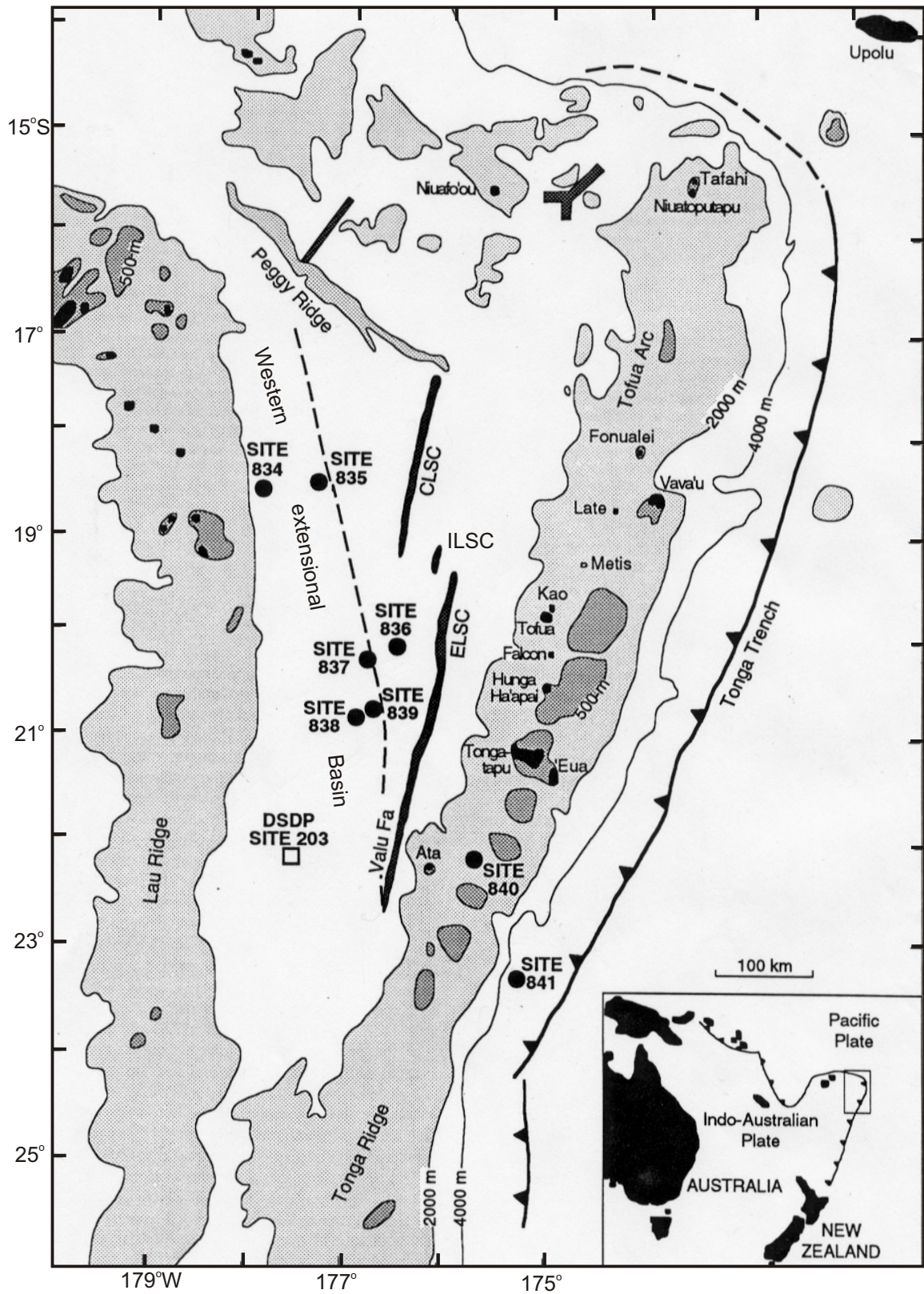


Figure 6.9: Location map of the Lau Basin

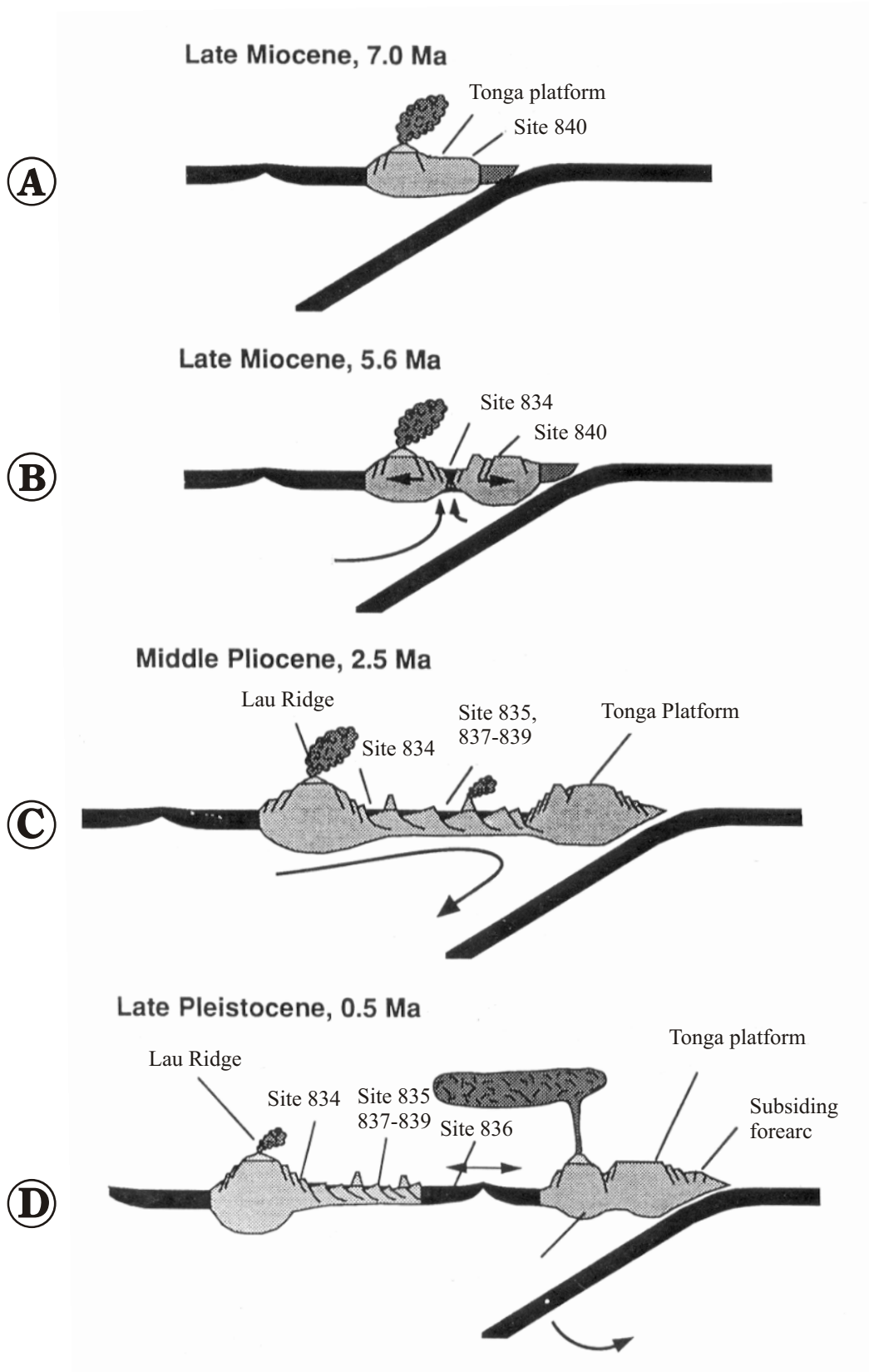


Figure 6.10: Diagram showing the tectonic evolution of the Lau Basin (after Clift and Dixon, 1994)

See text for details.

volcanoes formed at the margins of the half grabens (figure 6.10c) and were the proximal source of volcanoclastic infillings of the narrow, linear sub-basins (e.g., Clift and Dixon, 1994). The lavas range in composition from basalt to basaltic andesite. The Ta/Yb and Th/Yb ratios of sites 835, 837, and 839 differ significantly from each other indicating various degrees of mantle depletion and addition of a variable slab component (figure 6.11). The most primitive lavas at site 835 and 839 have lower Ta/Yb ratios than the lavas at site 834, indicating site 835 and 839 lavas were derived by higher degrees of melting and/or from a more depleted mantle source than earlier site 834 lavas. However, Site 837 lavas plot almost completely within the field for Site 834 lavas (figure 6.12) indicating that lavas similar in composition to earlier Site 834 lavas erupted at ≥ 2 Ma.

Lavas from site 839 have the highest subduction contribution and are geochemically very similar to lavas from the Tofua and Kermadec arc (figures 6.11). Site 839 is located very close to, but just west of, the boundary between the older western Lau Basin and younger eastern Lau Basin (figure 6.9). The latter formed by seafloor spreading at the ELSC. Site 839 lavas formed as the volcanic arc moved away from the trench because of fore-arc rifting (figure 6.10c). As a result, the rifted fore-arc moved over the locus of arc magmatism, explaining the eruption of lavas with a strong subduction contribution at Site 839. However, lavas similar in composition to earlier site-834 lavas continued to erupt (e.g. site 837) indicating a large compositional heterogeneity during the stage of fore-arc rifting. A correlation between proximity to the trench (at the time of eruption) and subduction component or mantle depletion is not found using the Th/Yb ratios as a measure of the subduction component, nor is there a correlation between proximity to the trench and the Ta/Yb ratios as a measure of mantle depletion (accounting for variations in partial melting and fractionation).

Unlike the other back-arc sites (835, 837, 838 and 839), which are assigned to the western Lau Basin, site 836 is believed to be located on crust formed by seafloor spreading at the ELSC. The recovered lavas are of basaltic composition and have distinctly elevated Th/Yb ratios compared to the MORB array suggesting the addition of a slab component (figure 6.12). Overall, the samples recovered at site 836 are more N-MORB-like than at sites 835, 837, 838 and 839. However, the variations in Ta/Yb and Th/Yb

ratios are similar to site 839 suggesting various degrees of melting and/or a variably depleted mantle source (figure 6.12).

Samples dredged from the spreading ridges (ELSC and CLSC) in the Lau Basin are predominantly N-MORB like, but some samples have slightly elevated Th/Yb ratios compared to the MORB array implying a subduction zone component. The CLSC and ELSC lavas are very similar to site 836 and have the same range of Ta/Yb ratios. An interesting observation is that two samples dredged at the ILSC have extremely low Ta/Yb ratios (and a very strong negative Ta- and Nb-anomaly on a N-MORB normalized diagram; not shown) suggesting they derived by melting of a highly depleted mantle source. Perhaps, the CLSC is propagating into a mantle that is depleted because of previous melting and melt extraction at the ELSC.

The lavas recovered at the ILSC may reflect a process of mantle depletion due to multi-stage melt extraction associated with rift propagation as suggested by Meffre et al. (1996) for the Koh ophiolite. Meffre et al. (1996) proposed a model invoking propagating rifts to explain the evolution of the Koh ophiolite, New Caledonia. This ophiolite was formed by two tholeiitic magmatic episodes separated by high-Ca boninites. The first island-arc tholeiitic magmatic episode in the Koh ophiolite is thought to be related to spreading in a supra-subduction zone setting. These tholeiitic lavas are overlain by a high-Ca boninitic suite that is inferred to have formed by shallow melting of residual mantle underneath a propagating rift augmented by fluids released into the mantle wedge. This episode was followed by deeper melting of more fertile mantle to produce the upper tholeiitic series. It appears that large geochemical heterogeneity can be introduced due to the initiation of propagating rifts.

The Valu Fa ridge is the southern extension of the ELSC, and its southernmost tip is propagating into the active Tofua arc thus representing a nascent back-arc basin. The samples dredged at this rift range in composition from basaltic andesite to andesite (Jenner et al., 1987; Boespflug et al., 1990; Hawkins, 1995). The lavas from the Valu Fa ridge have magmatic affinities between those of the ELSC (N-MORB) and the active volcanic front (IAT) (figures 6.11 and 6.12).

Kamenetsky et al. (1997) identified two types of magmas based on the analysis of melt inclusions trapped in primitive olivine phenocrysts of magmas erupted at near-axis seamounts on either side of the

Figure 6.11

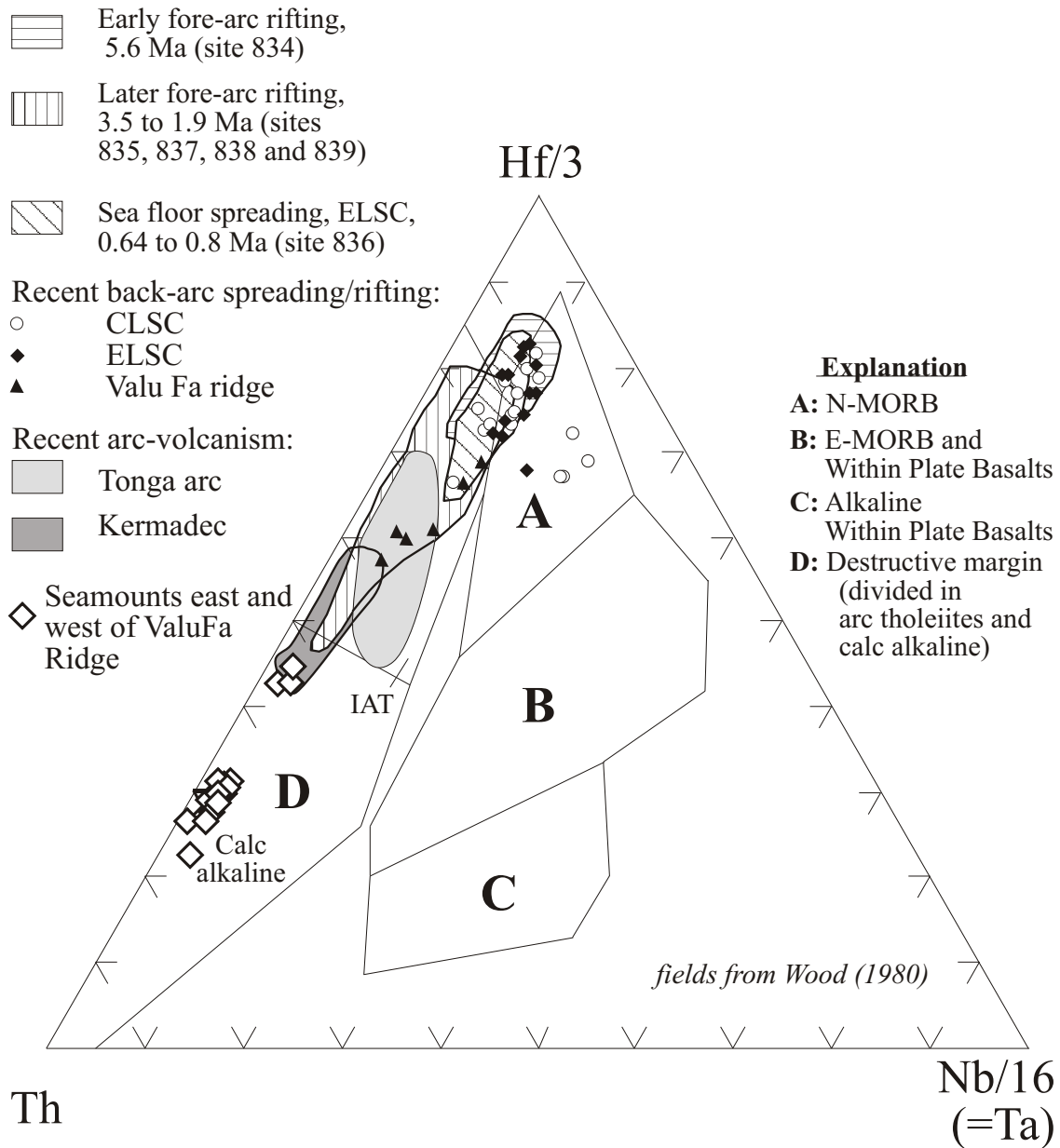
Published geochemical data from the Lau Basin, SW Pacific plotted in the Hf/3-Th-Ta discrimination diagram of Wood (1979).

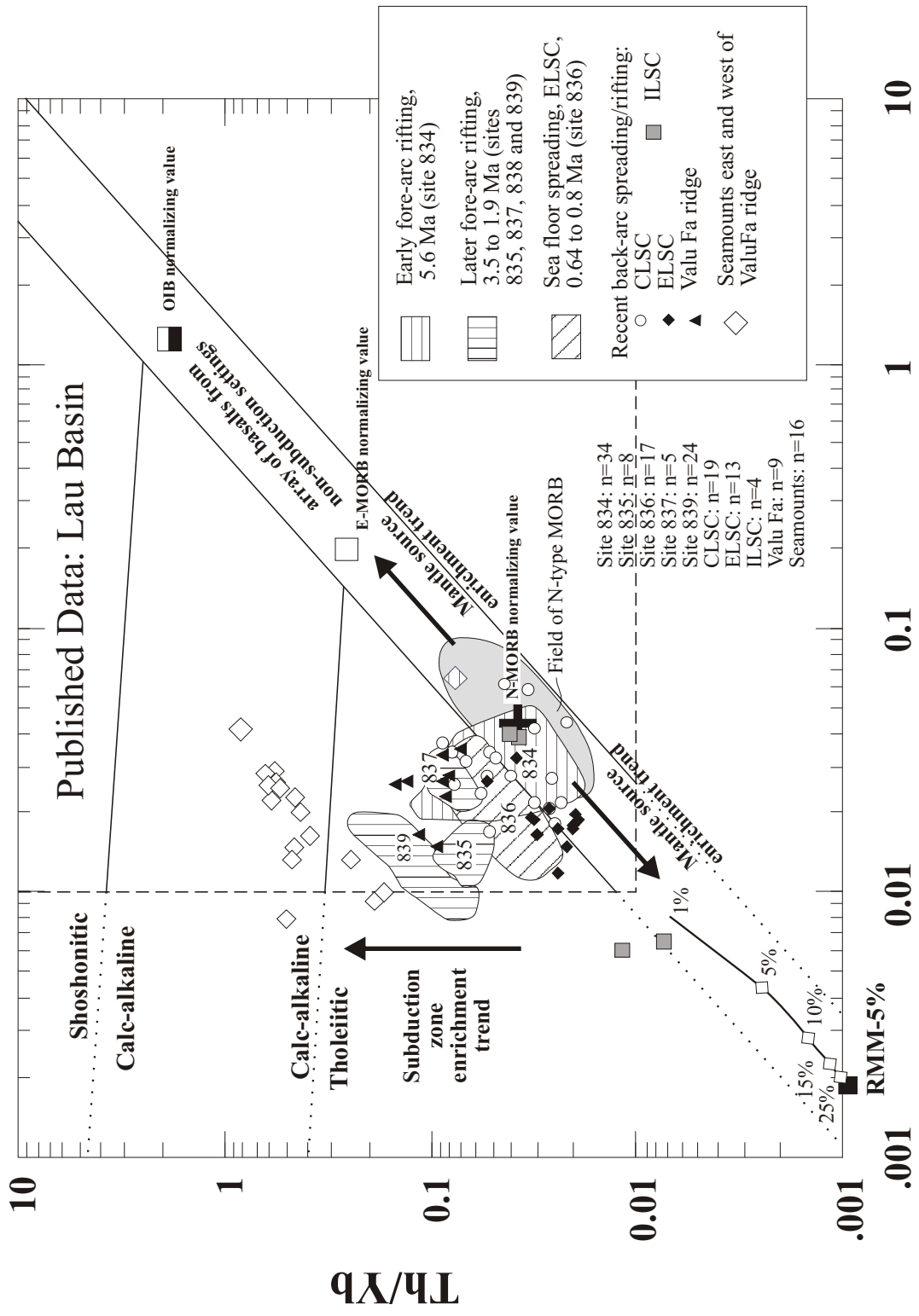
Figure 6.12

Published geochemical data from the Lau Basin, SW Pacific plotted in the Th/Yb vs. Ta/Yb discrimination diagram of Pearce (1982).

The analytical data shown in figures 6.11 and 6.12 are compiled mainly from ODP volume 135 and include the data reported in Ewart et al. (1994a), Ewart et al. (1994b), Hergt and Farley (1994), Allan (1994), Hawkins and Allan (1994), and Hergt and Hawkesworth (1994). Other data include those of Pearce et al. (1995b), Hawkins (1995), Hawkins and Melchior (1985), Kamenetsky et al. (1997), Jenner et al. (1987), Frenzel et al. (1990), and Boespflug et al. (1990).

Published Data: Lau Basin





Valu Fa ridge. One type of magma is a high-Ca (14%), low Al_2O_3 (~8%) magnesian basalt, and the other is a low-Ca boninite-like magma. These lavas plot in the calc-alkaline fields in the tectonic discrimination diagrams in figures 6.11 and 6.12. Kamenetsky et al. (1997) found large and systematic variations in incompatible trace element compositions that can be explained with the variable addition of LILE, Pb and Cl-rich component to the mantle wedge source with increased influence toward the Tofua arc. Pearce et al. (1995b) also reported that the relative enrichment of LILE and H_2O of basalts drilled and dredged in the Lau basin increases towards the volcanic front. Kamenetsky et al. (1997) as well as Pearce et al. (1995b) suggest that this component is a supercritical fluid with LILE, Cl and Pb-rich \gg LREE \gg HFSE-poor characteristics released as oceanic crust is dehydrated during subduction beneath the volcanic arc. However, high La/Yb and Sr/Y ratios in melt inclusions from lavas erupted at the western seamounts, are not consistent with the model of addition of an aqueous fluid low in LREE. Kamenetsky et al. (1997) suggest that a second component was added and could be a silicate melt of broadly tonalitic composition generated by partial melting of the subducting slab. The large variability of incompatible trace element ratios indicate that the back-arc mantle, prior to propagation and rifting of the Valu Fa ridge, was heterogeneous due to variable addition of a subduction component to the back-arc and subarc mantle (i.e., addition of aqueous fluid and silicic melt). Rifting on the Valu Fa ridge caused the upwelling and invasion of MORB-source mantle into the pre-existing, metasomatized arc-lithosphere which may have been veined by clinopyroxene-rich dikes (Kamenetsky et al., 1997). The heterogeneous sub-seamount mantle became entrained into the upwelling MORB-source mantle, which caused decompressional melting augmented by conductive heating. The model of Kamenetsky et al. (1997) is consistent with the lower Th/Yb and Th/Hf ratios in lavas dredges from the ValuFa ridge compared to the seamounts east and west of the ValuFa ridge (figures 6.11 and 6.12). The highly metasomatized mantle under the seamounts is apparently capable of producing magmas with boninitic affinities, while the lavas erupted at the ValuFa ridge have magmatic affinities between MORB and IAT.

6.4.2.3 Formation of the Wild Rogue Wilderness ophiolite by fore-arc rifting

Ophiolites which are thought to have formed in a suprasubduction-zone setting commonly have strong arc geochemical affinities and typically contain arc-like granitoids and related volcanic equivalents that are part of the ophiolite stratigraphy (Pearce et al., 1984b; Förster et al., 1997). These granitoids in ophiolites, often referred to as ‘oceanic plagiogranites’ (e.g., Coleman and Peterman, 1975), have trace element compositions indistinguishable from ‘volcanic arc granites’. Clearly, there is some confusion with the use of the term ‘oceanic plagiogranites’ and ‘volcanic arc granites’ and the implied tectonic setting of these granitoids. Nevertheless, the occurrence of large arc-like dioritic to tonalitic plutons, such as the metatonalite unit, is characteristic of many ophiolites that formed in suprasubduction zone settings (e.g., Upadhyay and Neale, 1979).

The metatonalite unit is a calc-alkaline granitoid with high Th/Yb and Th/Hf ratios, but low Zr/Y ratios and K₂O- and Rb-contents (K₂O and Rb are “mobile” but Zr and Y are not). Low-K arc basalts and their derivatives are typical of oceanic arcs and typically have Zr/Y < 3 (Pearce, 1983). The major- and trace element characteristics of the metatonalite are similar to high-Na (and low-K) arc rhyolites and dacites that have been described from various oceanic arc systems including the fore-arc region (e.g., Tonga: Bloomer et al., 1994; Marianas: Bloomer, 1987), the volcanic front (e.g., Tonga: Cunningham and Anscombe, 1985) and the back-arc region (Valu Fa ridge: Frenzel et al., 1990; Sumisu rift: Hochstaedter et al., 1990a and 1990b; Ikeda and Yuasa, 1989). Also, Sigurdsson et al. (1993) report that various high-Na rhyolites were dredged from the Hunter ridge located at the southern margin of the North Fiji Basin. High-Na rhyolites occur also at the southernmost end of the main spreading center of the North Fiji Basin. The southernmost tip of this spreading center propagates into the arc crust bordering the rim of the North Fiji Basin, almost perpendicular to the Hunter ridge (Maillet et al., 1989). Also, high-Na arc rhyolites and tonalites-trondhjemites are known from ophiolites (Pearce et al., 1984b, Coleman and Peterman, 1975, Coleman and Donato, 1979, Foerster et al., 1997 and references therein). However, they are commonly not as voluminous as the metatonalite unit in the Rogue Wilderness ophiolite. This suggests that the Wild Rogue Wilderness ophiolite formed very close to or within a volcanic arc where silicic plutonic and volcanic rocks having calc-alkaline affinity are more abundant than in a back-arc environment.

Most dikes of geochemical group 2 from the sheeted dike complex contain igneous quartz (see chapter 2) and have significantly higher Zr/TiO₂ ratios at a given Nb/Y ratio than dikes of geochemical group 1 (see chapter 5). These petrographic and geochemical data suggest that the calc-alkaline sheeted dikes are evolved (i.e., basaltic andesite to andesite). Note that the samples recovered from the Valu Fa ridge are more evolved (mostly basaltic andesite to andesite, some dacites) than lavas currently erupting at the Eastern Lau spreading center (Jenner et al., 1987; Davis et al., 1990; Frenzel et al., 1990). However, dacitic to rhyolitic volcanic rocks were recovered from the basin crust that formed by seafloor spreading at the Eastern Lau spreading center (e.g. Hawkins, 1995).

The occurrence of andesitic to rhyolitic lithologies at the ELSC and the Valu Fa ridge as well as the Hunter Ridge is consistent with the model of Christie and Sinton (1981) and Sinton et al. (1983) suggesting that the intermittent development of closed magma systems at any propagating ridge tip results in closed system fractionation. If the magma is a dry melt (normal N-MORB-like liquid), typical Fe-Ti rich basalts are produced, such as those at the Galapagos propagating rift tip (Christie and Sinton, 1981). Moderate amounts of fractionation of olivine, plagioclase, and pyroxene from a basaltic liquid cannot result in significant increase of SiO₂, but FeO* and TiO₂ increase sharply. In contrast, if the melt is hydrous, which is common in suprasubduction zone settings (e.g., Hochstaedter et al., 1990a,b; Pearce et al., 1995a,b), andesites to rhyolites are readily generated by crystal fractionation. Early fractionation of Fe-Ti oxides in a hydrous melt causes SiO₂ to become rapidly enriched and FeO* and TiO₂ depleted, while delayed fractionation of plagioclase results in elevated Al₂O₃ contents (Sisson and Grove, 1993a and 1993b). Therefore, lavas with high primary H₂O- and SiO₂-, and low FeO*- and TiO₂- contents should occur at propagating ridges in supra-subduction settings. Such lavas are found at the ValuFa ridge (Jenner et al., 1987; Davis et al., 1990; Frenzel et al., 1990), and southern-most tip of the main spreading center of the North Fiji basin (Hunter ridge) (Sigurdsson, 1993). However, a small number of lavas at the ValuFa ridge indicate strong enrichment of FeO* and TiO₂ with fractionation (Jenner et al., 1987; Davis et al., 1990; Frenzel et al., 1990) suggesting the generation of more than one magma type at this site. The andesites having high TiO₂ from the Valu Fa ridge probably developed from magma having low *f*O₂ and thus are not much different from Fe-Ti basalts.

Olivine xenocryst phyric dikes of geochemical group 2 (calc-alkaline sheeted dikes) and a pillow sample (IAT) from the pillow unit contain Cr-spinels having compositions similar to Cr-spinels in high-Ca boninites (chapter 5). This implies that high-Ca boninitic magmas were present and mixed with IAT and CAB. High-Ca boninites were dredged at the Hunter ridge where the southernmost spreading center of the North Fiji Basin propagates into arc-lithosphere (Sigurdsson et al., 1993). Also, melt inclusions of depleted high-CaO, low- Al_2O_3 magnesian basalts occur in olivine and clinopyroxene phenocrysts in lavas recovered from near-axis seamounts on either side of the ValuFa ridge, Lau Basin (Kamenetsky et al., 1997). These melt inclusions are very similar to high-CaO boninites or primitive ankaramites (Kamenetsky et al., 1997).

These examples indicate that depleted lavas similar to high-Ca boninites and primitive ankaramites are associated with propagating spreading centers in supra-subduction environments. Furthermore, high degrees of fractionation is likely to occur in a closed magma system at a propagating ridge tip (Christie and Sinton, 1981; Sinton et al. (1983) perhaps explaining the large volume of intermediate to silicic rocks in the Wild Rogue Wilderness ophiolite. The presence of both silicic rocks and boninitic components supports the idea that the Wild Rogue Wilderness ophiolite formed in a suprasubduction zone setting in which propagating spreading centers represented an essential mode of extension and marginal basin formation.

6.4.3 Discussion

The influence of tectonic processes on magma composition as inferred from the detailed study of the Lau Basin can be summarized as follows: (1) Fore-arc rifting was accompanied by MORB-like magmatism (site 834, figures 6.11 and 6.12), probably because Pacific-MORB mantle was drawn into the melting zone beneath the arc during fore-arc rifting (Hergt and Farley; 1994). (2) Continued crustal extension caused the Tonga ridge to move further away from the trench, and numerous arc-composition volcanoes erupting lavas of variable composition formed on the structurally extended older arc-crust (e.g. sites 835, 837, 838 and 839, figures 6.10c). The largest compositional heterogeneity is observed during this stage ranging between compositions similar to lavas from the Tonga-Kermadec arc and older Site 834 lavas (figure 6.11 and 6.12). (3) The southward propagating Eastern Lau spreading center formed and

seafloor spreading replaced fore-arc rifting (figures 6.9 and 6.10d). Currently, the ValuFa ridge propagates into the arc crust of the Tofua arc (figure 6.9). Magmatism at this site is highly diverse (figures 6.11 and 6.12). Valu Fa ridge lavas are predominantly andesitic in composition, and they are intermediate in composition between lavas erupting at the volcanic front and N-MORB. However, the melt inclusion composition of magmas erupted at near-axis seamounts on either side of the ValuFa ridge have boninitic affinities (depleted, residual arc mantle became entrained into the upwelling MORB-source mantle beneath the Valu Fa ridge). (4) Finally, a second southward propagating spreading ridge formed, the CLSC. The formation of a second southward-propagating spreading center (CLSC) probably introduced more magmatic diversity in the back-arc basin. Apparently, the ILSC erupts magmas that formed by melting of a depleted mantle source. The mantle depletion can be explained with previous melting and melt extraction at the ELSC.

Parson et al. (1990) suggested that the processes of arcward ridge migration, ridge propagation, and basinward arc migration is a common feature of the evolution of back-arc system. As shown in this chapter, the magmatism in a suprasubduction zone setting is closely interlinked with these processes, and, as a result, the marginal basin crust is compositionally heterogeneous. Basically, the Lau Basin consists of a compositionally heterogeneous marginal basin/island arc crust that reflects its complex tectonic evolution. Note that a change of the magma types with time does not follow a predictable pattern such as the model of Shervais et al. (in review) would predict. Based on the synthesis of the tectonic and magmatic evolution of the Lau Basin it is recognized that the composition of the magmas is fundamentally controlled by two factors: (1) the composition of the mantle prior to rifting (i.e., inherited mantle), and (2) the composition of the mantle that is drawn into the rift zone due to extension (i.e., mantle “invasion”).

Using the Lau Basin as an analogue, the large magmatic diversity of rocks from the Wild Rogue Wilderness ophiolite as well as from the entire CRO (figures 6.3, 6.4 and 6.5) and Josephine ophiolite, can be interpreted as indication of formation in a suprasubduction zone setting in which processes of fore-arc rifting, arcward ridge migration, ridge propagation, and basinward arc migration may have played an important role. Additionally, the mantle source of the Coast Range ophiolite could have been highly

heterogeneous prior to initiation of fore-arc or intra-arc rifting (inherited mantle sources). This could result in obscuring the effects on magma composition due to tectonic processes such as rift propagation.

The Josephine ophiolite has a similar range of magmatic affinities as the Coast Range ophiolite (section 6.3). This is consistent with the interpretation that the CRO and the Josephine ophiolite could have formed in the same arc-marginal basin system (section 6.2). However, the Josephine ophiolite does not contain calc-alkaline rocks reflecting perhaps the Josephine ophiolite formed at a greater distance to the active volcanic front (i.e., back-arc basin) than the Coast Range ophiolite (i.e., fore-arc or intra-arc basin) such as depicted in model 3 (figure 1.6, chapter 1) (e.g., Saleeby and Harper, 1993). Furthermore, Harper (in review) suggested that the Fe-Ti lavas in the upper pillows of the Josephine ophiolite (figure 6.7) could have formed by propagation of a back-arc spreading center into island arc crust. It is possible that several propagating spreading centers were active, but at different distances to the volcanic front similar to the modern Lau Basin (figure 6.9). Indication for rift propagation from the Josephine ophiolite and the Wild Rogue Wilderness ophiolite supports the idea that rift propagation could have played an important role in the tectonic and magmatic evolution of both belts of Jurassic ophiolites in California and Oregon.

Furthermore, the Lau basin, which formed by fore-arc rifting over an existing subduction zone (Parson and Wright, 1996), is thought to be an appropriate modern analogue for the CRO, because (1) a tectonic model for the CRO similar to that of the Tonga-Lau arc/back-arc basin system is consistent with the radiometric age data indicating arc-activity in the Sierran-Klamath arc in Mid-Jurassic time (e.g., Chen, 1992; Wright and Fahan, 1988); (2) the Lau Basin crust is heterogeneous similar to the CRO which comprises extrusive and intrusive hypabyssal rocks having a large range of magmatic affinities including MORB, IAT, CAB and boninites (section 6.3). Thus, the evolution of the Tonga-Lau arc/back-arc basin system represents a more appropriate modern analogue for the CRO than the Eocene Izu-Bonin-Mariana arc.

CHAPTER SEVEN

SUMMARY

- The geological map of the Wild Rogue Wilderness is shown in figure 7.1 (see also plate 1), and a cross section is shown in figure 7.2. The basement units in this area strike NE, are subvertical and fault bounded. The tectonostratigraphy, from east to west, include: (1) a sheeted dike complex having gabbro and “plagiogranite” screens; (2) a ductily, but heterogeneously deformed metatonalite unit containing abundant mylonites, mapped by previous workers as foliated “silicic tuff”; (3) a heterogeneously deformed metagabbro having a relic magmatic foliation overprinted by solid-state deformation at amphibolite facies and lower grade conditions; (4) a 0.5 - 0.9 km wide, high-strain zone consisting of mafic and silicic ultramylonites and mylonites (Blossom Bar shear zone); (5) undeformed pillow basalts cut by mafic and silicic dikes; (6) quartz gabbro to tonalite best exposed around Half Moon Bar (Half Moon Bar diorite), (7) poorly exposed metavolcanic rocks, including at least some volcanoclastics and radiolarian-bearing mudstones (tuffaceous? cherts) in the uppermost section of this unit (Mule Mountain Volcanics).
- The sheeted dike complex is dated at 163 ± 1 Ma (zircon U/Pb), the metatonalite unit at 163 ± 4 Ma (zircon U/Pb), the metagabbro unit at 171.4 ± 3.1 Ma (hornblende $^{40}\text{Ar}/^{39}\text{Ar}$ cooling age), and the Half Moon Bar diorite at 157-160 Ma (zircon U/Pb: 160 ± 1 Ma and 158 ± 1.5 Ma; hornblende K/Ar: 159 ± 3 Ma; hornblende $^{40}\text{Ar}/^{39}\text{Ar}$: 157.2 ± 2.0 Ma). A dacitic samples from the upper most section of the Mule Mountain volcanics is dated at 152.9 ± 1.8 Ma (hornblende $^{40}\text{Ar}/^{39}\text{Ar}$), and two deformed muscovite-garnet tonalite dikes in the metagabbro unit are dated at 147.99 ± 0.32 Ma and 148.52 ± 0.17 Ma (muscovite $^{40}\text{Ar}/^{39}\text{Ar}$ cooling ages) (chapter 2).
- The ophiolite and overlying sedimentary rocks occur on the east limb of a large Cretaceous syncline within a folded thrust sheet (chapter 4). It is suggested that the units can be restored to paleohorizontal by correcting for Cretaceous and Tertiary folding (rotation axis R = 045/00, ~90 clockwise rotation). The tectonostratigraphy from base to top after correcting for folding is as follows: Franciscan complex, sheeted dike complex, metatonalite unit, metagabbro unit Blossom Bar shear zone, Mule Mountain volcanics, and Myrtle Group. The terrane boundary occurs between the rocks of the Franciscan complex and the sheeted dike complex (figure 7.1).
- The sheeted dike complex, the metatonalite unit, metagabbro unit and Blossom Bar shear zone have undergone extensive retrogressive greenschist facies metamorphism, including local cataclasis, and are cut by numerous veins and mineralized faults containing epidote, prehnite, pumpellyite, quartz, and sulfides (chapter 2). The presence of epidote in faults and veins indicate $T \geq 200^\circ\text{C}$. Much of the

retrogressive greenschist facies metamorphism in the sheeted dike complex is interpreted to have occurred during subseafloor hydrothermal alteration near the ridge axis. However, at least three episodes of deformation and hydrothermal alteration have been identified in Wild Rogue Wilderness. These are outlined below (chapter 4):

- (1) Possible pre-ophiolite deformation and metamorphism: The oldest deformational phase is recognized in the metagabbro unit. Pillowed and attenuated mafic dikes intruding the gabbro occur subparallel to the mineral foliation. These structures are interpreted to have formed by intrusion of mafic magma in a deforming, partially crystallized gabbro (i.e., magmatic flow) (chapter 2 and 4). The magmatic texture and flow foliation are overprinted, but not completely erased by inferred amphibolite facies metamorphism. Equilibrium temperatures of hornblende-plagioclase pairs in three metagabbro samples range between $635 \pm 38\text{C}$ (assuming 2 kbar) and $670 \pm 28\text{C}$ (assuming 8 kbar) using the improved hornblende-plagioclase geothermometer of Holland and Blundy (1994) (chapter 3). The cooling age of 171.4 ± 3.1 Ma (cooling below 500C) is interpreted to mark the end of amphibolite-facies metamorphism. Similar, Mid-Jurassic cooling-ages (169-173 Ma) are reported by Hacker et al. (1995), and Wright and Fahan (1988) in the Klamath Mountains province and constrain the age of Middle Jurassic regional deformation and metamorphism in this area (Siskiyou event of Coleman et al., 1988).
- (2) Formation of the ophiolite, related deformation and hydrothermal alteration: The second phase of deformation is characterized by the formation of the metatonalite unit, sheeted dike complex, and the pillow unit marking an episode of construction of new oceanic crust by magmatic processes (e.g., intrusion of the sheeted dikes). This phase was also characterized by tectonic extension and subseafloor hydrothermal alteration near the spreading axis (brittle fragmentation, faulting, and pervasive lower amphibolite to greenschist grade and lower hydrothermal alteration; see chapters 2 and 4). Crosscutting relationships and paleostress analysis of amphibole shear bands in screens of cumulate gabbro suggest normal faulting followed closely upon the crystallization of the cumulate gabbro in the sheeted dike complex. This episode of normal faulting was essentially synchronous with the intrusion of dikes, and spreading and early normal faulting are interpreted to have occurred in SW-NE (present orientation) direction. The deformation of the ophiolite after the intrusion of most of the dikes could have involved large-magnitude tectonic extension associated with differential rotation of rigid fault blocks around a subvertical axis (rotation axis re-orientated to paleohorizontal). Fault-block rotation could explain the progressive change of the strike of the steeply dipping sheeted dikes as depicted in figure 7.1. Furthermore, the paleostress analysis of cemented faults in the sheeted dike complex indicates that the stress field changed after the intrusion of most of the dikes. The change of the stress field could be related to the formation of the ophiolite in or near a ridge discontinuity such as a propagating spreading center or ridge-transform intersection (chapter 4).

- (3) Post-ophiolite arc-related magmatism: Arc-related magmatism and associated hydrothermal alteration followed the formation of the ophiolite exposed in the Wild Rogue Wilderness. The intrusion of the 158-160 Ma calc-alkaline Half Moon Bar diorite into the pillow unit and the formation of the upper most section of the Mule Mountain volcanics (152.9 ± 1.8 Ma calc-alkaline dacite) mark the arc-related intrusive, extrusive and hydrothermal phase. Faulting and greenschist grade and lower hydrothermal alteration is much less intense in the Half Moon Bar diorite compared to that of the sheeted dike complex (chapter 2). The dated dacite sample was taken from the uppermost section of the Mule Mountain volcanics which consists mainly of volcanoclastic sandstone and breccia, dacitic extrusive and shallow intrusive rocks and minor thinly laminated, tuffaceous mudstone and chert. The presence of young intrusive and extrusive calc-alkaline rocks and associated volcanoclastics implies an extended magmatic history related to a nearby active volcanic arc, similar to several of the southern remnants of the Coast Range ophiolite, California (e.g., Llanada, Del Puerto).
- (4) Post-ophiolite deformation: This episode is characterized by the formation of the Blossom Bar shear zone, mylonite zones and penetrative foliation in the metatonalite unit, and localized shear foliation in the metagabbro unit, especially in quartz-rich rocks. The Blossom Bar shear zone represents a major ductile-brittle, greenschist facies shear zone with a width of ~900 m (chapters 2 and 4). The subparallel mylonitic zones in the metagabbro unit and metatonalite unit total about 150 m. With an estimated average shear strain ratio of 1:10, a transport distance of about 10 km is obtained. Microstructural data and metamorphic mineral assemblages indicate that temperatures of ductile deformation ranged between 300C to 500C in these three units. Mylonites and ultramylonites in the metatonalite unit, metagabbro unit and Blossom Bar shear zone developed within epidosite zones (epidote+quartz rocks indicate T300C) suggesting that extensive subseafloor hydrothermal alteration preceded or was contemporaneous with ductile deformation. Ductile deformation is inferred to have ended around 149 Ma (muscovite $^{40}\text{Ar}/^{39}\text{Ar}$ ages indicate time of cooling below ~350-400C, depending on cooling rate), and thus coincides with the Nevadan orogeny. After correcting for Cretaceous and Tertiary folding, the shear zone is subhorizontal with sense of shear indicating top (Mule Mountain volcanics) to the NW thrusting (see tectonostratigraphy after correction for Cretaceous and Tertiary folding, chapter 4).
- The origin of the metagabbro unit is controversial: it could be a plutonic unit that belongs to the ophiolite consisting of the metatonalite unit, sheeted dike complex and pillow unit. Alternatively, the metagabbro unit could be correlative with older basement terrane occurring in the rift facies of the Josephine ophiolite, western Klamath Mountain terrane.

Arguments for an ophiolite-related origin include: (1) the metagabbro unit occurs beneath the metatonalite unit and a coherent, mid-crustal rock sequence is present consisting of the sheeted dike complex, metatonalite unit, and metagabbro unit (see figure 7.2); (2) the geochemistry of the

metagabbro unit is broadly similar to other ophiolitic units indicating a suprasubduction zone origin (chapter 5); (3) if the metagabbro unit is related to the ophiolite, it is slightly younger, because it is not intruded by diabasic dikes similar to the sheeted dike complex (chapter 2). Also, the lack of sheeted dike diabases in the metagabbro unit is inconsistent with the hypothesis the metagabbro represents rift facies within the Wild Rogue Wilderness remnant of the CRO.

Arguments against an ophiolite-related origin include: (1) The $^{40}\text{Ar}/^{39}\text{Ar}$ cooling age of 171.4 ± 3.1 Ma does not overlap with the zircon age of the metatonalite unit (164 ± 1 Ma) and the sheeted dike complex (163 ± 1 Ma); (2) the geochemistry of the metagabbro unit differs in important aspects from that of the ophiolitic units (chapter 5). Samples from the metagabbro unit have convex-up REE patterns centered on Nd. Also, the samples do not plot within the fields for any of the other units on the Hf/3-Th-Ta, Th/Yb vs. Ta/Yb and Zr/Y vs. Y tectonic discrimination diagrams. This implies that the metagabbro unit cannot be related to any of the other units in the Wild Rogue Wilderness; that is, the metagabbro unit is derived from a distinctly different mantle source. (3) The uniform dark-green color of the hornblende in the metagabbro unit is uncharacteristic for ophiolitic and oceanic gabbros that were altered during seafloor hydrothermal metamorphism. The uniform dark-green color of the hornblende is typical for regionally metamorphosed rocks. This petrographic evidence as well as the results from geothermometry (chapter 3) suggest the hornblendes may have re-equilibrated during regional amphibolite facies metamorphism.

- The major and trace-element analyses by XRF and ICP-MS, respectively of samples from the Wild Rogue Wilderness, SW Oregon, indicate that the ophiolitic basement is compositionally heterogeneous. The different magma types identified in each unit are summarized below (see figure 7.2):
 - (1) The cumulate gabbro screens in the sheeted dike complex have island-arc tholeiite magmatic affinities. Dikes intruding cumulate gabbro include diabasic dikes having magmatic affinities to island-arc tholeiite and N-MORB (defined as geochemical group 1), and microdioritic and diabasic dikes which have magmatic affinities to calc-alkaline basalt (defined as geochemical group 2). Several dikes of geochemical group 2 contain Cr-spinel within olivine xenocrysts. The Cr/(Cr+Al) ratios of spinels are typical of high-Ca boninites, implying boninitic magmas were present and mixed with calc-alkaline magmas. Trace element modeling shows that mixing MORB and IAT end members results in transitional compositions occurring in the sheeted dike complex. Also, a strongly LREE-enriched calc-alkaline magma (i.e., group 2 sheeted dike or deformed dike in metatonalite unit) could have mixed with LREE-depleted IAT in crustal magma chambers. This could explain the large range of La/Yb and Th/Yb ratios observed in the calc-alkaline dikes (and perhaps in the metatonalite unit).
 - (2) The metatonalite unit consists of calc-alkaline plutonic rocks of tonalitic to trondhjemitic composition. A dioritic enclave and a deformed dike in the metatonalite unit are very similar in

- trace element composition to dikes of geochemical group 2 (calc-alkaline) in the sheeted dike complex. The large range of La/Yb ratios determined in samples from the metatonalite unit could be related to allanite fractionation, because of the strong inverse correlation between La/Yb ratios and SiO₂. Alternatively, the variations of a number of trace element ratios could be related to mixing of magmas derived from a heterogeneous source (mixing IAT and CAB) or contamination.
- (3) Samples from the metagabbro unit are similar to island-arc tholeiite, but they are distinct from all other units in that they have a pronounced convex-up REE pattern centered on Nd, and are significantly more depleted in Ta, Nb, Zr and Hf than samples from the other units (“depleted” IAT). A small intrusion of hornblende quartz diorite has a trace element composition transitional between that of the metagabbro and IAT-dikes from the sheeted dike complex suggesting an IAT magma intruded the metagabbro and assimilated wall rock or magma mixing occurred.
 - (4) The pillow unit consists of pillowed, submarine volcanic flows cut by diabasic and silicic dikes. Pillows and dikes have magmatic affinities to IAT. The samples from the pillow unit have in general lower Ta/Yb and Ta/Hf ratios than IAT-dikes in the sheeted dike complex implying the pillow unit was derived from a more depleted mantle source. Variations of incompatible trace element ratios in samples from the pillow unit can be explained with variable degrees of partial (dynamic?) melting and/or magma mixing. A pillow contains Cr-spinel xenocrysts and Cr-spinel within a clinopyroxene phenocryst. The Cr/(Cr+Al) ratios of the spinels within cpx and the matrix differ which is suggestive of magma mixing. Also, the Cr/(Cr+Al) ratios of the spinels are typical of high-Ca boninites, implying boninitic magmas were present and mixed with IAT magmas.
 - (5) The Mule Mountain volcanics consist largely of island arc tholeiites, but boninitic and calc-alkaline rocks occur as well in the uppermost section of the Mule Mountain volcanics. Samples having IAT magmatic affinities range in composition from basalt to dacite. Some of the basaltic, andesitic and dacitic samples have parallel chondrite and N-MORB normalized REE and trace element patterns suggesting they are related by crystal fractionation. Also, the IAT samples from the Mule Mountain volcanics plot in the field for the pillow unit in the Hf/3-Th-Ta and Th/Yb vs. Ta/Yb tectonic discrimination diagrams. Additionally, other incompatible trace element ratios are very similar suggesting the pillow unit and the lower part of the Mule Mountain volcanics could be related which is consistent with the age constraints (the pillow unit is intruded by and in fault contact with the 157-160 Ma Half Moon Bar diorite, and a sample from the uppermost section of the Mule Mountain volcanics is dated at 152.9 ± 1.8 Ma). A sample having IAT magmatic affinities from the lower section of the Mule Mountain volcanics contains Cr-spinel within cpx- and olivine-phenocrysts and in the matrix. The various Cr-spinels have a large range of Cr/(Cr+Al) ratios and are similar in composition to Cr-spinel in IAT and high-Ca boninites, implying boninitic magmas were present and mixed with IAT magmas. The dated dacitic sample

(153 Ma) from the uppermost section of the Mule Mountain volcanics has calc-alkaline magmatic affinity.

- (6) The Half Moon Bar diorite is a 157-160 Ma calc-alkaline pluton cut by porphyritic calc-alkaline dikes. The samples from this unit have parallel Chondrite and N-MORB normalized REE and trace element patterns suggesting they are related by crystal fractionation.
 - (7) The deformed muscovite garnet tonalite dikes in the metagabbro unit plot in the Hf/3-Th-Ta ternary diagram in the calc-alkaline field and are peraluminous in composition. For further interpretation, the age and origin of the muscovite garnet tonalite dikes must be constrained by determining the igneous age using zircon U/Pb dating and analyzing the dikes for Sr-, Nd-, and O-isotopes, respectively. For example, late-stage granitoids (peraluminous in composition) are associated with Mid-Jurassic volcanic arc plutons in the Klamath Mountains province. Sr-, Nd-, and O-isotopic data suggest these peraluminous granitoids could have formed by melting of a metagraywacke-like source (Barnes et al., 1990).
- The dikes of geochemical group 2 from the sheeted dike complex plot in the field for continental arcs in the Zr/Y vs Zr diagram of Pearce (1983) (chapter 5). The elevated Zr/Y ratios of the dikes of geochemical group 2 suggest an enriched mantle source having geochemical characteristics of subcontinental lithosphere (Pearce, 1983).
 - Overall, the compositional variations within units and between units cannot be explained with differences in the degree of partial melting and/or fractionation. A highly heterogeneous mantle source is inferred, which probably was variably depleted by previous melting and variably re-enriched with a subduction component (chapter 5).
 - The comparison of the tectonostratigraphy of the Wild Rogue Wilderness ophiolite with two belts of mid Late-Jurassic ophiolites in California and SW Oregon (i.e., CRO comprises the western belt and Josephine ophiolite and Smartville complex the eastern belt) shows that the Wild Rogue Wilderness ophiolite has a structural and stratigraphical evolution which is similar in part to that of the Josephine ophiolite and in part to that of the Coast Range ophiolite in California. The Wild Rogue Wilderness ophiolite may be the 'missing link' between these two belts of ophiolites, which, if present in California, is now buried beneath the sedimentary rocks of the Great Valley sequence. Based on this correlation, I conclude that the Coast Range ophiolite probably formed in the same arc-system as the Josephine ophiolite (chapter 6).
 - The comparison of the geochemical data compiled from several Coast Range ophiolite remnants in California (Point Sal, Llanada, Black Mountain, and Stonyford) and in Oregon (Snow Camp Mountain) shows that the range of magmatic affinities for the Wild Rogue Wilderness ophiolite (MORB, IAT, CAB and BON) overlaps that for the other CRO remnants in California (MORB, IAT, CAB, BON, OIB) and Oregon (MORB, IAT, BON) (chapter 6). Interestingly, the range of magmatic affinities for one of the CRO remnants closest to the Josephine ophiolite (i.e., Snow Camp Mountain,

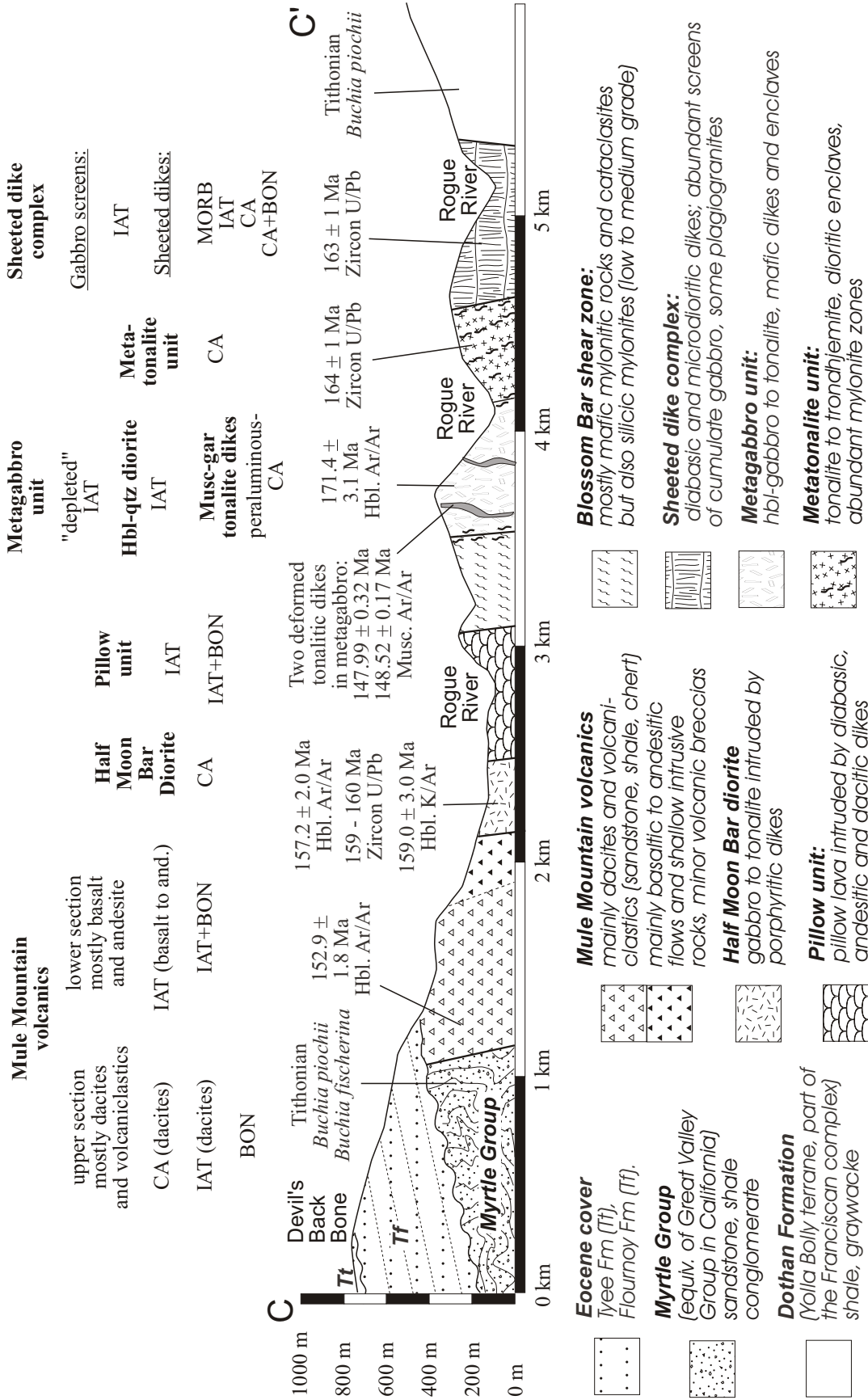


Figure 7.2: Cross section showing the units of the Wild Rogue Wilderness, sample ages and magmatic affinities.

- SW Oregon) overlaps that for the Josephine ophiolite (MORB, IAT and BON), suggesting the CRO and Josephine ophiolite could be related (i.e. they formed in the same suprasubduction zone setting).
- The Lau Basin crust consists of petrogenetically diverse rocks having a similar range of magmatic affinities (MORB, IAT, CAB, BON, and OIB-like rocks in the northern Lau Basin) as the Coast Range ophiolite and Josephine ophiolite. It seems that a large petrogenetic diversity, such as that of the Lau Basin and the Coast Range ophiolite, could be a characteristic feature of marginal basins that formed by fore-arc or intra-arc rifting.
 - Using the Lau Basin as a modern analogue, the large magmatic diversity of rocks from the Wild Rogue Wilderness ophiolite and perhaps from the entire CRO and Josephine ophiolite, can be interpreted as indication of formation in a suprasubduction zone setting in which processes of fore-arc rifting, arcward ridge migration, ridge propagation, and basinward arc migration may have played an important role. Additionally, the mantle source of the Coast Range ophiolite could have been highly heterogeneous prior to initiation of postulated fore-arc or intra-arc rifting (i.e., inherited mantle sources). Note that the paleostress analysis of cemented faults in the sheeted dike complex are consistent with a change of the stress field possibly related to a ridge discontinuity such as a propagating rift (chapter 4).

To summarize, the data collected for this study enabled to propose a correlation between the Coast Range ophiolite and the Josephine ophiolite (chapter 6). Thus, these data are consistent with previously proposed models for the tectonic evolution of the Coast Range ophiolite that invoke for both, the Josephine and the Coast Range ophiolite, rifting of the volcanic arc built on western North America (models 3 and 4, chapter 1). Additionally, the large petrogenetic diversity of rocks from the Rogue Wilderness ophiolite is suggestive of formation in a fore-arc or intra-arc setting similar to that of the Miocene Tonga arc, SW Pacific. Rift-propagation and melting of heterogeneous, inherited mantle may have played an important role in the magmatic evolution of the Coast Range ophiolite.

APPENDIX A

**PETROGRAPHIC SUMMARY OF SAMPLES FROM THE WILD ROGUE
WILDERNESS, SW OREGON**

Table A1a: Petrographic summary of representative samples from the metagabbro unit

| Sample-ID | Rock Type | A | Igneous (mode): | Mineralogy | Metamorphic: | % Alt. | Texture | Grain size | Veins oldest → youngest |
|------------|-------------------------------------------------|---|------------------------------------------------------|-----------------------------------------------------------|--------------|--------|----------------------------------------------------------|------------|----------------------------|
| GH-97-19A | foliated hbl qz metagabbro | - | pl(48, An ₇₂), hbl(41), qz(8), ox(2), ap | pl ^z → cz, ab, ep; hbl* → ep, ch, | | 30% | hypidomorphic granular, weak tectonic foliation | 2.5 mm | ep+qzch |
| MRH-23.1 | foliated hbl metagabbro (dike) | + | pl(42, An ₈₂), hbl(55), ox(3), ap | pl ^z → cz, ab, ep, mu; hbl → ep, ch, | | 40% | hypidomorphic granular, igneous foliation/lineation | 1.5 mm | ep+qzch |
| MRH-23.2 | foliated leuko hbl metagabbro (schlieren layer) | - | pl(70), hbl (25), ox(5), qz, ap | pl ^z → cz, ab, ep, mu; hbl → ep, ch, | | 80% | hypidomorphic granular, igneous foliation/lineation | 1.5 mm | ep+qzch |
| MRH-78.1 | foliated hbl metagabbro (enclave) | + | pl(45, An ₇₈₋₈₉), hbl(49), ox(6), ap | pl ^z → cz, ab, ep, mu; hbl → ep, ch, pu | other: | 30% | hypidomorphic granular, igneous foliation/lineation | 1.8 mm | |
| MRH-78.2 | foliated hbl metagabbro | + | pl(53, An ₇₆), hbl(40), ox(5), qz(2), ap | pl ^z → cz, ab, ep, mu; hbl → ep, ch, pu | other: | 40% | hypidomorphic granular, igneous foliation/lineation | 3 mm | ep, pr (probe data) |
| O/C-373A | foliated hbl metagabbro (dike 1) | + | pl(39, An ₈₁₋₁₆), hbl(57), ox(4), ap | pl ^z → cz, ab, ep, ±mu, ch, ±ser; hbl → ep, ch | | 20% | hypidomorphic granular, igneous foliation/lineation | 0.75 mm | sb (cz, ep, ch), ab |
| O/C-373A.1 | foliated hbl metagabbro (dike 2) | - | pl(47, An ₈₁₋₆₃), hbl(49), ox(4), ap | pl ^z → cz, ab, ep, ±mu, hbl → ep, ch, pu | other: | 30% | hypidomorphic granular, weak igneous foliation/lineation | 1 mm | sb (cz, ep, ch), ab |
| O/C-373B | foliated hbl metagabbro | + | pl(54, An ₈₁₋₅₉), hbl(45), ox(<1), ap | pl ^z cz, ab, ep, ±ch; ac, ep, ch, | | 55% | hypidomorphic granular, igneous foliation/lineation | 3 mm | ab |
| O/C-373C | foliated hbl metagabbro | - | pl(48), hbl(50), ox(2), ap, ti | pl → cz, ab, ep, ch, ±mu; hbl → ac, ch ±ep; other: pr | | 48% | hypidomorphic granular, igneous foliation/lineation | 3.5 mm | ab+cz |

Table: A1a: Petrographic summary of representative samples from the metagabbro unit (continued)

| Sample-ID | Rock Type | A | Igneous (mode): | Mineralogy | Metamorphic: | % Alt. | Texture | Grain size | Veins oldest → youngest |
|-------------|------------------------------------------------|---|--------------------------------------------------------------------------------|-----------------------------------------------------|---------------|--------|------------------------------------------------------------------------|------------|---------------------------|
| O/C-374B.1 | foliated hbl metagabbro | - | pl(63), hbl(36), ox(1), ap | pl → cz, ab, ep, ch; → ch, ep ± ac | hbl | 63% | hypidiomorphic granular, isotropic | 4 mm | epqz |
| O/C-374B.2 | foliated hbl metagabbro (dike 1) | + | pl(40, An ₈₂), hbl(55), ox(5), ap | pl ^z → cz, ab, ep; → ch, ep ± ac; pr | hbl other: | 10% | hypidiomorphic granular, strong igneous foliation ^t | 0.25 mm | sb (cz, ep, ch), ep+qz+ch |
| O/C-374B.3 | layered hbl metagabbro with schlieren layering | - | pl(45, An ₈₃), hbl(51), ox(4), ap | pl → cz, ab, ep, ch ± mu; hbl → ch, ep ± ac; | | 30% | hypidiomorphic granular, igneous schlieren-type foliation ^t | 2 mm | sb (cz, ep, ch), ep+qz+ch |
| O/C-374B.4 | foliated hbl metagabbro (dike or enclave) | - | pl(55), qz ^t (4), hbl(40), ox(<1), ap | pl → ep, ab, ch, ± cz; hbl → ep, ch, ac | | 60% | S/C-type foliation | 1 mm | ep+qz+ch |
| O/C-385.1 | foliated hbl metagabbro | - | pl(47, An ₆₉), qz(8), hbl(39), ox(5), bio(1), ap | pl → cz, ab, ep, ± ch, ± mu; hbl → ch, ep ± ac ± mt | | 40% | hypidiomorphic granular, weak igneous foliation ^t | 3 mm | ep |
| O/C-385.2 | foliated hbl metagabbro (enclave) | - | pl(41), hbl(53), bio(2), ox(4) | pl → cz, ab, ep → ch, ep ± ac | hbl | 35% | hypidiomorphic granular, igneous foliation ^t | 0.8 mm | ep |
| GH-97-15a | foliated hbl qz metagabbro | - | pl(33, An ₆₈₋₄₈), qz ^t (15), hbl(50), bio(1), ox(1), ap | pl ^z → cz, ab, ± ch; hbl → ch, ac | | 25% | relic igneous and strong tectonic foliation | 1 mm | |
| GH-97-16b.1 | metatonalite (host rock of GH-97-16b.2) | - | pl(54, An ₅₈), qz ^t (40), hbl(4), ox(2) | pl → cz, ab, ± ch; hbl → ch, ac | | 50% | strong tectonic foliation, strongly recrystallized qz | 3 mm | |
| GH-97-16b.2 | metadiorite (enclave in GH-97-16b.1) | - | pl(46, An ₄₇), qz ^t (8), hbl(38), ox(8), ap | pl → cz, ab, ep; hbl → ac, ± ch, other: ep | | 15% | xenomorphic granular | 0.3 mm | - |

Table A1b: Petrographic summary of representative samples from the hornblende quartz diorite in the metagabbro unit

| Sample-ID | Rock Type | A | Mineralogy | | % Alt. | Texture | G | Veins oldest → youngest |
|-----------|------------------------------------------------|---|------------------------------------------------------------------|--------------------------------------------------------|--------|-------------------------------------------------|--------|----------------------------|
| | | | Igneous (mode): | Metamorphic: | | | | |
| GH-97-14 | foliated hbl qz metadiorite | + | pl(45, An ⁶⁸⁻⁵⁸), hbl(49), qz(6), ox(<1), bio, ap | pl ^Z → cz, ab, ep, ch; hbl → ac, ep, ch; | 40% | hypidomorphic granular, weak tectonic foliation | 2 mm | ep+qz |
| SC-3 | foliated hbl qz metadiorite | - | pl(46, An ⁶⁸⁻³⁸), hbl(37), qz(14), ox(2), bio(1), ap | pl ^Z → cz, ab, ep; hbl → ep, ch, | 35% | hypidomorphic granular, weak tectonic foliation | 2.5 mm | ep+qzch |
| O/C-229.1 | foliated hbl qz metadiorite | - | pl(58, An ⁶⁸⁻⁴²), hbl(30), qz(6), ox(6), ap | pl ^Z → cz, ab, ep, ±mu, hbl → ep, ch | 50% | hypidomorphic granular, weak tectonic foliation | 2 mm | sb (cz, ep, ch, qz) |
| O/C-229.2 | foliated hbl qz metadiorite (enclave in 229.1) | - | pl(50, An ⁶⁸), hbl(40), qz(6), ox(4), ap | pl → cz, ab, ep, ±mu, hbl → ep, ch | 50% | hypidomorphic granular, weak tectonic foliation | 0.5 mm | |

Table A2: Petrographic summary of representative samples from the metatonalite unit

| Sample-ID | Rock Type | A | Igneous (mode): | Mineralogy | Metamorphic: | % Alt. | Ign. Texture | Grain size | Veins oldest → youngest |
|-------------|----------------------------------------------|---|--------------------------------------------|----------------------------------------------|--------------|--------|--------------------------------------------------|------------|----------------------------|
| GH-97-2b | mylonite (protolith is trondhjemite) | + | pl(~50), qz'(~45), hbl? Or cpx? (~5), ox<1 | pl → cz, ab, ep, ch; or cpx ep, ch, ac | | 55% | primary texture not preserved (mylonite) | 0.1 mm | qz+ep, pr |
| GH-97-3 | meta-trondhjemite | + | pl(55), qz'(39), cpx*(5), ox(<1), ti, ap | pl → cz, ab, ep, ch; cpx → ac ±mg, other: pr | | 55% | hypidiomorphic granular | 1.2 mm | qz |
| O/C-11S-16a | foliated meta-tonalite | + | pl(61), qz'(28), hbl*(10), ox(1), ap, ti | pl → cz, ab, ep, ch; → ac, ch ±ep | | 70% | primary texture not preserved (foliated) | 1.0 mm | qtz+ep |
| O/C-11S16b | foliated meta-quartz diorite ("pillow dike") | + | pl(50), qz'(12), hbl*(35), ox(3), ap | pl → cz, ab, ep, ch; → ac, ch ±ep; oxti | | 80% | primary texture not preserved (foliated) | 0.5 mm | qtz+ep |
| O/C-62 | metatonalite | - | pl(63), qz(20), hbl*(14), ox(3), ap, ti | pl → cz, ab, ep, ch ±mu; hbl → ac, ch, ep; | | 65% | granophyric | 1.8 mm | |
| O/C-250 | metatonalite | - | pl(57), qz(25), hbl*(15), ox(3), ap, ti | pl → cz, ab, ep, ch ±mu; hbl → ac, ch, ep; | | 65% | granophyric | 2 mm | |
| O/C-367 | metatonalite | + | pl(45), qz'(40), hbl(14), ox(<1), ap | pl → ep, ab, ch, ±cz; hbl → ep, ch, ac | | 60% | primary texture not preserved, strongly foliated | 2 mm | qtz |
| O/C-368A | metatonalite | - | pl(44), qz(40), hbl*(12), ox(4), ap, ti | pl → cz, ab, ep → ac, ch ±ep ±mg; | | 50% | granophyric | 0.5 mm | |
| O/C-368B | meta quartz-diorite | - | pl(50), qz(13), hbl*(37), ox(4) | pl → cz, ab, ep → ac, ch ±ep; | | 80% | hypidiomorphic granular | 0.5 mm | |

Table A2: Petrographic summary of representative samples from the metatonalite unit (continued)

| Sample-ID | Rock Type | A | Igneous (mode): | Mineralogy | Metamorphic: | % Alt. | Ign. Texture | Grain size | Veins oldest → youngest |
|-----------|-------------------------------|---|-----------------------------------------|----------------------------------------|--------------|---------|----------------------------|------------|----------------------------|
| O/C-368F | meta quartz diorite (enclave) | + | pl(54), qz(18), hbl*(23), ox(5) | pl → cz, ab, ep → ac, ch ± ep; oxti | | hbl 55% | hypidiomorphic granular | 0.3 mm | qz+ep, qz+su |
| O/C-368G | meta-trondhjemite | - | pl(52), qz(39), cpx*(9), ox(<1), ap, ti | pl → cz, ab, ep; → acmg, other: ch | | cpx 68% | granophyric and myrmekitic | 1.3 mm | |
| SC-2 | meta-trondhjemite | - | pl(55), qz(40), cpx*(5), ox(<1), ap, ti | pl → cz, ab, ep; → acmg, other: ch | | cpx 58% | granophyric | 1.0 mm | |

Table A3a: Petrographic summary of representative samples from the sheeted dike complex (gabbroic screens)

| Sample-ID | Rock Type | A (mode): | Mineralogy Metamorphic: | Igneous | % Alt. | Texture | Grain size | Veins oldest → youngest |
|------------|---------------------------------|-----------------------------------|---------------------------------------------------|---------|--------|------------------------------------------------|----------------------|----------------------------|
| GH-97-21 | pl-cpx cumulate gabbro | - pl(49), cpx*(50), ox(1), ol? | Pl → cz+ab, cpx → amphib other: ep, ac, ch, mu | amph | 90% | poikilitic mesocumulate pref. Orient. Of pl | pl.. 2mm cpx ~5mm | - |
| GH-97-22 | pl-cpx cumulate gabbro | - pl(55), cpx(45), ox(<1) | pl → cz+ab, cpx → amphib other: ep, ac, ch | amph | 100% | mesocumulate, weak pref. Orient. Of pl | 2 mm | qz, cc |
| GH-97-23 | pl-cpx cumulate leucogabbro | + pl(87), cpx(12), ox(<1) | pl → cz+ab, cpx → amphib other: ep, ac, ch | amph | 100% | mesocumulate, weak pref. Orient. Of pl | 1 mm | pr+qz |
| GH-97-24 | pl-cpx cumulate gabbro | - pl(58), cpx(41), ox(1) | pl → cz+ab, cpx → amphib other: ep, ac, ch | amph | 99% | adcumulate, weak pref. Orient. Of pl | 1 mm | ep |
| GH-97-25.1 | plagioclasite | + pl(95), cpx(5), ox(<1) | pl → cz+ab, cpx → amphib other: ep, ac, ch | amph | 100% | adcumulate, weak pref. Orient. Of pl | 1.5 mm | - |
| GH-97-25.2 | pl-cpx cumulate gabbro | - pl(58), cpx(41), ox(1) | pl → cz+ab, cpx → amphib other: ep, ac, ch, ti | amph | 99% | mesocumulate, pref. Orient. Of pl | 2 mm | cz, qz |
| GH-97-27 | anorthosite/ plagiogranite? | + pl, qz, ox(<1), zr | pl → cz+ab, cpx → amphib other: ep, ac, ch | amph | 100% | primary texture not preserved (epidosite) | ? | cz, qz |
| MIRH-76 | pl-cpx cumulate leucogabbro | - pl(66), cpx*(33), ox(1) | pl → cz+ab, cpx → amphib other: ep, ac, ch, mu | amph | 95% | adcumulate, strong pref. Orient. Of pl | pl 1.5 mm cpx~4mm | amph, ep |
| O/C-358 | pl-cpx cumulate gabbro | + pl(53), cpx(47), ox(<1) | pl → cz+ab, cpx → amphib other: ep, ac, ch | amph | 100% | poikilitic mesocumulate pref. Orient. Of pl | pl.. 1 mm cpx~4mm | amph, ep |
| O/C-358b | plagioclasite (anorthosite?) | - pl(96), cpx(4), ox(<1) | pl → cz+ab, cpx → amphib other: ep, ac | amph | 100% | adcumulate, weak pref. Orient. Of pl | 0.8 mm | ep |
| O/C-359 | pl-cpx cumulate gabbro | - pl(55), cpx(45), ox(<1) | pl → cz+ab, cpx → amphib other: ep, ac, ch, mu | amph | 100% | poikilitic orthocumulate | pl.. 1mm px~4mm | ep, ab |

Table A3a: Petrographic summary of representative samples from the sheeted dike complex (gabbroic screens) continued

| Sample-ID | Rock Type | A | Mineralogy (mode): | Metamorphic: | Igneous | % Alt. | Texture | Grain size | Veins oldest → youngest |
|-----------|------------------------------|---|-------------------------|-------------------------------------------------|---------|--------|------------------------------------------------|---------------------------------|-------------------------|
| O/C-360 | pl-cpx cumulate gabbro | + | pl(48), cpx(59), ox(1) | pl → cz+ab, cpx → amph other: ep, ac, ch, mu | amph | 99% | poikilitic mesocumulate pref. Orient. Of pl | pl 0.8 mm cpx 3 mm | ep, pr+qz |
| O/C-360.1 | pl-cpx cumulate leuco gabbro | - | pl(73), cpx(27), ox(<1) | pl → cz+ab, cpx → amph other: ep, ac, ch, mu | amph | 100% | adcumulate, weak pref. Orient. Of plag | pl. 0.8 mm mm cpx ~1.5 mm | cz, ab+qz |
| SC-1 | anorthosite | - | pl(95), px(5), ox(<1) | pl → cz+ab, cpx → amph other: ep, ac, ch | amph | 100% | adcumulate, weak pref. Orient. Of pl | 1 mm | pr |

Table A3b: Petrographic summary of representative samples from the sheeted dike complex (diabasic and microdioritic dikes)

| Sample ID | Rock Type | A | Igneous (mode) | Mineralogy | Metamorphic | % Alt. | Texture | grain size | % phenocrysts | size | Veins | |
|------------------------------------------------------------------------|--------------|---|------------------------------------------------|-----------------------------------------------------|-------------|--------|------------------------------|------------|-----------------------------|---------|----------------------|--|
| Three samples from same dike: MRH-45a.1, MRH-45a.3, MRH-45a.3 | | | | | | | | | | | | |
| MRH-45a.1 | Microdiorite | + | pl(44), cpx(50), qz(5), ox(1), sp ¹ | pl → cz+ab, cpx → amph other: ep, ac, ch, qz | | 95% | hyp. Granular to subophitic | 0.15 mm | 2% xenocrysts ² | 0.5 mm | epqz, qz+s, prqz, qz | |
| MRH-45a.2 | Metadiabase | - | pl(44), cpx(53), qz(2), ox(1), sp ¹ | pl → cz+ab, cpx → amph other: ep, ac, ch, qz, ti | | 97% | hyp. Granular to subophitic | 0.25 mm | 5% xenocrysts ² | 1 mm | - | |
| MRH-45a.3 | Metadiabase | - | pl(45), cpx(55), ox(1), ±qz, sp ¹ | pl → cz+ab, cpx → amph other: ep, ac, ch, qz, py | | 100% | subophitic | 0.5 mm | 10% xenocrysts ² | 3 mm | - | |
| MRH-45b | Microdiorite | + | pl(47), cpx(41), qz(12), ±ox | pl → cz+ab, cpx → amph other: ep, ac, ch, qz, ti | | 88% | hypidiomorphitic granular | 0.2 mm | 1% xenocrysts ² | 1 mm | ep, prqz | |
| MRH-111 | Metadiabase | + | pl, px | ac, cz, ep, ab, ch | | 100% | chilled marg. (micro-cryst.) | - | 2% cpx ³ | 0.05 mm | ep+qz, pr | |
| O/C-1-S1 | Metadiabase | + | pl, px, ox(1) | ac, cz, ep, ab, ch, qz | | 99% | 1 cm dike, (micro-cryst.) | - | - | - | ep, pr, qz+py | |
| O/C-1-S2 | Metadiabase | + | pl(45), cpx(51), ox(4), ti | pl → cz+ab, cpx → amph other: ep, ac, ch, qz | | 96% | subophitic | 0.3 mm | - | - | epqz | |
| Three samples taken from same dike: O/C-4-S3.1, O/C-4-S3.2, O/C-4-S3.3 | | | | | | | | | | | | |
| O/C-4-S3.1 | Microdiorite | + | pl(41), cpx(53), qz(4), ox(2), sp ¹ | pl → cz+ab, cpx → amph other: ep, ac, ch, qz, ti | | 94% | hyp. Granular to subophitic | 0.4 mm | 6% xenocrysts ² | 1.5 mm | - | |
| O/C-4-S3.2 | Metadiabase | - | pl(40), cpx(55), qz(3), ox(2), sp ¹ | pl → cz+ab, cpx → amph other: ep, ac, ch, qz | | 95% | hyp. Granular to subophitic | 0.5 mm | 10% xenocrysts ² | 2 mm | - | |
| O/C-4-S3.3 | Metadiabase | - | pl(41), cpx(56), ±qz, ox(2), sp ¹ | pl → cz+ab, cpx → amph other: ep, ac, ch, qz, py | | 95% | ophitic | 0.5 mm | 19% xenocrysts ² | 3 mm | - | |
| O/C-5-S4 | Metadiabase | + | pl(45), cpx(54), ox(1) | pl → cz+ab, cpx → amph other: ep, ac, ch, qz, pu | | 99% | subophitic to ophitic | 0.3 mm | - | - | ep, pr+qz, qz | |

Table A3b: Petrographic summary of representative samples from the sheeted dike complex (diabasic and microdioritic dikes) continued

| Sample ID | Rock Type | A | Igneous (mode) | Mineralogy | Metamorphic | % Alt. | Texture | grain size | phenocrysts % | size | Veins oldest → youngest |
|-----------|------------------------|---|----------------------------------|---------------------------------------------------------------|-------------|--------|--------------------------------|------------|------------------------------------------|---------|-------------------------|
| O/C-6-S5 | Microdiorite | + | pl(47), cpx(42), qz(10), ti(1) | pl ^z cz+ab, cpxamph other: ep, ac, ch | | 89% | hypidiomorphi cgranular | 1 mm | - | - | - |
| O/C-58 | Metadiabase | - | pl(43), cpx(56), ox(1) | pl → cz+ab, cpx → amph other: ep, ac, ch, qz, ti | | 99% | ophitic | 0.3 mm | - | - | ep+qz, ab+qz |
| O/C-325 | Metadiabase (cumulate) | + | pl, cpx, sp ¹ , ox(2) | ac, cz, ep, ab, ch, qz, cc | | 95% | foliated, stretched xeno. | 0.3 mm | 15% xenocrysts | 3 mm | qz+cc |
| O/C-333 | Metadiabase | + | pl(49), cpx(50), ox(<1), ti | pl → cz+ab, cpx → amph other: ep, ac, ch, qz | | 99% | subophitic | 0.4 mm | - | - | ep, pr, ch+qz |
| O/C-356 | Metadiabase | + | pl, cpx, ox(1) | ac, cz, ep, ab, ch, qz | | 99% | 5 cm wide dike (microcrystal.) | - | 2% pl ⁴ , 2% cpx ³ | 0.01 mm | ep+qz, pu+qz |
| O/C-357a | Metadiabase | - | pl, cpx, ox(<1) | ac, cz, ep, ab, ch, qz, ti | | 100% | chilled margin (microcrystal.) | 0.35 mm | 2% pl ⁴ , 4% cpx ³ | - | ep+qz, ch |
| O/C-357b | Metadiabase | + | pl(42), cpx(55), ox(3) | pl ^z → cz+ab, cpx → amph other: ep, ac, ch, qz, sp | | 98% | subophitic to ophitic | 0.3 mm | - | - | ep, pr+qz |
| O/C-357c | Metadiabase | - | pl(43), cpx(55), ox(2) | pl → cz+ab, cpx → amph other: ep, ac, ch, qz, ti | | 95% | subophitic to ophitic | 0.5 mm | - | - | - |
| O/C-362 | Microdiorite | + | pl(45), cpx(40), ox(14), ti (1) | pl → cz+ab, cpx → amph other: ep, ac, ch, qz | | 99% | hypidiomorphi cgranular | 0.2 mm | - | - | pr, cc |
| O/C-362b | Metadiabase | - | pl, cpx, ox(<1) | ac, cz, ep, ab, ch, qz | | 100% | chilled margin (microcrystal.) | - | 2% pl ⁴ | - | pr, cc |

Table A4: Petrographic summary of representative samples from the pillow unit

| Sample ID | Rock Type | A | Igneous (mode) | Mineralogy | Metamorphic | % Alt. | Ign. Texture | grain size | Phenocrysts | size | Veins |
|-----------|--------------------------|---|--------------------------------|--------------------------------------------------------------|-------------|--------|------------------------------|------------|-----------------------|------------|-----------------------------------------|
| O/C-113 | metadiabase (dike) | + | pl(53), cpx(45), ox(1), qz?(1) | pl ep, cz, ab, qz, ±ch; cpxamph ±mg; other: ti, py | | 65% | subophitic | 0.2 | aphyric | - | ep+qz, pr+cc |
| O/C-186 | metadiabase (dike) | + | pl(47), cpx(47), ox(6) | pl cz, ep, ch, ab, ±qz; cpx*amph, ch, mg, ep | | 75% | subophitic | 0.15 | aphyric | - | ep+qz, qz+cc |
| O/C-224A | metabasalt (pillow) | - | pl, cpx, ox(2) gl? | pl ep, cz, ch, ab, ±mu; cpx*amph, ch, ±mg; other: ti, qz, py | | 50% | intergranular (intersertal?) | - | pl: 5.6% cpx: 2.1% | 0.8 1.0 | ep, ep+qz Am: ep, ch, qz, ti |
| O/C-224B | metabasalt (pillow) | + | pl, cpx, ox(2), sp, gl? | pl cz, ep, ab, ch; cpx*amph, ch, ±mg; other: py, qz | | 60% | intergranular (intersertal?) | - | pl: 3.5% cpx: 1.4% | 1.0 1.0 | ep, ep+qz Am: ep, ch, qz, ab |
| O/C-226A | meta-microdiorite (dike) | - | pl(55), cpx(30), qz(10), ox(5) | pl ep, cz, ab, ±ch, ±mu; cpx ch, ±mg; other: qz, py | | 70% | granophyric | 0.5 | aphyric | - | ep, pr+cc |
| O/C-226B | metabasalt (pillow) | - | pl, cpx, ox(2), gl? | pl cz, ep, ab, ±ch; cpx amph, ch, cc, ±mg; other: qz, ep, py | | 80% | intergranular (intersertal?) | - | pl: 24% cpx: 14% | 2.0 1.2 | ep+qz, cc, Am: ch, ep, qz, su |
| O/C-226C | metadiabase (dike) | - | pl(50), qz(8), cpx(35), ox(7) | pl ep, cz, ab, ±ch; cpx ch, ±mg; other: ac, qz, pr | | 70% | hypidiomorph. granular | 0.25 | aphyric | - | ep+qz, cc+qz, prcc |
| O/C-227A | metabasalt (pillow) | + | pl, cpx, ox(<1), gl? | pl cz, ab, ±ep, cpx*ch, cc, other: pr | | 55% | intergranular (intersertal?) | - | cpx: 1.5% | 0.25 | ep, ep+qz, pr+cc, Am: cc, ep, ch, qz |
| O/C-227B | meta-microdiorite (dike) | + | pl(50), cpx(40), qz(6), ox(4) | pl cz, ab, ±ch, ±mu; cpx*ch, cc, amph; other: pr, qz, py | | 65% | hypidiomorph. granular | 0.5 | aphyric | - | pr+cc |

Table A4: Petrographic summary of representative samples from the pillow unit (continued)

| Sample ID | Rock Type | A | Igneous (mode) | Mineralogy | Metamorphic | % Alt. | Ign. Texture | grain size | Phenocrysts | size | Veins |
|-----------|---------------------|---|-------------------------|--------------------------------------------------|--------------------------------------------------|--------|---------------------------------|------------|----------------------|------------|------------------------------------------------------------|
| O/C-231A | metadacite (dike) | + | pl, qz, cpx ox(<<1) | pl ab, cz, ep; other: qz, pu | pl ab, cz, ep; other: qz, pu | 50% | xenomorph. granular | - | pl: 14%, qz: 5.5% | 1.2 1.0 | - |
| O/C-232B | metadacite (dike) | - | pl, qz, cpx, ox(<<1) | pl ab, cz, ep; other: qz | pl ab, cz, ep; other: qz | 60% | xenomorph. granular | - | pl: 17% qz: 6.8% | 1.0 0.8 | ep |
| O/C-379 | metabasalt (pillow) | + | pl, cpx, gl? ox(6) | pl ab, pr, ch; qz, pu | pl ab, pr, ch; qz, pu | 65% | intergranular (intersertal?) | - | aphyric | - | pr, cc; Am: pr, ch, cc |
| O/C-380 | metabasalt (pillow) | + | pl, cpx?, gl?, ox(8) | pl ab, pr, ch; qz, pu, cc, py | pl ab, pr, ch; qz, pu, cc, py | 55% | intergranular (intersertal?) | - | aphyric | - | qz, cc |
| Pb-1 | metabasalt (pillow) | + | pl, cpx, gl?, ox(<1) | pl ab, cz, ep, ch, cpxamph; other: ti, pu, py | pl ab, cz, ep, ch, cpxamph; other: ti, pu, py | 70% | intergranular (intersertal?) | - | pl: <<1% | 0.15 | ep+qz, pr+pu+py+qz+ch, Am: ep, ab, qz, ch, pu, ti |

Table A5: Petrographic summary of representative samples from the Mule Mountain volcanics

| Sample ID | Rock Type | A | Igneous (mode) | Mineralogy | Metamorphic | % Alt. | Ign. Texture (groundmass) | grain size | Phenocrysts | size | Veins |
|-----------|---------------------------------------|---|-------------------------------------------|----------------------------------------------------------------|-------------|------------------------------|---------------------------|-------------------------------------|-------------------|-------------------------------|-----------------------|
| GDH-1 | metadacite | + | pl, qz, cpx, ox (<1) | pl cz, pr, ab, \pm ch, \pm mu; cpx*ch, pr, pu other: py | 50% | trachytic | | pl: 12.3% qz: 9.1% cpx: 3.2% | 0.8 2.5 0.5 | | |
| GDH-2a | metadacite | + | pl, hbl, qz, ox(2), ap, | pl cz, ab, \pm ch, \pm mu; hbl*ch, pu, pr; other: py | 40% | xenomorphic granular | | pl: 14.7% hbl: 5.6% | 1.0 0.8 | | |
| GDH-2b | metadacite with broken qz phenocrysts | + | pl, qz, cpx, ap, ox (<1) | pl cz, ab, \pm ch, \pm mu; cpx*ch other: ti | 45% | trachytic | | pl: 16.2% qz: 10.4% cpx: 2.3% | 1.0 2.0 0.5 | | |
| GDH-4 | metadacite | - | pl, cpx, qz, ox (1) | pl cz, ab, \pm ch, \pm mu; cpx*ch, pr | 55% | xenomorphic granular | | pl: 30.6% cpx: 15.2% qz: <1% | 1.5 0.9 0.2 | | |
| GDH-5a | metadacite | + | pl, hbl, ap, qz ox(1.5) | pl cz, ab, \pm ch, \pm mu; hbl*ch, pu, pr; other: ti | 50% | xenomorphic granular | | pl: 19.5% hbl: 4.5% | 0.5 0.7 | ch | |
| GDH-7 | metabasalt | + | pl, cpx, ox(2), gl? | plab, cc, ch, mu; cpx*ch, cc; gl?ch | 50% | intergranular (intersertal?) | | pl: 7.9% cpx: 2.3% | 0.4 0.3 | qz+ep, ch, pr, Am: ch, qz, cc | |
| GDH-8 | metabasalt | + | pl, cpx, ox(3), | pl ab, ep, ch; ep, pr; | 45% | intergranular | | pl: 13.7% cpx: 2.3% | 0.7 0.8 | ep+qz, ch+qz, pr; | |
| O/C-80 | metaandesite | + | pl, gl, qz? ox(2) | pl ab, ep, ch; glch+qz | 55% | trachytic | | - | | | ep+az, cc; Am: qz, ch |
| O/C-81B | metabasalt | + | cpx, pl, ol, ox(1), sp (sp in cpx and ol) | plab, cz, pr, ch; amph, qz ch of qz, cc, | 45% | intergranular (intersertal?) | | pl: 6.3% cpx: 10.5% ol: 6.9% | 1.0 2.0 1.0 | Am: ch, qz | |

Table A5: Petrographic summary of representative samples from the Mule Mountain volcanics (continued)

| Sample ID | Rock Type | A | Igneous (mode) | Mineralogy Metamorphic | % Alt. | Ign. Texture (groundmass) | grain size | Phenocrysts | size | Veins oldest → youngest |
|-----------|--------------|---|-------------------------|---------------------------------------------------|-----------|---------------------------------|---------------|-----------------------------------|-------------------|-------------------------------|
| O/C-81A | metabasalt | + | pl, cpx, ox(<1) | pl cz, ab, ch, mu; cpx*ch, qz, amph ol?qz, cc, ch | 40% | intergranular | | pl: 2%, cpx: 3% ol: 2% | 0.8 1.0 0.7 | qz+ch |
| O/C-82 | metaandesite | + | pl, cpx, ox(2) | pl ab, ±cz, ±ep, ±ch; cpx*chl, other: qz | 50% | intergranular | | pl: 1.9% cpx 0.5% | 0.2 0.2 | qz+ch qz, ch, ep A: |
| O/C-104 | metaandesite | - | pl, cpx, ox(3), gl? | pl ab, ±cz, ±ep, ±pr; cpxch, qz | 60% | intergranular (intersertal?) | | pl: 4.1% cpx: 21% | 0.1 0.1 | Am: pr, ch, qz, cc |
| O/C-147 | metaandesite | + | pl, cpx?, gl?, ox(5) | pl ab, ±ep, ±cz,; glch; other: pr, cc, | 65% | trachytic | | aphytic | | ep, cc, Am: qz, ch, gar |
| O/C-217 | metaandesite | + | pl, cpx, gl?, ox(3) | pl ab, cz, ep, ±ch, ±mu; cpxch, pr, qz, | 55% | trachytic | | pl: 12.5%, cpx: 1.8% ox: 2% | 0.8 0.3 | qz+ep, lau, Am: qz, ch, pr |

Table A6 Petrographic summary of representative samples from tonalitic dikes in the metagabbro unit (muscovitebiotitegarnet bearing dikes)

| Sample-ID | Rock Type | A | Igneous (mode): | Mineralogy | Metamorphic: | % Alt. | Texture | Grain size | Veins oldest → youngest |
|------------|------------------------|---|---------------------------------------------------|----------------------------------|----------------------------------|--------|----------------------------------------------|------------|----------------------------|
| GH-97-6 | s/c-augen metatonalite | + | pl(45), qz(45), mu(8), bio(2), gar | pl cz, ab, ±ep ±ch, other: pr | pl cz, ab, ±ep ±ch, other: pr | 55% | mylonitic fabric, S/C-type foliation | 4 mm | ep ^{bound} , pr |
| GH-97-20 | metatonalite | + | pl(42, An ₁₂), mu(15), qz(36), gar(7) | pl cz, ab, ep, ±ch | pl cz, ab, ep, ±ch | 10% | tectonic foliation, recryst. qz | 2.5 mm | |
| O/C-30-S37 | metatonalite | - | pl(50, An ₂), qz(48), mafic?(2) | pl cz, ab, ±ep, mafic; other: pr | pl cz, ab, ±ep, mafic; other: pr | 49% | tectonic foliation and cataclastic overprint | 3 mm | ep ^{def} , ch, pr |
| O/C-12-S20 | metatonalite | - | pl(50, An), qz(45), mu(1), bio(4), ox(<1) | pl cz, ab, ch, ep, pr | pl cz, ab, ch, ep, pr | 47% | tectonic foliation | 3 mm | pr |
| O/C-372b | metatonalite | - | pl(50), qz(40), mu(10) | pl cz, ab, ep, ch, ep, pr | pl cz, ab, ep, ch, ep, pr | 55% | mylonitic fabric | 1.5 mm | pr |
| O/C-417a | metatonalite | - | pl(48), qz(38), bio(7), hbl(2), mu(2), ox(2), ap | pl cz, ab, ±ep, other: ch, pr | pl cz, ab, ±ep, other: ch, pr | 45% | mylonitic fabric | 1.5 mm | |

Table A7: Petrographic summary of representative samples from the Half Moon Bar diorite

| Sample-ID | Rock Type | A | Mineralogy | Metamorphic: | % Alt. | Ign. Texture | phenocrysts (%, size) | m- gs | Veins oldest → youngest |
|-----------|---------------------------------------------|---|----------------------------------------------------------------|---------------------------------------------------------------------|--------|-----------------------------------------------|----------------------------------------------|----------|----------------------------|
| | | | Igneous (mode): | | | | | | |
| SC-11 | Leuco-hornblende-diorite (dike) | - | pl(73, An ₈₂), cpx/hbl(27), ox(1.7), qz(1.2) | pl → chl, mu, ab; cpx → amph ± mt; other: ti, | 60% | seriate hypidiomorphic granular texture | pl (20, 2) | 1 | |
| SC-12 | meta-trondhjemite | - | pl(50), qz(47), hbl+bio(3), ox(<1) | pl* → cz, ab, ± ep, ± ch; hbl*+bio* → ac ± chl, mt, other: pr | 50% | xenomorphic granular | - | 1.5 | qz+ep |
| SC-13 | meta-trondhjemite | - | pl(50), qz(46) hbl(2), ox(1), bio, ap, ti | pl → cz, ab, ± ep, ± ch; hbl* → ac, ch ± ep | 50% | xenomorphic granular | - | 1.0 | qz+ep, qz+ch |
| O/C-118a | quartz bearing hornblende-diorite | + | pl(55, An ₇₆₋₁₈), cpx/hbl(39), qz(2), ox(4) | pl → cz, ep, chmu, ab; cpx → ac, ch ± ep; | 80% | hypidiomorphic granular | - | 3 | qz+ep, pr, lau |
| O/C-118b | diabase (dike) | - | pl(An ₇₈₋₉), cpx, ox(3) | pl → cz, ab, ep, ch ± mu; cpx* ac+mt, ± ch | 65% | porphyritic, cpx pseudomorphs | pl (15, 0.8) cpx (9, 0.7) ox(1.5, 0.4) | | ep+qz, qz |
| O/C-174A | quartz-hornblende-diorite | + | pl(45, An ₇₈₋₉), cpx+hbl?(45), qz(7), ox(3) | pl → cz, ab, ep, ch ± mu; cpx* → ac, ch, ep; | 60% | hypidiomorphic granular | - | 2 | |
| O/C-174B | diabase (dike) | + | pl, cpx, ox(4) | pl → ep, cz, ab, ch, ± mu cpx* → ac, mt, ± ch,; other: pr | 60% | porphyritic | pl (22, 0.6) cpx(19, 0.7) ox: (3, 0.4) | | pr, lau |
| O/C-174C | dacitic dike with xenoliths of O/C-174a & b | - | pl(35), qz(20) hbl(3), ox(1) | pl → ep, cz, ab hbl → ac, ch ± ep ± mt; | 85% | porphyritic, many broken phenocrysts | pl (30, 0.5) qz (20, 0.6) hbl (3, 0.4) | | qz+ep, lau |
| O/C-176A | leuco-hornblende diorite | + | pl(70, An ₇₆), hbl/ cpx?(30), ox(2) | pl → cz, ab, ep, ch cpx → ac, mt, ch ± ep; | 80% | hypidiomorphic granular | | 0.5 | ep, pr |

Table A7: Petrographic summary of representative samples from the Half Moon Bar gabbro (continued)

| Sample-ID | Rock Type | A | Mineralogy | | % Alt. | Ign. Texture | phenocrysts (%, size) | m- gs | Veins oldest → youngest |
|-----------|-----------------------------------|---|--------------------------------------------------------------|---------------------------------------------------------------|--------|---------------------------------|----------------------------------------------|----------|----------------------------|
| | | | Igneous (mode): | Metamorphic: | | | | | |
| O/C-176B | diabase (dike) | - | pl, cpx, ox(5) | pl → cz, ab, ep cpx → ac, mt, ch ± ep | 80% | porphyritic (seriate in places) | pl (25, 1) cpx (7, 0.6) ox (2, 0.3) | - | ep, qz+ep+ch, pr |
| O/C-178 | quartz bearing hornblende-diorite | - | pl(57, An ₇₅₋₁₇), qz(3) cpx?/ hbl(38), ox(2), ap | pl → cz, ab, ep; cpx → acmg, other: ch hbl → ac, ch, ep | 68% | idiomorphic granular | - | 2.5 | ductile-brittle shearbands |
| O/C-375B | hornblende-diorite | - | pl(53), hbl(45), cpx?, ox(2), ap | pl → cz, ab, ep; cpx → acmt, ch | 90% | hypidiomorphic granular | - | 2 | |
| O/C-375C | diabase (dike) | + | pl(An ₇₆), cpx, ox(1.5) | pl → cz, ab, ep; cpx → acmt, other: ch | 85% | porphyritic, cpx pseudomorphs | pl (14, 0.5) cpx (4, 0.4) ox: (1, 0.1) | - | ep+qz+ch |
| O/C-375D | diabase (dike) | + | pl(An ₆₃), cpx, ox(1.5) | pl → cz, ab, ep; cpx → acmt, other: ch | 70% | porphyritic, cpx pseudomorphs | pl (12, 0.4) cpx (7, 0.3) ox (1, 0.1) | | pr, lau, cc |
| O/C-376 | quartz-hornblende-diorite | + | pl(64, An ₇₅₋₁₇), hbl/cpx(30), qz(5), ox(1) | pl → cz, ab, ep, ch; cpx → acmt, | 65% | idiomorphic granular | - | 2.5 | cz |
| O/C-377 | quartz-hornblende-diorite | + | pl(58, An ₇₇₋₇₉), hbl/cpx(28), qz(12), ox(2) | pl → cz, ab, ep, ch; cpx* → acmt, | 75% | idiomorphic granular | - | 2.5 | |

Explanation to tables A1 through A7

Mineral abbreviations

| | | | | | |
|------|----------------------------|-----------------|------------------------------|-----|--------------------------|
| ab | albite | gar | garnet | pr | prehnite |
| ac | actinolite | gl | glass (altered to chlorite) | pu | pumpellyite |
| amph | amphibole (ac and ac-hbl) | hbl | hornblende | py | pyrite |
| An | anorthite | hbl* | relict igneous hbl present | qz | quartz |
| ap | apatite | lau | laumontite | qz' | weakly recrystallized qz |
| bio | biotite | mt | magnetite | ser | sericite |
| cc | calcite | mu | muscovite | sp | Chromian spinel |
| ch | chlorite | ol | olivine | su | sulfide |
| cpx | clinopyroxene | opx | orthopyroxene | ti | titanite (sphene) |
| cpx* | relict igneous cpx present | ox | Fe-Ti oxide (opaque) | | |
| cz | clinozoisite | pl | plagioclase | | |
| ep | epidote | pl ^z | relict zoning in plagioclase | | |

Other

- ¹ tectonic overprint of igneous foliation (commonly stress induced twinning in plagioclase)
 - ¹ cr-spinel in xenocrysts (olivine),
 - ² pseudomorphs after olivine, ³..pseudomorphs after clinopyroxene, ⁴..pseudomorphs after plagioclase,
- Veins: ^{boud}...boudinaged, ^{def}...deformed
- Am amygdules
- sb shear band
- Row A + analyzed for major and trace elements, - not analyzed

APPENDIX B

**AGE SPECTRA, K/CA AND RADIOGENIC YIELD DIAGRAMS FOR THE
DATED HORNBLENDES AND MUSCOVITES**

Figure 1

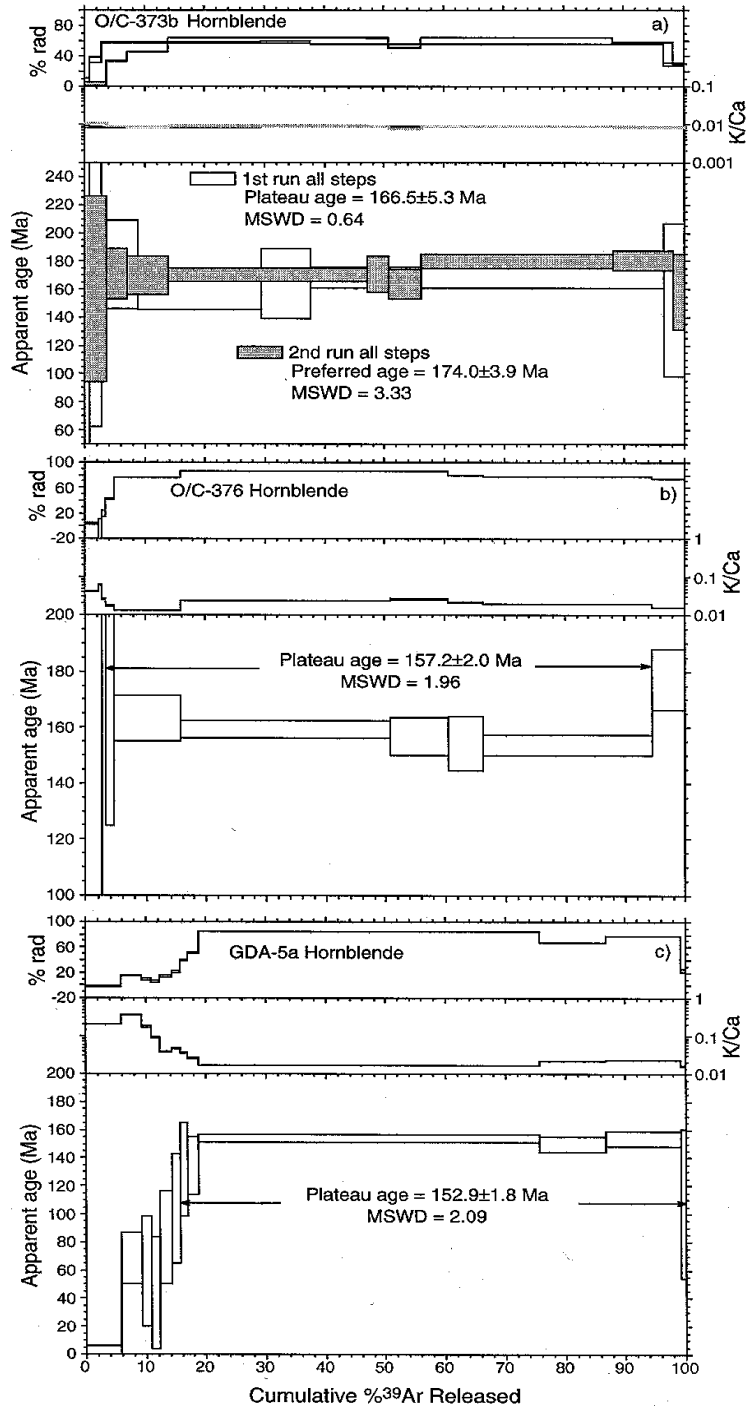


Figure 1. Age spectra, K/Ca and radiogenic yield diagrams for the dated hornblendes.

Figure B1: Age spectra, K/Ca and radiogenic yield diagrams for the dated hornblendes

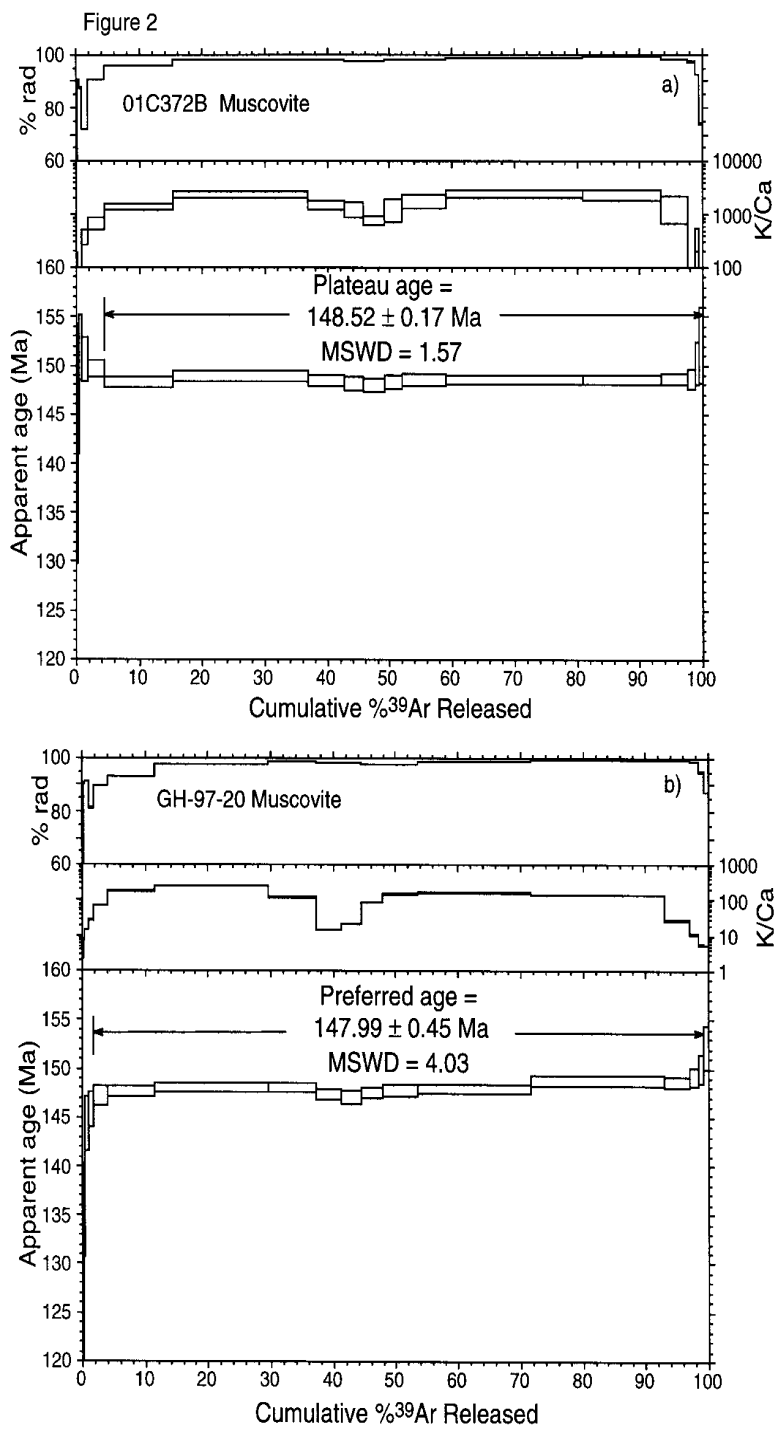


Figure 2. Age spectra, K/Ca and radiogenic yield diagrams for the dated muscovites.

Figure B2: Age spectra, K/Ca and radiogenic yield diagrams for the dated muscovites

Table B1: Analytical and age calculation methods

Sample preparation and irradiation:

Muscovite and hornblende separates obtained by standard heavy liquid, Franz magnetic and hand-picking techniques. Samples were packed in Cu foil and irradiated in machined Al discs for 100 hrs in L67 position of the Ford Reactor, University Michigan along with neutron flux monitor Fish Canyon sanidine, (FC-1) with an assigned age of 27.84 Ma (Deino and Potts, 1990).

Instrumentation

Mass Analyzer Products 215-50 mass spectrometer on line with automated all-metal extraction system.

Samples step-heated in Mo double-vacuum resistance furnace. Heating duration 7 to 8 minutes.

Reactive gases removed by reaction with SAES GP-50 getters, w operated at ~450°C and 1 at 20°C.

Gas also exposed to a W filament operated at ~2000°C.

Analytical parameters:

Electron multiplier sensitivity averaged 1×10^{-16} moles/pA.

Total system blanks plus backgrounds for the muscovites were about:

2000-6500, 15, 3.0, 2.0, 7-20 x 10^{-18} moles at masses 40, 39, 38, 37, 36, respectively for temperatures <1300°C.

Total system blanks plus backgrounds for the hornblendes were about:

1400-2000, 4, 1.5, 1.5, 4.5-8.5 x 10^{-18} moles at masses 40, 39, 38, 37, 36, respectively for temperatures <1300°C.

J-factors determined to a precision of $\pm 0.1\%$ by CO₂ laser-fusion of 4 single crystals from each 3 or 4 radial positions around the irradiation tray.

Correction factors for interfering nuclear reactions were determined using K-glass and CaF₂ and are as follows:

$$(^{40}\text{Ar}/^{39}\text{Ar})_{\text{K}} = 0.0262 \pm 0.0001; (^{36}\text{Ar}/^{37}\text{Ar})_{\text{Ca}} = 0.000279 \pm 0.00001 \text{ and } (^{39}\text{Ar}/^{37}\text{Ar})_{\text{Ca}} = 0.00077 \pm 0.00001.$$

Age calculations:

Total ages and errors calculated by weighting individual steps by fraction of ^{39}Ar released.

Plateau definition: 3 or more analytically indistinguishable contiguous steps comprising at least 50% of the total ^{39}Ar (Fleck et al., 1977). Preferred age calculated for indicated steps when rge sample does not meet plateau criteria or if MSWD outside of 95% confidence interval.

Plateau or preferred ages calculated weighting each step by the inverse of the variance.

Plateau and preferred age errors calculated using the method of Taylor (1982).

MSWD values are calculated for n-1 degrees of freedom for plateau and preferred ages.

If the MSWD is outside the 95% confidence window (cf. Mahon, 1996; Table 1), the error is multiplied by the square root of the MSWD.

Isochron ages, $^{40}\text{Ar}/^{36}\text{Ar}_i$ and MSWD values calculated form regression results obtained by the methods of York (1969).

All final errors reported at $\pm 2\sigma$, unless otherwise noted.

Table B2: Summary of Sample ages

| Sample | Mineral | Plateau or Preferred age (Ma $\pm 2\sigma$) | MSWD | % ^{39}Ar in plateau |
|------------------------------------------------------|------------|----------------------------------------------|------|-------------------------------|
| O/C-376 | hornblende | 157.2 \pm 2.0 | 1.96 | 91.1 |
| O/C-373b 1 st run | hornblende | 166.5 \pm 5.3 | 0.64 | 100.0 |
| O/C-373b 2 nd run | hornblende | 174.0 \pm 3.9 | 3.33 | 100.0 |
| GDH-5a | hornblende | 152.9 \pm 1.8 | 2.09 | 84.1 |
| GH-97-20 | muscovite | 147.99 \pm 0.32 | 4.03 | 97.4 |
| O/C-372B | muscovite | 148.52 \pm 0.17 | 1.57 | 98.2 |
| Weighted mean of O/C-373b runs is 171.4 \pm 3.1 Ma | | | | |

APPENDIX C

**COMPOSITION OF CLINOPYROXENE, PLAGIOCLASE AND CR-SPINEL IN
SAMPLES FROM THE WILD ROGUE WILDERNESS, SW OREGON
(ELECTRON MICROPROBE ANALYSIS)**

Table C1: Microprobe analysis of clinopyroxene in O/C-325

deformed dike (porphyritic), sheeted dike complex (see table A3)

| Analysis | 11 | 12 | 13 | 14 | 15 |
|--------------------------------|-------|-------|-------|-------|-------|
| Location | 3 | 3 | 4 | 4 | 4 |
| SiO ₂ | 53.75 | 53.83 | 52.51 | 53.62 | 53.27 |
| TiO ₂ | 0.16 | 0.19 | 0.24 | 0.17 | 0.15 |
| Al ₂ O ₃ | 1.84 | 1.70 | 2.30 | 1.51 | 1.64 |
| FeO* | 4.12 | 3.96 | 5.36 | 5.12 | 4.57 |
| Cr ₂ O ₃ | 0.90 | 0.78 | 0.75 | 0.61 | 0.80 |
| MgO | 18.40 | 18.25 | 17.29 | 18.73 | 17.94 |
| CaO | 20.21 | 21.02 | 20.57 | 19.47 | 20.60 |
| Na ₂ O | 0.21 | 0.25 | 0.20 | 0.19 | 0.22 |
| Total | 99.59 | 99.98 | 99.22 | 99.42 | 99.19 |
| Si | 1.960 | 1.955 | 1.933 | 1.960 | 1.955 |
| Al | 0.079 | 0.073 | 0.099 | 0.065 | 0.071 |
| Ti | 0.004 | 0.005 | 0.007 | 0.005 | 0.004 |
| Fe ³⁺ | 0.000 | 0.001 | 0.014 | 0.002 | 0.004 |
| Fe ²⁺ | 0.126 | 0.119 | 0.151 | 0.155 | 0.137 |
| Cr | 0.026 | 0.022 | 0.022 | 0.018 | 0.023 |
| Mg | 1.000 | 0.988 | 0.948 | 1.020 | 0.981 |
| Ca | 0.790 | 0.818 | 0.811 | 0.762 | 0.810 |
| Na | 0.015 | 0.018 | 0.014 | 0.013 | 0.016 |
| Sum | 4.000 | 3.999 | 3.999 | 4.000 | 4.001 |
| WO | 41.2 | 42.5 | 42.1 | 39.3 | 41.9 |
| EN | 52.2 | 51.3 | 49.3 | 52.6 | 50.8 |
| FS | 6.6 | 6.2 | 8.6 | 8.1 | 7.3 |

Data obtained by G.D. Harper

Table C2: Microprobe analysis of clinopyroxene in O/C-81acpx + plag \pm ol phyrlic basalt, Mule Mountain volcanics (see table A5)

| Analysis | 11 | 17 | 18 | 3.1 | 3.2 | 4.1 | 4.2 |
|--------------------------------|--------|-------|-------|-------|-------|-------|-------|
| Location | 5 | 3 | 3 | 8 | 8 | 8 | 8 |
| SiO ₂ | 53.91 | 53.09 | 53.29 | 53.47 | 53.47 | 52.62 | 52.62 |
| TiO ₂ | 0.07 | 0.10 | 0.17 | 0.10 | 0.10 | 0.24 | 0.24 |
| Al ₂ O ₃ | 1.47 | 1.61 | 1.95 | 1.88 | 1.88 | 2.44 | 2.44 |
| FeO* | 3.63 | 3.69 | 5.98 | 3.51 | 3.51 | 6.28 | 6.28 |
| Cr ₂ O ₃ | 0.53 | 0.45 | 0.19 | 0.74 | 0.74 | 0.29 | 0.29 |
| MgO | 17.68 | 17.41 | 17.41 | 17.53 | 17.53 | 16.71 | 16.71 |
| CaO | 22.63 | 22.76 | 19.99 | 22.25 | 22.25 | 20.57 | 20.57 |
| Na ₂ O | 0.10 | 0.11 | 0.13 | 0.12 | 0.12 | 0.17 | 0.17 |
| Total | 100.02 | 99.22 | 99.11 | 99.60 | 99.60 | 99.32 | 99.32 |
| Si | 1.961 | 1.947 | 1.965 | 1.954 | 1.954 | 1.941 | 1.941 |
| Al | 0.063 | 0.070 | 0.084 | 0.080 | 0.080 | 0.106 | 0.106 |
| Ti | 0.002 | 0.003 | 0.005 | 0.003 | 0.003 | 0.007 | 0.007 |
| Fe ³⁺ | 0.002 | 0.025 | 0.000 | 0.000 | 0.000 | 0.002 | 0.002 |
| Fe ²⁺ | 0.108 | 0.088 | 0.184 | 0.107 | 0.107 | 0.192 | 0.192 |
| Cr | 0.015 | 0.013 | 0.006 | 0.021 | 0.021 | 0.008 | 0.008 |
| Mg | 0.958 | 0.952 | 0.957 | 0.954 | 0.954 | 0.919 | 0.919 |
| Ca | 0.882 | 0.894 | 0.790 | 0.871 | 0.871 | 0.813 | 0.813 |
| Na | 0.007 | 0.008 | 0.009 | 0.009 | 0.009 | 0.012 | 0.012 |
| Sum | 3.998 | 4.000 | 4.000 | 3.999 | 3.999 | 4.000 | 4.000 |
| WO | 45.2 | 45.6 | 40.9 | 45.1 | 45.1 | 42.2 | 42.2 |
| EN | 49.1 | 48.6 | 49.6 | 49.4 | 49.4 | 47.7 | 47.7 |
| FS | 5.7 | 5.8 | 9.5 | 5.5 | 5.5 | 10.1 | 10.1 |

Data obtained by G.D. Harper

Table C3a: Microprobe analysis of plagioclase in O/C-118

Hornblende quartz diorite, Half Moon Bar diorite (see table A7)

Plagioclase coexisting with hornblende, table 3.1a (chapter 3)

| Analysis | 69 | 71 | 82 | 74 | 86 | 63 | 83 |
|--------------------------------|--------|--------|--------|--------|--------|--------|--------|
| Location | 1 | 2 | 5 | 3 | 4 | 5 | 5 |
| SiO ₂ | 58.92 | 59.28 | 59.29 | 63.07 | 66.38 | 67.76 | 59.21 |
| TiO ₂ | 0.00 | 0.00 | 0.00 | 0.00 | 0.00 | 0.00 | 0.00 |
| Al ₂ O ₃ | 25.77 | 25.68 | 25.80 | 22.60 | 21.16 | 20.22 | 25.82 |
| FeO* | 0.11 | 0.24 | 0.18 | 0.20 | 0.02 | 0.24 | 0.12 |
| MnO | 0.00 | 0.00 | 0.00 | 0.00 | 0.00 | 0.00 | 0.00 |
| MgO | 0.09 | 0.01 | 0.00 | 0.01 | 0.00 | 0.05 | 0.02 |
| CaO | 7.43 | 7.39 | 7.44 | 3.60 | 2.02 | 1.59 | 7.49 |
| Na ₂ O | 7.40 | 7.43 | 7.29 | 9.19 | 10.64 | 10.74 | 7.32 |
| K ₂ O | 0.14 | 0.13 | 0.15 | 0.03 | 0.00 | 0.00 | 0.10 |
| Total | 99.85 | 100.17 | 100.16 | 98.71 | 100.21 | 100.60 | 100.09 |
| Si | 10.542 | 10.575 | 10.570 | 11.270 | 11.628 | 11.805 | 10.562 |
| Al | 5.431 | 5.395 | 5.417 | 4.757 | 4.366 | 4.149 | 5.424 |
| Ti | 0.000 | 0.000 | 0.000 | 0.000 | 0.000 | 0.000 | 0.000 |
| Fe ²⁺ | 0.017 | 0.036 | 0.027 | 0.030 | 0.003 | 0.035 | 0.017 |
| Mn | 0.000 | 0.000 | 0.000 | 0.000 | 0.000 | 0.000 | 0.000 |
| Mg | 0.023 | 0.003 | 0.000 | 0.004 | 0.000 | 0.013 | 0.006 |
| Ba | n.d. | n.d. | n.d. | n.d. | n.d. | n.d. | n.d. |
| Ca | 1.424 | 1.411 | 1.422 | 0.688 | 0.378 | 0.298 | 1.431 |
| Na | 2.566 | 2.570 | 2.521 | 3.185 | 3.613 | 3.628 | 2.531 |
| K | 0.032 | 0.029 | 0.034 | 0.007 | 0.000 | 0.000 | 0.023 |
| Sum | 20.035 | 20.019 | 19.991 | 19.941 | 19.988 | 19.928 | 19.994 |
| Ab | 63.80 | 64.10 | 63.40 | 82.10 | 90.50 | 92.40 | 63.50 |
| An | 35.40 | 35.20 | 35.80 | 17.70 | 9.50 | 7.60 | 35.90 |
| Or | 0.80 | 0.70 | 0.90 | 0.20 | 0.00 | 0.00 | 0.60 |
| coexisting hbl analys. | 68 | 70 | 78 | 80 | 76 | 79 | 81 |

Analysis was performed at Rensselaer Polytechnique Institute using a JEOL 733X electron microprobe operating at 15 keV accelerating voltage and 15.5 nA sample current. Analyses were obtained using a defocused beam site and integrated count times of 5 seconds.

Total iron as FeO*

End members were determined after cation normalization per 32 oxygens.

Table C3b: Microprobe analysis of plagioclase in O/C-376

Hornblende quartz diorite, Half Moon Bar diorite (see table A7)

| Plagioclase coexisting with hornblende, table 3.1b (chapter 3) | | | | | | | | Plagioclase core |
|----------------------------------------------------------------|--------|--------|--------|--------|--------|--------|--------|------------------|
| Analysis | 46 | 47 | 60 | 59 | 56 | 57 | 67 | 44 |
| Location | 2 | 2 | 1 | 1 | 3 | 3 | 5 | 2 |
| SiO ₂ | 60.03 | 57.48 | 54.58 | 61.38 | 54.84 | 66.21 | 64.67 | 49.66 |
| TiO ₂ | 0.00 | 0.03 | 0.06 | 0.00 | 0.01 | 0.04 | 0.07 | 0.02 |
| Al ₂ O ₃ | 25.35 | 27.88 | 28.68 | 24.12 | 28.56 | 21.27 | 22.33 | 31.77 |
| FeO* | 0.16 | 0.27 | 0.48 | 0.22 | 0.35 | 0.22 | 0.21 | 0.55 |
| MnO | 0.00 | 0.06 | 0.00 | 0.04 | 0.00 | 0.01 | 0.02 | 0.00 |
| MgO | 0.03 | 0.05 | 0.02 | 0.01 | 0.02 | 0.03 | 0.00 | 0.02 |
| CaO | 6.67 | 8.52 | 11.60 | 5.75 | 10.76 | 2.50 | 3.41 | 14.84 |
| Na ₂ O | 7.57 | 5.92 | 5.14 | 8.01 | 5.38 | 10.15 | 9.56 | 3.20 |
| K ₂ O | 0.27 | 0.61 | 0.15 | 0.35 | 0.17 | 0.12 | 0.25 | 0.08 |
| Total | 100.07 | 100.82 | 100.71 | 99.87 | 100.10 | 100.56 | 100.52 | 100.13 |
| Si | 10.689 | 10.223 | 9.818 | 10.925 | 9.894 | 11.583 | 11.358 | 9.077 |
| Al | 5.315 | 5.840 | 6.075 | 5.056 | 6.068 | 4.382 | 4.618 | 6.840 |
| Ti | 0.000 | 0.004 | 0.008 | 0.000 | 0.001 | 0.005 | 0.010 | 0.003 |
| Fe ²⁺ | 0.024 | 0.040 | 0.072 | 0.032 | 0.053 | 0.033 | 0.031 | 0.083 |
| Mn | 0.000 | 0.009 | 0.000 | 0.006 | 0.000 | 0.002 | 0.003 | 0.000 |
| Mg | 0.007 | 0.014 | 0.004 | 0.002 | 0.006 | 0.007 | 0.000 | 0.006 |
| Ba | n.d. | n.d. | n.d. | n.d. | n.d. | n.d. | n.d. | n.d. |
| Ca | 1.273 | 1.623 | 2.236 | 1.096 | 2.079 | 0.468 | 0.641 | 2.906 |
| Na | 2.613 | 2.042 | 1.794 | 2.764 | 1.882 | 3.443 | 3.257 | 1.132 |
| K | 0.060 | 0.138 | 0.034 | 0.080 | 0.040 | 0.028 | 0.055 | 0.019 |
| Sum | 19.981 | 19.933 | 20.041 | 19.961 | 20.023 | 19.951 | 19.973 | 20.066 |
| Ab | 66.2 | 53.7 | 44.1 | 70.2 | 47.0 | 87.4 | 82.4 | 27.9 |
| An | 32.3 | 42.7 | 55.0 | 27.8 | 52.0 | 11.9 | 16.2 | 71.6 |
| Or | 1.5 | 3.6 | 0.8 | 2.0 | 1.0 | 0.7 | 1.4 | 0.5 |
| coexisting hbl analys. | 40 | 41 | 48 | 49 | 53 | 55 | 64 | - |

Analysis was performed at Rensselaer Polytechnique Institute using a JEOL 733X electron microprobe operating at 15 keV accelerating voltage and 15.5 nA sample current. Analyses were obtained using a defocused beam site and integrated count times of 5 seconds.

Total iron as FeO*

End members were determined after cation normalization per 32 oxygens.

Table C4: Microprobe analysis of plagioclase in O/C-229

Hornblende quartz diorite in metagabbro unit (see table A1b for petrography)

Plagioclase coexisting with hornblende, table 3.2 (chapter 3)

| Analysis | 129 | 131 | 130 | 121 | 127 | 126 | 133 |
|--------------------------------|--------|--------|--------|--------|--------|--------|--------|
| Location | 2 | 4 | 5 | 5 | 5 | 5 | 5 |
| SiO ₂ | 61.66 | 58.15 | 56.65 | 57.18 | 56.13 | 55.61 | 54.41 |
| TiO ₂ | 0 | 0 | 0 | 0.03 | 0.18 | 0 | 0.01 |
| Al ₂ O ₃ | 24.59 | 26.7 | 27.78 | 27.29 | 27.61 | 28.52 | 29.13 |
| FeO | 0.45 | 0.58 | 0.37 | 0.17 | 0.09 | 0.31 | 0.23 |
| MnO | 0.01 | 0.01 | 0.01 | 0.01 | 0.02 | 0 | 0.01 |
| MgO | 0.16 | 0.2 | 0.09 | 0 | 0 | 0.01 | 0.01 |
| CaO | 4.16 | 7.38 | 8.89 | 9.23 | 9.74 | 10.08 | 11.43 |
| Na ₂ O | 7.93 | 6.52 | 6.01 | 6.6 | 6.17 | 5.86 | 5.34 |
| K ₂ O | 1.03 | 0.78 | 0.54 | 0.07 | 0.11 | 0.33 | 0.06 |
| Total | 99.99 | 100.31 | 100.33 | 100.57 | 100.03 | 100.72 | 100.62 |
| Si | 10.948 | 10.394 | 10.152 | 10.214 | 10.095 | 9.963 | 9.78 |
| Al | 5.141 | 5.621 | 5.862 | 5.742 | 5.848 | 6.017 | 6.166 |
| Ti | 0 | 0 | 0 | 0.004 | 0.024 | 0 | 0.002 |
| Fe ₂ | 0.067 | 0.086 | 0.056 | 0.025 | 0.014 | 0.046 | 0.034 |
| Mn | 0.002 | 0.001 | 0.001 | 0.002 | 0.003 | 0 | 0.001 |
| Mg | 0.043 | 0.052 | 0.025 | 0.001 | 0 | 0.003 | 0.004 |
| Ba | 0 | 0 | 0 | 0 | 0 | 0 | 0 |
| Ca | 0.792 | 1.414 | 1.708 | 1.766 | 1.877 | 1.934 | 2.201 |
| Na | 2.73 | 2.26 | 2.087 | 2.287 | 2.151 | 2.036 | 1.862 |
| K | 0.234 | 0.177 | 0.123 | 0.015 | 0.024 | 0.076 | 0.013 |
| Sum | 19.957 | 20.005 | 20.014 | 20.056 | 20.036 | 20.075 | 20.063 |
| Ab | 72.7 | 58.7 | 53.3 | 56.2 | 53.1 | 50.3 | 45.7 |
| An | 21.1 | 36.7 | 43.6 | 43.4 | 46.3 | 47.8 | 54 |
| Or | 0.8 | 0.7 | 0.9 | 0.2 | 0 | 0 | 0.6 |
| Coexisting hbl analys. | 139 | 138 | 125 | 134 | 135 | 136 | 137 |

Analysis was performed at Rensselaer Polytechnique Institute using a JEOL 733X electron microprobe operating at 15 keV accelerating voltage and 15.5 nA sample current. Analyses were obtained using a defocused beam site and integrated count times of 5 seconds.

Total iron as FeO*

End members were determined after cation normalization per 32 oxygens.

Table C5a: Microprobe analysis of plagioclase in MRH-78/1

Metagabbro unit (see table A1a for petrography)

Plagioclase coexisting with hornblende, table 3.3 (chapter 3)

| Analysis | 142 | 144 | 149 | 152 | 160 |
|--------------------------------|---------|---------|---------|---------|---------|
| Location | 1 | 1 | 2 | 3 | 4 |
| SiO ₂ | 65.382 | 62.548 | 64.828 | 63.431 | 61.518 |
| TiO ₂ | 0.034 | 0.015 | 0.015 | 0.017 | 0.000 |
| Al ₂ O ₃ | 22.063 | 23.865 | 22.707 | 23.456 | 24.823 |
| FeO | 0.124 | 0.085 | 0.080 | 0.090 | 0.047 |
| MnO | 0.006 | 0.026 | 0.003 | 0.006 | 0.010 |
| MgO | 0.008 | 0.008 | 0.014 | 0.005 | 0.011 |
| CaO | 2.447 | 4.882 | 3.042 | 4.317 | 5.941 |
| Na ₂ O | 10.137 | 8.849 | 9.829 | 9.191 | 8.418 |
| K ₂ O | 0.049 | 0.058 | 0.070 | 0.033 | 0.026 |
| Total | 100.250 | 100.340 | 100.590 | 100.550 | 100.790 |
| Si | 11.469 | 11.042 | 11.351 | 11.152 | 10.844 |
| Al | 4.558 | 4.961 | 4.682 | 4.857 | 5.153 |
| Ti | 0.004 | 0.002 | 0.002 | 0.002 | 0 |
| Fe ₂ | 0.018 | 0.013 | 0.012 | 0.013 | 0.007 |
| Mn | 0.001 | 0.004 | 0 | 0.001 | 0.001 |
| Mg | 0.002 | 0.002 | 0.004 | 0.001 | 0.003 |
| Ba | 0 | 0 | 0 | 0 | 0 |
| Ca | 0.46 | 0.923 | 0.571 | 0.813 | 1.122 |
| Na | 3.448 | 3.029 | 3.337 | 3.133 | 2.877 |
| K | 0.011 | 0.013 | 0.016 | 0.007 | 0.006 |
| Sum | 19.971 | 19.989 | 19.975 | 19.979 | 20.013 |
| Ab | 88.00 | 76.40 | 85.00 | 79.30 | 71.80 |
| An | 11.7 | 23.3 | 14.6 | 20.6 | 28 |
| Or | 0.3 | 0.3 | 0.4 | 0.2 | 0.1 |
| Coexisting hbl analys. | 141 | 143,145 | 150 | 151 | 156,165 |

Analysis was performed at Rensselaer Polytechnique Institute using a JEOL 733X electron microprobe operating at 15 keV accelerating voltage and 15.5 nA sample current. Analyses were obtained using a defocused beam site and integrated count times of 5 seconds.

Total iron as FeO*

End members were determined after cation normalization per 32 oxygens.

Table C5b: Microprobe analysis of plagioclase in MRH-78/2

Metagabbro unit (see table A1a for petrography)

Plagioclase coexisting with hornblende, table 3.3 (chapter 3)

| Analysis | 42 | 47 | 50 | 55 | 40 |
|--------------------------------|---------|--------|---------|--------|--------|
| Location | 2 | 1 | 4 | 4 | 3 |
| SiO ₂ | 65.244 | 63.962 | 62.810 | 63.995 | 66.075 |
| TiO ₂ | 0.029 | 0.018 | 0.017 | 0.019 | 0.058 |
| Al ₂ O ₃ | 22.224 | 22.651 | 23.633 | 22.988 | 21.259 |
| FeO | 0.113 | 0.048 | 0.087 | 0.094 | 0.179 |
| MnO | 0.005 | 0.005 | 0.006 | 0.009 | 0.010 |
| MgO | 0.009 | 0.007 | 0.004 | 0.012 | 0.000 |
| CaO | 2.596 | 3.666 | 4.781 | 3.693 | 1.702 |
| Na ₂ O | 10.060 | 9.535 | 8.971 | 9.499 | 10.522 |
| K ₂ O | 0.055 | 0.041 | 0.028 | 0.061 | 0.024 |
| Total | 100.340 | 99.930 | 100.340 | 100.37 | 99.830 |
| Si | 11.439 | 11.292 | 11.083 | 11.253 | 11.616 |
| Al | 4.589 | 4.709 | 4.911 | 4.761 | 4.401 |
| Ti | 0.004 | 0.002 | 0.002 | 0.003 | 0.008 |
| Fe ₂ | 0.017 | 0.007 | 0.013 | 0.014 | 0.026 |
| Mn | 0.001 | 0.001 | 0.001 | 0.001 | 0.001 |
| Mg | 0.002 | 0.002 | 0.001 | 0.003 | 0 |
| Ba | 0 | 0 | 0 | 0 | 0 |
| Ca | 0.488 | 0.693 | 0.904 | 0.696 | 0.321 |
| Na | 3.42 | 3.264 | 3.069 | 3.239 | 3.587 |
| K | 0.012 | 0.009 | 0.006 | 0.014 | 0.005 |
| Sum | 19.972 | 19.979 | 19.99 | 19.984 | 19.965 |
| Ab | 87.2 | 82.3 | 77.1 | 82 | 91.7 |
| An | 12.4 | 17.5 | 22.7 | 17.6 | 8.2 |
| Or | 0.3 | 0.2 | 0.2 | 0.4 | 0.1 |
| Coexisting hbl analys. | 41,43 | 49 | 51 | 52 | 54 |

Analysis was performed at Rensselaer Polytechnique Institute using a JEOL 733X electron microprobe operating at 15 keV accelerating voltage and 15.5 nA sample current. Analyses were obtained using a defocused beam site and integrated count times of 5 seconds.

Total iron as FeO*

End members were determined after cation normalization per 32 oxygens.

Table C5c: Microprobe analysis of plagioclase in O/C-373

Metagabbro unit (see table A1a for petrography)

Plagioclase coexisting with hornblende, table 3.3 (chapter 3)

| Analysis | 8 | 12 | 17 | 20 | 24 | 30 |
|--------------------------------|---------|---------|---------|---------|---------|---------|
| Location | 1 | 4 | 4 | 3 | 3 | 3 |
| SiO ₂ | 63.424 | 61.447 | 63.222 | 61.510 | 64.412 | 62.790 |
| TiO ₂ | 0.020 | 0.044 | 0.020 | 0.000 | 0.000 | 0.049 |
| Al ₂ O ₃ | 23.423 | 24.404 | 23.488 | 24.795 | 23.189 | 23.692 |
| FeO | 0.133 | 0.169 | 0.076 | 0.259 | 0.047 | 0.060 |
| MnO | 0.011 | 0.027 | 0.007 | 0.000 | 0.000 | 0.009 |
| MgO | 0.018 | 0.004 | 0.010 | 0.060 | 0.018 | 0.010 |
| CaO | 4.009 | 5.482 | 4.372 | 5.162 | 3.489 | 4.792 |
| Na ₂ O | 9.235 | 8.417 | 9.164 | 8.347 | 9.598 | 8.995 |
| K ₂ O | 0.097 | 0.056 | 0.048 | 0.277 | 0.085 | 0.029 |
| Total | 100.370 | 100.050 | 100.410 | 100.410 | 100.840 | 100.430 |
| Si | 11.167 | 10.903 | 11.135 | 10.877 | 11.264 | 11.071 |
| Al | 4.857 | 5.099 | 4.872 | 5.163 | 4.776 | 4.919 |
| Ti | 0.003 | 0.006 | 0.003 | 0 | 0 | 0.006 |
| Fe ₂ | 0.02 | 0.025 | 0.011 | 0.038 | 0.007 | 0.009 |
| Mn | 0.002 | 0.004 | 0.001 | 0 | 0 | 0.001 |
| Mg | 0.005 | 0.001 | 0.003 | 0.016 | 0.005 | 0.003 |
| Ba | 0 | 0 | 0 | 0 | 0 | 0 |
| Ca | 0.756 | 1.042 | 0.825 | 0.978 | 0.654 | 0.905 |
| Na | 3.153 | 2.896 | 3.13 | 2.862 | 3.254 | 3.075 |
| K | 0.022 | 0.013 | 0.011 | 0.062 | 0.019 | 0.007 |
| Sum | 19.985 | 19.989 | 19.991 | 19.996 | 19.979 | 19.996 |
| Ab | 80.2 | 73.3 | 78.9 | 73.3 | 82.9 | 77.1 |
| An | 19.2 | 26.4 | 20.8 | 25.1 | 16.7 | 22.7 |
| Or | 0.6 | 0.3 | 0.3 | 1.6 | 0.5 | 0.2 |
| Coexisting hbl analys. | 6 | 13, 14 | 15 | 23 | 25, 26 | 27, 29 |

Analysis was performed at Rensselaer Polytechnique Institute using a JEOL 733X electron microprobe operating at 15 keV accelerating voltage and 15.5 nA sample current. Analyses were obtained using a defocused beam site and integrated count times of 5 seconds.

Total iron as FeO*

End members were determined after cation normalization per 32 oxygens.

Table C6a: Cr-spinel compositions in sample O/C-4-S3a (sheeted dike complex)

| analysis | 23 ¹ | 24 ¹ | 25 ¹ | 26 ¹ | 27 ¹ | 27 ¹ |
|----------|-----------------|-----------------|-----------------|-----------------|-----------------|-----------------|
| Location | 1 | 1 | 2 | 2 | 3 | 3 |
| TiO2 | 0.26 | 0.26 | 0.41 | 0.40 | 0.26 | 0.26 |
| Al2O3 | 10.30 | 10.47 | 10.00 | 9.88 | 10.67 | 10.64 |
| Fe2O3 | 3.99 | 3.79 | 4.83 | 4.83 | 3.81 | 3.98 |
| FeO | 13.02 | 13.37 | 17.01 | 16.69 | 14.00 | 17.49 |
| MgO | 14.03 | 14.04 | 12.07 | 12.22 | 14.03 | 11.63 |
| Cr2O3 | 55.60 | 56.35 | 54.74 | 54.74 | 56.93 | 55.45 |
| Ti | 0.0064 | 0.0064 | 0.0102 | 0.0100 | 0.0063 | 0.0064 |
| Al | 0.3993 | 0.4017 | 0.3872 | 0.3835 | 0.4041 | 0.4103 |
| Fe3 | 0.1398 | 0.1325 | 0.1703 | 0.1704 | 0.1318 | 0.1424 |
| Fe2 | 0.3172 | 0.3244 | 0.4164 | 0.4089 | 0.3367 | 0.4345 |
| Mg | 0.6878 | 0.6817 | 0.5912 | 0.5996 | 0.6720 | 0.5673 |
| Cr | 1.4459 | 1.4507 | 1.4217 | 1.4250 | 1.4468 | 1.4350 |
| Cr # | 78.4 | 78.3 | 78.6 | 78.8 | 78.2 | 77.8 |
| Mg # | 68.4 | 67.8 | 58.7 | 59.5 | 66.6 | 56.6 |

| analysis | 29 ^P | 30 ^P | 31 ^P | 32 ^P | 33 ^P | 34 ^P |
|----------|-----------------|-----------------|-----------------|-----------------|-----------------|-----------------|
| Location | 1 | 1 | 2 | 2 | 3 | 3 |
| TiO2 | 0.23 | 0.22 | 0.24 | 0.24 | 0.31 | 0.29 |
| Al2O3 | 10.45 | 10.41 | 10.35 | 10.39 | 10.97 | 10.58 |
| Fe2O3 | 3.22 | 3.17 | 3.45 | 3.54 | 3.84 | 4.06 |
| FeO | 11.63 | 11.76 | 18.26 | 18.41 | 21.50 | 23.60 |
| MgO | 15.20 | 15.09 | 10.89 | 10.78 | 9.13 | 7.48 |
| Cr2O3 | 57.97 | 58.06 | 55.09 | 54.87 | 53.23 | 52.56 |
| Ti | 0.0057 | 0.0053 | 0.0061 | 0.0059 | 0.0077 | 0.0073 |
| Al | 0.3964 | 0.3951 | 0.4062 | 0.4082 | 0.4319 | 0.4235 |
| Fe3 | 0.1114 | 0.1102 | 0.1273 | 0.1303 | 0.1427 | 0.1536 |
| Fe2 | 0.2795 | 0.2836 | 0.4676 | 0.4713 | 0.5545 | 0.6204 |
| Mg | 0.7291 | 0.7245 | 0.5405 | 0.5354 | 0.4546 | 0.3788 |
| Cr | 1.4750 | 1.4786 | 1.4503 | 1.4452 | 1.4057 | 1.4112 |
| | un. | un. | | | | |
| Cr # | 78.8 | 78.9 | 78.1 | 78.0 | 76.5 | 76.9 |
| Mg # | 72.3 | 71.9 | 53.6 | 53.2 | 45.0 | 37.9 |

¹ inclusion in olivine pseudomorph
^P microphenocryst

Data obtained by G.D. Harper

Table C6a: Cr-spinel compositions in sample O/C-4-S3 (sheeted dike complex)

| analysis | 35 ¹ | 36 ¹ | 37 ¹ | 38 ¹ | 39 ¹ | 40 ¹ |
|--------------------------------|-----------------|-----------------|-----------------|-----------------|-----------------|-----------------|
| Location | 1 | 1 | 2 | 2 | 3 | 3 |
| TiO ₂ | 0.35 | 0.32 | 0.52 | 0.59 | 0.24 | 0.25 |
| Al ₂ O ₃ | 12.06 | 11.92 | 9.94 | 10.34 | 11.21 | 11.17 |
| Fe ₂ O ₃ | 3.96 | 3.63 | 6.91 | 7.27 | 3.74 | 3.64 |
| FeO | 12.53 | 14.68 | 20.66 | 20.92 | 10.84 | 10.86 |
| MgO | 14.99 | 13.68 | 10.45 | 10.33 | 15.96 | 15.94 |
| Cr ₂ O ₃ | 55.46 | 55.58 | 51.56 | 50.27 | 57.93 | 57.72 |
| Ti | 0.0083 | 0.0077 | 0.0128 | 0.0147 | 0.0056 | 0.0060 |
| Al | 0.4524 | 0.4496 | 0.3862 | 0.4025 | 0.4172 | 0.4172 |
| Fe ₃ | 0.1339 | 0.1263 | 0.2411 | 0.2532 | 0.1245 | 0.1219 |
| Fe ₂ | 0.2943 | 0.3541 | 0.5004 | 0.5057 | 0.2507 | 0.2526 |
| Mg | 0.7110 | 0.6524 | 0.5138 | 0.5085 | 0.7513 | 0.7529 |
| Cr | 1.3953 | 1.4062 | 1.3442 | 1.3131 | 1.4466 | 1.4463 |
| Cr # | 75.5 | 75.8 | 77.7 | 76.5 | 77.6 | 77.6 |
| Mg # | 70.7 | 64.8 | 50.7 | 50.1 | 75.0 | 74.9 |

¹...inclusion in olivine pseudomorph

Data obtained by G.D. Harper

Table C6b Cr-spinel compositions in sample MRH-45a (sheeted dike complex)

| analysis | 1 ^l | 2 ^l | 3 ^l | 4 ^l | 5 ^l |
|--------------------------------|----------------|----------------|----------------|----------------|----------------|
| Location | 1 | 2 | 3 | 4 | 5 |
| TiO ₂ | 0.29 | 0.26 | 0.22 | 0.31 | 0.32 |
| Al ₂ O ₃ | 10.65 | 9.78 | 9.79 | 9.59 | 9.50 |
| Fe ₂ O ₃ | 3.81 | 3.11 | 3.03 | 3.68 | 3.36 |
| FeO | 17.56 | 32.49 | 33.98 | 28.97 | 26.09 |
| MgO | 11.49 | 1.49 | 0.31 | 4.06 | 5.70 |
| Cr ₂ O ₃ | 55.47 | 50.86 | 50.47 | 52.37 | 53.60 |
| Ti | 0.0071 | 0.0070 | 0.0059 | 0.0082 | 0.0083 |
| Al | 0.4120 | 0.4131 | 0.4176 | 0.3938 | 0.3871 |
| Fe ₃ | 0.1372 | 0.1282 | 0.1264 | 0.1456 | 0.1316 |
| Fe ₂ | 0.4387 | 0.9292 | 0.9844 | 0.7956 | 0.7099 |
| Mg | 0.5618 | 0.0797 | 0.0169 | 0.2110 | 0.2938 |
| Cr | 1.4389 | 1.4409 | 1.4438 | 1.4433 | 1.4648 |
| Cr # | 77.7 | 77.7 | 77.6 | 78.6 | 79.1 |
| Mg # | 56.2 | 7.9 | 1.7 | 21.0 | 29.3 |

| analysis | 6 ^l | 7 ^l | 8 ^l | 9 ^p | 10 ^p |
|--------------------------------|----------------|----------------|----------------|----------------|-----------------|
| location | 5 | 5 | 6 | 1 | 1 |
| TiO ₂ | 0.16 | 0.17 | 0.30 | 0.42 | 0.44 |
| Al ₂ O ₃ | 9.48 | 9.65 | 8.38 | 10.81 | 10.97 |
| Fe ₂ O ₃ | 3.15 | 3.08 | 3.42 | 7.11 | 7.06 |
| FeO | 11.39 | 11.29 | 33.36 | 22.91 | 22.84 |
| MgO | 15.13 | 15.18 | 0.69 | 8.74 | 9.04 |
| Cr ₂ O ₃ | 59.15 | 59.07 | 51.71 | 48.33 | 49.04 |
| Ti | 0.0040 | 0.0041 | 0.0083 | 0.0106 | 0.0109 |
| Al | 0.3618 | 0.3683 | 0.3587 | 0.4300 | 0.4309 |
| Fe ₃ | 0.1098 | 0.1074 | 0.1422 | 0.2557 | 0.2506 |
| Fe ₂ | 0.2756 | 0.2734 | 0.9639 | 0.5718 | 0.5635 |
| Mg | 0.7305 | 0.7325 | 0.0376 | 0.4397 | 0.4493 |
| Cr | 1.5152 | 1.5116 | 1.4841 | 1.2900 | 1.2929 |
| Cr # | 80.7 | 80.4 | 80.5 | 75.0 | 75.0 |
| Mg # | 72.6 | 72.8 | 3.8 | 43.5 | 44.4 |

^l...inclusion in olivine pseudomorph^p... microphenocryst

Data obtained by G.D. Harper

Table C6c: Cr-spinel compositions in sample O/C-325 (sheeted dike complex)

| analysis | 1 ^P | 2 ^P | 3 ^P | 4 ^P | 5 ^I | 6 ^I | 7 ^I | 8 ^I |
|----------|----------------|-----------------|-----------------|-----------------|-----------------|-----------------|-----------------|----------------|
| location | 1 | 1 | 2 | 2 | 1 | 2 | 3 | 4 |
| TiO2 | 0.27 | 0.28 | 0.22 | 0.21 | 0.21 | 0.22 | 0.19 | 0.30 |
| Al2O3 | 10.60 | 10.83 | 10.32 | 10.31 | 10.74 | 10.69 | 10.36 | 9.65 |
| Fe2O3 | 4.13 | 4.07 | 3.68 | 3.71 | 3.66 | 3.63 | 3.95 | 4.91 |
| FeO | 11.29 | 11.41 | 11.57 | 11.55 | 11.66 | 12.77 | 12.16 | 17.21 |
| MgO | 15.46 | 15.52 | 15.31 | 15.48 | 14.99 | 14.48 | 15.03 | 11.70 |
| Cr2O3 | 56.64 | 56.70 | 57.93 | 58.59 | 56.48 | 56.77 | 57.58 | 54.45 |
| Ti | 0.0066 | 0.0068 | 0.0052 | 0.0050 | 0.0052 | 0.0053 | 0.0047 | 0.0074 |
| Al | 0.4023 | 0.4090 | 0.3902 | 0.3870 | 0.4107 | 0.4075 | 0.3916 | 0.3779 |
| Fe3 | 0.1394 | 0.1370 | 0.1255 | 0.1254 | 0.1264 | 0.1261 | 0.1343 | 0.1751 |
| Fe2 | 0.2647 | 0.2668 | 0.2738 | 0.2709 | 0.2797 | 0.3078 | 0.2873 | 0.4259 |
| Mg | 0.7421 | 0.7415 | 0.7324 | 0.7346 | 0.7251 | 0.6982 | 0.7187 | 0.5798 |
| Cr | 1.4422 | 1.4366 | 1.4696 | 1.4745 | 1.4495 | 1.4523 | 1.4606 | 1.4305 |
| Cr # | 78.2 | 77.8 | 79.0 | 79.2 | 77.9 | 78.1 | 78.9 | 79.1 |
| Mg # | 73.7 | 73.5 | 72.8 | 73.1 | 72.2 | 69.4 | 71.4 | 57.6 |
| S | | | | | | | | |
| analysis | 9 ^I | 10 ^C | 16 ^C | 18 ^P | 19 ^P | 20 ^I | 21 ^I | |
| location | 4 | 5 | 6 | 3 | 3 | 7 | 7 | |
| TiO2 | 0.33 | 0.62 | 0.33 | 0.22 | 0.20 | 0.31 | 0.28 | |
| Al2O3 | 9.73 | 12.93 | 9.21 | 10.71 | 10.69 | 10.44 | 10.37 | |
| Fe2O3 | 4.85 | 5.53 | 3.69 | 3.60 | 3.75 | 4.15 | 4.59 | |
| FeO | 17.53 | 19.89 | 28.70 | 10.97 | 10.42 | 12.93 | 13.46 | |
| MgO | 11.76 | 10.32 | 2.63 | 15.82 | 15.92 | 14.40 | 13.82 | |
| Cr2O3 | 55.10 | 48.05 | 48.23 | 58.17 | 58.21 | 56.38 | 55.99 | |
| Ti | 0.0080 | 0.0156 | 0.0092 | 0.0053 | 0.0047 | 0.0075 | 0.0067 | |
| Al | 0.3772 | 0.5079 | 0.4062 | 0.4013 | 0.4011 | 0.3984 | 0.3975 | |
| Fe3 | 0.1717 | 0.1982 | 0.1564 | 0.1212 | 0.1254 | 0.1427 | 0.1575 | |
| Fe2 | 0.4307 | 0.4948 | 0.8452 | 0.2565 | 0.2420 | 0.3088 | 0.3209 | |
| Mg | 0.5767 | 0.5123 | 0.1469 | 0.7499 | 0.7554 | 0.6953 | 0.6701 | |
| Cr | 1.4329 | 1.2658 | 1.4262 | 1.4626 | 1.4652 | 1.4437 | 1.4397 | |
| Cr # | 79.2 | 71.4 | 77.8 | 78.5 | 78.5 | 78.4 | 78.4 | |
| Mg # | 57.2 | 50.9 | 14.8 | 74.5 | 75.7 | 69.2 | 67.6 | |

^I inclusion in olivine pseudomorph

^P microphenocryst

^C inclusion in clinopyroxene

Data obtained by G.D. Harper

Table C7: Cr-spinel compositions in sample O/C-224b (pillow unit)

| analysis location | 1 ^C 1 | 2 ^C 1 | 3 ^C 2 | 4 ^C 2 | 5 ^C 3 | 6 ^C 3 |
|-------------------|---------------------|---------------------|---------------------|---------------------|---------------------|---------------------|
| TiO2 | 0.25 | 0.24 | 0.25 | 0.24 | 0.23 | 0.24 |
| Al2O3 | 11.45 | 10.86 | 11.20 | 11.25 | 11.02 | 11.42 |
| Fe2O3 | 3.61 | 3.30 | 3.52 | 3.72 | 3.26 | 3.58 |
| FeO | 15.43 | 24.25 | 14.80 | 14.91 | 15.42 | 16.30 |
| MgO | 13.13 | 7.18 | 12.88 | 12.89 | 12.74 | 12.06 |
| Cr2O3 | 55.80 | 52.97 | 55.35 | 54.92 | 55.77 | 54.59 |
| Ti | 0.0061 | 0.0060 | 0.0061 | 0.0058 | 0.0056 | 0.0059 |
| Al | 0.4352 | 0.4344 | 0.4327 | 0.4347 | 0.4253 | 0.4425 |
| Fe3 | 0.1271 | 0.1266 | 0.1255 | 0.1322 | 0.1173 | 0.1290 |
| Fe2 | 0.3767 | 0.6459 | 0.3668 | 0.3684 | 0.3852 | 0.4076 |
| Mg | 0.6309 | 0.3632 | 0.6292 | 0.6302 | 0.6217 | 0.5912 |
| Cr | 1.4227 | 1.4209 | 1.4339 | 1.4235 | 1.4436 | 1.4189 |
| Cr # | 76.6 | 76.6 | 76.8 | 76.6 | 77.2 | 76.2 |
| Mg # | 62.6 | 36.0 | 63.2 | 63.1 | 61.7 | 59.2 |

| analysis location | 7 ^C 4 | 8 ^C 4 | 9 ^P 1 | 10 ^P 1 | 11 ^P 1 | 12 ^P 1 |
|-------------------|---------------------|---------------------|---------------------|----------------------|----------------------|----------------------|
| TiO2 | 0.23 | 0.25 | 0.23 | 0.23 | 0.21 | 0.24 |
| Al2O3 | 11.21 | 11.16 | 9.04 | 8.84 | 8.82 | 8.49 |
| Fe2O3 | 3.21 | 3.29 | 3.63 | 3.31 | 3.69 | 2.97 |
| FeO | 15.56 | 15.36 | 15.34 | 15.21 | 15.10 | 20.67 |
| MgO | 12.50 | 12.52 | 12.68 | 12.54 | 12.64 | 9.09 |
| Cr2O3 | 54.93 | 55.14 | 58.21 | 58.18 | 58.34 | 57.11 |
| Ti | 0.0057 | 0.0062 | 0.0057 | 0.0058 | 0.0051 | 0.0060 |
| Al | 0.4359 | 0.4334 | 0.3494 | 0.3448 | 0.3422 | 0.3394 |
| Fe3 | 0.1165 | 0.1192 | 0.1299 | 0.1202 | 0.1319 | 0.1134 |
| Fe2 | 0.3923 | 0.3858 | 0.3808 | 0.3834 | 0.3751 | 0.5485 |
| Mg | 0.6147 | 0.6150 | 0.6203 | 0.6191 | 0.6202 | 0.4594 |
| Cr | 1.4327 | 1.4365 | 1.5099 | 1.5228 | 1.5183 | 1.5312 |
| Cr # | 76.7 | 76.8 | 81.2 | 81.5 | 81.6 | 81.9 |
| Mg # | 61.0 | 61.5 | 62.0 | 61.8 | 62.3 | 45.6 |

^C inclusion in cpx(?) pseudomorph^P.... microphenocryst

Data obtained by G.D. Harper

Table C8: Cr-spinel compositions in sample O/C-81b (Mule Mountain volcanics)

| analysis location | 1 ^P 1 | 2 ^P 1 | 7 ^C 1 | 8 ^C 1 | 9 ^C 2 |
|-------------------|---------------------|---------------------|---------------------|---------------------|---------------------|
| TiO2 | 0.23 | 0.21 | 0.38 | 0.38 | 0.31 |
| Al2O3 | 10.48 | 10.40 | 11.11 | 10.94 | 9.25 |
| Fe2O3 | 3.41 | 3.34 | 5.22 | 5.30 | 5.08 |
| FeO | 21.70 | 22.36 | 18.22 | 18.23 | 20.50 |
| MgO | 8.60 | 8.11 | 11.22 | 11.13 | 9.83 |
| Cr2O3 | 54.04 | 53.79 | 52.28 | 52.43 | 54.04 |
| Ti | 0.0058 | 0.0055 | 0.0094 | 0.0094 | 0.0079 |
| Al | 0.4168 | 0.4164 | 0.4327 | 0.4267 | 0.3655 |
| Fe3 | 0.1291 | 0.1274 | 0.1852 | 0.1877 | 0.1849 |
| Fe2 | 0.5701 | 0.5928 | 0.4484 | 0.4488 | 0.5180 |
| Mg | 0.4325 | 0.4105 | 0.5528 | 0.5493 | 0.4909 |
| Cr | 1.4418 | 1.4443 | 1.3664 | 1.3720 | 1.4320 |
| Cr # | 77.6 | 77.6 | 75.9 | 76.3 | 79.7 |
| Mg # | 43.1 | 40.9 | 55.2 | 55.0 | 48.7 |

| analysis location | 10 ^C 2 | 13 ^P 2 | 16 ^P 3 | 19 ^C 3 |
|-------------------|----------------------|----------------------|----------------------|----------------------|
| TiO2 | 0.25 | 0.49 | 0.50 | 0.30 |
| Al2O3 | 7.94 | 14.98 | 18.12 | 10.89 |
| Fe2O3 | 4.64 | 9.75 | 8.76 | 7.43 |
| FeO | 20.13 | 21.13 | 20.87 | 18.95 |
| MgO | 9.71 | 10.64 | 10.68 | 9.82 |
| Cr2O3 | 56.33 | 41.73 | 38.42 | 49.38 |
| Ti | 0.0062 | 0.0120 | 0.0121 | 0.0075 |
| Al | 0.3155 | 0.5755 | 0.6947 | 0.4338 |
| Fe3 | 0.1708 | 0.3254 | 0.2948 | 0.2615 |
| Fe2 | 0.5149 | 0.4900 | 0.4874 | 0.4633 |
| Mg | 0.4881 | 0.5170 | 0.5178 | 0.4947 |
| Cr | 1.5024 | 1.0757 | 0.9878 | 1.3195 |
| Cr # | 82.6 | 65.1 | 58.7 | 75.3 |
| Mg # | 48.7 | 51.3 | 51.5 | 51.6 |

^C inclusion in cpx
^P microphenocrysts

APPENDIX D

**FAULT SLIP DATA AND SENSE OF SHEAR DETERMINED IN FOLIATED
AND MYLONITIC ROCKS FROM THE WILD ROGUE WILDERNESS,
SW OREGON**

Table D1: Fault slip data from Rogue River fault zone

| Outcrop Locality | Fault-# | Striated fault | | | Striation | | Hanging block |
|---------------------|---------|----------------|-----|----|-----------|--------|------------------|
| | | Strike | Dip | | Trend | Plunge | |
| <u>Rogue River</u> | | | | | | | |
| | 12* | 90 | 22 | S | 140 | 17 | down |
| | 14* | 234 | 22 | N | 340 | 70 | down |
| | | | | W | | | |
| | 31* | 14 | 60 | E | 137 | 48 | down |
| | 34* | 200 | 7 | N | 300 | 6 | down |
| | | | | W | | | |
| | 40* | 105 | 85 | SW | 272 | 67 | down |
| | 54* | 165 | 56 | W | 321 | 30 | down |
| | 56* | 15 | 30 | E | 125 | 29 | down |
| | 57* | 108 | 49 | SW | 116 | 8 | down |
| | 58* | 84 | 45 | S | 150 | 42 | down |
| <u>Mule Creek</u> | | | | | | | |
| | 106 | 173 | 50 | W | 312 | 37 | down |
| | 107 | 177 | 49 | W | 310 | 40 | down |
| | 105 | 110 | 10 | SW | 225 | 8 | down |
| | 110 | 130 | 74 | SW | 275 | 63 | down |
| | 112 | 209 | 39 | N | 291 | 39 | down |
| | | | | W | | | |
| | 114 | 20 | 85 | SE | 195 | 40 | down |
| | 117 | 56 | 55 | SE | 221 | 20 | down |
| | 121 | 26 | 20 | SE | 80 | 15 | down |
| | 122 | 24 | 68 | SE | 40 | 30 | down |
| | 123 | 240 | 40 | N | 347 | 38 | down |
| | | | | W | | | |
| | 124 | 186 | 89 | W | 2 | 70 | down |
| | 126 | 144 | 59 | SW | 310 | 22 | down |
| | 127 | 150 | 75 | SW | 216 | 73 | down |
| | 131 | 128 | 46 | SW | 246 | 42 | down |

Table D2: Fault-slip data of amphibole shear bands in cumulate gabbro screens

| Outcrop number | Sense of Slip* | Fault Strike | Fault Dip (rhr) | Striae Trend | Striae Plunge |
|----------------|----------------|--------------|-----------------|--------------|---------------|
| O/C-356 | down | 290 | 74 | 107 | 12 |
| O/C-360 | up | 284 | 85 | 286 | 23 |
| O/C-360 | down | 296 | 72 | 112 | 13 |
| O/C-360 | up | 117 | 70 | 128 | 28 |
| O/C-361 | up | 104 | 58 | 114 | 16 |
| O/C-361 | up | 312 | 82 | 316 | 28 |
| O/C-361 | up | 86 | 70 | 100 | 33 |
| O/C-362 | down | 130 | 70 | 180 | 65 |
| O/C-362 | down | 143 | 80 | 158 | 55 |
| O/C-362 | up | 66 | 67 | 87 | 40 |
| O/C-363 | up | 80 | 70 | 97 | 38 |

* indicates movement of the hanging block

rhr right hand rule

Table D3a: Fault-slip data of cemented faults in the sheeted dike complex, domain A

| Location | Sense of Slip* | Fault Strike | Fault Dip (rhr) | Striae Trend | Striae Plunge |
|-----------|----------------|--------------|-----------------|--------------|---------------|
| O/C-355.1 | up | 128 | 50 | 300 | 9 |
| O/C-355.2 | up | 123 | 27 | 185 | 24 |
| O/C-355.3 | down | 342 | 75 | 351 | 30 |
| O/C-355.4 | up | 350 | 50 | 74 | 50 |
| O/C-355.5 | down | 315 | 83 | 318 | 26 |
| O/C-355.6 | down | 355 | 55 | 24 | 35 |
| O/C-356.1 | up | 90 | 63 | 130 | 52 |
| O/C-356.2 | up | 305 | 78 | 85 | 72 |
| O/C-357.1 | up | 178 | 25 | 301 | 21 |
| O/C-357.2 | up | 253 | 20 | 330 | 20 |
| O/C-357.3 | up | 304 | 75 | 80 | 69 |
| O/C-357.4 | up | 295 | 32 | 300 | 3 |
| O/C-357.5 | up | 0 | 50 | 154 | 28 |
| O/C-357.6 | up | 337 | 33 | 155 | 1 |
| O/C-357.7 | up | 20 | 65 | 179 | 37 |
| O/C-358.1 | up | 358 | 65 | 55 | 61 |
| O/C-358.2 | up | 12 | 38 | 88 | 37 |
| O/C-358.3 | up | 57 | 66 | 105 | 59 |
| O/C-359.1 | up | 85 | 43 | 105 | 18 |
| O/C-359.2 | up | 303 | 54 | 104 | 24 |
| O/C-359.3 | up | 294 | 64 | 101 | 25 |
| O/C-359.4 | down | 294 | 29 | 325 | 16 |
| O/C-359.5 | up | 56 | 66 | 105 | 59 |
| O/C-359.6 | down | 140 | 52 | 180 | 39 |
| O/C-359.7 | up | 60 | 64 | 85 | 41 |
| O/C-359.8 | up | 320 | 82 | 123 | 64 |
| O/C-359.9 | up | 105 | 61 | 109 | 8 |

* Sense of slip of the hangingwall block
rhr right hand rule

Table D3b: Fault-slip data of cemented faults in the sheeted dike complex, domain B

| Location | Sense of Slip* | Fault Strike | Fault Dip (rhr) | Striae Trend | Striae Plunge |
|-----------|----------------|--------------|-----------------|--------------|---------------|
| O/C-360.1 | up | 174 | 61 | 177 | 5 |
| O/C-360.2 | down | 273 | 89 | 93 | 20 |
| O/C-360.3 | down | 285 | 86 | 103 | 25 |
| O/C-360.4 | up | 68 | 64 | 94 | 42 |
| O/C-360.5 | up | 35 | 75 | 87 | 71 |
| O/C-360.6 | down | 212 | 30 | 220 | 5 |
| O/C-360.7 | up | 224 | 49 | 355 | 41 |
| O/C-361.1 | up | 80 | 69 | 163 | 69 |
| O/C-361.2 | down | 312 | 80 | 317 | 28 |
| O/C-361.3 | up | 104 | 58 | 115 | 17 |
| O/C-361.4 | up | 337 | 29 | 95 | 26 |
| O/C-361.5 | up | 105 | 47 | 135 | 28 |
| O/C-362.1 | down | 105 | 85 | 273 | 67 |
| O/C-362.2 | up | 292 | 47 | 80 | 30 |
| O/C-362.3 | up | 297 | 54 | 89 | 33 |
| O/C-362.4 | up | 50 | 84 | 54 | 34 |
| O/C-362.5 | down | 225 | 70 | 33 | 30 |
| O/C-362.6 | up | 214 | 86 | 241 | 81 |
| O/C-362.7 | up | 145 | 70 | 178 | 56 |
| O/C-362.8 | up | 131 | 66 | 180 | 59 |
| O/C-363.1 | up | 92 | 43 | 110 | 16 |
| O/C-363.2 | up | 214 | 36 | 307 | 36 |
| O/C-363.3 | up | 165 | 65 | 324 | 38 |
| O/C-365.1 | up | 118 | 31 | 134 | 9 |
| O/C-365.2 | down | 140 | 41 | 296 | 19 |
| O/C-365.3 | up | 85 | 35 | 110 | 16 |
| O/C-365.4 | up | 73 | 15 | 127 | 12 |

* Sense of slip of the hangingwall block
rhr right hand rule

Table D4: Fault-slip data for cemented faults in the sheeted dike complex, domain D

| Outcrop number | Sense of Slip* | Fault Strike | Fault Dip (rhr) | Striae Trend | Striae Plunge |
|----------------|----------------|--------------|-----------------|--------------|---------------|
| | up | 18 | 76 | 26 | 30 |
| | up | 224 | 45 | 355 | 37 |
| | up | 158 | 30 | 248 | 30 |
| | down | 270 | 59 | 84 | 10 |
| | down | 165 | 89 | 166 | 37 |
| | up | 138 | 84 | 143 | 37 |
| | down | 145 | 45 | 156 | 11 |
| | down | 206 | 80 | 17 | 43 |
| | down | 234 | 58 | 45 | 14 |
| | down | 205 | 84 | 206 | 12 |
| | up | 241 | 48 | 18 | 37 |
| | down | 262 | 48 | 52 | 29 |
| | up | 312 | 41 | 60 | 40 |
| | up | 14 | 89 | 14 | 5 |
| | up | 164 | 54 | 187 | 28 |
| | up | 294 | 77 | 347 | 74 |
| | up | 322 | 63 | 347 | 40 |
| | up | 210 | 47 | 353 | 33 |
| | up | 302 | 89 | 302 | 4 |
| | down | 192 | 89 | 12 | 14 |
| | up | 340 | 74 | 351 | 34 |
| | down | 200 | 55 | 209 | 12 |
| | up | 132 | 62 | 184 | 56 |
| | down | 117 | 72 | 123 | 19 |

* indicates movement of the hanging wall

rhr right hand rule

Table D5 continued

| Sample-ID | Rock type | Foliation & SB | | | Microfaults in PC | | PC | Other fabric elements | | | | Brittle def. (comments) | |
|-----------------------------------------|---------------|----------------|------------|-------------|--------------------|----------------------|----|-----------------------|----------|----------|----------------------|-------------------------|----------------------|
| | | oblique GSF | C/S fabric | C'/S fabric | synth low \angle | antith high \angle | | σ | δ | Tiling ? | Folds ? | | Offset ! |
| Samples from the Blossom Bar shear zone | | | | | | | | | | | | | |
| O/C-17S31 | mylonite | D | - | D | - | - | - | D | - | - | - | LPO, R#, SG, U | R+R' \rightarrow D |
| O/C-17S34 | ultramylonite | - | - | D | - | - | - | - | - | - | - | LPO, R# | |
| O/C-17S35 | ultramylonite | - | - | D | - | - | S | - | S | - | - | LPO, R# | |
| O/C230S61 | mylonite | S | - | - | S | S | - | - | - | - | - | LPO, R#, SG, U | |
| O/C230S62 | protomylonite | - | - | - | D | - | - | - | D | - | - | SG, R#, LPO | (f.n.) |
| O/C-233 | mylonite | S | - | - | - | - | - | - | - | - | qz'v \rightarrow D | LPO, R#, SG, U | |

Table D5: Microstructures and fabric elements of foliated and mylonitic samples from the Wild Rogue Wilderness

II. Mylonites essentially consisting of chlorite, epidote, plagioclase (part. or compl. sauss.), quartz, ±hornblende, ±clinozoisite, ±actinolite

| Sample-ID | Rock type | Foliation & SB | | | Microfaults in PC | | | PC | | | Other fabric elements | | | Brittle def. (comments) |
|-----------------------------------------|---------------|----------------|------------|-------------|-------------------|---------------|---|----|----------|---------|-----------------------|-------------------------|---|-------------------------|
| | | oblique GSF | C/S fabric | C'/S fabric | synth low ∠ | antith high ∠ | σ | δ | Tiling ? | Folds ? | Offset ! | Crystal plasticity (qz) | | |
| Samples from the metatonalite unit | | | | | | | | | | | | | | |
| O/C11S16c | mylonite | - | - | S | S | - | S | - | - | - | - | - | - | LPO, R#, SG |
| O/C-368E | ultramylonite | - | - | S | S | S | - | S | - | S | - | - | - | LPO, R# |
| Samples from the Blossom Bar shear zone | | | | | | | | | | | | | | |
| O/C-45S42 | mylonite | - | - | S | - | - | - | - | - | - | - | - | - | LPO, R# |
| O/C-48S44 | Mylonite | - | - | - | S | S | - | S | S | - | - | - | - | LPO, R#, SG, U |
| O/C-236 | Mylonite | - | - | S | S | - | S | - | - | - | - | - | - | LPO, R#, SG |
| O/C-238 | Mylonite | - | - | S | - | - | - | - | - | - | - | - | - | R# cc |
| O/C-418A | Mylonite | - | - | D | - | - | D | - | - | - | - | - | - | LPO, R#, SG - |

Table D5: Microstructures and fabric elements of foliated and mylonitic samples from the Wild Rogue Wilderness

III. Mylonites essentially consisting of hornblende, plagioclase (part. or compl. sauss.), quartz, epidote, clinzoisite, chlorite, actinolite.

| Sample-ID | Rock type | Foliation & SB | | | Microfaults in PC | | | PC | | | Other fabric elements | | | Brittle def. (comments) |
|-------------------------------------------------------------------------|---------------|----------------|------------|------------|--------------------|----------------------|----------------|----------|----------|---------|-----------------------|-------------------------|--|-------------------------|
| | | oblique GSF | C/S fabric | C/S fabric | synth low \angle | antith high \angle | σ | δ | Tiling ? | Folds ? | Offset ! | Crystal plasticity (qz) | | |
| Samples from the contact zone between metatonalite and metagabbro units | | | | | | | | | | | | | | |
| O/C-13S28 | protomylonite | D | D | - | - | - | d ^a | - | - | - | SG, R#, U | | | |
| O/C371B.1 | protomylonite | S | - | - | - | - | s ^a | - | - | - | LPO, R#, SG | | | |
| O/C371B.2 | protomylonite | - | - | - | - | - | s ^a | - | - | - | LPO, R#, SG | | | R' → S |
| Samples from the metagabbro unit | | | | | | | | | | | | | | |
| GH-97-15a | protomylonite | - | - | - | - | - | - | - | - | - | R#, SG, U | | | |
| O/C-228 | protomylonite | - | - | - | - | - | - | - | - | - | R#, SG, U | | | |
| O/C-229 | mm-scale | - | - | - | - | - | - | - | - | - | SG, U | | | |
| sb's | | | | | | | | | | | | | | |
| Samples from the Blossom Bar shear zone | | | | | | | | | | | | | | |
| O/C-234 | protomylonite | - | D | D | D | - | - | - | - | - | R#, SG, U | | | |
| O/C-237 | protomylonite | - | - | - | - | - | - | - | - | - | R#, SG, U | | | |

Table D5: Microstructures and fabric elements of foliated and mylonitic samples from the Wild Rogue Wilderness

IV. Mylonites essentially consisting of hornblende, plagioclase (part. or compl. sauss.), epidote, actinolite, chlorite (no quartz present!)

| Sample-ID | Rock type | Foliation & SB | | | Microfaults in PC | | | PC | | | Other fabric elements | | | Brittle def. (comments) |
|-------------------------------------------------------------------------|-----------|----------------|------------|-------------|--------------------|----------------------|----------------|----------|----------|---------|-----------------------|-------------------------|----------|-------------------------|
| | | oblique GSF | C/S fabric | C'/S fabric | synth low \angle | antith high \angle | σ | δ | Tiling ? | Folds ? | Offset ! | Crystal plasticity (qz) | | |
| Samples from the contact zone between metatonalite and metagabbro units | | | | | | | | | | | | | | |
| O/C-13S22 | mylonite? | - | - | - | S | S | S ^a | - | S | - | - | no quartz | R+R' → S | |
| O/C-13S23 | mylonite? | - | - | - | S | S | S ^a | - | S | - | - | no quartz | cc F | |
| O/C-324 | | | | | | | | | | | | | | |
| O/C-325 | | | | | | | | | | | | | | |
| Samples from the metagabbro unit | | | | | | | | | | | | | | |
| O/C-216 | mylonite? | - | - | S | S | S | S ^a | - | - | - | - | no quartz | | |
| O/C-373C | mylonite? | - | S | - | - | S | S ^a | - | - | - | - | no quartz | R' → S | |
| O/C-374b.4 | mylonite? | - | S | - | - | S | S ^a | - | - | - | - | no quartz | R' → S | |
| O/C-384 | mylonite | - | - | D | - | - | d ^a | - | - | - | - | no quartz | | |
| O/C-417b | mylonite | - | - | - | - | - | D | - | - | - | - | no quartz | | |
| Samples from the Blossom Bar shear zone | | | | | | | | | | | | | | |
| O/C45aS41 | mylonite | - | S | - | - | - | S ^a | - | - | - | - | no quartz | | |

Table D5: Microstructures and fabric elements of foliated and mylonitic samples from the Wild Rogue Wilderness

V. Mylonites essentially consisting of plagioclase (part. or compl. sauss.), quartz and mica, ±epidote, ±clinozoisite, ±actinolite, ±chlorite

| Sample-ID | Rock type | Foliation & SB | | | Microfaults in PC | | | PC | | | Other fabric elements | | | Brittle def. (comments) |
|-----------------------------------------|-----------------|----------------|------------|------------|-------------------|---------------|---|----|----------|---------|-----------------------|-------------------------|----------------|-------------------------|
| | | oblique GSF | C/S fabric | C/S fabric | synth low ∠ | antith high ∠ | σ | δ | Tiling ? | Folds ? | Offset ! | Crystal plasticity (qz) | | |
| Samples from the metagabbro unit | | | | | | | | | | | | | | |
| O/C-12S20 | protomylonite | - | - | - | - | - | - | - | - | - | - | - | U, SG, R# | □ pl. |
| O/C-372b | mylonite | S | S | - | - | - | S | - | S | - | - | S | LPO, R#, SG, U | |
| O/C-417A | mylonite | S | S | - | - | - | - | - | - | - | - | - | LPO, R#, U, SG | |
| GDH-97-6 | protomylonite | - | S | - | - | - | S | - | S | - | - | - | U, SG, R# | |
| Samples from the Blossom Bar shear zone | | | | | | | | | | | | | | |
| O/C-17S32 | cataclastic o.p | - | - | - | - | - | - | - | - | - | - | - | U, SG, R# | □ pl. |
| O/C-19S34 | cataclastic o.p | - | - | - | - | - | - | - | - | - | - | - | U, SG, R# | □ pl. |

Explanation to table D5

The sense of shear indicators are described in detail in chapter.... The following abbreviations and symbols are used in the table:

| | | |
|-----------------------------|----------------------------------------------------------------|------------------------------------------------------------------------------|
| GSF | grain shape fabric | The following quartz fabrics are listed according to their importance |
| SB | shear band | in individual thin sections: |
| PC | porphyroblast | LPO: Lattice preferred orientation |
| synth. low \angle : | synthetic offset along low-angle microfault in porphyroblast | R#: Grain size reduction by recrystallization |
| antith. high \angle : | antithetic offset along high-angle microfault in porphyroblast | SG Subgrains |
| σ | σ -type winged porphyroblast | U Undulatory extinction |
| δ | δ -type winged porphyroblast | |
| D | sense of shear indicators are consistent with dextral shear | R' or R \rightarrow : R' or R-type Riedel shear indicate sense of shear |
| S | sense of shear indicators are consistent with sinistral shear | \square pl. strongly fractured plagioclase (albite) in fine grained matrix |
| s^a, d^a | asymmetry of augen-shaped amphibole indicates sense of shear | cc F cataclasis zone parallel foliation |
| qz ∇ \rightarrow : | offset of slightly recrystallized quartz vein | |

Table D6: Shear foliation, stretching lineation and sense of shear in present day coordinates; Blossom Bar shear zone

| Location (Sample) | Sense of Shear* | Sense of Shear** | Foliation Strike | Foliation Dip (rhr) | Lineation Trend | Lineation Plunge |
|----------------------------------------------|--------------------|---------------------|---------------------|------------------------|--------------------|---------------------|
| O/C-17S31 | D | down | 220 | 73 | 261 | 66 |
| O/C-17S34 | D | down | 212 | 74 | 12 | 51 |
| O/C-17S35 | D | down | 222 | 76 | 273 | 72 |
| O/C230S61 | S | down | 200 | 75 | 275 | 74 |
| O/C230S62 | S | down | 200 | 89 | 212 | 85 |
| O/C-233 | S | down | 210 | 88 | 300 | 88 |
| O/C-45S42 | S | down | 204 | 85 | 231 | 78 |
| O/C-48S44 | S | down | 230 | 61 | 278 | 52 |
| O/C-236 | S | down | 351 | 82 | 140 | 70 |
| O/C-238 | S(?) | ? | 215 | 80 | ? | ? |
| O/C-418A | D | down | 186 | 82 | 298 | 82 |
| O/C-234 | D | up | 18 | 89 | 28 | 84 |
| O/C45aS41 | S | down | 225 | 68 | 292 | 66 |
| O/C-17S32 | ? | ? | 383 | 52 | 306 | 52 |
| Foliation and lineation measured in outcrops | | | | | | |
| O/C-45 | ? | ? | 225 | 68 | 300 | 60 |
| O/C-46 | ? | ? | 34 | 85 | 50 | 73 |
| O/C-329 | ? | ? | 64 | 62 | 90 | 72 |
| O/C-330 | ? | ? | 25 | 75 | 120 | 76 |
| O/C-330 | ? | ? | 15 | 78 | 56 | 72 |
| O/C-331 | ? | ? | 204 | 64 | 350 | 37 |

* indicates sense of shear determined in thin section (see table D5)

** indicates motion of the hangingwall block in present day coordinates

Table D6: Shear foliation, stretching lineation and sense of shear in present day coordinates; metagabbro unit

| Location (Sample) | Sense of Shear* | Sense of Shear** | Foliation Strike | Foliation Dip (rhr) | Lineation Trend | Lineation Plunge |
|----------------------------------------------|--------------------|---------------------|---------------------|------------------------|--------------------|---------------------|
| O/C-228 | ? | ? | 56 | 83 | 63 | 49 |
| O/C-229 | ? | ? | 201 | 82 | 6 | 55 |
| O/C-216 | S | up | 55 | 53 | 228 | 12 |
| O/C-373C | S | up | 61 | 75 | 74 | 43 |
| O/C-374b.4 | S | up | 55 | 90 | 55 | 27 |
| O/C-384 | D | down | 54 | 75 | 56 | 10 |
| O/C-417b | D | up | 57 | 77 | 56 | 4 |
| O/C-372b | S | down | 180 | 80 | 351 | 44 |
| O/C-417A | S | up | 32 | 55 | 35 | 5 |
| GDH-97-6 | S | up | 353 | 85 | 356 | 37 |
| Foliation and lineation measured in outcrops | | | | | | |
| GH-97-14 | ? | ? | 175 | 74 | 343 | 38 |
| GH-97-19a | ? | ? | 16 | 88 | 15 | 19 |
| O/C-372 | ? | ? | 205 | 78 | 30 | 27 |
| O/C-372 | ? | ? | 37 | 72 | 35 | 42 |
| O/C-373 | ? | ? | 45 | 89 | 47 | 20 |
| O/C-374 | ? | ? | 40 | 59 | 63 | 35 |
| O/C-374 | ? | ? | 60 | 70 | 69 | 26 |

* indicates sense of shear determined in thin section (see table D5)

** indicates motion of the hangingwall block in present day coordinates

Table D6: Shear foliation, stretching lineation and sense of shear in present day coordinates; metatonalite unit

| Location (Sample) | Sense of Shear* | Sense of Shear** | Foliation Strike | Foliation Dip (rhr) | Lineation Trend | Lineation Plunge |
|-------------------------------------------------------------------------|--------------------|---------------------|---------------------|------------------------|--------------------|---------------------|
| Samples from the metatonalite unit | | | | | | |
| MRH-73 | D | up | 23 | 70 | 43 | 46 |
| O/C-9-S12 | S | up | 54 | 85 | 58 | 37 |
| O/C-14S21 | D | up | 46 | 75 | 52 | 25 |
| O/C-65 | D | up | 30 | 67 | 59 | 50 |
| O/C-366A | S | up | 53 | 85 | 63 | 63 |
| O/C-366B | S | down | 233 | 79 | 48 | 29 |
| O/C-366C | S | up | 61 | 81 | 71 | 48 |
| O/C-367 | D | up | 352 | 66 | 22 | 50 |
| O/C-368A | D | up | 40 | 84 | 45 | 44 |
| O/C-368c.1 | S | up | 11 | 78 | 23 | 47 |
| O/C-368c.2 | S | up | 28 | 50 | 80 | 44 |
| O/C-368d.1 | S | up | 7 | 68 | 19 | 30 |
| O/C-370B | D | up | 30 | 77 | 35 | 24 |
| O/C11S16c | S | up | 52 | 72 | 66 | 42 |
| O/C-368E | S | down | 183 | 63 | 325 | 52 |
| Samples from the contact zone between metatonalite and metagabbro units | | | | | | |
| O/C-371A | S | up | 40 | 70 | 51 | 30 |
| O/C-13S26 | D | up | 35 | 74 | 49 | 42 |
| O/C-13S28 | D | up | 52 | 71 | 59 | 23 |
| O/C371B.1 | S | down | 218 | 77 | 31 | 32 |
| O/C371B.2 | S | down | 211 | 77 | 23 | 35 |
| O/C-13S22 | S | down | 213 | 83 | 23 | 55 |
| O/C-13S23 | S | up | 58 | 83 | 64 | 44 |
| O/C-324 | ? | ? | 215 | 65 | 16 | 35 |
| O/C-325 | ? | ? | 233 | 89 | 53 | 5 |
| Foliation and lineation measured in outcrops | | | | | | |
| MRH-10 | ? | ? | 42 | 82 | 46 | 32 |
| MRH-73 | ? | ? | 35 | 77 | 23 | 33 |
| O/C-9-S14 | ? | ? | 20 | 68 | 32 | 30 |
| O/C-325 | ? | ? | 210 | 65 | 14 | 24 |
| O/C-370 | ? | ? | 47 | 79 | 57 | 45 |
| O/C-370 | ? | ? | 39 | 90 | 42 | 34 |
| O/C-370 | ? | ? | 211 | 83 | 32 | 36 |
| O/C-370 | ? | ? | 27 | 78 | 49 | 55 |
| O/C-371 | ? | ? | 216 | 76 | 26 | 35 |
| O/C-371 | ? | ? | 213 | 88 | 28 | 40 |

* indicates sense of shear determined in thin section (see table D5)

** indicates motion of the hangingwall block in present day coordinates

Table D7: Fault-slip data for cemented faults cutting mylonitic foliation in the metatonalite unit

| Outcrop number | Sense of Slip* | Fault Strike | Fault Dip (rhr) | Striae Trend | Striae Plunge |
|----------------|----------------|--------------|-----------------|--------------|---------------|
| | up | 263 | 65 | 64 | 35 |
| | up | 44 | 73 | 55 | 36 |
| | up | 280 | 85 | 96 | 39 |
| | up | 12 | 50 | 70 | 45 |
| | up | 265 | 88 | 85 | 5 |
| | up | 358 | 49 | 65 | 45 |
| | up | 285 | 80 | 100 | 38 |
| | up | 1 | 46 | 70 | 45 |
| | up | 38 | 76 | 48 | 39 |
| | down | 210 | 24 | 275 | 22 |
| | down | 70 | 67 | 157 | 67 |
| | down | 86 | 68 | 160 | 68 |
| | up | 117 | 45 | 253 | 35 |
| | up | 70 | 42 | 240 | 10 |
| | up | 83 | 54 | 250 | 18 |
| | up | 15 | 49 | 60 | 38 |
| | down | 133 | 82 | 144 | 51 |
| | up | 26 | 77 | 43 | 50 |
| | up | 105 | 60 | 264 | 34 |
| | up | 265 | 68 | 69 | 35 |
| | up | 5 | 54 | 53 | 46 |
| | up | 11 | 80 | 16 | 32 |
| | up | 23 | 75 | 38 | 45 |
| | up | 49 | 89 | 49 | 22 |
| | up | 40 | 79 | 45 | 31 |
| | down | 217 | 70 | 30 | 21 |
| | down | 226 | 88 | 44 | 43 |
| | down | 190 | 65 | 3 | 19 |
| | down | 181 | 80 | 354 | 38 |

* indicates movement of hanging-wall block
rhr right hand rule

APPENDIX E

QUALITY CHECK OF THE TRACE ELEMENT ANALYSIS BY INDUCTIVELY COUPLED PLASMA MASS SPECTROMETRY (ICP-MS) AT THE UNION COLLEGE GEOLOGY DEPARTMENT, SCHENECTADY, NY.

E.1 Introduction

In addition to the very good accuracy and precision of inductively coupled plasma mass spectrometry (ICP-MS) for trace element analysis, the detection limits are very low and are not easily matched by other analytical techniques (e.g., Longerich et al., 1990). ICP-MS is a suitable technique for the accurate measurement of low levels of incompatible elements in rock samples collected for this study. Yet, how capable is the ICP-MS, a VG PlasmaQuad2+, at the Union College Geology Department? The accuracy and precision of the ICP-MS as well as the sample preparation method by acid digestion have been tested and evaluated. Following the procedure for acid digestion routinely used at Union College, problems with Ta and Nb staying in solution became apparent. A modification of the routine procedure, adding 50 μl of 50% hydrofluoric acid to 15 ml analytical solutions, was found to be essential to stabilize Ta and Nb in solution.

ICP-MS results are only as good as sample preparation, i.e. the completeness of sample dissolution. Some of the analyzed rare earth and trace elements are partitioned into resistant minerals which are hard to dissolve by acid digestion, and can most easily be brought into solution using a fusion technique prior to dissolution. Hard to dissolve minerals include zircon, rutile, tourmaline, staurolite, and chromite. The fusion step is generally unnecessary for mafic subalkaline igneous rocks, because chemically resistant minerals such as zircon are not in equilibrium with subalkaline rocks of basaltic and andesitic composition. All of the collected basaltic and andesitic samples could be completely digested by a mixed acid attack in screw-top Teflon® vials using conventional heating. Samples that might contain well-crystallized zircon

and other refractory minerals were sent off for analysis at Washington State University Geoanalytic Laboratory. This laboratory routinely decomposes samples with a lithium borate fusion attack.

The quality of trace element data obtained by ICP-MS is evaluated in this chapter. Precision and accuracy of the determination of 28 trace elements is presented and discussed as well as data that show the effectiveness of adding hydrofluoric acid as a complexing agent to the analytical solutions to stabilize Ta and Nb in solution. Evidence for incomplete dissolution using acid digestion has not been found; however, the possibility is discussed.

E.2 Sample preparation

E.2.1 Internal standards

Internal standards, which are added to all solutions for interference and drift correction (section E.3.2 and E.3.3), are prepared by mixing Spex® 1000 $\mu\text{g ml}^{-1}$ single-element solutions and diluting to yield the desired element concentrations. To a 100 ml volumetric flask, 5 ml each of the Spex single-element solutions ($1000 \pm 2 \mu\text{g ml}^{-1}$) of In, Re, and Bi and 15 ml of Ga were added with a high-precision pipette (pipette error is less than $\pm 2\%$). Then, 8 ml of high purity HNO_3 was added and the flask filled to volume with de-ionized H_2O . The concentration of Ga in the internal standard solution is $150 \pm 3 \mu\text{g ml}^{-1}$ and of In, Re, and Bi $50 \pm 1 \mu\text{g ml}^{-1}$. The HNO_3 concentration is about 6%. This internal standard solution is enough for up to 650 samples.

E.2.2 Acid digestion procedure

Acid digestion has several advantages over flux fusion methods: it is less time consuming, it involves fewer steps reducing the risk of contamination, and analytical solutions have higher concentrations in the sample solution allowing better analytical precision and shorter run time. To keep the contamination at a minimum, only high purity (double distilled) acids and de-ionized H_2O were used. Disadvantages of acid digestion are: extremely hazardous hydrofluoric acid are used, and a number of chemically resistant

minerals may not completely dissolve, especially zircon and rutile, but possibly also tourmaline, staurolite, and chromite.

E.2.1.1 Weighing and dissolution procedure

17 ml Teflon screw-top vials were cleaned by soaking the open vials and screw-top caps for several hours in boiling 20% HNO₃. Then, the Teflon vials were rinsed with de-ionized H₂O, filled with 9 ml high purity HF and capped. After about ten minutes, the Teflon vials (half-filled with HF) were turned over and left to soak for another ten minutes standing on the caps. Finally, the acid was discarded and the Teflon vials and caps were rinsed with de-ionized H₂O and placed in an oven to dry.

The following dissolution procedure was applied to prepare sample, standard and blank solutions for each analytical run. Blank solutions do not contain any dissolved solids; therefore, step (1) of the following was omitted preparing the acid blanks. The steps were as follows:

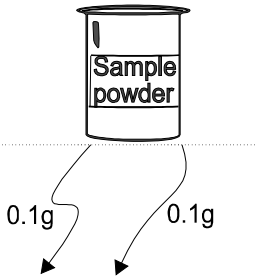
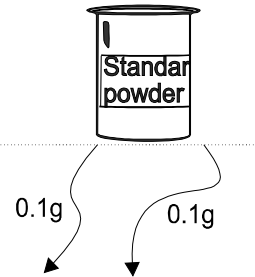
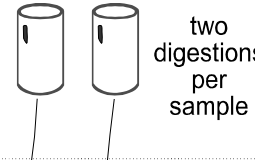
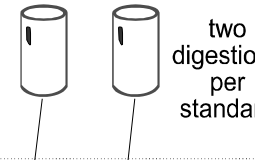
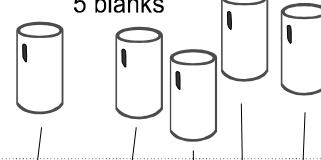
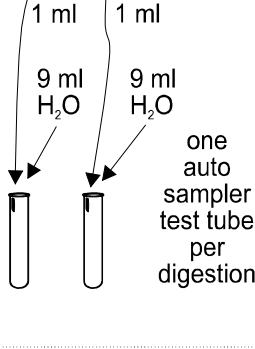
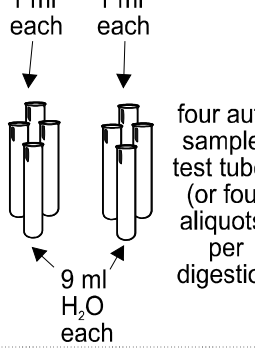
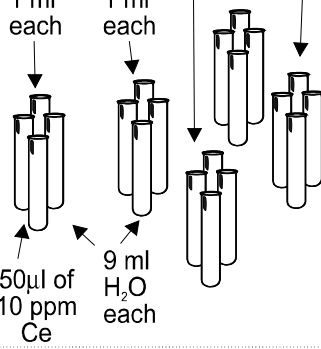
- (1) 0.1000 ± 0.0002 g of rock powder was weighed in a clean Teflon vial. As illustrated in figure E.1, duplicates of standards and samples were prepared (i.e., 0.1g of sample powder were weighed in each of two Teflon vials per sample). Any sample dust adhering to the weighing paper could affect the accuracy of the weighing procedure. It was, therefore, necessary to pre-contaminate the weighing paper with the rock powder being weighed. Furthermore, the rim of the Teflon vials must be cleaned from any rock dust to avoid damage of the rim when the vials are capped. The cleaning of the rims also ensures that the caps seal properly.
- (2) 0.5 ml of HNO₃ and 1.5 ml of HF were added to the rock powders in the Teflon vials. Five empty Teflon vials were also filled with 0.5 ml of HNO₃ and 1.5 ml of HF: these are the blanks (figure E1). All Teflon vials were capped, clamped into aluminum retainers and heated in an oven at 100°C overnight. Even though the aluminum retainers ensure that the Teflon vials remain sealed when the pressure inside the vials rises, the oven must be under an exhaust hood in case any vapor escapes. Fast reacting silicates and glass are decomposed in this step. Further dissolution of hard to dissolve minerals are made in the following steps.

- (3) Samples, standards and blanks were dried by placing the uncapped Teflon vials in a large Teflon bowl in which filtered hot air ($\sim 100^{\circ}\text{C}$) was pumped. Ventilation occurred through a conduit in the lid of the Teflon bowl. The evaporation apparatus was mounted beneath the exhaust hood.
- (4) 0.5 ml of HNO_3 and 1.5 ml of HF were again added to the Teflon vials. Then, the Teflon vials were capped, clamped into aluminum retainers, and heated in an oven at 120°C overnight.
- (5) Samples, standards and blanks were taken to dryness using the evaporation apparatus mounted in the hood (same as step 3)
- (6) 1 ml of HNO_3 and 1 ml of de-ionized H_2O were added. The Teflon vials were capped, clamped into aluminum retainers, and heated in an oven at 100°C overnight.
- (7) Samples, standards and blanks were again dried (same as step 3). During the last evaporation step, most fluoride escapes as HF and very little (or no) HF is retained. It is not desirable to dispel the complexing agent HF completely after the dissolution of aluminosilicate materials if Nb and Ta are to be kept in solution (Goguel, 1992). Because HF is almost completely driven out through step (7), it is necessary to add a certain amount of HF later (discussed in detail in sections 5.7.1.6 and 5.7.2.6).
- (8) 2.1 ml HNO_3 , 12.7 ml de-ionized H_2O , and 0.15 ml of the internal standard solution were added using high precision automatic pipettes. Teflon vials were capped, clamped into aluminum retainers, and heated in an oven at 100°C . After about two hours, the Teflon vials were taken out of the oven, shaken, then placed back in the oven and heated overnight.
- (9) All solutions were visually inspected for the completeness of dissolution. Precipitates or undissolved residue were not visually observed in any of the prepared solutions. Then, 0.05 ml of 50% HF was added to the solution in the Teflon vials.

Because 15 ml of solution was obtained by digesting 0.1g of rock powder in a screw-top Teflon vial (figure E.1a), the solution in the Teflon vial had a rock/solution proportion of 1:150 (except for the blanks which contained no dissolved solids). The final HNO_3 concentration was about 10% and HF concentration about 0.17%.

Figure E.1

- a. Illustration of the main steps of the preparation of samples, standards and blanks. The term “a digestion of a sample” is defined as weighing of 0.1g of rock powder in a Teflon vial and dissolving the rock powder to obtain 15 ml of solution (rock solution ratio 1:150). Typically, samples and standards are prepared in duplicates (two digestions per sample or standard) and the blanks in quintuplets. Then, the solutions in the Teflon vials are transferred to the auto sampler test tubes and diluted, and as many aliquots as necessary are prepared.
- b. Illustration of the sequence of the analysis. The aliquots of blanks and standards are arranged in four groups so that none of the aliquots in one group are from the same blank or the same digestion of a standard. All unknown samples are evenly distributed between the four groups of standards and blanks.

| A | Sample | Standard | Acid blanks |
|-----------------------------------------------------------------------------------------------------------------------------|-----------------------------------------------------------------------------------------------------------------------------------------------------------------------------------------------------------------------------------------------------------------------------------------------------------------------------------------------------------------------------------------------------------------------------------------------------------------------------------------------------------------------------------------------------------------------------------------------------------------------------------------------------------------------------------------------------------------------------------------------------------------|-------------------------------------------------------------------------------------|-----------------------------------------------------------------------------------------------------|
| Weighing: (step 1) |  |  | no rock powder in blanks |
| Dissolving: (steps 2-9) digestion = 0.1g sample dissolved in a Teflon vial |  |  |  |
| Diluting: transfer of 1 ml solution to auto sampler test tubes, addition of 9 ml H ₂ O (1:10 dilution) |  |  |  |
| Number of auto sampler test tubes: (= number of analyses) | 2 auto sampler test tubes per sample | 8 auto sampler test tubes per standard | 4 auto sampler tubes with Ce-spiked blank solutions 16 auto sampler tubes with blank solutions |
| B Sequence of test tubes in auto sampler: | <p>For the analysis, the auto sampler test tubes should be arranged in the auto sampler tray as follows:</p> <ol style="list-style-type: none"> 1. group of blanks and standards Unknowns * 2. group of blanks and standards Unknowns * 3. group of blanks and standards Unknowns * 4. group of blanks and standards (end of analytical run) <div style="margin-left: 200px;"> <p>arrangement of a group of blanks and standards</p> <ul style="list-style-type: none"> Ce-spiked blank 1 Blank 2 Blank 3 Blank 4 Blank 5 NIST-278 NIST-278 NIST-688 NIST-688 BCR-1 BCR-1 </div> | | |

E.2.1.2 Dilution procedure

The solutions in the Teflon vials were diluted prior to analysis by ICP-MS (figure E.1). 1 ml of solution was taken from the Teflon vials using a high-precision pipette and transferred to polypropylene auto sampler test tubes. Then, 9 ml of de-ionized H₂O was added using a high-precision pipette. The auto sampler test tubes were capped and shaken to homogenize the solutions. The analytical solution contained a rock/solution proportion of about 1:1500 (except for the blanks), an HNO₃ concentration of about 1%, and an HF concentration of about 0.017%. All sample and standard solutions should be transferred to the auto sampler tubes shortly before the analytical run because Ta and Nb may be lost in the dilute solutions when the solutions are stored for long periods of time in polypropylene.

E.3 ICP-MS instrument operation

E.3.1 Instrumentation

The results of the trace element analysis presented in this study were acquired with one single routine-procedure covering the complete element suite. The analyses were performed at the Union College Geology Department, Schenectady, NY, using a VG PlasmaQuad2+ ICP-MS instrument equipped with a VG multi-channel-analyzer. Kurt Hollocher is gratefully acknowledged for the set-up and operation of the ICP-MS instrument. The analyses were performed using a RF power of 1350 W, argon flow rates of 13 l min.⁻¹ (cooling), 0.6 l min.⁻¹ (auxiliary), and 0.78 l min.⁻¹ (nebulizer). For automatic sampling, an auto sampler was used. Liquid sample flow rates were controlled with a peristaltic pump, with a sample flow at 0.8 ml min.⁻¹. The glass Meinhard concentric nebulizer in a glass spray chamber was cooled to 15°C. The scan range, skipped mass regions, dwell times, and the selected isotopes are listed in table E1. The detector of the ICP-MS instrument was always run in pulse counting mode.

Table E1: Plasmaquad element menu for analytical runs

| Mass Range: 49.94 to 236.75 a.m.u. | | Skipped mass regions: | | | |
|-------------------------------------------|-------|------------------------------|-----------|-------------|-----------|
| Number of Channels: | 2048 | PULSE COUNTING | | ANALOG | |
| Number of Scan Sweeps: | 100 | <u>From</u> | <u>To</u> | <u>From</u> | <u>To</u> |
| Dwell Time (μ s): | 320 | | | | |
| Points per Peak: | 5 | | | | |
| DAC Step between Points: | 5 | 12.50 | 24.00 | 12.00 | 23.50 |
| Number of Peak Jump Sweeps: | 100 | 27.50 | 41.50 | 27.50 | 41.50 |
| Collector type: | Pulse | 79.50 | 80.50 | 79.50 | 80.50 |

| Analyzed elements/isotopes: | | | | |
|------------------------------------|---------------|-------------------------|------------------------|------------------|
| <u>Elements selected</u> | <u>Symbol</u> | <u>Selected isotope</u> | <u>Peak Jump Dwell</u> | <u>Collector</u> |
| Vanadium | V | 51 | 2560 | Pulse |
| Chromium | Cr | 53 | 5120 | Pulse |
| Gallium | Ga | 71 | 1280 | Pulse |
| Rubidium | Rb | 85 | 10240 | Pulse |
| Strontium | Sr | 86 | 5120 | Pulse |
| Yttrium | Y | 89 | 5120 | Pulse |
| Zirconium | Zr | 90 | 2560 | Pulse |
| Niobium | Nb | 93 | 10240 | Pulse |
| Indium | In | 115 | 1280 | Pulse |
| Cesium | Cs | 133 | 20480 | Pulse |
| Barium | Ba | 137 | 5120 | Pulse |
| Lanthanum | La | 39 | 5120 | Pulse |
| Cerium | Ce | 140 | 2560 | Pulse |
| Praseodymium | Pr | 141 | 5120 | Pulse |
| Neodymium | Nd | 146 | 10240 | Pulse |
| Europium | Eu | 151 | 40960 | Pulse |
| Samarium | Sm | 152 | 10240 | Pulse |
| Gadolinium | Gd | 158 | 10240 | Pulse |
| Terbium | Tb | 159 | 20480 | Pulse |
| Dysprosium | Dy | 163 | 10240 | Pulse |
| Holmium | Ho | 165 | 10240 | Pulse |
| Erbium | Er | 166 | 10240 | Pulse |
| Thulium | Tm | 169 | 20480 | Pulse |
| Ytterbium | Yb | 174 | 10240 | Pulse |
| Lutetium | Lu | 175 | 20480 | Pulse |
| Hafnium | Hf | 178 | 10240 | Pulse |
| Tantalum | Ta | 181 | 10240 | Pulse |
| Rhenium | Re | 185 | 1280 | Pulse |
| Lead | Pb | 206 | 5120 | Pulse |
| Lead | Pb | 207 | 5120 | Pulse |
| Lead | Pb | 208 | 5120 | Pulse |
| Bismuth | Bi | 209 | 1280 | Pulse |
| Thorium | Th | 232 | 5120 | Pulse |
| Uranium | U | 238 | 10240 | Pulse |

E.3.2 Drift

The sensitivity for any element can and does vary with time, as a result of changes in instrument parameters (Riddle et al, 1988). Generally, there is a loss of sensitivity with time, but increase and sudden jumps were observed as well, especially at the beginning of a run. Also, the sensitivity changes across the mass spectrum: larger changes of the sensitivity have been observed for lighter elements than for heavier.

The changes of the sensitivity with time as well as the mass-dependent signal drift was monitored by analyzing the selected internal standard elements Ga, In, Re, and Bi in all sample, blank, and standard solutions. The effectiveness of internal standardization to correct for mass and time dependent signal drift has repeatedly been demonstrated using various internal standard elements (e.g., Doherty, 1989). The best internal standardization is achieved when internal standard elements satisfy four requirements. First, they have to be in low and/or constant concentration in the samples. Second, internal standard elements have to be stable in dilute acid solutions. Third, oxides or doubly charged ions of internal standard elements must not interfere with analyzed elements. Fourth, the ionization potential of the internal standard elements should be closely matched to that of the analyzed elements. These requirements were met with the selected internal standard elements in the analytical runs.

E.3.3 Interference

There are a variety of potential mass spectral interferences possible, including isobaric (e.g., ^{144}Nd on ^{144}Sm), doubly charged ions (e.g., ^{138}Ba on ^{69}Ga), oxides (e.g., $^{135}\text{Ba}^{16}\text{O}$ on ^{151}Eu), hydrides (e.g., ^{85}RbH on ^{86}Sr), and fluorides (e.g., $^{138}\text{Ba}^{19}\text{F}$ on ^{157}Gd). Of these, oxide interferences are a significant problem for REE, Ta and Hf analysis (e.g., Jenner et al., 1990; Young-Sang et al., 1990).

In order to correct for these interferences, Ce was analyzed at mass 140 and Gd at mass 158. With the analysis of the Ce-spiked blanks, the production rate of $^{142}\text{Ce}^{16}\text{O}^+$ at mass 158 can be monitored throughout the run. The ratio $^{142}\text{Ce}^{16}\text{O} / ^{140}\text{Ce}$ served as a monitor of the production of all Ba oxides (BaO^+) and rare earths oxides (REO^+). The computer program VGFIX2, which was used to convert measured peak intensities to elemental concentrations, contains an empirical table of ratios of BaO^+ and REO^+ interferences on Ta, Hf, and the REE normalized to the $^{142}\text{Ce}^{16}\text{O}^+$ oxide. This table, however, does not

contain a complete list of normalized ratios of all possible oxide interferences on all isotopes of Ta, Hf, and the REE. Therefore, the isotope masses of the REE, Ta and Hf listed in table E1 must be analyzed, so that interference corrections can be made using the correction factors contained in the VGFIX2 program.

E.4 Calibration

E.4.1 Sequence of analysis

The blanks, standards and samples must be analyzed in a certain sequence (figure E.1), in order that measured peak intensities can be accurately converted to elemental concentrations and that necessary drift and interference corrections can be made. The blanks and standards must always be in groups. Special solutions to monitor interferences, such as Ce-spiked blanks, must be included among the other acid blanks. If there are two sets of standards and blanks; they must be at the beginning and end of each run with all unknowns in between. If there are more than two sets of standards and blanks, one set must be at the beginning, one at the end and the others evenly spaced between approximately equal numbers of unknowns. Typically, four groups of standards and blanks were analyzed with unknown samples evenly distributed between these groups (figure E.1).

E.4.2 Standards

Three standards were used for the calibration of all analytical runs. The standards are BCR-1, NIST-278 and NIST-688. As described in section E.2.2, the standard solutions were prepared by acid digestion along with the samples and blanks. For each analytical run, two digestions of each of the standards were prepared and four aliquots of each digestion analyzed (figure E1).

The elemental concentrations of BCR-1, NIST-278 and NIST-688 are listed in tables E2, E3 and E4, respectively. For the calibration of the analytical runs, the recommended standard values of Govindaraju (1994) were adopted for BCR-1, whereas for NIST-278 and NIST-688, the in-house standard values (K. Hollocher, personal communication 1995) were used.

Table E2: Standard values of BCR-1

| Element | recom- mended values | ID-SSMS (n=10) | method preferred values* | BCR-1 analyzed as unknown using NIST-278 and NIST-688 as standards | |
|---------|----------------------------|-------------------|--------------------------------|--------------------------------------------------------------------------|----------------------|
| | [1] | [2] | [3] | ICP-MS (n=32) | Element [this study] |
| V | <u>407</u> | - | - | V | 403 |
| Cr | 16 | - | - | Cr | 13.1 |
| Rb | <u>47.2</u> | 46.7 | 46.8 | Rb | 47.3 |
| Sr | <u>330</u> | 327 | 331 | Sr | 333 |
| Y | <u>38</u> | 37.9 | 36.8 | Y | 35.5 |
| Zr | <u>190</u> | 186 | 195 | Zr | 185 |
| Nb | 14 | 13.8 | 13.5 | Nb | 15.0 |
| Cs | <u>0.96</u> | 0.91 | 0.96 | Cs | 0.96 |
| Ba | <u>681</u> | 653 | 676 | Ba | 694 |
| La | <u>24.9</u> | 24.7 | 25.03 | La | 25.6 |
| Ce | <u>53.7</u> | 54 | 53.6 | Ce | 53.4 |
| Pr | <u>6.80</u> | 6.79 | - | Pr | 6.84 |
| Nd | <u>28.8</u> | 29.1 | 28.8 | Nd | 29.6 |
| Sm | <u>6.59</u> | 6.63 | 6.60 | Sm | 6.53 |
| Eu | <u>1.95</u> | 1.96 | 1.97 | Eu | 1.97 |
| Gd | <u>6.68</u> | 6.56 | 6.68 | Gd | 6.73 |
| Tb | <u>1.05</u> | 1.07 | - | Tb | 1.04 |
| Dy | <u>6.34</u> | 6.35 | 6.57 | Dy | 6.30 |
| Ho | <u>1.26</u> | 1.24 | - | Ho | 1.27 |
| Er | <u>3.63</u> | 3.77 | 3.64 | Er | 3.52 |
| Tm | <u>0.56</u> | 0.62 | - | Tm | 0.52 |
| Yb | <u>3.38</u> | 3.43 | 3.37 | Yb | 3.30 |
| Lu | <u>0.51</u> | 0.53 | 0.5 | Lu | 0.55 |
| Hf | <u>4.95</u> | 4.9 | - | Hf | 5.01 |
| Ta | <u>0.81</u> | - | - | Ta | 0.78 |
| Pb | <u>13.6</u> | 15.9 | - | Pb | 14.3 |
| Th | <u>5.98</u> | 6.02 | 6.02 | Th | 6.08 |
| U | <u>1.75</u> | 1.73 | 1.73 | U | 1.72 |

* Cs, Rb, Ba, and REE determined by ID-TIMS

U and Th determined by ID-SSMS

Nb, Zr, and Y determined by SSMS

[1] Govindaraju (1994), data underlined are recommended values; other values are proposed

[2] Jochum et al (1988)

[3] Jenner et al (1990)

Table E3: Standard values of NIST-278

| Element | preferred | recom- | UA | | UC | | ITNA/ | | consensus | |
|---------|--------------------------------|------------------------|-----------------------------|---------------------|----------------------------|---------------------|------------|---------------------|---------------|---------------------|
| | in-house standard values | ended values [1] | SSC-method ICP-MS [2] | error 1 σ | SA-method ICP-MS [2] | error 1 σ | XRF [3] | error 1 σ | values [4] | error 1 σ |
| V | 9 | 9 | - | - | - | - | 16 | 2 | 15 | 8 |
| Cr | 6.6 | <u>6.1</u> | - | - | - | - | 7.3 | 0.7 | 6.4 | 0.9 |
| Rb | 130 | <u>127.5</u> | 121 | 2 | - | - | 133 | 6 | 133 | 6 |
| Sr | 63.5 | <u>63.5</u> | 60 | 2 | - | - | 74 | 8 | 64 | 5 |
| Y | 39 | 39 | 35 | 1 | - | - | 42 | 4 | 39 | 5 |
| Zr | 290 | 290 | 276 | 9 | - | - | 338 | 30 | 290 | 30 |
| Nb | 21 | 18 | 22 | 4 | - | - | 22 | 2 | 18 | 5 |
| Cs | 5.2 | <u>5.5</u> | 5.3 | 0.2 | - | - | 5.2 | 0.3 | 5.2 | 0.2 |
| Ba | 947 | <u>1140</u> | 904 | 21 | 896 | 19 | 1000 | 90 | 970 | 60 |
| La | 31.3 | 32 | 30 | 1 | 31 | 2 | 31.9 | 1.7 | 32 | 2 |
| Ce | 61.8 | <u>62.2</u> | 65 | 2 | 61 | 2 | 68 | 3 | 60 | 6 |
| Pr | 7.2 | 7.2 | - | - | 7 | 0.2 | - | - | 7.0 | 1.3 |
| Nd | 28 | 30 | 27 | 1 | 26 | 1 | 33 | 3 | 30 | 3 |
| Sm | 5.6 | <u>5.7</u> | 5.6 | 0.3 | 5.6 | 0.1 | 4.73 | 0.22 | 5.9 | 0.5 |
| Eu | 0.78 | <u>0.84</u> | 0.67 | 0.07 | 0.8 | 0.04 | 0.74 | 0.04 | 0.78 | 0.03 |
| Gd | 5.7 | <u>5.3</u> | 5.7 | 0.1 | 5.8 | 0.1 | - | - | 5.5 | 0.4 |
| Tb | 0.97 | <u>1.0</u> | 1.01 | 0.04 | 0.92 | 0.02 | 0.99 | 0.09 | 1.06 | 0.14 |
| Dy | 6.2 | 6.3 | - | - | 6 | 0.1 | 6.1 | 0.5 | 6.3 | 0.4 |
| Ho | 1.33 | 1.26 | 1.31 | 0.04 | 1.29 | 0.02 | - | - | 1.26 | 0.17 |
| Er | 3.95 | 3.8 | 4.1 | 0.1 | 4.1 | 0.1 | - | - | 3.8 | 0.5 |
| Tm | 0.64 | 0.41 | 0.63 | 0.03 | 0.64 | 0.02 | - | - | 0.41 | 0.15 |
| Yb | 4.45 | <u>4.5</u> | 4.31 | 0.03 | 4.4 | 0.1 | 5.3 | 0.3 | 4.6 | 0.6 |
| Lu | 0.74 | <u>0.73</u> | 0.64 | 0.2 | 0.66 | 0.02 | 0.74 | 0.04 | 0.77 | 0.12 |
| Hf | 8.1 | <u>8.4</u> | 7.7 | 0.1 | - | - | 8.2 | 0.5 | 8.5 | 0.4 |
| Ta | 1.29 | <u>1.2</u> | 1.5 | 0.1 | - | - | 1.42 | 0.11 | 1.29 | 0.08 |
| Pb | 16.4 | <u>16.4</u> | 17.2 | 1 | - | - | - | - | 14 | 6 |
| Th | 12.6 | <u>12.4</u> | 12.1 | 0.8 | - | - | 12.8 | 0.5 | 12.6 | 0.6 |
| U | 4.55 | <u>4.58</u> | 4.7 | 0.3 | - | - | 4.89 | 0.18 | 4.55 | 0.18 |

[1] Govindaraju (1994); data underlined are recommended values, other values are proposed

[2] Hollocher (1993) UA ... University of Arizona UC ... Union College
SSC ... Standard solution comparison SA ... Standard addition

[3] Bower et al. (1992)

[4] Gladney et al. (1987, supplement 1 issued in 1993)

Table E4: Standard values of NIST-688

| Element | preferred in-house standard values | recom- mended values [1] | UA | | UC | | ITNA/ XRF | | consensus | |
|---------|---------------------------------------------|-----------------------------------|-----------------------------|---------------------|----------------------------|---------------------|---------------------|---------------------|---------------|---------------------|
| | | | SSC-method ICP-MS [2] | error 1 σ | SA-method ICP-MS [2] | error 1 σ | error 1 σ | error 1 σ | values [4] | error 1 σ |
| V | 238 | <u>250</u> | 240 | 3 | - | - | 228 | 9 | 238 | 7 |
| Cr | 321 | <u>332</u> | 298 | 6 | - | - | 315 | 18 | 332 | 9 |
| Rb | 1.91 | <u>1.91</u> | 1.9 | 0.1 | - | - | 10 | 4 | 5 | 4 |
| Sr | 169 | <u>169.2</u> | 162 | 5 | - | - | 166 | 8 | 169 | 3 |
| Y | 18 | 19 | 16.9 | 0.4 | - | - | 8 | 6 | 19 | 3 |
| Zr | 59 | 59 | 49 | 0.1 | - | - | 62 | 6 | 59 | 3 |
| Nb | 5.6 | 5.7 | - | - | 5.2 | 0.05 | 7 | 2 | 5.7 | 1.2 |
| Cs | 0.26 | 0.26 | - | - | - | - | <1.5 | - | - | - |
| Ba | 198 | <u>200</u> | 175 | 7 | 165 | 4 | 220 | 100 | 198 | 14 |
| La | 5.15 | 5.3 | 4.9 | 0.5 | 5.1 | 0.6 | 5 | 0.3 | 5.3 | 0.5 |
| Ce | 12.55 | <u>13.3</u> | 12 | 1 | 10.1 | 0.3 | 13.1 | 0.6 | 12.5 | 1.4 |
| Pr | 1.78 | 2.0 | - | - | 1.58 | 0.04 | - | - | 2.0 | 0.3 |
| Nd | 8.3 | 8.9 | 8.4 | 1.2 | 8 | 0.2 | <35 | - | 8.9 | 1 |
| Sm | 2.4 | <u>2.79</u> | 2.17 | 0.01 | 2.3 | 0.1 | 2.2 | 0.1 | 2.4 | 2 |
| Eu | 0.98 | <u>1.07</u> | 0.89 | 0.02 | 0.94 | 0.03 | 0.85 | 0.04 | 1.00 | 0.06 |
| Gd | 2.9 | 3.2 | 2.9 | 0.3 | 2.6 | 0.1 | - | - | 3.2 | 0.4 |
| Tb | 0.50 | <u>0.45</u> | 0.46 | 0.02 | 0.47 | 0.01 | 0.36 | 0.09 | 0.52 | 0.04 |
| Dy | 3.25 | 3.3 | - | - | 3.1 | 0.1 | 3.2 | 0.4 | 3.3 | 0.4 |
| Ho | 0.70 | 0.75 | 0.66 | 0 | 0.72 | 0.02 | - | - | 0.75 | 0.1 |
| Er | 1.99 | 2.09 | 1.9 | 0.1 | 2.04 | 0.04 | - | - | 2.09 | 0.2 |
| Tm | 0.31 | 0.31 | 0.27 | 0.04 | 0.31 | 0.01 | - | - | 0.30 | 0.05 |
| Yb | 2.00 | <u>2.09</u> | 1.9 | 0.1 | 2.00 | 0.04 | 2.1 | 0.3 | 2.03 | 0.16 |
| Lu | 0.31 | <u>0.34</u> | 0.26 | 0.01 | 0.31 | 0.01 | 0.33 | 0.02 | 0.33 | 0.03 |
| Hf | 1.55 | <u>1.6</u> | 1.4 | 0.1 | - | - | 1.46 | 0.1 | 1.55 | 0.1 |
| Ta | 0.31 | 0.31 | - | - | - | - | 0.28 | 0.12 | 0.31 | 0.07 |
| Pb | 3.6 | <u>3.3</u> | 3.16 | 0.05 | - | - | - | - | 4.6 | - |
| Th | 0.32 | <u>0.33</u> | - | - | - | - | 0.28 | 0.08 | 0.33 | 0.02 |
| U | 0.32 | <u>0.37</u> | - | - | - | - | 0.32 | 0.06 | 0.31 | 0.02 |

[1] Govindaraju (1994); data underlined are recommended values, other values are proposed

[2] Hollocher et al. (1995)

UA ... University of Arizona

UC ... Union College

SSC ... Standard solution comparison

SA ... Standard addition

[3] Bower et al. (1992)

[4] Gladney et al. (1987, supplement 1 issued in 1993)

In addition to the recommended standard values of BCR-1, two sets of values are listed in table E2 for comparison. The elemental concentrations determined by isotope-dilution spark-source mass spectrometry (ID-SSMS) represent the mean of ten independent measurements performed at the Max-Planck-Institut, Germany (Jochum et al., 1988). The method preferred values were compiled by Jenner et al. (1990): Cs, Rb, Ba, and the REE were determined by isotope-dilution thermal-ionization mass spectrometry (ID-TIMS) and Nb, Zr, and Y by spark-source mass spectrometry (SSMS). There is excellent agreement between the recommended standard values and the values determined by these highly accurate techniques. This clearly indicates that BCR-1 is a well-characterized standard.

The in-house standard values of NIST-278 and NIST-688 are listed in tables E3 and E4, respectively, and can be compared with five published sets of elemental concentrations arranged in the tables. The agreement between the in-house standard values and the other five sets of values is good, generally within indicated errors of the analytical techniques, or within the errors given for the compilation. Furthermore, there is very good evidence that the in-house standard values are very accurate: BCR-1 was analyzed in this study as unknown sample using NIST-278 and NIST-688 as standards for the calibration, and the recommended standard values of BCR-1 were accurately reproduced (table E2).

E.4.3 Blanks

As described in section E2.2, the blanks were prepared in five different Teflon vials for each analytical run together with the samples and standards. The blanks are dilute acid solutions which contain no dissolved solids except for the internal standard elements Ga, In, Re, and Bi. As illustrated in figure E1, four aliquots were taken from each of the five blanks and diluted. Then, four aliquots of one blank were spiked with 50 μl of 0.01 $\mu\text{g/ml}$ Ce single-element solution.

The analysis of acid blanks is important for several reasons. First, the calibration curves are generated by calculating a regression line between the measured peak intensities and known concentrations of the standards plus the blanks (the “known” concentrations of the blanks are assumed to be zero). A “zero-intercept” model is used for the linear regression; accordingly, the measured peak intensities of the blanks are subtracted from the data (the blank level is so low that its subtraction from the data results in no

significant change in the peak intensities). Second, the detection limits are determined from the analysis of the blanks. And third, possible contamination during sample preparation can be detected (unusually high blank levels would indicate that the blanks contain some amounts of dissolved solids). Contamination was not found to be a problem in all analytical runs performed at Union College. Only occasionally were blank solutions contaminated with Pb and very rarely with Rb.

E.5 Calculation of concentrations

The measured peak intensities were converted to elemental concentrations using VGFIX2, a computer program written by Kurt Hollocher, Union College, Schenectady, NY. This program was written in Turbo Pascal v. 6.0 and compiled for IBM-type personal computers running the DOS operating system, with or without a numeric coprocessor.

Prior to inputting data into the VGFIX2 program, the obtained peak intensities were read into spread-sheet format and arranged in the order in which the blanks, standards and samples were analyzed (see section E.4.1). The details on how to arrange the data table so it can be read by the VGFIX2 program are described in the unpublished program manual. For example, the type of analyzed solution, whether it is a blank, Ce-spiked blank, standard or unknown sample must be specified in the data table before the VGFIX2 program is put to use. The rows containing the elemental concentrations of the standards must be entered (in ppm) in the data table as well.

Two data tables per analytical run were arranged as outlined above. Both data tables contain the same measured peak intensities of the same analytical run. However, there are differences between the two tables. The information entered in the first data table tells VGFIX2 that BCR-1 is a unknown sample and NIST-278 and NIST-688 are the standards. The second data table is arranged so that NIST-278 and NIST-688 as well as BCR-1 are recognized as standards. Then, VGFIX2 was used to convert the peak intensities to elemental concentrations. The elemental concentrations of BCR-1 (treated as unknown sample) were calculated using NIST-278 and NIST-688 as standards. Then, the elemental concentrations of all other analyzed samples were calculated using NIST-278, NIST-688 and BCR-1 as standards.

The calculations performed by the VGFIX2 program are described in more detail in its program manual. Basically, linear calibration curves were calculated using the blank-subtracted peak intensities and known concentrations of standards and blanks. The unknown concentrations were calculated by comparing the blank-subtracted peak intensities of the samples to the (best-fit) calibration curves. Corrections were made by the program for internal standard drift, blank drift, calibration drift and interferences of BaO⁺ and REO⁺ on Hf, Ta and the REE.

The VGFIX2 program also calculated the “blank residuals”. In essence, the measured peak intensities of the blanks were compared to the calibration curves (similar to the calculation of concentrations of the unknown samples) deriving “concentrations” of the blanks given in “ppm”. These “concentrations” represent the blank residuals. The blank residuals calculated in this manner also indicate whether the calibration curves intercept the origin in plots of peak intensities vs. concentrations (mean of blank residuals $\cong 0$) or intercept the y-axis at notable positive or negative values (mean of blank residuals < 0 , or mean of blank residuals > 0). For instance, the absolute mean of the blank residuals of V, Cr, Zr and Ba typically indicate values between 0.5 ppm and 3 ppm. The absolute mean of the blank residuals calculated for all other elements is very close to zero.

E.6 Evaluation of data

E.6.1 Determination of detection limits

Limits of detection (LOD) are used as a measure of instrument performance. The ICP-MS instrument does not have a fixed LOD and must be calculated for each individual run with the formula:

$$LOD = \left| \bar{X} \right| + 3 \cdot \sigma \quad (1)$$

The limits of detection are given in ppm. $\left| \bar{X} \right|$ is the absolute mean and σ the standard deviation of twelve blank residuals. As mentioned in section E.5, the elements V, Cr, Zr and Ba indicated generally higher absolute means (0.5-3 ppm) of the blank residuals than any other element ($\cong 0$ ppm). Consequently, the detection limits of V, Cr, Zr and Ba are relatively higher than those for all other elements.

The detection limits of the ICP-MS instrument, as determined in this study, are generally well below chondrite level, and for most elements several orders of magnitude lower than element concentrations in the samples. The detection limits, calculated for each individual run, are listed in tables E6, E8, E9, E10, E11 and E12.

E.6.2 Determination of precision

In geochemical analyses, it is common practice to run a series of determinations, or replicates, on a single sample to determine the precision of the analytical technique. The most frequently measure adopted to express the spread or dispersion about the mean is the *standard deviation* denoted by the Greek letter σ :

$$\sigma = \sqrt{\frac{\sum (X_i - \bar{X})^2}{n^2}} \quad (2)$$

\bar{X} is the mean of n determinations with X_i being the value of i th measurement. A small σ indicates that the measurements are clustered tightly around the mean, indicating the multiple determinations were realized with “high” or “excellent” precision.

Furthermore, the standard deviation is commonly normalized and presented as the percentage of the respective mean value. This is called the relative standard deviation (RSD). The RSDs are calculated for each element using the formula:

$$RSD = (\sigma / \bar{X}) \bullet 100\% \quad (3)$$

Then, the RSDs are plotted using bar diagrams to illustrate the precision of the analysis for each run (e.g., figure E2). The classification of the precision as “excellent”, “good”, “acceptable”, and “poor” based on the %-RSD was arbitrarily chosen, although it is comparable to the precision of ICP-MS analysis discussed elsewhere (e.g., Jenner et al., 1990; Longrich et al., 1990; Holmes et al., 1995).

E.6.3 Determination of accuracy

E.6.3.1 Comparison with standards

In order to evaluate the accuracy of the ICP-MS analysis at Union College, two standards (BCR-1 and Pal-889) were analyzed as unknowns in each of the analytical runs. The accuracy is then assessed by comparing the determined values with the recommended standard values. However, no absolute values for the standard materials are available, only a consensus of the most likely values and, occasionally, values obtained by highly accurate techniques (e.g., ID-SSMS). Accordingly, an exact measurement of the accuracy cannot be made, and the accuracy must be determined with this deficiency in mind.

To facilitate the comparison, measured values are plotted against the standard values in bivariate diagrams having logarithmic scale on both axes (e.g., figures E3 and E4). Ideally, all points should plot close to or on the solid line with slope = 1. Generally, the accuracy of the analysis is considered “good” when the range of the multiple determinations is within $\pm 10\%$ of the corresponding standard values. To illustrate $\pm 10\%$ deviation from the line with slope = 1, two dashed lines are drawn on the diagrams. The upper line, limiting the dark gray field, is a line with slope of 1.1, the lower line, limiting the light gray field, is a line with slope of 0.9. Note that lines with different slopes plot parallel on diagrams having logarithmic scales on both axes.

The standard values compiled by Govindaraju (1994) were selected as the reference values to which the analyses of BCR-1 were compared (e.g., figure E2). The standard values of BCR-1 are listed in table E2. Cr and Nb standard values are not as well-established as the other values. Accordingly, Cr and Nb values are “proposed” instead of “recommended” (Govindaraju, 1994).

Pal-889 is an in-house standard used at Cornell University, Uthica, NY. It was sampled from the Palisade Sill at the same locality as the U.S.G.S. standard W-1 (Wirth, 1991). As shown in table E5, most standard values of W-1 agree well with the in-house standard values of Pal-889. However, some elements, such as Cr and Cs, indicate significant differences, confirming that Pal-889 and W-1 are actually two different rock samples. Nonetheless, both standards agree sufficiently well and the concentrations of the elements Y, Zr, Nb, Pr, Gd, Dy, Ho, Er and Tm determined in W-1 were used to complement the in-house standard values of Pal-889 (table E5). Accordingly, the reference values used in the comparative plots

Table E5: Standard values of Pal-889 and W-1

| Element | W-1 recom- mended values [1] | W-1 ID-SSMS (n=7) [2] | Pal-889 in-house standard values [3] |
|---------|------------------------------------------|--------------------------------|--------------------------------------------------|
| V | <u>257</u> | - | - |
| Cr | <u>119</u> | - | 314 |
| Rb | <u>21.4</u> | 21.6 | - |
| Sr | <u>186</u> | 193 | 183 |
| Y | <u>26</u> | 22.6 | - |
| Zr | <u>99</u> | 98.6 | - |
| Nb | <u>9.9</u> | 7.91 | - |
| Cs | <u>0.96</u> | 0.9 | 2.19 |
| Ba | <u>162</u> | 162 | 185 |
| La | <u>11</u> | 10.9 | 10.52 |
| Ce | <u>23.5</u> | 24 | 23.6 |
| Pr | <u>3.2</u> | 3.27 | - |
| Nd | <u>14.6</u> | 14.4 | 13 |
| Sm | <u>3.68</u> | 3.65 | 3.42 |
| Eu | <u>1.12</u> | 1.14 | 1.07 |
| Gd | <u>4.01</u> | 4.24 | - |
| Tb | <u>0.63</u> | 0.65 | 0.67 |
| Dy | <u>3.99</u> | 4.18 | - |
| Ho | <u>0.81</u> | 0.8 | - |
| Er | <u>2.3</u> | 2.25 | - |
| Tm | <u>0.34</u> | 0.33 | - |
| Yb | <u>2.03</u> | 2.17 | 2.18 |
| Lu | <u>0.32</u> | 0.34 | 0.3 |
| Hf | <u>2.5</u> | 2.68 | 2.56 |
| Ta | <u>0.48</u> | - | 0.63 |
| Pb | 7.5 | 7.83 | - |
| Th | <u>2.4</u> | 2.65 | 2.07 |
| U | <u>0.57</u> | 0.61 | 0.5 |

[1] Govindaraju (1994); data underlined are recommended values,
other values are proposed

[2] Jochum et al. (1988)

[3] Wirth (1991)

(e.g., figure E4) are a blending of the in-house standard values of Pal-889 and elemental concentrations of W-1 determined by ID-SSMS (Jochum et al, 1988). The elemental concentrations determined by ID-SSMS are preferred over the recommended standard values of Govindaraju (1994), because there are indications of bias in the compilation of the standard values (e.g. Jochum et al, 1988; Jenner et al, 1990). For instance, the Y concentration in W-1, determined by ID-SSMS, is 22.6 ppm (table E5), whereas the recommended standard value is notably higher (Y = 26 ppm). The discrepancy in the Nb concentrations could be due to bias in the compilation of the standard values as well. Nevertheless, all other values determined by ID-SSMS agree well with the recommended standard values of W-1 (Govindaraju, 1994).

The agreement, or disagreement, between recommended standard values of W-1 and the ID-SSMS data may be considered as an “accuracy gauge”. ID-SSMS is one of the most accurate methods of trace element analysis (Jochum et al, 1988), and the mean of seven independent analyses of W-1 agree within 2% to 10% of the recommended standard values of Govindaraju (1994), except for Y and Nb.

E.6.3.2 Inter-laboratory comparison

The comparison of results obtained at different analytical laboratories -- “inter-laboratory comparison” -- is another method to evaluate the accuracy of the analysis by ICP-MS. Accordingly, several samples analyzed at various laboratories were re-analyzed at Union College, and the different sets of data were compared. Similar to the comparison with standard values, the same type of bivariate diagrams are used for the inter-laboratory comparison (e.g., figures E5 and E6).

E.7 Test runs

E.7.1 First test run, 06/12/1995, synthetic standard used

E.7.1.1 Strategy and methods

Prior to analyzing any samples collected from the Snow Camp terrane, SW Oregon, the accuracy and precision of the analysis by ICP-MS were evaluated by analyzing three reference materials: BCR-1,

Cou-IL-6 and Pal-889. For the calibration of the analysis, several aliquots of a synthetic standard solutions were analyzed along with the sample and blank solutions.

Three digestions per reference material were prepared in order to assess the precision and accuracy of weighing of the sample (i.e. weighing three times $0.1000\text{g} \pm 0.0002\text{g}$ per sample), pipetting, and diluting. Also, the completeness of dissolution and whether contamination is a problem or not can be evaluated by analyzing aliquots of three separate digestions per sample. The rock powders were dissolved following the acid digestion procedure routinely used at the Union College Geology Department (see section E2.2 for detail). This, however, means HF was not added at the end of the digestion procedure, a step that was later added to keep Ta and Nb in solution (see section E7.2.6). As always, five blanks were prepared along with the samples.

The completeness of dissolution of the sample can be independently verified by using a standard which is already available in dissolved form. If a rock standard were used and the dissolution of the aluminosilicates and other minerals (e.g., oxides) were incomplete, an identical problem dissolving the samples may not be detected. Hence, a synthetic standard solution was prepared by mixing accurately measured volumes of $1000\ \mu\text{g ml}^{-1}$ Spex single-element solutions into a 150 ml volumetric flask. Then, 21 ml high purity HNO_3 and 1.5 ml of the internal standard solution were added and the flask filled to volume with de-ionized H_2O . The synthetic standard solution was prepared four days in advance of the analysis by ICP-MS.

The following number of aliquots of each of the sample, standard and blank solutions were transferred from the Teflon vials to a total of 39 polypropylene auto sampler test tubes, diluted and analyzed: two aliquots of three digestions per sample ($n=6$ per sample), six aliquots of the synthetic standard solution, and three aliquots of five blanks ($n=15$, three of which were spiked with Ce). All but three sample solutions ($n=15$) and all blank ($n=15$) and standard solutions ($n=6$) were transferred to 36 polypropylene auto sampler tubes three days in advance of the run. The remaining three auto sampler tubes were filled shortly before the analysis, each of which contained a different sample (i.e. BCR-1, Pal-889, and Cou-IL-6).

E.7.1.2 Limits of detection

The limits of detection calculated for the first test run are listed in table E6. Generally, the detection limits are at ppb levels or lower. The comparatively high detection limits of Rb and Pb could be due to very small amounts of contamination of the blanks. Three out of twelve analyzed blank solutions indicated perceptibly higher blank levels for Rb and Pb. However, this amount of contamination in the blanks is negligible and does not affect the determination of the element concentrations as long as the concentrations in analyzed samples are well above the determined limits of detection. Pb and Rb contamination have been reported from other laboratories and may cause poor precision analyzing Rb and Pb (e.g., Jenner et al., 1990). Pb and Rb are apparently more prone to contamination than any other analyzed element.

E.7.1.3 Precision

The mean values and standard deviation of the measured elemental concentrations are listed in table E6. For the purpose of the illustration of the precision, the relative standard deviations were calculated from the data in table E6 and plotted in figure E2. Excluding Ta, Nb, and Pb, the overall precision of the ICP-MS analysis is excellent as indicated by less than 3% relative standard deviation for most elements. However, Pal-889 indicates significantly higher (though still “good”) relative standard deviation for Rb, Y, and the light REE than BCR-1 and Cou-IL-6 (figure E2). This must be due to fluctuations in the performance of the ICP-MS instrument during the analytical run, because significant differences between the three separate digestions of Pal-889 were not found (table E7). Furthermore, notable differences among any of the three separate digestions of any of the samples do not exist, suggesting all samples were completely digested and no errors were made during weighing of the samples and subsequent dissolution.

The element Pb has been determined with excellent precision in BCR-1 and Pal-889 (figure E2) whereas the determination of Pb in Cou-IL-6 indicates poor precision. Because contamination with Pb can occur very easily, it is reasonable to conclude that the poor precision of the analysis of Pb in Cou-IL-6 is caused by various amounts of Pb contamination of the sample solutions (table E7). Also, three of the blank solutions analyzed in the test run indicated some Pb contamination supporting this hypothesis.

Table E6: Results of first test run, 12/6/95, synthetic standard used

| Element | Detection | BCR-1 | | Pal-889 | | Cou-IL-6 | |
|---------|------------------|---------------|---------------------|---------------|---------------------|-------------------|---------------------|
| | Limits in ppm | mean (n=6) | error 1 σ | mean (n=6) | error 1 σ | mean (n=6) | error 1 σ |
| V | - | n.d. | - | n.d. | - | n.d. | - |
| Cr | - | n.d. | - | n.d. | - | n.d. | - |
| Rb | 0.156 | 46.91 | 0.78 | 30.3 | 1.4 | 13.04 | 0.10 |
| Sr | - | n.d. | - | n.d. | - | n.d. | - |
| Y | 0.031 | 36.51 | 0.51 | 22.0 | 1.1 | 39.8 | 0.3 |
| Zr | - | n.d. | - | n.d. | - | n.d. | - |
| Nb | 0.039 | 15.7* | 2.0 | 9.71* | 1.97 | 5.73* | 0.14 |
| Cs | 0.0046 | 0.905 | 0.009 | 1.91 | 0.03 | 2.77 | 0.01 |
| Ba | 0.11 | 674.5 | 3.1 | 174.4 | 2.3 | 57.1 | 0.3 |
| La | 0.013 | 24.50 | 0.16 | 10.62 | 0.95 | 6.28 | 0.05 |
| Ce | 0.025 | 52.9 | 0.3 | 22.8 | 1.0 | 17.07 | 0.03 |
| Pr | 0.0072 | 6.82 | 0.04 | 3.02 | 0.09 | 2.73 | 0.02 |
| Nd | 0.016 | 28.4 | 0.3 | 13.0 | 0.4 | 14.0 | 0.1 |
| Sm | 0.0069 | 6.39 | 0.05 | 3.27 | 0.11 | 4.31 | 0.04 |
| Eu | 0.0018 | 1.98 | 0.02 | 1.12 | 0.04 | 1.44 | 0.01 |
| Gd | 0.0087 | 6.64 | 0.08 | 3.70 | 0.13 | 5.59 | 0.07 |
| Tb | 0.0016 | 1.06 | 0.01 | 0.624 | 0.018 | 0.996 | 0.016 |
| Dy | 0.0061 | 6.15 | 0.07 | 3.71 | 0.07 | 6.25 | 0.09 |
| Ho | 0.0020 | 1.28 | 0.01 | 0.779 | 0.012 | 1.37 | 0.02 |
| Er | 0.0063 | 3.61 | 0.03 | 2.18 | 0.03 | 3.96 | 0.06 |
| Tm | 0.00073 | 0.564 | 0.005 | 0.342 | 0.004 | 0.634 | 0.007 |
| Yb | 0.0075 | 3.36 | 0.03 | 2.03 | 0.02 | 3.80 | 0.04 |
| Lu | 0.00093 | 0.508 | 0.005 | 0.279 | 0.003 | 0.532 | 0.006 |
| Hf | 0.011 | 4.93 | 0.06 | 2.51 | 0.03 | 3.18 | 0.03 |
| Ta | 0.0043 | 3.21* | 1.70 | 2.47* | 1.39 | 0.83* | 0.06 |
| Pb | 0.44 | 13.9 | 0.1 | 4.68 | 0.11 | 0.87 [×] | 0.30 |
| Th | 0.0017 | 5.96 | 0.05 | 2.04 | 0.01 | 0.523 | 0.009 |
| U | 0.00085 | 1.77 | 0.01 | 0.513 | 0.004 | 0.185 | 0.003 |

* Ta and Nb unstable in solution

× Pb contamination detected

n.d. not determined

standard deviation:
$$\sigma = \sqrt{\frac{\sum(X_i - \bar{X})^2}{n^2}}$$

see tables 2 and 5 for recommended standard values of BCR-1 and Pal-889, respectively

see tables 14, 15 and 16 for compilation of analytical results

for BCR-, Pal-889, and Cou-IL-6, respectively

Table E7: %-Difference between three digestions per sample, first test run, 12/6/95

0.1g of sample powder were weighed in each of three Teflon vials per sample and dissolved (= three digestions per sample). Two aliquots of each digestion were prepared and analyzed, accordingly, listed values are the mean of two analyses.

| Sample: | BCR-1 | | | Pal-889 | | | Cot-IL-6 | | | | | |
|---------|-------|-------|---------|---------|-------|------|----------|--------|--------|--------|--------------------------|--------|
| | no.1 | no.2 | no.3 | %Diff. | no.1 | no.2 | no.3 | %Diff. | no.1 | no.2 | no.3 | %Diff. |
| Rb | 47.9 | 46.3 | 46.5 | 3.2% | 30.8 | 30.0 | 30.3 | 2.7% | 13.1 | 13.0 | 13.0 | 1.2% |
| Y | 36.8 | 36.7 | 36.1 | 2.0% | 22.6 | 21.7 | 21.6 | 4.6% | 40.1 | 39.5 | 39.7 | 1.5% |
| Cs | 0.91 | 0.90 | 0.91 | 0.8% | 1.94 | 1.89 | 1.89 | 2.3% | 2.77 | 2.76 | 2.77 | 0.4% |
| Ba | 676 | 673 | 674 | 0.4% | 177 | 173 | 173 | 1.9% | 57.0 | 57.1 | 57.2 | 0.3% |
| La | 24.3 | 24.6 | 24.6 | 1.1% | 11.03 | 10.8 | 10.0 | 9.1% | 6.31 | 6.26 | 6.27 | 0.7% |
| Ce | 53.0 | 52.8 | 53.1 | 0.5% | 23.3 | 22.8 | 22.2 | 4.6% | 17.0 | 17.1 | 17.1 | 0.2% |
| Pr | 6.81 | 6.83 | 6.82 | 0.4% | 3.07 | 3.00 | 2.98 | 2.9% | 2.74 | 2.72 | 2.74 | 0.8% |
| Nd | 28.6 | 28.4 | 28.2 | 1.4% | 13.2 | 12.9 | 12.9 | 2.5% | 14.0 | 14.0 | 14.0 | 0.5% |
| Sm | 6.43 | 6.39 | 6.36 | 1.1% | 3.33 | 3.23 | 3.24 | 3.0% | 4.34 | 4.32 | 4.26 | 1.8% |
| Eu | 1.99 | 1.98 | 1.97 | 1.1% | 1.14 | 1.11 | 1.11 | 2.8% | 1.45 | 1.44 | 1.42 | 1.6% |
| Gd | 6.70 | 6.62 | 6.58 | 1.8% | 3.78 | 3.65 | 3.68 | 3.3% | 5.65 | 5.62 | 5.52 | 2.3% |
| Tb | 1.06 | 1.06 | 1.05 | 1.3% | 0.64 | 0.62 | 0.61 | 3.4% | 1.01 | 1.00 | 0.98 | 2.4% |
| Dy | 6.19 | 6.14 | 6.12 | 1.1% | 3.76 | 3.66 | 3.70 | 2.6% | 6.27 | 6.26 | 6.22 | 0.9% |
| Ho | 1.29 | 1.28 | 1.28 | 1.1% | 0.79 | 0.77 | 0.78 | 3.0% | 1.38 | 1.37 | 1.36 | 1.1% |
| Er | 3.61 | 3.61 | 3.60 | 0.2% | 2.20 | 2.16 | 2.17 | 1.8% | 3.99 | 3.97 | 3.91 | 1.9% |
| Tm | 0.56 | 0.57 | 0.56 | 1.1% | 0.35 | 0.34 | 0.34 | 2.0% | 0.64 | 0.63 | 0.63 | 1.0% |
| Yb | 3.38 | 3.36 | 3.35 | 1.1% | 2.05 | 2.02 | 2.01 | 1.8% | 3.80 | 3.80 | 3.82 | 0.5% |
| Lu | 0.51 | 0.51 | 0.51 | 1.0% | 0.28 | 0.28 | 0.28 | 2.0% | 0.53 | 0.53 | 0.53 | 1.1% |
| Hf | 4.94 | 4.92 | 4.93 | 0.5% | 2.52 | 2.48 | 2.53 | 2.0% | 3.19 | 3.17 | 3.18 | 0.7% |
| Pb | 14.01 | 13.78 | 13.78 | 1.6% | 4.75 | 4.75 | 4.55 | 4.2% | 0.90 × | 1.23 × | 0.49 | 60% |
| Th | 5.92 | 5.94 | 6.02 | 1.8% | 2.04 | 2.04 | 2.02 | 0.9% | 0.52 | 0.51 | 0.53 | 4.0% |
| U | 1.76 | 1.77 | 1.78 | 0.7% | 0.51 | 0.51 | 0.52 | 0.9% | 0.19 | 0.18 | 0.19 | 3.1% |
| | | | average | 1.1% | | | average | 2.9% | | | average without Pb-value | 1.3% |

$$\%Diff = \frac{(\max - \min.)}{\max} \bullet 100\%$$

calculation of the %-Difference between the minimum and maximum value:

×Pb contamination detected

Precision based on multiple analyses of three samples

1st test run, 12/6/95,
synthetic standard used

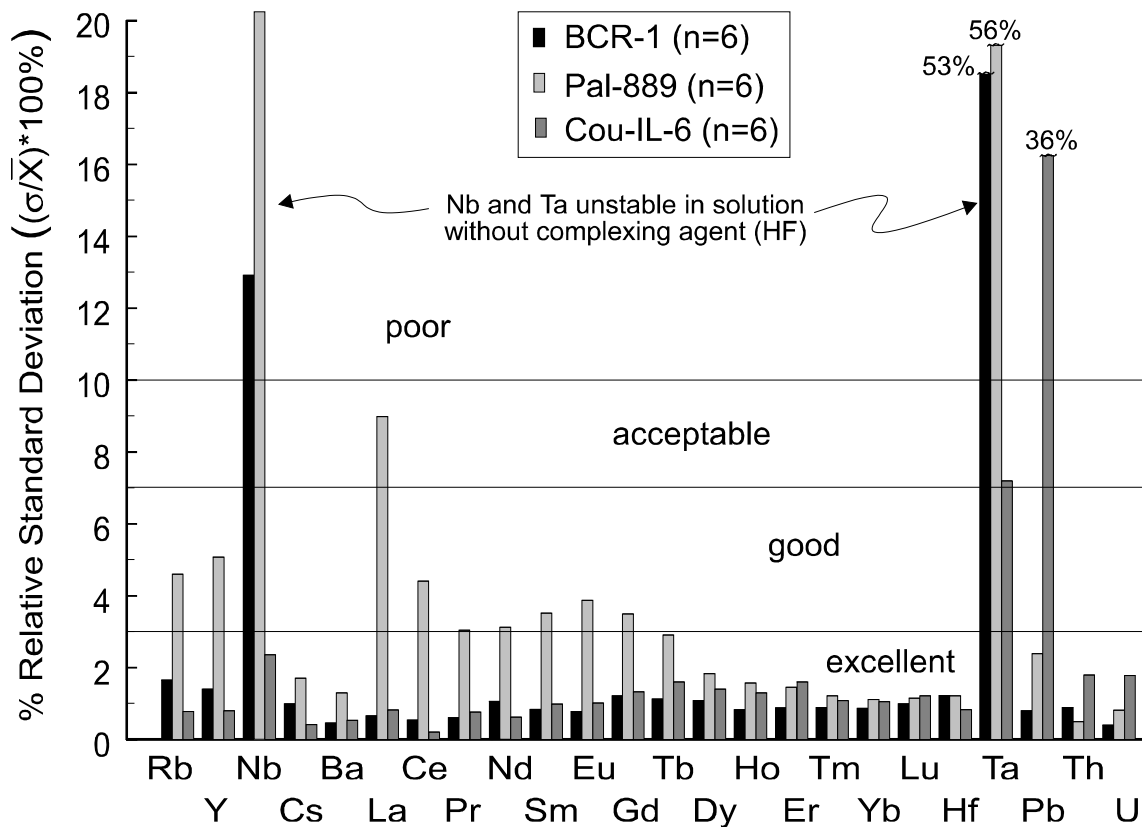


Figure E2

Diagram illustrating the precision of the analysis in the first test run. The analysis was performed by ICP-MS on two aliquots of three separate digestions per sample. Very low relative standard deviation indicate excellent precision of the determination of most elements. The poor precision of the determination of Ta and Nb is due to instability of these elements in solution (see text). Various amounts of Pb contamination were found in two of three digestions of Cou-IL-6, accordingly, large relative standard deviations were obtained (see table E6).

The poor precision of the analysis of Ta and Nb illustrated in figure E2 is interpreted as due to the instability of these elements in solution. This problem will be discussed below (section E7.1.6).

E.7.1.4 Accuracy

The elements Ta and Nb are excluded from the following discussion of the accuracy of the analysis, because Ta and Nb were apparently not stable in the analytical solutions and poor accuracy was the result. This problem was solved in the first analytical run and is discussed in more detail below (section E.7.1.6).

As illustrated in figure E3, very small differences between the measured and the recommended standard values of BCR-1 indicate that all trace elements were analyzed with very good accuracy. The results of the analysis of BCR-1 agree with the reference values within better than 5%.

The comparison of the analytical results of Pal-889 with the selected reference values reveals that some of the data points deviate more than 10% from the line with slope = 1 (figure E4). Perhaps because the reference values selected for Pal-889 are not as well-characterized as the recommended standard values of BCR-1, differences between the ICP-MS data and the reference values of Pal-889 are larger than 5% for many elements (compare figure E3 with figure E4). For example, Dy and Gd were analyzed in BCR-1 with excellent accuracy (figure E3), whereas in figure E4, the accuracy of the analysis of Pal-889 for Gd and Dy appears to be poorer, possibly due to the selection of the reference values (i.e., standard values of W-1 instead of Pal-889 were selected; see section E6.3 for more detail). Furthermore, lower precision for Y and the light REE result in slightly lower accuracy for Pal-889 as well (figure E4). Nonetheless, the mean of six analyses of Pal-889 are generally within $\pm 10\%$ of the reference values, indicating good accuracy of the analysis.

E.7.1.5 Inter-laboratory comparison

The samples Pal-889 (table E15) and Cou-IL-6 (table E16) were analyzed by ICP-MS at Washington State University Geoanalytical Laboratories. These ICP-MS data were used as reference values to which the results of the ICP-MS analysis at Union College (UC) were compared. Again, Ta and Nb are excluded from the discussion of the inter-laboratory comparison and discussed below (section E.7.1.6).

Sample: BCR-1

1st test run, 6/12/95,
synthetic standard used

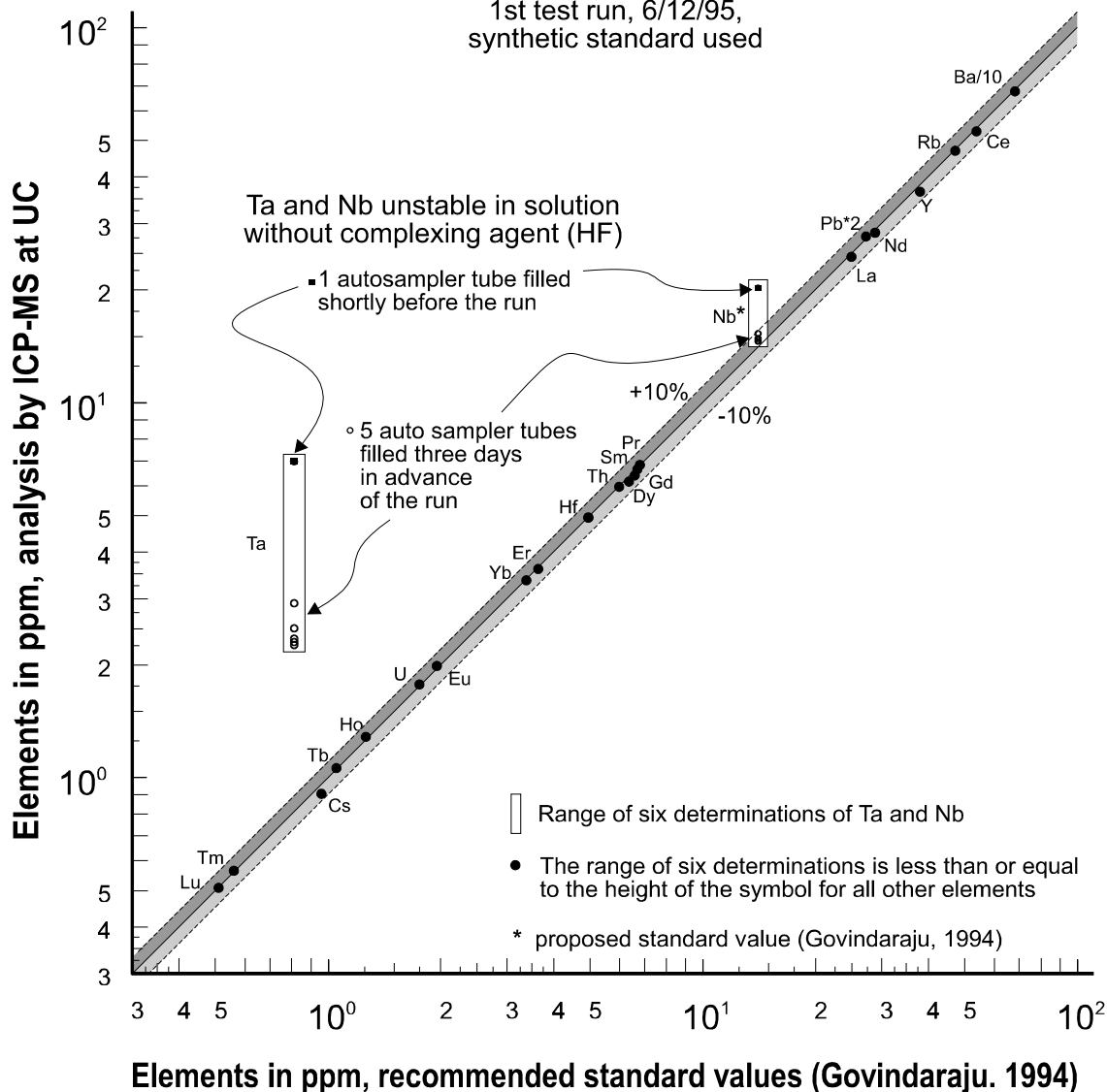


Figure E3

Comparative plot of the analytical data for BCR-1 versus the recommended standard values of Govindaraju (1994). All data points, except Ta and Nb, plot close to or on the line with slope = 1, indicating excellent accuracy of the analysis. The poor accuracy of Ta and Nb is due to the instability of these elements in solution. Three days in advance of the test run, BCR-1 solutions were transferred from the Teflon vials to five auto sampler test tubes and subsequently diluted. The sixth auto sampler tube was filled shortly before the test run and diluted. As illustrated, Ta and Nb concentrations apparently decreased with time of residence in the polypropylene auto sampler test tubes. This problem was resolved in subsequent runs.

Sample: Pal-889
(re-collected W-1)

1st test run, 06/12/95,
synthetic standard used

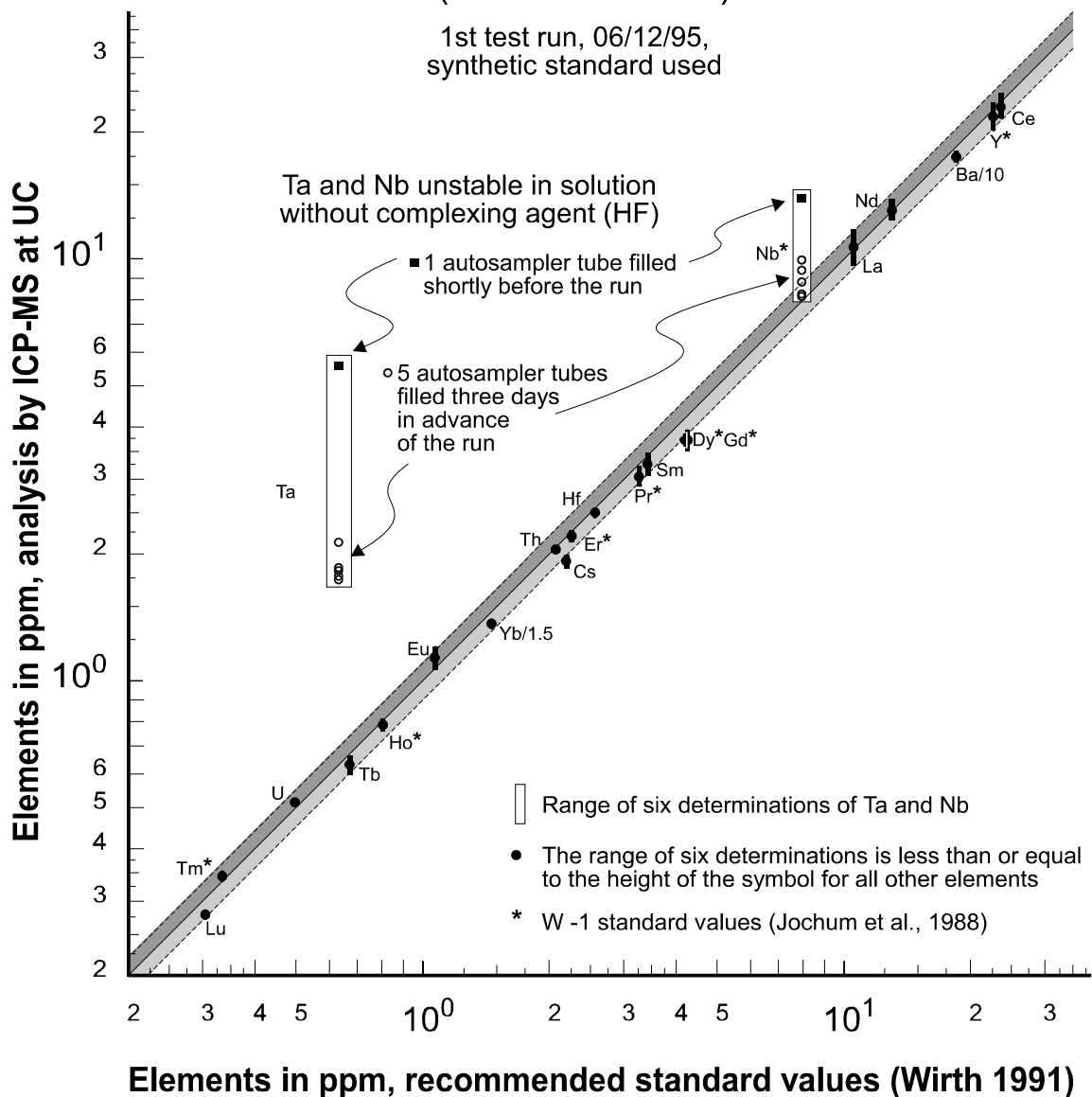


Figure E4

Comparative plot of the analytical data for Pal-889 versus the standard values of Pal-889 and W-1. The agreement between the analytical results for Pal-889 and the selected standard values is very good, indicating good accuracy of the analysis (except Ta and Nb). The deviation of the data points from the line with slope = 1 are generally larger than in figure E3 (e.g. Dy and Gd), suggesting that the selected reference values could be somewhat inaccurate as well. Again, the solution in the auto sampler tube, that was filled last, was analyzed with the highest Ta and Nb concentrations. The problem with Ta and Nb was resolved in subsequent runs.

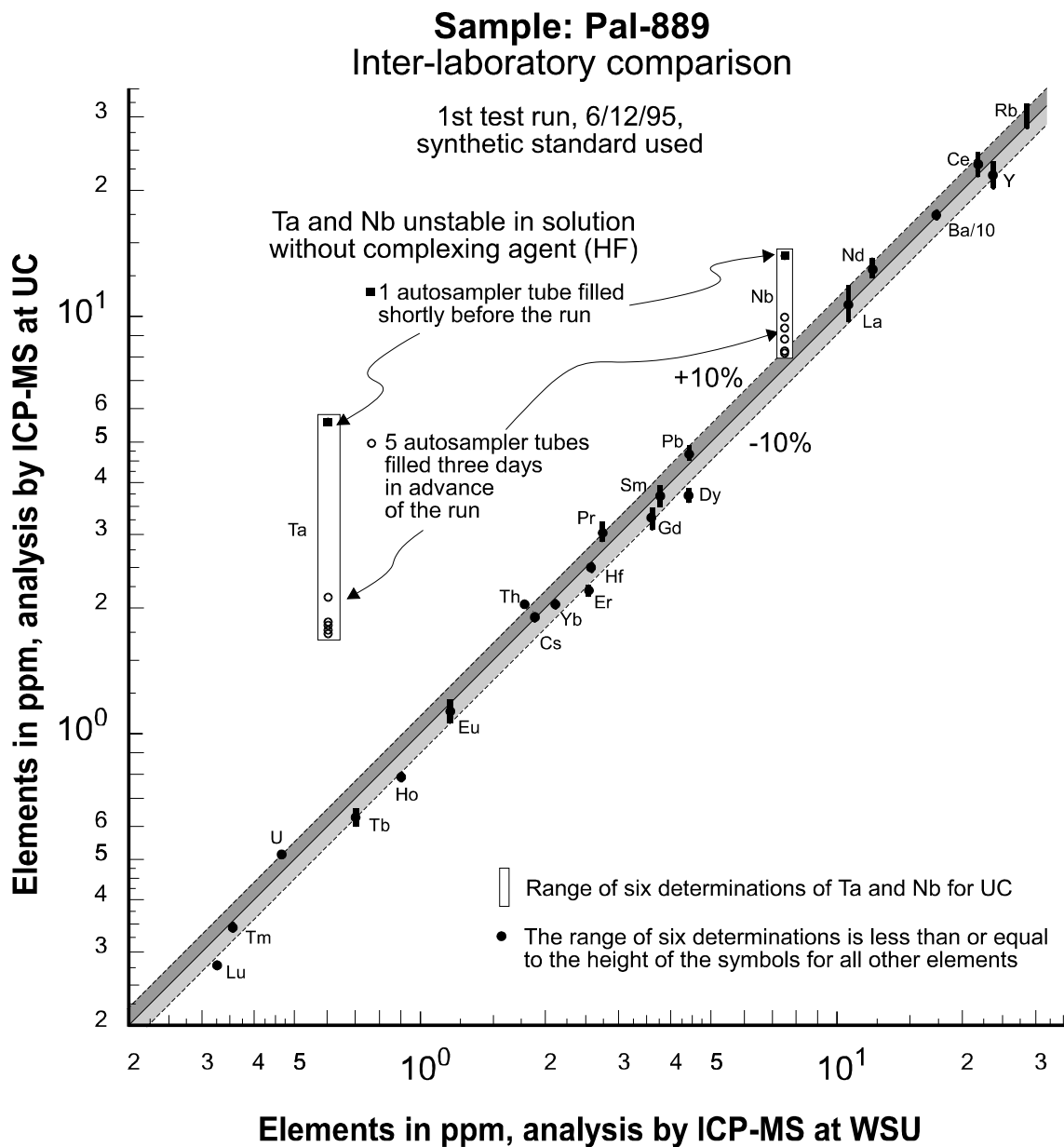


Figure E5

Comparative plot of analytical data for Pal-889 obtained at Union College (UC) versus the analytical data obtained at Washington State University (WSU). Most of the analytical results agree within 10%, indicating good accuracy of the analysis at UC as well as at WSU. The accuracy of Ta and Nb at UC is poor due to instability of Ta and Nb in solution. The sample preparation by acid digestion, routinely used at UC, does not include the addition of hydrofluoric acid (HF) to the analytical solutions. However, it is common practice at WSU to add couple drops of HF to the analytical solutions in order to stabilize Ta and Nb in the solutions. This procedure was used in later runs at UC (see section 7.1.6) resulting in good accuracy.

Sample: Cou-IL-6
Inter-laboratory comparison

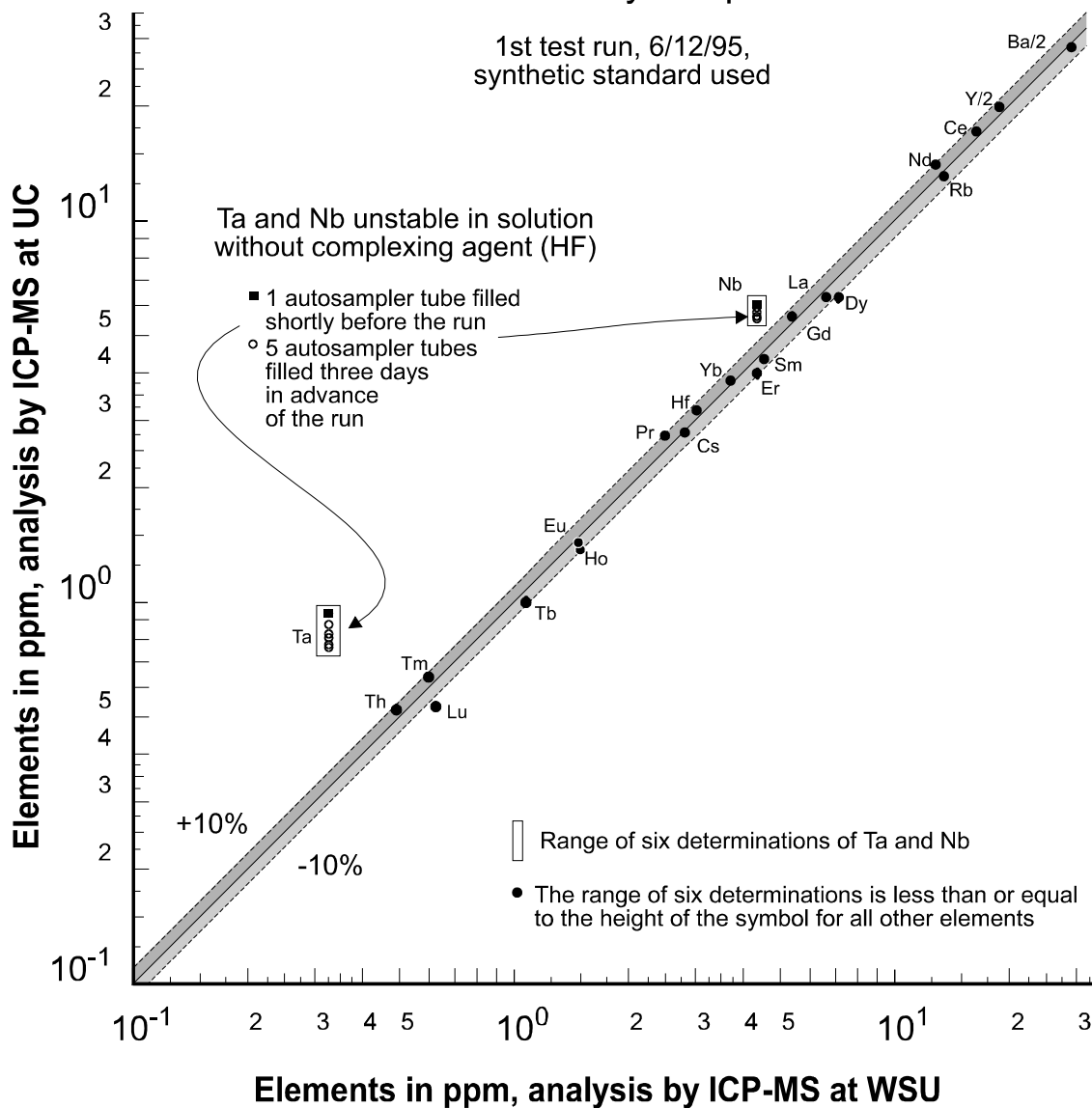


Figure E6

Comparative plot of analytical data for Cou-IL-6 obtained at Union College (UC) versus the analytical data obtained at Washington State University (WSU). Similar to the comparative diagram in figure 5, all analytical data, except for Ta, Nb and Lu, agree within 10%. Ta and Nb were determined with poor accuracy at UC because Ta and Nb were not stable in solution (the complexing agent HF was not added to the analytical solutions). The differences in the Lu values is insignificant considering the low levels of Lu in the sample.

There is generally good agreement between the two laboratories as illustrated for Pal-889 in figure E5. Most elemental concentrations, with view exceptions, agree within $\pm 10\%$. The average of six determinations of Lu, Er, and Dy plot below the line with slope = 0.9 (-10%), and the averages of Th and Pr above the line with slope = 1.1 (+10%). Differences of this kind are apparently not uncommon comparing results of different laboratories (e.g., ICP-MS, INAA and SSMS data compiled in Ewart et al., 1994a,b) differ as much as 15 - 20 % depending on the element). Using the standard values of Pal-889 in table E15 as reference values for the data obtained at WSU, the accuracy of the analysis at WSU can be assessed as well. For instance, Lu, Er and Dy concentrations measured at UC are 3% to 11% lower than the standard values, and the concentrations obtained at WSU are 5% to 14% higher than the standard values. Both laboratories determined Lu, Er and Dy with very similar accuracy; however, WSU measurements were too high and those for UC too low. Basically, the errors of both laboratories accumulate in the comparative diagram (figure E5). Furthermore, the Th and Pr concentrations determined at WSU are 16% lower than the standard values, whereas the Th data obtained at UC match exactly the standard value and Pr is only 6% lower. Consequently, the determinations of the Th and Pr concentrations are apparently more accurate at UC.

The results for Cou-IL-6 obtained at UC agree with the data obtained at WSU within $\pm 10\%$ (figure E6). Similar to the comparative diagram for Pal-889, Lu and a few other elements indicate larger than 10% variations from the 1:1 line (figure E6). As discussed above, such differences are probably the sum of the errors of both laboratories accumulating in the comparative diagram. However, such differences are inconsequential for petrogenetic interpretations.

E.7.1.6 Problems with Ta and Nb

The variations in the analytical results for BCR-1, Pal-889 and Cou-IL-6 suggest that Ta and Nb were not stable in the sample and standard solutions. Two observations were made supporting this hypothesis:

(1) Ta and Nb were determined with consistently higher concentrations in the three auto sampler tubes filled shortly before the test run, whereas all other sample solutions, which were transferred from the Teflon vials to the polypropylene auto sampler tubes three days in advance of the run, are up to 40% lower in Nb

and up to 70% lower in Ta (figures E3, E4, E5 and E6). Evidently, the concentrations of Ta and Nb in solution decreased with time of residence in the polypropylene auto sampler tubes. Possibly, Ta and Nb adhere to polypropylene when the solutions are stored in the auto sampler tubes, while Ta and Nb remain stable in solution when stored in Teflon vials (generally, polypropylene is chemically less inert than Teflon).

(2) The analytical results of Ta and Nb for BCR-1, Pal-889 and Cou-IL-6 are systematically higher than the corresponding reference values (figures E3, E4, E5 and E6), suggesting the synthetic standard solution lost relatively more Ta and Nb than the sample solutions. The elemental concentrations (= standard values) of the synthetic standard solution are accurately known as long as the elements remain stable in solution. However, Ta and Nb were apparently not stable in solution, and the concentrations may have decreased with time of residence in the polypropylene volumetric flask (1 day) and in the auto sampler tubes (3 days). Perhaps, Ta and Nb concentrations decreased more in the synthetic standard solution than in the sample solutions due to longer contact with polypropylene. As a result, the synthetic standard solution contained much less Ta and Nb in solution than originally added, and thus the standard values were much too high when applied to calibrate the analysis. Ultimately, the analytical results of Ta and Nb for BCR-1, Pal-889 and Cou-IL-6 derived from this calibration would be much higher than the corresponding reference values as observed (figures E3, E4, E5 and E6). Conversely, if Ta and Nb would have been stable in the synthetic standard solution, or would have lost relatively less Ta and Nb than the sample solutions, the analytical results for BCR-1, Pal-889 and Cou-IL-6 would be lower than the corresponding reference values.

As soon as the problem with Ta and Nb was recognized, other ICP-MS laboratories were contacted, and it was found that the instability of Ta and Nb in solution had been a problem at Washington State University (WSU) as well. The analysts at WSU solved this problem with addition of HF to the sample and standard solutions (C. Knaack, personal communication, 1995), which apparently keeps Ta and Nb in solution as fluorine complexes. This procedure, adding HF to the solutions (section E.2.2.1), was used with success at Union College beginning with first analytical run (section E8.2).

The instability of Ta and Nb in solution, however, had not been reported from the Union College Geology Department before, and Ta and Nb had been analyzed with good accuracy and precision (K. Hollocher, personal communication, 1995). The good results had apparently been obtained without adding

HF to sample and standard solutions. Presumably, the problem with Ta and Nb occurred in the first test run, because the test run was arranged in a different way than most analytical runs performed at Union College. The main differences were the following: a synthetic standard solution was used instead of rock standards, and all but three solutions were stored in the auto sampler tubes for three days instead of minimizing the exposure to polypropylene.

The hypothesis outlined below might explain why these differences could be critical. Perhaps, Ta and Nb were not stable in solution due to deficiency of HF in the synthetic standard solution (HF was not added). In contrast to the synthetic standard solution, which was prepared by mixing and diluting single-element solutions, the samples were dissolved by acid digestion and might have retained HF during the dissolution procedure (section E.2.2.1). Perhaps, not all HF was driven out in the last evaporation step (step 7 in section E.2.2.1). Provided that HF was retained, the amount of HF was probably insufficient to stabilize Ta and Nb in the sample solutions that were stored in the polypropylene auto sampler tubes for three days. However, the amount of retained HF might have been sufficient to stabilize Ta and Nb in the sample solutions that were stored in Teflon vials until transferred to polypropylene auto sampler tubes just prior to analysis.

Rock standards were used in a second test run, and the exposure of solutions to polypropylene was minimized as described in “Strategy and Methods” for the second test run (section E.7.2). Potentially, standards as well as samples might retain enough HF so that Ta and Nb are stable in solution for the duration of the analysis by ICP-MS (~7 hours). The second test run was designed to determine whether it is really necessary to add HF to the sample and standard solutions to stabilize Ta and Nb.

E.7.1.7 Evaluation of dissolution

High precision (figure E2) and accuracy (figures E3, E4, E5 and E6) were demonstrated in the first test run where 24 trace elements were determined for BCR-1, Pal-889 and Cou-IL-6. Several potential problems, such as incomplete digestion of the samples, weighing errors, poor instrumentation, or flawed calibration can be ruled out, because the test run was set up in a manner such that any of these

would be indicated by poor precision and/or accuracy. In fact, the test run proved to be very successful, revealing a major problem with Ta and Nb, which were apparently unstable in solution.

As argued below, it is well-constrained that incomplete digestion is not a problem dissolving samples of basaltic to andesitic composition using the sample preparation method described in section E.2.2. A synthetic standard prepared from Spex® single element solutions was used for the calibration. Therefore, the elemental concentrations in the synthetic standard solution do not depend on the complete dissolution of any mineral phases. If samples were not completely dissolved, then systematically lower values for the elements partitioned into chemically resistant minerals would have been observed. However, all elements (except Ta and Nb) were determined very accurately. Consequently, the complete dissolution of the samples was verified using a synthetic standard.

E.7.2 Second test run, 11/17/95, NIST-278 and NIST-688 used as standards

E.7.2.1 Strategy and methods

The second test run was set up similar to a typical analytical run: 16 samples from the Oregon Coast Range ophiolite and four samples from the Josephine ophiolite were analyzed, and two rock standards (NIST-278 and NIST-688) were used for the calibration. Five blanks and two digestions of each of the samples and standards were prepared using the acid digestion method described in section E.2.2. However, HF was not added to any of the solutions as done in following runs to stabilize Ta and Nb. The sequence of the analysis of solutions is similar to that of the analytical runs (figure E1). However, the four groups of blanks and standards in the second test run contained only aliquots of NIST-278, NIST-688, and blanks but none of BCR-1 (i.e., BCR-1 was not used as standard). Furthermore, the exposure of solutions to polypropylene was minimized: all blank, standard, and sample solutions were transferred to the auto sampler tubes and diluted within 3-9 hours of being analyzed. Two additional elements (Cr and Zr) were analyzed in the second test run.

Three reference materials (Z-83a, BCR-1 and Pal-889) were analyzed together with blanks standards and samples for the purpose of evaluating the accuracy and precision for the second test run. Two aliquots of two digestions of Z-83a (n=4) were evenly spaced throughout the run to test whether or not Ta

and Nb are stable in solution for the duration of the second test run (about 7 hours). If not, one would expect to see Ta and Nb values changing throughout the run. Additionally, these four analyses of Z-83a enable to evaluate drift corrections which the VGFIX2 program automatically performs. In contrast to the four auto sampler tubes containing Z-83a spaced throughout the run, two aliquots of two digestions of BCR-1 (n=4) and Pal-889 (n=4) were analyzed in series. If drift corrections were incorrect, the precision of the analysis would be significantly lower for Z-83a than for BCR-1 and Pal-889.

E.7.2.2 Limits of detection

Using equation (1), the detection limits were determined from the blank residuals of the second test run and are listed in table E8. The detection limits of Cr, Zr, and Ba are generally higher than those of the other elements (see section E.5 and E.6.1 for more detail). Nonetheless, all elemental concentrations determined in the samples are well above the calculated detection limits.

E.7.2.3 Precision

The mean values and standard deviations (1σ) of four analyses of BCR-1, Pal-889 and Z-83a are listed in table E8. To illustrate the precision of the analysis, the relative standard deviations of analyzed elements are plotted in figure E7. Generally, the precision is very good as suggested by the analytical results of BCR-1, Pal-889 and Z-83a, except for Ta. The problem with Ta (and Nb) is discussed separately in section E.7.2.6.

The four sample solutions of Z-83a were evenly spaced throughout the test run in order to evaluate the drift corrections performed by the VGFIX2 program. In general, the sample Z-83a does not indicate significantly higher relative standard deviations than BCR-1 and Pal-889 which were analyzed in series (figure E6). This shows clearly that the drift corrections, performed by the VGFIX2 program, are sufficient to compensate for instrument drift, even for very long analytical runs (7 hours).

Cr concentrations determined in the four Z-83a solutions do not change systematically with time; but vary randomly. Therefore, the marginally acceptable precision of determining Cr is most likely due to real limitations of the analysis and not due to any instability of Cr in solution.

Table E8: Results of second test run, 11/17/95, NIST-278 and NIST-688 used as standards

| Element | Detction Limits in ppm | BCR-1 | | Pal-889 | | Z-83a | | Z-83a | |
|---------|------------------------------|---------------|---------------------|---------------|---------------------|---------------|---------------------|-------------------------|---------------------|
| | | mean (n=4) | error 1 σ | mean (n=4) | error 1 σ | mean (n=4) | error 1 σ | <i>XRF</i> /INAA [1] | error 2 σ |
| V | n.d. | n.d. | - | n.d. | - | n.d. | - | 416 | - |
| Cr | 0.66 | 12.0 | 0.5 | 283 | 11 | 283 | 30 | 254 | 293 - |
| Rb | 0.019 | 52.6 | 2.2 | 31.5 | 0.4 | 2.05 | 0.11 | - | - |
| Sr | n.d. | n.d. | - | n.d. | - | n.d. | - | 598 | - |
| Y | 0.034 | 37.0 | 0.2 | 23.0 | 0.2 | 26.3 | 0.8 | 25 | - |
| Zr | 5.5 | 190 | 4 | 97.3 | 1.7 | 75.0 | 1.9 | 84 | - |
| Nb | 0.014 | 17.8* | 0.4 | 9.9* | 0.19 | 8.3* | 0.52 | - | - |
| Cs | 0.0040 | 1.037 | 0.027 | 2.19 | 0.06 | 0.06 | 0.00 | - | - |
| Ba | 0.62 | 684.4 | 17.9 | 185.0 | 3.2 | 11.7 | 0.7 | - | - |
| La | 0.010 | 26.83 | 1.24 | 11.27 | 0.19 | 7.09 | 0.10 | 6.89 | 0.15 |
| Ce | 0.031 | 57.3 | 1.7 | 23.7 | 0.6 | 16.85 | 0.46 | 18.36 | 1.19 |
| Pr | 0.0037 | 7.17 | 0.12 | 3.15 | 0.04 | 2.72 | 0.08 | - | - |
| Nd | 0.017 | 29.5 | 1.3 | 14.3 | 0.3 | 13.7 | 0.3 | - | - |
| Sm | 0.0048 | 6.44 | 0.27 | 3.45 | 0.09 | 3.90 | 0.12 | 3.82 | 0.05 |
| Eu | 0.0013 | 1.97 | 0.05 | 1.14 | 0.03 | 1.38 | 0.04 | 1.25 | 0.03 |
| Gd | 0.0047 | 7.17 | 0.19 | 3.87 | 0.08 | 4.69 | 0.23 | - | - |
| Tb | 0.0008 | 1.05 | 0.04 | 0.623 | 0.014 | 0.737 | 0.019 | 0.81 | 0.1 |
| Dy | 0.0043 | 6.33 | 0.16 | 3.86 | 0.09 | 4.60 | 0.12 | - | - |
| Ho | 0.0014 | 1.33 | 0.03 | 0.787 | 0.015 | 0.96 | 0.03 | - | - |
| Er | 0.0030 | 3.41 | 0.13 | 2.15 | 0.08 | 2.53 | 0.06 | - | - |
| Tm | 0.00088 | 0.521 | 0.010 | 0.314 | 0.006 | 0.373 | 0.012 | - | - |
| Yb | 0.0031 | 3.44 | 0.14 | 2.07 | 0.05 | 2.39 | 0.03 | 2.34 | 0.24 |
| Lu | 0.00080 | 0.575 | 0.014 | 0.322 | 0.006 | 0.370 | 0.008 | 0.35 | 0.3 |
| Hf | 0.006 | 5.31 | 0.12 | 2.63 | 0.03 | 2.51 | 0.07 | 2.37 | 0.24 |
| Ta | 0.0045 | 0.89* | 0.11 | 0.77* | 0.06 | 0.45* | 0.15 | 0.43 | 0.19 |
| Pb | 0.03 | 15.3 | 0.3 | 5.59 | 0.13 | 1.843 | 0.02 | - | - |
| Th | 0.0031 | 6.32 | 0.15 | 2.25 | 0.04 | 0.709 | 0.003 | 0.76 | 0.19 |
| U | 0.0022 | 1.80 | 0.05 | 0.516 | 0.007 | 0.255 | 0.012 | - | - |

* Ta (and Nb) unstable in solution

[1] unpublished data from Harper (pers. comm., 1995)

n.d. not determined

ICP-MS analysis; standard deviation:
$$\sigma = \sqrt{\frac{\sum(X_i - \bar{X})^2}{n^2}}$$

see tables 2 and 5 for recommended standard values of BCR-1 and Pal-889, respectively

see tables 14 and 15 for compilation of analytical results for BCR-1 and Pal-889, respectively

Precision based on multiple analyses of three samples

2nd test run, 17/11/95,
NIST-688 and NIST-278
used as standards

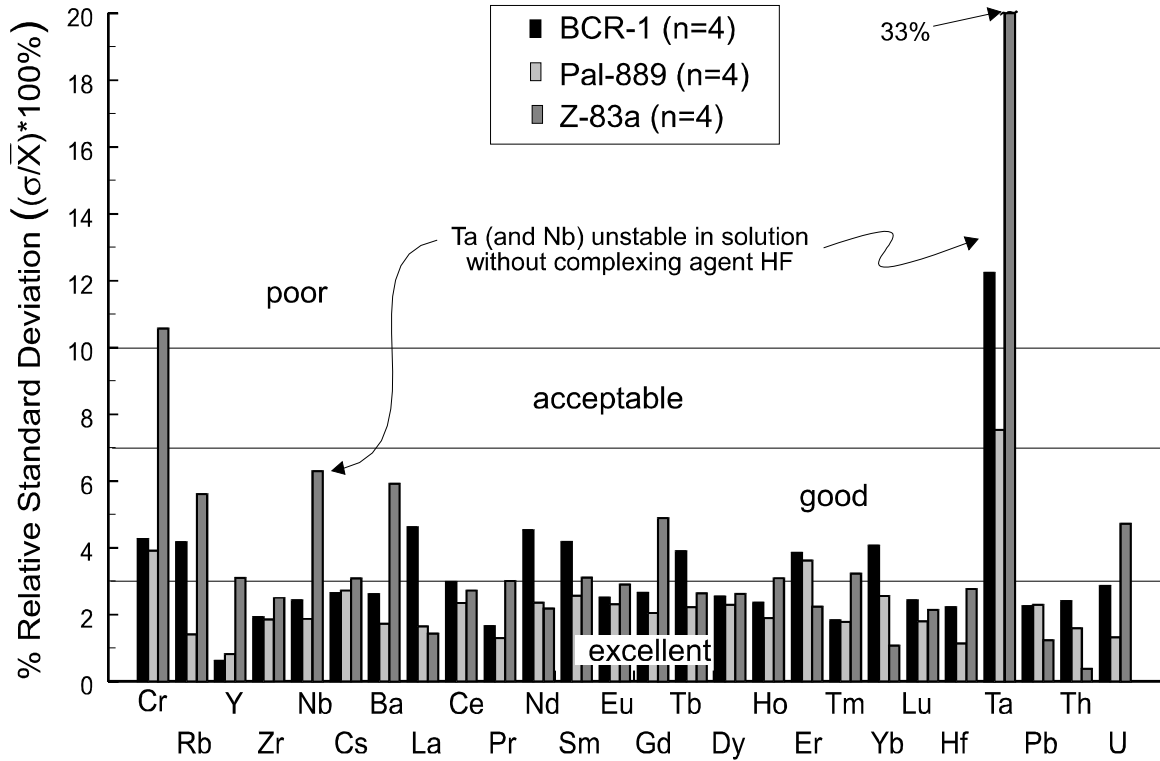


Figure E7

Diagram illustrating the precision of the analysis of the second test run. Two aliquots of two separate digestions per sample were analyzed. Except for the element Ta, good to excellent precision of the analysis is indicated by 2% to 5% relative standard deviation. In contrast to BCR-1 and Pal-889 which were analyzed in series, the four auto sampler tubes of Z-83a were evenly spaced throughout a ~7 hour run. The extremely poor precision of Ta for Z-83a is interpreted as due to the decrease of Ta concentrations with time of residence in the polypropylene auto sampler tubes.

E.7.2.4 Accuracy

The accuracy of the second test run is assessed by comparing the analytical results of BCR-1 and Pal-889 with the corresponding reference values. As illustrated in figures E8 and E9, the analytical results agree with the recommended standard values generally within 10%, and most points plot with very little departure from the line with slope = 1. However, the data points of Ta, Nb and Cr in figure E8 (BCR-1) and of Ta and Nb in figure E9 (Pal-889) indicate significant disagreement between the ICP-MS analysis and the corresponding standard values. Evidently, the problem with Ta and Nb was still not resolved in the second test run and is discussed in a separate section below (section E7.2.6).

The Cr concentration in BCR-1 was determined with seemingly poor accuracy as illustrated in figure E8. Perhaps, the standard value of Cr is not very good (it is “proposed” rather than “recommended”, table E2). The Cr values obtained by ICP-MS may be more accurate than the proposed standard value of Govindaraju (1994). Regardless, the difference of 25% between the standard value (16 ppm) and the analytical results (12 ppm) is inconsequential for petrogenetic interpretations considering the low level of Cr in the sample. Furthermore, the analytical results for samples with higher Cr concentrations are in good to acceptable agreement with the reference values (figures E9 and E10).

E.7.2.5 Inter-laboratory comparison

The analytical data of Z-83a obtained by XRF and INAA are listed in table E8, and the corresponding comparative plot is shown in figure E10. Generally, the analytical data agree within the errors of the analyses. The indicated mean values plot close to or on the line with slope = 1.

Cr is determined with much higher precision by XRF analysis and INAA than ICP-MS analysis (figure E10). Nonetheless, there is a notable difference between the Cr data obtained by INAA (293 ppm) and XRF analysis (254 ppm), and these Cr values do not overlap within 2σ error. The mean of the ICP-MS analysis of Cr (283 ppm) agrees best with the INAA data (table E8).

The analytical results for Y indicate good agreement between ICP-MS and XRF analyses (figure E10). Yet, the ICP-MS data for Zr are more than 10% lower than the XRF values, even though Zr concentrations in BCR-1 and Pal-889 were determined very accurately (figures E8 and E9). Probably, Zr

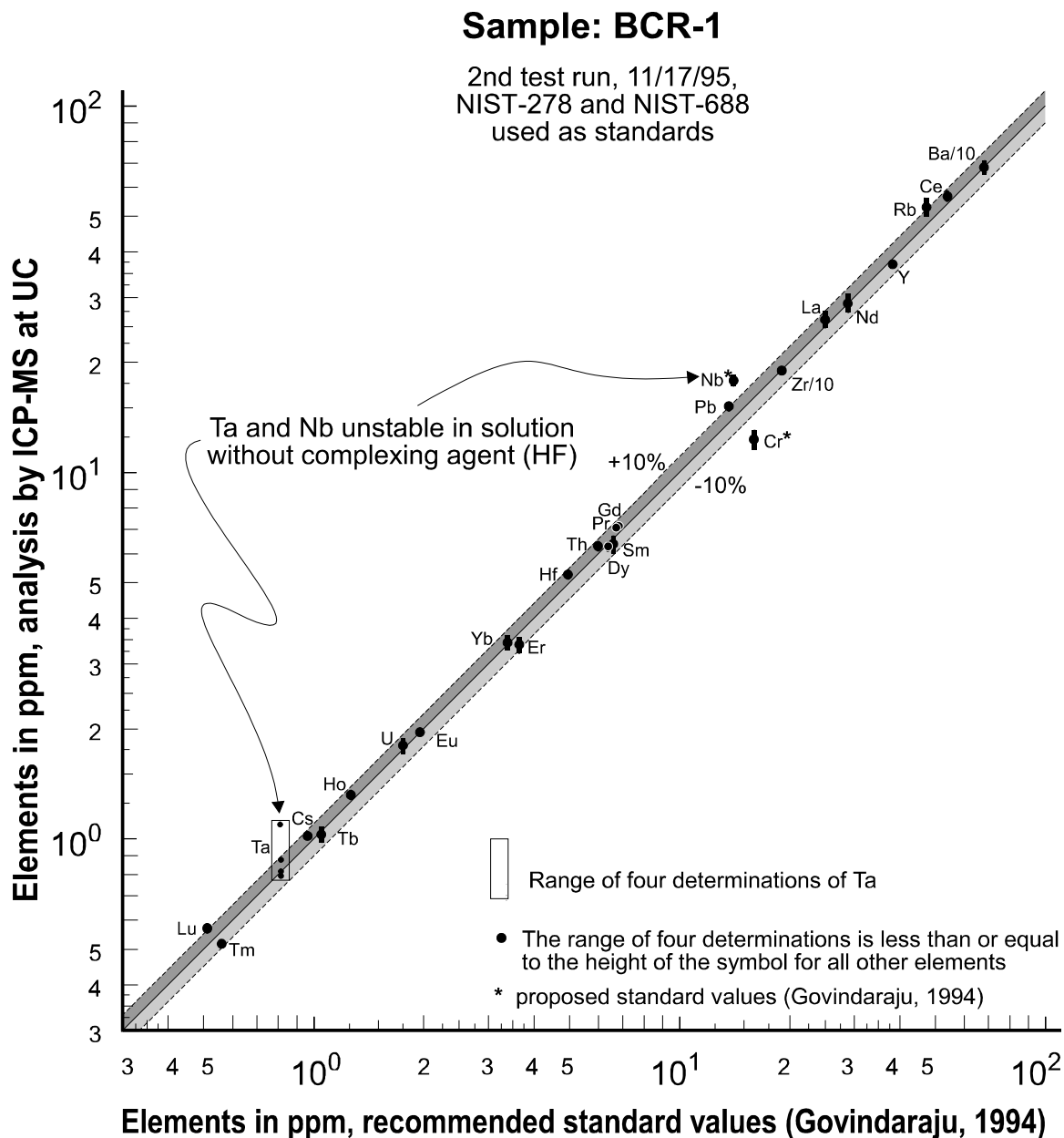


Figure E8

Comparative plot of the analytical data of the second test run versus the recommended standard values of BCR-1 (Govindaraju, 1994). Most data points plot close to or on the line with slope = 1, indicating excellent accuracy of the analysis. The analytical results of Ta and Nb suggest once again that Ta and Nb are unstable in solution, although accuracy was improved over the first test run (compare with figure 3). Note that the analytical results of Cr are notably lower than the proposed standard value of Cr. Either the standard value is too high, or the analysis by ICP-MS is too low for samples with low levels of Cr.

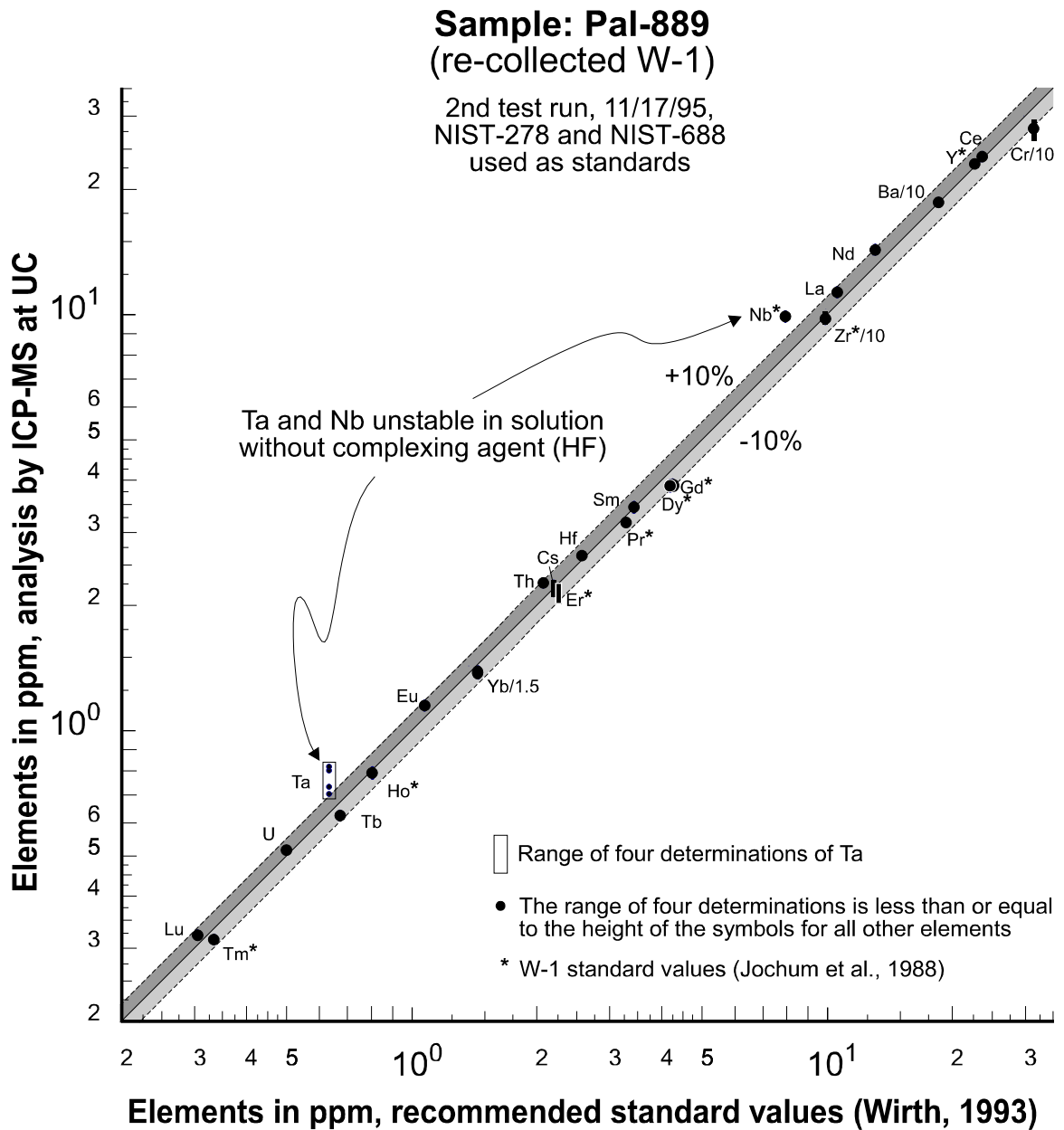


Figure E9

Comparative plot of the analytical data for Pal-889 versus the standard values of Pal-889 and W-1. All analytical results agree with the reference values within 10%, indicating very good accuracy of the analysis. Also in this diagram, Ta and Nb data plot at notably higher values than the corresponding standard values, indicating that the standard solutions (NIST-278 and NIST-688) lost some amount of Ta and Nb.

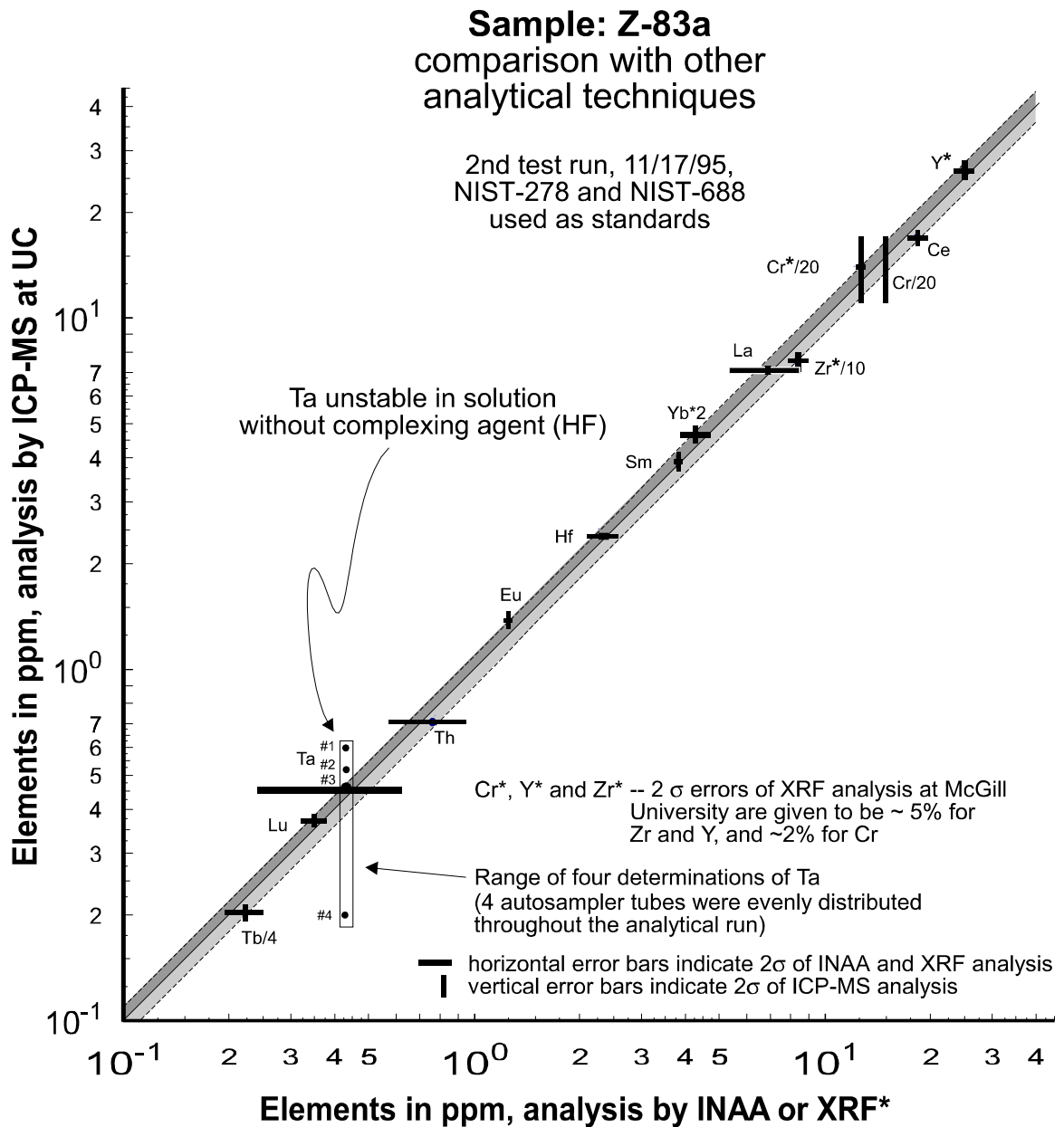


Figure E10

Comparative plot of analytical data for Z-83a obtained at Union College (UC) versus the analytical data obtained by XRF analysis and INAA. All of the analytical results agree within 10%, indicating good accuracy of the analysis at UC as well as by INAA and XRF analysis. The four auto sampler tubes containing Z-83a solutions were evenly distributed throughout the run. The first analyzed solution (#1) indicates the highest concentration and the last analysis (#4) the lowest, suggesting that Ta was not stable in solution for the duration of the test run. This problem was resolved with beginning of the first analytical run.

was determined at higher than standard concentration in the XRF analyses and lower than standard concentration using ICP-MS, therefore resulting in >10 % differences between the two techniques. For example, the XRF analysis of Pal-889 (table E.15) determined at the University of Massachusetts (Zr = 101.6 ppm) matches very closely the standard value of 98.6 ppm whereas five analyses by XRF at McGill University indicate significantly higher Zr values (116 ± 5 ppm). The ICP-MS data for Pal-889 show generally lower Zr concentrations (90.6 to 99.3 ppm) than the recommended standard value.

Evidently, the precision of La, Ce, Tb, Yb, Lu, Hf, and Th was better by ICP-MS analysis than by INAA as indicated by smaller 2σ errors calculated for the ICP-MS data. Only Eu and Sm were determined with better precision by INAA than by ICP-MS analysis. Generally, the agreement between the two techniques is very good (within 10%, figure E10), giving further evidence of good accuracy of the ICP-MS analysis.

E.7.2.6 Problems with Ta and Nb

Apparently, Ta and Nb were not stable in the sample and standard solutions analyzed in the second test run, in spite of the changes with respect to the first test run. Two observations support the hypothesis that Ta and Nb were not stable in solution:

- (1) The concentrations of Ta in Z-83a solutions, which were dispersed throughout the run, decreased with time of residence in the auto sampler tubes, resulting in the high relative standard deviation of 33% (figure E7). The Z-83a solution analyzed earliest in the run gave the highest Ta concentration (#1, figure E10). Subsequently, Ta concentrations decreased with time (#2 - #4, figure E10). Consequently, such variations in the analytical results are interpreted as due to the instability of Ta in solution (i.e., increased loss of Ta with time is possibly due to adherence to walls of polypropylene auto sampler tubes).
- (2) Similar to the first test run (figures E3 and E4), the Ta and Nb concentrations determined in the second test run are higher than the recommended standard values (figures E8 and E9). This suggests that the standard solutions (NIST-278 and NIST-688) must have lost relatively more Ta and Nb than the sample solutions, further indicating that the problem with Ta and Nb was still not solved.

Nonetheless, the accuracy and precision of Ta and Nb were clearly improved (figures E7, E8 and E9) compared to the first test run (figures E2, E3, and E4). Apparently, the use of rock standards instead of a synthetic standard solution and minimizing the exposure of the solutions to polypropylene were effective measures to improve the accuracy and precision of Ta and Nb. However, the analytical results of Ta and Nb were still not acceptable and had to be further improved. It was believed that further improvement might be achieved by adding HF to all solutions prior to analysis as done at Washington State University Geoanalytical Laboratories (C. Knaack, personal communication 1995)

In conclusion, the analytical results of the second test run suggest that the samples and standards probably retained some HF during acid digestion. However, this amount of retained HF was apparently not enough to stabilize Ta and Nb in all analytical solutions for the duration of the test run. The observed decrease of the Ta and Nb concentrations in analytical solutions during the 7 hour run could be partly due to the deterioration of the solutions when in prolonged contact with polypropylene. Consequently, some HF must be added to the sample and standard solutions in the Teflon vials before the solutions are transferred to the polypropylene auto sampler tubes and subsequently diluted. It appears that by adding a sufficient amount of HF to the solutions in the chemically inert Teflon vials, all of the Ta and Nb in solution form soluble complexes before the solutions are transferred to the chemically less inert polypropylene auto sampler tubes. This procedure was successfully used for all samples and standards in subsequent analytical runs, and excellent accuracy and precision were obtained for Ta and Nb in all samples.

E.8 Analytical runs

E.8.1 Introduction

A complete description of the sample preparation procedure, the acquisition of the data, and the methods of data evaluation are described above in sections E2 through E6. Nonetheless, some remarks regarding the procedure are made in order to emphasize parts of it (or differences with the test runs) which enhanced the accuracy and precision of the analysis, or at least provided the means to detect any problems with the analysis.

The unknown samples were prepared in duplicate, which means two separate solutions were prepared by weighing and dissolving 0.1 g of the sample powder in each of two Teflon vials (figure E1). The accuracy may be improved with the analysis of duplicates, and errors during sample preparation, such as weighing errors, pipetting errors, contamination and incomplete dissolution can be detected. In the analytical runs, the relative standard deviation of the analysis of four separate digestions for a number of samples were generally less than 5% (table E13), indicating no errors were made preparing the samples, and all samples were completely dissolved. Similar consistency of the analytical results of three separate digestions per sample were demonstrated in the first test run (table E7). The results of ICP-MS analyses reported in appendix A represent averages of the duplicate analyses. Note that two additional elements (V and Sr) were analyzed in all analytical runs.

The well-characterized U.S.G.S. standard BCR-1 was always included in the analytical runs, and obtained data for each analytical run were used in two ways (section E5). First, BCR-1 was treated as unknown sample, and the elemental concentrations of BCR-1 were calculated with NIST-278 and NIST-688 as standards. Obtained analytical results of BCR-1 were then used to assess the accuracy and precision of the analysis. Treating BCR-1 as an unknown sample has the additional benefit that any problems with the preparation of the standard solutions (NIST-278, NIST-688 and BCR-1), such as weighing errors, pipetting errors, or contamination, can be detected before the elemental concentrations of all other unknown samples are calculated. Second, NIST-278, NIST-688 and BCR-1 were used as standards in order to calculate the elemental concentrations of Pal-889, Cou-IL-6 and all other samples. The analytical results are most likely more accurate when all three standards, instead of only the two NIST-standards, are put to use. In other words, the accuracy of the analytical results of Pal-889, Cou-IL-6 and all other samples (derived from a calibration with three standards) is considered better characterized than the analytical results of BCR-1 (derived from a calibration with only two standards).

Finally, 0.05 ml of 50% HF was added to all blank, standard and sample solutions prior to transferring aliquots of the solutions to polypropylene auto sampler tubes. Any indications of instability of Ta and Nb in solution were not observed in any of the analytical runs. Ta and Nb were analyzed with excellent accuracy and precision in all analytical runs. Thus, the Ta and Nb problems were resolved. Of

course, new sample solutions for all unknown samples analyzed in the second test run were prepared again using acid digestion, and HF was added to the solutions. Thus, all samples analyzed in the second test run were re-analyzed in order to obtain accurate Ta and Nb values.

E.8.2 First analytical run, 02/23/96

E.8.2.1 Limits of detection

The detection limits were determined as described in section E.6.1 and are listed in table E9. None of the detection limits indicate problems with the analysis, and as usual, V, Cr, Zr and Ba have relatively higher detection limits than other elements. This is not a problem in that all determined elemental concentrations of the samples (appendix F) are well above the detection limits.

E.8.2.2 Precision

The precision of the analysis is based on multiple analyses of BCR-1 (treated as an unknown), Pal-889 and Cou-IL-6. The relative standard deviation is smaller than 7% for most elements in all three samples (figure E.11), indicating good precision of the analysis.

Cr and V show slightly higher relative standard deviations than the other elements (figure E11). This was also observed for Cr in the second test run (figure E7). Perhaps, the precision of Cr and V is in general not as good as for the other elements indicating limitations of ICP-MS for accurate analysis of Cr and V.

The poor precision for Pb in Cou-IL-6 may be related to the low levels of Pb in Cou-IL-6: samples with low Pb concentrations are affected by even very small amounts of Pb contamination whereas similar amounts of contamination would have no effect on samples with high Pb concentrations.

E.8.2.3 Accuracy

The accuracy is evaluated by comparing the analytical results of BCR-1 and Pal-889 (table E9) with the corresponding standard values. As illustrated in figure E12, the range of eight determinations of most

Table E9: Results of first analytical run, 02/23/96

| Element | Detection Limits in ppm | BCR-1 | | Pal-889 | | Cou-IL-6 | |
|---------|----------------------------|---------------|---------------------|---------------|---------------------|---------------|---------------------|
| | | mean (n=8) | error 1 σ | mean (n=4) | error 1 σ | mean (n=8) | error 1 σ |
| V | 0.35 | 411 | 26 | 269 | 16 | 501 | 28 |
| Cr | 1.27 | 14.5 | 1.3 | 310 | 21 | 89 | 5 |
| Rb | 0.035 | 47.2 | 0.7 | 29.7 | 1.1 | 12.8 | 0.2 |
| Sr | 0.18 | 342 | 9 | 174 | 4 | 273 | 5 |
| Y | 0.016 | 35.5 | 1.0 | 21.4 | 0.7 | 38.9 | 1.0 |
| Zr | 8.3 | 183 | 4 | 90.9 | 2.5 | 119 | 2 |
| Nb | 0.035 | 15.5 | 0.5 | 8.68 | 0.32 | 5.71 | 0.24 |
| Cs | 0.0062 | 0.96 | 0.02 | 1.95 | 0.02 | 2.82 | 0.13 |
| Ba | 0.60 | 686 | 17 | 169 | 8 | 53.5 | 3.4 |
| La | 0.028 | 25.7 | 0.5 | 10.1 | 0.3 | 6.11 | 0.26 |
| Ce | 0.056 | 52.5 | 1.1 | 21.8 | 0.8 | 15.9 | 0.8 |
| Pr | 0.0068 | 6.76 | 0.16 | 2.93 | 0.08 | 2.57 | 0.11 |
| Nd | 0.020 | 29.8 | 0.502 | 13.1 | 0.4 | 13.4 | 0.6 |
| Sm | 0.0038 | 6.52 | 0.15 | 3.26 | 0.10 | 4.18 | 0.22 |
| Eu | 0.0014 | 2.00 | 0.03 | 1.09 | 0.04 | 1.34 | 0.06 |
| Gd | 0.0040 | 6.73 | 0.22 | 3.69 | 0.12 | 5.31 | 0.30 |
| Tb | 0.00035 | 1.03 | 0.03 | 0.620 | 0.018 | 0.912 | 0.041 |
| Dy | 0.0025 | 6.29 | 0.11 | 3.82 | 0.11 | 6.06 | 0.19 |
| Ho | 0.00086 | 1.29 | 0.02 | 0.768 | 0.033 | 1.30 | 0.05 |
| Er | 0.0023 | 3.51 | 0.07 | 2.13 | 0.08 | 3.77 | 0.12 |
| Tm | 0.00080 | 0.506 | 0.017 | 0.319 | 0.011 | 0.575 | 0.023 |
| Yb | 0.0028 | 3.26 | 0.10 | 2.01 | 0.03 | 3.65 | 0.15 |
| Lu | 0.00052 | 0.563 | 0.014 | 0.305 | 0.004 | 0.557 | 0.014 |
| Hf | 0.0044 | 4.97 | 0.11 | 2.56 | 0.09 | 3.15 | 0.07 |
| Ta | 0.013 | 0.751 | 0.011 | 0.600 | 0.043 | 0.301 | 0.009 |
| Pb | 0.25 | 14.5 | 0.2 | 4.52 | 0.27 | 0.582 | 0.075 |
| Th | 0.017 | 6.22 | 0.09 | 2.07 | 0.06 | 0.541 | 0.012 |
| U | 0.0021 | 1.71 | 0.05 | 0.494 | 0.008 | 0.180 | 0.005 |

standard deviation : $\sigma = \sqrt{\frac{\Sigma(X_i - \bar{X})^2}{n^2}}$

see tables 2 and 5 for recommended standard values of BCR-1 and Pal-889, respectively
 see tables 14, 15 and 16 for compilation of analytical results
 for BCR-, Pal-889, and Cou-IL-6, respectively

Precision based on multiple analyses of three samples

1st analytical run, 02/23/96

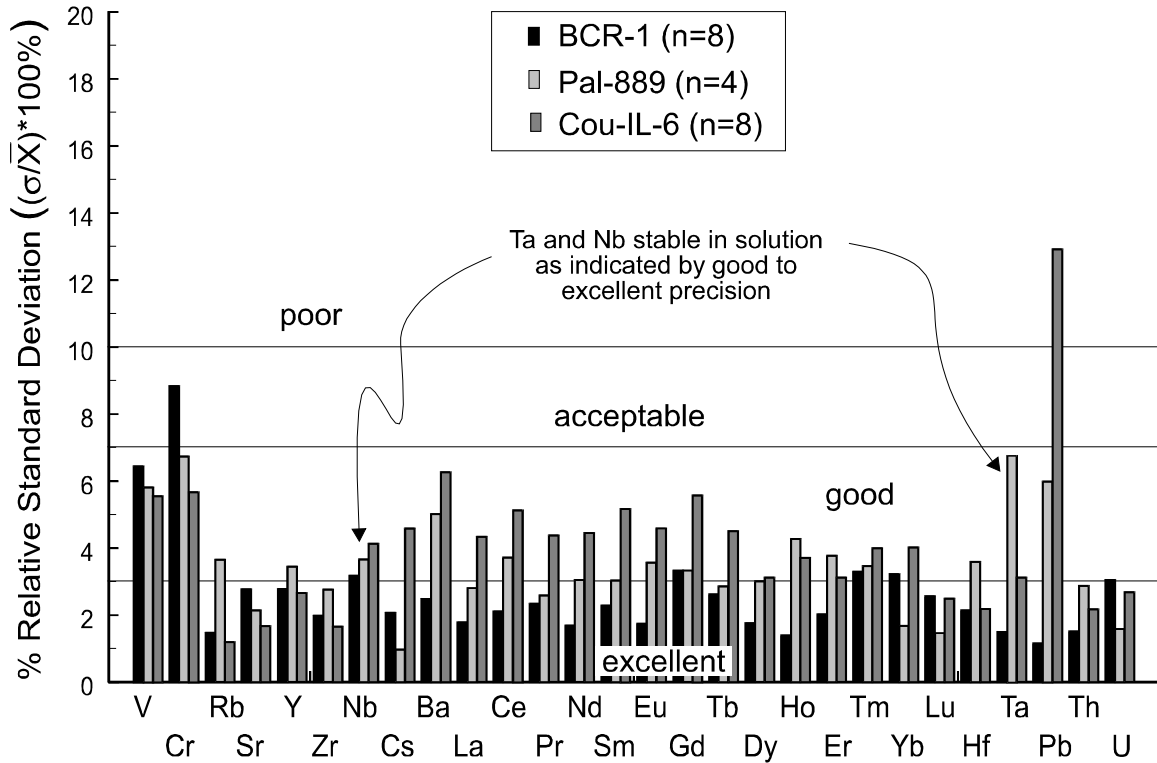


Figure E11

Diagram illustrating the precision of the analysis of the first analytical run. Four aliquots of two digestions of BCR-1 and Cou-IL-6 and two aliquots of two digestions of Pal-889 were analyzed. Except for Pb determined in Cou-IL-6, good to excellent precision of the analysis is indicated by 2% - 5% relative standard deviation on average. V and Cr have slightly higher relative standard deviations (~7%).

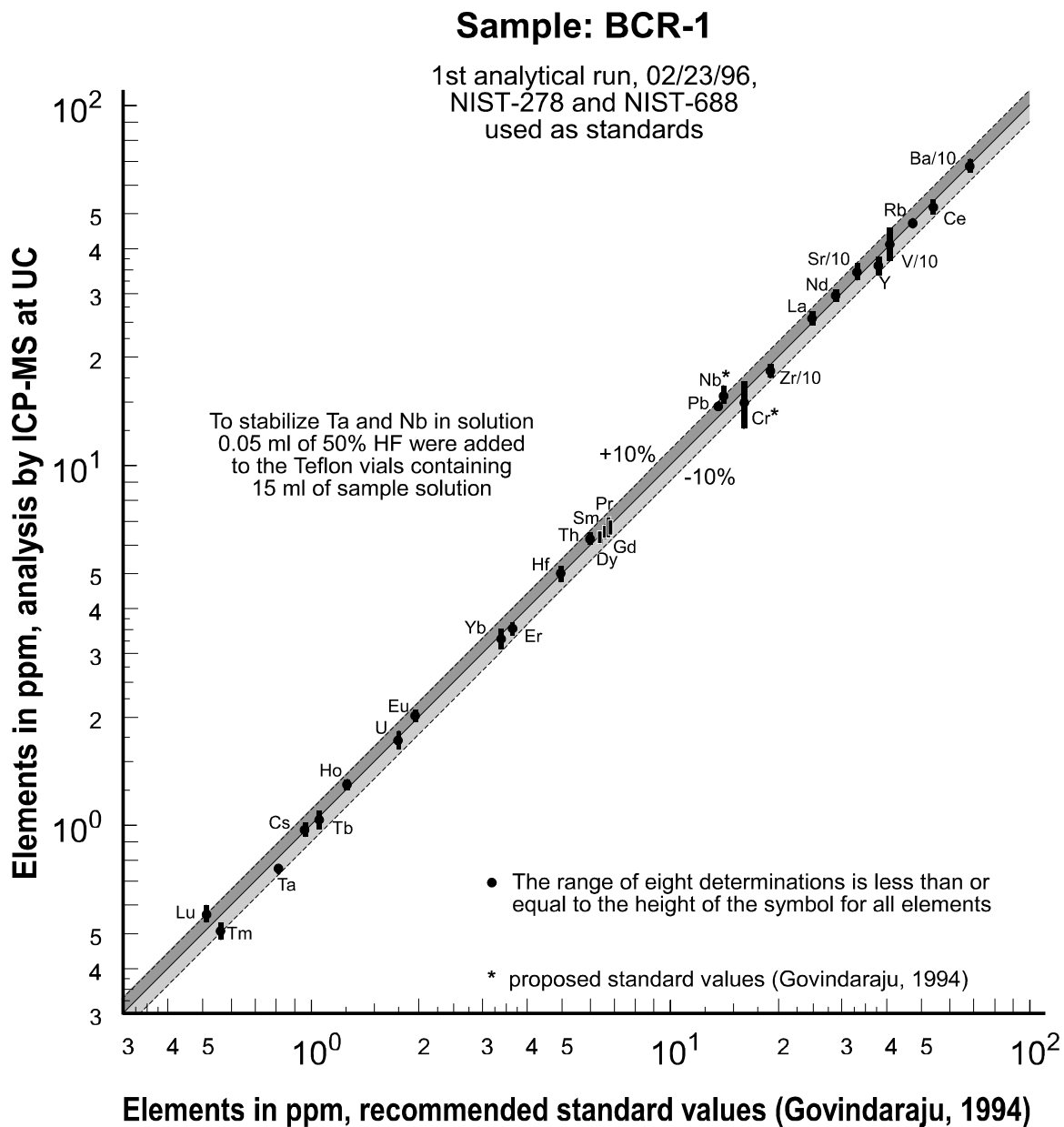


Figure E12

Comparative plot of the analytical results of the first analytical run versus the recommended standard values of BCR-1 (Govindaraju, 1994). All data points plot close to or on the line with slope = 1, indicating excellent accuracy of the analysis. The analytical results generally agree with the standard values within 10% (most within 5%). Furthermore, good analytical results obtained for Ta and Nb suggest that Ta and Nb are stable in solution. Similar to the second test run (figure 8) the analytical results of Cr are somewhat lower than the proposed standard value.

Sample: Pal-889
(re-collected W-1)

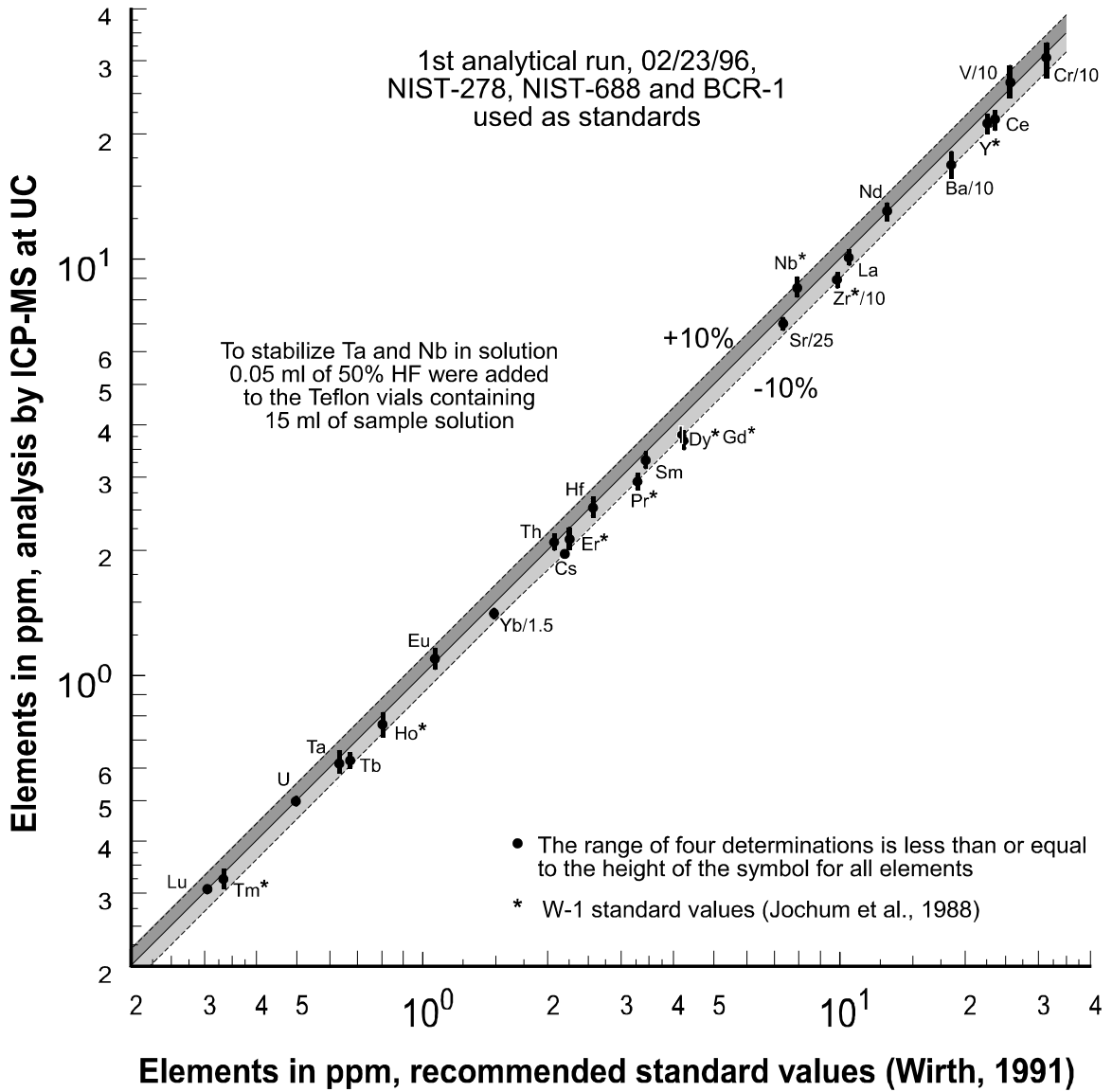


Figure E13

Comparative plot of the analytical data for Pal-889 versus the standard values of Pal-889 and W-1. The agreement between the analytical results for Pal-889 and the selected standard values is very good, indicating good accuracy of the analysis, including Cr. Also in this diagram, data points of Ta and Nb plot within 10% of the standard values, suggesting Ta and Nb are stable in solution and, therefore, could be analyzed with very good accuracy and precision.

elements is within $\pm 10\%$ of the recommended standard values of BCR-1. Only two determinations of Lu and Nb deviate more than $+10\%$ from the corresponding standard values, and two determinations of Tm and three determinations of Cr deviate more than -10% . Nonetheless, the average of eight determinations of all elements of BCR-1 agrees within $\pm 10\%$ of the recommended standard values. Furthermore, good agreement exists between the four determinations of Pal-889 and the recommended standard values (figure E13). The standard values of W-1 for Pr and Gd, used to supplement missing standard values of Pal-889, are more than 10% higher than the measured values of Pr and Gd. Possibly, this is due to real differences between Pal-889 and W-1 (table E5). As pointed out in section E.6.3.1, real differences do exist between Pal-889 and W-1 based on significantly different Cr and Cs values.

The eight determinations of Cou-II-6 agree well with the results from the first test run and also with the analysis at WSU (table E16), confirming good accuracy of the analysis.

E.8.2.4 Resolution of problem with Ta and Nb

The auto sampler tubes containing solutions of BCR-1, Pal-889 and Cou-IL-6 were evenly distributed throughout the entire run. If Ta and Nb were not stable in solution for at least the duration of the analytical run, poor precision and/or accuracy would have been the result. Apparently, addition of HF to all sample and standard solutions in this analytical run stabilized Ta and Nb as indicated by the good precision (figure E11) and accuracy (figures E12 and E13) for Ta and Nb. This clearly demonstrates the effectiveness of adding a complexing agent to the analytical solutions to stabilize Ta and Nb in solution. This technique, adding HF to the solutions, was developed at Washington State University and has been applied to subsequent runs with great success. It is also important to note that the HF concentration in the analytical solutions is so low, that damage to the glass spray chamber of the ICP-MS instrument has never been observed even after several years of applying this technique (C. Knaack, personal communication, 1995).

E.8.3 Second analytical run, 08/19/96

E.8.3.1 Limits of detection

The limits of detection for the second analytical run are presented in table E10 together with the mean values of twelve analyses of BCR-1 and of two analyses of Pal-889 and Cou-II-6. Two digestions of each sample were analyzed once, and the average of obtained elemental concentrations are presented in appendix F. Similar to previous runs, the detection limits of Cr, Zr, Ba, and Pb are relatively higher than of the other elements. However, this is not a problem in that all determined elemental concentrations are well above the detection limits.

E.8.3.2 Precision

Four auto sampler tubes were filled with solutions of BCR-1 left from the first analytical run and analyzed in addition to four aliquots of two new digestions of BCR-1. Accordingly, each of the four sets of standards and blanks (figure E1) consisted of the two NIST-standards, and two new and one old BCR-1 solution (stored in a Teflon vial). Consequently, twelve determinations of elemental concentrations in BCR-1 were made as indicated in figure E14. The old solution of BCR-1 was used to test the long-term stability of Ta and Nb in solution.

The precision is based on twelve analyses of BCR-1 (treated as unknown), and excellent precision are indicated by less than 3% relative standard deviations for all elements (figure E14). There was no systematic difference observed between new and old BCR-1 solutions suggesting that all elements, including Ta and Nb, are stable in solution stored in Teflon vials for long periods of time (>1/2 year). Both analyses of Pal-889 and Cou-II-6 indicate very good reproducibility (table E10), confirming the excellent precision achieved in the second analytical run.

4.8.3.3 Accuracy

As illustrated in the comparative plot in figure E15, all elements, except Lu and Cr, were determined within $\pm 10\%$ (most within $\pm 5\%$) of the recommended standard values of BCR-1 indicating very

Table E10: Results of second analytical run, 08/19/96

| Element | Detection Limits in ppm | BCR-1 | | Pal-889 | | Cou-IL-6 | |
|---------|----------------------------|---------------|---------------------|---------------------|-------|---------------------|-------|
| | | mean (n=8) | error 1 σ | doublicate analysis | | doublicate analysis | |
| | | | | no.1 | no.2 | no.1 | no.2 |
| V | 0.092 | 398 | 7 | 261 | 264 | 492 | 493 |
| Cr | 0.34 | 10.4 | 0.3 | 292 | 297 | 81 | 81 |
| Rb | 0.037 | 47.3 | 0.4 | 30.5 | 30.8 | 12.7 | 12.5 |
| Sr | 0.07 | 329 | 3 | 181 | 181 | 268 | 266 |
| Y | 0.028 | 34.6 | 0.3 | 21.9 | 22.1 | 38.1 | 38.0 |
| Zr | 4.8 | 184 | 4 | 92.9 | 93.0 | 117 | 116 |
| Nb | 0.012 | 15.4 | 0.2 | 8.77 | 8.70 | 5.60 | 5.55 |
| Cs | 0.0062 | 0.97 | 0.02 | 2.04 | 2.01 | 2.96 | 2.92 |
| Ba | 0.42 | 714 | 11 | 180 | 181 | 59.7 | 57.9 |
| La | 0.0059 | 26.5 | 0.4 | 10.2 | 10.3 | 6.56 | 6.46 |
| Ce | 0.020 | 54.7 | 0.5 | 22.3 | 22.4 | 17.2 | 16.9 |
| Pr | 0.0058 | 7.02 | 0.09 | 2.94 | 2.92 | 2.72 | 2.66 |
| Nd | 0.011 | 30.8 | 0.427 | 12.7 | 13.1 | 13.7 | 13.9 |
| Sm | 0.0069 | 6.51 | 0.16 | 3.37 | 3.32 | 4.30 | 4.22 |
| Eu | 0.0015 | 1.98 | 0.03 | 1.08 | 1.13 | 1.35 | 1.36 |
| Gd | 0.0036 | 6.86 | 0.12 | 3.71 | 3.77 | 5.60 | 5.47 |
| Tb | 0.0012 | 1.07 | 0.01 | 0.619 | 0.599 | 0.957 | 0.951 |
| Dy | 0.0034 | 6.40 | 0.07 | 3.72 | 3.80 | 6.30 | 6.20 |
| Ho | 0.0013 | 1.29 | 0.02 | 0.751 | 0.773 | 1.32 | 1.31 |
| Er | 0.0032 | 3.51 | 0.05 | 2.16 | 2.26 | 3.81 | 3.89 |
| Tm | 0.0011 | 0.512 | 0.009 | 0.319 | 0.320 | 0.597 | 0.598 |
| Yb | 0.0046 | 3.32 | 0.05 | 2.00 | 2.02 | 3.77 | 3.76 |
| Lu | 0.0012 | 0.578 | 0.006 | 0.301 | 0.304 | 0.581 | 0.572 |
| Hf | 0.028 | 5.15 | 0.09 | 2.48 | 2.51 | 3.24 | 3.22 |
| Ta | 0.003 | 0.764 | 0.006 | 0.600 | 0.606 | 0.314 | 0.315 |
| Pb | 0.31 | 14.2 | 0.1 | 4.37 | 4.48 | 0.661 | 0.574 |
| Th | 0.0046 | 6.12 | 0.06 | 2.06 | 2.06 | 0.526 | 0.554 |
| U | 0.0036 | 1.72 | 0.01 | 0.494 | 0.483 | 0.186 | 0.183 |

standard deviation :
$$\sigma = \sqrt{\frac{\sum(X_i - \bar{X})^2}{n^2}}$$

see tables 2 and 5 for recommended standard values of BCR-1 and Pal-889, respectively
 see tables 14, 15 and 16 for compilation of analytical results
 for BCR-, Pal-889, and Cou-IL-6, respectively

Precision based on multiple analyses of BCR-1

2nd analytical run, 08/19/96

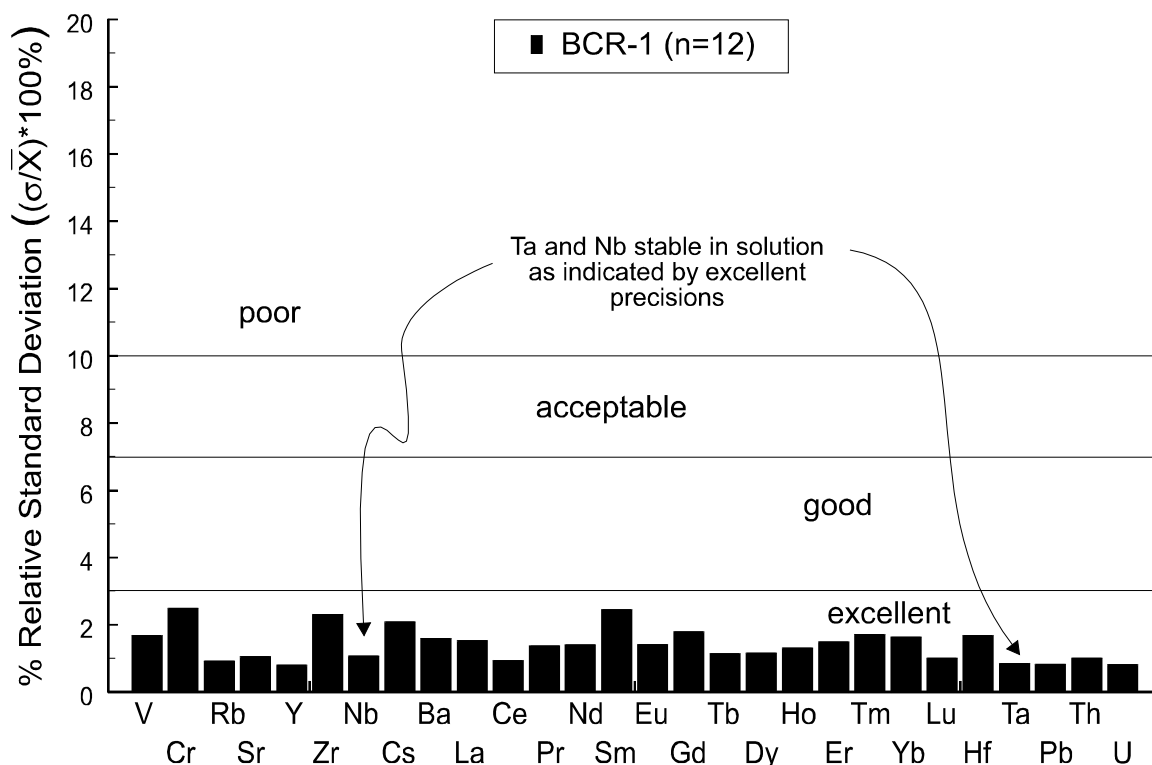


Figure E14

Diagram illustrating the precision of the analysis of the second analytical run. Four aliquots of two new digestions of BCR-1 and four aliquots of an old BCR-1 solution were analyzed. The old BCR-1 solution left from the first analytical run was stored in a Teflon vial. Excellent precision of the analysis is indicated by $< 3\%$ relative standard deviation for all elements. This suggests, that all elements, including Ta and Nb were stable in solution for long periods of time ($\sim 1/2$ year). Furthermore, extremely good run performance of the ICP-MS instrument is demonstrated as well as high reproducibility preparing samples by acid digestion (i.e., there are no systematic differences between new and old BCR-1 solutions).

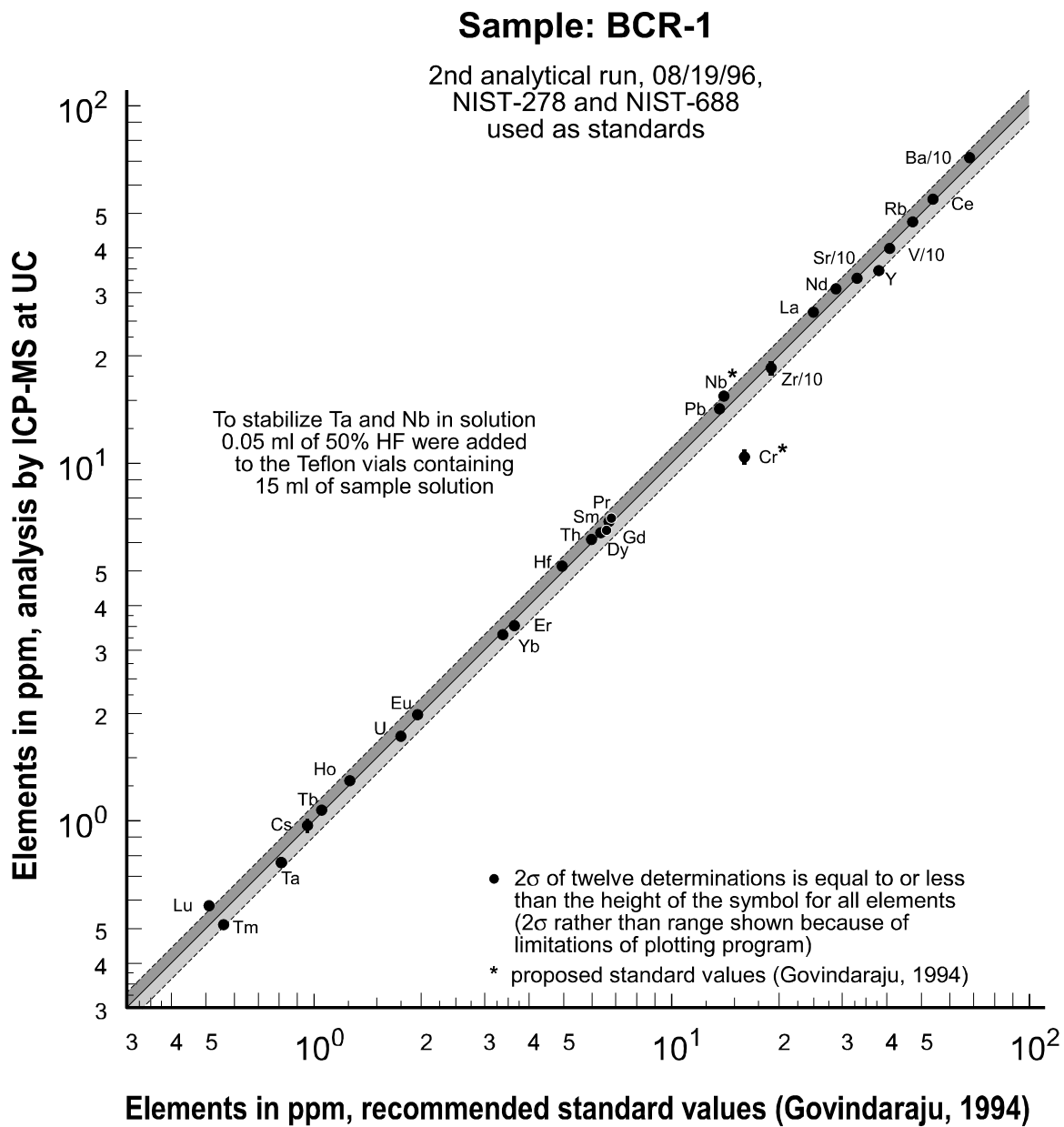


Figure E15

Comparative plot of the analytical results of the second analytical run versus the recommended standard values of BCR-1 (Govindaraju, 1994). The mean values of twelve analyses of BCR-1 plot close to or on the line with slope = 1, indicating excellent accuracy of the analysis. Generally, the analytical results agree with the standard values within 10% (most within 5%). Furthermore, good accuracy of Ta and Nb was obtained verifying Ta and Nb were stable in solution. The analytical results of Cr are once again lower than the standard value suggesting the standard value of Cr might be too high.

Sample: Pal-889
(re-collected W-1)

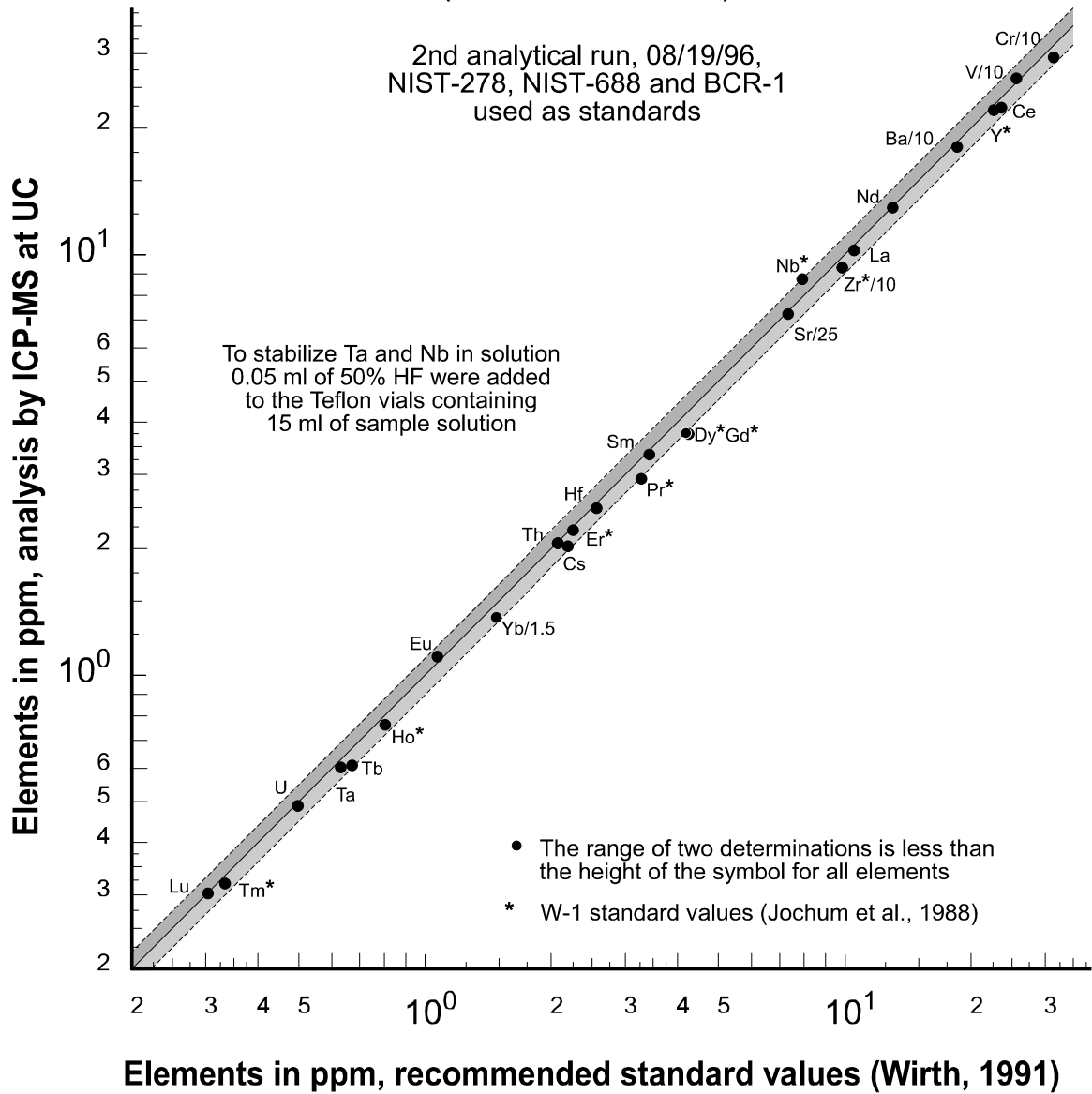


Figure E16

Comparative plot of the analytical data for Pal-889 versus the standard values of Pal-889 and W-1. The agreement between the analytical results for Pal-889 and the selected standard values is very good, indicating good accuracy of the analysis, including Cr. Also in this diagram, data points of Ta and Nb plot within 10% of the standard values, suggesting Ta and Nb are stable in solution and, therefore, could be analyzed with very good accuracy and precision.

good accuracy. It appears that either the determination of Cr using ICP-MS is not very accurate in samples with low Cr concentrations or the reference value of BCR-1 is high. Note that consistently lower Cr values were obtained for BCR-1 in previous runs (12 ppm and 14.5 ppm), suggesting the proposed value of Govindaraju (1994) is indeed high. Also similar to previous runs, the Cr concentration in Pal-889 was analyzed with good accuracy (figure E16), suggesting there are no significant problems analyzing Cr using ICP-MS.

In contrast to BCR-1, Lu was determined in Pal-889 matching exactly the recommended standard value (figure E16). This suggests that the results for Lu are more accurate when three rock standards were used for the calibration instead of only the two NIST-standards. Furthermore, all other elements in Pal-889 were analyzed with good accuracy as indicated by small or no disagreement between measured and recommended standard values (figure E16). The discrepancies between analytical results for Pal-889 and W-1 standard values (e.g. Pr, Dy and Gd) are very similar to the differences observed in earlier runs (figures E4, E9, and E13). Most likely, the discrepancies are due to actual differences between Pal-889 and W-1.

Both analyses of Cou-IL-6 agree well with earlier analyses at Union College and at WSU (table E16) giving further evidence for the good accuracy achieved in the second analytical run.

E.8.3.4 Evaluation of dissolution

It was demonstrated in the first test run that incomplete dissolution of samples is not a problem in this study (section E.7.1.7). This observation is also in agreement with the study of Jarvis (1990) showing that Y, Zr, Nb, Hf, Ta, Pb, Th, U, and the REE can be measured with good accuracy in a range of silicate (i.e., basalt, dolerite, andesite, norite) and carbonate (i.e. limestone, dolomite) matrices, both in samples brought into solution by acid digestion and lithium metaborate fusion. Jarvis (1990) observed poor agreement between reference values of Zr, Ta, Nb, and HREE and the analytical results only when rock samples containing refractory minerals, such as zircon and rutile (i.e. granite, syenite, shale), were brought into solution by acid digestion. Evidently, zircon and rutile did not dissolve using open acid digestion. Since samples analyzed in this study (i.e. subalkaline basalts and andesites) do not contain refractory

minerals such as zircon and rutile, inaccurate determination of elemental concentrations due to incomplete dissolution of samples is very unlikely.

Possibly, further evidence for complete dissolution of samples in this study was obtained through repeating the duplicate analysis of samples analyzed in the second test run. Two separate digestions of 20 samples were prepared and analyzed in the second test run (section E.7.2.1). Duplicates of 19 of these 20 samples were prepared and analyzed in the first and second analytical runs (11 and 8 samples, respectively), because of problems with Ta and Nb in the second test run (section E.7.2.6). Thus, a total of four separate digestions of each of these 19 samples were prepared and analyzed. Supposing four 0.1g-units of a sample weighed in four different Teflon vials would not dissolve completely, systematic and relatively large variations in the analytical data of the four digestions of this sample should be expected (this is based on the assumption that four 0.1g-units of a sample would dissolve differently if incomplete dissolution would occur). The analytical results for all samples, however, indicate high reproducibility suggesting that incomplete dissolution was not a problem. The relative standard deviations of the multiple analyses of the 19 samples are presented in table E13. As shown, the variations in the analytical results are generally less than 5% on average, indicating very good precision of the ICP-MS analysis as well as completeness of dissolution of the samples.

E.8.4 Third analytical run, 09/10/97

E.8.4.2 Limits of detection

As before, BCR-1 solutions left from the second analytical run were re-analyzed together with two new digestions of BCR-1. Consequently, twelve determinations of elemental concentrations in BCR-1 were made. The limits of detection for the third analytical run are listed in table E11 together with the mean values of twelve analyses of BCR-1 and of four analyses of Pal-889 and Cou-IL-6. Compared to previous runs, the detection limit of Ta is about ten times higher than normal, which is still rather low (0.013 ppm). The reason for the higher detection limit is not known and was still significantly below values in most samples. The results of the third analytical run are presented in appendix F, and the listed concentrations

represent the mean value of duplicate analysis made for two digestions per sample (note that the Ta values obtained in the fourth analytical run are preferred over the Ta data of the third analytical run, see section 8.5.4).

E.8.4.3 Precision

The precision, based on the multiple analyses of BCR-1 is excellent for most elements as indicated by $\leq 3\%$ relative standard deviations (figure E17). Only Cr is determined with poor precision in BCR-1 possibly due to difficulties analyzing low levels of Cr. Similar to the second analytical run, there are no systematic differences observed between stored BCR-1 solutions and the new solutions of BCR-1. The good reproducibility between old and new solutions of BCR-1 not only indicates a high degree of consistency preparing the samples, but also that all elements are stable in solution stored in Teflon containers for more than a year.

E.8.4.4 Accuracy

The comparison of the analytical results of BCR-1 with recommended standard values indicates that all elements (except Cr) were accurately determined (figure E18). The mean values as well as $\pm 2\sigma$ of twelve determinations plot within 10% of the recommended standard values.

It was noted in previous runs that the analytical results of Cr for BCR-1 are consistently lower than the proposed standard value (16 ppm). Also in this analytical run, the mean value is significantly lower than the reference value suggesting the proposed standard value is high.

As illustrated in figure E19, Pal-889 was analyzed with good accuracy as well, including Cr. All elements, except Nb, were determined within $\pm 10\%$ of the recommended standard values. Measured Nb concentrations of Pal-889 from this and previous runs are higher by about 0.5 to 1 ppm than the adopted reference value of 7.91 ppm (compare figures E13, E16 and E19) suggesting that the selected reference value could be too low. Actually, an alternative standard value of Nb is listed in table 5 (9.9 ppm recommended by Govindaraju, 1994) which is significantly higher than the selected reference value (ID-SSMS). Consequently, depending on the selection of the reference value, analytical data of Nb for Pal-889

Table E11: Results of third analytical run, 09/10/97

| Element | Detection Limits in ppm | BCR-1 | | Pal-889 | | Cou-IL-6 | |
|---------|----------------------------|----------------|---------------------|---------------|---------------------|---------------|---------------------|
| | | mean (n=12) | error 1 σ | mean (n=4) | error 1 σ | mean (n=4) | error 1 σ |
| V | 0.77 | 393 | 18 | 275 | 17 | 476 | 16 |
| Cr | 1.3 | 10.6 | 1.3 | 312 | 11 | 85 | 1 |
| Rb | 0.018 | 47.6 | 1.0 | 30.1 | 0.1 | 13.1 | 0.2 |
| Sr | 0.45 | 335 | 8 | 173 | 2 | 273 | 4 |
| Y | 0.045 | 35.3 | 1.0 | 22.1 | 0.2 | 40.2 | 0.9 |
| Zr | 3.8 | 194 | 6 | 100.5 | 4.4 | 131 | 5 |
| Nb | 0.020 | 14.5 | 0.5 | 8.51 | 0.34 | 5.70 | 0.20 |
| Cs | 0.0046 | 0.96 | 0.01 | 2.15 | 0.03 | 2.96 | 0.04 |
| Ba | 0.78 | 688 | 11 | 193 | 1 | 59.7 | 0.6 |
| La | 0.012 | 24.6 | 1.0 | 10.9 | 0.1 | 6.51 | 0.09 |
| Ce | 0.096 | 53.6 | 1.4 | 23.6 | 0.0 | 17.7 | 0.1 |
| Pr | 0.0042 | 6.79 | 0.24 | 3.15 | 0.01 | 2.81 | 0.02 |
| Nd | 0.016 | 28.4 | 0.982 | 13.2 | 0.2 | 14.2 | 0.2 |
| Sm | 0.0048 | 6.59 | 0.19 | 3.46 | 0.05 | 4.45 | 0.07 |
| Eu | 0.0015 | 1.94 | 0.04 | 1.12 | 0.02 | 1.41 | 0.02 |
| Gd | 0.0049 | 6.58 | 0.15 | 3.89 | 0.09 | 5.68 | 0.12 |
| Tb | 0.00082 | 1.04 | 0.02 | 0.649 | 0.022 | 0.984 | 0.019 |
| Dy | 0.0053 | 6.20 | 0.14 | 4.01 | 0.09 | 6.47 | 0.09 |
| Ho | 0.00094 | 1.25 | 0.03 | 0.811 | 0.016 | 1.37 | 0.02 |
| Er | 0.0030 | 3.48 | 0.06 | 2.35 | 0.07 | 3.99 | 0.07 |
| Tm | 0.00077 | 0.531 | 0.011 | 0.360 | 0.010 | 0.623 | 0.010 |
| Yb | 0.0034 | 3.29 | 0.07 | 2.12 | 0.04 | 3.84 | 0.07 |
| Lu | 0.00055 | 0.517 | 0.010 | 0.314 | 0.007 | 0.552 | 0.006 |
| Hf | 0.015 | 4.95 | 0.07 | 2.62 | 0.04 | 3.27 | 0.04 |
| Ta | 0.037 | 0.821 | 0.009 | 0.677 | 0.008 | 0.330 | 0.006 |
| Pb | 0.18 | 14.0 | 0.4 | 4.75 | 0.23 | 0.598 | 0.013 |
| Th | 0.013 | 5.87 | 0.23 | 2.02 | 0.01 | 0.520 | 0.005 |
| U | 0.00088 | 1.71 | 0.05 | 0.492 | 0.006 | 0.181 | 0.003 |

standard deviation :
$$\sigma = \sqrt{\frac{\Sigma(X_i - \bar{X})^2}{n^2}}$$

see tables 2 and 5 for recommended standard values of BCR-1 and Pal-889, respectively
 see tables 14, 15 and 16 for compilation of analytical results
 for BCR-, Pal-889, and Cou-IL-6, respectively

Precision based on multiple analyses of BCR-1

3rd analytical run, 09/10/97

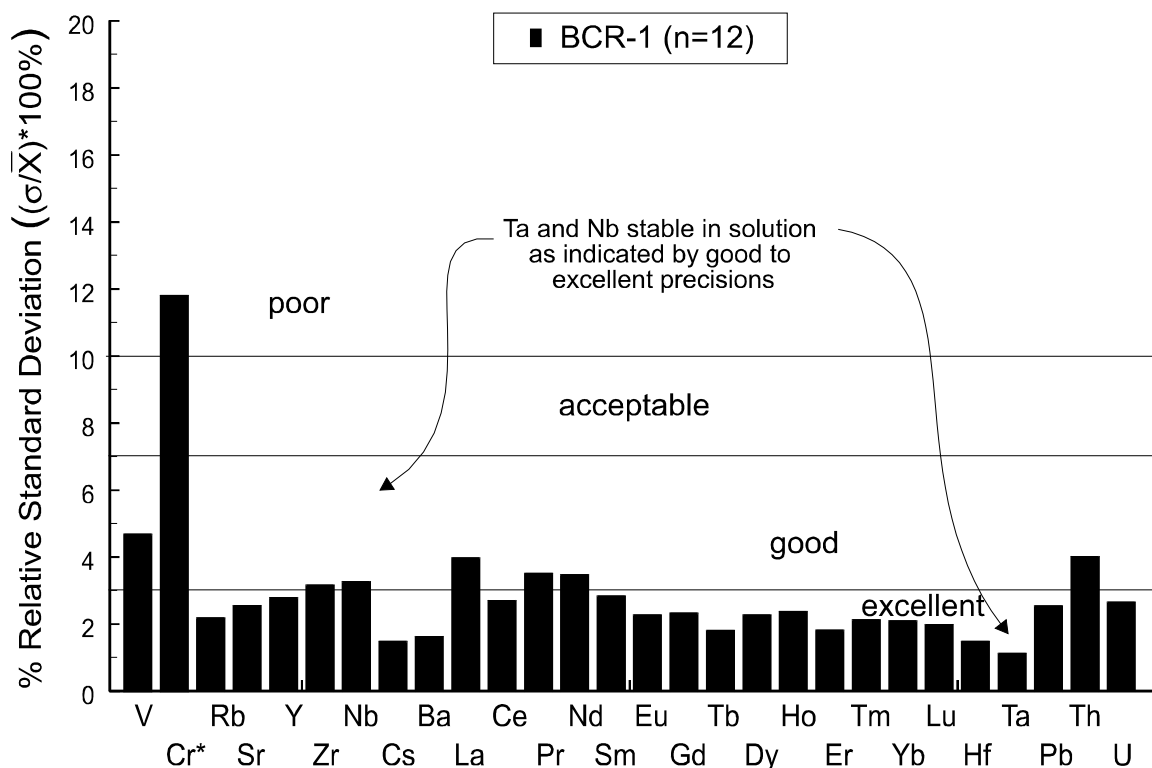


Figure E17

Diagram illustrating the precision of the analysis of the second analytical run. Four aliquots of two new digestions of BCR-1 and four aliquots of an old BCR-1 solution were analyzed. The old BCR-1 solution left from the second analytical run was stored in a Teflon vial. Excellent precision of the analysis is indicated by ~3% relative standard deviation for most elements. Good run performance of the ICP-MS instrument is demonstrated as well as high reproducibility preparing samples by acid digestion (i.e., there are no systematic differences between new and old BCR-1 solutions).

* The high relative standard deviation for Cr is misleading in that the Cr level in BCR-1 is very low (proposed standard value of 16 ppm). The precision of Cr for samples with higher levels of Cr is very good as demonstrated with the duplicate analyses of Pal-889 and Cou-IL-6 (table E11).

Sample: BCR-1

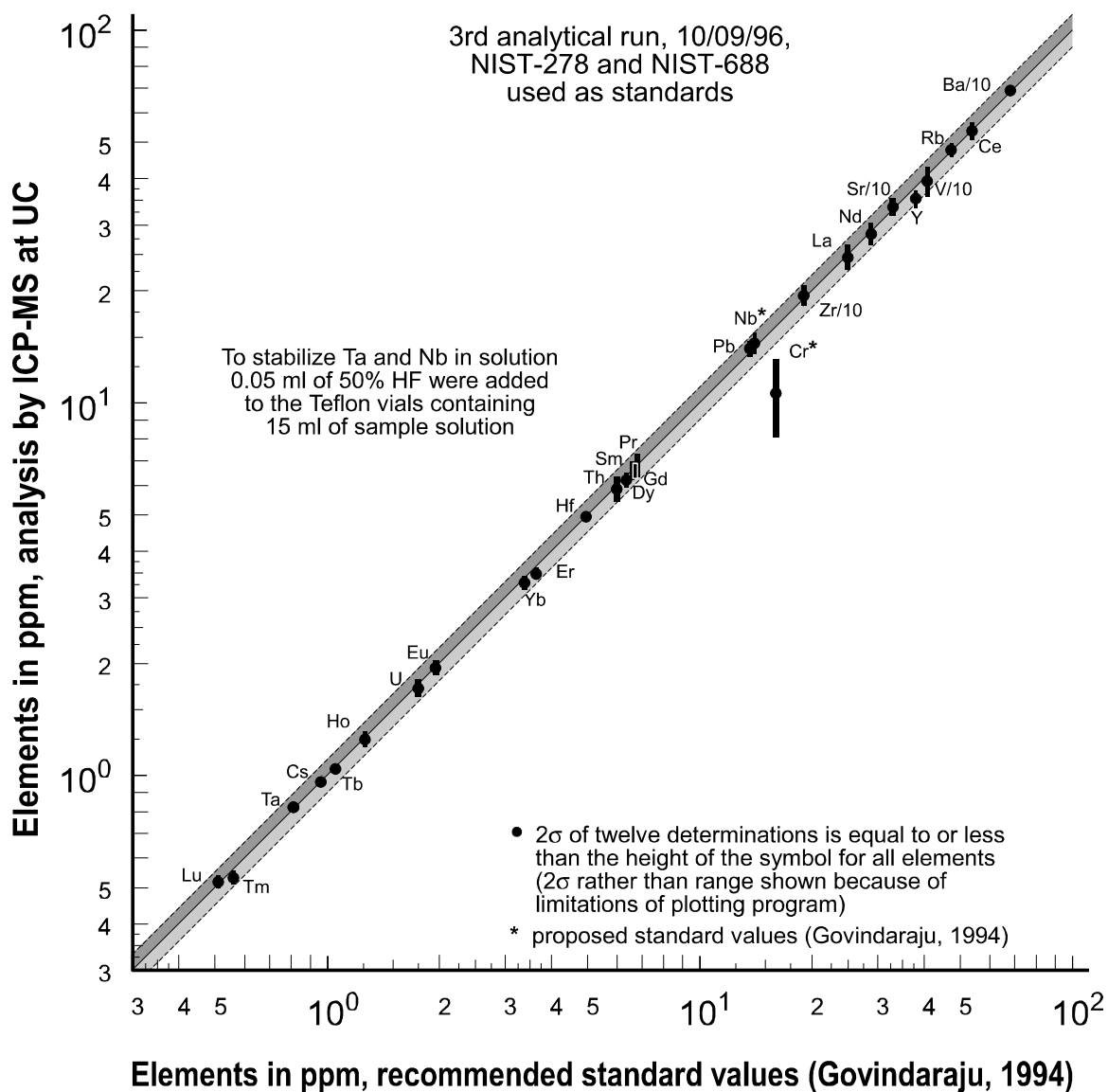


Figure E18

Comparative plot of the analytical results of the third analytical run versus the recommended standard values of BCR-1 (Govindaraju, 1994). All data points plot close to or on the line with slope = 1, indicating excellent accuracy of the analysis. The analytical results generally agree with the standard values within 10% (most within 5%). Furthermore, good analytical results obtained for Ta and Nb suggest that Ta and Nb are stable in solution. The analytical results of Cr are once again lower than the standard value, suggesting the proposed standard value of Cr might be too high.

Sample: Pal-889
(re-collected W-1)

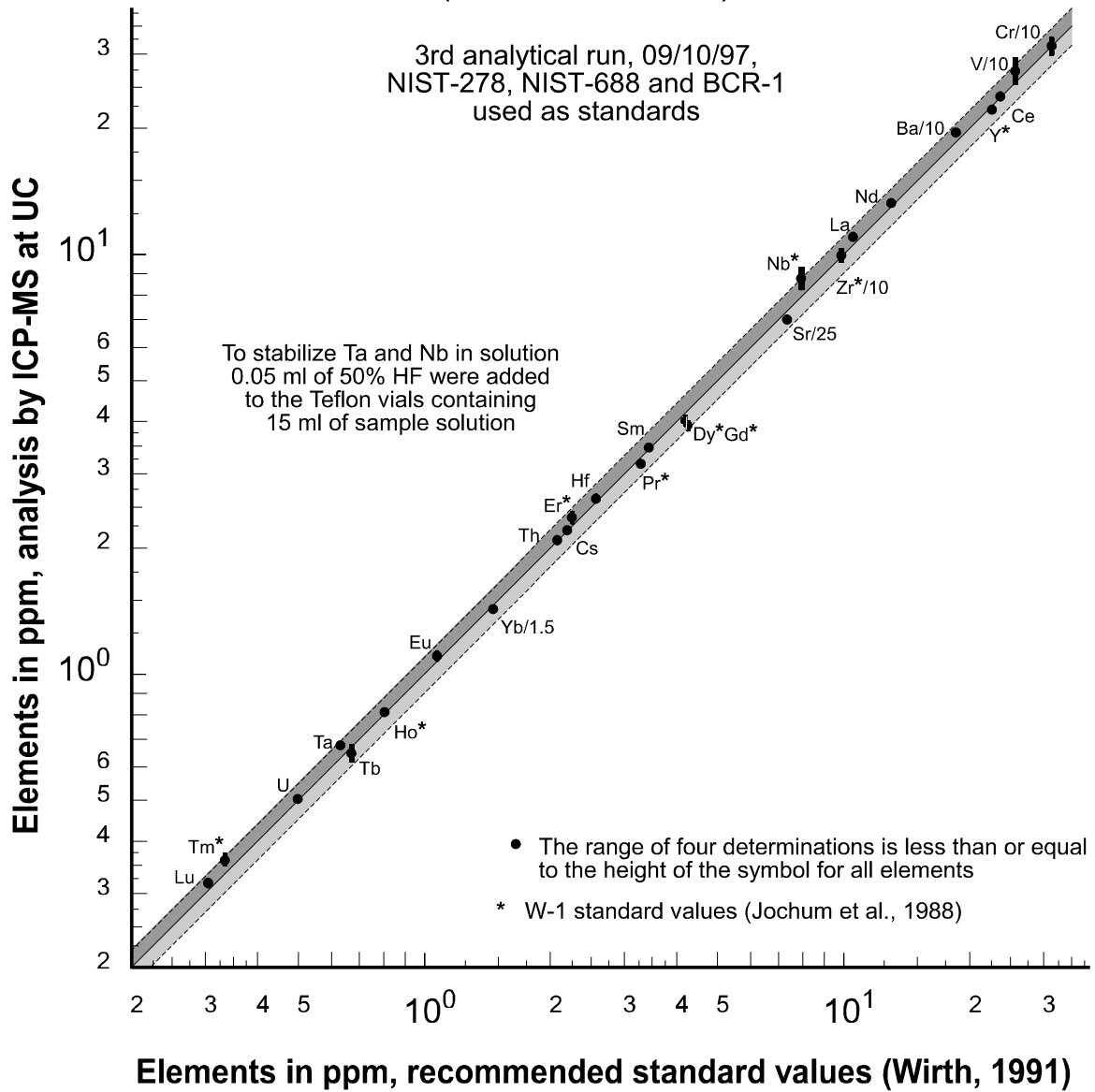


Figure E19

Comparative plot of the analytical data for Pal-889 versus the standard values of Pal-889 and W-1. The agreement between the analytical results for Pal-889 and the selected standard values is very good, indicating good accuracy of the analysis, including Cr. Note that the analytical data of Nb obtained in all analytical runs are consistently higher than the standard value of Nb (see figures E12 and E15), suggesting the selected W-1 standard value is too low (see text).

(8.40 to 8.74 ppm) would either plot significantly above the line with slope = 1 (reference value of 7.91 ppm selected) or significantly below the line with slope = 1 (reference value of 9.9 ppm selected).

E.8.5 Fourth analytical run, 09/19/97

E.8.5.1 Limits of detection

The analysis of some samples analyzed in the third analytical run was repeated, because the detection limits of Ta were approximately ten times higher in the third analytical run (table E11) than those in the preceding runs (tables E9 and E10). Samples with Ta concentrations near or below the unusually high detection limits were re-analyzed. New solutions of the samples and standards were not prepared for the fourth analytical run; that is, the same standard and sample solutions were analyzed as in the third analytical run.

In the fourth analytical run, lower detection limits of Ta were obtained (table E12), providing accurate values for the re-analyzed samples (Appendix F). The Ta values obtained in run 3 were replaced by Ta values obtained in run 4 in the data table in appendix F.

E.8.5.2 Precision

The precision is based on 6 analyses of BCR-1 treated as unknown. Unlike the other analytical runs, the light REE and medium REE were determined with poor to acceptable precision (figure E20). All other elements were analyzed with good to excellent precision. The generally poor precision obtained for the fourth run must be due to a decline of the performance of the ICP-MS instrument, because the same solutions were analyzed with much higher precision in the third analytical run (figure E17). Apparently, a vacuum leak occurred in the ICP-MS instrument that was repaired between third and fourth analytical run. Nonetheless, Ta was determined with excellent precision, not only in BCR-1 (figure E19), but also in Cou-II-6 and Pal-889 (table E12).

Table E12: Results of fourth analytical run, 09/19/97*

(partial repeat of third analytical run: same sample and standard solutions re-analyzed)

| Element | Detection Limits in ppm | BCR-1 | | Pal-889 | | Cou-IL-6 | |
|---------|----------------------------|---------------|---------------------|---------------------|-------|---------------------|-------|
| | | mean (n=6) | error 1 σ | doublicate analysis | | doublicate analysis | |
| | | | | no.1 | no.2 | no.1 | no.2 |
| V | 0.143 | 370 | 13 | 246 | 265 | 467 | 476 |
| Cr | 0.71 | 13.3 | 3.0 | 302 | 325 | 84 | 83 |
| Rb | 0.112 | 47.0 | 3.2 | 27.4 | 29.5 | 12.0 | 12.4 |
| Sr | 0.22 | 331 | 16 | 178 | 188 | 269 | 281 |
| Y | 0.024 | 34.5 | 1.9 | 23.0 | 24.9 | 37.3 | 37.5 |
| Zr | 0.4 | 185 | 5 | 97.7 | 99.5 | 118 | 119 |
| Nb | 0.019 | 15.3 | 0.4 | 8.15 | 8.66 | 5.59 | 5.58 |
| Cs | 0.0059 | 1.05 | 0.04 | 2.26 | 2.12 | 2.86 | 2.81 |
| Ba | 0.71 | 738 | 55 | 192 | 177 | 60.3 | 57.1 |
| La | 0.0109 | 27.4 | 2.6 | 11.0 | 10.0 | 6.63 | 6.28 |
| Ce | 0.033 | 56.0 | 5.7 | 24.6 | 22.5 | 17.9 | 16.5 |
| Pr | 0.0036 | 7.20 | 0.82 | 3.32 | 3.07 | 2.75 | 2.58 |
| Nd | 0.029 | 31.2 | 4.448 | 13.7 | 12.3 | 14.2 | 13.1 |
| Sm | 0.0078 | 6.58 | 0.90 | 3.61 | 3.21 | 4.41 | 4.04 |
| Eu | 0.0069 | 1.92 | 0.13 | 1.13 | 1.00 | 1.34 | 1.23 |
| Gd | 0.0079 | 6.78 | 0.85 | 4.24 | 3.73 | 5.70 | 5.22 |
| Tb | 0.0018 | 1.05 | 0.12 | 0.710 | 0.625 | 1.005 | 0.920 |
| Dy | 0.0155 | 6.36 | 0.67 | 4.18 | 3.78 | 6.48 | 6.09 |
| Ho | 0.0022 | 1.28 | 0.12 | 0.841 | 0.776 | 1.39 | 1.30 |
| Er | 0.0030 | 3.47 | 0.32 | 2.42 | 2.17 | 4.02 | 3.79 |
| Tm | 0.0011 | 0.508 | 0.040 | 0.355 | 0.324 | 0.609 | 0.582 |
| Yb | 0.0041 | 3.29 | 0.18 | 2.24 | 2.12 | 3.88 | 3.76 |
| Lu | 0.0021 | 0.568 | 0.026 | 0.314 | 0.293 | 0.592 | 0.576 |
| Hf | 0.009 | 4.96 | 0.17 | 2.63 | 2.48 | 3.33 | 3.22 |
| Ta | 0.0029 | 0.753 | 0.020 | 0.633 | 0.626 | 0.295 | 0.299 |
| Pb | 0.06 | 13.6 | 0.2 | 4.59 | 4.24 | 0.677 | 0.597 |
| Th | 0.0045 | 6.06 | 0.19 | 2.03 | 2.11 | 0.549 | 0.542 |
| U | 0.0017 | 1.70 | 0.03 | 0.492 | 0.502 | 0.184 | 0.177 |

standard deviation :
$$\sigma = \sqrt{\frac{\Sigma(X_i - \bar{X})^2}{n^2}}$$

see tables 2 and 5 for recommended standard values of BCR-1 and Pal-889, respectively

see tables 14, 15 and 16 for compilation of analytical results

for BCR-, Pal-889, and Cou-IL-6, respectively

* only Ta values for samples used

Precision based on multiple analyses of BCR-1

fourth analytical run, 09/19/97

partial repeat of 3rd analytical run: same standard and sample solutions were re-analyzed (only Ta values used)

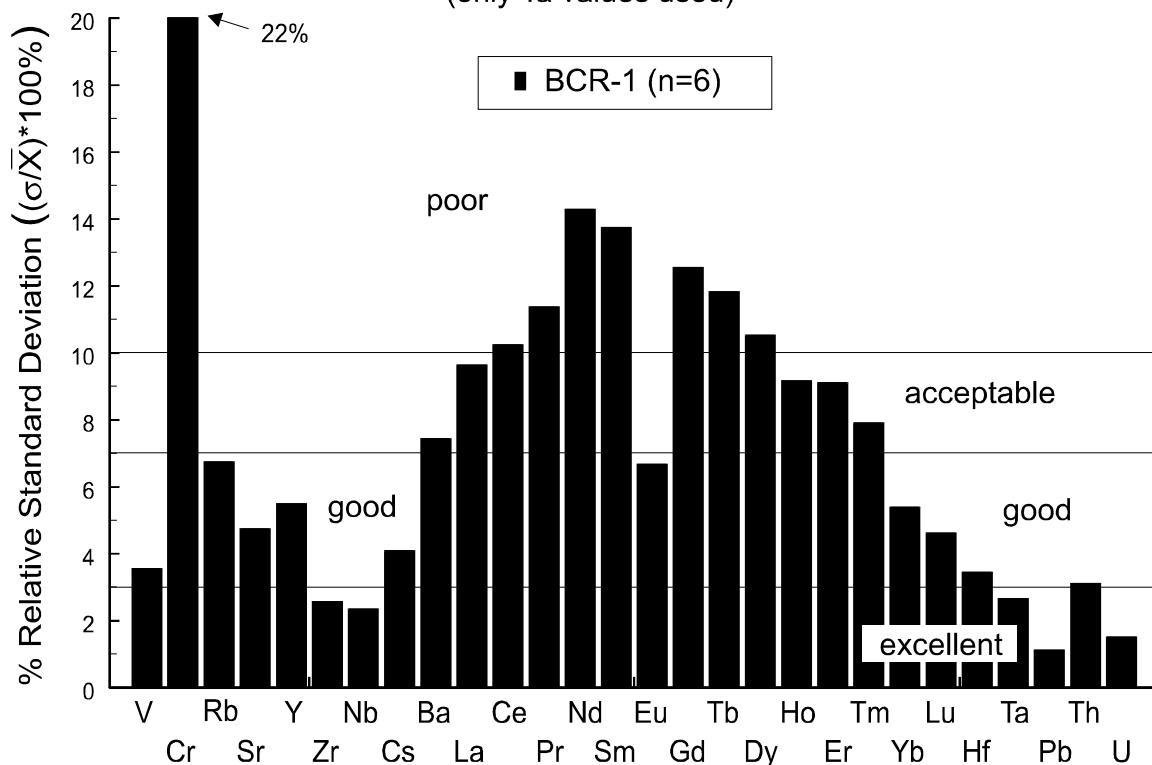


Figure E20

Diagram illustrating the precision of the analysis of the fourth analytical run. The standard and sample solutions prepared for the third analytical run were stored in Teflon vials and re-analyzed in the fourth analytical run (i.e., the samples with very low levels of Ta, near or below detection of third analytical run, were re-analyzed). Compared to the third analytical run (figure 17), the overall precision of the fourth analytical run is notably worse suggesting that a decline of the performance of the ICP-MS instrument occurred (see text). Nonetheless, the analytical results of Ta obtained in the fourth analytical run are very good as indicated by very low detection limits (table 12), good accuracy (figures 21 and 22), and excellent precision (< 3% relative standard deviation).

Sample: BCR-1

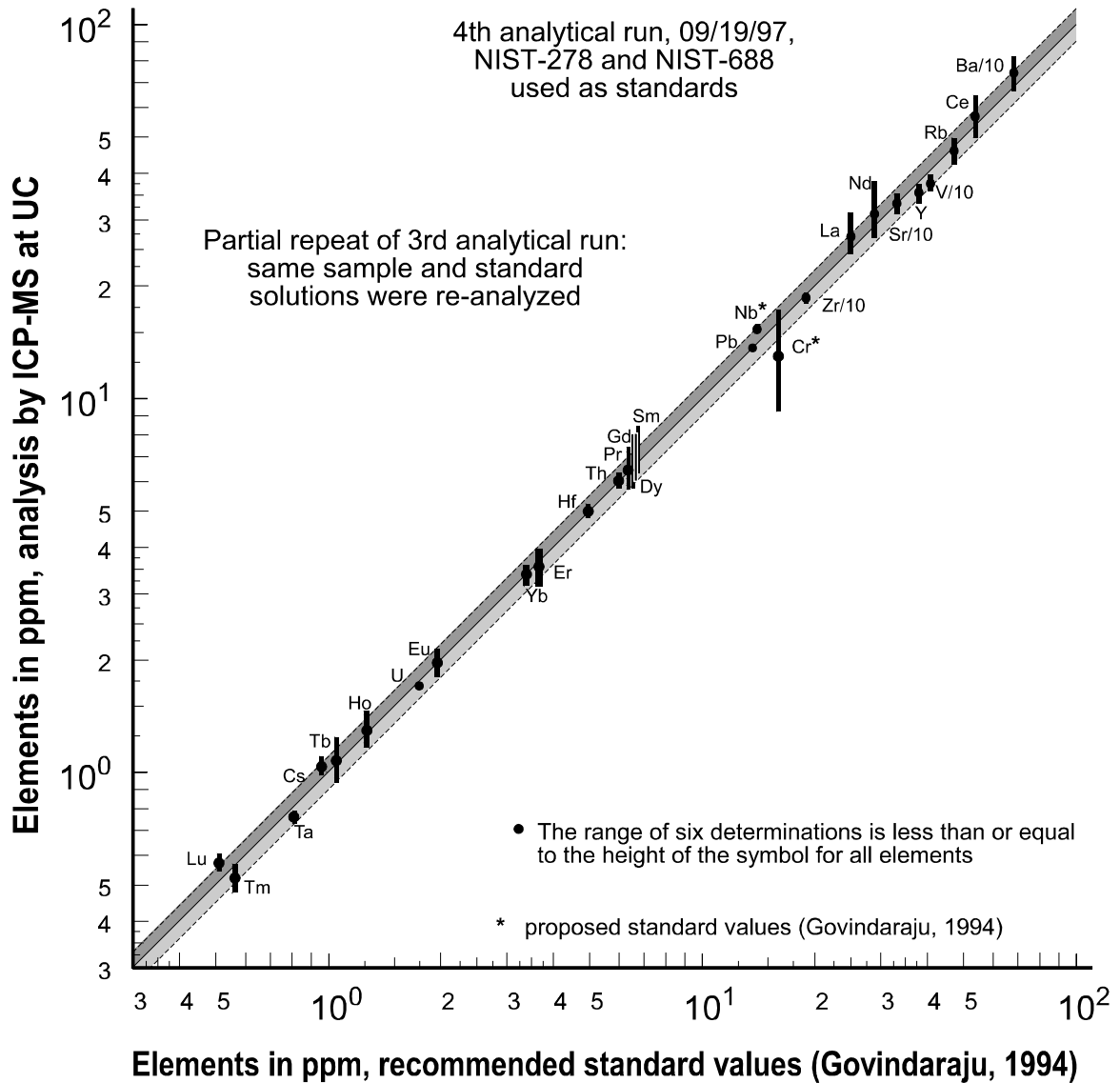


Figure E21

Comparative plot of the analytical results of the fourth analytical run versus the recommended standard values of BCR-1 (Govindaraju, 1989). Many data points deviate significantly from the line with slope = 1, indicating poor accuracy of La, Ce, Pr, Nd, Sm, Gd, Tb, and Dy (elements analyzed with poor precision). For the other elements, the analytical results generally agree with the standard values within 10%. Furthermore, good analytical results obtained for Ta and Nb suggest that Ta and Nb are stable in solution. Even though the precision of Cr is extremely poor in this run, the analytical results of Cr are once again lower than the reference value, suggesting the proposed standard value of Cr might be too high.

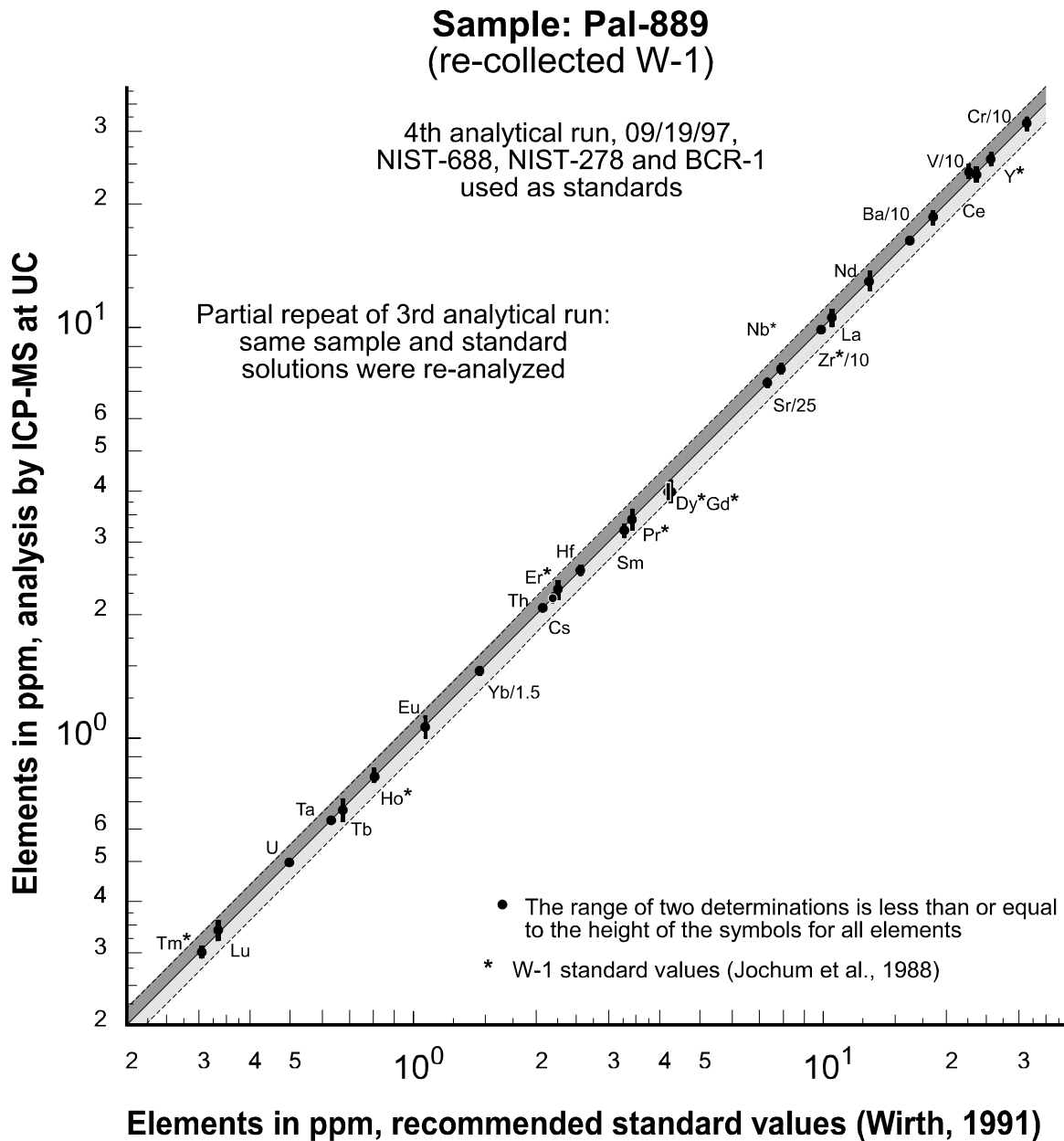


Figure E22

Comparative plot of the analytical data for Pal-889 versus the standard values of Pal-889 and W-1. The agreement between the analytical results for Pal-889 and the selected standard values is surprisingly good considering the poor precision of some elements analyzed in the fourth run (figure 20). Ta was analyzed with excellent precision (figure 20), good accuracy (figure 21 and 22) and low detection limits (table 12). The Ta values obtained with fourth analytical run are preferred over those of the third run because of relatively high detection limits for Ta in the third analytical run.

E.8.5.3 Accuracy

The agreement between recommended standard values and the average of measured values of BCR-1 is good (figure E21). Generally, two or three of the twelve determinations of the light REE and medium REE for BCR-1 are significantly higher than the corresponding standard values due to the poor precision for these elements. It is surprising that both analyses of Pal-889 agree very well with the recommended standard values (figure E22), considering the large variations for BCR-1. Also, both analyses of Cou-II-6 agree well with the results obtained earlier at UC and also with the analysis at WSU (table E16).

E.8.5.4 Selection of data

Because of the poor accuracy and precision determining the light REE and medium REE in BCR-1 (figure E20 and E21), only Ta values obtained in the fourth analytical run are used, and all other analytical data of this run are not reported in appendix F. The detection limits of Ta were ten times lower than in the third analytical run (table E12) and Ta was also determined with good accuracy (figure E21) and precision (figure E20). Therefore, the Ta concentrations obtained in the fourth analytical run are preferred over those of the third analytical run; that is, the Ta values obtained in run 3 were replaced by the Ta values obtained in run 4 (appendix F).

E.9 Comments on use of ICP-MS at Union College and conclusions

It was demonstrated in preceding sections that the analytical results obtained by ICP-MS at Union College are of high quality. Overall, high accuracy, very good precision and low detection limits were realized analyzing samples from the Oregon Coast Range ophiolite (and samples from the Josephine ophiolite). The following summary outlines the main points of the sections E7 and E8:

- Multiple analyses of solutions prepared from separate digestions (weighing of 0.1g of sample in a Teflon vial and dissolving is defined as a digestion of a sample, figure E1) show that sample preparation errors are very small, in general < 3% (table E7). Thus, sample preparation errors are within the precision of the analysis by ICP-MS.

- The complete dissolution of samples was verified using a synthetic standard in the first test run (section E.7.1.7). Furthermore, absence of chemically resistant minerals in analyzed samples (section E.8.3.4) and high reproducibility of analytical data (i.e., multiple analyses of solutions prepared from separate digestions) suggest that incomplete dissolution of the samples did not occur (tables E7 and E13).
- Ta and Nb were accurately analyzed in this study, only when HF was added to all sample and standard solutions to stabilize Ta and Nb in solution (section E.8.2.4). The problem with Ta and Nb has not been detected previously at Union College (K. Hollocher, personal communication 1995), even though HF has not been added to the solutions.
- The analysis of BCR-1 as an unknown sample is extremely accurate as indicated by comparing the analytical results for BCR-1 (obtained in analytical runs 1, 2 and 3) with the recommended standard values: V, Rb, Sr, Cs, Ba, Ce, Pr, Sm, Eu, Gd, Tb, Dy, Ho, Hf, Th and U were analyzed within better than 2%; Zr, La, Nd, and Yb within better than 3%; Er, Ta, and Pb within better than 5%; and Y, Nb, Tm, and Lu within better than 8% of the recommended standard values of BCR-1.
- The precision analyzing the samples might be obtained from the average relative standard deviations listed in table E13 in addition to the relative standard deviations shown in figures E11, E14, and E17. The average relative standard deviation (1σ) for Dy, Ho, Er and Tm is estimated to be smaller than 3%; for Y, Zr, Nb, Ba, La, Ce, Pr, Nd, Sm, Eu, Gd, Tb, Yb, Lu, Hf, Ta and Th smaller than 4%; for V, Cr, Rb and U smaller than 8% and for Pb smaller than 10%.
- The analytical results obtained at Union College agree well with the ICP-MS data of the Washington State University Geoanalytical Laboratories (tables E15 and E16). Furthermore, the agreement is very good between the ICP-MS data obtained at Union College and the data obtained by other analytical techniques (figure E10, tables E15 and E16).
- Much poorer precision was obtained in the fourth analytical run than in the third analytical run (compare figures E17 and E20), even though the same solutions stored in Teflon vials were analyzed in both runs. Consequently, observed differences in precision (and accuracy) are interpreted as due to machine problems in the fourth analytical run. As discussed in section E.8.4, the third analytical run was repeated because of relatively high detection limits of Ta (table E12). Therefore, only Ta values

were needed in the fourth analytical run. Fortunately, good accuracy, excellent precision, and low detection limits of Ta were obtained. Thus, the analytical results of Ta in the fourth run are given for those samples in appendix A rather than the Ta data of the third run.

- Multiple analyses of standards as unknowns is essential to evaluate accuracy and precision, and thus, evaluate performance of the ICP-MS instrument at the Union College Geology Department. The machine performance may change drastically from one run to another (e.g., third and fourth analytical run). The cause of varying machine performance is unknown.

Nonetheless, very good results can be obtained with the ICP-MS instrument at the Union College Geology Department (e.g., table E14). The accuracy and precision of the presented data of this study is similar to that of published ICP-MS data (Jenner et al., 1990). For example the analytical results for BCR-1 of the study of Jenner et al. (1990) are very similar in precision (figure E23) and accuracy (figure E24) to the results obtained at Union College (precision figures E11, E14, and E17; accuracy figures E12, E15, and E18).

- Occasionally, small amounts of Pb and Rb contamination affected accuracy and precision of the analysis of samples with low levels of Pb (< 1 ppm) and Rb (< 1 ppm) as indicated in table E13.
- Low precision and accuracy was obtained analyzing low levels of Cr in some samples (e.g., figures E17 and E18). The relatively large differences observed between the analytical results for BCR-1 and the proposed standard value of 16 ppm (Govindaraju, 1994) is partly due to large uncertainty of the proposed standard value. Generally, the precision of Cr is better than 5% relative standard deviation for samples with > 35 ppm Cr (table E13), and Cr concentrations of Pal-889 were determined within 10% of the reference values (e.g., figures E13, E16 and E19). Nonetheless, the accuracy and precision of Cr by XRF analysis might be better than by ICP-MS analysis (e.g., results for Z-83a shown in figure E10). Additionally, Cr concentrations in many samples exceed the highest standard of 321 ppm. For that reason, the analysis of Cr by XRF is preferred over the ICP-MS values (note: the differences between XRF and ICP-MS values is inconsequential for petrogenetic interpretations).

To summarize, the high precision and accuracy achieved for analytical runs 1, 2 and 3 (and for Ta in run 4), as well as the duplicate digestion and analyses of each unknown sample, which agree within 3% (e.g., table E7), leads to the conclusion that ICP-MS analytical data reported for samples in this study (appendix A) are very accurate.

E.10 Supplement: Evaluation of the fifth analytical run; analysis of samples from the Coast Range ophiolite remnants at Llanada and Black Mountain

E.10.1 Introduction

The samples from the Coast Range ophiolite remnant at Black Mountain and Llanada were supplied by Glenn MacPherson for re-analysis by ICP-MS at Union College. The samples from these CRO remnants were previously analyzed by XRF and INAA, and these analytical data are reported in Giaramita et al., (1998). In this section, the analysis of these samples by ICP-MS is evaluated and compared to the XRF and INAA data in Giaramita et al., (1998).

The samples from the Coast Range ophiolite remnant at Black Mountain and Llanada were prepared using acid digestion and analyzed as outlined in sections E2 through E5. Duplicates of the standards as well as of the samples were prepared. Thus, the presented analytical results for the samples (appendix F) are the average of two analyses by ICP-MS.

The analytical results of the fifth analytical run are perhaps not as good (i.e., accuracy and precision) as the results of the analytical runs 1, 2 and 3 (section E8.2, E8.3, and E8.4). However, the data obtained with the fifth analytical run are of much higher quality than the data obtained with the fourth analytical run (section E.8.5). Furthermore, the precision and accuracy of most elements appear to be good so that the analytical results can be used for meaningful petrogenetic interpretations. The analytical results for standards analyzed as unknowns generally agree within 10% of the corresponding reference values. Additionally, the agreement between the available XRF / INAA data and the ICP-MS values is good as well.

Precision based on multiple analyses
of three rock standards

Analysis by ICP-MS at Memorial University of
Newfoundland (MUN), data published by
Jenner et al., (1990)

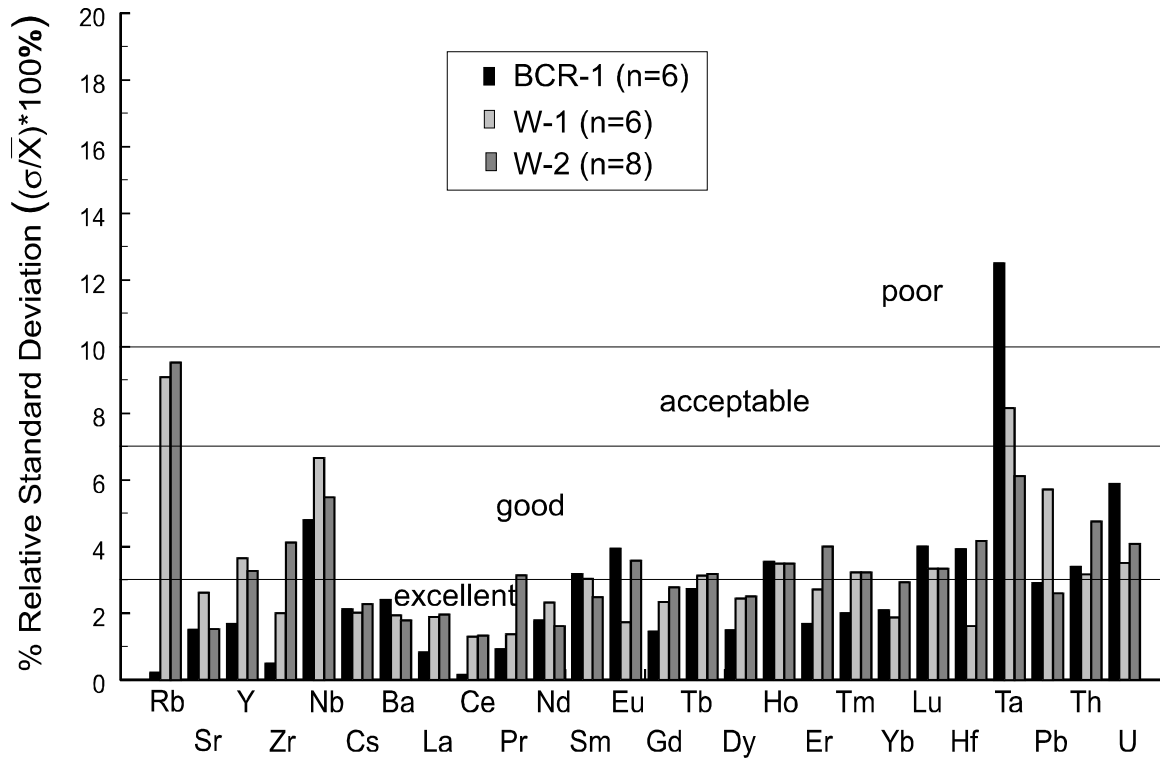


Figure E23

Diagram illustrating the precision of the analysis by ICP-MS at the Memorial University of Newfoundland. The precision of the analysis indicated by the relative standard deviation is very similar to the typical precision achieved in this study using the ICP-MS instrument at the Union College Geology Department (compare figures E11, E14 and E17).

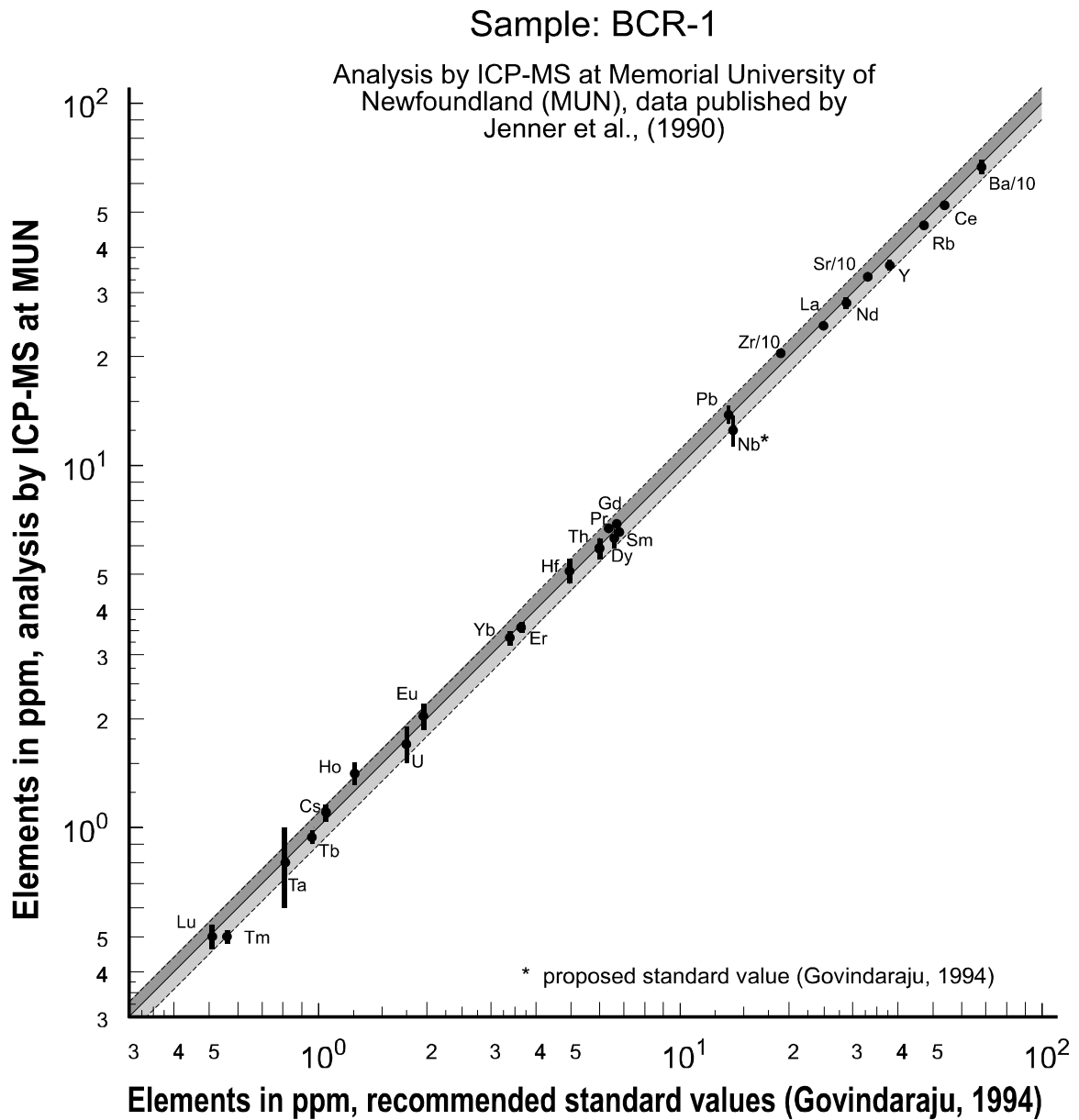


Figure E24

Comparative plot of the analytical data for BCR-1 obtained at MUN versus the recommended standard values of Govindaraju (1994). Similar accuracy is achieved using the ICP-MS at the Union College Geology Department (compare with figures E12, E15 and E18).

Table E13: Relative standard deviation (RSD) of multiple analyses of 19 samples
(table continued on next page)

| Sample: | Z-91a | Z-91b | Z-94 | MRH-45a | MRH-45b | MRH-111 | OC-1-S1 | OC-1-S2 | OC-5-S4 | OC-6-S5 |
|------------------------|---------|---------|---------|---------|----------|----------|---------|---------|----------|---------|
| Analyzed in runs: | (2),[1] | (2),[1] | (2),[1] | (2),[2] | (2),[1*] | (2),[1*] | (2),[2] | (2),[2] | (2),[1*] | (2),[2] |
| Total no. of analyses: | 4 | 4 | 4 | 4 | 6 | 6 | 4 | 4 | 6 | 4 |
| Cr | 6.4% | 3.7% | 3.1% | 2.6% | 2.9% | 10.1% + | 2.8% | 5.0% + | 4.3% | 4.8% |
| Rb | 4.8% | 2.8% | 1.3% | 3.0% | 1.8% | 2.6% | 17.4% × | 1.0% | 8.9% × | 2.1% |
| Y | 3.2% | 1.3% | 3.8% | 3.7% | 1.5% | 4.3% | 1.3% | 1.0% | 2.2% | 3.6% |
| Zr | 3.4% | 1.1% | 2.3% | 3.5% | 1.7% | 2.7% | 1.9% | 4.9% | 3.8% | 4.8% |
| Nb ◁ | 3.0% | 1.9% | 16.7% | 1.2% | 3.5% | 4.6% | 5.7% | 3.0% | 3.7% | 2.8% |
| Cs | 2.5% | 2.5% | 7.3% | 1.0% | 2.3% | 3.0% | 4.3% | 2.8% | 2.7% | 2.7% |
| Ba | 5.4% | 4.0% | 8.8% | 1.4% | 3.2% | 2.7% | 1.8% | 1.7% | 4.2% | 3.7% |
| La | 5.1% | 2.2% | 5.9% | 1.9% | 0.9% | 1.8% | 3.7% | 3.8% | 1.3% | 6.4% |
| Ce | 4.0% | 2.9% | 6.1% | 1.4% | 1.5% | 2.5% | 1.5% | 0.9% | 2.8% | 3.1% |
| Pr | 4.6% | 2.8% | 4.9% | 1.3% | 1.3% | 1.6% | 2.9% | 3.5% | 1.4% | 3.8% |
| Nd | 4.6% | 2.0% | 6.0% | 3.5% | 1.5% | 2.3% | 3.9% | 4.0% | 1.2% | 4.1% |
| Sm | 1.4% | 0.2% | 6.0% | 4.5% | 2.4% | 5.1% | 1.4% | 3.1% | 0.8% | 3.8% |
| Eu | 2.4% | 1.4% | 5.4% | 4.8% | 1.8% | 1.8% | 2.9% | 3.7% | 1.1% | 4.8% |
| Gd | 1.8% | 1.0% | 6.8% | 3.7% | 2.8% | 4.0% | 1.3% | 1.6% | 1.6% | 3.3% |
| Tb | 1.1% | 2.6% | 5.3% | 3.9% | 1.6% | 2.1% | 1.9% | 2.4% | 1.7% | 2.4% |
| Dy | 1.9% | 2.5% | 3.9% | 3.7% | 1.5% | 2.1% | 1.7% | 2.5% | 1.5% | 2.5% |
| Ho | 1.1% | 0.6% | 3.5% | 2.6% | 1.2% | 3.3% | 2.1% | 1.9% | 2.3% | 3.0% |
| Er | 0.3% | 1.8% | 4.2% | 1.9% | 1.5% | 4.0% | 1.3% | 2.1% | 1.2% | 1.9% |
| Tm | 2.3% | 1.8% | 3.2% | 1.3% | 2.7% | 5.9% | 3.0% | 1.9% | 1.5% | 1.3% |
| Yb | 6.7% | 2.0% | 7.6% | 3.1% | 2.7% | 3.2% | 4.0% | 2.5% | 4.2% | 3.5% |
| Lu | 3.1% | 0.8% | 8.3% | 5.2% | 3.8% | 1.0% | 3.3% | 5.4% | 5.2% | 5.2% |
| Hf | 0.9% | 1.9% | 7.9% | 3.3% | 2.9% | 1.2% | 3.4% | 8.4% | 7.4% | 9.1% |
| Pb | 9.1% | 9.6% | 4.8% | 11.1% | 8.6% | 3.2% | 9.2% | 4.9% | 25.2% × | 11.7% |
| Th | 2.6% | 3.1% | 3.8% | 2.6% | 3.6% | 2.9% | 4.7% | 3.4% | 4.7% | 5.4% |
| U | 5.7% | 7.6% | 6.1% | 6.7% | 9.0% | 6.7% | 14.1% | 7.6% | 10.0% | 8.7% |
| Average | 3.5% | 2.6% | 5.7% | 3.3% | 2.7% | 3.4% | 3.5% | 3.3% | 3.0% | 4.3% |

Note that the solutions of four separate digestions per sample were analyzed:

Relative standard deviation:

$$RSD = (\sigma/\bar{X}) \bullet 100\%$$

- (2) duplicate analyses of sample in second test run (n=2)
- [1] duplicate analyses of sample in first analytical run (n=2)
- [1*] analysis of two aliquots of two digestions (n=4)
- [2] duplicate analyses of sample in second analytical run (n=2)
- [1,2] duplicate analyses in first analytical run, analyzed once in second analytical run (n=3)

Table E13 cont.

| Sample: | OC-58 | OC-113 | OC-186 | OC-224 | OC-227a | OC-227b | OC-379 | OC-380 | PB-1 | Aver-age of 19 samples |
|------------------------|-----------|---------|---------|---------|---------|---------|---------|---------|---------|------------------------|
| Analyzed in runs: | (2),[1,2] | (2),[1] | (2),[1] | (2),[2] | (2),[2] | (2),[1] | (2),[2] | (2),[1] | (2),[2] | |
| Total no. of analyses: | 5 | 4 | 4 | 4 | 4 | 4 | 4 | 4 | 4 | |
| Cr | 3.9% | 1.6% | 17.0% + | 4.9% | 4.8% | 5.4% | 9.3% + | 24.7% + | 3.7% | 6.4% |
| Rb | 3.3% | 2.3% | 2.4% | 4.5% | 3.3% | 1.2% | 22.3% × | 5.9% | 17.3% × | 2.8% |
| Y | 2.7% | 2.8% | 4.9% | 3.6% | 0.8% | 2.5% | 2.6% | 3.3% | 3.1% | 2.7% |
| Zr | 1.1% | 4.2% | 5.4% | 4.5% | 3.2% | 2.6% | 3.2% | 4.0% | 1.7% | 3.2% |
| Nb \triangleleft | 2.8% | 3.6% | 0.8% | 3.1% | 5.3% | 3.8% | 3.0% | 2.7% | 3.4% | 3.9% |
| Cs | 3.9% | 2.8% | 6.5% | 6.5% | 7.2% | 7.3% | 4.7% | 3.6% | 14.5% | 4.6% |
| Ba | 4.6% | 2.3% | 8.0% | 1.5% | 1.3% | 6.7% | 4.0% | 2.4% | 2.5% | 3.7% |
| La | 3.2% | 0.8% | 9.4% | 3.7% | 7.2% | 7.5% | 2.8% | 3.4% | 2.0% | 3.9% |
| Ce | 4.0% | 2.8% | 7.4% | 2.2% | 3.9% | 7.0% | 2.9% | 2.4% | 2.1% | 3.2% |
| Pr | 4.3% | 2.4% | 8.5% | 2.3% | 0.7% | 4.7% | 2.0% | 3.3% | 1.1% | 3.0% |
| Nd | 4.2% | 1.2% | 9.0% | 5.5% | 5.7% | 6.7% | 2.6% | 4.1% | 1.5% | 3.9% |
| Sm | 3.6% | 3.0% | 6.1% | 6.2% | 2.9% | 5.5% | 3.7% | 1.4% | 2.3% | 3.3% |
| Eu | 4.0% | 1.0% | 7.5% | 6.9% | 3.7% | 5.0% | 2.6% | 2.6% | 1.9% | 3.4% |
| Gd | 3.8% | 1.5% | 8.0% | 5.6% | 3.3% | 5.2% | 2.6% | 2.6% | 0.9% | 3.2% |
| Tb | 3.5% | 1.2% | 8.2% | 4.4% | 2.8% | 4.6% | 3.3% | 2.9% | 1.4% | 3.0% |
| Dy | 2.7% | 1.8% | 6.1% | 3.4% | 1.9% | 3.4% | 3.5% | 2.3% | 0.9% | 2.6% |
| Ho | 2.1% | 1.2% | 4.3% | 4.3% | 2.3% | 2.3% | 2.4% | 2.7% | 2.4% | 2.4% |
| Er | 2.5% | 0.4% | 4.0% | 3.7% | 1.6% | 3.4% | 4.6% | 1.9% | 1.7% | 2.3% |
| Tm | 2.1% | 2.0% | 1.9% | 1.5% | 2.1% | 2.6% | 3.8% | 2.7% | 2.4% | 2.4% |
| Yb | 3.6% | 1.4% | 4.8% | 4.0% | 3.3% | 5.4% | 3.6% | 5.2% | 0.5% | 3.8% |
| Lu | 4.9% | 1.7% | 5.4% | 3.0% | 3.5% | 5.5% | 3.8% | 2.4% | 2.1% | 3.9% |
| Hf | 4.4% | 0.6% | 2.5% | 6.7% | 1.4% | 2.5% | 1.8% | 2.3% | 2.0% | 3.7% |
| Pb | 59.5% × | 7.0% | 3.5% | 4.2% | 5.1% | 7.0% | 2.3% | 8.2% | 3.1% | 6.6% |
| Th | 5.4% | 4.4% | 3.1% | 2.9% | 8.2% | 2.5% | 4.6% | 2.0% | 2.7% | 3.8% |
| U | 11.2% | 3.2% | 7.1% | 9.5% | 5.5% | 6.8% | 2.3% | 4.4% | 4.1% | 7.2% |
| Average | 3.8% | 2.3% | 6.1% | 4.3% | 3.6% | 4.7% | 3.4% | 4.1% | 3.3% | |

× Samples with very low levels (< 1 ppm) of Rb or Pb which are affected by small amounts of Rb or Pb contamination have high relative standard deviations (average relative standard deviation of Rb and Pb calculated without marked values)

+ In general, samples with the lowest levels of Cr have the highest RSDs (e.g., OC-380 with 8 ppm Cr)

\triangleleft The accuracy and precision of Nb were improved with second test run; Nb values of second test run agree well with those of the first and second analytical run.

Table E14: Compilation of analytical results, BCR-1 analyzed as unknown

| Element | recom- mended values [1] | Analysis by ICP-MS at Union College: | | | | | | |
|---------|-----------------------------------|--------------------------------------|-----------------|------------------|-------------------|-------------------|------------------|--------------------|
| | | test 1 (n=6) | test 2 (n=4) | analy.1 (n=8) | analy.2 (n=12) | analy.3 (n=12) | analy.4 (n=6) | analy.5 × (n=8) |
| | | [----- this study -----] | | | | | | |
| V | <u>407</u> | n.d. | n.d. | 411 | 398 | 393 | 370 | 373 |
| Cr | 16 | n.d. | 12.0 | 14.5 | 10.4 | 10.6 | 13.3 | 26 |
| Rb | <u>47.2</u> | 46.91 | 52.6 | 47.2 | 47.3 | 47.6 | 47 | 47.7 |
| Sr | <u>330</u> | n.d. | n.d. | 342 | 329 | 335 | 331 | 336 |
| Y | <u>38</u> | 36.51 | 37.0 | 35.5 | 34.6 | 35.3 | 34.5 | 34.7 |
| Zr | <u>190</u> | n.d. | 190 | 183 | 184 | 194 | 185 | 184 |
| Nb | 14 | 15.7* | 17.8* | 15.5 | 15.4 | 14.5 | 15.3 | 15.3 |
| Cs | <u>0.96</u> | 0.905 | 1.04 | 0.96 | 0.97 | 0.959 | 1.05 | 1.04 |
| Ba | <u>681</u> | 674.5 | 684 | 686 | 714 | 688 | 738 | 727 |
| La | <u>24.9</u> | 24.50 | 26.8 | 25.7 | 26.5 | 24.6 | 27.4 | 26.5 |
| Ce | <u>53.7</u> | 52.9 | 57.3 | 52.5 | 54.7 | 53.6 | 56.0 | 55.2 |
| Pr | <u>6.8</u> | 6.82 | 7.17 | 6.76 | 7.02 | 6.79 | 7.20 | 7.03 |
| Nd | <u>28.8</u> | 28.4 | 29.5 | 29.8 | 30.8 | 28.4 | 31.2 | 30.3 |
| Sm | <u>6.59</u> | 6.39 | 6.44 | 6.52 | 6.51 | 6.59 | 6.58 | 6.58 |
| Eu | <u>1.95</u> | 1.98 | 1.97 | 2.00 | 1.98 | 1.94 | 1.92 | 1.93 |
| Gd | <u>6.68</u> | 6.64 | 7.17 | 6.73 | 6.86 | 6.58 | 6.78 | 6.79 |
| Tb | <u>1.05</u> | 1.06 | 1.05 | 1.03 | 1.07 | 1.04 | 1.05 | 1.05 |
| Dy | <u>6.34</u> | 6.15 | 6.33 | 6.29 | 6.40 | 6.20 | 6.36 | 6.20 |
| Ho | <u>1.26</u> | 1.28 | 1.33 | 1.29 | 1.29 | 1.25 | 1.28 | 1.25 |
| Er | <u>3.63</u> | 3.61 | 3.41 | 3.51 | 3.51 | 3.48 | 3.47 | 3.40 |
| Tm | <u>0.56</u> | 0.564 | 0.52 | 0.506 | 0.512 | 0.531 | 0.508 | 0.50 |
| Yb | <u>3.38</u> | 3.36 | 3.44 | 3.26 | 3.32 | 3.29 | 3.29 | 3.21 |
| Lu | <u>0.51</u> | 0.508 | 0.575 | 0.563 | 0.578 | 0.517 | 0.568 | 0.56 |
| Hf | <u>4.95</u> | 4.93 | 5.31 | 4.97 | 5.15 | 4.95 | 4.96 | 4.98 |
| Ta | <u>0.81</u> | 3.21* | 0.89* | 0.751 | 0.764 | 0.821 | 0.753 | 0.76 |
| Pb | <u>13.6</u> | 13.9 | 15.3 | 14.5 | 14.2 | 13.97 | 13.61 | 13.6 |
| Th | <u>5.98</u> | 5.96 | 6.32 | 6.22 | 6.12 | 5.87 | 6.06 | 5.81 |
| U | <u>1.75</u> | 1.77 | 1.80 | 1.71 | 1.72 | 1.71 | 1.70 | 1.59 |

[1] Govindaraju (1994), data underlined are recommended values, other values are proposed

* Ta and Nb unstable in solution

× analytical run for MacPherson (11/11/97)

Table E15: Compilation of analytical results for Pal-889
(table continued on next page)

| selected reference values [1] | Analysis by ICP-MS at Union College | | | | | | | | | | WSU ICP-MS (n=2) [2] | UM XRF (n=1) [2] | McGill XRF (n=1) [2] | McGill XRF (n=5) [3] | Cornell INAA error (n=13) [3] |
|-------------------------------|-------------------------------------|--------------|---------------|---------------|---------------|---------------|---------------|------------------|---------------|---------------|----------------------|------------------|----------------------|----------------------|-------------------------------|
| | test 1 (n=6) | test 2 (n=4) | analy.1 (n=4) | analy.2 (n=2) | analy.3 (n=4) | analy.4 (n=2) | analy.5 (n=3) | ICP-MS (n=2) [2] | XRF (n=1) [2] | XRF (n=5) [3] | | | | | |
| V | n.d. | n.d. | 269 | 263 | 275 | 256 | 285 | - | 252.4 | 260 | 249 | 21 | - | | |
| Cr | n.d. | 283 | 310 | 294 | 312 | 313 | 310 | - | 284.4 | 310 | - | - | 312 | | |
| Rb | 30.3 | 31.5 | 29.7 | 30.7 | 30.1 | 28.5 | 30.6 | 28.5 | - | - | 32 | 3 | - | | |
| Sr | n.d. | n.d. | 174 | 181 | 173 | 183 | 172 | 180.5 | 181.8 | 177 | 179 | 8 | - | | |
| Y | 22.0 | 23.0 | 21.4 | 22.0 | 22.1 | 24.0 | 21.4 | 23.7 | - | - | 22 | 1 | - | | |
| Zr | n.d. | 97.3 | 90.9 | 93.0 | 100.5 | 98.6 | 94.9 | - | 101.6 | 110 | 116 | 5 | - | | |
| Nb | 9.71* | 9.9* | 8.68 | 8.74 | 8.51 | 8.41 | 8.53 | 7.47 | 7.3 | [15] | 9 | 1 | - | | |
| Cs | 2.19 | 2.19 | 1.95 | 2.03 | 2.15 | 2.19 | 2.04 | 1.88 | - | - | - | - | - | | |
| Ba | 174.4 | 185.0 | 169 | 180 | 193 | 185 | 184 | 173.1 | 195.5 | 231 | - | - | 183 | | |
| La | 10.62 | 11.27 | 10.1 | 10.2 | 10.9 | 10.5 | 10.4 | 10.64 | [6.5] | - | - | - | 10.51 | | |
| Ce | 22.8 | 23.7 | 21.8 | 22.4 | 23.6 | 23.6 | 22.9 | 21.73 | 23.8 | - | - | - | 23.9 | | |
| Pr | 3.27 | 3.15 | 2.93 | 2.93 | 3.15 | 3.19 | 2.97 | 2.73 | - | - | - | - | - | | |
| Nd | 13.0 | 14.3 | 13.1 | 12.9 | 13.2 | 13.0 | 13.2 | 12.11 | - | - | - | - | 12.2 | | |
| Sm | 3.42 | 3.45 | 3.26 | 3.34 | 3.46 | 3.41 | 3.23 | 3.60 | - | - | - | - | 3.44 | | |
| Eu | 1.12 | 1.14 | 1.09 | 1.11 | 1.12 | 1.07 | 1.06 | 1.18 | - | - | - | - | 1.04 | | |
| Gd | 4.24 | 3.87 | 3.69 | 3.74 | 3.89 | 3.98 | 3.68 | 3.76 | - | - | - | - | - | | |
| Tb | 0.67 | 0.624 | 0.620 | 0.609 | 0.649 | 0.667 | 0.614 | 0.70 | - | - | - | - | - | | |
| Dy | 4.18 | 3.71 | 3.86 | 3.76 | 4.01 | 3.98 | 3.79 | 4.40 | - | - | - | - | - | | |
| Ho | 0.8 | 0.779 | 0.768 | 0.762 | 0.811 | 0.809 | 0.768 | 0.90 | - | - | - | - | - | | |
| Er | 2.25 | 2.18 | 2.13 | 2.21 | 2.35 | 2.29 | 2.15 | 2.54 | - | - | - | - | - | | |
| Tm | 0.33 | 0.342 | 0.319 | 0.319 | 0.360 | 0.339 | 0.327 | 0.36 | - | - | - | - | - | | |
| Yb | 2.18 | 2.03 | 2.01 | 2.01 | 2.12 | 2.18 | 2.03 | 2.11 | - | - | - | - | - | | |
| Lu | 0.3 | 0.279 | 0.305 | 0.303 | 0.314 | 0.304 | 0.304 | 0.33 | - | - | - | - | - | | |
| Hf | 2.56 | 2.51 | 2.63 | 2.49 | 2.62 | 2.56 | 2.60 | 2.58 | - | - | - | - | 2.58 | | |
| Ta | 0.63 | 2.47* | 0.600 | 0.603 | 0.677 | 0.630 | 0.596 | 0.60 | - | - | - | - | 0.65 | | |
| Pb | - | 4.68 | 5.59 | 4.43 | 4.75 | 4.41 | 4.69 | 4.42 | - | - | - | - | - | | |
| Th | 2.04 | 2.25 | 2.07 | 2.06 | 2.02 | 2.07 | 2.05 | 1.78 | - | - | - | - | 1.98 | | |
| U | 0.513 | 0.516 | 0.494 | 0.489 | 0.492 | 0.497 | 0.417 | 0.47 | - | - | - | - | 0.5 | | |

Table E15 cont.

[1] data underlined are in-house standard values of Pal-889 used at Cornell University (Wirth, 1991)
other values are from the analysis of the U.S.G.S. standard W-1 using ID-SSMS (Jochum et al., 1988)
V - reference value: average of XRF analyses at McGill and UM

[2] unpublished data (Harper pers. com., 1995)

[3] Wirth (1991)

WSU ... Washington State University Geoanalytical Laboratories

UM ... University of Massachusetts

* Ta and Nb unstable in solution

× analytical run for MacPherson (11/11/97)

Table E16: Compilation of analytical results for Cou-IL-6

| Element | Analysis by ICP-MS at Union College: [----- this study -----] | | | | | | WSU ICP-MS | WSU XRF | |
|---------|--------------------------------------------------------------------|-----------------|------------------|------------------|------------------|------------------|-------------------------------|--------------|--------------|
| | test 1 (n=6) | test 2 (n=0) | analy.1 (n=8) | analy.2 (n=2) | analy.3 (n=4) | analy.4 (n=6) | analy.5 [×] (n=3) | (n=2) [1] | (n=2) [1] |
| V | n.d. | | 501 | 493 | 476 | 472 | 492 | - | 472 |
| Cr | n.d. | | 89 | 81 | 85 | 83 | 99 | - | - |
| Rb | 13.04 | | 12.8 | 12.6 | 13.1 | 12.2 | 13.5 | 13.5 | 11 |
| Sr | n.d. | | 273 | 267 | 273 | 275 | 279 | - | 257 |
| Y | 39.8 | | 38.9 | 38.0 | 40.2 | 37.4 | 38.8 | 37.6 | 39 |
| Zr | n.d. | | 119 | 117 | 131 | 119 | 122 | - | 120 |
| Nb | 5.73* | | 5.71 | 5.57 | 5.70 | 5.59 | 5.87 | 4.33 | 5.9 |
| Cs | 2.77 | | 2.82 | 2.94 | 2.96 | 2.83 | 2.99 | 2.80 | - |
| Ba | 57.1 | | 53.5 | 58.8 | 59.7 | 58.7 | 63 | 58.0 | 31 |
| La | 6.28 | | 6.11 | 6.51 | 6.51 | 6.46 | 6.65 | 6.60 | 3 |
| Ce | 17.1 | | 15.9 | 17.1 | 17.7 | 17.2 | 17.7 | 16.3 | 18 |
| Pr | 2.73 | | 2.57 | 2.69 | 2.81 | 2.67 | 2.75 | 2.48 | - |
| Nd | 14.0 | | 13.4 | 13.8 | 14.2 | 13.6 | 14.2 | 12.8 | - |
| Sm | 4.31 | | 4.18 | 4.26 | 4.45 | 4.23 | 4.17 | 4.51 | - |
| Eu | 1.44 | | 1.34 | 1.36 | 1.41 | 1.28 | 1.34 | 1.48 | - |
| Gd | 5.59 | | 5.31 | 5.53 | 5.68 | 5.46 | 5.32 | 5.37 | - |
| Tb | 0.996 | | 0.912 | 0.954 | 0.984 | 0.962 | 0.946 | 1.08 | - |
| Dy | 6.25 | | 6.06 | 6.25 | 6.47 | 6.29 | 6.16 | 7.09 | - |
| Ho | 1.37 | | 1.30 | 1.32 | 1.37 | 1.35 | 1.31 | 1.49 | - |
| Er | 3.96 | | 3.77 | 3.85 | 3.99 | 3.90 | 3.76 | 4.35 | - |
| Tm | 0.634 | | 0.575 | 0.598 | 0.623 | 0.596 | 0.581 | 0.60 | - |
| Yb | 3.80 | | 3.65 | 3.76 | 3.84 | 3.82 | 3.76 | 3.70 | - |
| Lu | 0.532 | | 0.557 | 0.577 | 0.552 | 0.584 | 0.58 | 0.62 | - |
| Hf | 3.18 | | 3.15 | 3.23 | 3.27 | 3.27 | 3.23 | 3.02 | - |
| Ta | 0.83* | | 0.301 | 0.314 | 0.330 | 0.297 | 0.31 | 0.33 | - |
| Pb | 0.87 [○] | | 0.582 | 0.617 | 0.598 | 0.637 | 0.82 | 2.04 | - |
| Th | 0.523 | | 0.541 | 0.540 | 0.520 | 0.545 | 0.54 | 0.49 | - |
| U | 0.185 | | 0.180 | 0.185 | 0.181 | 0.181 | 0.17 | 0.13 | - |

[1] unpublished data (G. Harper, pers. com., 1995)

* Ta and nb unstable in solution

○ contamination detected

× analytical run for MacPherson (11/11/97)

E.10.2 Fifth analytical run, 11/11/97

E.10.2.1 Limits of detection

Using equation (1) in section 6.1, the detection limits were determined from the blank residuals of the fifth analytical run and are listed in table E17. The detection limits of V, Cr, Rb, Sr, Zr, Ba and Pb are relatively higher than those of the other elements. Overall, the detection limits of the fifth analytical run are very similar to previous analytical runs (see tables E9, E10, E11 for comparison) and do not indicate problems with the performance of the ICP-MS instrument (i.e., back ground levels were very low as usual). Most importantly, all elemental concentrations determined in the samples (appendix F) are well above the detection limits (table E17).

E.10.2.2 Precision

The analytical results for BCR-1, Pal-889 and Cou-II-6 are listed in table E17 as well as the standard deviation of the multiple analyses of these reference materials. The precision is based on eight analyses of BCR-1 treated as an unknown sample and three analyses of Pal-889 and Cou-IL-6 (figure E25). The overall precision achieved in the fifth analytical run is poorer than the precision of analytical runs 1, 2 and 3 (figures E11, E14, and E17, respectively), however, notably better than for the fourth analytical run (figure E20). As shown in figure E25, the precision of light REE and medium REE is acceptable to good, and the precision of Nb, Cs, heavy REE, Hf, Ta, Pb, Th and U is good to excellent based on the % relative standard deviation. The precision of the remaining elements (i.e., V, Cr, Rb, Sr, Y and Zr) might be unacceptable as indicated by high relative standard deviations. Overall, the precision of the fifth analytical run is poorer than usual which might be related to a decline of the performance of the ICP-MS instrument (see section E.10.2.4).

E.10.2.3 Accuracy

The agreement between the recommended standard values of BCR-1 and the mean of measured values is good (figure E26). Generally, the mean values agree within $\pm 10\%$ of the reference values, except

Table E17: Results of fifth analytical run 11/11/97

| Element | Detection Limits in ppm | BCR-1 | | Pal-889 | | Cou-IL-6 | |
|---------|----------------------------|---------------|---------------------|---------------|---------------------|---------------|---------------------|
| | | mean (n=8) | error 1 σ | mean (n=3) | error 1 σ | mean (n=3) | error 1 σ |
| V | 0.36 | 373 | 42 | 285 | 17 | 492 | 27 |
| Cr | 1.29 | 26.2 | 4.1 | 310 | 40 | 99 | 16 |
| Rb | 0.111 | 47.7 | 4.5 | 30.6 | 2.7 | 13.5 | 1.2 |
| Sr | 0.60 | 336 | 31 | 172 | 7 | 279 | 20 |
| Y | 0.038 | 34.7 | 3.5 | 21.4 | 1.8 | 38.8 | 3.8 |
| Zr | 0.3 | 184 | 17 | 94.9 | 8.1 | 122 | 14 |
| Nb | 0.022 | 15.3 | 0.7 | 8.53 | 0.35 | 5.87 | 0.50 |
| Cs | 0.0105 | 1.04 | 0.05 | 2.04 | 0.10 | 2.99 | 0.21 |
| Ba | 2.41 | 727 | 54 | 184 | 8 | 63.4 | 1.6 |
| La | 0.084 | 26.5 | 2.0 | 10.4 | 0.6 | 6.65 | 0.54 |
| Ce | 0.159 | 55.2 | 4.2 | 22.9 | 1.2 | 17.7 | 1.5 |
| Pr | 0.0206 | 7.03 | 0.49 | 2.97 | 0.18 | 2.75 | 0.25 |
| Nd | 0.068 | 30.3 | 2.242 | 13.2 | 0.8 | 14.2 | 1.1 |
| Sm | 0.0117 | 6.58 | 0.40 | 3.23 | 0.14 | 4.17 | 0.27 |
| Eu | 0.0037 | 1.93 | 0.11 | 1.06 | 0.05 | 1.34 | 0.09 |
| Gd | 0.0075 | 6.79 | 0.38 | 3.68 | 0.16 | 5.32 | 0.26 |
| Tb | 0.00119 | 1.05 | 0.04 | 0.614 | 0.032 | 0.946 | 0.051 |
| Dy | 0.0110 | 6.20 | 0.25 | 3.79 | 0.19 | 6.16 | 0.33 |
| Ho | 0.00199 | 1.25 | 0.05 | 0.768 | 0.032 | 1.31 | 0.08 |
| Er | 0.0047 | 3.40 | 0.09 | 2.15 | 0.10 | 3.76 | 0.22 |
| Tm | 0.00115 | 0.500 | 0.012 | 0.327 | 0.011 | 0.581 | 0.024 |
| Yb | 0.0032 | 3.21 | 0.07 | 2.03 | 0.06 | 3.76 | 0.07 |
| Lu | 0.00083 | 0.564 | 0.012 | 0.304 | 0.008 | 0.576 | 0.021 |
| Hf | 0.0048 | 4.98 | 0.08 | 2.60 | 0.06 | 3.23 | 0.06 |
| Ta | 0.002 | 0.761 | 0.014 | 0.596 | 0.014 | 0.312 | 0.008 |
| Pb | 0.39 | 13.6 | 0.4 | 4.69 | 0.21 | 0.818 | 0.026 |
| Th | 0.021 | 5.81 | 0.34 | 2.05 | 0.02 | 0.539 | 0.003 |
| U | 0.0062 | 1.59 | 0.12 | 0.417 | 0.014 | 0.167 | 0.002 |

standard deviation :
$$\sigma = \sqrt{\frac{\sum(X_i - \bar{X})^2}{n^2}}$$

see tables 2 and 5 for recommended standard values of BCR-1 and Pal-889, respectively

see tables 14, 15 and 16 for compilation of analytical results

for BCR-, Pal-889, and Cou-IL-6, respectively

Precision based on multiple analyses of three samples

5th analytical run, 11/11/97

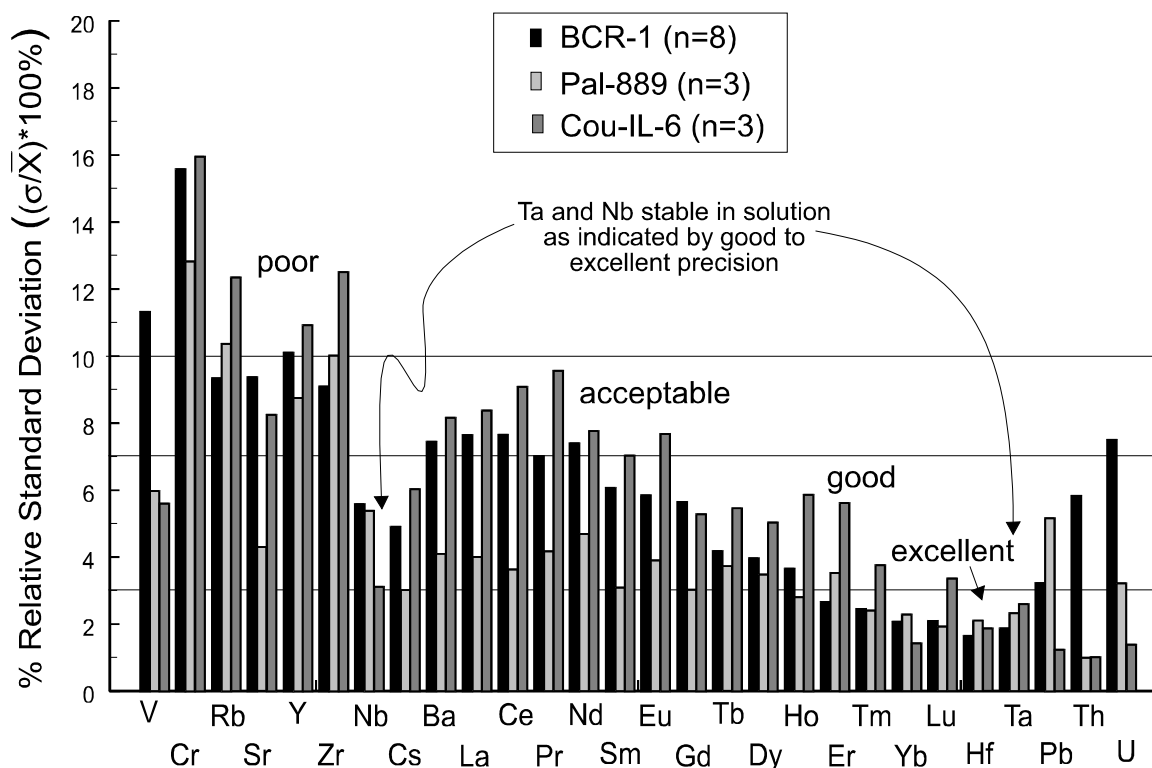


Figure E25

Diagram illustrating the precision of the analysis of the fifth analytical run. Four aliquots of an old BCR-1 solution and four aliquots of a new BCR-1 solution were analyzed. The old BCR-1 solution left from the third analytical run was stored in a Teflon vial. Systematic differences between the old and new BCR-1 solutions were not observed. Poor precision of V, Cr, Rb, Sr (compared to previous runs), and Zr is indicated by $\geq 10\%$ relative standard deviation. Acceptable to good precision of Sr, Ba and the light REE is indicated by 5% to 9% relative standard deviation. The remaining elements were analyzed with good to excellent precision (1% to 5% relative standard deviation).

Sample: BCR-1

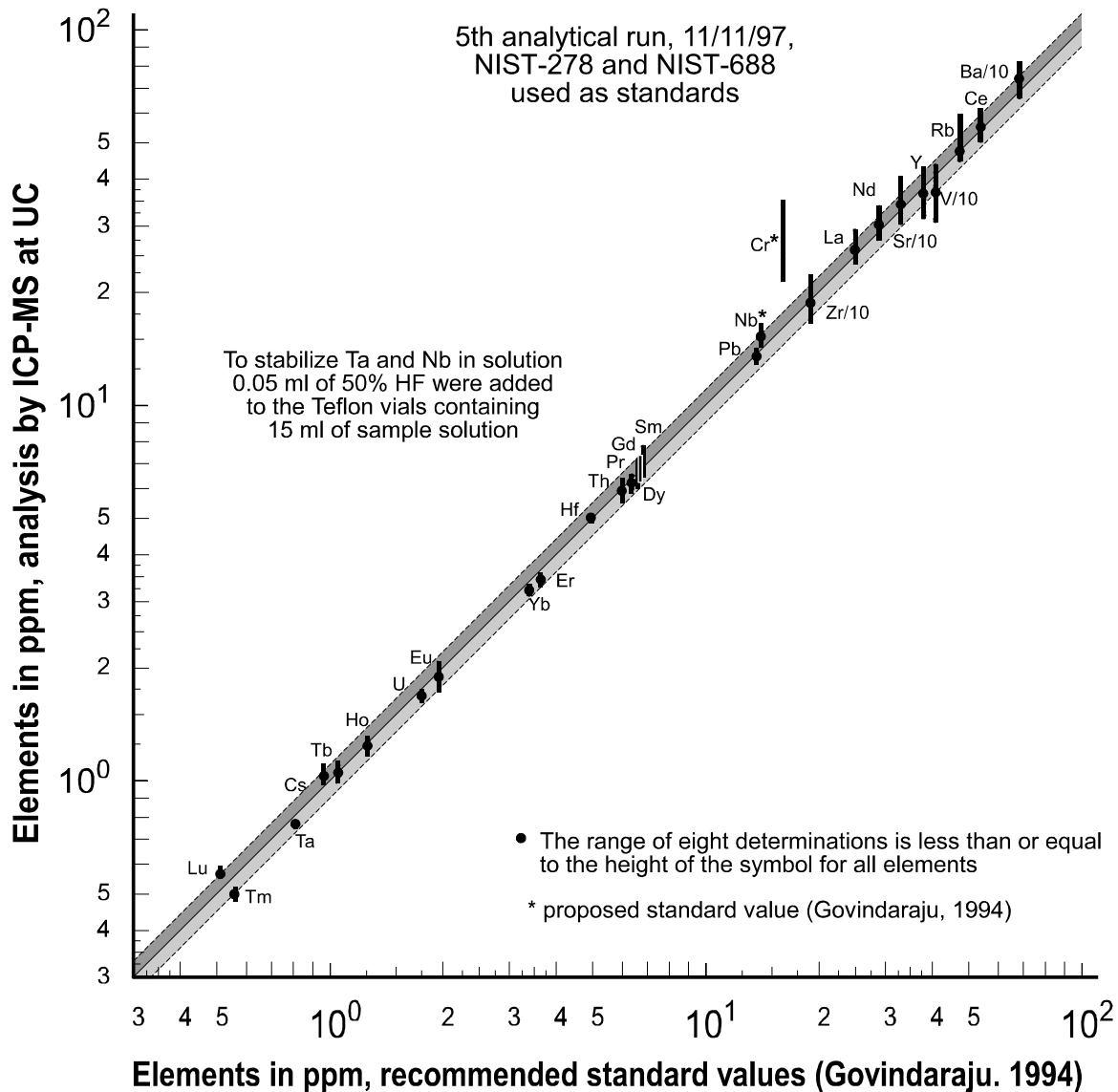


Figure E26

Comparative plot of the analytical results of the fifth analytical run versus the recommended standard values of BCR-1 (Govindaraju, 1994). The mean values of eight analyses of BCR-1 plot close to or on the line with slope = 1. However, due to poor precision of V, Cr, Rb, Sr, Y, and Zr, several data points plot outside the shaded fields indicating some analytical results differ more than 10% from the standard values. Nonetheless, most elemental concentrations were determined within $\pm 10\%$ of the standard values indicating good accuracy of the analysis.

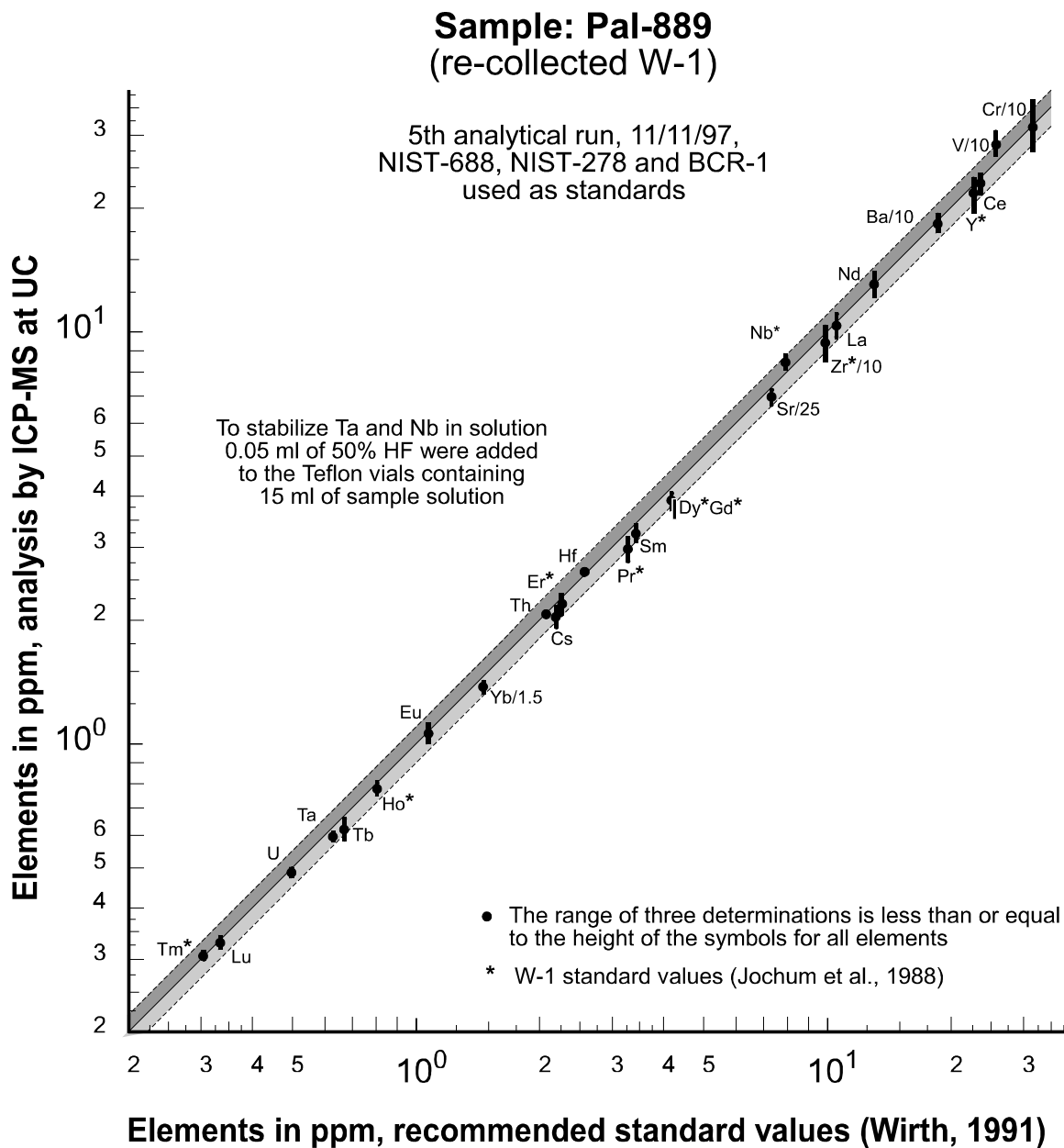


Figure E27

Comparative plot of the analytical data for Pal-889 versus the standard values of Pal-889 and W-1. The agreement between the analytical results for Pal-889 and the selected standard values is very good, indicating good accuracy of the analysis. In the fifth analytical run, the accuracy of V, Cr, Y and Zr may not be as good as for all other elements due to poor precision (figure E25). Note that the analytical data of Nb obtained in all analytical runs are consistently higher than the standard value of Nb (see figures E12 and E15), suggesting the selected W-1 standard value is too low (see section E.8.4.4).

for Cr. The analytical data of Cr are significantly higher than the proposed standard value (16 ppm). This is rather unusual because much lower Cr values (10-14 ppm) were obtained in all other analytical runs (table E14). This possibly indicates a problem analyzing low levels of Cr in the fifth analytical run.

Two or three of eight determinations of V, Rb, Sr, and Y and one of eight determinations of Zr, Ba, La and Nd do not agree within 10% of the corresponding reference values (figure E26). Thus, the accuracy (and precision) of the fifth analytical run is apparently not as good as the accuracy (and precision) of analytical runs 1, 2 and 3. Nonetheless, most data points agree within $\pm 10\%$ of the recommended standard values suggesting that the analytical results are acceptably accurate.

The analytical results for Pal-889 agree well with the selected standard values (figure E27), indicating good accuracy of the analysis. As observed in previous comparative plots (e.g., figure E13), the analytical results for Pal-889 differ more than 10% from the W-1 standard values (i.e., Nb, Pr, Dy, and Gd), however, agree well with the Pal-889 standard values (most analytical results agree within 5-6% of the Pal-889 standard values). Furthermore, the three analyses of Pal-889 and Cou-II-6 agree well with the results obtained earlier at Union College and also with the ICP-MS analysis at Washington State University (tables E15 and E16, respectively).

E.10.2.4 Varying performance of the ICP-MS instrument or incomplete dissolution ?

Poor precision of the fifth analytical run (figure E25) is interpreted as due to a decline of the performance of the ICP-MS instrument. Such decline of the performance was observed before: aliquots of the same sample, standard, and blank solutions (stored in Teflon vials) were analyzed in the third and fourth analytical run. If there would have been no change in the performance of the ICP-MS instrument, very similar precision of the analyses of the same solutions should have been obtained. However, the precision of the fourth analytical (figure E20) run is much poorer than that of the third analytical run (figure E17) indicating varying machine performance. Probably, the fifth analytical run was affected by similar problems with the ICP-MS instrument (i.e., a vacuum leak apparently occurred several times during 1997).

Furthermore, it has been demonstrated in this study that samples of basaltic to andesitic composition are completely dissolved using the mixed acid attack as described in section E2 (see also

sections E.7.1.7 and E.8.3.4). Also, duplicates of the samples (i.e. weighing of 0.1g sample in each of two Teflon vials per sample and dissolving using acid digestion) were analyzed in the fifth analytical run. Systematic differences between the two digestions of a sample were not observed suggesting incomplete dissolution is not a problem in the fifth analytical run.

To summarize, poorer than usual precision of the fifth analytical run is most likely due to a decline of the performance of the ICP-MS instrument and not due to incomplete dissolution of the samples.

E.10.3 Comparison with XRF and INAA data

E.10.3.1 Comparison with XRF data

The precision of XRF as well as of ICP-MS analysis should be given for a meaningful comparison of the analytical results. The precision of ICP-MS analysis is given in figure E25. In lack of more detailed information, the precision of XRF analysis was roughly estimated using data obtained at McGill University and the University of Massachusetts. The relative standard deviation (1σ) was estimated as follows: Sr ~4.5%; V ~8.5%; Y ~4.5%; Zr ~4.5%; Ba ~50% to ~12% for concentrations ranging from 20 ppm to 100 ppm). Evidently, the precision of Sr, V, Y, and Zr is better by XRF than by ICP-MS analysis. Thus, the XRF data for these elements are preferred over the ICP-MS data. However, the precision of Ba by ICP-MS analysis (figure E25) is much better than by XRF analysis, especially at low levels of Ba (detection limit at ~20 ppm, figure E28a).

Overall, the analytical results agree within errors of the analyses (most data agree within 1σ and all data within 2σ). Nonetheless, a systematic difference between ICP-MS and XRF data can be seen in figure 28d (element Y). Unusual low and/or variable count rates analyzing Y in the standards (due to varying machine performance?) probably affected the calibration of the ICP-MS analysis. As a result, Y concentrations obtained by ICP-MS in the fifth analytical run are lower than the XRF values.

E.10.3.2 Comparison with INAA data

The comparative diagrams are shown in figures E29, E30 and E31. In general, the analytical

results obtained by ICP-MS analysis and INAA agree fairly well: the agreement is within errors of the analyses, and differences are usually not larger than 10% (except for Cr, Rb, Cs, Ta and U).

Probably, the analysis of elements with very low concentrations is more accurate by ICP-MS than by INAA, because the detection limits of ICP-MS are 1 to 3 orders of magnitude lower than the detection limits of INAA. Consequently, more accurate results for Rb (figure E29b), Cs (figure E29c), Ta (figure E31c) and U (figure E31e) were obtained by ICP-MS. Considering the large uncertainty analyzing low levels of Th by INAA (figure E10), the Th data obtained by ICP-MS is probably more accurate as well.

Systematic differences between the two analytical techniques observed for Sm (figure E30b) and Yb (figure E30e) is possibly due to differences in the standardization (calibration) of the analyses.

Documentation of accurate calibration of the analytical runs using ICP-MS is given in table E2: recommended standard values of BCR-1 (Govindaraju, 1994) were accurately reproduced analyzing BCR-1 as an unknown sample (NIST-278 and NIST-688 used as standards). Note that all samples were analyzed using BCR-1, NIST-278 and NIST-688 as standards.

E.10.4. Summary

Precision and accuracy of Nb, Cs, Ba, REE, Hf, Ta, Pb, Th and U are good to acceptable as shown in figures E25, E26 and E27. The analytical results of V, Cr, Sr, Y, and Zr obtained in the fifth analytical run are less than adequate compared to the data obtained by XRF analysis. In spite of poor precision of Rb, the analytical data of Rb obtained by ICP-MS are more accurate than by INAA. Overall, the ICP-MS data represent a valuable addition to previous data (mainly because of the low detection limits of ICP-MS) and may prove to be useful for petrogenetic interpretations. Nonetheless, petrogenetic interpretations of the geochemical data should be made within the limits of the precision and accuracy achieved in the fifth analytical run (figures E25, E26, and E27).

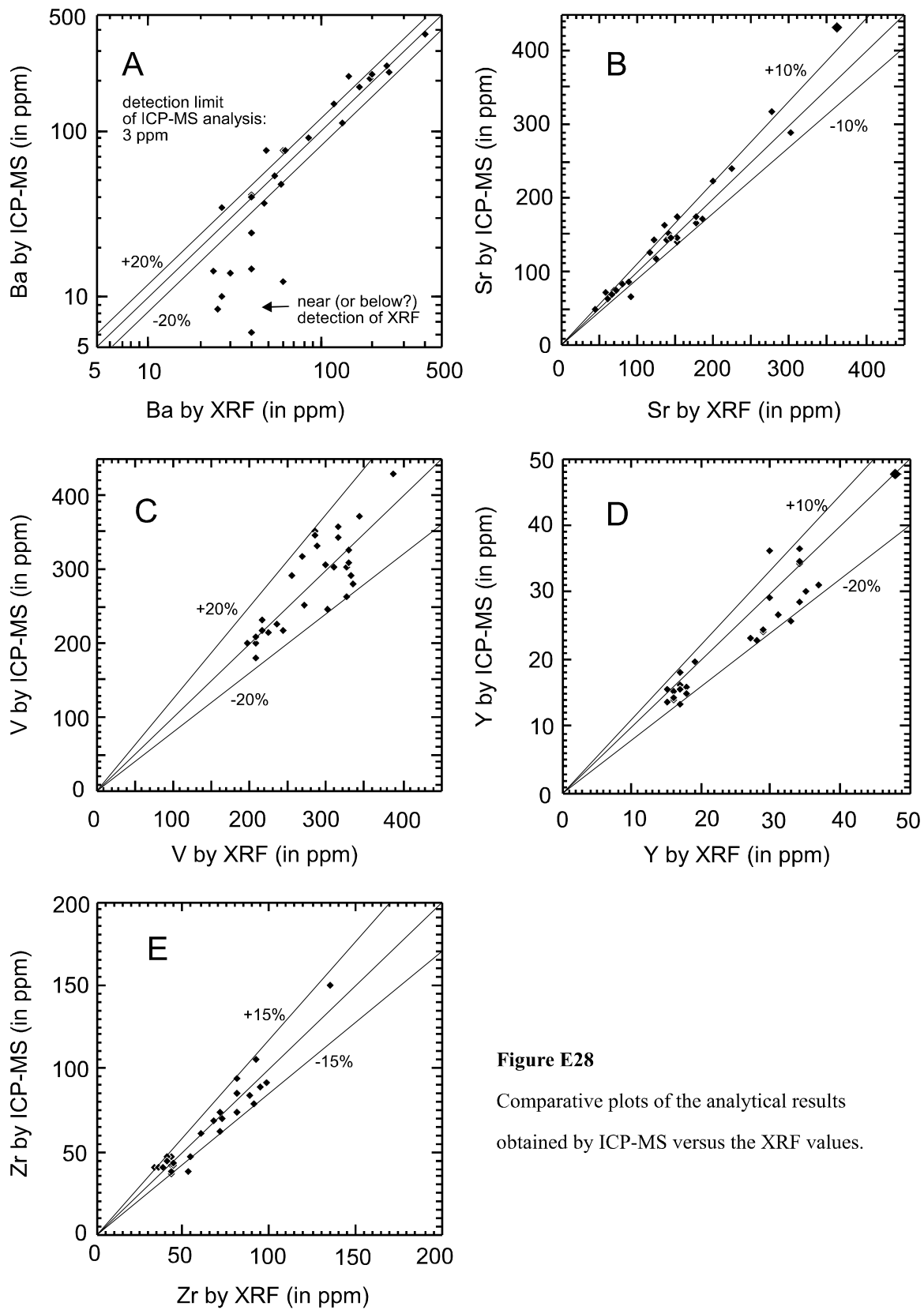


Figure E28

Comparative plots of the analytical results obtained by ICP-MS versus the XRF values.

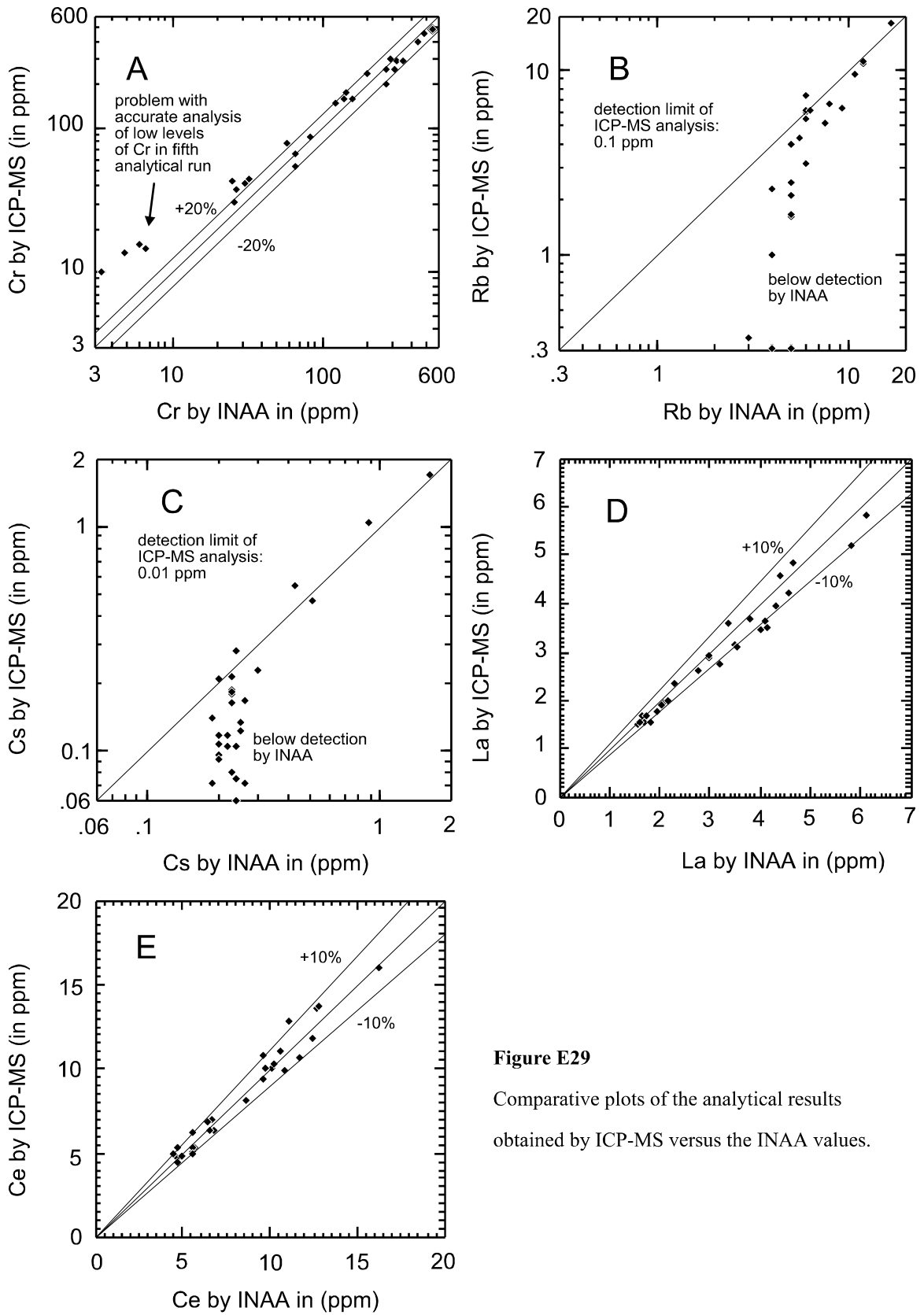


Figure E29

Comparative plots of the analytical results obtained by ICP-MS versus the INAA values.

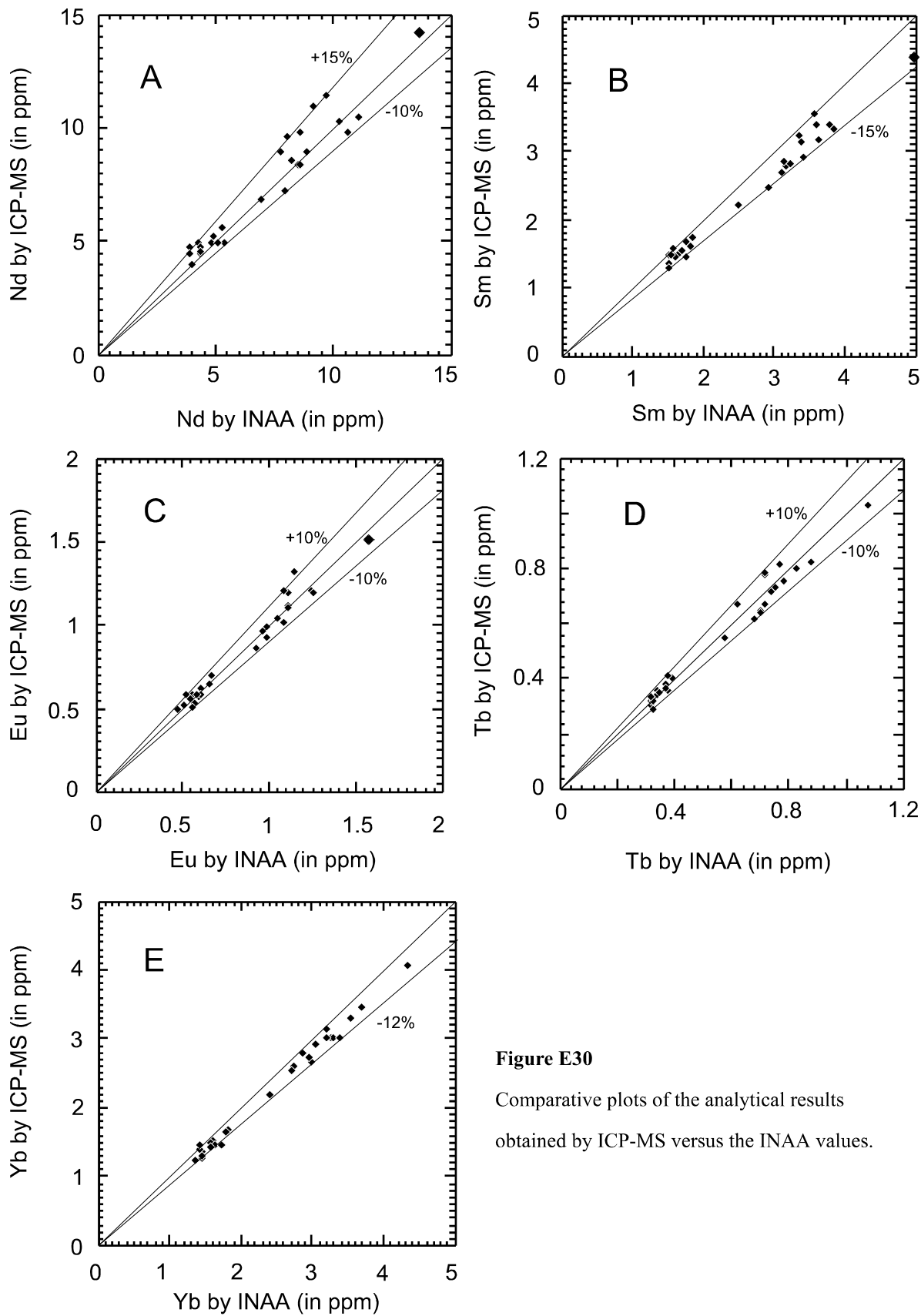


Figure E30

Comparative plots of the analytical results obtained by ICP-MS versus the INAA values.

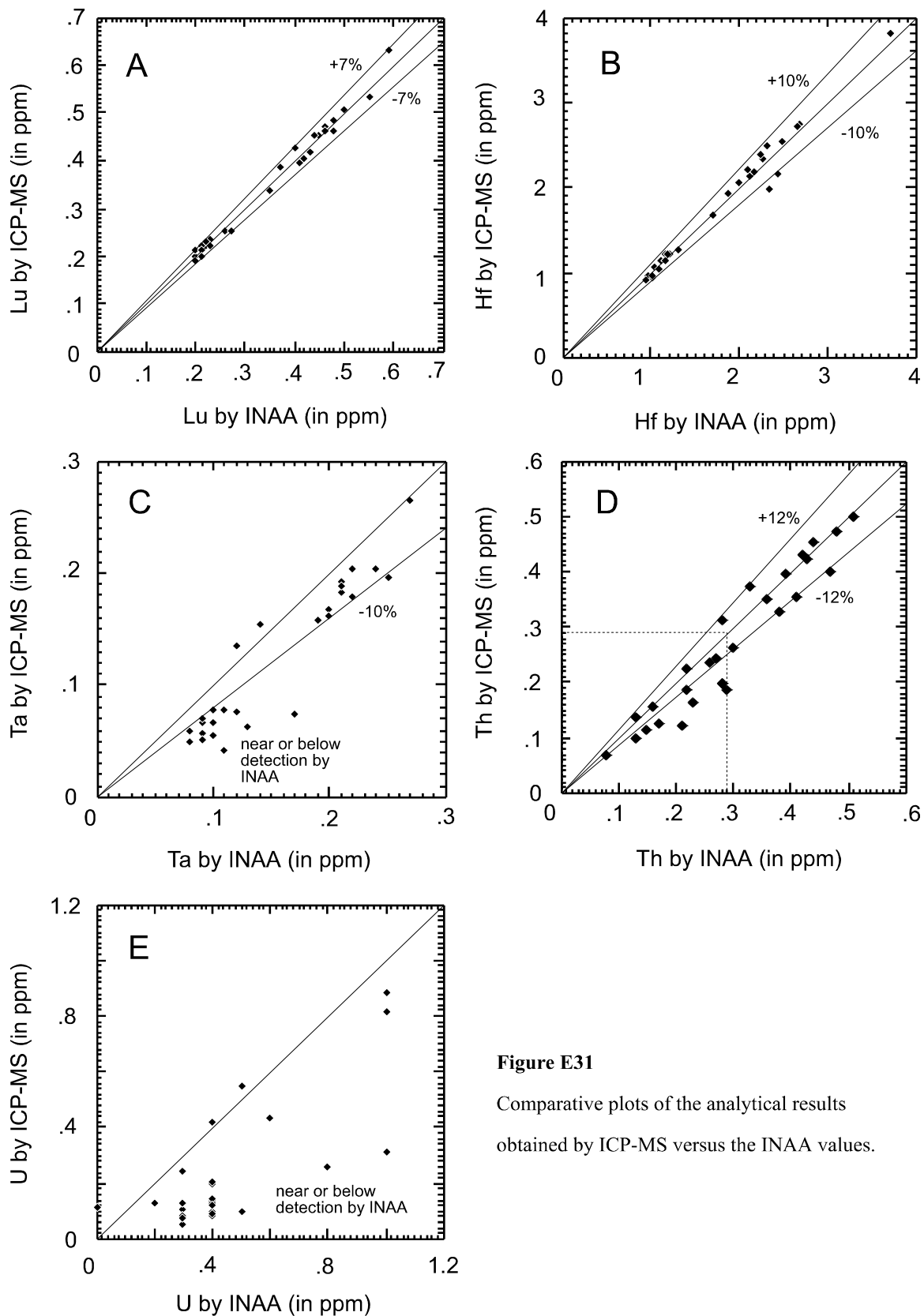


Figure E31

Comparative plots of the analytical results obtained by ICP-MS versus the INAA values.

APPENDIX F

**ANALYTICAL DATA OBTAINED BY ICP-MS AT THE UNION COLLEGE
GEOLOGY DEPARTMENT, SCHENECTADY, NY (WILD ROGUE
WILDERNESS, SNOW CAMP MOUNTAIN, BLACK MOUNTAIN AND
LLANADA)**

Table F1: Metagabbro unit**Sample:** O/C-373a O/C-373b O/C-373b OC-374b MRH-23 MRH-78/1 MRH-78/2

| | [3],[4]* 2 | R.C. 1 | [3],[4]* 2 | [2] 2 | [2] 2 | [3],[4]* 2 | [3],[4]* 2 |
|----|---------------|-----------|---------------|----------|----------|---------------|---------------|
| V | 373 | - | 333 | 247 | 343 | 372 | 285 |
| Cr | 29 | - | 46 | 9 | 75 | 27 | 37 |
| Rb | 1.83 | 1.90 | 1.61 | 2.51 | 1.51 | 3.58 | 3.11 |
| Sr | 448 | 449 | 454 | 436 | 386 | 476 | 510 |
| Y | 24.4 | 24.1 | 22.3 | 10.9 | 18.6 | 19.5 | 20.3 |
| Zr | 23.2 | 21.0 | 21.7 | 14.1 | 18.4 | 24.4 | 19.0 |
| Nb | 0.37 | 0.40 | 0.40 | 0.22 | 0.28 | 0.45 | 0.42 |
| Cs | 0.33 | 0.33 | 0.32 | 0.41 | 0.20 | 0.76 | 0.41 |
| Ba | 31.3 | 34.0 | 29.3 | 42.9 | 29.5 | 46.6 | 55.2 |
| La | 2.55 | 3.26 | 3.00 | 1.61 | 1.92 | 3.57 | 3.80 |
| Ce | 9.98 | 10.84 | 11.06 | 5.38 | 7.63 | 11.91 | 12.3 |
| Pr | 2.15 | 2.16 | 2.27 | 1.04 | 1.63 | 2.24 | 2.30 |
| Nd | 13.4 | 12.8 | 13.5 | 6.00 | 9.75 | 12.4 | 12.9 |
| Sm | 4.10 | 4.27 | 4.08 | 1.77 | 2.96 | 3.50 | 3.67 |
| Eu | 1.31 | 1.40 | 1.29 | 0.66 | 1.11 | 1.20 | 1.18 |
| Gd | 4.69 | 4.52 | 4.50 | 1.88 | 3.11 | 3.74 | 4.07 |
| Tb | 0.74 | 0.74 | 0.68 | 0.30 | 0.49 | 0.58 | 0.62 |
| Dy | 4.54 | 4.60 | 4.15 | 1.89 | 3.14 | 3.53 | 3.80 |
| Ho | 0.88 | 0.94 | 0.81 | 0.39 | 0.66 | 0.70 | 0.73 |
| Er | 2.64 | 2.57 | 2.43 | 1.14 | 1.95 | 2.05 | 2.20 |
| Tm | 0.42 | 0.37 | 0.38 | 0.18 | 0.30 | 0.32 | 0.34 |
| Yb | 2.44 | 2.35 | 2.30 | 1.14 | 1.90 | 1.96 | 2.05 |
| Lu | 0.35 | 0.37 | 0.34 | 0.18 | 0.29 | 0.28 | 0.30 |
| Hf | 0.893 | 1.00 | 0.843 | 0.55 | 0.77 | 0.90 | 0.73 |
| Ta | 0.013 | 0.020 | 0.014 | 0.017 | 0.020 | 0.014 | 0.016 |
| Pb | 0.500 | 0.64 | 0.459 | 0.51 | 0.18 | 0.51 | 0.57 |
| Th | 0.025 | 0.140 | 0.043 | 0.024 | 0.020 | 0.039 | 0.062 |
| U | 0.017 | 0.040 | 0.019 | 0.016 | 0.011 | 0.022 | 0.032 |

[2] ... 2nd analytical run

[3] ... 3rd analytical run

[4]*... 4th analytical run; *only Ta data used, replacing Ta values of 3rd analytical run

R.C. ... analyzed at Washington State University, courtesy of Richard Conrey (1998)

Table F2: Metatonalite unit

| Sample: | OC-11- S16b | OC-368f |
|------------|----------------|----------|
| Reference: | [2] 2 | [2] 2 |
| V | 177 | 210 |
| Cr | 9 | 32 |
| Rb | 0.42 | 1.08 |
| Sr | 380 | 286 |
| Y | 23.6 | 26.4 |
| Zr | 61.6 | 38.8 |
| Nb | 2.34 | 1.69 |
| Cs | 0.04 | 0.05 |
| Ba | 46.0 | 86.2 |
| La | 17.1 | 8.99 |
| Ce | 37.2 | 24.0 |
| Pr | 4.76 | 3.43 |
| Nd | 19.9 | 15.5 |
| Sm | 4.46 | 3.90 |
| Eu | 1.07 | 0.94 |
| Gd | 4.48 | 4.22 |
| Tb | 0.68 | 0.68 |
| Dy | 4.10 | 4.48 |
| Ho | 0.82 | 0.94 |
| Er | 2.35 | 2.78 |
| Tm | 0.35 | 0.43 |
| Yb | 2.29 | 2.75 |
| Lu | 0.35 | 0.42 |
| Hf | 1.88 | 1.37 |
| Ta | 0.13 | 0.082 |
| Pb | 0.64 | 0.40 |
| Th | 2.48 | 1.25 |
| U | 0.55 | 0.30 |

[2] 2nd analytical run

2 ... number of digestions (equals number of analyses)

Table F3: Sheeted dike complex

| Sample: | OC-1-S1 | OC-1-S2 | OC-4-S3 | OC-5-S4 | OC-6-S5 | OC-58 | O/C-325 |
|------------|---------------|---------------|----------|-------------------|---------------|---------------------|----------------|
| Reference: | {2}, [2] 4 | {2}, [2] 4 | [2] 2 | {2}, [1] 4 (6) | {2}, [2] 4 | {2}, [1,2] 4 (5) | [3], [4]* 2 |
| V | 270 | 376 | 258 | 200 | 260 | 233 | 200 |
| Cr | 204 | 14 | 326 | 54 | 190 | 73 | 1125 |
| Rb | 0.37 | 3.08 | 9.11 | 0.13 | 0.92 | 3.92 | 0.20 |
| Sr | 181 | 253 | 282 | 73 | 279 | 197 | 113 |
| Y | 21.3 | 23.3 | 18.7 | 19.9 | 12.8 | 17.1 | 15.0 |
| Zr | 72.8 | 50.7 | 61.5 | 43.9 | 46.8 | 43.7 | 49.5 |
| Nb | 2.77 | 1.72 | 1.66 | 1.25 | 1.22 | 1.84 | 1.02 |
| Cs | 0.12 | 0.27 | 0.36 | 0.03 | 0.05 | 0.24 | 0.08 |
| Ba | 37.2 | 86.2 | 155.5 | 20.5 | 85.2 | 51.8 | 10.7 |
| La | 3.45 | 5.51 | 5.90 | 1.82 | 7.80 | 4.05 | 5.63 |
| Ce | 8.61 | 14.82 | 12.48 | 4.80 | 14.70 | 9.73 | 11.79 |
| Pr | 1.33 | 2.30 | 1.78 | 0.79 | 1.86 | 1.49 | 1.72 |
| Nd | 6.91 | 11.20 | 8.32 | 4.27 | 7.94 | 7.43 | 7.54 |
| Sm | 2.19 | 2.93 | 2.31 | 1.52 | 1.90 | 2.17 | 2.07 |
| Eu | 0.73 | 1.28 | 0.68 | 0.58 | 0.79 | 0.87 | 0.63 |
| Gd | 2.89 | 3.50 | 2.73 | 2.31 | 2.12 | 2.71 | 2.33 |
| Tb | 0.52 | 0.60 | 0.46 | 0.47 | 0.35 | 0.47 | 0.38 |
| Dy | 3.42 | 3.82 | 3.01 | 3.34 | 2.17 | 3.06 | 2.43 |
| Ho | 0.73 | 0.82 | 0.63 | 0.75 | 0.46 | 0.64 | 0.52 |
| Er | 2.08 | 2.36 | 1.85 | 2.24 | 1.32 | 1.82 | 1.56 |
| Tm | 0.32 | 0.36 | 0.29 | 0.35 | 0.21 | 0.28 | 0.24 |
| Yb | 2.11 | 2.35 | 1.91 | 2.23 | 1.38 | 1.80 | 1.52 |
| Lu | 0.32 | 0.36 | 0.29 | 0.34 | 0.22 | 0.28 | 0.23 |
| Hf | 1.86 | 1.57 | 1.81 | 1.42 | 1.51 | 1.26 | 1.37 |
| Ta | 0.18 | 0.10 | 0.10 | 0.079 | 0.088 | 0.13 | 0.063 |
| Pb | 0.42 | 0.58 | 0.54 | 0.33 | 0.71 | 0.12 | 0.85 |
| Th | 0.29 | 0.61 | 1.06 | 0.32 | 1.39 | 0.32 | 0.83 |
| U | 0.12 | 0.37 | 0.40 | 0.12 | 0.39 | 0.12 | 0.31 |

{2} 2nd test run (Ta and Nb values not used!)

[1] ... 1st analytical run

[2] 2nd analytical run

[3] ... 3rd analytical run

[4]*... 4th analytical run; *only Ta data used which Ta values of 3rd analytical run

2, 4 ... total number of digestions per sample (usually equal to number of analyses)

e.g., {2}, [1]: average of data from second test run (n=2) and first analytical run (n=2)

(6), (5) ... total number of analyses per sample when larger than number of digestions

Table F3 (continued)

| Sample: | OC-333 | OC-356 | OC-357b | OC-362 | MRH-45a | MRH-45b | MRH-111 |
|------------|----------|----------|----------|----------|---------------|-------------------|---------------|
| Reference: | [2] 2 | [2] 2 | [2] 2 | [2] 2 | {2}, [2] 4 | {2}, [1] 4 (6) | {2}, [1] 4 |
| V | 200 | 251 | 186 | 231 | 241 | 269 | 194 |
| Cr | 260 | 185 | 79 | 69 | 278 | 84 | 35 |
| Rb | 1.34 | 3.00 | 1.92 | 1.98 | 6.49 | 5.00 | 0.34 |
| Sr | 146 | 179 | 202 | 310 | 256 | 347 | 252 |
| Y | 16.9 | 22.2 | 13.8 | 17.9 | 13.4 | 21.4 | 19.1 |
| Zr | 34.8 | 64.9 | 32.5 | 55.8 | 47.8 | 68.7 | 34.9 |
| Nb | 1.73 | 3.07 | 0.93 | 1.43 | 1.32 | 1.99 | 0.73 |
| Cs | 0.10 | 0.25 | 0.29 | 0.11 | 0.21 | 0.14 | 0.06 |
| Ba | 37.8 | 92.5 | 85.2 | 77.5 | 96.3 | 93.1 | 20.2 |
| La | 2.39 | 3.32 | 2.39 | 8.05 | 6.26 | 19.10 | 3.90 |
| Ce | 6.36 | 9.30 | 4.99 | 17.81 | 12.23 | 37.27 | 9.42 |
| Pr | 1.02 | 1.44 | 0.73 | 2.56 | 1.62 | 4.98 | 1.56 |
| Nd | 5.22 | 7.48 | 3.65 | 11.85 | 7.45 | 22.37 | 8.39 |
| Sm | 1.68 | 2.37 | 1.27 | 2.98 | 1.86 | 5.21 | 2.58 |
| Eu | 0.65 | 0.91 | 0.45 | 1.00 | 0.57 | 1.80 | 0.87 |
| Gd | 2.32 | 3.11 | 1.78 | 3.14 | 2.10 | 4.87 | 3.17 |
| Tb | 0.42 | 0.57 | 0.32 | 0.49 | 0.35 | 0.69 | 0.52 |
| Dy | 2.74 | 3.68 | 2.18 | 2.99 | 2.22 | 3.92 | 3.32 |
| Ho | 0.57 | 0.78 | 0.46 | 0.61 | 0.47 | 0.77 | 0.71 |
| Er | 1.68 | 2.22 | 1.35 | 1.74 | 1.36 | 2.11 | 2.02 |
| Tm | 0.26 | 0.34 | 0.21 | 0.27 | 0.21 | 0.31 | 0.31 |
| Yb | 1.64 | 2.18 | 1.40 | 1.71 | 1.45 | 1.99 | 1.99 |
| Lu | 0.25 | 0.32 | 0.21 | 0.26 | 0.24 | 0.30 | 0.32 |
| Hf | 1.03 | 1.71 | 0.92 | 1.70 | 1.50 | 2.04 | 1.09 |
| Ta | 0.11 | 0.19 | 0.067 | 0.083 | 0.081 | 0.10 | 0.044 |
| Pb | 0.29 | 0.44 | 0.24 | 0.44 | 0.46 | 0.60 | 0.69 |
| Th | 0.18 | 0.22 | 0.25 | 1.53 | 0.99 | 2.19 | 0.53 |
| U | 0.09 | 0.08 | 0.14 | 0.60 | 0.27 | 0.68 | 0.18 |

Table F3 (continued)

Sample: O/C-358 O/C-360
Reference: [3], [4]* [3], [4]*
2 2

| | | |
|----|--------|--------|
| V | 191 | 156 |
| Cr | 291 | 157 |
| Rb | 3.71 | 1.38 |
| Sr | 188 | 274 |
| Y | 6.49 | 4.70 |
| Zr | 8.50 | 6.76 |
| Nb | 0.15 | 0.12 |
| Cs | 0.08 | 0.06 |
| Ba | 28.9 | 46.4 |
| La | 0.72 | 0.67 |
| Ce | 1.68 | 1.48 |
| Pr | 0.28 | 0.24 |
| Nd | 1.56 | 1.28 |
| Sm | 0.61 | 0.45 |
| Eu | 0.29 | 0.25 |
| Gd | 0.87 | 0.62 |
| Tb | 0.15 | 0.11 |
| Dy | 1.05 | 0.75 |
| Ho | 0.22 | 0.16 |
| Er | 0.66 | 0.48 |
| Tm | 0.10 | 0.08 |
| Yb | 0.63 | 0.47 |
| Lu | 0.090 | 0.070 |
| Hf | 0.27 | 0.18 |
| Ta | 0.0084 | 0.0070 |
| Pb | 0.45 | 0.54 |
| Th | 0.052 | 0.068 |
| U | 0.040 | 0.026 |

Table F4: Pillow unit

| Sample: | OC-113 | OC-186 | OC-224 | OC-227a | OC-227b | OC-379 | OC-380 |
|------------|----------|----------|----------|----------|----------|----------|----------|
| Reference: | {2}, [1] | {2}, [1] | {2}, [2] | {2}, [2] | {2}, [1] | {2}, [2] | {2}, [1] |
| | 4 | 4 | 4 | 4 | 4 | 4 | 4 |
| V | 277 | 375 | 387 | 263 | 428 | 312 | 167 |
| Cr | 53.5 | 18.0 | 42.5 | 27.0 | 32.5 | 9.7 | 8.0 |
| Rb | 3.87 | 0.74 | 0.84 | 5.38 | 3.98 | 0.20 | 0.19 |
| Sr | 163 | 87 | 161 | 179 | 169 | 58 | 61 |
| Y | 13.4 | 28.8 | 17.5 | 19.2 | 22.9 | 25.5 | 32.1 |
| Zr | 30.8 | 68.4 | 30.0 | 49.4 | 45.4 | 57.6 | 35.5 |
| Nb | 0.61 | 1.62 | 0.83 | 1.39 | 0.68 | 1.29 | 0.64 |
| Cs | 0.07 | 0.02 | 0.10 | 0.76 | 0.32 | 0.05 | 0.05 |
| Ba | 62.5 | 38.7 | 46.7 | 99.2 | 74.7 | 24.0 | 28.7 |
| La | 2.14 | 3.35 | 2.13 | 2.90 | 2.15 | 3.16 | 1.84 |
| Ce | 5.17 | 8.99 | 5.29 | 7.19 | 5.59 | 8.36 | 4.78 |
| Pr | 0.85 | 1.56 | 0.89 | 1.16 | 1.03 | 1.46 | 0.90 |
| Nd | 4.64 | 8.86 | 4.98 | 6.37 | 5.88 | 7.90 | 5.22 |
| Sm | 1.57 | 2.97 | 1.71 | 2.05 | 2.00 | 2.65 | 2.03 |
| Eu | 0.59 | 1.02 | 0.64 | 0.78 | 0.75 | 0.94 | 0.85 |
| Gd | 2.04 | 3.98 | 2.41 | 2.67 | 2.70 | 3.56 | 3.03 |
| Tb | 0.36 | 0.70 | 0.44 | 0.47 | 0.50 | 0.63 | 0.56 |
| Dy | 2.36 | 4.76 | 2.92 | 3.11 | 3.41 | 4.20 | 3.85 |
| Ho | 0.51 | 1.03 | 0.64 | 0.66 | 0.74 | 0.92 | 0.85 |
| Er | 1.51 | 3.03 | 1.87 | 1.97 | 2.16 | 2.63 | 2.45 |
| Tm | 0.23 | 0.46 | 0.30 | 0.30 | 0.33 | 0.41 | 0.39 |
| Yb | 1.58 | 3.00 | 1.98 | 2.06 | 2.21 | 2.63 | 2.55 |
| Lu | 0.25 | 0.48 | 0.31 | 0.32 | 0.37 | 0.42 | 0.42 |
| Hf | 0.99 | 2.09 | 1.02 | 1.39 | 1.40 | 1.79 | 1.25 |
| Ta | 0.037 | 0.092 | 0.063 | 0.096 | 0.037 | 0.087 | 0.038 |
| Pb | 2.29 | 1.06 | 0.52 | 0.90 | 1.13 | 1.46 | 0.91 |
| Th | 0.33 | 0.38 | 0.32 | 0.32 | 0.30 | 0.34 | 0.21 |
| U | 0.14 | 0.16 | 0.14 | 0.14 | 0.12 | 0.16 | 0.11 |

{2} 2nd test run (Ta and Nb values are not used!)

[1] ... 1st analytical run

[2] 2nd analytical run

4 ... number of digestions per sample (equals number of analyses)

e.g., {2}, [1]: average of data from second test run (n=2) and first analytical run (n=2)

Table F4 (continued)

Sample: PB-1 O/C-231
Reference: {2}, [2]
4

| | |
|----|-------|
| V | 314 |
| Cr | 19.9 |
| Rb | 0.42 |
| Sr | 61 |
| Y | 21.0 |
| Zr | 40.4 |
| Nb | 0.69 |
| Cs | 0.02 |
| Ba | 22.6 |
| La | 1.93 |
| Ce | 5.30 |
| Pr | 0.96 |
| Nd | 5.47 |
| Sm | 1.92 |
| Eu | 0.63 |
| Gd | 2.73 |
| Tb | 0.49 |
| Dy | 3.33 |
| Ho | 0.74 |
| Er | 2.14 |
| Tm | 0.34 |
| Yb | 2.26 |
| Lu | 0.36 |
| Hf | 1.34 |
| Ta | 0.060 |
| Pb | 0.47 |
| Th | 0.25 |
| U | 0.15 |

Table F5: Mule Mountain volcanics

| Sample: | OC-80 | OC-81a | OC-81b | OC-82 | OC-88 | GDH-96-7 | GDH-96-8 |
|------------|----------|----------|----------|----------|----------|---------------|---------------|
| Reference: | [2] 2 | [2] 2 | [2] 2 | [2] 2 | [2] 2 | [3],[4]* 2 | [3],[4]* 2 |
| V | 130 | 239 | 238 | 328 | 363 | 232 | 281 |
| Cr | 7 | 381 | 515 | 33 | 94 | 49 | 75 |
| Rb | 9.59 | 6.72 | 7.13 | 6.17 | 0.18 | 2.66 | 4.44 |
| Sr | 134 | 150 | 148 | 228 | 233 | 220 | 194 |
| Y | 17.9 | 12.9 | 12.5 | 19.8 | 23.1 | 19.9 | 17.8 |
| Zr | 73.7 | 25.1 | 23.1 | 40.6 | 47.9 | 38.2 | 35.6 |
| Nb | 1.57 | 0.39 | 0.37 | 0.76 | 0.72 | 0.69 | 0.72 |
| Cs | 0.12 | 0.34 | 0.36 | 0.34 | 0.04 | 0.25 | 0.32 |
| Ba | 608 | 140 | 137 | 103 | 17 | 52 | 90 |
| La | 3.67 | 1.29 | 1.28 | 2.63 | 2.33 | 2.97 | 3.02 |
| Ce | 8.51 | 3.37 | 3.27 | 6.58 | 6.48 | 6.69 | 7.09 |
| Pr | 1.30 | 0.59 | 0.57 | 1.07 | 1.15 | 1.16 | 1.17 |
| Nd | 6.37 | 3.21 | 3.17 | 5.86 | 6.48 | 5.62 | 5.76 |
| Sm | 2.01 | 1.18 | 1.11 | 2.01 | 2.29 | 1.88 | 1.86 |
| Eu | 0.56 | 0.48 | 0.45 | 0.68 | 0.85 | 0.64 | 0.67 |
| Gd | 2.56 | 1.64 | 1.59 | 2.65 | 3.11 | 2.65 | 2.44 |
| Tb | 0.44 | 0.30 | 0.29 | 0.46 | 0.56 | 0.47 | 0.43 |
| Dy | 2.95 | 2.09 | 1.99 | 3.18 | 3.77 | 3.16 | 2.90 |
| Ho | 0.62 | 0.45 | 0.43 | 0.70 | 0.81 | 0.68 | 0.65 |
| Er | 1.87 | 1.33 | 1.27 | 2.09 | 2.36 | 2.04 | 1.98 |
| Tm | 0.30 | 0.21 | 0.20 | 0.33 | 0.37 | 0.32 | 0.32 |
| Yb | 1.97 | 1.40 | 1.34 | 2.15 | 2.41 | 2.02 | 1.99 |
| Lu | 0.32 | 0.22 | 0.21 | 0.33 | 0.37 | 0.30 | 0.31 |
| Hf | 2.25 | 0.76 | 0.71 | 1.34 | 1.51 | 1.19 | 1.15 |
| Ta | 0.097 | 0.033 | 0.035 | 0.051 | 0.053 | 0.041 | 0.041 |
| Pb | 1.19 | 0.99 | 1.05 | 1.78 | 1.06 | 2.93 | 2.87 |
| Th | 0.69 | 0.20 | 0.19 | 0.39 | 0.30 | 0.38 | 0.42 |
| U | 0.32 | 0.10 | 0.08 | 0.19 | 0.12 | 0.17 | 0.35 |

[2] 2nd analytical run

[3] 3rd analytical run

[4] ... 4th analytical run; * only Ta data used which replace Ta values of 3rd analytical run

2 ... number of digestions per sample (equals number of analyses)

Table F5 (continued)

| Sample: | OC-147 | OC-217 |
|------------|--------|--------|
| Reference: | [2] | [2] |
| | 2 | 2 |
| V | 26 | 31 |
| Cr | 14 | 11 |
| Rb | 0.25 | 0.79 |
| Sr | 75 | 59 |
| Y | 44.6 | 41.0 |
| Zr | 111.8 | 112.8 |
| Nb | 2.18 | 2.14 |
| Cs | 0.02 | 0.04 |
| Ba | 96 | 321 |
| La | 5.59 | 4.99 |
| Ce | 14.93 | 13.57 |
| Pr | 2.53 | 2.33 |
| Nd | 13.65 | 12.68 |
| Sm | 4.57 | 4.18 |
| Eu | 1.39 | 1.21 |
| Gd | 6.04 | 5.38 |
| Tb | 1.06 | 0.94 |
| Dy | 7.01 | 6.49 |
| Ho | 1.49 | 1.43 |
| Er | 4.42 | 4.31 |
| Tm | 0.70 | 0.67 |
| Yb | 4.46 | 4.29 |
| Lu | 0.67 | 0.66 |
| Hf | 3.59 | 3.58 |
| Ta | 0.14 | 0.14 |
| Pb | 1.18 | 2.87 |
| Th | 0.75 | 0.72 |
| U | 0.31 | 0.39 |

Table F6: Half Moon Bar Gabbro (diabasic dikes)

| Sample: | OC-174b | OC-375c | OC-375d |
|---------|---------|---------|---------|
| Run: | [2] | [2] | [2] |
| | 2 | 2 | 2 |
| V | 242.7 | 235 | 256 |
| Cr | 44.0 | 18.5 | 18.1 |
| Rb | 5.19 | 2.94 | 2.88 |
| Sr | 357.9 | 370 | 410 |
| Y | 16.9 | 18.6 | 17.4 |
| Zr | 51 | 56.8 | 50.3 |
| Nb | 1.45 | 1.67 | 1.45 |
| Cs | 0.528 | 0.665 | 0.66 |
| Ba | 216 | 157.7 | 188 |
| La | 5.47 | 6.10 | 5.21 |
| Ce | 11.9 | 13.30 | 11.8 |
| Pr | 1.75 | 1.95 | 1.76 |
| Nd | 8.2 | 8.97 | 8.20 |
| Sm | 2.20 | 2.35 | 2.16 |
| Eu | 0.70 | 0.68 | 0.65 |
| Gd | 2.36 | 2.58 | 2.42 |
| Tb | 0.40 | 0.43 | 0.42 |
| Dy | 2.70 | 2.95 | 2.79 |
| Ho | 0.59 | 0.64 | 0.60 |
| Er | 1.75 | 1.89 | 1.81 |
| Tm | 0.27 | 0.30 | 0.28 |
| Yb | 1.81 | 1.97 | 1.86 |
| Lu | 0.28 | 0.31 | 0.30 |
| Hf | 1.55 | 1.74 | 1.55 |
| Ta | 0.08 | 0.094 | 0.083 |
| Pb | 0.53 | 0.68 | 0.75 |
| Th | 1.06 | 1.22 | 1.01 |
| U | 0.39 | 0.44 | 0.29 |

[2] 2nd analytical run

Table F7: Snow Camp Mountain area

| Sample: | SM-96-2a | SM-96-2b.1 | SM-96-2c.1 | SM-96-2c.2 | SM-96-2d.1 | SM-96-3b | SM-96-3d |
|------------|----------------|------------|----------------|----------------|----------------|----------------|----------|
| Reference: | [3], [4]* 2 | [3] 2 | [3], [4]* 2 | [3], [4]* 2 | [3], [4]* 2 | [3], [4]* 2 | [3] 2 |
| V | 232 | 237 | 225 | 245 | 203 | 226 | 257 |
| Cr | 119 | 145 | 91 | 393 | 282 | 140 | 365 |
| Rb | 5.81 | 6.27 | 3.36 | 8.29 | 4.07 | 1.75 | 12.76 |
| Sr | 154 | 381 | 295 | 316 | 276 | 217 | 444 |
| Y | 14.2 | 21.6 | 15.9 | 15.6 | 15.2 | 21.5 | 23.1 |
| Zr | 33.2 | 65.9 | 38.4 | 41.0 | 42.0 | 70.8 | 60.8 |
| Nb | 0.83 | 2.03 | 0.84 | 0.97 | 1.35 | 1.82 | 2.51 |
| Cs | 0.10 | 0.31 | 0.30 | 0.61 | 0.55 | 0.13 | 2.49 |
| Ba | 127 | 369 | 553 | 893 | 723 | 61.2 | 257 |
| La | 2.43 | 3.79 | 2.61 | 4.22 | 1.79 | 3.78 | 3.70 |
| Ce | 6.16 | 10.0 | 6.04 | 10.1 | 5.04 | 9.52 | 10.1 |
| Pr | 0.98 | 1.58 | 0.98 | 1.62 | 0.84 | 1.54 | 1.68 |
| Nd | 4.98 | 8.05 | 4.74 | 8.11 | 4.54 | 7.53 | 8.32 |
| Sm | 1.57 | 2.48 | 1.59 | 2.46 | 1.58 | 2.36 | 2.69 |
| Eu | 0.51 | 0.82 | 0.60 | 0.85 | 0.51 | 0.73 | 0.99 |
| Gd | 1.98 | 3.08 | 2.07 | 2.75 | 1.99 | 2.99 | 3.49 |
| Tb | 0.34 | 0.54 | 0.37 | 0.43 | 0.36 | 0.51 | 0.60 |
| Dy | 2.26 | 3.46 | 2.47 | 2.64 | 2.38 | 3.36 | 3.94 |
| Ho | 0.49 | 0.74 | 0.54 | 0.54 | 0.51 | 0.72 | 0.82 |
| Er | 1.46 | 2.19 | 1.62 | 1.52 | 1.54 | 2.16 | 2.41 |
| Tm | 0.23 | 0.35 | 0.26 | 0.24 | 0.25 | 0.34 | 0.37 |
| Yb | 1.46 | 2.19 | 1.63 | 1.49 | 1.52 | 2.13 | 2.21 |
| Lu | 0.21 | 0.32 | 0.25 | 0.22 | 0.22 | 0.32 | 0.33 |
| Hf | 0.98 | 1.79 | 1.12 | 1.16 | 1.22 | 1.87 | 1.55 |
| Ta | 0.044 | 0.10 | 0.051 | 0.059 | 0.088 | 0.11 | 0.16 |
| Pb | 2.61 | 2.87 | 1.63 | 2.21 | 0.45 | 1.12 | 1.13 |
| Th | 0.28 | 0.41 | 0.29 | 0.46 | 0.29 | 0.43 | 0.24 |
| U | 0.11 | 0.17 | 0.15 | 0.17 | 0.11 | 0.19 | 0.085 |

Table F7 (continued)

| Sample: | SM-96-5a.1 | SM-96-8b | SM-96-10b | SM-96-10c | SM-96-10d | SM-96-11 | SM-96-12a |
|------------|------------|----------|-----------|-----------|-----------|----------|-----------|
| Reference: | [3], [4]* | [3] | [3], [4]* | [3] | [3] | [3] | [3], [4]* |
| | 2 | 2 | 2 | 2 | 2 | 2 | 2 |
| V | 237 | 162 | 473 | 399 | 375 | 333 | 136 |
| Cr | 83 | 13 | 28 | 11 | 15 | 24 | 432 |
| Rb | 7.26 | 23.61 | 1.00 | 0.57 | 0.20 | 7.26 | 19.17 |
| Sr | 537 | 515 | 293 | 93 | 117 | 329 | 319 |
| Y | 15.6 | 20.8 | 24.3 | 31.1 | 35.8 | 22.3 | 8.7 |
| Zr | 39.4 | 95.8 | 65.7 | 84.1 | 110 | 83.8 | 34.1 |
| Nb | 1.11 | 19.0 | 1.86 | 2.45 | 3.29 | 3.48 | 0.77 |
| Cs | 1.93 | 0.55 | 0.12 | 0.31 | 0.12 | 7.36 | 0.92 |
| Ba | 212 | 463 | 266 | 151 | 105 | 166 | 712 |
| La | 3.20 | 18.81 | 5.40 | 4.03 | 3.60 | 10.74 | 4.49 |
| Ce | 7.64 | 40.4 | 12.0 | 11.8 | 10.8 | 24.6 | 9.12 |
| Pr | 1.23 | 5.66 | 1.83 | 1.99 | 1.84 | 3.44 | 1.12 |
| Nd | 6.28 | 23.8 | 9.02 | 10.34 | 9.95 | 15.5 | 5.23 |
| Sm | 1.98 | 5.39 | 2.77 | 3.34 | 3.49 | 3.72 | 1.52 |
| Eu | 0.62 | 1.62 | 1.00 | 1.05 | 1.22 | 1.08 | 0.54 |
| Gd | 2.38 | 5.09 | 3.47 | 4.28 | 4.74 | 3.78 | 1.56 |
| Tb | 0.40 | 0.75 | 0.60 | 0.77 | 0.86 | 0.59 | 0.25 |
| Dy | 2.52 | 4.15 | 3.97 | 5.04 | 5.74 | 3.69 | 1.53 |
| Ho | 0.53 | 0.78 | 0.84 | 1.08 | 1.21 | 0.76 | 0.31 |
| Er | 1.55 | 2.08 | 2.53 | 3.25 | 3.61 | 2.24 | 0.91 |
| Tm | 0.25 | 0.30 | 0.40 | 0.51 | 0.57 | 0.36 | 0.14 |
| Yb | 1.56 | 1.74 | 2.50 | 3.11 | 3.54 | 2.24 | 0.88 |
| Lu | 0.23 | 0.25 | 0.36 | 0.44 | 0.50 | 0.33 | 0.13 |
| Hf | 1.20 | 2.87 | 2.00 | 2.40 | 2.89 | 2.38 | 0.90 |
| Ta | 0.066 | 1.14 | 0.10 | 0.14 | 0.20 | 0.18 | 0.046 |
| Pb | 1.31 | 4.92 | 2.82 | 1.48 | 1.72 | 0.84 | 2.07 |
| Th | 0.46 | 1.78 | 0.59 | 0.37 | 0.29 | 1.74 | 0.48 |
| U | 0.18 | 0.62 | 0.32 | 0.13 | 0.21 | 0.61 | 0.074 |

Table F7 (continued)

| Sample: | SM-96- 12d | SM-96- 12e | SM-96- 13a | SM-96- 13b | SM-96- 13c |
|------------|----------------|----------------|---------------|---------------|---------------|
| Reference: | [3], [4]* 2 | [3], [4]* 2 | [3] 2 | [3] 2 | [3] 2 |
| V | 186 | 218 | 313 | 402 | 348 |
| Cr | 45 | 399 | 58 | 12 | 6 |
| Rb | 2.05 | 1.27 | 1.12 | 6.14 | 0.46 |
| Sr | 133 | 95 | 79 | 72 | 55 |
| Y | 20.5 | 14.8 | 30.2 | 23.2 | 23.2 |
| Zr | 57.3 | 36.9 | 77.5 | 63.2 | 69.6 |
| Nb | 1.59 | 0.70 | 2.11 | 1.80 | 1.96 |
| Cs | 0.11 | 0.04 | 0.12 | 0.65 | 0.17 |
| Ba | 62.4 | 41.2 | 88.7 | 136 | 136 |
| La | 2.86 | 5.54 | 5.03 | 3.67 | 2.60 |
| Ce | 7.44 | 9.04 | 12.7 | 9.55 | 7.11 |
| Pr | 1.19 | 1.66 | 2.06 | 1.61 | 1.31 |
| Nd | 5.91 | 7.97 | 10.4 | 8.06 | 7.01 |
| Sm | 1.90 | 2.13 | 3.25 | 2.64 | 2.43 |
| Eu | 0.51 | 0.69 | 1.01 | 0.90 | 0.76 |
| Gd | 2.57 | 2.61 | 4.12 | 3.54 | 3.12 |
| Tb | 0.47 | 0.41 | 0.70 | 0.61 | 0.57 |
| Dy | 3.20 | 2.59 | 4.57 | 4.00 | 3.78 |
| Ho | 0.69 | 0.54 | 0.99 | 0.86 | 0.80 |
| Er | 2.10 | 1.55 | 2.89 | 2.58 | 2.33 |
| Tm | 0.34 | 0.23 | 0.45 | 0.41 | 0.37 |
| Yb | 2.12 | 1.38 | 2.76 | 2.47 | 2.26 |
| Lu | 0.31 | 0.20 | 0.41 | 0.38 | 0.32 |
| Hf | 1.55 | 1.08 | 2.17 | 1.90 | 1.95 |
| Ta | 0.091 | 0.040 | 0.13 | 0.10 | 0.12 |
| Pb | 0.48 | 1.27 | 1.07 | 1.60 | 1.17 |
| Th | 0.37 | 0.42 | 0.59 | 0.50 | 0.50 |
| U | 0.14 | 0.083 | 0.31 | 0.26 | 0.28 |

Table F8: Analytical data by ICP-MS, XRF and INAA, Black Mountain

| Sample: | BM91-11C | | BM91-12A | | BM91-14 | |
|------------|----------|------|----------|------|---------|------|
| Reference: | [5] | {1} | [5] | {1} | [5] | {1} |
| Ba | 226 | 249 | 77.7 | 61 | 448 | 404 |
| Ni | - | 24 | - | 63 | - | 55 |
| Sr | 178 | 178 | 139 | 125 | 166 | 153 |
| V | 328 | 317 | 268 | 286 | 230 | 268 |
| Y | 34.0 | 35 | 40.8 | 37 | 32.7 | 29 |
| Zr | 99.1 | 95 | 103 | 89 | 83.1 | 68 |
| Nb | 3.31 | 5 | 3.50 | 5 | 2.52 | 5 |
| Sc | - | 35.6 | - | 38.8 | - | 38.5 |
| Cr | 39.1 | 25.5 | 131 | 125 | 154 | 146 |
| Co | - | 38.1 | - | 38.2 | - | 39.0 |
| Zn | - | 84.4 | - | 85.2 | - | 85.9 |
| Cu | - | 40.0 | - | 32.0 | - | 67 |
| Rb | 3.84 | 5 | 1.77 | 5 | 4.72 | 6 |
| Cs | 0.10 | 0.26 | 0.04 | 0.24 | 0.19 | 0.23 |
| La | 4.31 | 4.57 | 3.84 | 3.99 | 4.16 | 4.15 |
| Ce | 11.8 | 12.4 | 11.9 | 11.7 | 11.8 | 10.9 |
| Pr | 1.99 | - | 2.18 | - | 2.08 | - |
| Nd | 10.6 | 10.2 | 10.4 | 10.6 | 9.29 | 8.54 |
| Sm | 3.51 | 3.77 | 3.86 | 3.84 | 3.35 | 3.16 |
| Eu | 1.25 | 1.24 | 1.27 | 1.26 | 1.11 | 1.08 |
| Gd | 4.78 | - | 5.68 | - | 4.71 | - |
| Tb | 0.85 | 0.83 | 1.01 | 0.88 | 0.85 | 0.70 |
| Dy | 5.54 | - | 6.79 | - | 5.67 | - |
| Ho | 1.16 | - | 1.31 | - | 1.07 | - |
| Er | 3.35 | - | 3.89 | - | 3.13 | - |
| Tm | 0.52 | - | 0.59 | - | 0.47 | - |
| Yb | 3.41 | 3.54 | 4.05 | 3.69 | 3.25 | 2.98 |
| Lu | 0.51 | 0.50 | 0.54 | 0.55 | 0.41 | 0.42 |
| Hf | 2.74 | 2.68 | 2.73 | 2.67 | 2.15 | 2.12 |
| Ta | 0.19 | 0.22 | 0.22 | 0.24 | 0.18 | 0.20 |
| Pb | 1.12 | - | 0.32 | - | 1.01 | - |
| Th | 0.34 | 0.41 | 0.22 | 0.27 | 0.29 | 0.28 |
| U | 0.12 | 0.40 | 0.10 | 0.30 | 0.12 | 0.40 |

[5] ... analysis by ICP-MS at Union College (fifth analytical run 11/11/97)

{1} ... analysis by XRF and INAA, Giaramita et al. (1998)

Table F8 (continued)

| Sample: | BM91-15 | | BM91-16 | | BM91-19 | |
|------------|---------|------|---------|------|---------|------|
| Reference: | [5] | {1} | [5] | {1} | [5] | {1} |
| Ba | 190 | 193 | 229 | 147 | 32.4 | 40 |
| Ni | - | 60 | - | 36 | - | 47 |
| Sr | 182 | 177 | 434 | 363 | 72.3 | 91 |
| V | 281 | 255 | 256 | 328 | 307 | 329 |
| Y | 26.1 | 29 | 35.9 | 30 | 28.3 | 33 |
| Zr | 73.8 | 73 | 84.0 | 98 | 79.9 | 82 |
| Nb | 2.57 | 5 | 3.44 | 5 | 2.68 | 5 |
| Sc | - | 38.7 | - | 38.4 | - | 28.0 |
| Cr | 146 | 140 | 65.1 | 66.6 | 37.9 | 30.5 |
| Co | - | 37.2 | - | 38.2 | - | 35.4 |
| Zn | - | 79.4 | - | 139 | - | 75.9 |
| Cu | - | 61 | - | 54 | - | 40 |
| Rb | 6.96 | 8 | 5.20 | 6 | 1.25 | 5 |
| Cs | 0.11 | 0.23 | 1.13 | 0.89 | 0.03 | 0.2 |
| La | 3.49 | 4.08 | 5.41 | 4.67 | 3.98 | 4.29 |
| Ce | 9.30 | 10.1 | 15.2 | 12.7 | 10.8 | 10.6 |
| Pr | 1.50 | - | 2.61 | - | 1.71 | - |
| Nd | 8.17 | 8.60 | 12.5 | 9.68 | 9.11 | 8.88 |
| Sm | 2.62 | 3.10 | 4.13 | 3.58 | 2.89 | 3.22 |
| Eu | 0.99 | 0.98 | 1.46 | 1.15 | 1.02 | 0.96 |
| Gd | 3.57 | - | 5.44 | - | 3.91 | - |
| Tb | 0.63 | 0.70 | 0.96 | 0.77 | 0.69 | 0.62 |
| Dy | 4.12 | - | 6.40 | - | 4.39 | - |
| Ho | 0.88 | - | 1.26 | - | 0.94 | - |
| Er | 2.55 | - | 3.53 | - | 2.73 | - |
| Tm | 0.39 | - | 0.52 | - | 0.43 | - |
| Yb | 2.59 | 2.75 | 3.31 | 3.27 | 2.82 | 2.87 |
| Lu | 0.40 | 0.41 | 0.46 | 0.45 | 0.43 | 0.40 |
| Hf | 2.04 | 2 | 2.18 | 2.43 | 2.21 | 2.09 |
| Ta | 0.14 | 0.14 | 0.19 | 0.25 | 0.14 | 0.19 |
| Pb | 0.63 | - | 0.27 | - | 0.61 | - |
| Th | 0.31 | 0.38 | 0.35 | 0.36 | 0.38 | 0.39 |
| U | 0.11 | 0.4 | 0.14 | 0.4 | 0.79 | 1.04 |

Table F8 (continued)

| Sample: | BM91-2 | | BM91-25 | | BM91-27 | |
|------------|--------|------|---------|------|---------|------|
| Reference: | [5] | {1} | [5] | {1} | [5] | {1} |
| Ba | 32.7 | 47 | 137 | 120 | 72.1 | 48 |
| Ni | - | 24 | - | 45 | - | 62 |
| Sr | 239 | 224 | 226 | 201 | 311 | 302 |
| V | 275 | 334 | 286 | 331 | 294 | 289 |
| Y | 34.0 | 34 | 36.7 | 34 | 27.1 | 28 |
| Zr | 97.4 | 93 | 89.0 | 82 | 69.6 | 72 |
| Nb | 3.01 | 9 | 3.11 | 5 | 2.21 | 5 |
| Sc | - | 32.2 | - | 36.7 | - | 42.6 |
| Cr | 36.88 | 26.3 | 75.13 | 66.6 | 208 | 203 |
| Co | - | 28.1 | - | 37.5 | - | 41.3 |
| Zn | - | 90.3 | - | 93.2 | - | 67.1 |
| Cu | - | 49 | - | 65 | - | 64 |
| Rb | 0.47 | 5 | 6.50 | 6 | 11.4 | 12.0 |
| Cs | 0.05 | 0.22 | 0.17 | 0.30 | 0.06 | 0.25 |
| La | 4.75 | 4.40 | 3.56 | 3.37 | 2.89 | 3.19 |
| Ce | 13.2 | 11.0 | 10.5 | 9.59 | 8.28 | 8.64 |
| Pr | 2.28 | - | 1.85 | - | 1.44 | - |
| Nd | 11.04 | 9.18 | 9.40 | 8.56 | 7.57 | 7.97 |
| Sm | 3.66 | 3.59 | 3.32 | 3.34 | 2.66 | 2.93 |
| Eu | 1.24 | 1.11 | 1.20 | 1.09 | 0.99 | 0.99 |
| Gd | 4.83 | - | 4.65 | - | 3.83 | - |
| Tb | 0.86 | 0.72 | 0.83 | 0.72 | 0.68 | 0.68 |
| Dy | 5.75 | - | 5.70 | - | 4.46 | - |
| Ho | 1.16 | - | 1.15 | - | 0.92 | - |
| Er | 3.30 | - | 3.33 | - | 2.67 | - |
| Tm | 0.50 | - | 0.51 | - | 0.41 | - |
| Yb | 3.22 | 3.29 | 3.30 | 3.21 | 2.72 | 2.70 |
| Lu | 0.47 | 0.46 | 0.49 | 0.48 | 0.39 | 0.37 |
| Hf | 2.52 | 2.49 | 2.32 | 2.27 | 1.95 | 1.87 |
| Ta | 0.17 | 0.21 | 0.17 | 0.22 | 0.12 | 0.12 |
| Pb | 0.39 | - | 1.35 | - | 0.30 | - |
| Th | 0.37 | 0.33 | 0.23 | 0.26 | 0.18 | 0.28 |
| U | 0.08 | 0.40 | 0.09 | 0.4 | 0.07 | 0.4 |

Table F8 (continued)

| Sample: | BM91-31 | | BM91-4 | | BM91-5 | |
|------------|---------|------|--------|-------|--------|------|
| Reference: | [5] | {1} | [5] | {1} | [5] | {1} |
| Ba | 36.6 | 40 | 33.8 | 40 | 77.3 | 63 |
| Ni | - | 54 | - | 31 | - | 38 |
| Sr | 178 | 153 | 74.0 | 71 | 195 | 187 |
| V | 295 | 300 | 415 | 386 | 278 | 285 |
| Y | 35.5 | 34 | 48.1 | 48 | 33.7 | 31 |
| Zr | 75.9 | 91 | 143 | 135 | 87.6 | 72 |
| Nb | 3.42 | 5 | 4.33 | 12 | 2.98 | 10 |
| Sc | - | 38.4 | - | 34.1 | - | 36.1 |
| Cr | 182 | 160 | 54.0 | 32.3 | 67.9 | 57.9 |
| Co | - | 36.3 | - | 36.6 | - | 35.7 |
| Zn | - | 34.7 | - | 111 | - | 81.6 |
| Cu | - | 39 | - | 47 | - | 52 |
| Rb | 1.92 | 5 | 2.05 | 5 | 9.37 | 11 |
| Cs | 0.02 | 0.26 | 0.06 | 0.22 | 0.11 | 0.23 |
| La | 3.11 | 3.49 | 5.53 | 6.13 | 3.48 | 3.52 |
| Ce | 9.69 | 9.75 | 15.3 | 16.2 | 10.5 | 9.64 |
| Pr | 1.75 | - | 2.66 | - | 1.87 | - |
| Nd | 9.02 | 8.06 | 12.9 | 13.63 | 9.35 | 8.23 |
| Sm | 3.20 | 3.37 | 4.39 | 4.98 | 3.40 | 3.43 |
| Eu | 1.01 | 1.05 | 1.44 | 1.58 | 1.20 | 1.11 |
| Gd | 4.52 | - | 6.11 | - | 4.86 | - |
| Tb | 0.81 | 0.78 | 1.09 | 1.08 | 0.88 | 0.75 |
| Dy | 5.56 | - | 7.47 | - | 5.82 | - |
| Ho | 1.08 | - | 1.48 | - | 1.14 | - |
| Er | 3.13 | - | 4.27 | - | 3.36 | - |
| Tm | 0.48 | - | 0.65 | - | 0.51 | - |
| Yb | 3.22 | 3.37 | 4.37 | 4.35 | 3.42 | 3.21 |
| Lu | 0.47 | 0.48 | 0.63 | 0.59 | 0.47 | 0.46 |
| Hf | 1.97 | 2.35 | 3.77 | 3.72 | 2.40 | 2.24 |
| Ta | 0.19 | 0.21 | 0.27 | 0.27 | 0.19 | 0.21 |
| Pb | 0.07 | - | 0.85 | - | 0.32 | - |
| Th | 0.19 | 0.28 | 0.42 | 0.43 | 0.21 | 0.22 |
| U | 0.08 | 0.3 | 0.91 | 0.96 | 0.09 | 0.5 |

Table F8 (continued)

| Sample: | BM91-7B | | BM91-9 | |
|------------|---------|------|--------|------|
| Reference: | [5] | {1} | [5] | {1} |
| Ba | 20.3 | 40 | 206 | 201 |
| Ni | - | 40 | - | 38 |
| Sr | 62.8 | 61 | 148 | 153 |
| V | 358 | 342 | 298 | 309 |
| Y | 29.5 | 30 | 29.4 | 34 |
| Zr | 80.9 | 81 | 86.9 | 82 |
| Nb | 2.58 | 5 | 3.26 | 15 |
| Sc | - | 38.8 | - | 30.8 |
| Cr | 102 | 84.8 | 36.2 | 26.7 |
| Co | - | 40.4 | - | 33.7 |
| Zn | - | 84.0 | - | 74.0 |
| Cu | - | 47 | - | 20 |
| Rb | 0.29 | 5 | 5.54 | 6 |
| Cs | 0.02 | 0.24 | 0.06 | 0.25 |
| La | 3.71 | 3.80 | 5.09 | 5.80 |
| Ce | 10.31 | 10.2 | 13.1 | 12.8 |
| Pr | 1.78 | - | 1.99 | - |
| Nd | 8.70 | 7.79 | 10.4 | 11.1 |
| Sm | 3.01 | 3.13 | 3.13 | 3.62 |
| Eu | 1.12 | 1.11 | 1.12 | 1.11 |
| Gd | 4.20 | - | 4.14 | - |
| Tb | 0.75 | 0.72 | 0.71 | 0.74 |
| Dy | 5.07 | - | 4.69 | - |
| Ho | 1.01 | - | 0.99 | - |
| Er | 2.91 | - | 2.89 | - |
| Tm | 0.44 | - | 0.45 | - |
| Yb | 2.97 | 2.94 | 2.91 | 3.06 |
| Lu | 0.42 | 0.43 | 0.45 | 0.44 |
| Hf | 2.17 | 2.16 | 2.48 | 2.31 |
| Ta | 0.15 | 0.20 | 0.17 | 0.21 |
| Pb | 1.41 | - | 0.98 | - |
| Th | 0.26 | 0.30 | 0.49 | 0.51 |
| U | 0.12 | 0.3 | 0.23 | 0.8 |

Table F9: Analytical data by ICP-MS, XRF and INAA, Llanada

| Sample Reference: | LL91-1 | | LL91-10 | | LL91-11 | |
|----------------------|--------|------|---------|------|---------|------|
| | [5] | {1} | [5] | {1} | [5] | {1} |
| Ba | 14.7 | 24 | 115 | 135 | 11.5 | 60 |
| Ni | - | 113 | - | 12 | - | 325 |
| Sr | 45.6 | 46 | 150 | 138 | 83.2 | 82 |
| V | 205 | 225 | 296 | 316 | 194 | 198 |
| Y | 16.1 | 18 | 18.4 | 18 | 16.1 | 18 |
| Zr | 38.7 | 33 | 44.9 | 44 | 42.3 | 44 |
| Nb | 1.15 | 5 | 0.69 | 5 | 1.21 | 5 |
| Sc | - | 29 | - | 37 | - | 34 |
| Cr | 295 | 316 | 22.3 | 6 | 397 | 434 |
| Co | - | 31 | - | 26 | - | 57 |
| Zn | - | 46 | - | 73 | - | 65 |
| Cu | - | 33 | - | 67 | - | 63 |
| Rb | 0.29 | 3 | 5.07 | 9.2 | 0.37 | 4 |
| Cs | 0.16 | 0.2 | 0.47 | 0.51 | 0.01 | 0.24 |
| La | 1.89 | 2.09 | 2.96 | 2.97 | 1.31 | 1.58 |
| Ce | 5.00 | 5.63 | 7.26 | 6.71 | 3.81 | 4.68 |
| Pr | 0.86 | - | 1.24 | - | 0.68 | - |
| Nd | 4.62 | 4.83 | 5.43 | 5.30 | 3.76 | 4.34 |
| Sm | 1.51 | 1.71 | 1.81 | 1.75 | 1.29 | 1.75 |
| Eu | 0.60 | 0.60 | 0.59 | 0.56 | 0.46 | 0.57 |
| Gd | 2.10 | - | 2.37 | - | 1.75 | - |
| Tb | 0.37 | 0.37 | 0.41 | 0.34 | 0.32 | 0.38 |
| Dy | 2.41 | - | 2.65 | - | 2.08 | - |
| Ho | 0.52 | - | 0.53 | - | 0.45 | - |
| Er | 1.47 | - | 1.55 | - | 1.31 | - |
| Tm | 0.23 | - | 0.24 | - | 0.21 | - |
| Yb | 1.50 | 1.60 | 1.64 | 1.57 | 1.42 | 1.63 |
| Lu | 0.22 | 0.22 | 0.23 | 0.23 | 0.22 | 0.21 |
| Hf | 1.03 | 1.04 | 1.22 | 1.30 | 1.10 | 1.12 |
| Ta | 0.061 | 0.10 | 0.044 | 0.08 | 0.061 | 0.11 |
| Pb | 0.52 | - | 0.82 | - | 0.68 | - |
| Th | 0.13 | 0.13 | 0.49 | 0.44 | 0.18 | 0.22 |
| U | 0.03 | 0.3 | 0.20 | 0.40 | 0.51 | 0.47 |

[5] ... analysis by ICP-MS at Union College (fifth analytical run 11/11/97)

{1} ... analysis by XRF and INAA, Giaramita et al (in press)

Table F9 (continued)

| Sample Reference: | LL91-13 | | LL91-14 | | LL91-16 | |
|----------------------|---------|------|---------|------|---------|------|
| | [5] | {1} | [5] | {1} | [5] | {1} |
| Ba | 91 | 86 | 47.9 | 59 | 52.1 | 54 |
| Ni | - | 13 | - | 23 | - | 232 |
| Sr | 153 | 141 | 90.2 | 90 | 161 | 137 |
| V | 294 | 327 | 209.3 | 301 | 197 | 207 |
| Y | 13.9 | 15 | 15.3 | 17 | 15.5 | 15 |
| Zr | 44.8 | 41 | 39.4 | 45 | 41.4 | 41 |
| Nb | 0.73 | 5 | 0.61 | 5 | 1.00 | 5 |
| Sc | - | 38 | - | 36 | - | 28 |
| Cr | 17.7 | 5 | 17.6 | 3 | 520 | 557 |
| Co | - | 29 | - | 28 | - | 34 |
| Zn | - | 51 | - | 80 | - | 72 |
| Cu | - | 13 | - | 90 | - | 51 |
| Rb | 5.13 | 7.52 | 3.01 | 5.48 | 6.19 | 6.38 |
| Cs | 0.14 | 0.23 | 0.24 | 0.24 | 0.09 | 0.19 |
| La | 2.40 | 2.28 | 2.62 | 2.75 | 1.99 | 2.05 |
| Ce | 6.08 | 5.60 | 6.50 | 6.77 | 4.96 | 5.55 |
| Pr | 1.03 | - | 1.08 | - | 0.85 | - |
| Nd | 4.89 | 4.28 | 4.69 | 5.35 | 4.48 | 3.93 |
| Sm | 1.56 | 1.51 | 1.58 | 1.65 | 1.40 | 1.52 |
| Eu | 0.50 | 0.47 | 0.56 | 0.55 | 0.53 | 0.51 |
| Gd | 1.98 | - | 2.08 | - | 1.86 | - |
| Tb | 0.34 | 0.32 | 0.36 | 0.32 | 0.32 | 0.33 |
| Dy | 2.24 | - | 2.39 | - | 2.07 | - |
| Ho | 0.44 | - | 0.48 | - | 0.43 | - |
| Er | 1.29 | - | 1.38 | - | 1.23 | - |
| Tm | 0.20 | - | 0.22 | - | 0.19 | - |
| Yb | 1.37 | 1.45 | 1.51 | 1.46 | 1.31 | 1.35 |
| Lu | 0.21 | 0.20 | 0.21 | 0.20 | 0.20 | 0.20 |
| Hf | 1.22 | 1.17 | 1.17 | 1.21 | 0.94 | 1.02 |
| Ta | 0.040 | 0.1 | 0.043 | 0.09 | 0.051 | 0.09 |
| Pb | 0.38 | - | 3.55 | - | 0.77 | - |
| Th | 0.42 | 0.42 | 0.45 | 0.47 | 0.14 | 0.16 |
| U | 0.20 | 0.40 | 0.45 | 0.57 | 0.41 | 0.44 |

Table F9 (continued)

| Sample Reference: | LL91-18 | | LL91-2 | | LL91-3A | |
|----------------------|---------|------|--------|------|---------|------|
| | [5] | {1} | [5] | {1} | [5] | {1} |
| Ba | 32.8 | 27 | 14.9 | 30 | 7.1 | 40 |
| Ni | - | 118 | - | 170 | - | 228 |
| Sr | 141 | 122 | 73.2 | 58 | 73.8 | 69 |
| V | 222 | 235 | 202 | 217 | 194 | 209 |
| Y | 18.3 | 17 | 18.1 | 17 | 16.6 | 16 |
| Zr | 38.9 | 36 | 36.9 | 39 | 35.8 | 44 |
| Nb | 0.47 | 5 | 0.77 | 5 | 1.05 | 5 |
| Sc | - | 31 | - | 37 | - | 29 |
| Cr | 309 | 350 | 346 | 291 | 503 | 544 |
| Co | - | 28 | - | 37 | - | 45 |
| Zn | - | 53 | - | 52 | - | 57 |
| Cu | - | 57 | - | 72 | - | 111 |
| Rb | 3.66 | 6.27 | 1.33 | 4 | 0.63 | 4 |
| Cs | 0.06 | 0.20 | 0.13 | 0.23 | 0.03 | 0.23 |
| La | 1.77 | 1.96 | 1.67 | 1.70 | 1.67 | 1.64 |
| Ce | 4.96 | 5.60 | 5.27 | 4.48 | 4.68 | 5.51 |
| Pr | 0.88 | - | 0.99 | - | 0.82 | - |
| Nd | 4.63 | 4.38 | 4.80 | 3.90 | 4.15 | 3.86 |
| Sm | 1.50 | 1.59 | 1.81 | 1.83 | 1.44 | 1.61 |
| Eu | 0.57 | 0.59 | 0.71 | 0.66 | 0.57 | 0.61 |
| Gd | 2.02 | - | 2.54 | - | 2.01 | - |
| Tb | 0.35 | 0.34 | 0.47 | 0.39 | 0.35 | 0.35 |
| Dy | 2.34 | - | 3.16 | - | 2.35 | - |
| Ho | 0.48 | - | 0.62 | - | 0.48 | - |
| Er | 1.44 | - | 1.75 | - | 1.38 | - |
| Tm | 0.22 | - | 0.27 | - | 0.21 | - |
| Yb | 1.46 | 1.59 | 1.85 | 1.82 | 1.41 | 1.43 |
| Lu | 0.23 | 0.23 | 0.25 | 0.26 | 0.21 | 0.21 |
| Hf | 0.97 | 0.97 | 1.11 | 1.16 | 0.93 | 1.02 |
| Ta | 0.025 | 0.11 | 0.053 | 0.1 | 0.057 | 0.17 |
| Pb | 0.34 | - | 0.44 | - | 0.76 | - |
| Th | 0.17 | 0.29 | 0.17 | 0.21 | 0.12 | 0.15 |
| U | 0.06 | 0.3 | 0.13 | 0.19 | 0.09 | - |

Table F9 (continued)

| Sample Reference: | LL91-5 | | LL91-6 | | LL91-7 | |
|----------------------|--------|------|--------|------|--------|------|
| | [5] | {1} | [5] | {1} | [5] | {1} |
| Ba | 248 | 245 | 8.0 | 25 | 9.3 | 27 |
| Ni | - | 119 | - | 123 | - | 83 |
| Sr | 324 | 277 | 79.0 | 73 | 128 | 117 |
| V | 213 | 245 | 153 | 207 | 214 | 216 |
| Y | 19.8 | 19 | 16.8 | 16 | 16.5 | 17 |
| Zr | 45.1 | 55 | 36.3 | 43 | 37.8 | 53 |
| Nb | 0.86 | 5 | 1.06 | 5 | 1.11 | 5 |
| Sc | - | 38 | - | 29 | - | 27 |
| Cr | 224 | 267 | 522 | 479 | 245 | 272 |
| Co | - | 37 | - | 29 | - | 23 |
| Zn | - | 70 | - | 52 | - | 47 |
| Cu | - | 60 | - | 46 | - | 33 |
| Rb | 16.8 | 16.6 | 0.65 | 4 | 1.00 | 3 |
| Cs | 1.75 | 1.62 | 0.03 | 0.20 | 0.02 | 0.19 |
| La | 1.74 | 1.72 | 1.35 | 1.59 | 1.33 | 1.84 |
| Ce | 5.15 | 4.75 | 4.13 | 4.91 | 3.49 | 4.73 |
| Pr | 0.93 | - | 0.76 | - | 0.59 | - |
| Nd | 4.94 | 5.10 | 3.60 | 4.34 | 3.26 | 3.99 |
| Sm | 1.78 | 1.85 | 1.36 | 1.56 | 1.08 | 1.50 |
| Eu | 0.69 | 0.67 | 0.49 | 0.58 | 0.43 | 0.56 |
| Gd | 2.50 | - | 1.99 | - | 1.57 | - |
| Tb | 0.44 | 0.38 | 0.36 | 0.37 | 0.28 | 0.33 |
| Dy | 2.99 | - | 2.53 | - | 1.85 | - |
| Ho | 0.61 | - | 0.50 | - | 0.41 | - |
| Er | 1.76 | - | 1.42 | - | 1.19 | - |
| Tm | 0.27 | - | 0.22 | - | 0.19 | - |
| Yb | 1.77 | 1.78 | 1.54 | 1.72 | 1.24 | 1.45 |
| Lu | 0.26 | 0.27 | 0.21 | 0.23 | 0.19 | 0.21 |
| Hf | 1.15 | 1.17 | 0.99 | 1.09 | 0.89 | 0.93 |
| Ta | 0.047 | 0.13 | 0.064 | 0.12 | 0.053 | 0.09 |
| Pb | 0.23 | - | 0.52 | - | 1.09 | - |
| Th | 0.15 | 0.23 | 0.14 | 0.13 | 0.11 | 0.17 |
| U | 0.11 | 0.4 | 0.07 | 0.28 | 0.10 | 0.3 |

Table F9 (continued)

| Sample Reference: | LL91-8 | | LL91-9 | |
|----------------------|--------|------|--------|------|
| | [5] | {1} | [5] | {1} |
| Ba | 178 | 169 | 13.4 | 40 |
| Ni | - | 14 | - | 111 |
| Sr | 154 | 144 | 63.9 | 67 |
| V | 273 | 329 | 252 | 272 |
| Y | 16.3 | 16 | 24.3 | 27 |
| Zr | 41.9 | 45 | 61.3 | 61 |
| Nb | 0.59 | 5 | 0.41 | 6 |
| Sc | - | 33 | - | 29 |
| Cr | 20.6 | 6.6 | 249 | 311 |
| Co | - | 26 | - | 28 |
| Zn | - | 83 | - | 66 |
| Cu | - | 229 | - | 45 |
| Rb | 9.78 | 12.4 | 0.48 | 4.72 |
| Cs | 0.54 | 0.43 | 0.06 | 0.20 |
| La | 2.91 | 2.96 | 1.78 | 2.17 |
| Ce | 6.82 | 6.47 | 5.26 | 6.49 |
| Pr | 1.13 | - | 1.01 | - |
| Nd | 4.95 | 4.91 | 5.85 | 6.90 |
| Sm | 1.65 | 1.57 | 1.95 | 2.51 |
| Eu | 0.56 | 0.52 | 0.76 | 0.93 |
| Gd | 2.12 | - | 2.75 | - |
| Tb | 0.36 | 0.32 | 0.48 | 0.58 |
| Dy | 2.42 | - | 3.18 | - |
| Ho | 0.48 | - | 0.70 | - |
| Er | 1.41 | - | 2.05 | - |
| Tm | 0.23 | - | 0.32 | - |
| Yb | 1.56 | 1.43 | 2.06 | 2.40 |
| Lu | 0.23 | 0.22 | 0.33 | 0.35 |
| Hf | 1.17 | 1.19 | 1.63 | 1.71 |
| Ta | 0.04 | 0.09 | 0.030 | 0.08 |
| Pb | 2.11 | - | 1.03 | - |
| Th | 0.49 | 0.48 | 0.05 | 0.08 |
| U | 0.30 | 1 | 0.21 | 0.32 |

REFERENCES

- Ague, J.J., 1997, Thermodynamic calculation of emplacement pressures for batholithic rocks, California: Implications for the aluminum-in-hornblende barometer: *Geology*, vol. 25, no. 6, p. 563-566.
- Ague, J.J., and Brimhall, G.H., 1988, Magmatic arc asymmetry and distribution of anomalous plutonic belts in the batholiths of California: Effects of assimilation, crustal thickness, and depth of crystallization: *Geological Society of America Bulletin*, vol. 100, p. 912-927.
- Ague, J.J., and Brandon, M.T., 1996, Regional tilt of the Mount Stuart Batholith, Washington, determined using aluminum-in-hornblende barometry; implications for the northward translation of Baja British Columbia: *Geological Society of America Bulletin*, vol. 108, p. 471-488.
- Alt, J.C., Honnorez, J. Laverne, C., and Emmermann, R., 1986, Hydrothermal alteration of a 1 km section through the upper oceanic crust, DSDP Hole 504b: mineralogy, chemistry, and evolution of seawater-basalt interactions: *Journal of Geophysical Research*, vol. 91, p. 10,309-10335.
- Anderson, J.L., 1997, Regional tilt of the Mount Stuart Batholith, Washington, determined using aluminum-in-hornblende barometry; implications for the northward translation of Baja British Columbia: Discussion and reply: *Geological Society of America Bulletin*, vol. 109, p. 1223-1227.
- Anderson, J.L., and Smith, D.R., 1995, The effects of temperature and oxygen fugacity on the Al-in-hornblende barometer: *American Mineralogist*, vol. 80, p. 549-559.
- Anderson, J.L., and Smith, D.R., 1993, Success and failure of the Al-in-hornblende barometer: *Geological Society of America Abstracts with programs*, vol. 25, p. A41.
- Aleksandrowski, P., 1985, Graphical determination of principal stress directions for slickenside populations: an attempt to modify Arthaud's method: *Journal of Structural Geology*, vol. 7, no. 1, p. 73-82 .

Alexander, R.J., Harper, G.D., and Bowman, J.R., 1993, Oceanic faulting and fault-controlled subseafloor hydrothermal alteration in the sheeted dike complex of the Josephine ophiolite: *Journal of Geophysical Research*, vol. 98, p. 9731-9759.

Alexander, R.J., and Harper, G.D., 1992, The Josephine ophiolite: an ancient analogue for slow- to intermediate-spreading oceanic ridges, in Parson, L.M., Murton, B.J., and Browning, P., (eds.), *Ophiolites and their modern oceanic analogues: Geological Society of America Special Publication No. 60*, p. 3-38.

Allan, J., 1994, Cr-spinel in depleted basalts from the Lau Basin Backarc: Petrogenetic history from Mg-Fe crystal-liquid exchange, in Hawkins, J., Parson, L., Allan, J., et al., (eds.), *Proceedings of the Ocean Drilling Program, Scientific Results, College Station, TX (Ocean Drilling Program)*, vol. 135, p. 565-583.

Allerton, S., and Vine, F.J., 1987, Spreading structure of the Troodos ophiolite, Cyprus: some paleomagnetic constraints: *Geology*, vol. 15, p. 593-597.

Anderson, J.L., and Smith, D.R., 1995, The effects of temperature and oxygen fugacity on the Al-in-hornblende barometer: *American Mineralogist*, vol. 80, p. 549-559.

Angelier, J., 1979, Determination of the mean principal directions of stresses for a given fault population: *Tectonophysics*, vol. 56, p. T17-T26.

Angelier, J., and Mecheler, 1977, Sur une methode graphique de recherche des contraintes principales egalemente utilisable en technique et en seismologique: la methode des diedres droits: *Bulletin Societe Geologique France*, vol. 19, p. 1309-13-18.

Angelier, J., Tarantola, A., Valette, B., and Manoussis, S., 1981, Inversion of field data in fault tectonics to obtain the regional stress-I. Single phase fault populations: a new method of computing the stress tensor: *Geophysical Journal of the Royal Astronomical Society*, vol. 69, p. 607-621.

- Arth, J.G., 1979, Some trace elements in trondhjemites - their implications to magma genesis and paleotectonic setting, *in*, Barker, F., *ed.*, Trondhjemites, dacites and related rocks: Elsevier, Amsterdam, Oxford, New York, p. 123-132.
- Ayers J.C., and Watson, E.B., 1991, Solubility of apatite, monazite, zircon, and rutile in supercritical aqueous fluids with implications for the subduction zone geochemistry: Royal Society of London Philosophical Transactions, vol. 335, p. 365-375.
- Baldwin, E.M., 1969, Thrust faulting along the lower Rogue River, Klamath Mountains, Oregon: Geological Society of America Bulletin, vol. 80, p. 2047-2052.
- Baldwin, E.M., and Rud, J.O., 1972, Thrusting of the Rogue Formation near Marial on the lower Rogue River, Oregon: The Ore Bin, Oregon Department of Geology and Mineral Industries, vol. 34, no. 4, p. 57-66.
- Baldwin, E.M., 1974, Eocene stratigraphy of southwestern Oregon: State of Oregon Department of Geology and Mineral Industries Bulletin, vol. 83, pp. 40.
- Barker, F., 1979, Trondhjemite: definition, environment, and hypothesis of origin, *in*, Barker, F., *ed.*, Trondhjemites, dacites and related rocks: Elsevier, Amsterdam, Oxford, New York, p. 1-12.
- Barnes, C.G., Allan, C.M., Hoover, J.D., and Brigham, R.H., 1990, Magmatic components of a tilted plutonic system, Klamath Mountains, California: Geological Society of America Memoir 174, P. 331-346.
- Barnes, C.G., Peterson, S.W., Kistler, R.W., Prestvik, T., and Sundvoll, B., 1992, Tectonic implications of isotopic variation among Jurassic and Early Cretaceous plutons, Klamath Mountains: Geological Society of America, vol. 104, p. 117-126.
- Barrat, J.A., and Nesbitt R.W., 1996, Geochemistry of the Tertiary volcanism of Northern Ireland: Chemical Geology, vol. 129, p. 15-38.
- Barsdell, M., 1988, Petrology and petrogenesis of clinopyroxene-rich tholeiitic lavas, Merelava volcano, Vanuatu: Journal of Petrology, vol. 29, p. 927-964.

- Beard, J.S., and Lofgren, G.G., 1991, Dehydration melting and water-saturated melting of basaltic and andesitic greenstones and amphibolites at 1.3 and 6.9 kb: *Journal of Petrology*, vol. 32 p. 365-401.
- Beccaluva, L., and Serri, G., 1988, Boninitic and low-Ti subduction-related lavas from intraoceanic arc - backarc systems and low-Ti ophiolites: a reappraisal of their petrogenesis and original tectonic setting: *Tectonophysics*, vol. 146, p. 291-315.
- Best, M.G., and Christiansen, E.H., 1997, Origin of broken phenocrysts in ash-flow tuffs: *Geological Society of America Bulletin*, vol. 109, p. 63-73.
- Bettison-Varga, L., Schiffmann, P. and Janecky D.R., 1995, Fluid-rock interaction in the hydrothermal upflow zone of the Solea graben, Troodos ophiolite, Cyprus: *in Schiffmann, P. and Day, H., eds., Low Grade metamorphism of Mafic Rocks: Geological Society of America Special Paper 296*, p. 81-100.
- Bierman, C., 1981, (100) deformation twins in naturally deformed amphiboles: *Nature*, vol. 292, p. 821-823.
- Blake, M.C., Page, N.J., Smith, J.G., Griscom, A., Coleman, R.G., and Loney R.A., 1982, Geological cross section from Cape Sebastian to Upper Klamath Lake, Southwest Oregon: *Geological Society of America, Map and Chart Series, MC-280*.
- Blake, M.C., Jr., and Jones, D.L., 1974, Origin of Franciscan melanges in northern California, *in* Dott, R.H., Jr., and Shaver, R.H., (eds.), *Modern and ancient geosynclinal sedimentation; problems of palinspastic restoration: Society of Economic Paleontologists and Mineralogists Special Publication 19*, p. 345-357.
- Blake, M.C., Jr. and Jones D.L., 1981, The Franciscan assemblage and related rocks in northern California: A reinterpretation *in*, Ernst, W.G., (ed.): *The geotectonic development of California*; Englewood Cliffs, New Jersey, Prentice-Hall, p.306-328.
- Blake, M.C., Jr., Jayko, A.S., McLaughlin, R.J., and Underwood, M.B., 1988, Metamorphic and tectonic evolution of the Franciscan Complex, northern California, *in* Ernst, W.G., (ed.), *Metamorphic and*

crustal evolution of the western United States (Rubey Volume 7): Englewood Cliffs, New Jersey, Prentice-Hall, pp. 1035-1060.

Blake, M.C., Jr, Jayko, A.S., and McLaughlin, R.J., 1985b, Tectonostratigraphic Terranes of the northern Coast Ranges, California, *in* Howell, D.G., (ed.), Tectonostratigraphic Terranes of the Circum Pacific Region: Circum Pacific Council for Energy and Mineral Resources Earth Science Series, vol. 1, p. 159-171.

Blake, M.C., Jr, Engebretson, D.C., Jayko, A.S., and Jones, D.L., 1985a, Tectonostratigraphic Terranes in Southwest Oregon, *in* Howell, D.G., (ed.), Tectonostratigraphic Terranes of the Circum Pacific Region: Circum Pacific Council for Energy and Mineral Resources Earth Science Series, vol. 1, p. 147-157.

Blakely, R.J., and Senior, L., 1983, Map and interpretation of aeromagnetic data for the Wild Rogue Wilderness, Coos and Curry Counties, Oregon: U.S. Geological Survey Miscellaneous Field Studies Map MF-1381-C, scale 1:48,000.

Bloomer, S.H., 1987, Geochemical characteristics of boninite-, and tholeiite-series volcanic rocks from the Marianas forearc and the role of an incompatible element-enriched fluid in arc petrogenesis: Geological Society of America Special Paper, vol. 215, p. 151-164.

Bloomer, S.H., Ewart, A., Hergt, J.M., Bryan, W.B., 1994, Geochemistry and origin of igneous rocks from the outer Tonga forearc (site 841), *in* Hawkins, J., Parson, L., Allan, J., et al., (eds.), Proceedings of the Ocean Drilling Program, Scientific Results, College Station, TX (Ocean Drilling Program), v. 135, p. 625-646

Blundy, J.D., and Holland, T.J.B., 1990, Calcic amphibole equilibria and a new amphibole-plagioclase geothermometer: Contributions to Mineralogy and Petrology, vol. 104, p. 208-224.

Blundy, J.D., and Holland, T.J.B., 1992a, Calcic amphibole equilibria and a new amphibole-plagioclase geothermometer: Reply to the comments of Hammarstrom and Zen, and Rutherford and Johnson: Contributions to Mineralogy and Petrology, vol. 111, p. 269-272.

- Blundy, J.D., and Holland, T.J.B., 1992b, "Calcic amphibole equilibria and a new amphibole-plagioclase geothermometer" - reply to the comment of Poli and Schmidt: *Contributions to Mineralogy and Petrology*, vol. 111, p. 278-283.
- Boespflug, X., Dosso, L., Bougault, H., Joron, J.L., 1990, Trace element and isotopic (Sr, Nd) geochemistry of volcanic rocks from the Lau Basin: *Geologisches Jahrbuch*, vol. D92, p. 503-516.
- Borg, L.E., Clyne, M.A., and Bullen, T.D., 1997, The variable role of slab-derived fluids in the generation of a suite of primitive calc-alkaline lavas from the southernmost Cascades, California: *The Canadian Mineralogist*, vol. 35, p. 425-452.
- Bouchez, J.L., Delas, C., Gleizes, G., and Nédélec, A., 1992, Submagmatic microfractures in granites: *Geology*, vol. 20. P. 35-38.
- Bower, N.W., Lewis, C.M., Neifert, P.E., Gladney, E.S., 1992, Elemental concentrations in twenty NIST standards of geochemical interest: *Geostandard Newsletters*, vol. 16, pp. 27-40.
- Brodie, K.H., and Rutter, E.H., 1985, On the relationship between deformation and metamorphism, with special reference to the behavior of basic rocks, *in* Thompson, A.B., and Rubie, D.C., (eds.), *Metamorphic reactions, Kinetics, Textures and Deformation*: Springer, New York, Berlin, Heidelberg, Tokyo, p. 138-179.
- Cameron, W.E., 1985, Petrology and the origin of primitive lavas from the Troodos ophiolite, Cyprus, *Contributions to Mineralogy and Petrology*, vol. 89, p. 239-255.
- Cann, J.R., 1977, Metamorphism in the ocean crust, *in* Talwani, M., Harrison, C.G., and Hayes, Dennis (eds.), *Deep Drilling Results in the Atlantic Ocean: Oceanic Crust: Maurice Ewing series 2*, American Geophysical Union, Washington, D.C., p. 230-238.
- Cannat, M., Mevel, C., and Stakes, D.S., 1991, Normal ductile shear-zones at an oceanic spreading ridge; tectonic evolution of site 735 gabbros (Southwest Indian Ridge): *Proceedings of the Ocean Drilling Program, Scientific Results*, vol. 118, p. 415-429.

- Casey, J.F., Dewey, J.F., Fox, P.Y., Karson, J.A., Rosencrantz, E., 1981, Heterogeneous nature of oceanic crust and upper mantle: A perspective from the Bay of Islands Ophiolite Complex, in Emiliani, C., (ed.), *The Sea*, vol. 7: John Wiley, New York, p. 305-338.
- Chan, M.A., and Dott, R.H., Jr., Shelf and deep-sea sedimentation in Eocene fore-arc basin, Western Oregon - Fan or Non-Fan?: *American Association of Petroleum Geologists Bulletin*, vol 67, p. 2100-2116.
- Chen, J.C., and Moore, J.G., 1982, Uranium-lead isotopic ages from the Sierra Nevada batholith: *Journal of Geophysical Research*, vol. 87, p. 4761-4784.
- Chow, T.J., and Patterson, C.C., 1962, On the occurrence and significance of lead isotopes in pelagic sediments: *Geochimic et Cosmochimica Acta*, vol. 26, p. 263-308.
- Christensen, N.I., and Salisbury, M.H., 1975, Structure and Constitution of the Lower Oceanic Crust: *Reviews of Geophysics and Space Physics*, vol. 13, no. 1, p. 57-86.
- Christenson, N.I., and Smewing, J.D., 1981, Geology and seismic structure of the northern section of the Oman ophiolite: *Journal of Geophysical Research*, vol. 86, p. 2545-2555.
- Christie, D.M., and Sinton, 1981, Evolution of abyssal lavas along propagating segments of the Galapagos spreading center: *Earth and Planetary Science Letters*, vol. 56, p. 321-335.
- Clift, P.D., and Dixon, J.E., 1994, Variations in arc volcanism and sedimentation related to rifting of the Lau Basin (southwest Pacific), *in* Hawkins, J., Parson, L., Allan, J., et al., (eds.), *Proceedings of the Ocean Drilling Program, Scientific Results*, College Station, TX (Ocean Drilling Program), vol. 135, p.23-49.
- Clynne, M.A., and Borg, L.E., 1997, Olivine and Chromian spinel in primitive calc-alkaline and tholeiitic lavas from the southernmost Cascade Range, California: a reflection of relative fertility of the source: *The Canadian Mineralogist*, vol. 35, p. 453-472.
- Cole, J.W., 1979, Structure, petrology, and genesis of Cenozoic volcanism, Taupo Volcanic Zone, New Zealand - a review: *New Zealand Journal of Geology and Geophysics* vol. 6, p. 31-657.

- Cole, J.W., 1981, Genesis of lavas of the Taupo Volcanic Zone, North Island, New Zealand: *Journal of Volcanology and Geothermal Research*, vol. 10, p. 317-337.
- Coleman, R.G., 1972, The Colebrook Schist of southwestern Oregon and its relation to the tectonic evolution of the region: *U.S. Geological Survey Bulletin*, 1339, 61 pages.
- Coleman, R.G., 1977, *Ophiolites, Ancient Oceanic Lithosphere?: Springer-Verlag, Berlin, Heidelberg, New York*, pp. 229.
- Coleman, R.G., and Lanphere, 1991, The Briggs Creek amphibolite, Klamath Mountains, Oregon: its origin and dispersal: *New Zealand Journal of Geology and Geophysics*, vol. 34, p. 271-284.
- Coleman, R.G., and Donato, M.M., 1989, Oceanic Plagiogranite Revisited, in *Trondhjemites, Dacites and Related Rocks*, F. Barker (ed.): *Developments in Petrology 6*, Elsevier, Amsterdam, Oxford and New York, p. 149-166.
- Coleman, R.G., and Peterman, Z.E., 1975, Oceanic Plagiogranites: *Journal of Geophysical Research*, vol. 80, p. 1099-1108.
- Coleman, R.G., Manning, C.E., Mortimer, N., Donato, M.M., and Hill, L.B., 1988, Tectonic and regional metamorphic framework of the Klamath Mountains and adjacent Coast Ranges. California and Oregon, in Ernst, W.G., (ed.), *Metamorphism and Crustal Evolution of the western United States, Pacific Section, Society of Economic Paleontologists and Mineralogists Pacific Coast Paleogeography Symposium 1*, p. 1-32.
- Collier, J.S., Dañobeitia, J.J., and CD82 Scientific party, 1997, Evidence for asymmetric accretion and low-angle planar faults in slow-spreading oceanic crust: *Geology*, vol. 25, p. 1075-1078.
- Conrey, R.M., Sherrod, D.R., Hooper, P.R., and Swanson, D.A., 1997, Diverse primitive magmas in the Cascade Arc, northern Oregon and southern Washington: *Canadian Mineralogist*, vol. 35, p. 367-396.

- Coulton, A.J., Harper, G.D., and O'Hanley, D.S., 1995, Oceanic vs. emplacement-age serpentinization in the Josephine ophiolite: Implications for the nature of the Moho at intermediate and slow spreading ridges: *Journal of Geophysical Research*, vol. 100, p. 22,245-22,260.
- Cox, K.G., Bell, J.D., and Pankhurst, R.J., 1979, *The interpretation of igneous rocks*: Unwin, London, pp 231.
- Crawford, A.J., Falloon, T.J., and Green, D.H., 1989, Classification, petrogenesis and tectonic setting of boninites, *in* Crawford, A.J., (ed.), *Boninites and Related Rocks*: Unwin Hyman, London, p. 2-49.
- Cunningham, J.K., and Anscombe, K.J., 1985, Geology of 'Eua and other islands, Kingdom of Tonga, in Scholl, D.W., and Vallier, T.L., eds., *Geology and Offshore Resources of Pacific Island Arcs - Tonga region*: Circum-Pacific Council for Energy and Mineral Resources, Earth Science Series, vol. 2, p., 221-258.
- Czamanske, G.K., and Wones, D.R., 1973, Oxidation during crystallization during magmatic differentiation, Finnmarka complex, Oslo area, Norway; part 2: the mafic silicates: *Journal of Petrology*, vol. 14, p. 349-380.
- Davis, A.S., Clague, D.A. and Morton, J.L., 1990, Volcanic Glass Compositions from two spreading centers in Lau Basin, South West Pacific Ocean: *Geologisches Jahrbuch* vol. D92, p. 481-501.
- Debon, F., and Le Fort, P., 1982, A chemical-mineralogical classification of common plutonic rocks and associations: *Transactions of the Royal Society of Edinburgh: Earth Sciences* vol. 73, p. 135-149.
- DeLong, S.E., and Chatelain, C., 1990, Trace element constraints on accessory-phase saturation in evolved MORB magma: *Earth and Planetary Science Letters*, 101, p. 206-215.
- Dewey, J.F., and Kidd, W.S.F., 1977, Geometry of plate accretion: *Geological Society of America Bulletin*, vol. 88, p. 960-968.
- Dick, H.J.B., and Bullen T., 1984, Chromian spinel as a petrogenetic indicator in abyssal and alpine-type peridotites and spatially associated lavas; *Contributions to Mineralogy and Petrology*, vol. 86, p. 54-76.

- Dickinson, W.R., and Seely, D.R., 1979, Structure and stratigraphy of forearc regions: American Association of Petroleum Geologists Bulletin, vol. 63, p. 2-31.
- Dickinson, W.R., Hopson, C.A., and Saleeby, J.B., 1996, Alternate origins of the Coast Range ophiolite (California): Introduction and Implications: GSA Today, vol. 6, no. 2., p. 2-10.
- Dilek, Y., and Delaloye, M., 1992, Structure of the Kizildag ophiolite, a slow-spreading Cretaceous ridge segment north of the Arabian promontory: Geology, vol. 20, p. 19-22.
- Dilek, Y., and Thy, P., 1998, Structure, petrology and seafloor spreading tectonics of the Kizildag ophiolite, Turkey, in Mills, R.A., and Harrison, K., (eds.), Modern ocean floor processes and geological record: Geological Society Special Publications 148, p. 43-69.
- Dilek, Y., Moores, E.M., and Furnes, H., 1998, Structure of modern oceanic crust and ophiolites and implications for faulting and magmatism at oceanic spreading centers, in, Buck, W.R., Delaney, P.T., Karson, J.A., and Lagabriele, Y. (eds.), Faulting and magmatism at mid-ocean ridges: Geophysical Monograph 106, American Geophysical Union, p. 219-265.
- Diller, J.S., 1898, Description of the Roseburg Quadrangle: U.S. Geological Survey Geological Atlas Roseburg Folio 49, pp. 4, maps.
- Dixon-Spulber, S., and Rutherford, M.J., 1979, Plagiogranites as late-stage immiscible liquids in ophiolite and mid-ocean ridge suites: an experimental study: Earth and Planetary Science Letters, vol. 45, p. 45-60.
- Dixon-Spulber, S., and Rutherford, M.J., 1983, The origin of rhyolite and plagiogranite in oceanic crust: an experimental study: Journal of Petrology, vol. 24, p. 1-25.
- Doherty, William, 1989, An internal standardization procedure for the determination of yttrium and the rare earth elements in geological materials by inductively coupled plasma - mass spectrometry; Spectrochimica Acta, vol. 44b, no. 3, pp. 263-280.
- Dollinger, G.S., and Blacic, J.D., 1975, Deformation mechanisms in experimentally and naturally deformed amphiboles: Earth and Planetary Science Letters, vol. 26, p. 409-416.

- Dott, R.H. Jr, 1965, Mesozoic-Cenozoic tectonic history of the southwestern Oregon coast in relation to Cordilleran orogenesis; *Journal of Geophysical Research*, vol. 70, no. 18, p. 4687-4707.
- Dudas, F.O., 1992, Petrogenetic evaluation of trace element discrimination diagrams, *in* Batholomew, M.J., Hyndman, D.W., Mogk, D.W., and Marson, R., (eds.), *Basement Tectonics 8*: Kluwer, Dordrecht, p. 93-127.
- Eberz, G.W., and Nicholls, I.A., 1988, Microgranitoid enclaves from the Swift Creek Pluton SE Australia: textural and physical constraints on the nature of magma mingling processes in the plutonic environment: *Geologische Rundschau*, vol. 77/3, p. 713-736.
- Edelman, S.H., Day, H.W., and Bickford, M.E., 1989, Implications of U-Pb zircon ages for the tectonic settings of the Smartville and Slate Creek complexes, northern Sierra Nevada, California: *Geology*, vol. 17, p. 1032-1035.
- Edwards, C.M.H., Morris, J.D., and Thirlwall, M.F., 1993, Separating mantle from slab signatures in arc lavas using B/Be and radiogenic isotopic systematics: *Nature*, vol. 362p. 530-533.
- Elderfield and Greaves, 1982, The Rare Earth elements in Seawater: *Nature*, vol., 296, p. 214-219.
- Ellam, R.M., and Hawkesworth, C.J., 1988, Elemental and isotopic variations in subduction related basalts: evidence for a three component model: *Contributions to Mineralogy and Petrology*, vol. 98, p. 72-80.
- Elthon, D., 1981, Metamorphism in oceanic spreading centers, *in* Emiliani, C., ed.: *The Sea*, Vol. 7, *The Oceanic Lithosphere*, New York, John Wiley and Sons, p. 285-303.
- Escartin, J., and Lin, J., 1998, Tectonic modification of axial crustal structure, evidence from spectral analyses, residual gravity and bathymetry of Mid-Atlantic Ridge flanks: *Earth and Planetary Science letters*, vol. 154, p. 279-293.
- Evarts, R.C., 1977, Petrology of the Del Puerto ophiolite central California Coast Ranges, *in* Coleman R.G., and Irwin W.P. (eds), *North American Ophiolites*: Oregon Department of Geology and Mineral Industries, Bulletin 95, p. 121-145.

- Evarts, R.C., and Schiffmann, P., 1983, Submarine hydrothermal metamorphism of the Del Puerto ophiolite, California: *American Journal of Science*, vol. 283, p. 289-340.
- Evarts, R.C., Sharp, R.D., and Phelps, D.W., 1992, The Del Puerto Canyon Remnant of the Great Valley ophiolite: Geochemical and Age Constraints on its Formation and Evolution: *American Association of Petroleum Geologists Bulletin*, vol. 76, no. 3, p. 418.
- Ewart, A., 1976, Mineralogy and chemistry of modern orogenic lavas - some statistics and implications: *Earth and Planetary Science Letters*, vol. 31, p. 417-432.
- Ewart, A., Hergt, J.M., Hawkins, J.W., 1994a, Major element, trace element, and isotope (Pb, Sr and Nd) geochemistry of site 839 basalts and basaltic andesites: implications for arc-volcanism: *Proceedings of the Ocean Drilling Program, Scientific Results College Station, TX (Ocean Drilling Program)*, vol. 135, p. 519-531.
- Ewart, A., Bryan, W.B., Chappell, B.W., and R.L. Rudnick, 1994b, Regional Geochemistry of the Lau-Tonga Arc and back-arc systems: *Proceedings of the Ocean Drilling Program, Scientific Results College Station, TX (Ocean Drilling Program)*, vol. 135, p. 385-425.
- Fallon, T.J., and Crawford, A.J., 1991, The petrogenesis of high-calcium boninite lavas dredged from the northern Tonga ridge: *Earth and Planetary Science Letters*, vol. 102, p. 375-394.
- Fitz Gerald, J.D., and Stünitz, H., 1993a, Deformation of granitoids at low metamorphic grade. I: Reactions and grain size reduction: *Tectonophysics*, vol. 221, p. 269-297.
- Fitz Gerald, J.D., and Stünitz, H., 1993b, Deformation of granitoids at low metamorphic grade. II: Granular flow in albite-rich mylonites: *Tectonophysics*, vol. 221, p. 299-324.
- Fjäder, K., Gudmundsson, A. and Forslund, T., 1994, Dikes, minor faults and mineral veins associated with transform fault in North Iceland: *Journal of Structural Geology*, vol. 16, p. 109-119.
- Förster, H.-J., Tischendorf, G., and Trumbull, R.B., 1997, An evaluation of the Rb v. (Y+Nb) discrimination diagram to infer the tectonic setting of silicic igneous rocks: *Lithos*, vol. 40, p. 261-293.

- Forsythe, L.M., and Fisk, M.R., 1994, Comparison of experimentally crystallized and natural spinels from Leg 135, in Hawkins, J., Parson, L., Allan, J., et al., (eds.), Proceedings of the Ocean Drilling Program, Scientific Results, College Station, TX (Ocean Drilling Program), v. 135, p. 585-594.
- Frei, L.S., Magill, J.R., and Cox, A., 1982, Paleomagnetic results from the central Sierra Nevada; constraints on reconstructions of the Western United States: *Tectonics*, vol. 3, p. 157-177.
- Frenzel, G. Mühe, R., and Stoffers, P., 1990, Petrology of the Volcanic Rocks from the Lau Basin, South West Pacific: *Geologisches Jahrbuch* vol. D92, p. 395-479.
- Fujii, T., 1989, Genesis of Mid-ocean ridge basalts, in Saunders, A.D. and Norry, M.J., (eds.), *Magmatism in the Ocean Basins: Geological Society of America Special Publication 42*, p. 137-146.
- Garver, J., 1988, Stratigraphy, depositional setting, and tectonic significance of the clastic cover to the Fidalgo Ophiolite, San Juan Islands, Washington: *Canadian Journal of Earth Sciences*, vol. 25, p. 417-432.
- Giaramita, M., MacPherson, G.J., and Phipps, S.P., Petrologically diverse basalts from a fossil oceanic forearc in California: The Llanada and Black Mountain remnants of the Coast Range ophiolite: *Geological Society of America Bulletin*, vol. 110, p. 2-20.
- Gladney, E.S., O'Malley, B., Roelandts, I. and Gills, T., 1987, Compilation of elemental concentration data for NBS Clinical biological, geological, and environmental standard reference materials: *NBS Special Publication*, vol. 2, pp. 60-111; Supplement 1 issued in 1993.
- Govindaraju, K., 1994, 1994 compilation of working values and sample descriptions for 383 geostandards: *Geostandard Newsletters*, vol. 18, special issue, pp. 1-159.
- Gray F., L. Ramp, B. Moring, I. Douglas, and J. Donahoe, 1982, Geologic map of the Wild Rogue Wilderness, Coos, Curry and Douglas Counties, Oregon: U. S. Geological Survey Miscellaneous Field Studies Map MF-1381-A, scale 1:48,000.
- Gray, F., and McKee, E.H., 1981, New K-Ar dates from the Wild Rogue Wilderness, Southwestern Oregon: *Isochron/West*, no. 32, p. 27-29.

- Gray, F., and Peterson, J.A., 1982, Geochemical analyses of rock and stream-sediment samples from the Wild Rouge Wilderness area, Coos, Curry, and Douglas Counties, Oregon: U.S. Geological Survey Open-File Report 82-186.
- Gregory, R.T. and Taylor, H.P., Jr., 1984, An oxygen isotope profile in a section of Cretaceous oceanic crust, Semail ophiolite, Oman: Evidence for $\delta^{18}\text{O}$ buffering of the oceans by >5 km seawater-hydrothermal circulation at mid-ocean ridges: *Journal of Geophysical Research*, vol. 86, p. 2737-2755.
- Hacker, B.R., Donato, M.M., Barnes, C.G., McWilliams, M.O., and Ernst W.G., 1995, Timescales of orogeny: Jurassic construction of the Klamath Mountains: *Tectonics*, vol. 14, p. 677-703.
- Hacker, B.R., Ernst, W.G., and McWilliams, M.O., Genesis and evolution, of a Permian-Jurassic magmatic arc/accretionary wedge, and reevaluation of terranes in the central Klamath Mountains: *Tectonics*, vol. 12, p. 387-409.
- Hagstrum, J.T., and Murchey, B.L., 1996, Paleomagnetism of Jurassic radiolarian chert above the Coast Range ophiolite at Stanley Mountain, California, and implications for its paleogeographic origins: *Geologic Society of America Bulletin*, vol. 108, no. 6, p. 643-652.
- Hall, P.C., 1984, Some aspects of deformation fabrics along the Highland/Lowland Boundary, Northwest Adirondacks, New York State: M.S. thesis, State University of New York at Albany, 124pp.
- Hames, W.E., and Bowring, S.A., 1994, An empirical evaluation of the argon diffusion geometry in muscovite: *Earth and Planetary Science Letters*, vol. 124, p. 161-169.
- Hamilton, W., 1969, Mesozoic California and the underflow of Pacific mantle: *Geological Society of America Bulletin*, vol. 80, p. 2409-2430.
- Hamilton, Warren, 1978, Mesozoic tectonics of the western United States, *in* Howell D.G., and McDougall, K.A., (eds.), *Mesozoic paleogeography of the Western United States: Pacific Section*, Society of Economic Paleontologists and Mineralogists, Pacific Coast Paleogeography Symposium 2, pp. 33-70.

- Hammarstrom, J.M., and Zen, E-An, 1986, Aluminum in hornblende: an empirical igneous geobarometer: *American Mineralogist*, vol. 71, p. 1297-1313.
- Hammarstrom, J.M., and Zen, E-an, 1992, Discussion of Blundy and Holland's (1990) "Calcic amphibole equilibria and a new amphibole-plagioclase geothermometer": *Contributions to Mineralogy and Petrology*, vol. 111, p. 264-266.
- Hanmer, S., and Passchier, C., 1991, Shear-sense indicators: a review: Geological Survey of Canada, paper 90-17, pp. 72.
- Harms, T., Jayko, A.S., and Blake, M.C., 1992, Kinematic evidence for extensional unroofing of the Franciscan complex along the Coast Range fault, northern Diabolo Range, California: *Tectonics*, vol. 11, p. 228-241.
- Harper, G.D., 1982a, Inferred high primary volatile contents in lavas erupted in an ancient back-arc basin California: *Journal of Geology*, vol. 90., p. 187-194.
- Harper, G.D., 1982b, Evidence for large-scale rotations at spreading centers from the Josephine ophiolite: *Tectonophysics*, vol. 82, p. 25-44.
- Harper, G.D., 1984, The Josephine ophiolite, northwestern California, *Geol. Soc. Amer. Bull.*, v. 95, p. 1,009-1,026.
- Harper, G.D., 1983, A depositional contact between the Galice Formation and a Late Jurassic ophiolite northwestern California and southwestern Oregon: *Oregon Geology*, vol. 45, no. 1, p. 3-7.
- Harper, G.D., Saleeby, J.B., and Norman, E.A.S., 1985, Geometry and tectonic setting of the sea-floor spreading for the Josephine ophiolite, and implications for Jurassic accretionary events along the California margin, *in* Howell, D.G., (ed.), *Tectonostratigraphic Terranes of the Circum-Pacific Region*: Circum Pacific Council for Energy and Mineral Resources, Earth Science Series, vol. 1, p. 239-257.
- Harper, G.D., 1995, Pumpellyosite and prehnite associated with epidosite in the Josephine ophiolite - Ca metasomatism during upwelling of hydrothermal fluids at spreading axis, *in* Schiffmann, P. and

- Day, H., *eds.*, Low Grade metamorphism of Mafic Rocks: Geological Society of America Special Paper 296, p. 101-122.
- Harper, G.D., Bowman, J.R., and Kuhns, R., 1988, A Field, chemical, and stable isotope study of submarine hydrothermal metamorphism of the Josephine ophiolite, California-Oregon: *Journal of Geophysical Research*, vol. 93, p. 4,625-4,656.
- Harper, G.D., Grady, K., and Wakabayashi, J., 1990, A structural study of a metamorphic sole beneath the Josephine ophiolite, western Klamath terrane, California-Oregon, *in* Howell, D.S., and Miller, M.M., (eds.), Paleozoic and Early Mesozoic paleogeographic relations in the Klamath Mountains, Sierra Nevada, and related terranes: Geological Society of America Special Paper 255, p. 379-396.
- Harper, G.D., Saleeby, J.B., and Heizler, M., 1994, Formation and Emplacement of the Josephine ophiolite and the age of the Nevadan orogeny in the Klamath Mountains, California-Oregon: U/Pb zircon and $^{40}\text{Ar}/^{39}\text{Ar}$ geochronology: *Journal of Geophysical Research*, vol. 99, p. 4293-4321.
- Harper G.D., and Wright, J.E., 1984, Middle to late Jurassic tectonic evolution of the Klamath Mountains, California-Oregon: *Tectonics* vol. 3, p. 759-772.
- Harper, G.D., 1996, A review of hemipelagic and Flysch sedimentation associated with the Josephine ophiolite, California: *Ofioliti*, vol. 19, no 2b., p. 397-411.
- Harper, G.D., in review, Fe-Ti basalts and propagating rift tectonics in the Josephine ophiolite.
- Harrison, T.M., 1981, The diffusion of ^{40}Ar in Hornblende: *Contributions to Mineralogy and Petrology*, vol. 78, p. 324-331.
- Hawkesworth, C.J., 1988, Heterogeneous mantle domains: signatures, genesis, and mixing chronologies: *Earth and Planetary Science Letters*, 90, p 273-296).
- Hawkesworth, C.J., Hergt, J.M., Ellam, R.M., and McDermott, F., 1991, Element fluxes associated with subduction related magmatism: *Philosophical Transactions of the Royal Society of London, Series A.*, vol. 335, p. 393-403.

- Hawkins, J.W., 1995, Evolution of the Lau Basin-Insights from ODP Leg 135; *in* Active margins and marginal basins of the western Pacific; Geophysical Monograph, vol. 88, p. 125-173.
- Hawkins, J.W., and Allan J.F., 1994, Petrologic evolution of Lau Basin Sites 834 through 839, *in* Hawkins, J., Parson, L., Allan, J., et al., (eds.), Proceedings of the Ocean Drilling Program, Scientific Results, College Station, TX (Ocean Drilling Program), vol. 135, p. 427-470.
- Hawkins, J.W., and Melchior, J.T., 1985, Petrology of the Mariana Trough and Lau Basin Basalts: Journal of Geophysical Research, vol. 90, no. B13, p. 11,431-11,468.
- Hawkins, J.W., Lonsdale, P.F., Macdougall, J.D., and Volpe, A.M., 1990, Petrology of the axial ridge of the Mariana Trough backarc spreading center: Earth and Planetary Science Letters, vol. 100, p. 226-250.
- Helz, R.T., 1976, Phase relations of basalts in their melting ranges at $p_{H_2O} = 5$ kbar. Part II. Melt compositions: Journal of Petrology, 17, p. 139-193.
- Hergt, J.M., and Farley, K.N., 1994, Major element, trace element and isotope (Pb, Sr and Nd) variations in site 834 basalts: Implications for the initiation of backarc opening, *in* Hawkins, J., Parson, L., Allan, J., et al., eds., Proceedings of the Ocean Drilling Program, Scientific Results, College Station, TX (Ocean Drilling Program), v. 135, p. 471-485.
- Hergt, J.M., and Hawkesworth, C.J., 1994, Pb-, Sr-, and Nd-, isotopic evolution of the Lau Basin: implications for mantle dynamics during backarc opening, *in* Hawkins, J., Parson, L., Allan, J., et al., (eds.), Proceedings of the Ocean Drilling Program, Scientific Results, College Station, TX (Ocean Drilling Program), vol. 135, p. 505-517.
- Hertogen, J, and Gubels, R. 1976, Calculation of trace element fractionation during partial melting: Geochimica and Cosmochimica Acta, vol. 40, pp. 313-322.
- Higgins, M., 1991, The origin of laminated and massive anorthosite, Sept Iles layered intrusion, Quebec, Canada: Contributions to Mineralogy and Petrology, vol. 106, p. 340-354.

- Hildreth, W., and Moorbath, S., 1988, Crustal contributions to arc magmatism in the Andes of Central Chile: *Contributions to Mineralogy and Petrology*, vol. 98, p. 455-489.
- Hochstедter A.G., Gill, J.B., and Morris, J.D., 1990b, Volcanism in the Sumisu Rift, II. Subduction and non-subduction related components: *Earth and Planetary Science Letters*, vol. 100, p. 195-209.
- Hochstедter A.G., Gill, J.B., Kusakabe, M., Newman S., Pringle, M., Taylor, B., and Fryer, P., 1990a, Volcanism in the Sumisu Rift, I. Major element volatile, and stable isotope geochemistry: *Earth and Planetary Science Letters* vol. 100, p. 179-194.
- Hochstедter A.G., Kepezhinskas, P., Defant, M., Drummond, M., and Koloskov, A., 1996, Insights into the volcanic arc mantle wedge from magnesian lavas from the Kamtchatka arc: *Journal of Geophysical Research*, vol. 101, no. B1, p. 697-712.
- Hoepfner, R., 1955, Tektonik im Schiefergebirge: *Geologische Rundschau*, vol. 44, p. 26-58.
- Hole, M.J., Saunders, A.D., Marriner, G.F., and Tarney, J., 1984, Subduction of pelagic sediments: implications for the origin of Ce-anomalous basalts from the Mariana Islands: *Journal of the Geological Society London*, vol. 141, p. 453-472.
- Holland, T., and Blundy, J., 1994, Non-ideal interactions in calcic amphiboles and their bearing on amphibole-plagioclase thermometry: *Contributions to Mineralogy and Petrology*, vol., 116, p. 433-447.
- Hollister, L.S., Grissom, G.C., Peters, E.K., Stowell, H.H., and Sisson, V.B., 1987, Confirmation of the empirical correlation of Al in hornblende with pressure of solidification of calc-alkaline plutons: *American Mineralogist*, vol. 72, p. 231-239.
- Hollocher, K., Fakhry, A., Ruiz, J., 1995, Trace element determinations for USGS Basalt BHVO-1 and NIST standard reference materials 278, 688 and 694 by inductively coupled plasma - mass spectrometry: *Geostandards Newsletter*. vol. 19, no., 1, pp. 35 - 40.
- Holloway, J.R., and Burnham, C.W., 1972, Melting relations of basalt with equilibrium water pressures less than total pressure: *Journal of Petrology*, vol. 13, p. 1-29.

- Holmes, L.J., Robinson, V.J., Makinson, P.R., Livens, F.R., 1995, Multi-element determination in complex matrices by inductively coupled plasma - mass spectrometry: *The Science of the Total Environment*, vol. 173/174, pp. 345-350.
- Honthaas, C., Réhault, J-P., Maury, R.C., Bellon, H., Hémond, C., Malod, J-A., Cornée, J-J., Villeneuve, M., Cotton, J., Burhanuddin, S., Guillou, H., and Arnaud, N., 1998, A Neogene back-arc origin for the Banda Sea basins: geochemical and geochronological constraints from the Banda ridges (East Indonesia): *Tectonophysics*, vol. 298, p. 297-317.
- Honza, E., 1995, Spreading mode of backarc basins in the western Pacific; *Tectonophysics*, vol. 251, p. 139-152.
- Hoogewerff, J.A., Van Bergen, M.J., Vroon, P.Z., Hertgen, J., Wordel, R., Sneyers, A., Nasution, A., Varenkamp, J.C., Moens, H.L.E., and Mouchel, D., 1997, U-series, Sr-Nd-Pb isotope and trace-element systematics across an active island arc-continent collision zone: implications for the element transfer at the slab-wedge interface: *Geochim. et Cosmochim. Acta*, v. 61, p. 1057-1072.
- Hopson, C.A., and Frano, C.J., 1977, Igneous history of the Point Sal ophiolite, Southern California: Oregon Department of Geology and Mineral Industries Bulletin, vol. 95, p.161-183.
- Hopson, C.A., Mattinson, J.M., and Passagno, E.A., Jr., 1981, Coast Range Ophiolite, western California, *in*, Ernst, W.G., ed., *The geotectonic development of California Englewood Cliffs*: New Jersey, Prentice-Hall, p. 418-510.
- Hopson, C.A., Mattinson, J.M., Luyendyk, B.P., Beebe, W.J., Pessagno, E.A., Jr, Hull, D.M., Munoz, I.M., and Blome, C.D., 1997, Coast Range ophiolite; paleoequatorial ocean ridge lithosphere: American Association of Petroleum Geologists Pacific section meeting in AAPG Bulletin, vol. 81, no. 4, p. 687.
- Hull, D.M., Blome, C.D., Pessagno, E.A., Murchey, B.L., and Hagstrum, J.T., 1997, Paleomagnetism of Jurassic radiolarian chert above the Coast Range ophiolite at Stanley Mountain, California, and implications for its paleogeographic origins; discussion and reply: *Geological Society of America Bulletin*, vol. 109, p. 1633-1639.

- Hussong, D.M., and Uyeda, S., 1981, Tectonic processes and the history of the Mariana arc: a synthesis of the results of Deep Sea Drilling Project Leg 60, *in*, D.M. Hussong and Uyeda (eds.), Initial Report Deep Sea Drilling Program, vol. 60, pp. 909-929.
- Ikeda, Y., and Yuasa M., 1989, Volcanism in nascent back-arc basins behind the Shichito Ridge and adjacent areas in the Izu-Ogasawara arc, northwest Pacific: evidence for mixing between E-type MORB and island arc magmas at the initiation of back-arc rifting: *Contribution to Mineralogy and Petrology*, vol. 101., p. 377-393.
- Imlay, R.W., Dole, H.M., Wells, F.G., and Peck, D., 1959, Relations of certain upper Jurassic and lower Cretaceous Formations in southwestern Oregon: *Bulletin of the American Association of Petroleum Geologists*, vol. 43, no. 12, pp. 2770-2785.
- Ingersoll, R.V., and Schweickert, R.A., 1986, A plate-tectonic model for Late Jurassic ophiolite genesis, Nevadan orogeny and forearc initiation, northern California: *Tectonics*, vol. 5, p. 901-912.
- Ingersoll, R.V., 1979, Evolution of the Late Cretaceous forearc basin, northern and central California: *Geological Society of America*, vol. 90, p. 813-826.
- Irvine, T.N., 1982, Terminology for layered intrusions: *Journal of Petrology*, vol.23, p. 127-162.
- Jarvis, Kym E., 1990, A critical evaluation of two sample preparation techniques for low-level determination of some geologically incompatible elements by inductively coupled plasma - mass spectrometry; *Chemical Geology*, vol. 83, pp. 89-103.
- Jayko, A.S., Blake, M.C., Jr., and Harms, T., 1987, Attenuation of the Coast Range ophiolite by extensional faulting and nature of the Coast Range "thrust", California: *Tectonics*, vol. 6, p. 475-488.
- Jenner, G.A., Cawood, P.A., Rautenschlein, M., and White, W.M., 1987, Composition of Back-Arc Basin Volcanics, ValuFa Ridge, Lau Basin: Evidence for Slab-derived component in their Mantle Source: *Journal of Volcanology and Geothermal Research*, vol. 32, p. 209-222.

- Jenner, G.A., Longerich, H.P., Jackson, S.E., and Fryer, B.J., 1990, ICP-MS - a powerful tool for high precision trace element analysis in Earth Sciences: Evidence from analysis of selected U.S.G.S. reference samples, *Chemical Geology*, vol. 83, pp. 133-148.
- Jochum, K. P., Seufert, H. M., Midinet-Best, S., Rettmann, E., Schönberger, K., and Zimmer, M., 1988, Multi-element analysis by isotope dilution-spark source mass spectrometry (ID-SSMS): *Fresenius Zeitschrift für Analytische Chemie*, vol. 331, pp.104-110.
- Johnson, L.E., and Fryer, P., 1990, The first evidence for MORB-like lavas from the outer Mariana fore-arc: geochemistry, petrography and tectonic implications: *Earth and Planetary Science Letters*, vol. 100, p. 304-316.
- Johnson, M.C., and Rutherford, M.J., 1989, Experimental calibration of an Aluminum-in-hornblende geobarometer applicable to calc-alkaline rocks: *Transactions of the Geophysical Union, EOS*, vol. 69, p. 1511.
- Kamenetsky, V.S., Crawford, A.J., Eggins, S., and Mühe, R., 1997, Phenocrysts and melt inclusion chemistry of near-axis seamounts, Valu Fa Ridge, Lau Basin: insight into mantle wedge melting and the addition of subduction components: *Earth and Planetary Science Letters*, Vol. 151, p. 205-223.
- Kamenetsky, V.S., Sobolev, A.V., Joron, J.-L., and Semet, M.P., 1995, Petrology and geochemistry of Cretaceous ultramafic volcanics from East Kamtchatka: *Journal of Petrology*, vol. 36, 637-662.
- Karson, J.A., 1990, Seafloor spreading on the Mid-Atlantic Ridge: implications for the structure of ophiolites and oceanic lithosphere produced in slow-spreading environments, in Malpas, J., Moore, E.M., Panayiotou, A., and Xenophontos, C., (eds.), *Geological Survey Department Cyprus, Nicosia*, p. 547-555.
- Kent, R.C., 1972, The geology of the southeast quarter of the Bone Mountain quadrangle, Oregon: Portland, Oregon, Portland State University, M.S. thesis, pp. 132.

- Kingsley, R.H., and Schilling, J.-G., 1995, Carbon in Mid-Atlantic ridge basalt glasses from 28 degrees S to 63 degrees N; evidence for Carbon-enriched Azores mantle plume: *Earth and Planetary Science Letters*, vol. 129, p. 31-53.
- Kidd, R.G.W., and Cann, J.R., 1974, Chilling statistics indicate an oceanic-floor spreading origin for the Troodos complex, Cyprus: *Earth and Planetary Science Letters*, 24, 151-155.
- Klein, E.M., and Karsten, J.L., 1995, Ocean-ridge basalts with convergent-margin geochemical affinities from the Chile Ridge: *Nature*, vol. 374, p. 52-57.
- Kosanke, S.B., and Harper, G.D., 1996, High-T ductile deformation in 164 Ma ophiolitic basement of the Snow Camp terrane, SW Oregon: *Geological Society of America Abstracts with Program*, vol. 28, p. 83.
- Kosanke, S.B. Harper, G.D., and Heizler, M. 1999, Younger extrusive and intrusive volcanic arc rocks and Nevadan-age ductile deformation in the 164 Ma Coast Range ophiolite, SW Oregon: *Geological Society of America Abstracts with Programs*, vol. 31, p. A71.
- Lagabrielle, Y, Auzende, J-M., Eissen, J-P., Janin, M-C., and Cotton, J., 1994, Geology and geochemistry of a 800 m section through young upper oceanic crust in the North Fiji Basin (Southwest Pacific): *Marine Geology*, vol. 116, p. 113-132.
- Lagabrielle, Y., Roure, F., Coutell, A., Maury, R.C., Joron J.L., and Thonon, P. 1986, The Coast Range ophiolite (northern California): possible arc and back-arc basin remnants; their relations with the Nevadan orogeny; *Bulletin Société géologique France*, vol. 8, no. 6, p. 981-999.
- Laird, J., 1982, Amphiboles in metamorphosed basaltic rocks: greenschist facies to amphibolite facies, *in* Veblen, D.R. and Ribbe, P.H. (eds.), *Amphiboles: Petrology and experimental phase relations: Reviews in Mineralogy*, vol. 9B, Mineralogical Society of America, Washington D.C., p. 113-137.
- Law, B., Anders, D.E., Fouch, T.D., Pawlewica, M.J., Lickus, M.R., and Molenaar, C.M., 1984, Petroleum source rock evaluations of outcrop samples from Oregon and northern California, Oregon *Geology*, 46, 77-81.

- Lattard, D., 1995, Experimental evidence for the exsolution of ilmenite from titaniferous spinel: *American Mineralogist*, vol. 80, p. 9-10.
- Le Maitre, R.W., Bateman P., Dudek A., Keller, J., Lameyre Le Bas, M.J., Sabine, P.A., Schmid, R., Sørensen, H., A., Streckeisen, A., Wooley, A.R., and Zanettin, B., 1989, A classification of igneous rocks and glossary of terms: Blackwell, Oxford, London, Edinburgh, Boston, Melbourne, p. 1-197.
- Letterier, J., Maury, R.C., Thonon, P., and Girard, D., 1982, Clinopyroxene composition as a method of identification of the magmatic affinities of paleovolcanic series, *Earth Planet. Sci. Lett.*, v. 59, p. 139-154.
- Lisle, R.J., 1988, Romsa: A BASIC program for paleostress analysis using fault striation data: *Computers and Geosciences*, vol. 14, no. 2, p. 255-259.
- Lister, G.S., and Snoke, A.W., S-C mylonites: *Journal of Structural Geology*, vol. 6, p. 617-638.
- Liou, J.G., 1971, P-T stabilities of laumontite, wairakite, lawsonite, and related minerals in the system $\text{CaAl}_2\text{Si}_2\text{O}_8\text{-SiO}_2\text{-H}_2\text{O}$: *Journal of Petrology*, vol. 12, p. 379-411.
- Longerich, H.P., Jenner, G.A., Fryer B.J., Jackson, S.E., 1990, Inductively coupled plasma - mass spectrometric analysis of geological samples: A critical evaluation based on a case study: *Chemical Geology*, vol. 83, pp. 105-118.
- Ludden, J.N., and Thompson, G., 1979, An evaluation of the behavior of the rare earth elements during the weathering of sea floor basalt: *Earth and Planetary Science Letters.*, vol. 43 p. 85-92.
- MacDonald, K.C., Fox, P.J., Perrain, L.J., Eisen, M.F., Haymon, R.M., Miller, S.P., Carbotte, S.M., Cormier, M.-H., and Shor, A.N., 1988, A new view of the mid-ocean ridge from the behavior of ridge axis discontinuities: *Nature*, vol. 335, p. 217-225.
- MacPherson, G.J., Phipps S.P. and Grossman J.N., 1990, Diverse sources for igneous blocks in Franciscan Melanges, California Coast Ranges: *Journal of Geology*, vol. 98, p. 845-862.
- MacPherson, G.J., 1983, The Snow Mountain volcanic complex: An on-land seamount in the Franciscan terrain, California: *Journal of Geology*, vol. 91, p. 73-92.

- Maillet P., Monzier, M., Eissen, J.-P., and Louat R., 1989, Geodynamics of an arc-ridge junction: the case of the New Hebrides Arc, North Fiji Basin: *Tectonophysics*, vol. 165, p. 251-268.
- Maniar, P.D., and Piccoli, P.M., 1989, Tectonic discrimination of granitoids: *Geological Society of America Bulletin*, vol. 101, p. 635-643.
- Marrett, R.A., and Allmendinger, 1990, Kinematic analysis of fault-slip data: *Journal of Structural Geology*, vol. 12, p. 973-986.
- Matveyenko, V.V., and Khain, V.V., 1988, Vesicularity of basalts as an index of volcanic activity of back-arc basins: *Oceanology*, vol. 28, p. 203-207.
- McCarthy, J., Mutter, J.C., Morton, J.L., Sleep, N.H., and Thompson, G.A., 1988, Relic magma chamber structure preserved within the Mesozoic North Atlantic crust?: *Geological Society of America Bulletin*, vol. 100, p. 1423-1436.
- McDougall, I., and Harrison, T.M., 1988, *Geochronology and thermochronology by the $^{40}\text{Ar}/^{39}\text{Ar}$ method*: Oxford University Press, Oxford, United Kingdom, pp. 212.
- McLaughlin, R.J., Blake, M.C., Jr., and Griscom, A., 1988, Tectonics of formation, translation and dispersal of the Coast Range ophiolite of California: *Tectonics*, vol. 7, p. 1033-1056.
- McLaughlin, R.J., Kling, S.A., Poore, R.Z., McDougall, K., and Beutener, E.C., 1982, Post-middle Miocene accretion of Franciscan rocks, northwestern California: *Geological Society of America Bulletin*, vol. 93, pp. 595-605.
- Means, W.D., 1981, The concept of steady state foliation: *Tectonophysics*, vol. 78, p. 179-199.
- Means, W.D., 1987, A newly recognized type of slickenside striation: *Journal of Structural Geology*, vol. 9, p. 585-590.
- Means, W.D., 1989, A construction for shear stress on a generally-oriented plane: *Journal of Structural Geology*, vol. 11, no. 5, p. 625-627.
- Means, W.D., and Park, Y., 1994, New experimental approach to understanding igneous texture: *Geology*, vol. 22, p. 323-326.

- Means, W.D., and Park, Y., 1993, Analog experiments suggest need for caution in interpreting strains and flow processes from fabrics in plutons: Geological Society of America Abstracts with Programs, vol. 25, no. 6., p. A96.
- Meffre, S., Aitchison, J.C., and Crawford, A.J., 1996, Geochemical evolution and tectonic significance of boninites and tholeiites from the Koh ophiolite, New Caledonia: Tectonics, vol. 15, no. 1, p. 67-83.
- Menzies, M., Blanchard, D., and Jacobs, J., 1977a, Rare earth and trace element geochemistry of metabasalts from the Point Sal ophiolite, California: Earth and Planetary Science Letters, vol. 37, p. 203-215.
- Menzies, M., Blanchard, D., Brannon, J., Korotev, R., 1977b, Rare Earth and trace element geochemistry of a fragment of Jurassic seafloor, Point Sal, California: Geochimica and Cosmochimica Acta, vol. 41, p. 1419-1430.
- Miller, M.M., and Saleeby, J.B., 1987, Detrital Zircon studies of the Galice Formation: Common provenance of strata overlying the Josephine ophiolite and the Rogue Island arc, western Klamath Mountains, terrane: Geological Society of America Abstract with Programs, vol. 19, p. 772-773.
- Minshull, T.A., and Hall, B.D., 1997, Geometry of a mid-ocean-ridge normal fault: Geology, vol. 25, p. 835-838.
- Miyashiro, A., 1974, Volcanic rock series in island arcs and active continental margins: American Journal of Science, vol. 274, p. 321-355.
- Molenaar, C.M., Depositional relations of Umpqua and Tyee Formations (Eocene), southwestern Oregon: American Association of petroleum Geologists Bulletin, vol. 69, p. 1217-1229.
- Monzier, M., Danyushevsky, L.V., Crawford, A.J., Bellon, H., and Cotton, J., 1993, High-Mg andesites from the southern termination of the New Hebrides island arc, SW Pacific: Journal of Volcanology and Geothermal Research, vol. 57, p. 193-217.
- Morton J.L., and Sleep, N.H., 1985, A mid-ocean ridge thermal model: Constraints on the volume of axial hydrothermal heat flux: Journal of Geophysical Research, vol. 90, p. 11345-11353.

- Mottl, M.J., 1983, Metabasalts, axial hot springs, and structure of hydrothermal systems at mid-ocean ridges: Geological Society of America Bulletin, vol. 94, p. 161-180.
- Mutter, J.C., and Karson, J.A., 1992, Structural Processes at slow-spreading ridges: Science, vol 257, p. 627-634.
- Murton, B.J., Peate, D.W., Arculus, R.J., Pearce, J.A., van-der-Laan, S.R., 1992, Trace element geochemistry of volcanic rocks from Site 786; the Izu-Bonin forearc, *in*, Dearmont, L.H., Mazullo, E.K., Stewart, N.J. and Winkler, W.R., (eds.), Proceedings of the Ocean Drilling Program, Scientific Results, vol. 125, p. 211-235.
- Nicholas, A., 1992, Kinematics in Magmatic Rocks with special Reference to Gabbros: Journal of Petrology, vol. 33, p. 891-915.
- Nicholas, A., Reuber, I., and Benn, K., 1988, A new magma chamber model based on structural studies in the Oman ophiolite: Tectonophysics, vol. 151, p. 87-106.
- Nicolas, A., Freydier, C., Godard, M., and Vauchez, A., 1993, Magma chambers at oceanic ridges; how large?: Geology, vol. 21, p. 53-56.
- Niem, R.A., and Niem, W.A., 1990, Geology and oil, gas and coal resources, southern Tyee Basin, southern Coast Range, Oregon, Open-File Report 0-89-3, Department of Geology and Mineral Industries, Portland, Oregon.
- Norell, G.N., Tiexell, A., and Harper, G.D., 1989, Microstructure of serpentinite mylonites from the Josephine ophiolite and serpentinization in retrogressive shear zones, California: Geological Society of America Bulletin, vol. 101, p. 673-682.
- Norell G.T., and Harper, G.D., 1988, Detachment faulting and amagmatic extension at mid-ocean ridges: The Josephine ophiolite as an example: Geology, vol. 16, p. 827-830.
- Passchier, C.W., and Trouw, R.A.J., 1996, Microtectonics: Springer, Berlin, Heidelberg, pp. 289.
- Passchier, C.W, and Williams, P.R., 1996, Conflicting shear sense indicators in shear zones; the problem of non-ideal sections: Journal of Structural Geology, vol. 18, p. 1281-1284.

- Page, B.M., 1972, Oceanic crust and mantle fragment in subduction complex near San Luis Obispo, California: Geological Society of America Bulletin, vol. 83, p. 957-972.
- Parson, L.M., and Wright, I.C., 1996, The Lau-Havre-Taupo back-arc basin: A southward-propagating, multi-stage evolution from rifting to spreading: Tectonophysics, vol. 263, p. 1-22.
- Parson, L.M., Pearce, J.A., Murton, B.J., Hodkinson, R.A., and RRS Charles Darwin Scientific Party, 1990, Role of ridge jumps and ridge propagation in the tectonic evolution of the Lau back-arc basin, southwest Pacific, *in* Hawkins, J., Parson, L., Allan, J., et al., (eds.), Proceedings of the Ocean Drilling Program, Scientific Results, College Station, TX (Ocean Drilling Program), vol. 135, p. 819-828.
- Parson L.M., Rothwell, R.G., and MacLeod, C.J., 1994, Tectonics and sedimentation in the Lau Basin (southwest Pacific), *in* Hawkins, J., Parson, L., Allan, J., et al., (eds.), Proceedings of the Ocean Drilling Program, Scientific Results, College Station, TX (Ocean Drilling Program), vol. 135, p. 9-22.
- Parson, L.M., and Hawkins, J.W., 1994, Two-stage ridge-propagation and geological history of the Lau backarc basin: *in* Hawkins, J., Parson, L., Allan, J., et al., (eds.), Proceedings of the Ocean Drilling Program, Scientific Results, College Station, TX (Ocean Drilling Program), vol. 135, p. 819-828.
- Paterson, S.R., Vernon, R.H., and Tobisch, O.T., 1989, A review of criteria for the identification of magmatic and tectonic foliations in granitoids: Journal of Structural geology, vol. 11 p. 349-363.
- Paterson, S.R., and, Miller, R.B., 1998, Regional tectonics of the Mount Stuart batholith, Washington, determined using aluminum-in-hornblende barometry: implications for northward translation of Baja British Columbia: Discussion and reply: Geological Society of America Bulletin, vol. 110, p. 685-690.
- Pessagno, E.A., and Blome, C.D., 1990, Implications of new Jurassic stratigraphic, geochronometric, and paleolatitudinal data from the western Klamath terrane (Smith River and Rogue Valley subterranean): Geology, vol. 18, p. 665-668.

- Pessagno, E.A., Jr., Blome, C.D., Hull, D.M., and Six, W.M., 1993, Jurassic radiolaria from the Josephine ophiolite and overlying strata, Smith River subterrane (Klamath Mountains), northwestern California and southwestern Oregon: *Micropaleontology*, vol. 39, p. 93-166.
- Pessagno, E.A., Jr., Hopson, C.A., Mattinson, J.M., Blome, C.D., Luyendyk, B.P., Hull, D.M., and Beebe, W., 1996, Coast Range ophiolite and its sedimentary cover (California Coast Ranges): Jurassic stratigraphy and northward tectonic transport: *Tectonics*
- Perfit, M.R., Langmuir, C.H., Baekisapa, M., Chappell, B., Johnson, R.W., Staudigel, H., and Geological Research Division A-015 Scripps Institution of Oceanography, 1987, Geochemistry and petrology of volcanic rocks from the Woodlark Basin: addressing questions of ridge subduction, in Taylor, B., and Exon, N.F., (eds.), *Marine Geology, Geophysics, and Geochemistry of the Woodlark Basin-Solomon islands: Circum Pacific Council for Energy and Mineral Resources Earth Science Series*, vol. 7., p. 113-154.
- Petit, J.P., 1987, Criteria for the sense of movement of fault surfaces in brittle rocks: *Journal of Structural Geology*, vol. 9, p. 597-608.
- Pearce, J.A., Harris, N.B.W., and Tindle, A.G., 1984b, Trace element discrimination diagrams for the tectonic interpretation of granitic rocks: *Journal of Petrology*, vol. 25, p. 956-983.
- Pearce, J.A., 1982, Trace element characteristics of lavas from destructive plate boundaries, *in* Thorpe, R.S., (ed.), *Andesites: John Wiley and Sons*, p. 525-548.
- Pearce, J.A., 1983, Role of the sub-continental lithosphere in magma genesis at active continental margins, *in* Hawksworth, C.J., and Norry, M.J., (eds.), *Continental Basalts and Mantle Xenoliths: Shiva Publishing, Nantwich, Great Britain*, p. 230-249.
- Pearce, J.A., and Norry, M.J., 1979, Petrogenetic implications of Ti, Zr, Y, and Nb variations in volcanic rocks: *Contributions to Mineralogy and Petrology*, vol. 69, p. 33-47
- Pearce, J.A., and Parkinson, I. J., 1993, Trace element models for mantle melting: application to volcanic arc petrogenesis, *in* H. Prichard, H.M., Alabaster, T., Harris N.B.W., and Neary, C.R., (eds.),

- Magmatic Processes and Plate Tectonics: Geological Society London Special Publication 76 (I.G. Gass Memorial Volume), p. 373-403.
- Pearce, J.A., and Peate, D.W., 1995, Tectonic implications of the composition of volcanic arc magmas: Annual Reviews of Earth and Planetary Sciences, vol. 23, p. 251-285.
- Pearce, J.A., Baker, P.E., Harvey, P.K. and Luff, I.W., 1995a, Geochemical evidence for subduction fluxes, mantle melting and fractional crystallization beneath the South Sandwich island arc: Journal of Petrology, vol. 36, no. 4, p. 1073-1109.
- Pearce, J.A., Ernewein, M., Bloomer, S.H., Parson, L.M., Murton, B.J., and Johnson, L.E., 1995b, Geochemistry of Lau Basin volcanic rocks: influence of ridge segmentation and arc proximity, *in* Smellie, J.L., (ed.), Volcanism Associated with Extension at Consuming Plate Margins: Geological Society of America Special Publication No. 81, p. 53-75.
- Pearce, J.A., Lippard, S.J., and Roberts, S., 1984a, Characteristics and tectonic significance of supra-subduction zone ophiolites, *in* Kokelaar, B.P., and Howells, M.F., (eds.), Geology of Marginal Basins: Geological Society of London, Special Publication 16, p 77-94.
- Peate, D.W., Pearce, J.A., Hawkesworth, C.J., Colley, H., Edwards, C.M.H. and Hirose, K., 1997, Geochemical variations in Vanuatu arc lavas: the role of subducted material and a variable mantle wedge composition: Journal of Petrology, vol. 38, p. 1331-1358.
- Penrose conference report (anonymous), 1972, Penrose field conference on ophiolites: Geotimes vol. 17, p. 24-25.
- Pegram, W.P., 1990, Development of continental lithospheric mantle as reflected in the chemistry of the Mesozoic Appalachian Tholeiites, U.S.A.: Earth and Planetary Science Letters vol. 97, p. 316-333.
- Pearce, J.A., 1996, A user's guide to basalt discrimination diagrams, *in* Wyman, D.A. (ed.), Trace element geochemistry of volcanic rocks: application for massive sulfide exploration: Geological Association of Canada Short Course Notes vol. 12, p. 79-113.

- Philipot, P., and Selverstone, J., 1991, Trace-element-rich brines in eclogite veins: implications for fluid composition and transport during subduction: *Contributions to Mineralogy and Petrology*, vol. 106, p. 417-430.
- Phipps, S. P., 1984, Ophiolitic olistostromes in the basal Great Valley sequence, Napa County, northern California Coast Ranges, in Raymond, L., ed., *Melanges: Their Nature, Origin, and Significance: Geological Society of America Special Paper 198*, 103-125.
- Phipps, S.P., and Unruh, 1992, Crustal-scale wedging beneath an imbricate roof-thrust system: Geology of a transect across the western Sacramento Valley and northern Coast Ranges, California, in, Bartow, A., Erskine, M., and Unruh, J., (eds.), *Field Guide to the Tectonics of the Boundary between the California Coast Ranges and the Great Valley of California: Pacific Section, Society of Economic Paleontologists and Mineralogists Field Trip[Guide Book: Bakersfield, CA, Pacific Section, American Association of Petroleum Geologists*, p. 117-140.
- Pichavant M., and Montel, M.-J., 1988, Petrogenesis of a two-mica ignimbrite suite: the Macusani volcanics, SE Peru: *Transactions of the Royal Society Edinburgh Earth Sciences*, vol. 79, p. 197-207.
- Pichavant M., Herrera, J.V., Boulmier, S., Brique, L., Joron, J.-L., Juteau, M., Marin, L., Michard, L., Sheppard, S.M.F., Treuil, M., and Vernet, M., 1987, The Macusani glasses, SE Peru: evidence of fractionation in peraluminous magmas, *in*, Mysen, B.O., ed., *Magmatic processes: Physicochemical Principles: Geol. Society of London Special Publication*, vol. 241, p 127-144.
- Piwinskii, A.J., 1973, Experimental studies bearing on the origin of the Central and Southern Coast Range granitoids, California: *Tschermaks Mineralogische and Petrographische Mitteilungen*, vol. 20, p. 107-130.
- Plank T, and Langmuir, C.H., 1988, An evaluation of the global variations in the major element chemistry of arc basalts: *Earth and Planetary Science Letters*, vol. 90, p. 349-370.
- Poli, S., 1993, The amphibolite, eclogite transformation: an experimental study on basalt: *American Journal of Science*, vol. 293, p. 1061-1107.

- Poli, S., and Schmidt, M.W., 1992, A comment on "Calcic amphibole equilibria and a new amphibole-plagioclase geothermometer" by J.D. Blundy and T.J.B. Holland (Contrib Mineral Petrol (1990) 104: 208-224): Contributions to Mineralogy and Petrology, vol. 111, p. 273-278.
- Powell, R., 1984, Inversion of the assimilation and fractional crystallization (AFC) equations; characterization of contaminants from isotopes and trace element relationships in volcanic suites: Journal of the Geological Society of London, vol. 141, p. 447-452.
- Ramp, L., 1969, Dothan(?) fossils discovered: The Ore Bin, vol. 31, no. 12, p. 256-264.
- Ramp, L., Schlicker, H.G., and Gray, J.J., 1977, Geology, Mineral Resources and rock material of Curry County, Oregon: Oregon Department of Geology and Mineral Industries Bulletin vol. 93, pp. 79.
- Ramp, L. and Gray, F., 1980, Sheeted dikes of the Rogue Wilderness, Oregon: Oregon Geology, vol. 42, no. 7 p. 119-124.
- Ramp, L., and Moring, B., 1986, Reconnaissance Geologic Map of the Marial Quadrangle: U.S. Geological Survey Miscellaneous Field Studies Map MF-1735, scale 1:62:500
- Rapp, R.P, Watson, E.B., and Miller, C.F., 1991, Partial melting of amphibolite and eclogite and the origin of Archean trondhjemites: Precambrian Research, 51, p. 1-25.
- Raymond, L.A., 1984, Classification of melanges: Geological Society of America Special Paper 198, p. 7-20.
- Reches, Z., 1987, Determination of the tectonic stress tensor from slip along faults that obey the Coulomb yield condition: Tectonic, vol. 6, p. 849-861.
- Reston, T.J., Ruoff, O., McBride, J.H., Ranero, C.R., and White, R.S., Detachment and steep normal faulting in Atlantic oceanic crust west of Africa: Geology, vol. 24, p. 811-814.
- Riddle, C., Vander Voet, A., and Doherty, W., 1988, Rock analysis using inductively coupled plasma mass spectrometry: a review: Geostandard Newsletters, vol. 12, page 203-234.
- Ring, U., and Brandon, M.T., Kinematic data for the Coast Range fault and implications for exhumation of the Franciscan subduction complex: Geology, vol. 22, p. 735-738.

- Ringwood, 1974, A.E., The petrological evolution of island arc systems: *Journal of the Geological Society of London*, vol. 130, p. 183-204.
- Robertson, A.H.F., 1989, Paleooceanography and tectonic setting of the Jurassic Coast Range ophiolite, central California: evidence from the extrusive rocks and volcanoclastic sediment cover: *Marine and Petroleum Geology*, vol. 6, p. 194-220.
- Robertson, A.H.F., 1990, Sedimentology and tectonic implications of ophiolite-derived clastics overlying the Jurassic Coast Range ophiolite, northern California: *American Journal of Science*, vol. 290, p. 109 - 163.
- Robinson, P., Schumacher, J.C., Spear, F.S., 1982, Formulation of electron probe analyses, *in* Veblen, D.R. and Ribbe, P.H. (eds.), *Amphiboles: Petrology and experimental phase relations: Reviews in Mineralogy*, vol. 9B, Mineralogical Society of America, Washington D.C., p. 6-9.
- Rollinson, H., 1993, *Using Geochemical Data: Evaluation, presentation, interpretation*: Longman Group, Essex, England, 352 pp.
- Ross, M.E., 1986, Flow differentiation, phenocryst alignment, and compositional trends within a dolerite dike at Rockport, Massachusetts: *Geological Society of America Bulletin*, vol. 97, p 232-240.
- Roure, F., and Blanchet, R., 1983, A geological transect between the Klamath Mountains and the Pacific ocean (Southwestern Oregon): A model for paleosubduction: *Tectonophysics*, vol. 91, p. 53-72.
- Rutherford, M.J., and Johnson, M.C., 1992, Comment on Blundy and Holland's (1990) "Calcic amphibole equilibria and a new amphibole-plagioclase geothermometer": *Contributions to Mineralogy and Petrology*, vol. 111, p. 266-268.
- Rud, J.O., 1971, The geology of the southwest quarter of the Bone Mountain quadrangle, Oregon: Portland, Oregon, Portland State University, M.S. thesis, pp. 73.
- Sajona, F.G., Maury, R.C., Bellon, H., Cotton, J., Defant, M.J., and Pubellier, M., 1993, Initiation of subduction and the generation of slab melts in western and eastern Mindanao, Philippines: *Geology*, vol. 21, p. 1007-1010.

- Saleeby, J.B. and Harper, G.D., 1993, Tectonic relations between the Galice Formation and the schists of Condrey Mountain, Klamath Mountains, northern California, *in* Dunne, G., and McDougall, K., (eds.), Mesozoic paleogeography of the western United States-II: Pacific section SEPM, Book 71, p. 61-80.
- Saleeby, J.B., 1984, Pb/U zircon ages from the Rogue River area, western Jurassic belt Klamath Mountains, Oregon: Geological Society of America Abstracts with Program, v. 16, p. 331.
- Saleeby, J.B., Busby-Spera, C., Oldow, J.S., Dunne, G.C., Wright, J.E., Cowan, D.S., Walker, N.W., and Allmendinger, R.W., 1992, Early Mesozoic tectonic evolution of the western U.S. Cordillera, *in* Burchfield, B.C., Lipman, P.W., Zoback, M.L., (eds.), The Cordilleran orogen; conterminous U.S.: Boulder Colorado, Geological Society of America; Geology of North America, vol. G-3, p. 107-168.
- Saleeby, J.B., Blake, M.C., and Coleman, R.G., 1984, Pb/U Zircon Ages on Thrust Plates of the West Central Klamath Mountains and Coast Ranges, Northern California and Southern Oregon: EOS Transactions, American Geophysical Union, vol. 65, p. 1147.
- Saleeby, J.B., Shaw, H.F., Niemeyer, S., Moores, E.M., and Edelman, S.H., 1989, U/Pb, Sm/Nd, and Rb/Sr geochronological and isotopic study of northern Sierra Nevada ophiolitic assemblages, California: Contributions to Mineralogy and Petrology, vol. 102, p. 205-220.
- Saleeby, J.B., Harper, G.D., Snoke, A.W., and Sharp, W.D., 1982, Time relations and structural-stratigraphic patterns in ophiolite accretion, west central Klamath Mountains, California: Journal of Geophysical Research, vol. 87, p. 3831-3848.
- Saunders, A.D. Tarney, J. and Weaver, S.D., 1980, Transverse geochemical variations across the Antarctic Peninsula: implications for the genesis of calc-alkaline magmas: Earth and Planetary Science Letters vol. 46, p. 344-360.
- Saunders, A.D., Norry, M.J., and Tarney, J., 1991, Fluid influence on the trace element compositions of subduction zone magmas: Royal Society of London Philosophical Transactions, series A, vol. 117, p. 377-392.

- Schiffmann, P., and Smith, B.M., 1988, Petrology and oxygen isotope-geochemistry of a fossil sea water hydrothermal system within the Solea graben, northern Troodos ophiolite, Cyprus: *Journal of Geophysical Research*, vol. 93, p. 4612-4624.
- Schiffmann, P., Evarts, R.C., Williams, A.E., and Pickthorn, W.J., 1991, Hydrothermal metamorphism in Oceanic Crust from the Coast Range ophiolite of California: Fluid-rock interaction in a rifted island arc, in Peters., T., Adolphe, N., and Coleman, R.J., (eds.), *Ophiolite genesis and evolution of the Oceanic Lithosphere: Dordrecht-Boston-London, Netherlands*, p. 399-425.
- Schimmrich, S.H., 1991, Evaluation of computational methods of paleostress analysis using fault striation data, M.S. thesis, State University of New York at Albany, 394 pp.
- Schmidt, M.W., 1992, Amphibole compositions in tonalite as a function of pressure: An experimental study at 650°C: *Contributions to Mineralogy and Petrology*, vol.110, p. 304-310.
- Sclater J.G., Anderson, R.N., and Bell, L.M., 1971, Elevation of Ridges and Evolution of the Central Eastern Pacific: *Journal of Geophysical Research*, vol. 76, no. 32, p. 7888-7915.
- Sclater, J.G., 1972, Heat Flow and elevation of the Marginal Basins of the Western Pacific: *Journal of Geophysical Research*, vol. 77, no. 29, p. 5688-5696.
- Seewald, J.S., and Seyfried, W.E., Jr., 1990, The effect of temperature on metal mobility in seafloor hydrothermal systems: constraints from basalt alteration experiments: *Earth and Planetary Science Letters*, vol. 101, p. 388-403.
- Seiders, V.M., and Blome, C.D., 1988, Implications of upper Mesozoic conglomerate for suspect terrane in western California and adjacent areas: *Geological Society of America Bulletin*, vol. 100, p. 374-391.
- Seyfried, W.E., Jr., 1987, Experimental and theoretical constraints on hydrothermal alteration processes at mid-ocean ridges: *Annual Reviews Earth and Planetary Sciences*, vol. 15, p. 317-335.

- Seyfried, W.E., Berndt, M.E., and Seewald, J.S., 1988, Hydrothermal alteration processes at mid-ocean ridges: constraints for diabase alteration, experiments, hot-spring fluids and composition of the oceanic crust: *Canadian Mineralogist*, vol. 26, p. 787-804.
- Shand, S.J., 1951, *Eruptive rocks*: J. Wiley, New York, pp.
- Shervais J.W, 1990; Island arc and oceanic crust ophiolites: Contrasts in the petrology, geochemistry and tectonic style of ophiolite assemblages in the California Coast Ranges, *in* Malpas, J., Moores, E., Panayiotou A., and Xenophontos, C., *eds.*, *Ophiolites: Oceanic Crust Analogues*: Nicosia, Cyprus, Geological Survey Department of Cyprus, p. 507-520.
- Shervais, 1982, Ti-V plots and the petrogenesis of modern and ophiolitic lavas: *Earth and Planetary Science letters*, vol. 59, p. 101-118.
- Shervais, J. W., and Kimbrough, D.L., 1985, Geochemical evidence for the tectonic setting of the Coast Range ophiolite: A composite island arc - oceanic crust terrane in western California: *Geology*, vol. 13, p. 35-38.
- Shervais, J. W., and Kimbrough, D.L., 1987, Alkaline and transitional subalkaline metabasalts in the Franciscan Complex melange, California: *Geological Society of America Special Paper* 215, p. 165-182.
- Shervais, J.W, 1990, Island arc and oceanic crust ophiolites: Contrasts in the petrology, geochemistry and tectonic style of ophiolite assemblages in the California Coast Ranges, *in* Malpas, J., Moore, E.M., Panayiotou, A., and Xenophontos, A., (eds.), *Ophiolites: oceanic crustal analogues*: Geological Survey Department, Nicosia, Cyprus, p. 507-520.
- Shervais, J.W., Murchey, B., Kimbrough, D.L., Hanan, B.B., and Renne, P., in review, New insights into the origin and development of the Coast Range ophiolite, California.
- Shervais J.W, 1990; Island arc and oceanic crust ophiolites: Contrasts in the petrology, geochemistry and tectonic style of ophiolite assemblages in the California Coast Ranges, *in* Malpas, J., and development of the Coast Range ophiolite, California.

- Schiffman, P., and Smith, B.M., 1988, Petrology and oxygen isotope geochemistry of a fossil seawater hydrothermal system within the Solea Graben, northern Troodos ophiolite, Cyprus; *Journal of Geophysical Research, B, Solid Earth and Planets*, vol. 93, no. 5, p. 4612-4624.
- Sigurdsson, I.A., Kamenetsky, V.S., Crawford, A.J., Eggins, S.M., and Zlobin, S.K., 1993, Primitive Island Arc and Oceanic Lavas from the Hunter-Ridge Fracture Zone. Evidence from Glass, Olivine and Spinel compositions: *Mineralogy and Petrology* vol. 47, p. 149-169.
- Sibson, R.H., 1977, Fault rocks and fault mechanisms: *Journal of the Geological Society of London*, vol. 133, p. 190-213.
- Simpson, C., and Schmid, S.M., 1983, An evaluation of criteria to determine the sense of movement in sheared rocks: *Geological Society of America Bulletin*, vol. 94, p. 1281-1288.
- Simpson, C., 1986, Determination of movement sense in mylonites: *Journal of Geological Education*, vol. 34, p. 246-261.
- Sinton, J. M., Wilson, D.S., Christie, D.M., Hey, R.N., and Delaney, J.R., 1983, Petrologic consequences of rift propagation on ocean spreading ridges: *Earth and Planetary Science Letters*, vol. 62, p. 193-207.
- Sisson, T.W., and Grove, T.L., 1993a, Experimental investigation of the role of H₂O in calc-alkaline differentiation and subduction zone magmatism: *Contributions to Mineralogy and Petrology*, vol. 113, p. 143-166.
- Sisson, T.W., and Grove, T.L., 1993b, Temperatures and H₂O contents of low-MgO high-Al basalts: *Contributions to Mineralogy and Petrology*, vol. 113, p. 167-184.
- Sleep, N.H., 1975, Formation of Oceanic Crust: Some Thermal Constraints: *Journal of Geological Research*, vol. 80, no. 29, p. 4037-4042.
- Sliter, W.V., Jones, D.L., and Throckmorton, C.K., 1984, Age and correlation of the Cretaceous Hornbrook Formation, California and Oregon, in, Nilson, Tor H., *Geology of the Upper Cretaceous Hornbrook Formation, Oregon and California: Pacific Section Society of Economic Paleontologists and Mineralogists*, vol. 42, p. 89-98.

- Sobolev, A., and Danyushevsky, L.V., 1994, Petrology and Geochemistry of Boninites from the North Termination of the Tonga Trench: Constraints on the Generation Conditions of Primary High-Ca Boninite Magmas: *Journal of Petrology*, vol. 35, p. 1183-1211.
- Spear, F.S., 1981, An experimental study of hornblende stability and compositional variability in amphibolites: *American Journal of Science*, vol. 281, p. 697-734.
- Spear, F.S., 1993, *Metamorphic Phase Equilibria and Pressure-Temperature-Time Paths: Mineralogical Society of America (Monograph)*, Washington, DC, pp. 799.
- Spear, F.S., and Kimball, C., 1984, RECOMP - a Fortran IV program for estimating Fe³⁺ contents in amphiboles: *Computers in Geology*, vol. 10, p.317-325.
- Staudigel, H., Plank, T., White, B., and Schmincke, H-U., 1996, Geochemical Fluxes during seafloor alteration of the basaltic upper oceanic crust: DSDP Sites 417 and 418, *in*, Bebout, G.E., Scholl, D.W, Kirby, S.H., and Platt, J.P., *eds.*, *Subduction Top to Bottom: American Geophysical Union, Geophysical Monograph 96*, p. 19-36.
- Stern, R.J., and Bloomer, S.H., 1992, Subduction zone infancy: Example from the Eocene Izu-Bonin-Mariana and Jurassic California arcs: *Geological Society of America Bulletin*, vol. 104, p. 1621-1636.
- Stern, R.J., Jackson, M.C., Fryer, P., and Ito, E., 1993, O, Sr, Nd, and Pb isotopic composition of the Kasuga Cross-Chain in the Mariana Arc: a new perspective on the K-h relationship: *Earth and Planetary Science Letters*, vol. 119, p. 459-475.
- Stern, R.J., Lin, P-N., Morris, J.D., Jackson, M.C., Fryer, P., Bloomer, S.H., and Ito, E., 1990, Enriched back-arc basin basalts from the northern Mariana Trough: implications for the magmatic evolution of back-arc basins: *Earth and Planetary Science Letters*, vol. 100, p. 210-225.
- Stern, T.W., Bateman, P.C., Morgan, B.A., Newell, M.F., and Peck, D.L., 1981, Isotopic U-Pb ages of zircon from the granitoids of the central Sierra Nevada, California: *U.S. Geological Survey Professional Paper 1185*, pp. 17.

- Stolper, E., and Newman, S., 1994, The role of water in the petrogenesis of Mariana trough magmas: Earth and Planetary Science Letters, vol. 121, p. 293-325.
- Stolz, A.J., Jochum, K.P., Spettel, B., and Hofmann, A.W., 1996, Fluid- and melt-related enrichment in the subarc mantle: Evidence from Nb/Ta variations in island-arc basalts: Geology, vol. 24, no. 7, p. 587-590.
- Stormer J.C., and Nicholls, J., 1978, XLFRAC: a program for the interactive testing of magmatic differentiation models: Computers and Geosciences, vol. 4, pp. 143-159.
- Streckeisen, A., 1973, Classification and Nomenclature of Plutonic Rocks: Geologische Rundschau, Band 63, p. 773-786
- Streckeisen, A., 1976, To each plutonic rock its proper name: Earth Science Reviews, vol. 12, p. 1-33.
- Sun, S.-s., and McDonough, W.F., 1989, Chemical and isotopic systematics of oceanic basalts: implications for mantle composition and processes, *in* Saunders, A.D., and Norry, M.J., (eds.), Magmatism in the Ocean Basins: Geological Society Special Publication No. 42, p. 313-345.
- Suppe, J., 1979, Structural interpretation of the southern part of the northern Coast Ranges and Sacramento Valley, California: Summary: Geological Society of America Bulletin, vol. 90, p. 327-330.
- Tatsumi, Y., Hamilton, D.L., and Nesbitt, R.W., 1986, Chemical characteristics of fluid phase released from a subducted lithosphere and origin of arc magma: Evidence from high-pressure experiments and natural rocks: Journal of Volcanology and Geothermal Research, vol. 29, p. 294-309.
- Taylor, B, 1992, Rifting and the volcanic-tectonic evolution of the Izu-Bonin-Mariana arc; *in* Taylor, B, Fujioka., et al. (eds.), Proceedings of the Ocean Drilling Program, Scientific results, vol. 126, p. 627-648.
- Taylor, R.N., Murton, B.J., and Nesbitt, R.W., 1992, Chemical transects across intra-oceanic arcs: implications for the tectonic setting of ophiolites, *in*, Parson, L.M., Murton, B.J., and Browning, P., (eds.), Ophiolites and their modern Analogues: Geological Society Special Publication No. 60, p. 117-132.

- Tröger, W.E., 1974, *Optische Bestimmung der wichtigsten gesteinsbildenden Minerale*: Umschau Verlag, Frankfurt, Germany, 308 pp.
- Umino, S., 1986, Magma mixing in boninite sequence of Chichijima, Bonin Islands, *Journal of Volcanological and Geothermal Research*, vol. 29, p. 125-157.
- Unruh, J.R., Ramirez, V.R., Phipps, S.P., Moores, E., 1991, Tectonic wedging beneath fore-arc basins: Ancient and modern examples from California and the Lesser Antilles: *GSA Today*, vol. 1, p. 185-190.
- Upadhyay, H.D., and Neale, 1979, On the tectonic regimes of ophiolite genesis: *Earth and Planetary Science Letters*, vol. 43, p. 93-102.
- Valsami, E., and Cann, J.R., 1992, Mobility of rare earth elements in zones of intense hydrothermal alteration in the Pindos ophiolite, Greece, *in*, Parson, L.M., Murton, B.J., and Browning, P., (eds.), *Ophiolites and their modern oceanic analogues: Geological Society Special Publication No. 60.*, p. 219-232.
- Van der Molen, I., and Paterson, M.S., 1979, Experimental deformation of partially melted granite: *Contribution to Mineralogy and Petrology*, vol. 70, p. 299-318.
- Vernon, R.H., 1984, Microgranitoid enclaves in granites - globules of hybrid magma quenched in a plutonic environment: *Nature*, vol. 309, p 438-439.
- Vernon, R.H., 1991, Interpretation of microstructures of microgranitoid enclaves, *in* Didier, J., and Barbarin, B., (eds.), *Enclaves and granite petrology*: Elsevier, Amsterdam, New York, p. 277-291.
- Vernon, R.H., Etheridge, M.A., and Wall, V.J., 1988, Shape and microstructure of microgranitoid enclaves: indicators of magma mingling: *Lithos*, vol. 22, p. 1-11.
- Vogt, P.R., Schneider, E.D., and Johnson, G.L. 1969, *The Crust and Upper Mantle beneath the Sea*: American Geophysical Union, Geophysical Monograph, no. 13, p. 556-517.

- Volpe, A.M., Macdougall, J.D., Lugmair, G.W., Hawkins, J.W., and Lonsdale, P.F., 1990, Fine-scale isotopic variation in Mariana Trough basalts: evidence for heterogeneity and recycled component in backarc basin mantle: *Earth and Planetary Science Letters*, vol. 100, p. 251-264.
- Wager, L.R., Brown, G.M., and Wadsworth, W.J., 1960, Types of igneous cumulates: *Journal of Petrology*, vol. 1. P 73-85.
- Walker, G. W., and MacLeod, N. S., 1991, *Geologic Map of Oregon*, U.S. Geological Survey.
- Wells, F.G., 1955, Preliminary geologic map of southwestern Oregon west of meridian 122° west and south of parallel 43° north: U.S. Geological Survey Miscellaneous Field Studies Map MF-38, scale 1:250,000.
- Wells, F.G., and Peck, D.L., 1961, Geologic map of Oregon west of the 121st meridian: U.S. Geological Survey Geologic Investigations Map I-325, scale 1: 500,000.
- Wentworth, C.W., Blake, M.C., Jones, D.L., Walter, A.W., and Zoback, M.D., 1984, Tectonic wedging associated with the emplacement of the Franciscan assemblage, California Coast Ranges, in Blake, M.C., (ed.), *Franciscan Geology of northern California: Pacific Section, Society of Economic Paleontologists and Mineralogists, Field Trip Guidebook 43*, p. 163-173.
- Watson, E.B., and Harrison, M.H., 1983, Zircon saturation revisited: temperature and composition effects in a variety of crustal magma types: *Earth and Planetary Science Letters*, vol. 64, p. 295-304.
- Wilson, M., 1989, *Igneous Petrogenesis*: Unwin Hyman, London, UK, pp. 275.
- White, A.J.R., and Chappell, B.W., 1977, Ultrametamorphism and granitoid genesis: *Tectonophysics*, vol. 43., p. 7-22.
- Wirth, K. Rudolf, 1991, Processes of lithosphere evolution; geochemistry and tectonics of mafic rocks in the Brooks Range and Yukon-Tanana region, Alaska: PhD thesis Cornell University, 384pp.
- White, M.W., and Patchett, J., 1984, Hf-Nd-Sr isotopes and incompatible element abundances in island arcs: implications for magma origins and crust-mantle evolution: *Earth and Planetary Science Letters*, vol. 67, p. 167-185.

- Winchester, J.A., and Floyd, P.A., 1977, Geochemical discrimination of different magma series and their differentiation products using immobile elements: *Chemical Geology*, vol. 20 p. 325-343.
- Wiggins, B.D., 1980, Volcanism and sedimentation of a late Jurassic to Early Cretaceous Franciscan Terrane Near Bosley Butte, Southwestern Oregon: Ph.D. thesis, University of California, Berkeley.
- Wood, D.A., 1980, The application of a Th-Hf-Ta diagram to problems of tectonomagmatic classification and to establishing the nature of crustal contamination of basaltic lavas of the British Tertiary Volcanic Province: *Earth and Planetary Science Letters*, vol. 50, p. 11-30.
- Wood, D.A., Joron, J.L., and Treuil, 1979, A re-appraisal of the use of trace elements to classify and discriminate between magma series erupted in different tectonic settings: *Earth and Planetary Science Letters*, vol. 45, P. 326-336.
- Wooldridge, A.L., Haggerty, S.E., Rona, P.A., and Harrison, C.G.A., 1990, Magnetic properties and opaque mineralogy of rocks from selected seafloor hydrothermal sites at oceanic ridges: *Journal of Geophysical Research*, vol. 95, p. 123,351-12,374.
- Wright, J. E., and Wyld, S.J., 1994, The Rattlesnake Creek terrane, Klamath Mountains, California: An early Mesozoic volcanic arc and its basement of tectonically disrupted oceanic crust: *Geological Society of America Bulletin*, vol. 106, p. 1033-1056.
- Wright, J.E. and Fahan M.R., 1988, An expanded view of Jurassic orogenesis in the western United States Cordillera: Middle Jurassic (pre-Nevadan) regional metamorphism and thrust faulting within an active arc environment, Klamath Mountains, California: *Geological Society of America Bulletin*, vol. 100, p. 859-876.
- Wyld, S.J., and J.E. Wright, 1988, The Devils Elbow ophiolite remnant and overlying Galice Formation: New constraints on the Middle to Late Jurassic evolution of the Klamath Mountains, California, *Geological Society of America Bulletin*, vol. 100, p. 29-44.

- Young-Sang Kim, Hiroshi Kawaguchi, Tomokazu Tanaka, Atsushi Mitsuike, 1990, Non-spectroscopic matrix interferences in inductively coupled plasma - mass spectrometry; *Spectrochimica Acta*, vol. 45b, no. 3, pp. 333-339.
- Yoder, H.S., Jr., and Tilley C.E., 1962, Origin of basalt magmas: an experimental study of synthetic rock systems: *Journal of Petrology*, vol. 3, p. 342-532.
- Yogodzinski, G.M., Volynets, O.N., Koloskov, A.V., Seliverstov, N.I. and Matvenkov, V.V., 1994: Magnesian andesites and the subduction component in a strongly calc-alkaline series at Piip volcano, far western Aleutians: *Journal of Petrology*, 35, 163-204.
- Yule, J.D., and J.B. Saleeby, 1994, Geochemistry of Rattlesnake Creek terrane fragments contained within the western Jurassic belt, Oregon Klamath Mountains, *Geological Society of America Abstract with Program*, vol. 26, p. 106.
- Yule, J.D., J.B. Saleeby, D.L. Jones, and M. Silk, 1992, Correlation of basement terranes across the Late Jurassic Josephine inter-arc basin, southwestern Oregon and northern California *Geological Society of America Abstract with Program*, vol. 24, p 93.
- Yule, J.D., 1996, Geologic and tectonic evolution of the Jurassic Marginal Basin Lithosphere, Klamath Mountains, Oregon: Ph.D. Dissertation, California Institute of Technology, Pasadena, USA, pp. 308.